Aerodynamic Characteristics of Yawed Inclined Circular Cylinders

by

Michael Shane Hoftyzer

A thesis submitted to the Faculty of Graduate and Postdoctoral Studies
in partial fulfilment of the requirements for the degree of

Doctor of Philosophy

In

Civil Engineering



uOttawa

Department of Civil Engineering

University of Ottawa

Ottawa, Canada

May 2016

© Michael Hoftyzer, Ottawa, Canada, 2016

Abstract

The wind-induced vibration of bridge stay cables has been a long studied and documented topic including a vast literature presenting experimental and numerical investigation results. There are several aerodynamic phenomena which can be associated with the wind-induced vibrations of bridge stay cables, such as vortex-induced vibration, rain-wind induced vibrations, buffeting phenomenon, dry cable galloping, and high-speed vortex excitation, to name a few. One of the most critical types of vibrations for slender structures exposed to wind is the galloping instability. This is typically not encountered for round structures, like circular cylinders or cables, due to their symmetrical nature, and therefore a lack of negative slope in the lift coefficient. However, vibrations of inclined cables of cable-stayed bridges have been noticed for several bridges, and were associated with partial damage of the cable stays, and damaged noted to cable anchors. It is still unclear if these cable vibrations are caused by dry inclined cable galloping, or by high speed vortex excitation. For this reason, stay cables construction guidelines (FHWA, 2005) have not been able to clearly identify the aerodynamic instability resulting in the recommended use of high structural damping, and high Scruton numbers used to limit bridge stay cable vibrations.

The current research addresses these issues by performing numerical CFD (computational fluid dynamics) simulations of wind flow around inclined and yawed cables in order to identify the flow behaviour around the circumference and downstream of the cable. Such numerical models provide a new understanding regarding the flow conditions around an inclined cable and the beginning of dry galloping instability. The simulation was performed for full scale cables in the form of cylinder models with high aspect ratios. The arrangement for the cable was considered as a combination of the inclination and yaw angles, in such a way that it should match the experimental setting considered by Cheng et al (2003), based on which a validating comparison

of results was performed. A LES (Large Eddy Simulation) model was developed with a constant Smagorinsky model for simulating the turbulent flow around the cylinders. Reynolds numbers (Re) ranging from 1.1×10^5 to 6.7×10^5 were investigated for various combinations of the inclination angles of 0° to 60° and yaw angles of 0° to 40°. The diameter of the circular cylinder was set to D = 0.089 m and the length of the cable was 2.67 m (30D). Pressure on the surface of the cylinder was monitored on 5 rings arranged along the circular cylinder at equal intervals and velocities were recorded for intervals of 0.1 – 0.5D downstream the cylinder. Also pressure, vorticity and streamlines distributions were recorded for several plans along and across the cylinder. The flow pattern visualisations were clearly established and wind speed profiles were presented.

An axial flow along the leeward side of the cylinder was identified for inclined circular cylinders. The predominant axial flows were noted at intervals of 0.1D to 0.3D downstream of the cylinder. As the distance from the leeward side of the cylinder increased, the effect of the far field flow increased as well, for the flow around the leeward side of the cylinder. The drag crisis encountered as a sudden drop in the drag coefficient C_D, with the increase of Re number, was confirmed.

The preliminary results for inclined cylinders showed good agreement with the experimental results available in the literature. Slight discrepancies for the upper and lower branches of the drag crisis were found between the published data and results obtained in the current study.

A new flow classification for inclined and/or yawed circular cylinders was proposed based on the velocity profiles, eddy viscosity, and swirl threads formations, as a combination of the TrSL

and TrBL regimes similar with the ones defined by Zdravkovich (1997), for flow perpendicular to cylinders.

Four cases showed a potential aerodynamic instability when results of the current study were employed into the theoretical aerodynamic damping equation derived by MacDonald and Larose (2006). Three of these cases demonstrated a similar flow phenomenon to the TrSL-Short flow phenomenon defined in this study, which occurs when the major axis of the ellipse is close to the direction of flow, and the turbulent shear layers detach almost on the leeward side of the cylinder.

The coherence, cross-coherence and cross-bicoherence were calculated for the frequency components of the coefficient of lift, the pressure coefficient along the leeward side of the cylinder, and the total velocity along the leeward side of the cylinder, and it was found that three cases of low non-linear interaction, intermediate non-linear interaction, and high non-linear interaction could be identified. Also it was concluded that the interaction between the lift and pressure coefficients monitored for the cylinder and the variation of the total velocity component, did not have a significant influence on the flow regimes, or on the transition between the flow regimes. The high-nonlinear interactions relate more to the potential coupling between the frequencies of the parameters mentioned above, especially for the critical case of 60° relative angle.

Table of Contents

Abstract ii

Table of Content v

List of Figures x

List of Tables xvii

Nomenclature xviii

Chapter 1: Introduction 1

1.1: Research Motivation 2

1.2: Objectives 4

1.3: Thesis Layout 5

Chapter 2: Literature Review 7

2.1: Wind-Induced Vibration Phenomena for Stay Cables 7

2.1.1: Vortex Shedding Vibration (Vortex-Induced Oscillations) 8

2.1.2: Buffeting Induced Vibrations 11

2.1.3: Wake Effects/Resonant Buffeting 12

2.1.4: Parametric Excitation 14

2.1.5: Aerodynamic Instability 15

2.1.5.1: Reynolds Number-related Instability 16

2.1.5.2: Rain-wind Induced Vibrations 16

2.1.5.3: Dry Galloping of Single Inclined Cables 20

2.1.5.4: High Speed Vortex Excitation of Dry, Inclined Cables 23

2.2: CFD Numerical Simulations Involving Flow around Circular Cylinders 23

2.3: Wind Tunnel Experiments for Flow around Circular Cylinders 31

2.4: Flow Regimes for Circular Cylinders 40

2.5: .... Experimental Visualizations for Flow around Circular Cylinder Perpendicular to Flow 45

2.6: Field Observations for Flow around Inclined Cables 49

2.7: Aeroelastic Stay-Cable Models 55

Chapter 3: Computational Fluid Dynamics Modelling – Background and Modelling Consideration 57

3.1: Laminar Flow Modelling 57

3.2: *k*-ε Trubulence Model 58

3.2.1: OverviewR 58

3.2.2: *k*-ε Theory 58

3.3: Large Eddy Simulation Theory 62

3.3.1: Governing Equations of Fluid Dynamics 63

3.3.2: Filtered Equations 65

3.3.3: Closure Models 69

3.3.4: Modelling Theory and Assumptions 71

3.4: Circular Cylinder Computational Geometry 73

3.5: Circular Cylinder Computational Mesh 74

3.6: Comparison of Laminar Flow, *k-e* Model and LES Model 80

3.6.1: Study Results for Flow Velocity and Eddy Viscosity 80

3.6.2: Comparison of Study Results with Published Data 81

3.7: Model Validation for Flow around a Circular Cylinder 90

3.7.1: Coefficient of Drag Force on a Circular Cylinder 90

3.7.2: Coefficient of Lift Force on a Circular Cylinder 97
3.7.3: Coefficient of Pressure on the Surface of a Circular Cylinder 99
Chapter 4: Pressure and Velocity Distributions for Inclined and Perpendicular Cylinders 105
4.1: Pressure Distributions on the Surface of the Cylinder 106
4.2: Velocity and Pressure Distributions around the Cylinder 114
4.3: Axial Flow along the Length of the Cylinder 119
4.4: Interpretation and Identification of the Axial Flow 126
4.5: Characteristics of Axial Flow around Circular Cylinder 128
4.6: Velocity Streamlines in a Two-dimensional Plane 135
4.7: Dominant Velocity Zones and Flow Patterns 138
4.8: Tendencies of the Pressure and Velocity Distributions for Inclined and Perpendicular Cylinders 140
Chapter 5: Flow Characteristics around Inclined and Perpendicular Circular Cylinders 142
5.1: Flow Regimes for Inclined and Yawed Circular Cylinders 142
5.2: Flow Characteristics around Inclined and Perpendicular Circular Cylinders 142
5.2.1: Transition to Turbulent Shear Layers and Turbulent Boundary Layer for Flow around Inclined Cylinders 146
5.3: Wake Profiles Following the Leeward Side of the Cylinder 152
5.3.1: Eddy Viscosity Following the Leeward Side of the Cylinder 153
5.3.2: Pressure Distribution Following the Leeward Side of the Cylinder 157
5.3.3: Velocity Profiles Following the Leeward Side of the Cylinder 160
5.3.4: Comparison of Velocities in the Wake of the Cylinder 163
5.4: Proposed Flow Classification for Inclined and Yawed Cylinders 167

5.5: Influence of Yaw Angle on Flow Characteristics around Circular Cylinders 171
5.6: MacDonald Equation 172
5.6.1: Contribution of Each Term to the Total Aerodynamic Damping 174
Chapter 6: Fast Fourier Transform and Coherence 180
6.1: Fast Fourier Transform (FFT) Results for C_D 181
6.2: Fast Fourier Transform (FFT) Results for C_L 189
6.3: Fast Fourier Transform (FFT) Results for Leeward Points 198
6.4: Fast Fourier Transform (FFT) Results for Leeward Velocity 216
6.5: Coherence and Cross-Coherence 223
6.5.1: Summary of the Spectral Coherence Function 224
6.5.2: Summary of the Cross-Bicoherence 225
6.6: Coherence and Cross-Coherence Results 228
Chapter 7: Conclusions 247
References 255
Appendix A: Cable Vibrations of Cable Stayed Bridges 263
Appendix B: Pressure Distribution on the Front Side and Leeward Side of the Cylinder Model 265
Appendix C: Pressure Distribution around the Cylinder 276
Appendix D: Velocity Distribution around the Cylinder 287
Appendix E: Axial and Along Stream Flow 298
Appendix F: Velocity Vectors 319
Appendix G: Axial Flow Visualization, Velocity Streamlines 330
Appendix H: Velocity Streamlines 341

Appendix I: Dominant Velocity Zones and Flow Patterns 352

Appendix J: Two-dimensional Eddy Viscosity Profiles and Associated Three-dimensional Visualization of the Q-criterion 363

Appendix K: Mean Pressure Distribution about a Circular Cylinder 374

Appendix L: Fast Fourier Transform (FFT) Results for C_D 385

Appendix M: Fast Fourier Transform (FFT) Results for C_L 396

Appendix N: Fast Fourier Transform (FFT) Results for Leeward Points 407

Appendix O: Fast Fourier Transform (FFT) Results for Leeward Velocity 459

Appendix P: Coherence and Cross-Coherence 509

Appendix Q: Comparison of Laminar, k-ε and LES 559

List for Figures

Figure 2.1: Vortex shedding frequency with wind velocity over elastic structure (Simiu and Scanlan, 1978)..... 10

Figure 2.2: Computational domain for cable model with water rivulet, (a) Full simulation domain, (b) Grid near cable model with rivulet position θ = 60°, (Qingkuan, 2007)..... 28

Figure 2.3: Grids of a yawed and inclined cylinder (L = 30D, β = 30, θ = 45), a) Grids on the domain, b) Zoom-in around the cylinder (Yeo and Jones, 2011)..... 29

Figure 2.4: Schematic of the computational domain with boundary conditions (Yeo and Jones, 2011)..... 29

Figure 2.5: Physical space around two circular cylinders (a) coordinate system and boundary conditions, (b) grid system near the cylinder, (c) deformation of grid system (Kim and Kitagawa, 2011)..... 30

Figure 2.6: Visualized axial vortex in the wake of inclined cable (without end plate, β = 45°, V = 0.5 m/s, in smooth flow) (Matsumoto et al, 2001)..... 32

Figure 2.7: Visualized axial vortex and intermittently enhanced Karman vortex in the wake of inclined cable (without end plate, β = 45°, in smooth flow)..... 33

Figure 2.8: Power spectrum density of fluctuating wind velocity in the wake of stationary inclined circular cylinder, where f_v denotes the dominating frequency of fluctuating wind velocity (in smooth flow, without rivulet, with 100mm windows, V = 6.0 m/s, β = 45°) 34

Figure 2.9: Flow visualization around cable model, smooth surface (α = 0°, β = 0°, U = 5 m/s) (Yagi, 2011) 40

Figure 2.10: Transition in free shear layers: (a) Re = 2,000; (b) Re = 8,000 and (c) Re = 1.1×10^5 (Zdravkovich, M. M., 1997) 42
Figure 2.11: Transition in boundary layers: (a) TrBL0, (b) TrBL1, (c) TrBL2, (d) TrBL3 (Zdravkovich, M. M., 1997) 43
Figure 2.12: Variation of aerodynamic force coefficients for disturbance-free flow (reproduced from Zdravkovich, 1997) 44
Figure 2.13: Influence of Reynolds number and surface roughness on drag coefficient (Simiu and Scanlan, 1987) 45
Figure 2.14: Transition in free shear layers, Re = 1.1×10^5 (Zdravkovich, 1997) 46
Figure 2.15: Visualization of a turbulent vortex street. Streamwise vorticity, in the braid between Karman vortices, is indicated by the white regions and is visible for Re = 2.7×10^5 (Williamson, 1996) 46
Figure 2.16: (a) Subcritical symmetric state, Re = 2.0×10^5; (b and c) possible asymmetric states near the transition, Re = 3.0×10^5; (d) supercritical state, 4.0×10^5 (Coutanceau and Defaye, 1991) 47
Figure 2.17: Mean pressure distribution around a circular cylinder (ESDU, 1986) 47
Figure 2.18: Sequence of high-speed visualization of flow vortex street couple in the near wake for one period: Re = 10^5 (Coutanceau and Defaye, 1991) 48
Figure 2.19: Vibration amplitude of stay vs. wind speed (Main and Jones, 1999) 50
Figure 2.20: Vibration amplitude for stay vs. wind direction for different wind speeds (Main and Jones, 1999) 50
Figure 2.21: Visualized axial flow by light string for a proto-type cable (Matsumoto et al, 2010) 52

Figure 2.22: Aerodynamic force coefficients as a function of ϕ for $3 \times 10^4 < Re < 9 \times 10^4$ (Hoang et al, 2015) 54

Figure 2.23: Aerodynamic coefficients as a function of ϕ for $3 \times 10^4 < Re < 9 \times 10^4$ (Hoang et al, 2015) 54

Figure 3.1: Details of the geometry and monitoring point details for the cylinder model 74

Figure 3.2a) Cylinder model and computational domain, b) Computational domain details..... 76

Figure 3.3a) Mesh details for flow perpendicular to the cylinder, b) Mesh details for cylinder inclined to flow 77

Figure 3.4: Velocity profiles; study results for $\alpha = 0°$, $\beta = 0°$, compared to flow visualizations 82

Figure 3.5: Study results for $\alpha = 0°$, $\beta = 0°$; velocity profiles 88

Figure 3.6: Study results for $\alpha = 0°$, $\beta = 0°$; eddy viscosity 89

Figure 3.7: Variation of aerodynamic force coefficients for disturbance-free flow (reproduced from Zdravkovich, 1997) 91

Figure 3.8: Aerodynamic force coefficients for cylinder inclined/yawed and perpendicular to flow: drag coefficient, C_D. 92

Figure 3.9: Aerodynamic force coefficients for cylinder inclined/yawed and perpendicular to flow: drag coefficient, C_D 93

Figure 3.10: Aerodynamic force coefficients for cylinder inclined/yawed and perpendicular to flow: drag coefficient, C_D: (a) perpendicular to flow; (b) cylinder inclination 60°, (c) cylinder inclination 54.7°; (d) cylinder inclination 50°. 95

Figure 3.11: Aerodynamic force coefficients for cylinder inclined/yawed and perpendicular to flow: lift coefficient, C_L 98

Figure 3.12: Aerodynamic force coefficients for cylinder inclined/yawed and perpendicular to flow: lift coefficient, C_L 98

Figure 3.13: Pressure coefficient for flow perpendicular to the cylinder ($\theta = 0°$) at Re = 2.74×10^5 to 4.65×10^5, adapted from Zdravkovich (1997) 100

Figure 3.14: Pressure profile for flow perpendicular to the cylinder at Re = 1.1×10^5 to 6.7×10^5, current study 101

Figure 3.15: Pressure profile for flow around an inclined cylinder (60°) at Re = 1.1×10^5 to 6.7×10^5, current study 101

Figure 3.16: Pressure profile results for current study for $\alpha = 0°$, $\beta = 0°$, for Re = 1.1×10^5 to 4.4×10^5, for LES, k-ε and laminar flow 103

Figure 4.1: Pressure distribution on the front side and leeward side of the cylinder model 108

Figure 4.2: Pressure distribution around the cylinder 116

Figure 4.3: Velocity distribution around the cylinder 118

Figure 4.4: Axial and along stream flow 123

Figure 4.5: Velocity vectors 127

Figure 4.6: Axial flow visualization, velocity streamlines 131

Figure 4.7: Velocity streamlines in a two-dimensional plane 137

Figure 4.8: Dominant velocity zones and flow patterns 139

Figure 5.1: Dominant velocity zones and flow patterns 145

Figure 5.2: Two-dimensional eddy viscosity profiles and associated three-dimensional visualization of the Q-criterion 148

Figure 5.3: Two-dimensional eddy viscosity profiles for flow inclined to the cylinder; (a): case (a) $\alpha = 54.7°$, $\beta = 40°$, $\phi = 64°$, Re = 1.1×10^5; (b): case (j) $\alpha = 0°$, $\beta = 0°$, $\phi = 0°$, Re = 6.7×10^5 shown with monitoring locations highlighted 153

Figure 5.4: Eddy viscosity at various monitoring locations on the leeward side of the cylinder 155

Figure 5.5: Pressure at various monitoring locations on the leeward side of the cylinder 158

Figure 5.6: Velocity at various monitoring locations on the leeward side of the cylinder 161

Figure 5.7: Comparison of the normalized *u* velocity and the total velocity on the leeward side of the cylinder..... 163

Figure 5.8: Flow regimes for inclined cylinders 168

Figure 5.9: Coefficient of drag (C_D) vs. Reynolds number (Re) for study data 176

Figure 5.10: Coefficient of lift (C_L) vs. Reynolds number (Re) for study data 176

Figure 5.11: Coefficient of drag (C_D) vs. cable-wind angle (degrees) for study data 177

Figure 5.12: Coefficient of lift (C_L) vs. cable-wind angle (degrees) for study data 177

Figure 5.13: Aerodynamic damping vs. Reynolds number (Re) for study data 178

Figure 5.14: Aerodynamic damping vs. Reynolds number (Re) for study data 178

Figure 6.1: Time histories for C_D, $\phi = 60°$; $\alpha = 60°$, $\beta = 0°$ 183

Figure 6.2: Time histories for C_D, $\phi = 57.1°$; $\alpha = 54.7°$, $\beta = 20°$ 184

Figure 6.3: Fast Fourier Transform (FFT) results for C_D, $\phi = 60°$; $\alpha = 60°$, $\beta = 0°$ 185

Figure 6.4: Fast Fourier Transform (FFT) results for C_D, $\phi = 57.1°$; $\alpha = 54.7°$, $\beta = 20°$ 186

Figure 6.5: Relative angle vs. Stroudal number for C_D, plotted for each Reynolds number tested 188

Figure 6.6: Reynolds number vs. Stroudal number for C_D, plotted for each relative angle tested 189

Figure 6.7: Time histories for C_L, $\phi = 60°$; $\alpha = 60°$, $\beta = 0°$ 192

Figure 6.8: Time histories for C_L, $\phi = 57.1°$; $\alpha = 54.7°$, $\beta = 20°$ 193

Figure 6.9: Fast Fourier Transform (FFT) results for C_L, $\phi = 60°$; $\alpha = 60°$, $\beta = 0°$ 194

Figure 6.10: Fast Fourier Transform (FFT) results for C_L, $\phi = 57.1°$; $\alpha = 54.7°$, $\beta = 20°$ 195

Figure 6.11: Relative angle vs. Stroudal number for C_L, plotted for each Reynolds number tested 197

Figure 6.12: Reynolds number vs. Stroudal number for C_L, plotted for each relative angle tested 197

Figure 6.13: Details of the geometry and monitoring points for the cylinder model 199

Figure 6.14: Fast Fourier Transform (FFT) results for leeward points, $\phi = 60°$; $\alpha = 60°$, $\beta = 0°$ 201

Figure 6.15: Fast Fourier Transform (FFT) results for leeward points, $\phi = 57.1°$; $\alpha = 54.7°$, $\beta = 20°$ 206

Figure 6.16: Variation in *St* leeward pressures along the length of the cylinder 211

Figure 6.17: Variation in *St* with Reynolds number; leeward pressure 213

Figure 6.18: Fast Fourier Transform (FFT) results for leeward velocity, $\phi = 60°$; $\alpha = 60°$, $\beta = 0°$ 217

Figure 6.19: Variation in *St* for leeward velocity along the length of the cylinder 222

Figure 6.20: Variation in *St* with Reynolds number 223

Figure 6.21: Coherence, and cross-coherence, $\phi = 60°$; $\alpha = 60°$, $\beta = 0°$ 232

Figure 6.22: Coherence, and cross-coherence, $\phi = 57.1°$; $\alpha = 54.7°$, $\beta = 20°$ 237

Figure 6.23: Coherence, and cross-coherence, $\phi = 54.7°$; $\alpha = 54.7°$, $\beta = 0°$ 242

List for Tables

Table 2.1: Response characteristics of the two observed critical cases in the tests (Cheng et al, 2011) 39

Table 3.1: Number of elements per simulation case 75

Table 3.2: Performed cases for cable model orientations at various Re numbers 56

Table 4.1: Representative sample cases of study 105

Table 5.1: Flow regimes classifications for study results 170

Table 6.1: Fast Fourier Transform (FFT) results for C_D 187

Table 6.2: Fast Fourier Transform (FFT) results for C_L 196

Nomenclature

a amplitude of vibration (m)

c constant (dimensionless)

e internal energy per unit mass

f natural frequency (Hz)

f_i body force vector per unit mass

f_v frequency of the vortex shedding (Hz)

k turbulent kinetic energy

m mass per unit length (kg/m)

q_i conductive heat flux

u_i velocity component in the i-th direction,

y coordinate normal to the wall (m)

A projected area of cylinder at the right angle to the flow (m^2)

C_D coefficient of drag (dimensionless)

C_D' fluctuating fluid-dynamic drag coefficient (dimensionless)

C_{Dp} portion of mean drag coefficient due to asymmetric pressure distribution on the upstream and downstream side (dimensionless)

C_{Df} portion of mean drag coefficient due to viscous friction on the surface of the cylinder (dimensionless)

C_L coefficient of lift $C_L = \frac{F_L}{\frac{1}{2}\rho V_f^2 A}$(dimensionless)

C_L mean lift coefficient (dimensionless)

C_L' fluctuating fluid-dynamic lift coefficient (dimensionless)

C_P coefficient of pressure (dimensionless)

C_S empirical Smagorinsky constant

D diameter of the section (m)

D_{crit} critical cable diameter (m)

E_T total energy per unit volume

F_L lift force

G filter function that determines the scale of the resolved eddies

K turbulent kinetic energy

L cable length (m)

Pr_T Prandtl number

P_{xy} cross-spectral density between x and y

P_{xx} autospectral density of x

P_{yy} autospectral density of y

Re Reynolds number $Re = \frac{UD}{\nu}$ (dimensionless)

Re_T turbulent Reynolds number $Re_T = \frac{\rho k^2}{(\varepsilon^* \mu_L)}$ (dimensionless)

Sc Scruton number $Sc = \frac{m\varsigma}{\rho D^2}$

$\tilde{S}_{ij}$ Farve-averaged strain rate

$\bar{S}_{ij}$ Reynolds averaged strain-rate tensor

S_t Strouhal number (dimensionless)

$S_{xyz}(f_1,f_2)$ averaged estimate of the cross-bispectrum

$S_x(f)$ averaged estimate of the power spectra of x

$S_y(f)$ averaged estimate of the power spectra of y

$S_z(f)$ averaged estimate of the power spectra of z

T fully turbulent state

TrBL transition-in-boundary layers

TrSL transition-in-shear layers

TrW transition-in-wake state of flow

V control volume

V_f flow velocity (m/s^2)

X position along the cylinder from the most forward location of the cylinder

U flow velocity, mean wind speed (m/s)

U_R reduced wind speed $U_R = \overline{U}/_{(fD)}$

V_{axial} axial velocity (m/s)

V_U along stream velocity (m/s)

W_k FFT for the kth segment of w

X_k FFT for the kth segment of x

Y_k FFT for the kth segment of y

α inclination angle of the cable (degrees)

β yaw angle of the cable (degrees)

δ logarithmic damping decrement

δ_{ij} Kronecker delta function

ε energy dissipation

ε_w dissipation rate at the wall

ϕ relative angle of attack of the cable; $\cos\phi = \cos\alpha\cos\beta$ (degrees)

ϕ_ε explicit wall term

ζ structural damping

μ mass per unit length of the cable (kg/m)

μ dynamic (absolute) fluid viscosity

μ_T eddy viscosity

$\mu_t(\boldsymbol{x}, t)$ turbulent eddy viscosity

ρ density of the fluid (kg/m^3)

σ_{ij} stress tensor

τ_{ij} viscous stress tensor

τ_{ij}^F Favre-average turbulent stresses

τ_{ij}^r stress tensor

τ_{ij}^R residual stress tensor

μ_T turbulent eddy viscosity

ρ density of the air (kg/m^3)

ν airflow's kinematic viscosity (m^2/s)

υ_s velocity parallel to the wall (m/s)

y_n coordinate normal to the wall (m)

ω frequency (radians per second)

ω_n undamped circular natural frequency (radians per second)

Δ filter width

Δt time step (s)

Δt^* non-dimension timestep (dimensionless)

1 Introduction

The construction of cable-stayed bridges has expanded beyond precedent, as these structures are prefered to the more expensive cable suspension bridges. In Canada alone there were 5 cable-stayed bridges constructed in the last 5 years. Also with the increase of the main span, the number of stay cables used for bridge structures has multiplied, and the cable related aerodynamic phenoma showed particular characteristics, which were not described through the well-known aerodynamic vibration theories. During construction, or upon completion of a cable-stayed bridge, stay cables have been known to vibrate. These vibrations might be caused by rain-wind effect, wind buffeting turbulent effect, parametric excitations, wake effects, or combinaiton of these mechanisms. The stay cable vibrations which captured the particular attention of wind engineers and aerodynamicisits worldwide are caused by a phenomenon that is not well understood at this time, known as dry cable galloping. Several researchers have carried out rigorous experimental programs in an attempt to better understand this phenomenon (Larose et al., 2003; Cheng et al., 2008, Matsumoto et al., 1990, Jakobsen et al., 2008; Katsuchi et al., 2009, etc.). This new aerodynamic instability of the structural stay cable was found to occur around the Reynolds number of Re = 2.2×10^5, for cable inclined at the angles of 57° and greater (Larose et al., 2003, Jakobsen et al., 2008).

A new formulation for the aerodynamic forces for inclined cables has been developed for verifying the galloping criterion based on the variation of aerodynamic coefficients with the Re number, and the inclination of the cable. This was provided by MacDonald et al. (2003) as a result of their study. A structural damping recommendation has been developed for cable-stayed bridges (FHWA, 2005) in an attempt to reduce the galloping of stay cables. However the tests performed in the wind tunnel, and in the field on similar cable models tested within the same Reynolds number

range, resulted in different structural responses and different aerodynamic coefficients (Jakobsen et al., 2008; Cheng et al., 2008: Katsuchi et al., 2009; Zuo, 2014). This phenomenon is of concern as it indicates that the increase in structural damping of inclined cables is not necesarly effective in reducing the dry inclined cable galloping vibration (Saito et al., 1994).

The presence of an axial flow on the leeward side of the cylinder inclined at 42.5°, and yaw varying between 0° and 45° has been shown through oil film visualization techniques in wind tunnel tests, for a Reynolds number of $Re = 1.5 \times 10^5$ (Matsumoto et al., 1990), and noted in the wind tunnel studies performed by Matsumoto et al. (1995b), for up to $Re = 1.65 \times 10^5$. A connection has been established between the on-set wind speed for dry inclined cable galloping, and the presence of the axial flow along the leeward side of the cylinder. This interpretation was similar to the presence of the water rivulet causing the on-set of rain-wind vibration, though the Re, and the inclination of the cables for which the two phenomena would occur, dry inclined galloping and rain-wind vibration, are different (Matsumoto et al. 2010).

The current research looks at numerically simulating the flow around an inclined circular cylinder and verify the formation of the axial flow along the leeward side of the cylinder. This is to assist in clarifying the conditions for the occurrence of dry cable galloping of inclined cable.

Reynolds numbers of 1.1×10^5 to 6.7×10^5 were used in the investigation to simulate flow around cylinder for inclinaiton angles of 0° to 60° and yaw angles of 0° to 40°. The diameter of the cylinder was D = 0.089 m with a cylinder length of 30D. Pressure on the surface of the cylinder was monitored around 5 rings arranged along the cable at equal intervals.

1.1 Research Motivation

Stay cables of cable stayed bridges are prone to vibrations induced by many natural and manmade sources due to the flexible nature of the cables. A major source of this instability is the

lack of bending stiffness of the cable due to its length, and its composition. The cables can span as much as 575 m (Wang and Wu, 2009) as is the case for the Sutong Bridge in China. Moreover, given the extremely low/virtually no structural damping provided by the stay cable, any relatively small force can excite the cable vibration to considerably large amplitudes.

The extensive research and in-situ measurements of bridge stay cables (Ramsey, K., 2005, Matsumoto, M., 1998) show that the fundamental frequencies of interest to the present study have values in the range of 0.3 Hz to 3 Hz. Increasing the sag, as a function of the stay cable's tension and self weight, will increase the vertical vibration frequency of the stay cable (Starossek, 1994). On the other hand, the horizontal vibration frequency is initially unaffected by this increase in the cable sag. The flexibility at the cable supports adds to the complexity of the frequencies and vibration characteristics. The stay cable attachment points at the towers and at the deck are far from being fixed supports in the classical, analytical sense of the term.

Structural damping of stay cables is typically in the range of 0.01% to 0.2% of the critical damping. This level of self-damping is a function of the type of cable used. For traditional engineering structures constructed of concrete or steel, it is normal engineering practice to assume a critical damping value of 3% to 5% of critical damping. This means that the optimum case of structural damping for a stay cable is a full order of magnitude smaller than that of traditional engineering structures. Vibrations in traditional engineered structures can be controlled with an economical increase in the stiffness, or adjustment in the mass of the structural system. However, this is not the case with stay cables, as little can be done to economically increase its effective damping. For this reason the study of the wind-induced vibrations caused by the flow formed around inclined cables requires further investigation, as supressing cable vibrations after they occur has been established as uneconomical.Also if cable vibrations remain uncontrolled, various

consequences can occur such as damage from fatigue, or full rupture of the cable anchorage would result. These would require expensive repairs, or even worst could lead to catastrophic failure of the entire bridge structure. Serviceability requirements limit the movement of the deck, for safe passage of traffic even if the structure is perfectly able to withstand such vibrations. The perception of the public needs to be considered since a bridge that is perceived to be unsafe will not be used.

The current research investigates in depth the characteristics and the patterns of the axial flow formed on the leeward surface of the stay cables inclined, and yawed at angles of up to 60 deg in an attempt to clarify the potential causes of dry galloping vibrations of the stay cables. Also the turbulence formed behind the cables is detailed for determining transitions in the flow regimes which could be used for identifying the critical yaw/inclination angles for stay cables. Bi- and tri-correlation expressions are determined between the lift coefficient, the axial flow velocity and the pressure at the surface of the cable for establishing the relationship, and the direct effect the axial flow has on the cross-wind galloping vibrations of the stay cables.

1.2 Objectives

The goal of this research is to provide a better understanding of the flow around inclined cables and the resulting wind induced vibrations caused by this flow. This will be accomplished by the use of a computational fluid dynamics model to study the air flow around an inclined and yawed circular cylinder. The circular cylinder was used to simulate a section of an inclined cable exposed to wind to better understand the wind flow around the cable and the resulting aerodynamic forces on the cable causing wind-induced vibrations.

The presence of a flow along the leeward side of the cylinder, called an axial flow, will be confirmed. An axial flow has been observed in wind tunnel tests on a cylinder inclined to the flow

direction. With the use of the CFD-LES model the axial flow will be clearly identified and validated. Also, the role of the axial flow will be identified and the possible interaction with the vortices shedding from around the cylinder will be better illustrated. Once the CFD-LES model is validated, the test cases will be expanded for more Re cases, for a wide range of yaw and inclination angles of stay cables. The flow visualizations from the CFD modelling will be employed, and a flow regime classification specific to yaw/inclined stay cables will be proposed. These regimes will follow a similar flow classification system as the one used by Zdravkovich (1997) to classify the flow regimes around a cylinder placed normal to the flow.

The relationship between the coefficient of lift, pressure, and total velocity will be examined using both fast Fourier transforms and different forms of coherences. The use of frequency domain analysis, obtained from the use of fast Fourier analysis, and the coherences can provide additional insight about the interaction within the wake vortices of an inclined circular cylinder, and the interaction of these variables (Elgar et al, 1990).

This study will build on the current research in the area of wind flow effect on inclined and/or yawed circular cylinders, and will add valuable knowledge, novel flow characteristics, and classifications to the understanding of the mechanisms that cause vibrations of inclined and yawed cables.

1.3 Thesis Layout

The study presented in the current manuscript involves modelling the flow around a circular cylinder inclined to the flow using compuational fluid dynamics. Pressure measurements around the circumference of the circular cylinder were monitored to determine the mean and instantansous flow characteristics around the circular cylinder. The objective was to examine and

clarify the flow patterns around the circular cylinder to provide a better understanding for the conditions of inclined cables dynamics, in particular for cable-stayed bridges.

The motivation for conducting the current research was outlined, and the objectives of this research were presented in this chapter.

In Chapter 2, a general overview of the vibration phenomena associated with inclined stay cables will be presented. The summary includes known phenomina that affect stay cables, and some proposed methods for surpressing and controlling stay cable vibration. A review of currently available data is also summarized for experimental studies, computational studies, and any field observations. The historical development of the flow around a circular placed prependicular to the flow has also been presented in Chapter 2, including the flow classification developed to describe the five flow states and fifteen flow regimes. Chapter 3 provides an overview of the computational approach including a description of the computational model, and an outline of the cases studied. An anylsis and discussion of the study results are presented in Chapter 4 reviewing the pressure and velocity distributions around the circular cylinder model. This is followed by the discussion of the flow characteristics around the model in Chapter 5. The Fast Fourier Transform (FFT) of the pressure coefficients, and the velocity fluctuation along the leeward side of the cylinder are presented in Chapter 6. The results are summarized for each variable and comparisons made. The coherence and cross-coherence is also calculated between pressure coefficients, and the velocity fluctuation along the leeward side of the cylinder. A brief description of each of coherence and cross-coherence is provided followed by a summary of the results. The conclusions and discussions are presented in Chapter 7 along with recommendations for future study.

2 Literature Review

The topic of wind-induced vibrations of inclined stay cables has been studied from many different perspectives. These include the type of cable excitations observed for inclined cables resulting from the wind flow past the inclined cable. Also, the flow around an inclined cylinder has been investigated by various researchers both in the wind tunnel with flow visualization and with the use of computer simulations with the aid of computational fluid dynamics (CFD). The wind flow and cable vibration phenomena, and the latest studies in this field which are most pertinent to current research are reviewed in this chapter.

2.1 Wind-Induced Vibration Phenomena for Stay Cables

When compared to all other types of possible excitations, the most important type of dynamic loading on cables appears to be the wind. Bridge stay cables can register various types of vibrations due to wind loads comprising the mean wind component and the dynamic loading due to the direct pressure gusts and the inertia loading due to the cable motions. The major stay cable vibration phenomena identified until present are:

- vortex shedding vibration
- buffeting phenomena
- wake effects/resonant buffeting
- parametric excitation
- aerodynamic instability
    - Reynolds number-related instability
    - rain-wind induced vibration
    - dry inclined cable galloping
    - high-speed vortex excitation of dry, inclined cables

Wind buffeting is considered to be a normal type of loading, while the others are classified as instabilities and may lead to significant cable vibrations. The design objective is to either suppress the vibrations down to acceptable levels and/or eliminate the instabilities. A summary of the observed cable vibrations and remedies on various cable-stayed bridges is shown in the table in Appendix A (Stoyanoff et al., 2009). All of these mechanisms require careful consideration at the design stage of the bridge project (FHWA, 2007).

2.1.1 Vortex Shedding Vibrations (Vortex-Induced Oscillations)

The flow behaviour around circular cross-sections is controlled by the viscous and inertial forces of the flow. This is quantified by the Reynolds number (Re), which is defined as the ratio of the inertial forces to viscous forces (Fox et al., 2009):

$$\mathrm{Re} = \frac{UD}{\nu} \tag{2-1}$$

where U is the flow velocity (m/s)

D is the diameter of the section (m)

ν is the airflow's kinematic viscosity (m^2/s)

With the variation of Re number, characteristics of several flow patterns and different regimes have been identified for the flow around circular cylinders (Zdravkovich, 1997).

At very low velocities, for Re around 1, the flow approaching the cylinder will follow the surface around the circumference and detach at the most leeward point. Viscous forces dominate in this flow regime. As the flow velocity increases the pressure around the cylinder will no longer be strong enough to maintain the flow attached to the cylinder's surface as it approaches the leeward side, approximately Re = 20. At this point the viscous forces are no longer strong enough

to overcome the developing inertia forces and the inertia forces begin to dominate. The flow detaches from the surface of the cylinder prematurely, referred to as the separation point, forming a region of eddies on the leeward side of the cylinder.

A region known as the wake extends from the separation point on each side of the cylinder containing the slow moving region of eddies. The velocity outside of these shear layers is faster moving than the slow moving fluid within the wake region resulting in the shear layer rolling up on themselves forming vortices.

Increasing the velocity further causes the flow to separate along a line where the shear layers roll into line-like vortices extending along the cylinder. The resulting vortices are formed and shed from alternating side of the cylinder and move downstream from the leeward side of the cylinder at a slower velocity than the adjacent flow. This phenomenon is known as Kármán vortex formation and is characterized by the Strouhal relationship:

$$f_v = \frac{US_t}{D} \tag{2-2}$$

where f_v is the frequency of the vortex shedding (Hz)

U is the mean wind speed (m/s)

D is the diameter of the cylinder (m)

S_t is the Strouhal number (dimensionless)

Strouhal numbers of approximately 0.2 are typical for circular cross-sections (Simiu and Scanlan, 1996). The flow across the surface of the cylinder will become turbulent if the velocity continues to increase. The separation point of the flow from the cylinder will no longer be an organized line. This will result in regular vortices no longer being formed and the flow in the cylinder's wake becoming turbulent.

Alternating vortex formation results in a varied pressure distribution around the circumference of the cable inducing strong cable vibrations normal to the flow direction. The vibrations are characterized by limited-amplitude vibration at sustained wind speeds. When the natural frequency of the cylinder matches the frequency of the vortex formation, resonance occurs due to the pressure variations driving the motion of the cable at a particular frequency. The flow is altered by the movement of the cylinder which controls the formation of the vortices. However, the vibration will not be suppressed if the flow would increase slightly as the frequency of the vortex formation is still governed by the cable's motion and resonance continues. This is known as the lock-in phenomenon.

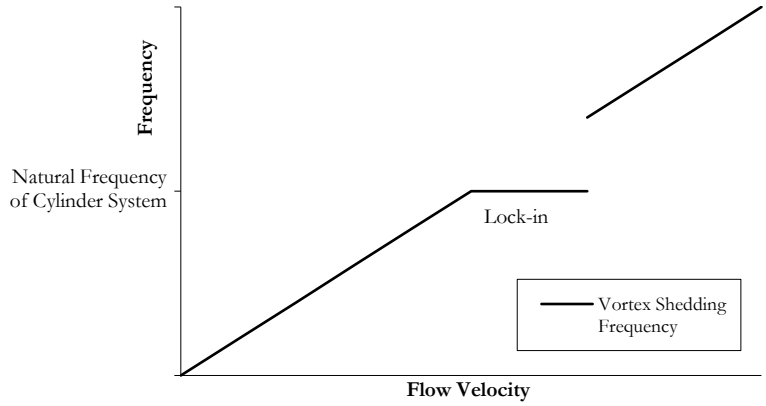


Figure 2.1: Vortex shedding frequency with wind velocity over elastic structure (Simiu and Scanlan, 1978)

Lock-in is a self-limiting phenomenon. As the amplitude increases the shedding pattern around the cylinder loses its uniformity and the vortices break up. The maximum sustained vibration amplitude tends to be limited to approximately one diameter (Blevins, 1997).

The mass-damping characteristics of the cable, quantified by the Scruton Number (S_c), limits the amplitude of the vibration (FHWA, 2007):

$$S_c = \frac{\mu\varsigma}{\rho D^2}$$

(2-3)

where μ is the mass per unit length of the cable (kg/m)

ζ is the structural damping (which will be different for every mode)

ρ is the density of the air (kg/m3)

D is the cable diameter (m)

Typical displacement amplitudes for vortex induced vibrations are relatively low and are in the range of one-half of the cable diameter without additional damping provided. This can be reduced to a few percent of the diameter provided a minimal damping is used to obtain $S_c \geq 2.5$ (Stoyanoff et al., 2009). Whenever the higher wind speeds are reached, higher modes of vibration may be excited; however as the frequency of vibration increases, the amplitude decreases. Fatigue however has to be taken into consideration. The damping requirements for the suppression of responses due to other excitation mechanisms are generally sufficient for prevention of noticeable oscillations. The assessment of a bridge cable's susceptibility to vortex-induced oscillations involves the estimation of the wind speed at which it would occur and the resulting cable amplitudes expected at these wind speed, and the required damping to achieve the minimum $S_c \approx 2.5$ for the first four modes of vibration.

2.1.2 Buffeting Induced Vibrations

Buffeting is described as the unsteady, random loading resulting from the fluctuations in the oncoming airflow. This is generally not harmful for stay cables, except for the possible concerns of potential fatigue as it is a normal loading condition. Due to the high tension in the cables supporting the dead load of the deck, and due to the relatively small cable's projected area which is directly exposed to wind, the amplitude of the vibrations tend to be limited to 1D at the design wind speeds (Stoyanoff et al., 2009). Buffeting effects become a more serious concern

with high-voltage transmission lines as the tension is a function of the cable's self-weight. Hence, due to insufficient pre-tensioning, sudden shocks provoked by the fluctuations in the oncoming flow can be induced into the cross tie cables of cable stays. It has been shown that the aerodynamic instability may occur in bridges composed of two planes of stay cables. This is due to the travel time of the wind speed from one stay plane to the next corresponds to half of a cycle of the deck's torsional vibration exciting the motion of the deck (Virlogeux, 1998). However, this is not likely to result in prolonged vibration in randomly fluctuating airflow.

2.1.3 Wake Effects/Resonant Buffeting

Wake galloping is characterised by the elliptical movement of the cables caused by variations in the drag, and across-wind force. This occurs when one cable lies in the wake of another, and the wind is along the span of the bridge. Wake galloping is a concern in unusual cable arrangements where the stays are closely spaced.

Cables used in tandem arrangement can be used instead of a single stay to limit the diameter of the cable. If the two cables are closely spaced and if the wind flows along a line joining the two cables the downwind cable's dynamic behaviour may be influenced by the wake of the upwind cable. The resulting vibration would not be significant and the wind speed producing the vortices from the upwind cable is low. If the cables are within a few diameters (spaced less than six diameters apart) of each other the wake of the upwind cable will excite the downwind cable to vibrate. The resulting vibration of the downwind cable will affect the flow around the upwind cable, in turn increasing the effects on the downwind cable. The increased movement of the downwind cable continues to affect the flow around the upwind creating a continuous intercorrelation between the vibration of the downwind cable and the wind flow around the upwind cable. The phenomenon has been observed on the cables of the Yobuko Bridge in Japan

(Yoshimura et al., 1995). In this case, the downwind cables which had diameters of 76 mm to 84 mm and were separated by two diameters from the upwind cables vibrated. The vibration amplitude was approximately two diameters. As the space between the two cables increases, the effect of the interaction between the downwind movement and the upwind cable diminished.

During construction of individual parallel strands of stay cables the external strands of the stays can be excited by the wind contacting the neighbouring strands while vibrating. This can result in a significant level of unsettling and undesirable rattling called 'breathing of strands' (Virlogeux, 1998). The vibrations occur only during construction and are suppressed once the ducts are installed over the strands.

An approximate equation has been proposed for the minimum wind velocity above which instability can be expected (FHWA, 2007):

$$U_{crit} = cfD\sqrt{S_c} \tag{2-4}$$

where c is a constant (dimensionless)

f is the natural frequency (Hz)

D is the cable diameter (m)

S_c is the Scruton number (dimensionless)

The constant c has an approximate median value of 40 for circular cross-sections. For cable-stayed bridges, the constant depends on the clear spacing between the cables:

c = 25 for closed spaced cables (2D to 6D spacing);

c = 80 for normally spaced cables (generally 10D and higher).

Wake galloping therefore has the potential to cause serviceability concerns as the critical wind speeds may be low enough to commmonly occur during the life of the bridge.

2.1.4 Parametric Excitation

Stay cables can be excited to vibrate by either the movement of the deck at the bottom end, or movement of the pylon at the top of the cable. This phenomenon is characterized by motion of the stay induced by motion of the deck and/or towers due to wind loads, traffic, or pedestrian excitation. These loads may result in large amplitude motion of the stay cables even from small movements in the deck or pylons. The cable's low self-damping does little to limit these vibrations. This type of vibration can be serious if the fundamental frequency of the stay cable matches the fundamental frequency of the overall structure.

The excitation of the cable is only expected to occur under condition where there is prolonged deck and/or tower motions due to vortex-induced excitation of the deck. The random excitation from wind buffeting would not generally result in stationary motions at the deck and/or tower anchorages of a sufficient duration to result in a resonance condition of the cable.

The fundamental frequencies of the stay cables of the Normandy Bridge closely matched the fundamental frequencies of the structure. If it was not for the presence of cross ties installed to increase the fundamental frequencies, parametric excitation would have been a concern for the safety of the bridge (Virlogeux, 1995). Resolving the problem might not be as simple as modifying the frequencies of the stay cables. In 1995, it was determined that occasionally the motion of the bridge deck matched the frequencies of the cables of the Second Severn Crossing in England. This resulted in extremely large amplitude vibration of the stay cables. With cross ties in place to restrict the vibrations of the cables the vibrations of the deck increased substantially (Stubler, 1999). It was assumed that the cables were acting like dampers by accepting energy from the vibrating deck. Once the motion of the cable was restricted by the cross ties the cables could no longer accept the same level of energy resulting in the increase of the deck's vibration amplitude.

A set of criteria has been suggested for parametric excitation. Stubler et al. (1999) suggested the following:

- appearance and comfort (at U=15 m/s):

  $$\frac{a}{L} < 0.0006$$

  where a is the amplitude of vibration (m),

  L is the cable length (m)

- admissible deviation angle:

  $$\frac{a}{L} < \frac{\alpha}{\pi}$$

  where α is the admissible deviation angle at the cable anchor point (rad)

2.1.5 Aerodynamic Instability

There are a number of aerodynamic instabilities of inclined cables identified in the last few decades. These instability phenomena include the following:

- Reynolds number effects
- rain-wind induced vibration
- dry, inclined cable galloping
- high-speed vortex excitation

When compared to the other three phenomena, Reynolds number effects on stability are relatively minor. The latter three vibration phenomena are specific to inclined cables. Rain-wind induced vibration has been reported in the field observations and is a very serious concern. Little is understood about the last two, dry, inclined cable galloping and high-speed vortex excitation, though both are potentially serious aerodynamic instabilities.

2.1.5.1 Reynolds Number-related Instability

A significant and abrupt reduction in the drag force is known to occur within a specific Reynolds number range. This reduction is in the range of 40% to 60%. This is known as the critical Reynolds number range. The range varies as it is affected by the roughness of the section's surface and is lower when the surface of the section is rougher. This phenomenon becomes a problem when cable is vibrating parallel to the direction of the wind resulting in a fluctuating relative wind velocity. If the range of the fluctuating relative wind velocity corresponds to the critical Reynolds range, a drag crisis may occur. As the cable sways back and forth in the wind the relative velocity increases and decreases accordingly. As the relative velocity increases the drag force acting on the cable is lower and when the relative velocity decreases the drag force increases. As the cables swings back and forth the vibration amplitude of the cable continues to increase. This is a known concern with power transmission lines. The construction of the cable contributes to the problem as the helical stranding increases the effective roughness. No instances of this phenomenon have been reported for stay cable, but stay cables are not immune to such excitation.

2.1.5.2 Rain-wind Induced Vibrations

When the airflow is symmetric about a circular section, the section does not experience any sustained lift force transverse to the flow. When this symmetry is lost the section will experience a resultant lift force. With the presence of water on the section due to rain, the rainwater can vary the shape of the section by various factors causing instability of the section.

Large, limited amplitude vibrations of stay cables can occur in the presence of moderate wind and rain, but when the stay cable is exposed to the same wind conditions without rain the vibrations would not occur. These vibrations emerged during the mid-1980s and are of concern

to bridge engineers. Large amplitudes may be experienced under relatively low wind speeds making this phenomenon quite significant. Field observations and wind tunnel testing conducted by several researchers have clarified the conditions favourable for this vibration mechanism beginning with Hikami and Shiraishi (1988).

The conditions favourable for rain-wind vibrations are smooth stay cable surfaces exposed to moderate rain which is neither light drizzle nor a downpour. The wind speed ranges from 8-15 m/s (FHWA, 2007). The cable diameter of the stays ranges from 140 mm to 225 mm with a fundamental frequency ranging from 0.4 Hz to 2.5 Hz. The resulting Reynolds number is in the transition range from sub-critical to critical: $6 \times 10^4 - 2 \times 10^5$. Cables on the leeward side of the pylons are susceptible resulting from the wind tending to lift the cables as the cables are declined in the direction of the wind. The cables are inclined at 20° - 60° from horizontal with the worst around 30°. This is not always the case as near vertical hanger on arch bridges have also been known to vibrate from this mechanism. The angle of the wind relative to the wind direction is within the range of 20° - 60°. A build-up of dirt and grit on the surface of the duct, which is usually polyethylene, results in a certain small scale roughness on the duct under normal service conditions. A low level of turbulence and a fairly uniform flow over the length of the cable is required resulting in the bridge being located near a large body of water or near flat surroundings. The resulting vibrations lead to amplitudes ranging from 0.25 m to 1.0m.

The formation of water rivulets on cable changes their aerodynamics. Wind tunnel tests have shown the formation of rivulets of water on the upper and lower surfaces of the cable in rainy weather are essential for the development of this instability. The rivulet on the lower surface of the cable is drawn by gravity. The combined effects of gravity, wind, and capillary help create other stream on the upper face of the cable. The cross-section of the cable is altered by the presence

of the rivulet of water resulting in a change of the aerodynamic forces acting on the cable leading to the vibration of the stay cable.

Japanese researchers have linked rain-wind vibration with the presence of the upper stream of water. Other researchers (Ruscheweyh, 1999b, Verwiebe, 1998) have shown that vibrations can occur with just the lower stream of water. In general, rain-wind vibration can result from three mechanisms (Verwiebe 1998). The first two involve both the upper and lower rivulets resulting in a predominantly across-wind or a predominantly along-wind vibration. The third involves only the lower rivulet with the resulting motion predominantly across-wind including a significant along-wind component.

The streams of water will move circumferentially around the cable surface at the same frequency as the cable vibration, due to the inertia of the water streams combined with the motion of the cable. The vibration of the cable produces cyclical changes in the aerodynamic response by varying the separation point of the flow. The change in the separation point results in a change in the lift and drag forces resulting in an increase in the oscillation (Ruscheweyh, 1999b). This mechanism helps to sustain the vibration of the cables.

The motion of the vibration tends to be in the plane of the cables with some transverse motion. The peak-to-peak responses of the vibrations can reach two metres in magnitude (Matsumoto et al, 1992). This can be a serious concern for bridge designers.

To limit or avoid vibrations measures can be taken to break up the formation of the water streams on the surface of the cable. In cases where no specific measures are taken, Irwin (1997) suggests the following Scruton number limit to avoid vibration problems:

$$S_C = \frac{m\,\delta}{2\pi\rho D^2} > 10 \qquad (2\text{-}5)$$

where m is the mass per unit length (kg/m);

δ is the logarithmic damping decrement;

ρ is the air density (kg/m^3); and

D is the cable diameter (m).

This results in a logarithmic decrement greater than 3 – 6% (Stubler et al, 1999) for typical stay cables. This requirement needs to be achieved for all cable modes having frequencies up to 2.5 Hz for smooth cables (PTI).

The mechanism resulting in rain-wind vibration is well known qualitatively and various different methods have been developed to suppress such vibrations. It is difficult to predict if vibrations will occur at any given location, and if it is going to occur the amount of damping required to suppress the oscillations. Further study is required to determine effective, reliable and practical prevention and control of the vibration as the mechanism is well understood.

As a means of suppressing rain-wind vibration, experimental studies over the past ten years have indicated the positive effect of added mass and structural damping. The Post-Tensioning Institute Committee on Cable-Stayed Bridges recommended a minimum Scruton number of 10 ($S_c \geq 10$) to suppress excessive rain-wind cable vibration based on experimental studies by Saito et al (1994). This is difficult to achieve without the use of auxiliary damping devices and/or surface modification such as helical filets for stay cables on most of the existing long-span bridges.

The stability criterion proposed by Saito et al (1994) to predict the critical wind speed for the galloping of dry inclined cables is approximately given by:

$$(U_R)_{cr} = 35\sqrt{Sc} \qquad (2\text{-}6)$$

where U_R is the reduced wind speed $U_R = \bar{U}/(fD)$

Sc is the Scruton number $Sc = \frac{m\varsigma}{\rho D^2}$

It was indicated that this criterion is applicable to the cases where the angle between cable axis and wind direction is 30° to 60°. With this criterion bridge stay cables with a diameter of 150 mm to 200 mm would be considered prone to galloping.

2.1.5.3 Dry Galloping of Single Inclined Cables

The inclination of cable causes a complex flow regime. When the airflow is approaching a circular section normal to the cable axis or a symmetric elliptical section due to the varying aspect ratio from the relative angle between the wind and the cable, a resultant lift force independent of the wind speed and due to the cross-sectional geometry will not occur. When this is no longer the case and the wind approaches the stay cable from an angle other than normal to the cable axis, vibrations and instability due to a more complicated flow regime initiated by the relative angle between wind and cable axis can occur.

Vibration caused by the formation of ice on cable. Ice can built up on one side and towards the bottom of the cable driven by wind and gravity. The resulting shape is somewhat egg-shaped. This leads to an unstable aerodynamic phenomenon of galloping which long been associated with power transmission cables. In this case the cables have been partially coated with ice by freezing rain. This change in shape causes the aerodynamic forces to produce extremely large amplitude vibrations leading to clashing of adjacent cables, failure of the cable or the failure of the connections to the transmission tower. The aerodynamic forces augment the vibrations rather than suppress them and are referred to as *negative aerodynamic damping*.

Dry, inclined cable galloping was first reported in wind tunnel studies performed in Japan. It differs from the traditional form of galloping (described above, previous paragraph) in that it occurs for cables of circular cross-section. This is a divergent self-excited vibration observed in a very narrow region of wind speed for any given cable. This wind speed corresponds to the critical

Reynolds number region where the aerodynamic drag force is reduced. If the wind speed increases above or decreases below this range the instability disappears. This type of vibration has not been observed in actual bridge cables but Irwin et al. (1999) have indicated that some field observations appear more consistent with galloping than rain/wind oscillations. It was originally thought that these vibrations are not significantly affected by additional damping. Additional research has shown that added damping on the cable stays could minimize the possibility of dry galloping occurring (Stoyanoff et al., 2009). The potential exists that many existing cable-stayed bridges are susceptible to this vibration mechanism.

An instability criterion for galloping of dry inclined cables (Irwin, 1981):

$$\frac{U}{fD_{crit}} = 40\sqrt{S_c} \tag{2-7}$$

where U is the wind velocity (m/s)

f is the natural frequency (Hz)

D_{crit} is the critical cable diameter (m)

S_c is the Scruton number

The mechanism of dry galloping is not well defined as the actual aerodynamic mechanism producing this reaction has yet to be clearly defined. This phenomenon seems to be very sensitive to support conditions in wind tunnel studies; as a consequence, it may be more a function of the conditions in the wind tunnel model than the behaviour of an actual stay cable. It has been suggested that motion observed in some wind tunnel tests which were described as galloping were in fact limited-amplitude vibration in which the maximum amplitude was not yet achieved and simply the limits of the test equipment were reached (Cheng et al, 2003). Further investigation is required as many existing stay cables seem to be surviving without suffering this instability.

Raeese et al (2013) proposed a quasi-steady analytical model to study the qualitative effects of the turbulence intensity of the natural wind on the aerodynamic behaviour of an inclined cable. The Discrete Wavelet Transform was applied to a set of wind data to develop an unsteady wind model. Subsequently, a quasi-steady analytical model was proposed for an inclined cable oscillating in unsteady wind to determine its aerodynamic instability. This model is an extension of the one proposed by Macdonald and Larose (2006) with the addition of the turbulent characteristics of the natural wind. Along with the emergence of the critical number regime for the development of the aerodynamic damping on a cable, the presence of turbulence in the natural wind could increase the risk of a galloping type response of a stayed cable.

Raeese et al (2014) developed the two degrees-of-freedom formulation of the above model, considering the elliptical nature of the cable motion with the occurrence of an unstable galloping type response. A set of non-linear equations were derived to describe the two degree-of-freedom motion of a rigid cylinder subjected to unsteady wind to provide a better understanding into the factors which could promote and/or suppress the occurrence of dry inclined cable galloping. The results were compared to a previous wind tunnel study (Cheng et al, 2003) to validate the proposed analytical model. The authors noted that since the reduced wind speed Ur cannot uniquely reflect the actual flow conditions the Reynolds number range must be included when defining a specific Ur-Sc relation for the likelihood of the cable vibration. There are three key elements which dictate the occurrence of dry inclined cable galloping: the emergence of the critical Reynolds number regime; the spanwise correlation of the aerodynamic forces acting on a cable; and the sustained duration of the critical flow conditions. The first element is necessary for the onset condition of instability. The latter two determine the growth of the response amplitude. All three elements can be met in the wind tunnel, the latter two are more unlikely to be satisfied in the field under natural

wind. This could probably be the reason why such an aerodynamic instability is not common on actual cable-stayed bridges.

2.1.5.4 High Speed Vortex Excitation of Dry, Inclined Cables

High-speed vortex excitation produce limited amplitude vibration excitation which excites the lower vibration modes. These vibrations occur at higher velocities than those produced at normal Kármán vortex and without the presence of moisture due to rain. However, the presence of an axial airflow along the leeward side of an inclined cable is thought to be involved in the cable vibrations. Through testing, it has been noted that the Kármán vortices are enhanced at every third shedding by an axial vortex for a certain discrete wind velocity (Matsumoto et al., 1998). The amplified vortices are produced on alternating sides of the cable. As a result, the cable is excited in a similar manner to normal vortex vibration, but builds to a greater amplitude.

The amount of damping required to suppress cable vibrations is unknown. Cross ties between stay cables were installed on the Meiko West Bridge I in Japan to control cable vibrations and the tie-to-stay connections were damaged due to severe vibrations (Matsumoto et al. 1997). Therefore further study is required to understand its mechanism in order to predict it and efficiently prevent or control it.

2.2 CFD Numerical Simulations Involving Flow around Circular Cylinder

Kawamura and Tsutomu (1994) studied the flow around a yawed circular cylinder for a Reynolds number of 2000 using the finite difference method to study the detailed flow structure especially in the wake region. Three cases were performed with end plates for a cylinder of finite length of 5 times, 9 times, and 15 times the diameter of the cylinder. These were compared to the case of a cylinder of infinite length with an imposed periodic boundary condition in the axial direction. The pressure distributions resulting from the simulations compared with experimental

data. The pressure on the leeward side of the cylinder varied along the length of the cylinder with the pressure on the upstream end being higher than that of the downstream side. The study showed the existence of end plates greatly affects the location of the separation point of the flow. Flow along the length of the cylinder was noted using particle traces with a periodic nature.

Kalro and Tezduyar (1997) presented a parallel 3D finite element computation of unsteady incompressible flow around circular cylinders. Results are shown for three Reynolds numbers, 300, 800, and 10 000. Results for Reynolds number of 10 000 will be summarized here. The use of large eddy simulation was employed for the simulations with a Reynolds number of 10 000. To capture all the flow details very fine grids need to be utilized. An approximate number of grid points required for a simulation can be approximated by $Re^{2.25}$. This is due to the requirement to resolve the Kolmogoroff scale, the scale at which all the turbulent energy is dissipated. The mesh used contained 1 177 600 hexahedral elements, 14 720 elements in a 2D section, 80 along the cylinder span and 160 along its circumference. An initial condition of a 2D unsteady solution was used. The authors were able to capture the 3D characteristics of the flow in the wake of the cylinder. The drag coefficients were in excellent agreement with experimental results including the LES computations.

Selvam (1997) used large eddy simulation with finite element method to study the flow around circular cylinder. The drag-crisis phenomena was simulated using a two-dimensional model for Reynolds numbers of 10^4, 10^5, 5×10^5, and 10^6, and compared with available experimental and computational results. The computational domain was 2D domain for the length of 23.2D, 6.6D upstream of the cylinder and 16.6D downstream of the cylinder, and 13.2D in width, balanced to either side of the domain. A uniform velocity of one and zero in the x and y directions respectively are assumed. The time step for the computational ranged around 0.01s for

a total length of 90s. The drag crisis was captured, but did not match reported in the wind tunnel measurements. The resulting model will be used to study flow around bridges.

Breuer (2000) preformed a thorough numerical investigation of a high Reynolds number flow ($Re = 1.4 \times 10^5$) around a circular cylinder using large eddy simulation. Two types of curvilinear O-type orthogonal grids were used, a course grid with 165 × 165 control volumes in the cross-sectional plane and 64 control volumes in the spanwise direction, and a second fine grid with 325 × 325 control volumes in the cross-sectional plane and the same number of control volumes in the spanwise direction, for a total of 6.76 million control volumes. The study demonstrated that LES can be used for relevant high-Re flows. Also, the study showed that grid refinement did not automatically lead to improved results for all quantities, where improvement was defined as better agreement with experimental results.

Mittal (2001) presented the results of a finite element analysis study for three-dimensional unsteady flow past cylinders with low aspect ratios. For flow past a finite cylinder, a mesh with 2 944 500 nodes with 2 880 000 hexahedral elements was utilized. A low aspect ratio of 4 times the diameter was used. The results presented show that the flow was still developing and more time is required to reach a developed solution. The author's objective was to look into the possibility of studying the phenomenon of drag-crisis by utilizing a direct numerical simulation.

Tutar and Holdø (2001) preformed numerical simulations around a two-dimensional stationary circular cylinder for two turbulence models in the sub-critical flow regime. The first group use two-equation turbulence models which includes k-ε model. The second group uses the large eddy simulation method, with standard sub-grid scale model and near wall approach. The circular cylinder for the model has a non-dimensional unit diameter and placed in the middle of the domain. The domain extended far enough downstream of the cylindrical model to eliminate

the far field effects on the near wake and to produce a full development of the vortex street. The length of domain was 22D, 7D from the center of the cylinder to the inlet and 15D from the center of the cylinder to the outlet of the domain. The domain was 14D wide. The grid contained 11 474 nodes for the *k*-ε model and 21 864 and 34 804 nodes for the LES model. All simulations were performed at a Reynolds number of 1.4×10^5 in the sub-critical flow regime. The LES methods with the SGS model was able to yield much more realistic pictures for the vortex shedding flow in the transitional flow regime. This shows the applicability of the SGS model for the calculation of the vortex shedding flow.

Catalano et al (2003) performed large-eddy simulations for high Reynolds numbers of 5×10^5, 1×10^6, and 2×10^6 for flow around a circular cylinder. The results were compared to Reynolds-averaged Navier-Stokes (RANS) and available experimental data. It was shown that the LES results to be considerably more accurate than the RANS solutions. It was noted that the LES solution become less accurate at increased Reynolds number.

Singh and Mittal (2004) computed the unsteady flow past a circular cylinder for Reynolds numbers of 100 to 10^7. The upstream and downstream boundary conditions were located 8D and 30D from the center of the cylinder respectively. The sides of the domain were placed 8D from the cylinder. The mesh used consists of two parts, a structured mesh close to the cylinder to provide the desired grid resolution to capture the boundary layer flow, and unstructured mesh in the far field. Three mesh resolutions were used: 68 858 elements for the lower Reynolds number models, 93 574 for the intermediate Reynolds number models, and 231 484 for the higher Reynolds number models. The time averaged drag coefficient for a Reynolds number of 10^5 was 1.07, for a Reynolds number of 10^6 a value of 0.607, and for a Reynolds number of 10^7 a value of 0.897.

They were able to capture the drag crisis at a Reynolds number of 2×10^5 in two-dimensional computations.

Singh and Mittal (2005) is a continuation of study performed by Singh and Mittal (2004). The objective of the study was to investigate possible connection between the shear layer instability and the drag crisis. Direct numerical simulation (DNS) is not possible for flows at large Re due to the heavy demands placed on computational resources. Large eddy simulation was used with and without a suitable turbulence model and the two sets of computations are almost indistinguishable for the 2D computations. The agreement of the shear layer between the laboratory results and the computational results at $Re = 10^6$ is poor due to the transition point at which the separated shear layers becomes unstable and it reaches the cylinder surface. The pressure distribution around the circumference of the cylinder showed a delay in the flow separation for $Re = 10^6$ resulting in high peak suction near the shoulder of the cylinder and a higher base pressure. The resulting higher base pressure results in a lower drag coefficient. The authors were able to capture almost all the flow features with a 2D model qualitatively, but a three-dimensional model is required to obtain good quantitative comparisons with experimental results.

Qingkuan et al (2007) simulated the flow around a cable model with a water rivulet on the cable surface using large eddy simulation. The computational domain was circular with the following dimensions: $20D \times 20D \times 0.2D$. Tests included a case without a rivulet, and 13 cases with a rivulet. The time step used was $\Delta t = 0.002$. The authors confirmed that for some water rivulet positions Kármán vortex shedding can be suppressed while at other positions it can be enhanced.

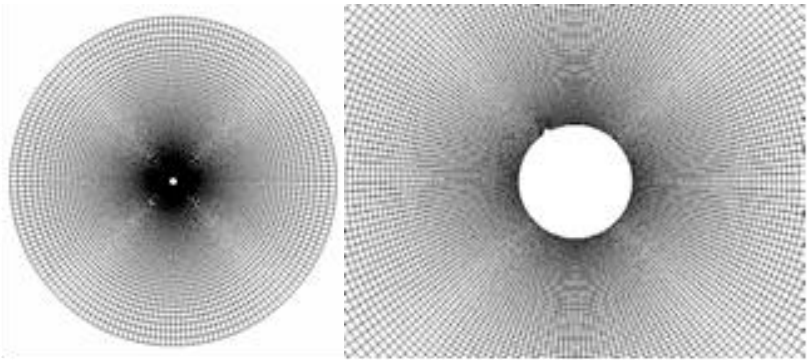


Figure 2.2: Computational domain for cable model with water rivulet, (a) Full simulation domain, (b) Grid near cable model with rivulet position $\theta = 60°$, (Qingkuan, 2007)

Yeo and Jones (2008) preformed a three-dimensional detached eddy simulation to investigate the three-dimensional characteristics of flow past a yawed and inclined circular cylinder. The three lengths of cylinders used in the study were 10D, 20D and 30D, where D is the diameter of the cylinder, and a resulting Reynolds number of 1.4×10^5. It was shown that the spanwise wall boundary conditions influence the vortex flow structure on the leeward side of the cylinder. The authors also studied the force coefficients of a yawed and inclined circular cylinder. It was noted that the force coefficients were not correlated along the length of the cylinder showing a regular pattern along the length of the cylinder for cylinder of length 10D and 20D with less periodicity for the cylinder of 30D. A cylinder of 30D can reduce the influence on the flow structures caused by the periodic boundary conditions.

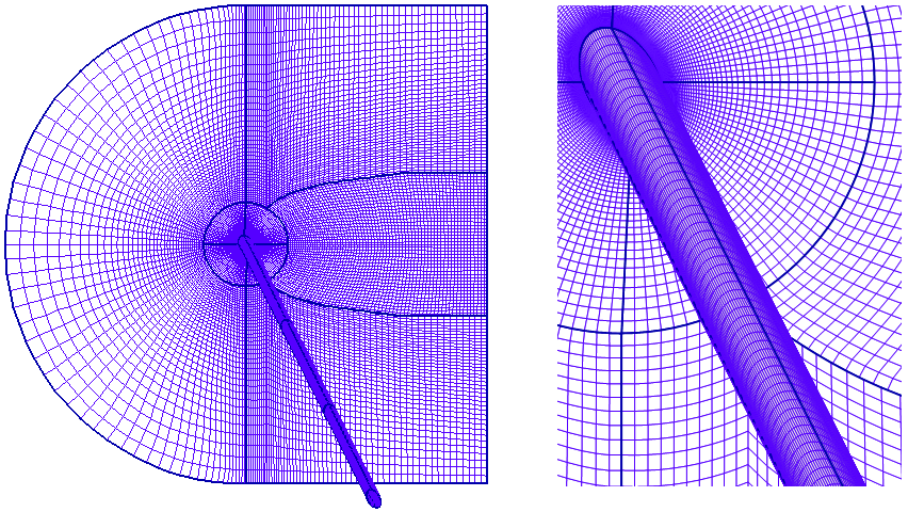


Figure 2.3: Grids of a yawed and inclined cylinder (L = 30D, β = 30, θ = 45), a) Grids on the domain, b) Zoom-in around the cylinder (Yeo and Jones, 2011)

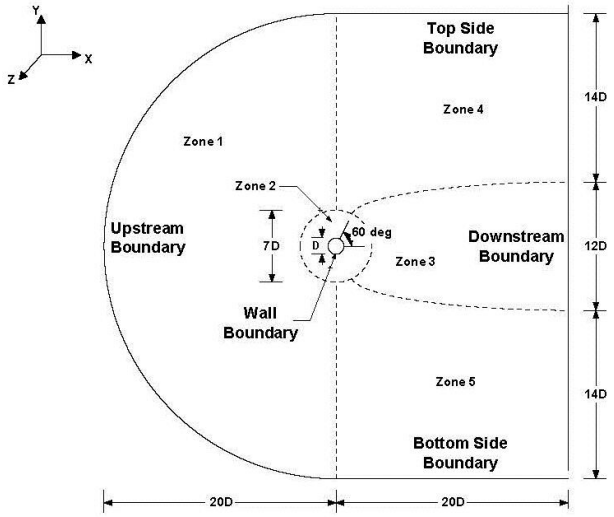


Figure 2.4: Schematic of the computational domain with boundary conditions (Yeo and Jones, 2011)

Yeo and Jones (2010) studied the flow around a yawed cylinder with various strake patterns using three-dimensional detached eddy simulation. The three-dimensional simulations were conducted for flow past a 40° yawed cylinder at a Re = 1.4×10^5. The computational domain extended 35D in the streamwise direction, 15D upstream of the cylinder and 20D downstream of the cylinder, 25D in the cross-stream direction, 12.5D from the center of the cylinder to the top

and bottom sides, with a cylinder length of 10D in the spanwise direction. The total number of elements was approximately 1.2×10^6. The non-dimensional timestep of 0.01 was used; calculated as $\Delta t^* = Ut/D$. The results demonstrated the effect of the strakes patterns on the development of the flow structures around the cylinder and the resulting forces on the cylinder.

Kim and Kitagawa (2011) performed three-dimensional computations around two closely spaced circular cylinders to clarify the mechanism of wake galloping. Large eddy simulations with the Smagorinsky subgrid-scale model was employed. The computational domain was an O-type grid system with a major axis of 60D along the direction of flow, and a minor axis of 30D in the cross wind direction. The number of grid point on the circumference of the cylinder was 200. They presented results for the response of the downstream cylinder, response displacement, lift coefficient, and pressure distribution on the downstream-cylinder surface.

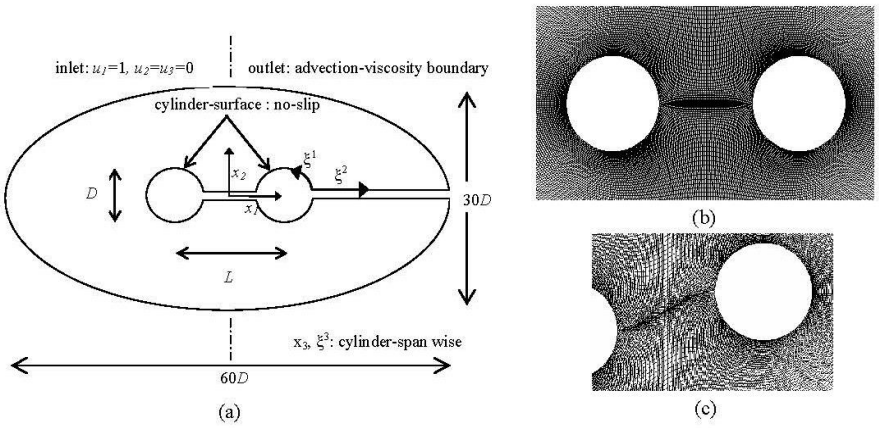


Figure 2.5: Physical space around two circular cylinders (a) coordinate system and boundary conditions, (b) grid system near the cylinder, (c) deformation of grid system (Kim and Kitagawa, 2011)

Yeo and Jones (2011) tried to understand the effects of the cable motion on the wind-induced aerodynamic forces acting on the cylinder. To simulate the motion the uniform incoming flow had an addition of an oscillating component exposed to a stationary yawed cylinder. Detached Eddy Simulation (DES), a hybrid approach to turbulence modeling, uses a combination

of Reynolds Averages Navier Storkes (RANS) and a LES approach. Simulations were performed on a cylinder inclined at 20° for a Reynolds number of 1.4×10^5. The computational domain consisted of a parallelepiped who's upstream and downstream boundaries were shewed at the same angle as the cylinder. The length of the domain was 32D (where D is the diameter of the cylinder), 13.5D in the upstream direction of the cylinder and 18.5D in the downstream direction; 28D in the cross-stream direction, 14D from the center of the cylinder to the top and bottom; and 20D along the length of the cylinder. The computation domain was approximately 2.5×10^5 was used with 128 nodes around the circumference of the cylinder. A non-dimension timestep of $\Delta t^* = 0.01$ as defined by the following: $\Delta t^* = U \Delta t/D$. Yeo and Jones (2011) noted that the swirling flow around the cylinder had a rotational and axial components.

2.3 Wind Tunnel Experiments for Flow around Circular Cylinder

Matsumoto et al (1990) performed a series of wind tunnel tests to clarify the fundemental aerodynamic characteristics of a yawed and/or inclined circular cylinder. This was done in an attempt to clarify the mechanism of of rain-wind vibration of stay cables of cable stayed bridges. The authors confirmed an intense secondary axial flow on the leeward surface of a yawed circular cylinder in flow visualization tests. The experiments were conduited in a wind tunnel of 1.0 m by 0.7 m at a Reynolds number of 1.5×10^5. Two cylinders were used, one with a diameter of 50 mm and the other with a diameter of 160 mm, for a length of 1.5 m and 1.6 m respectively. Visualizations were carried out with a stationary yawed cylinder at yaw of 45° and vibrating cylinder inclined at 45° and yawed at 42.5°.

Matsumoto et al (2001) presented the mechanisms of vortex-induced vibrations of inclined cables at high reduced wind speeds resulting from a series of wind tunnel studies. It was noted that the three-dimensional properties of the vortex shedding around the cable plays an important

role in vortex-induced vibration. A cylinder model with a diameter of 50 mm or 54 mm was placed in a wind tunnel with a yaw angle. Tests were done with and without an artificial rivulet attached to the cylinder model. The pressure on the surface of the model was measured with 48 surface taps along a single line along the length of a cylinder. Flow visualization was completed in the wake of the cylinder using smoke wire techniques which confirmed an axial vortex in the wake of the yawed cylinder. It is suggested that the axial vortex is shed once every three Kármán vortices as shown in the figures below.

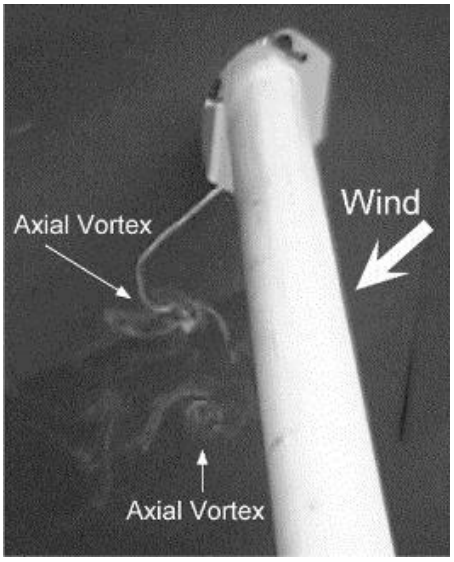


Figure 2.6: Visualized axial vortex in the wake of inclined cable
(without end plate, $\beta = 45°$, $V = 0.5$ m/s, in smooth flow) (Matsumoto et al, 2001)

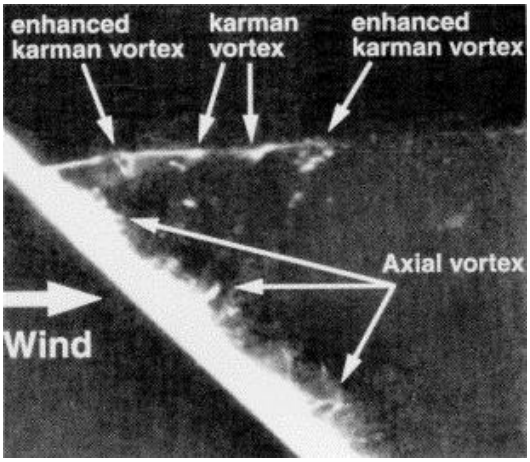


Figure 2.7: Visualized axial vortex and intermittently enhanced Kármán vortex in the wake of inclined cable (without end plate, $\beta = 45°$, in smooth flow) (Matsumoto et al, 2001)

This observation is in agreement with Shirakashi (1985) where the vortex shedding of the axial flow is 1/3 times the frequency of the conventional Kármán street. The unsteady pressure distribution along the length of the cylinder showed the dominance of the low frequency components at X/D = 2.5 to 6 whereas the frequency components of the Kármán vortex shedding are dominating in the range of X/D = 14 to 18, where X is the position along the cylinder from the most forward location of the cylinder.

Matsumoto et al (2003) preformed a wind tunnel study in a tunnel with a working section of 1.8m high and 1.0 m wide. A rigid circular cylinder with a diameter of 54 mm and a length of 1.5 m was used with a horizontal yaw angle of 45°. Holes were placed in the walls of the wind tunnel to prevent the reduction of the axial flow along the length of the cylinder. Three measurements were conducted during the tests: aerodynamic lift force on a stationary cable; fluctuating wind velocity in the wake of the stationary cylinder using a hot-wire anemometer along the length of the cable model placed 0.6D from the leeward side of the cylinder; and the dynamic response of a spring supported cable model. The model was set at a yaw angle of 45° for all tests. Tests were performed up to a Reynolds number of 3.6×10^4. The power spectral densities of all

the results are presented. The results of the power spectral density for fluctuating velocity along the leeward side of the cylinder is presented below.

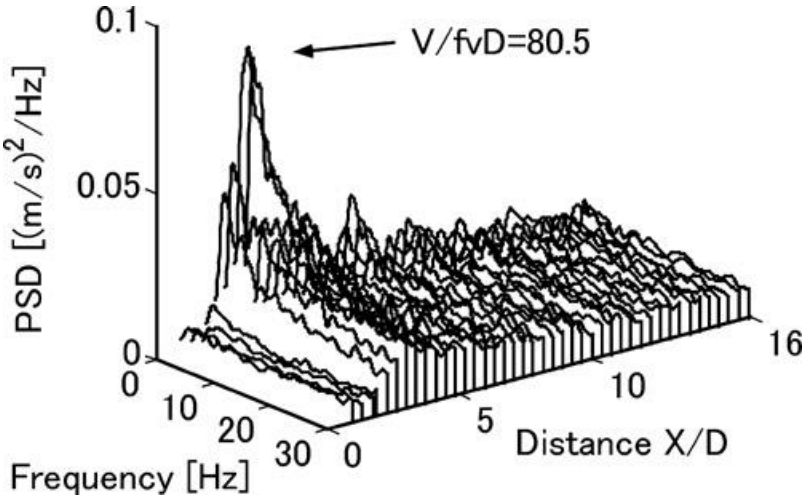


Figure 2.8: Power spectrum density of fluctuating wind velocity in the wake of stationary inclined circular cylinder, where f_v denotes the dominating frequency of fluctuating wind velocity (in smooth flow, without rivulet, with 100mm windows, V = 6.0 m/s, β = 45°)

Cheng et al (2003) tried to clarify the driving mechanisms of high-speed vortex-induced vibrations, and dry inclined cable galloping. The results of their study resulted in fairly large amplitude motion and divergent motion causing aerodynamic concerns in design of bridges. Two phases were involved in the study. A dynamic wind tunnel test where a polyethylene wrapped cable model with a diameter of 160 mm and a length of 6.7 m was tested in an open-circuit wind tunnel. The second phase was a static model test as outlined below in Larose et al (2003). Both types of motion outlined above, high-speed vortex-induced vibrations and dry inclined cable galloping, were observed. The dynamic model was set-up with an orientation equivalent to a full-scale cable inclination and yaw at 45° for both against the mean wind direction. Divergent motion was noted, having a response characteristic similar to that of galloping at 32 m/s. In the static modelling testing it was noted that there was a significant decrease of the drag coefficient and negative slope of the lift coefficient curve within the expected critical Reynolds number range suggesting divergent type motion could be possible.

Larose et al. (2003) tested a steel tube with an outside diameter of 89 mm with an exposed length within the wind tunnel varying from 1.93 m to 2.4 m depending on the inclination of the cylinder. This leads to a length-to-diameter ratio between 21 and 25. A length-to-diameter ratio was set at a minimum of 20 for a circular cylinder. The end effects associated with smaller aspect ratios leads to the contamination for the unsteady aerodynamic forces along the length of the cylinder and reduction of the correlation of the forces. The Reynolds number range of interest was from 1.0×10^5 to 6.0×10^5. The cylinder was instrumented with 192 pressure taps on 5 circumferential strips along the length of the model. The inclination of the model was 60° and 54.7°. It was shown that there is a high degree of variability in the pressure distribution along the cylinder when 2 different rings were compared. Axial vortices were present on the cylinder at certain Reynolds numbers with the use of oil film visualizations.

Poulin and Larsen (2007) required cable drag coefficients for wind along the bridge for two long span bridge designs; SuTong Bridge spanning the Yangtze River in China, and Stonecutters Bridge in Hong Kong. The design value of the cable drag coefficient were then compared with the measured drag coefficients for various types of cable surface treatments introduced to suppress rain-wind vibration. A cable diameter of 158 mm was tested for the SuTong Bridge for the inclination angles of 10°, 20°, 30°, 40°, 50°, and 60°, for both transverse and longitudinal wind. Two cable configurations were tested for the Stonecutters Bridge, one at cylinder diameter of 169 mm with an inclination of 21° (representing the longest main span cable), and the second cable of diameter 139 mm with an inclination of 36°. The test models were a scale of 1:1 with the two cable-stayed bridges to ensure Reynolds number similarity between cable model and prototype. A 1.8 m long cable model was attached to a force balance on each end. The Reynolds numbers for the tests 2×10^5 to 4.1×10^5 for Sutong Bridge and a Reynolds number of

2.2×10^5 to 5.1×10^5 for Stonecutters. The drag forces were calculated and a modified design specification for cable drag coefficients for along the bridge were proposed.

Pastò (2008) studied the behaviour of a freely vibrating circular cylinder in laminar and turbulent flows. Varying degrees of cylinder roughness and mass-damping were used in the wind tunnel tests. The cable model was a circular cylinder with an outside diameter of 155 mm and 2.3 m long. Anemometers were placed in the wake of the cylinder at an interval of 2 diameter downstream and 3 diameters downstream of the cylinder axis. The three anemometers were positioned at L/2, L/3, L/6, where L is the length of the cylinder, from the middle of the cylinder. The Reynolds number varied from 3.1×10^4 to 3.9×10^5. It was noted that the Reynolds number plays an important role in influencing the response of a cylinder. Also, the oscillating cylinder influences the vortex shedding process in the critical Reynolds number range, where a sharp drop in the drag force is associated with the end of coherent vortex shedding. Further study may be necessary to assess the nature of the wake during lock-in, before and after the boundary layer transition Reynolds number.

Anderson et al (2009) and Jakobsen et al (2012) present a continuation of the tests performed by Cheng et al (2003) and Larose et al (2003). The diameter of the model was 160 mm and elastically supported as previously done by Cheng et al (2003) with the addition of along the cylinder to monitor the pressures during the vibrations. Conditions on the leeward side of the cylinder was monitored by a cobra probe, the dynamic response was recorded by 4 translation laser transducers at each support, and the response of the cylinder was recorded by 4 accelerometers. Results were reproduced for large responses observed at a cable-wind angle of 60° with sustained results and double amplitudes exceeding 190 mm. Anderson et al (2009) noted that the angle of incidence, i.e. the angle between the wind and the cable axis, is a major parameter with the largest

responses occurring at 60°. The force coefficients were also calculated using the mean pressures as well as the dynamic response from the model. For a model inclined at 60°, the mean force coefficients from the mean cable response was generally higher than the mean force coefficients from the pressure data, but showed similar variation with Reynolds number. The difference was attributed to the possibility of a larger spatial variation of the surface pressures on the inclined model of 60°.

Katsuchi and Yamada (2009) placed two types of cylinders in a wind tunnel for study; a smooth cylinder and one with an indented pattern on the surface of the cable. The pattern on the indented surface cable was similar to the one used on the Tatara Bridge in Japan. The depth of the indent was 1mm. A cable model with a diameter of 86 mm was chosen. The model was placed in the wind tunnel in the horizontal direction with an angle to the wind of 0, 30, and 45 degrees and supported by springs with one degree of freedom in the vertical direction. A divergent response, reported as dry galloping, occurred around 25 m/s and 23 m/s for the normal and indented surface cables respectively. The pressure distribution around the cylinder was noted at three different locations along the length of the cylinder; the center, 1D downstream and 4D upstream from the center of the cylinder. In general, similar patterns were noted with the coefficient of pressure taking a larger value in the upstream position. The axial flow was measured along the leeward side of the cylinder using an X-type hot wire anemometer. The hot wire was placed at a distance of 0.2D and moved along the leeward side of the cylinder. The axial intensity along the length of the cylinder changed with different end conditions used; with and without end plates.

Matsumoto et al (2010) studied the end effects of end conditions in the wind tunnel on the axial flow velocity. Three types of end conditions were used: free cable ends without tunnel walls; with end plates and without tunnel walls; and with tunnel walls with suitable openings at the cable

ends. For the case of a yaw angle of 45° and a wind speed of 8 m/s in smooth flow the axial flow velocity were not so different except at the upstream end of the cylinder where the axial velocity 70%, 50%, and 80% near the upstream end of the cylinder for the three cases mentioned above. From the quarter point of the cylinder length to the downstream end the axial velocity varied from 40% to 60% and the velocity decreasing to the downstream end of the cylinder for all three cases.

Qingkuan et al (2011) studied the effects of surface roughness, and the velocity of the wind corresponding to the critical Reynolds number. Three models were tested with varying degrees of surface roughness from smooth to a model wrapped with wall paper to add surface roughness. Reynolds numbers for the tests ranged from 1.2×10^5 to 5.1×10^5. The authors concluded that surface roughness of the cable reduces the critical Reynolds number to values more obtainable by natural wind speeds, and therefore resulting in the possibility of large amplitude vibrations, and dry cable galloping.

Yagi et al (2009) noted that end plates reduce the axial flow in the wake of the inclined cylinder. This was concluded with the unsteady pressure distribution on the surface of a forced vibrating cylinder inclined to the air flow. Variation of the end condition of the upstream end of the inclined circular cylinder influences the surface pressure along the cable axis. A rigid circular cylinder with a diameter of 50 mm, and a length of 1500 mm with an angle of inclination of 45° exposed to a wind speed of 30 m/s. The model had monitor locations around the cylinder, and along the leeward side of the cylinder. The frequency of vibration was 2.0 Hz.

Cheng et al (2011) studied the possible mechanisms associated with the divergent type response, and limited-amplitude instability of circular cylinder. It was concluded that there are three factors that lead to the excitation mechanism of these two phenomena: wind velocity, the cable orientation, and the dominant cable motion direction. Two cases were identified for the two

types of responses, and are repeated below. It was noted that the two types of cable aerodynamic instability with different response characteristics occurred at the same cable wind relative angle of 60° for different Reynolds numbers. The authors noted that it is "essential to investigate the variation of flow pattern in different Re ranges at this particular orientation to better understand the physics behind the excitation mechanisms."

Table 2.1: Response characteristics of the two observed critical cases in the tests (Cheng et al, 2011)

Response Type	Full-Scale Cable Angles (°)		Cable-Wind Relative Angle	Major Motion Direction (°)	Static Model Orientation Angles (°)		Unstable Range	
	α_f	β_f	ϕ	γ	α	β	Re ($\times 10^5$)	U_r*
Divergent	45	45	60	54.7	54.7	30	3.16-3.37	79-84
Limited Amplitude	60	0	60	90	60	0	1.86-1.96	106-114

*Reduced wind velocity $U_r = U/f{\cdot}D$, where f is the model frequency and D is the model diameter

Yagi et al (2011) studied the modification of the cable surface for the reduction of drag force, but also aerodynamic stabilization. They studied different surface configurations, including parallel protuberances in attempt to reduce rain-wind vibrations. The static wind-tunnel model was 156 mm in diameter with a length of 900 mm. The length of the model for the outdoor measurement with water was 1700 mm. The number of protuberances were varied to demonstrate its advantages. Flow visualizations for different surface configurations including smooth surface were presented.

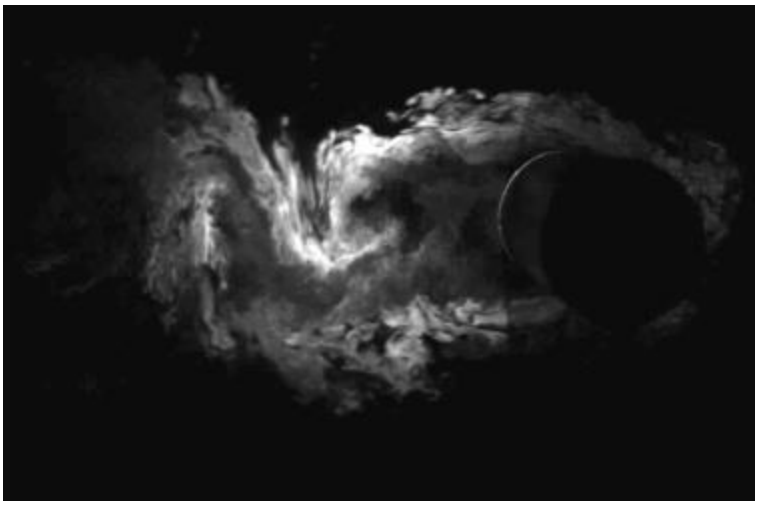


Figure 2.9: Flow visualization around cable model, smooth surface (α = 0°, β = 0°, U = 5 m/s) (Yagi, 2011)

2.4 Flow Regimes for Circular Cylinders

The study of the characteristics and the effects of flow about circular cylinders placed normal to the flow direction has a long history dating back into the 19th century, when Rayleigh applied the use of the Reynolds number to the flow around spheres and cylinders (Zdravkovich 1997). The study still attracts much attention nowadays. The flow regime can be broken down into several categories spanning the flow velocity spectrum from fully laminar to fully turbulent flow. Each category can be separated into sub-categories based on the characteristics of the flow.

The flow around a circular cylinder placed perpendicular to the flow can be regarded as a two-dimensional flow phenomenon. Simplifying the flow into nominally two-dimensional flow about a circular section is sufficient for most applications even though there is a span-wise variation in the flow. The flow behaviour and the resulting aerodynamic forces on the cylinder are predominantly governed by Reynolds number. As summarized in Zdravkovich (1997), the flow around a circular cylinder can be separated into five separate states which are sub-divided into fifteen regimes:

Laminar state of flow (L) can be divided into three basic flow regimes:

L1: creeping flow or non-separation regime (Re= 0 to 4-5): The flow is continuously attached to the surface of the cylinder all around the circumference of the section. There is no visible wake in this regime;

L2: steady separation or closed near-wake regime (Re = 4-5 to 30-48): Separation initiates and a distinct, steady, symmetric, and closed near-wake is formed;

L3: periodic laminar regime (Re = 30-48 to 180-200): The elongated closed near wake becomes unstable and a sinusoidal oscillation of the shear layers commences at the confluence point. The amplitude of the trail oscillations increases with increasing Re.

Transition-in-wake state of flow (TrW) is the second state of flow and can be divided into two flow regimes:

TrW1: transition of laminar eddies in the wake - far wake (Re = 180-200 to 220-250): Downstream from the cylinder the laminar periodic wake becomes unstable and transitions to turbulent;

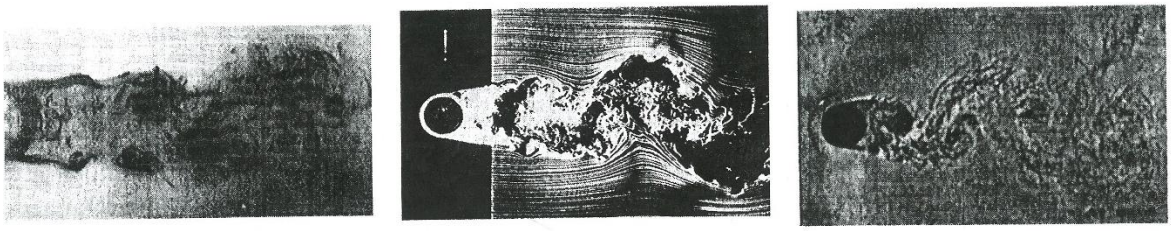
TrW2: transition of an irregular eddy during its formation - near-wake (Re = 220-250 to 350-400): The transition of the eddies moves upstream in the wake and becomes turbulent during its formation.

Transition-in-shear layers (TrSL) is the third state of flow and can be divided into three flow regimes. It is known as the sub-critical state of flow:

TrSL1: development of transition waves - lower (Re = 350-400 to 1×10^3 – 2×10^3): development of transition waves as undulations of the free shear layers;

TrSL2: formation of the transition eddies - intermediate (Re = 1×10^3 – 2×10^3 to 2×10^4 – 4×10^4): The transition waves roll up into discrete eddies along the free shear layer before becoming turbulent and roll into alternate eddies behind the cylinder;

TrSL3: burst to turbulence - upper (Re = $2\times10^4 - 4\times10^4$ to $1\times10^5 - 2\times10^5$): The formation of eddies takes place close to the rear of the cylinder when the sudden burst into turbulence in the free shear layers occurs near the side of the cylinder.



(a) (b) (c)

Figure 2.10: Transition in free shear layers: (a) Re = 2,000; (b) Re = 8,000 and (c) Re = 1.1×10^5 (Zdravkovich, , 1997)

Transition-in-boundary layers (TrBL) is the fourth state of flow and can be divided into five regimes. It is known as the critical state of flow and is where the drag crisis occurs.

TrBL0: pre-critical regime (Re = $1\times10^5 - 2\times10^5$ to $3\times10^5 - 3.4\times10^5$): The transition to turbulence in the free shear layers along separation lines on the surface of the section. The initial fall in the drag coefficient occurs while the eddy shedding remains prominent;

TrBL1: one-bubble regime (Re = $3\times10^5 - 3.4\times10^5$ to $3.8\times10^5 - 4\times10^5$): Begins with a discontinuous fall in the drag coefficient known as the "drag crisis" and with a jump in the frequency of eddy shedding. The formation of a laminar separation bubble on one side of the cylinder results in an asymmetrical pressure distribution resulting in a net lift on the cylinder. This laminar separation bubble reattaches to the surface a short time later before becoming turbulent;

TrBL2: two-bubble regime (Re = $3.8\times10^5 - 4\times10^5$ to $5\times10^5 - 1\times10^6$): Another discontinuous fall of the drag coefficient occurs at the start of the regime along with a jump in the shedding frequency when a second bubble is formed on the other side of the cylinder. The result is the net lift force disappears;

TrBL3: supercritical regime (Re = $5\times10^5 - 1\times10^6$ to $3.5\times10^6 - 6\times10^6$): The disruption and fragmentation of the separation bubbles along the span of the cylinder is a result of the transition of the primary laminar separation line in an irregular manner. Periodic eddy shedding is prevented by the irregularly fragmented separation lines;

TrBL4: post-critical regime (Re = $3.5\times10^6 - 6\times10^6$ to unknown values): The transition in boundary layer occurs between the stagnation point and separation lines. With the increase in R_e the transition region moves towards the stagnation line asymptotically.

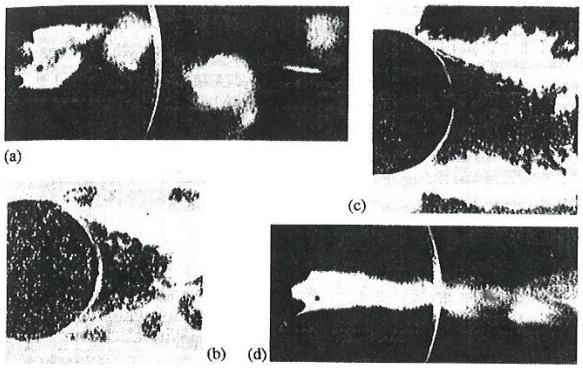


Figure 2.11: Transition in boundary layers: (a) TrBL0, (b) TrBL1, (c) TrBL2, (d) TrBL3 (Zdravkovich,, 1997)

The fifth state is the fully turbulent state and is divided into two regimes: T1: invariable and T2: ultimate. When the disturbed flow region around the cylinder becomes fully turbulent, this state of flow is reached. The associated drag and eddy shedding is unknown because the compressibility effects in air and the cavitations in water cannot be avoided at very high R_e.

Other parameters that influence the characteristics of flow include surface roughness, flow turbulence, blockage, and oscillation of the cylinder. Surface roughness is especially known to alter the onset of the Transition in Boundary Layer (TrBL) state.

The current study will concentrate on clarifying the conditions of occurrence of turbulence during the transition state for an inclined and perpendicular to flow cylinder, namely will investigate the transition between the TrBL1 and TrBL2 flow regimes.

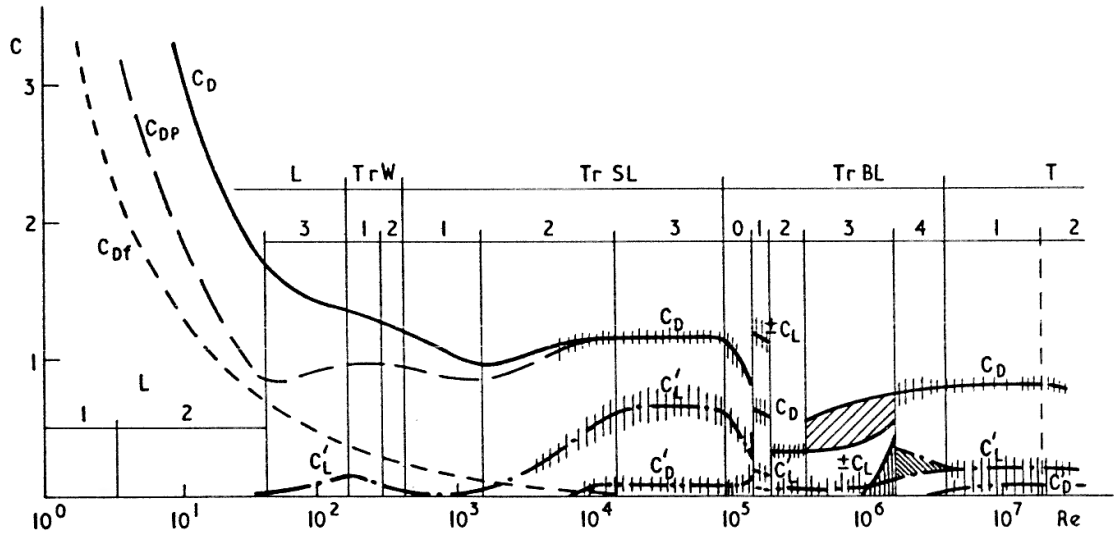


Figure 2.12: Variation of aerodynamic force coefficients for disturbance-free flow (reproduced from Zdravkovich, 1997)

In the Figure 2.12 the following notations were considered:

C_D – mean drag coefficient; $C_D = C_{Dp} + C_{Df}$;

C_{Dp} – portion of mean drag coefficient due to asymmetric pressure distribution on the upstream and downstream side;

C_{Df} – portion of mean drag coefficient due to viscous friction on the surface of the cylinder;

C_D' – fluctuating fluid-dynamic drag coefficient;

C_L – mean lift coefficient;

C_L' – fluctuating fluid-dynamic lift coefficient;

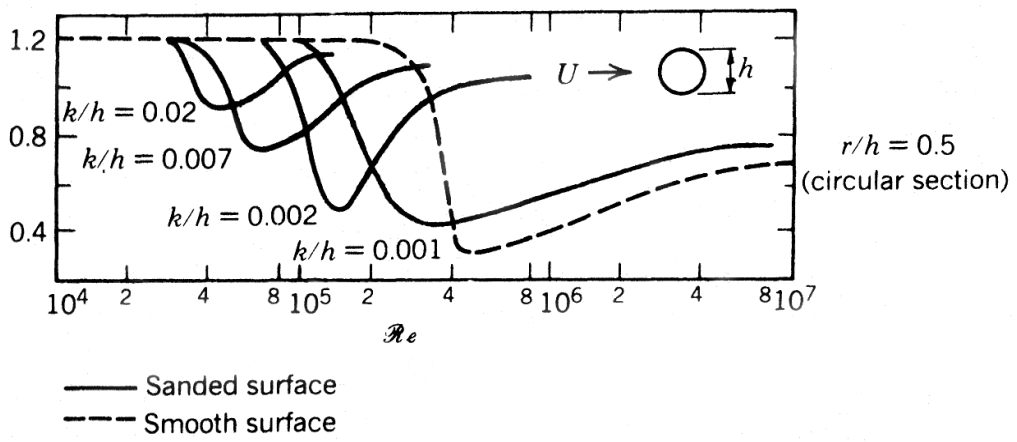


Figure 2.13: Influence of Reynolds number and surface roughness on drag coefficient (Simiu and Scanlan, 1987)

2.5 Experimental Visualizations for Flow around Circular Cylinder Perpendicular to Flow

Many experimental visualization have been found and will be compared to the computational models from this study to show the convergence of the flow. These and subsequent computational models will be used to estimate the flow around a circular cylinder in various configurations. The first figure shows transition in the shear layers for flow around a circular cylinder for Re = 1.1×10^5 (Figure 2.10) (Zdravkovich, 1997). Figure 2.15 shows the development of the Kármán vortex street for a flow with Re = 2.7×10^5 (Williamson, 1996). The next two figures (Zdravkovich, 1997; Coutanceau and Defaye, 1991) shows the change in the vortex pattern on the leeward side of the side as the Reynolds number is increased from approximately Re = 1.1×10^5 to Re = 5×10^5 (Figure 2.11 and Figure 2.16). This is followed by a typical mean pressure distribution around the circumference of the cylinder (Figure 2.17) (ESDU, 1986). And the final experimental visualization shows a sequence of high-speed visualization of flow vortex street couple in the near wake for one period for Re = 10^5 (Figure 2.18) (Coutanceau and Defaye, 1991). The flow in all cases is shown from left to right.



Figure 2.14: Transition in free shear layers, Re = 1.1×10^5 (Zdravkovich, 1997)

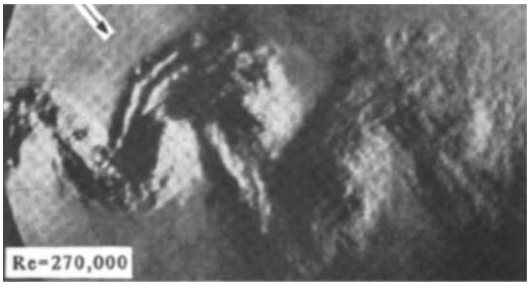


Figure 2.15: Visualization of a turbulent vortex street. Streamwise vorticity, in the braid between Karman vortices, is indicated by the white regions and is visible for Re = 2.7×10^5 (Williamson, 1996)

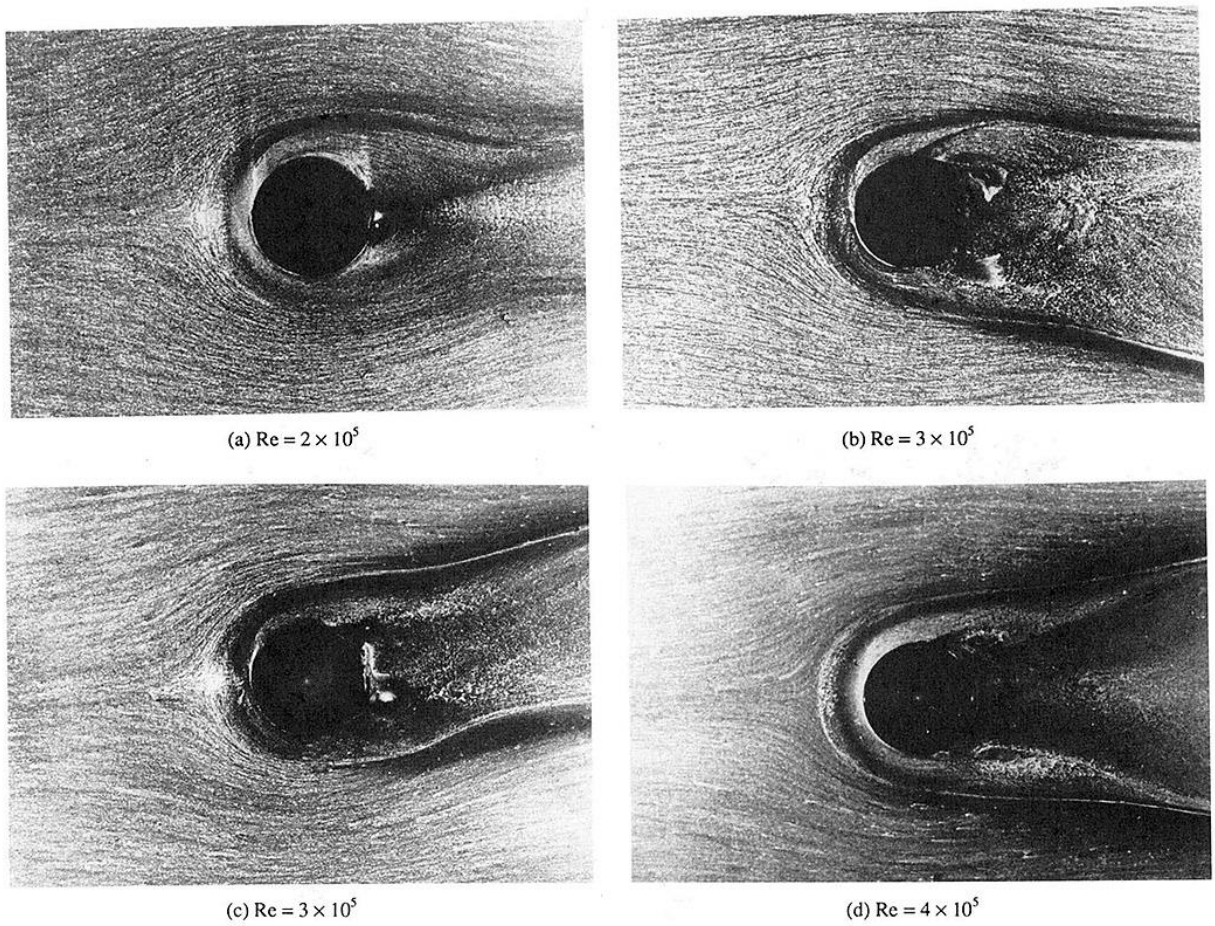


Figure 2.16: (a) Subcritical symmetric state, Re = 2.0×10^5; (b) and (c) possible asymmetric states near the transition, Re = 3.0×10^5; (d) supercritical state, 4.0×10^5
(Coutanceau and Defaye, 1991)

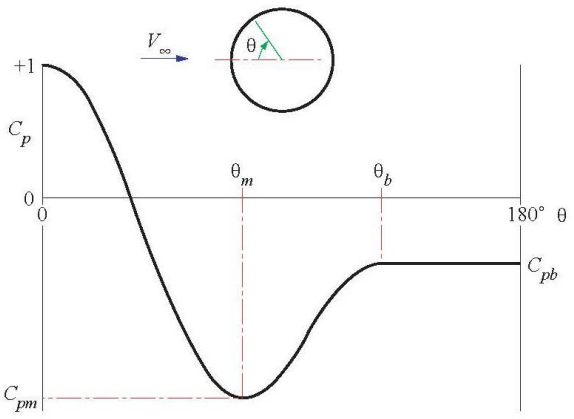


Figure 2.17: Mean pressure distribution around a circular cylinder (ESDU, 1986)

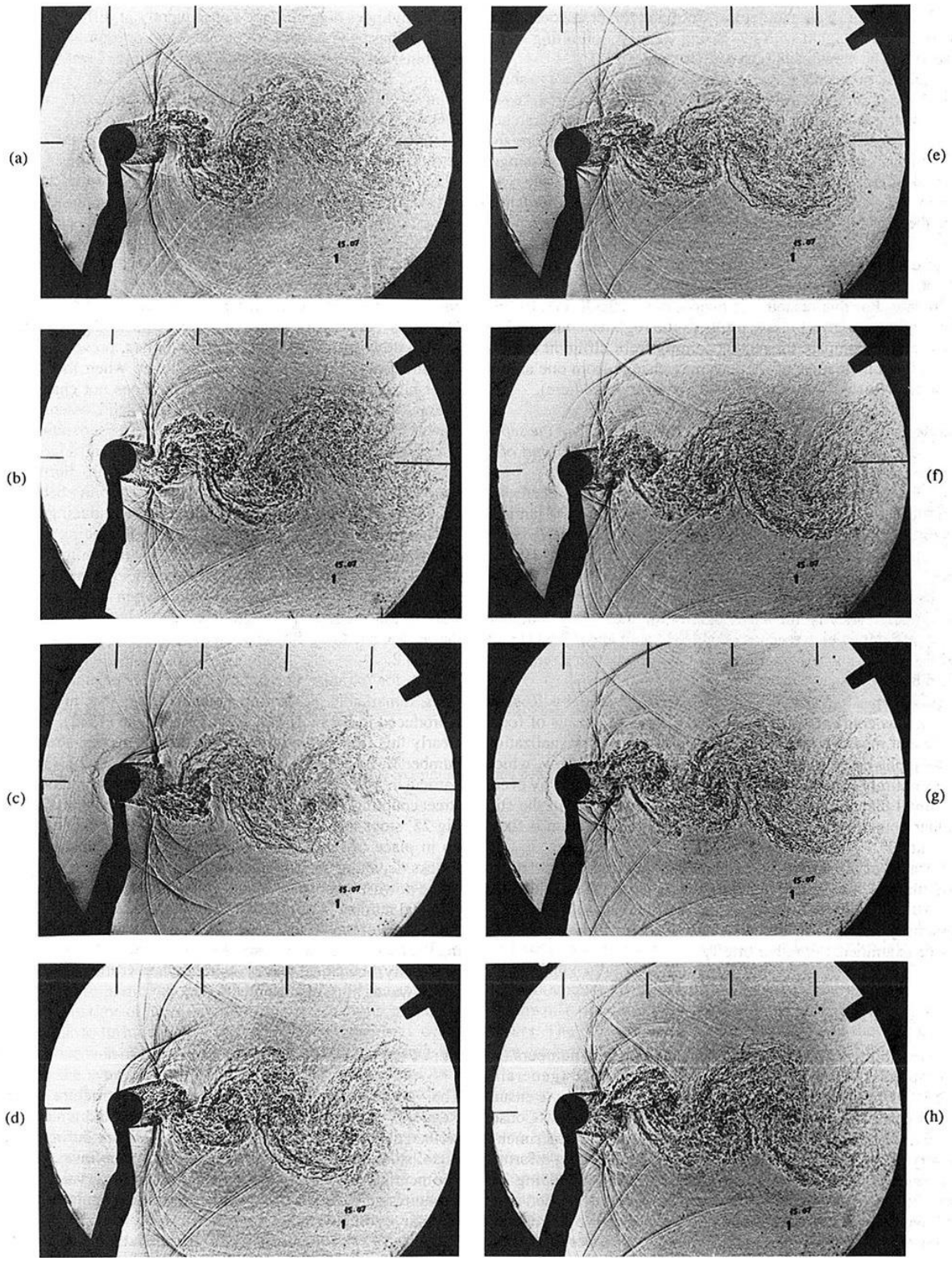


Figure 2.18: Sequence of high-speed visualization of flow vortex street couple in the near wake for one period: Re = 10^5 (Coutanceau and Defaye, 1991)

2.6 Field Observations for Flow around Inclined Cables

Hikami and Shiraishi (1988) reported on the cable vibrations observed during the construction of the Meikonishi Bridge located in the Nagoya Harbour inlet in Japan. The Meikonshi Bridge is a three span cable-stayed bridge. The cables became unstable with rain with an observed vibration of 55 cm peak-to-peak amplitude under a 14 m/s wind. The stayed cables varied from 65 m to 200 m made up of bundles of parallel wires using a polyethylene pipe and cement grout for corrosion protection. The typical outside diameter of the polyethylene pipe was 140 mm. The following variables were monitored: cable transverse vibration in the vertical plane, wind speed and direction, and the cable damping. It was noted that vibrations were limited to cables which declined in the direction of wind. Wind tunnel testing was performed in order to produce the cable vibration in the wind tunnel. The cable model was the same polyethylene pipe with an outer diameter of 140 mm, and a cable length of 2.6 m. The model was mounted on springs to mimic the bridge cable motion. The wind tunnel used was 2.5m by 1.5 m. The model was tested at α = 45° and β = 45°, and α = 45° and β = 45°, corresponding to the cable directions in which the vibrations were observed and were not observed on the bridge. The authors were able to reproduce the vibrations in the wind tunnel in a similar wind speed range of 9 m/s to 13 m/s.

The Fred Hartman Bridge in Houston, TX is a twin-deck cable-stayed bridge with a main span of 381 m. The deck was supported by 192 stays arranged in 4 inclined planes. The stays range in length from 59 m to 198 m of varying diameters. Vibrations were noted for a stay cable with relatively small vibration amplitudes, and relatively low wind speeds, as shown in Figure 2.19 below (Main and Jones, 1999). The vibrations appear to be velocity-restricted, but the authors were unable to confirm. The vibrations occur over a wide range of wind directions where the stay cable is inclined in the direction of the wind, as shown in the figure below.

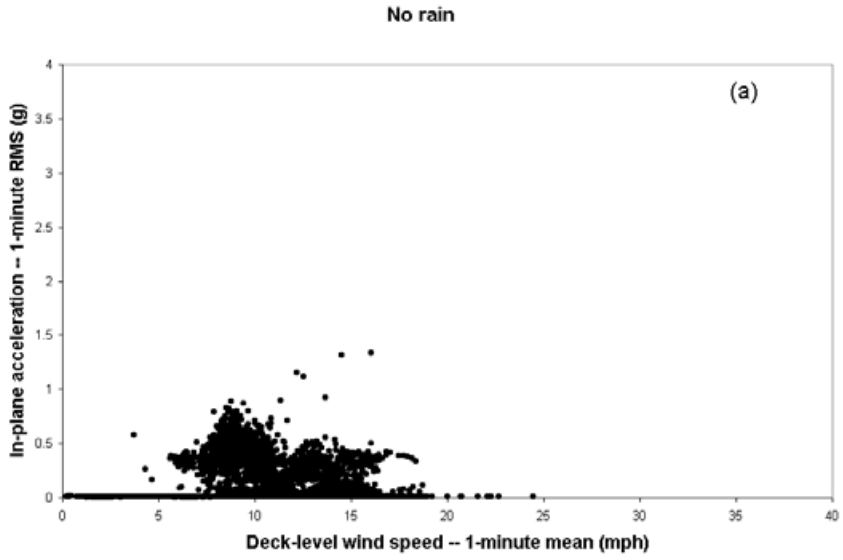


Figure 2.19: Vibration amplitude of stay vs. wind speed (Main and Jones, 1999)

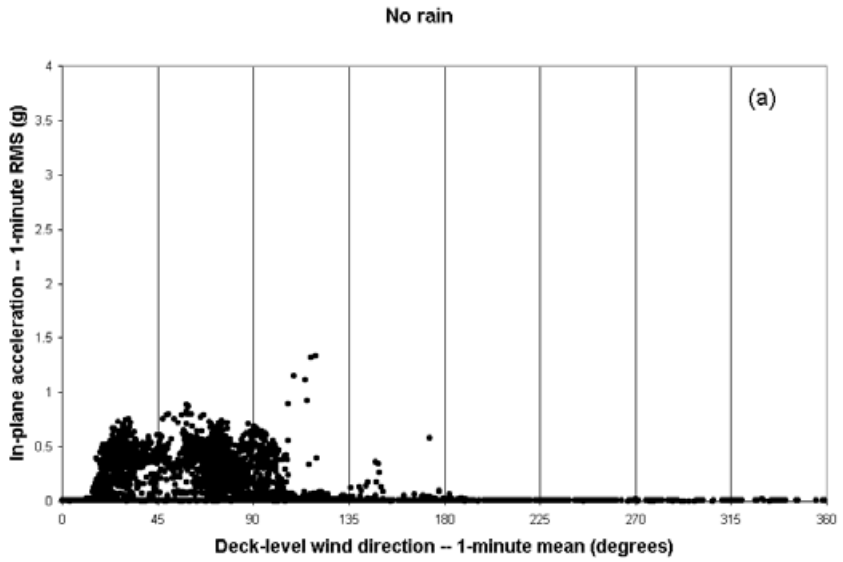


Figure 2.20: Vibration amplitude for stay vs. wind direction for different wind speeds (Main and Jones, 1999)

Matsumoto, Shirato et al (2003) setup a full-scale cable model in the field to observe the response of the cable under various weather conditions. A 30 m long polyethylene pipe from a cable-stayed bridge was exposed to natural wind in order to investigate the wind-induced vibration. The cable was supported by a steel tower at a height of 21.1 m with a cable model made up of an aluminum pipe wrapped with a polyethylene pipe used in cable-stayed bridges. The exterior

diameter of the cable was 110 mm. The cable force was monitored with a load cell and an accelerometer was used to study the vibration of the cable. The cable model was setup to simulate a cable on the leeward side of the tower and at approximately 45° from the dominant wind direction. Wind direction and velocity was monitored with an anemometer near the cable model. Two data results were present of cable vibration without the occurrence of rain with a velocity of 12.28 m/s at approximately 45° from the plane of the cylinder and 15.54 m/s also at approximately 45° from the plane of the cylinder.

Boujard and Grillaud (2007) initiated as study of the Iroise Bridge due to the observations of crack in the bottom anchorages of 4 stay-cables along the main span. The deck, piers, and 9 stay cables were monitored along with the wind speed and direction. Vibrations were observed for a cable of length of 172.0 m, diameter of 180 mm, and an inclination angle of 25.2°. Most of the vibrations occurred over a limited range of wind speeds, from 11 to 18 m/s, and for yaw angles between 10° and 40°. Wind tunnel tests were performed on an inclined circular cylinder with a diameter of 200 mm and length of 4.7 m. Pressure readings were monitored at 32 pressure taps arranged in two different cross-sectional rings around the middle of the cylinder. The pressure distribution obtained were similar to those observed for a horizontal cylinder in the critical regime, where the transition to turbulent flow occurs in the separated shear layers and induces a re-attachment on the cylinder.

Matsumoto et al (2010) also performed axial visualizations in the field by the use of light strings for a cable inclined at 30° with the vertical resulting in an equivalent yaw angle with the wind of 40°-50° as shown in the figure below. The velocity of the axial flow was measured with soap bubble movement with the aid of a video camera. The axial velocities were measured between 40% and 80% of the corresponding approaching wind speed.



Figure 2.21: Visualized axial flow by light string for a proto-type cable (Matsumoto et al, 2010)

Zuo and Jones (2010) presented full scale measurement for two bridges. The first, the Fred Hartman Bridge in Houston, TX is a twin-deck cable-stayed bridge with a main span of 381 m. Cable arrangement is described above in Main and Jones (1999). Results were presented for cables with a diameter varying from 141 mm to 194 mm, fundamental frequencies from 0.57 to 1.26, and inclination angles from 21.1 to 48.9. The details for the Veterans' Memorial Bridge were not provided. The authors suggested that Kármán-vortex-induced vibration occurred at relatively low wind speeds and over a broad range of wind directions. They also suggest that when the angle of attack increases beyond about 120°, the required reduced velocity for the vibrations becomes much higher than 5. The authors noted that due to the limited nature of full-scale measurement, additional work is required to investigate the three-dimensional nature of the flow around yawed and inclined circular cylinders, including the use of wind tunnel experiments and computational fluid dynamics.

Zuo (2014) measured the wind pressure on the surface of a circular cylinder placed in the atmospheric boundary layer while simultaneously the acceleration of the cylinder. A cylinder was

placed horizontally in a field experiment to investigate the effects of the natural turbulence and shear in the atmospheric boundary layer. This also allow for the variation of the yaw angle with the change in direction of the wind. The test specimen was a 7.62 m long circular cylinder with an outer diameter of 0.224 m mounted 6 m above the ground. The pressure was monitored with 36 pressure taps at selected locations around the circumference of the PVC section of the circular cylinder. An accelerometer was used to measure the vibration of the cylinder. The site meteorological conditions were monitored by an ultrasonic anemometer, a temperature and relative humidity sensor, and a barometric pressure sensor. Results were presented for both flow approximately normal to the cylinder, and inclined to the cylinder. The field data when the cylinder is inclined to the flow showed a reduction of the drag coefficient with the increase in wind speed above Re of 1.12×10^5, and a significant deviation of the mean lift coefficient from zero starting at a Reynolds number of approximately 0.5×10^5. These tendencies are occurring at much lower Reynolds numbers than other tests due to the inclusion of tests with higher turbulence intensities.

Hoang et al (2015) preformed wind tunnel studies on an aluminum circular cylinder with a diameter of 50.8 mm within a 1.82 m square wind tunnel. The circular cylinder was supported by a three axis load cell at either end of the model, and supported outside the tunnel section. Tests were performed to determine the three aerodynamic force coefficients in the case of a circular cylinder inclined, and yawed with respect to the flow, and study the applicability of the Independence Principle. The flow phenomena around a circular cylinder placed normal to the flow has been studied extensively with the results being observed partly applicable to the more complicated cases of flow past an inclined and yawed circular cylinder by using the Independence Principle, or also known as the cross-flow principle, or cosine law. The level of inaccuracy in this

principle is consistent with the increase of the relative angle between the circular cylinder and the wind flow. This principle does not take into account the possible development of an axial flow in the near wake of the circular cylinder with the increase in relative angle. The Re tested varied from 8500 to 90 000. The horizontal yaw angle varied from 25° to 155°, and the inclination angle varied from 22° to 60°. The authors confirmed that the Independence Principle becomes inaccurate for yaw angles larger than 40°, and highlighted the importance of the 3D aspects of the flow around an inclined cylinder even for these lower Reynolds numbers.

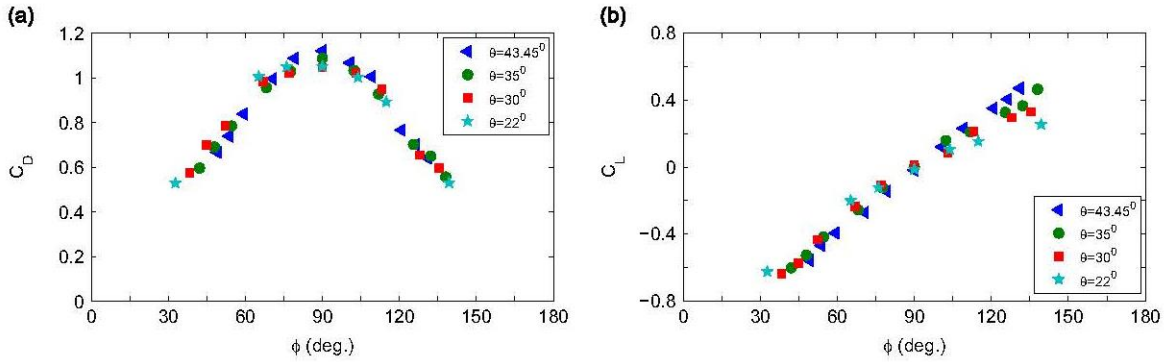


Figure 2.22: Aerodynamic force coefficients as a function of ϕ for $3 \times 10^4 < Re < 9 \times 10^4$ (Hoang et al, 2015)

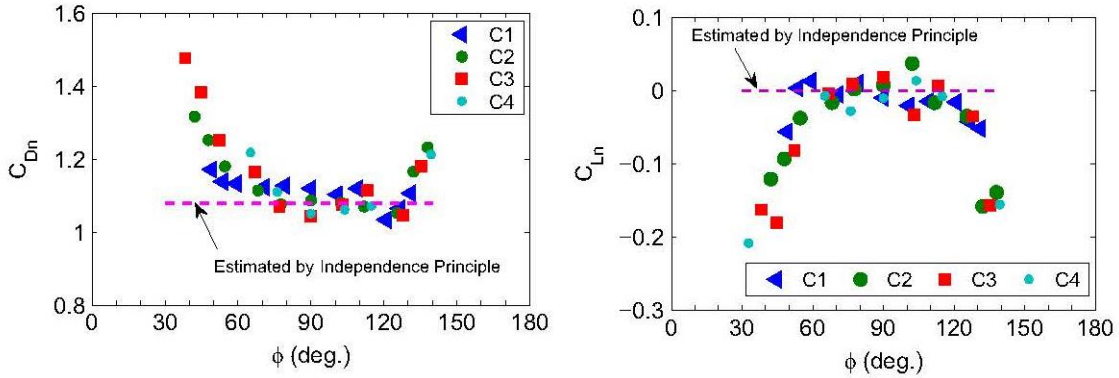


Figure 2.23: Aerodynamic coefficients as a function of ϕ for $3 \times 10^4 < Re < 9 \times 10^4$ (Hoang et al, 2015)

This area of research has drawn a lot of attention from many researchers over the past number of years with the increase in the length of the stay cables of cable stayed bridges. Many researchers have looked at the problem of inclined cable vibrations from a number of different perspectives, both in the laboratory and in the field, to better understand the cause of these vibrations. The current study continues to build on this current area of research in flow around inclined and/or yawed circular cylinders, and add to the understanding of the flow characteristics and pattern that cause vibrations of inclined cables.

2.7 Aeroelastic Stay-Cable Models

Raeesi et al (2104) proposed to study the wind-induced response of bridge stay cables with the development of a two-degree of freedom aeroelastic model. This was done to provide a better understanding of the excitation mechanism assoicated with dry inclined cable galloping in an attempt to clarify its contributing factors. The model consisted of a rigid circular cylinder model oscillating in an arbitary orientation with respect to the on-coming flow. Two unsteady wind models and a case study have been used to examine the impact of the flow unsteadiness on the aerodynamic response of a dry inclined stay cable. The results of the study indicate that different segments of a stay cable could be exposed to different flow regimes along the length of the cable. This indicates that a stay cable might be triggered along the portion of its length. The researchers concluded that the emergance of the critical Reynolds number regime, the spanwise corelation of the aerodynamic forces acting along the cylinder, and the sustained duration of the critical flow conditions are all key elements in the onset of dry inclined cable galloping.

The concept was further developed by Raeesi et al (2106) who proposed a three-dimensional aeroelastic model to further clarify the aerodynamic response of an inclined and/or yawed slender flexible cylinder subject to unsteady mean flow. The role of several practical factors

on the aerodynamic response of the dry inclined cable were investigated. The researchers studied the impact of the atmospheric boundary layer wind velocity profile, and any pre-existing cable motion on the galloping response of a dry inclinded stay cable. It was concluded that the aerodynamic response of a stay cable could be reduced it multi-mode oscillaitons, or cable motion higher than the fundemental frequency is present prior to exposure to cirtical flow conditions. Also, the wind-induced response of a dry inclined cable is dependent on the fluctuation frequency of the wind.

3 Computational Fluid Dynamics Modelling – Background and Modelling Consideration

The application of CFD in wind engineering has increased rapidly over the past number of years. This is due to both the advancement of numerical techniques, and the computational technology used to solve these problems.

In this section the basic methodology of CFD will be covered. This will include the governing equations of fluid dynamics, and the numerical methods of turbulence modelling. Also, a general introduction to LES will be provided along with how it is applied by ANSYS in Fluent in Sections 3.3 and 3.5, the software used in this study.

3.1 Laminar Flow Modelling

Laminar flow calculations are governed by the unsteady Navier-Stokes equations. There is no turbulence model applied to the simulation which results in making the laminar option only appropriate if the flow is laminar (ANSYS, 2010a). This only applies for low Reynolds number flow, for example for flow around a circular cylinder with a Reynolds number less than 200. The energy transfer in the fluid for the laminar option is accomplished by molecular interaction, or diffusion of the fluid. As the speed of the flow increases, viscous stresses also contribute to the energy transfer within the fluid. If the flow is turbulent, and the simulation was set-up using the laminar flow option, convergence will be difficult, and the simulation will not reach the correct solution. The output of the model should be checked to confirm the maximum Reynolds number reached, and that Reynolds number is within the laminar flow regime.

3.2 *k-ε* Turbulence Model

The *k-ε* turbulence model is based on the solution of equations for the turbulent kinetic energy *k* and the turbulent dissipation rate *ε*. This model is the most widely employed two-equation eddy-viscosity model used. The *k-ε* turbulence model date back to work by Chou (1945).

3.2.1 Overview

Two-equation turbulence models allow for the determination of both the turbulent length scale and the time scale by the solution of two separate transport equations. The standard *k-ε* turbulence model is within this class of models. It is a robust model, and provides reasonable economy and accuracy for a wide range of turbulent flows. This is the reason it is popular in industrial flows. This model is a semi-empirical, as it relies on empirical observations.

The standard *k-ε* turbulence model is based on model transport equations for the turbulence kinetic energy (*k*), and its dissipation rate (*ε*). The model transport equation for the turbulence kinetic energy (*k*) is derived for the exact equation, whereas the model transport equation for the dissipation rate (*ε*) is a result of physical reason.

It is assumed that the flow for a *k-ε* turbulence model is fully turbulent, and the effect of the molecular viscosity are negligible.

3.2.2 *k-ε* Theory

The *k-ε* turbulence model requires the addition of a damping function in order to stay valid through the viscous sublayer to the wall. The goal of the damping function is to properly limit the behaviour of *k* and *ε* at the wall, for example:

$$k \sim y^2 \tag{3-1}$$

and

$$\frac{\varepsilon}{k} \sim \frac{2\nu}{y^2} \tag{3-2}$$

for

$$y \to 0$$

where *y* represents the coordinate normal to the wall.

The Reynolds shear stress behaves as follows:

$$\tau_{ij}^{R} \sim y^3 \tag{3-3}$$

for

$$y \to 0, i \neq j.$$

The *k*-ε turbulence models are denoted as low Reynolds number models. They are more difficult to solve numerically, as the damping function leads to turbulence equations with stiff source terms. High resolution is required near the wall surface in order to resolve the viscous sublayer.

A *k*-ε model can be written as

$$\frac{\partial \rho k}{\partial t} + \frac{\partial}{\partial x_j}\left(\rho v_j k\right) = \frac{\partial}{\partial x_j}\left[\left(\mu_L + \frac{\mu_T}{\sigma_k}\right)\frac{\partial k}{\partial x_j}\right] + \tau_{ij}^{F} S_{ij} - \rho\varepsilon \tag{3-4}$$

$$\frac{\partial \rho \varepsilon^*}{\partial t} + \frac{\partial}{\partial x_j}\left(\rho v_j \varepsilon^*\right) = \frac{\partial}{\partial x_j}\left[\left(\mu_L + \frac{\mu_T}{\sigma_\varepsilon}\right)\frac{\partial \varepsilon^*}{\partial x_j}\right] + C_{\varepsilon 1} f_{\varepsilon 1} \frac{\varepsilon^*}{k} \tau_{ij}^{F} S_{ij} - C_{\varepsilon 2} f_{\varepsilon 2} \rho \frac{(\varepsilon^*)^2}{k} + \phi_\varepsilon \tag{3-5}$$

On the right hand side of the equation the terms represent the conservative diffusion, eddy-viscosity production and dissipation, respectively. The explicit wall term is denoted by ϕ_ε.

The term τ_{ij}^F is the Favre-average turbulent stresses, and is defined as

$$\tau_{ij}^F = -\bar{\rho}\widetilde{v_i''v_j''} = 2\mu_T\tilde{S}_{ij} - \left(\frac{2\mu_T}{3}\right)\frac{\partial\tilde{v}_k}{\partial x_k}\delta_{ij} - \frac{2}{3}\bar{\rho}\tilde{k}\delta_{ij} \tag{3-6}$$

where

$\tilde{S}_{ij}$ is the Farve-averaged strain rate

$\tilde{k}$ is the turbulent kinetic energy

The turbulent eddy viscosity is defined as

$$\mu_T = C_u f_u \rho \frac{k^2}{\varepsilon^*} \tag{3-7}$$

The turbulent kinetic energy is used in the evaluation of the eddy viscosity with the term τ_{ij}^F, the Favre-average turbulent stresses defined above and the following:

$$\tau_{ij}^R = -\rho\overline{v_i'v_j'} = 2\mu_T\overline{S_{ij}} - \frac{2}{3}\rho K\delta_{ij} \tag{3-8}$$

where

$\bar{S}_{ij}$ denotes the Reynolds averaged strain-rate tensor

K is the turbulent kinetic energy $\left(K = \left(\frac{1}{2}\right)\overline{v_i'v_i'}\right)$, and

μ_T is the eddy viscosity.

The quantity ε^* and the turbulent dissipation rate ε are related by the following

$$\varepsilon = \varepsilon_w + \varepsilon^*$$

(3-9)

where

ε_w is the dissipation rate at the wall

The near wall damping functions, and the wall term vary between the various *k*-ε models. The Launder-Sharma model provides good results for a wide range of applications. For this model the constants (ANSYS, 2010b), and Prandtl number are as follows:

C_μ = 0.09,

$C_{\varepsilon 1}$ = 1.44,

$C_{\varepsilon 2}$ = 1.92,

σ_k = 1.0,

σ_ε = 1.3,

Pr_T = 0.9.

The wall damping function is defined as:

$$f_\mu = exp\left(\frac{-3.4}{(1 + 0.02Re_T)^2}\right)$$

(3-10)

$$f_{\varepsilon 1} = 1$$

(3-11)

$$f_{\varepsilon 2} = 1 - 0.3exp(Re_T^2)$$

(3-12)

where $Re_T = \frac{\rho k^2}{(\varepsilon^* \mu_L)}$ is the turbulent Reynolds number.

The value of ε_w and the explicit wall term ϕ_ε are defined as:

$$\phi_\varepsilon = 2\mu_T \frac{\mu_L}{\rho}\left(\frac{\partial^2 \upsilon_s}{\partial y_n^2}\right)^2$$

(3-13)

$$\varepsilon_w = \frac{2\mu_L}{\rho}\left(\frac{\partial\sqrt{k}}{\partial y_n}\right)^2$$

(3-14)

where

υ_s is the velocity parallel to the wall, and

y_n is the coordinate normal to the wall.

Using the Cartesian tensor form to compute the wall term, ϕ_ε, and ε_w avoids having to know the wall distance and orientation.

$$\phi_\varepsilon = 2\mu_T \frac{\mu_L}{\rho}\left(\frac{\partial^2 \upsilon_i}{\partial x_j \partial x_k}\right)^2$$

(3-15)

$$\varepsilon_w = \frac{2\mu_L}{\rho}\left(\frac{\partial\sqrt{k}}{\partial x_j}\right)^2$$

(3-16)

3.3 Large Eddy Simulation Theory

Large Eddy Simulation (LES) was first used by Smagorinsky (1963) in meteorology with the first engineering application of LES by Deardorff (1970) (Blazek, 2005). LES is increasingly used for physically and geometrically complex flows in engineering.

LES is based on the observation that the small turbulent flow structures are more universal in character than the larger eddies. Therefore, the idea is to compute the contributions of the large,

energy carrying flow structures from momentum, and energy transfer and to model the effects of the small flow structures.

3.3.1 Governing Equations of Fluid Dynamics

In computational fluid dynamics, the governing equations of fluid dynamics are solved in calculating the flow around a bluff body. These equations ensure the conservation of mass, momentum, and energy (Zikanov, 2010), and are listed below:

Mass continuity equation

$$\frac{\partial \rho}{\partial t} + \frac{\partial}{\partial x_k}(\rho u_k) = 0 \tag{3-17}$$

Momentum conservation equation

$$\rho \frac{\partial u_i}{\partial t} + \rho u_j \frac{\partial u_i}{\partial x_j} = \frac{\partial \sigma_{ji}}{\partial x_j} + \rho f_i \tag{3-18}$$

Energy conservation equation

$$\rho \frac{\partial e}{\partial t} + \rho u_j \frac{\partial e}{\partial x_j} = \sigma_{ji} \frac{\partial u_i}{\partial x_j} - \frac{\partial q_j}{\partial x_j} \tag{3-19}$$

where

u_i is the velocity component in the i-th direction,

ρ is the density of the fluid,

σ_{ij} is the stress tensor,

f_i is the body force vector per unit mass,

e is the internal energy per unit mass, and

q_i is the conductive heat flux.

Constitutive equations are needed since these governing equations above have more unknowns than the available number of equations. These constitutive equations are needed to fully close the system of equations.

The conservation of momentum equation combined with the constitutive equations of a Newtonian fluid are known as the Navier-Strokes equations

$$\rho\frac{\partial u_i}{\partial t}+\rho u_j\frac{\partial u_i}{\partial x_j}=-\frac{\partial p}{\partial x_i}+\frac{\partial}{\partial x_i}\left(\lambda\frac{\partial u_j}{\partial x_j}\right)+\frac{\partial}{\partial x_j}\left[\mu\left(\frac{\partial u_i}{\partial x_j}+\frac{\partial u_j}{\partial x_i}\right)\right]+\rho f_i \tag{3-20}$$

where μ and λ are the coefficients of viscosity, and can be determined from experimental data.

In order to apply numerical algorithms the above governing equations are rearranged in vector form. The Navier-Stokes equation without body force, mass diffusion, finite-rate chemical reactions, or external heat addition in Cartesian coordinates can be represented as

$$\frac{\partial q}{\partial t}+\frac{\partial f_i}{\partial x_i}=\frac{\partial r_i}{\partial x_i} \tag{3-21}$$

where

$$q=\left[\rho,\rho u_j,E_t\right]^T \tag{3-22}$$

$$f_i=\left[\rho u_i,\rho u_i u_j+p\delta_{ij},(E+p)u_i\right]^T \tag{3-23}$$

$$r_i=\left[0,\tau_{ij},u_j\tau_{ij}-q_i\right]^T$$

(i = 1, 2, 3; j = 1, 2, 3; in 3D) (3-24)

where

$[\ \ ]^T$ is the transpose operation,

δ_{ij} is the Kronecker delta function ($\delta_{ij} = 1$ if $i = j$; $\delta_{ij} = 0$ if $i \neq j$),

$E_t = \rho e + \frac{1}{2}\rho u_j u_j$ is the total energy per unit volume,

τ_{ij} is the viscous stress tensor, and

q_i is the heat flux transfer due to temperature gradient.

The above Navier-Stokes equation in vector form is a matrix which consists of five rows: the first row is the continuity equation; the second to fourth rows are the momentum equations; and the fifth row is the energy equation.

The above equations are solved for a time-dependent velocity field in the simulation of turbulent flow. It is not feasible to resolve all the details of the turbulent flow in most engineering applications. As an alternative of computing the fluid flow for all length and time scales of turbulence the equations are solved for an appropriately averaged flow quantities in a turbulence model.

3.3.2 Filtered Equations

Filtering is a key concept of LES. Variables of the Navier-Stokes system of equations are filtered to define a velocity field containing only the large-scale components of the total flow. The filtered velocity may be written as:

$$\overline{\boldsymbol{u}}(\boldsymbol{x}, t) \equiv \int G(\boldsymbol{r}, \boldsymbol{x})\boldsymbol{u}(\boldsymbol{x} - \boldsymbol{r}, t)d\boldsymbol{r} \tag{3-25}$$

where the integral is over the flow domain,

G is a filter function that satisfies the normalization condition

$$\int G(\boldsymbol{r}, \boldsymbol{x}) d\boldsymbol{r} = 1$$

(3-26)

and is nearly zero at

$$r = |\boldsymbol{r}| > \frac{\Delta}{2}$$

(3-27)

where Δ is called the filter width.

Various forms of a filtering function have been suggested. Two popular versions are a uniform filter, where *G* does not depend on $\boldsymbol{x}$, and isotropic, where the dependence on $\boldsymbol{r}$ is limited to the dependence on its absolute value *r*

$$G(r) = \begin{cases} 1/\Delta & \text{if} \quad r < \Delta/2 \\ 0 & \text{if} \quad r > \Delta/2 \end{cases}$$

(3-28)

and the Gaussian filter

$$G(r) = \left(\frac{6}{\pi\Delta^2}\right)^{\frac{1}{2}} exp\left(-\frac{6r^2}{\Delta^2}\right)$$

(3-29)

The isotopic filtering operations is simply a weighted and localized averaging, in the sphere of diameter Δ. Fluctuations with length scales significantly smaller than Δ are smoothed out. The result is the smallest scales remaining in the filtered signal are of the order of Δ. This is the reason for the computational efficiency of LES.

The relationship between the filter width and grid steps in taken as far as assuming near identity between them. The filtered fields, $\bar{\boldsymbol{u}}$, are called resolved fields, and the term subgrid-scale can be used for the filtered out fluctuations

$$\boldsymbol{u'} = \boldsymbol{u} - \bar{\boldsymbol{u}}$$

(3-30)

Assuming the grid steps are different size than the filter width the appropriate terms in this case are filtered fields for $\bar{\boldsymbol{u}}$ and residual fields for $\boldsymbol{u'}$.

$$\overline{\left(\frac{\partial u}{\partial t}\right)} = \int G(\boldsymbol{r}, \boldsymbol{x}) \frac{\partial u}{\partial t}(\boldsymbol{x} - \boldsymbol{r}, t) d\boldsymbol{r}$$

(3-31)

$$= \frac{\partial}{\partial t} \int G(\boldsymbol{r}, \boldsymbol{x}) u(\boldsymbol{x} - \boldsymbol{r}, t) d\boldsymbol{r} = \frac{\partial \bar{u}}{\partial t}$$

(3-32)

The result of the filtering for the Navier-Stokes equation

$$\rho \frac{\partial \bar{u}_i}{\partial t} + \rho \frac{\partial}{\partial x_j}\left(\overline{u_i u_j}\right) = -\frac{\partial \bar{p}}{\partial x_i} + \mu \nabla^2 \bar{u}_i$$

(3-33)

$$\frac{\partial \bar{u}_i}{\partial x_i} = 0$$

(3-34)

The above equations is the main challenge of LES due to the nonlinearity of the momentum equation. The filtered product of $\overline{u_i u_j}$ cannot be expressed as a function of the filtered velocity, for example

$$\overline{u_i u_j} \neq \bar{u}_i \bar{u}_j$$

(3-35)

Rewriting the filtered equations

$$\rho \frac{\partial \bar{u}_i}{\partial t} + \rho \frac{\partial}{\partial x_j}\left(\bar{u}_i \bar{u}_j\right) = -\frac{\partial \bar{p}}{\partial x_i} + \mu \nabla^2 \bar{u}_i - \frac{\partial \tau_{ij}^R}{\partial x_j}$$

(3-36)

$$\frac{\partial \bar{u}_i}{\partial x_i} = 0$$

(3-37)

where

$$\tau_{ij}^R \equiv \rho\overline{u_i u_j} - \rho\bar{u}_i\bar{u}_j$$

(3-38)

is the residual stress tensor.

This only includes the effects of fluctuations with length scales smaller than the LES filter width.

By expanding the τ_{ij}^R term as a sum of anisotropic and trace parts

$$\tau_{ij}^R = \tau_{ij}^r + \frac{1}{3}\delta_{ij}\tau_{ii}^R$$

(3-39)

and by introducing the modified pressure field

$$\bar{p}^* = \bar{p} + \frac{1}{3}\tau_{ii}^R$$

(3-40)

the final LES equation becomes

$$\rho\frac{\partial \bar{u}_i}{\partial t} + \rho\frac{\partial}{\partial x_j}\left(\bar{u}_i\bar{u}_j\right) = -\frac{\partial \bar{p}^*}{\partial x_i} + \mu\nabla^2\bar{u}_i - \frac{\partial \tau_{ij}^r}{\partial x_j}$$

(3-41)

$$\frac{\partial \bar{u}_i}{\partial x_i} = 0$$

(3-42)

The LES equations listed above is not a closed system. To obtain a numerical solution the stress tensor τ_{ij}^r will need to be modelled in terms of the filtered flow fields.

3.3.3 Closure Models

Models used to approximate the stress tensor τ_{ij}^r are called closure and subgrid-scale models. The first name comes from the fact that the model closes the LES equations to allow them to be solved numerically. The latter name reflects the fact that the stress tensor τ_{ij}^r represents the effect of the residual, or subgrid-scale, fluctuations on the filtered part of the flow.

Three things are required from a model. First, the model must provide true closure. An approximation of the stress tensor τ_{ij}^r should depend only on filtered flow fields and known parameters such as the filter width. Second is a geometric requirement in which a model is invariant to the principal coordinate transformations. In other words a model should represent the effect of residual fluctuations as accurately as possible. And lastly, the model should provide an energy sink of the appropriate strength at the length scale approximately equal to the filter width since the small-scale fluctuations are not simulated in LES.

There exist many closure models. One of the simplest and oldest models is the Smagorinsky model which was proposed in 1963. This model has served as a basis for many other more advanced models.

The eddy viscosity hypothesis is used in the Smagorinsky model:

$$\tau_{ij}^r = -2\mu_t \bar{S}_{ij} \tag{3-43}$$

where $\mu_t(\boldsymbol{x}, t)$ is the turbulent eddy viscosity, and

$$\bar{S}_{ij} \equiv \frac{1}{2}\left(\frac{\partial \bar{u}_i}{\partial x_j} + \frac{\partial \bar{u}_j}{\partial x_i}\right)$$

(3-44)

is the rate of strain tensor of the filtered flow.

The eddy viscosity is modeled as, based on the Prandtl's mixing length theory:

$$\mu_t(\boldsymbol{x}, t) = \rho \ell_S^2 |\bar{S}| = \rho (C_S \Delta)^2 |\bar{S}|$$

(3-45)

where

$$|\bar{S}| = \left(2 S_{ij} S_{ij}\right)^{1/2}$$

(3-46)

where the summation over *i* and *j* are assumed.

The filter width Δ and the empirical Smagorinsky constant C_S is used as an approximation the characteristic length scale $\mathbf{l}_s$. The rate of energy sink by the closure model is

$$P_t = -\tau_{ij}^r \bar{S}_{ij} = 2\mu_t \bar{S}_{ij} \bar{S}_{ij} = \mu_t |\bar{S}|^2$$

(3-47)

The Smagorinsky model is not difficult to implement numerically. A filtered flow computed at a previous time step can be used or extrapolated from a number of previous time steps to evaluate the terms $\bar{S}_{ij}$ and $|\bar{S}|$. These results are put into the above equations to compute the eddy viscosity and residual tensor. The filter width Δ is usually assumed to be the typical grid cell size and is estimated as $\Delta = (\Delta x \Delta y \Delta z)^{1/3}$.

The popularity of the Smagorinsky model is due to its simplicity and computational efficiency. The model does have its downsides related to its accuracy and flexibility when compared to more complex models. A single optimal value or a functional dependency of the Smagorinsky constant C_S has no theoretical origin.

3.3.4 Modelling Theory and Assumptions

As noted above, the rationale behind the large-eddy simulation technique is to separate the large scale eddies from the small scale eddies (ANSYS, 2010b). The time-dependent Navier-Stokes equations are filtered to obtain the governing equations for LES. The eddies whose scales are smaller than the filter width or grid spacing used in the computations are effectively filtered out. The dynamics of the large eddies are governed by the resulting equations.

A filtered variable is denoted by an overbar as outlined below:

$$\bar{\Phi}(x) = \int_D \Phi(x')G(x,x')\,dx' \tag{3-48}$$

where *D* is the fluid domain, and

G is the filter function that determines the scale of the resolved eddies.

For the unresolved part of the quantity Φ:

$$\Phi' = \Phi - \bar{\Phi} \tag{3-49}$$

And the filtered fluctuations are not zero:

$$\overline{\Phi'} \neq 0 \tag{3-50}$$

The filtering operation is implicitly provided by the discretization of the spatial domain into finite control volumes:

$$\bar{\Phi}(x) = \frac{1}{V}\int_V \Phi(x')\,dx' \tag{3-51}$$

$$x' \in V$$

where V is the control volume.

The filter function implied here is

$$G(x;x') = \begin{cases} 1/V\,, x' \in V \\ 0\ otherwise \end{cases}$$

(3-52)

Additional unknown quantities are a result of filtering the Navier-Stokes equations. The filtered momentum equation for incompressible flow can be expressed as:

$$\frac{\partial \bar{U}_\iota}{\partial t} + \frac{\partial}{\partial x_j}\left(\bar{U}_\iota \bar{U}_J\right) = -\frac{1}{\rho}\frac{\partial \bar{p}}{\partial x_i} + \frac{\partial}{\partial x_j}\left[\nu\left(\frac{\partial \bar{U}_\iota}{\partial x_j} + \frac{\partial \bar{U}_J}{\partial x_i}\right)\right] - \frac{\partial \tau_{ij}}{\partial x_j}$$

(3-53)

where τ_{ij} denotes the subgrid-scale stress.

It includes the effect of the small scales and is defined by

$$\tau_{ij} = \overline{U_\iota U_J} - \bar{U}_i \bar{U}_j$$

(3-54)

The influence of the small scales is taken into account by appropriate subgrid-scale (SGS) models and the large scale turbulent flow is solved directly. An eddy viscosity approach is used which relates the subgrid-scale stresses τ_{ij} to the large-scale strain rate tensor $\bar{S}_{ij}$:

$$-\left(\tau_{ij} - \frac{\delta_{ij}}{3}\tau_{kk}\right) = 2\nu_{sgs}\bar{S}_{ij}$$

(3-55)

$$\bar{S}_{ij} = \frac{1}{2}\left(\frac{\partial \bar{U}_i}{\partial x_j} + \frac{\partial U_j}{\partial x_i}\right)$$

(3-56)

The isotropic part of τ_{kk} are added to the filtered static pressure and not modelled.

The Dynamic Smagorinsky-Lilly model was used in this study. In order to overcome the deficiencies of the Smagorinsky model (Germano et al., 1991), the Dynamic Smagorinsky-Lilly model (Lilly, 1992) is based on the Germano-identity, and uses information contained in the resolved turbulent velocity field to evaluate the model coefficient. The model coefficient adjusts automatically with the flow type, and as a result is no longer a constant value. This method is more time consuming as it requires explicit (secondary) filtering.

3.4 Circular Cylinder Computational Geometry

For the current research a cable model was created with a diameter (D) of 0.089 m and a length (L) of 30D. The inclination angle (α) and the yaw angle (β) were used to orient the cylinder in regard to the wind flow direction. The inclination angle is defined as the angle of rotation of the cable in the vertical plane, and the yaw angle describes the rotation of its projection in the horizontal plane as shown in Figure 3.1. In order to capture the instantaneous and average pressure coefficients, and aerodynamic forces coefficients profiles around the circumference of the cylinder 5 rings of 36 points each were created at intervals of 5D centred at the midspan of the cylinder. Velocity vectors and streamlines visualizations were also captured for middle rings of the cylinder, and eddy viscosity profiles were as a representation of the turbulence around the cylinder. Detailed records of axial velocity (along the cable axis), and along wind velocity were extracted on the leeward side of the cylinder at intervals 0.1D, 0.2D, 0.3D, 0.4D, and 0.5D downstream the cylinder, in order to determine the characteristics of the flow directionality in this area.

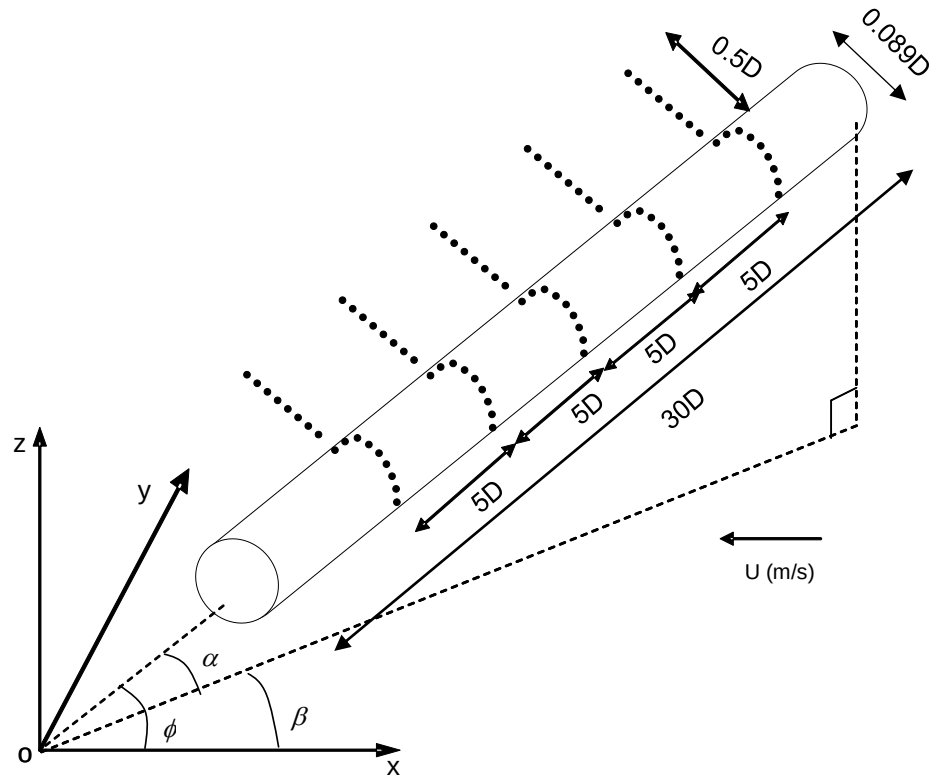


Figure 3.1: Details of the geometry and monitoring points for the cylinder model

The relative angle of attack ϕ is considered as the angle between the wind flow and the cable measured in the plane of the flow which was determined based on the following equation (Cheng et al. 2008)

$$\cos\phi = \cos\alpha \cos\beta \tag{3-57}$$

where ϕ is uniquely given for a given set of α and β

This is an important parameter in modeling as it best describes how the wind 'sees' the cylinder as it approaches, and the resulting flow around the cylinder.

3.5 Circular Cylinder Computational Mesh

The computational domain employed for the present investigation is a closed space rectangular field extending 30D along the length of the cylinder L, 22.5D in the direction of flow,

11.25D upstream and downstream from the center of the cylinder, and 22.5D in the direction perpendicular to the direction of flow centered around the cylinder, as illustrated in Figure 3.2(a) below. The height of the domain changed with the inclination of the cylinder to match the cylinder length of 30D. A tetrahedral mesh with over 3,000,000 cells were used for the entire domain with over 200,000 elements for the mesh of the cylinder surface, as outlined in the table below for each inclination and yaw angle combination in this study. A number of Re were examined for each of the cases listed. Figure 3.2(b) shows the mesh in greater detail.

Table 3-1: Number of elements per simulation case

Inclination angle α (deg)	Yaw angle β (deg)	Relative angle of attack, ϕ (deg)	Number of Mesh Elements	Number of Element on Cylinder
0	0	0	3444162	234433
60	0	60	3028457	250080
60	20	62	3374249	237516
60	40	67.5	3406126	247444
54.7	0	54.7	3265166	252528
54.7	20	57.1	3339564	253262
54.7	40	64	3459561	252294
50	20	53	3498177	234052
50	40	60.5	3500466	234252
30	20	35.5	3130210	231534

The cable models were exposed to various wind speeds ranging between 18.0 m/s to 90.3 m/s resulting in high Reynolds numbers of $Re = 1.1 \times 10^5 – 6.7 \times 10^5$. This is assuming a smooth circular cylinder which is modelled in this study. These values are characteristic to the precritical regime of the TrBL (Transition in Boundary Layers) flow regime as defined by Zdravkovich (1997), and as detailed above. This regime is characterized by the abrupt decrease in drag force as

a result of an increase in wind speed, and is known as the drag crisis (Simiu and Scanlan, 1987; Zdravkovich, 1997).

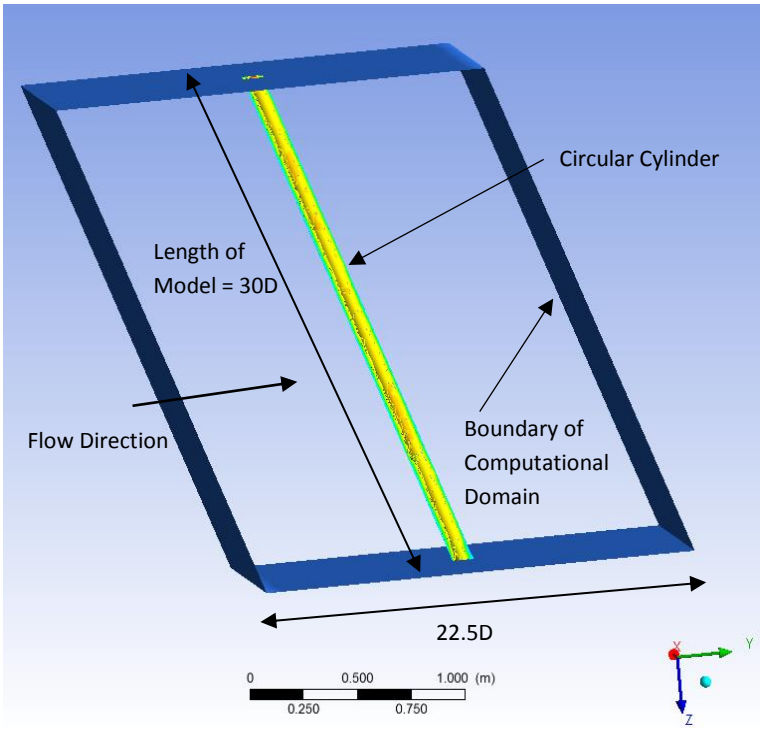


Figure 3.2(a) Cylinder model and computational domain

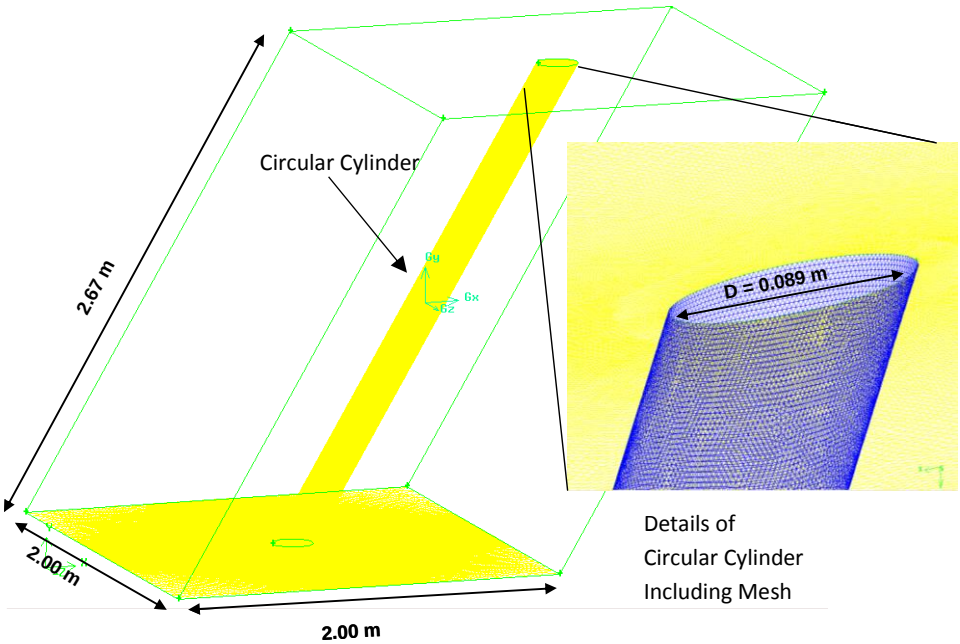


Figure 3.2 (b) Computational domain details

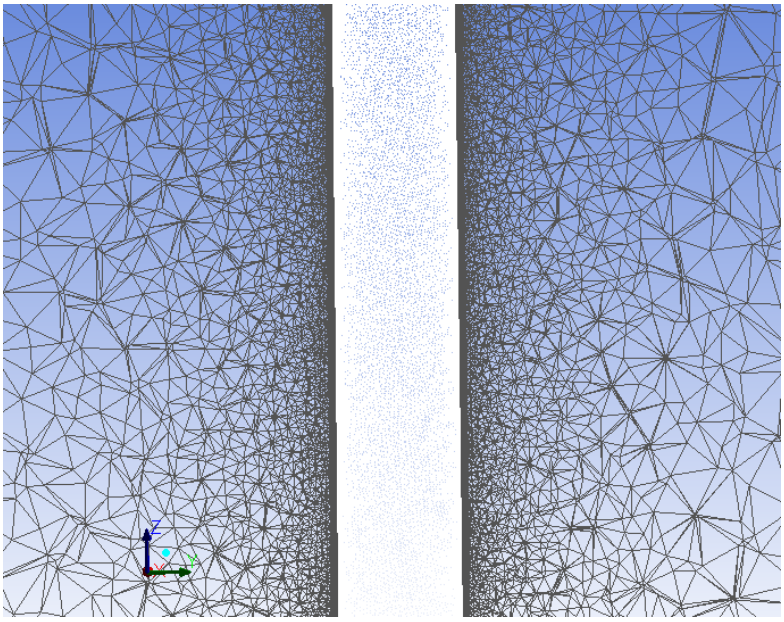


Figure 3.3 (a) Mesh details for flow perpendicular to the cylinder

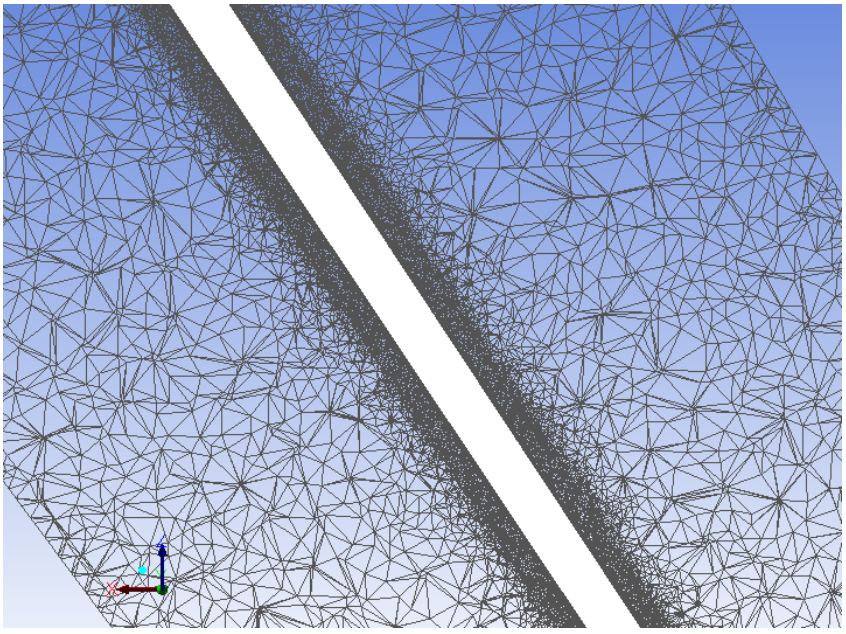


Figure 3.3 (b) Mesh details for cylinder inclined to flow

Several combinations of inclinaiton and yaw angles were investigated at various Re numbers for a total of 52 cases as outlined in the Table 3.2 below, where the cases simulated in this study are indicated by the mark "X". The relative angle of 60° was identified as a critical angle for different yaw angles (Saito et al (1994) and Cheng et al (2011)), therefore the inclination

and yaw angles of interest considered in the current research were selected such that would concentrate around these values. The relative angle of attack was determined using the inclination angle, yaw angle, and Equation 3-57 to calculate the angle between the approaching wind and the inclined/yawed cable.

Table 3-2: Performed cases for cable model orientations at various Re numbers

Inclination angle α (deg)	Yaw angle β (deg)	Relative angle of attack, ϕ (deg)	Re = 1.1 $\times 10^5$	Re = 2.2 $\times 10^5$	Re = 3.3 $\times 10^5$	Re = 4.4 $\times 10^5$	Re = 5.5 $\times 10^5$	Re = 6.7 $\times 10^5$
0	0	0	X	X	X	X	X	X
60	0	60	X	X	X	X	X	X
60	20	62	X	X	X	X	X	N/A
60	40	67.5	X	X	X	X	X	N/A
54.7	0	54.7	X	X	X	X	X	N/A
54.7	20	57.1	X	X	X	X	X	N/A
54.7	40	64	X	X	X	X	X	N/A
50	20	53	X	X	X	X	X	N/A
50	40	60.5	X	X	X	X	X	N/A
30	20	35.5	X	X	X	X	X	N/A

To achieve a faster convergence a laminar model was initially used followed by a *k-ε* model to initialize the flow. To develop the flow the LES model with the Smagorinsky-Lilly algorithm for the eddy viscosity at subgrid-scale was employed. The advection term in non-dimensional Navier-Stokes equations was discretized with the finite difference method (FDM) and was solved through a second-order implicit time integration. Spatial discretization was estimated through the second-order upwind scheme and the diffusion term in the transport equation was discretized through central-differenced method. A Smagorinsky constant of $C_s = 0.1$ was considered, and the non-dimensional time step Δt was set to 0.01. The filter width was taken as the cubic-root of grid volume. The continuous x-component velocity for the inflow condition and advection-viscous condition for the outflow region were employed. The cylinder had the no slip, no penetration

conditions while along the walls a solely no penetration condition was considered. Built-in modules within the Fluent Ansys Software were used for the application of the above mentioned algorithms.

The current study uses the turbulent LES model throughout the entire domain with Smagorinsky model for turbulent viscosity. Several cases of perpendicular, and inclined/yawed circular cylinders of diameter D = 0.089 m, and length of 30D = 2.67 m, for high Re numbers from 1.1×10^5 to 6.7×10^5 were investigated. Aerodynamic characteristics of inclined/yawed slender cylinders, and the three-dimensional character of the axial flow which appeared for certain cases are discussed.

This size of mesh for the computational domain was chosen as a balance between the convergence rate of the model, computational time of the model, and accuaracy of the model. Increasing the number of elements in the model in Fluent would significantly increase the computational time required for the model with minimal change on the results obtained.

In deciding on the size of the compuational domain for this study, two studies were used in balancing the size of the domain with the compuational requirements to model the flow. As discussed in the literature review, Qingkuan et al (2007) simulated the flow around a cable model with a water rivulet on the cable surface using large eddy simulation using a circular computational domain with dimensions of 20D × 20D × 0.2D. Using a slightly larger domain, Yeo and Jones (2008) performed a three-dimensional detached eddy simulation to investigate the three-dimensional characteristic flow past a yawed and inclined circular cylinder using varying length of the cylinder. The resulting domain was 40D × 40D × 30D with the analysis on the flow structures developing around and downstream of the cylinder giving the best results due to the length of the cylinder used of 30D. For this study, a balance between the two domains mentioned

above were used to concentrate on the flow around and along the leeward side of the cylinder while also focussing the computational power at this location.

3.6 Comparison of Laminar Flow, k-ε Model and LES Models

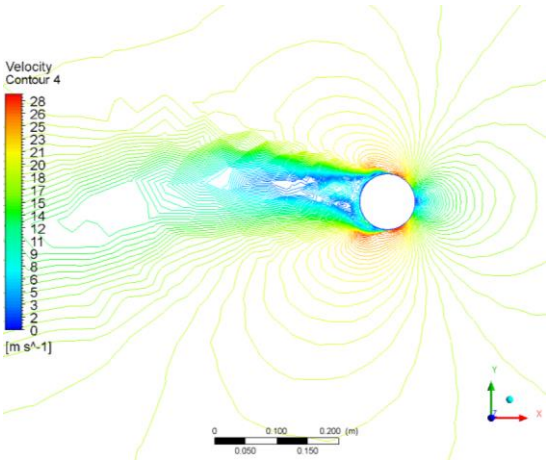
As mentioned above, a laminar, inviscid model was initially used followed by a k-ε model to initialize the flow to achive a faster convergence. To develop the flow the LES model with the Smagorinsky-Lilly algorithm for the eddy viscosity at subgrid-scale was employed. The results of the three modelling techniques are presented in this section, and compared with flow visualizations from wind tunnel studies to show the convergence of the flow around a circular cylinder with the use of the LES model.

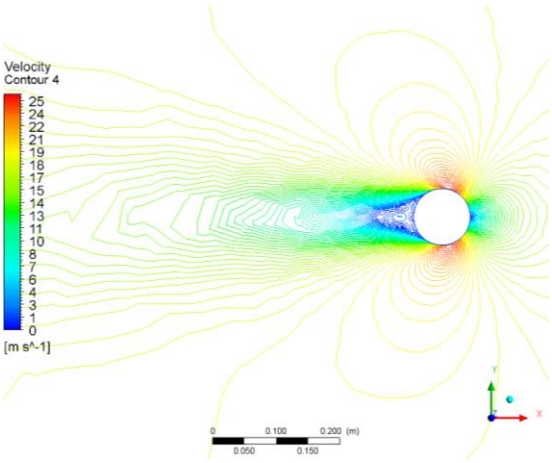
3.6.1 Study Results for Flow Velocity and Eddy Viscosity

The results of the models for the standard and well-studied case of flow perpendicular to the cylinder, $\alpha = 0°$, $\beta = 0°$, for Re = 1.1×10^5, Re = 2.2×10^5, Re = 3.3×10^5, and Re = 4.4×10^5 are presented in this section, and compared with published the flow visualizations. The results for other cases of $\alpha = 0°$, $\beta = 0°$, for Re = 5.5×10^5, and Re = 6.7×10^5 as well as the 6 cases of $\alpha = 60°$, $\beta = 0°$, for Re = 1.1×10^5, Re = 2.2×10^5, Re = 3.3×10^5, Re = 4.4×10^5, Re = 5.5×10^5, and Re = 6.7×10^5 are presented in Appendix Q. Velocity profiles are shown in two different planes for each of the computational models used in the study. One plane cuts a section through the circular cylinder parallel to the flow and perpendicular to the cylinder for flow perpendicular to the cylinder, and at an angle to the cylinder for the case of the circular cylinder inclined to the flow at the same angle of the flow, in Figure 3.4. The flow is from right to left. The other plane also is in the direction of flow but cuts the length of the circular cylinder, in Figure 3.5. The flow for this case is left to right. The eddy viscosity is shown for the k-ε and LES models for which the flow is shown right to left, in Figure 3.6.

3.6.2 Comparison of Study Results with Published Data

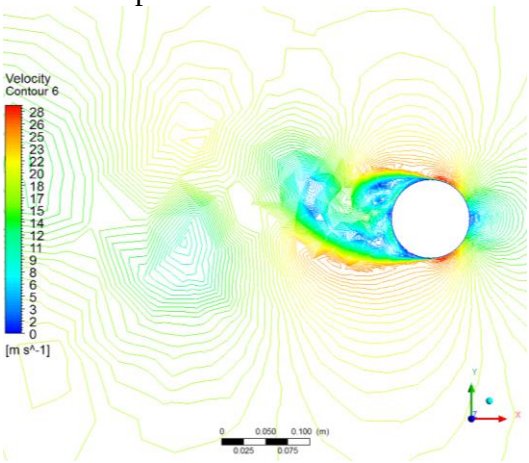
The velocity profile results of the models for the flow prependicular to the cylinder, α = 0°, β = 0°, for Re = 1.1 × 10^5 are presented in Figure 3.4(a), and compared with the flow visualization showing the transition in the shear layers for flow around a circular cylinder for a Re = 1.1 × 10^5 (Zdravkovich, 1997). The velocity profiles for the laminar option and the k-ε model produce wake region on the leeward side of the cylinder showing little to no recirculation within the region, with the laminar option producing the longer tail. The velocity results using the LES model shows a recirculation zone near to the leeward side of the cylinder, and the vortex strength diminishes as the flow move downstream of the circular cylinder. This is similar to the visualization from (Zdravkovich, 1997) for the same Re = 1.1 × 10^5 except the recirculation zone is shorter in the visualization.



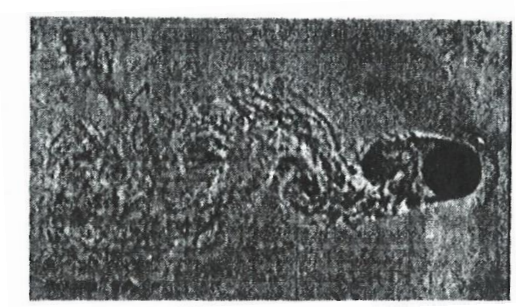


Velocity profiles, $\alpha = 0°$, $\beta = 0°$, Re = 1.1×10^5.
Laminar option

Velocity profiles, $\alpha = 0°$, $\beta = 0°$, Re = 1.1×10^5.
k-ε model

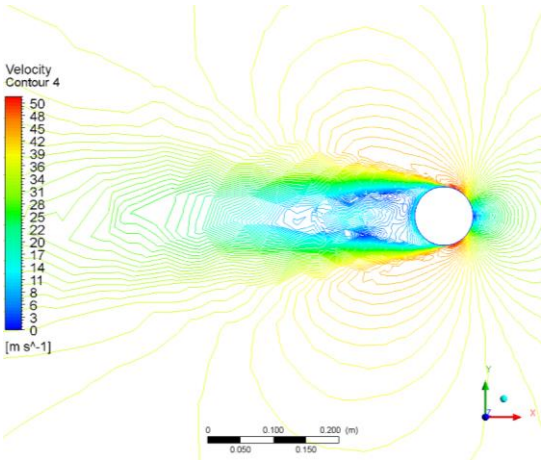


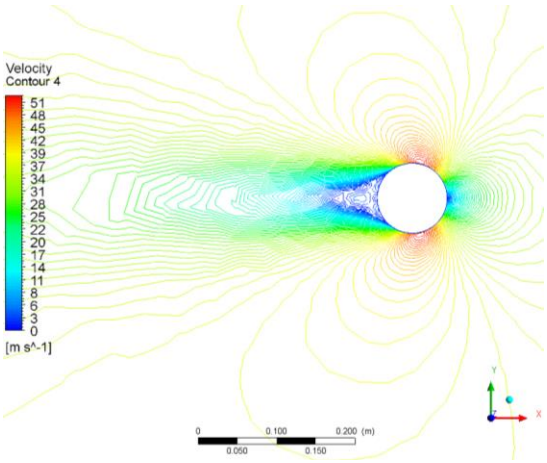
a) Velocity profiles, $\alpha = 0°$, $\beta = 0°$, Re = 1.1×10^5.
LES model



Transition in free shear layers,
Re = 1.1×10^5 (Zdravkovich, 1997)

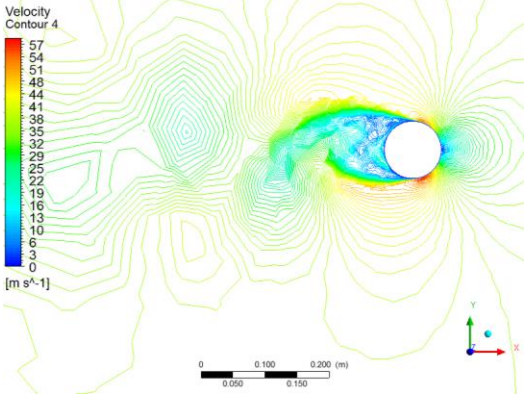
Figure 3.4: Study results for $\alpha = 0°$, $\beta = 0°$, Re = 1.1×10^5, compared to flow visualizations for $\phi = 0°$, Re = 1.1×10^5.



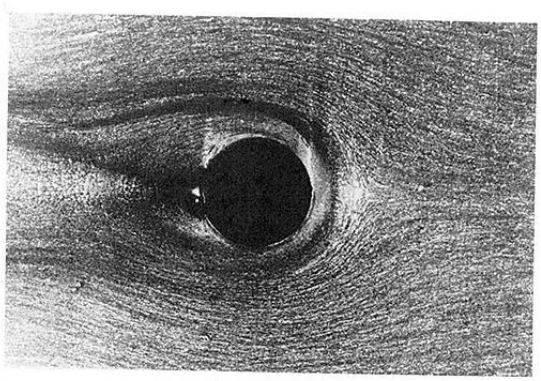


Velocity profiles, $\alpha = 0°$, $\beta = 0°$, Re = 2.2×10^5.
Laminar option

Velocity profiles, $\alpha = 0°$, $\beta = 0°$, Re = 2.2×10^5.
k-ε model



b) Velocity profiles, $\alpha = 0°$, $\beta = 0°$, Re = 2.2×10^5.
LES model

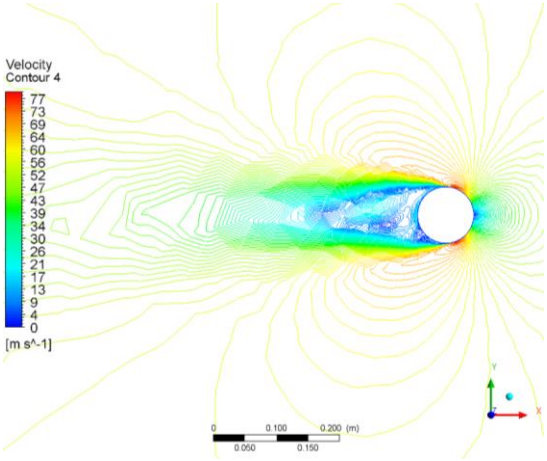


Flow visualization, Re = 2.0×10^5.
(Zdravkovich, 1997)

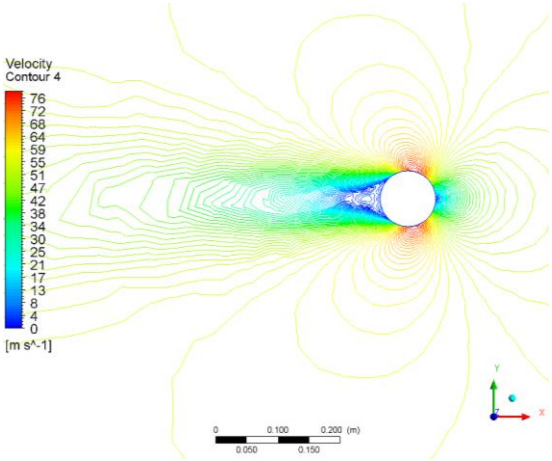
Figure 3.4: Study results for $\alpha = 0°$, $\beta = 0°$, Re = 2.2×10^5, compared to flow visualizations for $\phi = 0°$, Re = 2.0×10^5.

The velocity profiles for the flow perpendicular to the cylinder, $\alpha = 0°$, $\beta = 0°$, for Re = 2.2×10^5 are compared in Figure 3.4(b) with the flow visualization Re = 2.0×10^5 (Coutanceau and Defaye, 1991) which is presented separately from the visualizations for other Reynolds number for comparison purposes. It should be noted that there is a small area retarted flow directly behind the circular cylinder. This area is of substantial length in the model using the laminar option, shorter in length in the model using the k-ε model, and shorter yet, and of similar length when using the LES model when compared to the flow visualization.

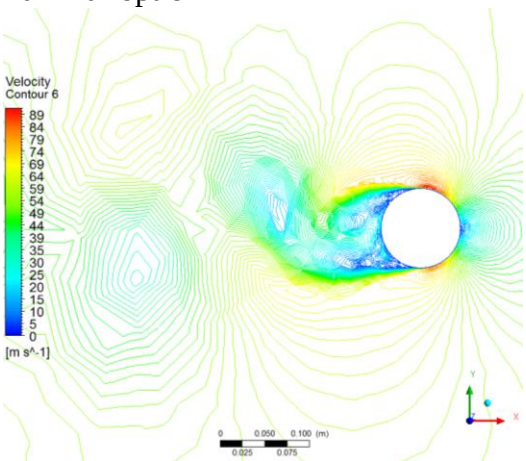
The velocity profiles along the length of the cylinder, eddy viscosity and pressure profiles around the circumference of the cylinder for Re = 2.2×10^5 show similar patterns in the data as described above for Re = 1.1×10^5. The variation of the flow along the length of the cylinder for the simulation using the LES model matching the velocity profiles mentioned above, eddy viscosity distribution on the leeward side of the cylinder for the LES model, and the pressure distribution varying from a coefficient of pressure of 1 on the windward side to a variation of the distribution on the leeward side of the circular cylinder.



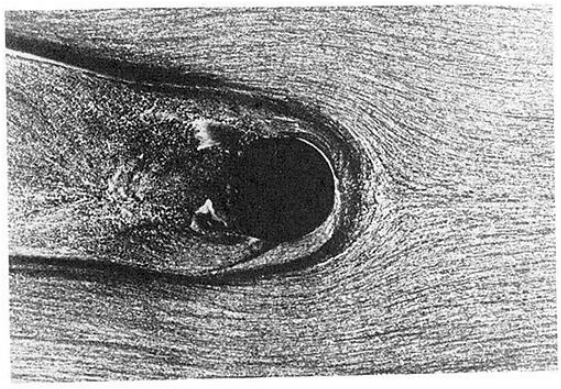
Velocity profiles, $\alpha = 0°$, $\beta = 0°$, Re = 3.3×10^5.
Laminar option



k-ε model



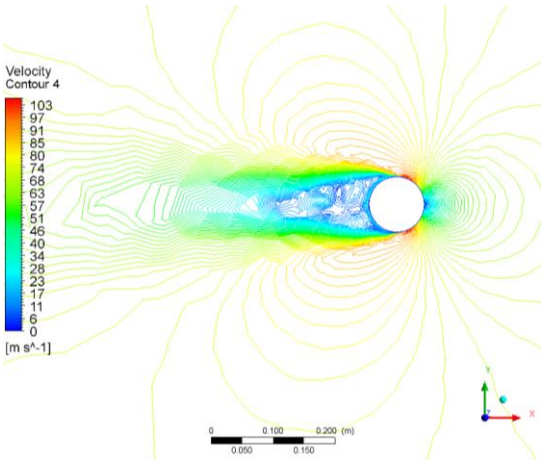
c) Velocity profiles, $\alpha = 0°$, $\beta = 0°$, Re = 3.3×10^5.
LES model

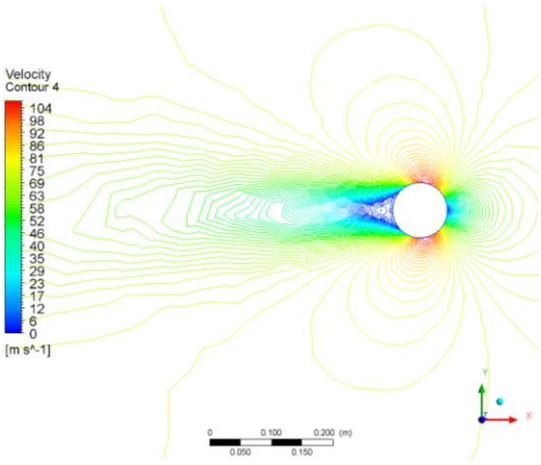


Flow visualization, Re = 3.0×10^5.
(Zdravkovich, 1997)

Figure 3.4: Study results for $\alpha = 0°$, $\beta = 0°$, Re = 3.3×10^5, compared to flow visualizations for $\phi = 0°$, Re = 3.0×10^5.

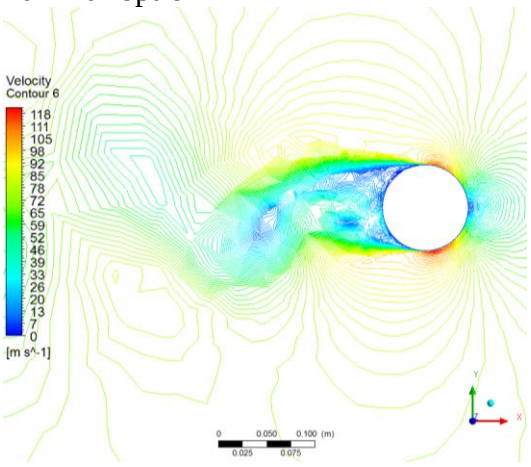
The velocity profiles for the flow perpendicular to the cylinder, $\alpha = 0°$, $\beta = 0°$, for Re = 3.3×10^5 in Figure 3.4(c) are compared with the flow visualization Re = 3.0×10^5 (Coutanceau and Defaye, 1991) which is presented separately from the visualizations for other Reynolds number for comparison purposes. As seen above for the flow of Re = 2.2×10^5, the length of the wake region changes from the longest point for the laminar option to the shortest and most similar to the flow visualization for the LES model.

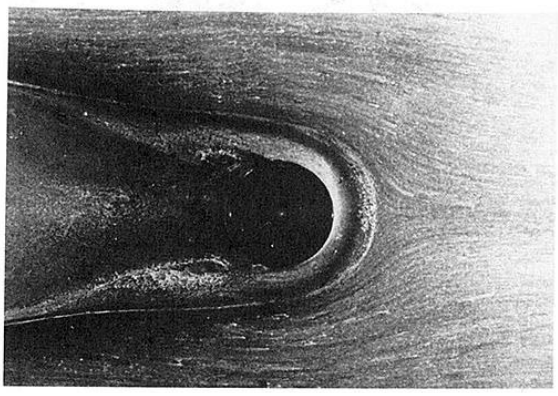




Velocity profiles, $\alpha = 0°$, $\beta = 0°$, Re = 4.4×10^5.
Laminar option

Velocity profiles, $\alpha = 0°$, $\beta = 0°$, Re = 4.4×10^5.
k-ε model





d) Velocity profiles, $\alpha = 0°$, $\beta = 0°$, Re = 4.4×10^5.
LES model

Flow visualization, Re = 4.0×10^5.
(Zdravkovich, 1997)

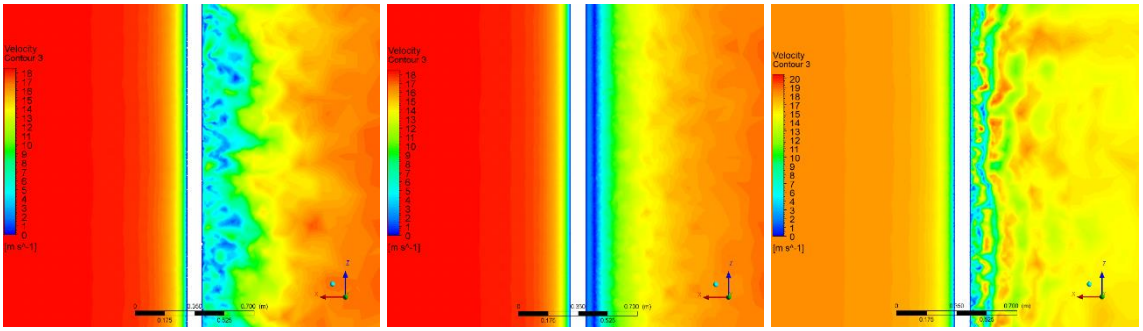
Figure 3.4: Study results for $\alpha = 0°$, $\beta = 0°$, Re = 4.4×10^5, compared to flow visualizations for $\phi = 0°$, Re = 4.0×10^5.

The velocity profiles for the flow perpendicular to the cylinder, $\alpha = 0°$, $\beta = 0°$, for Re = 4.4×10^5 in Figure 3.4(d) are compared with the flow visualization Re = 4.0×10^5 (Coutanceau and Defaye, 1991). Again, the length of the wake from the cylinder changes with computational model used. The length of the wake changes from the longest wake for the laminar option to a shorter wake for the k-ε model. For the LES computational model, the wake is wider when compared to the widths of the laminar option and the k-ε model. This matches the flow visualization for Re = 4.0×10^5 (Coutanceau and Defaye, 1991) which also has a wider wake on the leeward side of the circular cylinder. There is a wider region of increased flow velocity on both sides of the wake when compared with the lower Reynolds numbers which is similar to what is being seen in the flow visualization. The velocity profiles along the length of the cylinder and the eddy viscosity show similar tendencies with the results from the lower Reynolds numbers. The same results occur for the pressure profiles around the circumference of the cylinder with the exception of the pressure coefficient for the k-ε model is now 1 instead of being greater than 1 as seen for the lower Reynolds numbers.

The velocity profiles along the length of the cylinder shown in Figure 3.5 illustrates a variation in the velocity along the leeward side of the cylinder for the model using the laminar option. The velocity profile is much more consistent along the leeward side of the model using the k-ε model. The variation of the velocity returns for the distribution produced by the LES model showing the variation in the recirculation length along the length of the circular cylinder as seen in the LES model velocity distribution and flow visualization shown previously.

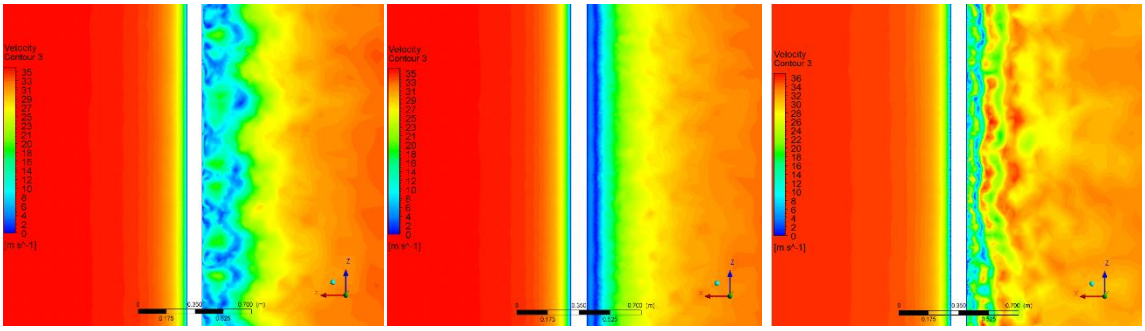
The results for eddy viscosity around the cylinder are shown in Figure 3.6. As the laminar flow calculations are governed by the unsteady Navier-Stokes equations, there is no turbulence model applied to the simulation resulting in no eddy viscosity calculations shown here. The eddy

viscosity for the k-ε model an area of high viscosity in front of the circular cylinder and a symmetric distribution on either side of the cylinder, which is not the expected flow development around the cylinder. This is not the expected flow around a cylinder. The variation in the eddy viscosity for the LES model shows a variation in distribution in the wake of the circular cylinder due to the turbulence created in this area. This variation between the two models comes from the assumptions made in the formulation of the models, and the assumptions made for the eddy viscosity calculations. This illustrates that the k-ε turbulence models are denoted as low Reynolds number models, as stated above.



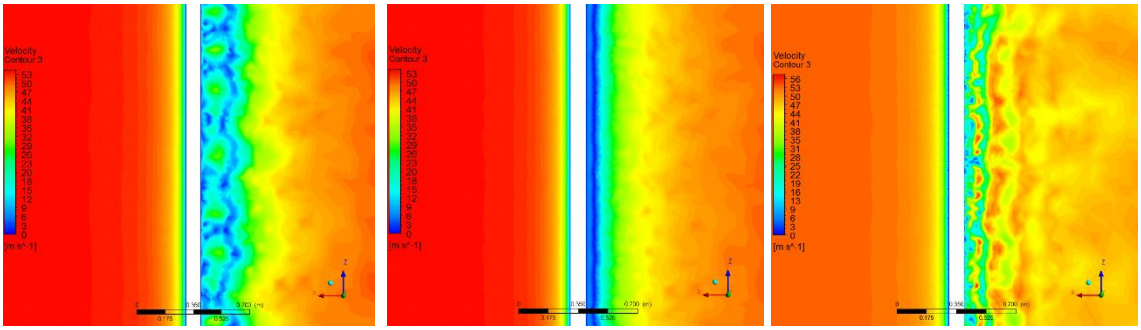
Laminar option k-ε model LES model

Figure 3.5: Study results for $\alpha = 0°$, $\beta = 0°$, Re = 1.1×10^5, i) velocity profiles.



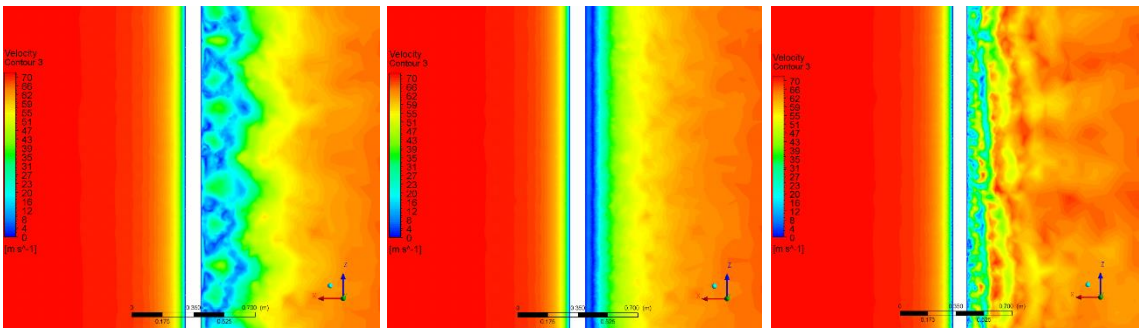
Laminar option k-ε model LES model

Figure 3.5: Study results for $\alpha = 0°$, $\beta = 0°$, Re = 2.2×10^5, ii) velocity profiles.



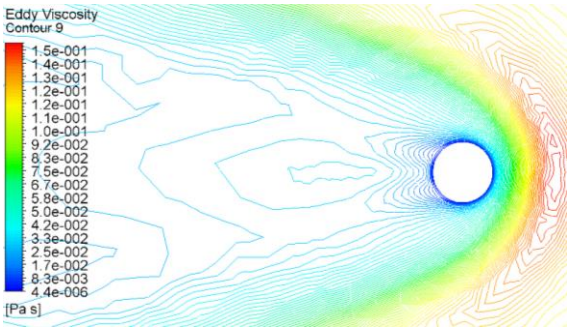
Laminar option k-ε model LES model

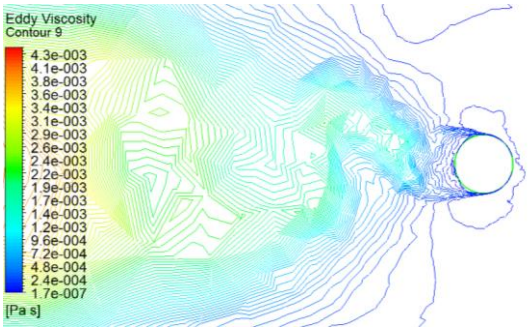
Figure 3.5: Study results for $\alpha = 0°$, $\beta = 0°$, Re = 3.3×10^5, iii) velocity profiles.



Laminar option k-ε model LES model

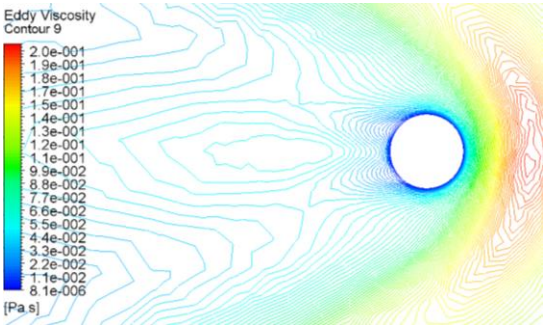
Figure 3.5: Study results for $\alpha = 0°$, $\beta = 0°$, Re = 4.4×10^5, iv) velocity profiles.

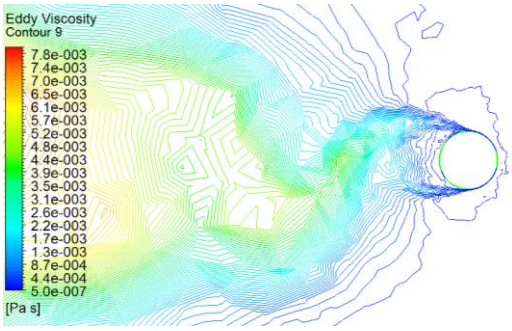




k-ε model LES model

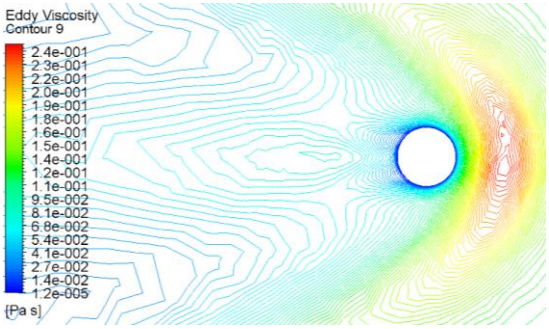
Figure 3.6: Study results for $\alpha = 0°$, $\beta = 0°$, Re = 1.1×10^5, i) eddy viscosity.

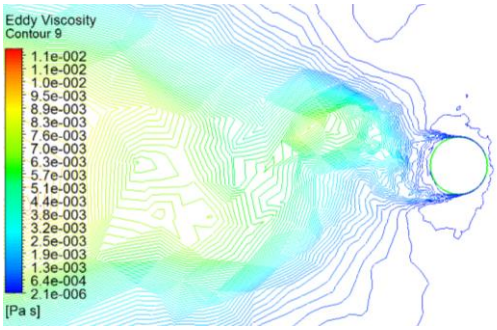




k-ε model LES model

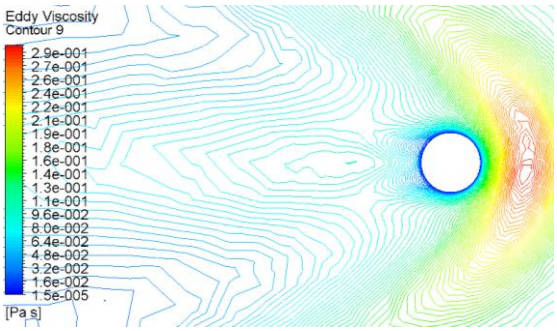
Figure 3.6: Study results for $\alpha = 0°$, $\beta = 0°$, Re = 2.2×10^5, ii) eddy viscosity.

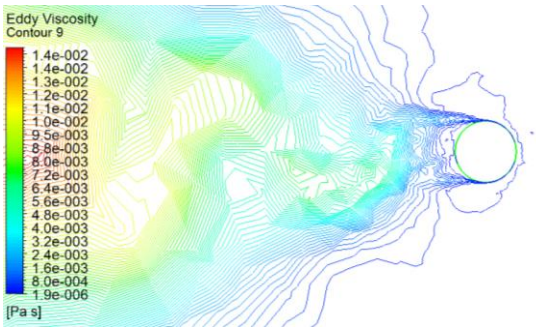




k-ε model LES model

Figure 3.6: Study results for $\alpha = 0°$, $\beta = 0°$, Re = 3.3×10^5, iii) eddy viscosity.





k-ε model LES model

Figure 3.6: Study results for $\alpha = 0°$, $\beta = 0°$, Re = 4.4×10^5, iv) eddy viscosity.

3.7 Model Validation for Flow around a Circular Cylinder

The results for the coefficients of drag (C_D), coefficients of lift (C_L), and pressure around the circumference of the circular cylinder are presented for the current study. The data is validated against currently available experimental data.

The validation was chosen for flow perpendicular to the cylinder, and for the cylinder inclined to the flow at 60°, as these cases provided the most published literature for comparison and validation. The flow perpendicular to the cylinder is highly studied and well understood. The range of Reynolds numbers provide for cases before, though, and following the drag crisis, and is the areas of interest in this study for all cases.

3.7.1 Coefficient of Drag Force on a Circular Cylinder

The drag crisis for flow perpendicular to circular cylinders was reported by Scruton et al. (1963), and later by Zdravkovich (1997). The decay of the drag coefficient begins around Reynolds number of 1.2×10^5, and does not begin to recover until a Reynolds number of 5.0×10^5 (ESDU, 1980). A similar result phenomena occurs for cylinders inclined to the flow. Recent wind tunnel studies have been performed, and obtain the same drag crisis with a drop in the drag coefficient from 0.8 to 0.2 within a similar Reynolds number range (Zurrel, 2004). In order to express the drag along the structural axes of the cylinder the aerodynamic drag coefficients for the inclined models were normalized with squared value of $\sin(\beta)$ as recommended in ESDU (1980), and in FHWA (2005).

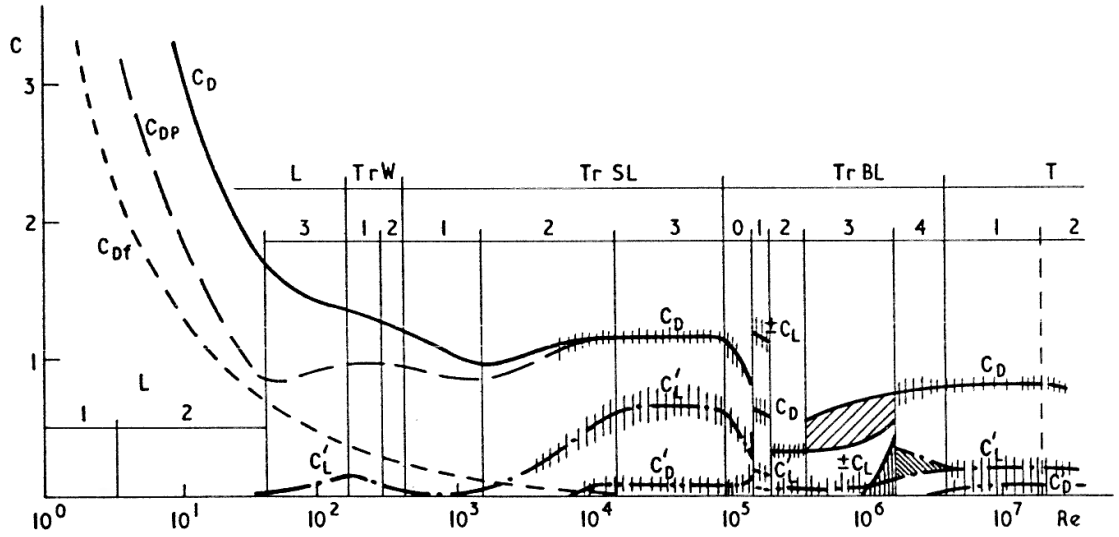


Figure 3.7: Variation of aerodynamic force coefficients for disturbance-free flow (reproduced from Zdravkovich, 1997)

The results of this study are presented in Figure 3.8 below. The results are separated into different yaw angles tested: flow perpendicular to the cylinder, cylinder inclined at 60°, 54.7°, and 50°. The results show a similar drop in the drag coefficient over similar Reynolds numbers. This will be discussed further when compared to other published data later.

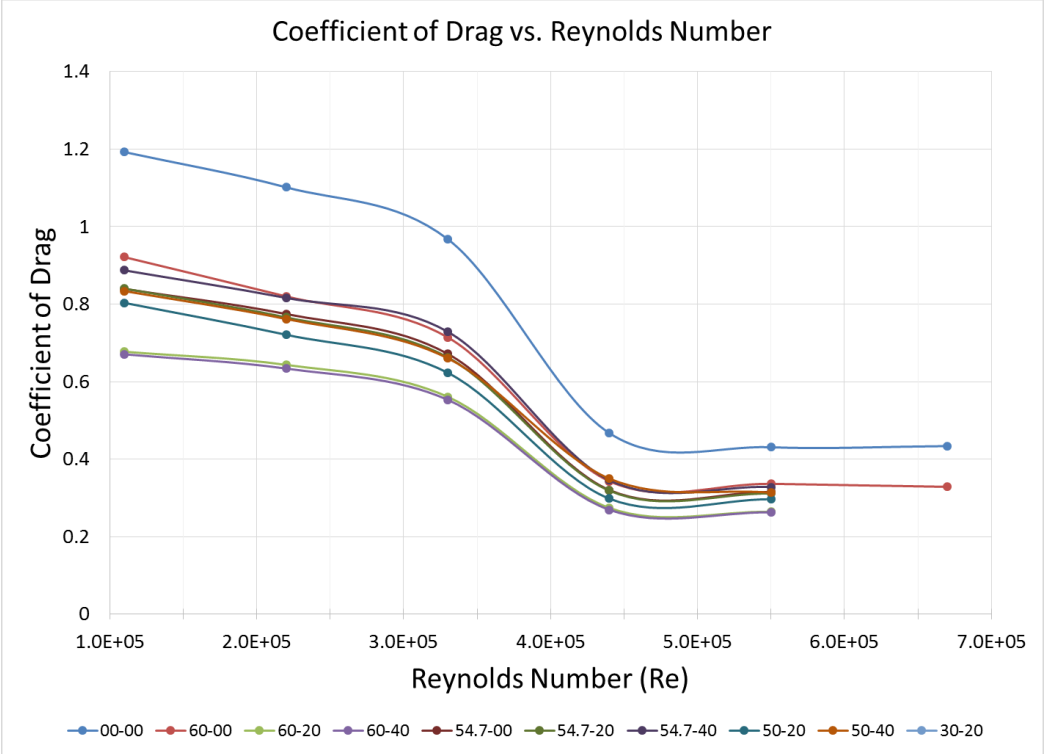


Figure 3.8: Aerodynamic force coefficients for cylinder inclined/yawed and perpendicular to flow: drag coefficient, C_D.

The results for inclined, and inclined and yawed cylinders showed a good agreement with the experimental results reported in literature. The experiments performed at NRC on inclined and inclined and yawed cables (Zurrel, 2004) showed a reduction of the drag coefficient for the 60° inclined cables around the drag crisis when compared with the data available for 0° angle of attack (ESDU, 1980; Scruton, 1960). The currently investigated case of 0° angle of attack, for lowest and highest Re numbers of 1.1×10^5 and 6.7×10^5 have indicated the lower and upper branches of the drag crisis. This varies slightly when compared with the published data. On the basis of the flow regimes classification and the data provided by Zdravkovich, a drag coefficient of around 1.2 was expected for the TrBL regime (as shown in Figure 3.10 below) while the numerical simulation indicates a value of 1.1, which is considered to be in the error limits of 10%, and therefore acceptable. A drag coefficient of around 0.45 is expected for the Upper TrBL regime while the

current result of the numerical simulation provided a drag coefficient of 0.35 (Figure 3.9) for the same case of 0°.

For the cases of inclined cylinders the experimental tests performed by Zurrel (2004) showed a value of less than 0.2 for the drag coefficient beyond the drag crisis for high Re numbers which is in good agreement with the data obtained from the current numerical simulation (Figure 3.8 above) and which will be presented in more detail in Figure 3.10 below.

Again, the data is separated into the four different yaw angles tested: flow perpendicular to the cylinder, cylinder inclined at 60°, 54.7°, and 50°. The results are compared with results obtained by ESDU (1980), Scruton et al. (1963), and Zurrel (2004).

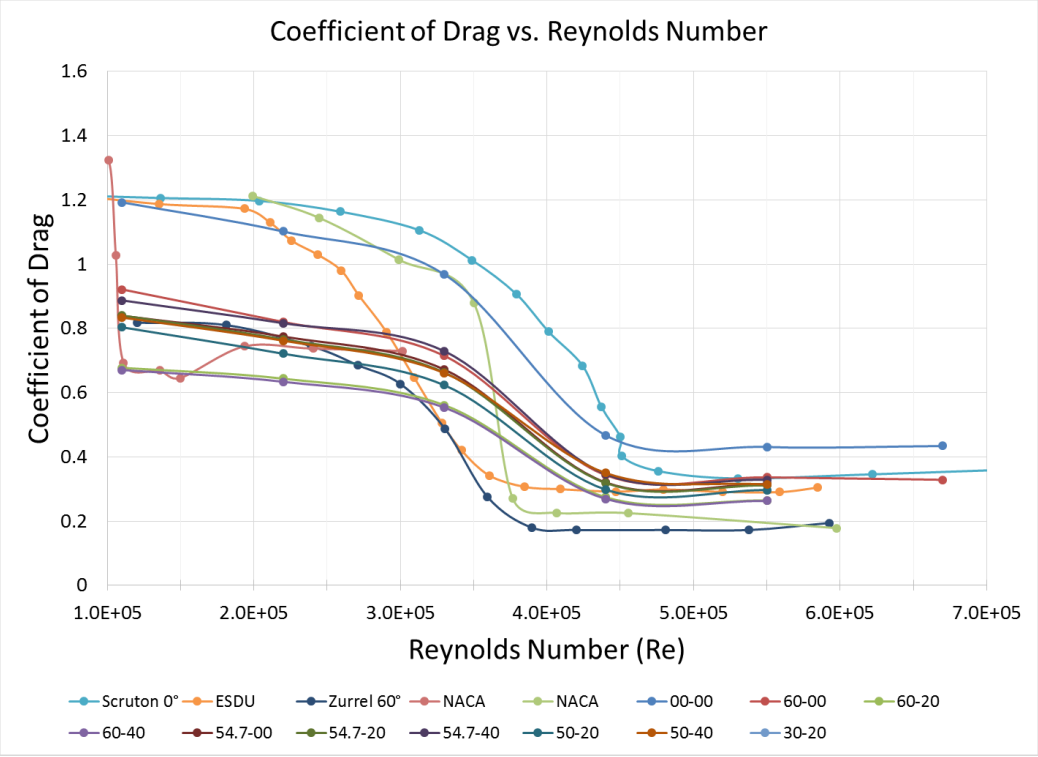


Figure 3.9: Aerodynamic force coefficients for cylinder inclined/yawed and perpendicular to flow: drag coefficient, C_D.

As mentioned above, the drag coefficient results from this study for the flow perpendicular to the cylinder show a similar drop in magnitude in a similar Re range as previous experimental

studies. The magnitude of the drag coefficient is not as high as the experimental values for lower Re, 1.2 compared to 1.1 for this study, but is higher for higher Re, 0.35 compared to 0.4 for this study. With the inclusion of the inclination angle (60°) the values of the Re drop compared to flow perpendicular to the cylinder, but show good comparison to experimental results with similar cylinder inclinations. This is seen in Figure 3.10(b) with a drop of the C_D in the similar Reynolds number range as the experimental results. The change in yaw angle of the cylinder also shows a drop of the C_D for all cases studied. Similar results are seen for cylinder inclinations of 54.7° and 50° as shown in Figure 3.10(c) and (d).

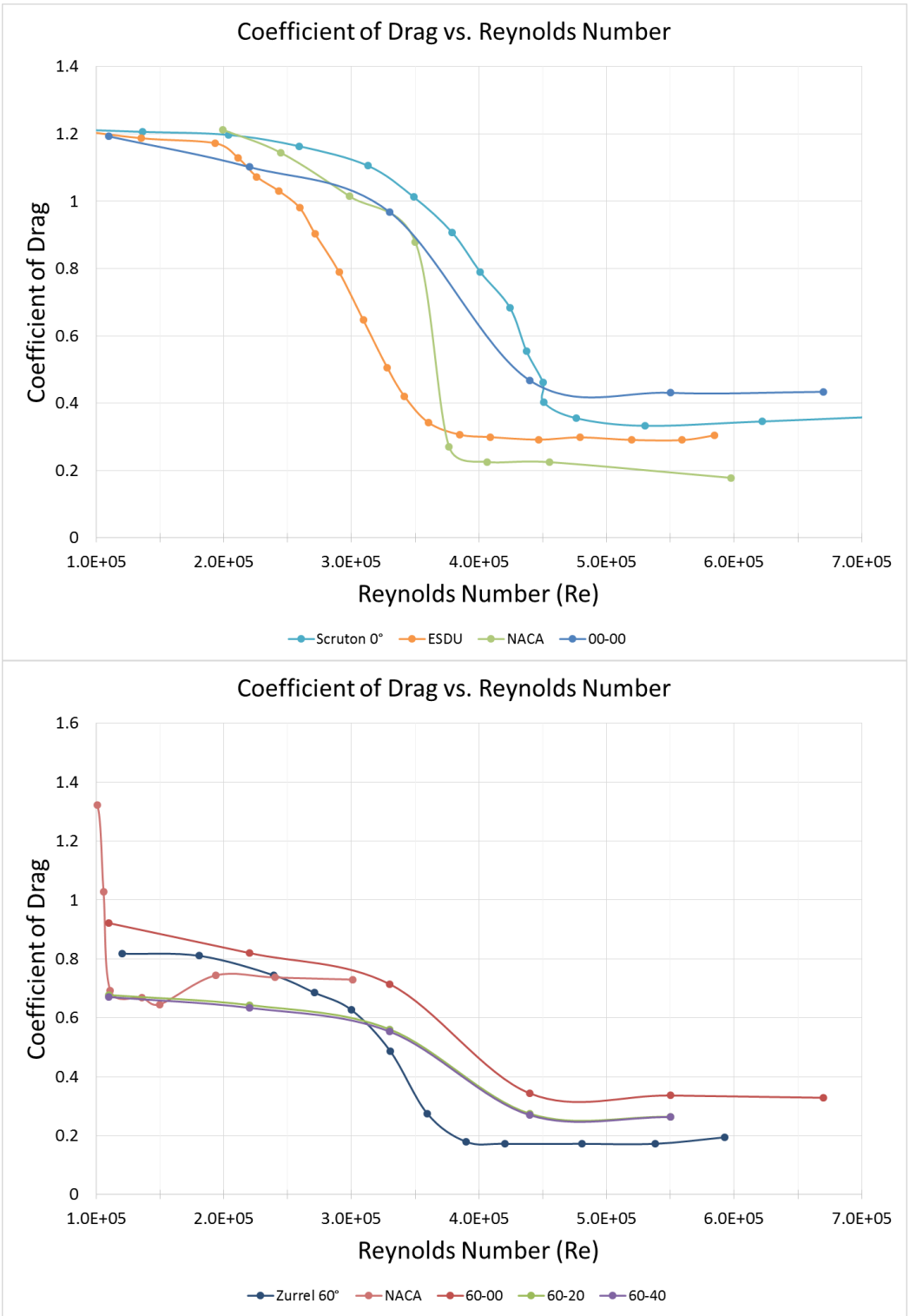
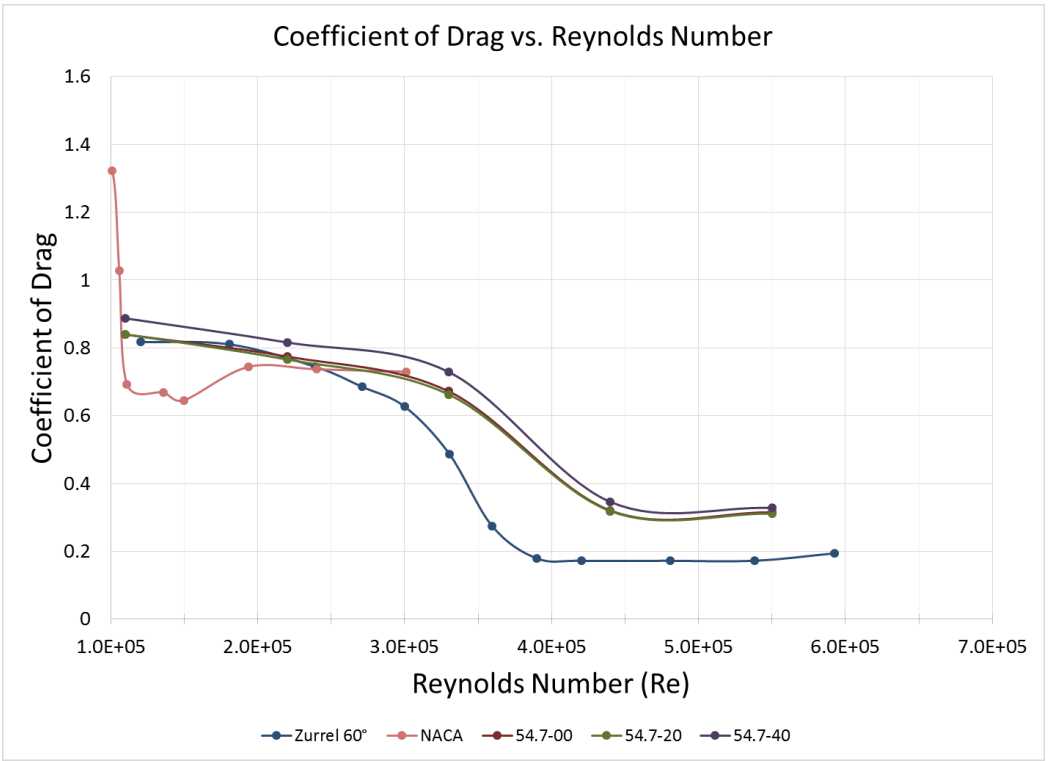


Figure 3.10: Aerodynamic force coefficients for cylinder inclined/yawed and perpendicular to flow: drag coefficient, C_D: (a) perpendicular to flow; (b) cylinder inclination 60°;



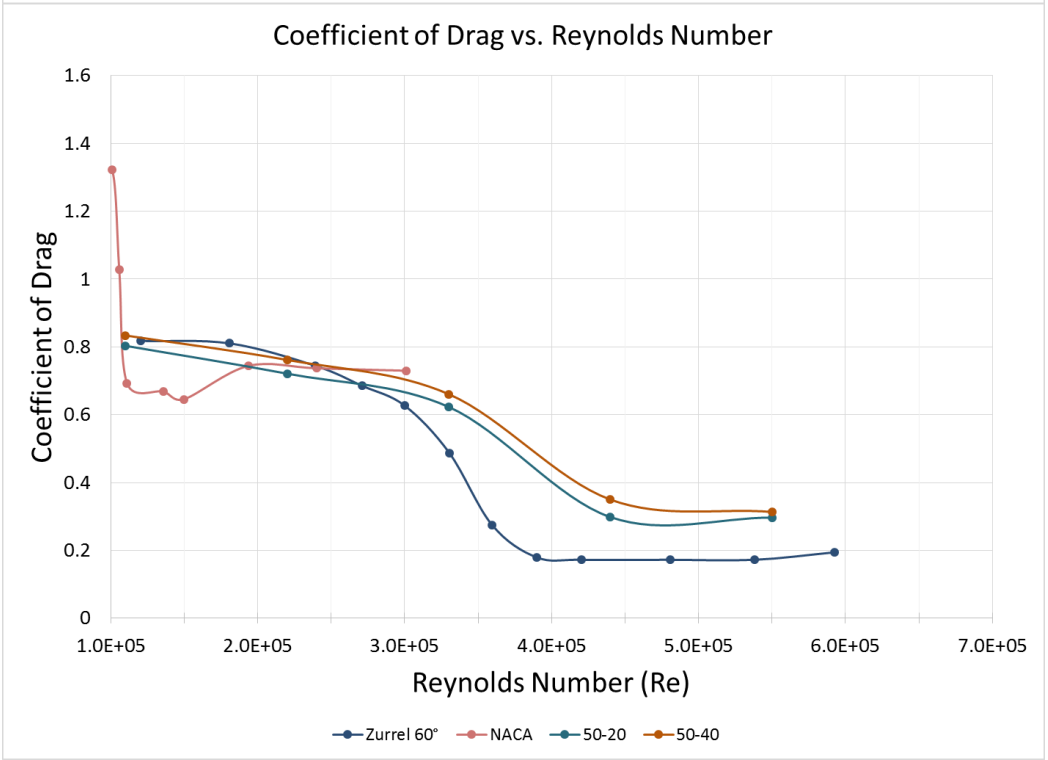


Figure 3.10: Aerodynamic force coefficients for cylinder inclined/yawed and perpendicular to flow: drag coefficient, C_D: (c) cylinder inclination 54.7°; (d) cylinder inclination 50°.

3.7.2 Coefficient of Lift Force on a Circular Cylinder

The lift coefficient (C_L) varies around 0.0 for the majority of Re numbers investigated in this study. The drop in the lift coefficient of the Re around 3.5×10^5 presented in the experimental work performed by Zurrel (2004), for 0° and 60° inclination was not registered in the numerical simulation performed in the current study, for any of the angles analysed. Also Zdravkovich acknowledged that the C_L coefficient has a discontinuous evolution, for the first interval of Re 1.0×10^5 (TrBL0 regime) not registering significant values, while it appears in the second interval, for the TrBL1 regime, where values of C_L = (- or +) 1.5 are registered, again dropping to values very close to 0 for the TrBL2 regime. Hence, considering the ideal conditions used for the numerical simulation when compared with the experimental settings, it seems that current data is located at the very sensitive limit between the TrBL0 and TrBL1, or TrBL1 and TrBL2 regimes (as defined above for flow perpendicular to the cylinder, $\phi = 0°$).

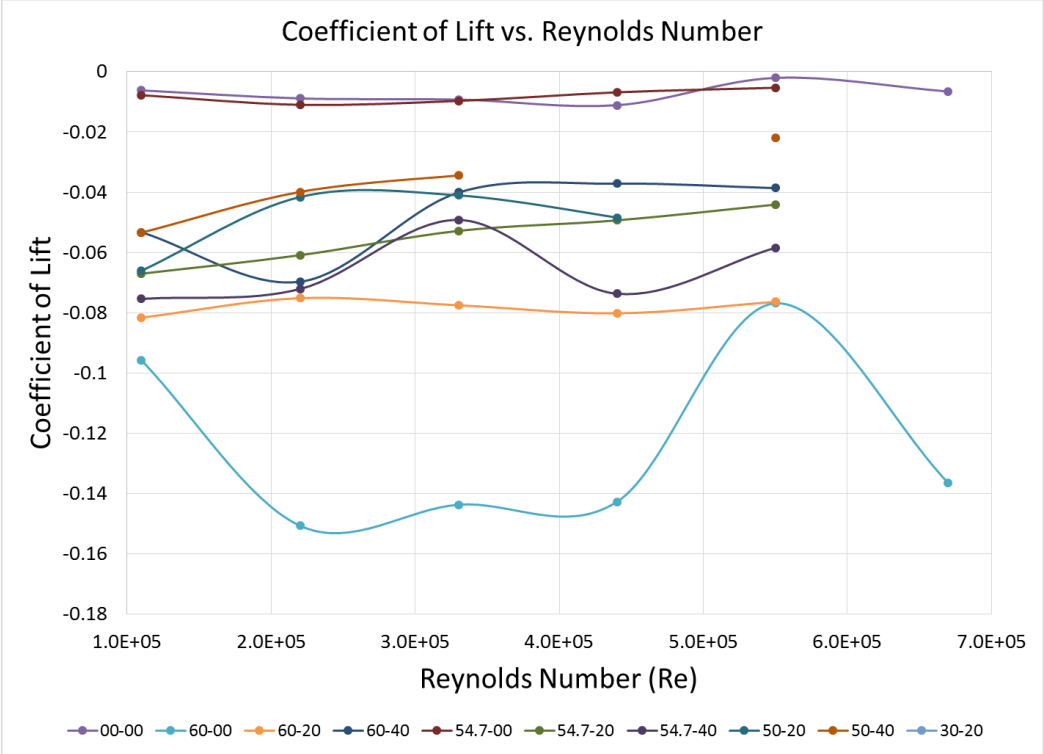


Figure 3.11: Aerodynamic force coefficients for cylinder inclined/yawed and perpendicular to flow: lift coefficient, C_L.

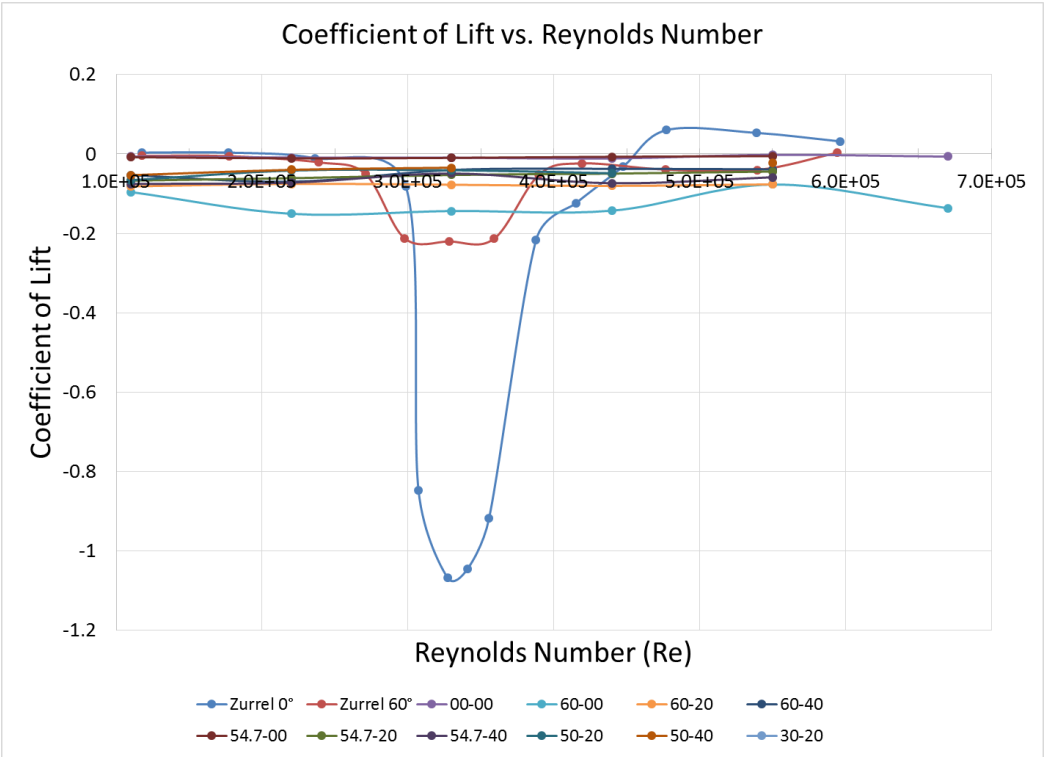


Figure 3.12: Aerodynamic force coefficients for cylinder inclined/yawed and perpendicular to flow: lift coefficient, C_L.

3.7.3 Coefficient of Pressure on the Surface of a Circular Cylinder

For flow perpendicular to the cylinder Zdravkovich (1997) showed that the pressure coefficient (C_P) distribution will vary with the increase of Re number, as shown in Figure 3.13. That is to say the minimum value of the C_P will decrease, and its position will move around the circumference of the cylinder towards downstream side. For the inclined cylinders investigated in the current research, the relative angle of attack had more influence upon the variation of the values and distribution of C_P than the Re number. Also the pressure distribution was not symmetric around the cylinder as it would be for the flow perpendicular to the cable due to the elliptic shape of the cross section; hence the entire distribution for the results from this study is plotted in Figure 3.16.

The pressure profiles for the six Re number used in this study for the flow perpendicular to the cylinder, and inclined to the cylinder (60°) for Re 1.1×10^5 to 6.7×10^5, are presented in Figure 3.14 and Figure 3.15 respectively. As can be seen comparing the results for flow perpendicular to the flow from the current study with the published experimental results of Figure 3.13, a similar change in position along the circumference of the cylinder is seen with the change in Re number as well as the variation is the pressure distribution along the leeward side of the cylinder. More will be discussed on this later with comparisons with published results. The results for the flow inclined to the cylinder at 60° showed less variation in the distribution for the range of Re numbers both for the separation point and along the leeward side of the cylinder. The major difference between the two inclinations of the cylinder is the change along the leeward side of the cylinder for the flow inclined to the cylinder when compared to the flow perpendicular to the

cylinder. More will be discussed on the pressure distribution around the circumference of the cylinder including the variation in the distribution along the length of the cylinder in Chapter 4.

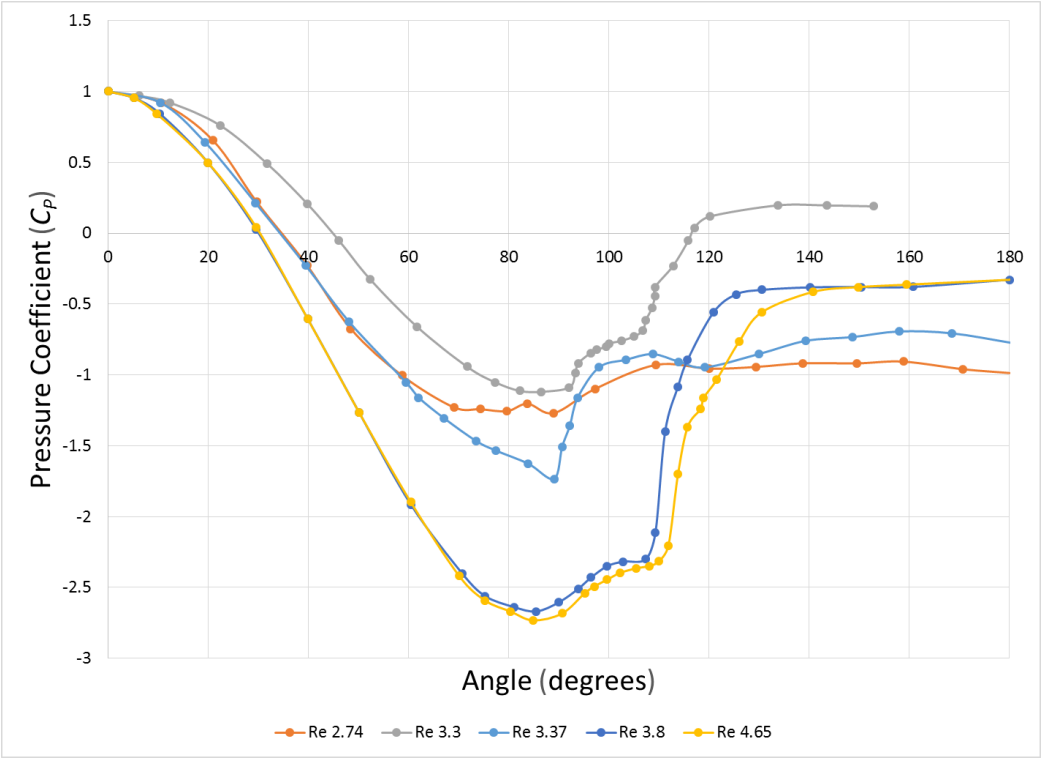


Figure 3.13: Pressure coefficient for flow perpendicular to the cylinder ($\phi = 0°$) at Re = 2.74×10^5 to 4.65×10^5, adapted from Zdravkovich (1997)

Comparing the current study results using LES simulations in Figure 3.14, and comparing them to the published experimental results of Figure 3.13 shows that the study results lie between the experimental results for Re = 3.37×10^5, 3.8×10^5, and Re = 4.65×10^5. For the study results, the peak pressure coefficients around the sides of the cylinder are around -1.25 to -2 compared to -1.5 to -2.25 for the published experimental results for the three cases mentioned above.

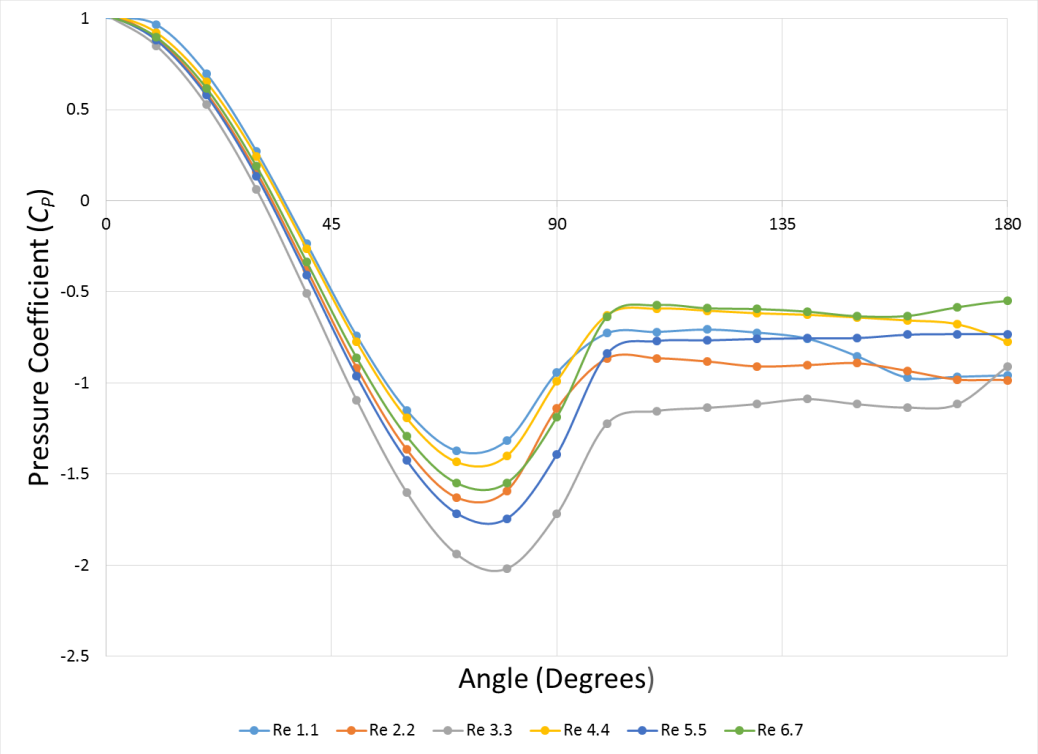


Figure 3.14: Pressure profile for flow perpendicular to the cylinder at Re = 1.1×10^5 to 6.7×10^5, current study

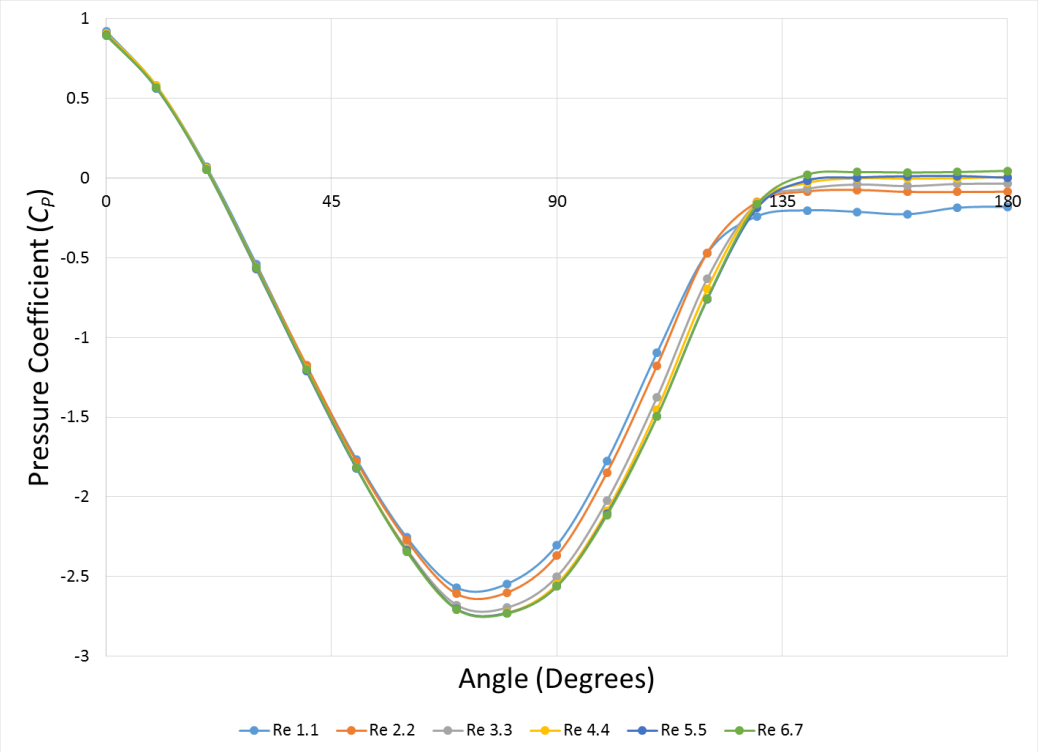
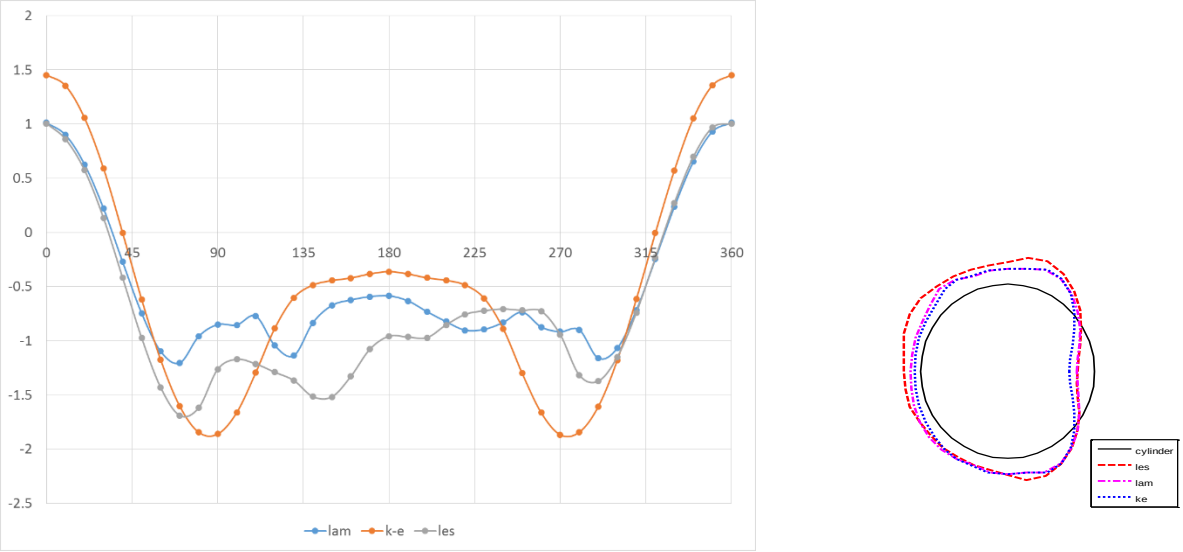


Figure 3.15: Pressure profile for flow around an inclined cylinder (60°) at Re = 1.1×10^5 to 6.7×10^5, current study

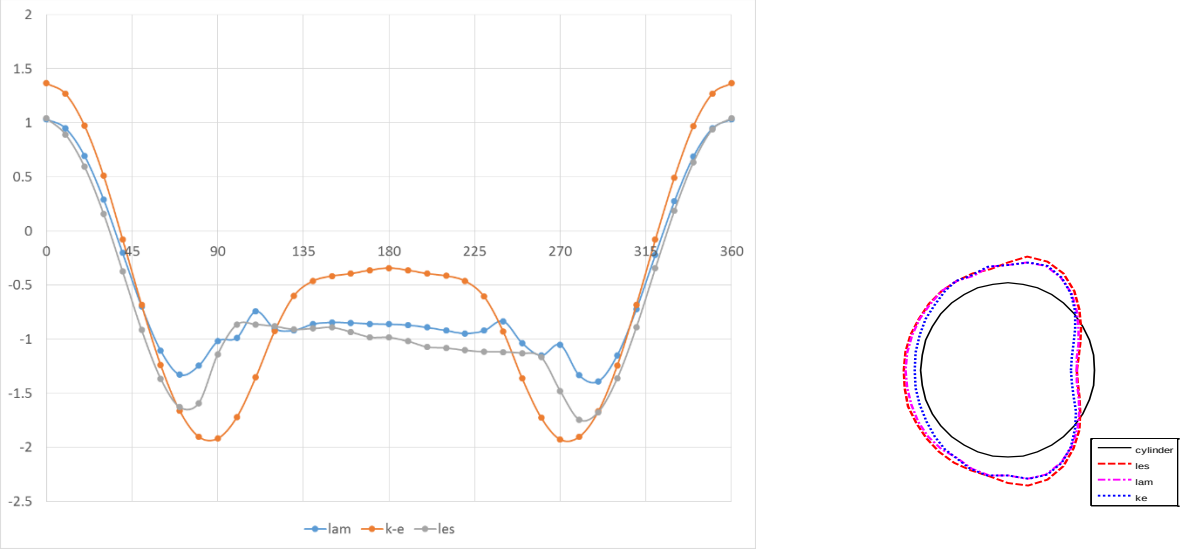
The pressure distribution around the circumference of the cylinder also varies with the three computational models used. The distribution for the laminar option produces a high coefficient of pressure of 1 at the windward point of the circumference (shown as 0° and 360° in the graph and to the right of the visualization). The pressure changes from positive to negative around the circumference of the circular cylinder resulting is a variation in the pressure distribution on the leeward side of the cylinder. The results from the k-ε model show a higher starting coefficient of pressure on the windward side of the cylinder, and also higher than is expected from the mean pressure distribution in experimental results as seen in the mean pressure distribution around a cylinder (ESDU, 1986). The pressure is also symmetric around the circumference of the cylinder which is not expected for an instantaneous pressure distribution captured here. The pressure distribution for the LES model again starts with a coefficient of pressure of 1 at the windward side of the cylinder and a variation pressure along the leeward side of the cylinder. It also appears similar to the mean pressure distribution around a cylinder (ESDU, 1986) with an area of high negative pressure followed by an area of lower negative pressure on the leeward side of the cylinder.

As can be seen in the above results, LES simulation results produce the best results of the three computational results calculated as part of this study when compared to experimental and published results. These results include velocity profiles both around the circular cylinder, and along the length of the circular cylinder. The flow around the circular cylinder illustrates an area of recirculation near to the leeward side of the cylinder and the vortex strength diminishing as the flow moves downstream of the circular cylinder. The velocity profile along the length of the cylinder also varies along the length for the distribution produced by the LES model showing the variation in the recirculation length along the length of the circular cylinder, as expected for the

flow around the cylinder. The variation in the eddy viscosity for the LES model shows a variation in distribution in the wake of the circular cylinder due to the turbulence created in this region as expected for flow around a circular cylinder. The pressure distributions around the circumference of the cylinder, and the drop in drag coefficient are in good agreement for result produced using LES. For this reason the LES results from the current study will be used in the remainder of this study.

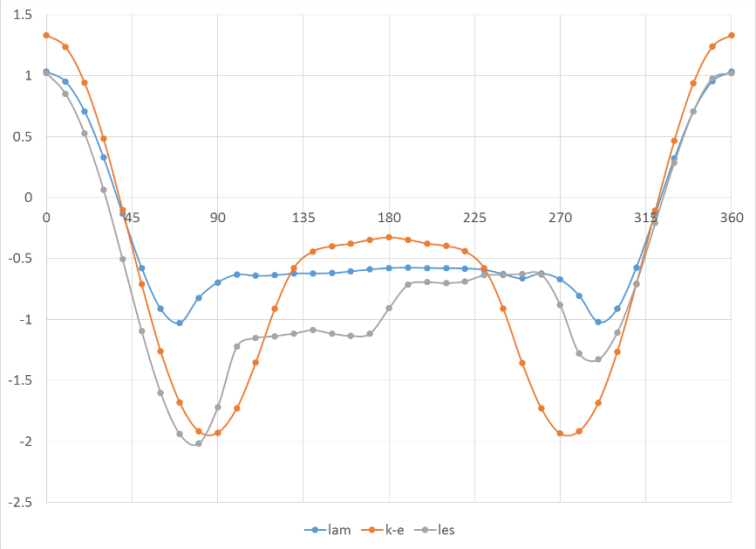


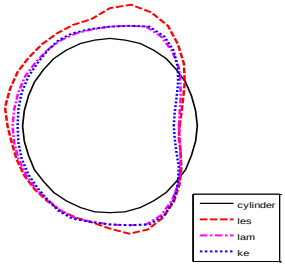
a) Pressure profiles, $\alpha = 0°$, $\beta = 0°$, Re = 1.1×10^5.



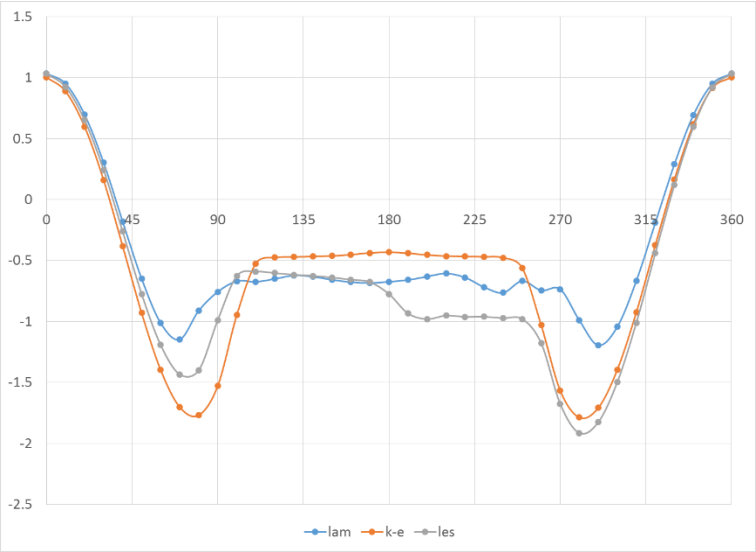
b) Pressure profiles, $\alpha = 0°$, $\beta = 0°$, Re = 2.2×10^5.

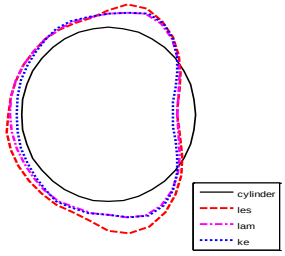
Figure 3.16: Pressure profile results for current study for $\alpha = 0°$, $\beta = 0°$.





c) Pressure profiles, $\alpha = 0°$, $\beta = 0°$, Re = 3.3×10^5.





d) Pressure profiles, $\alpha = 0°$, $\beta = 0°$, Re = 4.4×10^5.

Figure 3.16: Pressure profile results for current study for $\alpha = 0°$, $\beta = 0°$.

4 Pressure and Velocity Distributions for Inclined and Perpendicular Cylinders

The pressure and velocity distributions will be presented in this chapter for the flow around an inclined and yawed cylinder, and the standard well known cases of flow perpendicular to the cylinder.

This will include the pressure distribution around the circumference of the cylinder, the pressure and velocity distribution approaching the cylinder and downstream of the cylinder, plots of the axial and along stream flow velocity along the leeward side of the cylinder, vector plots showing the instantaneous flow distribution in the area of disturbed flow around the cylinder, velocity streamlines showing the disturbed flow around the cylinder and the development of the axial flow, and the dominant velocity zones and flow patterns as seen with the velocity contours around the cylinder.

The following ten cases will be presented as representative samples of the 52 total cases studied as part of the current work showing various inclination angles (α), yaw angles (β), relative angles of attack of the cable (ϕ), and Reynolds numbers (Re):

Table 4-1: Representative sample cases of study

Case	Inclination Angle (α)	Yaw Angle (β)	Relative Angle of Attack (ϕ)	Reynolds Numbers (Re)
a)	$\alpha = 54.7°$	$\beta = 40°$	$\phi = 64°$	$Re = 1.1 \times 10^5$
b)	$\alpha = 50°$	$\beta = 20°$	$\phi = 53°$	$Re = 3.3 \times 10^5$
c)	$\alpha = 50°$	$\beta = 40°$	$\phi = 60.5°$	$Re = 3.3 \times 10^5$
d)	$\alpha = 60°$	$\beta = 20°$	$\phi = 62°$	$Re = 3.3 \times 10^5$
e)	$\alpha = 54.7°$	$\beta = 40°$	$\phi = 64°$	$Re = 3.3 \times 10^5$
f)	$\alpha = 50°$	$\beta = 20°$	$\phi = 53°$	$Re = 4.4 \times 10^5$
g)	$\alpha = 60°$	$\beta = 20°$	$\phi = 62°$	$Re = 5.5 \times 10^5$
h)	$\alpha = 60°$	$\beta = 0°$	$\phi = 60°$	$Re = 6.7 \times 10^5$
i)	$\alpha = 60°$	$\beta = 0°$	$\phi = 60°$	$Re = 3.3 \times 10^5$
j)	$\alpha = 0°$	$\beta = 0°$	$\phi = 0°$	$Re = 6.7 \times 10^5$

4.1 Pressure Distributions on the Surface of the Cylinder

The windward and leeward pressure distributions on the surface of the cylinder were recorded and are presented in Figure 4.1. The pressure distribution shown here corresponds to the ten sample cases detailed in Table 4-1, for briefness and clarity of data interpretation. The pressure distribution for all the simulation cases investigated in this study are presented, along the entire length of the cylinder, in Appendix B.

High pressures are noted on the windward side of the cylinder ranging from 200 Pa up to 3,000 Pa for Re numbers of Re = 1.1×10^5 and up to 6.7×10^5 respectively. Along the leading edge of the cylinder the pressure distribution was symmetric with a constant band width of high pressure with a width of approximate 0.5D (Figures 4.1(a) - (j)). Along the sides of the cylinder where the shear layers are detaching from the model areas with lower levels of pressures are alternating with areas of fluctuating pressures, as noted on the leeward side of the model for various patterns as follows.

Small areas of low pressure intensity, alternating with high intensity pressure along the length of the cable, formed wave shapes for the cases $\alpha = 50°$, $\beta = 20°$, $\phi = 53°$, Re = 3.3×10^5; $\alpha = 50°$, $\beta = 40°$, $\phi = 60.5°$, Re = 3.3×10^5; and $\alpha = 50°$, $\beta = 20°$, $\phi = 53°$, Re = 4.4×10^5 (Figures 4.1(b), (c), and (f) respectively).

Longer areas of positive and negative pressures in a non-alternating pattern, but dominated a longer region on the surface of the cable model, for the cases $\alpha = 60°$, $\beta = 20°$, $\phi = 62°$, Re = 3.3×10^5 and $\alpha = 60°$, $\beta = 20°$, $\phi = 62°$, Re = 5.5×10^5 (Figure 4.1(d) and (g)). Regions of high pressure interrupted periodically by small patches of lower pressures were noted for cases $\alpha = 54.7°$, $\beta = 40°$, $\phi = 64°$, Re = 1.1×10^5 and $\alpha = 54.7°$, $\beta = 40°$, $\phi = 64°$, Re = 3.3×10^5 (Figures 4.1(a) and (e)). Also alternation of high pressures and low pressure patches formed along the edges

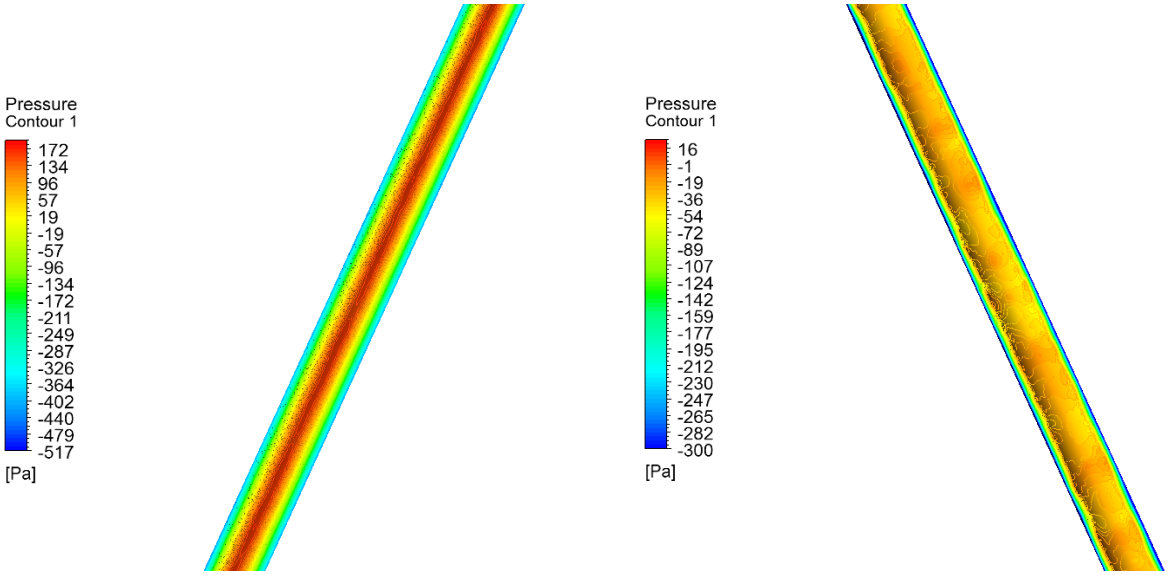
of the model were noticed for $\alpha = 60°$, $\beta = 0°$, $\phi = 60°$, Re = 6.7×10^5 (Figure 4.1(h)). The pressure along the leeward side of the cylinder was higher for this orientation and wind speed when compared to the other cases presented.

A random pressure distribution was noted along the leeward side of the cylinder for the case of flow perpendicular to the cylinder at Re = 6.7×10^5 (Figure 4.1(j)). This is in good agreement with the description of the turbulent boundary layer (TrBL) regime defined by Zdravkovich (1997). This pressure distribution pattern is absolutely different, when compared with the previously presented cases of inclined, and inclined and yawed cylinders.

When capturing the leeward side of the cylinder, along its length, some cases showed a lower pressure along the length of the cylinder. Continuous shear layers detachment occurs, and flow is directed along the length of the cylinder where the pressure is in the negative range of 0 Pa up to -250 Pa, as it can be noticed in the following cases: $\phi = 64°$, Re = 1.1×10^5; $\phi = 53°$, Re = 3.3×10^5; $\phi = 60.5°$, Re = 3.3×10^5 and $\phi = 64°$, Re = 3.5×10^5 (Figures 4.1(b), (c) and (e)). Positive pressures along the leeward side of the cylinder indicated attachment of the flow in this region, running along the entire length of the cylinder. This is seen for the following cases: $\phi = 62°$, Re = 5.5×10^5 and $\phi = 64°$, Re = 6.7×10^5 (Figures 4.1(g) and (h)) for which only positive pressures of up to 750 Pa and 550 Pa respectively were registered.

Other cases showed alternating positive and negative pressures indicating detachment and reattachment of flow along the length of the cylinder, such as case $\phi = 62°$, Re = 3.3×10^5 in Figure 4.1(d)), and $\phi = 53°$, Re = 4.4×10^5, Figure 4.1(f), where pressures in the range of -700 up to 700 Pa were noticed. For the flow perpendicular to the cylinder, $\phi = 0°$, Re = 6.7×10^5, (Figure 4.1(j)) alternation from negative to positive pressures without presenting any identifiable pattern along the length of the cylinder was noted.

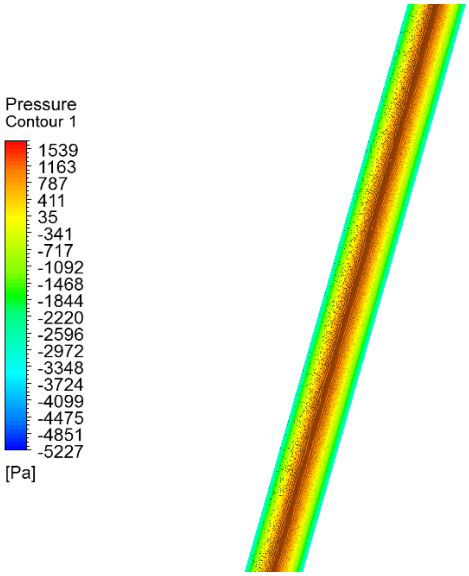
Noting the differences in the pressure distributions, and the associated flow patterns around the cylinder, a possible change in the flow regimes might be encountered, as it will be discussed in the later chapters. These regimes include different properties such as lower pressure along the leeward side of the cylinder, higher pressure along the leeward side of the cylinder, and altering between lower and higher pressure along the leeward side of the cylinder. More information regarding the evolution of the velocity, pressures and eddy viscosity distributions in the vicinity of the cylinder will be presented to verify this change is flow regime.

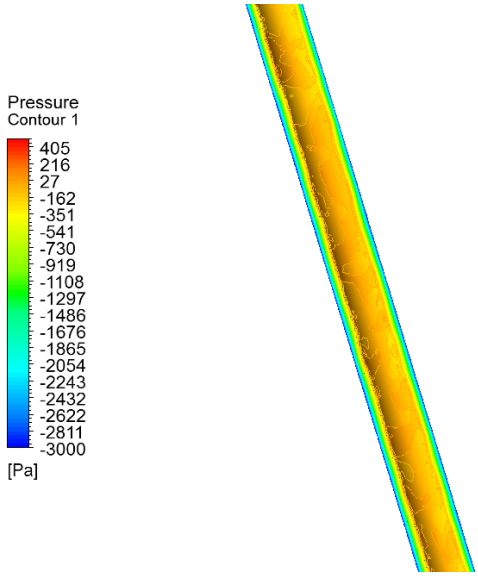


i) Windward side of the cylinder model ii) Leeward side of the cylinder model

a) $\alpha = 54.7°$, $\beta = 40°$, $\phi = 64°$, Re = 1.1×10^5;

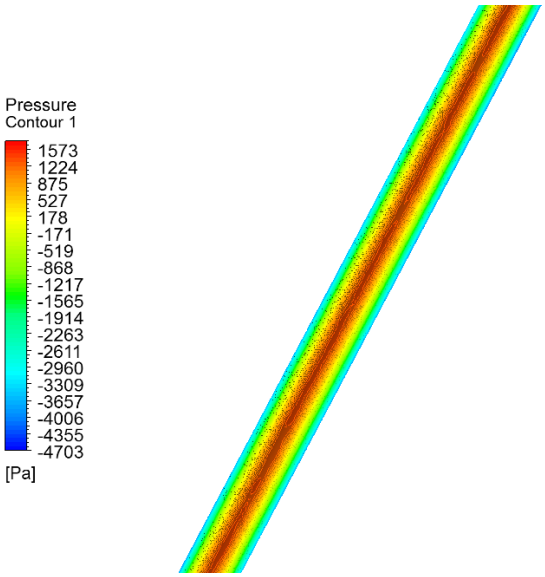
Figure 4.1: Pressure distribution on the windward side and leeward side of the cylinder model

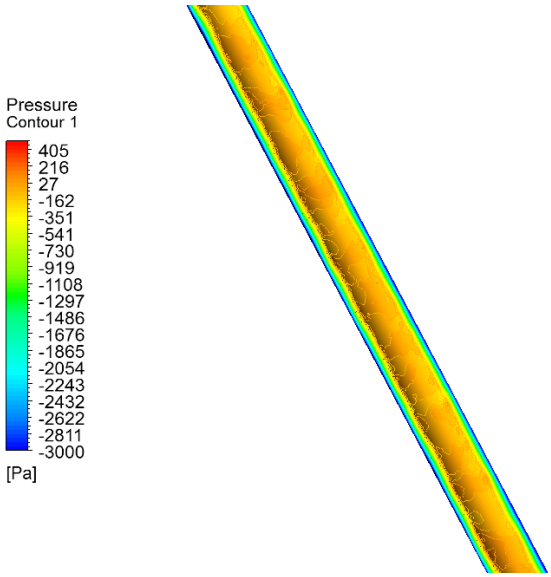




i) Windward side of the cylinder model ii) Leeward side of the cylinder model

b) $\alpha = 50°$, $\beta = 20°$, $\phi = 53°$, Re = 3.3×10^5;

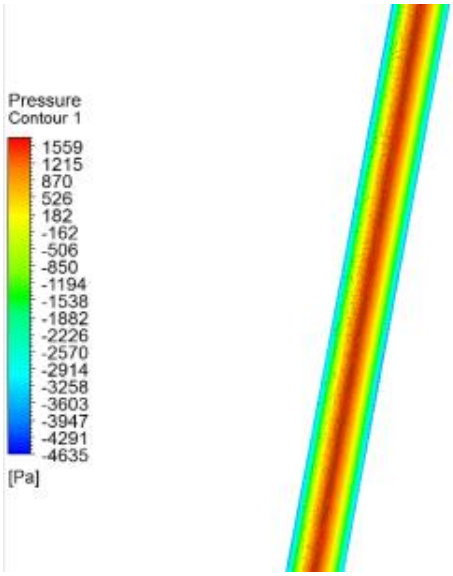


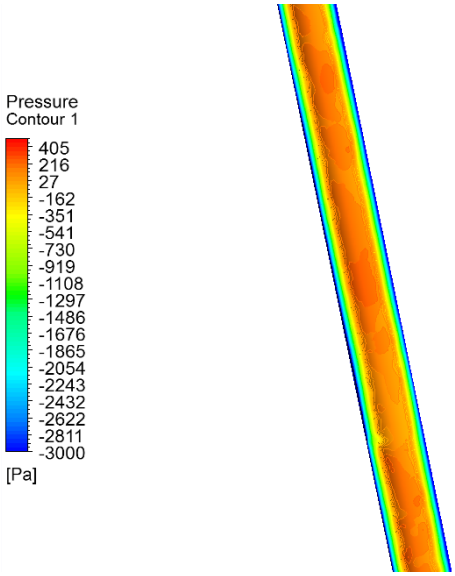


i) Windward side of the cylinder model ii) Leeward side of the cylinder model

c) $\alpha = 50°$, $\beta = 40°$, $\phi = 60.5°$, Re = 3.3×10^5;

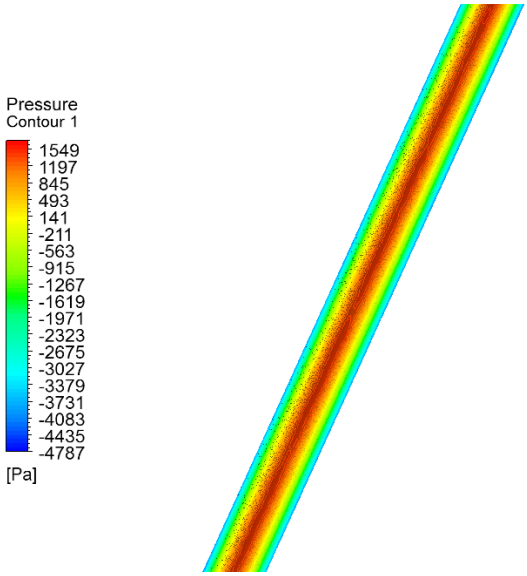
Figure 4.1: Pressure distribution on the windward side and leeward side of the cylinder model

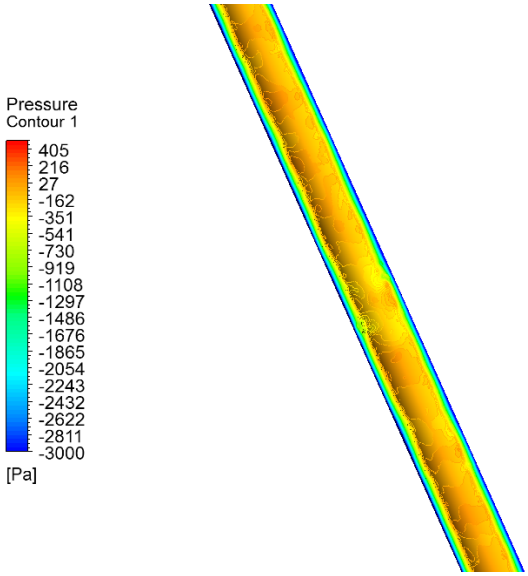




i) Windward side of the cylinder model ii) Leeward side of the cylinder model

d) $\alpha = 60°$, $\beta = 20°$, $\phi = 62°$, Re = 3.3×10^5;

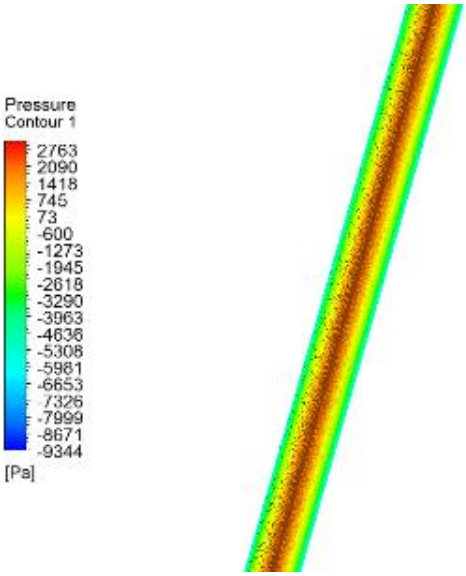


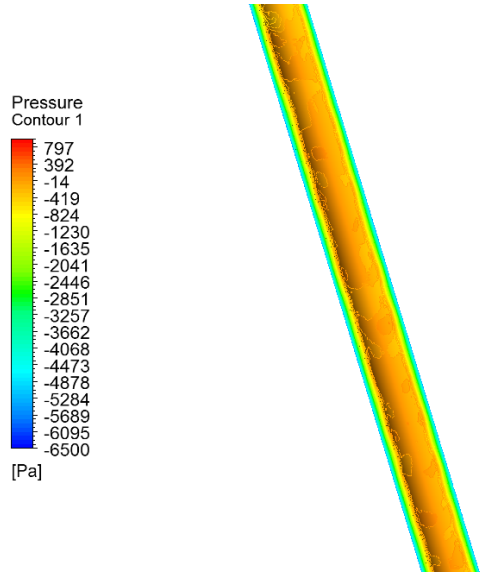


i) Windward side of the cylinder model ii) Leeward side of the cylinder model

e) $\alpha = 54.7°$, $\beta = 40°$, $\phi = 64°$, Re = 3.3×10^5;

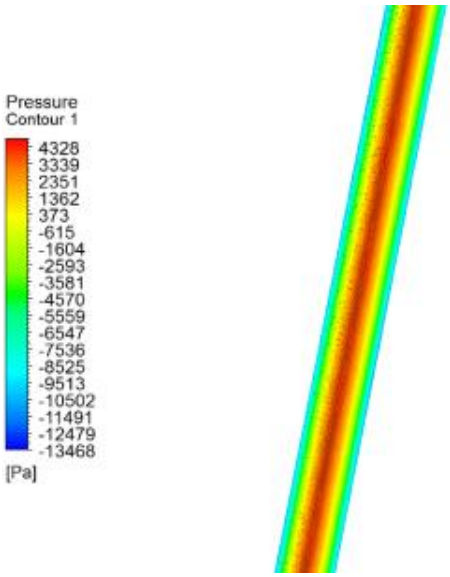
Figure 4.1: Pressure distribution on the windward side and leeward side of the cylinder model

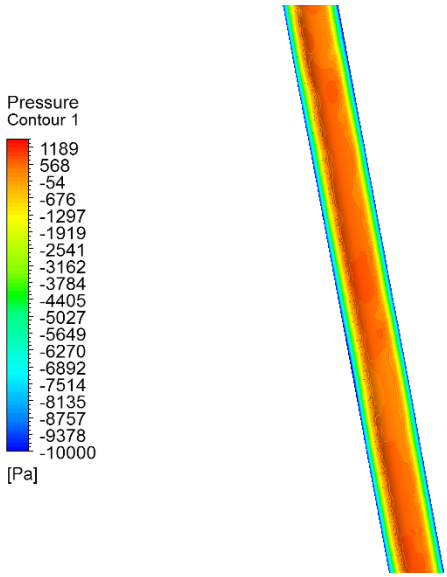




i) Windward side of the cylinder model ii) Leeward side of the cylinder model

f) $\alpha = 50°$, $\beta = 20°$, $\phi = 53°$, Re = 4.4×10^5;

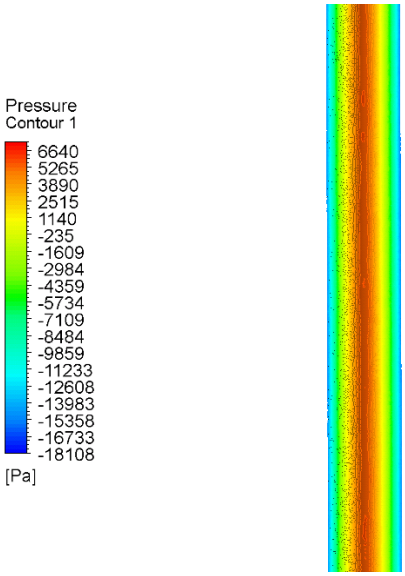




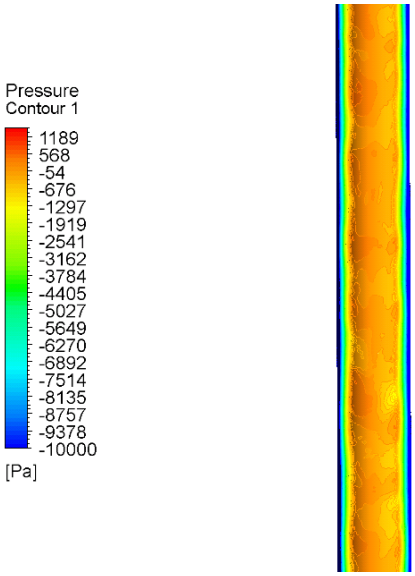
i) Windward side of the cylinder model ii) Leeward side of the cylinder model

g) $\alpha = 60°$, $\beta = 20°$, $\phi = 62°$, Re = 5.5×10^5;

Figure 4.1: Pressure distribution on the windward side and leeward side of the cylinder model

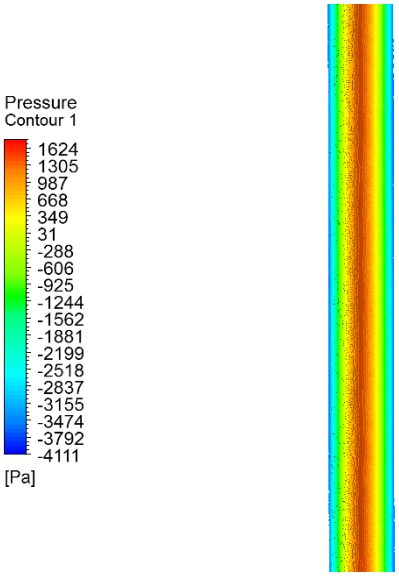


i) Windward side of the cylinder model

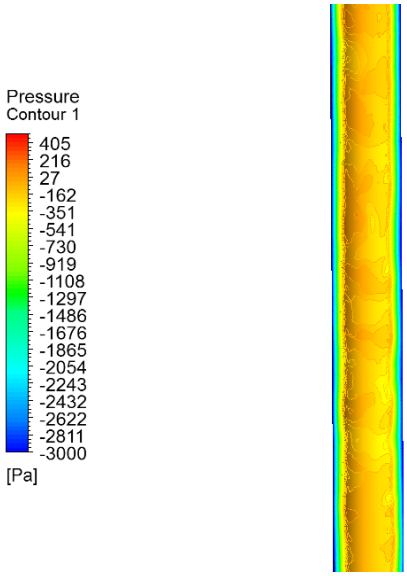


ii) Leeward side of the cylinder model

h) $\alpha = 60°$, $\beta = 0°$, $\phi = 60°$, Re = 6.7×10^5;



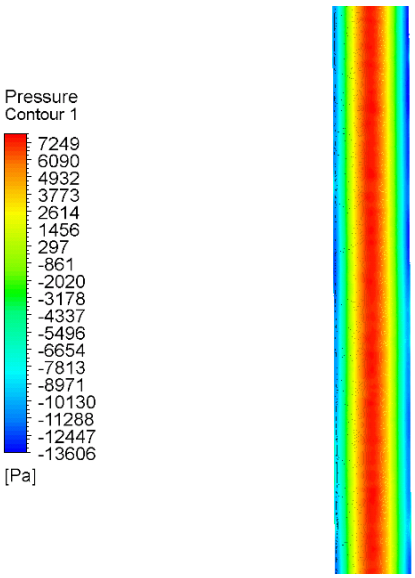
i) Windward side of the cylinder model

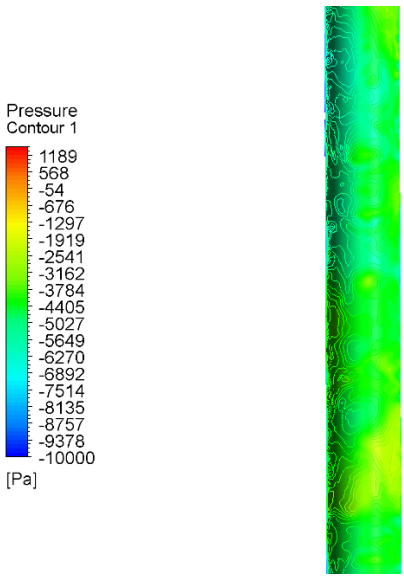


ii) Leeward side of the cylinder model

i) $\alpha = 60°$, $\beta = 0°$, $\phi = 60°$, Re = 3.3×10^5;

Figure 4.1: Pressure distribution on the windward side and leeward side of the cylinder model





i) Windward side of the cylinder model ii) Leeward side of the cylinder model

j) $\alpha = 0°$, $\beta = 0°$, $\phi = 0°$, Re = 6.7×10^5.

Figure 4.1: Pressure distribution on the windward side and leeward side of the cylinder model

The entire leeward surface of the cylinder was represented, however it was noticed that the width of the pressure distribution along the leeward side of the cylinder also varied for the different cases. The pressure distribution varied as follows:

a) from very wide band for $\alpha = 54.7°$, $\beta = 40°$, $\phi = 64°$, Re = 1.1×10^5 and $\alpha = 0°$, $\beta = 0°$, $\phi = 0°$, Re = 6.7×10^5 (Figure 4.1 (a) and (j));

b) to fairly wide band for $\alpha = 50°$, $\beta = 20°$, $\phi = 53°$, Re = 3.3×10^5; $\alpha = 50°$, $\beta = 40°$, $\phi = 60.5°$, Re = 3.3×10^5; $\alpha = 54.7°$, $\beta = 40°$, $\phi = 64°$, Re = 3.3×10^5; $\alpha = 50°$, $\beta = 20°$, $\phi = 53°$, Re = 4.4×10^5; $\alpha = 60°$, $\beta = 0°$, $\phi = 60°$, Re = 6.7×10^5; and $\alpha = 60°$, $\beta = 0°$, $\phi = 60°$, Re = 3.3×10^5 (Figure 4.1 (b), (c), (e), (f), (h) and (i)),

c) to narrow band for $\alpha = 60°$, $\beta = 20°$, $\phi = 62°$, Re = 3.3×10^5 and $\alpha = 60°$, $\beta = 20°$, $\phi = 62°$, Re = 5.5×10^5 (Figure 4.1 (d) and (g)).

This could be an indication that there is a variation in the detachment points of the shear layers shedding from the sides of the cylinder, as also detailed in the description of the flow

regimes provided by Zdravkovich (1997). In the current study the position along the circumference of the cylinder is expected to vary even more than the cases of flow perpendicular to the cylinder due to the inclination and the yaw angles of the models investigated.

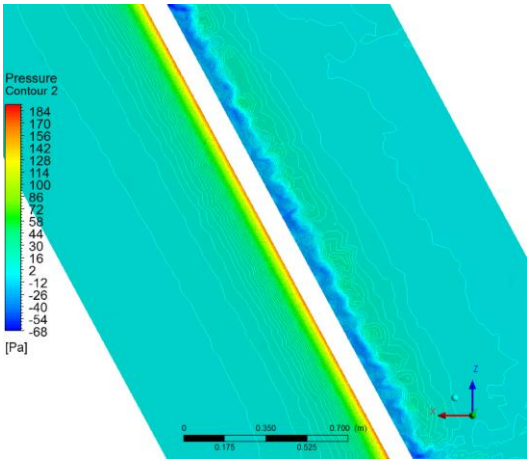
4.2 Velocity and Pressure Distributions around the Cylinder

In order to determine the effect of the flow pattern on the pressure induced at the surface of the cylinder the velocity and pressure distributions around the cylinder (upstream and downstream) are shown in Figure 4.2 and Figure 4.3. The distributions are shown on a plane parallel to the initial flow and passing through the center of the cylinder for its entire length. The development of pressure and velocity distributions for all cases is presented in Appendix C and Appendix D respectively.

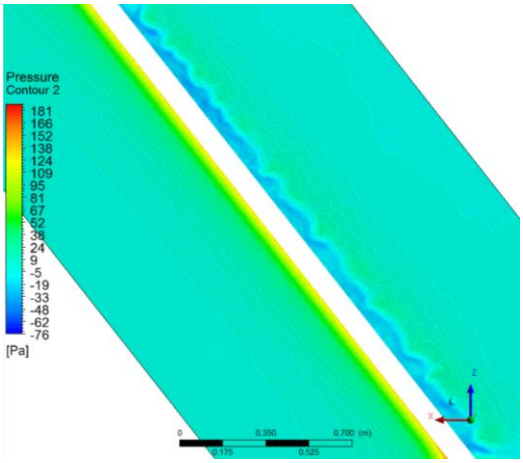
Examining the pressure distributions for the ten cases represented in Table 4-1, a strong layer of suction was noted for the entire length of the cylinder and immediately downstream for cases $\alpha = 54.7°$, $\beta = 40°$, $\phi = 64°$, Re = 1.1×10^5; $\alpha = 50°$, $\beta = 40°$, $\phi = 60.5°$, Re = 3.3×10^5 and $\alpha = 54.7°$, $\beta = 40°$, $\phi = 64°$, Re = 3.3×10^5 (Figures 4.3(a), (c), (e), and (h)). This layer was smaller than expected, when the increase in Re is taken into consideration, but still distinguishable for the cases $\alpha = 50°$, $\beta = 20°$, $\phi = 53°$, Re = 3.3×10^5; $\alpha = 50°$, $\beta = 20°$, $\phi = 53°$, Re = 4.4×10^5; and $\alpha = 60°$, $\beta = 0°$, $\phi = 60°$, Re = 3.3×10^5 (Figures 4.3(b), (f) and (i)). The pressure distributions for cases $\alpha = 60°$, $\beta = 20°$, $\phi = 62°$, Re = 3.3×10^5 and $\alpha = 60°$, $\beta = 20°$, $\phi = 62°$, Re = 5.5×10^5 (Figures 4.3(d) and (g)) showed a weak layer of suction with little variation along the leeward length of the cylinder. This included a non-periodic variation in the pressures distribution registered in this area. The velocity distributions clearly shows that the rotational formations of low velocity intensity are generated along the leeward side of the cylinder. These formations are closely spaced for the cases where high negative pressures were reported: $\alpha = 54.7°$, $\beta = 40°$, $\phi =$

64°, Re = 1.1×10^5; $\alpha = 50°$, $\beta = 40°$, $\phi = 60.5°$, Re = 3.3×10^5; $\alpha = 54.7°$, $\beta = 40°$, $\phi = 64°$, Re = 3.3×10^5; and $\alpha = 60°$, $\beta = 0°$, $\phi = 60°$, Re = 6.7×10^5 (Figures 4.3(a), (c), (e) and (h)).

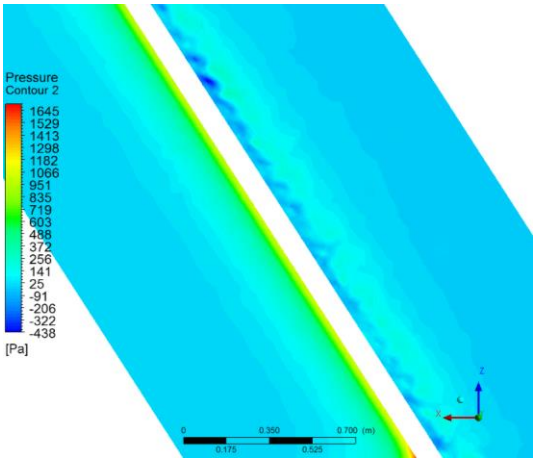
Low intensity rotational formations, but more widely spaced with gaps between them, were noticed for areas of lower negative pressure: $\alpha = 50°$, $\beta = 20°$, $\phi = 53°$, Re = 3.3×10^5; $\alpha = 50°$, $\beta = 20°$, $\phi = 53°$, Re = 4.4×10^5; and $\alpha = 60°$, $\beta = 0°$, $\phi = 60°$, Re = 3.3×10^5 (Figures 4.3(b), (f) and (i)). For the cases $\alpha = 60°$, $\beta = 20°$, $\phi = 62°$, Re = 3.3×10^5 and $\alpha = 60°$, $\beta = 20°$, $\phi = 62°$, Re = 5.5×10^5 (Figures 4.3(d) and (g)), the velocity distribution along the leeward side of the cylinder showed a very weak variation along the length of the cylinder, indicating no rotational flow formations within the region of delayed flow, along the leeward side.



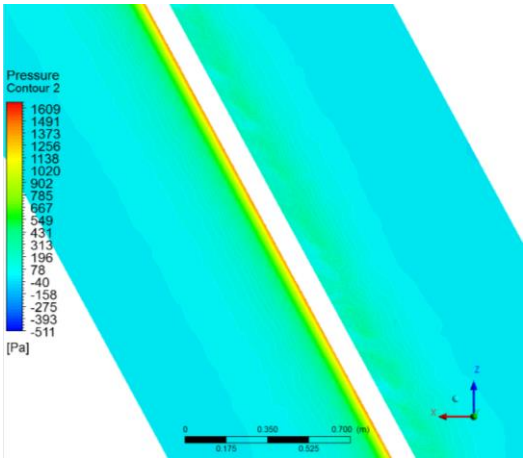
a) $\alpha = 54.7°$, $\beta = 40°$, $\phi = 64°$, Re = 1.1×10^5;



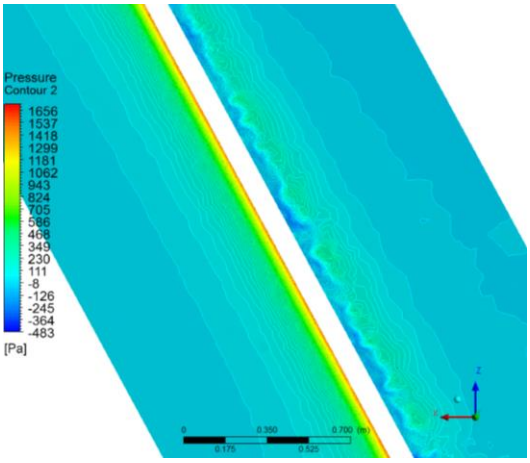
b) $\alpha = 50°$, $\beta = 20°$, $\phi = 53°$, Re = 3.3×10^5;



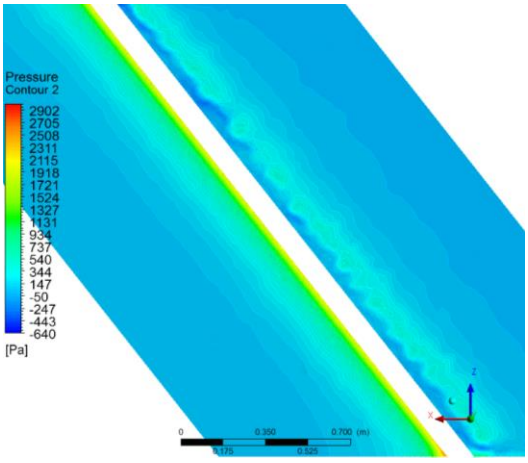
c) $\alpha = 50°$, $\beta = 40°$, $\phi = 60.5°$, Re = 3.3×10^5;



d) $\alpha = 60°$, $\beta = 20°$, $\phi = 62°$, Re = 3.3×10^5;

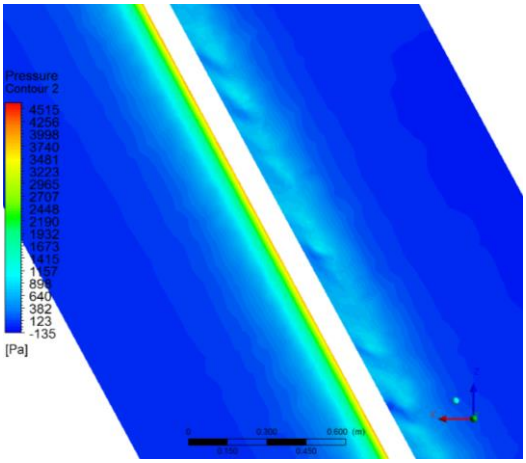


e) $\alpha = 54.7°$, $\beta = 40°$, $\phi = 64°$, Re = 3.3×10^5;

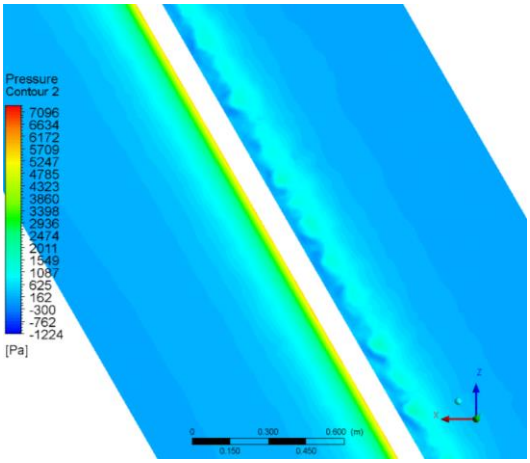


f) $\alpha = 50°$, $\beta = 20°$, $\phi = 53°$, Re = 4.4×10^5;

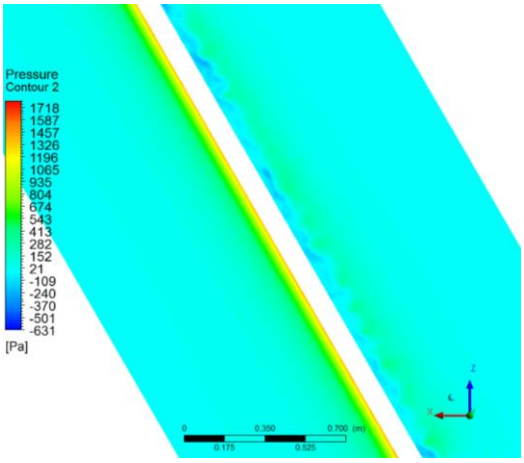
Figure 4.2: Pressure distribution around the cylinder



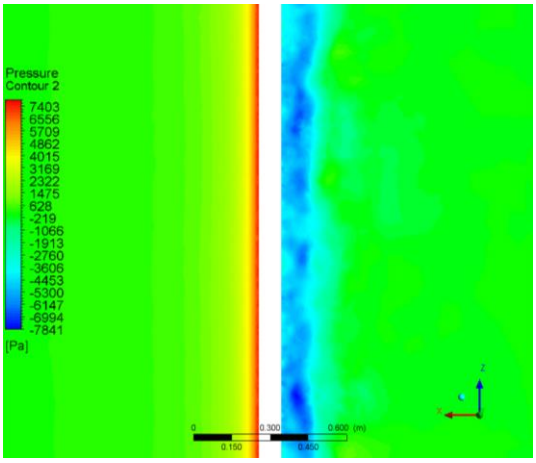
g) $\alpha = 60°$, $\beta = 20°$, $\phi = 62°$, Re = 5.5×10^5;



h) $\alpha = 60°$, $\beta = 0°$, $\phi = 60°$, Re = 6.7×10^5;

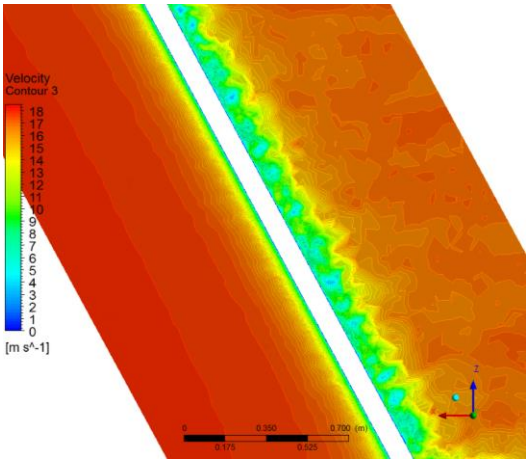


i) $\alpha = 60°$, $\beta = 0°$, $\phi = 60°$, Re = 3.3×10^5;

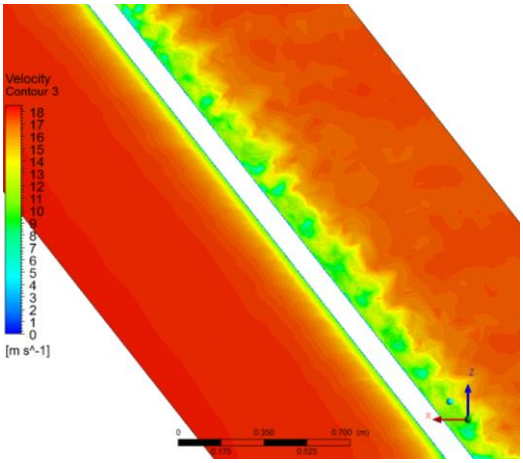


j) $\alpha = 0°$, $\beta = 0°$, $\phi = 0°$, Re = 6.7×10^5.

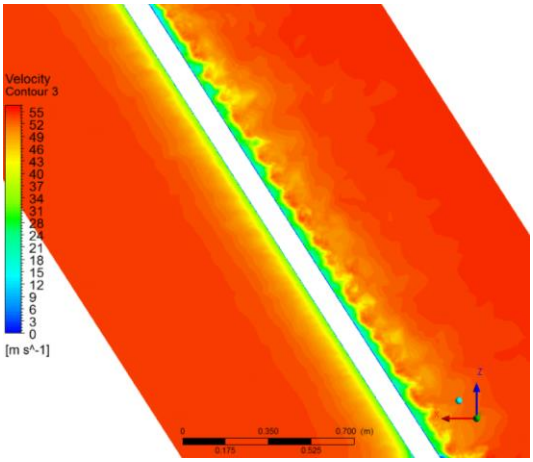
Figure 4.2: Pressure distribution around the cylinder



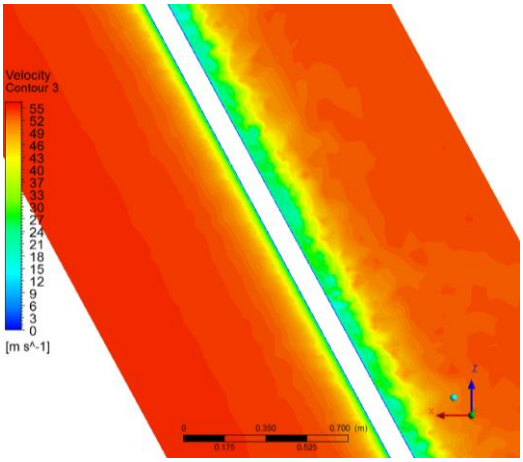
a) $\alpha = 54.7°$, $\beta = 40°$, $\phi = 64°$, Re = 1.1×10^5;



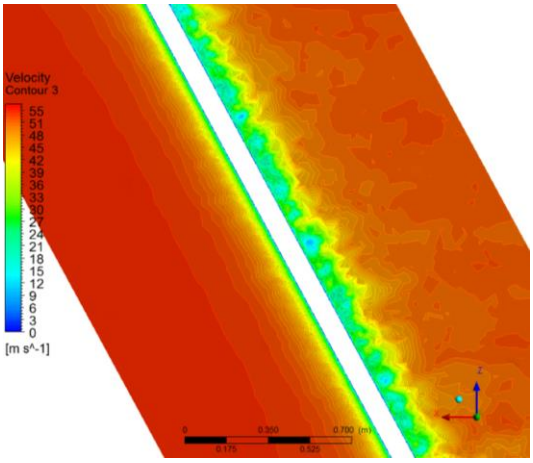
b) $\alpha = 50°$, $\beta = 20°$, $\phi = 53°$, Re = 3.3×10^5;



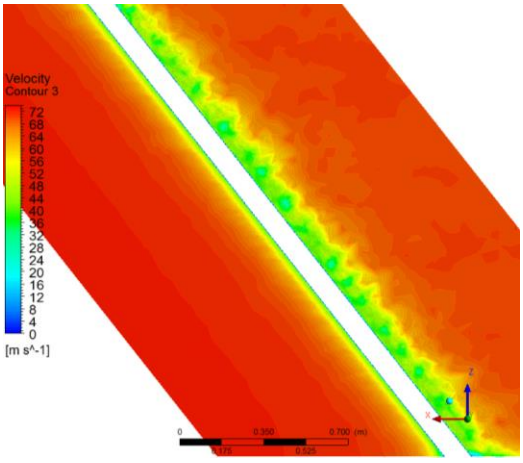
c) $\alpha = 50°$, $\beta = 40°$, $\phi = 60.5°$, Re = 3.3×10^5;



d) $\alpha = 60°$, $\beta = 20°$, $\phi = 62°$, Re = 3.3×10^5;

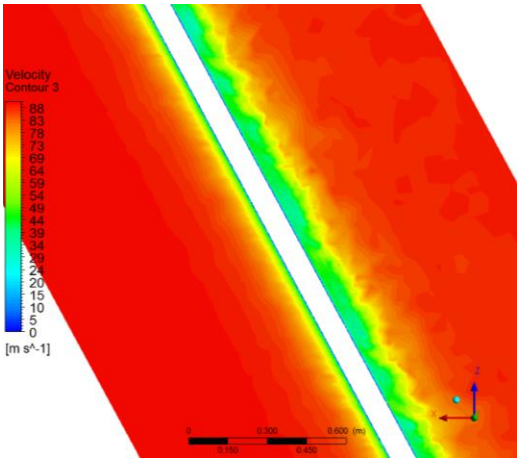


e) $\alpha = 54.7°$, $\beta = 40°$, $\phi = 64°$, Re = 3.3×10^5;

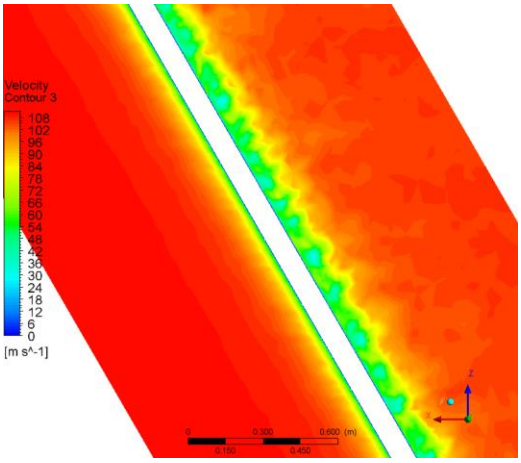


f) $\alpha = 50°$, $\beta = 20°$, $\phi = 53°$, Re = 4.4×10^5;

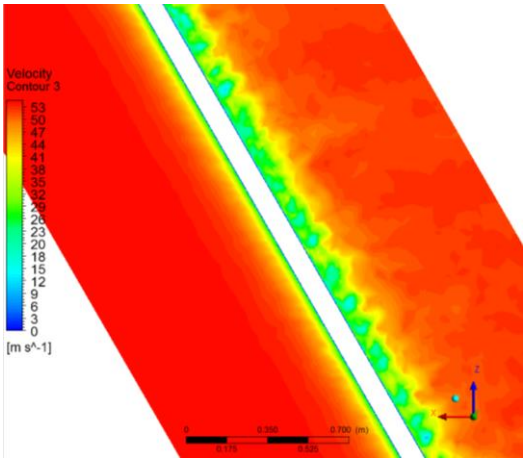
Figure 4.3: Velocity distribution around the cylinder



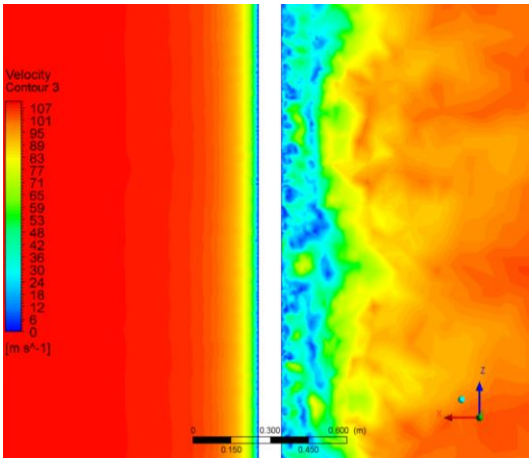
g) $\alpha = 60°$, $\beta = 20°$, $\phi = 62°$, Re = 5.5×10^5;



h) $\alpha = 60°$, $\beta = 0°$, $\phi = 60°$, Re = 6.7×10^5;



i) $\alpha = 60°$, $\beta = 0°$, $\phi = 60°$, Re = 3.3×10^5;



j) $\alpha = 0°$, $\beta = 0°$, $\phi = 0°$, Re = 6.7×10^5.

Figure 4.3: Velocity distribution around the cylinder

4.3 Axial Flow along the Length of the Cylinder

A possible flow formation attached onto the leeward surface of the cylinder model was indicated in the previous sections, as well as in several experiments performed by Matsumoto et al (2010) and Katsuchi et al (2009). Along the leeward side of an inclined cylinder the incoming flow changes direction, part of it following the structural axes of the cylinder, and is referred to as the "axial flow". However its exact properties and conditions of occurrence in relation to the aerodynamic phenomena encountered by inclined stay cables is not well understood at this time.

Hence, in the current study the flow along the leeward side of a cylinder was monitored at intervals of 0.1D, 0.2D, 0.3D, 0.4D and 0.5D downstream the cylinder in an attempt to identify this potential axial flow. The wind speed in the direction of the incoming flow along the leeward side of the cylinder and the axial wind speed determined by the Equation 4-1 below, as recommended by Cheng et al (2008), are reported in Figure 4.4.

$$u\cos\alpha\cos\beta + v\sin\alpha + w\sin\alpha\cos\beta \tag{4-1}$$

where u is the velocity along the x axis,

v is the velocity along the y axis, and

w is the velocity along the z axis.

The non-dimensional value of the velocity was considered, by dividing the measured axial flow with the incoming wind speed. The data from the upper 10% and the lower 10% of the cylinder length is not presented in the graphs, to avoid the end effects of the flow region on the flow observations. In experiments, when sampling the axial flow velocity components, the probe was situated at 0.2 D downstream the cylinder (Katsuchi et al., 2009). Non-dimensional values were reported for this study by considering the ratio of axial velocity over freestream velocity, V_{axial}/U, for the axial flow component, and the ratio of the along stream flow over the freestream flow, V_U/U, for the along flow component.

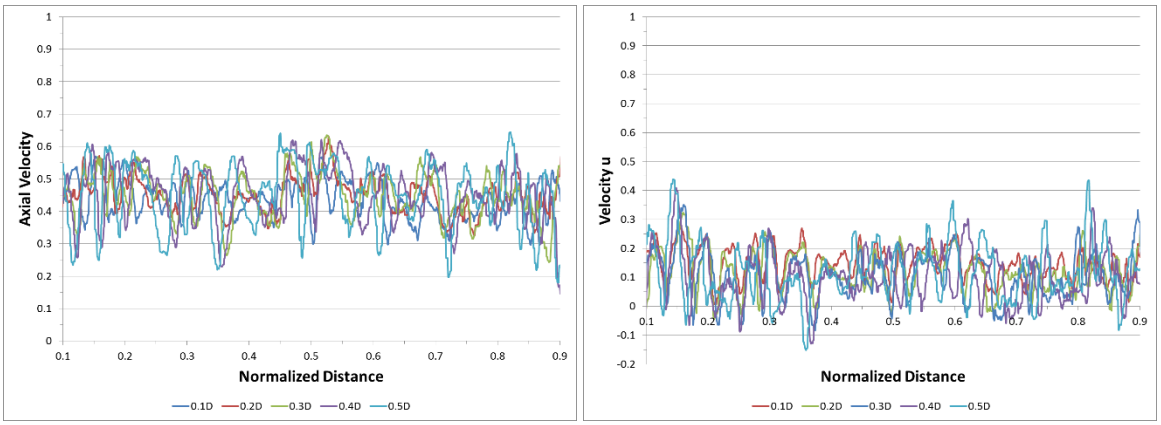
For the highest relative angle, $\phi = 64°$, it was noticed that the velocity fluctuation in the axial flow direction, and the incoming flow direction increased with the distance from the leeward side of the cylinder for the lower half of the cylinder. This occurred for both cases of Re = 1.1×10^5 and 3.5×10^5 as shown in Figures 4.4 (a) and (e) respectively. As the relative angle decreased the variation in the axial flow, and the flow in the direction of the incoming flow also decreased,

as shown in cases $\alpha = 50°$, $\beta = 40°$, $\phi = 60.5°$, Re = 3.3×10^5; $\alpha = 50°$, $\beta = 20°$, $\phi = 53°$, Re = 4.4×10^5; and $\alpha = 60°$, $\beta = 0°$, $\phi = 60°$, Re = 3.3×10^5 (Figures 4.4 (c), (f) and (i)). The case of $\alpha = 60°$, $\beta = 0°$, $\phi = 60°$, Re = 6.7×10^5 (Figure 4.4 (h)) shows an increase of velocity in the incoming flow direction at distances 0.4D and 0.5D, indicating the width of the axial flow is not as wide in this case as it appears to be in the other cases; this observation is somehow contradictory to the data presented in Figure 4.5 below. For the flow perpendicular to the cylinder, $\alpha = 0°$, $\beta = 0°$, $\phi = 0°$, Re = 6.7×10^5 (Figure 4.4 (j)), the velocity flow reversed its direction in the area behind the cylinder as expected, due to the three-dimensional nature of the flow near the leeward side of the cylinder. This flow pattern is not the same as the one seen in the other cases investigated in the current study, for an inclined cylinder, for which the flow has a no mean flow along the leeward side of the cylinder.

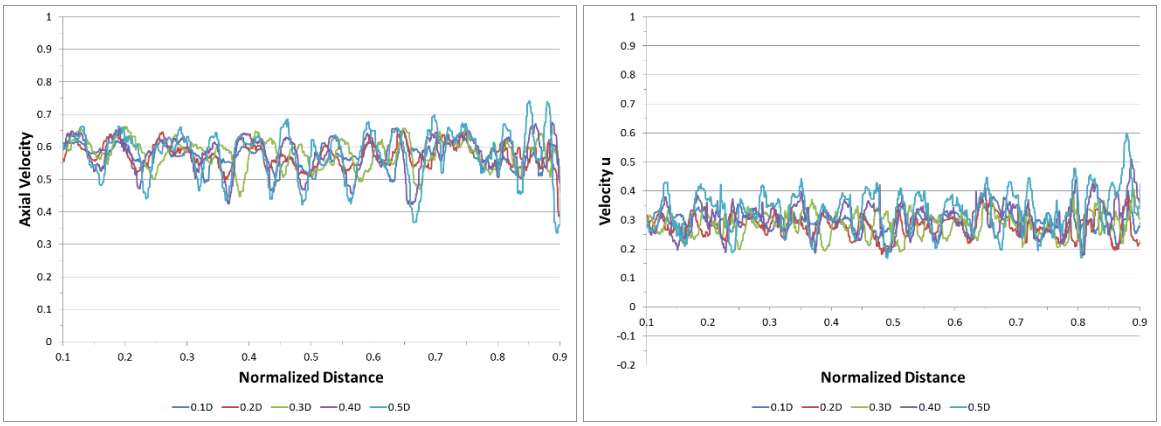
If only the axial flow component of the velocity is regarded, it is noted that a stronger flow is formed in the immediate vicinity of the cylinder surface, at 0.1D for cases $\alpha = 54.7°$, $\beta = 40°$, $\phi = 64°$, Re = 1.1×10^5; $\alpha = 50°$, $\beta = 40°$, $\phi = 60.5°$, Re = 3.3×10^5; and $\alpha = 50°$, $\beta = 20°$, $\phi = 53°$, Re = 4.4×10^5. The flow runs along the leeward side of the cylinder streaming parallel to the cylinder axis with a magnitude of $V_{axial}/U = 0.55 – 0.65$. This reduced to $V_{axial}/U = 0.5 – 0.45$ at distances 0.4D and 0.5D downstream from the cylinder (Figures 4.4 (a), (c) and (f)). No significant variation was noticed between the intensity of the axial flow component for the cases of $\alpha = 60°$, $\beta = 20°$, $\phi = 62°$, Re = 3.3×10^5; $\alpha = 60°$, $\beta = 20°$, $\phi = 62°$, Re = 5.5×10^5; $\alpha = 60°$, $\beta = 0°$, $\phi = 60°$, Re = 6.7×10^5; $\alpha = 60°$, $\beta = 0°$, $\phi = 60°$, Re = 3.3×10^5 (Figure 4.4 (d), (g), (h) and (i)), with $V_{axial}/U = 0.55 – 0.7$. Still higher axial flow intensities were observed as the distance away from the cylinder increased to 0.4D and 0.5D for $\alpha = 50°$, $\beta = 20°$, $\phi = 53°$, Re = 3.3×10^5; $\alpha = 60°$, $\beta = 20°$, $\phi = 62°$, Re = 3.3×10^5; and $\alpha = 54.7°$, $\beta = 40°$, $\phi = 64°$, Re = 3.3×10^5 (Figures 4.4 (b),

(d), and (e)) with similar $V_{axial}/U = 0.55 – 0.7$. As expected, the axial flow for the case of flow perpendicular to the cylinder, $\alpha = 0°$, $\beta = 0°$, $\phi = 0°$, $Re = 6.7 \times 10^5$, fluctuated up and down the length of the cylinder where the maximum value of $V_{axial}/U = 0.25$ were registered. The recorded values for the axial flow components were found to be in good agreement with the experiments performed by Matsumoto et al. (2010), and very close to the results reported by Katsuchi et al. (2009) as detailed below.

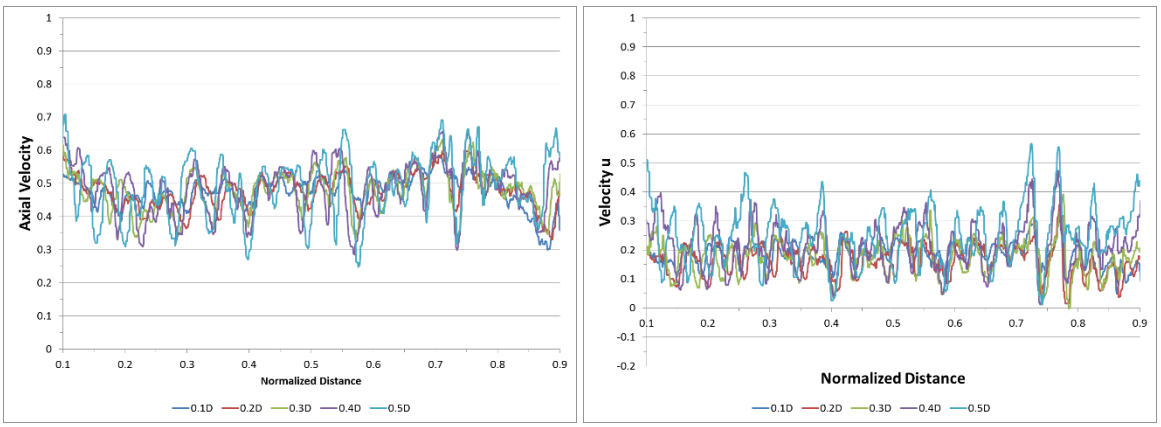
Katsuchi et al. (2009) performed wind tunnel experiments measuring the axial flow behind cylinders with a smooth surface and with an indented surface, as a countermeasure against rain-induced cable vibrations. The velocities along the axis of the cylinder measured on its leeward side were found to be in the range of $V_{axial}/U = 0.12 – 0.34$ for a $Re = 5.0 \times 10^3$ and for the inclination angle 45°. Matsumoto et al. (2010) completed a study on yawed cables of 45° with smooth surface and the axial flow measurements reported from these wind tunnel experiments varied from $V_{axial}/U = 0.42$ to 0.78. The cylinder used in this case however, was shorter, at approximately 15D, while the cylinder model used in the present study has the length of 30D.



a) $\alpha = 54.7°$, $\beta = 40°$, $\phi = 64°$, Re = 1.1×10^5;

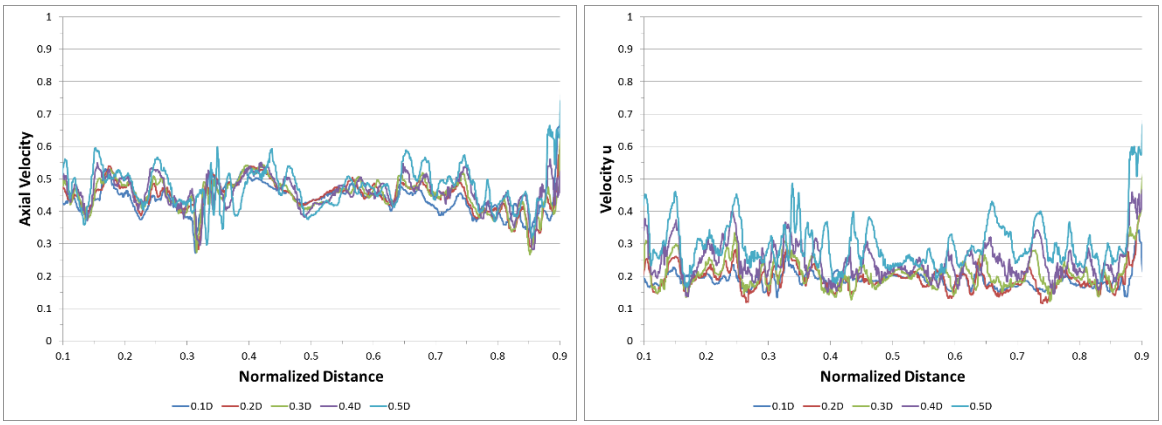


b) $\alpha = 50°$, $\beta = 20°$, $\phi = 53°$, Re = 3.3×10^5;

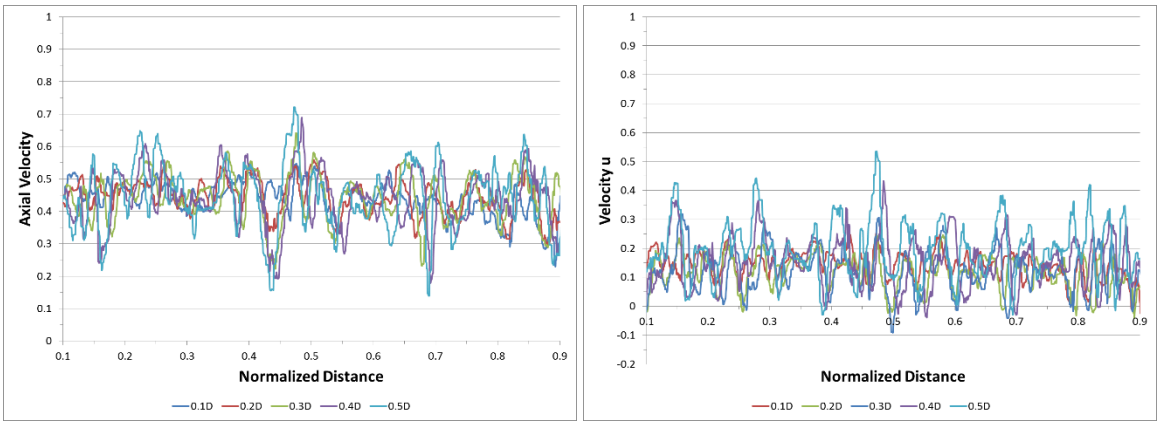


c) $\alpha = 50°$, $\beta = 40°$, $\phi = 60.5°$, Re = 3.3×10^5;

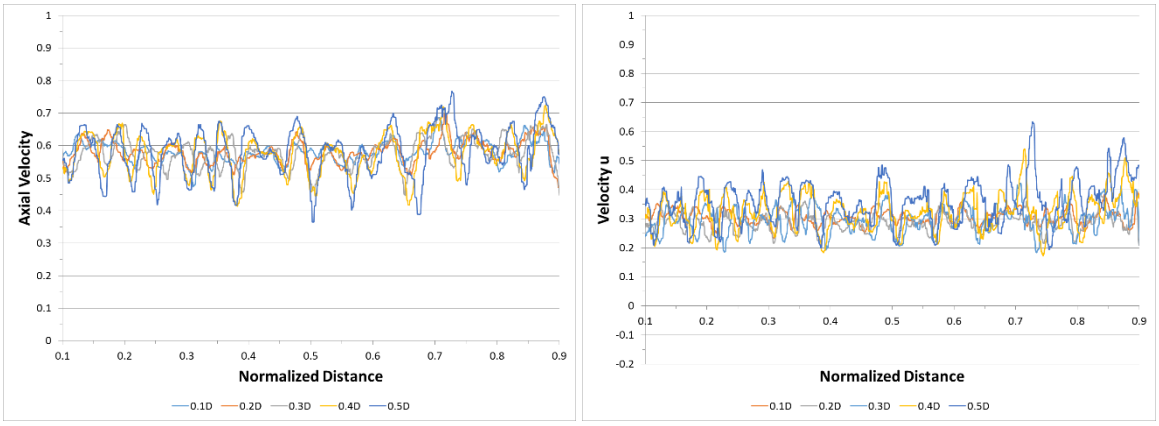
Figure 4.4: Axial and along stream flow



d) $\alpha = 60°$, $\beta = 20°$, $\phi = 62°$, Re = 3.3×10^5;

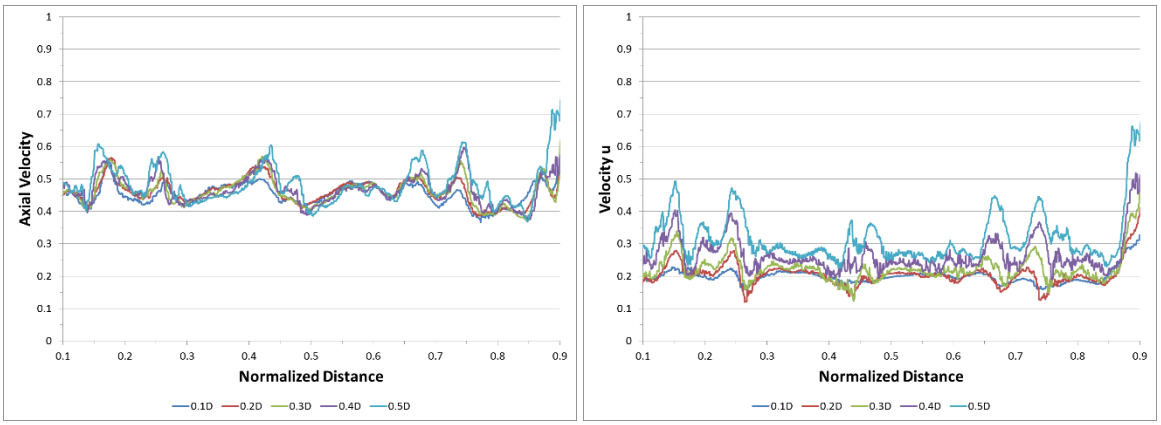


e) $\alpha = 54.7°$, $\beta = 40°$, $\phi = 64°$, Re = 3.3×10^5;

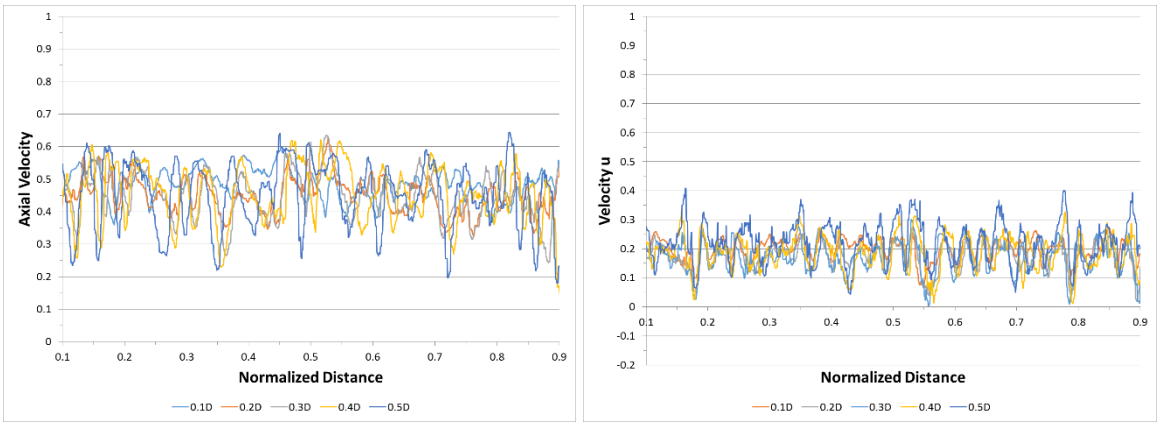


f) $\alpha = 50°$, $\beta = 20°$, $\phi = 53°$, Re = 4.4×10^5;

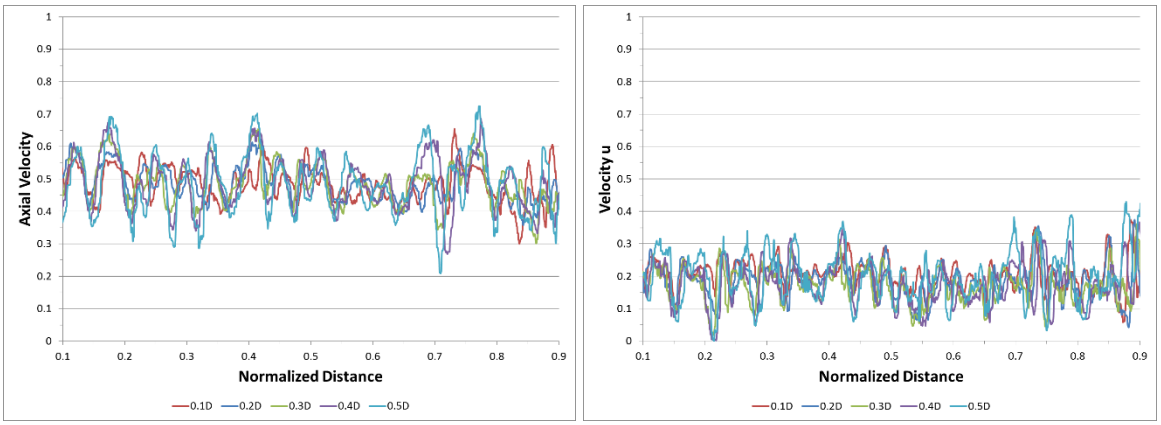
Figure 4.4: Axial and along stream flow



g) $\alpha = 60°$, $\beta = 20°$, $\phi = 62°$, Re = 5.5×10^5;

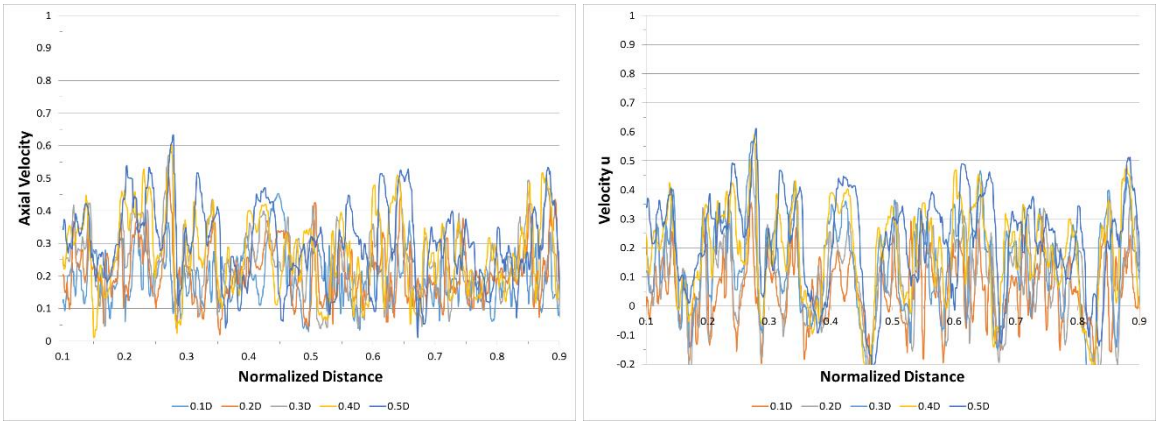


h) $\alpha = 60°$, $\beta = 0°$, $\phi = 60°$, Re = 6.7×10^5;



i) $\alpha = 60°$, $\beta = 0°$, $\phi = 60°$, Re = 3.3×10^5;

Figure 4.4: Axial and along stream flow



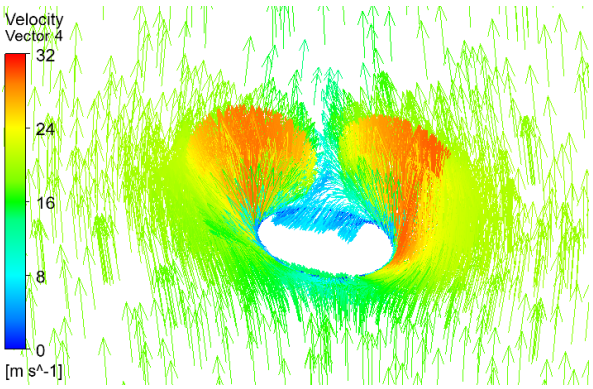
j) $\alpha = 0°$, $\beta = 0°$, $\phi = 0°$, Re = 6.7×10^5.

Figure 4.4: Axial and along stream flow

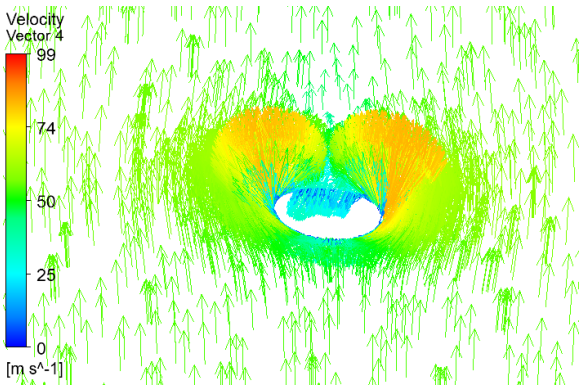
4.4 Interpretation and Identification of the Axial Flow

The velocity vector plots are presented in this section showing the magnitude and direction of the flow around the cylinder for a plane cutting through the middle of the cylinder. The vector representation for the 10 samples cases is shown in Figure 4.5(a) to (j), and Appendix F contains the vector plots for all cases performed in this study. As the flow approaches the cylinder the velocity tends to decrease when the flow is redirected around the sides of the cylinder where the shear layers detach under a slight upwards direction. As the flow reaches the leeward side of the cylinder the vectors indicate that the flow is directed down the cylinder, moving along the axis of the model, and not downstream with the flow. The flow along the leeward side of the cylinder is limited and fairly concentrated for the cases: $\alpha = 60°$, $\beta = 20°$, $\phi = 62°$, Re = 3.3×10^5; $\alpha = 60°$, $\beta = 20°$, $\phi = 62°$, Re = 5.5×10^5; $\alpha = 60°$, $\beta = 0°$, $\phi = 60°$, Re = 6.7×10^5; (Figures 4.5(d), (g), and (h)); and more widespread for $\alpha = 54.7°$, $\beta = 40°$, $\phi = 64°$, Re = 1.1×10^5; $\alpha = 50°$, $\beta = 20°$, $\phi = 53°$, Re = 3.3×10^5; $\alpha = 50°$, $\beta = 40°$, $\phi = 60.5°$, Re = 3.3×10^5; $\alpha = 54.7°$, $\beta = 40°$, $\phi = 64°$, Re = 3.3×10^5; $\alpha = 50°$, $\beta = 20°$, $\phi = 53°$, Re = 4.4×10^5; i) $\alpha = 60°$, $\beta = 0°$, $\phi = 60°$, Re = 3.3×10^5 (Figures 4.5(a), (b), (c), (e), (f), and (i). Also, for the case of flow perpendicular to the cylinder, ϕ

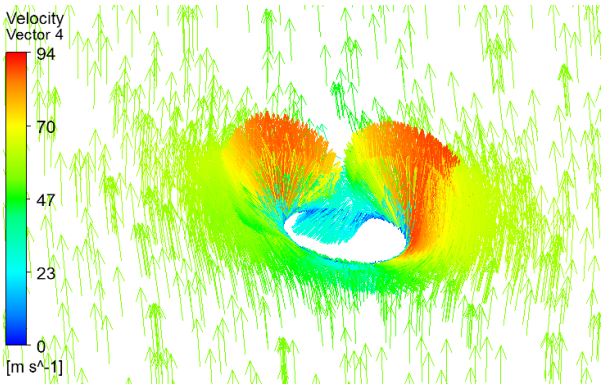
= 0°, Re = 6.7 × 10^5 (Figure 4.5 (j)), the velocity vectors are not aligned along one direction, indicating a turbulent flow generated behind the cable model, but not necessary along the model.



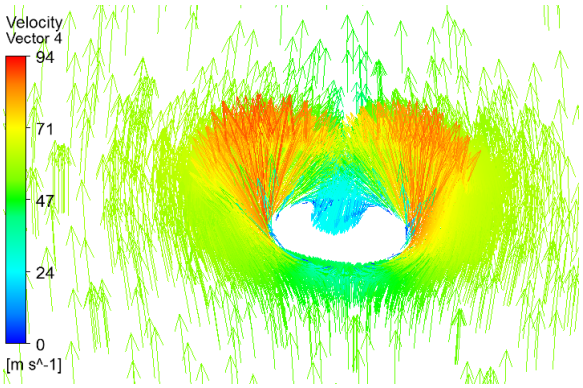
a) α = 54.7°, β = 40°, ϕ = 64°, Re = 1.1 × 10^5;



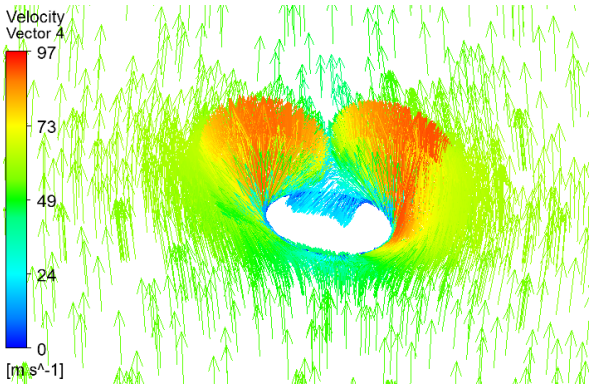
b) α = 50°, β = 20°, ϕ = 53°, Re = 3.3 × 10^5;



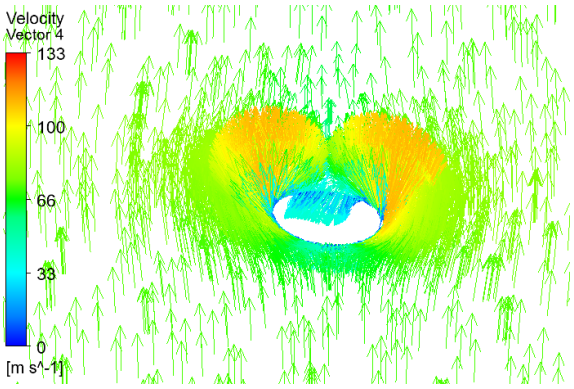
c) α = 50°, β = 40°, ϕ = 60.5°, Re = 3.3 × 10^5;



d) α = 60°, β = 20°, ϕ = 62°, Re = 3.3 × 10^5;

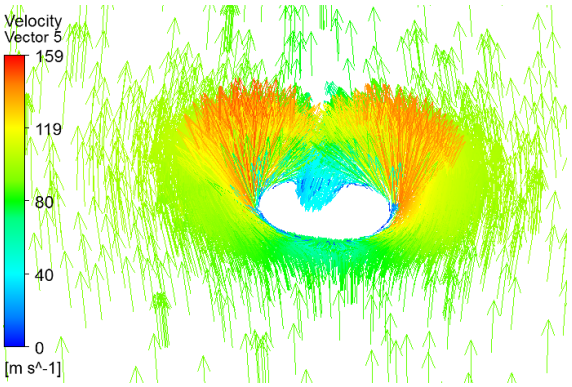


e) α = 54.7°, β = 40°, ϕ = 64°, Re = 3.3 × 10^5;

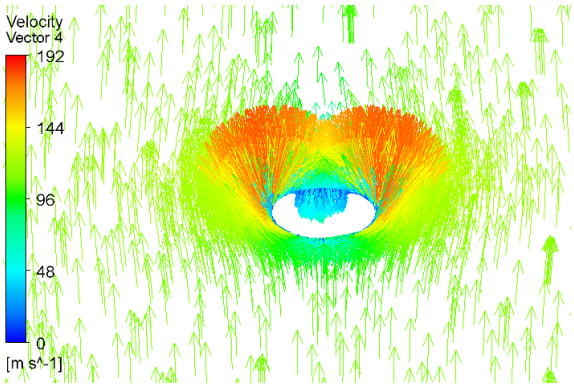


f) α = 50°, β = 20°, ϕ = 53°, Re = 4.4 × 10^5;

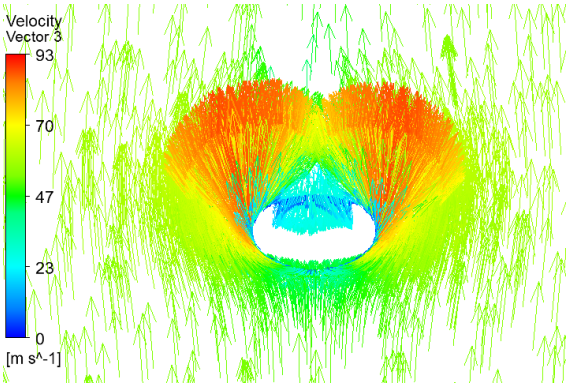
Figure 4.5: Velocity vectors



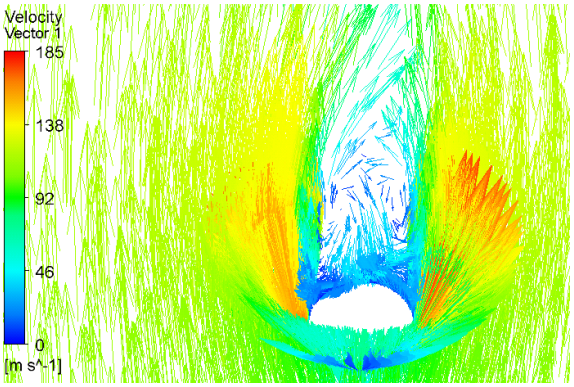
g) $\alpha = 60°$, $\beta = 20°$, $\phi = 62°$, Re = 5.5×10^5;



h) $\alpha = 60°$, $\beta = 0°$, $\phi = 60°$, Re = 6.7×10^5;



i) $\alpha = 60°$, $\beta = 0°$, $\phi = 60°$, Re = 3.3×10^5;



j) $\alpha = 0°$, $\beta = 0°$, $\phi = 0°$, Re = 6.7×10^5.

Figure 4.5: Velocity vectors

4.5 Characteristics of Axial Flow around Circular Cylinder

To continue with the flow visualizations, and to provide a better understanding of the flow formation around the cylinder the three-dimensional visualizations showing the flow streamlines are shown in Figures 4.6(a) to (j). This will also help illustrate the amount of flow which is redirected along the leeward side of the cylinder as an axial flow. The streamlines results obtained for all the cases investigated in this study are shown in Appendix G. The streamlines start from a plane parallel to the direction of flow that crosses the cylinder, and the resulting paths of the flow contained in that plane are shown for three different locations along the cylinder.

The difference between the flow around a cylinder inclined to the flow (Figures 4.6(a) to (i)), and the flow around a cylinder perpendicular to the flow (Figure 4.6(j)) becomes clear when

the streamlines are represented. For the cases of inclined, and inclined and yawed cylinders, the streamlines approach the cylinder along the same plane, where they are deviated around the sides, and then along the leeward side of the cylinder streaming along the length of the cylinder, and detaching at various intervals downstream. The flow shown by the streamlines for the flow perpendicular to the cylinder case are shown, as expected, streaming along the same plane after which they are deviated around the sides of the cylinder, developing into a turbulent formation behind the cylinder, and continuing to travel downstream along in the same direction as the initial flow. Several features of the formation of the axial flow formed on the leeward side of the inclined and/or yawed cylinders were identified as described below.

From the detachment point, majority of streamlines continued in the direction of the incoming flow spreading on planes adjacent to the incoming flow forming a "curtain" of different widths: wide for $\alpha = 60°$, $\beta = 0°$, $\phi = 60°$, Re = 6.7×10^5 (Figure 4.6(h)); medium for $\alpha = 54.7°$, $\beta = 40°$, $\phi = 64°$, Re = 1.1×10^5; $\alpha = 50°$, $\beta = 20°$, $\phi = 53°$, Re = 3.3×10^5; $\alpha = 54.7°$, $\beta = 40°$, $\phi = 64°$, Re = 3.3×10^5; $\alpha = 50°$, $\beta = 20°$, $\phi = 53°$, Re = 4.4×10^5; $\alpha = 60°$, $\beta = 0°$, $\phi = 60°$, Re = 3.3×10^5 (Figures 4.6 (a), (b), (e), (f), and (i)); and thin for $\alpha = 50°$, $\beta = 40°$, $\phi = 60.5°$, Re = 3.3×10^5; $\alpha = 60°$, $\beta = 20°$, $\phi = 62°$, Re = 3.3×10^5; $\alpha = 60°$, $\beta = 20°$, $\phi = 62°$, Re = 5.5×10^5 (Figures (c), (d), and (g)). The "curtain" widths were defined to be wide if approximately 75% of the zone between the contributing planes are shown to have redirected streamlines. The zone between contributing planes was 10D, as defined above. The medium "curtain" width was defined as 50% of the zone showing redirected streamlines, and the thin "curtain" width was identified for zones showing approximately 25% of the redirected stream lines. The bottom two zones were used as a better indication of the redirected flow, as they are the zone further downstream in the flow. For example, case $\alpha = 50°$, $\beta = 20°$, $\phi = 53°$, Re = 4.4×10^5 illustrated in Figure 4.6(f) shows a wide

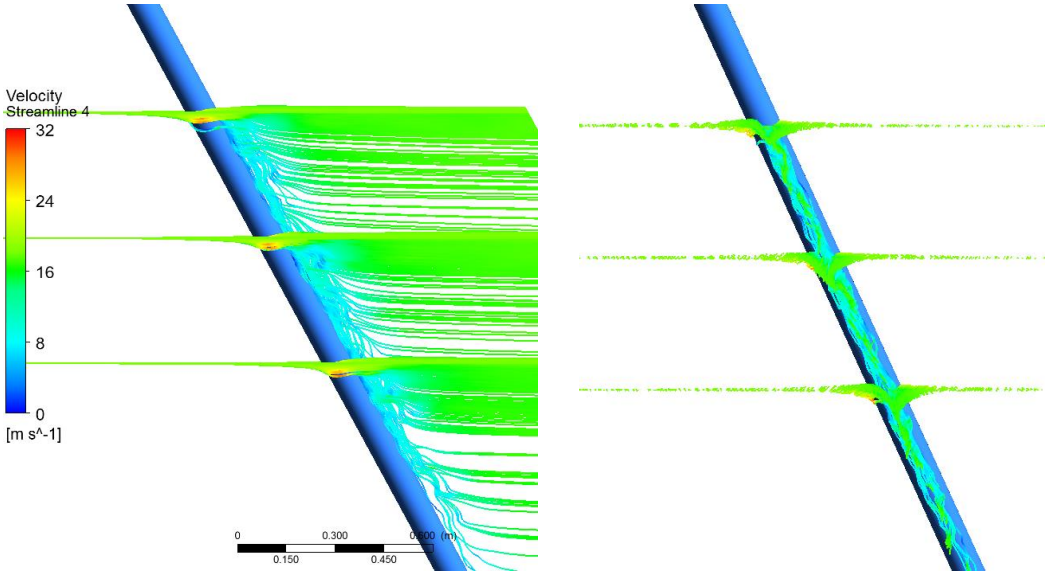
"curtain" width for the upper zone, but medium width in the middle and the lower zone, so it was classified in the medium group.

The streamlines were redirected along the leeward side of the cylinder, and detached at irregular intervals along the length of the cylinder. The flow remaining attached to the cylinder from the contributing velocity plane reduced significantly, and almost disappeared towards the lower extremity of the cylinder for cases $\alpha = 54.7°$, $\beta = 40°$, $\phi = 64°$, Re = 1.1×10^5; $\alpha = 50°$, $\beta = 40°$, $\phi = 60.5°$, Re = 3.3×10^5; $\alpha = 60°$, $\beta = 20°$, $\phi = 62°$, Re = 3.3×10^5; $\alpha = 54.7°$, $\beta = 40°$, $\phi = 64°$, Re = 3.3×10^5; $\alpha = 50°$, $\beta = 20°$, $\phi = 53°$, Re = 4.4×10^5 (Figures 4.6 (a), (c), (d), (e), and (f)). For other cases of $\alpha = 50°$, $\beta = 20°$, $\phi = 53°$, Re = 3.3×10^5; $\alpha = 60°$, $\beta = 20°$, $\phi = 62°$, Re = 5.5×10^5; $\alpha = 60°$, $\beta = 0°$, $\phi = 60°$, Re = 6.7×10^5; $\alpha = 60°$, $\beta = 0°$, $\phi = 60°$, Re = 3.3×10^5; (Figures 4.6 (b), (g), (h), and (i)), a limited number of streamlines detached at downwards points, but a significant portion of the flow remained attached along the leeward side of the cylinder for a significant duration downstream of the incoming flow.

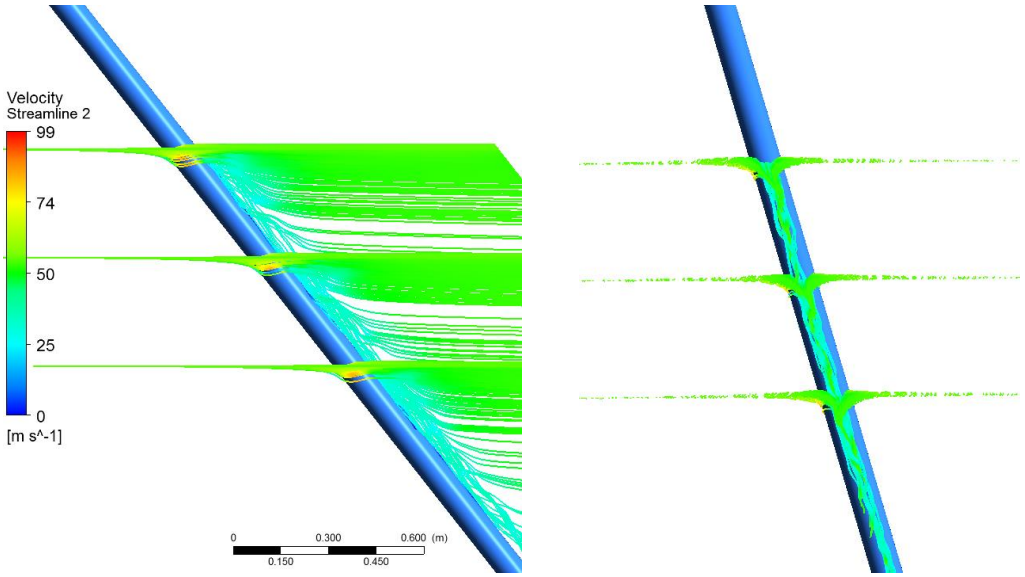
All cases showed a very strong flow disturbance along the axis of the cylinder, and undulating streamlines along the leeward side of the cylinder. This illustrates that the axial flow is not uniform along the axis of the cylinder, but is influenced by the continuous contribution of the flow along the length of the cylinder.

Regardless of the Reynolds number, and the inclination of the cylinder in this study the flow developed along the leeward side of the cylinder in spite of the detachment of the flow along the length. As shown above the presence of the axial flow along the leeward side of the cylinder is the major difference between the flow mechanism around a cylinder perpendicular, and a cylinder inclined or inclined and yawed cylinder to the flow. Therefore we could conclude that the axial flow, which was identified and measured in experiments by several researchers (Matsumoto

1998, Cheng et al. 2008, Katsuchi et al. 2009), is not a localized flow pattern, but is a characteristic of the flow regime for inclined cylinders.

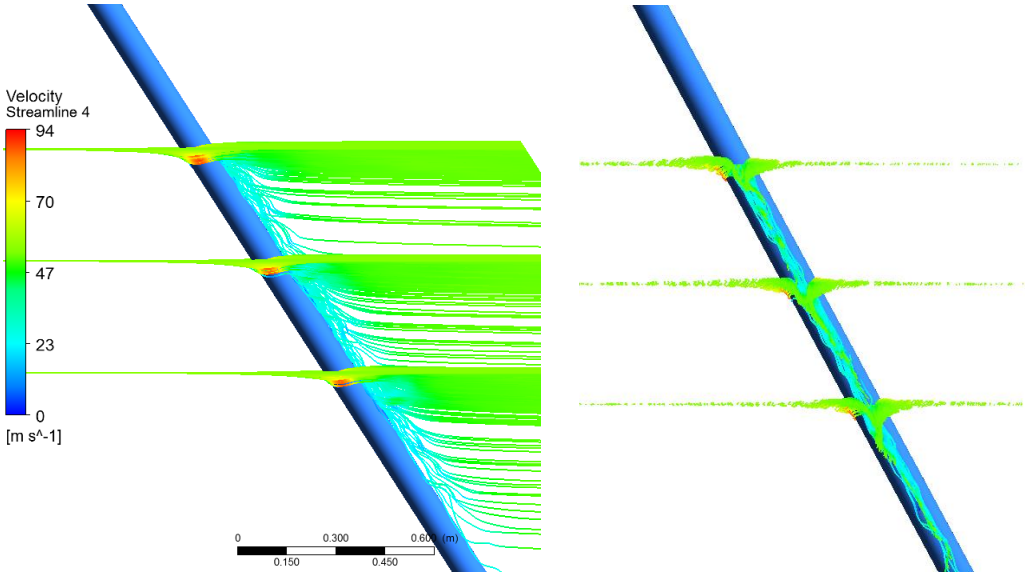


a) $\alpha = 54.7°$, $\beta = 40°$, $\phi = 64°$, Re = 1.1×10^5;

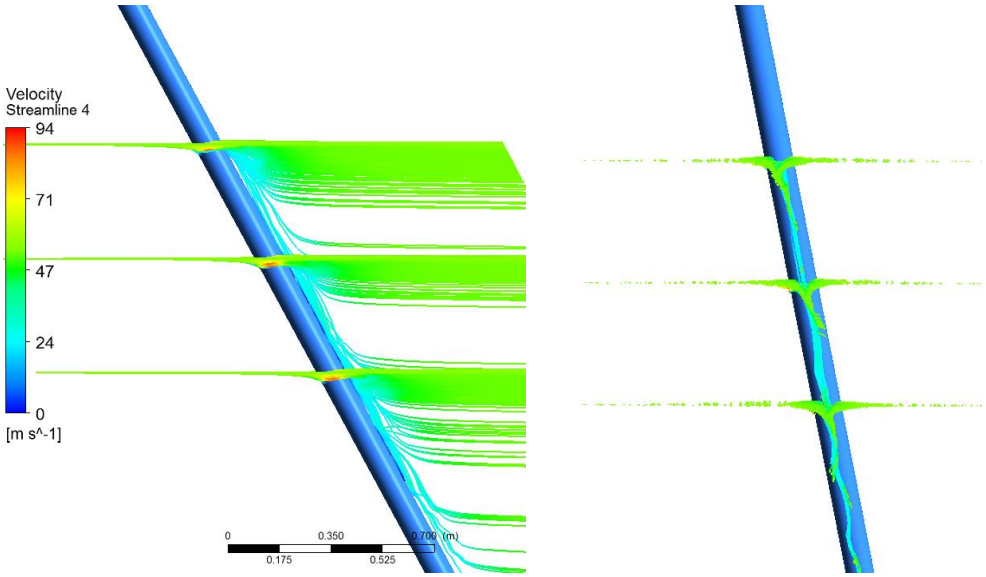


b) $\alpha = 50°$, $\beta = 20°$, $\phi = 53°$, Re = 3.3×10^5;

Figure 4.6: Axial flow visualization, velocity streamlines

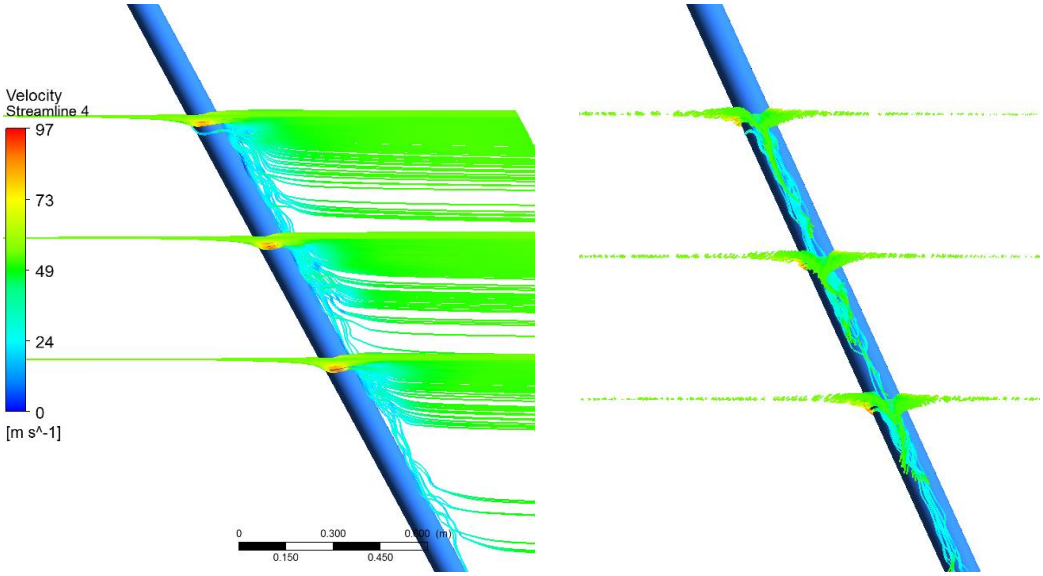


c) $\alpha = 50°$, $\beta = 40°$, $\phi = 60.5°$, Re = 3.3×10^5;

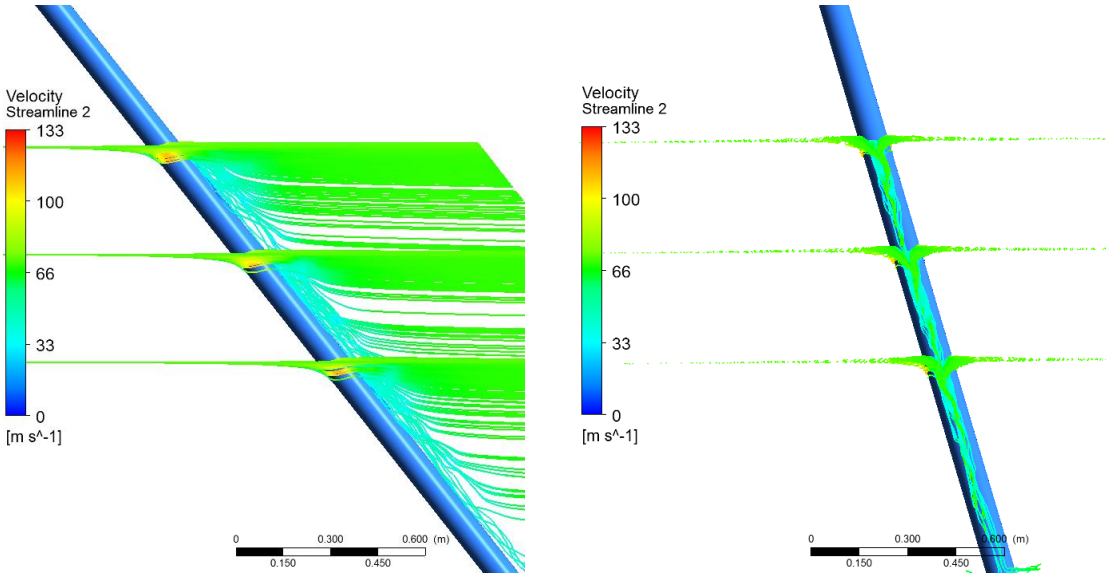


d) $\alpha = 60°$, $\beta = 20°$, $\phi = 62°$, Re = 3.3×10^5;

Figure 4.6: Axial flow visualization, velocity streamlines

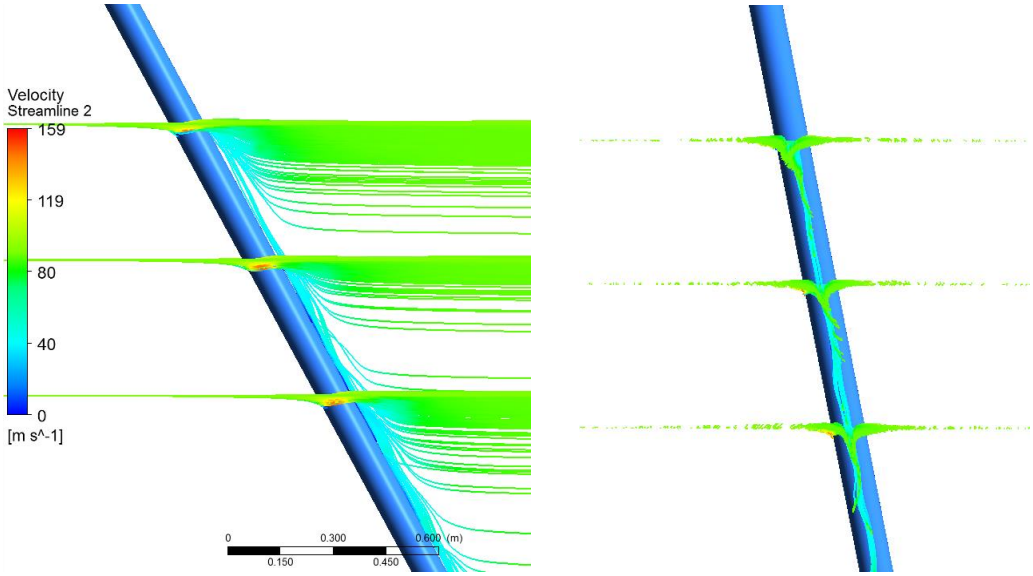


e) $\alpha = 54.7°$, $\beta = 40°$, $\phi = 64°$, Re = 3.3×10^5;

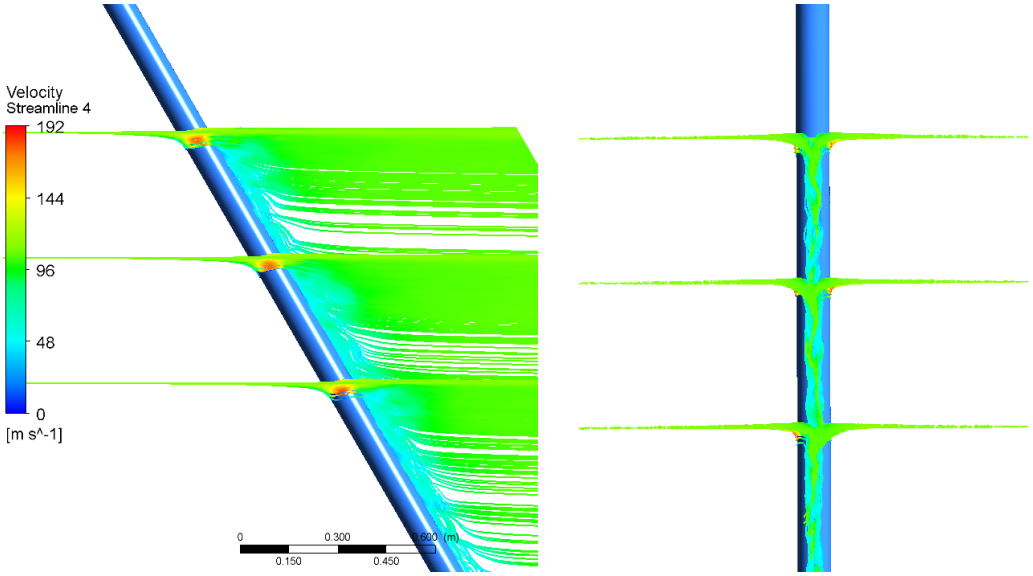


f) $\alpha = 50°$, $\beta = 20°$, $\phi = 53°$, Re = 4.4×10^5;

Figure 4.6: Axial flow visualization, velocity streamlines

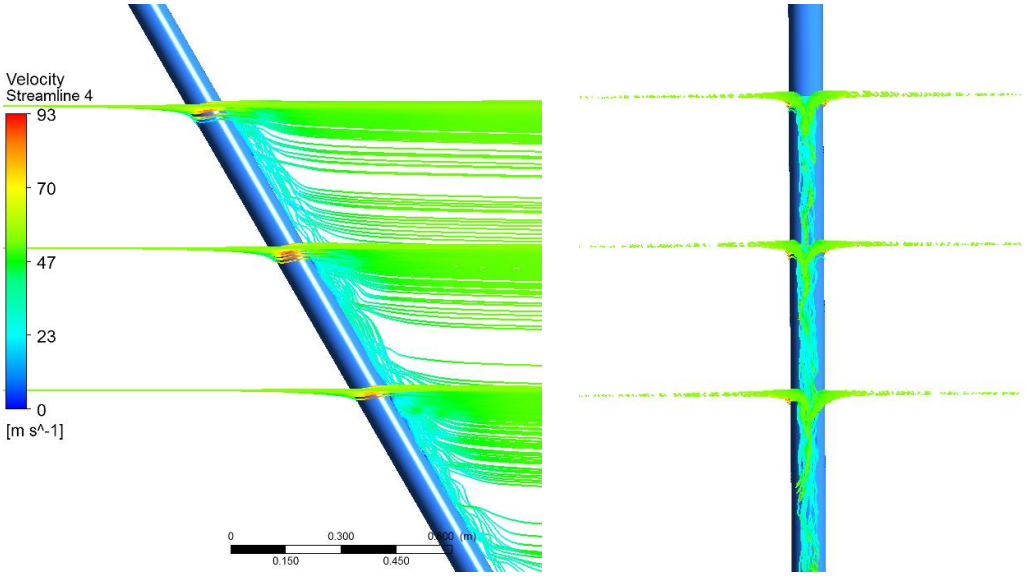


g) $\alpha = 60°$, $\beta = 20°$, $\phi = 62°$, Re = 5.5×10^5;

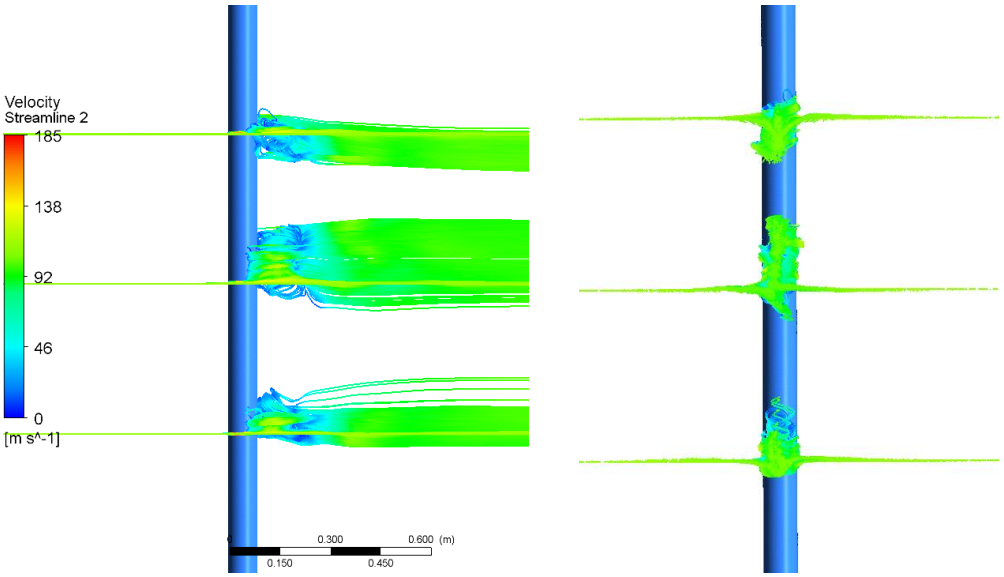


h) $\alpha = 60°$, $\beta = 0°$, $\phi = 60°$, Re = 6.7×10^5;

Figure 4.6: Axial flow visualization, velocity streamlines



i) $\alpha = 60°$, $\beta = 0°$, $\phi = 60°$, Re = 3.3×10^5;



j) $\alpha = 0°$, $\beta = 0°$, $\phi = 0°$, Re = 6.7×10^5.

Figure 4.6: Axial flow visualization, velocity streamlines

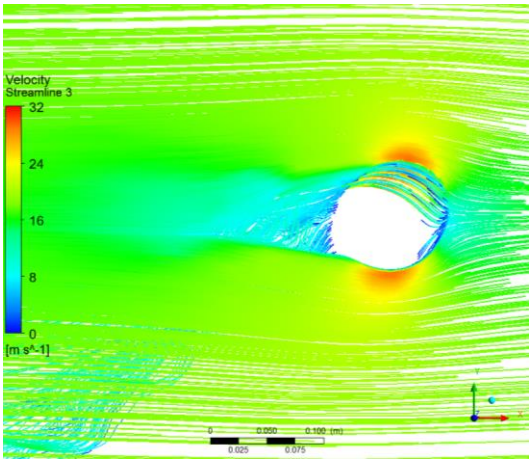
4.6 Velocity Streamlines in a Two-dimensional Plane

To provide a different view of the velocity streamlines, and a more comparable representation to the velocity vectors discussed in the section above, the velocity streamlines are presented in a two-dimensional plane cutting the cylinder in its center, used as the starting for the velocity streamlines. This is the same plane as the one outlined in the previous section on velocity

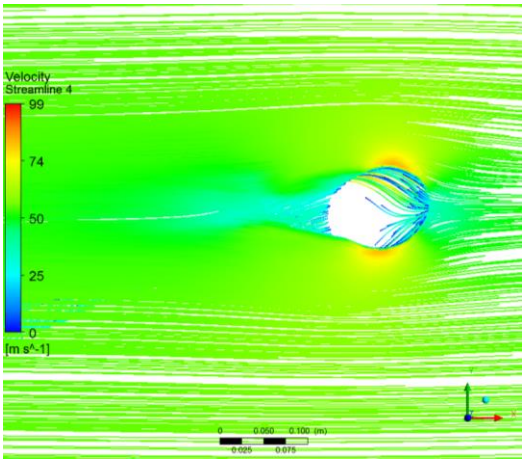
streamlines. The results are presented in Figures 4.7(a) – (j), and Appendix H contains the velocity streamlines for all cases performed in this study.

A very smooth flow pattern resulted by viewing the velocity streamlines for the flow inclined to the cylinder at 60°, and yawed at 0° at Re = 6.7×10^5. The shear layers uniformly surrounding the cylinder until they reach the leeward side of the cylinder (Figure 4.7(h)) where they detach from its surface, and converge towards a joining point downstream the cylinder. The velocity vectors shown above for the same location indicated a change in the flow along the leeward side of the cylinder, and not downstream (Figure 4.7(h)). In Figure 4.7(c), for $\alpha = 50°$, $\beta = 40°$, $\phi = 60.5°$ and Re = 3.3×10^5 also a very smooth flow pattern with shear layers uniformly distributed around the cylinder detaching as they approach the leeward side of the cylinder, and converging downstream of the cylinder are shown. This is a common flow configuration for a majority of cases investigated ($\phi = 64°$, Re = 1.1×10^5; $\phi = 53°$, Re = 3.3×10^5; $\phi = 62°$, Re = 3.3×10^5; $\phi = 64°$, Re = 3.5×10^5; $\phi = 53°$, Re = 4.4×10^5; and $\phi = 62°$, Re = 5.5×10^5); shown in Figures 4.7(a), (b), (d), (e), (f), (g), and (i).

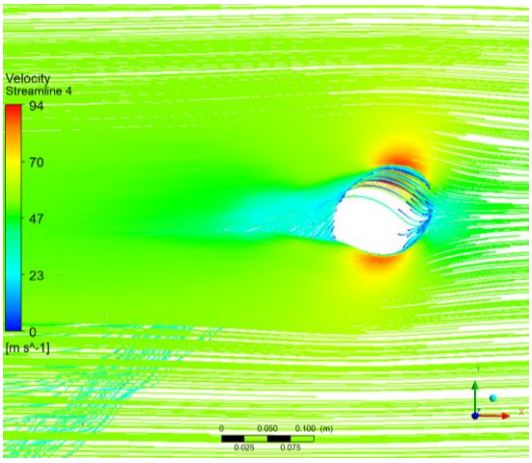
For the cylinder perpendicular to the flow at that same Re = 6.7×10^5 ($\alpha = 0°$, $\beta = 0°$, $\phi = 0°$), it was noticed that the streamlines will keep their parallel tracks until the detachment points on the sides of the cylinder were encountered, from where these will depart downstream with the flow. However behind the cylinder, and in the immediate vicinity of its leeward surface alternate vortices were identified (Figure 4.7(j)). The same tendency was noticed for the above velocity vectors (Figure 4.5 (j)), which showed the velocity alternating directions along the leeward side of the cylinder. This is in addition to the streamlines alternating directions up and down the leeward side of the cylinder as represented in Figure 4.6 (j).



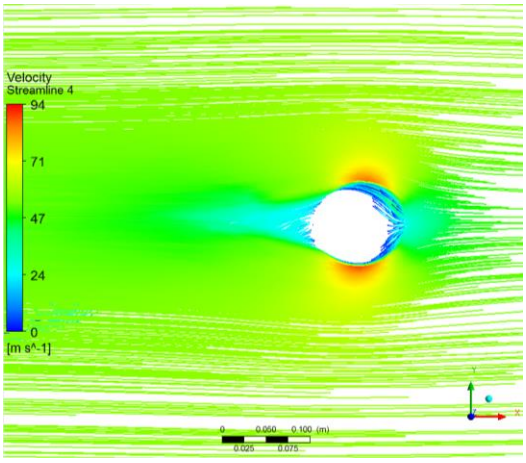
a) $\alpha = 54.7°$, $\beta = 40°$,
$\phi = 64°$, Re = 1.1×10^5;



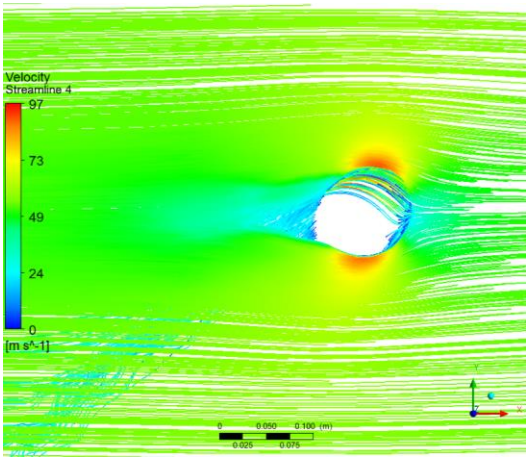
b) $\alpha = 50°$, $\beta = 20°$,
$\phi = 53°$, Re = 3.3×10^5;



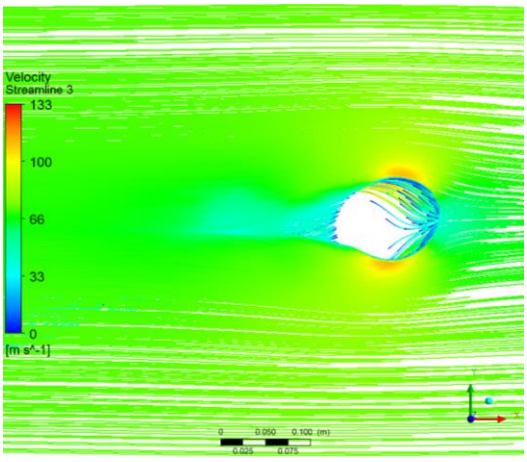
c) $\alpha = 50°$, $\beta = 40°$,
$\phi = 60.5°$, Re = 3.3×10^5;



d) $\alpha = 60°$, $\beta = 20°$,
$\phi = 62°$, Re = 3.3×10^5;

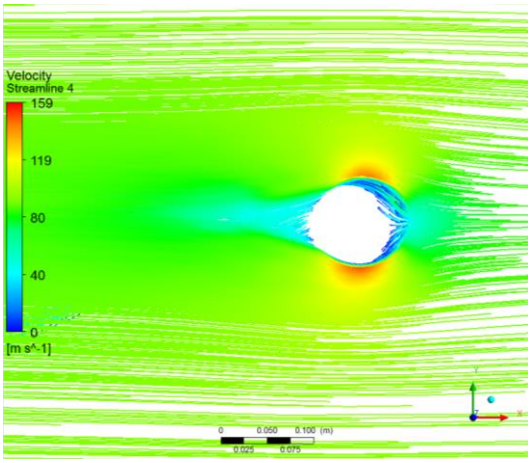


e) $\alpha = 54.7°$, $\beta = 40°$,
$\phi = 64°$, Re = 3.3×10^5;

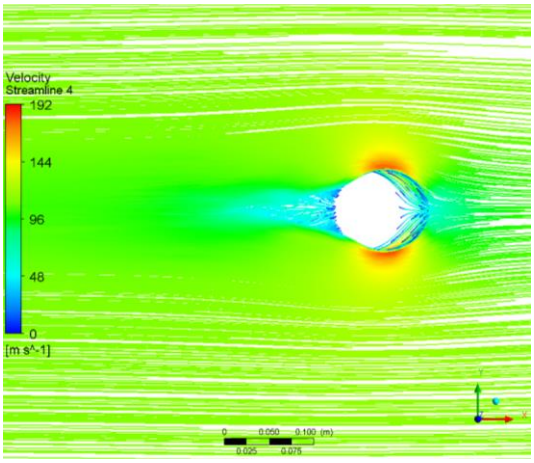


f) $\alpha = 50°$, $\beta = 20°$,
$\phi = 53°$, Re = 4.4×10^5;

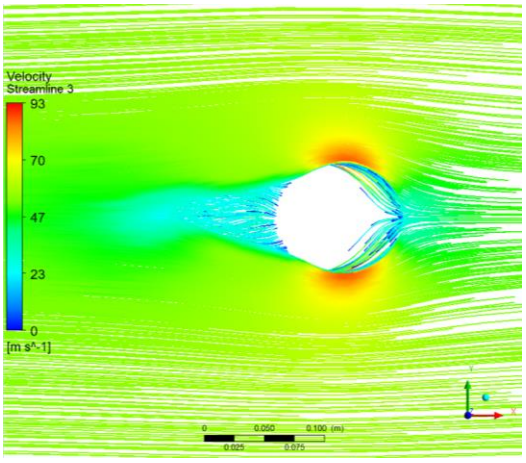
Figure 4.7: Velocity streamlines in a two-dimensional plane



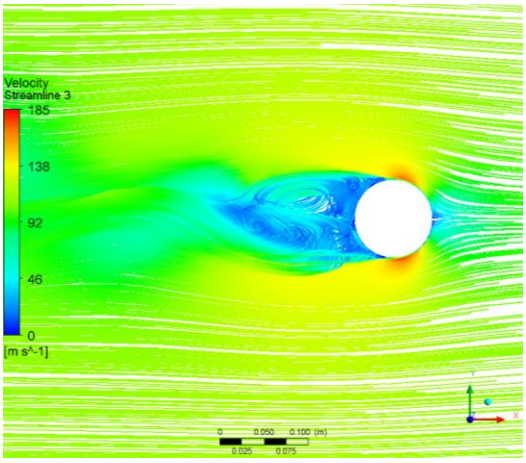
g) $\alpha = 60°$, $\beta = 20°$, $\phi = 62°$, Re = 5.5×10^5;



h) $\alpha = 60°$, $\beta = 0°$, $\phi = 60°$, Re = 6.7×10^5;



i) $\alpha = 60°$, $\beta = 0°$, $\phi = 60°$, Re = 3.3×10^5;



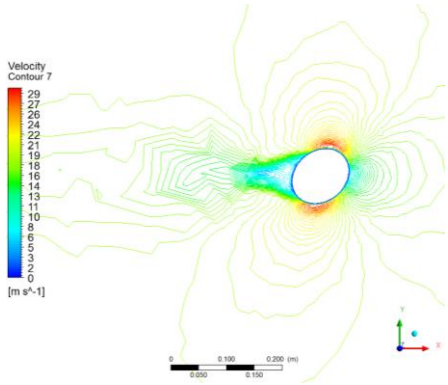
j) $\alpha = 0°$, $\beta = 0°$, $\phi = 0°$, Re = 6.7×10^5.

Figure 4.7: Velocity streamlines in a two-dimensional plane

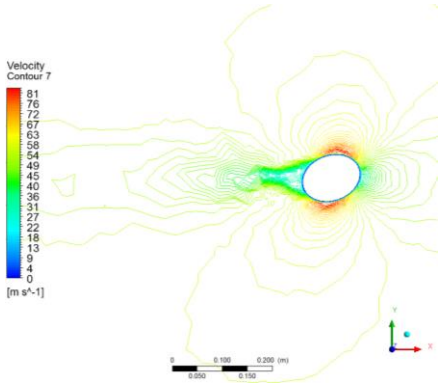
4.7 Dominant Velocity Zones and Flow Patterns

To help identifying the flow characteristics around an inclined cylinder the velocity contours are plotted in Figure 4.8(a) to (j). The distributions are shown in a plane parallel to the initial flow field, intersecting the center of the cylinder, and parallel to the computational domain at the ends of the cylinder. The ten sample cases are shown below with all cases presented in Appendix I. It was noticed that the flow patterns for the first 9 cases (Figures 4.8(a)-(i)), which are the cases of the inclined and yawed to the cylinder, showed narrower flow patterns when compared to the flow

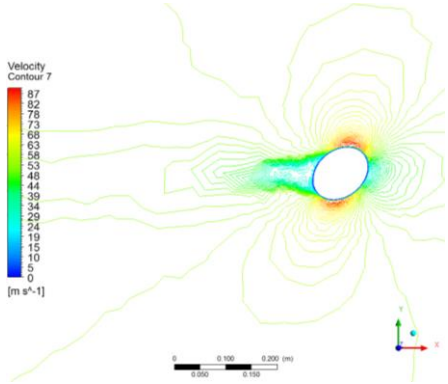
perpendicular to the flow (Figure 4.8(j)). A full description of these cases is presented in the next section along with the description of the flow characteristics shown in the velocity profiles.



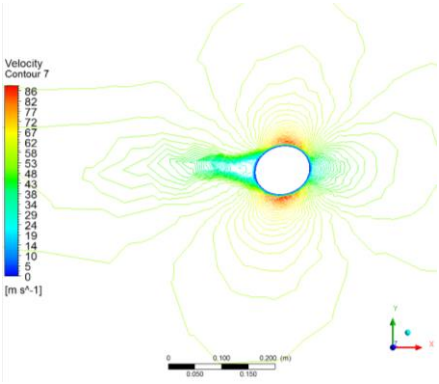
a) $\alpha = 54.7°$, $\beta = 40°$, $\phi = 64°$, Re = 1.1×10^5;



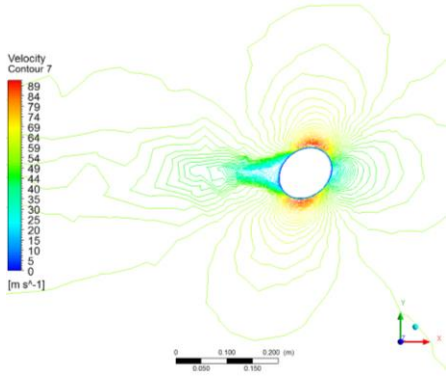
b) $\alpha = 50°$, $\beta = 20°$, $\phi = 53°$, Re = 3.3×10^5;



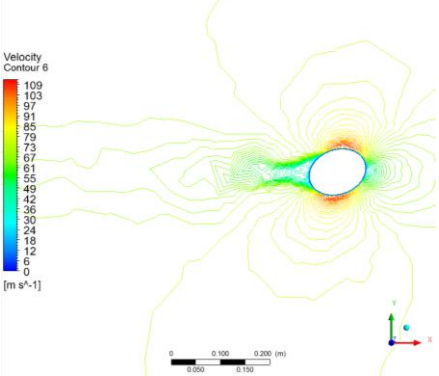
c) $\alpha = 50°$, $\beta = 40°$, $\phi = 60.5°$, Re = 3.3×10^5;



d) $\alpha = 60°$, $\beta = 20°$, $\phi = 62°$, Re = 3.3×10^5;

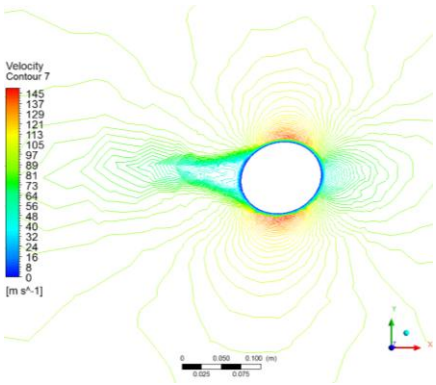


e) $\alpha = 54.7°$, $\beta = 40°$, $\phi = 64°$, Re = 3.3×10^5;

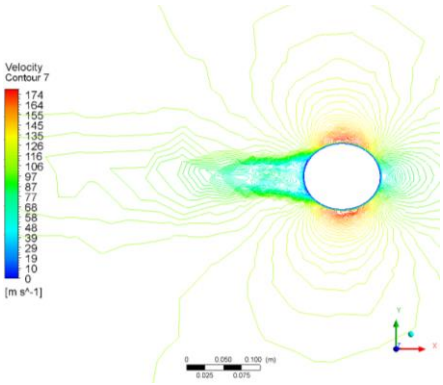


f) $\alpha = 50°$, $\beta = 20°$, $\phi = 53°$, Re = 4.4×10^5;

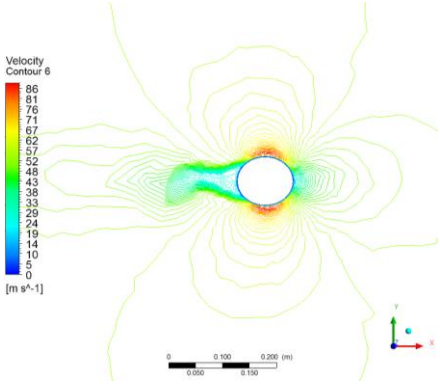
Figure 4.8: Dominant velocity zones and flow patterns



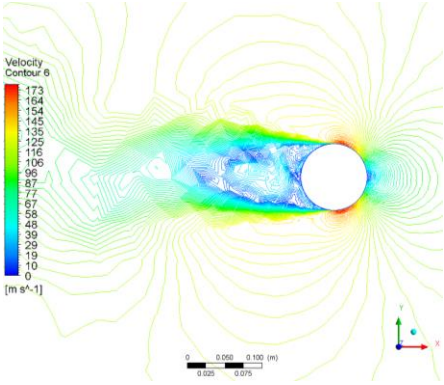
g) $\alpha = 60°$, $\beta = 20°$, $\phi = 62°$, Re = 5.5×10^5;



h) $\alpha = 60°$, $\beta = 0°$, $\phi = 60°$, Re = 6.7×10^5;



i) $\alpha = 60°$, $\beta = 0°$, $\phi = 60°$, Re = 3.3×10^5;



j) $\alpha = 0°$, $\beta = 0°$, $\phi = 0°$, Re = 6.7×10^5.

Figure 4.8: Dominant velocity zones and flow patterns

4.8 Tendencies of the Pressure and Velocity Distributions for Inclined and Perpendicular Cylinders

As can be seen in the above sections, there is a change in the flow patterns when the cylinder is inclined and yawed with respect to the incoming flow. This is most evident with the development of an axial flow along the leeward side of the cylinder. The intensity of this axial flow changes due to different variables of the approaching flow including the relative angle of the cylinder with respect to the flow, and the Re.

Also, a new flow pattern is developing for which the same cases are showing similar characteristics, at the different parameters analysed, as used in this section. The model parameters were $\alpha = 54.7°$, $\beta = 40°$, $\phi = 64°$, Re = 1.1×10^5; and $\alpha = 54.7°$, $\beta = 40°$, $\phi = 64°$, Re = 3.3×10^5;

or cases (a) and (e) which are grouped together, when comparing the different parameters. These include the regions of high pressures along the leeward surface of the cylinder which was characterised by discontinuities of areas of low pressure patches, while the velocity distribution along the leeward side of the cylinder showed a formation of rotational vortices; the axial flow fluctuations increased as the distance from the cylinder increased to locations 0.1D to 0.5D downstream the cylinder, including the amount of flow redirected along the leeward side of the cylinder. The model parameters $\alpha = 60°$, $\beta = 20°$, $\phi = 62°$, Re = 3.3×10^5; and $\alpha = 60°$, $\beta = 20°$, $\phi = 62°$, Re = 5.5×10^5; or cases (d) and (g) were also grouped because these showed similar tendencies for many of the model parameters. Some of these parameters were shown in this chapter, including areas of positive and negative pressures in a non-alternating pattern along the leeward surface of the cylinder, a narrow pressure distribution along the leeward surface of the cylinder, the velocity distribution showing no rotational formations along the leeward side of the cylinder, and the intensity of the axial flow along the cylinder. These tendencies of the pressure and velocity distributions will be further examined in the next chapter along with additional parameters in developing a classification system for the flow regimes around inclined and yawed cylinders.

5 Flow Characteristics around Yawed/Inclined and Perpendicular Circular Cylinders

5.1 Flow Regimes for Inclined and Yawed Circular Cylinders

The classification of the flow regimes for flow perpendicular on the cylinder, as provided by Zdravkovich (1997), compiles extensive data from several researchers, and is conducted mainly based on the flow visualization in one plane. Zdravkovich (1997) reported the averaged pressure coefficient at the circumference of the cylinder, aerodynamic force coefficients, and visual identification of the flow patterns. Several flow regimes were identified spanning from laminar regime for low Re numbers of 0 to 180-200, transition in wake regime (TrW) for Re = 180 - 200 to 350 - 400, transition in shear layer regime (TrSL) for Re = 350 - 400 to 1.0×10^5 - 2.0×10^5 and transition in boundary layers (TrBL) for Re = 1.0×10^5 - 2.0×10^5 to more than 6.0×10^6. The higher the Re number, the more difficult capturing the flow pattern around cylinders perpendicular to flow due to the limited dimensions of the experimental facilities and the turbulent conditions of the flow. However, for inclined cylinders, the flow mechanism is different, and flow visualization in one plane is not sufficient to completely describe the flow regime. This requires a three-dimensional representation to best describe the flow.

5.2 Flow Characteristics around Inclined and Perpendicular Circular Cylinders

Several cases were investigated for different inclinations α = 50° - 60° and yaw angles of β = 0° - 40° of the cylinder (corresponding to relative angles of attack between ϕ = 53° and 64°) for Re numbers of 1.1×10^5 to 6.7×10^5. Using a similar delimitation of the velocity field as the one used by Zdravkovich (1997): the regions of retarded flow (the boundary layers attached to the surface of the cylinder which developed into free shear layers); the regions of displaced and

accelerated flow (sidewise the cylinder); and the downstream region of separated flow (or the wake) were defined.

It was noted for all the above mentioned flow characteristics, such as retarded flow, accelerated flow, and separated flow, for the inclined and yawed circular cylinders investigated that the retarded flow region on the windward side of the cylinder is not so narrow as for the case of the flow perpendicular to a circular cylinder, as is the case reported by Zdravkovich, (1997). This region is as wide as the wake region downstream the cylinder, for most of the cases. The difference might be caused by the broad simulation domain used in the current analysis, and therefore the increase visualization area available, when compared with the limited sampling points, and streamline dye techniques used for the flow visualization in the wind tunnel experiments.

For clarity in the visualizations the areas of retarded, accelerated, wake flow, and the location of the boundary and shear layers were detailed only for Figure 5.1(a). For the remaining cases reported in Figures 5.1(b) – (j), only the lines representation for delimiting the velocities zones were adopted.

It was noticed that the inclination angle has a dominant effect upon the flow pattern. For higher relative angles of attack, e.g. $\phi = 64°$, both the retarded and the wake flow regions had a very wide width, regardless of the Re number, while the shear layers shedding from the cylinder formed a long and open wake behind the cylinder, as shown in Figures 5.1(a) and (e). For lower angles of attack of $\phi = 62°$, the retarded and wake regions were not very wide, leaving more space for the accelerated flow regions on the sides of the cylinder (Figures 5.1(d) and (g)). Moreover the wake formed behind the cylinder had a sharp and long shape with the shear layers intersecting at around 1D distance downstream the cylinder. The lowest angles of attack $\phi = 53°$ (Figures 5.1(b)

and (f)) had the retarded and wake regions of medium width, but the wake behind the cylinder was sharp and short, with shear layers intersecting at around 0.5 D downstream the cylinder. For the case of $\phi = 60.5°$ (Figure 5.1(c)) the flow pattern had a similar evolution as for the $\phi = 64°$, however the $\phi = 60°$ case showed a very abrupt and short wake behind the cylinder with the streamlines meeting in the vicinity of the leeward side of the cylinder (Figures 5.1(h) and (i)). For the flow perpendicular to the cylinder, a different evolution of velocity isolines was noticed (Figure 5.1(j)). The retarded flow extended over a bigger region behind the cylinder and the shear layers detaching from the sides of the cylinder did not intersect each other, entirely engulfing the strong wake created behind the cylinder. This distribution compares well with the TrBL regime described by Zdravkovich (1997), however, due to the ideal flow conditions used in the analytical simulation, no separation bubbles were noticed, and hence the TrBL1, TrBL2, and TrBL3 could not be discussed herewith.

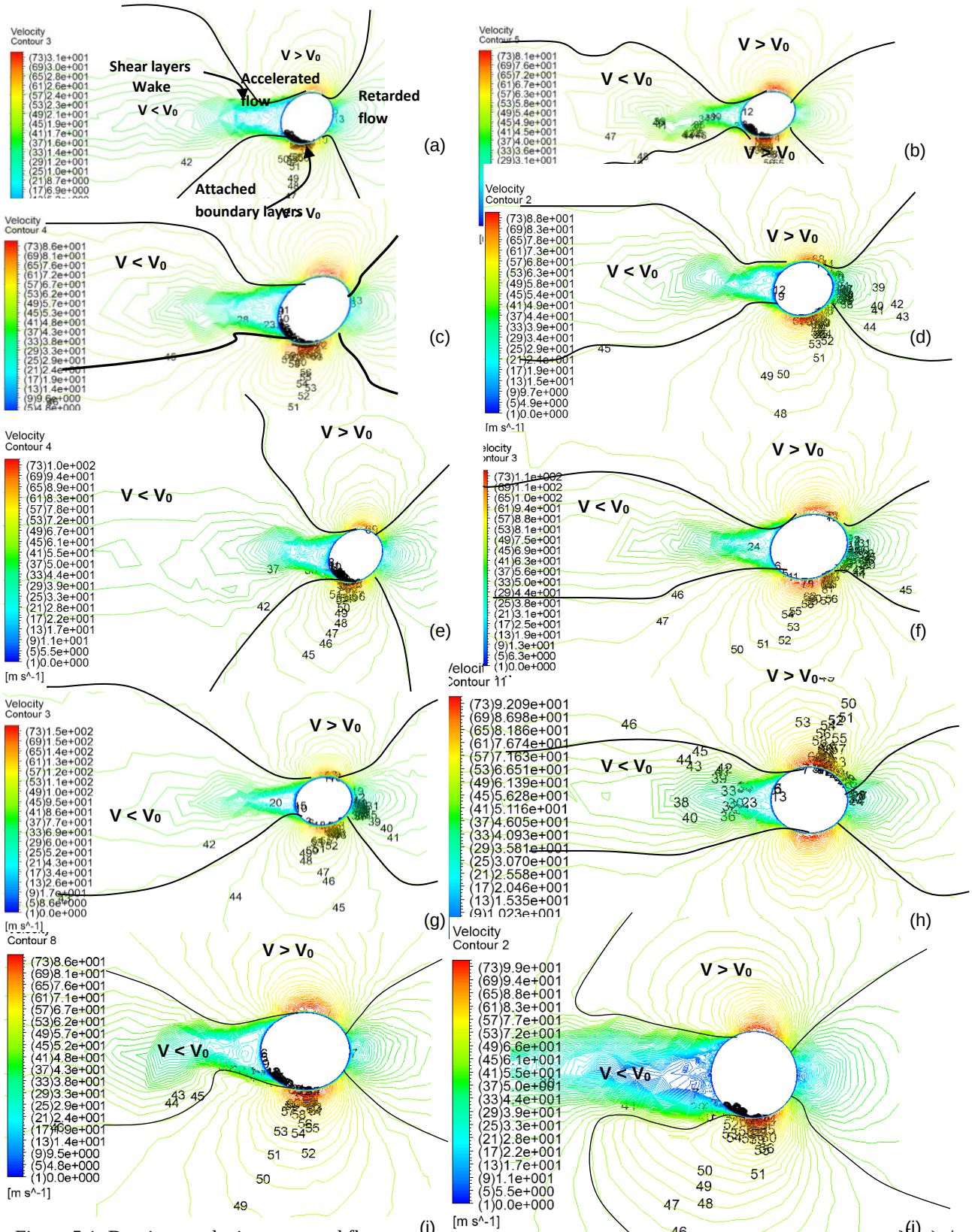


Figure 5.1: Dominant velocity zones and flow pattern for a) ϕ = 64°, Re = 1.1 × 10^5; b) ϕ = 53°, Re = 3.3 × 10^5; c) ϕ = 60.5°, Re = 3.3 × 10^5; d) ϕ = 62°, Re = 3.3 × 10^5; e) ϕ = 64°, Re = 3.5 × 10^5; f) ϕ = 53°, Re = 4.4 × 10^5; g) ϕ = 62°, Re = 5.5 × 10^5; h) ϕ = 60°, Re = 6.7 × 10^5; i) ϕ = 60°, Re = 3.3 × 10^5; and j) ϕ = 0°, Re = 6.7 × 10^5.

As a feature of the flow around bluff bodies, earlier researchers (Roshko and Fiszdon, 1969) indicated that the transition from laminar to turbulent flow states, with the increase of the Re number will take place gradually, and over a number of flow states. The transition in the flow first occurs with a change in the wake (TrW) then a change in the shear layers (TrSL), and then a transition to the boundary layers (TrBL) regime. Considering the velocities isolines zones in Figures 5.1(a) – (j), the transition regions could be determined given the intensities of the flow velocity, however no concrete information regarding the turbulence encountered in the wake, shear layers, and the boundary layer could be extracted only from the velocity isolines, therefore the eddy viscosities were discussed in the following section.

5.2.1 Transition to Turbulent Shear Layers and Turbulent Boundary Layers for Flow around Inclined Cylinders

There are numerous turbulence properties, such as turbulence intensity, Monin-Obukov length, Kolmogorov wavelength, turbulent kinetic energy k, energy dissipation ε, etc., which are equally used in fluid mechanics, and in engineering applications for characterizing the turbulence developed in the atmospheric boundary layer. In the current research, the Large Eddy Simulation (LES) was employed as a turbulence model, and two-dimensional eddy viscosity profiles along with three-dimensional Q-criterion velocity gradient method were used for determining the regions where the rotational formations of the fluid dominates over the strain rate (Figures 5.2(a) to (j)), and Appendix J contains the eddy viscosity profiles, and associated three-dimensional visualization of the Q-criterion for all cases performed in this study.

The two-dimensional eddy viscosity pattern plotted for the plane parallel with the wind direction, and intersecting the cylinder at the middle point, same as the one used for the velocity isolines in Figure 5.1, pointed out that the turbulence in the shear layers occurs in the near wake

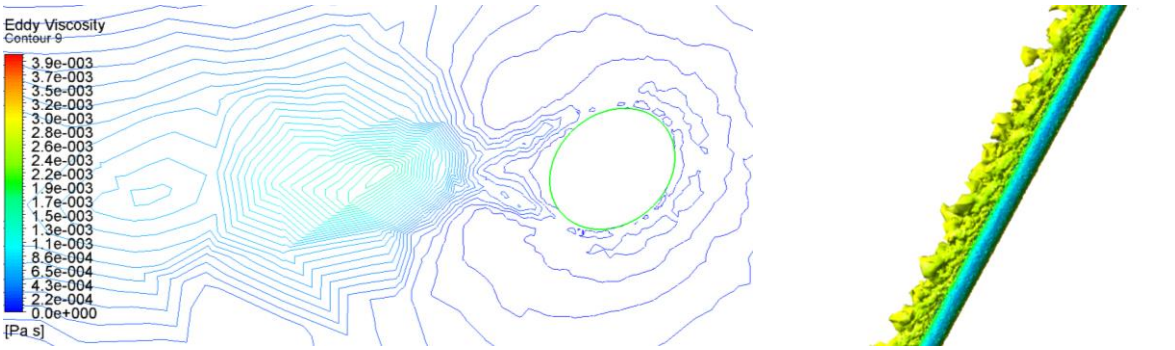
region behind the cylinder. Also, the three-dimensional velocity field given by the Q-criterion was plotted along the entire length of the cylinder, and it showed that there is a change in direction of the wind flow and the threads of swirl flow developing along the leeward side of the cylinder, streaming along its axis, and not along the initial wind speed direction (Figures 5.1(a) to (h)). Depending on the relative angle of attack and the Re number it was noticed that length of the generated swirl threads, and that the points along the cylinder from where these detached varied, and also the wake structure in the two-dimensional profiles varied as described below.

For a wide range of relative angles the turbulent shear layers detached from the cylinder, intersecting each other very close to the leeward side of the cylinder. This generated a main turbulent wake around 0.5D downstream of the cylinder as shown is Figure 5.2(c), (f), and (i) for cases: $\alpha = 50°$, $\beta = 40°$, $\phi = 60.5°$, Re = 3.3×10^5; $\alpha = 50°$, $\beta = 20°$, $\phi = 53°$, Re = 4.4×10^5; and $\alpha = 60°$, $\beta = 0°$, $\phi = 60°$, Re = 3.3×10^5. The three-dimensional profiles associated with the same figures showed long, intermittent swirl threads of flow streaming downwards along the leeward side of the cylinder, and detaching from it at periodic intervals.

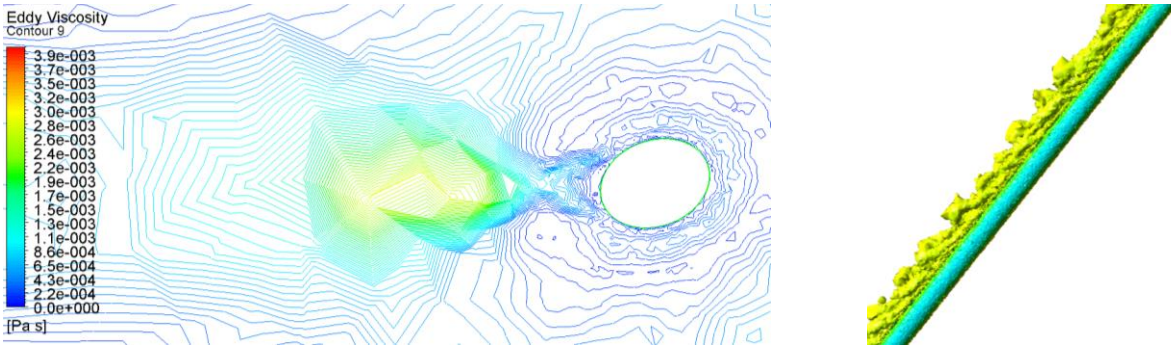
Other cases showed a similar flow behaviour with the turbulent wake separating from the cylinder, and intersecting further downstream from the cylinder at distances greater than 0.5D. This is shown in Figure 5.2(b), (d), and (g), for cases: $\alpha = 50°$, $\beta = 20°$, $\phi = 53°$, Re = 3.3×10^5; $\alpha = 60°$, $\beta = 20°$, $\phi = 62°$, Re = 3.3×10^5; and $\alpha = 60°$, $\beta = 20°$, $\phi = 62°$, Re = 5.5×10^5. Also the three-dimensional visualization showed similar swirl threads which will stream along the cylinder, however these will detach much earlier from its surface.

For the higher relative angles and yaw of $\beta = 40°$, the turbulent shear layers did not intersect after the detachment from the cylinder before reaching the turbulent wake downstream the cylinder. This left a gap, or opening between the turbulent shear layers, as shown in Figures 5.2(a)

and (e). Such flow pattern corresponds to the highest relative angles of attack of $\phi = 64°$: for $\alpha = 54.7°$, $\beta = 40°$, $\phi = 64°$, Re = 1.1×10^5; and $\alpha = 54.7°$, $\beta = 40°$, $\phi = 64°$, Re = 3.3×10^5. The swirl threads were similar to the ones encountered for the $\phi = 62°$ cases with an earlier detachment of the flow from the leeward side of the cylinder.

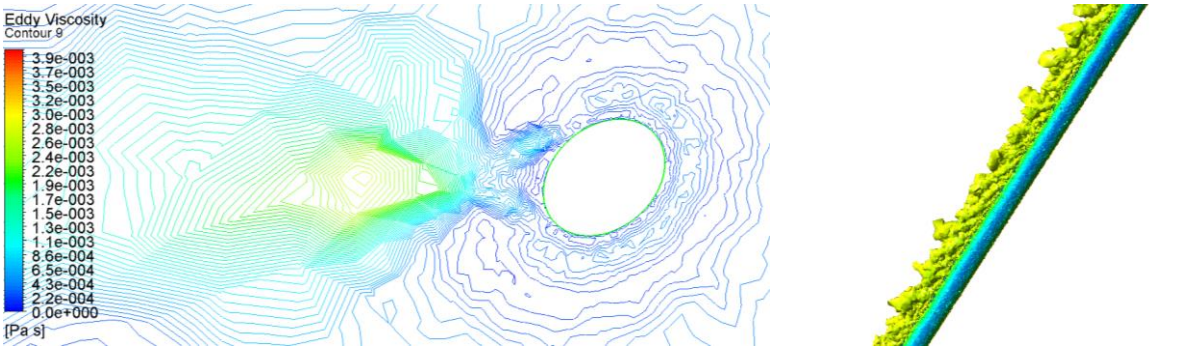


a) $\alpha = 54.7°$, $\beta = 40°$, $\phi = 64°$, Re = 1.1×10^5;

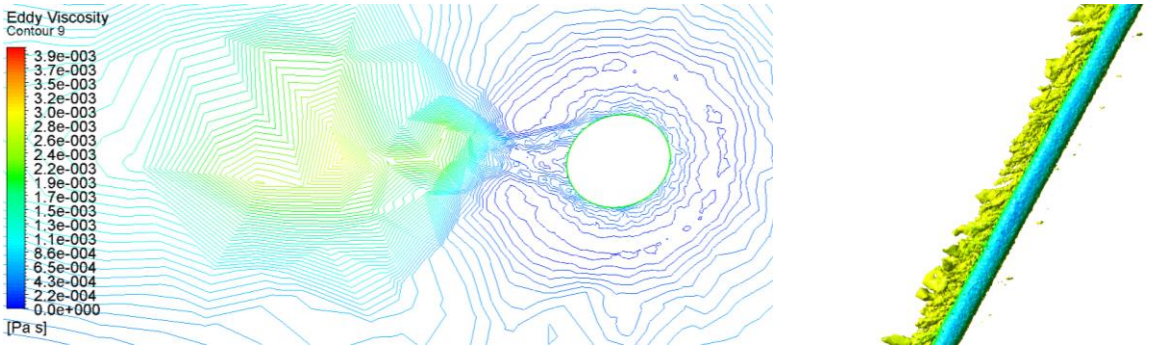


b) $\alpha = 50°$, $\beta = 20°$, $\phi = 53°$, Re = 3.3×10^5;

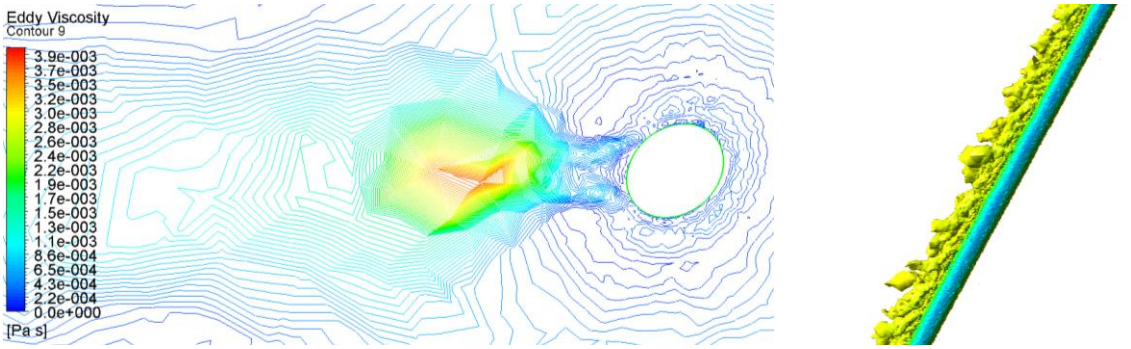
Figure 5.2: Two-dimensional eddy viscosity profiles and associated three-dimensional visualization of the Q-criterion



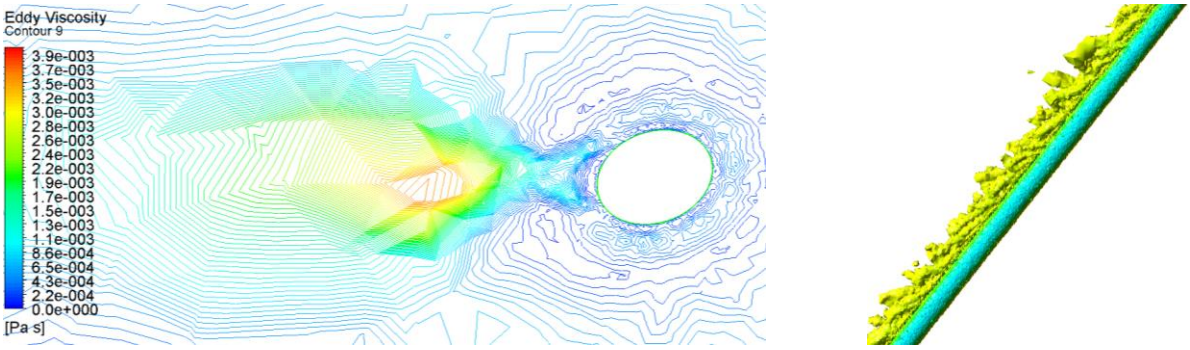
c) $\alpha = 50°$, $\beta = 40°$, $\phi = 60.5°$, Re = 3.3×10^5;



d) $\alpha = 60°$, $\beta = 20°$, $\phi = 62°$, Re = 3.3×10^5;

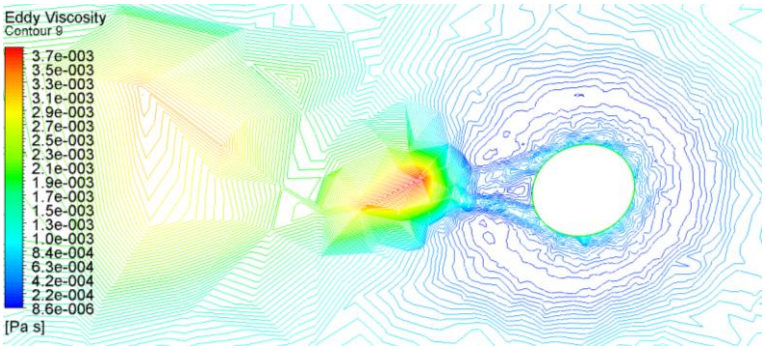


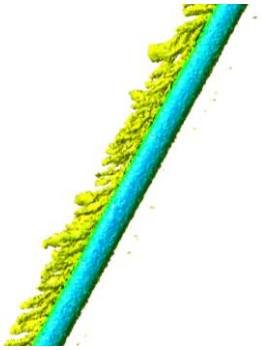
e) $\alpha = 54.7°$, $\beta = 40°$, $\phi = 64°$, Re = 3.3×10^5;



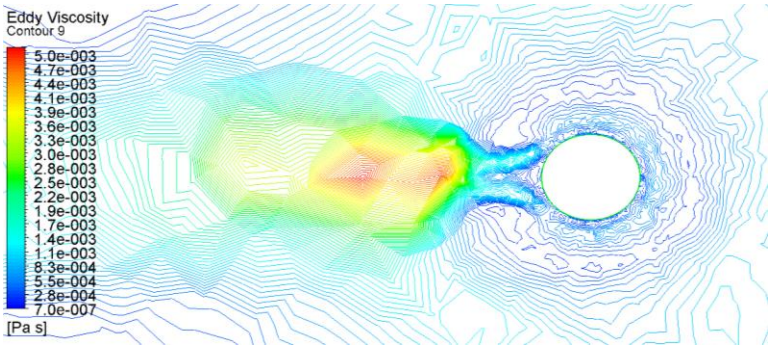
f) $\alpha = 50°$, $\beta = 20°$, $\phi = 53°$, Re = 4.4×10^5;

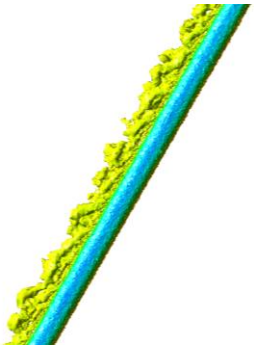
Figure 5.2: Two-dimensional eddy viscosity profiles and associated three-dimensional visualization of the Q-criterion



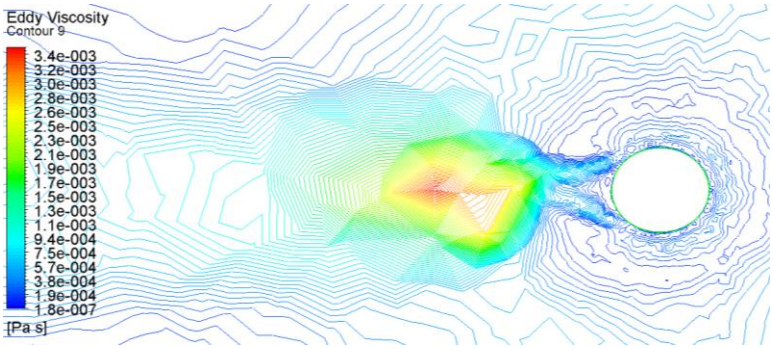


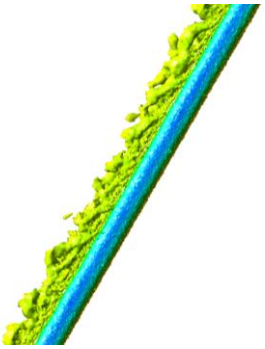
g) $\alpha = 60°$, $\beta = 20°$, $\phi = 62°$, Re = 5.5×10^5;



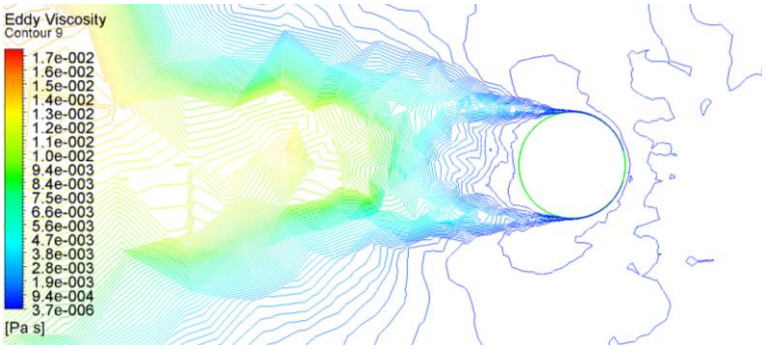


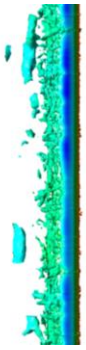
h) $\alpha = 60°$, $\beta = 0°$, $\phi = 60°$, Re = 6.7×10^5;





i) $\alpha = 60°$, $\beta = 0°$, $\phi = 60°$, Re = 3.3×10^5;





j) $\alpha = 0°$, $\beta = 0°$, $\phi = 0°$, Re = 6.7×10^5.

Figure 5.2: Two-dimensional eddy viscosity profiles and associated three-dimensional visualization of the Q-criterion

A transition of flow regimes was noted between $\phi = 60°$ and 60.5° for Re = 3.3×10^5, and Re = 6.7×10^5, as shown in Figures 5.2(c), (h), and (i). As there is little to no change in the relative angle between the flow and the cylinder, this change in the flow regime may be caused by the increase in Reynolds number more than the change of its inclination angle, yaw angle, or relative angle of attack. For $\alpha = 50°$, $\beta = 40°$, $\phi = 60.5°$, Re = 3.3×10^5, as described above, short turbulent shear layers were shedding from both sides of the cylinder which intersect downstream of the cylinder and formed a turbulent wake. This pattern is represented by the short flow threads visualized in the three-dimensional detail of the eddy viscosity profile. For the case $\alpha = 60°$, $\beta = 0°$, $\phi = 60°$, Re = 6.7×10^5, the turbulent flow formed much closer to the leeward side of the cylinder. An undulating turbulent flow could be noticed along the leeward side of the cylinder, and streaming along it with less detachment of the flow downstream, as noted for the rest of the inclined angles cases.

Also, it was observed that for the standard case of $\phi = 0°$, the eddy viscosity indicated the occurrence of turbulent wake in the immediate vicinity of the leeward side of the cable. The shear layers which are shed from the cylinder engulfed the turbulent wake (Figure 5.2 (j)) which is in conformity with the TrBL regime identified by Zdravkovich (1997). The visual information extracted from the analytical simulation did not show any shear layer reattachment, hence a discussion regarding the formation for the separation bubbles was not made, and the general TrBL notation was used instead of the detailed TrBL2 or TrBL3 as categorized by Zdravkovich (1997). Actually the cylinder inclined with $\phi = 60°$, (Figure 5.2(h)) presented a very similar flow pattern with turbulent wake directly attached to the cable's leeward side, which is actually caused by the axial flow indicated in Figure 4.6(h). It should be mentioned that the wind tunnel tests performed by various researchers (Matsumoto 1998, Jakobsen et al. 2008, Cheng et al. 2008, Katsuchi et al.

2009) have indicated a critical vibration for the same case of $\phi = 60°$ at high Re numbers, and a possible connection with the occurrence of an axial flow on the leeward side of the cable was discussed.

5.3 Wake Profiles Following the Leeward Side of the Cylinder

To assist in the visualization of the flow along the leeward side of the cylinder the eddy viscosity, pressure, and velocity were plotted for 9 locations along the leeward side of the cylinder. These locations include 0.1D, 0.2D, 0.3D, 0.4D, and 0.5D as previously used, but also locations further downstream of the cylinder at 0.7D, 1.0D, 1.5D and 2.0D for the full cross flow width of the computational domain. The locations of the plots are shown in Figure 5.3(a) for the inclined and yawed case for $\alpha = 54.7°$, $\beta = 40°$, $\phi = 64°$, Re = 1.1×10^5 and in Figure 5.3(b) for the flow perpendicular to the cylinder for case $\alpha = 0°$, $\beta = 0°$, $\phi = 0°$, Re = 6.7×10^5.

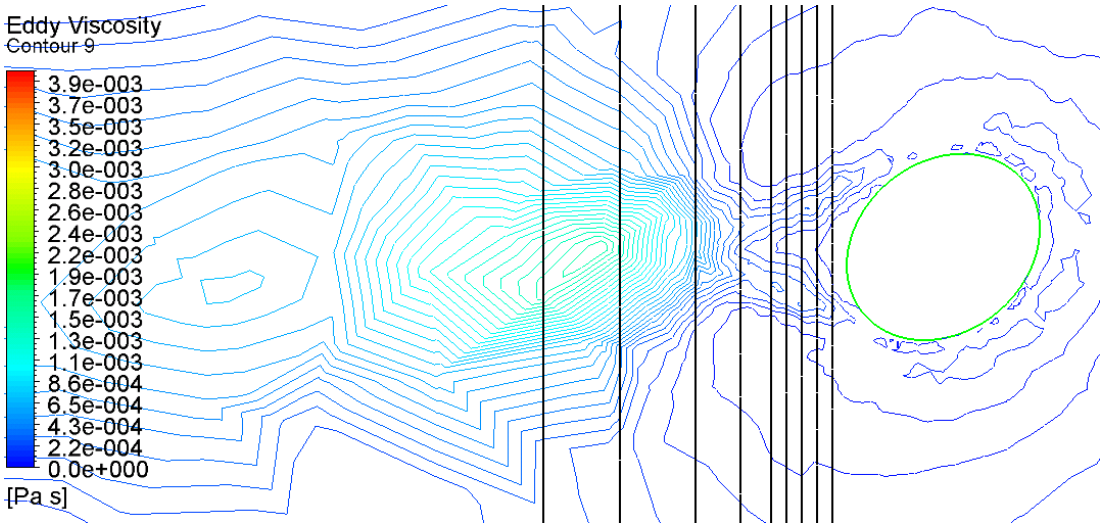


Figure 5.3(a): Two-dimensional eddy viscosity profiles for flow inclined to the cylinder, case (a) $\alpha = 54.7°$, $\beta = 40°$, $\phi = 64°$, Re = 1.1×10^5 shown with monitoring locations highlighted;

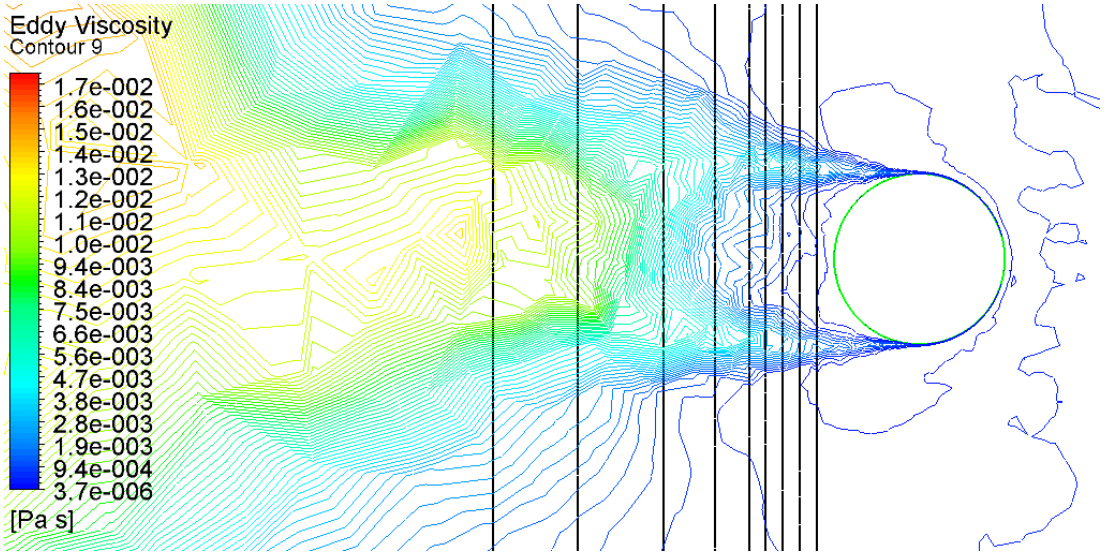


Figure 5.3(b): Two-dimensional eddy viscosity profiles for flow perpendicular to the cylinder, case (j) $\alpha = 0°$, $\beta = 0°$, $\phi = 0°$, Re = 6.7×10^5 with monitoring locations highlighted;

5.3.1 Eddy Viscosity Following the Leeward Side of the Cylinder

The results of the eddy viscosity evolution for several locations downstream of the leeward side of the cylinder are shown in Figure 5.4 below. As noted from all the cases, the eddy viscosity showed an asymmetric distribution along the center of the domain, and therefore the center of the cylindrical model. This is an indication of the asymmetrical flow around an inclined circular cylinder for higher Re numbers. As shown in the Figure 5.4 below, the eddy viscosity intensity

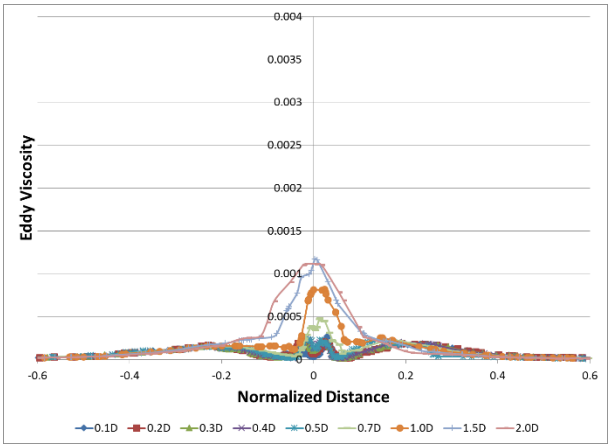
increased with the increase in the Re number. The eddy viscosity flow at the locations monitored closest to the leeward side of the cylinder, less than 0.5D, showed a similar tendency with vary similar magnitude for $\phi = 64°$, Re = 1.1×10^5, as shown in Figure 5.4(a). As the distance increased to 0.7D the eddy viscosity increases to 5.0×10^{-3}, and to a value of 0.001 at distances 1.5D and 2.0D from the leeward side of the cylinder for this case. Also, as the Re number increased to Re = 3.3×10^5, the magnitude of the eddy viscosity also increased in both the near wake locations (less than 0.5D), and also as the distance increases showing approximately 1.0×10^{-3} for 0.7D, and around 2.5×10^{-3} for distances of 1.5D and 2.0D, as represented in Figures 5.4(b), (c), (d), (e), and (i). With the gradual increase in Re up to 4.4×10^5, the increase in magnitude of the eddy viscosity continued to increase in both the near wake, and the far wake regions reaching values of approximate 3.0×10^{-3} and 3.5×10^{-3} for the cases shown in Figures 5.4(f) and (g) respectively. The greatest values for eddy viscosity are for the remaining cases shown in Figure 5.4(h) and (j) show the highest values of the eddy viscosity of all the cases shown for the highest Re = 6.7×10^5.

The eddy viscosity values were around 5.0×10^{-3} for locations monitored at less than 0.5D from the leeward side of the cylinder, and jumped when the distance from the cylinder increased to 0.7D, as shown in Figures 5.2(c), and (f), for cases: $\alpha = 50°$, $\beta = 40°$, $\phi = 60.5°$, Re = 3.3×10^5 and $\alpha = 50°$, $\beta = 20°$, $\phi = 53°$, Re = 4.4×10^5. This eddy viscosity distributions are similar when compared to other monitoring locations of 0.5D from the leeward side of the cylinder and less, and lower in magnitude when compared to other cases. The exception to this pattern was the case of $\alpha = 60°$, $\beta = 0°$, $\phi = 60°$, Re = 3.3×10^5 shown in Figure 5.2(i), where there was no jump in the eddy viscosity value at a distance of 0.7D.

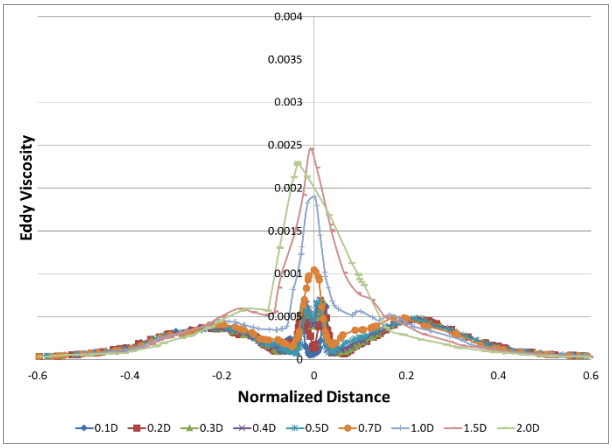
The eddy viscosity distributions shown in Figures 5.2(b), (d), and (g), for cases: $\alpha = 50°$, $\beta = 20°$, $\phi = 53°$, Re = 3.3×10^5; $\alpha = 60°$, $\beta = 20°$, $\phi = 62°$, Re = 3.3×10^5; and $\alpha = 60°$, $\beta = 20°$,

ϕ = 62°, Re = 5.5 × 10^5 had a similar distribution as for the cases mentioned above, with the exception of the increase in eddy viscosity values were higher in magnitude and showed greater variation in magnitude across the monitored locations at distances lower than 0.5D.

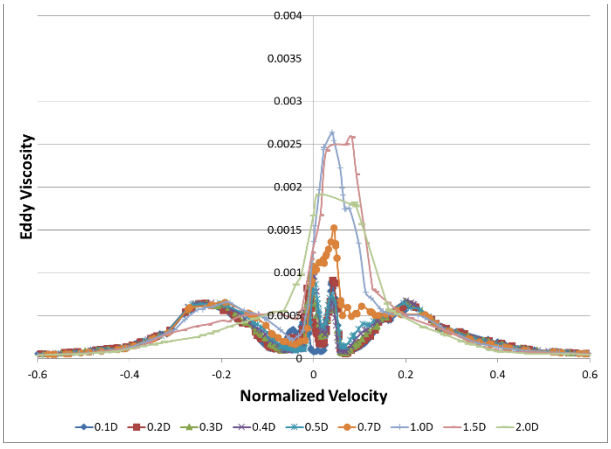
The width of the influence of the eddy viscosity also varied with the Re number. The width of influence for all inclined cases was wider when compared to the one shown for flow perpendicular to the cylinder shown in Figure 5.4(j). The width of influence for the eddy viscosity varied from approximately 0.8D, 0.4D on either side of the cylinder, to less than 0.4D, 0.2 on either side of the cylinder.



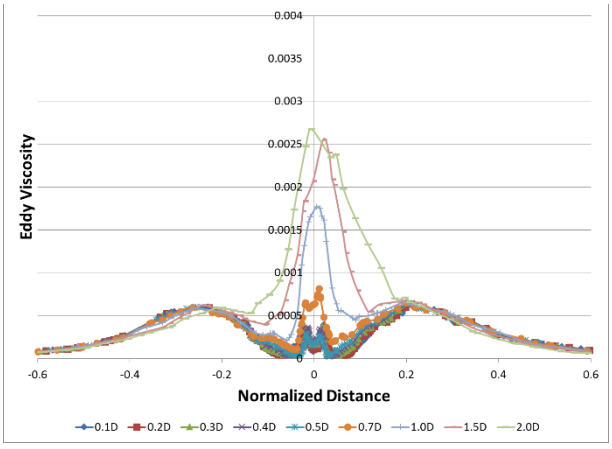
a) α = 54.7°, β = 40°, ϕ = 64°, Re = 1.1 × 10^5;



b) α = 50°, β = 20°, ϕ = 53°, Re = 3.3 × 10^5;

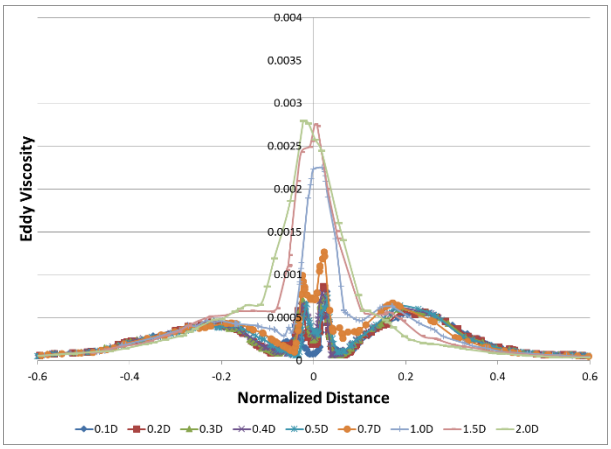


c) α = 50°, β = 40°, ϕ = 60.5°, Re = 3.3 × 10^5;

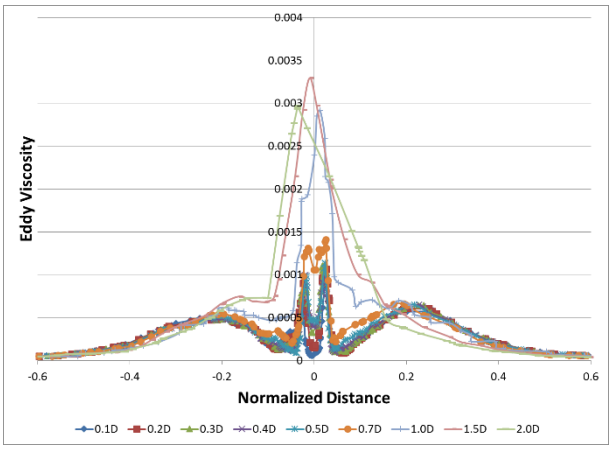


d) α = 60°, β = 20°, ϕ = 62°, Re = 3.3 × 10^5;

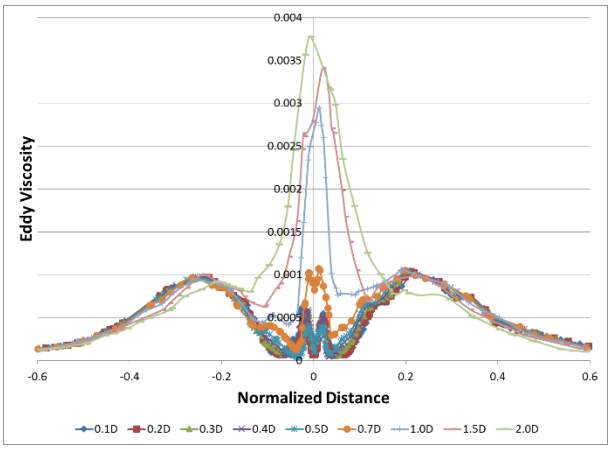
Figure 5.4: Eddy viscosity at various monitored locations on the leeward side of the cylinder



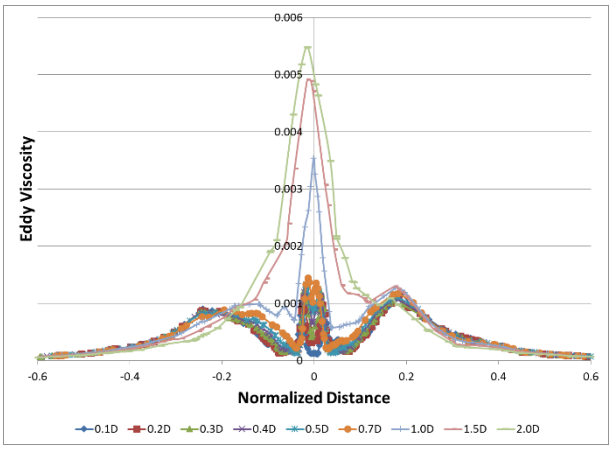
e) $\alpha = 54.7°$, $\beta = 40°$, $\phi = 64°$, Re = 3.3×10^5;



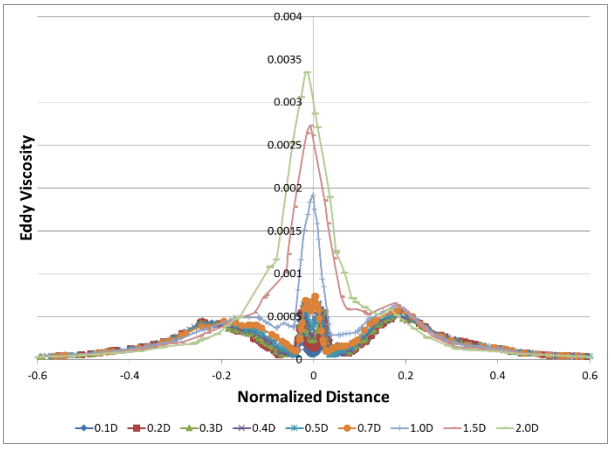
f) $\alpha = 50°$, $\beta = 20°$, $\phi = 53°$, Re = 4.4×10^5;



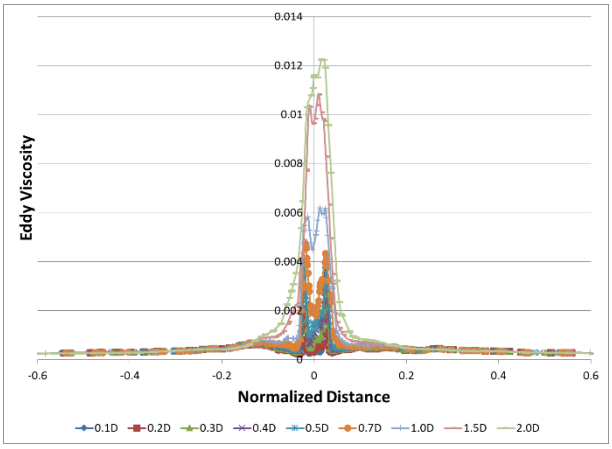
g) $\alpha = 60°$, $\beta = 20°$, $\phi = 62°$, Re = 5.5×10^5;



h) $\alpha = 60°$, $\beta = 0°$, $\phi = 60°$, Re = 6.7×10^5;



i) $\alpha = 60°$, $\beta = 0°$, $\phi = 60°$, Re = 3.3×10^5;



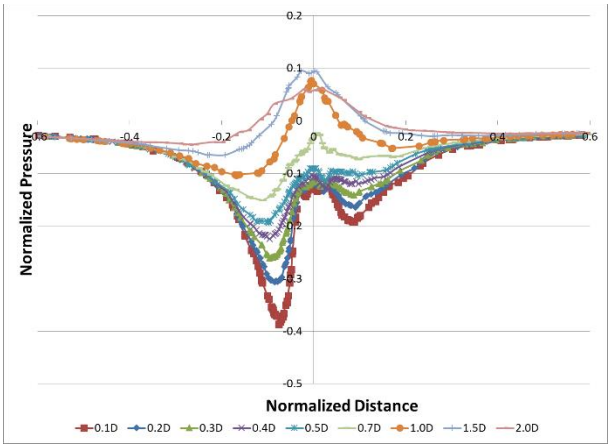
j) $\alpha = 0°$, $\beta = 0°$, $\phi = 0°$, Re = 6.7×10^5.

Figure 5.4: Eddy viscosity at various monitored locations on the leeward side of the cylinder

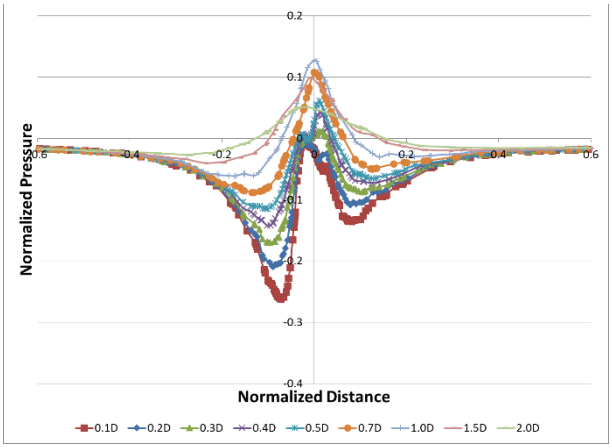
5.3.2 Pressure Distribution on the Leeward Side of the Cylinder

The flow formations which detach from the leeward surface of the cylinder, and the intensity of the wake formed immediately downstream the cylinder, both directly influence the pressure variation on the leeward side of the cylinder. Figure 5.5 shows the pressure distribution across the computational domain at different locations on the leeward side of the cylinder. The graphs show the normalized pressure versus the width across the computational domain. It was noticed that the distribution of pressure is asymmetric about the center of the computational domain, and therefore about the center of the cylinder similar to the eddy viscosity distributions, and especially for the cases of high yaw of the cylinder. For the yaw angle of $\beta = 40°$, the greatest normalized pressure drop from 0.35 to 0.4 occurred on one side of the wake while a drop in pressure was registered on the other side of the wake, varying from 0.15 to 0.2; thus the normalized pressure differential was approximately 0.2 from one side of the wake to the other, as it can be seen in Figures 5.5(a), (c), and (e). For lower yaw angles of the cylinder the normalized pressure dropped, reducing to 0.25 to 0.3 for one side of the wake, and to 0.1 to 0.15 on the other side of the wake, as illustrated in Figures 5.5(b), (d), (f), and (g). For the cases of zero yaw of the cylinder model the distribution was much more consistent from one side of the cylinder to the other. Also the differences in normalized pressure from one side of the wake to the other, caused by the asymmetric formation of eddies, from one side of the cylinder compared to the other, as shown in Figures 5.5(h), (i), and (j) where there is no yaw angle for the cylinder. The pressure distribution on the leeward side of the cylinder directly reflects the difference in flow patterns developed for different orientations of the cylinder. Comparing the pressure results shown in Figures 5.5(h) and (j) for the same Re number, but for different orientations of the flow inclined to the cylinder and flow perpendicular to the cylinder respectively, it can be noticed that different normalized pressure

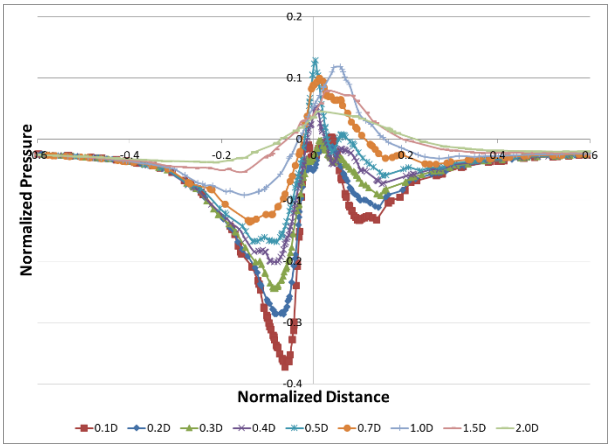
distributions will be formed for different flow phenomena. An area of high recirculation in the flow on the leeward side of the cylinder, for flow perpendicular to the cylinder creates a high drop in the normalized pressure in the wake, and the development of axial flow was related to the increase in inclination of the cylinder which created an increase in the normalized pressure in the wake region.



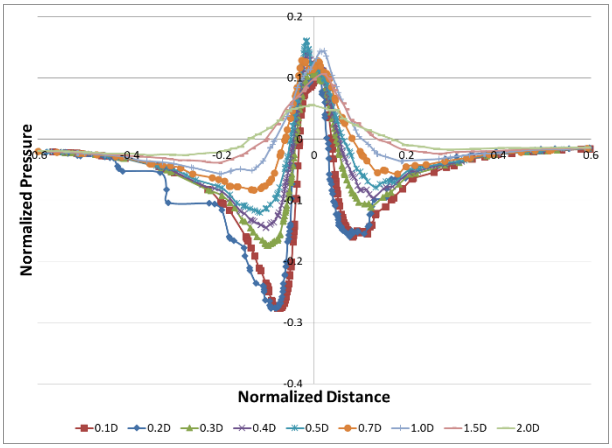
a) $\alpha = 54.7°$, $\beta = 40°$, $\phi = 64°$, Re = 1.1×10^5;



b) $\alpha = 50°$, $\beta = 20°$, $\phi = 53°$, Re = 3.3×10^5;

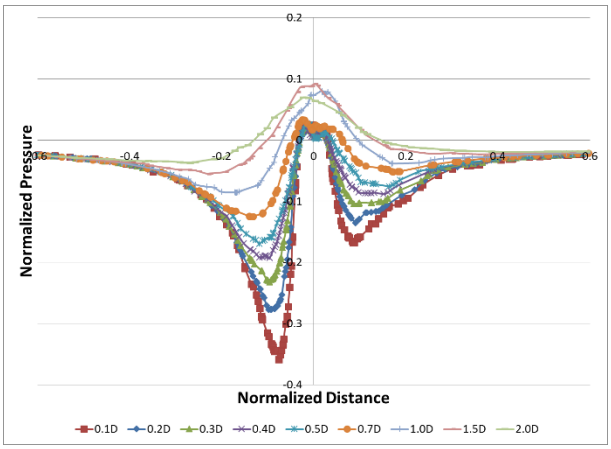


c) $\alpha = 50°$, $\beta = 40°$, $\phi = 60.5°$, Re = 3.3×10^5;

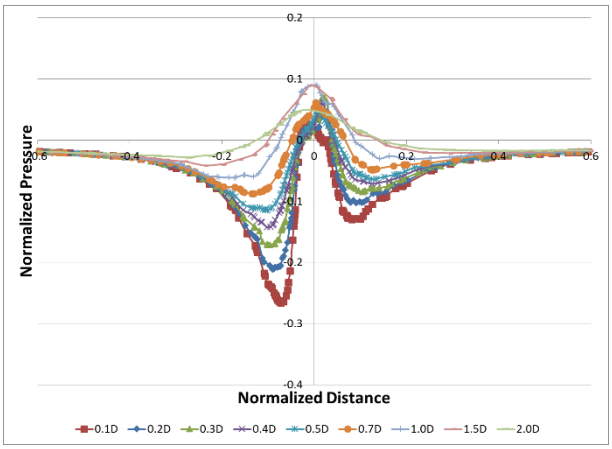


d) $\alpha = 60°$, $\beta = 20°$, $\phi = 62°$, Re = 3.3×10^5;

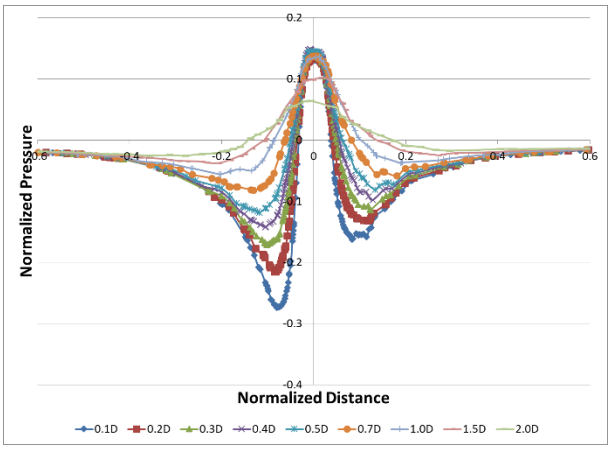
Figure 5.5: Pressure at various monitored locations on the leeward side of the cylinder



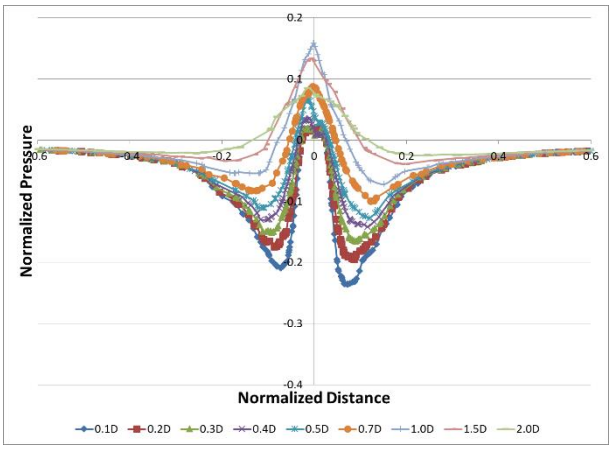
e) $\alpha = 54.7°$, $\beta = 40°$, $\phi = 64°$, Re = 3.3×10^5;



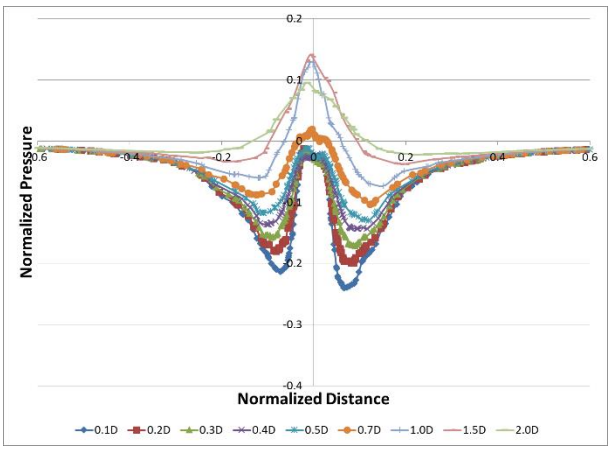
f) $\alpha = 50°$, $\beta = 20°$, $\phi = 53°$, Re = 4.4×10^5;



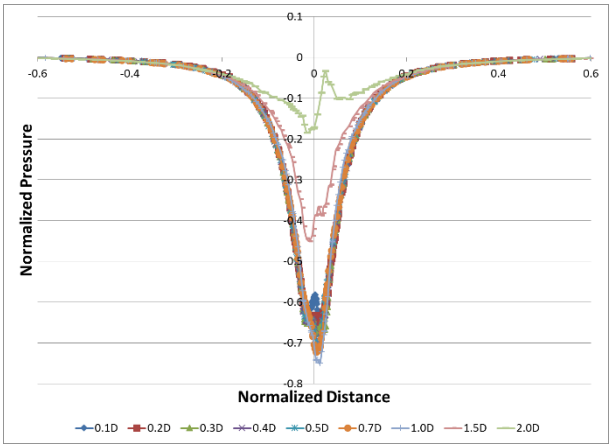
g) $\alpha = 60°$, $\beta = 20°$, $\phi = 62°$, Re = 5.5×10^5;



h) $\alpha = 60°$, $\beta = 0°$, $\phi = 60°$, Re = 6.7×10^5;



i) $\alpha = 60°$, $\beta = 0°$, $\phi = 60°$, Re = 3.3×10^5;



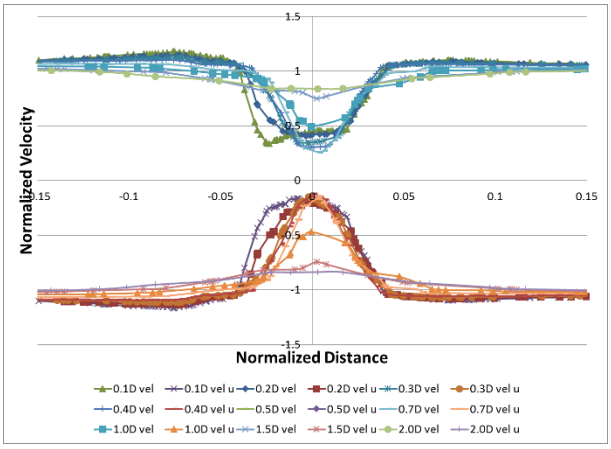
j) $\alpha = 0°$, $\beta = 0°$, $\phi = 0°$, Re = 6.7×10^5.

Figure 5.5: Pressure at various monitored locations on the leeward side of the cylinder

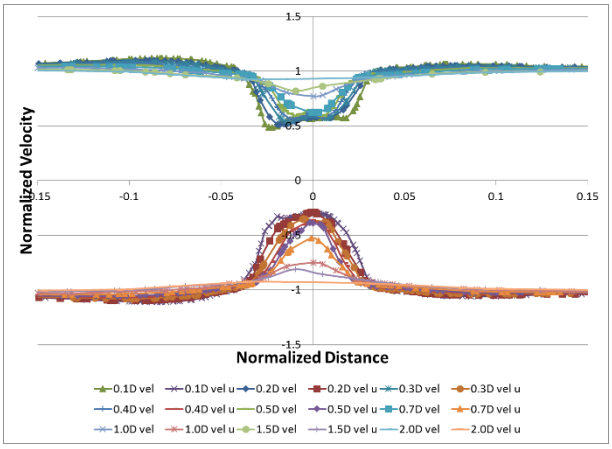
5.3.3 Velocity Profiles on the Leeward Side of the Cylinder

The distribution of the eddy viscosity, and the variation in pressure on the leeward side of the cylinder presented in the above sections are a function of the magnitude of wind velocity and its direction along the leeward side of the cylinder. The velocity isolines represented in Figure 5.1 showed the different flow zones which developed on the leeward side of the cylinder, however to establish the contribution of the axial flow the change in direction of the wind velocity must be interpreted. Therefore the velocity profiles monitored for the same locations as defined above are shown in Figure 5.6. The normalized total velocity is represented in the upper part of the graph, while the normalized velocity in the x-direction (direction of the far field flow) is plotted in the lower part of the graph, for each case. Both the total velocity, and the x-direction velocity were normalized at the monitoring locations with the use of the far field flow velocity. This representation allows for a direct comparison between the two velocity profiles. All velocity profiles showed similar tendencies with the increase of the flow velocity on either side of the wake closer to the cylinder, which diminishes as the flow travels further downstream the cylinder. The same asymmetry in the flow profiles is shown below which caused the asymmetry in the pressures profiles above. For the cases with the high yaw angle, shown in Figures 5.6(a), (c) and (e) registered the highest difference between the two velocity profiles from one side of the wake to the other. Also shown with the pressure profiles above is the decrease in the difference between the velocity profile from one side of the cylinder to the other with the decrease in the yaw angle of the cylinder, as expected, and shown in Figures 5.6(b), (d), (f), and (g). For the case of zero yaw, a minimal asymmetry in the distribution of the velocity from one side of the wake to the other was noticed, and was shown in Figures 5.6(h), (i), and (j). This asymmetry in the velocity profiles is due to the asymmetry of the flow in the wake formed on the leeward side of the cylinder, and not

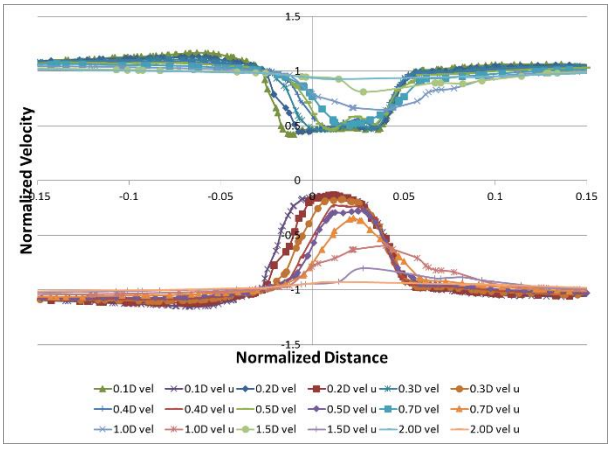
because of the geometry or inclination of the cylinder in respect to the flow. The area of flow recirculation is shown for the case of flow perpendicular to the cylinder where the change in direction of the flow was identified, as represented in Figure 5.6(j).



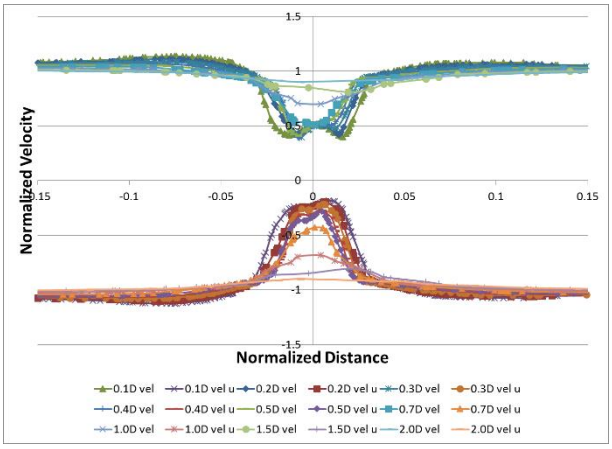
a) $\alpha = 54.7°$, $\beta = 40°$, $\phi = 64°$, Re = 1.1×10^5;



b) $\alpha = 50°$, $\beta = 20°$, $\phi = 53°$, Re = 3.3×10^5;

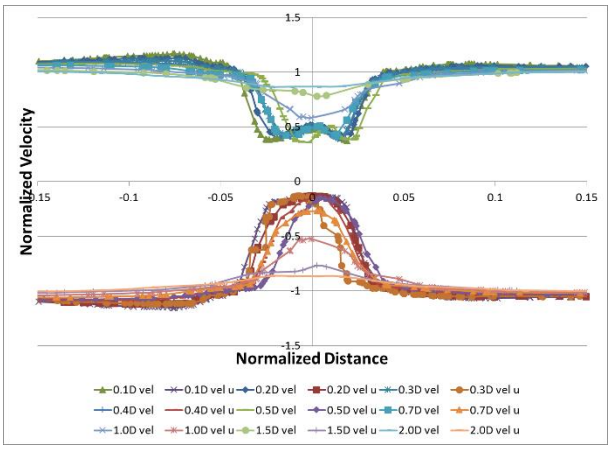


c) $\alpha = 50°$, $\beta = 40°$, $\phi = 60.5°$, Re = 3.3×10^5;

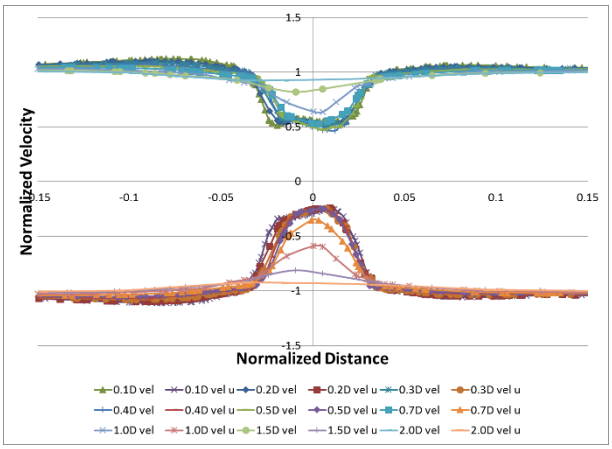


d) $\alpha = 60°$, $\beta = 20°$, $\phi = 62°$, Re = 3.3×10^5;

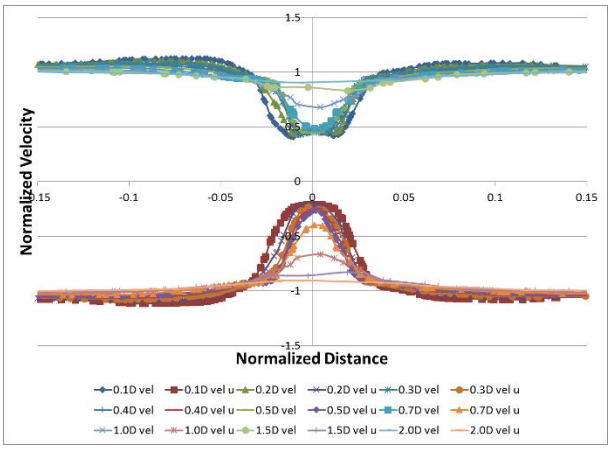
Figure 5.6: Velocity at various monitored locations on the leeward side of the cylinder



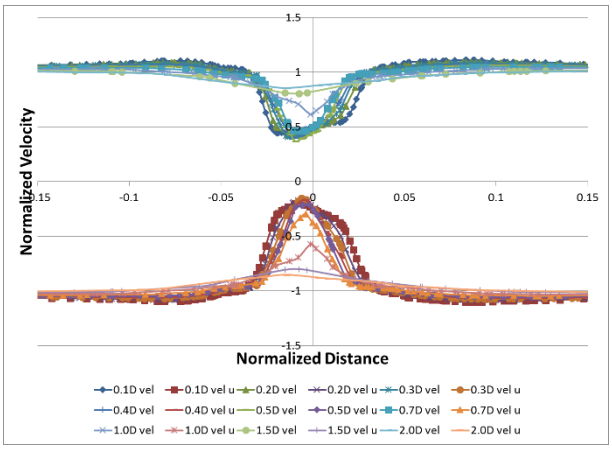
e) $\alpha = 54.7°$, $\beta = 40°$, $\phi = 64°$, Re = 3.3×10^5;



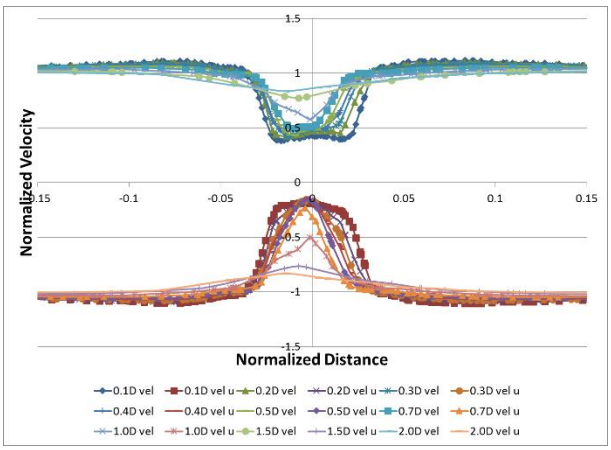
f) $\alpha = 50°$, $\beta = 20°$, $\phi = 53°$, Re = 4.4×10^5;



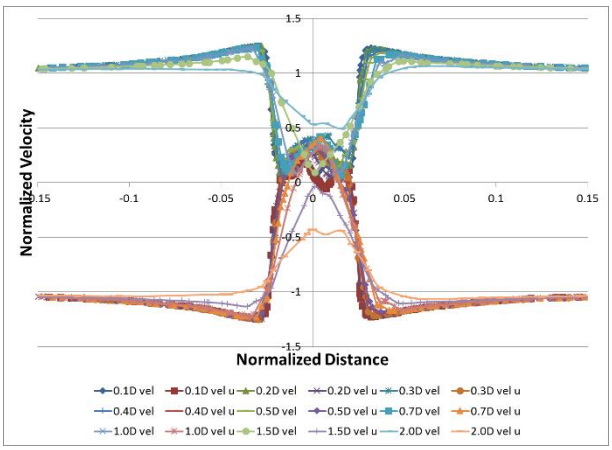
g) $\alpha = 60°$, $\beta = 20°$, $\phi = 62°$, Re = 5.5×10^5;



h) $\alpha = 60°$, $\beta = 0°$, $\phi = 60°$, Re = 6.7×10^5;



i) $\alpha = 60°$, $\beta = 0°$, $\phi = 60°$, Re = 3.3×10^5;

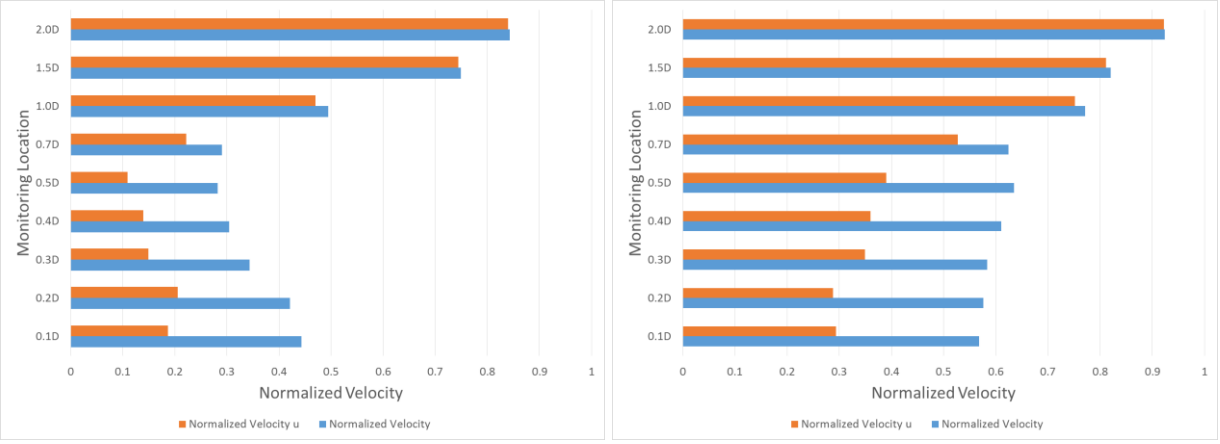


j) $\alpha = 0°$, $\beta = 0°$, $\phi = 0°$, Re = 6.7×10^5.

Figure 5.6: Velocity at various monitored locations on the leeward side of the cylinder

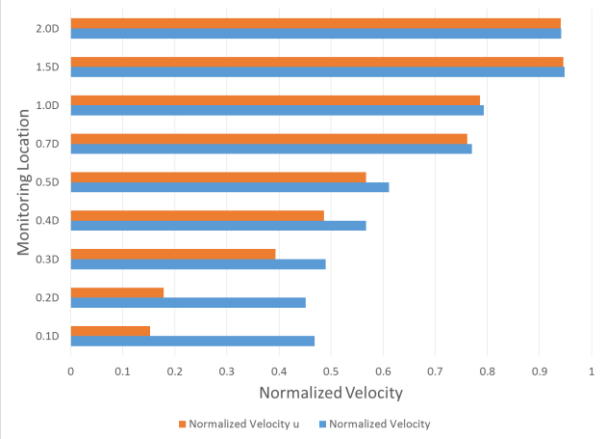
5.3.4 Comparison of the Flow Velocities for Different Directions in the Wake of the Cylinder

The results for the velocity profiles in the wake of the cylinder, for both the normalized total velocity, and the normalized velocity in the *x* direction are presented in the section, and are represented in Figure 5.7 below. As defined above, the velocity magnitudes were normalized at the monitoring locations with the use of the far field flow velocity. The velocity profiles are shown for the same locations defined in the previous sections. As a reminder, the locations of the sampling points are from the midpoint of the cylinder, starting at 0.1D from the leeward side of the cylinder to 0.5D at intervals of 0.1D, including 0.7D, 1.0D, 1.5D, and 2.0D downstream, in the wake of the cylinder.

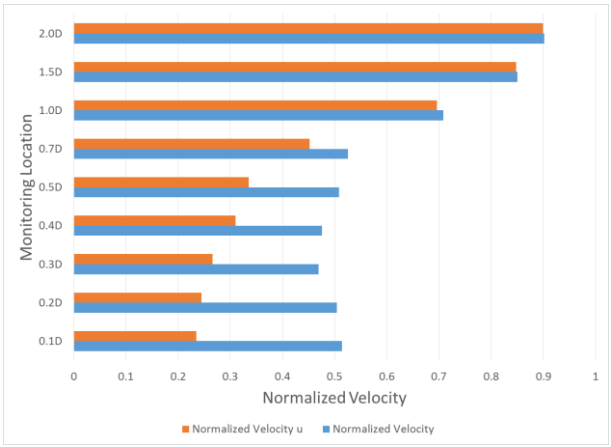


a) $\alpha = 54.7°$, $\beta = 40°$, $\phi = 64°$, Re = 1.1×10^5; b) $\alpha = 50°$, $\beta = 20°$, $\phi = 53°$, Re = 3.3×10^5;

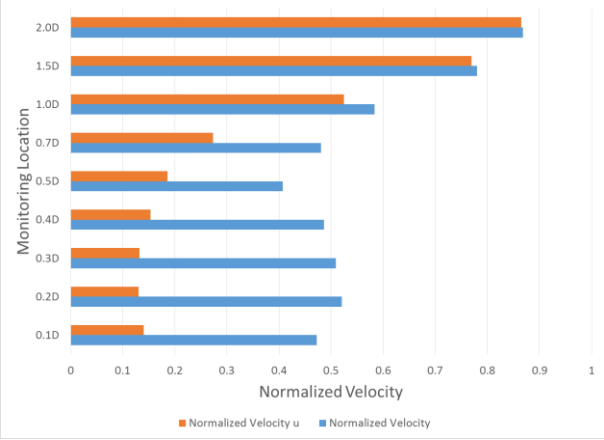
Figure 5.7: Comparison of the normalized *u* velocity and the total velocity on the leeward side of the cylinder



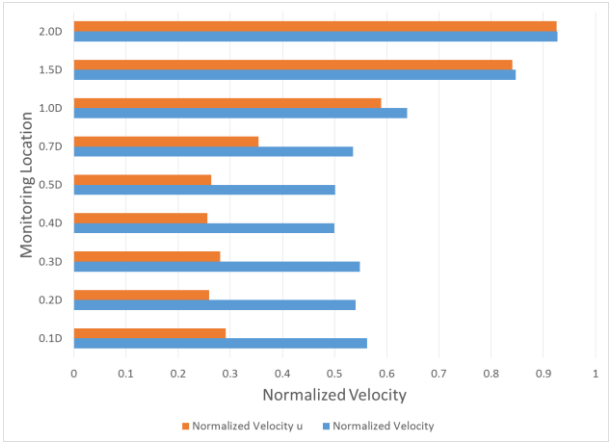
c) $\alpha = 50°$, $\beta = 40°$, $\phi = 60.5°$, Re = 3.3×10^5;



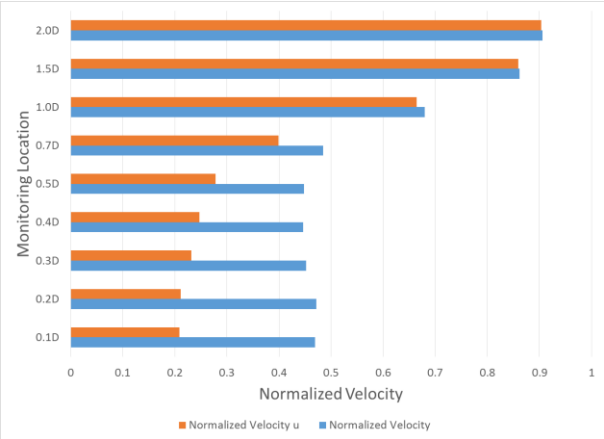
d) $\alpha = 60°$, $\beta = 20°$, $\phi = 62°$, Re = 3.3×10^5;



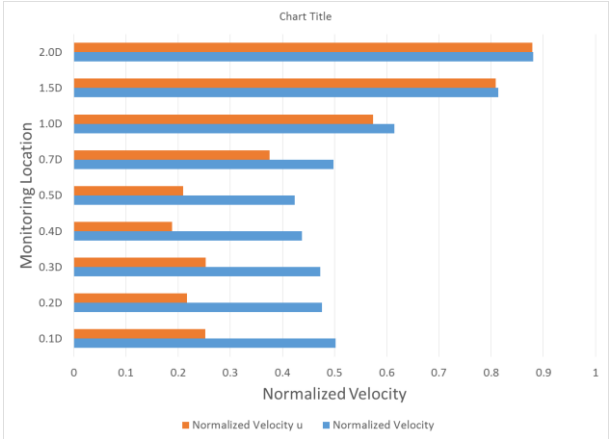
e) $\alpha = 54.7°$, $\beta = 40°$, $\phi = 64°$, Re = 3.3×10^5;



f) $\alpha = 50°$, $\beta = 20°$, $\phi = 53°$, Re = 4.4×10^5;

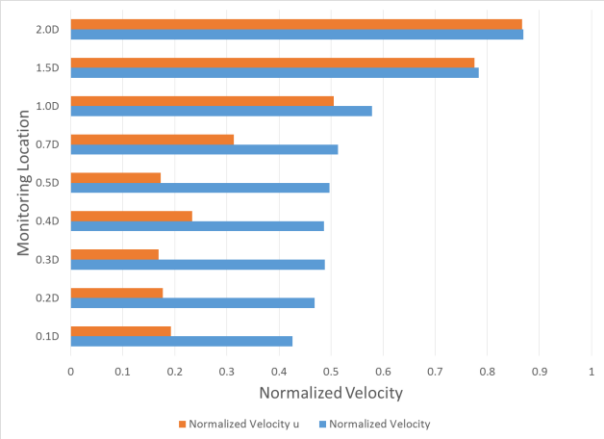


g) $\alpha = 60°$, $\beta = 20°$, $\phi = 62°$, Re = 5.5×10^5;

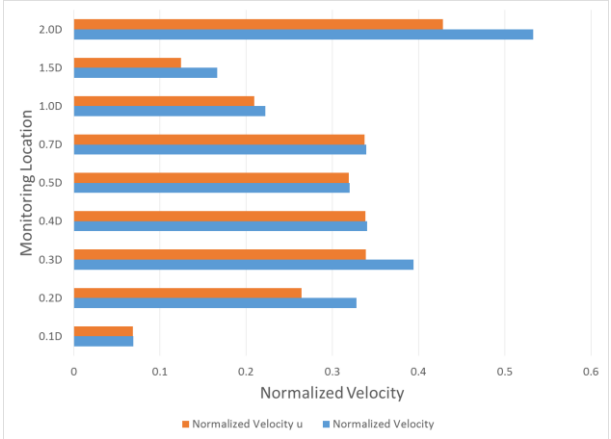


h) $\alpha = 60°$, $\beta = 0°$, $\phi = 60°$, Re = 6.7×10^5;

Figure 5.7: Comparison of the normalized *u* velocity and the total velocity on the leeward side of the cylinder



i) $\alpha = 60°$, $\beta = 0°$, $\phi = 60°$, Re = 3.3×10^5;



j) $\alpha = 0°$, $\beta = 0°$, $\phi = 0°$, Re = 6.7×10^5.

Figure 5.7: Comparison of the normalized *u* velocity and the total velocity on the leeward side of the cylinder

The normalized *u* velocity, shown in the Figure 5.7 above, is for the *x* direction of the computation domain which corresponds to the flow direction of the far field flow. The normalized total velocity was represented for the same locations as the normalized *u* velocity, for allowing a direct comparison between the two velocities, and thus to illustrate the development of the shifts in the wind flow direction.

Figure 5.7 above shows the percentage of the flow in the same direction of the far field flow in comparison to the total velocity at the same point in space. The larger the difference between the component velocity and the total velocity confirms the stronger axial flow along the leeward side of the cylinder, as seen for smaller distances of up to 0.7D. It also demonstrates the flow recovery in the wake on the leeward side of the cylinder for higher distances of up to 2.0D, for most of the cases investigated.

For lower Re numbers, of Re = 1.1×10^5, as shown in Figure 5.7(a) an area of recirculation can be noticed, as also seen in a similar flow pattern for the cylinder placed perpendicular to the flow represented in Figure 5.7(j). The velocity tendencies of following a certain direction are slightly different, as the flow perpendicular to the cylinder showed lower magnitude of velocity at

a distance of 0.1D from the leeward side of the cylinder, with an increase in both total and u velocities for the higher distances of 0.2D to 0.7D; however these decreased again at 1.0D and 1.5D. A partial flow recovery was noticed at 2.0D from the leeward side of the cylinder. The same tendency of a decreasing flow velocity was observed for the lower Re, for an inclined cylinder with the flow decreasing from the leeward side of the cylinder to the distance closer to the cylinder of 0.4D, 0.5D and 0.7D. This change is caused by the axial flow formed along the leeward side of the cylinder for the inclined cylinder, as compared to the flow perpendicular to the cylinder. The flow recovery occurred gradually for distances of 1.0D, 1.5D and 2.0D for the low Re flows inclined to the cylinder.

When reviewing the cases presented in Figure 5.7 above it was noted that the velocity profiles for the cases with the same Re that the magnitude of the total and *u* component velocities varied for each of the cases. Thus, for the same Re of 3.3×10^5, and for relative angles of attack of $\phi = 53°$, $\phi = 60.5°$, $\phi = 62°$, $\phi = 64°$, $\phi = 60°$, as represented in Figures 5.7(b), (c), (d), (e), and (i) respectively, it could be concluded that the angle of inclination of the cylinder plays an important role in the velocity in the wake of the cylinder. For the two cases of $\phi = 60°$ and $\phi = 60.5°$ the total velocities followed the same tendency of gradually increasing from 0.1D to 2.0D, but the magnitude of the *u* velocity did not increase, indicating a possible link between the axial flow formation, and the relative angle of the cylinder.

When comparing Figures 5.7 (h) and (j), flow inclined to the cylinder, and flow perpendicular to the cylinder for the same Re, it was clear that for inclined cylinders the flow velocity in the vicinity of the leeward side of the cylinder develops differently. For flow inclined to the cylinder ($\phi = 60°$), there is a notable difference between the *u* direction velocity, and the total velocity, ranging from approximately 40%, for closer locations to the cylinder, and

approaching 100%, for higher locations of up to 2.0D from the leeward side of the cylinder. For the flow perpendicular to the cylinder ($\phi = 0°$) there was a minimal change noted between the flow velocity predominantly in the *u* direction of the total flow velocity, meaning that the majority of the wind flow always streams is in the far flow field direction. At a distance of 2.0D, the flow in the wake downstream the flow was completely recovered streaming in the downstream direction, as shown in Figure 5.6(j).

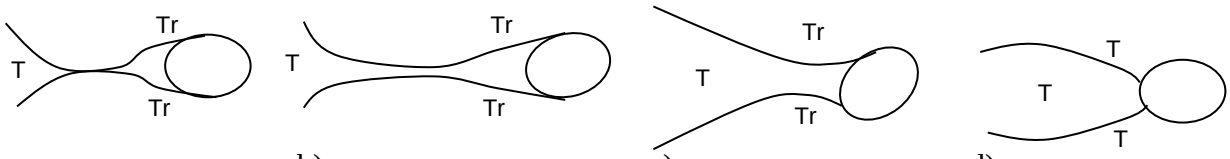
5.4 Proposed Flow Classification for Inclined and Yawed Cylinders

The predominant features of the flow developed around inclined and yawed cylinders differs from the characterization of the flow perpendicular to the cylinder, as described by Zdravkovich (1997). At the same time, there is currently no flow regime description for the inclined yawed cylinders. Therefore, based on the velocity profiles described in Figure 5.1(a) – (i), the eddy viscosity, and swirl threads formations presented in Figure 5.2(a) – (i), and supported by the eddy viscosity, normalized pressures, and the normalized velocity charts in Figures 5.3(a) – (i), Figures 5.4(a) – (i), and Figures 5.5(a) – (i) respectively, the following three flow regimes have been suggested for the inclined and yawed cylinders analysed herewith, which are combinations of the TrSL and TrBL regimes:

- TrSL-Short and Long (Figure 5.2(c), (f), (i) and (b), (d), (g) respectively) are encountered when the major axis of the ellipse, representing the cross-section of the inclined/yawed cable seen by the flow, is close to the direction of flow, and the turbulent shear layers detach almost on the leeward side of the cylinder, and they intersect immediately after at 0.5D (TrSL-Short) or at 1D from the cylinder (TrSL-Long), forming a turbulent wake downstream. TrSL-Short is applicable for cases: $\alpha = 50°$, $\beta = 40°$, $\phi = 60.5°$, Re = 3.3×10^5; $\alpha = 50°$, $\beta = 20°$, $\phi = 53°$, Re = 4.4×10^5; and $\alpha = 60°$, $\beta = 0°$, $\phi = 60°$, Re = $3.3 \times$

10^5; TrSL-Long is applicable for cases: $\alpha = 50°$, $\beta = 20°$, $\phi = 53°$, Re = 3.3×10^5; $\alpha = 60°$, $\beta = 20°$, $\phi = 62°$, Re = 3.3×10^5; and $\alpha = 60°$, $\beta = 20°$, $\phi = 62°$, Re = 5.5×10^5.. Schematic representation of both TrSL-Short and TrSL-Long can be found in Figure 5.8(a) and (b) below.

- TrSL-Open (Figure 5.2(a) and (e)) can be noticed when the major axis of the ellipse moves away from the direction of flow and the shear layers detach sidewise from the cylinder for $\alpha = 54.7°$, $\beta = 40°$, $\phi = 64°$, Re = 1.1×10^5; and $\alpha = 54.7°$, $\beta = 40°$, $\phi = 64°$, Re = 3.3×10^5. The TrSL-Open was represented in Figure 5.8(c).
- TrBL (Figure 5.2(h)) develops when the transition to turbulent regime occurs in the boundary layer surrounding the cylinder and the turbulent wake forms from in the immediate vicinity of the leeward side of the cylinder. This was noticed for Re of 6.7×10^5 for $\phi = 0°$, and also for the critical case of $\phi = 60°$. Schematic representation of TrBL is shown in Figure 5.8(d).



a) b) c) d)

Figure 5.8: Flow regimes for inclined cylinders (a) TrSL-Short, (b) TrSL-Long, (c) TrSL-Open and (d) TrBL (T = Transition, Tr = Turbulent)

It is worth mentioning that the free shear layers detaching from the inclined and/or yawed cylinders do not develop in the same manner as the shear layers for flow perpendicular to the cylinder presented in Zdravkovich (1997) for the flow regime classification. The flow perpendicular to the cylinder detach symmetrically from the sides of the cylinder, and engulf the wake region. In the present case, the shear layers will detach at various locations at the

circumference of the ellipse, sometimes not symmetric and in most of the cases the turbulent wake will be formed after their intersection downstream the cylinder.

The flow regimes for all the cases investigated in the current study have been classified, and are presented in the Table 5-1 below. The classifications for flow perpendicular to the cylinder are completed using the flow classification system proposed by Zdravkovich (1997), however the classifications for the flow for inclined and/or yawed cylinders are completed with the classification system proposed above (Figure 5.8).

Also for the case of flow perpendicular to the cylinder, the flow classification differs from Transition in Shear Layers (TrSL) to Transition in Boundary Layers (TrBL) due to the increase in Re from $Re = 3.3 \times 10^5$ to $Re = 4.4 \times 10^5$. This is in a similar Re range as outlined by Zdravkovich (1997) where the transition between the TrSL and TrBL flow regimes occurs in a slightly lower Re range of $Re = 1.0 \times 10^5$ and $Re = 2.0 \times 10^5$.

Table 5-1: Flow regimes classifications for the current study results

Inclination angle α (deg)	Yaw angle β (deg)	Relative angle of attack, ϕ (deg)	Re = 1.1×10^5	Re = 2.2×10^5	Re = 3.3×10^5	Re = 4.4×10^5	Re = 5.5×10^5	Re = 6.7×10^5
0	0	0	TrSL	TrSL	TrSL	TrBL	TrBL	TrBL
60	0	60	TrSL-Short	TrSL-Long	TrSL-Short	TrSL-Short	TrSL-Long	TrBL
60	20	62	TrSL-Long	TrSL-Long	TrSL-Long	TrSL-Long	TrSL-Long	-
60	40	67.5	TrSL-Open	TrSL-Open	TrSL-Long	TrSL-Long	TrSL-Open	-
54.7	0	54.7	TrSL-Long	TrSL-Long	TrSL-Long	TrSL-Long	TrSL-Long	-
54.7	20	57.1	TrSL-Open	TrSL-Long	TrSL-Long	TrSL-Long	TrSL-Long	-
54.7	40	64	TrSL-Open	TrSL-Open	TrSL-Open	TrSL-Open	TrSL-Open	-
50	20	53	TrSL-Long	TrSL-Long	TrSL-Long	TrSL-Short	TrSL-Long	-
50	40	60.5	TrSL-Short	TrSL-Short	TrSL-Short	TrSL-Short	TrSL-Short	-
30	20	35.5	TrSL-Short	TrSL-Short	TrSL-Short	TrSL-Short	TrSL-Short	-

For the flow inclined and/or yawed to the circular cylinder, the classification of the flow regimes varied with the change in yaw angle of the circular cylinder. As shown in the Table 5-1 above, for an inclination angle of the circular at 60°, the flow was classified as either TrSL-Short, or TrSL-Long for a yaw angle of 0°. Increasing the yaw angle to 20°, and maintaining the angle of inclination at 60°, the classification of the flow regime changed to TrSL-Long, for all Re, and finally to TrSL-Open as the yaw angle increased to 40°. This could be due to the flow encountering a "wider" obstacle as it approaches the cylinder, as the yaw angle of the inclined circular cylinder increases, thus creating a larger wake on the leeward side of the cylinder. A similar tendency is shown for the cylinder inclination of 54.7°, except for the fact that the flow regime classification

changes from TrSL-Long to TrSL-Open only. The results for cylinder inclination of 50°, do not show the same tendency as the above described flow regimes classification, but contrary the flow varies from TrSL-Open, for lower yaw angles to TrSL-Long, for higher yaw angles. If only the relative angle between the flow and the cylinder is considered, then it is noted that the flow classification for both cases near 60° correspond to a consistent flow classification, regardless the Re numbers, for up to Re = 6.7×10^5. These cases are $\alpha = 50°$, $\beta = 40°$, $\phi = 60.5°$; and $\alpha = 60°$, $\beta = 0°$, $\phi = 60°$. The results for a cylinder inclination of 30° are also shown, for which the TrSL-Short flow regime was consistent for all the Re numbers investigated.

5.5 Influence of the Yaw Angle on Flow Characteristics around Circular Cylinders

The yaw angle of an inclined cylinder has a major influence on the flow characteristics around a circular cylinder, as it can be seen in the above sections detailing the wind flow characteristics. In this section different aspects of the flow, including the dominant velocity zones, the eddy viscosity plots, the pressure plots downstream of the cylinder, and the velocity plots downstream of the cylinder were investigated, for different yaw angles. The yaw angle influenced the detachment of the turbulent shear layers, and the transition to the wake region by creating an open profile for the cases with larger yaw angles studied. The turbulent shear layers intersected each other downstream of the cylinder for intermediate yaw angles, and the intersection point moved closer to the leeward side of the cylinder as the yaw angles approached zero. The eddy viscosity plots downstream of the cylinder showed similar tendencies. The single exception to this observation was the case where the cylinder was not yawed to the flow, and the two-dimensional eddy viscosity profiles, and the eddy viscosity graphs showed different tendencies, for case $\alpha = 60°$, $\beta = 0°$, $\phi = 60°$, Re = 3.3×10^5, as shown in Figure 5.2(i) and Figure 5.3(i).

The pressure distribution downstream of the cylinder showed a significant variation with the change of the yaw angle. The highest difference was registered in the normalized pressure from one side of the cylinder to the other, for the highest yaw angle, and this difference decreased with the decrease in yaw angle. As expected, the velocity profiles on the downstream side of the cylinder showed a similar tendency.

5.6 MacDonald Equation for the Galloping Verification

A general expression for the theoretical aerodynamic damping has been derived by MacDonald and Larose (2006) which is based on the quasi-steady theory. The resulting theoretical aerodynamic damping approximated by this equation (Eq. (5-1)) may be positive or negative. Unless counteracted by a sufficient structural damping, a galloping-type aerodynamic stability is indicated when the aerodynamic equation is negative.

$$\zeta_a = \frac{\mu \mathrm{Re}}{4m\omega_n}\cos\alpha\left\{\cos\alpha\left[C_D\left(2\sin\phi + \frac{\tan^2\alpha}{\sin\phi}\right) + \frac{\partial C_D}{\partial \mathrm{Re}}\mathrm{Re}\sin\phi + \frac{\partial C_D}{\partial\phi}\cos\phi - \frac{\partial C_D}{\partial\alpha}\frac{\tan\alpha}{\sin\phi}\right]\right.$$
$$\left. - \sin\alpha\left[C_L\left(2\sin\phi - \frac{1}{\sin\phi}\right) + \frac{\partial C_L}{\partial \mathrm{Re}}\mathrm{Re}\sin\phi + \frac{\partial C_L}{\partial\phi}\cos\phi - \frac{\partial C_L}{\partial\alpha}\frac{\tan\alpha}{\sin\phi}\right]\right\}$$

Eq. (5-1)

where

μ is the dynamic (absolute) fluid viscosity,

Re is the Reynolds number,

m is the cylinder mass per unit length,

ω_n is the undamped circular natural frequency,

α is the direction between the cable motion and cable-wind plane,

ϕ is the cable-wind angle,

C_D is the drag coefficient, and

C_L is the lift coefficient.

For a cylinder of circular cross-section the drag and lift force coefficients C_D and C_L are invariant with the angle of attack. Therefore:

$$\frac{\partial C_D}{\partial \alpha} = \frac{\partial C_L}{\partial \alpha} = 0$$

(5-2)

Even though a circular cylinder always has a symmetric cross-section the forces developed by the flow around the circular cylinder may be asymmetrical. This occurs in the critical Reynolds number range when a laminar separation bubble forms on one side of the cylinder before the other with an increase in Reynolds number. This asymmetric flow generates a mean lift force over a narrow range of Reynolds number.

The direction of the mean lift force is arbitrary due to side of the symmetric section of the circular cylinder where the first laminar separation bubble forms. For this reason, the terms in the above formulation (Eq. (5-1)) related to the lift force may be either positive or negative. This lift force may be either beneficial or detrimental, depending on the direction of the lift force and the velocity.

For the case of a circular cylinder the following expression should be employed

$$\zeta_a = \frac{\mu \mathrm{Re}}{4m\omega_n} \cos\alpha \left\{ \cos\alpha \left[C_D \left(2\sin\phi + \frac{\tan^2\alpha}{\sin\phi} \right) + \frac{\partial C_D}{\partial \mathrm{Re}} \mathrm{Re} \sin\phi + \frac{\partial C_D}{\partial \phi} \cos\phi \right] \right.$$
$$\left. \pm \sin\alpha \left[C_L \left(2\sin\phi - \frac{1}{\sin\phi} \right) + \frac{\partial C_L}{\partial \mathrm{Re}} \mathrm{Re} \sin\phi + \frac{\partial C_L}{\partial \phi} \cos\phi \right] \right\}$$

Eq. (5-3)

5.6.1 Contribution of Each Term to the Total Aerodynamic Damping

The six terms contributing to the total aerodynamic damping in the above equation, Eq. (5-3), the drag and lift coefficients (C_D and C_L), their derivatives with respect to Reynolds number ($\partial C_D/\partial \mathrm{Re}$ and $\partial C_L/\partial \mathrm{Re}$), and cable-wind angle ($\partial C_D/\partial \phi$ and $\partial C_L/\partial \phi$) are reviewed for the current study. Positive aerodynamic damping is considered beneficial.

The contribution from the C_D term is always positive, and in the sub-critical range ($\mathrm{Re} < 2 \times 10^5$) it is the dominant term. As the Reynolds number increased to the critical Reynolds number region the contribution of the C_D term decreases. The $\partial C_D/\partial \mathrm{Re}$ has a significant negative contribution in the critical Reynolds number range ($2.8 \times 10^5 < \mathrm{Re} < 3.6 \times 10^5$), due to the drag crisis. This is of particular importance as the cable-wind relative angle (ϕ) tends towards 90°. The $\partial C_D/\partial \phi$ has little or no effect on the aerodynamic damping as it is small in magnitude for the full range of parameters investigated.

The C_L term contribution is not very significant because it is always small when compared with the other terms. The $\partial C_L/\partial \mathrm{Re}$ is the dominant term in causing the major instability in the critical Reynolds number range for the wind-cable relative angles of $75° < \phi < 90°$. This term has large negative values in this region, due to the asymmetrical pressure distribution created by the single laminar separation bubble over this narrow range of Reynolds numbers. The $\partial C_L/\partial \phi$ has little or no effect on the aerodynamic damping, except for a small region around the cable-wind relative angle of $\phi = 55°$ and $\phi = 60°$, where its contribution is dominant.

All terms related to the lift coefficient may be either positive or negative, depending on which side of the cable the first laminar separation bubble forms.

The data from the current study were analysed to identify if a possible aerodynamic instability would be defined as critical. The contribution of each term was plotted in the Figures

5.9 to 5.13 below, to estimate the derivatives of the drag and lift coefficients (C_D and C_L) with respect to Reynolds number ($\partial C_D/\partial$Re and $\partial C_L/\partial$Re), as shown in Figure 5.9 and Figure 5.10 respectively, and with respect to the cable-wind relative angle ($\partial C_D/\partial\phi$ and $\partial C_L/\partial\phi$), as shown in Figure 5.11 and Figure 5.12 respectively, over the entire range of Reynolds number studied. The data is plotted for the nine cases detailed in this study, or cable orientations, and a sample of a linear approximation for one of the sets of data, across the full data set for each case, is shown in each of the figures.

The aerodynamic damping calculated using the above formula (Eq. (5-3)) based on the results obtained in the current study, was plotted for the different Reynolds numbers also as employed in this study. The formulation indicated that the aerodynamic stability was achieved for the entire Reynolds numbers tested except for one case: $\alpha = 50°$, $\beta = 40°$, $\phi = 60.5°$, for Re = 4.4×10^5. This is shown in the negative aerodynamic damping values represented in Figure 5.13 below, and falls within the expected range of relative angles for the aerodynamic instability of inclined cables.

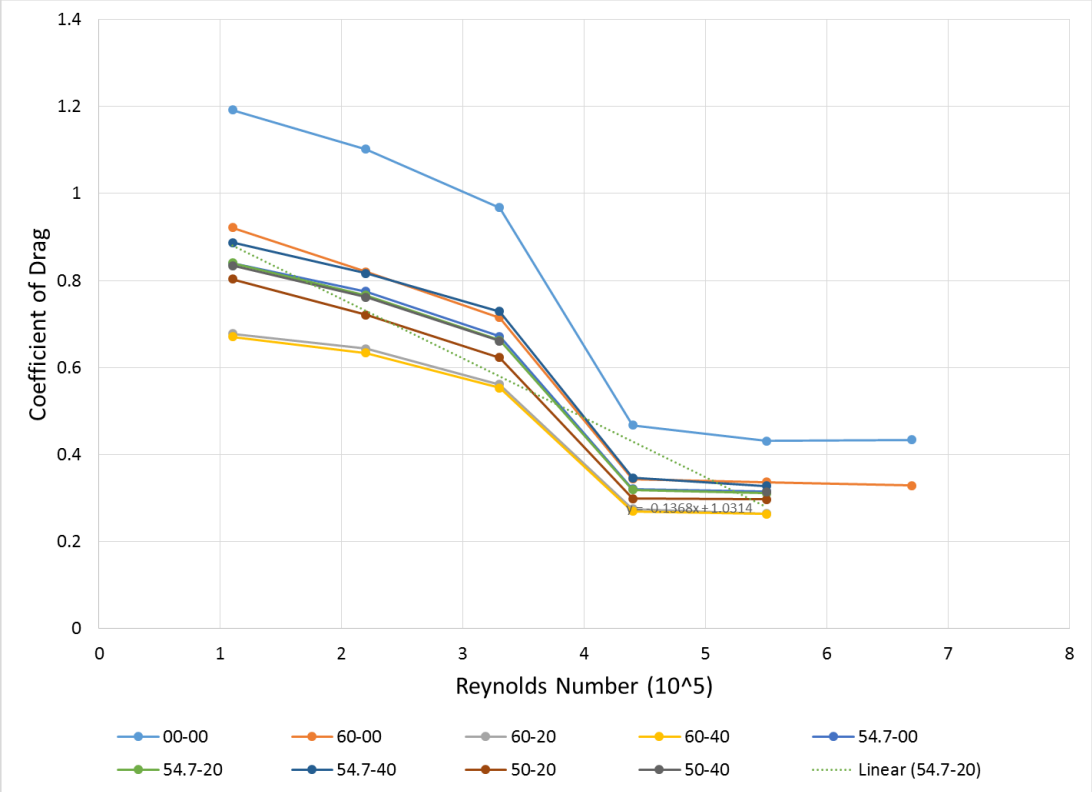


Figure 5.9: Coefficient of drag (C_D) vs. Reynolds number (Re) for the current study.

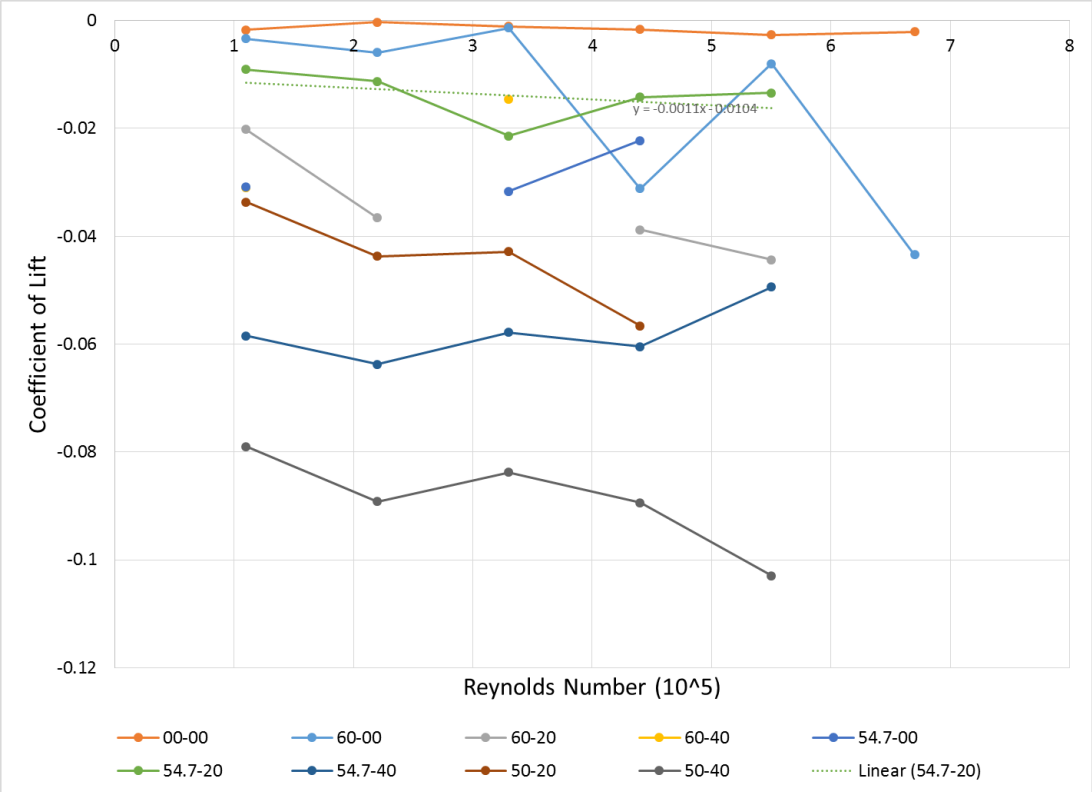


Figure 5.10: Coefficient of lift (C_L) vs. Reynolds number (Re) for the current study.

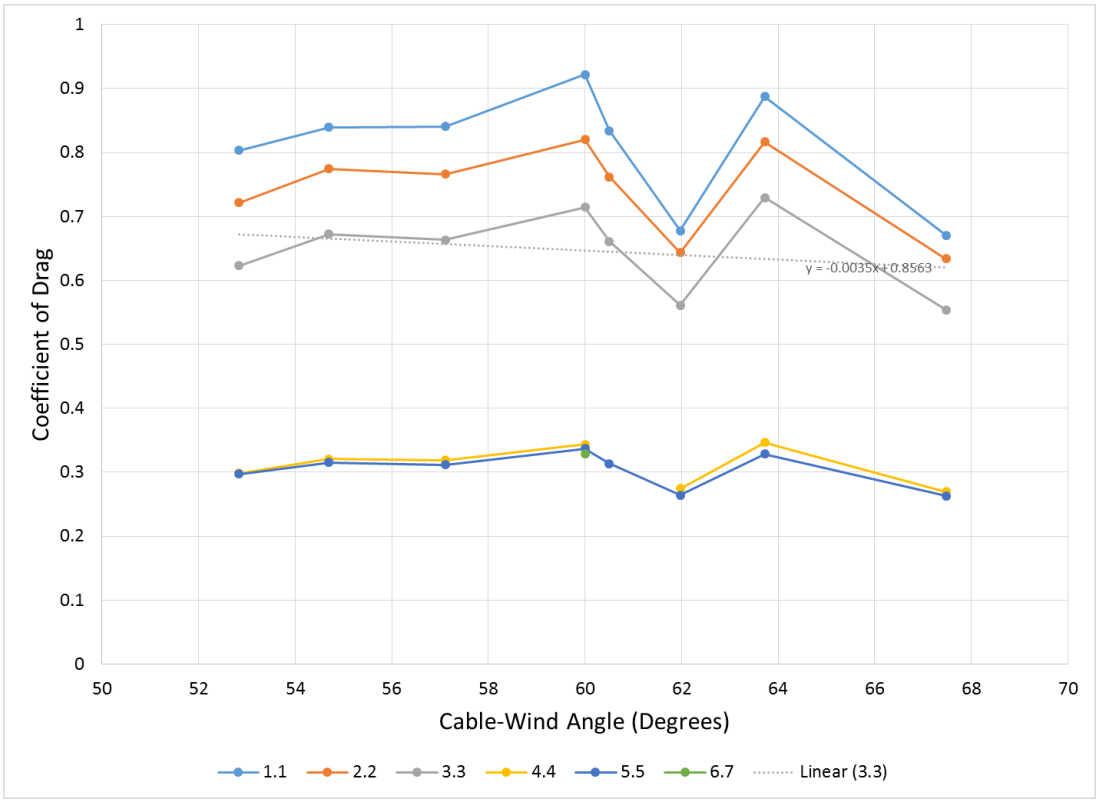


Figure 5.11: Coefficient of drag (C_D) vs. cable-wind relative angle (degrees) for the current study.

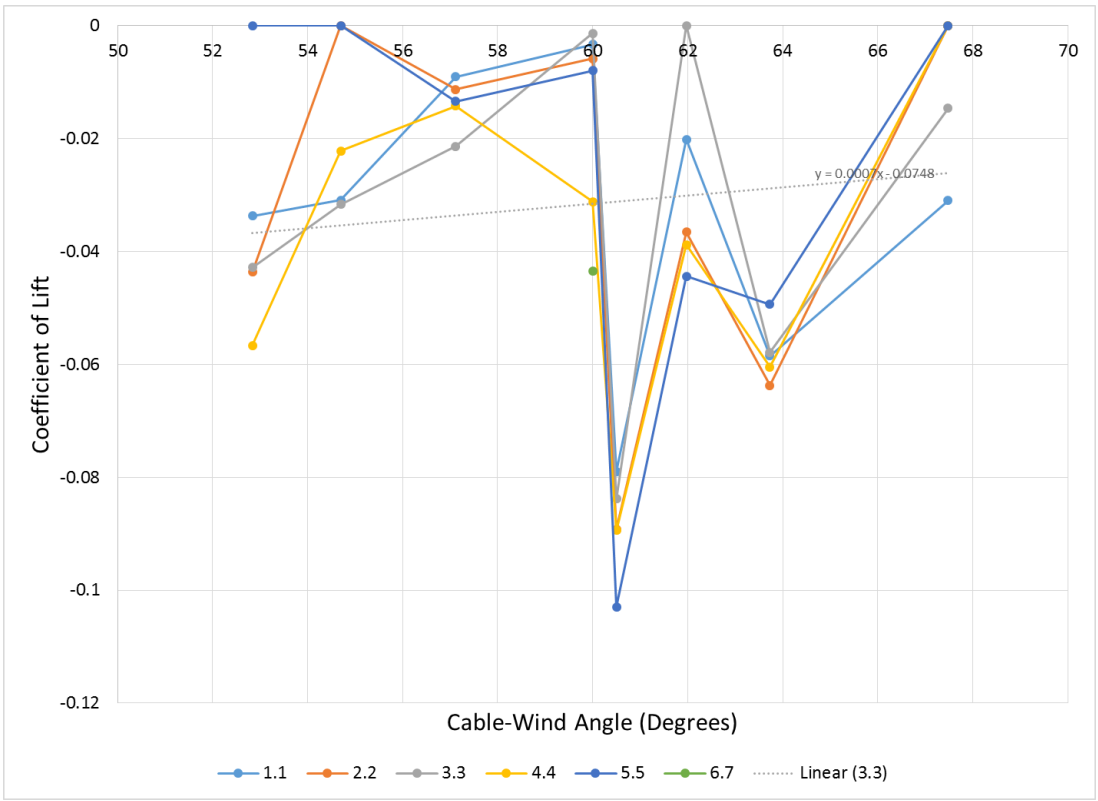


Figure 5.12: Coefficient of lift (C_L) vs. cable-wind relative angle (degrees) for the current study.

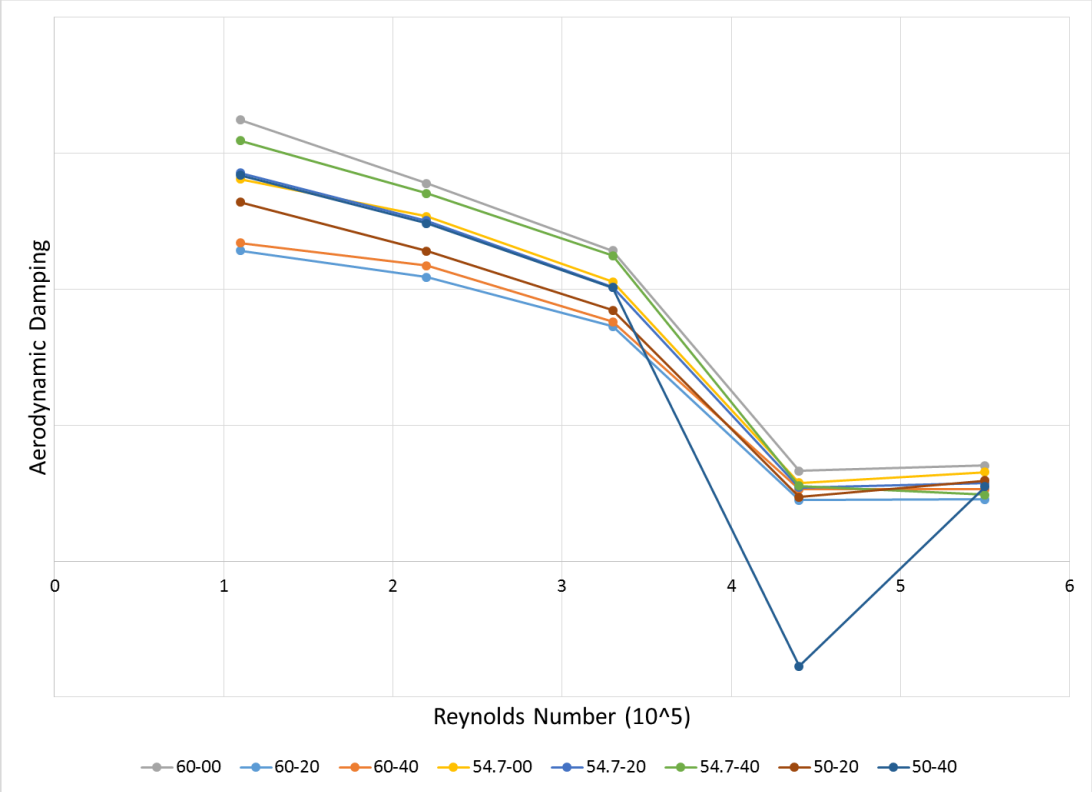


Figure 5.13: Aerodynamic damping vs. Reynolds number (Re) for the current study.

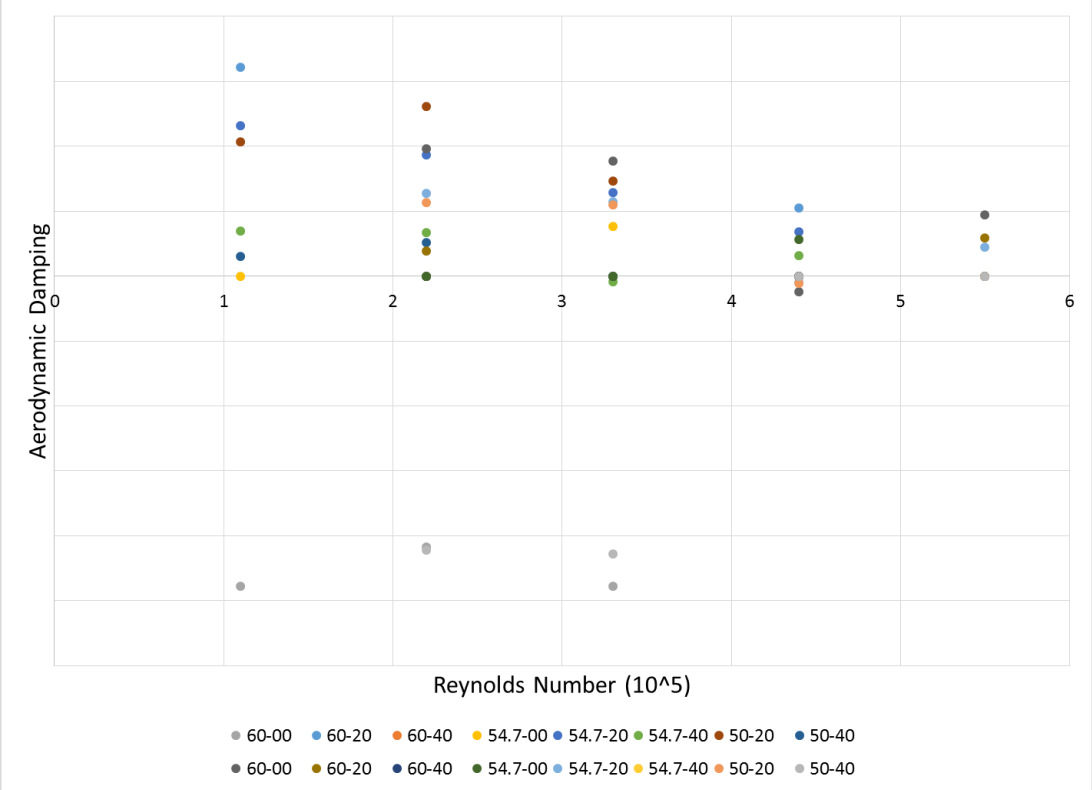


Figure 5.14: Aerodynamic damping vs. Reynolds number (Re) for the current study.

The data is presented for the current study data, using an estimation of the localized derivatives with respect to Reynolds number ($\partial C_D/\partial \mathrm{Re}$ and $\partial C_L/\partial \mathrm{Re}$), and cable-wind angle ($\partial C_D/\partial \phi$ and $\partial C_L/\partial \phi$), and are shown in Figures 5.9 to 5.12. The following cases showed that the aerodynamic instability was achieved, using the localized derivatives:

$\alpha = 54.7°$, $\beta = 40°$, $\phi = 63.7°$, for $\mathrm{Re} = 3.3 \times 10^5$

$\alpha = 60°$, $\beta = 0°$, $\phi = 60°$, for $\mathrm{Re} = 4.4 \times 10^5$

$\alpha = 54.7°$, $\beta = 20°$, $\phi = 57.1°$, for $\mathrm{Re} = 4.4 \times 10^5$

$\alpha = 50°$, $\beta = 20°$, $\phi = 52.8°$, for $\mathrm{Re} = 4.4 \times 10^5$

These cases were therefore identified as critical, and it was noticed that these belong to the typical cases of inclined and yawed cylinders known as reaching aerodynamic instability. This is known for the relative angle between the wind and cylinder at 60°, at the Reynolds numbers in the range of 3.3×10^5 to 4.4×10^5.

The cases $\alpha = 60°$, $\beta = 20°$, $\phi = 62°$ and $\alpha = 50°$, $\beta = 40°$, $\phi = 60.5°$ for $\mathrm{Re} < 3.3 \times 10^5$ also showed indications of aerodynamic instability. Again, the relative angle between the wind direction and cylinder of approximately $\phi = 60°$ is present in both cases. This is due to the large change in the lift coefficient variation at the relative angle ϕ in the vicinity of 60°, for all cases tested in this study, when using the local derivatives. More investigations are required however for clarifying the effect of the cable inclinations (α) and yaw angle (β) on this large variation of lift coefficient, for this relative angle of attack (ϕ). Currently the Eq. (5-3) considers only the partial derivatives terms as function of Re, and relative angle of attack ϕ.

6 Fast Fourier Transforms and Coherence

The coherence and cross-coherence is calculated between the coefficient of lift, the pressure coefficient along the leeward side of the cylinder, and the velocity fluctuation along the leeward side of the cylinder to study the relationship, and interaction between these parameters. A brief description of coherence and cross-coherence is provided, followed by the summary of the results.

The use of the frequency domain in analyzing the flow along the leeward side of the cylinder can provide additional information compared to the time domain analysis (Elgar et al, 1990) completed in the previous chapters. This will be performed through the coherence analysis. The cross-coherence will yield information on the phase coupling between two degrees-of-freedom parameters, because this characterizes the quadratic nonlinear transfer between the variables considered (Pezeshki et al, 1992).

Presented in this section is the Fast Fourier Transform (FFT) of some of the cases presented in the above chapters. The results are summarized for two cases which were identified as critical; first, the case of the cylinder inclined to the flow by 60° ($\phi = 60°$; $\alpha = 60°$, $\beta = 0°$), and the second is the case of the cylinder inclined to the flow by 54.7° and yawed 20° ($\phi = 57.1°$; $\alpha = 54.7°$, $\beta = 20°$); both cases were interpreted for the range of Re from 1.1×10^5 to 5.5×10^5. These cases were chosen as the most pertinent examples of flow around an inclined cylinder, and the frequency analysis is used to provide a concise summary of the vast amount of data obtained in the current study. FFT results from the coefficient of drag, coefficient of lift, the pressure coefficient along the leeward side of the cylinder, and the velocity fluctuation along the leeward side of the cylinder are summarized, and compared with each other at the end of the section.

6.1 Fast Fourier Transform (FFT) Results for C_D

Ten cases for the flow characteristics around the cylinder inclined to the flow by 60° (ϕ = 60°; α = 60°, β = 0°), and inclined to the flow by 54.7° and yawed 20° (ϕ = 57.1°; α = 54.7°, β = 20°) for Re of 1.1×10^5 to 5.5×10^5 are presented below. The time histories for C_D are presented in Figure 6.1 and Figure 6.2 respectively for the two cases, followed by the FFT results of C_D time histories in Figure 6.3 and Figure 6.4. The FFT results for all the cases in this study were presented in Appendix L. The time histories for the two cases are presented in Figure 6.1 and Figure 6.2 for a sample period of one second. The changes in the scale for the five parts of each figure, representing each Re investigated in this study, adjusted as the flow transitions through the drag crisis region. The data was presented such that it provides the greatest detail in the time history plots of the coefficients of drag.

As indicated in the previous chapter, the drag coefficient decreased as the Re increased for both cases. The magnitude of the fluctuations of the drag coefficient time history from the mean value remains consistent for both cases, and for all five Re numbers investigated. Of special note are the drag coefficient time histories for ϕ = 60°, for Re of both 3.3×10^5 and 4.4×10^5, which show a change in the fluctuation tendency, as it can be noticed in Figure 6.1iii) and Figure 6.1iv) respectively. The change is situated between 1.0 sec and 1.2 sec for Re = 3.3×10^5, and 0.8 sec and 1.0 sec for Re = 4.4×10^5. Also a particular feature is the greater magnitude of fluctuations of the drag coefficient time history for ϕ = 57.1° and Re = 4.4, as shown in Figure 6.2iv). The Fast Fourier Transforms corresponding to the drag coefficient time histories shown in Figure 6.1 and Figure 6.2 are represented in Figure 6.3 and Figure 6.4 respectively. The results of the power spectral densities (PSD) for ϕ = 60° in Figure 6.3 are showing a PSD energy component less than 0.4, for a reduced frequency lower than 0.3. The reduced frequency increased to values greater

than 0.37 for the next three Re numbers of 2.2×10^5, 3.3×10^5, and 4.4×10^5, with the power spectral density peaking around 0.8 for Re = 2.2×10^5. The PSD reduced thereafter for the next two Re tested, and the PSD for Re = 5.5×10^5 showed no dominant reduced frequency across the domain of interest. The results of the Fast Fourier Transforms above are plotted against reduced frequencies for enabling the direct comparison between different cases investigated. The reduced frequency is defined as a normalized frequency with respect to a reference chord length, and the far field flow velocity (Koochesfahani, 1989). In this case the reference chord length is the cylinder diameter. The inclination of the cable is also included within the normalization expression for the reduced frequency by taking into account the trigonometric function of the velocity along the cable inclination:

$$St = \frac{fL}{v \sin \varphi} \tag{6-1}$$

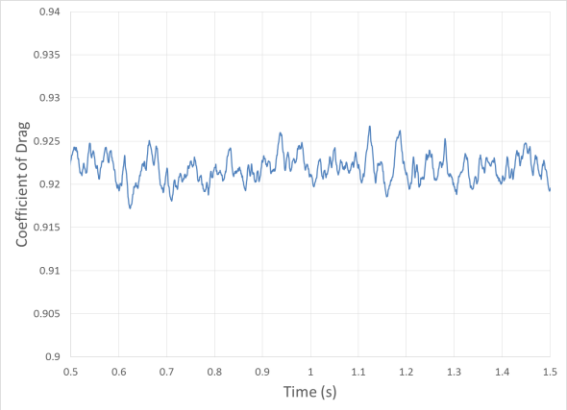
where f is the coresponding frequency

L is the diameter of the cylinder

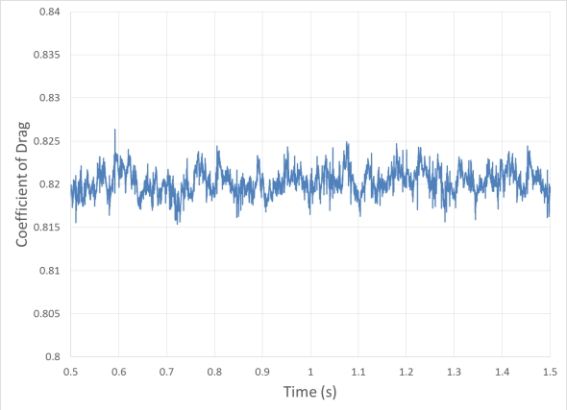
v is the far field flow velocity

ϕ is the cable inclination

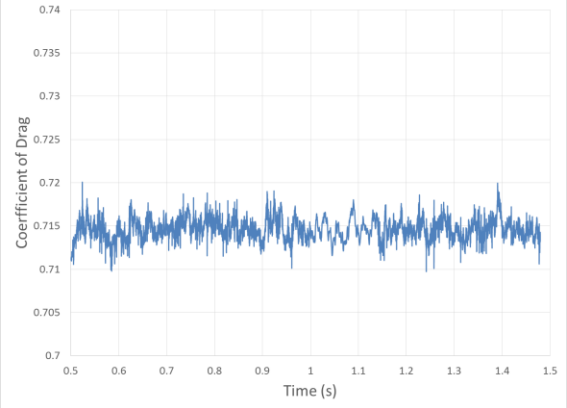
The PSDs for all Re cases investigated at $\phi = 57.1°$ are represented in Figure 6.4; these results showed a similar trend: this time the PSD peaks at Re = 1.1×10^5 for a reduced frequency value below 0.3, as shown in Figure 6.4i). The PSD reduced for each subsequent Re number tested, decreasing to a value of around 0.5 for Re = 2.2×10^5, and less than 0.4 for each of the next two Re numbers. The PSD for Re = 5.5×10^5 showed a peak of the power spectral density of 0.1 just below a reduced frequency of 0.4, as shown in Figure 6.4 iv).



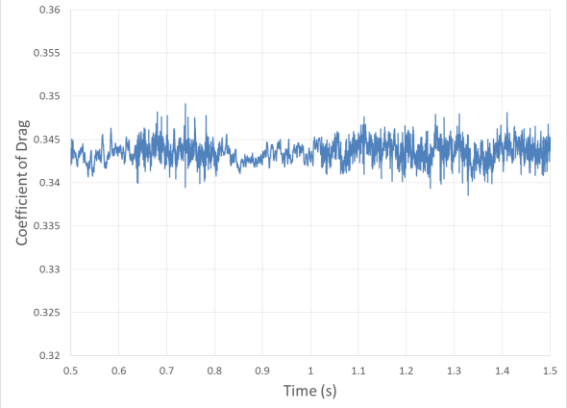
$\phi = 60°$; $\alpha = 60°$, $\beta = 0°$
i) Re = 1.1×10^5;



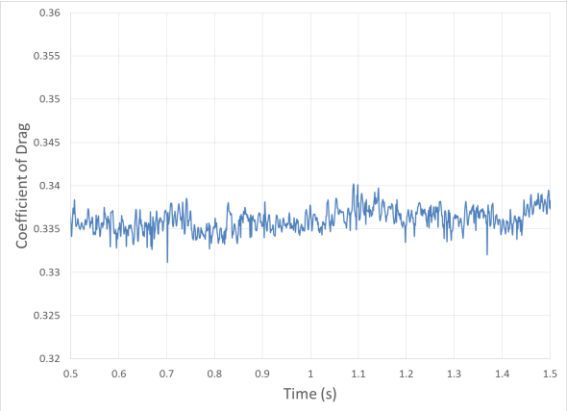
$\phi = 60°$; $\alpha = 60°$, $\beta = 0°$
ii) Re = 2.2×10^5;



$\phi = 60°$; $\alpha = 60°$, $\beta = 0°$
iii) Re = 3.3×10^5;

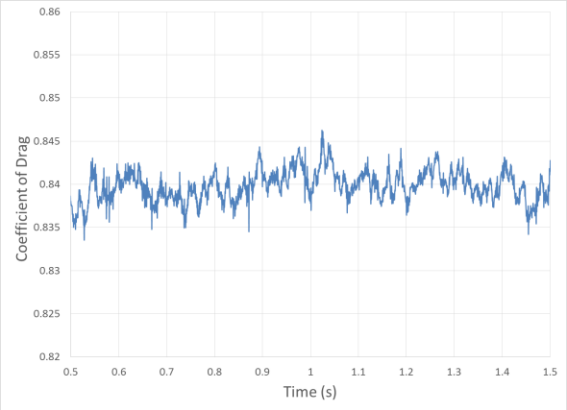


$\phi = 60°$; $\alpha = 60°$, $\beta = 0°$
iv) Re = 4.4×10^5;

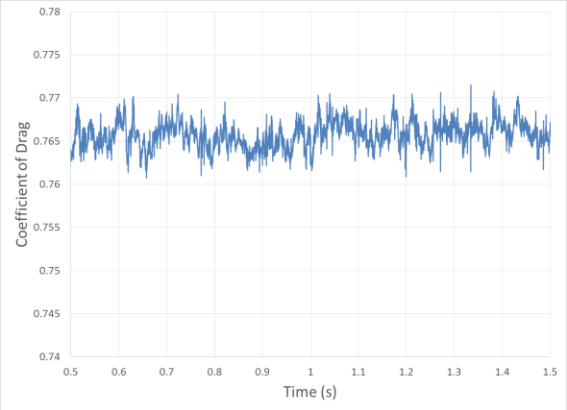


$\phi = 60°$; $\alpha = 60°$, $\beta = 0°$
v) Re = 5.5×10^5;

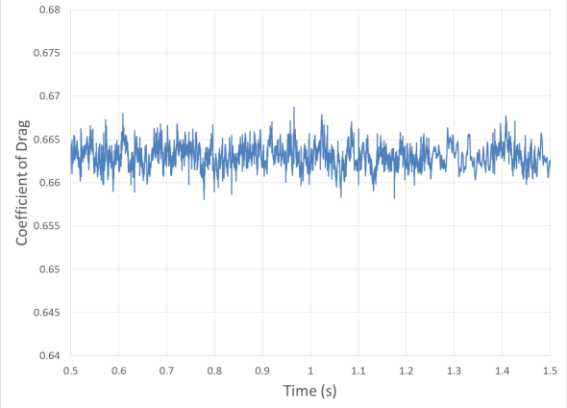
Figure 6.1: Time histories for C_D



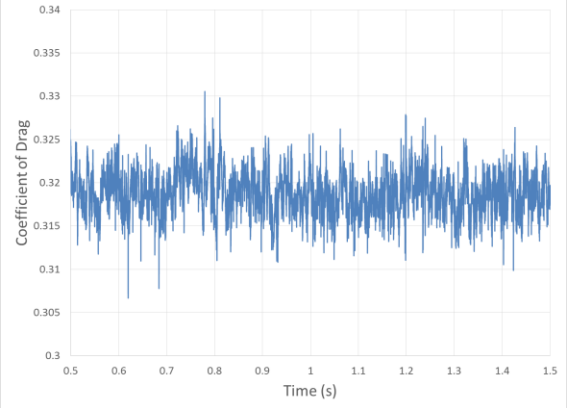
$\phi = 57.1°$; $\alpha = 54.7°$, $\beta = 20°$
i) Re = 1.1×10^5;



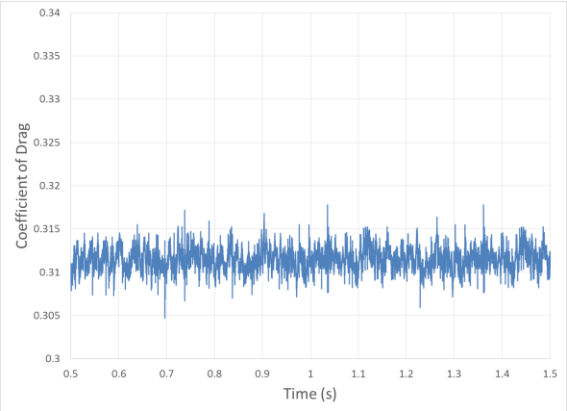
$\phi = 57.1°$; $\alpha = 54.7°$, $\beta = 20°$
ii) Re = 2.2×10^5;



$\phi = 57.1°$; $\alpha = 54.7°$, $\beta = 20°$
iii) Re = 3.3×10^5;

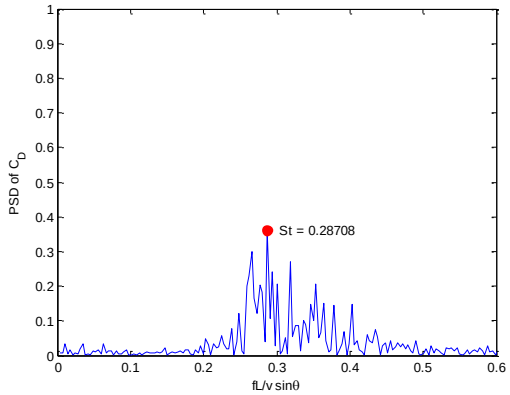


$\phi = 57.1°$; $\alpha = 54.7°$, $\beta = 20°$
iv) Re = 4.4×10^5;

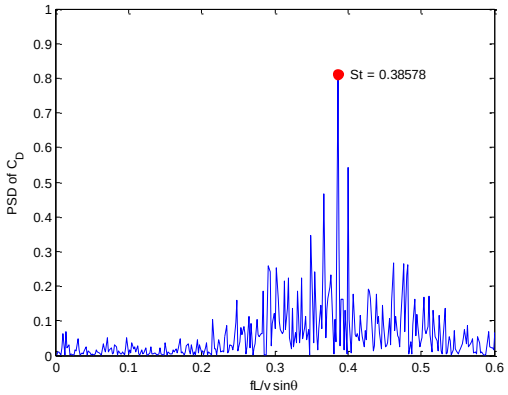


$\phi = 57.1°$; $\alpha = 54.7°$, $\beta = 20°$
v) Re = 5.5×10^5;

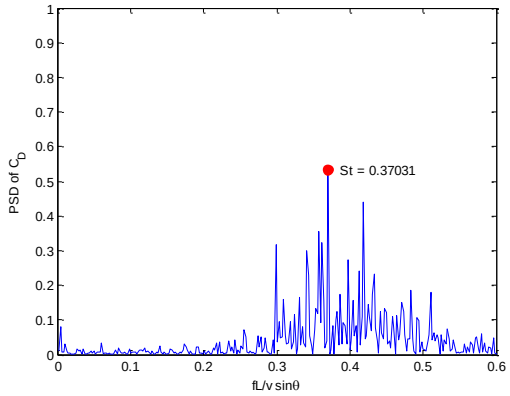
Figure 6.2: Time histories for C_D



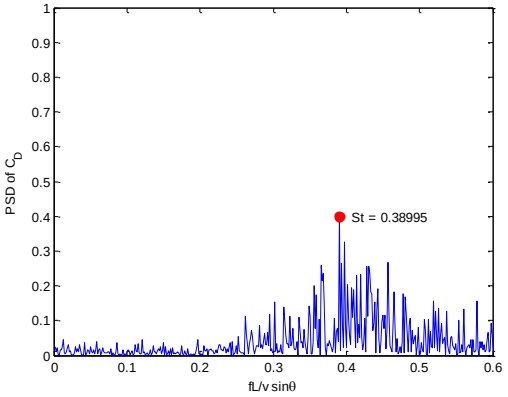
$\phi = 60°$; $\alpha = 60°$, $\beta = 0°$
i) Re = 1.1×10^5;



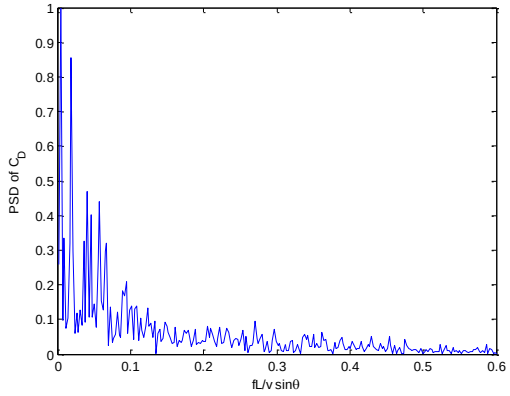
$\phi = 60°$; $\alpha = 60°$, $\beta = 0°$
ii) Re = 2.2×10^5;



$\phi = 60°$; $\alpha = 60°$, $\beta = 0°$
iii) Re = 3.3×10^5;

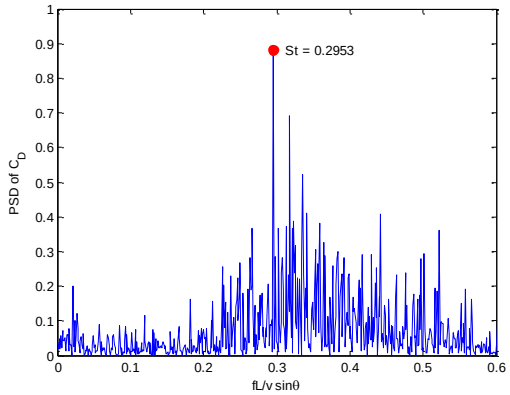


$\phi = 60°$; $\alpha = 60°$, $\beta = 0°$
iv) Re = 4.4×10^5;

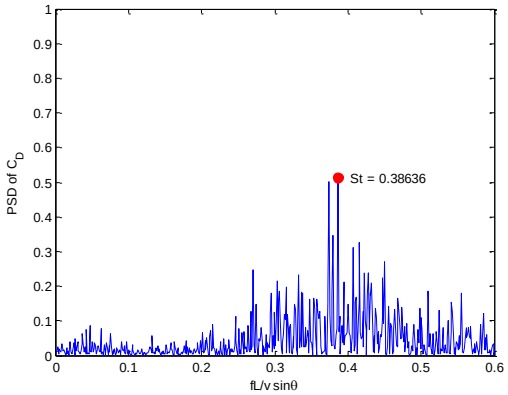


$\phi = 60°$; $\alpha = 60°$, $\beta = 0°$
v) Re = 5.5×10^5;

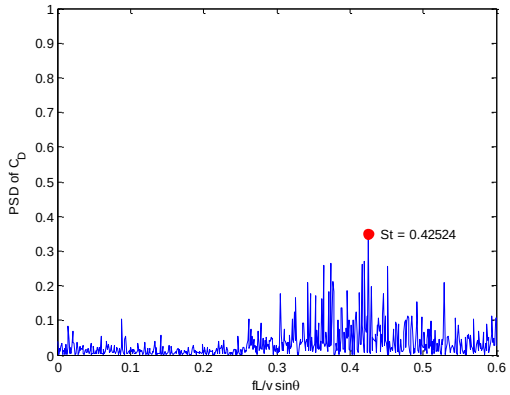
Figure 6.3: Fast Fourier Transform (FFT) results for drag coefficient C_D



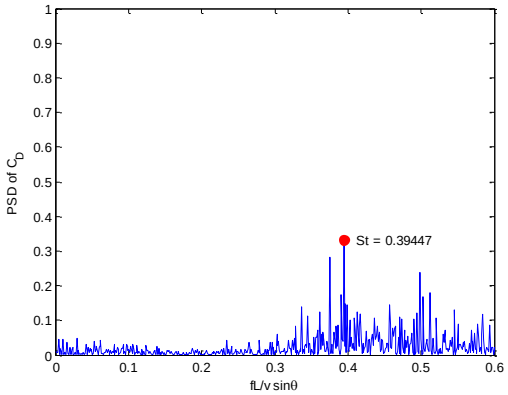
$\phi = 57.1°$; $\alpha = 54.7°$, $\beta = 20°$
i) Re = 1.1×10^5;



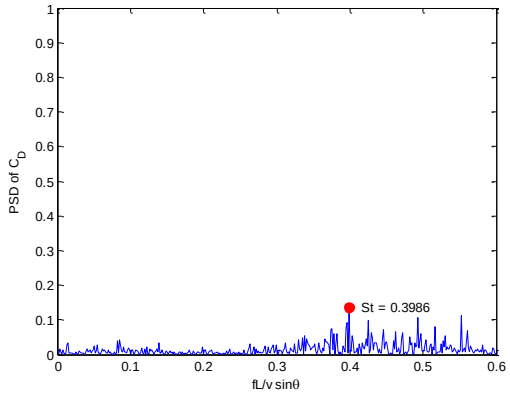
$\phi = 57.1°$; $\alpha = 54.7°$, $\beta = 20°$
ii) Re = 2.2×10^5;



$\phi = 57.1°$; $\alpha = 54.7°$, $\beta = 20°$
iii) Re = 3.3×10^5;



$\phi = 57.1°$; $\alpha = 54.7°$, $\beta = 20°$
iv) Re = 4.4×10^5;



$\phi = 57.1°$; $\alpha = 54.7°$, $\beta = 20°$
v) Re = 5.5×10^5;

Figure 6.4: Fast Fourier Transform (FFT) results for drag coefficients C_D

A summary of the results for the FFT results for the coefficient of drag (C_D) are detailed in Table 6.1, for all the cases calculated in this study. The results are summarized in the graphs below showing the FFT results as function of the relative angle between the cylinder and the wind flow (Figure 6.5), and the FFT results and Reynolds number (Figure 6.6). For the cases for which the reduced frequency could be clearly identified in the PSD graph, this value was represented in the Table 6.1, however for some cases no clear peak was identified indicating a noisy signal, thus no values were assigned in the Table 6.1. The case which were not performed were indicated as N/A. There is no clear pattern for the FFT results plotted as function of the relative angle, but a tendency for the Strouhal number to increase with Reynolds number for each of the relative angles investigated was noticed.

Table 6.1: Fast Fourier Transform (FFT) results for drag coefficient C_D

Inclination angle α (deg)	Yaw angle β (deg)	Relative angle of attack, ϕ (deg)	Re = 1.1 $\times 10^5$	Re = 2.2 $\times 10^5$	Re = 3.3 $\times 10^5$	Re = 4.4 $\times 10^5$	Re = 5.5 $\times 10^5$	Re = 6.7 $\times 10^5$
0	0	0	0.411	0.416	0.437	0.438	Noise	Noise
50	20	53	0.395	0.375	0.511	0.493	0.529	N/A
54.7	0	54.7	0.376	0.423	0.4	0.472	0.443	N/A
54.7	20	57.1	0.295	0.386	0.425	0.394	0.399	N/A
60	0	60	0.287	0.386	0.37	0.39	Noise	0.459
50	40	60.5	0.42	0.39	0.458	0.476	0.483	N/A
60	20	62	0.422	0.43	0.533	0.561	Noise	N/A
54.7	40	64	0.291	0.361	0.323	0.489	Noise	N/A
60	40	67.5	Noise	0.359	0.326	0.37	0.334	N/A

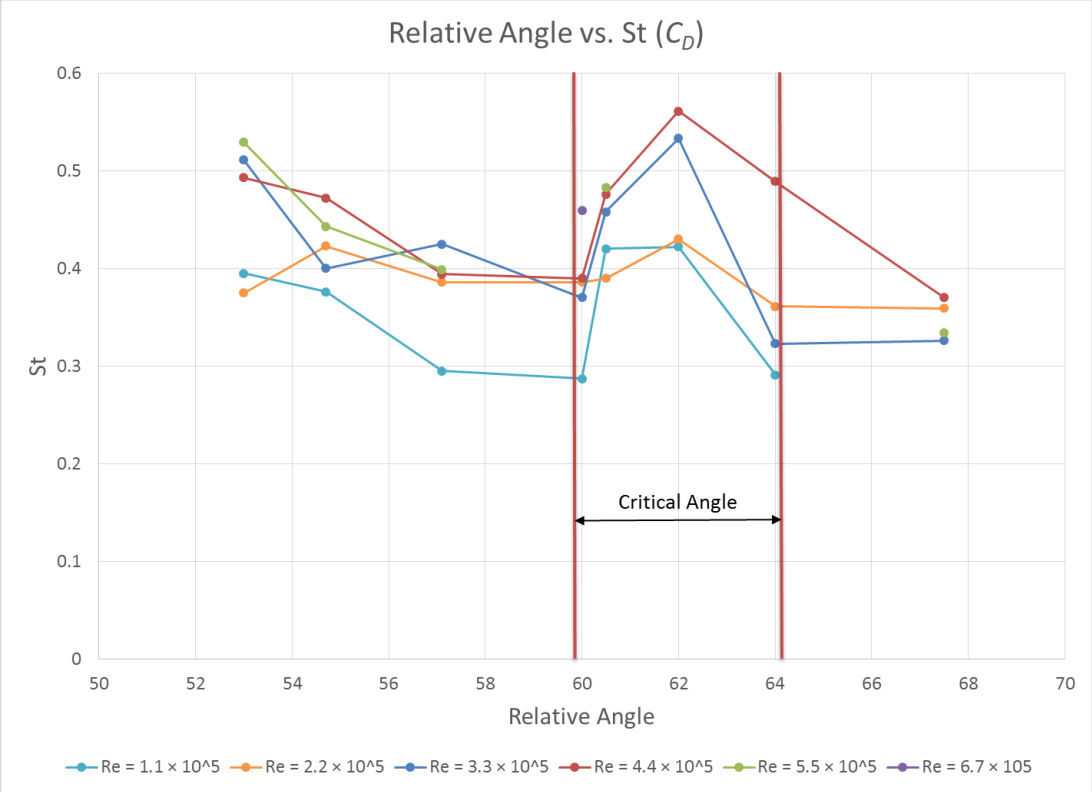


Figure 6.5: Relative angle vs. Strouhal number for C_D, plotted for each Reynolds number tested

As can be observed in the above graph (Figure 6.5) there are data points not connected to any lines. These stand-alone points are surrounded by either cases not calculated in this study, or cases where no dominant frequency was identified for the neighbouring cases in that respective series. This can be related to the cases noted as N/A, or as noise in Table 6.1.

Between the relative angles of 60° and 64° it is obvious that there is a peak in the dominant frequency for the cases investigated. In the current section, these cases will be referred to as critical cases.

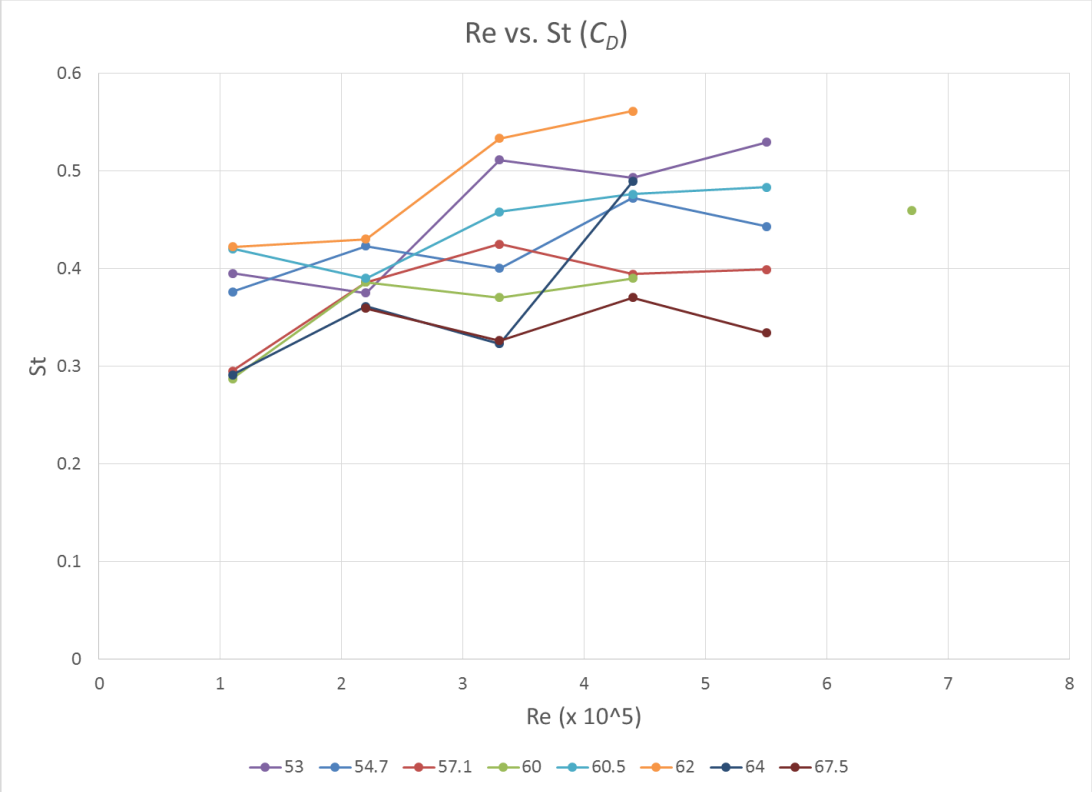


Figure 6.6: Reynolds number vs. Strouhal number for drag coefficient C_D, plotted for each relative angle

6.2 Fast Fourier Transform (FFT) Results for C_L

The same ten cases presented above for C_D coefficient for a cylinder inclined to the flow by 60° ($\phi = 60°$; $\alpha = 60°$, $\beta = 0°$), and inclined to the flow by 54.7° and yaw of 20° ($\phi = 57.1°$; $\alpha = 54.7°$, $\beta = 20°$) for Re of 1.1×10^5 to 5.5×10^5 are presented below. The across flow results has more of an influence on the vibration of the cable. The time histories for C_L coefficients are presented in Figure 6.7 and Figure 6.8 respectively for the two cases followed by the FFT results of C_L coefficients time histories in Figure 6.9 and Figure 6.10. The FFT results of all cases in this study have been presented in Appendix M.

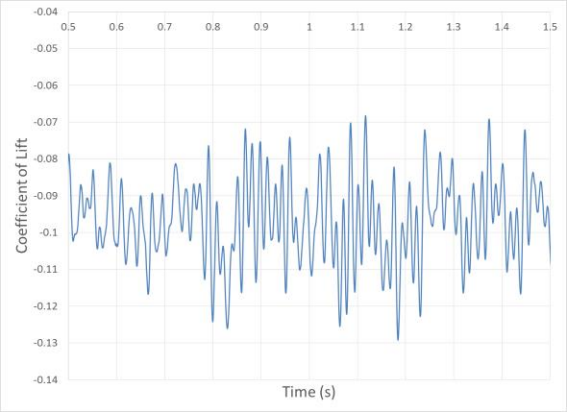
The time histories for two cases are presented in Figure 6.7 and Figure 6.8 for a sample period of one second for the coefficient of lift. In these graphs the time histories are presented against the same scale for each Re tested in this study for easy comparison. All time histories

show a consistent pattern throughout the sampled time period. The largest fluctuations in C_L coefficients for the first case of the cylinder inclined to the flow of 60° was at Re = 1.1×10^5, as shown in Figure 6.7, with a value greater than 0.04. The middle three Re tested, Re = 2.2×10^5, 3.3×10^5, and 4.4×10^5, show less fluctuation in the C_L coefficient time history of less than 0.04. For the higher Re tested, Re = 5.5×10^5, the fluctuations in the C_L coefficient time history are much less than the other four cases. Again, the time histories for the other case of flow inclined to the cylinder by $\phi = 57.1°$, as shown in Figure 6.8, showed a similar tendency. The time history for Re = 1.1×10^5 shows the greatest fluctuations in the time history with all other cases being about the same magnitude, but less than the fluctuations of the time history of Re = 1.1×10^5.

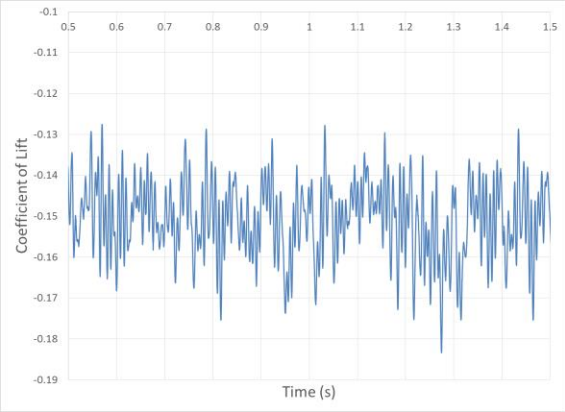
The FFT results for time histories shown in Figure 6.7 and Figure 6.8 are shown in Figure 6.9 and Figure 6.10 respectively. The PSDs of C_L coefficient shows the same tendency in magnitude variation when compared to the PSDs of C_D coefficient for the case of the cylinder inclined to the flow by 60°. The results of the power spectral densities (PSD) for $\phi = 60°$ in Figure 6.9 shows a maximum value greater than 25 for the case of Re = 2.2×10^5. All other Re tested for this angle of inclination was less than this case with no dominant frequency showing for the case of Re = 5.5×10^5.

The PSDs for all cases tested at $\phi = 57.1°$ as shown in Figure 6.10 again show a similar trend to that of the PSDs of C_D coefficient. This time the PSD peaks at Re = 1.1×10^5 again with a reduced frequency value below 0.3, as shown in Figure 6.10 i). The PSD reduce for each subsequent Re tested decreasing to a value less than 5 for Re = 5.5×10^5. The reduced frequencies are greater than 0.4 for Re = 2.2×10^5 and Re = 3.3×10^5, and less than 0.3 for Re = 4.4×10^5 and 5.5×10^5.

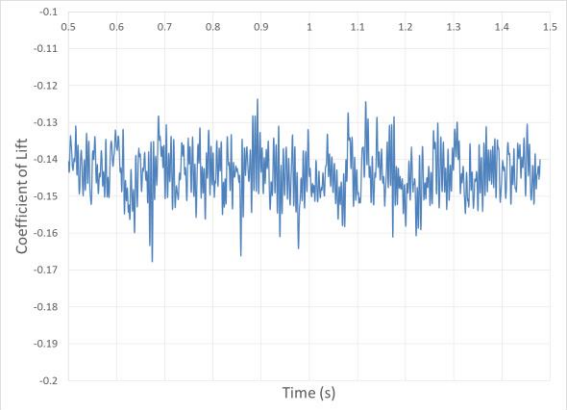
A summary of the results for the FFT results for the coefficient of lift (C_L) are summarized in the Table 6.2, for all cases calculated in this study. The results are summarized in the graphs below showing the FFT results vs relative angle between the cylinder and the wind flow (Figure 6.11), and the FFT results and Reynolds number (Figure 6.12). A peak value was noted for many of the Re cases plotted when transitioning from an angle of 60° to an angle of 62°. There is no other clear tendency for the FFT results plotted vs. the relative angle, or Reynolds number for each of the relative angles tested.



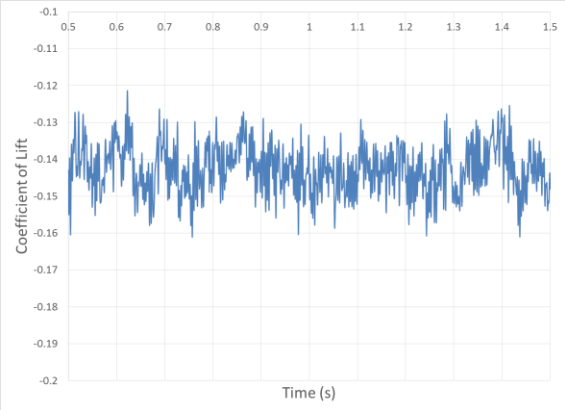
$\phi = 60°$; $\alpha = 60°$, $\beta = 0°$
i) Re = 1.1×10^5;



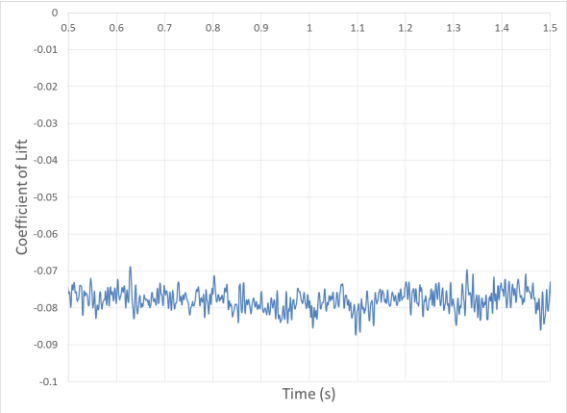
$\phi = 60°$; $\alpha = 60°$, $\beta = 0°$
ii) Re = 2.2×10^5;



$\phi = 60°$; $\alpha = 60°$, $\beta = 0°$
iii) Re = 3.3×10^5;

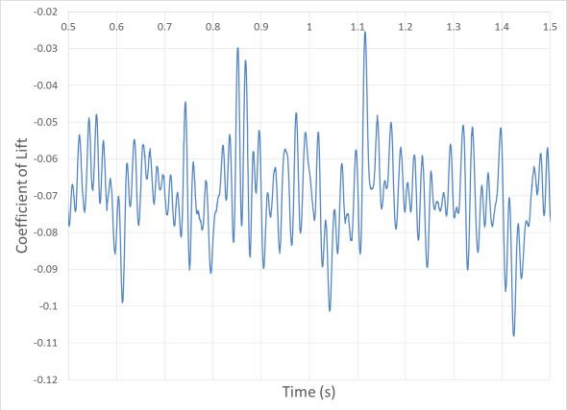


$\phi = 60°$; $\alpha = 60°$, $\beta = 0°$
iv) Re = 4.4×10^5;

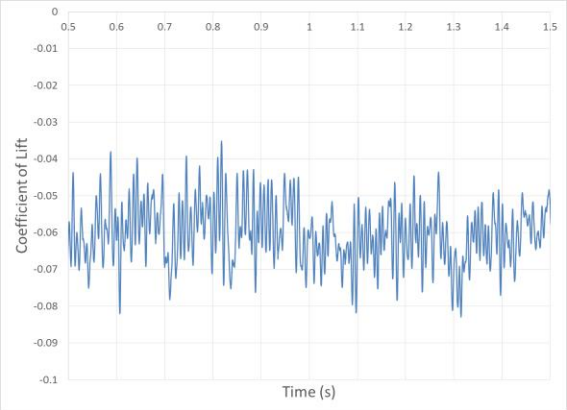


$\phi = 60°$; $\alpha = 60°$, $\beta = 0°$
v) Re = 5.5×10^5;

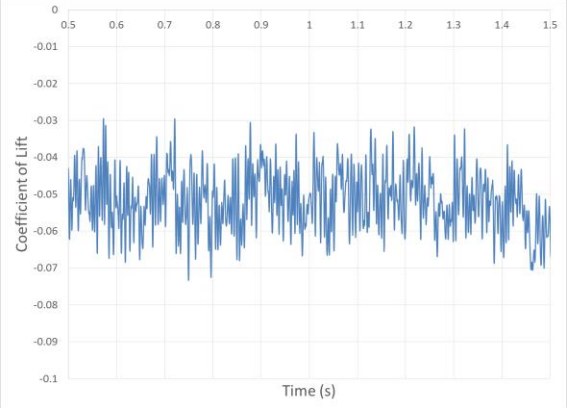
Figure 6.7: Time histories for C_L



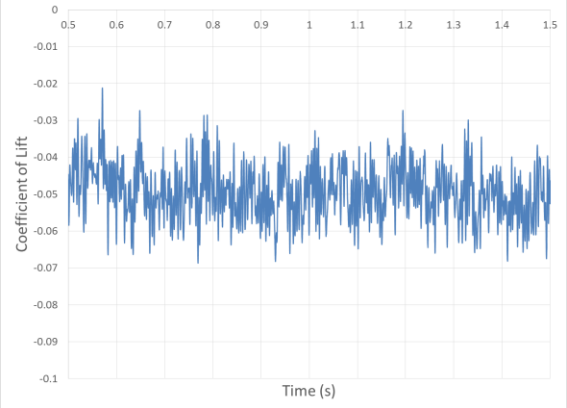
$\phi = 57.1°$; $\alpha = 54.7°$, $\beta = 20°$
i) Re = 1.1×10^5;



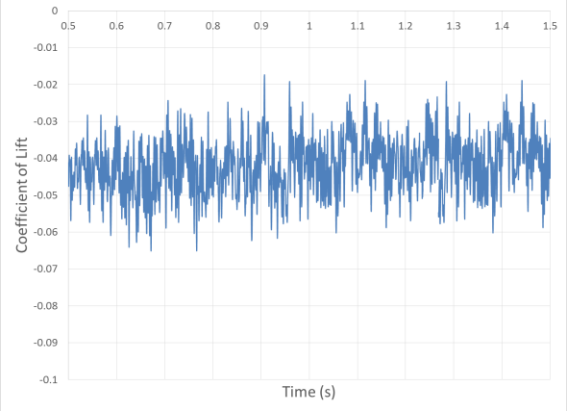
$\phi = 57.1°$; $\alpha = 54.7°$, $\beta = 20°$
ii) Re = 2.2×10^5;



$\phi = 57.1°$; $\alpha = 54.7°$, $\beta = 20°$
iii) Re = 3.3×10^5;

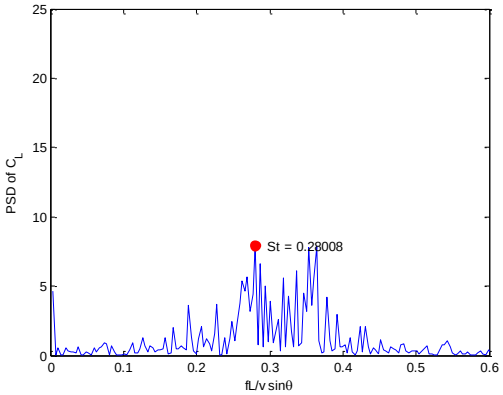


$\phi = 57.1°$; $\alpha = 54.7°$, $\beta = 20°$
iv) Re = 4.4×10^5;

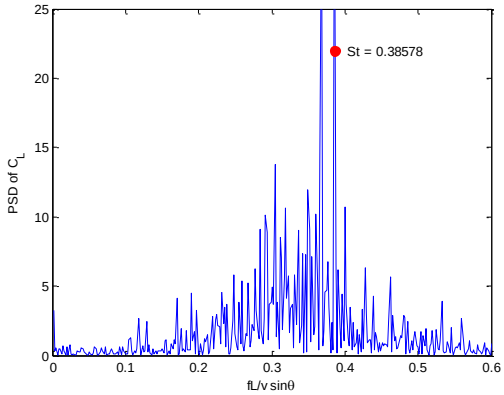


$\phi = 57.1°$; $\alpha = 54.7°$, $\beta = 20°$
v) Re = 5.5×10^5;

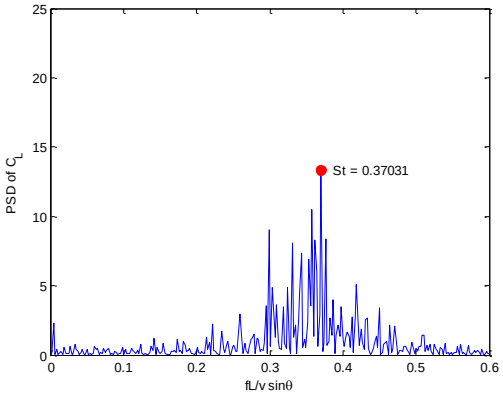
Figure 6.8: Time histories for C_L



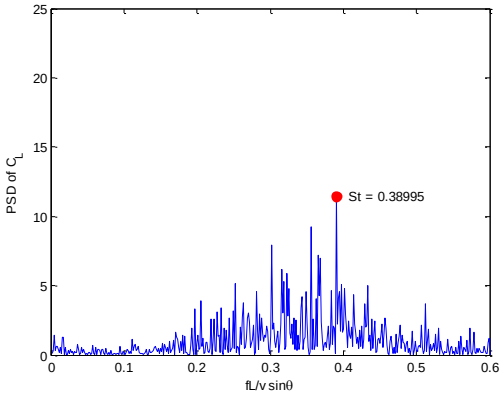
$\phi = 60°$; $\alpha = 60°$, $\beta = 0°$
i) Re = 1.1×10^5;



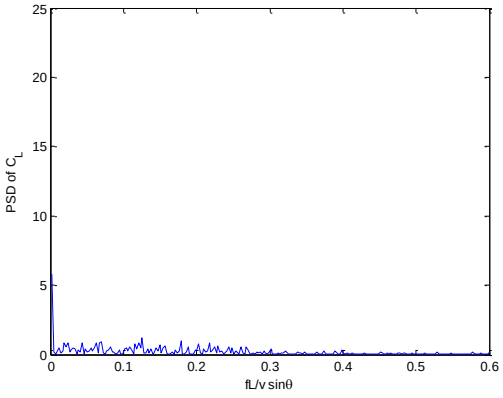
$\phi = 60°$; $\alpha = 60°$, $\beta = 0°$
ii) Re = 2.2×10^5;



$\phi = 60°$; $\alpha = 60°$, $\beta = 0°$
iii) Re = 3.3×10^5;

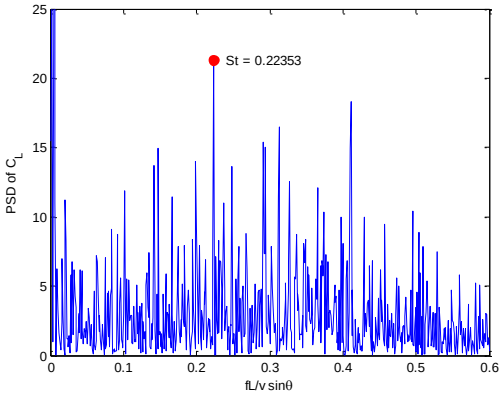


$\phi = 60°$; $\alpha = 60°$, $\beta = 0°$
iv) Re = 4.4×10^5;

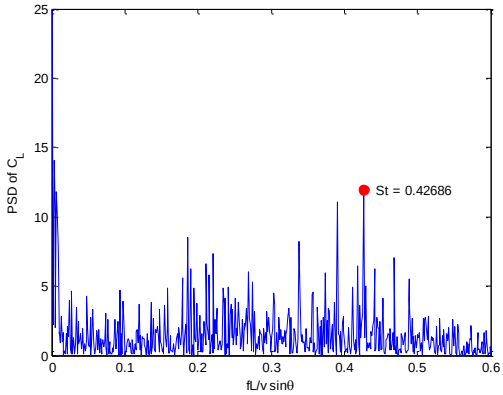


$\phi = 60°$; $\alpha = 60°$, $\beta = 0°$
v) Re = 5.5×10^5;

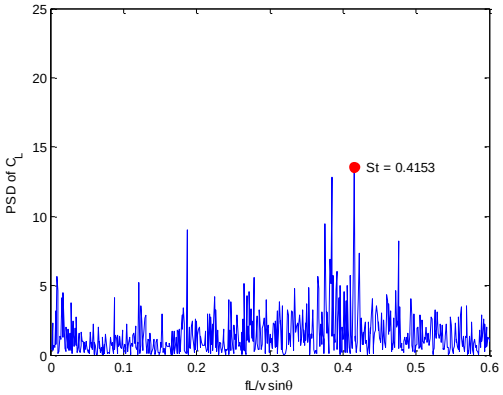
Figure 6.9: Fast Fourier Transform (FFT) results for C_L



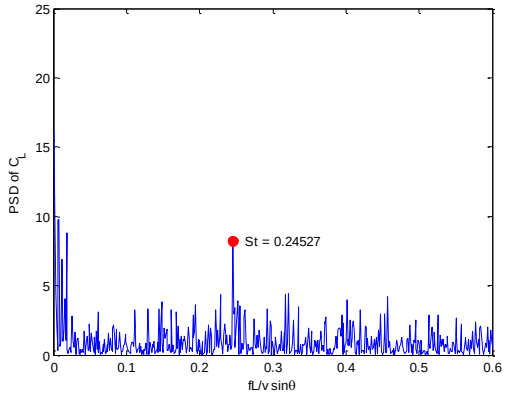
$\phi = 57.1°$; $\alpha = 54.7°$, $\beta = 20°$
i) Re = 1.1×10^5;



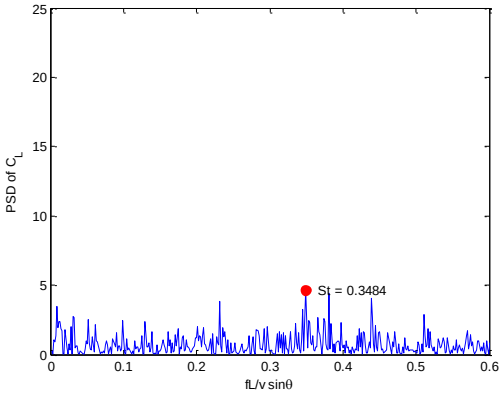
$\phi = 57.1°$; $\alpha = 54.7°$, $\beta = 20°$
ii) Re = 2.2×10^5;



$\phi = 57.1°$; $\alpha = 54.7°$, $\beta = 20°$
iii) Re = 3.3×10^5;



$\phi = 57.1°$; $\alpha = 54.7°$, $\beta = 20°$
iv) Re = 4.4×10^5;



$\phi = 57.1°$; $\alpha = 54.7°$, $\beta = 20°$
v) Re = 5.5×10^5;

Figure 6.10: Fast Fourier Transform (FFT) results for C_L

The results for the Fast Fourier Transforms for the C_L coefficients are similar to the values for the C_D coefficients reported above for the flow inclined to the circular cylinder at 60°, (ϕ = 60°; α = 60°, β = 0°). This is not the same for the other case presented with a yaw angle of 20°, ϕ = 57.1°; α = 54.7°, β = 20°, with different results between the Fast Fourier Transform results for C_D report above, and the C_L reported here.

Table 6.2: Fast Fourier Transform (FFT) results for C_L

Inclination angle α (deg)	Yaw angle β (deg)	Relative angle of attack, ϕ (deg)	Re = 1.1 × 10^5	Re = 2.2 × 10^5	Re = 3.3 × 10^5	Re = 4.4 × 10^5	Re = 5.5 × 10^5	Re = 6.7 × 10^5
0	0	0	0.203	0.209	0.218	0.217	0.215	0.205
50	20	53	0.365	0.5	0.461	0.493	0.551	N/A
54.7	0	54.7	0.23	0.47	0.448	0.439	0.443	N/A
54.7	20	57.1	0.224	0.427	0.415	0.245	0.348	N/A
60	0	60	0.28	0.386	0.37	0.39	Noise	0.363
50	40	60.5	0.419	0.423	0.474	0.443	0.387	N/A
60	20	62	0.422	0.429	0.408	0.189	Noise	N/A
54.7	40	64	0.5	0.379	0.407	0.383	Noise	N/A
60	40	67.5	Noise	0.484	Noise	Noise	Noise	N/A

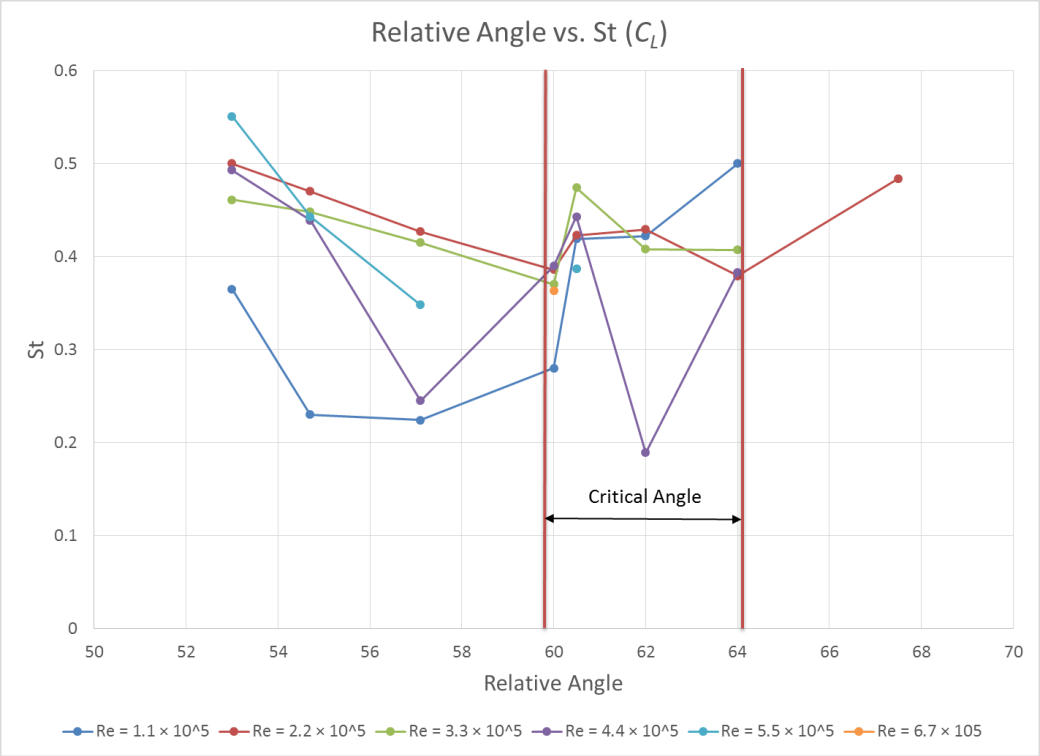


Figure 6.11: Relative angle vs. Stroudal number for C_L, plotted for each Reynolds number tested

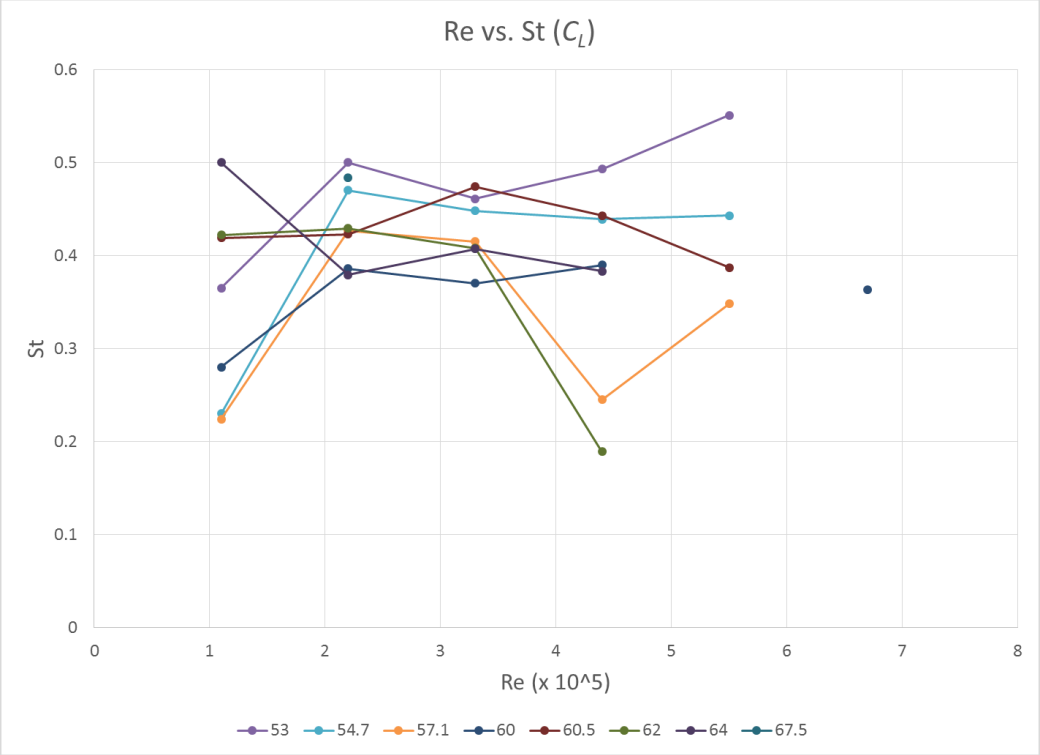


Figure 6.12: Reynolds number vs. Stroudal number for the lift coefficient C_L, plotted for each relative angle tested

6.3 Fast Fourier Transform (FFT) Results for Leeward Points Pressures

Several points were chosen on the leeward side of the circular cylinder to monitor the flow along its length. The monitor locations were separated by a length of 5D along the length of the cylinder (Figure 6.13). The ten cases highlighted in the previous two sections are shown in Figure 6.14 and Figure 6.15 below, for the FFT results of the pressure time histories of the on a leeward point situated on the circumference of the cylinder. The locations of the monitoring rings are as outlined in Chapter 3, and as reproduced below in Figure 6.13. The results for 3 of the 5 rings have been shown in Figure 6.14 and Figure 6.15 for the summarization of the data. Ring 1 is located at 10 cylinder diameters (+10D) upstream from the midspan of the cylinder, Ring 3 is at the midspan (0D) of the cylinder, and Ring 5 is 10 cylinder diameters (-10D) downstream of the midspan of the cylinder. The three points for which detailed results are presented, are at the leeward side of the cylinder, 10° around the circumference of the cylinder, and an additional 10° around the circumference of the cylinder for a total of 20° from the leeward side of the cylinder. A FFT analysis was performed using the pressure time history sampled from these points on the surface of the cylinder. As it can be seen in all the cases presented, the end effect of the computational domain was noticed in the results for the FFT results. The results of all cases and all 5 rings for the cases presented below have been detailed in Appendix N.

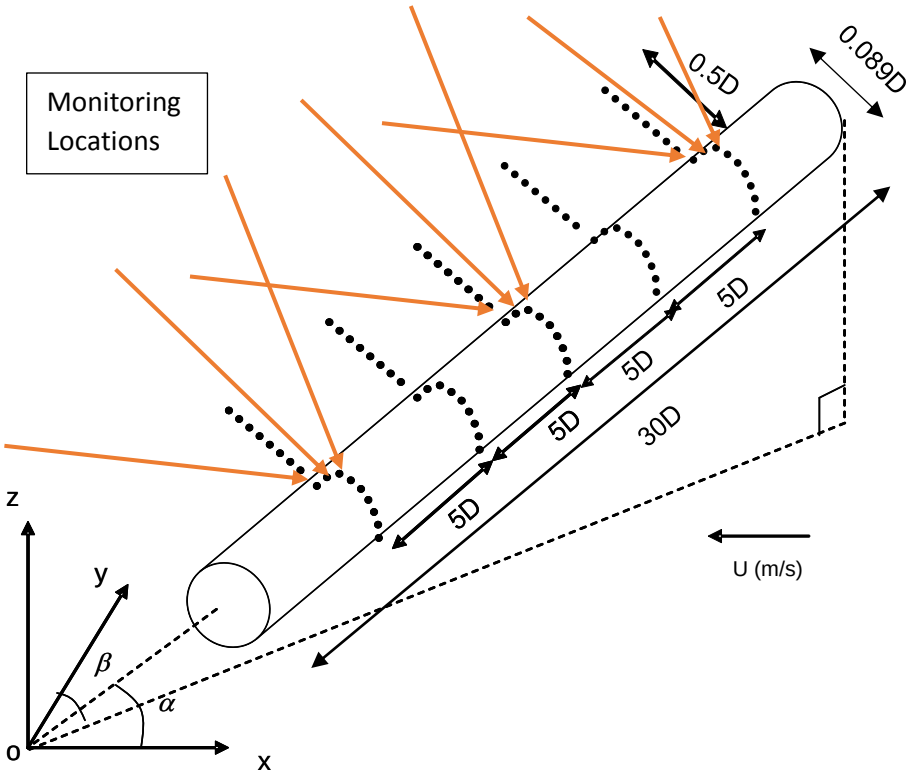


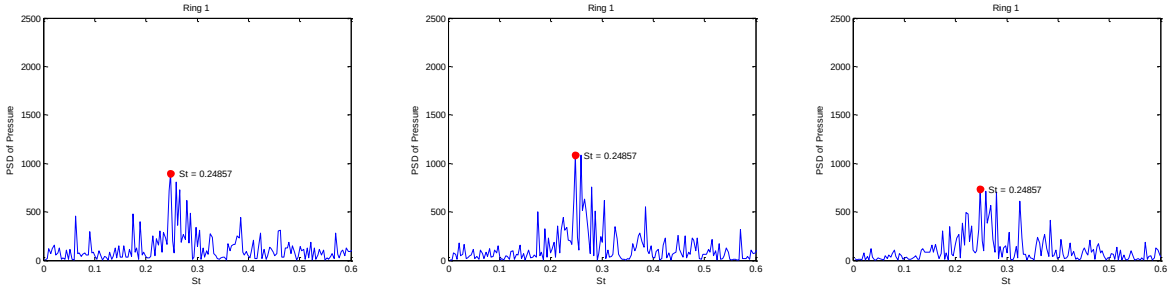
Figure 6.13: Details of the geometry and monitoring points for the cylinder model

The results of the FFTs for different inclinations $\alpha = 50°$ to 60° and yaw angles of $\beta = 0°$ to 40° of the cylinder (corresponding to relative angles of attack between $\phi = 53°$ and 64°), and for Re numbers of 1.1×10^5 to 6.7×10^5 varied along the length of the cylinder. This would lead to the conclusion that the end effects of the computational domain used in this study have a significant influence on the flow properties along the length of the cylinder. Also, the location of the dominant frequency changes along the length of the cylinder. For the case of the cylinder inclined to the flow by 60° at Re = 1.1×10^5, a maximum PSD was reached for a value of approximately *St* = 0.25 for Ring 1, a higher value of *St* of approximately 0.3 for the midspan of the cylinder at Ring 3, and no dominant frequency was noticed for downstream Ring 5, as represented in Figure 6.14 (i). A similar tendency is shown for the results obtained at Re = 2.2×10^5, with *St* values between 0.25 and 0.3 for Ring 1 at the various locations around the circumference of the cylinder shown,

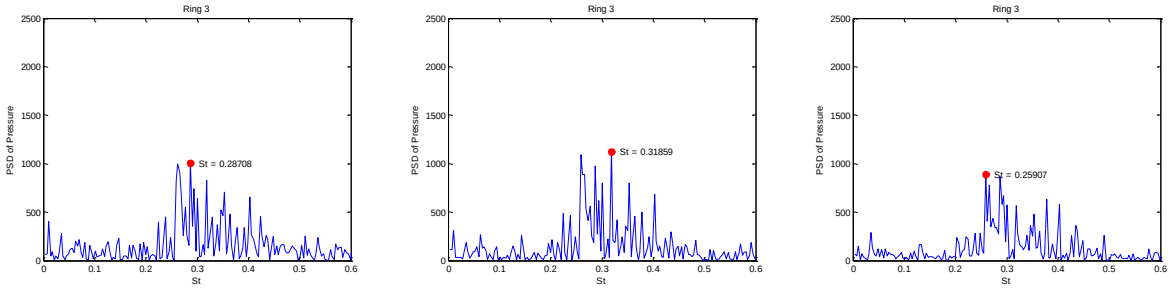
increasing in value to approximately 0.4 for Ring 3, and varying again for Ring 5 with an increase or decrease is *St* depending on the location of the monitoring point around the circumference of the cylinder, as shown in Figure 6.14 (ii). The results of Re = 3.3×10^5 and Re = 4.4×10^5 show similar result to Re = 2.2×10^5. The PSDs for Re = 5.5×10^5 showed no dominant frequency and the energy content was minimal (Figure 6.14 (iii)).

The results of the FFT analysis for the second case are shown for all cases tested at ϕ = 57.1°. A similar tendency as seen above with a variation in the dominant *St* along the length of the cylinder was noticed. A higher amount of energy was revealed in the results, for this cable geometry, and wider spectrum of results especially for the lower Re were obtained. For the case of Re =1.1×10^5, the *St* results varied between 0.3 to 0.6 for the three location along the circumference of the cylinder. The maximum PSD varied for both the circumference around the cylinder and along the length of the cylinder. For Re = 2.2×10^5, the spectrum of frequencies was not as wide as seen for the case of Re = 1.1×10^5, and its maximum value varied along the length of the cylinder. For Ring 1 a maximum *St* value of 0.47 was obtained for the leeward side of the cylinder, at Ring 3 a lower value of *St* of 0.37 is obtained, but increases again for Ring 5 with a value of 0.47. The same tendency in maximum PSD for *St* is shown for Re = 3.3×10^5 and Re = 5.5×10^5, which is opposite to the pattern showed for all cases of ϕ = 60°. For Re = 4.4×10^5, a maximum value for the PSD is approximately *St* = 0.40 for Ring 1, increasing to 0.51 for Ring 3, and dropping to a value of 0.13 for Ring 5. For this case the tendency in *St* variation followed that reported for all ϕ = 60° cases studied.

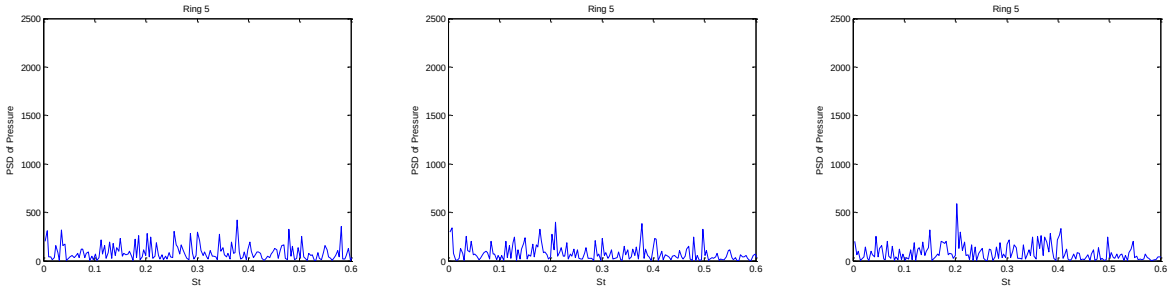
Leeward side | 10° from leeward | 20° from leeward



(+10D)



(0D)



(-10D)

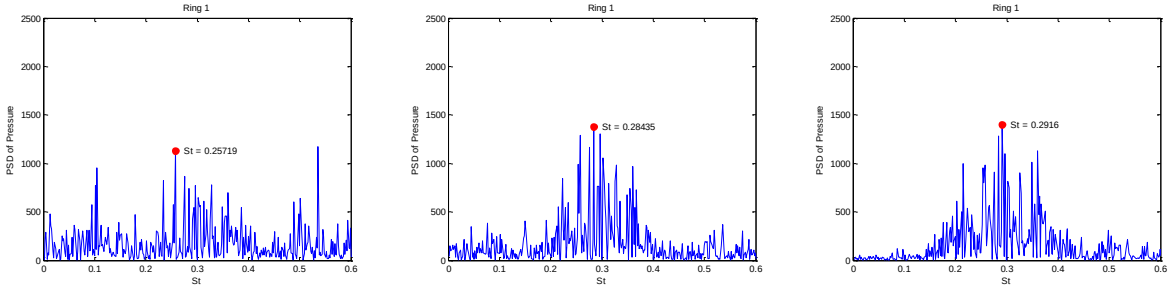
FFT results leeward points:

$\phi = 60°$; $\alpha = 60°$, $\beta = 0°$

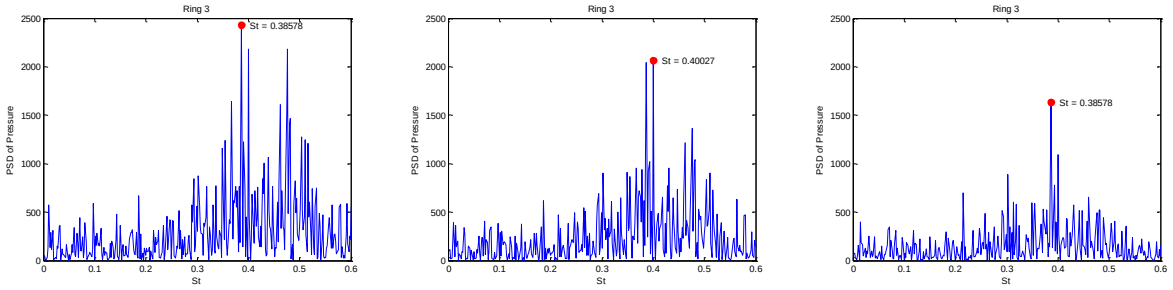
i) Re = 1.1×10^5;

Figure 6.14: Fast Fourier Transform (FFT) results for leeward points

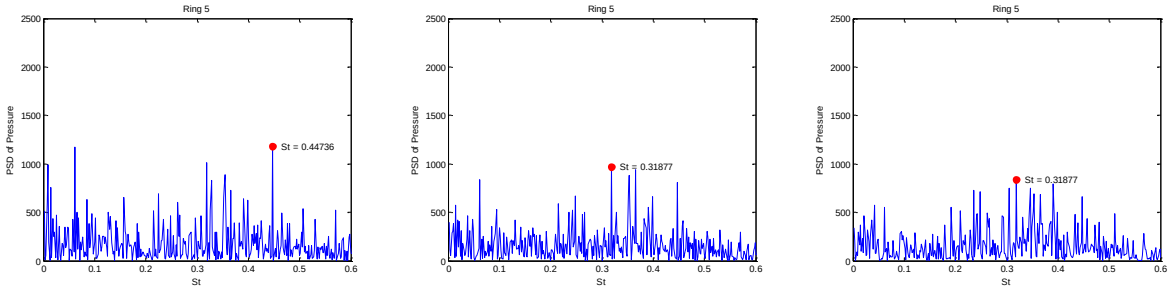
Leeward side | 10° from leeward | 20° from leeward



(+10D)



(0D)



(-10D)

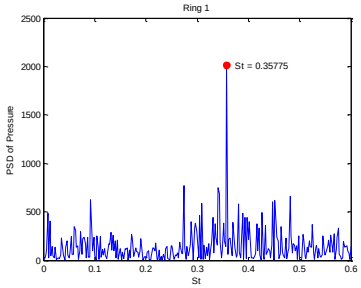
FFT results leeward points:

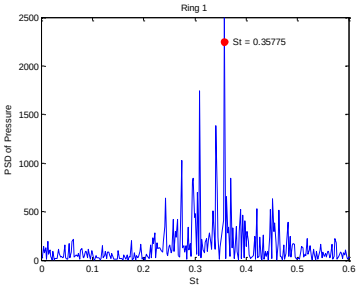
$\phi = 60°$; $\alpha = 60°$, $\beta = 0°$

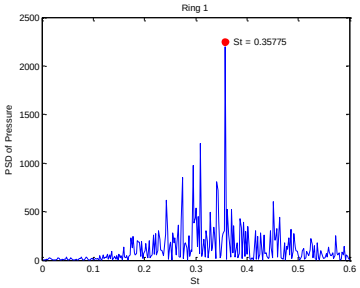
ii) Re = 2.2×10^5;

Figure 6.14: Fast Fourier Transform (FFT) results for leeward points

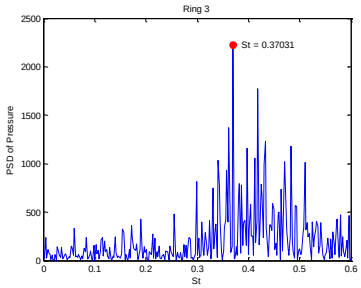
Leeward side | 10° from leeward | 20° from leeward

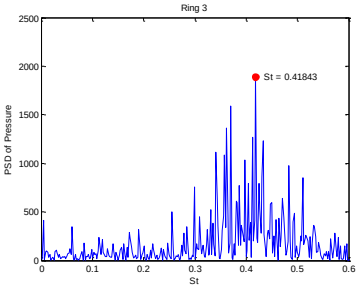


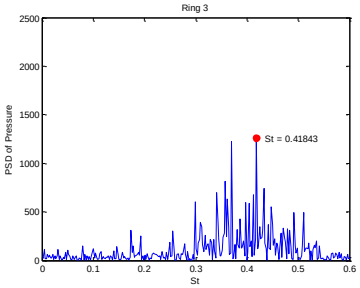




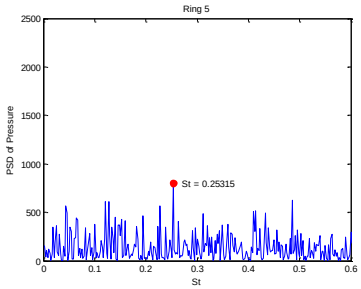
(+10D)

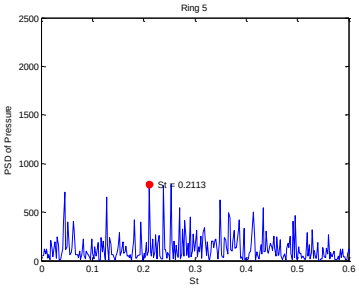


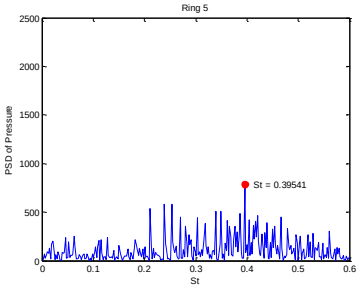




(0D)







(-10D)

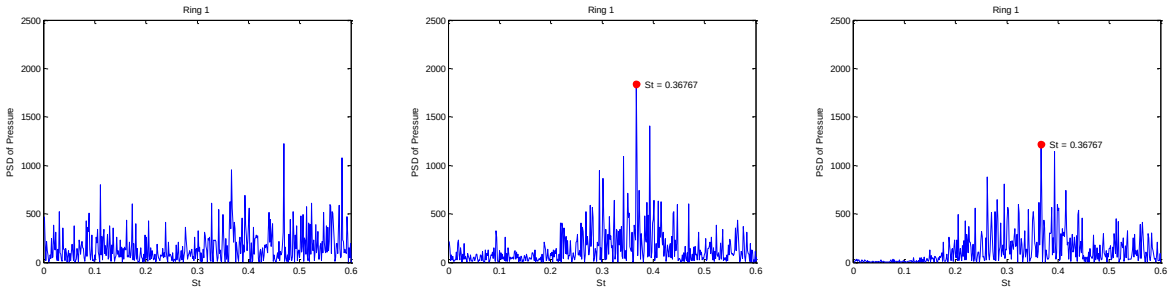
FFT results leeward points:

$\phi = 60°$; $\alpha = 60°$, $\beta = 0°$

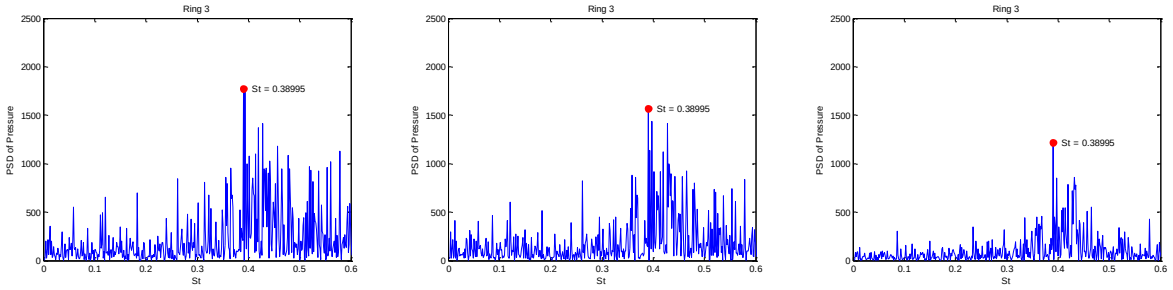
iii) Re = 3.3×10^5;

Figure 6.14: Fast Fourier Transform (FFT) results for leeward points

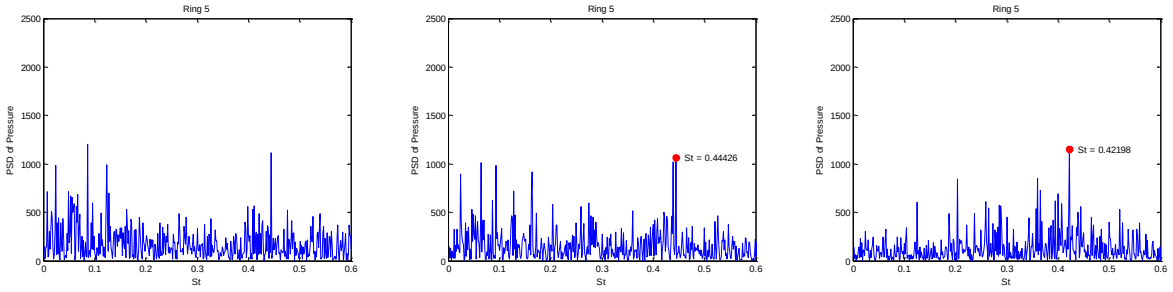
Leeward side | 10° from leeward | 20° from leeward



(+10D)



(0D)



(-10D)

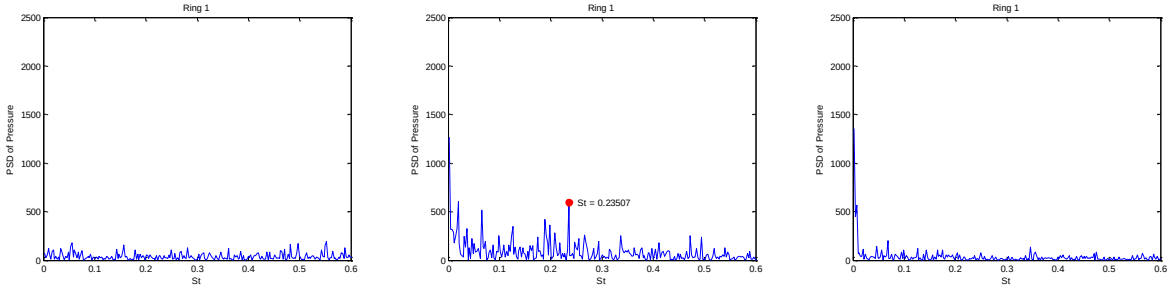
FFT results leeward points:

$\phi = 60°$; $\alpha = 60°$, $\beta = 0°$

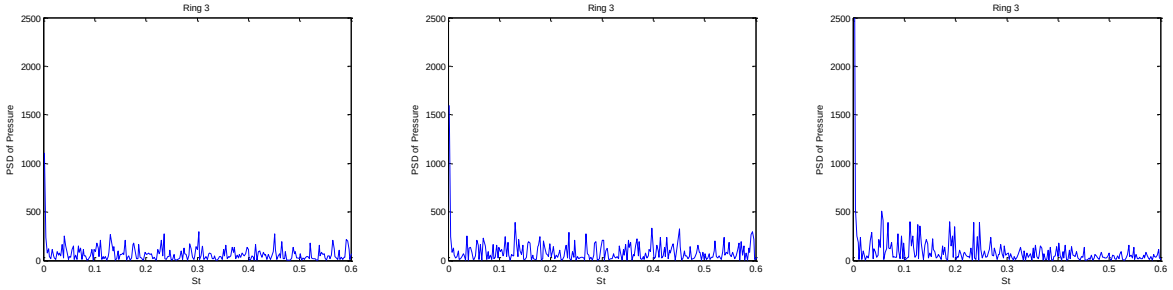
iv) Re = 4.4×10^5;

Figure 6.14: Fast Fourier Transform (FFT) results for leeward points

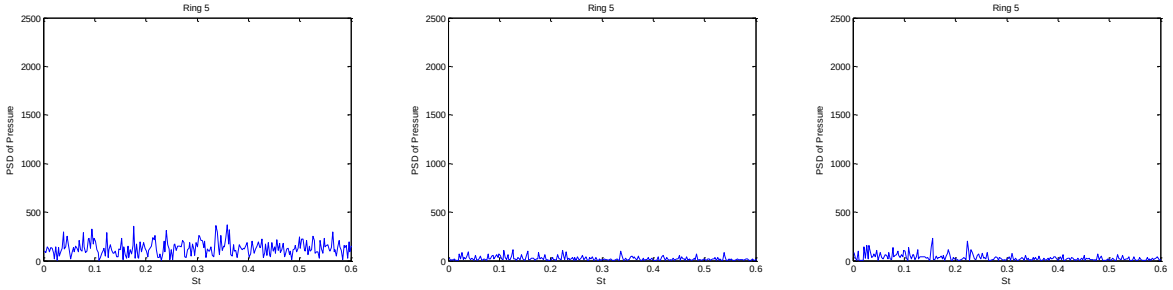
Leeward side | 10° from leeward | 20° from leeward



(-10D)



(0D)



(10D)

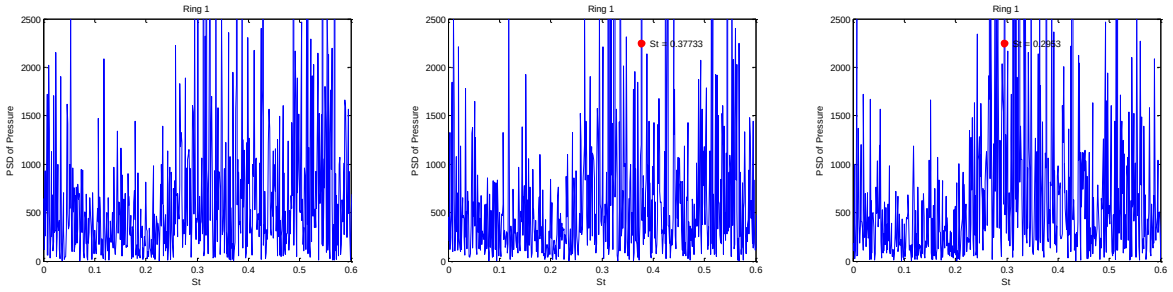
FFT results leeward points:

$\phi = 60°$; $\alpha = 60°$, $\beta = 0°$

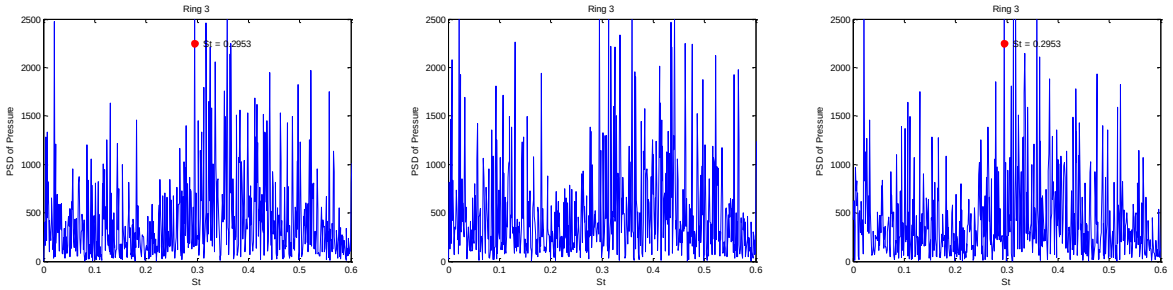
v) Re = 5.5×10^5;

Figure 6.14: Fast Fourier Transform (FFT) results for leeward points

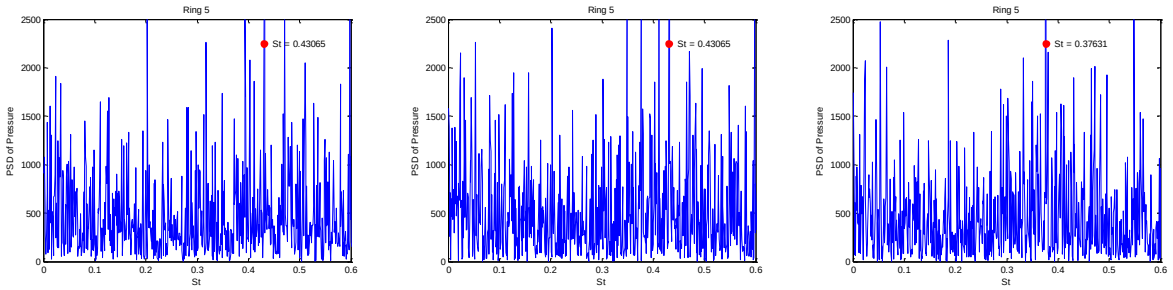
Leeward side | 10° from leeward | 20° from leeward



(+10D)



(0D)



(-10D)

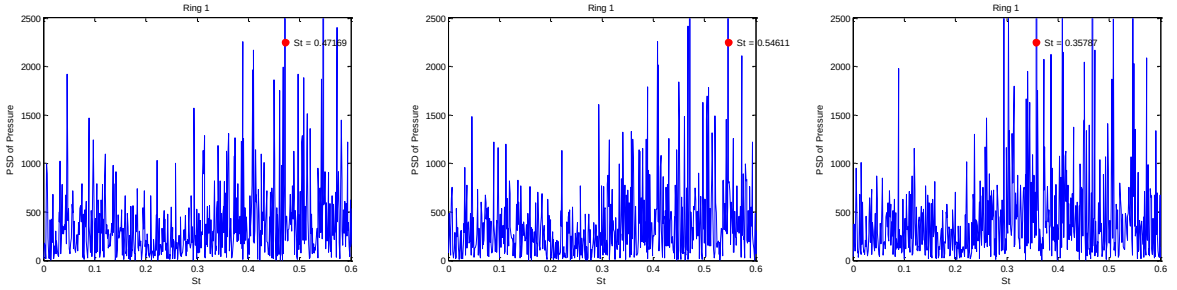
FFT results leeward points:

$\phi = 57.1°$; $\alpha = 54.7°$, $\beta = 20°$

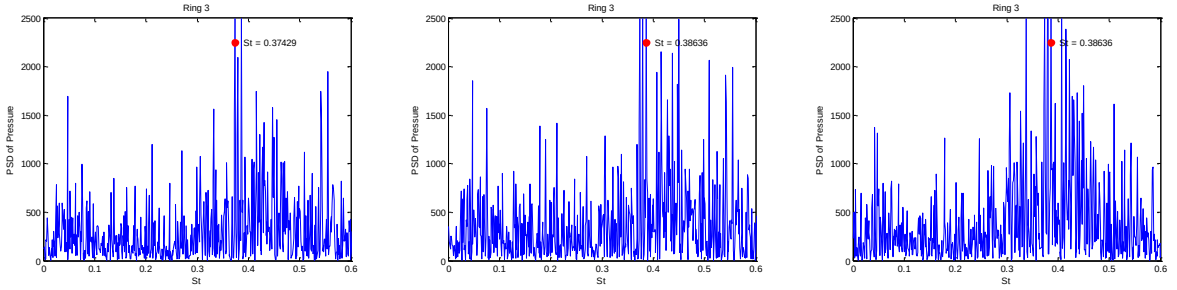
i) Re = 1.1×10^5;

Figure 6.15: Fast Fourier Transform (FFT) results for leeward points

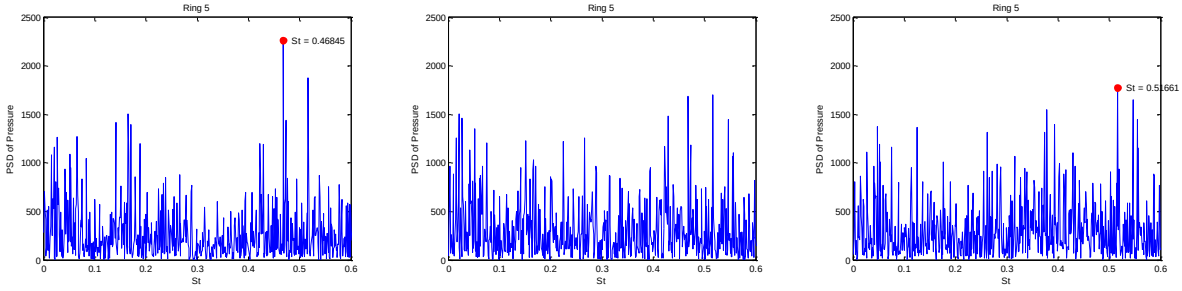
Leeward side | 10° from leeward | 20° from leeward



(+10D)



(0D)



(-10D)

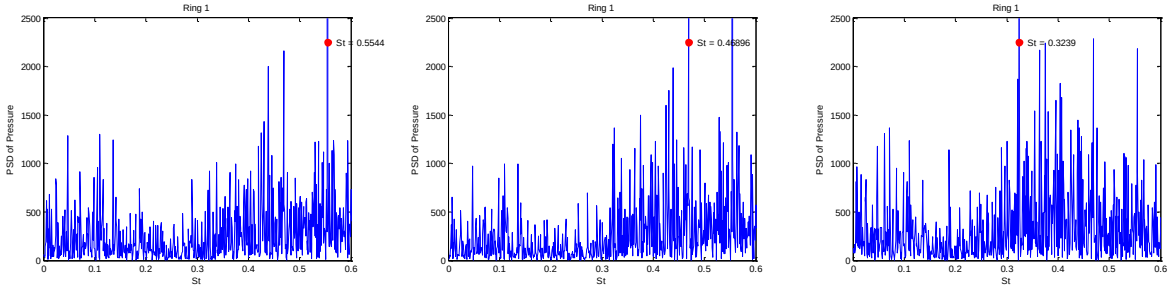
FFT results leeward points:

$\phi = 57.1°$; $\alpha = 54.7°$, $\beta = 20°$

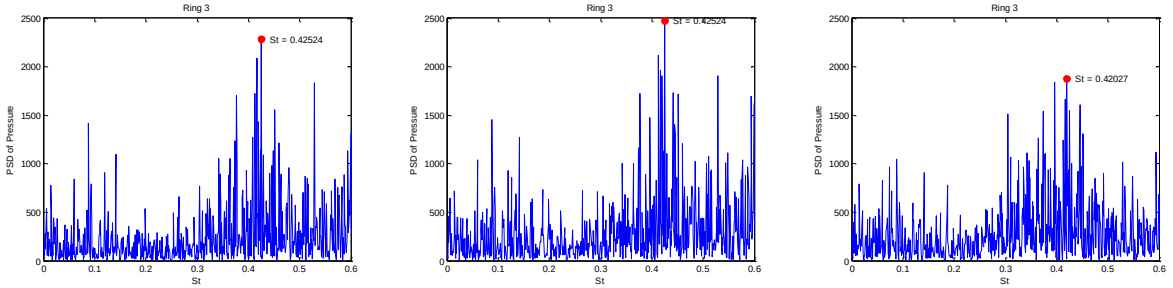
ii) Re = 2.2×10^5;

Figure 6.15: Fast Fourier Transform (FFT) results for leeward points

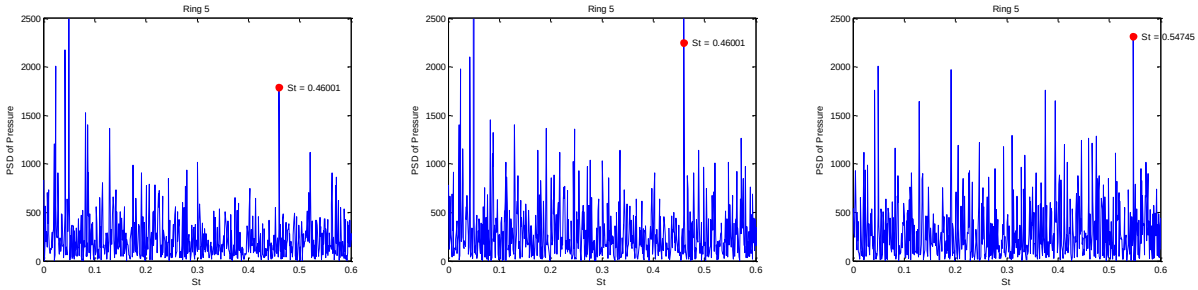
Leeward side | 10° from leeward | 20° from leeward



(+10D)



(0D)



(-10D)

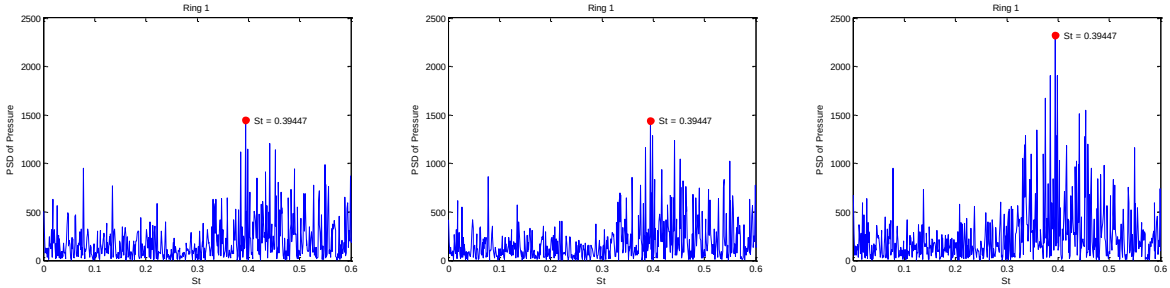
FFT results leeward points:

$\phi = 57.1°$; $\alpha = 54.7°$, $\beta = 20°$

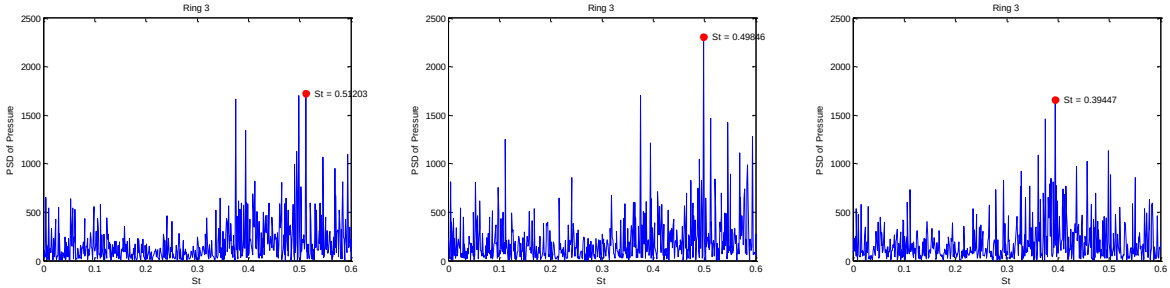
iii) Re = 3.3×10^5;

Figure 6.15: Fast Fourier Transform (FFT) results for leeward points

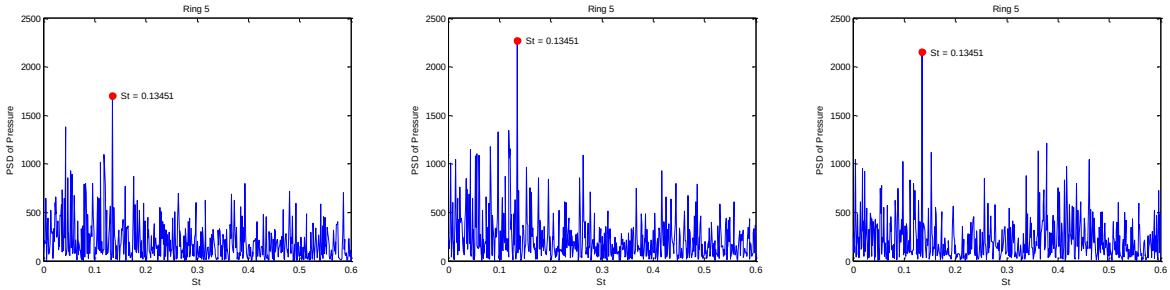
Leeward side | 10° from leeward | 20° from leeward



(+10D)



(0D)



(-10D)

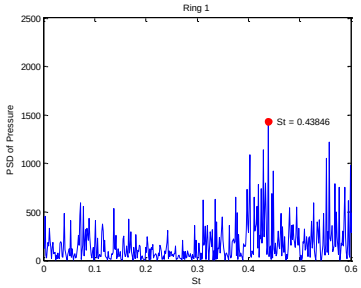
FFT results leeward points:

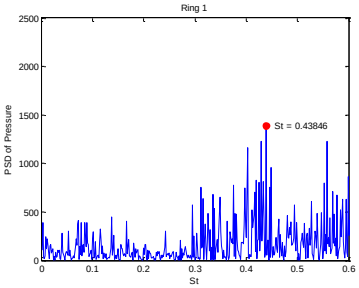
$\phi = 57.1°$; $\alpha = 54.7°$, $\beta = 20°$

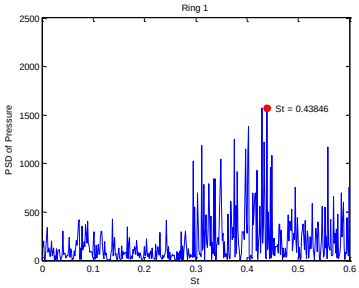
iv) Re = 4.4×10^5;

Figure 6.15: Fast Fourier Transform (FFT) results for leeward points

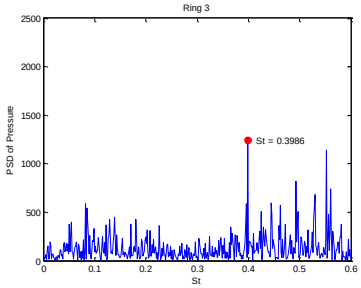
Leeward side | 10° from leeward | 20° from leeward

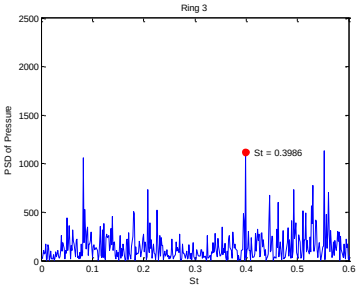


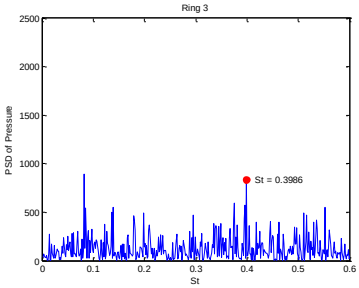




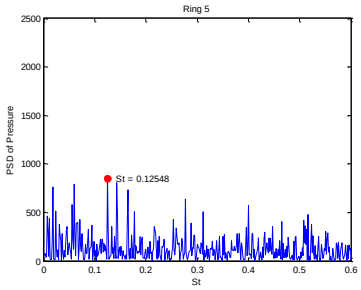
(-10D)

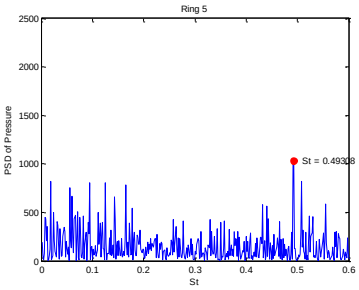


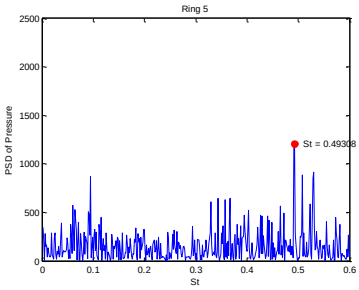




(0D)







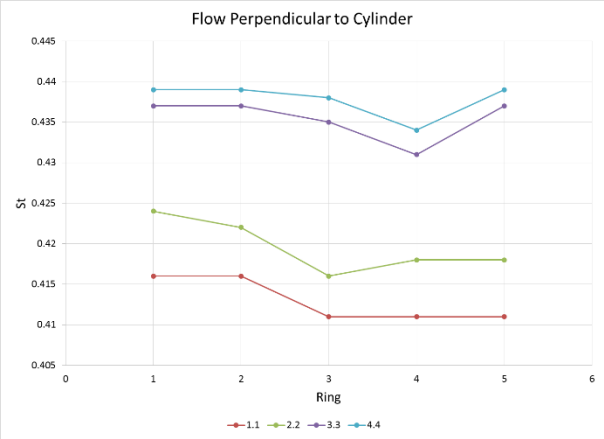
(-10D)

FFT results leeward points:

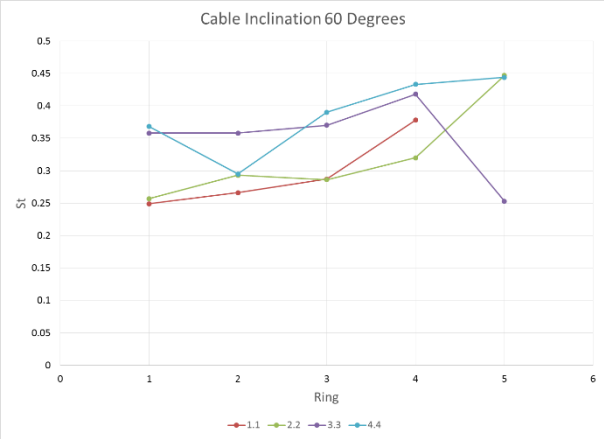
$\phi = 57.1°$; $\alpha = 54.7°$, $\beta = 20°$

v) Re = 5.5×10^5;

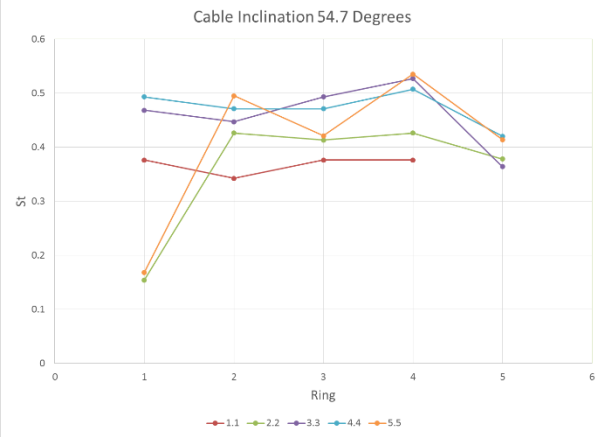
Figure 6.15: Fast Fourier Transform (FFT) results for leeward points



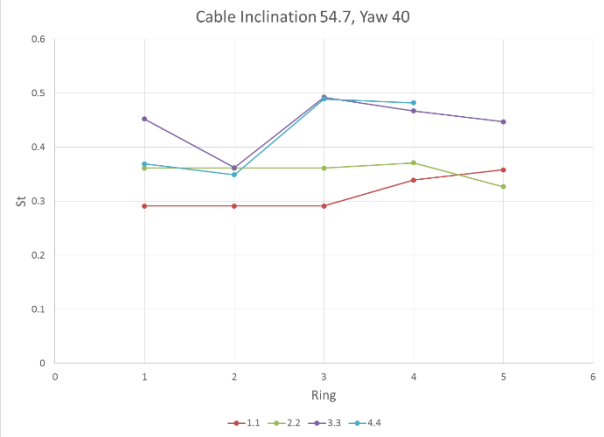
a) $\phi = 0°$; $\alpha = 0°$, $\beta = 0°$



b) $\phi = 60°$; $\alpha = 60°$, $\beta = 0°$



c) $\phi = 54.7°$; $\alpha = 54.7°$, $\beta = 0°$



d) $\phi = 64°$; $\alpha = 54.7°$, $\beta = 40°$

Figure 6.16: Variation in *St* leeward pressures along the length of the cylinder

The results for the variation of the *St* along the length of the cylinder for all locations monitored in this study are summarized in Figures 6.16(a) to (d) for four cases. The cases include flow perpendicular to the cylinder, $\phi = 0°$, flow inclined to the cylinder at 60°, $\phi = 60°$, flow inclined to the cylinder at 54.7°, $\alpha = 54.7°$, $\beta = 0°$, and flow inclined and yawed at $\alpha = 54.7°$ and $\beta = 40°$ respectively.

As described in detail for the two cases above, *St* is not uniform along the length of the cylinder, which means that the flow does not maintain the same frequency at all positions along the length of the cylinder. This is expected due to the 3D nature of the flow for this Reynolds

number, as well as the inclined nature of the cylinder. The end effects of the computational domain will have influence on this variation of *St* along the length of the cylinder. For the flow perpendicular to the cylinder, the variation of St along the length of the cylinder showed a drop at the middle of the cylinder, for lower Re numbers, and further down the cylinder for higher Re numbers. For this case effects from the boundaries of the domain were negligible.

It was also noticed from Figure 6.16(a) that there is a gap in the St evolution, for flow perpendicular to the cylinder ($\phi = 0°$) when Re ranges between Re = 1.1×10^5 and 2.2×10^5. The St was smaller in this range varying between 0.41 and 0.425. For higher Re of 3.3×10^5 and 4.4×10^5, again for flow perpendicular to the cylinder ($\phi = 0°$) case, the St numbers were much higher with values reaching 0.43 to 0.44, with a brief decrease for ring 4 which is situated on the lower half of the cylinder.

A similar evolution was noticed for $\phi = 60°$, as shown in Figure 6.16(b), for which Re = 1.1×10^5 and 2.2×10^5 increased gradually as the flow traveled down the cylinder; however for Re of 3.3×10^5 and 4.4×10^5, the St values also steadily increased with the exception of the Ring 2, for which a sudden decrease was noticed. This might be due to the development of the axial flow along the leeward side of the cylinder, associated with a change in the two-dimensional flow near the top of the cylinder (upstream part) to a more three-dimensional flow further downstream of the cylinder

For the other cases of $\phi = 54.7°$ and $\phi = 64°$ as seen in Figures 6.15(c) and (d) respectively, the discrepancy between the St at low Re is higher. For the case of $\phi = 54.7°$, and Re = 1.1×10^5 the St value is lower than 0.4, while the other four Re values tested were higher than 0.4. This is different from the first two cases for $\phi = 64°$ where the values of St were grouped together for the two lower Re (Re = 1.1×10^5 and 2.2×10^5), and the next two Re tested (Re = 3.3×10^5 and $4.4 \times$

10^5). The end effects were also noticeable for these two cases, especially for $\phi = 54.7°$ where sudden decrease of St was noticed for the first and last rings, located at the upper and lower monitoring locations along the cable. The case of Re = 5.5×10^5 was reported only for the cases of $\phi = 0°$, $\phi = 60°$, and $\phi = 64°$, as the dominant frequency could not be identified for the power spectral density of the pressure for this Re number, due to a high noise content in the pressure time history. The results for the power spectral density of the pressure along the leeward side of the cylinder are plotted this time in a different configuration, in Figure 6.17. The results are plotted for each case for Re versus resulting St.

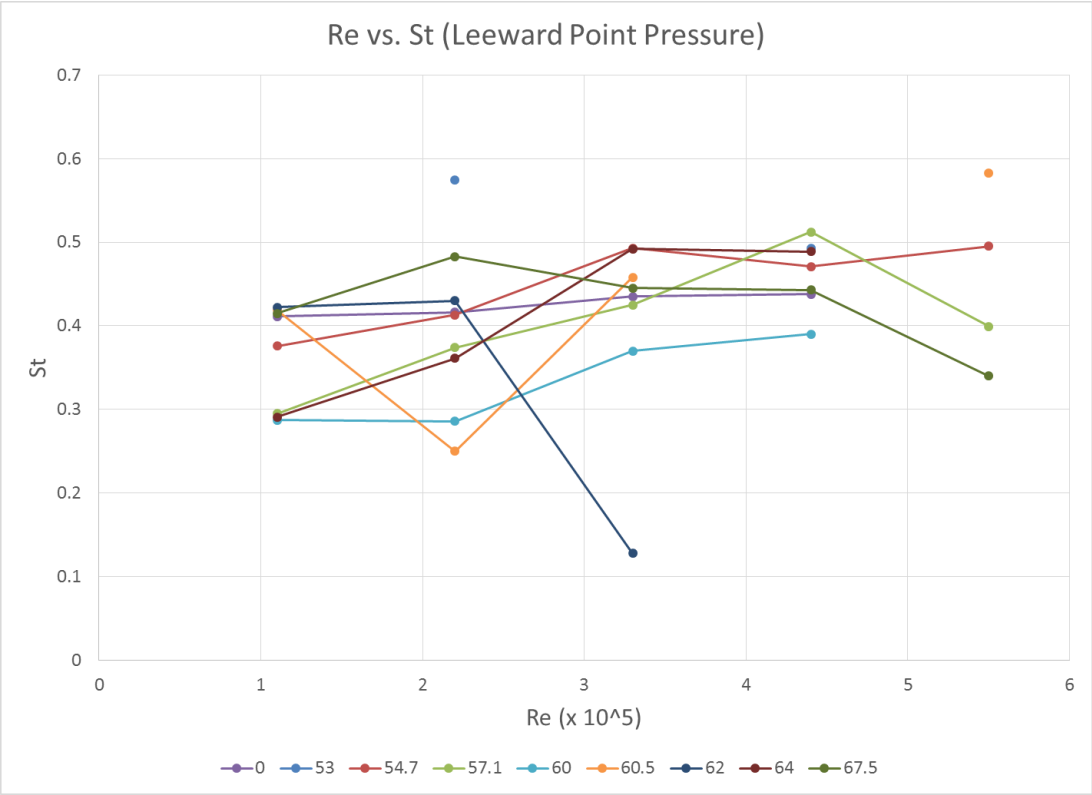


Figure 6.17: Variation in *St* with Reynolds number; leeward pressure

For the case of flow perpendicular to the cylinder, $\phi = 0$, the St value for all results obtained were fairly consistent across the results obtained, for Re cases tested, with a value just above 0.4. For the flow perpendicular to the cylinder the results are also consistent across all monitored

locations. This was expected due to the two dimension nature of the flow in comparison to the other cases in this study where the flow is more three dimensional in nature especially when the addition of the axial flow along the cylinder is considered. The St value for the flow perpendicular to the cylinder ($\phi = 0°$) was much higher than the St for the other cases studied, however this was relatively similar to the case of $\phi = 67.5°$, for which the value of St increased at Re = 2.2×10^5, had a stagnation for the cases of Re = 3.3×10^5 and Re = 4.4×10^5, and decreased at the highest Re of 5.5×10^5.

For $\phi = 60°$, the St increased with the increase in Re, but its evolution started out as the lowest, when compared to the other cases investigated. The St values started at less than 0.3 for Re = 1.1×10^5 and 2.2×10^5, and increased with the increase of Re to 3.3×10^5, and 4.4×10^5 to 0.37, and 0.39 respectively. Again, the results for Re = 5.5×10^5 was not reported for this case, as there was no dominant frequency identified by the power spectral density of the pressure, due to a high noise content in the pressure time history. This gradual increase in St is also shown for the following cases: $\phi = 54.7°$, $\phi = 57.1°$, and $\phi = 64°$.

The case for $\phi = 60.5°$ showed a particular evolution, when compared to the similar case of $\phi = 60°$. For $\phi = 60.5°$ there was a drop is St for Re = 2.2×10^5, and a sudden increase for Re = 5.5×10^5, leading to one of the highest results of this study. Both cases of $\phi = 53°$ and $\phi = 62°$ showed no significant variaiton with the change in Re, while for many Re tested the noise signal was registered, and therefore these were not reported in the graph.

Not all cases investigated in this study were reported in Figure 6.17, because no data point could be represented, if dominant frequency could not be identified for the power spectral density of the pressure for this Re, due to a high noise content in the pressure trace. This will lead to several gaps in the data presented in Figure 6.17.

Thus it can be concluded that for lower Re of 1.1×10^5, and 2.2×10^5, the results for the St will allow the following cases to be grouped together:

Group 1_LowRe (60°);

Group 2_LowRe (57.1°, 64°);

Group 3_LowRe (0°, 54.7°, 62°);

Group 4_LowRe (67.5°);

Group 5_LowRe (60.5°).

However for higher Re of 3.3×10^5 the evolution of St changed, and it was noticed that some of the angle cases shifted the groups as follows:

Group 1_HighRe (60°);

Group 2_HighRe (0°, 67.5°);

Group 3_HighRe (54.7°, 64°);

Group 4_HighRe (57.1°);

Group 5_HighRe (60.5°).

Groups 1 and 5 represent the critical relative angles of 60° and 60.5°, with a distinct evolution of the St number; on the other hand the relative angle 62° could not be included in the second category of groups, because of the sudden decrease in the St and the lack of dominant reduced frequency for higher Re, however this can be an indication of a critical inclination angle as well.

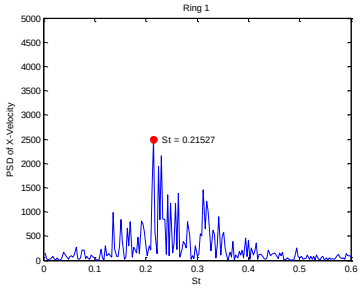
The shift in grouping for the Groups 2, 3 and 4, represent the switch from one flow regime at low Re numbers to a different regime characterized by higher St frequencies for 64°inclination angle, or by lower St frequencies, for 67.5°. Such transitions are too sensitive to be clearly identified herewith, however the sudden increase in St frequency can be considered as an indication of high-speed vortex occurrence.

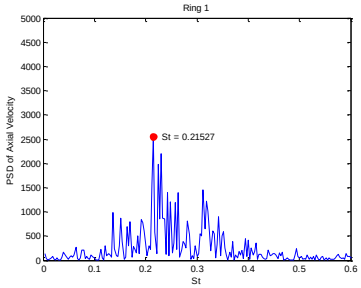
6.4 Fast Fourier Transform (FFT) Results for Leeward Velocity

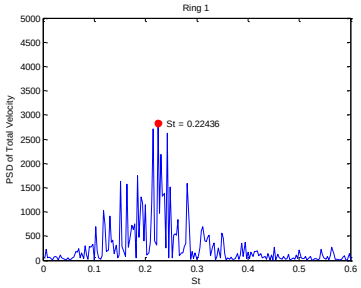
In this section the FFT results for the time histories of the velocities measured on the leeward side of the cylinder are shown in Figure 6.18. The results for the three middle rings are shown in Figure 6.18, following the same location convention as per the previous section. The position along the length of the cylinder for the monitoring points are as outlined in the model section presented in Chapter 3. Rings 1, 3, and 5 as per the previous section with the leeward points were positioned 0.1D from the leeward side of the cylinder, for the velocity measurements. The end effects of the computational domain are again noticed in the results presented, and will be detailed below. The results of all the cases investigated in this study, and for all the 5 rings for each case have been included in Appendix O.

For the case of flow inclined to the cylinder by 60° the results showed a similar tendency as the results for the pressure distribution, as shown in the previous section, as the location of the dominant frequency changes along the length of the cylinder. For the case of Re = 1.1×10^5, a maximum dominant frequency was reached for a value of approximately *St* = 0.21 for Ring 1, a higher value of *St* of approximately 0.24 for the midspan of the cylinder at Ring 3, and the dominant frequency of approximately 0.32 for downstream Ring 5 with minimal energy. For Re = 2.2×10^5, 3.3×10^5, and 4.4×10^5, all the reduced frequencies showed a similar tendency in variation of St with an increase from Ring 1 to Ring 3 to Ring 5; Ring 1 and Ring 3 registered very similar *St* values. The PSDs for Re = 5.5×10^5 showed no dominant frequency and minimal energy was determined.

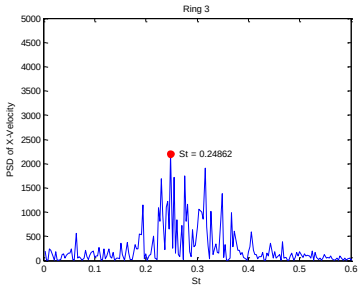
Direction of flow (x-vel) Axial flow Total velocity

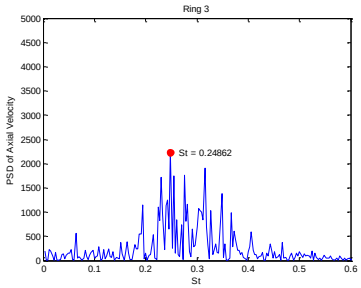


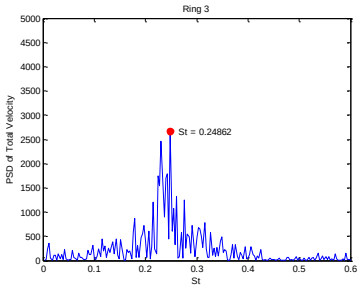




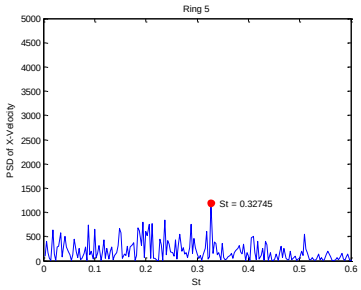
(+10D)

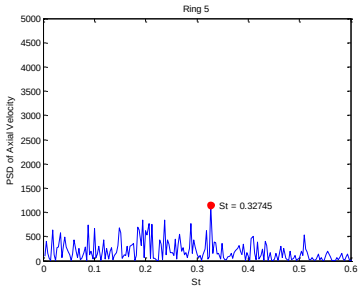


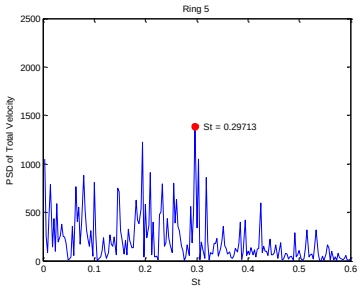




(0D)







(-10D)

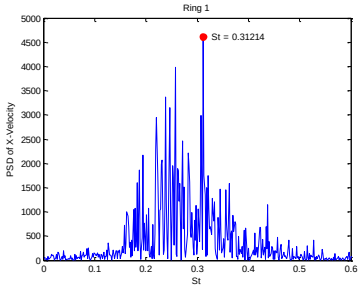
FFT results leeward velocity:

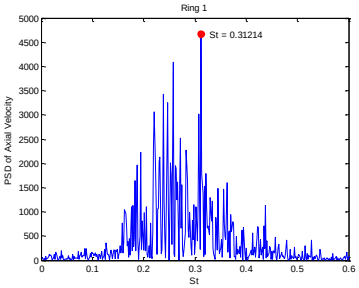
$\phi = 60°$; $\alpha = 60°$, $\beta = 0°$

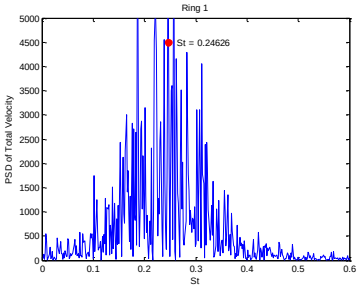
i) Re = 1.1×10^5;

Figure 6.18: Fast Fourier Transform (FFT) results for leeward velocity

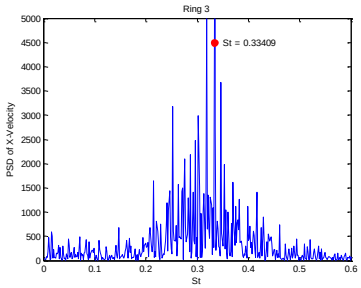
Direction of flow (x-vel) Axial flow Total velocity

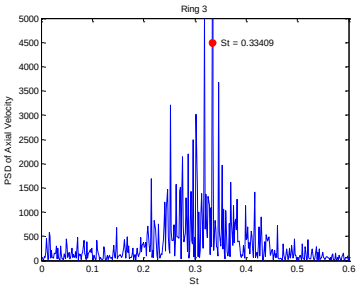


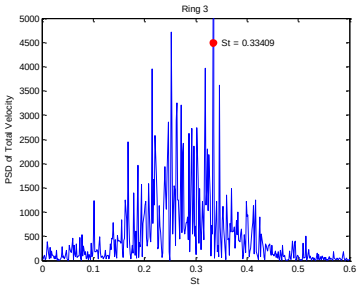




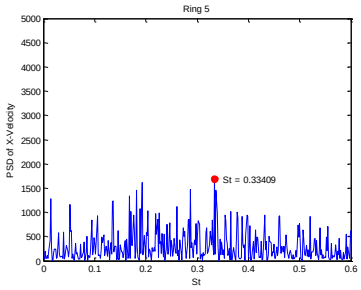
(+10D)

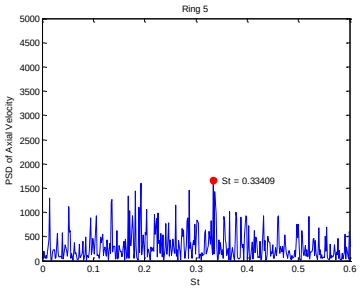


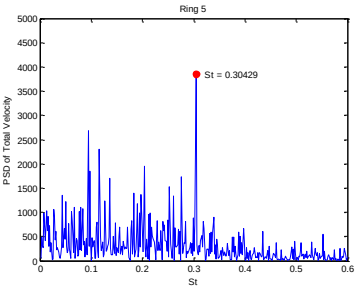




(0D)







(-10D)

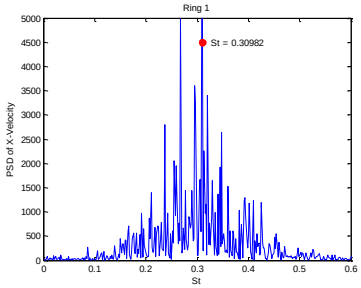
FFT results leeward velocity:

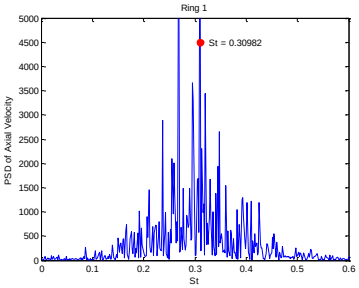
$\phi = 60°$; $\alpha = 60°$, $\beta = 0°$

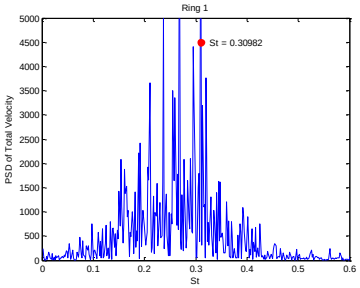
ii) Re = 2.2×10^5;

Figure 6.18: Fast Fourier Transform (FFT) results for leeward velocity

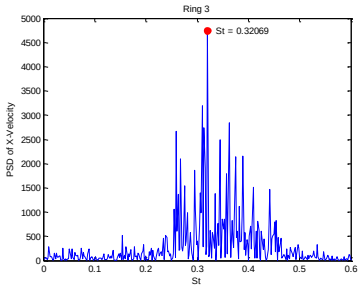
Direction of flow (x-vel) Axial flow Total velocity

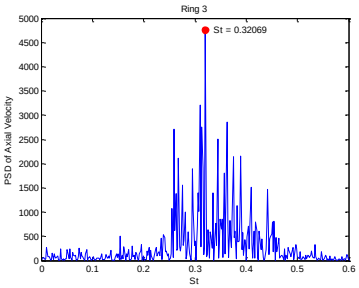


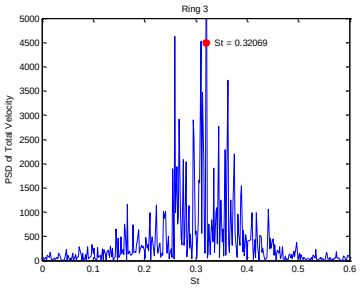




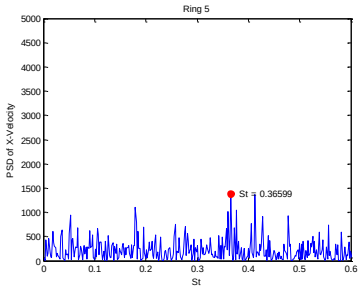
(-10D)

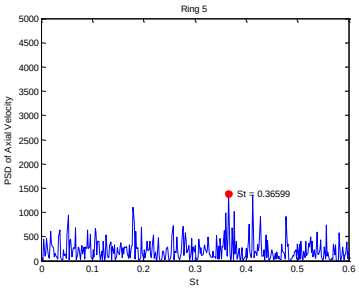


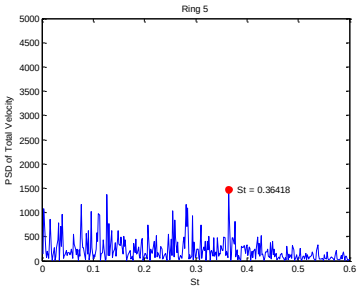




(0D)







(-10D)

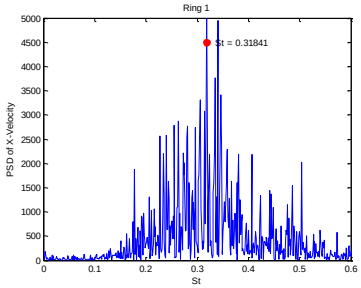
FFT results leeward velocity:

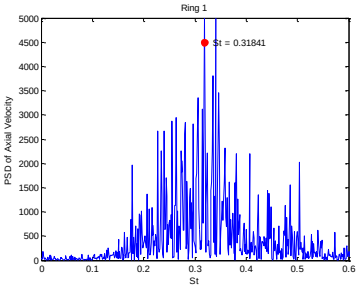
$\phi = 60°$; $\alpha = 60°$, $\beta = 0°$

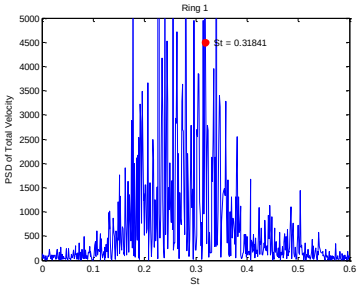
ii) Re = 3.3×10^5;

Figure 6.18: Fast Fourier Transform (FFT) results for leeward velocity

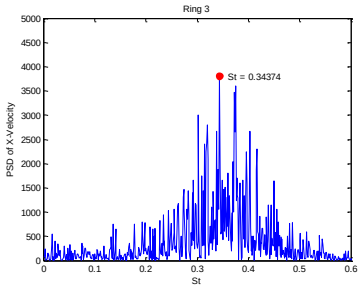
Direction of flow (x-vel) Axial flow Total velocity

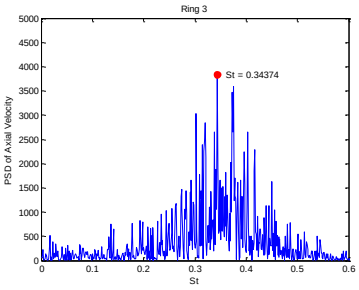


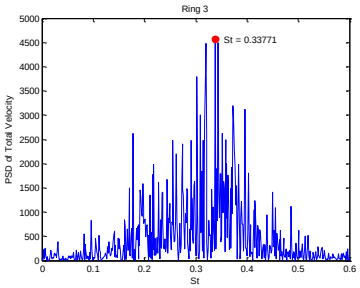




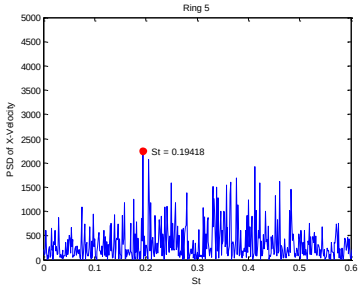
(+10D)

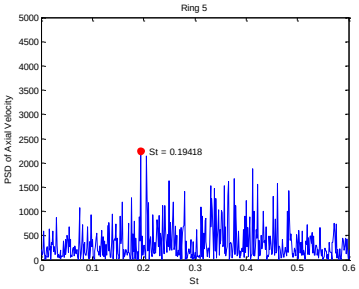


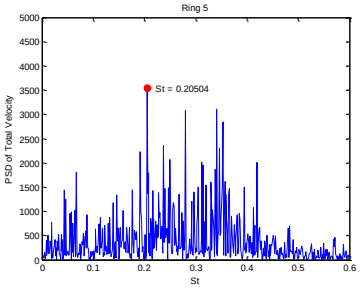




(0D)







(-10D)

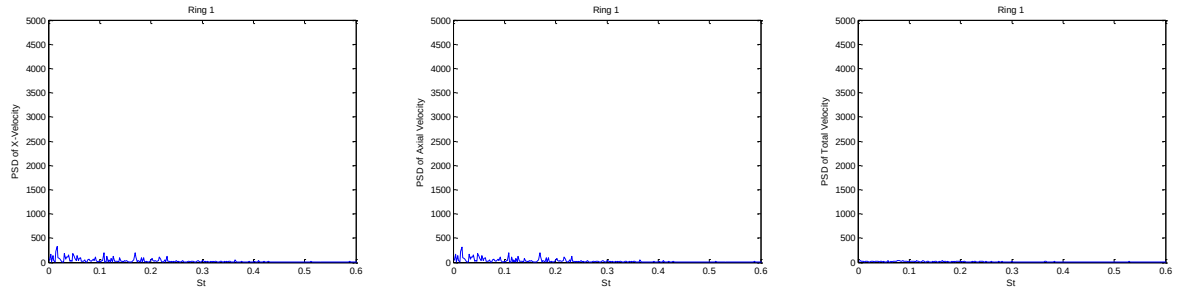
FFT results leeward velocity:

$\phi = 60°$; $\alpha = 60°$, $\beta = 0°$

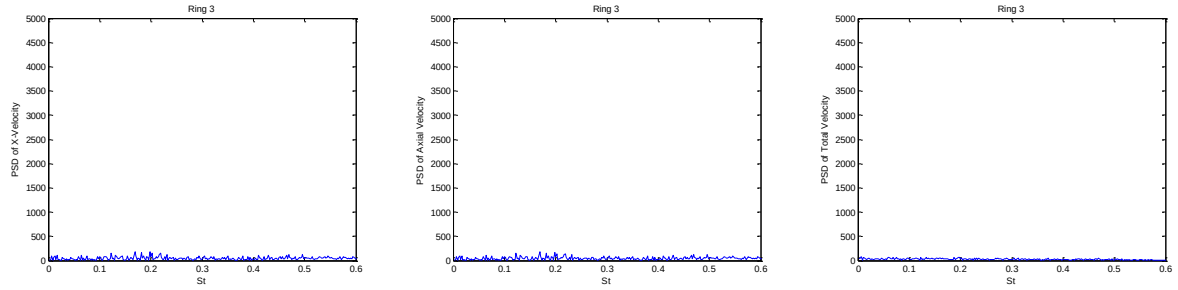
ii) Re = 4.4×10^5;

Figure 6.18: Fast Fourier Transform (FFT) results for leeward velocity

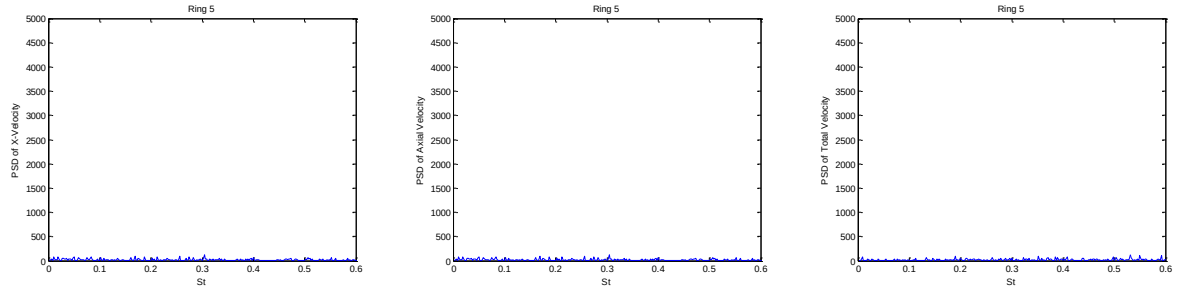
Direction of flow (x-vel) Axial flow Total velocity



(+10D)



(0D)



(-10D)

FFT results leeward velocity:

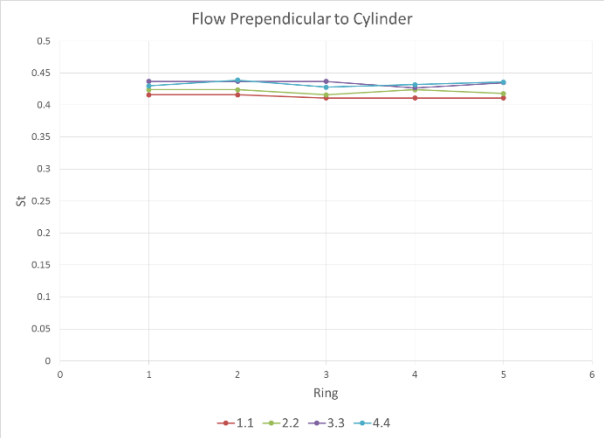
$\phi = 60°$; $\alpha = 60°$, $\beta = 0°$

ii) Re = 5.5×10^5;

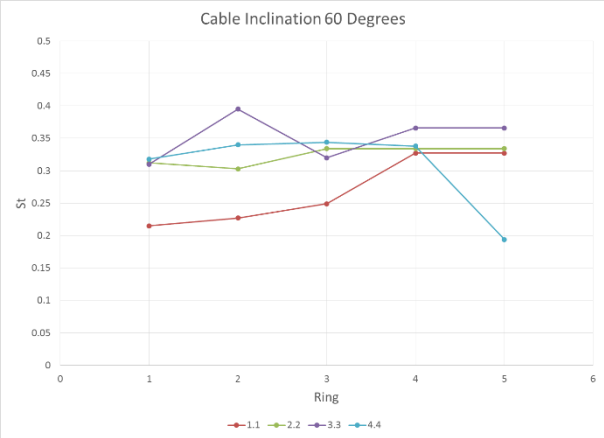
Figure 6.18: Fast Fourier Transform (FFT) results for leeward velocity

The results for the variation of the *St* for the leeward velocity along the length of the cylinder are summarized in Figure 6.19, for the same four cases as shown in the previous section. The cases are as follows: flow perpendicular to the cylinder, $\phi = 0°$; flow inclined to the cylinder at 60°, $\phi = 60°$; flow inclined to the cylinder at 54.7°, $\phi = 54.7°$. The results showed similar frequencies to the previous section, where the pressure of the cylinder was monitored on the leeward side of the cylinder. As it can be noticed in Figure 6.19(a), for the flow perpendicular to

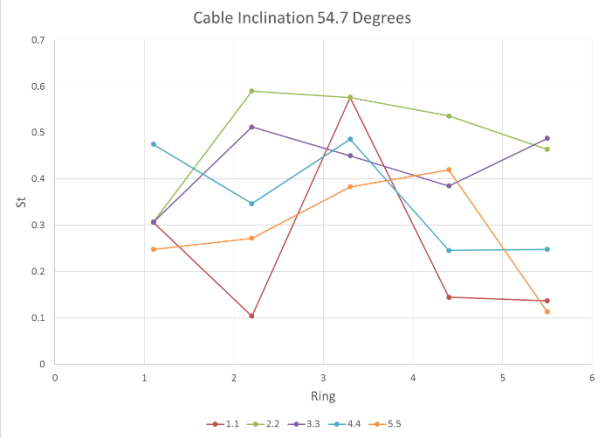
the cylinder, the variation of St along the cylinder length does not vary, but for the other three cases there is a variation in St along the length of the cylinder, as it can be seen in Figures 6.19(b), and (c). This was expected considering the three-dimensional nature of the flow formed around an inclined and yawed cylinder at this Reynolds number. The end effects of the computational domain can also contribute to the variation of *St* along the length of the cylinder.



a) $\phi = 0°$; $\alpha = 0°$, $\beta = 0°$



b) $\phi = 60°$; $\alpha = 60°$, $\beta = 0°$



c) $\phi = 54.7°$; $\alpha = 54.7°$, $\beta = 0°$

Figure 6.19: Variation in *St* for leeward velocity along the length of the cylinder

Figure 6.20 shows the results of the variation of St for the leeward velocity. These results are plotted for all cases with respect to the Re tested.

It was noticed that, for the cases reported in Figure 6.20, there is a high variation in the St value presented for the first two cases, Re = 1.1×10^5 and 2.2×10^5, but a more consistent evolution

of the St was noticed, for higher Re, with slight increases and decreases in the values for certain cases.

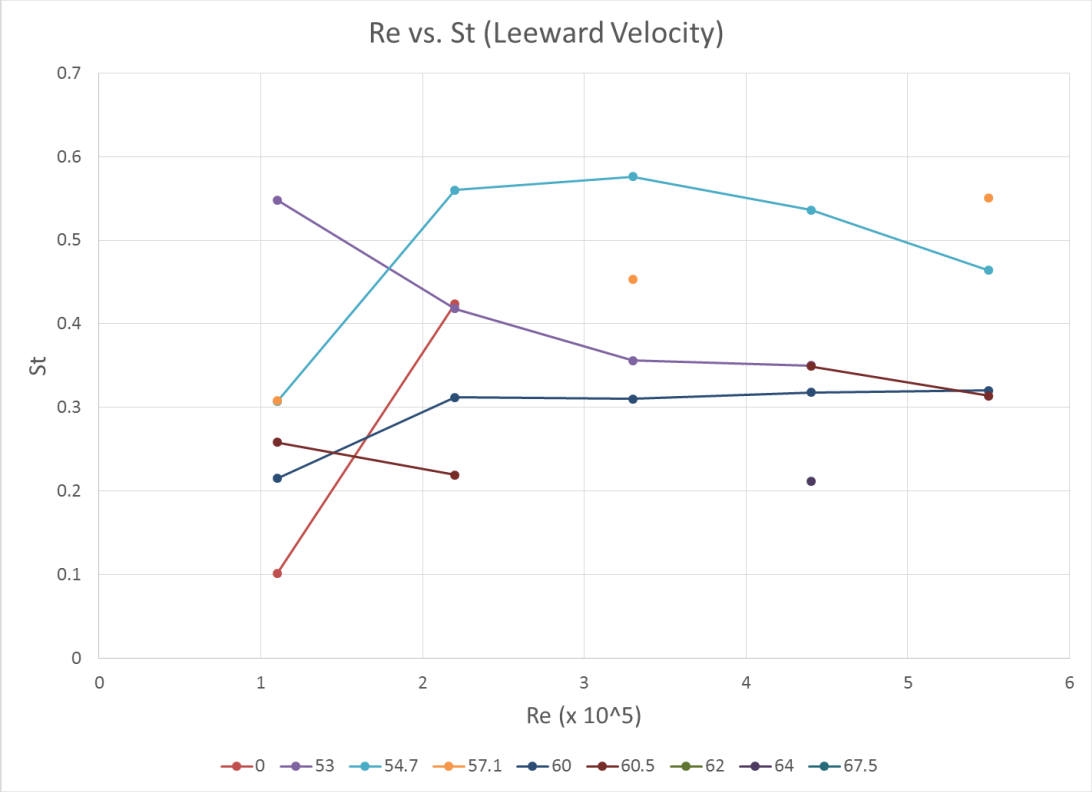


Figure 6.20: Variation in *St* with Reynolds number

6.5 Coherence and Cross-Coherence

In most of the investigations performed the time domain is primarily used to study the vortices in the wake of the cylinder, similar to the analysis carried out in the previous chapters of this study. These flow visualizations are used to show the characteristics of the wake velocities, in addition to the information provided by the time series for the wake velocities. With the use of frequency domain analysis additional information about the wake vortices may be obtained (Elgar et al, 1990).

The coherence and cross-coherence is calculated between coefficient of lift, the pressure coefficient along the leeward side of the cylinder, and the velocity fluctuation along the leeward

side of the cylinder presented in the previous section. It is assumed that these are ergodic processes. In the subsequent sections, a brief description will be provided for the coherence function and cross-coherence function followed by a summary of the results.

6.5.1 Summary of the Spectral Coherence Function

The spectral coherence was used to examine the relationship between pressure, total velocity, and coefficient of lift. Two signals were compared with one another and presented.

The coherence function between two signals $x(n)$ and $y(n)$ is defined as

$$C_{xy}(\omega) = \frac{\left|P_{xy}(\omega)\right|^2}{P_{xx}(\omega)P_{yy}(\omega)} \tag{6-1}$$

where

P_{xy} is the cross-spectral density between x and y,

P_{xx} is the autospectral density of x, and

P_{yy} is the autospectral density of y.

The result is a real number between 0, and 1, which shows measures the correlation between $x(n)$ and $y(n)$ at the frequency ω. The function takes sequence x and y, and computes the power spectra and CPSD (cross power spectral density). The result is the quotient of the magnitude squared of the CPSD and the product of the power spectra. The result of the coherence function is an estimate of the extent to which $y(t)$ may be predicted from $x(t)$ by an optimum linear least squares function.

6.5.2 Summary of the Cross-Bicoherence

Bicoherence is a squared normalised version of the bispectrum. The bispectrum is a statistic used to search for nonlinear interactions. The cross-bicorrelation measures the

relationship between three sets of variables (Swami et al, 1998) in the time domain, and gives an indication of the persistence of that interaction. The cross-bispectrum density is the measure in the frequency domain of such interaction. Three data sets are segmented into possibly overlapping records. The mean from each record is removed, and then the time-domain window is applied. The FFT is computed on the result.

The cross-bispectrum is computed for the *k*th record as

$$B_{wxy,k}(m,n) = W_k(m)X_k(n)Y_k^*(m+n) \tag{6-2}$$

where

W_k is the FFT for the *k*th segment of *w*,

X_k is the FFT for the *k*th segment of *x*, and

Y_k is the FFT for the *k*th segment of *y*,

The spectra are computed as

$$P_{w,k}(m) = |W_k(m)|^2$$

$$P_{x,k}(m) = |X_k(m)|^2$$

$$P_{y,k}(m) = |Y_k(m)|^2 \tag{6-3}$$

The cross-bicoherence is estimated by averaging the spectral and cross-bispectral estimates across records.

The cross-bicoherence is defined as (Swami et al, 1998)

$$bic_{xyz}(f_1,f_2) = \frac{S_{xyz}(f_1,f_2)}{\sqrt{S_{2x}(f_1+f_2)S_{2y}(f_1)S_{2z}(f_2)}} \tag{6-4}$$

where

$S_{xyz}(f_1,f_2)$ is the averaged estimate of the cross-bispectrum,

$S_x(f)$ is the averaged estimate of the power spectra of x,

$S_y(f)$ is the averaged estimate of the power spectra of y, and

$S_z(f)$ is the averaged estimate of the power spectra of z.

The resulted spectrum of the cross-bicoherence ranges from zero to one, for comparisons between two variables. The bicoherence functions are presented as three-dimensional plots, one axis for each frequency f_1 and f_2 and a magnitude axis (Van Diver and Jong, 1987). To enhance visualization and interpretation of the cross-bicoherence the results are shown in contour plots (Silva et al, 2005). The result is an estimate of the cross-biocherence of the three variables. Therefore this is an *nfft*-by-*nfft* array, with the origin at the center, and the axes pointing down and to the right (Swami et al, 1998).

Cross-bispectral analysis has been used previously to study the flow around circular cylinders. Elgar et al (1990) used cross-bispectral analysis to investigate the coupling between a vibrating cylinder and the velocity fluctuations in the wake at low Reynolds numbers ($40 < Re < 100$). This study was done by conducting an experiment in a low speed, low turbulence wind tunnel on a pair of steel music wires. The wires were mounted horizontally in the wind tunnel at the mid-height of the tunnel and passing through the tunnel walls to different mounting locations. The tension of the wire was adjusted using a guitar string machine head, and the tension was measured using a small cantilever beam with a strain gauge. The diameters of the music wires used for this experiment were D = 0.356 mm and D = 0.254 mm. The vibrations of the wires were measured using an infrared photo detector and a constant temperature hot wire anemometer was used to measure the velocity fluctuations in the cylinder wake. The hot wire anemometer was

placed at the mid-point of the wire, and 5 cylinder diameters downstream of the cylinder. With the use of the cross-bicoherence the authors were able to show that the flow field in the wake of the cylinder did respond to the change in the dominant modes of vibration of the cylinder.

Van Diver and Jong (1987) studied the vibration characteristics of long flexible cylinder subjected to vortex-induced vibrations. Two experiments were completed, one, for a 22.86 m long PVC cable with an external diameter of 3.18 cm which was placed in the tidal zone of the Atlantic Ocean off the coast of Maine. The vibration of the cable was monitored with biaxial accelerometers along the length of the cable. The second experiment was for a 610 m long cable suspended vertically in the Artic Ocean again monitored with bidirectional accelerometers. The authors used cross-bicoherence spectrum to demonstrate the non-linear interaction between cross-flow and in-line response of a flexible cylinder.

Pezeshki et al (1992) were able to confirm the capacity of the bispectral techniques to identify a nonlinear system that possesses chaotic motions. The use of the cross-bicoherence spectra indicates that most of the nonlinear energy transfer was from the cross-coupling between the phase modulations rather than between amplitude modulations. The power spectral techniques are adequate for the analysis of linear systems, but were unable to provide any information about the nonlinear interactions between components in a non-linear way.

Hajj et al (1990) indicated that by using the cross-bicoherence they could provide evidence of coupling between modes, but they were not able to provide information on the efficiency of the coupling, and the role of the exchange in energy between the modes. Other methods were required to confirm the transfer functions between the modes.

Silva et al (2005) illustrated the usefulness of higher-order spectral methods in the visualization of the transfer of energy from one frequency to another. This is a hallmark of a

nonlinear phenomenon that is not visible using traditional spectral methods. An advantage of the higher-order spectra is that they provide information regarding the interaction of frequencies due to the nonlinear process. If a phase relationship exist among frequency components of different systems the corresponding cross-spectral value will be large in magnitude. On the other hand, if the phase relationship does not exist among these frequencies components the value of the cross-bicoherence will be between zero and one to indicate partial coupling.

6.6 Coherence and Cross-Coherence Results

The coherence and cross-coherence were calculated between coefficient of lift, the pressure coefficient along the leeward side of the cylinder, and the total velocity along the leeward side of the cylinder. A brief description of each of coherence and cross-coherence is presented below. To assist in the descriptions of the results, the coherence between the lift, pressure coefficient, and leeward velocity will be loosely categorized as either ordered, or chaotic (Van Atta & Gharib, 1987). An ordered result will be characterized by a power spectrum dominated by a narrow primary spectral peak, and associated side band peaks. A chaotic result will be characterized by a relatively broad band power spectrum.

Fifteen cases for the flow characteristics around a cylinder inclined to the flow by 60° (ϕ = 60°; α = 60°, β = 0°), inclined to the flow by 54.7° and yaw of 20° (ϕ = 57.1°; α = 54.7°, β = 20°) and inclined to the flow by 54.7°, and a yaw of 0° (ϕ = 54.7°; α = 54.7°, β = 0°); for Re of 1.1×10^5 to 5.5×10^5 are presented in the upper part of the Figures 6.21, 6.22, and 6.23. For each case the coherence was calculated between the coefficient of lift (C_L) and pressure coefficient along the leeward side of the cylinder, between the coefficient of lift and the total velocity fluctuation along the leeward side of the cylinder, and between the pressure coefficient and the total velocity along the leeward side of the cylinder. Most of the results presented can be categorized as an ordered

signal with narrow peaks throughout the analysed range. The exception to this are the coherences between the coefficient of lift and the total velocity fluctuation along the leeward side of the cylinder for Re = 1.1×10^5 to 4.4×10^5. These coherences can be categorized as a chaotic signal with a broader band in the power spectrum. The coherences for Re = 5.5×10^5 differ from the other cases as there is no broad band within the power spectrum presented in these results.

As introduced in the previous section, the cross-bicorrelation measures the relationship between three sets of variables in the time domain, and gives an indication of the persistence of that interaction. The cross-bispectrum density is the measure of the frequency domain of such interaction. The result is a contour plot of the magnitude of the estimated cross-bicoherence which is displayed (Swami et al, 1998).

The results of the cross-coherence between the coefficient of lift, the pressure coefficient along the leeward side of the cylinder, and the velocity fluctuation along the leeward side of the cylinder for the same fifteen cases, as the coherence calculated previously in this section, are presented in the lower part of the same Figures 6.21, 6.22, and 6.23 below. As shown in the colour scale, the darker the colour the less cross-coherence is present between the variables, and the lighter the colour the more intensive coherence is between the variables for the St numbers. Most cases show little to low cross-coherence between the three variables. For the three cases presented in this section, for a cylinder inclined to the flow by 60°, and inclined to the flow by 54.7° and yaw of 20°, and inclined to the flow by 54.7° and yaw of 0°, the magnitude of the cross-coherence generally decreased with the increase in Re. The exception to this observation is the case of a cylinder inclined to the flow by 60° for Re = 5.5×10^5, where a pattern develops within the contour plot as St increased in both the horizontal and vertical axes. The other case is for a cylinder inclined to the flow by 54.7° and yaw of 20°, at Re = 1.1×10^5, where peaks in the cross-coherence occur

at St combinations of approximately 0.1 and 0.5, and 0.2 and 0.3. Moreover, for Re = 3.3×10^5 and Re = 4.4×10^5 for a cylinder inclined to the flow by 54.7° and yaw of 0° peaks were noted for the cross-coherence, but an unstructured pattern in the results was noticed.

The results were categorized under three cases, low non-linear interaction, intermediate non-linear interaction, and high non-linear interaction, as illustrated by the cross-coherence. The following cases showed low non-linear interaction between the coefficient of lift, the pressure coefficient along the leeward side of the cylinder, and the velocity fluctuation along the leeward side of the cylinder:

$\phi = 60°$; $\alpha = 60°$, and $\beta = 0°$; for Re = 4.4×10^5;

$\phi = 57.1°$; $\alpha = 54.7°$, and $\beta = 20°$; for Re = 3.3×10^5;

$\phi = 57.1°$; $\alpha = 54.7°$, and $\beta = 20°$; for Re = 4.4×10^5;

$\phi = 57.1°$; $\alpha = 54.7°$, and $\beta = 20°$; for Re = 5.5×10^5;

$\phi = 54.7°$; $\alpha = 54.7°$, and $\beta = 0°$; for Re = 1.1×10^5;

$\phi = 54.7°$; $\alpha = 54.7°$, and $\beta = 0°$; for Re = 2.2×10^5;

$\phi = 54.7°$; $\alpha = 54.7°$, and $\beta = 0°$; for Re = 5.5×10^5.

Cases considered with intermediate non-linear interaction were:

$\phi = 60°$; $\alpha = 60°$, and $\beta = 0°$; for Re = 1.1×10^5;

$\phi = 60°$; $\alpha = 60°$, and $\beta = 0°$; for Re = 2.2×10^5;

$\phi = 60°$; $\alpha = 60°$, and $\beta = 0°$; for Re = 3.3×10^5;

$\phi = 57.1°$; $\alpha = 54.7°$, and $\beta = 20°$; for Re = 2.2×10^5.

Finally cases considered with high non-linear interaction were:

$\phi = 60°$; $\alpha = 60°$, and $\beta = 0°$; for Re = 5.5×10^5;

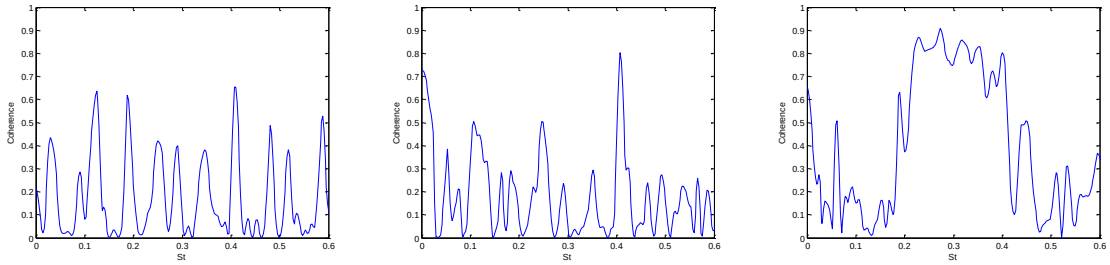
$\phi = 57.1°$; $\alpha = 54.7°$, and $\beta = 20°$; for Re = 1.1×10^5;

$\phi = 54.7°$; $\alpha = 54.7°$, and $\beta = 0°$; for Re = 3.3×10^5;

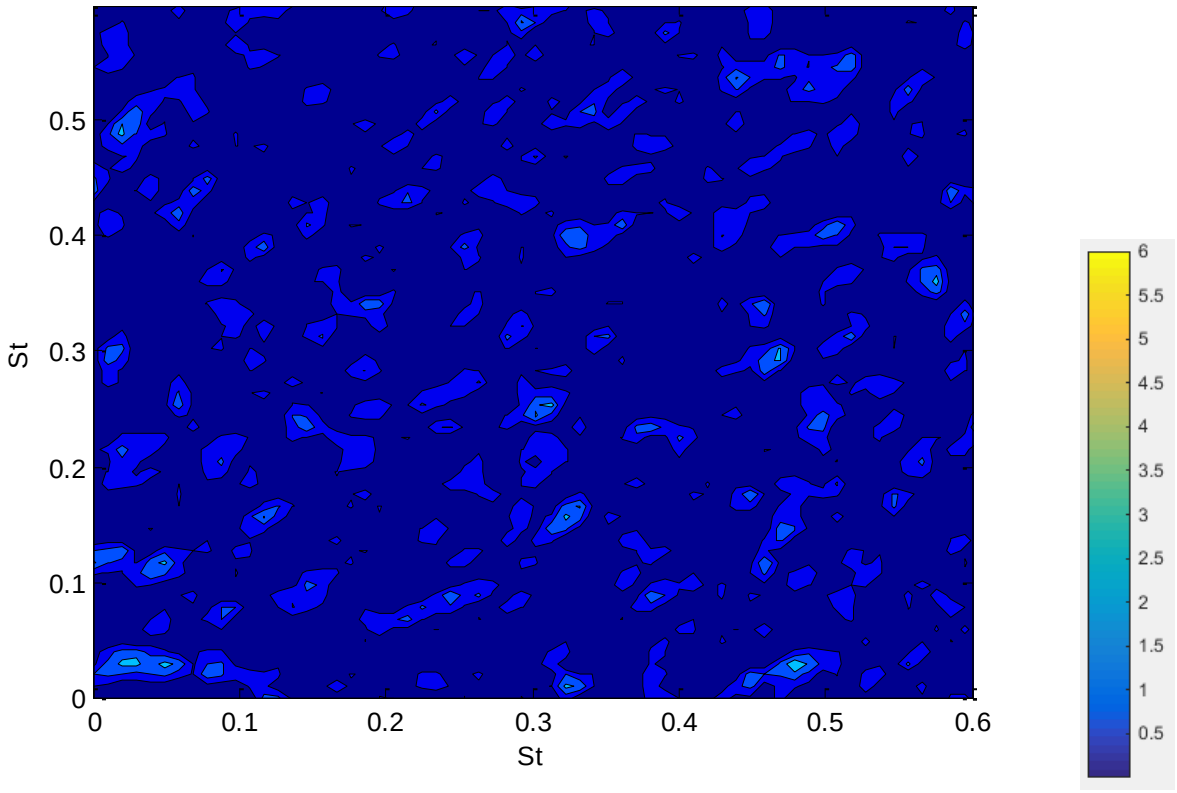
$\phi = 54.7°$; $\alpha = 54.7°$, and $\beta = 0°$; for Re = 4.4×10^5.

It is interesting to notice that the high non-linear interaction cases reported above correspond to the TrSL-Long regime, as described in Table 5-1, and Figure 5.8 discussed in Chapter 5. The single exception is the $\phi = 60°$; $\alpha = 60°$, and $\beta = 0°$, for Re = 4.4×10^5 case which follows a TrSL-Short flow regime. In general intermediate non-linear interaction was noticed for the $\phi = 60°$, $\alpha = 60°$, and $\beta = 0°$ case, for other Re numbers investigated, however the flow regime alternated between TrSL-Long, for Re 2.2×10^5 and 5.5×10^5, and TrSL-Short for Re 1.1×10^5, and 3.3×10^5, which shows the unstable flow conditions achieved for the critical case of relative angle of attack of $\phi = 60°$.

For the high non-linear interaction of the reduced frequencies of the three parameters the lift coefficient, the pressure coefficient, and the total velocity, more critical regimes were expected, however the cases reported under this category classified as the TrSL-Long regime, except for the $\phi = 57.1°$; $\alpha = 54.7°$, and $\beta = 20°$; for Re = 1.1×10^5 case, which followed a TrSL-Open flow regime. Therefore it can be concluded that the influence of the total component velocity, and implicitly the Re number, on the interaction between the lift and pressure coefficients monitored for the cylinder does not have a significant influence on the flow regimes, or on the transition between the flow regimes. The high-nonlinear interactions relate more to the potential coupling between the frequencies of the parameters mentioned above, especially for cases like $\phi = 60°$; $\alpha = 60°$, and $\beta = 0°$; for Re = 5.5×10^5, where a periodic structure of the nonlinear interaction can be noticed (Figure 6.25). This proves once more that the aerodynamic instability for the $\phi = 60°$ case is more complex than expected.



C_L-Pressure C_L-Total velocity Pressure-Total velocity

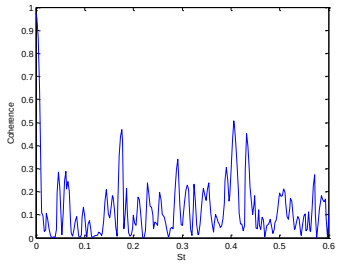


Cross-coherence: C_L-Pressure-Total velocity

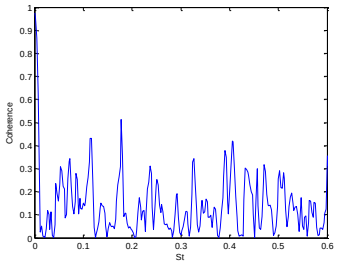
Figure 6.21: Coherence

$\phi = 60°$; $\alpha = 0°$, $\beta = 60°$

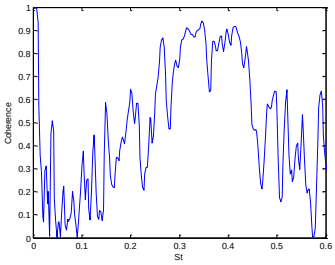
i) Re = 1.1×10^5;



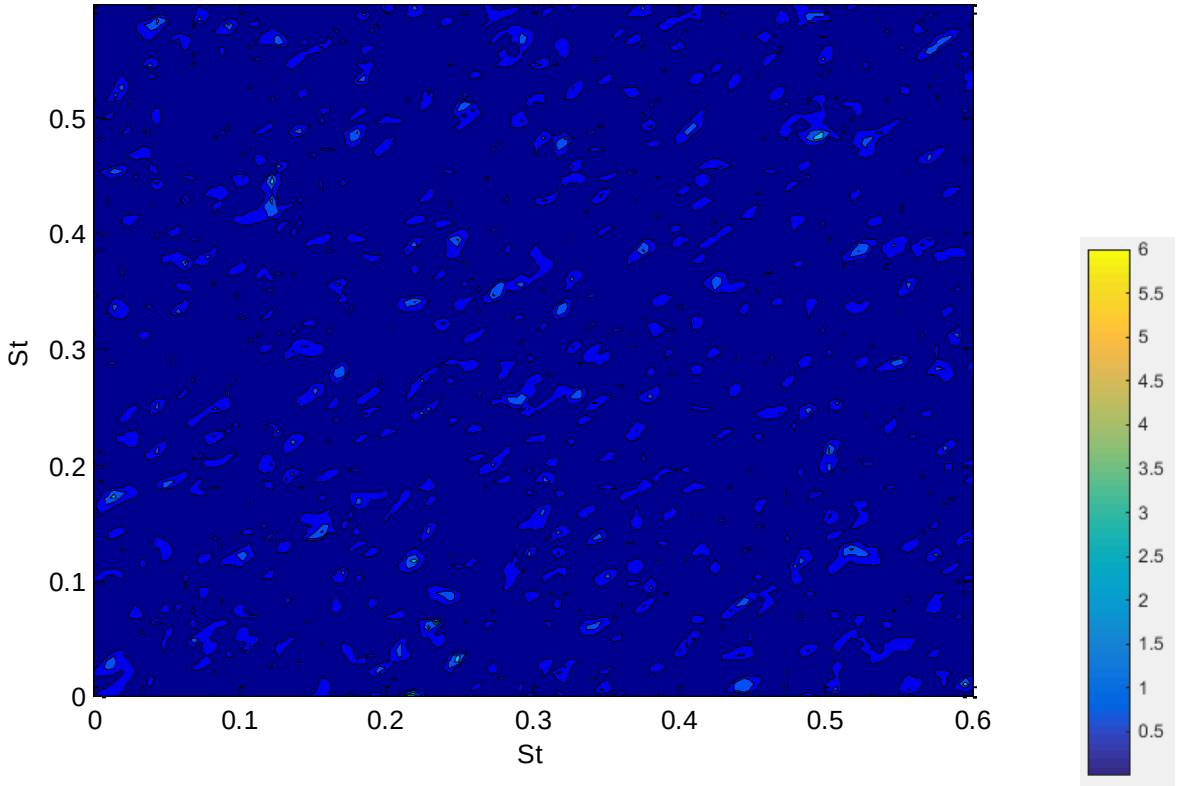
C_L-Pressure



C_L-Total velocity



Pressure-Total velocity

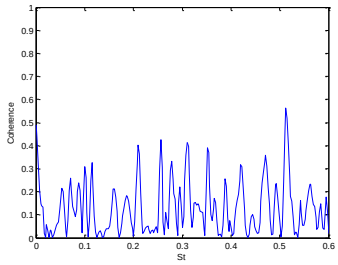


Cross-coherence: C_L-Pressure-Total velocity

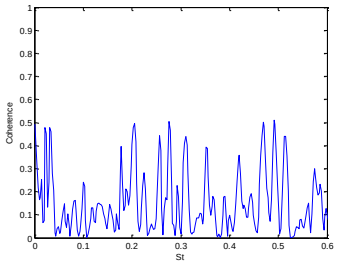
Figure 6.21: Coherence

$\phi = 60°$; $\alpha = 0°$, $\beta = 60°$

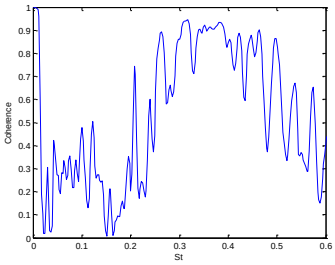
ii) Re = 2.2×10^5;



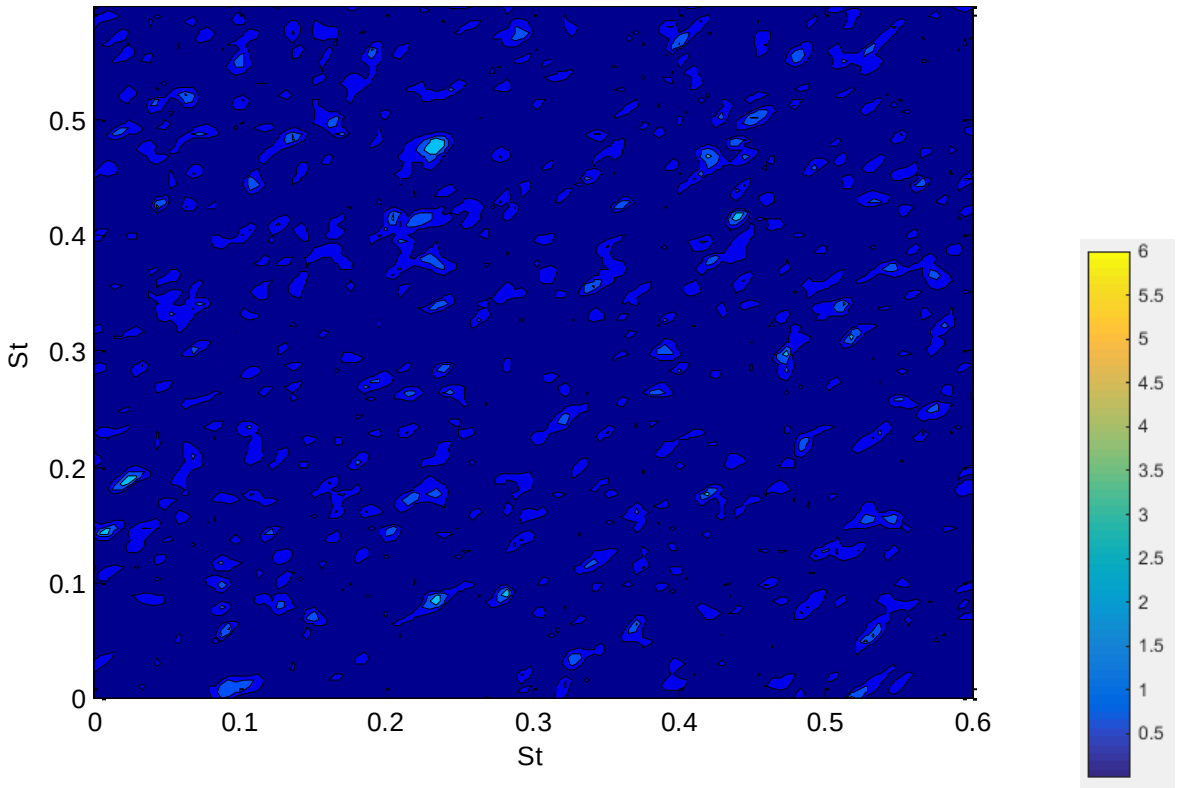
C_L-Pressure



C_L-Total velocity



Pressure-Total velocity

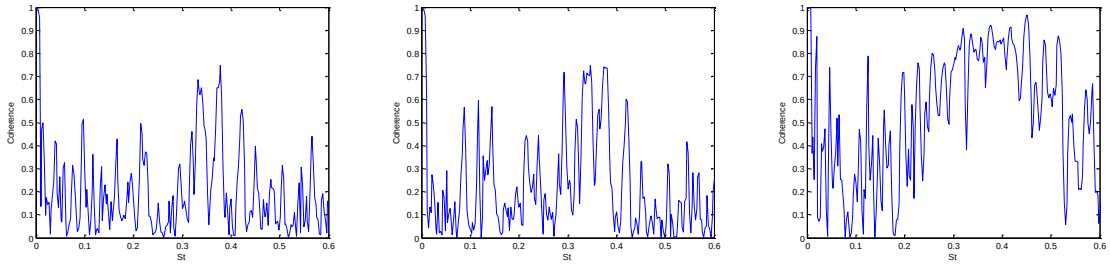


Cross-coherence: C_L-Pressure-Total velocity

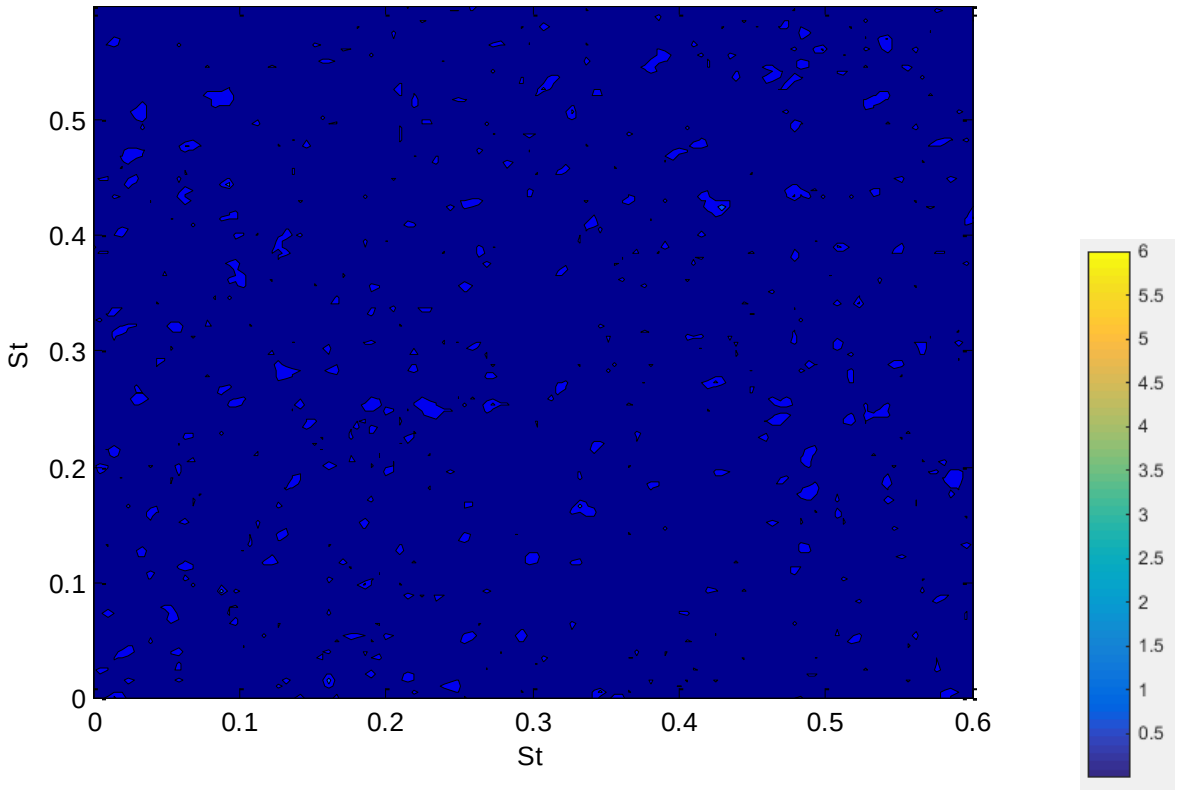
Figure 6.21: Coherence

$\phi = 60°$; $\alpha = 0°$, $\beta = 60°$

iii) Re = 3.3×10^5;



C_L-Pressure C_L-Total velocity Pressure-Total velocity

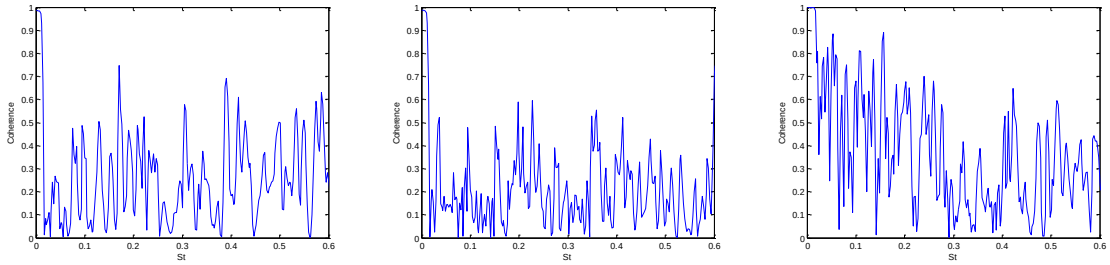


Cross-coherence: C_L-Pressure-Total velocity

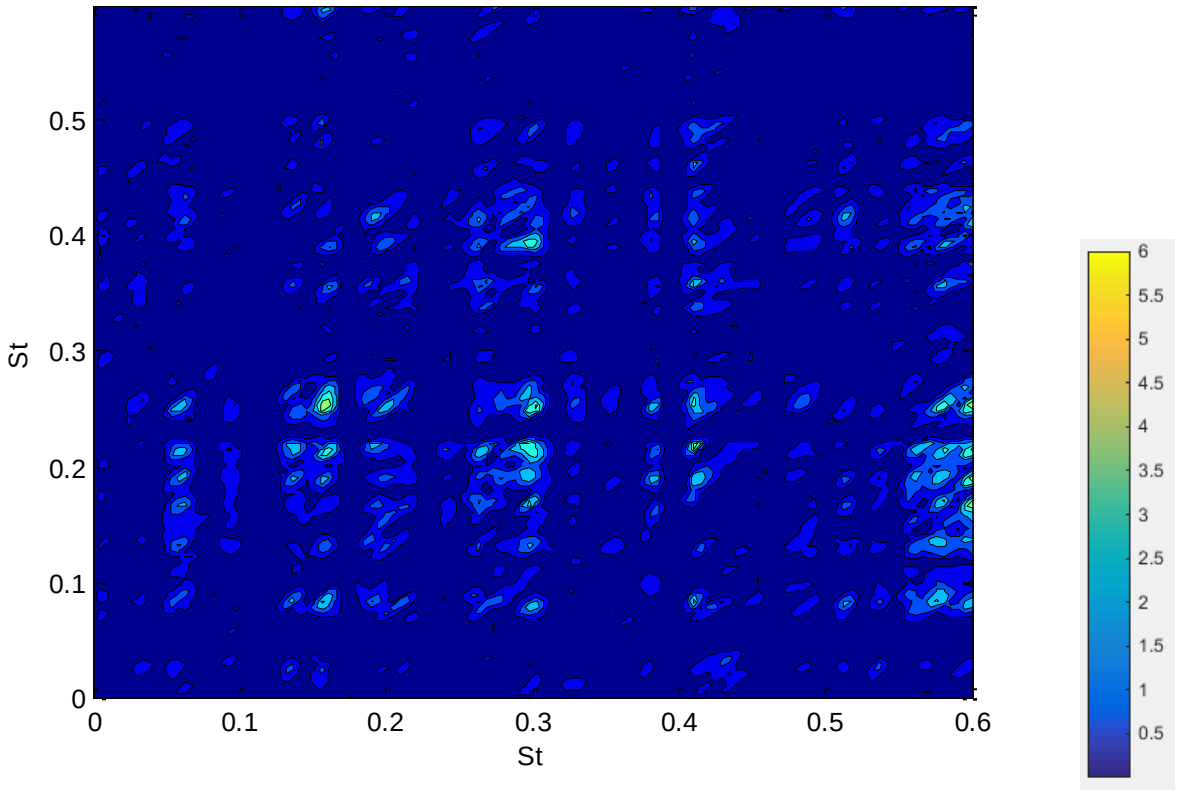
Figure 6.21: Coherence

$\phi = 60°$; $\alpha = 0°$, $\beta = 60°$

iv) Re = 4.4×10^5;



C_L-Pressure C_L-Total velocity Pressure-Total velocity

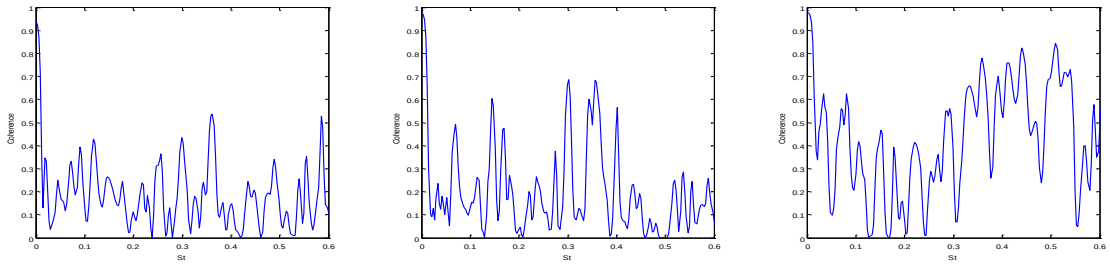


Cross-coherence: C_L-Pressure-Total velocity

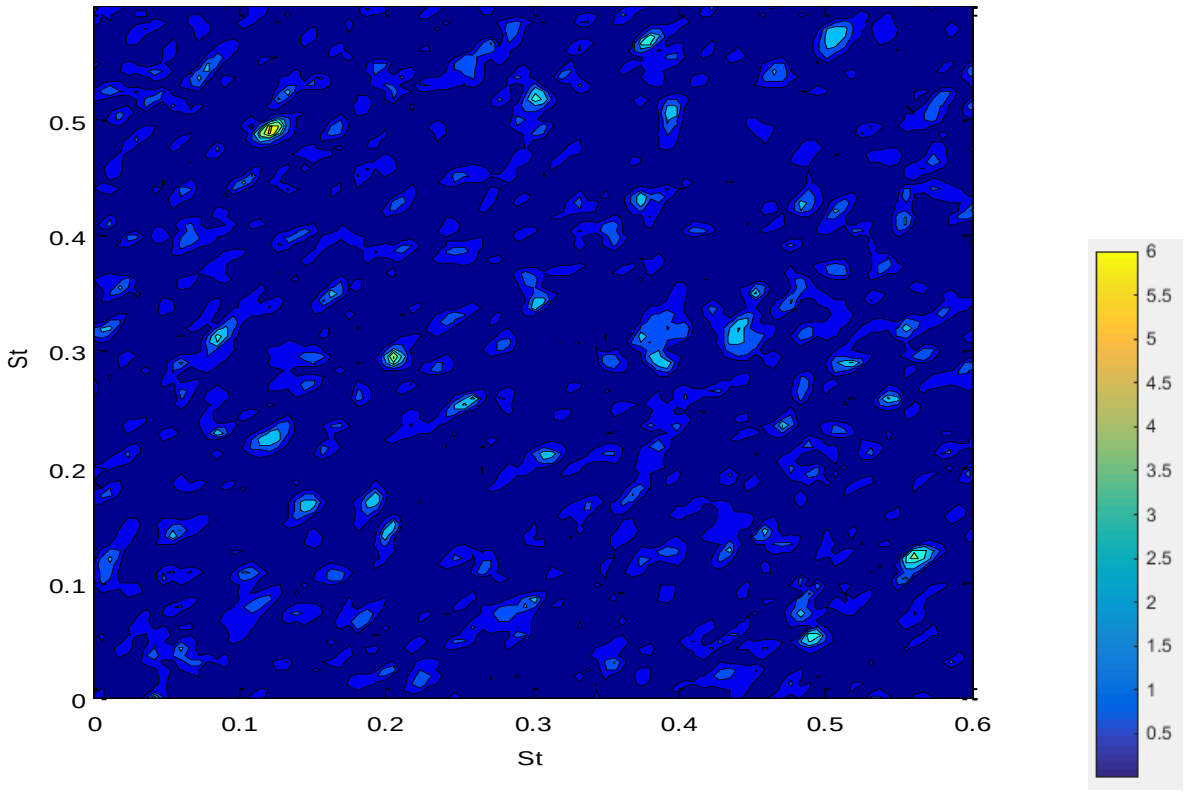
Figure 6.21: Coherence

$\phi = 60°$; $\alpha = 0°$, $\beta = 60°$

v) Re = 5.5×10^5;



C_L-Pressure C_L-Total velocity Pressure-Total velocity

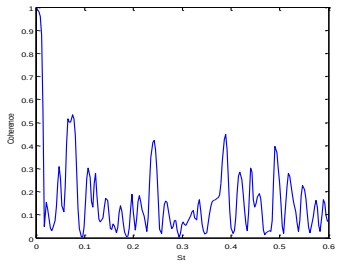


Cross-coherence: C_L-Pressure-Total velocity

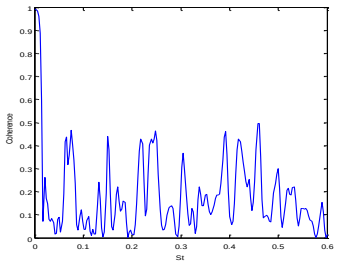
Figure 6.22: Coherence

$\phi = 57.1°$; $\alpha = 54.7°$, $\beta = 20°$

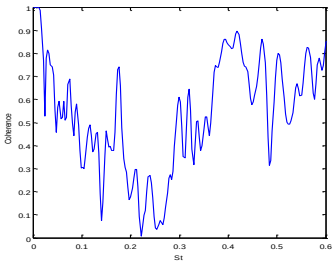
i) Re = 1.1×10^5;



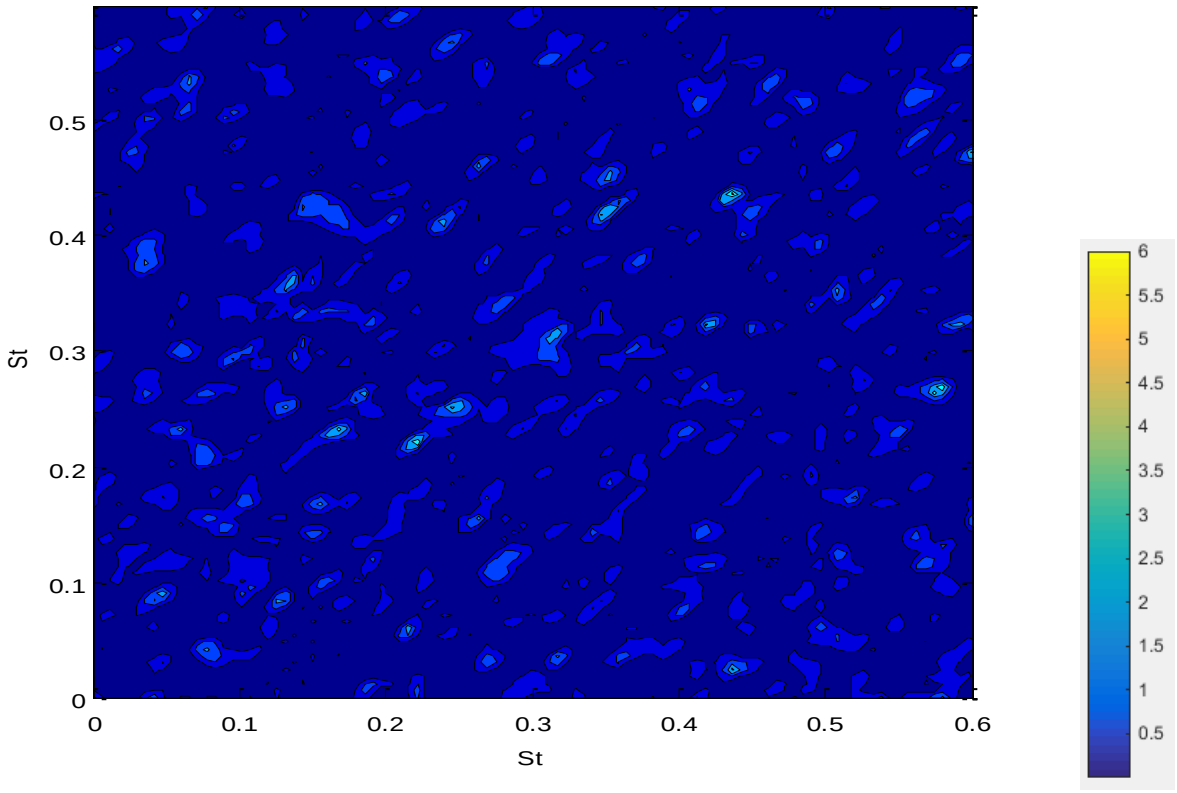
C_L-Pressure



C_L-Total velocity



Pressure-Total velocity

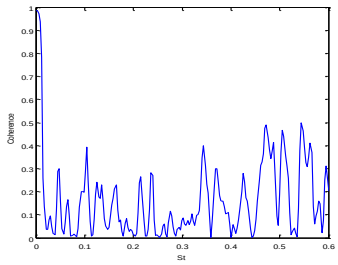


Cross-coherence: C_L-Pressure-Total velocity

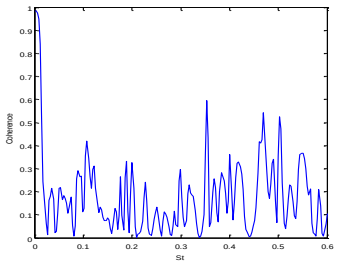
Figure 6.22: Coherence

$\phi = 57.1°$; $\alpha = 54.7°$, $\beta = 20°$

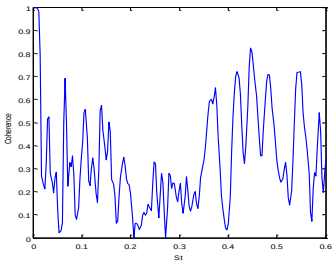
ii) Re = 2.2×10^5;



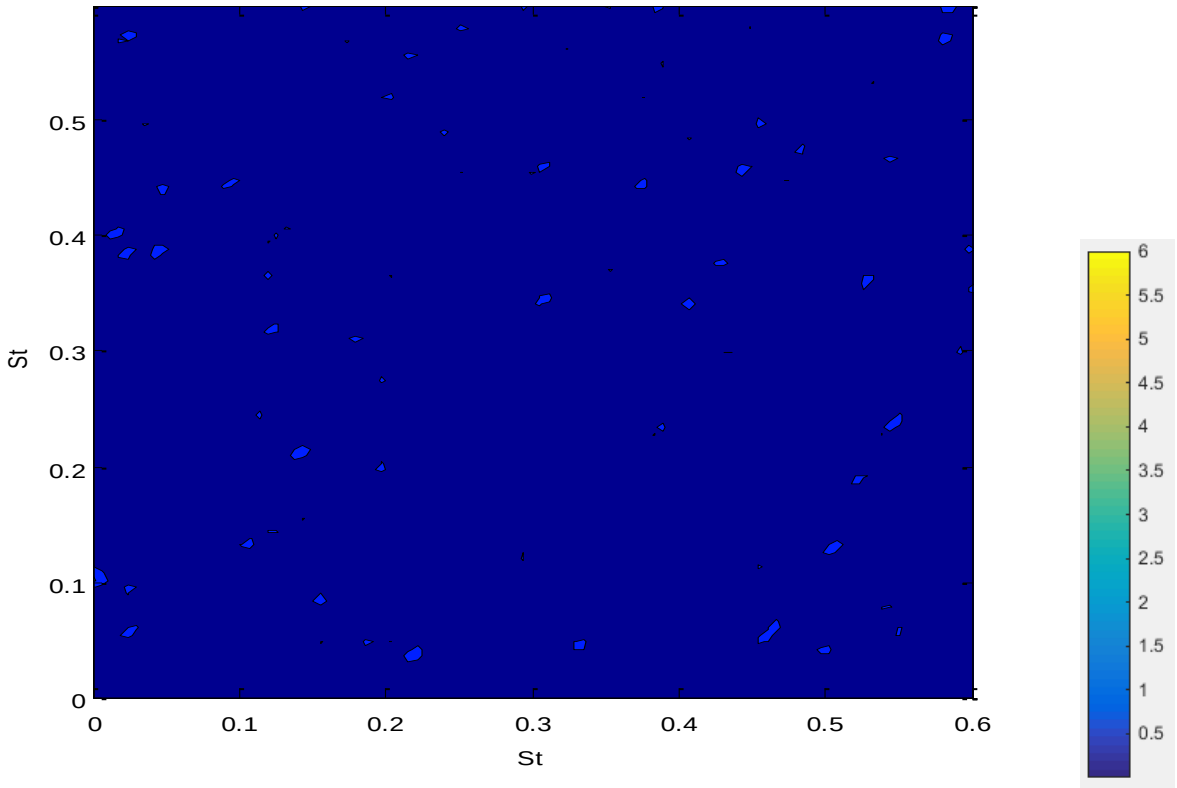
C_L-Pressure



C_L-Total velocity



Pressure-Total velocity

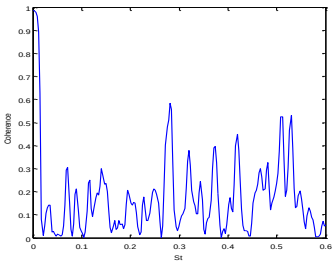


Cross-coherence: C_L-Pressure-Total velocity

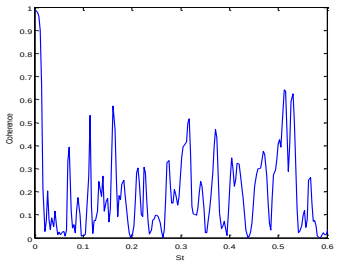
Figure 6.22: Coherence

$\phi = 57.1°$; $\alpha = 54.7°$, $\beta = 20°$

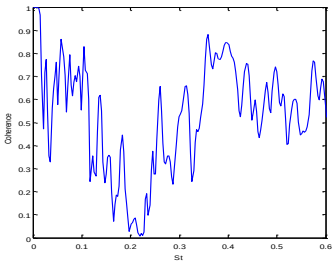
iii) Re = 3.3×10^5;



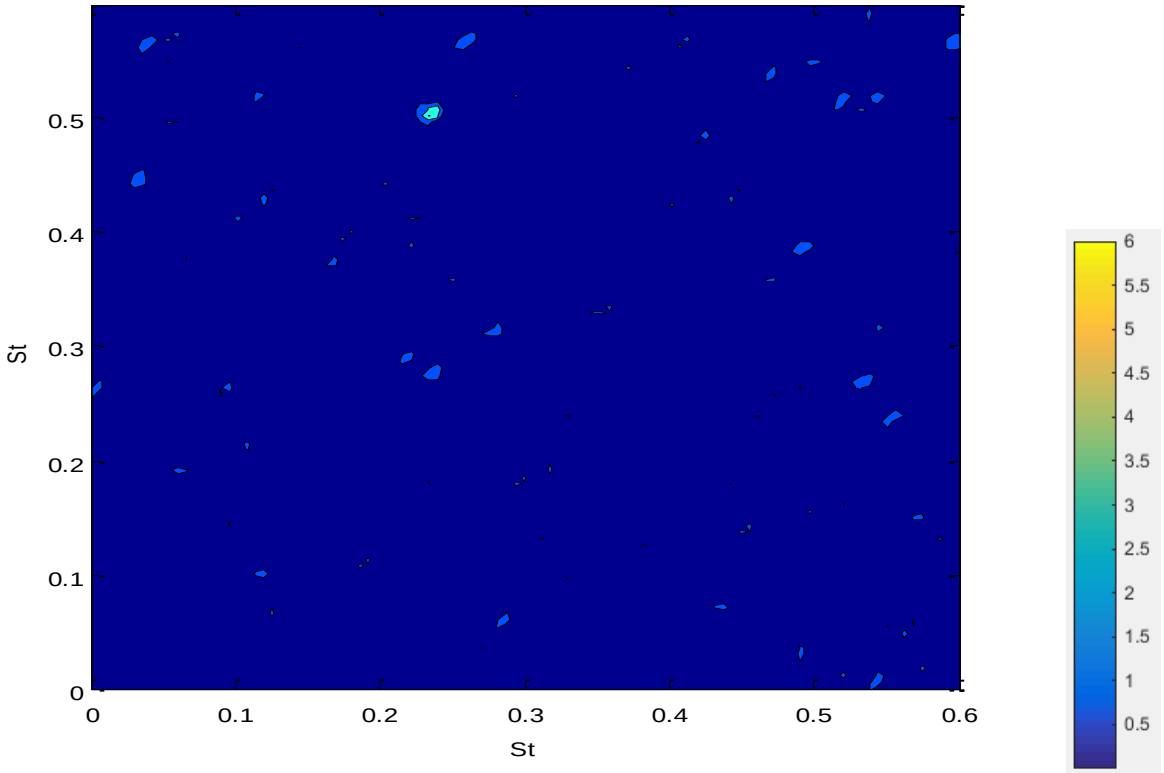
C_L-Pressure



C_L-Total velocity



Pressure-Total velocity

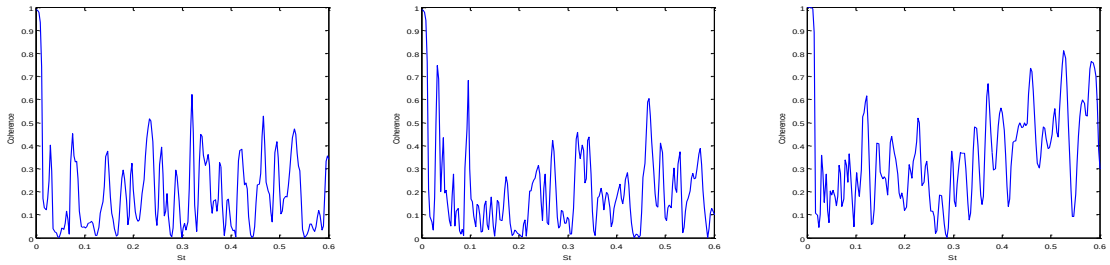


Cross-coherence: C_L-Pressure-Total velocity

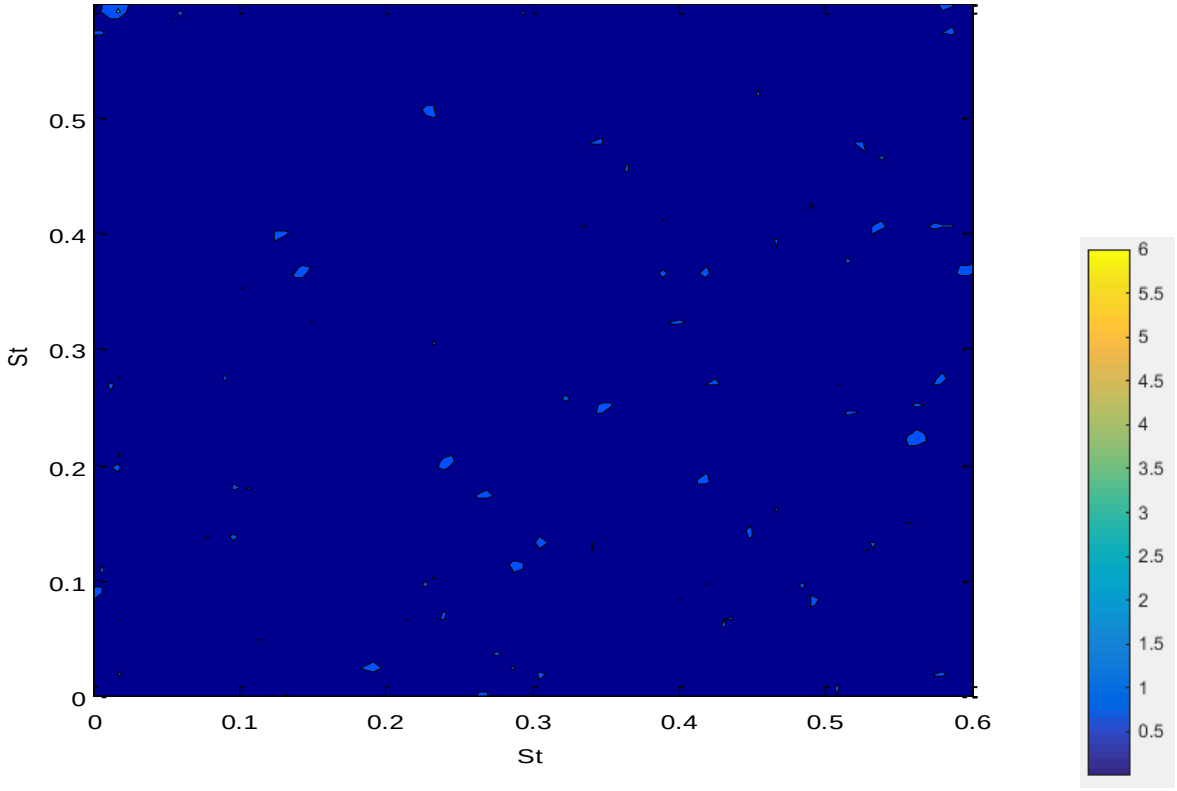
Figure 6.22: Coherence

$\phi = 57.1°$; $\alpha = 54.7°$, $\beta = 20°$

iv) Re = 4.4×10^5;



C_L-Pressure C_L-Total velocity Pressure-Total velocity

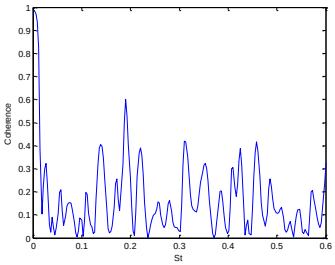


Cross-coherence: C_L-Pressure-Total velocity

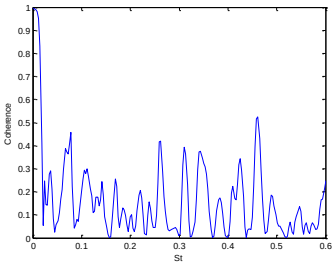
Figure 6.22: Coherence

$\phi = 57.1°$; $\alpha = 54.7°$, $\beta = 20°$

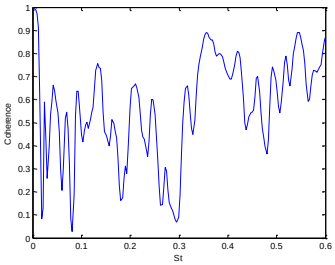
v) Re = 5.5×10^5;



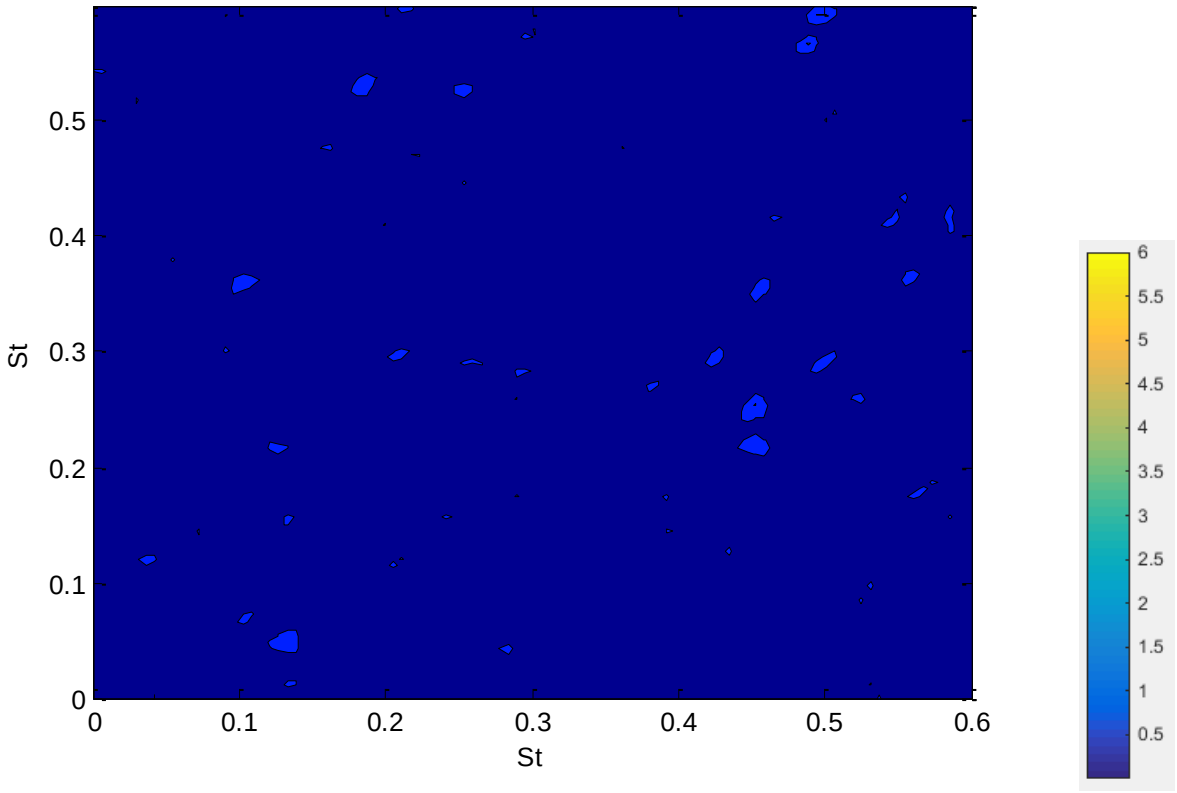
C_L-Pressure



C_L-Total velocity



Pressure-Total velocity

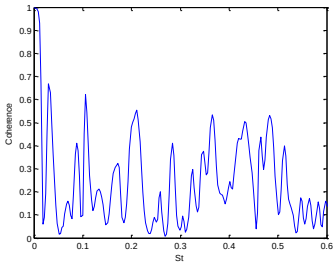


Cross-coherence: C_L-Pressure-Total velocity

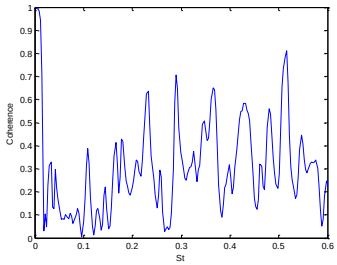
Figure 6.23: Coherence

$\phi = 54.7°$; $\alpha = 54.7°$, $\beta = 0°$

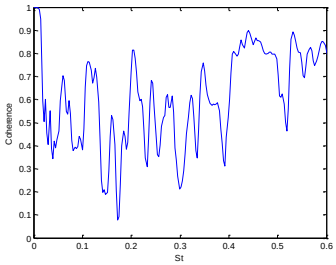
i) Re = 1.1×10^5;



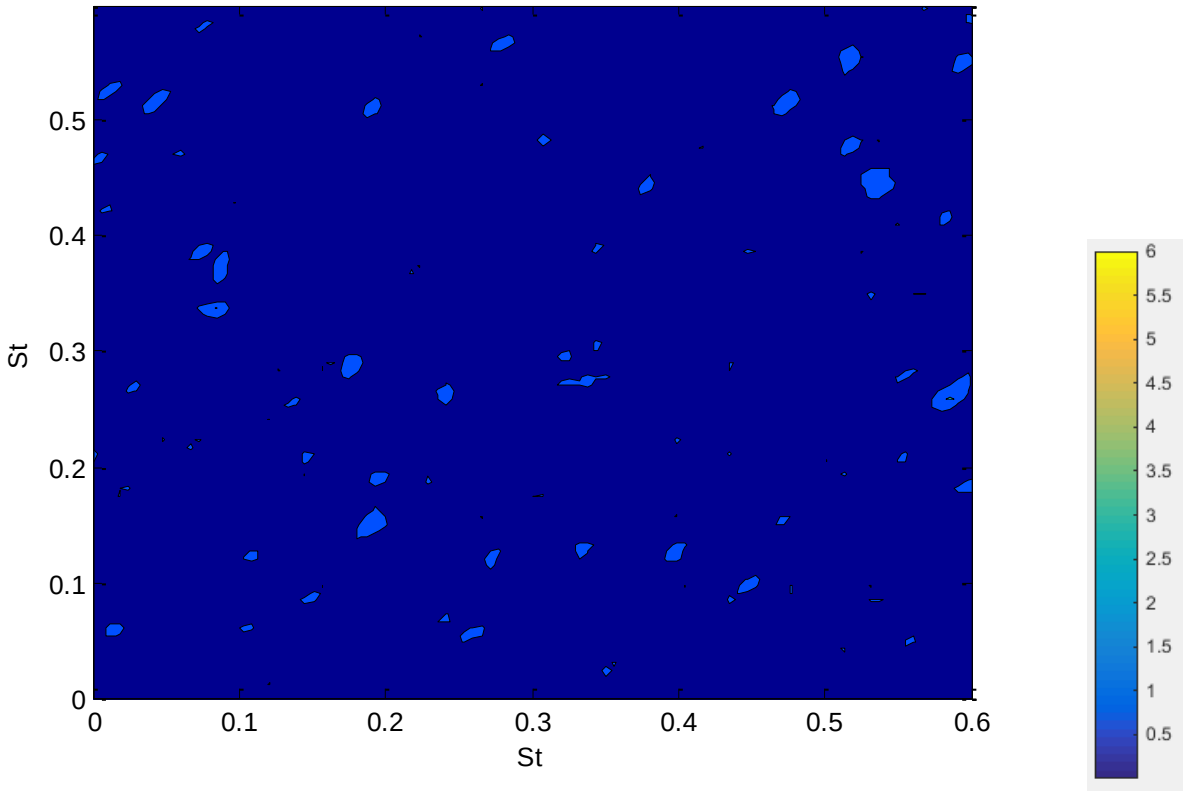
C_L-Pressure



C_L-Total velocity



Pressure-Total velocity

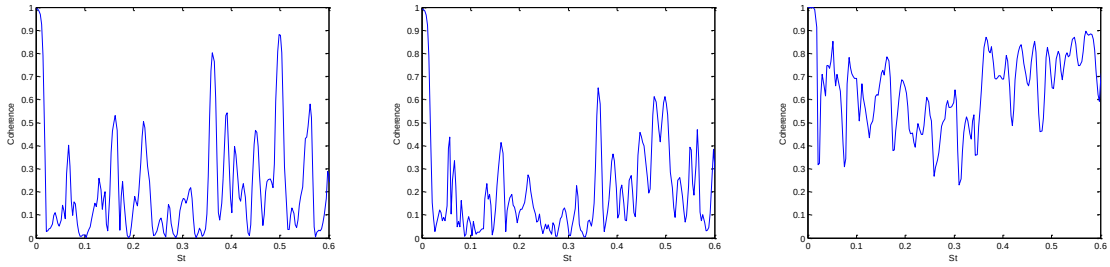


Cross-coherence: C_L-Pressure-Total velocity

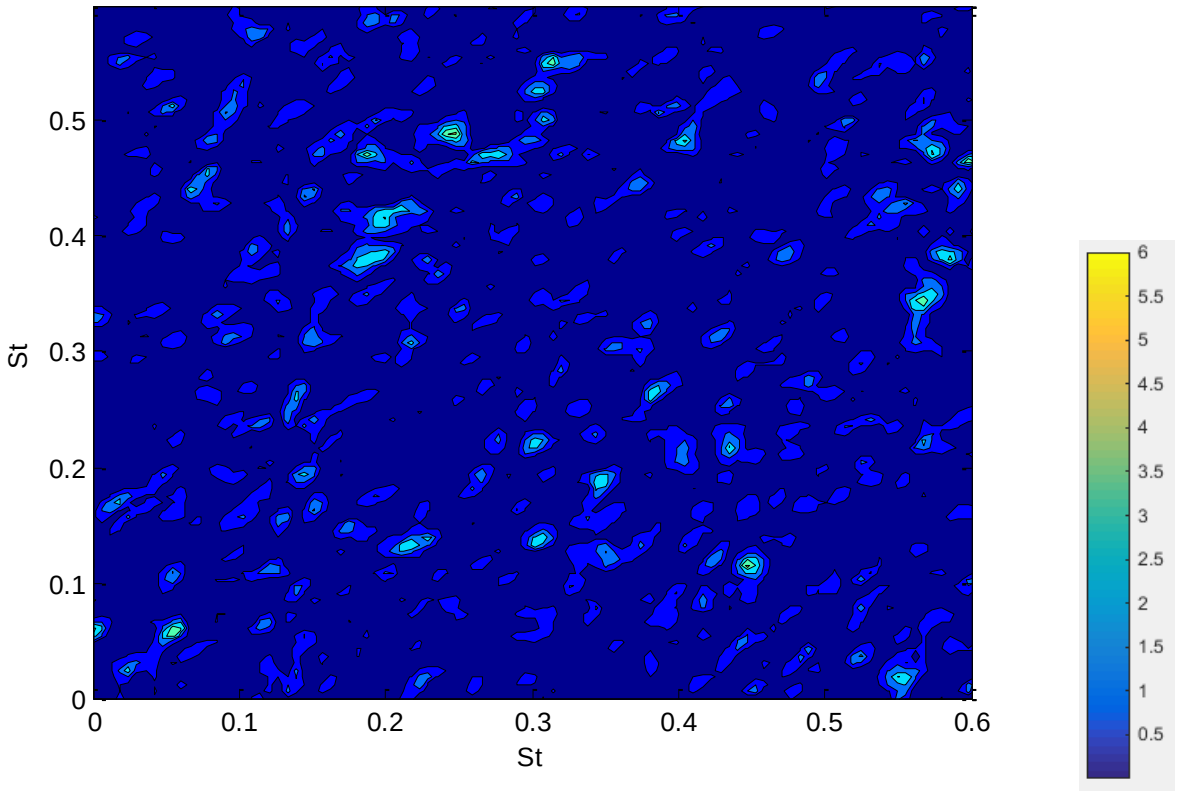
Figure 6.23: Coherence

$\phi = 54.7°$; $\alpha = 54.7°$, $\beta = 0°$

ii) Re = 2.2×10^5;



C_L-Pressure C_L-Total velocity Pressure-Total velocity

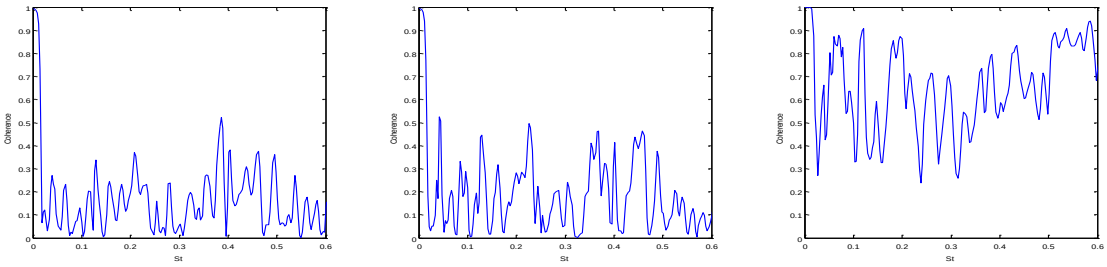


Cross-coherence: C_L-Pressure-Total velocity

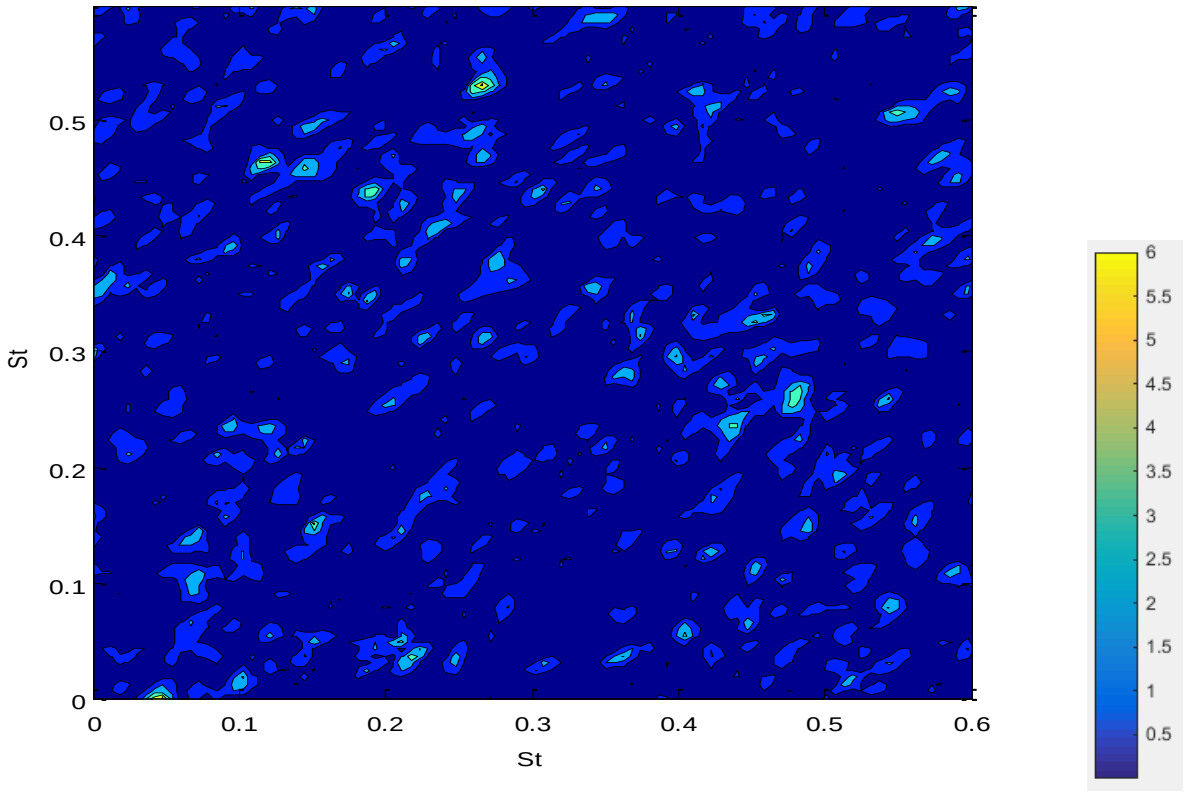
Figure 6.23: Coherence

$\phi = 54.7°$; $\alpha = 54.7°$, $\beta = 0°$

iii) Re = 3.3×10^5;



C_L-Pressure C_L-Total velocity Pressure-Total velocity

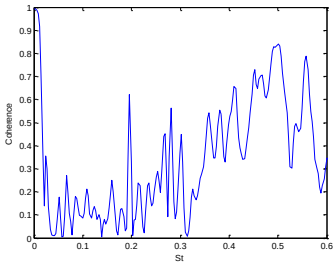


Cross-coherence: C_L-Pressure-Total velocity

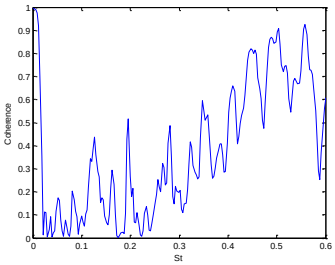
Figure 6.23: Coherence

$\phi = 54.7°$; $\alpha = 54.7°$, $\beta = 0°$

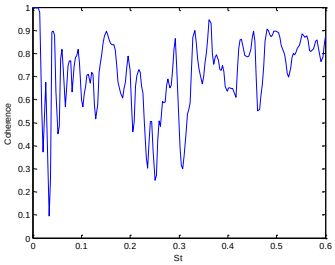
iv) Re = 4.4×10^5;



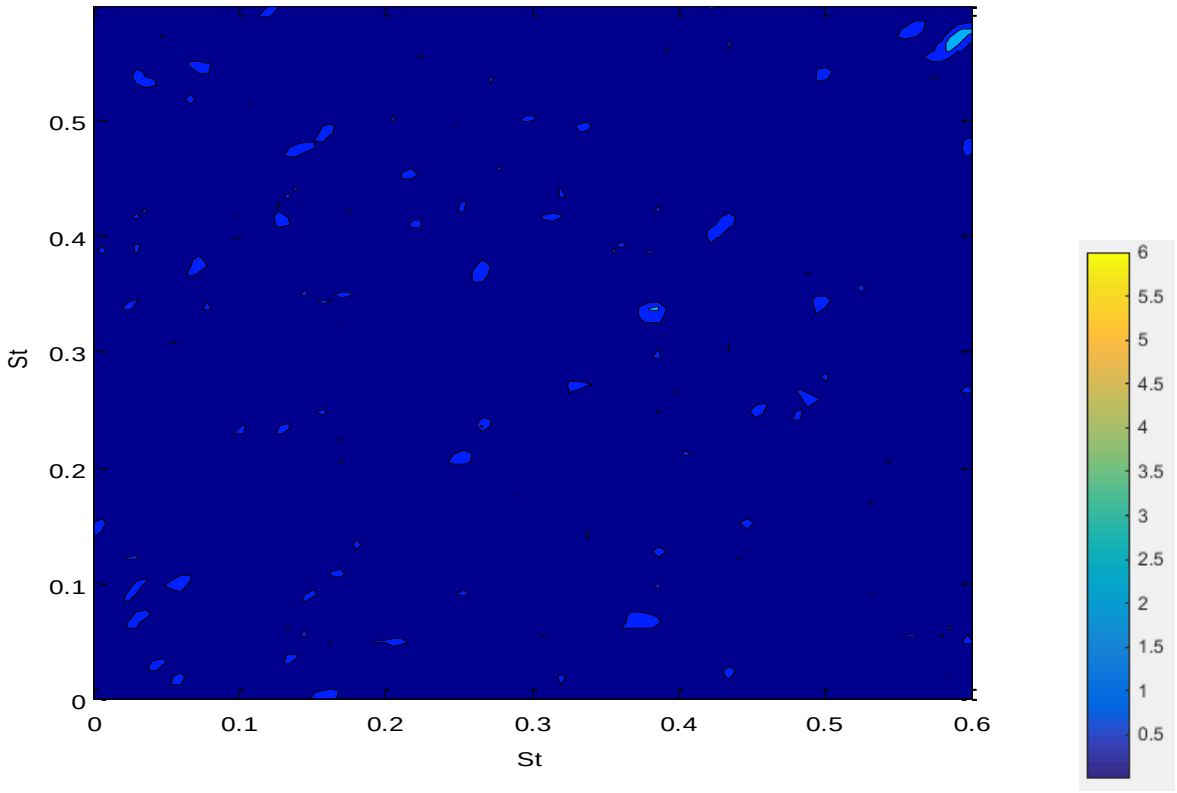
C_L-Pressure



C_L-Total velocity



Pressure-Total velocity



Cross-coherence: C_L-Pressure-Total velocity

Figure 6.23: Coherence

$\phi = 54.7°$; $\alpha = 54.7°$, $\beta = 0°$

v) Re = 5.5×10^5;

7 Conclusions

The current study focused on numerically investigating the flow behaviour around the inclined and yawed cylinders aiming at clarifying the occurrence, and properties of the axial flow attached on the leeward side of the cylinder, and the effect this could have on dry inclined cable galloping phenomenon. Several cases of inclined (α) and yawed (β) circular cylinders with angles between 0° and 60°, and 0° and 40° respectively were numerically investigated for Reynolds numbers ranging from 1.1 to 6.7×10^5. The numerical results from this study were used to identify if a potential aerodynamic instability would be defined as critical using the galloping equation developed by MacDonald and Larose (2006), and necessary interpretations were made to clarify the relatively new aerodynamic instability observed for the inclined and yawed cylinders.

The computational domain used in this study was 30D along the length of the cylinder, 22.5D in the direction of flow, and in the direction perpendicular to the flow, with a very fine mesh around the cylinder, and coarser in the rest of the domain. The circular cylinder was exposed to various wind speeds ranging from 18.0 m/s to 90.3 m/s, corresponding to high Reynolds numbers of Re = $1.1 \times 10^5 – 6.7 \times 10^5$. The current study used Ansys – Fluent software, with the turbulent LES algorithm throughout the entire domain with the Smagorinsky model for the turbulent viscosity. Several cases of flow perpendicular and inclined/yawed circular cylinders of diameter D = 0.089 m and length of 30D = 2.67 m were preformed and presented.

The results of this study showed the appearance of an axial flow on the leeward side of the cylinder when the cylinder is inclined at 60° for Re = 3.3×10^5 and 6.7×10^5. For the rest of the investigated cases of inclined and yawed cylinders, a lower intensity flow will be formed on the leeward side of the cylinder. However this will detach periodically from the cylinder's surface.

The measurements of the axial flow velocity at distances of 0.1D to 0.5D showed, however, that for 60° and 60.5° at Re = 3.3×10^5 and 6.7×10^5 the intensity of the flow along the cylinder axis does not vary very much within this distance downstream the cylinder. Also the position where the measurements were taken might have an influence upon this result, considering the undulated flow reported in Figure 4.6.

The ten cases were presented as representative samples of the cases studied as part of the current work showing various inclination angles (α), yaw angles (β), relative angles of attack of the cable (ϕ), and Reynolds numbers (Re). The rest of the cases were included in the Appendices. When reviewing the results, it was noticed that a flow pattern developed for the same cases, showing similar characteristics for different parameters used in this study.

The parameters presented in Chapter 4 include pressure distribution on the windward and leeward side of the cylinder, velocity and pressure distributions around the cylinder, axial flow along the length of the cylinder, vector plots showing the magnitude and direction of flow around the cylinder, and axial flow visualizations using velocity streamlines. The cases developing the same flow pattern were grouped as follows: $\phi = 64°$, Re = 1.1×10^5; and $\phi = 64°$, Re = 3.3×10^5, or cases (a) and (e), for the regions of high pressures along the leeward surface of the cylinder interrupted by areas of low pressure patches, the velocity distribution along the leeward side of the cylinder, showing a formation of rotational vortices; also the axial flow fluctuations increased as the distance from the cylinder increased for location 0.1D to 0.5D from the cylinder, including the amount of flow redirected along the leeward side of the cylinder. The model parameters $\alpha = 60°$, $\beta = 20°$, $\phi = 62°$, Re = 3.3×10^5; and $\alpha = 60°$, $\beta = 20°$, $\phi = 62°$, Re = 5.5×10^5, or cases (d) and (g), also showed similar evolutions for many of the model parameters studied. Results from this

study have added to the database of flow visualizations for flow around the inclined circular cylinders.

In addition to the axial flow visualizations discussed in the previous paragraph, data was sampled at 9 locations along the leeward side of the cylinder, for the full cross flow width of the computational domain. These locations include 0.1D, 0.2D, 0.3D, 0.4D, and 0.5D as previously presented, but also locations further downstream of the cylinder at 0.7D, 1.0D, 1.5D and 2.0D. Results were presented for eddy viscosity, pressure and velocity. The pressure distribution downstream of the cylinder showed the greatest change with the change of the yaw angle. The highest difference was noticed for the normalized pressure from one side of the cylinder to the other for the highest yaw angle, difference which decreased with the decrease in yaw angle. As expected, the velocity profiles on the downstream side of the cylinder showed a similar tendency. Also, the velocity profiles showed a recovery of the along flow profiles only for further locations of 0.7D up to 2.0D downstream of the cylinder. This proves a stronger axial flow in the vicinity of the cylinder, diminishing downstream of the cylinder. As a result, a proposed location has been recommended for the measurement of the axial flow along the leeward side of the cylinder. Experimental measurements of the axial flow are recommended within the interval of 0.1D-0.3D.

When the first results were obtained for the inclined, and inclined and yawed cylinders it was noticed that the flow behaviour does not fall into any of the flow regimes classified by Zdravkovich (1997). Comparing the currently obtained results with the data available for the TrBL regime, as described by Zdravkovich (1997), the turbulence intensities contours showed major discrepancies with this category of regime, only for inclined, and inclined and yawed cables. For the case of flow perpendicular to the cylinder the standard TrBL regime was obtained in the current simulation, for Re = 6.7×10^5. Therefore, a similar procedure as Zdravkovich (1997) was

followed for establishing the flow regimes, and the velocity contours, intensity isolines and pressure coefficient distributions, around the surface of the cylinder were investigated. Several new flow regimes were identified including TrSL-Short, TrSL-Long and TrSL-Open as follows: for TrSL-short the following cases were identified as: $\phi = 60.5°$, Re = 3.3×10^5; $\phi = 53°$, Re = 4.4×10^5; and $\phi = 60°$, Re = 3.3×10^5; for TrSL-Long: $\phi = 53°$, Re = 3.3×10^5; $\phi = 62°$, Re = 3.3×10^5; and $\phi = 62°$, Re = 5.5×10^5; for TrSL-Open: $\phi = 64°$, Re = 1.1×10^5; and $\phi = 64°$, Re = 3.3×10^5. The TrSL (Transition in Shear Layers) regimes defined herewith does not have many common features with the TrSL described by Zdravkovich (1997) for much lower Re numbers of Re = 350 - 400 to 1×10^3 - 2×10^3, however the same terminology was used because phenomenological, a transition towards turbulent flow takes place in the shear layers in the currently investigated cases. One major difference is that the shear layers for the inclined cables analyzed in the current research will detach from the cylinder, and will intersect downstream the cylinder thereafter, the plume of turbulent wake being generated. While for most of the regimes described by Zdravkovich (1997), the shear layers detach from the sides of the cylinder, and the evolution of the wake takes place between the upper and lower shear layers and immediately behind the cylinder.

A general expression for the theoretical aerodynamic damping derived by MacDonald and Larose (2006) based on the quasi-steady theory was used, with the data from this study, to estimate of the localized derivatives with respect to Reynolds number ($\partial C_D/\partial$Re and $\partial C_L/\partial$Re) and cable-wind angle ($\partial C_D/\partial\phi$ and $\partial C_L/\partial\phi$). It was found that the following four cases indicated that possibility of an aerodynamic instability:: $\alpha = 54.7°$, $\beta = 40°$, $\phi = 63.7°$, Re = 3.3×10^5; $\alpha = 60°$, $\beta = 0°$, $\phi = 60°$, Re = 4.4×10^5; $\alpha = 54.7°$, $\beta = 20°$, $\phi = 57.1°$, for Re = 4.4×10^5; $\alpha = 50°$, $\beta = 20°$, $\phi = 52.8°$, for Re = 4.4×10^5.

This is the typical range known as critical cases for the yawed and inclined cylinders, because aerodynamic instability was reported for the relative angle of 60° and the Reynolds number in the 3.3×10^5 to the 4.4×10^5. These inclinations and yaw angles are similar to the cases noted by Cheng et al (2008) for their critical onset for their static model tests. In the Cheng et al (2008) study, the inclination and yaw angles for the two cases of instability were $\alpha = 54.7°$ and $\beta = 30°$, and $\alpha = 60°$ and $\beta = 0°$, but at slightly lower Re than this study. Other cases at lower Reynolds number were noticed to tend to aerodynamic instability in this study, but may be due to the calculation of the derivatives, and the influence of the relative angle.

The Fast Fourier transforms were calculated for the drag coefficients, lift coefficients, pressures along the leeward point of the cylinder, and the velocity along the leeward side of the cylinder. Three cases were presented in detail in this study: $\alpha = 60°$, $\beta = 0°$, resulting in $\phi = 60°$ for a Re = 3.3×10^5; $\alpha = 50°$, $\beta = 20°$, resulting in $\phi = 53°$, with Re = 4.4×10^5; and $\alpha = 50°$, $\beta = 40°$; resulting in $\phi = 60.5°$, for Re = 3.3×10^5. The other cases were detailed in the Appendices L, M, N, and O. All three cases are mid-range Reynolds numbers within the drag crisis with the first case having a relative angle of 60°, and the second case having a relative slightly lower angle, of 53°. All three cases showed similar or the same evolution for the coefficient of drag, coefficient of lift, and the pressure at the leeward side of the cylinder.

The coherence and cross-coherence has been calculated between the coefficient of lift, the pressure coefficient along the leeward side of the cylinder, and the velocity fluctuation along the leeward side of the cylinder. The cross-bicorrelation which measures the relationship between three sets of variables in the time domain, and gives an indication of the persistence of that interaction was also reported. The cross-bispectrum density is the measure in the frequency domain of such interaction. The three cases highlighted above, namely, $\alpha = 60°$, $\beta = 0°$, $\phi = 60°$,

Re = 3.3 × 10^5; α = 50°, β = 20°, ϕ = 53°, Re = 4.4 × 10^5; and α = 50°, β = 40°; ϕ = 60.5°, for Re = 3.3 × 10^5, were used for the fast Fourier analysis with respect to the coefficient of drag, coefficient of lift, pressure along the leeward point of the cylinder, and the velocity along the leeward side of the cylinder. Coherence and cross-coherence between three of these variables were determined for the same cases. The cross-coherence results for the same three cases showed a consistent distribution, indicating a linear interaction among the variables. Both the coherence and cross-coherence did not show the same tendencies among the other cases, which can be found in Appendix P.

The cases demonstrating the TrSL-Short regime (Figure 5.2(c), (f), (i)), were also grouped together when looking at the velocity and pressure distributions on the leeward side of the cylinder. In particular, the pressure distribution along the cylinder, the magnitude of the axial flow along the cylinder, and the vector distribution showed the flow around the cylinder. One of the cases showed similar results for the Fast Fourier analysis of the coefficient of drag, coefficient of lift, and the pressure at the leeward side of the cylinder, and thus it was identified as a case for possible aerodynamic instability. The case is for cable inclination of α = 50°, cable yaw of β = 20°, and relative angle of ϕ = 53°, at Re = 4.4 × 10^5. This illustrates some of the conditions are possibly required for the aerodynamic instability of the cylinder, in particular the velocity and pressure distributions along the leeward side of the cylinder, and a TrSL-Short flow regimes as defined in this study.

Limited number of experimental results are available showing the flow visualization for flow inclined to a cylinder. If visualizations do exist, these are for a limited length of the cylinder showing limited turbulent formations along the length of the cylinder. In addition to further experimental testing focused on the development of the instability phenomenon discussed in this

study, flow visualization should be performed to better understand the flow occurring during the aerodynamic instabilities, but also for comparison to numerical results for convergence studies.

The cases $\alpha = 60°$, $\beta = 20°$, $\phi = 62°$, and $\alpha = 50°$, $\beta = 40°$, $\phi = 60.5°$ for $\mathrm{Re} < 3.3 \times 10^5$ also show indications of aerodynamic instability in this study. Again, the relative angle between the wind direction and cylinder of approximately $\phi = 60°$ was present in both cases. The cause of instability is due to the large change in the lift coefficient variation at ϕ close to 60°, for all cases investigated in this study, when using the local derivatives. More investigations are required for clarifying the effect of cable inclination angle (α) and yaw angle (β) on this large variation of lift coefficient for this relative angle of attack (ϕ).

An advantage of conducting numerical studies is the ability to use a continuous or repetitive computational domain. The wind tunnel studies, and the computational investigations shown are for a limited length of a stay cable due to the size limitations of the wind tunnel, or the computational resources restrains for solving the problem at hand. This is not the case for a full scale stay cable, which could have the required length of the segment being studied. The use of a periodic or cyclic boundary conditions could be used to help model this full scale condition more accurately. Computational models like the one used in this study are valuable for helping understanding the simulation conditions within the wind tunnel tests for flow around an inclined cylinder, including the effects of the boundary conditions created by the presence of the wind tunnel wall.

Four cases were highlighted as cases showing the possibility of developing aerodynamic instability:

$\alpha = 54.7°$, $\beta = 40°$, $\phi = 63.7°$, for $\mathrm{Re} = 3.3 \times 10^5$;

$\alpha = 60°$, $\beta = 0°$, $\phi = 60°$, for $\mathrm{Re} = 4.4 \times 10^5$;

$\alpha = 54.7°$, $\beta = 20°$, $\phi = 57.1°$, for Re = 4.4×10^5;

$\alpha = 50°$, $\beta = 20°$, $\phi = 52.8°$, for Re = 4.4×10^5.

These cases are among the critical cases known for encountering aerodynamic instability with the relative angle between the wind, and cylinder of 60°, and at Reynolds number in the range of 3.3×10^5 to the 4.4×10^5. Further clarification is required for the influence of the yaw angle for flow around a circular cylinder inclined to the flow especially around the relative angle of 60°. Wind tunnel tests could be performed to see if similar results can be obtained.

The natural wind contains a varying degree of turbulence. The effect of turbulence of the approaching wind speed should be examined, and the role this plays in the flow formation around the inclined and/or yawed circular cylinders, and the development of the axial flow. This could be done in both the computational domain and in the wind tunnel.

References

Andersen, T.L., Jakobsen, J.B., Macdonald, J.H.G., Nikitas, N., Larose, G.L., Savage, M.G., McAuliffe, B.R., (2009) Drag-crisis response of elastic cable-model, Eighth International Symposium on Cable Dynamics, Paris, France.

ANSYS, (2010) Theory Guide, CFX-Solver Modeling Guide.

ANSYS, (2010) Theory Guide, Large Eddy Simulation Theory.

Blazek, J., (2005) Computational Fluid Dynamics: Principles and Applications, Elsevier.

Blevins, R., (1997) Flow-induced Vibration, Van Nostrand Reinhold Company, New Yrk.

Breuer, M., (2000) A challenging test case for large eddy simulation: high Reynolds number circular cylinder flow, International Journal of Heat and Fluid Flow, 21, pp. 648-654.

Boujard, O., Grillaud, G., (2007) Inclined stay-cable vibrations: confrontation of full-scale measurements and quasi-steady analysis of wind-tunnel tests, International Conference in Wind Engineering, Cairns, pp. 927-934.

Catalano, P., Wang, M., Iaccarino, G., Moin, P., (2003) Numerical simulation of the flow around a circular cylinder at high Reynolds numbers, International Journal of Heat and Fluid Flow, 24, pp. 463-469.

Chen, W., Duan, L., (1999) Bridge Engineering Handbook, CRC Press, New York.

Cheng, S., Tanaka, H., (2002) Dynamics of dry inclined cables, Proceedings of the 2nd International Symposium on Advances in Wind and Structures, Busan, pp. 361-368.

Cheng, S., Irwin, P.A., Jakobsen, J.B., Lankin, J., Larose, G.L., Savage, M.G., Tanaka, H., Zurell, C., (2003) Divergent motion of cables exposed to skewed wind, Proceedings of the 5th International Symposium on Cable Dynamics, Santa Margherita, pp. 271-278.

Cheng, S., Tanaka, H., (2003) Correlation of aerodynamic forces on inclined circular cylinder, Proceedings of the 5th International Symposium on Cable Dynamics, Santa Margherita, pp. 361-369.

Cheng, S., Tanaka, H., Irwin, P.A., Jakobsen, J.B., (2003) Aerodynamic instability of inclined cables, Proceedings of the 5th International Symposium on Cable Dynamics, Santa Margherita, pp. 69-76.

Cheng, S., Larose, G.L., Savage, M.G., Tanaka, H., Irwin, P.A., (2008) Experimental study on the wind-induced vibration of a dry inclined cable—Part I: Phenomena. Journal of Wind Engineering and Industrial Aerodynamics, 96, pp. 2231-2253.

Cheng, S., Raeesi, A., Ting, D., (2011) Advances in the understanding of wind-induced cable vibration phenomena in the subcritical Reynolds number regimes. Canadian Society of Civil Engineering National Conference, Ottawa, pp. GC-1-GC-10.

Chou, P.Y., (1945) On velocity correlations and the solutions of the equations of turbulent fluctuations, Quarterly of Applied Mathematics, 3, pp. 38-45.

Coutanceau, M., Defaye, J-R, (1991) Circular Cylinder Wake Configurations: A Flow Visualization Survey, Applied Mechanics Reviews, Vol. 44, No 6, pp. 255-305.

Chung, T.J., (2010) Computational Fluid Dynamics, 2nd Edition, Cambridge University Press.

Deardorff, J.W., (1970). A numerical study of three-dimensional turbulent channel flow at large Reynolds numbers, Journal of Fluid Mechanics, 41, pp 453-480.

Elgar, S., Van Atta, C.W., Gharib, M., (1990) Cross-bispectral analysis of a vibrating cylinder and its wake in low Reynolds number flow, Jounal of Fluid and Structures, 4, pp. 59-71.

ESDU, (1980) Mean forces pressure and flow velocities for circular cylindrical structures. External Report no. 80025.

FHWA/HNTB, (2005) Wind induced vibration of stay cables. Interim final report, RDT 05-004.

FHWA, (2007) Wind-Induced Vibration of Stay Cables, U.S. Department of Transportation, Federal Highway Administration, Publication No. FHWA-HRT-05-083.

Fox, R.W., Pritchard, P.J., McDonald, A.T., (2009), Introduction to Fluid Mechanics, 7th Edition, John Wiley and Sons, Inc.

Ge, Y., (2011) Challenging aerodynamic concerns of cable-supported bridges with super long span, The 13th International Conference on Wind Engineering, Amsterdam.

Germano, M., Piomelli, U., Moin, P., Cabot, W.H., (1991) A dynamic subgrid-scale eddy viscosity model, Physics of Fluids A: Fluid Dynamics 3 (7), pp. 1760-1765.

Hajj, M.R., Miksad, R.W., Powers, E.J., (1991) Experiments on the effect of mean flow unsteadiness on the subharmonic growth in a plane mixing layer. Advances in Turbulence 3/Proceedings of the Third European Turbulence Conference, pp. 155-161.

Hikami, Y., Shiraishi, N., (1988) Rain-wind Vibrations of Cables in Cable Stayed Bridges, Journal of Wind Engineering and Industrial Aerodynamics, 29, pp. 409-418.

Hoang, M.C., Laneville, A., Legeron, F., (2015) Experimental study on aerodynamic coefficients of yawed cylinders, Journal of Fluids and Structures, 54, pp. 597-611.

Honda, A., Yamanaka, T., Fujiwara, T., Saito, T., (1995) Wind tunnel test on rain-induced vibration of the stay-cable, Proceedings of the 1st International Symposium on Cable Dynamics, Liege, pp. 255-262.

Irwin, H. M., (1981) Cable Structures, MIT Press, Cambridge, Massachusetts.

Irwin, P., (1997) Wind Vibrations of Cables on Cable-Stayed Bridges, Proceedings of the Structures Congress XV, Portland, pp. 383-387.

Irwin, P., Alca, N., Telang., N., (1999) Wind Induced Stay Cable Oscillations – A Case Study, Proceedings of the 3rd International Symposium on Cable Dynamics, Trondheim, pp. 171-176.

Jakobsen, J.B., Andersen, T.L., Macdonald, J.H.G., Nikitas, N., Larose, G.L., Savage, M.G., McAuliffe, B.R., (2012) Wind-induced response and excitation characteristics of an inclined cable model in the critical Reynolds number range, Journal of Wind Engineering and Industrial Aerodynamics, 110, pp. 100-112.

Kalro, V., Tezduyar, T., (1997) Parallal 3D computation of unsteady flows around circular cylinders. Parallel Computing, 23, pp. 1235-1248.

Katsuchi, H., Yamada, H., (2009) Surface pressure and axial flow measurements for indented-surface stay cable. Proceedings of 8th International Symposium on Cable Dynamics '09, Paris, France 215 - 222.

Kawamura, T., Tsutomu, T., (1994) Computation of flow around a yawed circular cylinder. Japan Society of Mechanical Engineers International Journal, Series B, 37(2), 229–236.

Kim, H., Kitagawa, T., (2011) Numerical investigation of wake galloping around two circular cylinders, International Conference on Wind Engineering, Amsterdam.

Koochesfahani, M.M., (1989) Vertical patterns in the wake of an oscillating airfoil, American Institute of Aeronautics and Astronautics Journal, Vol. 27, No. 9, pp 1200-1205.

Larose, G.L., Zan, S.J., (2001) The aerodynamic forces on the stay cables of cable-stayed bridges in the critical Reynolds number range, Proceedings of the 4th International Symposium on Cable Dynamics, Montreal, pp. 77-84.

Larose, G.L., Savage, M.G., Jakobsen, J.B., (2003) Wind tunnel experiments on an inclined and yawed circular cylinder in the critical Reynolds number range. Proceedings of the Eleventh International Conference on Wind Engineering, Lubbock, TX, pp. 1705–1712.

Lilly, D.K., (1992) A proposed modification of the Germano subgrid-scale closure method", Physics of Fluids A: Fluid Dynamics 4 (3), pp. 633-635.

Macdonald, J.H.G., Larose, G.L., (2003) Two-degree-of-freedom inclined cable galloping—Part 1: General formulation and solution for perfectly tuned system. Journal of Wind Engineering and Industrial Aerodynamics, 96, pp. 291-307.

MacDonald, J.H.G., (2005), Quasi-steady analysis of 2DOF inclined cable galloping in the critical Reynolds number range, Proceeding of the 6th International Symposium on Cable Dynamics, Charleston.

Macdonald, J.H.G., Larose, G.L. (2006) A unified approach to aerodynamic damping and drag/lift instabilities, and its application to dry inclined cable galloping, Journal of Fluids and Structures.

Main, J.A., Jones, N.P., (1999) Full-scale measurements of stay cable vibration, International Conference in Wind Engineering, Copenhagen, Denmark.

Matsumoto, M., Shiraishia, N., Kitazawab, M., Kniselya, C., Shiratoa, H., Kimc, Y., Tsujiia, M., (1990). Aerodynamic behaviour of inclined circular cylinders-cable aerodynamics, Jounal of Wind Engineering and Industrial Aerodynamics, 33 (1-2), pp. 63-72.

Matsumoto, M., Shiraishi, N., Shirato, H., (1992) Rain-wind Induced Vibration of Cables of Cable-stayed Bridges, Journal of Wind Engineering and Industrial Aerodynamics, 41-44, pp. 2011-2022.

Matsumoto, M., Yamagishi, M., Aoki, J., Shiraishi, N., (1995) Various Mechanisms of Inclined Cable Aerodynamics, Proceedings of the 9th International Conference Wind Engineering, New Delhi, Volume 2, pp. 759-770.

Matsumoto, M., Shirato, H., Yagi, T., Goto, M., Sakai, S., Ohya, J. (1995) Field Observation of th Full-Scale Wind-Induced Cable Vibration, Journal of Wind Engineering and Industrial Aerodynamics, 91, pp. 13-26.

Matsumoto, M., Shigemura, Y., Daito, Y., Kanamura, T., (1997) High Speed Vortex Shedding Vibration of Inclined Cables, Proceedings of the 2nd International Symposium on Cable Dynamics, Tokyo, pp. 27-35.

Matsumoto, M. (1998) Observed Behaviour of Prototype Cable Vibration and Its Generation Mechanism. Bridge Aerodynamics, Larsen & Esdahl (eds.), Balkema, Rotterdam, pp. 189-211.

Matsumoto, M., Yagi, T., Shigemura, Y., Tsushima, D., (2001) Vortex-induced cable vibration of cable-stayed bridges at high reduced wind velocity, Journal of Wind Engineering and Industral Aerodynamics, 89, pp. 633-647.

Matsumoto, M., Yagi, T., Goto, M., Sakai, S., (2003) Rain-wind-induced vibration of inclined cables at limited high reduced wind velocity region, Journal of Wind Engineering and Industral Aerodynamics, 91, pp. 1-12.

Matsumoto, M., Shirato, H., Yagi, T., Goto, M., Sakai, S., Ohya, J., (2003) Field Observation of the full-scale wind-induced cable vibration, Journal of Wind Engineering and Industral Aerodynamics, 91, pp. 13-26.

Matsumoto, M., Yagi T., Hatsudab, H., Shimac, T., Tanakad, M., Naitoa, H., (2010) Dry galloping characteristics and its mechanism of inclined/yawed cables. Journal of Wind Engineering and Industrial Aerodynamics, 98: 317-327.

Mittal, S., (2001) Computation of three-dimensional flow past circular cylinder of low aspect ratio, Physics of Fluids, 13, pp. 177-191.

Miyata, T., Yamada, H., Hojo, T., (1994) Aerodynamic response of PE stay cables with pattern indented surface, Proceeding of the International Conference on Cable-Stayed and Suspension Bridges, Deauville, pp. 515-522.

Pastò, S., (2008) Vortex-induced vibrations of a circular cylinder in laminar and turbulent flows. Jounal of Fluid and Structures, 24, pp. 977-993.

Pezeshki, C., Elger, S., Krishna, R., Burton, T.D., (1992) Auto and cross-bispectral analysis of a system of two coupled oscillators with quadratic nonlinearities possessing chaotic motion. Journal of Applied Mechanics, Volume 59, pp. 657-663.

Poulin, S., Larsen, A., (2007) Drag loading of circular cylinders inclined in the along-wind direction, Journal of Wind Engineering and Industral Aerodynamics, 95, pp. 1350-1363.

Qingkuan, L., Matsumoto, M., Yagi, T., Hori, K., (2007) LES study on the mechanism of rain-wind vibration of cables of cable-stayed bridge, International Confernce on Wind Engineering, Cairns, pp. 895-902.

Qingkuan, L., Zhang, F., Wenyong, M., Yi, W., (2011) Experimental study on Reynolds number effect on dry cable galloping of stay cables, International Conference on Wind Engineering, Amsterdam.

Raeesi, A., Cheng, S., Ting, D., (2014) A two-degree-of-freedom aeroelastic model for the vibration of dry cylindrical body along unsteady air flow and its application to aerodynamic response of dry inclined cables. Journal of Wind Engineering and Industrial Aerodynamics, 130, pp. 108-124.

Raeesi, A., Cheng, S., Ting, D., (2016) Application of a three-dimensional aeroelastic model to study the wind induced response of bridge stay cables in unsteady wind conditions. Journal of Sound and Vibration, 375, pp. 217-236.

Ramsey, K., (2005) Monitoring and Mitigation of Stay-Cable Vibrations on the Fred Hartman and Veterans Memorial Bridges, Texas, Sixth International Bridge Engineering Conference, Boston, MA, pp. 547-555.

Roshko, H., Fiszdon, W., (1969) On the persistence of transition in the near-wake. Problems in Hydrodynamics and Continuum Mechanics, Philadelphia, SIAM, 606-16.

Ruscheweyh, H. P., (1999) Vortex-induced Vibrations – Physical Background, Risk and Reliability of Estimations, Wind Engineering into the 21st Century, Larsen, Larose & Livesey (eds.) Balkema, Rotterdam, Volume 1, pp. 545-549.

Ruscheweyh, H. P., (1999) The Mechanism of Rain-wind-induced Vibration, Wind Engineering into the 21st Century, Larsen, Larose & Livesey (eds.) Balkema, Rotterdam, Volume 2, pp. 1041-1047.

Saito, T., Matsumoto, M., Kitazawa, M., (1994) Rain-wind excitation of cables on cable- stayed Higashi-Kobe Bridge and cable vibration control. Proceedings of the International Conference A.I.P.C.-F.I.P. Cable-Stayed and Suspension Bridges, pp. 507–514.

Selvam, R.P., (1997) Finite element modelling of flow around a circular cylinder using LES, Journal of Wind Engineering and Industral Aerodynamics, 67 & 68, pp. 129-139.

Shirakashi, M., Ishida, Y., Wakiya, S., (1985) Higher velocity resonance of circular cylinder in crossflow, Journal of Fluids Engineering ASME, 107, pp. 392-396.

Silva, W.A., Strganac, T.W., Hajj, M.R., (2005) Higher-order spectral analysis of a nonlinear pitch and plunge apparatus. Proceedings of the 46th American Institute of Aeronautics and Astronautics, pp. 1-20.

Simiu, E., Scanlan, R.H., (1978) Wind Effects of Structures: An Introduction to Wind Engineering. John Wiley & Sons, New York.

Simiu, E., Scanlan, R.H., (1987) Wind Effect on Structures. 1st ed., John Wiley & Sons, New York, NY, USA.

Singh, S.P., Mittal, S., (2004) Energy spectra of flow past a circular cylinder, International Journal of Computational Fluid Dynamics, 18, pp. 671-679.

Singh, S.P., Mittal, S., (2005) Flow past a cylinder: shear layer instability and drag crisis, International Journal for Numerical Methods in Fluids, 47, pp. 75-98.

Smagorinsky, J., (1963) General circulation experiments with the primitive equations, Monthly Weather Review, 91, pp. 99-164.

Starossek, U., (1994) Cable Dynamics – A Review, Structural Engineering International, 3/94, pp. 171-176.

Stoyanoff, S., Goodyear, D., Neff, T.L., (2009) PTI Recommendations for Stay Cables - Wind Design Considerations, Proceedings of the 8th International Symposium on Cable Dynamics, Paris, pp. 269-276.

Stubler, J., Ladret, P., Domage, J.B., Peltier, M., (1999) Bridge Stay Cable Vibration: Phenomena, Criteria and Damper Technology, Proceedings of the 3rd International Symposium on Cable Dynamics, Trondheim, pp. 163-170.

Swami, A., Mendel, J.M., Nikias, C.L., (1998) Higher-Order Spectral Analysis Toolbox for Use with Matlab, The MathWorks.

Tutar, M., Holdø, A.E., (2001) Computational modelling of flow around a circular cylinder in sub-critical flow regime with various turbulence models, International Journal for Numerical Methods in Fluids, 35, pp. 763-784.

Van Atta, C.W., Gharib, M., (1987) Ordered and chaotic vortex streets behind circular cylinders at low Reynolds numbers. Journal of Fluid Mechanics, 174, pp. 113-133.

Van Diver, J.K., Jong, J.-Y., (1987) The relationship between in-line and cross-flow vortex-induced vibration of cylinders. Journal of Fluids and Structures, 1, pp. 381-399.

Verwiebe, C., (1998) Exciting Mechanisms of Rain-Wind-Induced Vibrations, Structural Engineering International, Volume 2, pp. 112-117.

Virlogeux, M. (1995) Design of Cables for Cable-Stayed Bridges: The Example of the Normandie Bridge, Proceedings of the International Symposium on Cable Dynamics, Liège, pp.13-31.

Virlogeux, M., (1998) Cable Vibrations in Cable-Stayed Bridges, Bridge Aerodynamics, Larsen & Esdahl (eds.), Balkema, Rotterdam, pp. 213-233.

Wang, X., Wu, Z., (2009) Dynamic Behaviour of Thousand-Meter Scale Cable-Stayed Bridge with Hybrid FRP Cables, Journal of Applied Mechanics, Vol. 12, pp. 935-943.

Williamson, C.H.K., (1996) Vortex Dynamics in the Cylinder Wake, Annual Review of Fluid Mechanics, Vol. 208, pp. 477-539

Yagi, T., Haito, H., Liang, Z., Shirato, H., (2009) Evaluation of aerodynamic forces on inclined cable in consideration of end conditions of model for wind tunnel tests, Eighth International Symposium on Cable Dynamics, Paris, pp. 151-158.

Yagi, T., Okamoto, K., Sakaki, I., Koroyasu, H., Liang, Z., Narita, S., Shirato, H., (2011) Modification of surface configurations of stay cables for drag force reduction and aerodynamic stabization, International Conference on Wind Engineering, Amsterdam.

Yeo, D., Jones, N.P., (2008) Investigation on 3-D characteristics of flow around a yawed and inclined circular cylinder. Journal of Wind Engineering and Industrial Aerodynamics 96: 1947-1960.

Yeo, D., Jones, N.P., (2010) Aerodynamic effects of strake patterns on flow around a yawed circular cylinder, The Fifth International Conference on Computational Wind Engineering, Chapel Hill, North Carolina.

Yeo, D., Jones, N.P., (2011) Effects of oscillation incoming flow on flow-induced forces on a yawed circular cylinder, International Conference on Wind Engineering, Amsterdam.

Yeo, N.C.G., Neshyba, S., (1976) Bispectrum and cross-bispectrum anaylsis of wind and currents off the Oregon coast: I development. School of Oceanography, Oregon State University

Yoshimura, T., Savage, M.G., Tanaka, H., (1995) Wind-induced Vibrations of Bridge Stay-cables, Proceedings of the International Symposium on Cable Dynamics, Liège, pp. 437-444.

Zdravkovich, M. M., (1997) Flow around Circular Cylinders Vol 1: Fundamentals. 1st ed., Oxford University Press, New York, NY, USA.

Zikanov, O., (2010) Essential Computational Fluid Dynamics, John Wiley & Sons, Inc.

Zurrel, C., (2004) Aerodynamics of circular cylinders inclined to airflow and wind-induced vibrations of dry inclined cable at high wind speeds. PhD Thesis, University of Ottawa. Ottawa, ON, Canada.

Zuo, D., Jones, N.P., (2010) Interpretation of field observations of wind- and rain-wind-induced stay cable vibrations. Journal of Wind Engineering and Industrial Aerodynamics, pp. 73-87.

Zuo, D., (2014) Full-scale measurement of wind pressure on the surface of an oscillating circular cylinders, Journal of Wind Engineering and Industrial Aerodynamics, 133, pp. 65-72.

Appendix A: Cable Vibrations of Cable-Stayed Bridges

Table: Summary of Observed cable vibrations and remedies (Stoyanoff et al., 2009)

Name	Location	Main Span (m)	Observation, likely excitation mechanism	Vibration Amplitude (m)	Remedy
Normandy	France	856	Cable vibration during steady 1-2 m/s winds	0.8	Viscous dampers installed
Skarnsundet	Norway	530	Single occurrence, low turbulent wind, parametric excitation, 13 m/s winds	0.8	Although vibrations were monitored no retrofit was implemented
Oresundsbron	Denmark-Sweden	490	Rain/Wind, Iced Galloping	0.5	Dashpot dampers
Second Severn	United Kingdom	456	Cable vibrations with and without rain	0.2-0.8	Cross cables installed
Kap Shui Mun	Hong Kong	430	Severe winds, rain/wind	LA	Friction dampers
Helgeland	Norway	425	Large cable vibrations; depending on deck motion	0.3	Cross cables installed
Meiko Nishi	Japan	406	Vibration during light wind rain/low wind speed	0.3	Cross cables installed
Työrn Bridge	Sweden	386	Vibration during light rain	N/A	Viscous dampers installed
Fred Hartman	USA	381	Rain/wind, dry galloping, motion induced vibration	>1.5	Passive viscous damper and cross-ties
Tenpozan	Japan	350	Vibration during rain and 10 m/s winds	1.0	-
Kohlbrandt	Germany	326	-	0.5	Viscous dampers installed
Brotonne	France	320	Vibration in 15 m/s winds	0.3	Viscous dampers installed
Dongting	China	310	Vibration with rainfall	N/A	MR dampers
Erazmus	Netherlands	284	Rain/wind, wind speed 14 m/s	0.7	Cross-ties
W/Steubenville	USA	250	Vibrations noted when winds are parallel to deck	0.3	Visco-elastic dampers installed in the tower
Yobuko	Japan	250	Vibration during light rain	0.5	Manila ropes attached to cables

Veterans' Memorial	Texas, USA	195	Rain/wind, vortex shedding, dry galloping	0.3	Passive viscous dampers and cross-ties
Aratsu	Japan	185	Vibration during light rain	0.3	Viscous dampers installed
Wandre	Belgium	168	Vibration during light rain and 10 m/s winds	0.3	Petroleum wax fill in the guide pipe
Ben-Ahin	Belgium	168	Vibration noted during light drizzle and 10 m/s	0.5	Petroleum wax grout/cross-cables
Puente Real	Spain	136	Strong vibrations, parametric excitation, rain/wind	0.4	Friction dampers proposed at tower
Alzette	Luxembourg	130	Vibration during drizzles and light winds	N/A	Neoprene guides inside the guide pipe at deck and petroleum wax in the guide pipe

Notes: 1. LA – Large amplitudes were reported without being quantified;

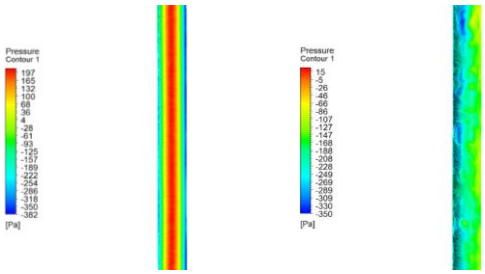
2. N/A – Although vibrations were reported no description was found.

Appendix B: Pressure Distribution on the Front Side and Leeward Side of the Cylinder Model

Figure B: Pressure distribution on the front side and leeward side of the cylinder model for:

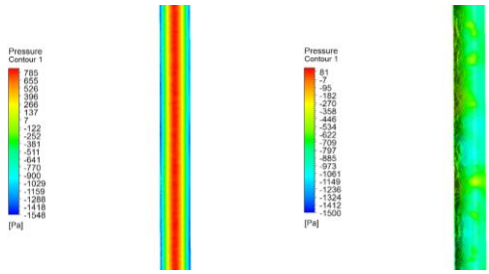
a) $\phi = 0°$; $\alpha = 0°$, $\beta = 0°$

i) Re = 1.1×10^5;



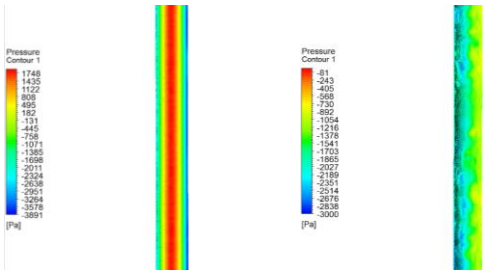
a) $\phi = 0°$; $\alpha = 0°$, $\beta = 0°$

ii) Re = 2.2×10^5;



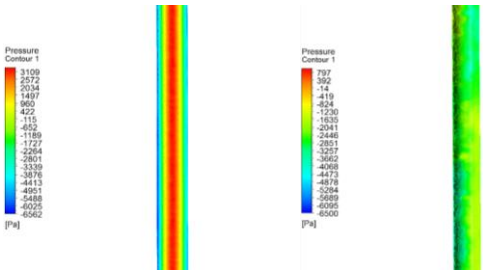
a) $\phi = 0°$; $\alpha = 0°$, $\beta = 0°$

iii) Re = 3.3×10^5;



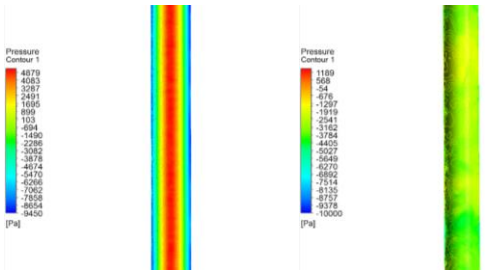
a) $\phi = 0°$; $\alpha = 0°$, $\beta = 0°$

iv) Re = 4.4×10^5;



a) $\phi = 0°$; $\alpha = 0°$, $\beta = 0°$

v) Re = 5.5×10^5;



a) $\phi = 0°$; $\alpha = 0°$, $\beta = 0°$

vi) Re = 6.7×10^5;

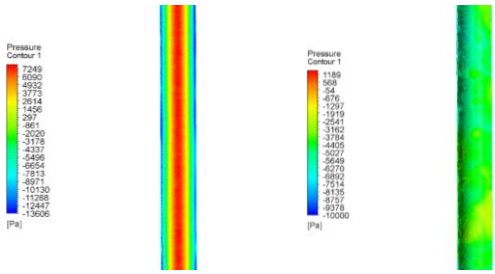
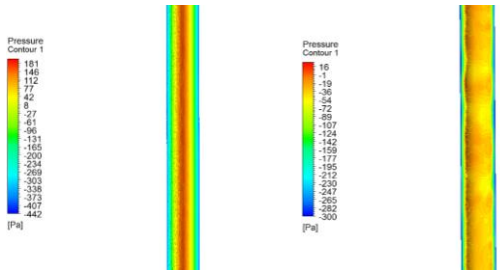


Figure B: Pressure distribution on the front side and leeward side of the cylinder model for:

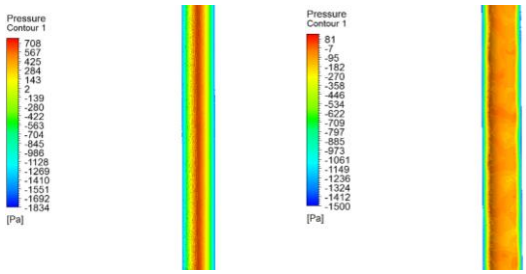
b) $\phi = 60°$; $\alpha = 60°$, $\beta = 0°$

i) Re = 1.1×10^5;



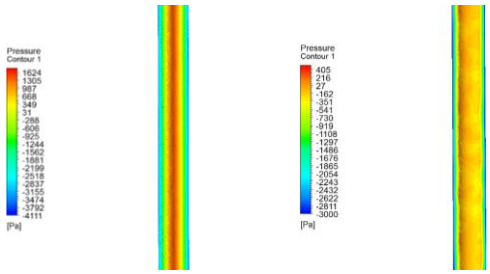
b) $\phi = 60°$; $\alpha = 60°$, $\beta = 0°$

ii) Re = 2.2×10^5;



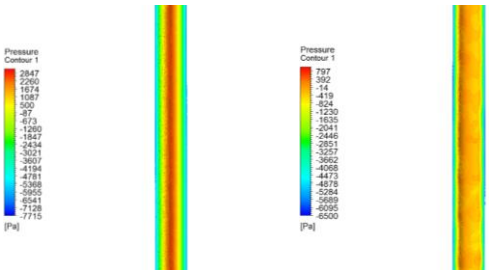
b) $\phi = 60°$; $\alpha = 60°$, $\beta = 0°$

iii) Re = 3.3×10^5;



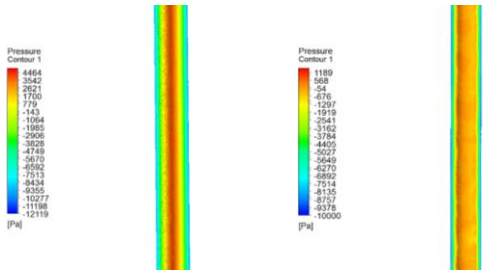
b) $\phi = 60°$; $\alpha = 60°$, $\beta = 0°$

iv) Re = 4.4×10^5;



b) $\phi = 60°$; $\alpha = 60°$, $\beta = 0°$

v) Re = 5.5×10^5;



b) $\phi = 60°$; $\alpha = 60°$, $\beta = 0°$

vi) Re = 6.7×10^5;

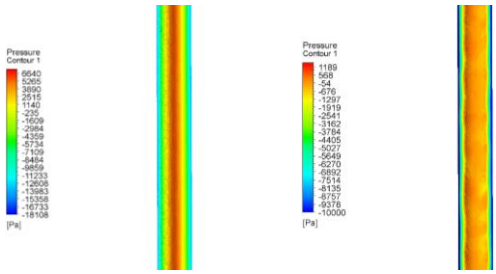
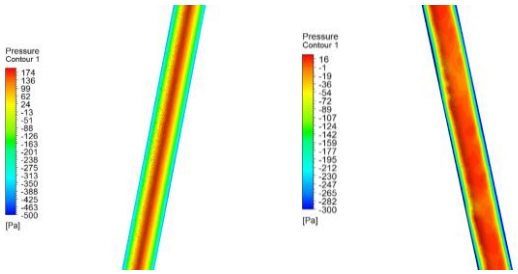
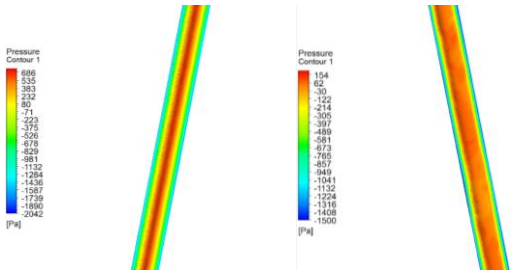


Figure B: Pressure distribution on the front side and leeward side of the cylinder model for:

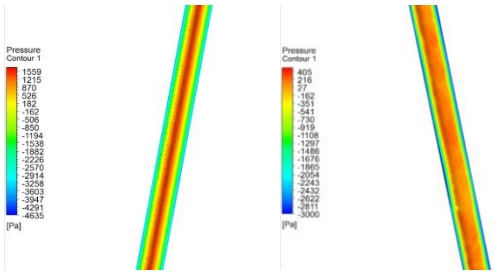
c) $\phi = 62°$; $\alpha = 60°$, $\beta = 20°$
i) Re = 1.1×10^5;



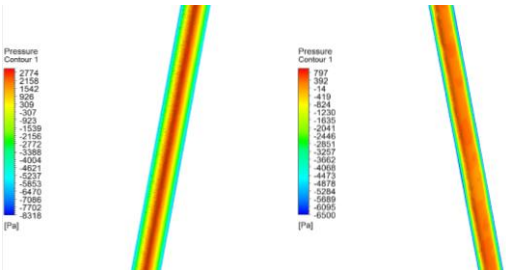
c) $\phi = 62°$; $\alpha = 60°$, $\beta = 20°$
ii) Re = 2.2×10^5;



c) $\phi = 62°$; $\alpha = 60°$, $\beta = 20°$
iii) Re = 3.3×10^5;



c) $\phi = 62°$; $\alpha = 60°$, $\beta = 20°$
iv) Re = 4.4×10^5;



c) $\phi = 62°$; $\alpha = 60°$, $\beta = 20°$
v) Re = 5.5×10^5;

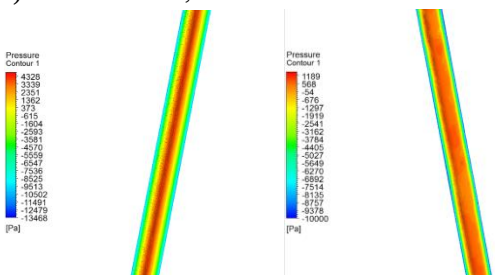
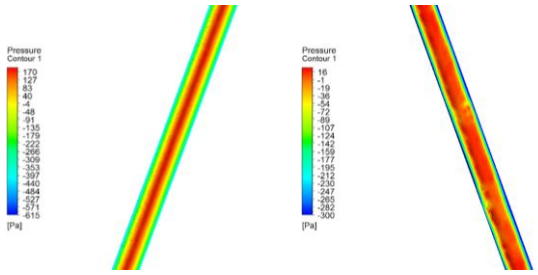
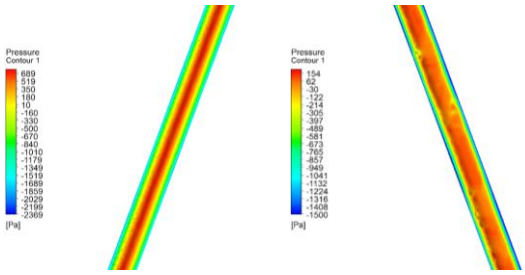


Figure B: Pressure distribution on the front side and leeward side of the cylinder model for:

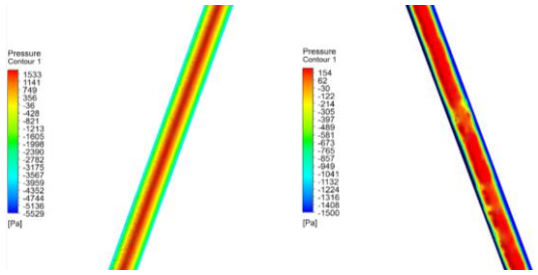
d) $\phi = 67.5°$; $\alpha = 60°$, $\beta = 40°$
i) Re = 1.1×10^5;



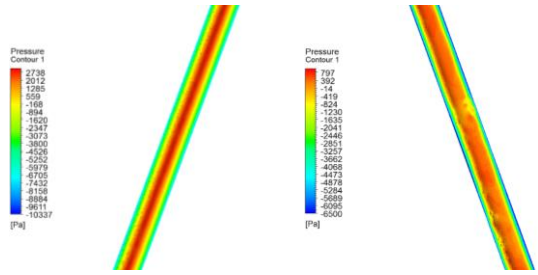
d) $\phi = 67.5°$; $\alpha = 60°$, $\beta = 40°$
ii) Re = 2.2×10^5;



d) $\phi = 67.5°$; $\alpha = 60°$, $\beta = 40°$
iii) Re = 3.3×10^5;



d) $\phi = 67.5°$; $\alpha = 60°$, $\beta = 40°$
iv) Re = 4.4×10^5;



d) $\phi = 67.5°$; $\alpha = 60°$, $\beta = 40°$
v) Re = 5.5×10^5;

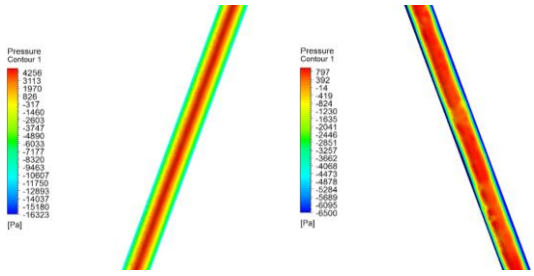
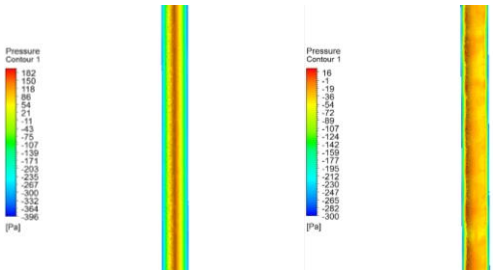
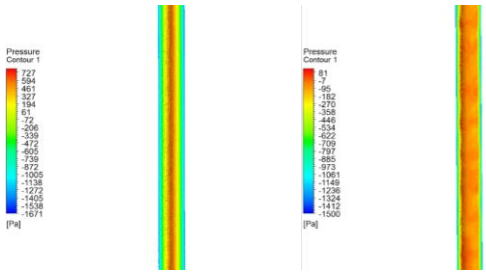


Figure B: Pressure distribution on the front side and leeward side of the cylinder model for:

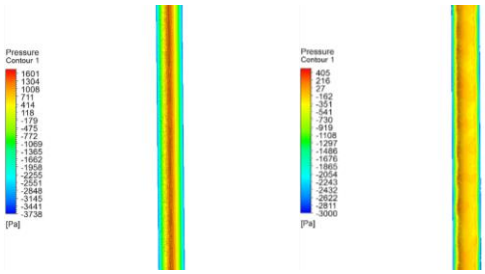
e) $\phi = 54.7°$; $\alpha = 54.7°$, $\beta = 0°$
i) Re = 1.1×10^5;



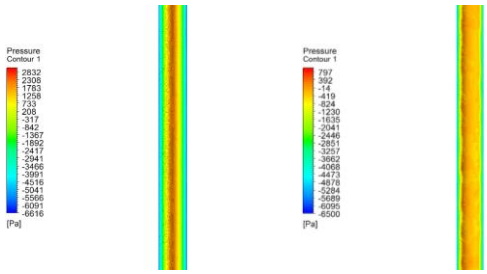
e) $\phi = 54.7°$; $\alpha = 54.7°$, $\beta = 0°$
ii) Re = 2.2×10^5;



e) $\phi = 54.7°$; $\alpha = 54.7°$, $\beta = 0°$
iii) Re = 3.3×10^5;



e) $\phi = 54.7°$; $\alpha = 54.7°$, $\beta = 0°$
iv) Re = 4.4×10^5;



e) $\phi = 54.7°$; $\alpha = 54.7°$, $\beta = 0°$
v) Re = 5.5×10^5;

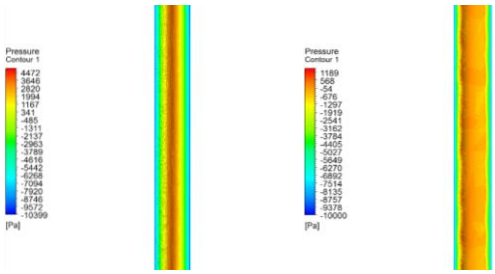
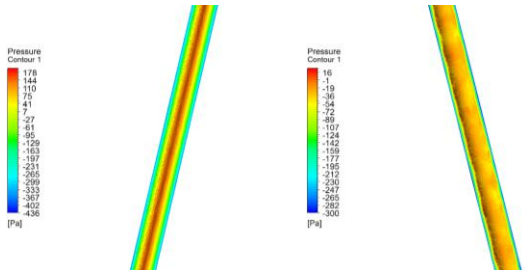
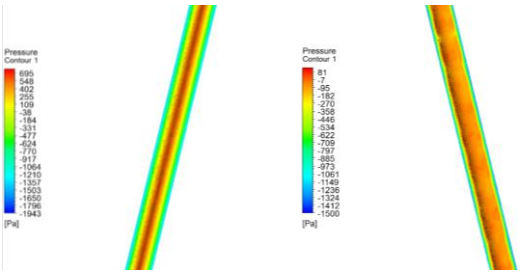


Figure B: Pressure distribution on the front side and leeward side of the cylinder model for:

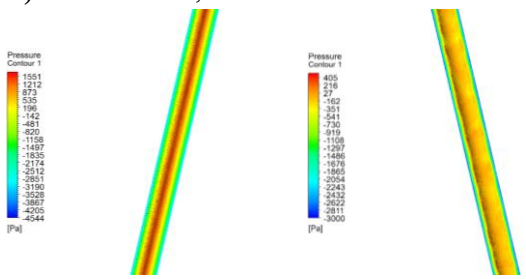
f) $\phi = 57.1°$; $\alpha = 54.7°$, $\beta = 20°$
i) Re = 1.1×10^5;



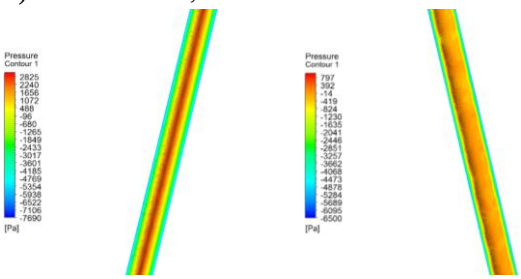
f) $\phi = 57.1°$; $\alpha = 54.7°$, $\beta = 20°$
ii) Re = 2.2×10^5;



f) $\phi = 57.1°$; $\alpha = 54.7°$, $\beta = 20°$
iii) Re = 3.3×10^5;



f) $\phi = 57.1°$; $\alpha = 54.7°$, $\beta = 20°$
iv) Re = 4.4×10^5;



f) $\phi = 57.1°$; $\alpha = 54.7°$, $\beta = 20°$
v) Re = 5.5×10^5;

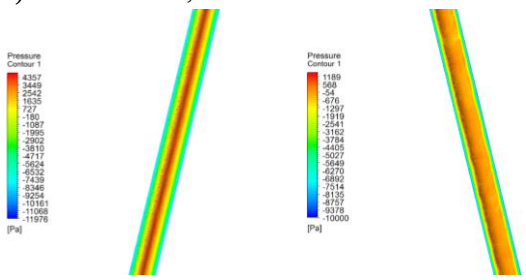
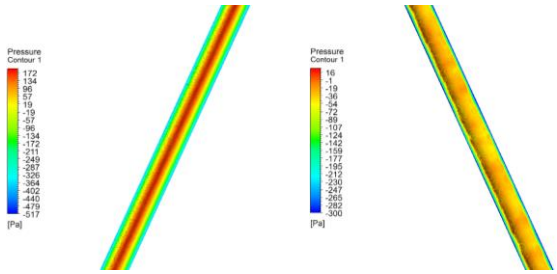
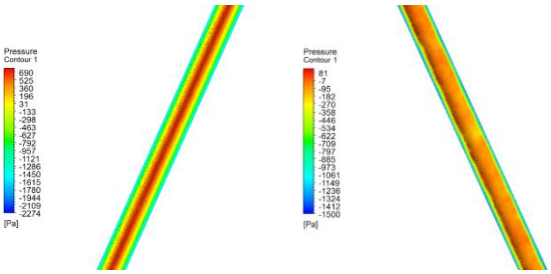


Figure B: Pressure distribution on the front side and leeward side of the cylinder model for:

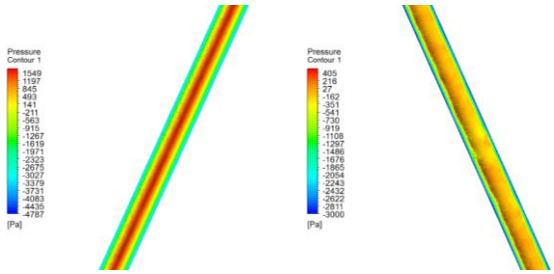
g) $\phi = 64°$; $\alpha = 54.7°$, $\beta = 40°$
i) Re = 1.1×10^5;



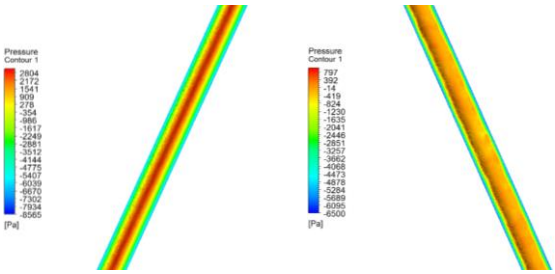
g) $\phi = 64°$; $\alpha = 54.7°$, $\beta = 40°$
ii) Re = 2.2×10^5;



g) $\phi = 64°$; $\alpha = 54.7°$, $\beta = 40°$
iii) Re = 3.3×10^5;



g) $\phi = 64°$; $\alpha = 54.7°$, $\beta = 40°$
iv) Re = 4.4×10^5;



g) $\phi = 64°$; $\alpha = 54.7°$, $\beta = 40°$
v) Re = 5.5×10^5;

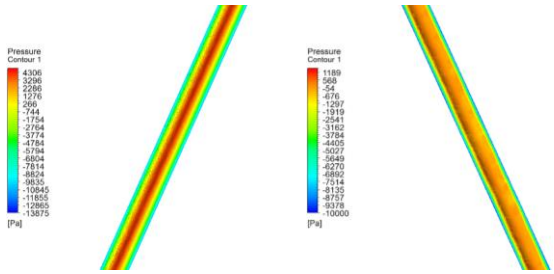
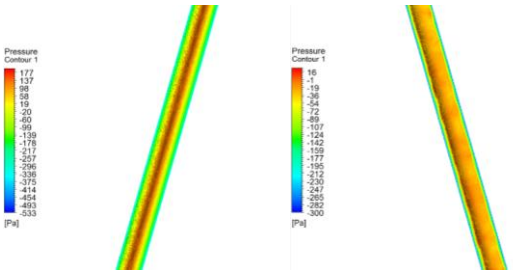
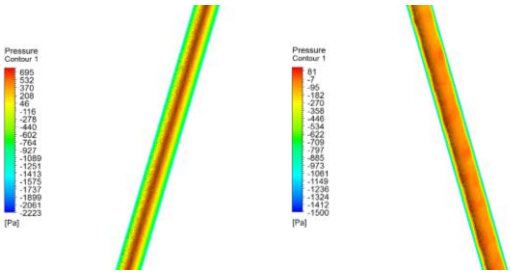


Figure B: Pressure distribution on the front side and leeward side of the cylinder model for:

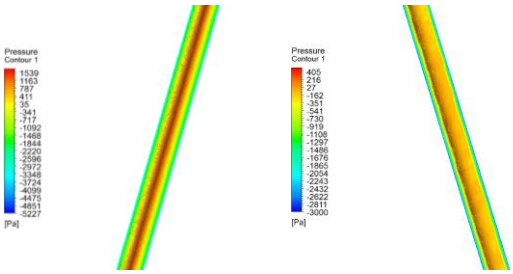
h) $\phi = 53°$; $\alpha = 50°$, $\beta = 20°$ i) Re = 1.1×10^5;



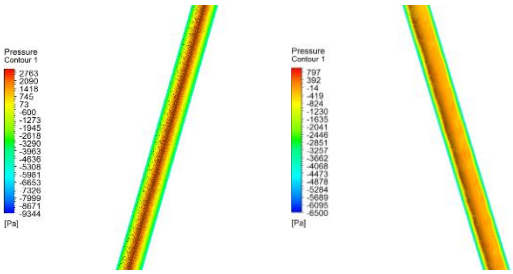
h) $\phi = 53°$; $\alpha = 50°$, $\beta = 20°$ ii) Re = 2.2×10^5;



h) $\phi = 53°$; $\alpha = 50°$, $\beta = 20°$ iii) Re = 3.3×10^5;



h) $\phi = 53°$; $\alpha = 50°$, $\beta = 20°$ iv) Re = 4.4×10^5;



h) $\phi = 53°$; $\alpha = 50°$, $\beta = 20°$ v) Re = 5.5×10^5;

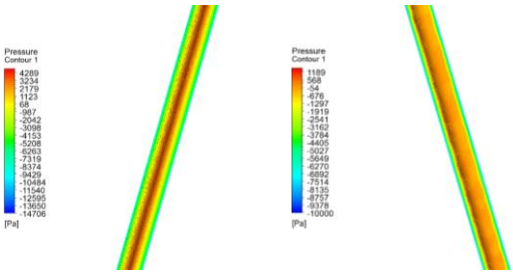
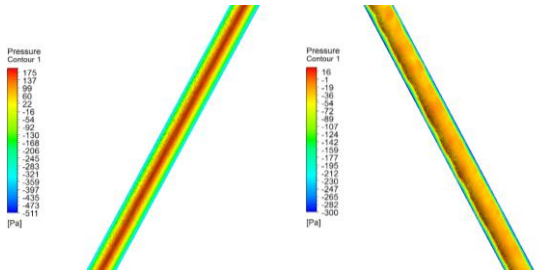
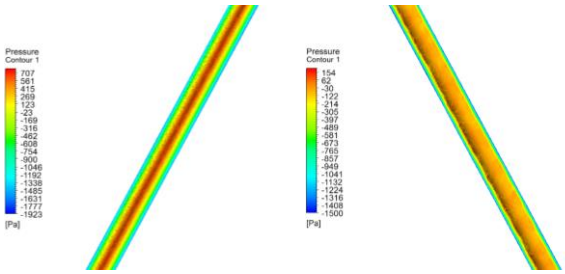


Figure B: Pressure distribution on the front side and leeward side of the cylinder model for:

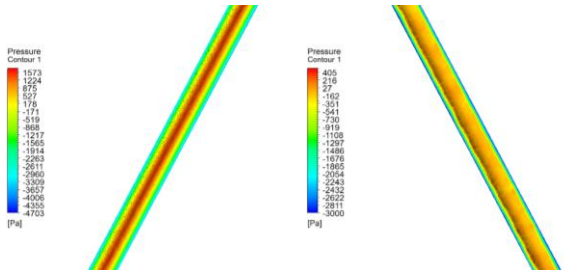
i) $\phi = 60.5°$; $\alpha = 50°$, $\beta = 40°$
Re = 1.1×10^5;



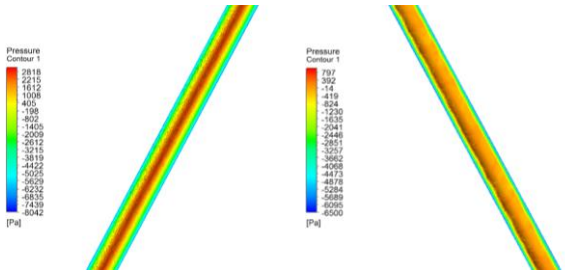
i) $\phi = 60.5°$; $\alpha = 50°$, $\beta = 40°$
Re = 2.2×10^5;



i) $\phi = 60.5°$; $\alpha = 50°$, $\beta = 40°$
Re = 3.3×10^5;



i) $\phi = 60.5°$; $\alpha = 50°$, $\beta = 40°$
Re = 4.4×10^5;



i) $\phi = 60.5°$; $\alpha = 50°$, $\beta = 40°$
Re = 5.5×10^5;

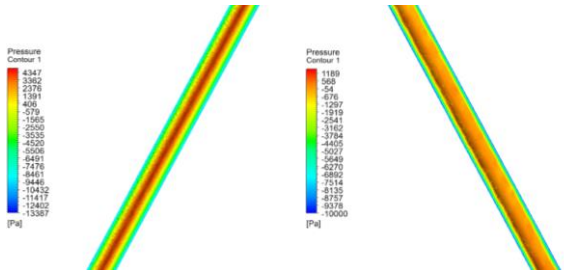
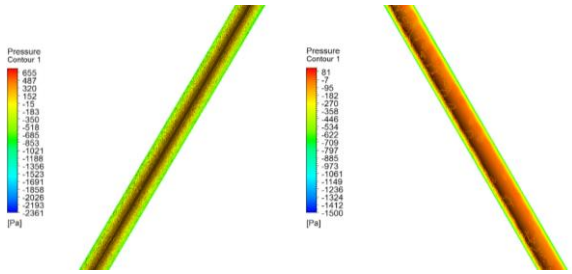
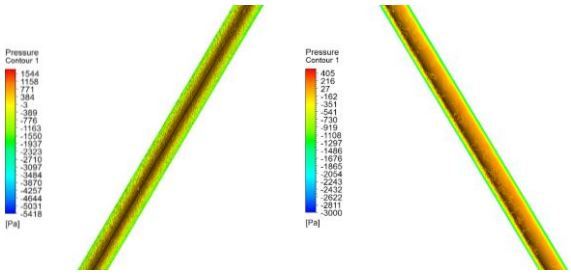


Figure B: Pressure distribution on the front side and leeward side of the cylinder model for:

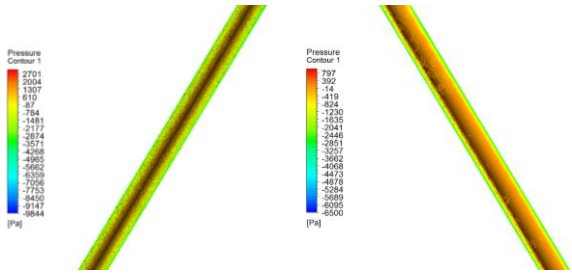
j) $\phi = 35.5°$; $\alpha = 30°$, $\beta = 20°$ ii) Re = 2.2×10^5;



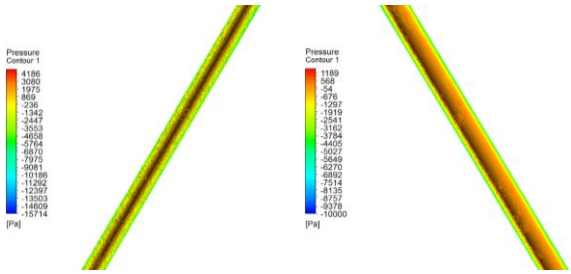
j) $\phi = 35.5°$; $\alpha = 30°$, $\beta = 20°$ Re = 3.3×10^5;



j) $\phi = 35.5°$; $\alpha = 30°$, $\beta = 20°$ Re = 4.4×10^5;



j) $\phi = 35.5°$; $\alpha = 30°$, $\beta = 20°$ Re = 5.5×10^5;

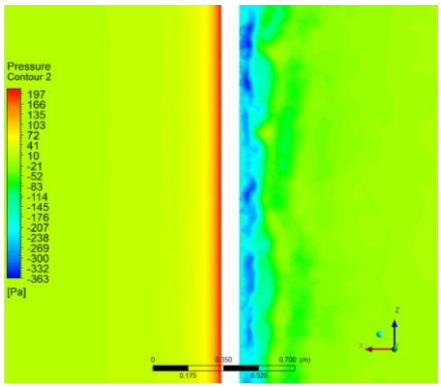


Appendix C: Pressure Distribution around the Cylinder

Figure C: Pressure distributions around the cylinder for:

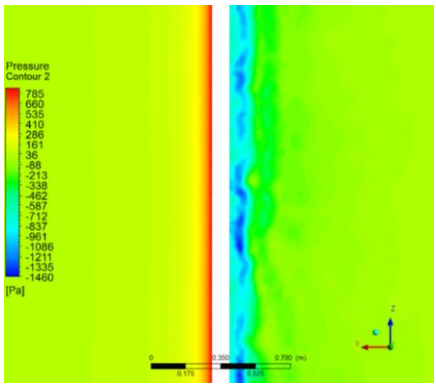
a) $\phi = 0°$; $\alpha = 0°$, $\beta = 0°$

i) Re = 1.1×10^5;



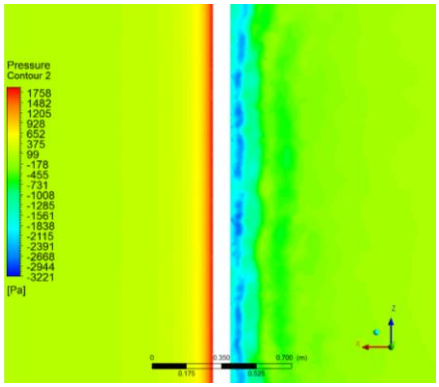
a) $\phi = 0°$; $\alpha = 0°$, $\beta = 0°$

ii) Re = 2.2×10^5;



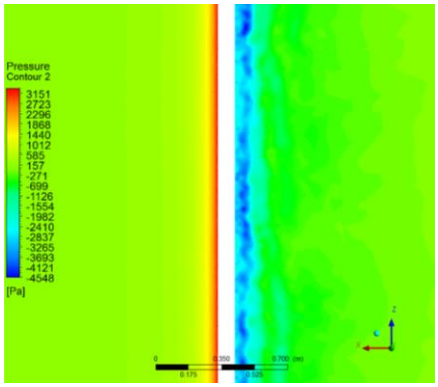
a) $\phi = 0°$; $\alpha = 0°$, $\beta = 0°$

iii) Re = 3.3×10^5;



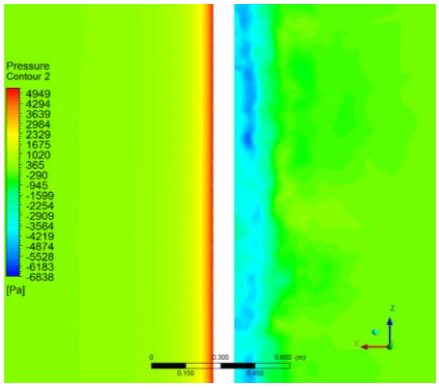
a) $\phi = 0°$; $\alpha = 0°$, $\beta = 0°$

iv) Re = 4.4×10^5;



a) $\phi = 0°$; $\alpha = 0°$, $\beta = 0°$

v) Re = 5.5×10^5;



a) $\phi = 0°$; $\alpha = 0°$, $\beta = 0°$

vi) Re = 6.7×10^5;

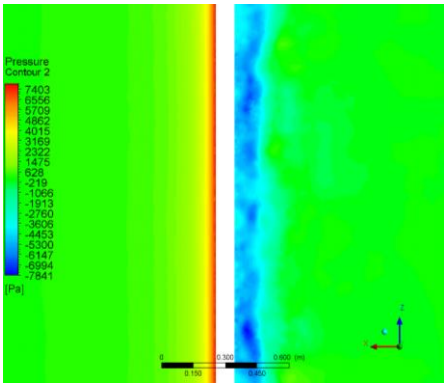
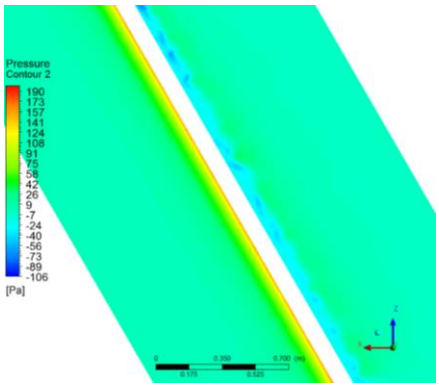
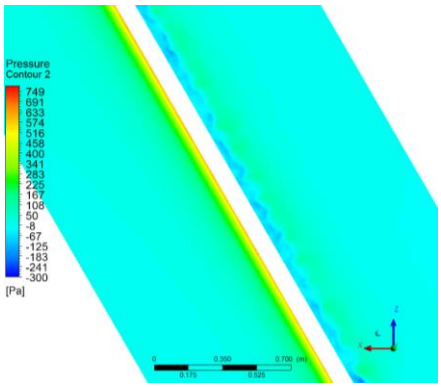


Figure C: Pressure distributions around the cylinder for:

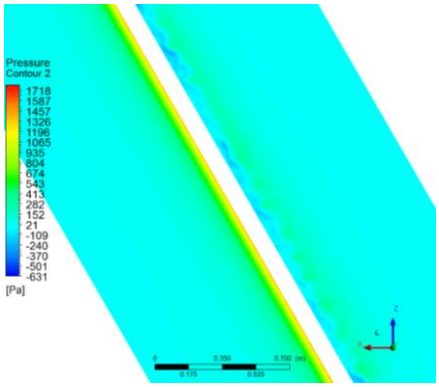
b) $\phi = 60°$; $\alpha = 60°$, $\beta = 0°$
i) Re = 1.1×10^5;



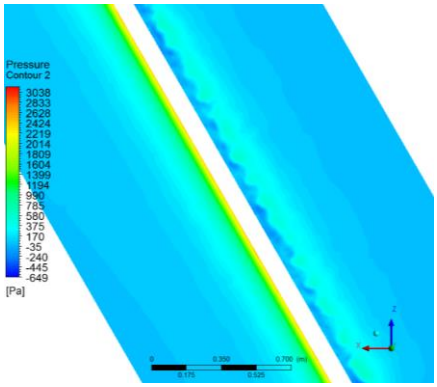
b) $\phi = 60°$; $\alpha = 60°$, $\beta = 0°$
ii) Re = 2.2×10^5;



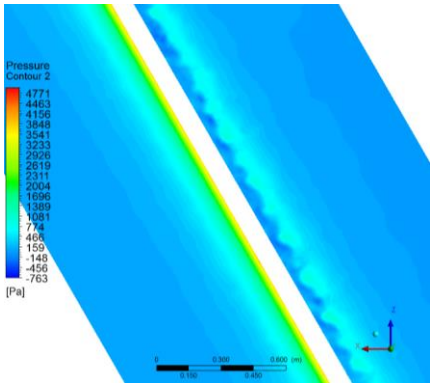
b) $\phi = 60°$; $\alpha = 60°$, $\beta = 0°$
iii) Re = 3.3×10^5;



b) $\phi = 60°$; $\alpha = 60°$, $\beta = 0°$
iv) Re = 4.4×10^5;



b) $\phi = 60°$; $\alpha = 60°$, $\beta = 0°$
v) Re = 5.5×10^5;



b) $\phi = 60°$; $\alpha = 60°$, $\beta = 0°$
vi) Re = 6.7×10^5;

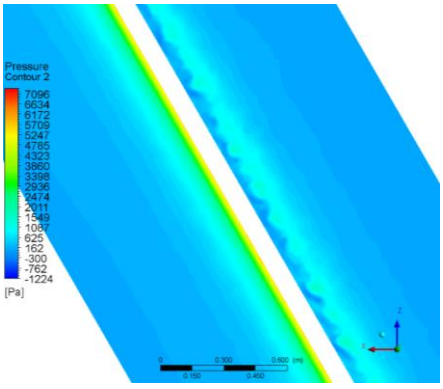
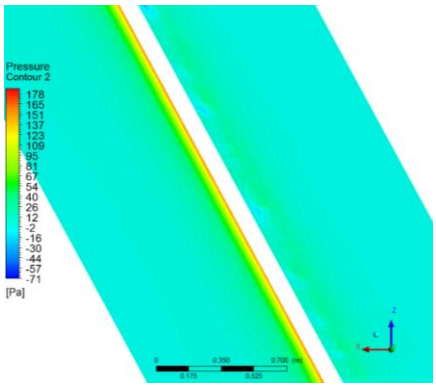
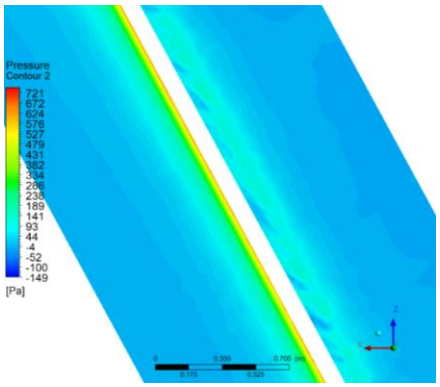


Figure C: Pressure distributions around the cylinder for:

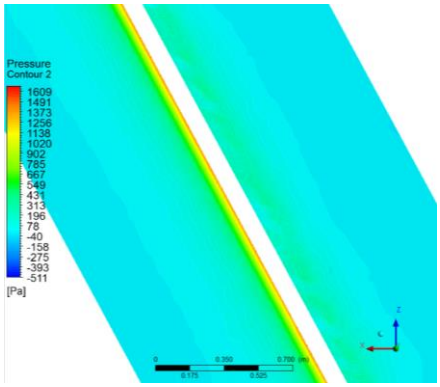
c) $\phi = 62°$; $\alpha = 60°$, $\beta = 20°$
i) Re = 1.1×10^5;



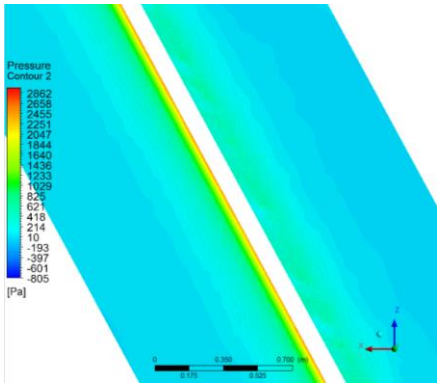
c) $\phi = 62°$; $\alpha = 60°$, $\beta = 20°$
ii) Re = 2.2×10^5;



c) $\phi = 62°$; $\alpha = 60°$, $\beta = 20°$
iii) Re = 3.3×10^5;



c) $\phi = 62°$; $\alpha = 60°$, $\beta = 20°$
iv) Re = 4.4×10^5;



c) $\phi = 62°$; $\alpha = 60°$, $\beta = 20°$
v) Re = 5.5×10^5;

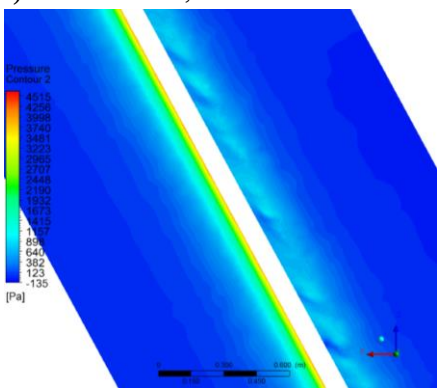
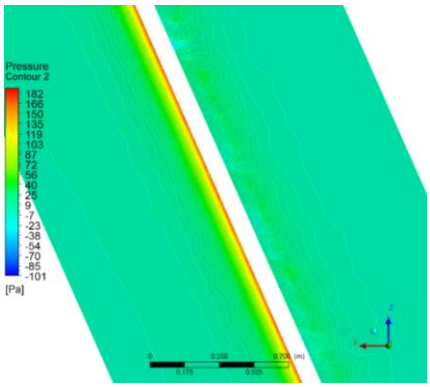
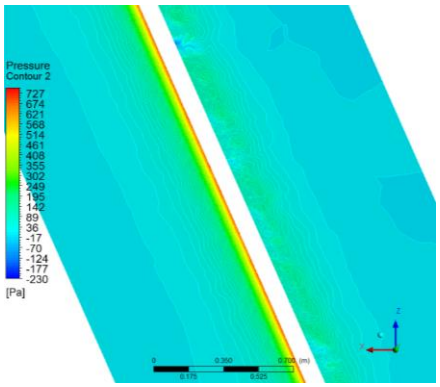


Figure C: Pressure distributions around the cylinder for:

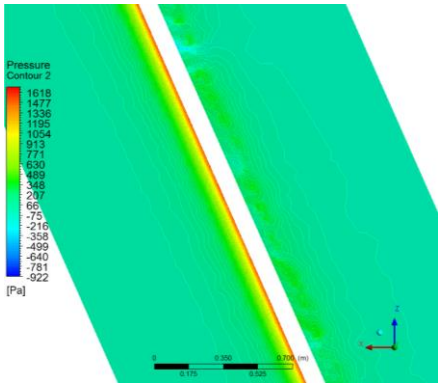
d) $\phi = 67.5°$; $\alpha = 60°$, $\beta = 40°$
i) Re = 1.1×10^5;



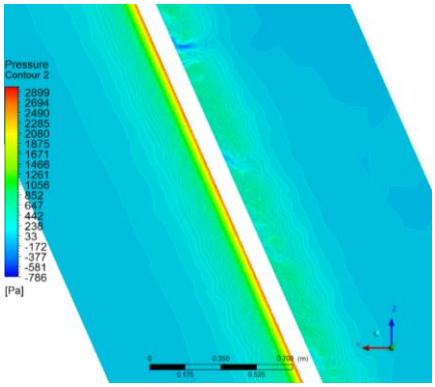
d) $\phi = 67.5°$; $\alpha = 60°$, $\beta = 40°$
ii) Re = 2.2×10^5;



d) $\phi = 67.5°$; $\alpha = 60°$, $\beta = 40°$
iii) Re = 3.3×10^5;



d) $\phi = 67.5°$; $\alpha = 60°$, $\beta = 40°$
iv) Re = 4.4×10^5;



d) $\phi = 67.5°$; $\alpha = 60°$, $\beta = 40°$
v) Re = 5.5×10^5;

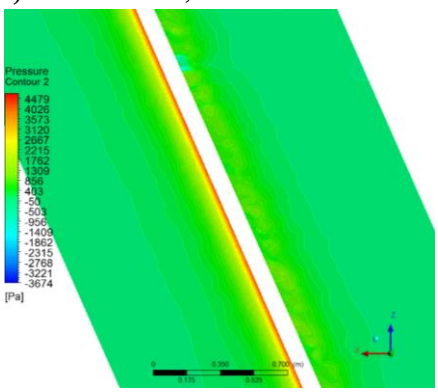
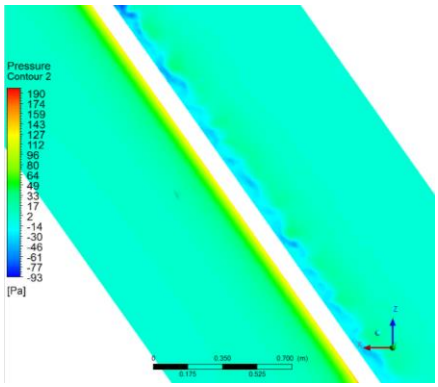
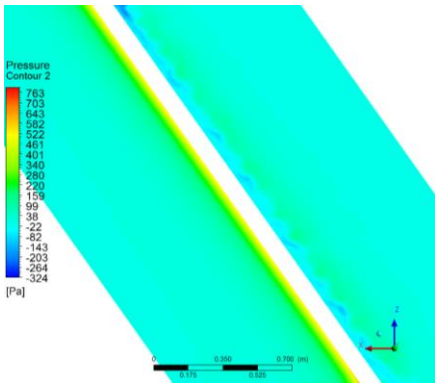


Figure C: Pressure distributions around the cylinder for:

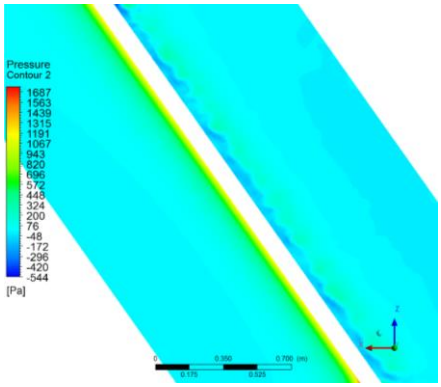
e) $\phi = 54.7°$; $\alpha = 54.7°$, $\beta = 0°$
i) Re = 1.1×10^5;



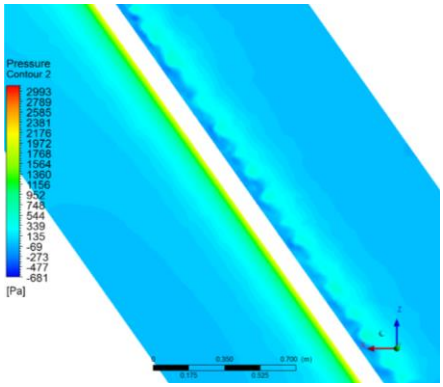
e) $\phi = 54.7°$; $\alpha = 54.7°$, $\beta = 0°$
ii) Re = 2.2×10^5;



e) $\phi = 54.7°$; $\alpha = 54.7°$, $\beta = 0°$
iii) Re = 3.3×10^5;



e) $\phi = 54.7°$; $\alpha = 54.7°$, $\beta = 0°$
iv) Re = 4.4×10^5;



e) $\phi = 54.7°$; $\alpha = 54.7°$, $\beta = 0°$
v) Re = 5.5×10^5;

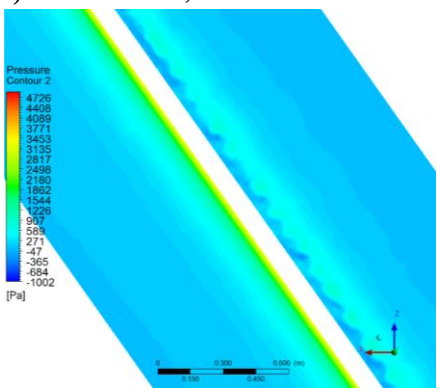
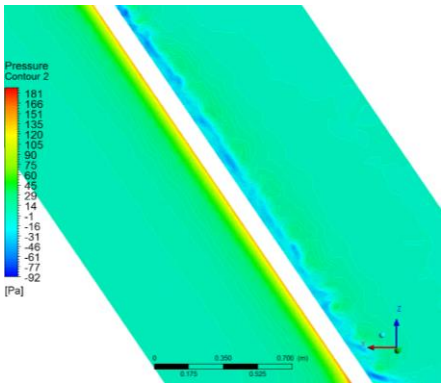
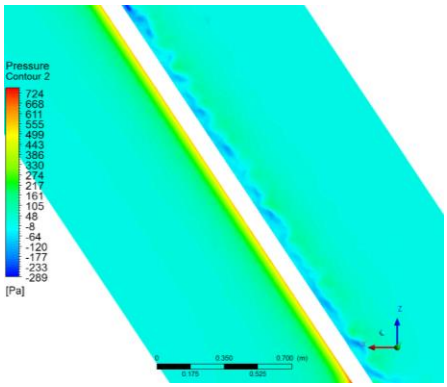


Figure C: Pressure distributions around the cylinder for:

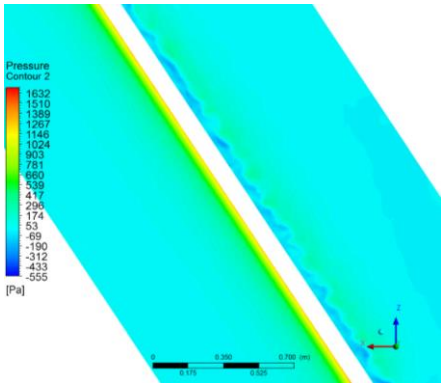
f) $\phi = 57.1°$; $\alpha = 54.7°$, $\beta = 20°$
i) Re = 1.1×10^5;



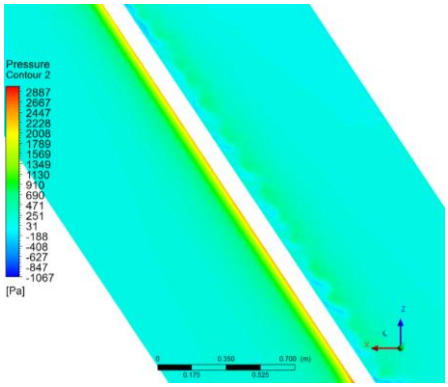
f) $\phi = 57.1°$; $\alpha = 54.7°$, $\beta = 20°$
ii) Re = 2.2×10^5;



f) $\phi = 57.1°$; $\alpha = 54.7°$, $\beta = 20°$
iii) Re = 3.3×10^5;



f) $\phi = 57.1°$; $\alpha = 54.7°$, $\beta = 20°$
iv) Re = 4.4×10^5;



f) $\phi = 57.1°$; $\alpha = 54.7°$, $\beta = 20°$
v) Re = 5.5×10^5;

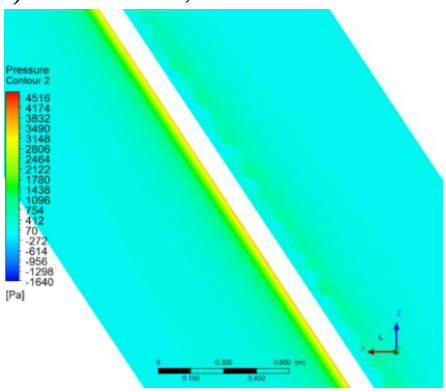
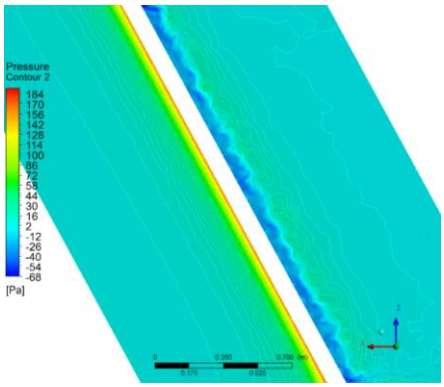
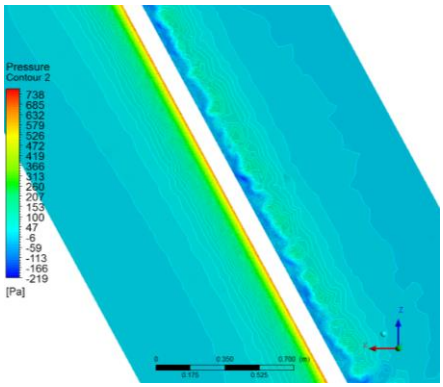


Figure C: Pressure distributions around the cylinder for:

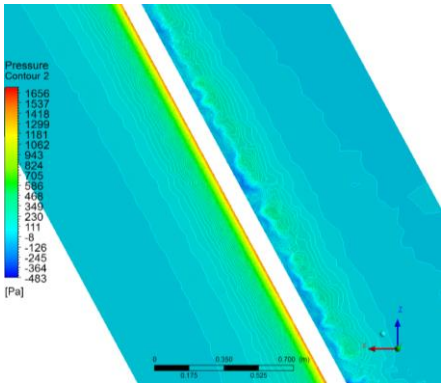
g) $\phi = 64°$; $\alpha = 54.7°$, $\beta = 40°$
i) Re = 1.1×10^5;



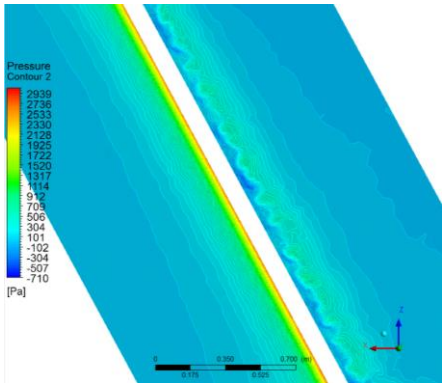
g) $\phi = 64°$; $\alpha = 54.7°$, $\beta = 40°$
ii) Re = 2.2×10^5;



g) $\phi = 64°$; $\alpha = 54.7°$, $\beta = 40°$
iii) Re = 3.3×10^5;



g) $\phi = 64°$; $\alpha = 54.7°$, $\beta = 40°$
iv) Re = 4.4×10^5;



g) $\phi = 64°$; $\alpha = 54.7°$, $\beta = 40°$
v) Re = 5.5×10^5;

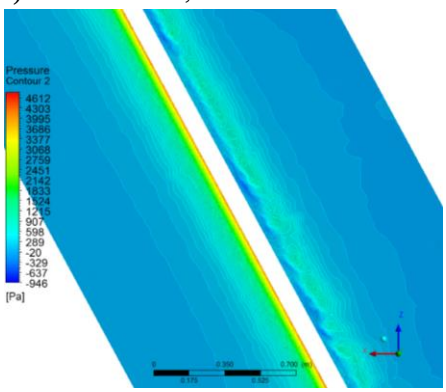
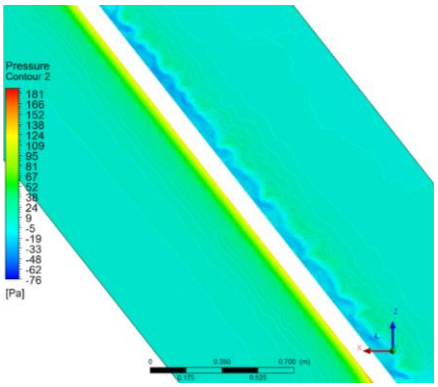
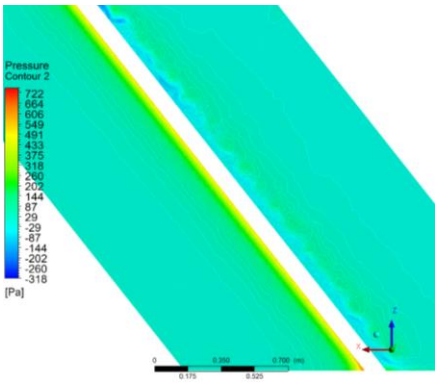


Figure C: Pressure distributions around the cylinder for:

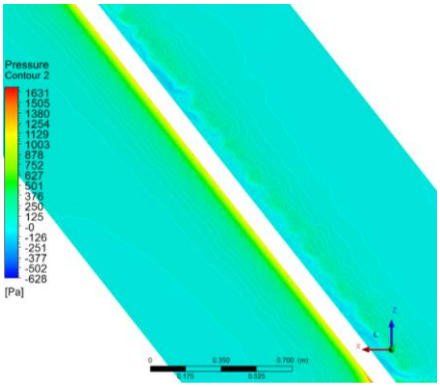
h) $\phi = 53°$; $\alpha = 50°$, $\beta = 20°$
i) Re = 1.1×10^5;



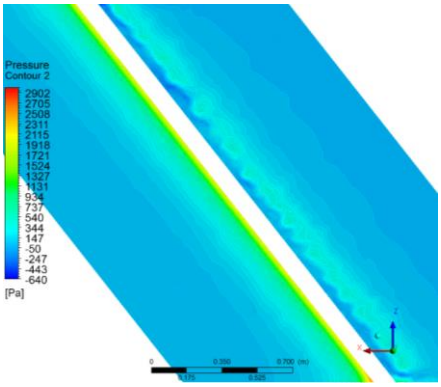
h) $\phi = 53°$; $\alpha = 50°$, $\beta = 20°$
ii) Re = 2.2×10^5;



h) $\phi = 53°$; $\alpha = 50°$, $\beta = 20°$
iii) Re = 3.3×10^5;



h) $\phi = 53°$; $\alpha = 50°$, $\beta = 20°$
iv) Re = 4.4×10^5;



h) $\phi = 53°$; $\alpha = 50°$, $\beta = 20°$
v) Re = 5.5×10^5;

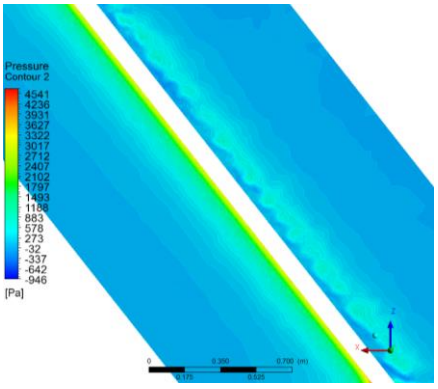
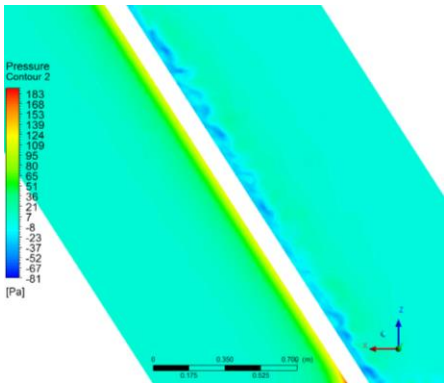
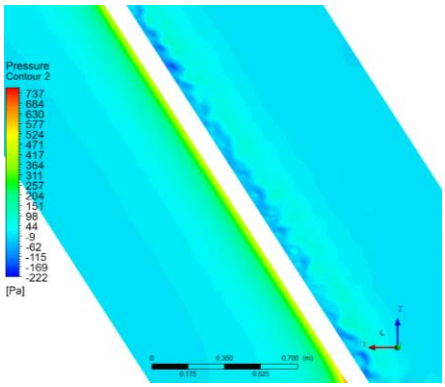


Figure C: Pressure distributions around the cylinder for:

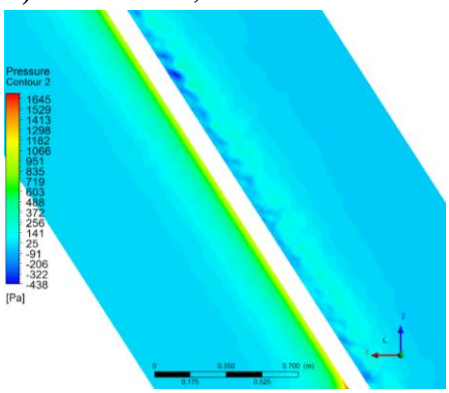
i) $\phi = 60.5°$; $\alpha = 50°$, $\beta = 40°$
i) Re = 1.1×10^5;



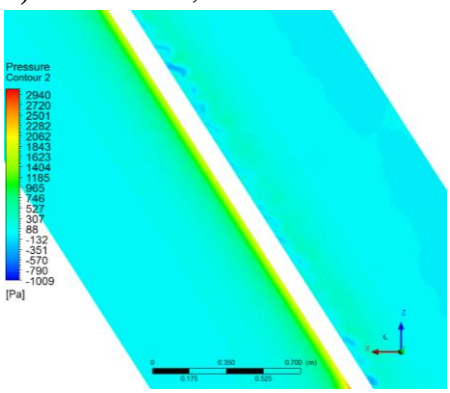
i) $\phi = 60.5°$; $\alpha = 50°$, $\beta = 40°$
ii) Re = 2.2×10^5;



i) $\phi = 60.5°$; $\alpha = 50°$, $\beta = 40°$
iii) Re = 3.3×10^5;



i) $\phi = 60.5°$; $\alpha = 50°$, $\beta = 40°$
iv) Re = 4.4×10^5;



i) $\phi = 60.5°$; $\alpha = 50°$, $\beta = 40°$
v) Re = 5.5×10^5;

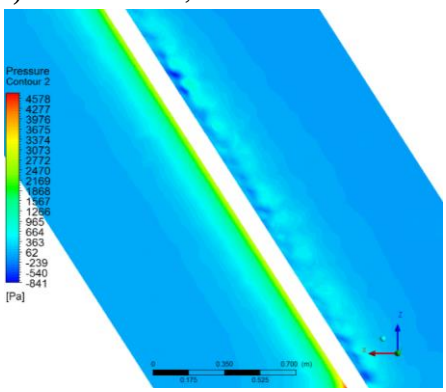
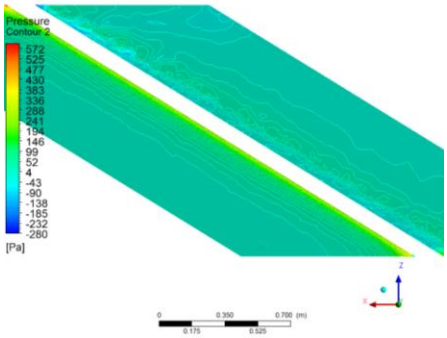
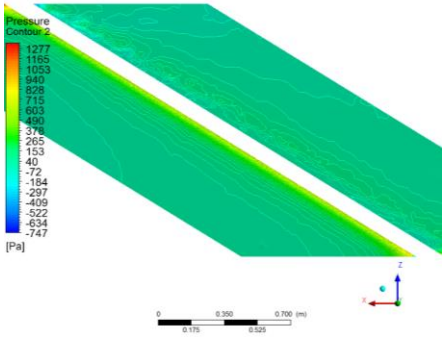


Figure C: Pressure distributions around the cylinder for:

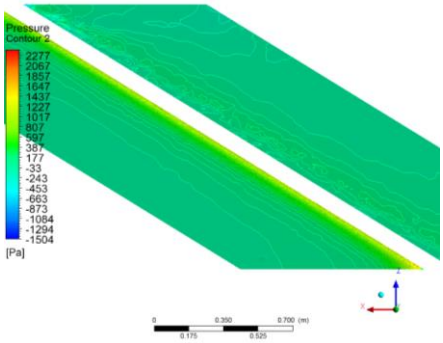
j) $\phi = 35.5°$; $\alpha = 30°$, $\beta = 20°$
ii) Re = 2.2×10^5;



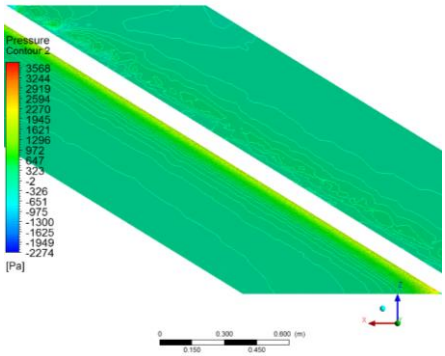
j) $\phi = 35.5°$; $\alpha = 30°$, $\beta = 20°$
iii) Re = 3.3×10^5;



j) $\phi = 35.5°$; $\alpha = 30°$, $\beta = 20°$
iv) Re = 4.4×10^5;



j) $\phi = 35.5°$; $\alpha = 30°$, $\beta = 20°$
v) Re = 5.5×10^5;

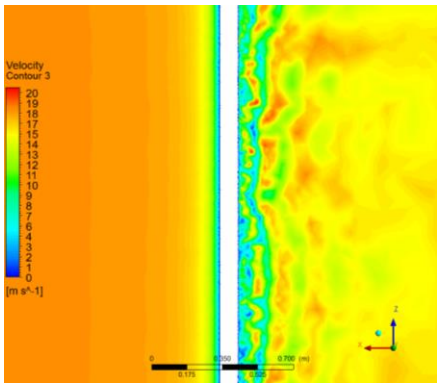


Appendix D: Velocity Distribution around the Cylinder

Figure D: Velocity distributions around the cylinder for:

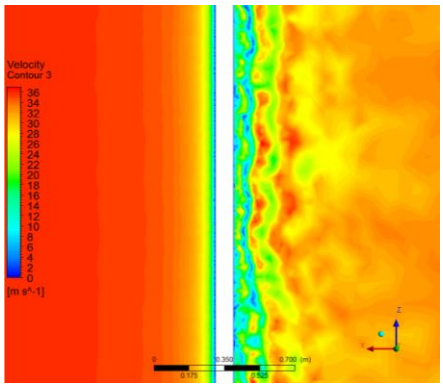
a) $\phi = 0°$; $\alpha = 0°$, $\beta = 0°$

i) Re = 1.1×10^5;



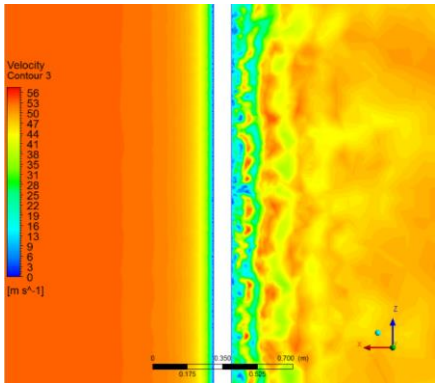
a) $\phi = 0°$; $\alpha = 0°$, $\beta = 0°$

ii) Re = 2.2×10^5;



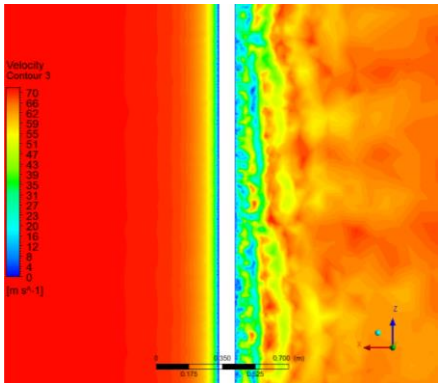
a) $\phi = 0°$; $\alpha = 0°$, $\beta = 0°$

iii) Re = 3.3×10^5;



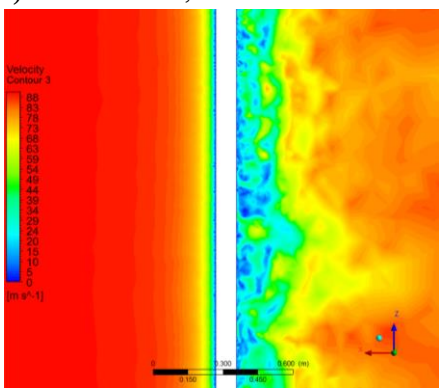
a) $\phi = 0°$; $\alpha = 0°$, $\beta = 0°$

iv) Re = 4.4×10^5;



a) $\phi = 0°$; $\alpha = 0°$, $\beta = 0°$

v) Re = 5.5×10^5;



a) $\phi = 0°$; $\alpha = 0°$, $\beta = 0°$

vi) Re = 6.7×10^5;

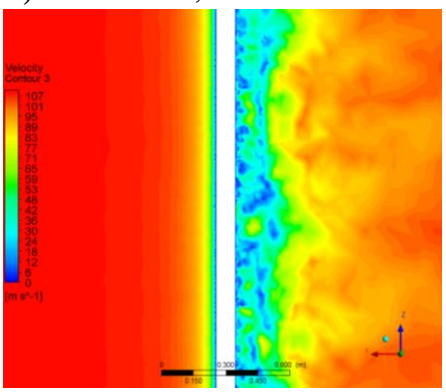
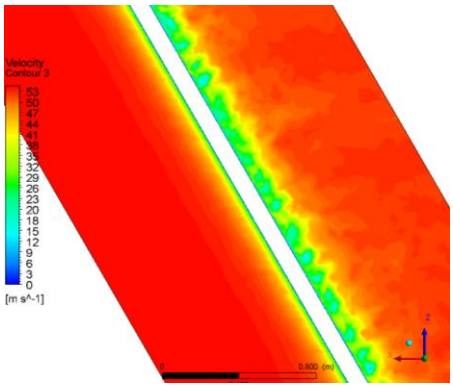
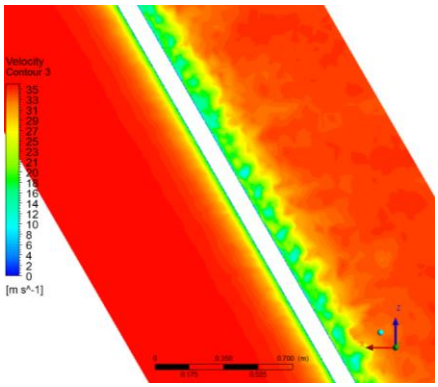


Figure D: Velocity distributions around the cylinder for:

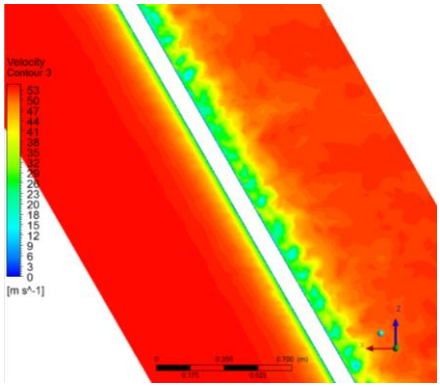
b) $\phi = 60°$; $\alpha = 60°$, $\beta = 0°$
i) Re = 1.1×10^5;



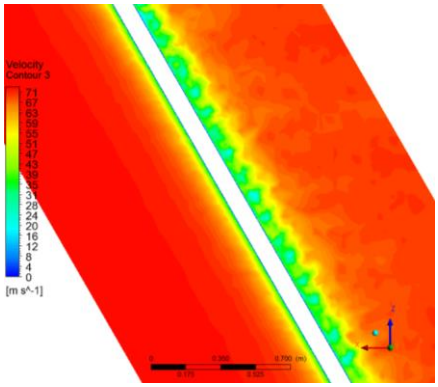
b) $\phi = 60°$; $\alpha = 60°$, $\beta = 0°$
ii) Re = 2.2×10^5;



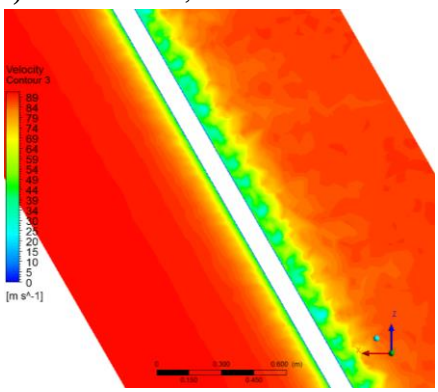
b) $\phi = 60°$; $\alpha = 60°$, $\beta = 0°$
iii) Re = 3.3×10^5;



b) $\phi = 60°$; $\alpha = 60°$, $\beta = 0°$
iv) Re = 4.4×10^5;



b) $\phi = 60°$; $\alpha = 60°$, $\beta = 0°$
v) Re = 5.5×10^5;



b) $\phi = 60°$; $\alpha = 60°$, $\beta = 0°$
vi) Re = 6.7×10^5;

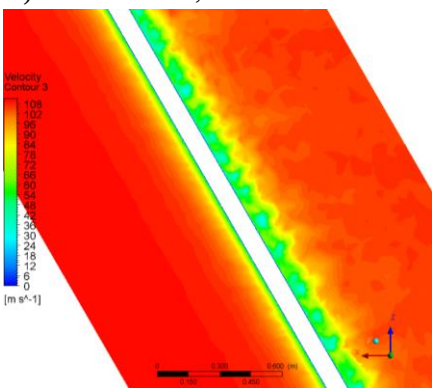
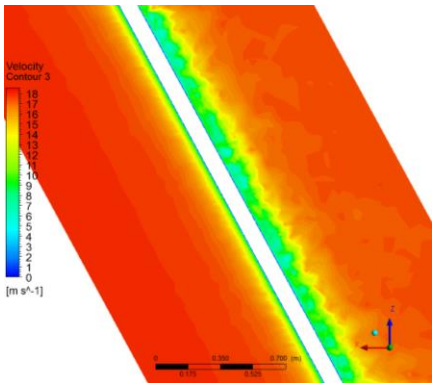
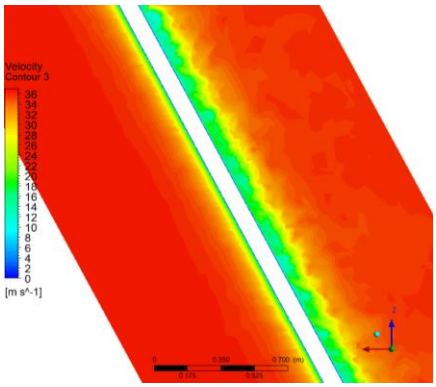


Figure D: Velocity distributions around the cylinder for:

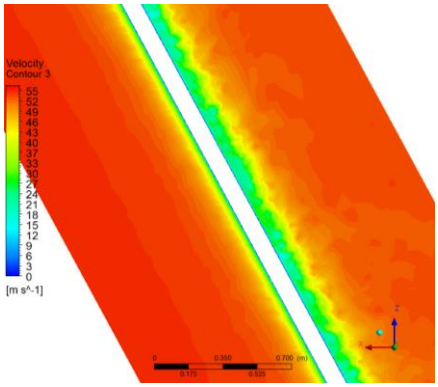
c) $\phi = 62°$; $\alpha = 60°$, $\beta = 20°$
i) Re = 1.1×10^5;



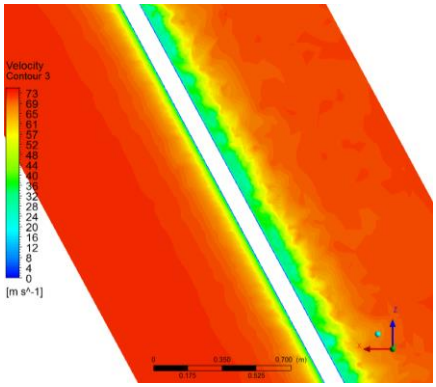
c) $\phi = 62°$; $\alpha = 60°$, $\beta = 20°$
ii) Re = 2.2×10^5;



c) $\phi = 62°$; $\alpha = 60°$, $\beta = 20°$
iii) Re = 3.3×10^5;



c) $\phi = 62°$; $\alpha = 60°$, $\beta = 20°$
iv) Re = 4.4×10^5;



c) $\phi = 62°$; $\alpha = 60°$, $\beta = 20°$
v) Re = 5.5×10^5;

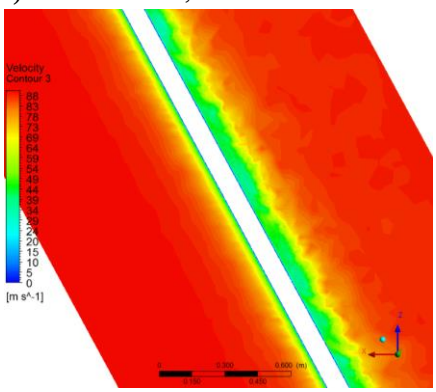
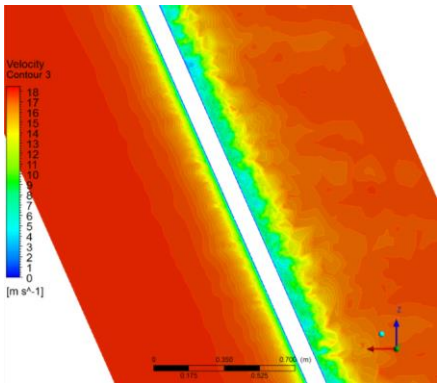
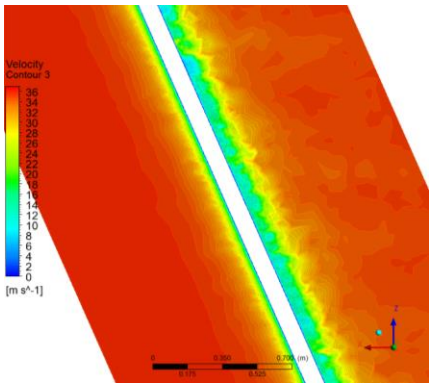


Figure D: Velocity distributions around the cylinder for:

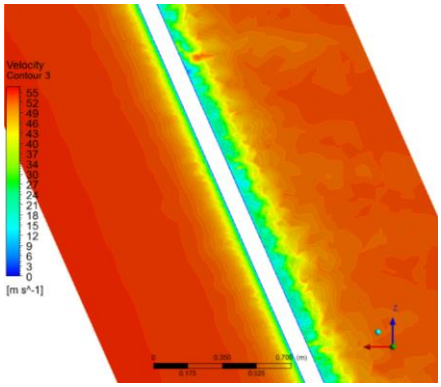
d) $\phi = 67.5°$; $\alpha = 60°$, $\beta = 40°$
i) Re = 1.1×10^5;



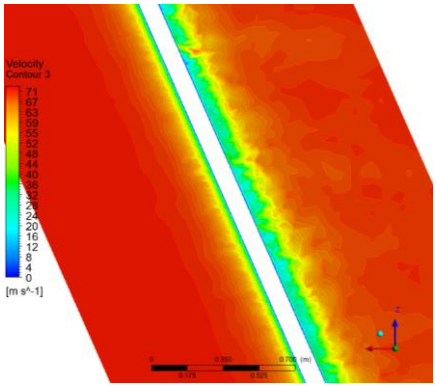
d) $\phi = 67.5°$; $\alpha = 60°$, $\beta = 40°$
ii) Re = 2.2×10^5;



d) $\phi = 67.5°$; $\alpha = 60°$, $\beta = 40°$
iii) Re = 3.3×10^5;



d) $\phi = 67.5°$; $\alpha = 60°$, $\beta = 40°$
iv) Re = 4.4×10^5;



d) $\phi = 67.5°$; $\alpha = 60°$, $\beta = 40°$
v) Re = 5.5×10^5;

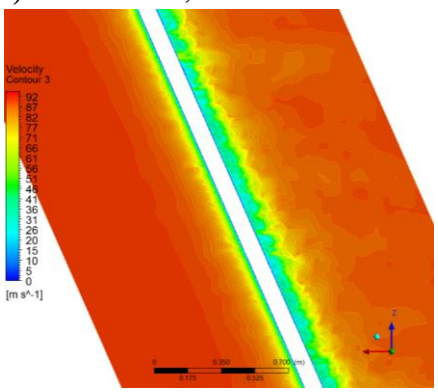
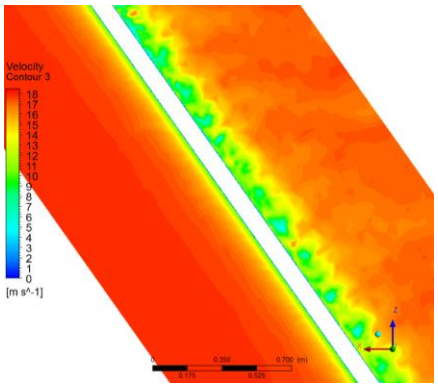
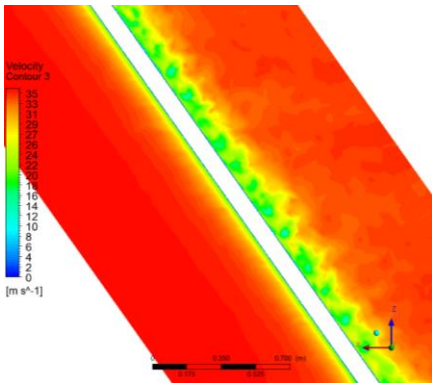


Figure D: Velocity distributions around the cylinder for:

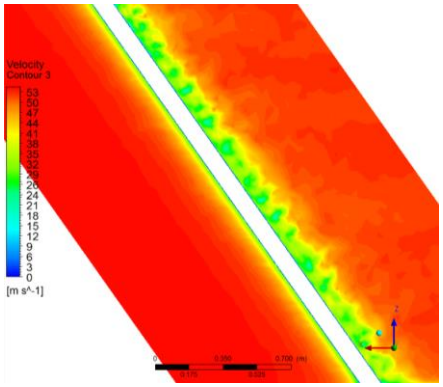
e) $\phi = 54.7°$; $\alpha = 54.7°$, $\beta = 0°$
i) Re = 1.1×10^5;



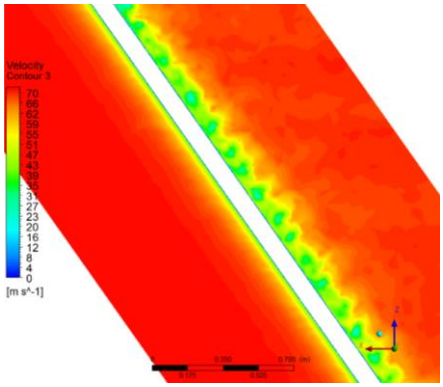
e) $\phi = 54.7°$; $\alpha = 54.7°$, $\beta = 0°$
ii) Re = 2.2×10^5;



e) $\phi = 54.7°$; $\alpha = 54.7°$, $\beta = 0°$
iii) Re = 3.3×10^5;



e) $\phi = 54.7°$; $\alpha = 54.7°$, $\beta = 0°$
iv) Re = 4.4×10^5;



e) $\phi = 54.7°$; $\alpha = 54.7°$, $\beta = 0°$
v) Re = 5.5×10^5;

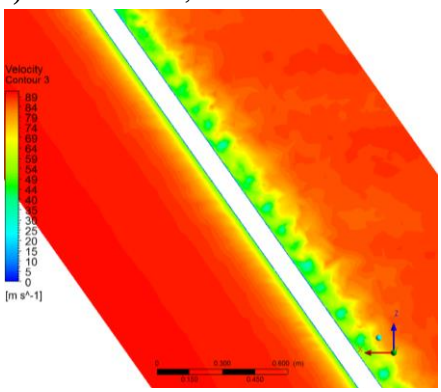
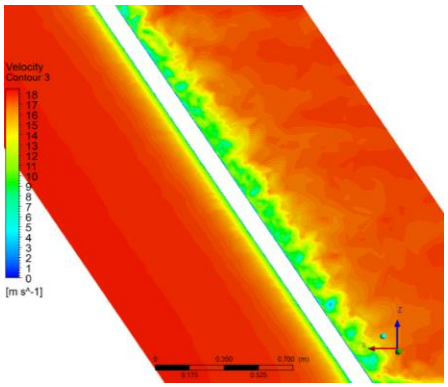
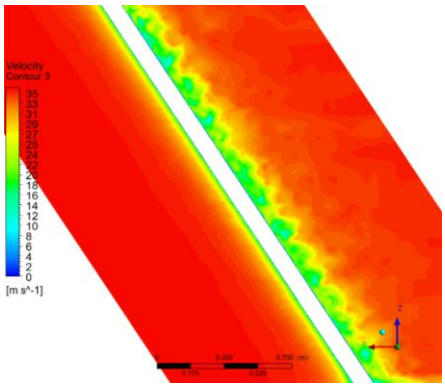


Figure D: Velocity distributions around the cylinder for:

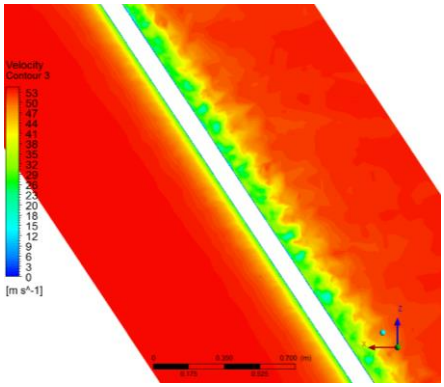
f) $\phi = 57.1°$; $\alpha = 54.7°$, $\beta = 20°$
i) Re = 1.1×10^5;



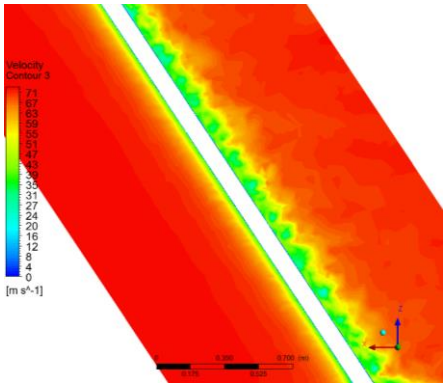
f) $\phi = 57.1°$; $\alpha = 54.7°$, $\beta = 20°$
ii) Re = 2.2×10^5;



f) $\phi = 57.1°$; $\alpha = 54.7°$, $\beta = 20°$
iii) Re = 3.3×10^5;



f) $\phi = 57.1°$; $\alpha = 54.7°$, $\beta = 20°$
iv) Re = 4.4×10^5;



f) $\phi = 57.1°$; $\alpha = 54.7°$, $\beta = 20°$
v) Re = 5.5×10^5;

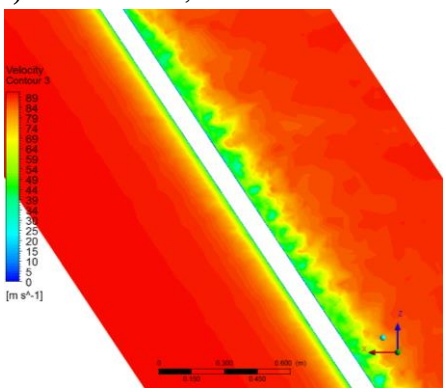
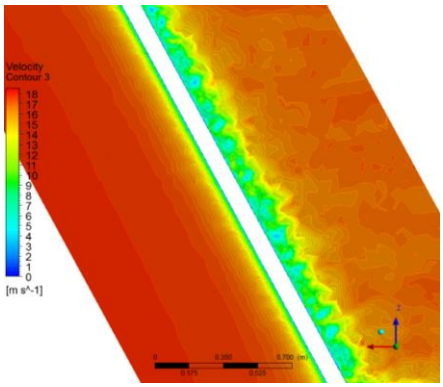
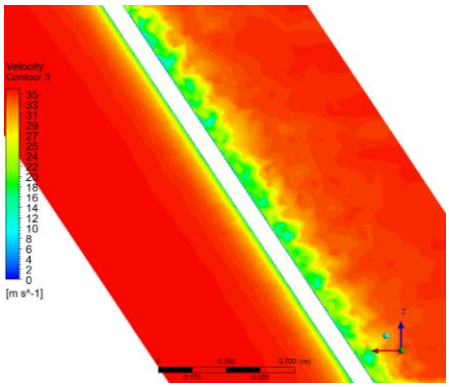


Figure D: Velocity distributions around the cylinder for:

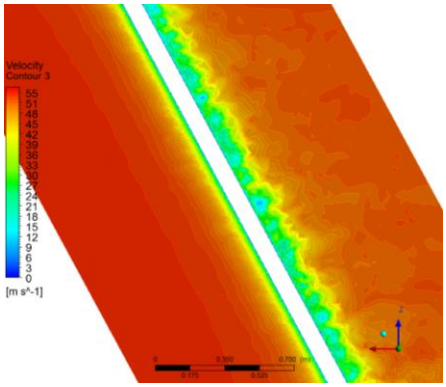
g) $\phi = 64°$; $\alpha = 54.7°$, $\beta = 40°$
i) Re = 1.1×10^5;



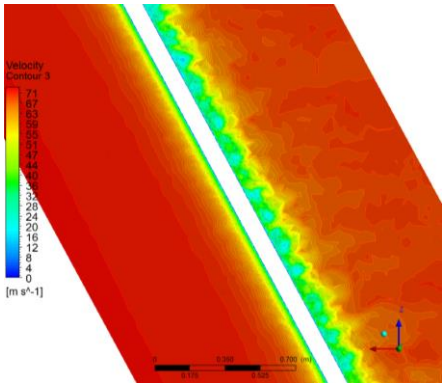
g) $\phi = 64°$; $\alpha = 54.7°$, $\beta = 40°$
ii) Re = 2.2×10^5;



g) $\phi = 64°$; $\alpha = 54.7°$, $\beta = 40°$
ii) Re = 3.3×10^5;



g) $\phi = 64°$; $\alpha = 54.7°$, $\beta = 40°$
iv) Re = 4.4×10^5;



g) $\phi = 64°$; $\alpha = 54.7°$, $\beta = 40°$
v) Re = 5.5×10^5;

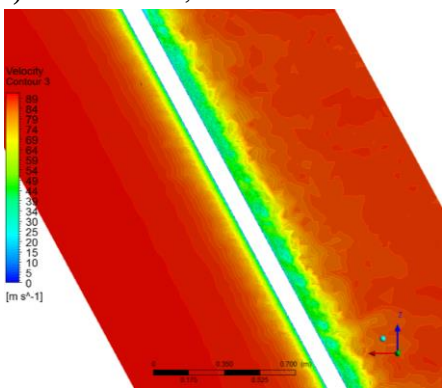
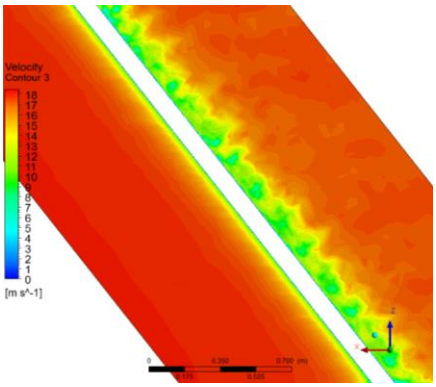
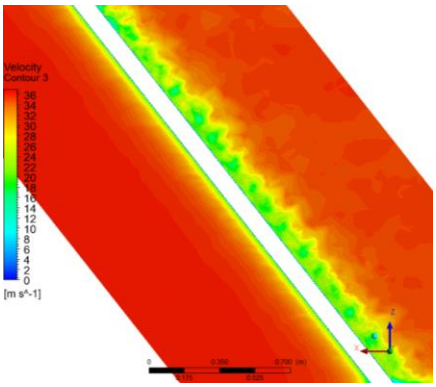


Figure D: Velocity distributions around the cylinder for:

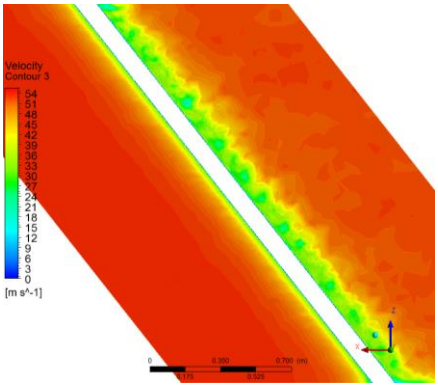
h) $\phi = 53°$; $\alpha = 50°$, $\beta = 20°$
i) Re = 1.1×10^5;



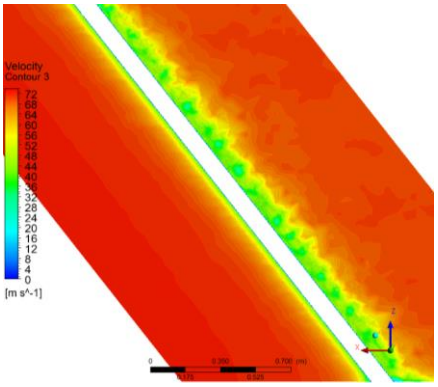
h) $\phi = 53°$; $\alpha = 50°$, $\beta = 20°$
ii) Re = 2.2×10^5;



h) $\phi = 53°$; $\alpha = 50°$, $\beta = 20°$
iii) Re = 3.3×10^5;



h) $\phi = 53°$; $\alpha = 50°$, $\beta = 20°$
iv) Re = 4.4×10^5;



h) $\phi = 53°$; $\alpha = 50°$, $\beta = 20°$
v) Re = 5.5×10^5;

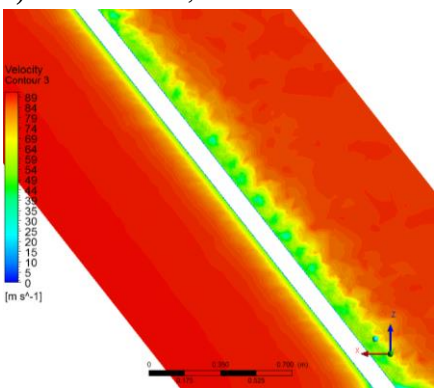
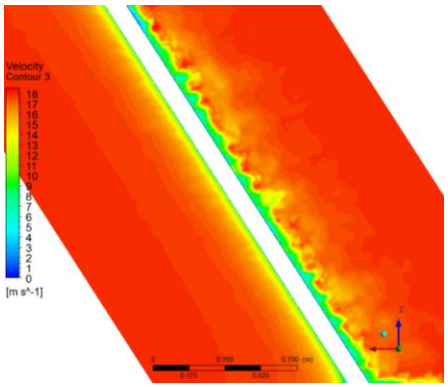
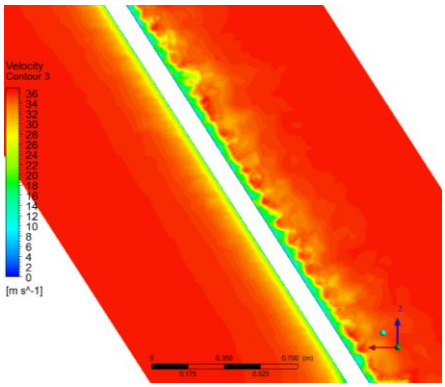


Figure D: Velocity distributions around the cylinder for:

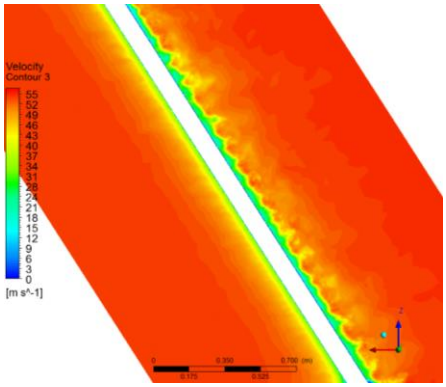
i) $\phi = 60.5°$; $\alpha = 50°$, $\beta = 40°$
i) Re = 1.1×10^5;



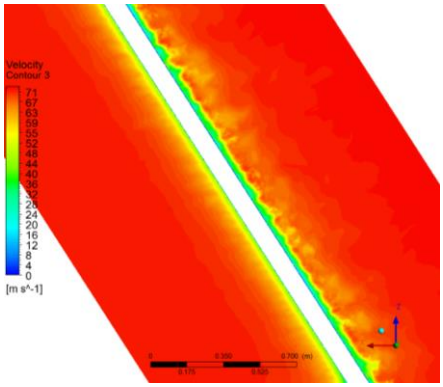
i) $\phi = 60.5°$; $\alpha = 50°$, $\beta = 40°$
ii) Re = 2.2×10^5;



i) $\phi = 60.5°$; $\alpha = 50°$, $\beta = 40°$
iii) Re = 3.3×10^5;



i) $\phi = 60.5°$; $\alpha = 50°$, $\beta = 40°$
iv) Re = 4.4×10^5;



i) $\phi = 60.5°$; $\alpha = 50°$, $\beta = 40°$
v) Re = 5.5×10^5;

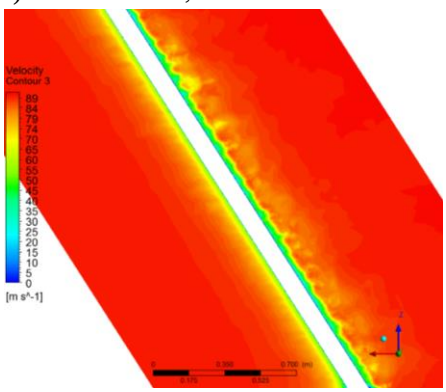
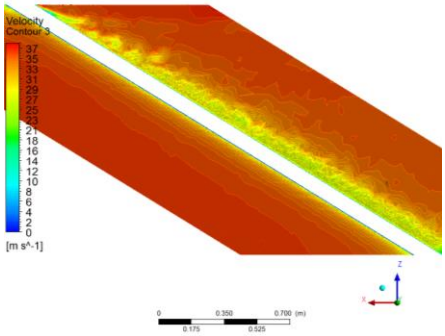


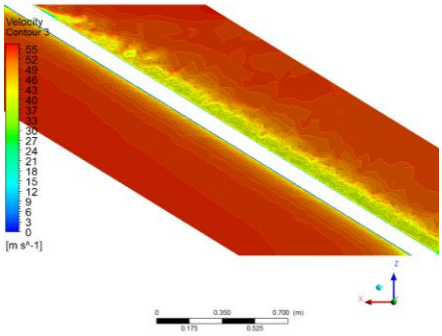
Figure D: Velocity distributions around the cylinder for:

j) $\phi = 35.5°$; $\alpha = 30°$, $\beta = 20°$

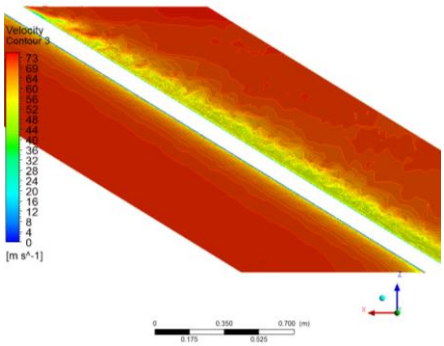
ii) Re = 2.2×10^5;



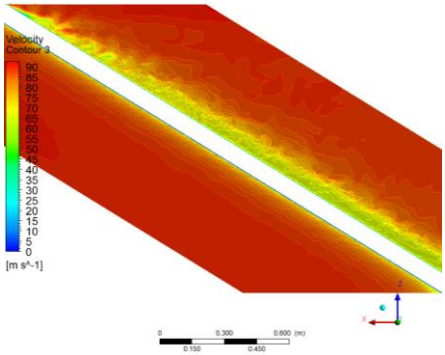
iii) Re = 3.3×10^5;



iv) Re = 4.4×10^5;



v) Re = 5.5×10^5;



Appendix E: Axial and Along Stream Flow

Figure E: Axial and along stream flow:

a) $\phi = 0°$; $\alpha = 0°$, $\beta = 0°$

i) Re = 1.1×10^5;

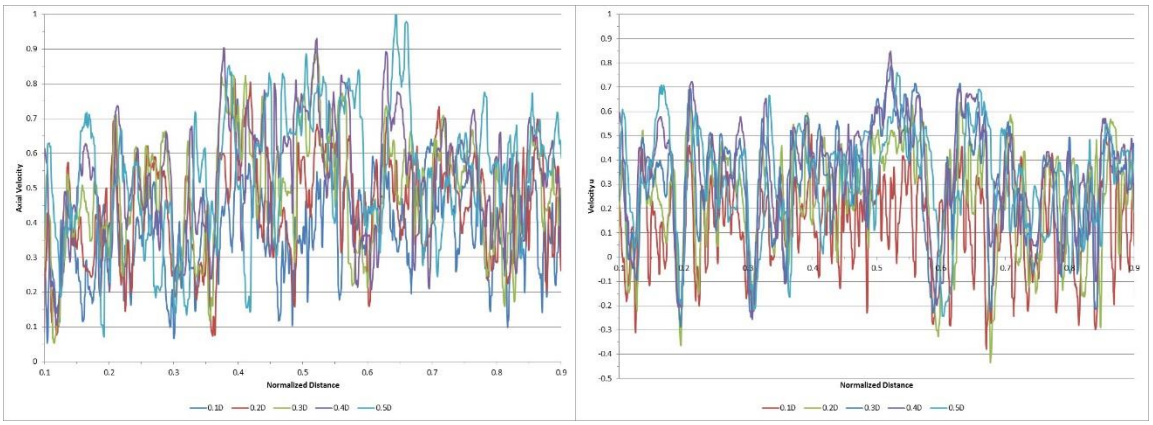


Figure E: Axial and along stream flow:

a) $\phi = 0°$; $\alpha = 0°$, $\beta = 0°$

ii) Re = 2.2×10^5;

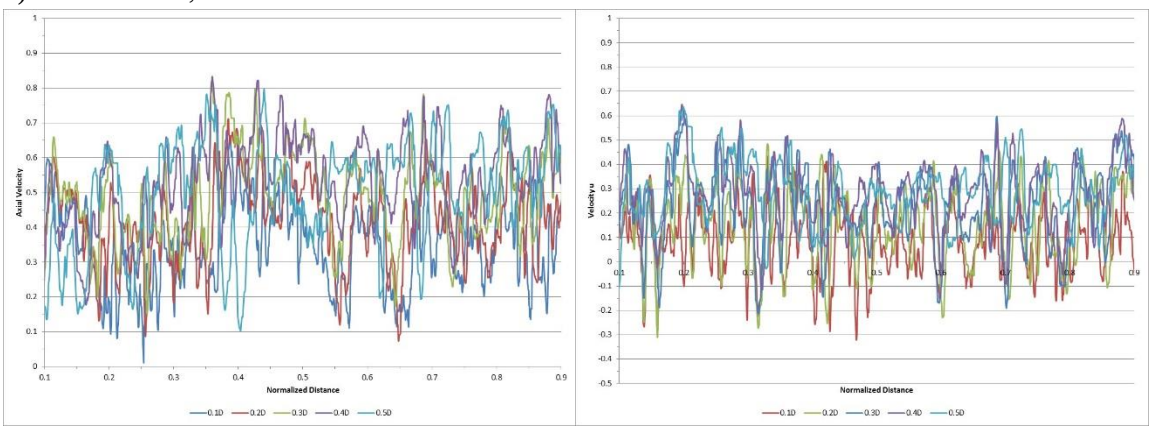


Figure E: Axial and along stream flow:

a) $\phi = 0°$; $\alpha = 0°$, $\beta = 0°$

iii) Re = 3.3×10^5;

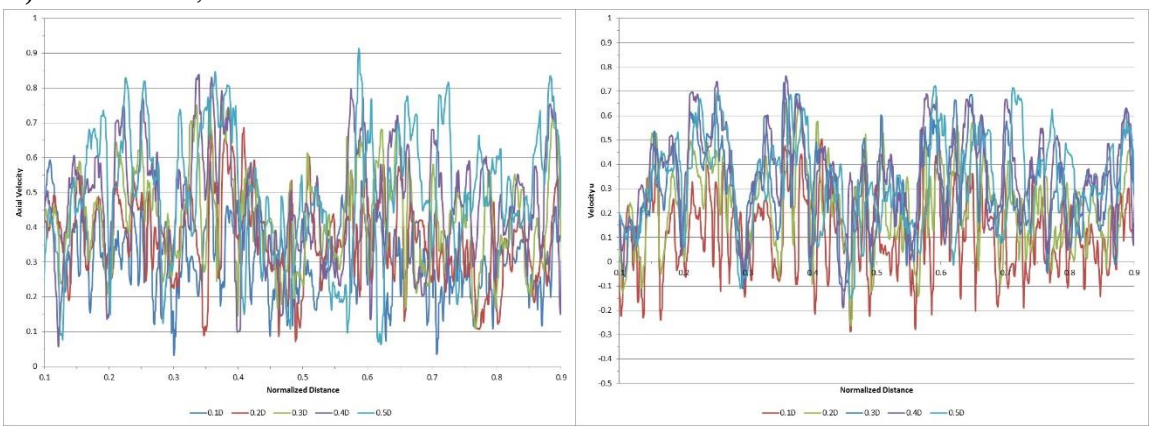


Figure E: Axial and along stream flow:

a) $\phi = 0°$; $\alpha = 0°$, $\beta = 0°$

iv) Re = 4.4×10^5;

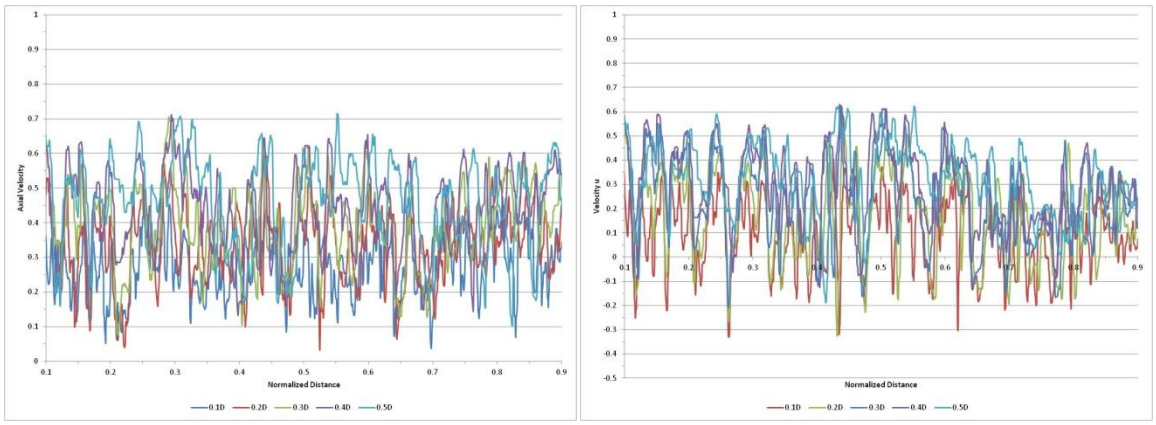


Figure E: Axial and along stream flow:

a) $\phi = 0°$; $\alpha = 0°$, $\beta = 0°$

v) Re = 5.5×10^5;

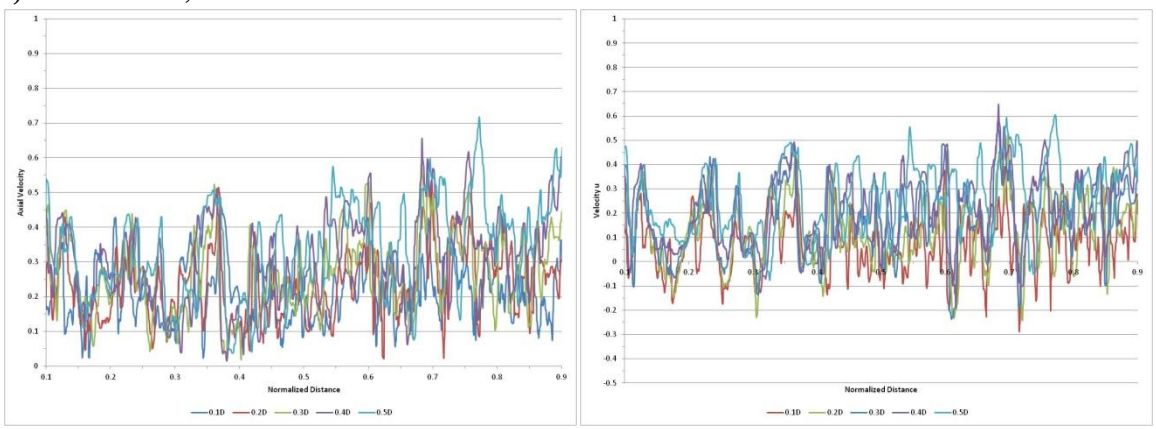


Figure E: Axial and along stream flow:

a) $\phi = 0°$; $\alpha = 0°$, $\beta = 0°$

vi) Re = 6.7×10^5;

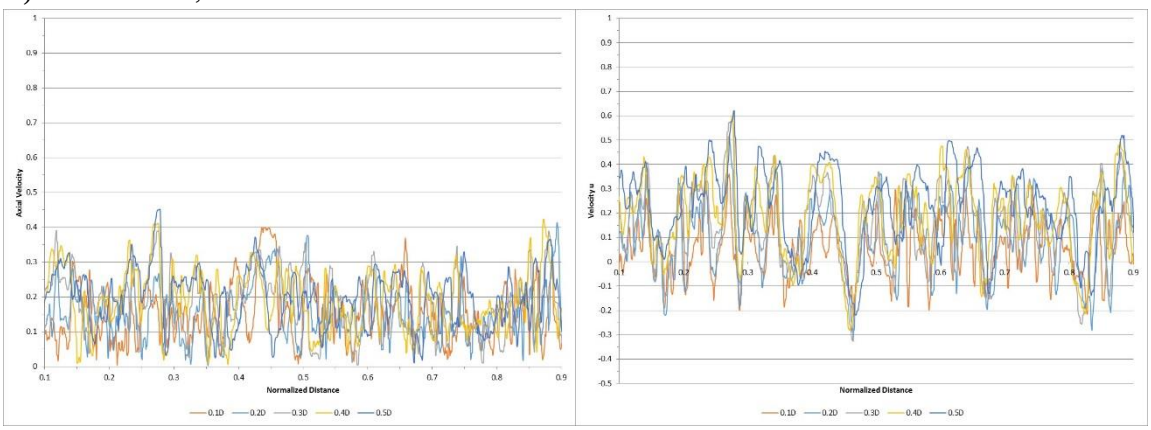


Figure E: Axial and along stream flow:
b) $\phi = 60°$; $\alpha = 60°$, $\beta = 0°$
i) Re = 1.1×10^5;

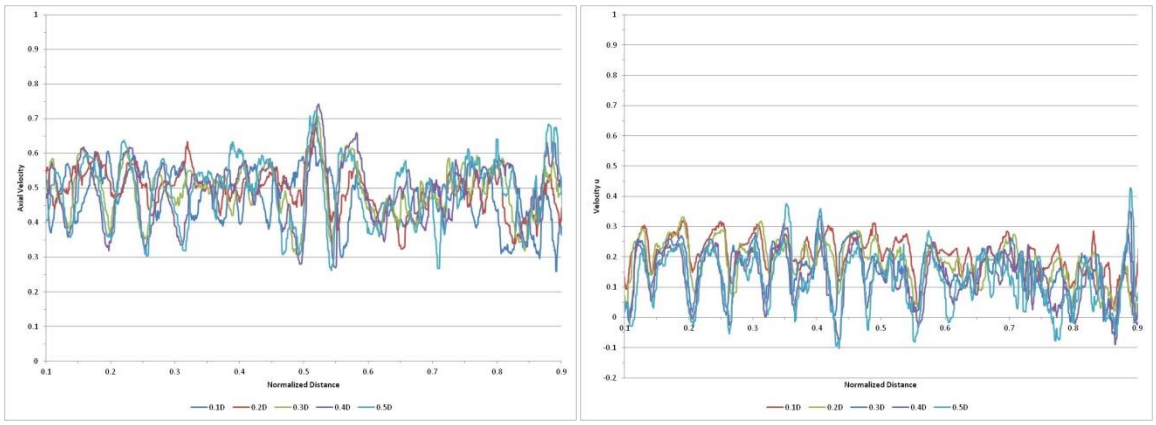


Figure E: Axial and along stream flow:
b) $\phi = 60°$; $\alpha = 60°$, $\beta = 0°$
ii) Re = 2.2×10^5;

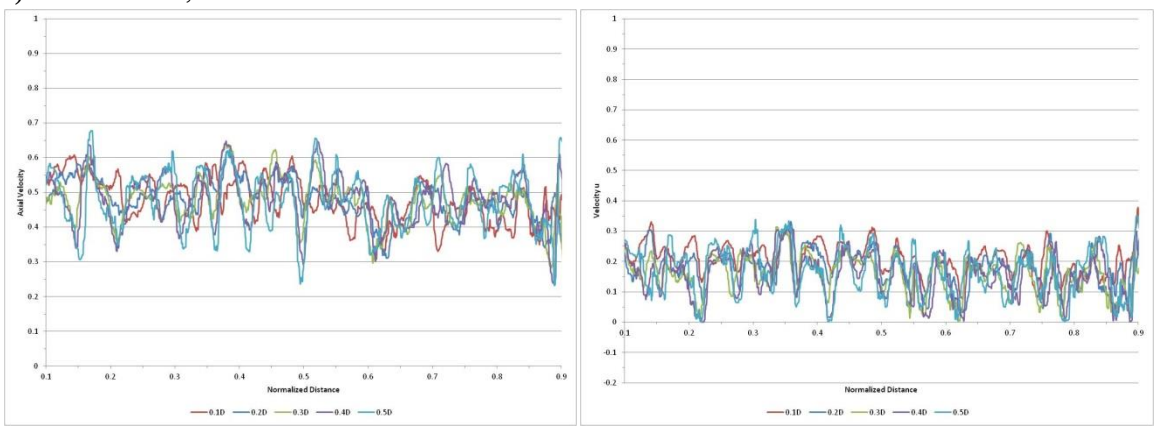


Figure E: Axial and along stream flow:
b) $\phi = 60°$; $\alpha = 60°$, $\beta = 0°$
iii) Re = 3.3×10^5;

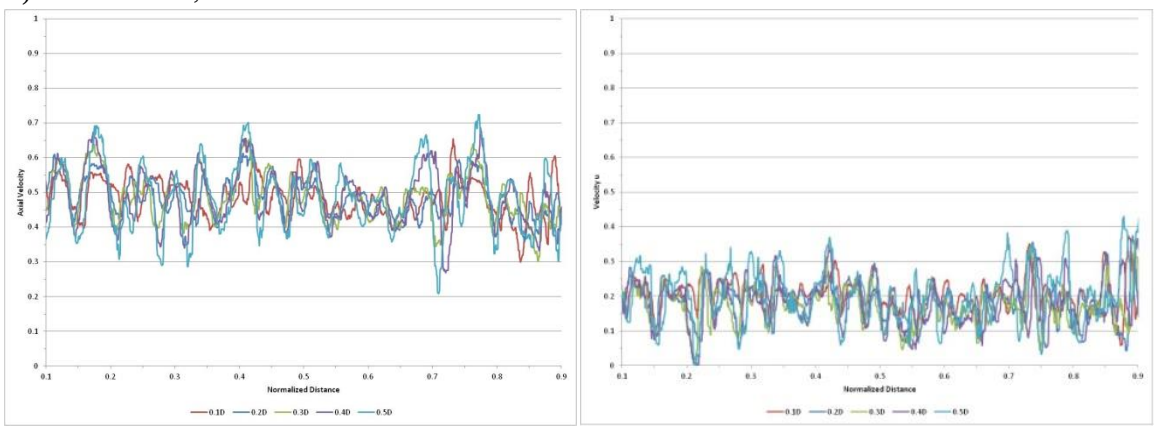


Figure E: Axial and along stream flow:

b) $\phi = 60°$; $\alpha = 60°$, $\beta = 0°$

iv) Re = 4.4×10^5;

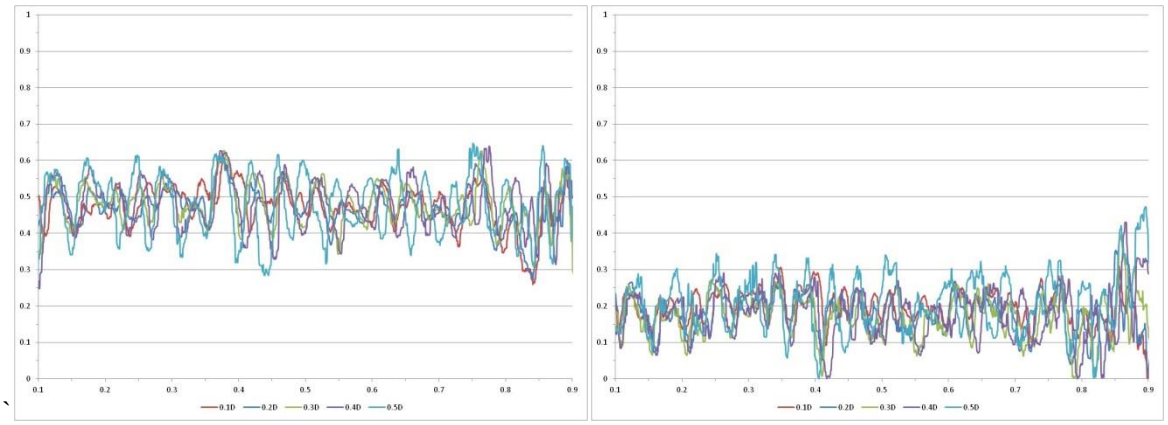


Figure E: Axial and along stream flow:

b) $\phi = 60°$; $\alpha = 60°$, $\beta = 0°$

v) Re = 5.5×10^5;

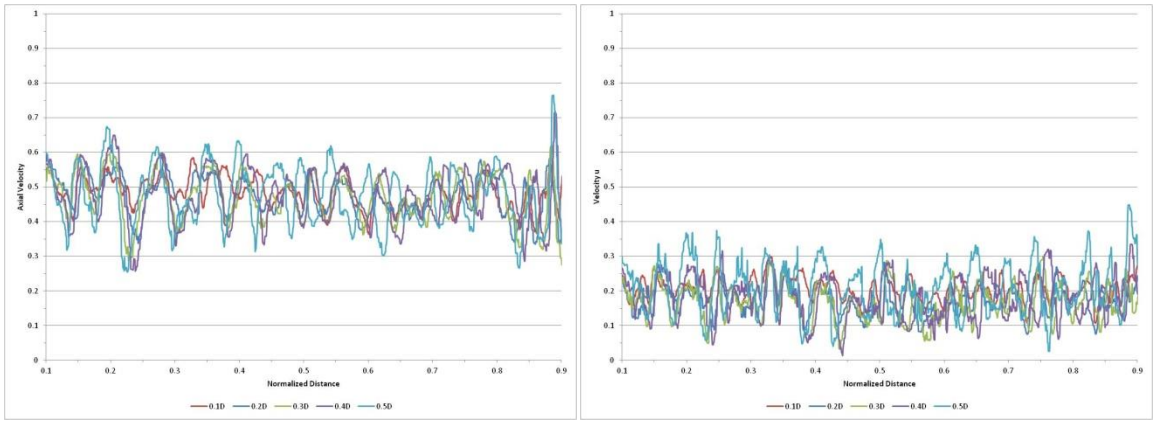


Figure E: Axial and along stream flow:

b) $\phi = 60°$; $\alpha = 60°$, $\beta = 0°$

vi) Re = 6.7×10^5;

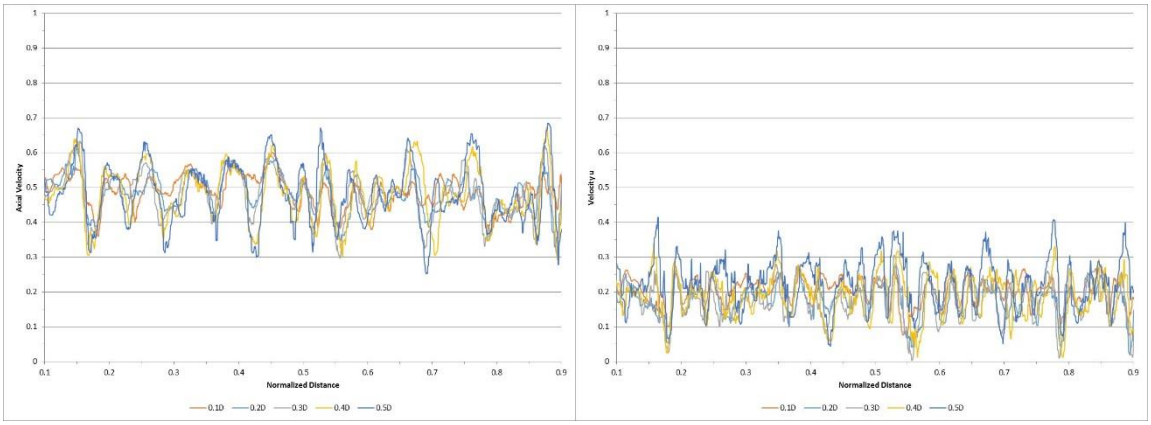


Figure E: Axial and along stream flow:
c) $\phi = 62°$; $\alpha = 60°$, $\beta = 20°$
i) Re = 1.1×10^5;

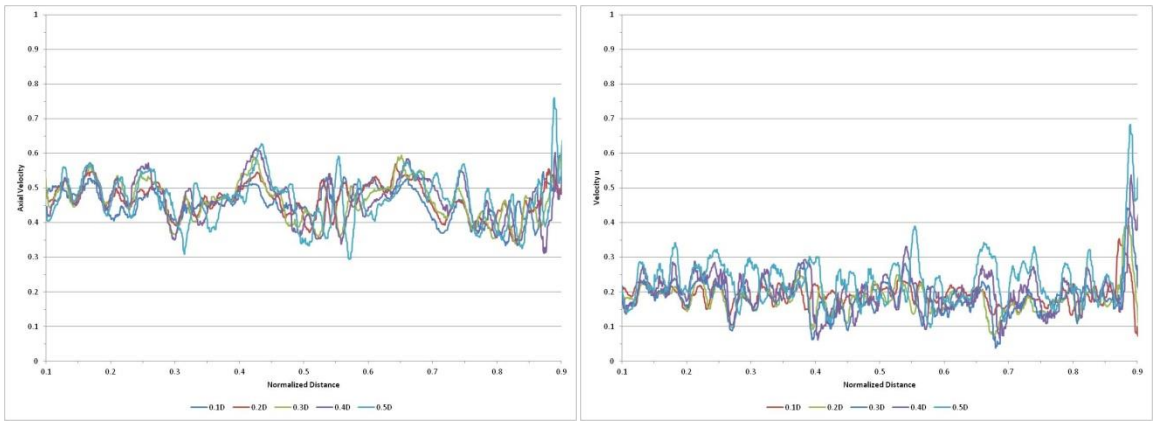


Figure E: Axial and along stream flow:
c) $\phi = 62°$; $\alpha = 60°$, $\beta = 20°$
ii) Re = 2.2×10^5;

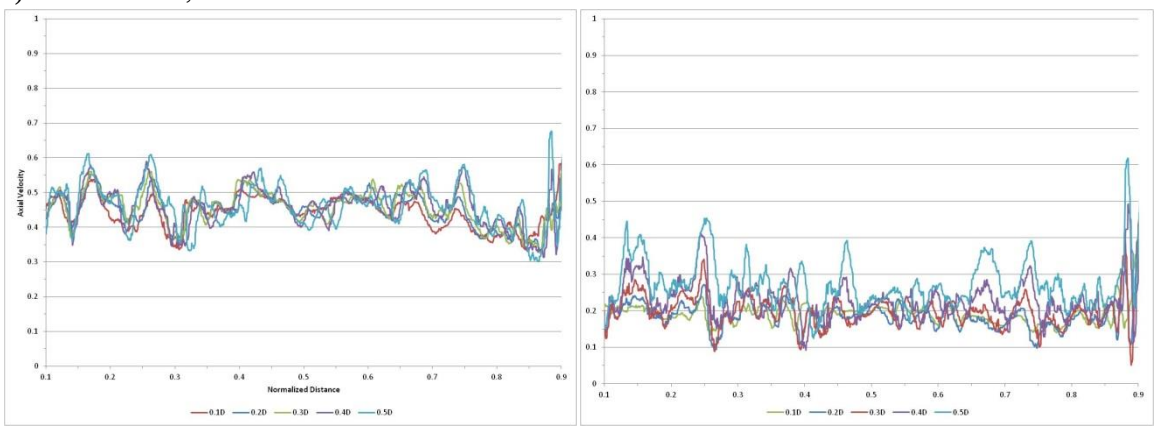


Figure E: Axial and along stream flow:
c) $\phi = 62°$; $\alpha = 60°$, $\beta = 20°$
iii) Re = 3.3×10^5;

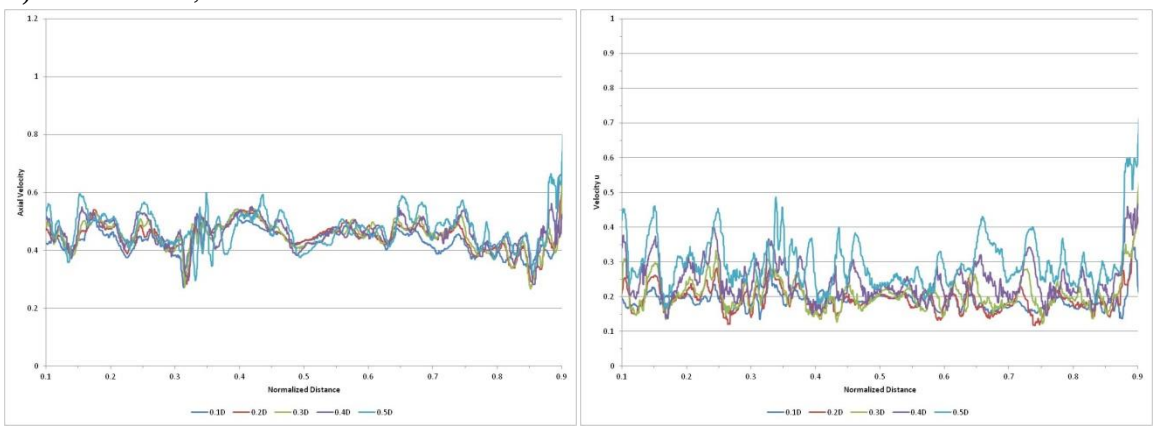


Figure E: Axial and along stream flow:
c) $\phi = 62°$; $\alpha = 60°$, $\beta = 20°$
iv) Re = 4.4×10^5;

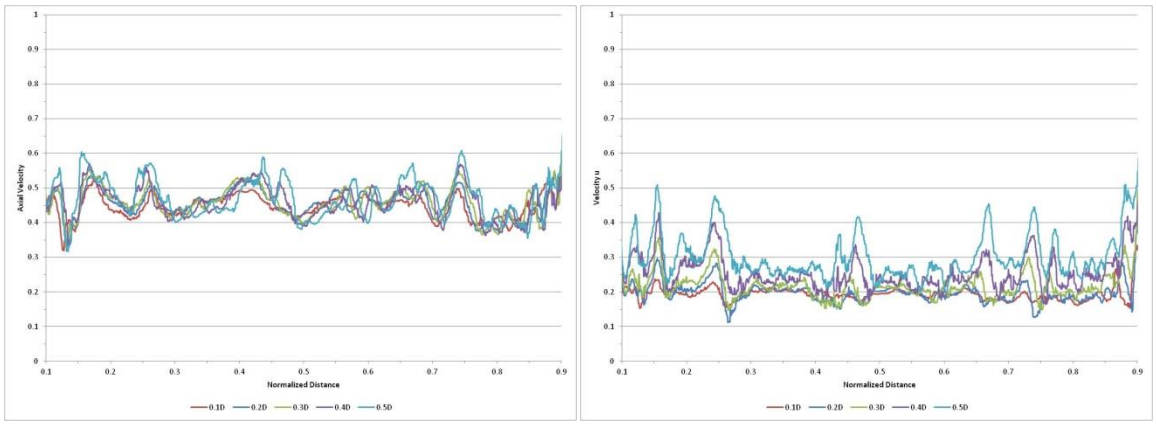


Figure E: Axial and along stream flow:
c) $\phi = 62°$; $\alpha = 60°$, $\beta = 20°$
v) Re = 5.5×10^5;

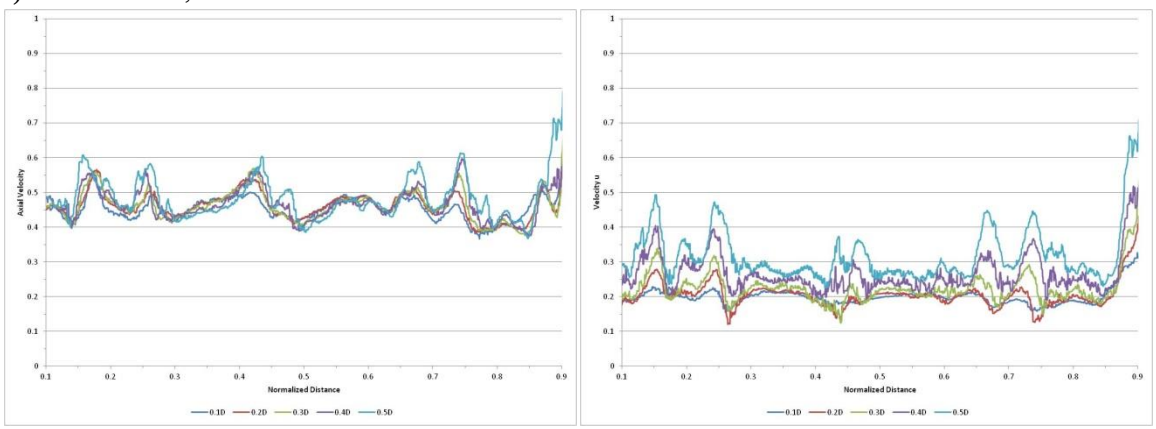


Figure E: Axial and along stream flow:
d) $\phi = 67.5°$; $\alpha = 60°$, $\beta = 40°$
i) Re = 1.1×10^5;

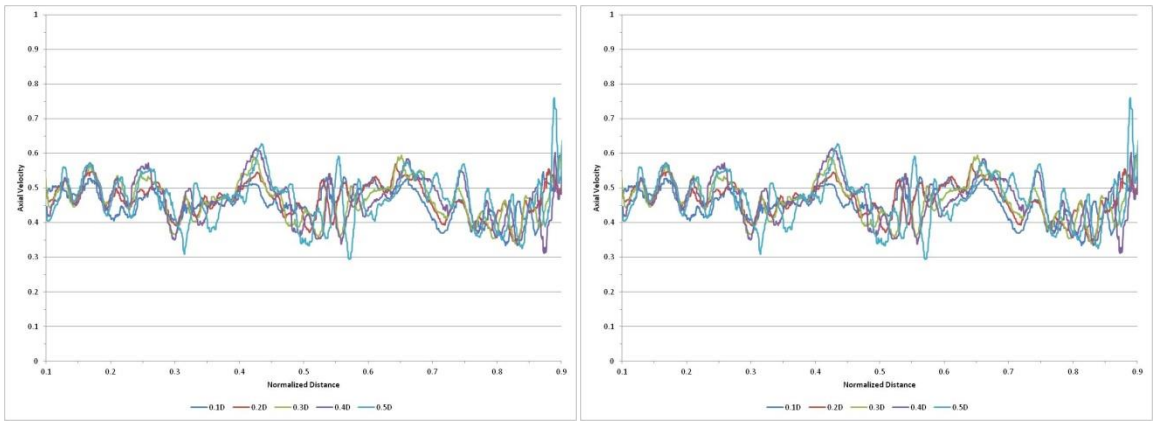


Figure E: Axial and along stream flow:
d) $\phi = 67.5°$; $\alpha = 60°$, $\beta = 40°$
ii) Re = 2.2×10^5;

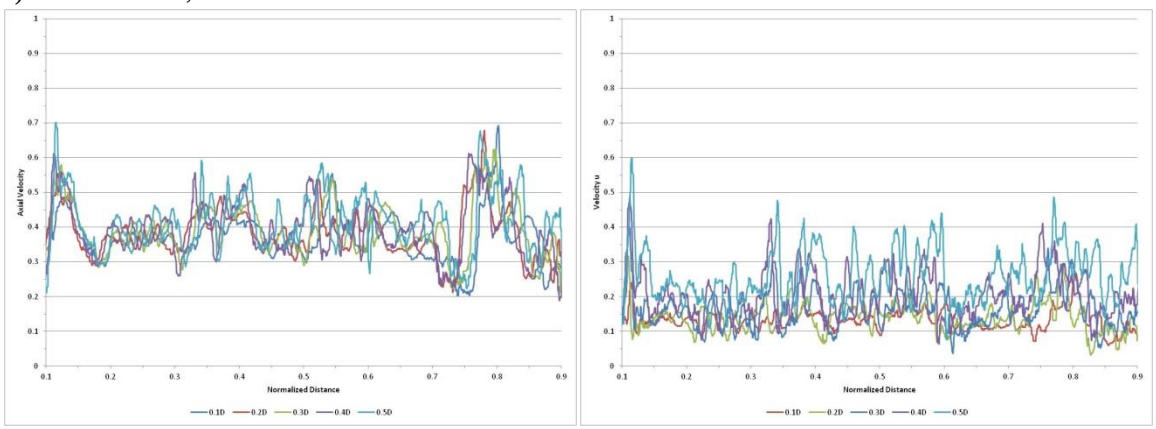


Figure E: Axial and along stream flow:
d) $\phi = 67.5°$; $\alpha = 60°$, $\beta = 40°$
iii) Re = 3.3×10^5;

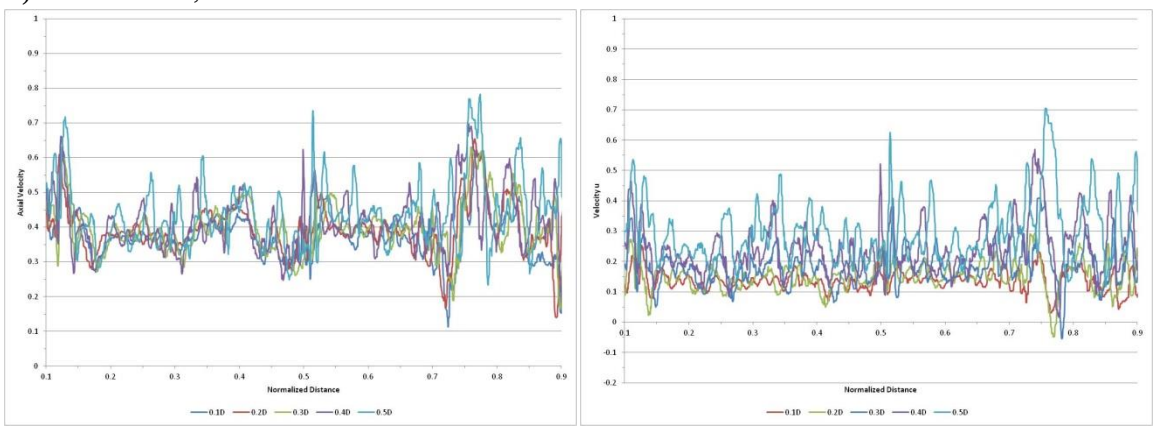


Figure E: Axial and along stream flow:
iv) d) $\phi = 67.5°$; $\alpha = 60°$, $\beta = 40°$
Re = 4.4×10^5;

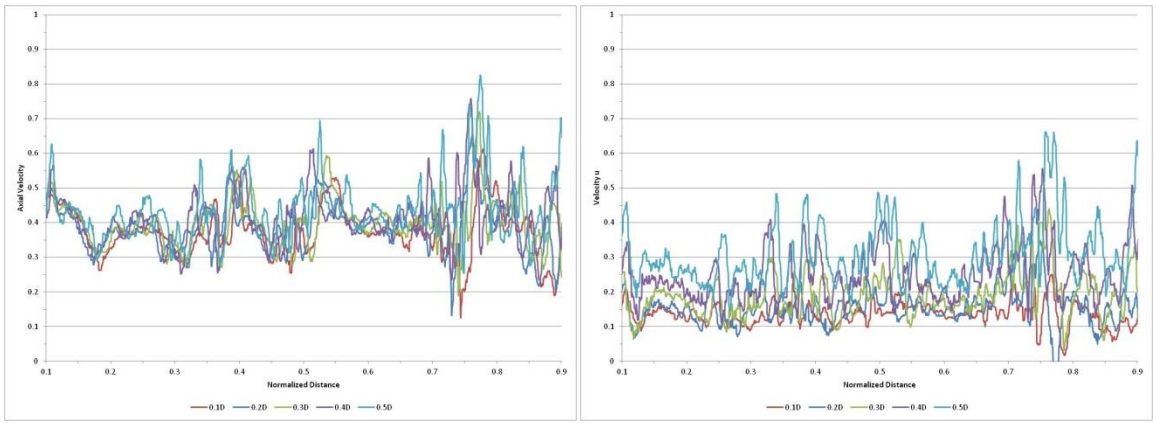


Figure E: Axial and along stream flow:
d) $\phi = 67.5°$; $\alpha = 60°$, $\beta = 40°$
v) Re = 5.5×10^5;

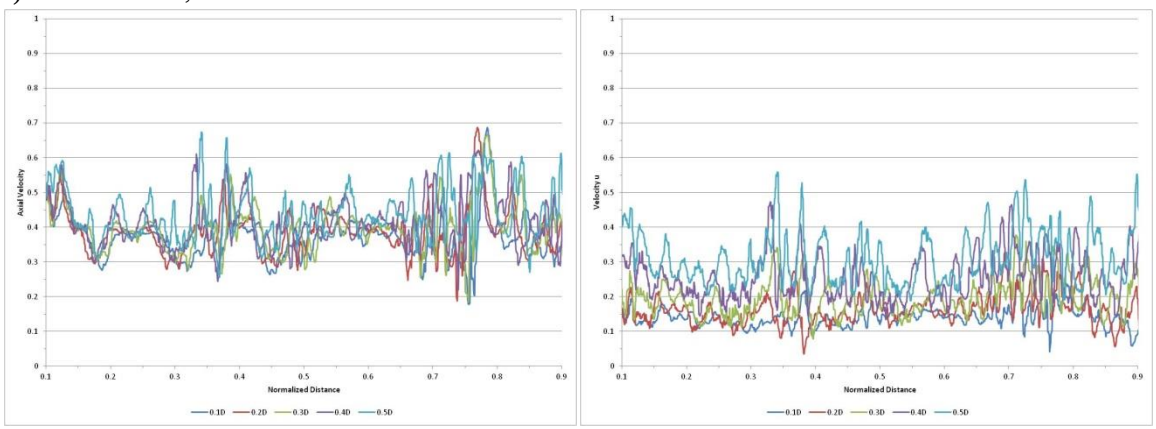


Figure E: Axial and along stream flow:
e) $\phi = 54.7°$; $\alpha = 54.7°$, $\beta = 0°$
i) Re = 1.1×10^5;

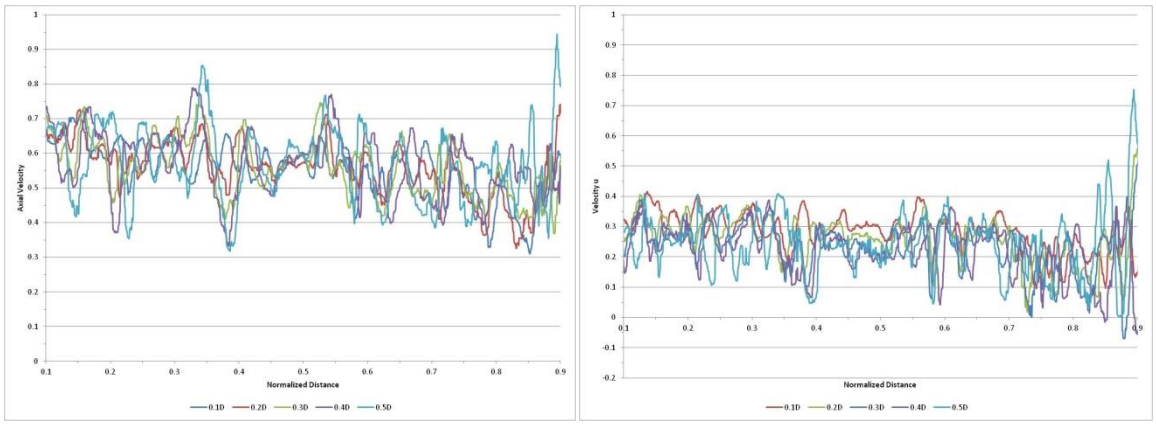


Figure E: Axial and along stream flow:
e) $\phi = 54.7°$; $\alpha = 54.7°$, $\beta = 0°$
ii) Re = 2.2×10^5;

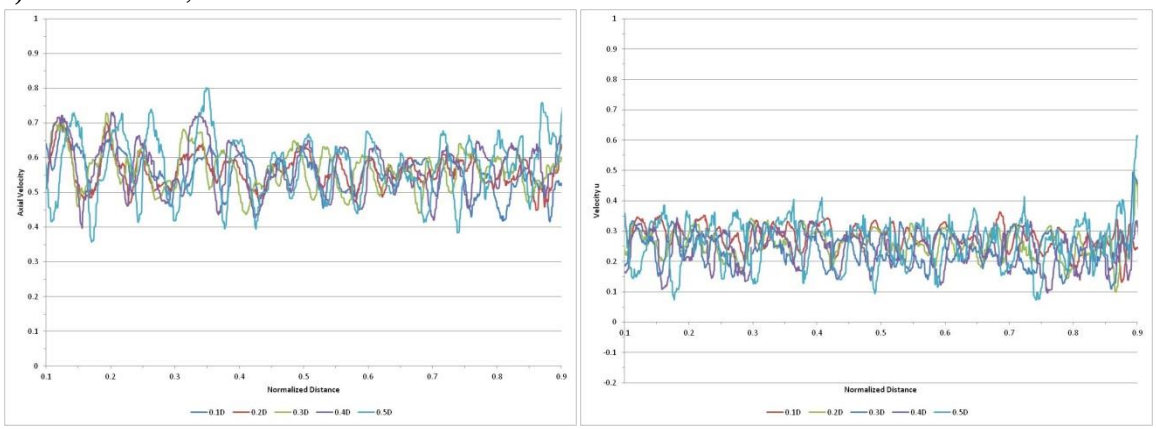


Figure E: Axial and along stream flow:
e) $\phi = 54.7°$; $\alpha = 54.7°$, $\beta = 0°$
iii) Re = 3.3×10^5;

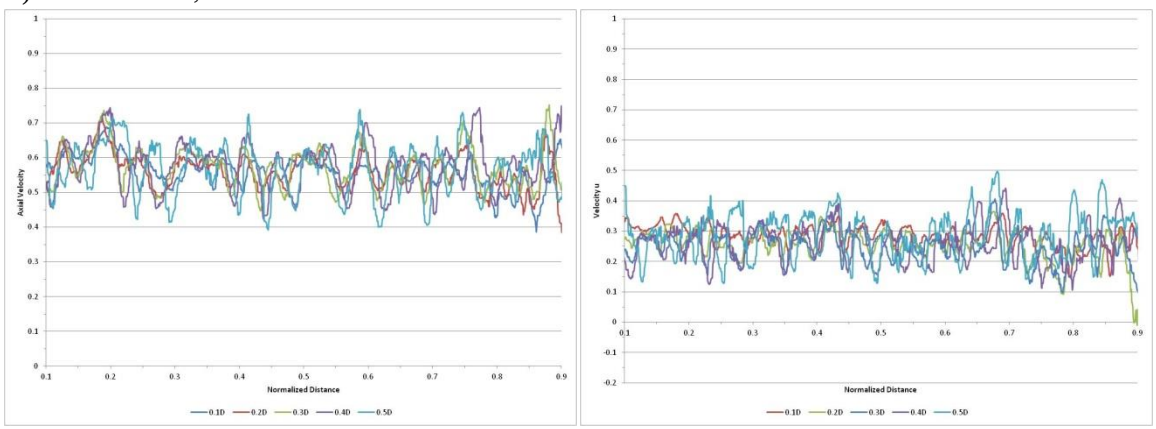


Figure E: Axial and along stream flow:

e) $\phi = 54.7°$; $\alpha = 54.7°$, $\beta = 0°$

iv) Re = 4.4×10^5;

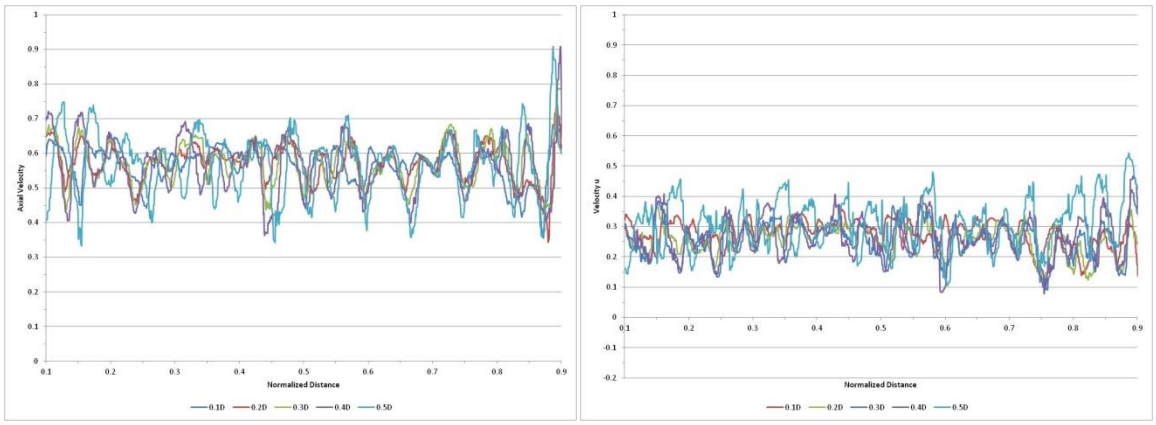


Figure E: Axial and along stream flow:

e) $\phi = 54.7°$; $\alpha = 54.7°$, $\beta = 0°$

v) Re = 5.5×10^5;

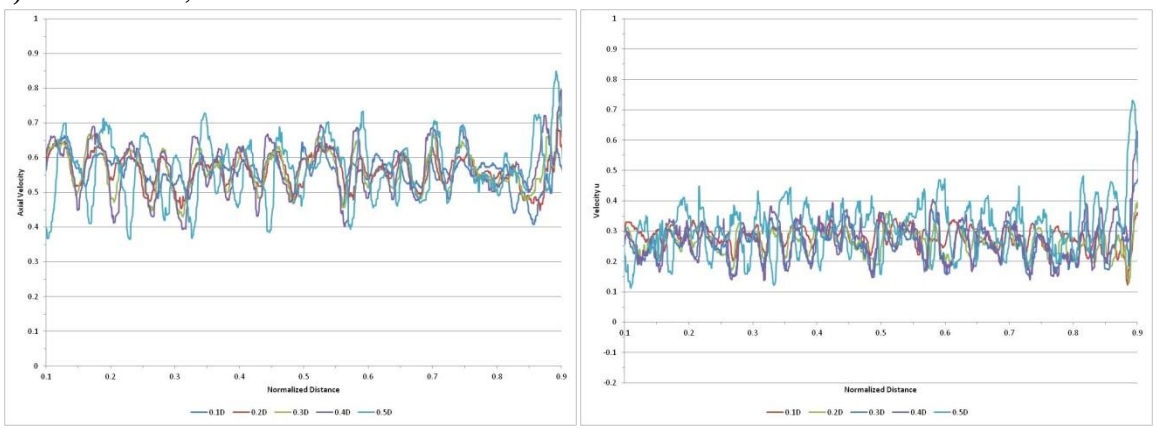


Figure E: Axial and along stream flow:

f) $\phi = 57.1°$; $\alpha = 54.7°$, $\beta = 20°$

i) Re = 1.1×10^5;

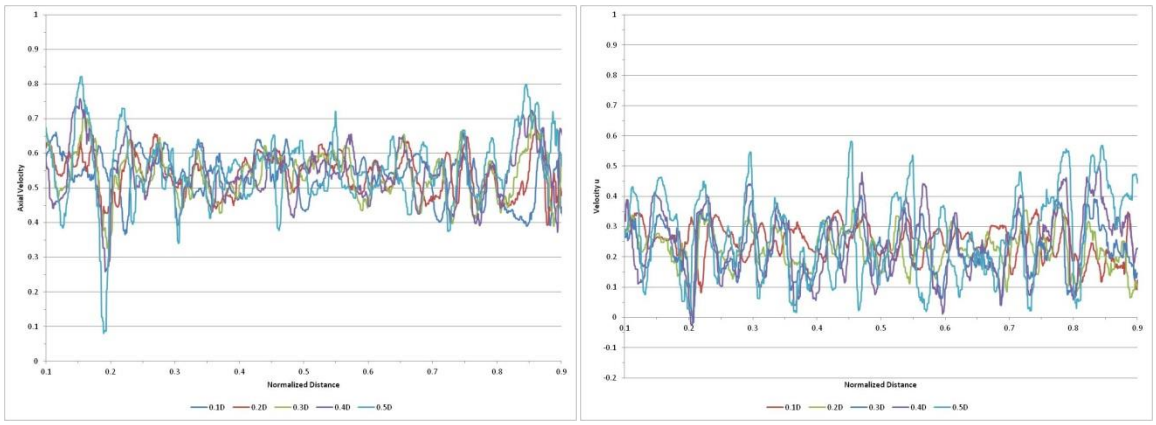


Figure E: Axial and along stream flow:

f) $\phi = 57.1°$; $\alpha = 54.7°$, $\beta = 20°$

ii) Re = 2.2×10^5;

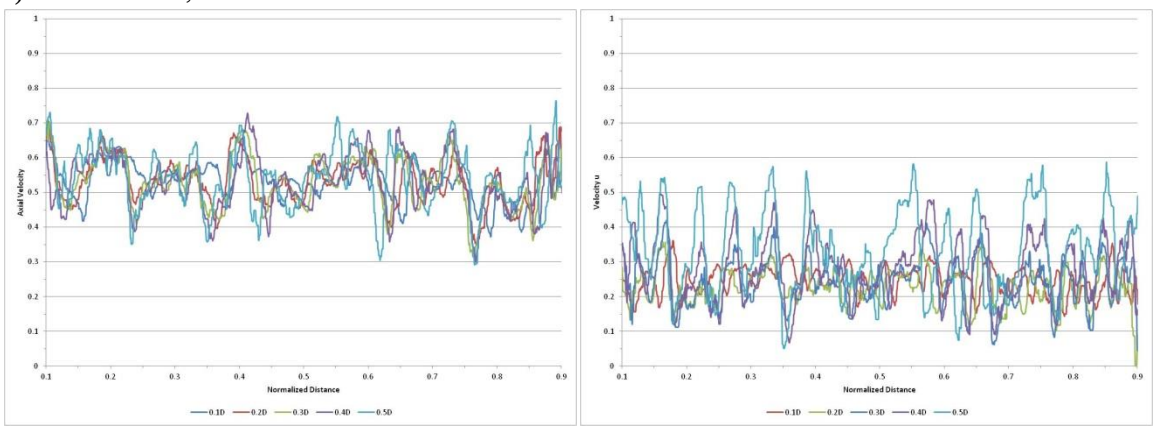


Figure E: Axial and along stream flow:

f) $\phi = 57.1°$; $\alpha = 54.7°$, $\beta = 20°$

iii) Re = 3.3×10^5;

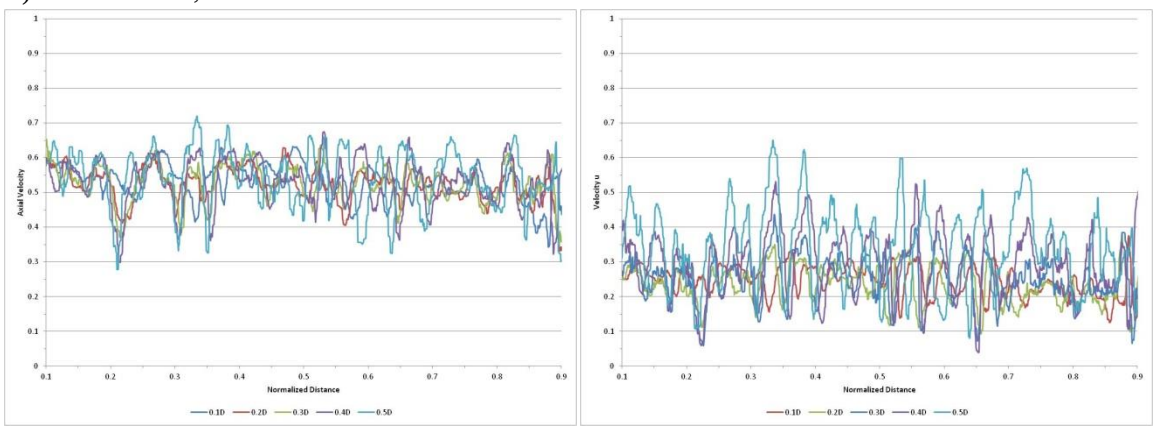


Figure E: Axial and along stream flow:

f) $\phi = 57.1°$; $\alpha = 54.7°$, $\beta = 20°$

iv) Re = 4.4×10^5;

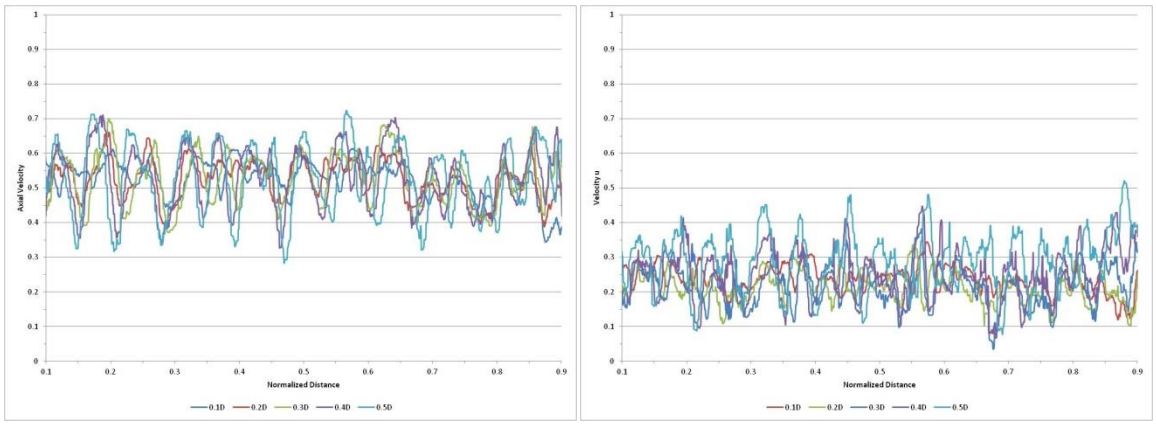


Figure E: Axial and along stream flow:

f) $\phi = 57.1°$; $\alpha = 54.7°$, $\beta = 20°$

v) Re = 5.5×10^5;

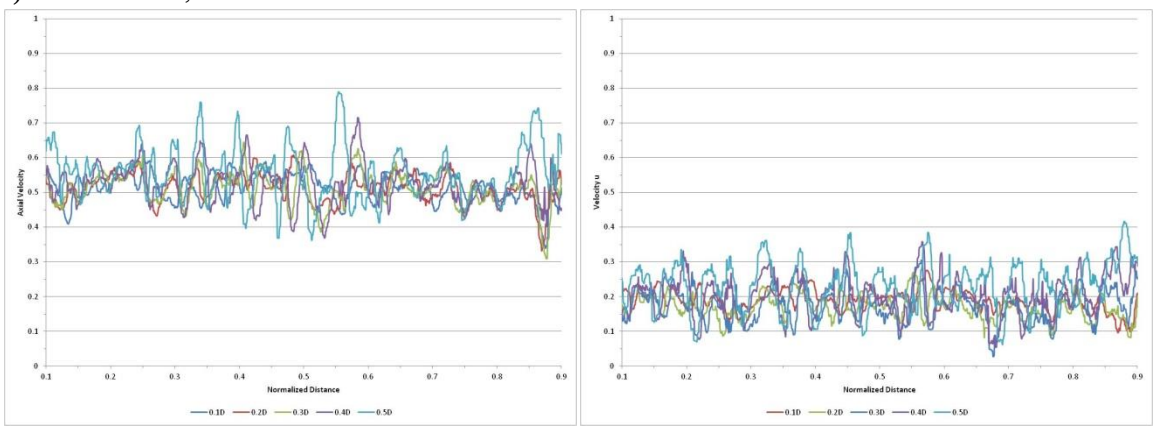


Figure E: Axial and along stream flow:
g) $\phi = 64°$; $\alpha = 54.7°$, $\beta = 40°$
i) Re = 1.1×10^5;

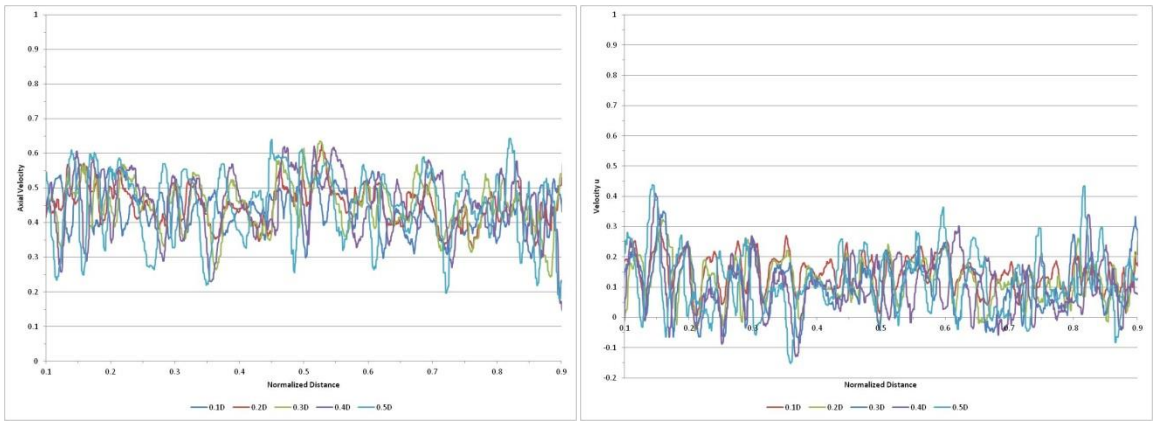


Figure E: Axial and along stream flow:
g) $\phi = 64°$; $\alpha = 54.7°$, $\beta = 40°$
ii) Re = 2.2×10^5;

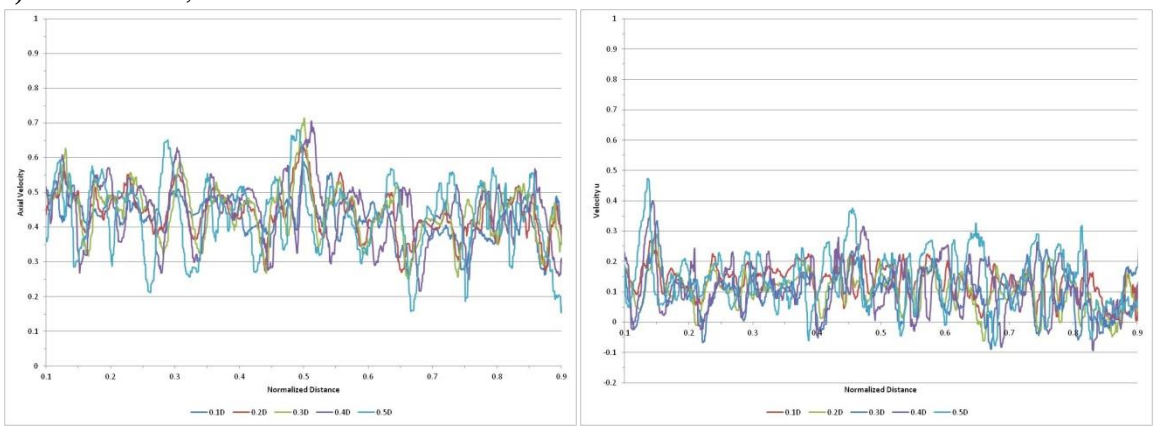


Figure E: Axial and along stream flow:
g) $\phi = 64°$; $\alpha = 54.7°$, $\beta = 40°$
iii) Re = 3.3×10^5;

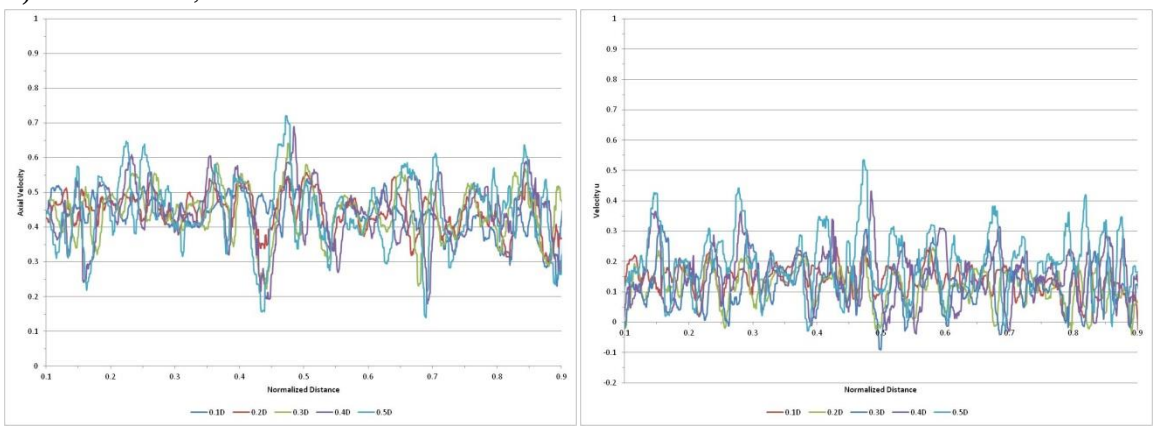


Figure E: Axial and along stream flow:

g) $\phi = 64°$; $\alpha = 54.7°$, $\beta = 40°$

iv) Re = 4.4×10^5;

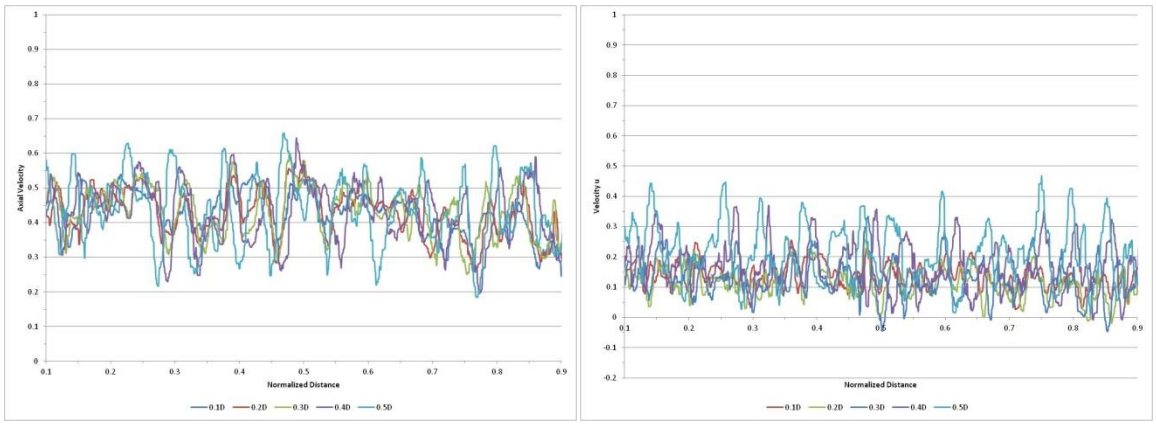


Figure E: Axial and along stream flow:

g) $\phi = 64°$; $\alpha = 54.7°$, $\beta = 40°$

v) Re = 5.5×10^5;

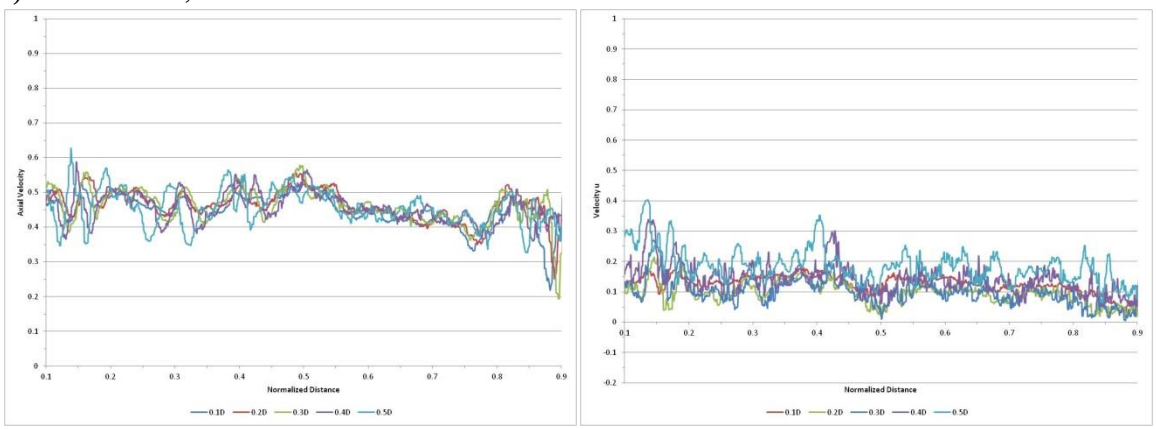


Figure E: Axial and along stream flow:
h) $\phi = 53°$; $\alpha = 50°$, $\beta = 20°$
i) Re = 1.1×10^5;

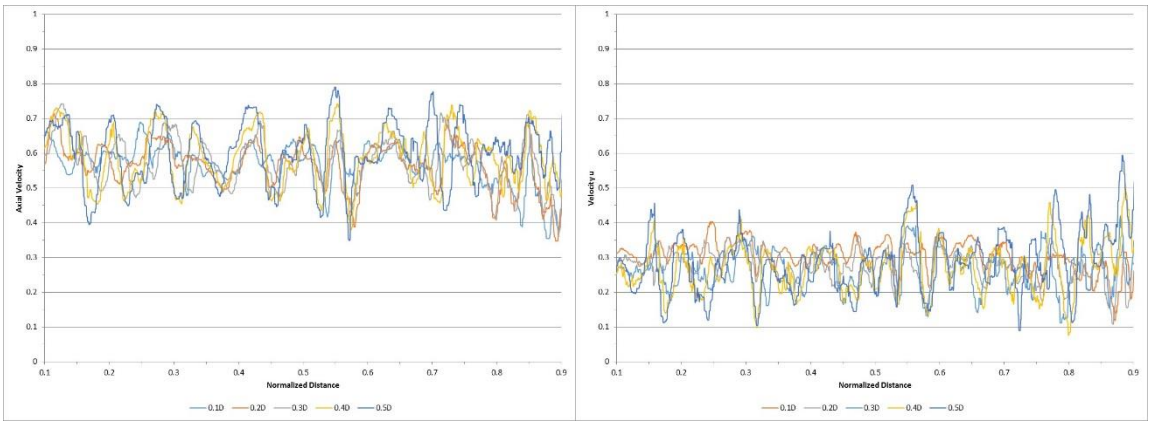


Figure E: Axial and along stream flow:
h) $\phi = 53°$; $\alpha = 50°$, $\beta = 20°$
ii) Re = 2.2×10^5;

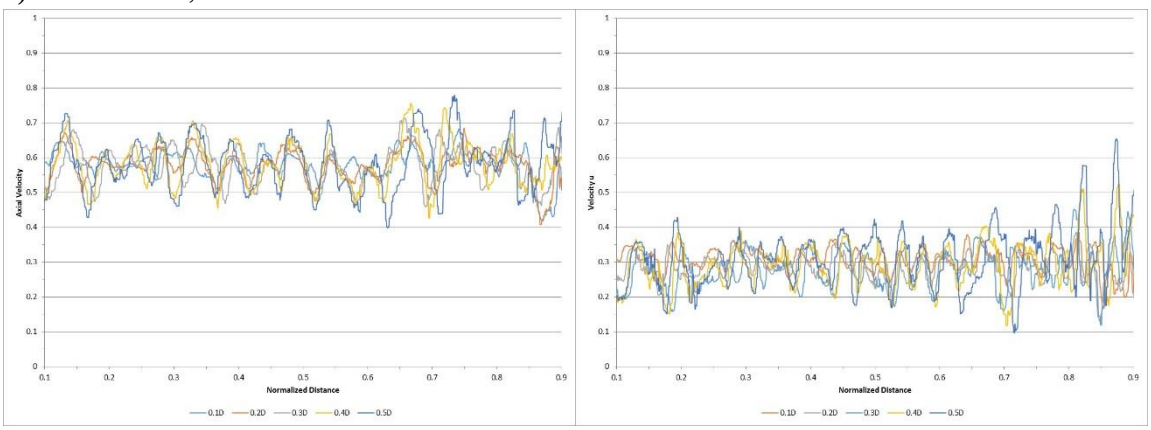


Figure: Axial and along stream flow:
h) $\phi = 53°$; $\alpha = 50°$, $\beta = 20°$
iii) Re = 3.3×10^5;

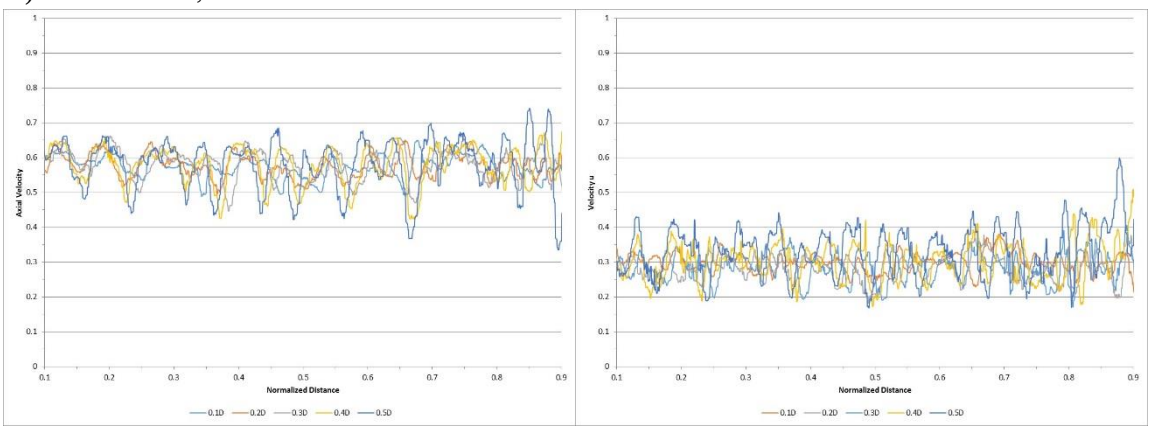


Figure E: Axial and along stream flow:
h) $\phi = 53°$; $\alpha = 50°$, $\beta = 20°$
iv) Re = 4.4×10^5;

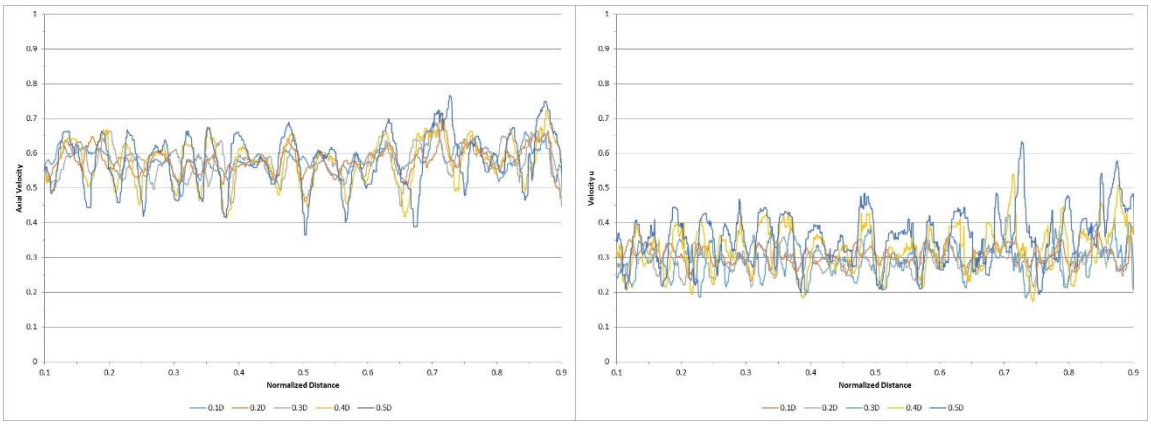


Figure E: Axial and along stream flow:
h) $\phi = 53°$; $\alpha = 50°$, $\beta = 20°$
v) Re = 5.5×10^5;

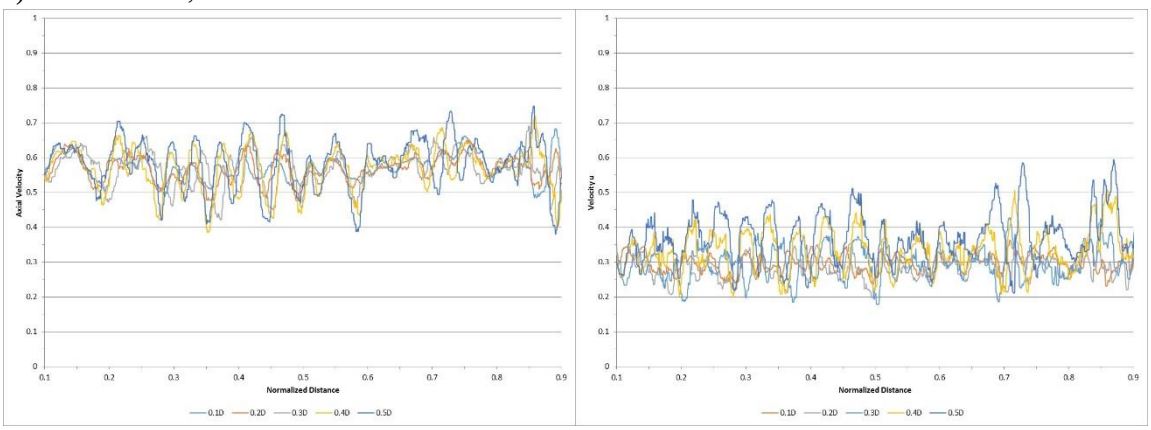


Figure E: Axial and along stream flow:

i) $\phi = 60.5°$; $\alpha = 50°$, $\beta = 40°$

i) Re = 1.1×10^5;

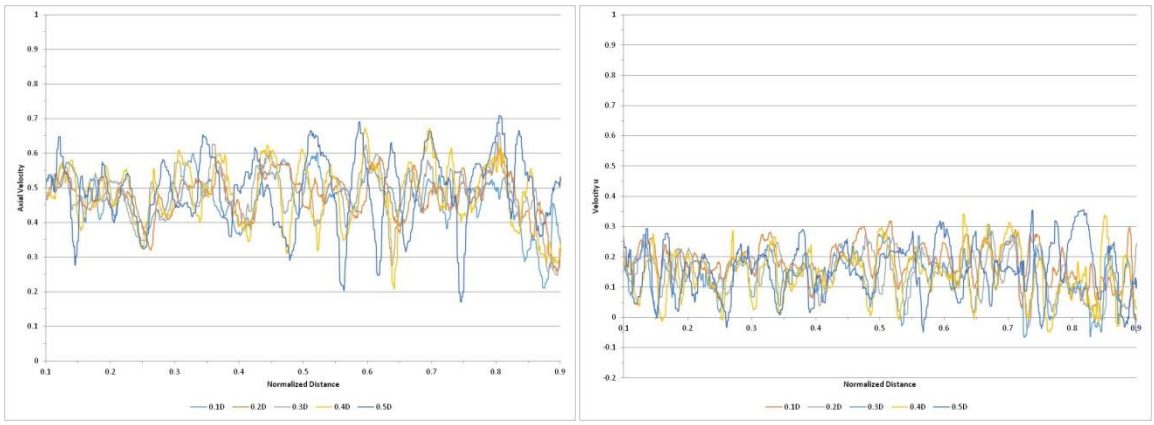


Figure E: Axial and along stream flow:

i) $\phi = 60.5°$; $\alpha = 50°$, $\beta = 40°$

ii) Re = 2.2×10^5;

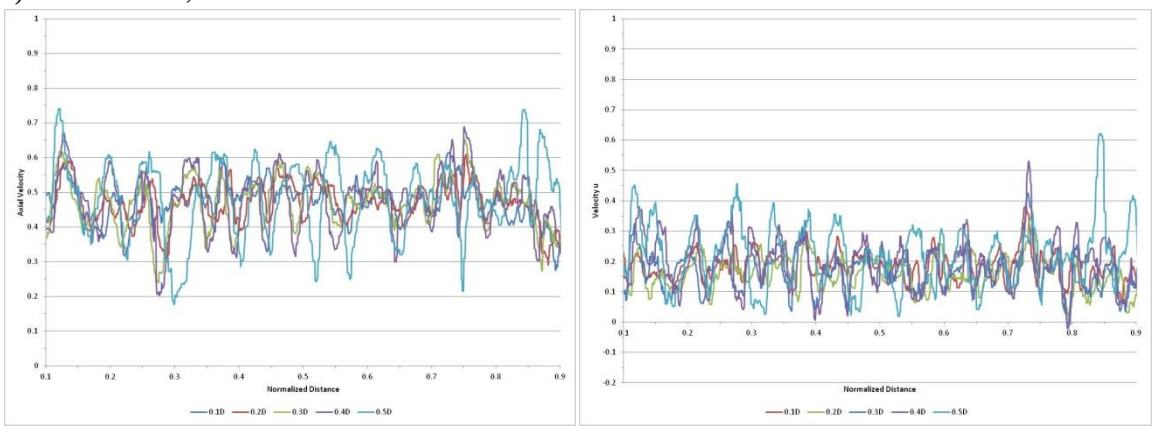


Figure E: Axial and along stream flow:

i) $\phi = 60.5°$; $\alpha = 50°$, $\beta = 40°$

iii) Re = 3.3×10^5;

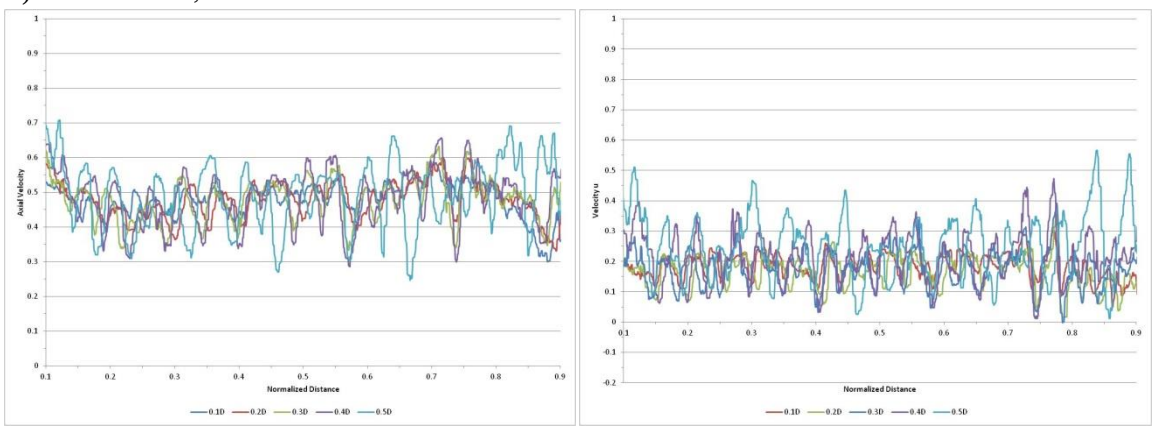


Figure E: Axial and along stream flow:

i) $\phi = 60.5°$; $\alpha = 50°$, $\beta = 40°$

iv) Re = 4.4×10^5;

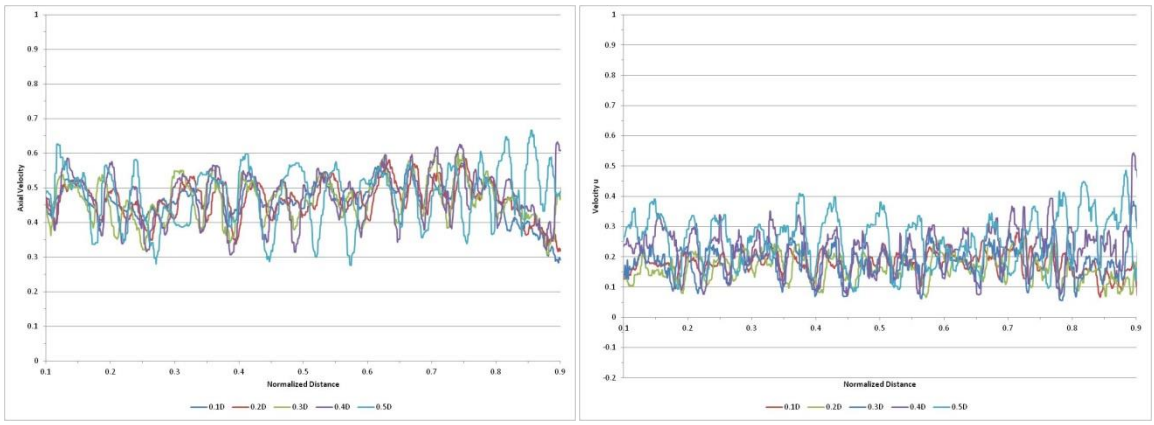


Figure E: Axial and along stream flow:

i) $\phi = 60.5°$; $\alpha = 50°$, $\beta = 40°$

v) Re = 5.5×10^5;

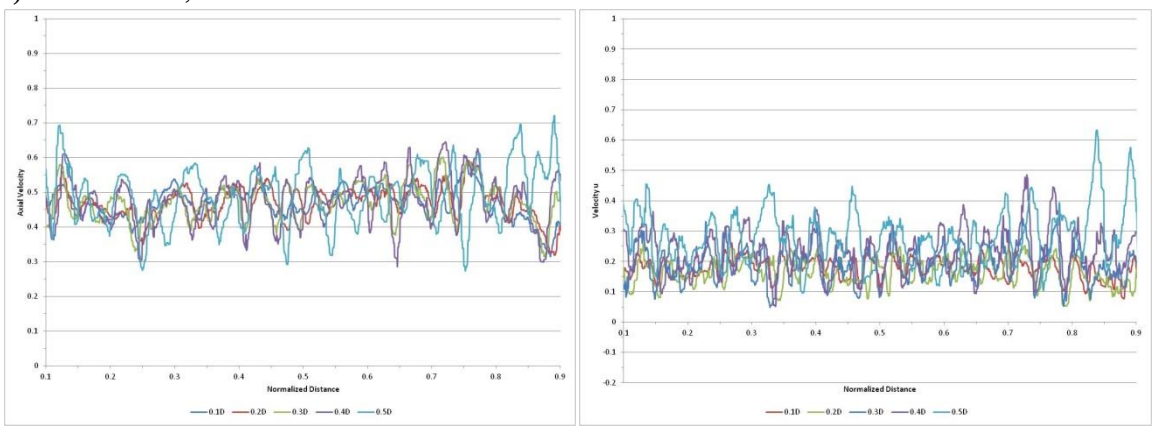


Figure E: Axial and along stream flow:

j) $\phi = 35.5°$; $\alpha = 30°$, $\beta = 20°$

ii) Re = 2.2×10^5;

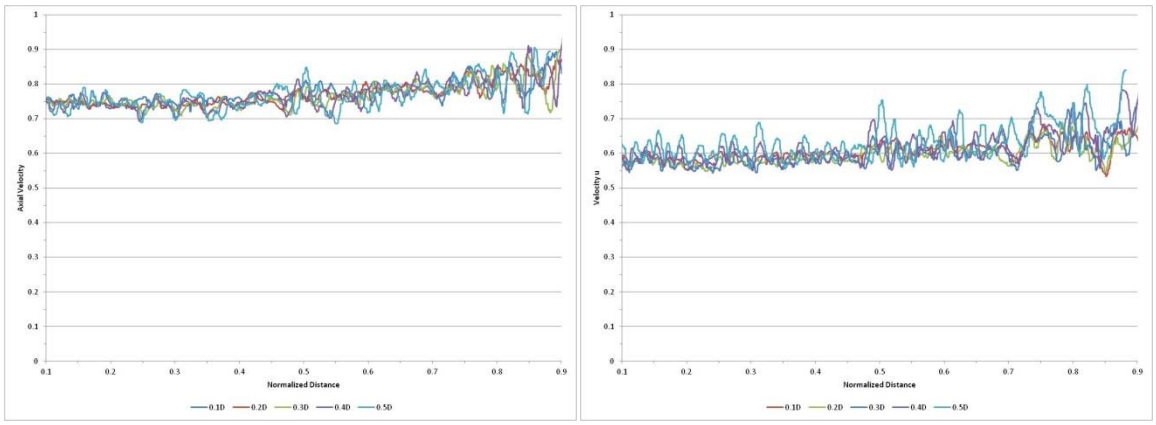


Figure E: Axial and along stream flow:

j) $\phi = 35.5°$; $\alpha = 30°$, $\beta = 20°$

iii) Re = 3.3×10^5;

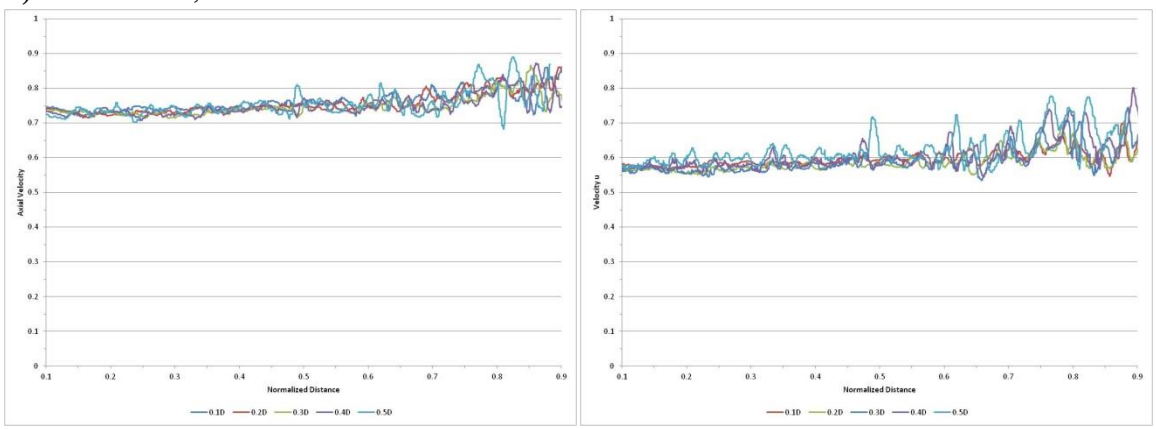


Figure E: Axial and along stream flow:

j) $\phi = 35.5°$; $\alpha = 30°$, $\beta = 20°$

iv) Re = 4.4×10^5;

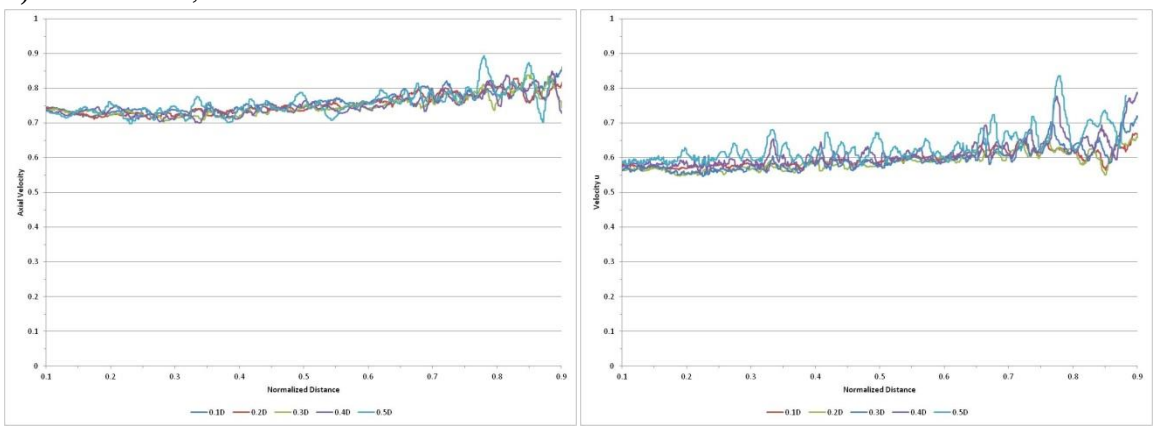
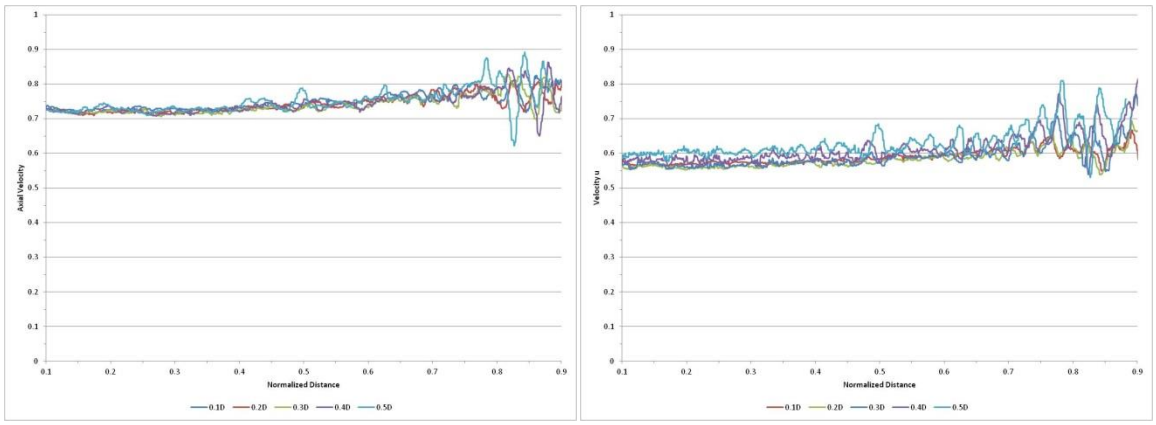


Figure E: Axial and along stream flow:
j) $\phi = 35.5°$; $\alpha = 30°$, $\beta = 20°$
v) Re = 5.5×10^5;

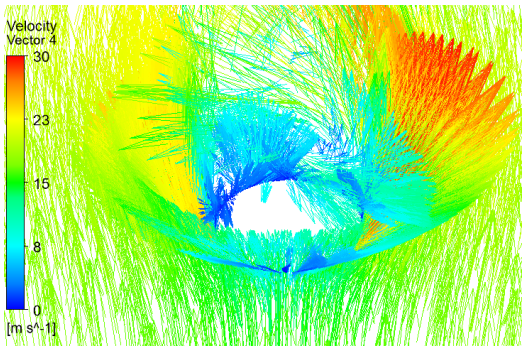


Appendix F: Velocity Vectors

Figure F: Velocity vectors

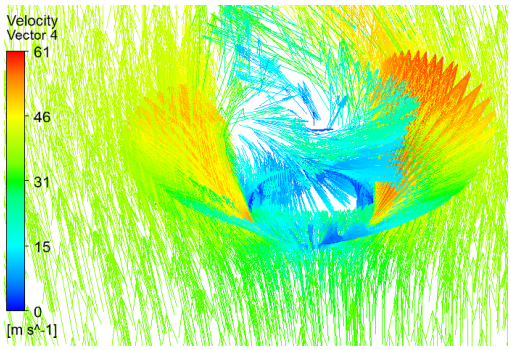
a) $\phi = 0°$; $\alpha = 0°$, $\beta = 0°$

i) Re = 1.1×10^5;



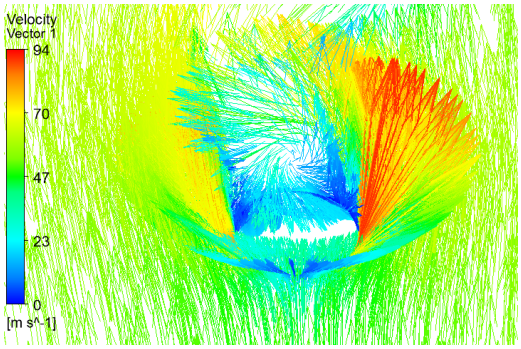
a) $\phi = 0°$; $\alpha = 0°$, $\beta = 0°$

ii) Re = 2.2×10^5;



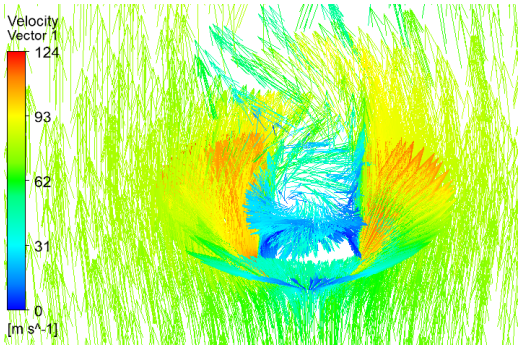
a) $\phi = 0°$; $\alpha = 0°$, $\beta = 0°$

iii) Re = 3.3×10^5;



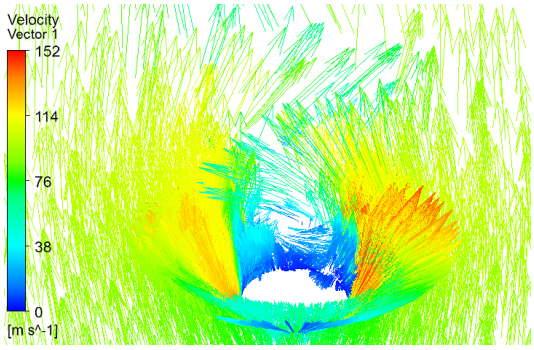
a) $\phi = 0°$; $\alpha = 0°$, $\beta = 0°$

iv) Re = 4.4×10^5;



a) $\phi = 0°$; $\alpha = 0°$, $\beta = 0°$

v) Re = 5.5×10^5;



a) $\phi = 0°$; $\alpha = 0°$, $\beta = 0°$

vi) Re = 6.7×10^5;

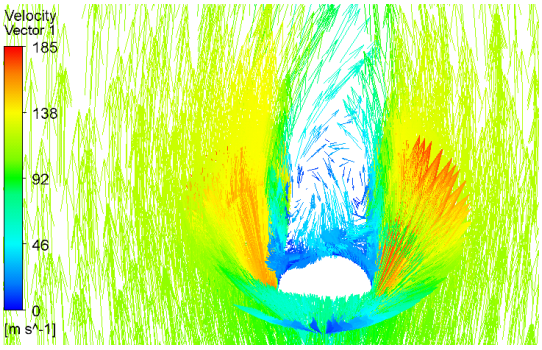
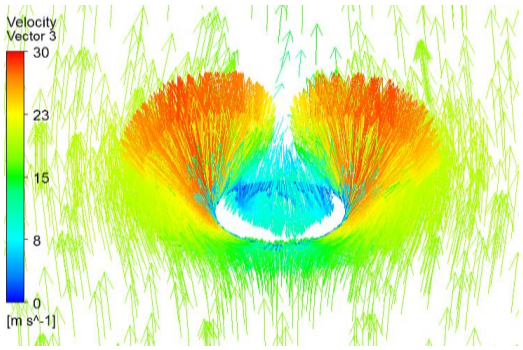


Figure F: Velocity vectors

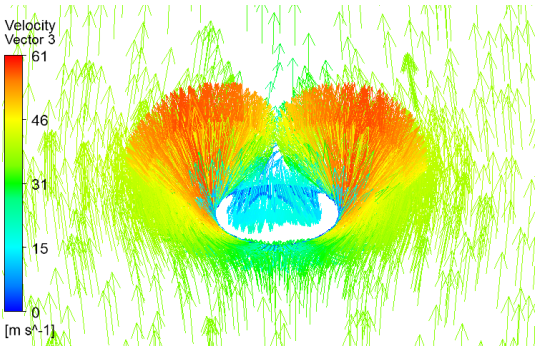
b) $\phi = 60°$; $\alpha = 60°$, $\beta = 0°$

i) Re = 1.1×10^5;



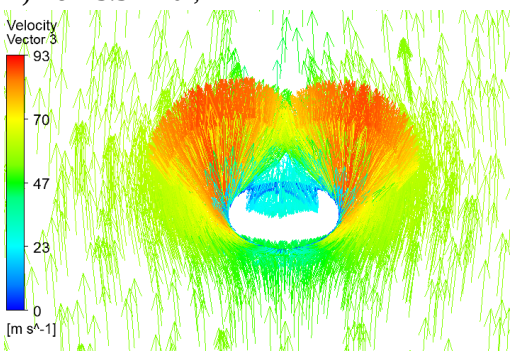
b) $\phi = 60°$; $\alpha = 60°$, $\beta = 0°$

ii) Re = 2.2×10^5;



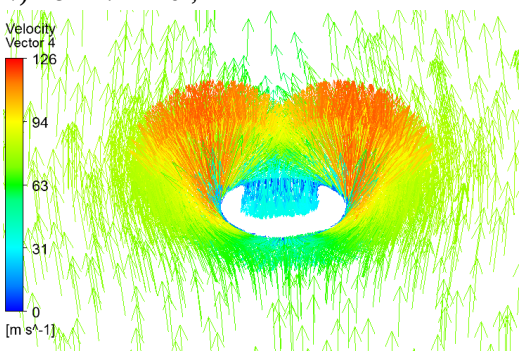
b) $\phi = 60°$; $\alpha = 60°$, $\beta = 0°$

iii) Re = 3.3×10^5;



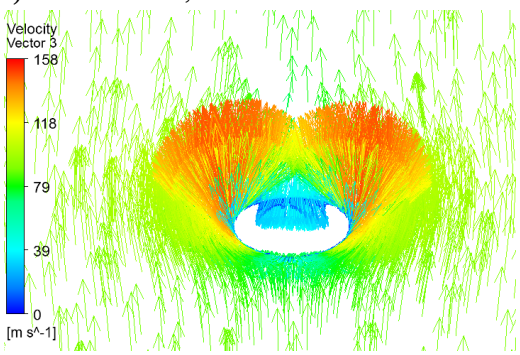
b) $\phi = 60°$; $\alpha = 60°$, $\beta = 0°$

iv) Re = 4.4×10^5;



b) $\phi = 60°$; $\alpha = 60°$, $\beta = 0°$

v) Re = 5.5×10^5;



b) $\phi = 60°$; $\alpha = 60°$, $\beta = 0°$

vi) Re = 6.7×10^5;

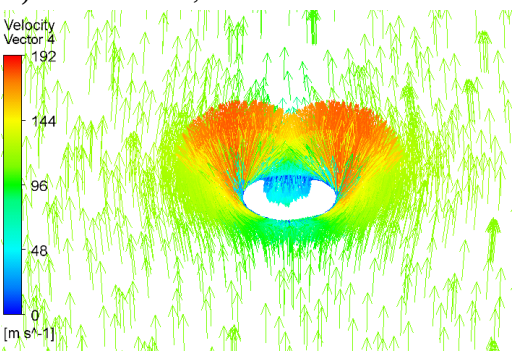
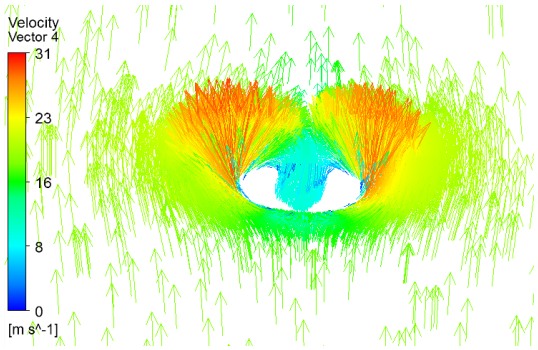


Figure F: Velocity vectors

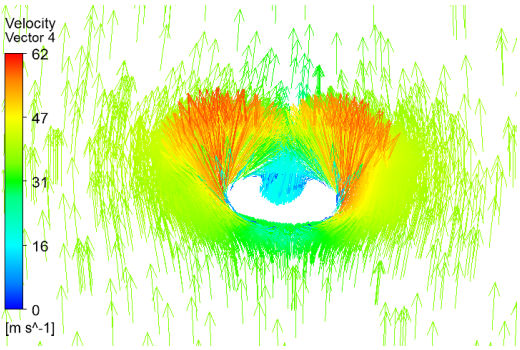
c) $\phi = 62°$; $\alpha = 60°$, $\beta = 20°$

i) Re = 1.1×10^5;



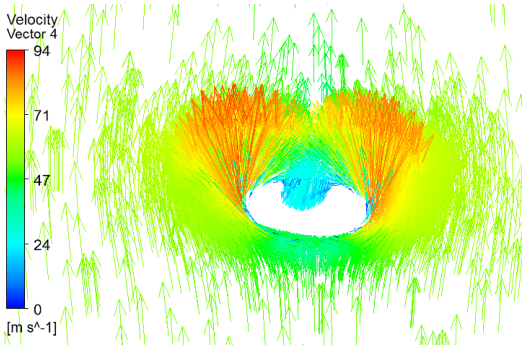
c) $\phi = 62°$; $\alpha = 60°$, $\beta = 20°$

ii) Re = 2.2×10^5;



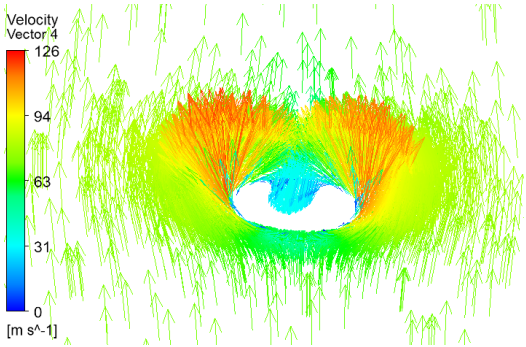
c) $\phi = 62°$; $\alpha = 60°$, $\beta = 20°$

iii) Re = 3.3×10^5;



c) $\phi = 62°$; $\alpha = 60°$, $\beta = 20°$

iv) Re = 4.4×10^5;



c) $\phi = 62°$; $\alpha = 60°$, $\beta = 20°$

v) Re = 5.5×10^5;

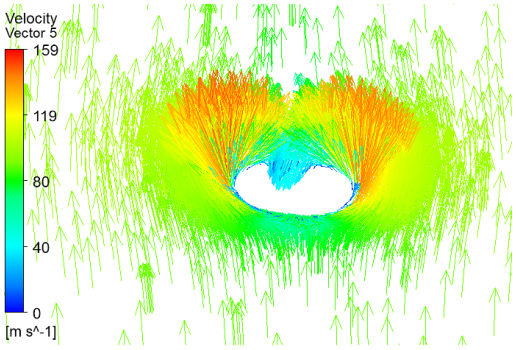
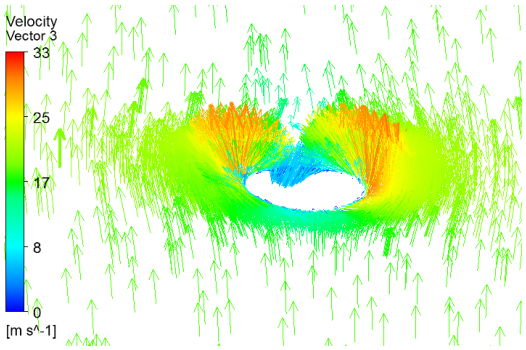


Figure F: Velocity vectors

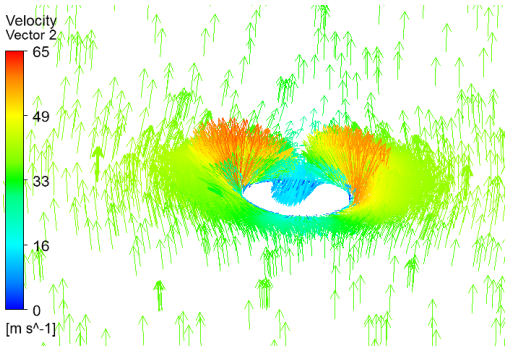
d) $\phi = 67.5°$; $\alpha = 60°$, $\beta = 40°$

i) Re = 1.1×10^5;



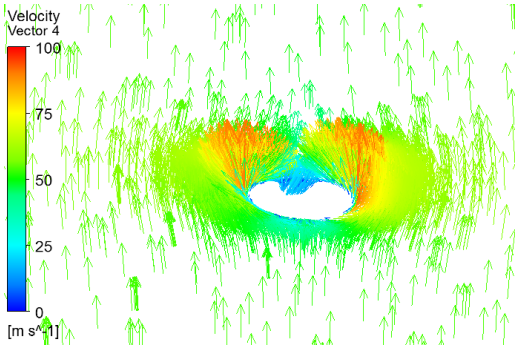
d) $\phi = 67.5°$; $\alpha = 60°$, $\beta = 40°$

ii) Re = 2.2×10^5;



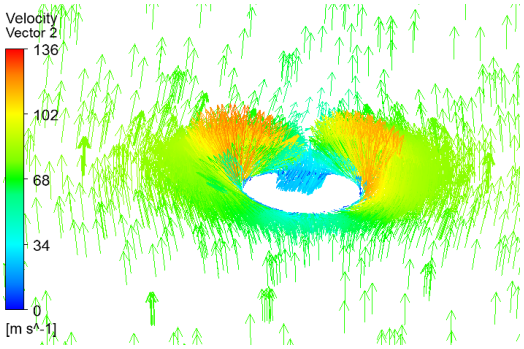
d) $\phi = 67.5°$; $\alpha = 60°$, $\beta = 40°$

iii) Re = 3.3×10^5;



d) $\phi = 67.5°$; $\alpha = 60°$, $\beta = 40°$

iv) Re = 4.4×10^5;



d) $\phi = 67.5°$; $\alpha = 60°$, $\beta = 40°$

v) Re = 5.5×10^5;

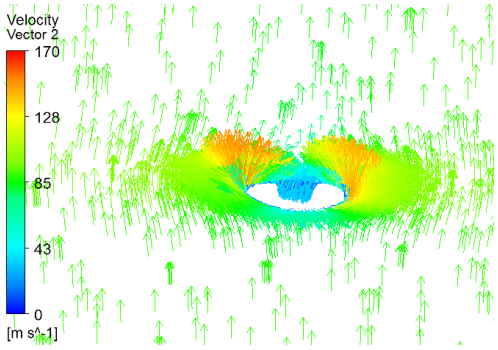
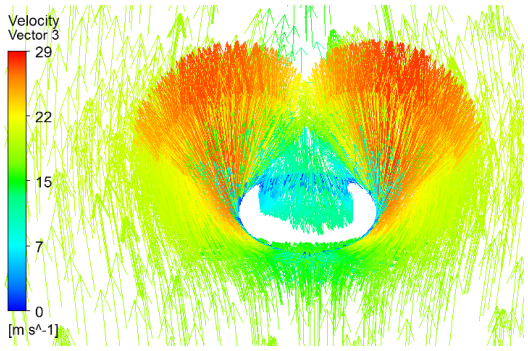


Figure F: Velocity vectors

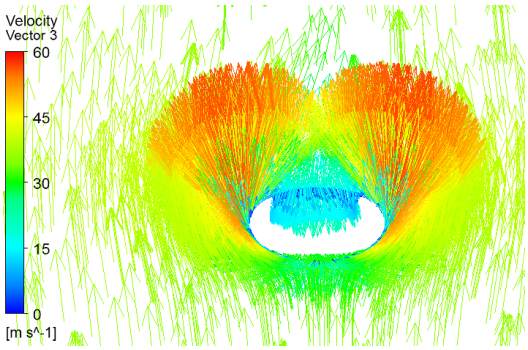
e) $\phi = 54.7°$; $\alpha = 54.7°$, $\beta = 0°$

i) Re = 1.1×10^5;



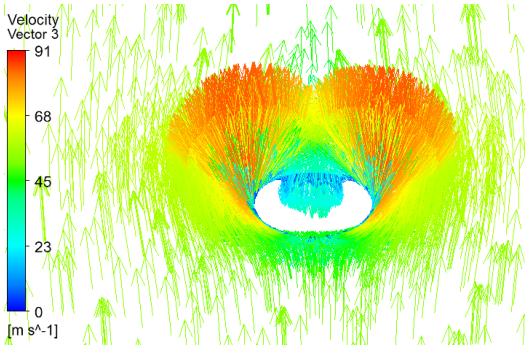
e) $\phi = 54.7°$; $\alpha = 54.7°$, $\beta = 0°$

ii) Re = 2.2×10^5;



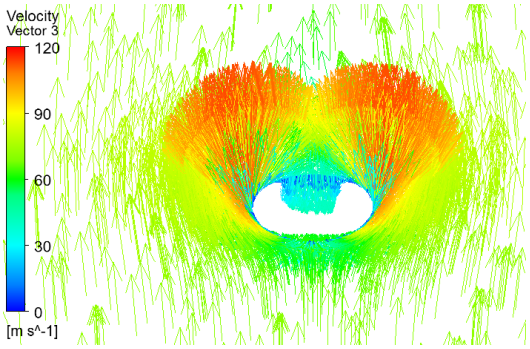
e) $\phi = 54.7°$; $\alpha = 54.7°$, $\beta = 0°$

iii) Re = 3.3×10^5;



e) $\phi = 54.7°$; $\alpha = 54.7°$, $\beta = 0°$

iv) Re = 4.4×10^5;



e) $\phi = 54.7°$; $\alpha = 54.7°$, $\beta = 0°$

v) Re = 5.5×10^5;

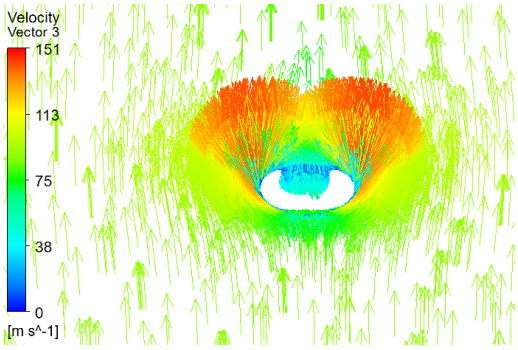
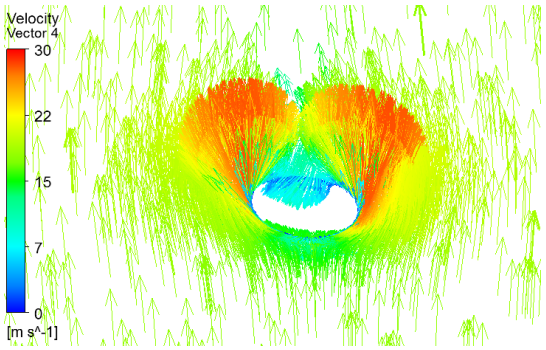


Figure F: Velocity vectors

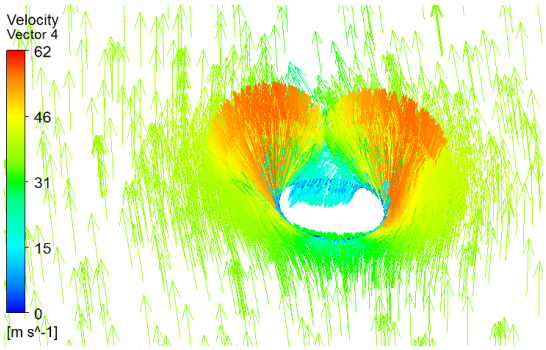
f) $\phi = 57.1°$; $\alpha = 54.7°$, $\beta = 20°$

i) Re = 1.1×10^5;



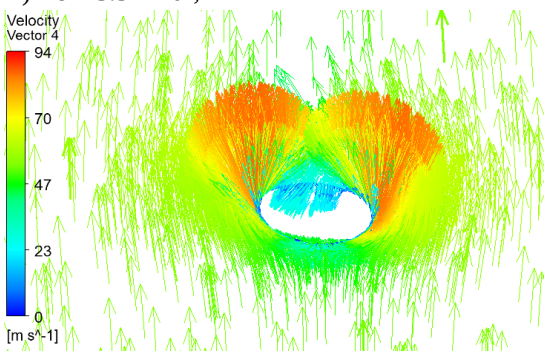
f) $\phi = 57.1°$; $\alpha = 54.7°$, $\beta = 20°$

ii) Re = 2.2×10^5;



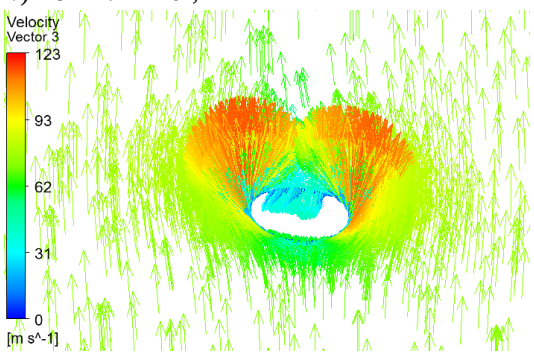
f) $\phi = 57.1°$; $\alpha = 54.7°$, $\beta = 20°$

iii) Re = 3.3×10^5;



f) $\phi = 57.1°$; $\alpha = 54.7°$, $\beta = 20°$

iv) Re = 4.4×10^5;



f) $\phi = 57.1°$; $\alpha = 54.7°$, $\beta = 20°$

v) Re = 5.5×10^5;

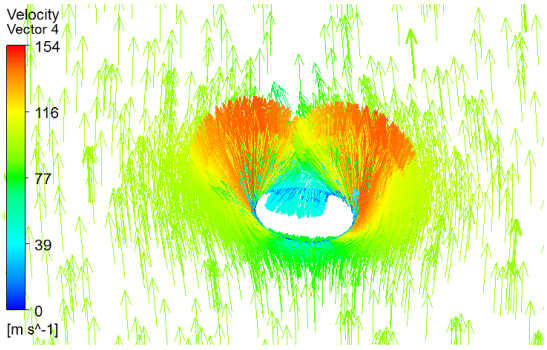
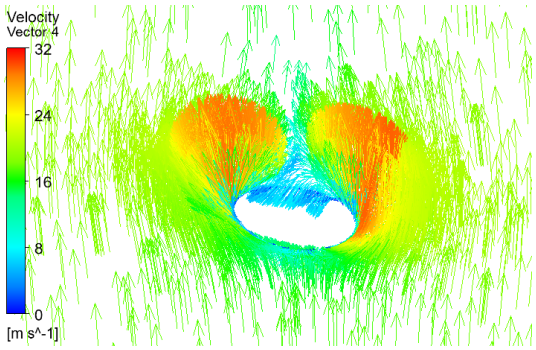


Figure F: Velocity vectors

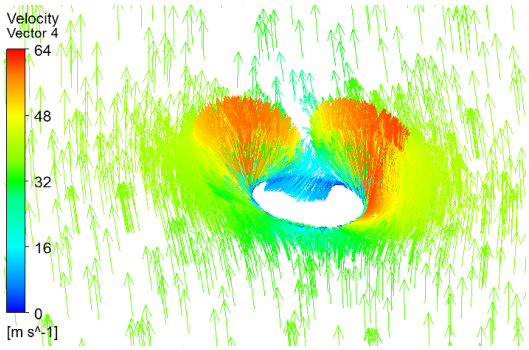
g) $\phi = 64°$; $\alpha = 54.7°$, $\beta = 40°$

i) Re = 1.1×10^5;



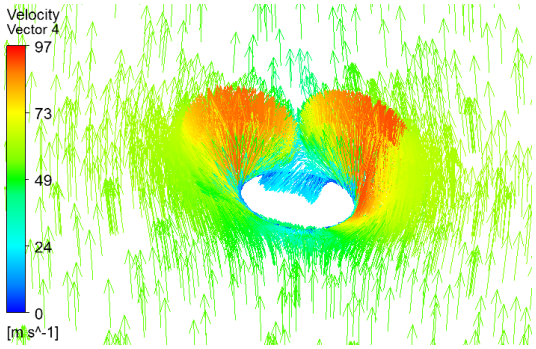
g) $\phi = 64°$; $\alpha = 54.7°$, $\beta = 40°$

ii) Re = 2.2×10^5;



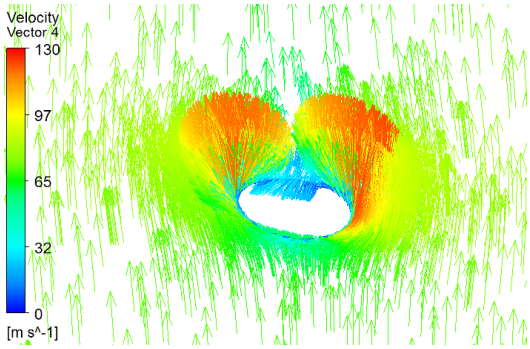
g) $\phi = 64°$; $\alpha = 54.7°$, $\beta = 40°$

iii) Re = 3.3×10^5;



g) $\phi = 64°$; $\alpha = 54.7°$, $\beta = 40°$

iv) Re = 4.4×10^5;



g) $\phi = 64°$; $\alpha = 54.7°$, $\beta = 40°$

v) Re = 5.5×10^5;

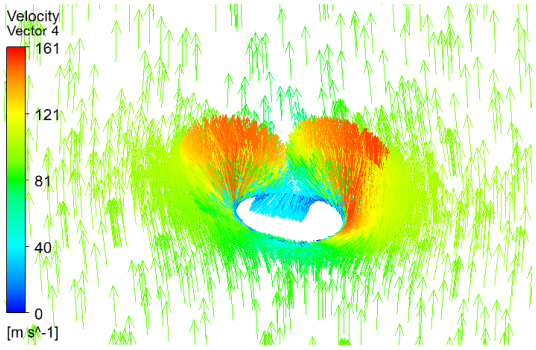
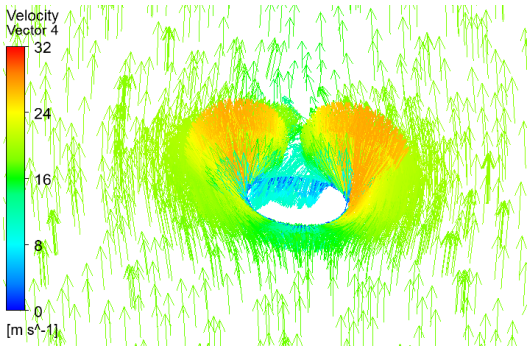


Figure F: Velocity vectors

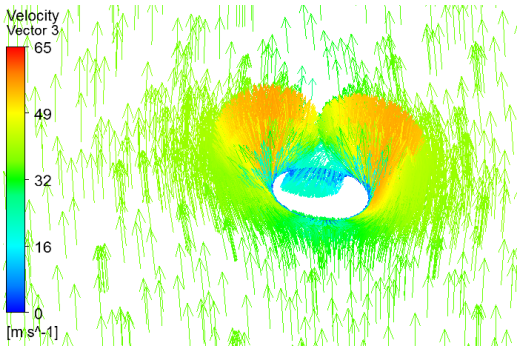
h) $\phi = 53°$; $\alpha = 50°$, $\beta = 20°$

i) Re = 1.1×10^5;



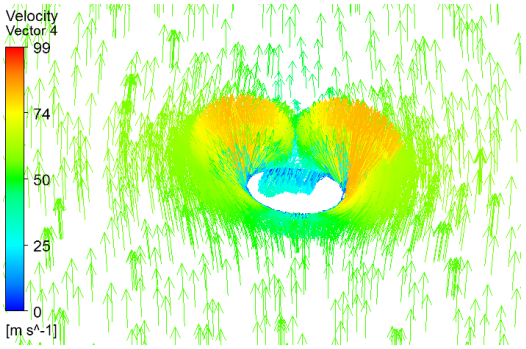
h) $\phi = 53°$; $\alpha = 50°$, $\beta = 20°$

ii) Re = 2.2×10^5;



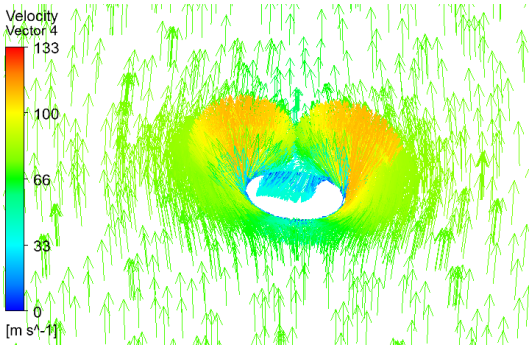
h) $\phi = 53°$; $\alpha = 50°$, $\beta = 20°$

iii) Re = 3.3×10^5;



h) $\phi = 53°$; $\alpha = 50°$, $\beta = 20°$

iv) Re = 4.4×10^5;



h) $\phi = 53°$; $\alpha = 50°$, $\beta = 20°$

v) Re = 5.5×10^5;

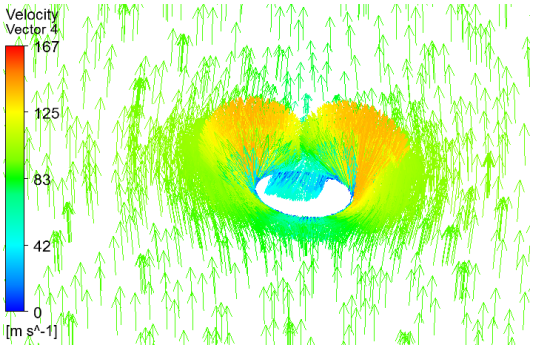
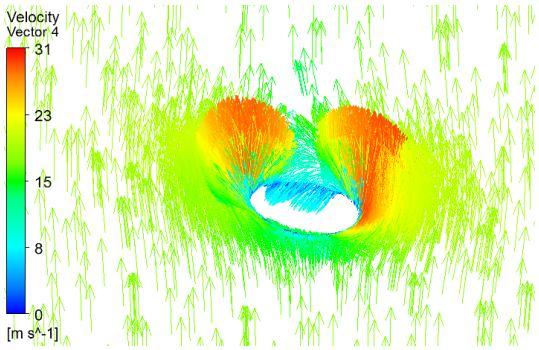


Figure F: Velocity vectors

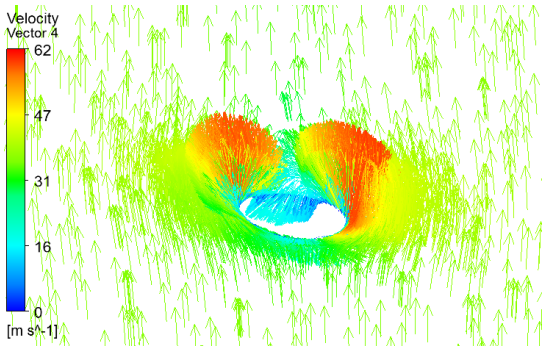
i) $\phi = 60.5°$; $\alpha = 50°$, $\beta = 40°$

i) Re = 1.1×10^5;



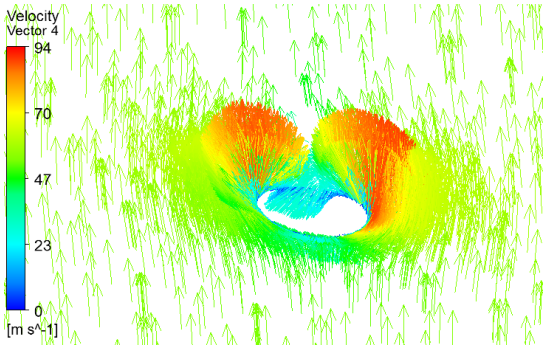
i) $\phi = 60.5°$; $\alpha = 50°$, $\beta = 40°$

ii) Re = 2.2×10^5;



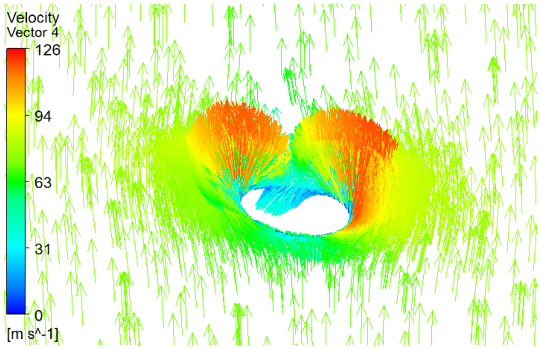
i) $\phi = 60.5°$; $\alpha = 50°$, $\beta = 40°$

iii) Re = 3.3×10^5;



i) $\phi = 60.5°$; $\alpha = 50°$, $\beta = 40°$

iv) Re = 4.4×10^5;



i) $\phi = 60.5°$; $\alpha = 50°$, $\beta = 40°$

v) Re = 5.5×10^5;

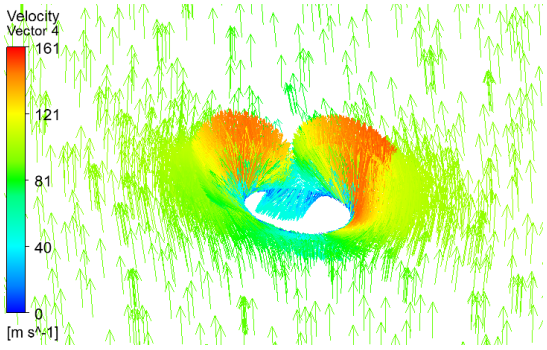
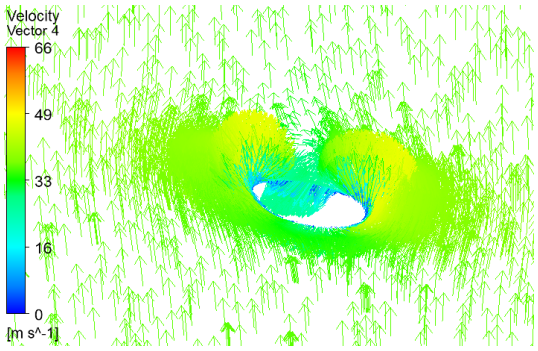


Figure F: Velocity vectors

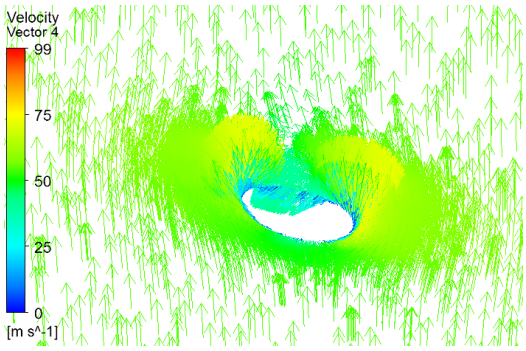
j) $\phi = 35.5°$; $\alpha = 30°$, $\beta = 20°$

ii) Re = 2.2×10^5;



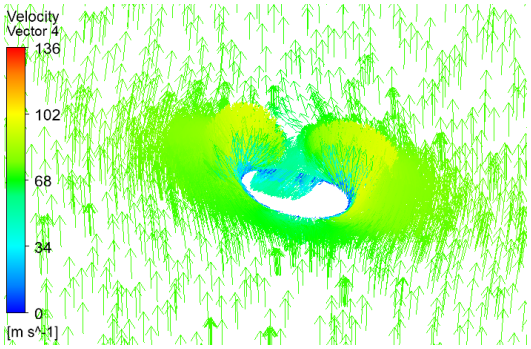
j) $\phi = 35.5°$; $\alpha = 30°$, $\beta = 20°$

iii) Re = 3.3×10^5;



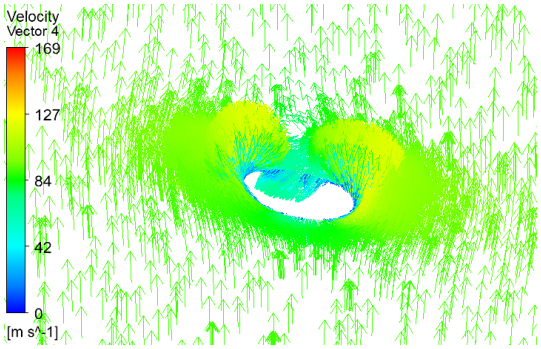
j) $\phi = 35.5°$; $\alpha = 30°$, $\beta = 20°$

iv) Re = 4.4×10^5;



j) $\phi = 35.5°$; $\alpha = 30°$, $\beta = 20°$

v) Re = 5.5×10^5;

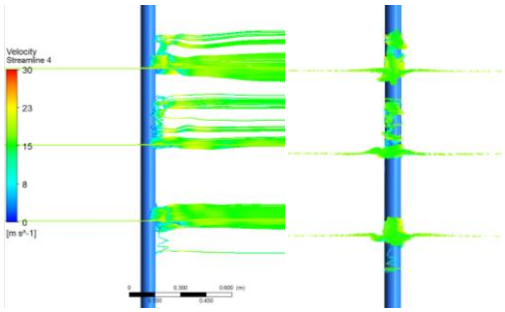


Appendix G: Axial Flow Visualization, Velocity Streamlines

Figure G: Axial flow visualization, velocity streamlines

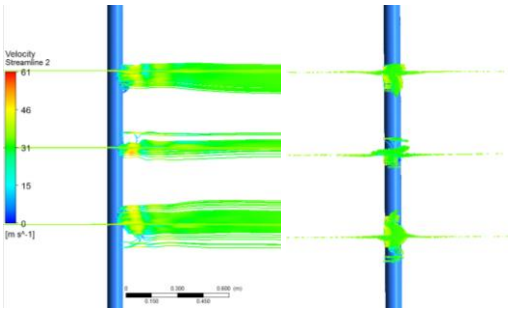
a) $\phi = 0°$; $\alpha = 0°$, $\beta = 0°$

i) Re = 1.1×10^5;



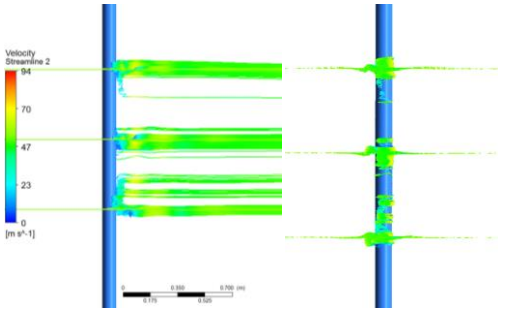
a) $\phi = 0°$; $\alpha = 0°$, $\beta = 0°$

ii) Re = 2.2×10^5;



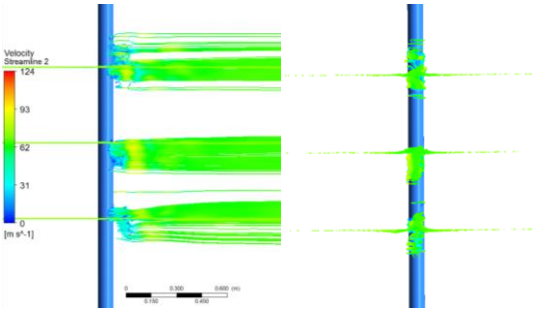
a) $\phi = 0°$; $\alpha = 0°$, $\beta = 0°$

iii) Re = 3.3×10^5;



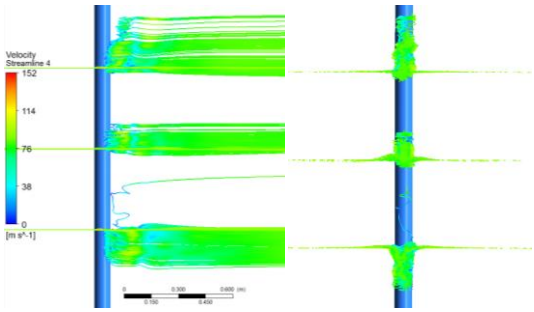
a) $\phi = 0°$; $\alpha = 0°$, $\beta = 0°$

iv) Re = 4.4×10^5;



a) $\phi = 0°$; $\alpha = 0°$, $\beta = 0°$

v) Re = 5.5×10^5;



a) $\phi = 0°$; $\alpha = 0°$, $\beta = 0°$

vi) Re = 6.7×10^5;

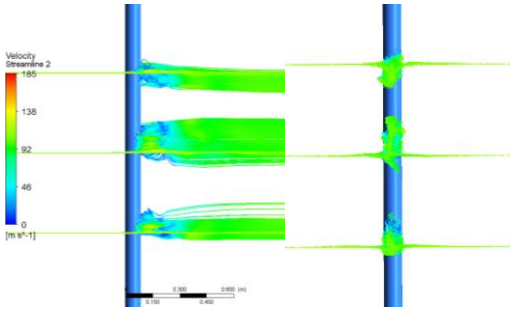
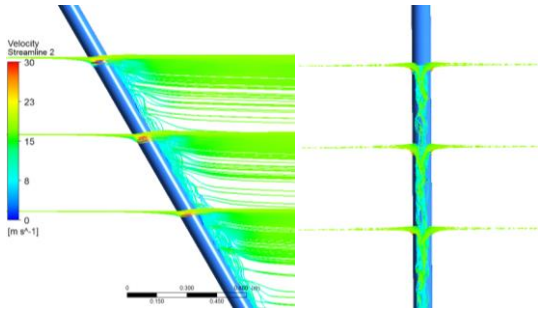


Figure G: Axial flow visualization, velocity streamlines

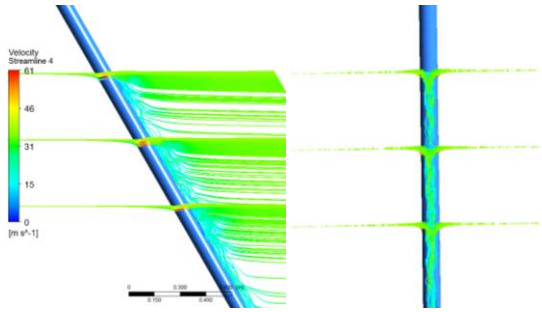
b) $\phi = 60°$; $\alpha = 60°$, $\beta = 0°$

i) Re = 1.1×10^5;



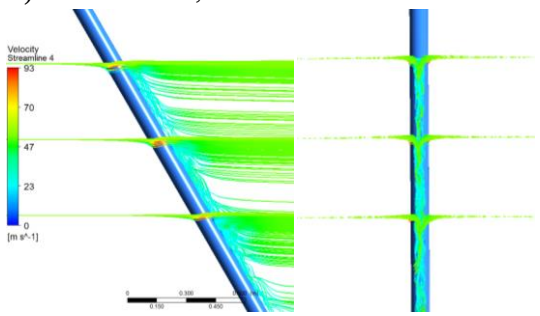
b) $\phi = 60°$; $\alpha = 60°$, $\beta = 0°$

ii) Re = 2.2×10^5;



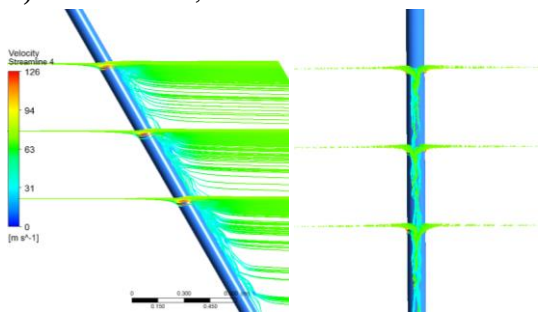
b) $\phi = 60°$; $\alpha = 60°$, $\beta = 0°$

iii) Re = 3.3×10^5;



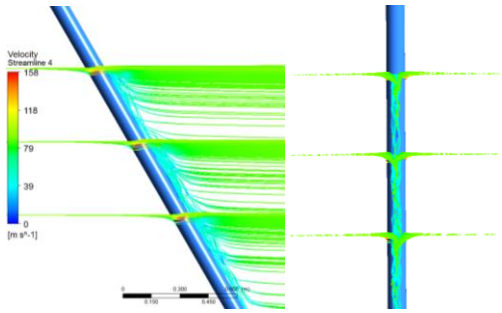
b) $\phi = 60°$; $\alpha = 60°$, $\beta = 0°$

iv) Re = 4.4×10^5;



b) $\phi = 60°$; $\alpha = 60°$, $\beta = 0°$

v) Re = 5.5×10^5;



b) $\phi = 60°$; $\alpha = 60°$, $\beta = 0°$

vi) Re = 6.7×10^5;

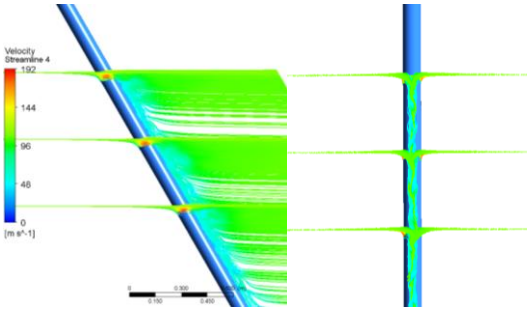
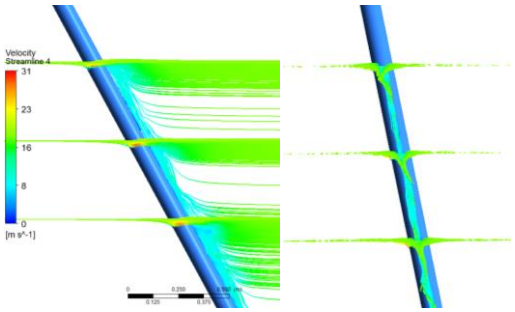
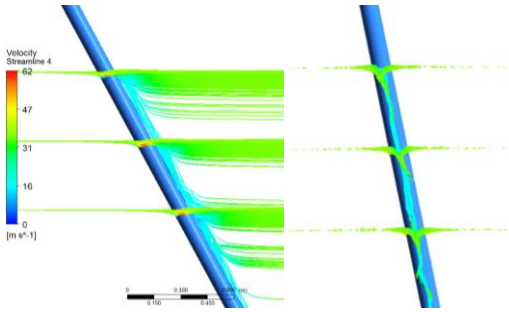


Figure G: Axial flow visualization, velocity streamlines

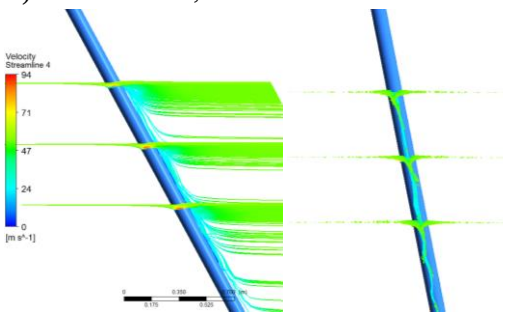
c) $\phi = 62°$; $\alpha = 60°$, $\beta = 20°$
i) Re = 1.1×10^5;



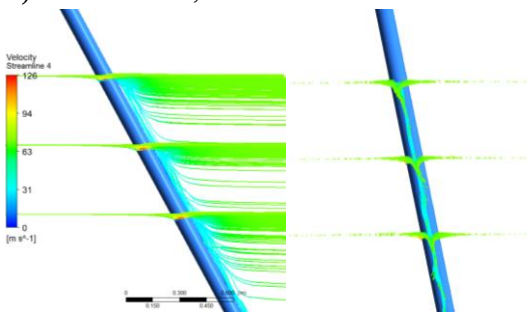
c) $\phi = 62°$; $\alpha = 60°$, $\beta = 20°$
ii) Re = 2.2×10^5;



c) $\phi = 62°$; $\alpha = 60°$, $\beta = 20°$
iii) Re = 3.3×10^5;



c) $\phi = 62°$; $\alpha = 60°$, $\beta = 20°$
iv) Re = 4.4×10^5;



c) $\phi = 62°$; $\alpha = 60°$, $\beta = 20°$
v) Re = 5.5×10^5;

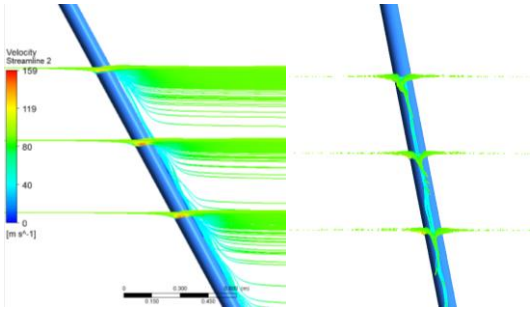
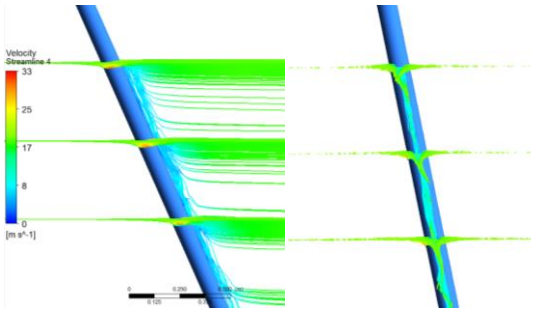
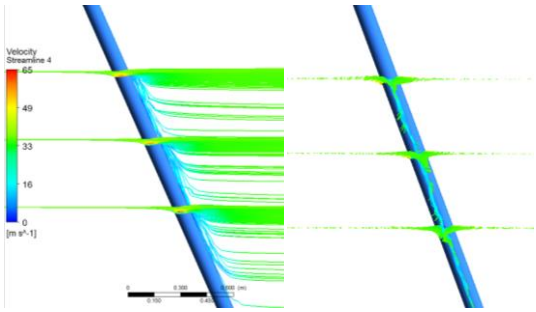


Figure G: Axial flow visualization, velocity streamlines

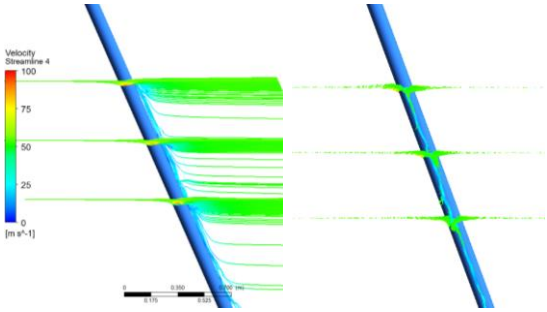
d) $\phi = 67.5°$; $\alpha = 60°$, $\beta = 40°$
i) Re = 1.1×10^5;



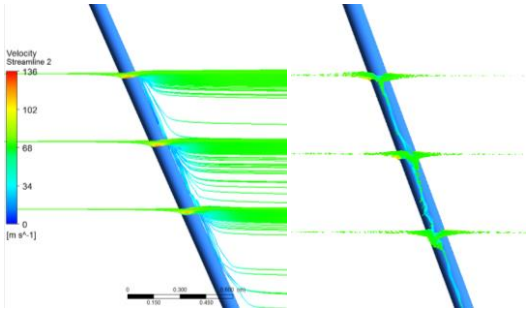
d) $\phi = 67.5°$; $\alpha = 60°$, $\beta = 40°$
ii) Re = 2.2×10^5;



d) $\phi = 67.5°$; $\alpha = 60°$, $\beta = 40°$
iii) Re = 3.3×10^5;



d) $\phi = 67.5°$; $\alpha = 60°$, $\beta = 40°$
iv) Re = 4.4×10^5;



d) $\phi = 67.5°$; $\alpha = 60°$, $\beta = 40°$
v) Re = 5.5×10^5;

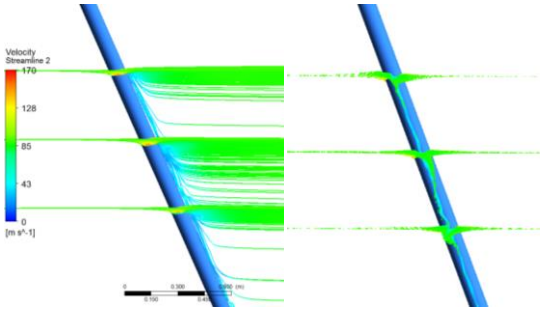
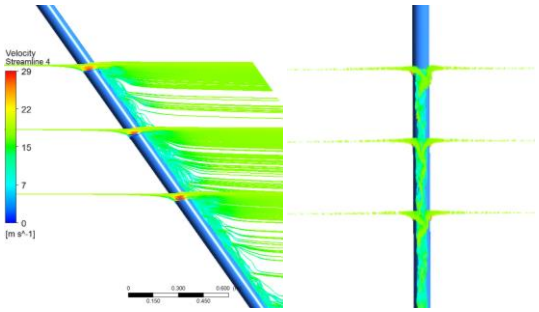


Figure G: Axial flow visualization, velocity streamlines

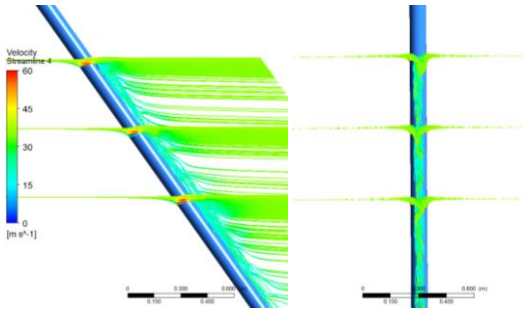
e) $\phi = 54.7°$; $\alpha = 54.7°$, $\beta = 0°$

i) Re = 1.1×10^5;



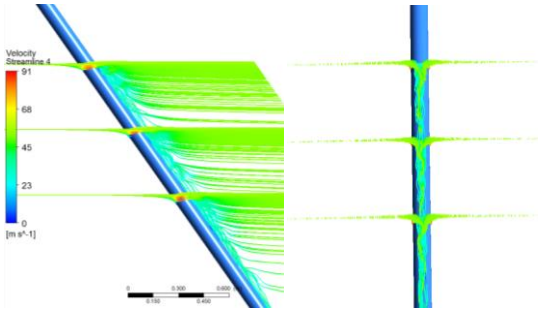
e) $\phi = 54.7°$; $\alpha = 54.7°$, $\beta = 0°$

ii) Re = 2.2×10^5;



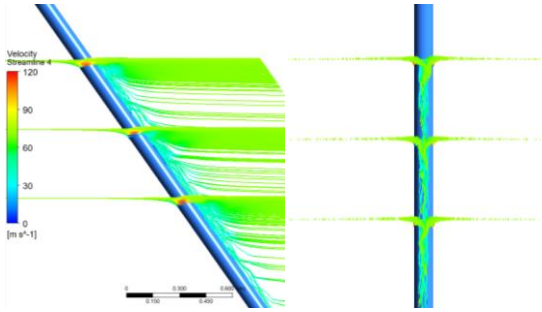
e) $\phi = 54.7°$; $\alpha = 54.7°$, $\beta = 0°$

iii) Re = 3.3×10^5;



e) $\phi = 54.7°$; $\alpha = 54.7°$, $\beta = 0°$

iv) Re = 4.4×10^5;



e) $\phi = 54.7°$; $\alpha = 54.7°$, $\beta = 0°$

v) Re = 5.5×10^5;

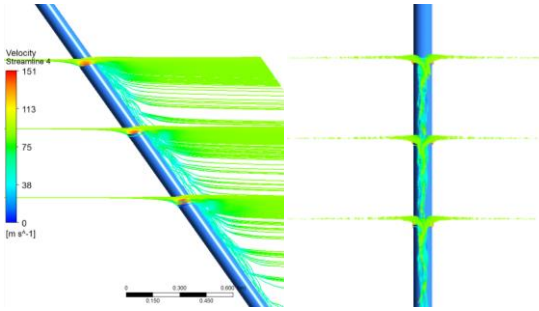
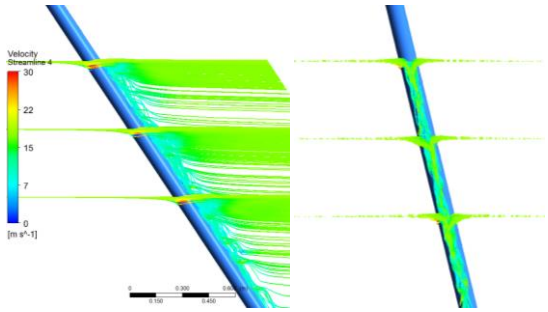
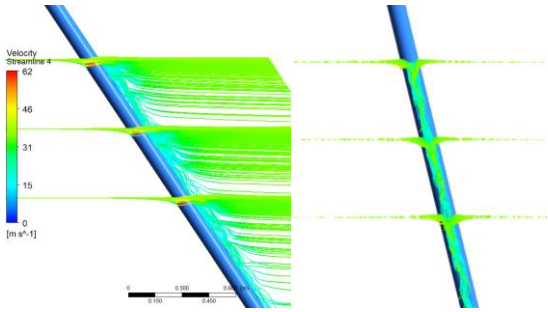


Figure G: Axial flow visualization, velocity streamlines

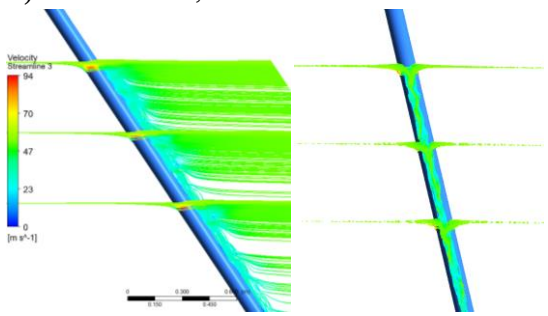
f) $\phi = 57.1°$; $\alpha = 54.7°$, $\beta = 20°$
i) Re = 1.1×10^5;



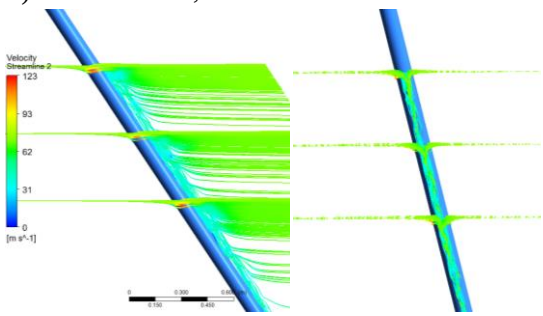
f) $\phi = 57.1°$; $\alpha = 54.7°$, $\beta = 20°$
ii) Re = 2.2×10^5;



f) $\phi = 57.1°$; $\alpha = 54.7°$, $\beta = 20°$
iii) Re = 3.3×10^5;



f) $\phi = 57.1°$; $\alpha = 54.7°$, $\beta = 20°$
iv) Re = 4.4×10^5;



f) $\phi = 57.1°$; $\alpha = 54.7°$, $\beta = 20°$
v) Re = 5.5×10^5;

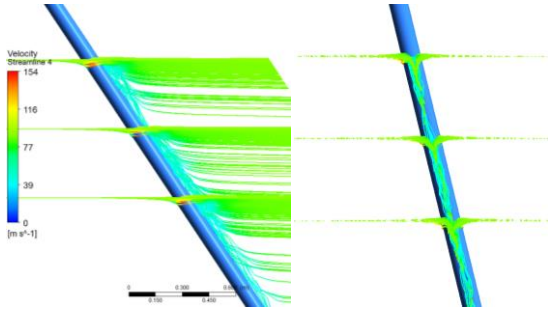
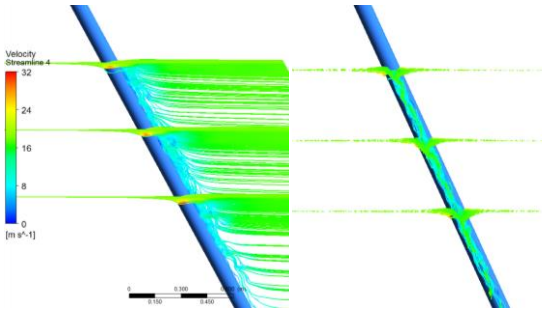
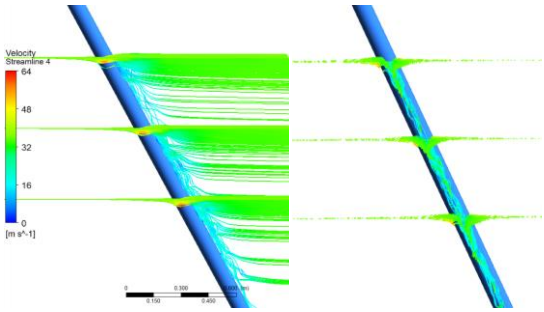


Figure G: Axial flow visualization, velocity streamlines

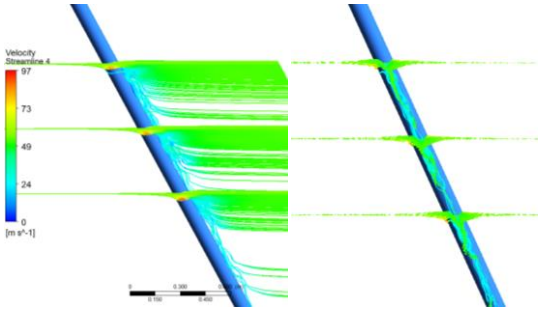
g) $\phi = 64°$; $\alpha = 54.7°$, $\beta = 40°$
i) Re = 1.1×10^5;



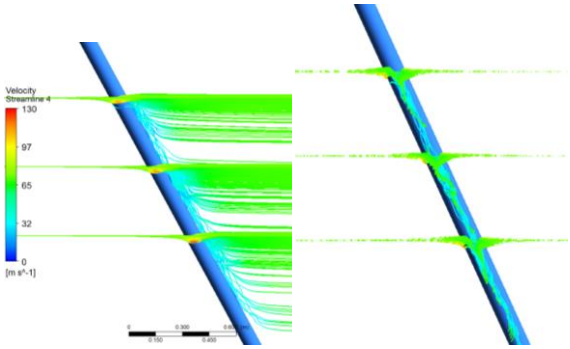
g) $\phi = 64°$; $\alpha = 54.7°$, $\beta = 40°$
ii) Re = 2.2×10^5;



g) $\phi = 64°$; $\alpha = 54.7°$, $\beta = 40°$
iii) Re = 3.3×10^5;



g) $\phi = 64°$; $\alpha = 54.7°$, $\beta = 40°$
iv) Re = 4.4×10^5;



g) $\phi = 64°$; $\alpha = 54.7°$, $\beta = 40°$
v) Re = 5.5×10^5;

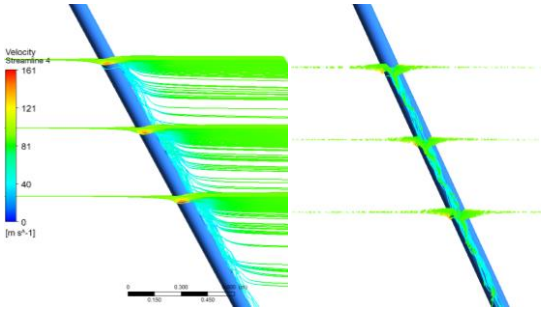
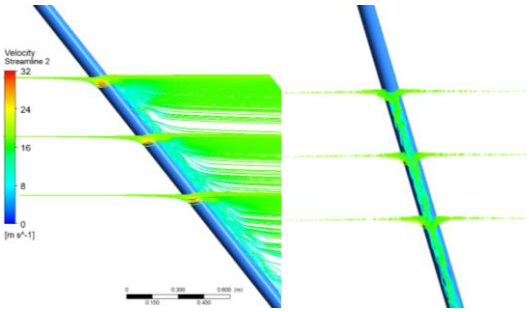
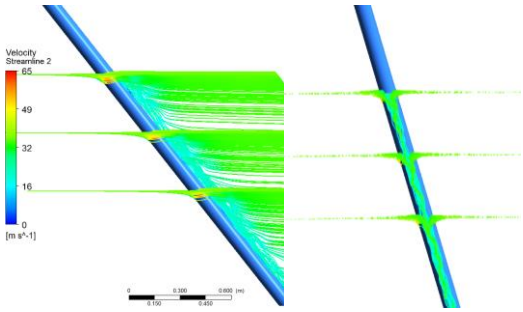


Figure G: Axial flow visualization, velocity streamlines

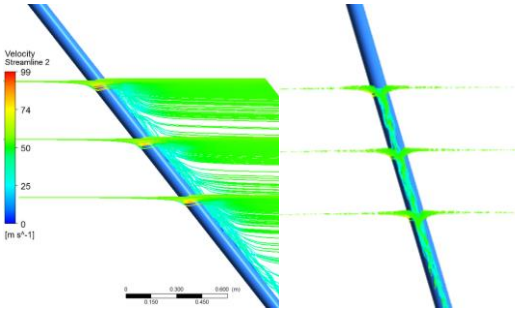
h) $\phi = 53°$; $\alpha = 50°$, $\beta = 20°$
i) Re = 1.1×10^5;



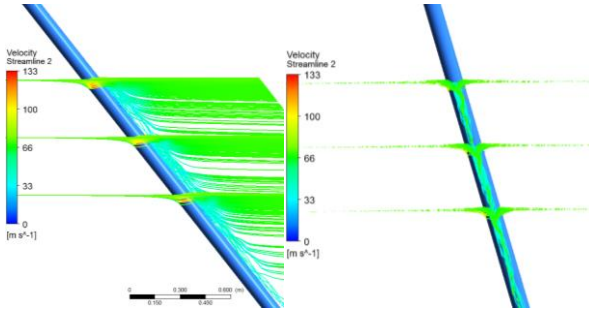
h) $\phi = 53°$; $\alpha = 50°$, $\beta = 20°$
ii) Re = 2.2×10^5;



h) $\phi = 53°$; $\alpha = 50°$, $\beta = 20°$
iii) Re = 3.3×10^5;



h) $\phi = 53°$; $\alpha = 50°$, $\beta = 20°$
iv) Re = 4.4×10^5;



h) $\phi = 53°$; $\alpha = 50°$, $\beta = 20°$
v) Re = 5.5×10^5;

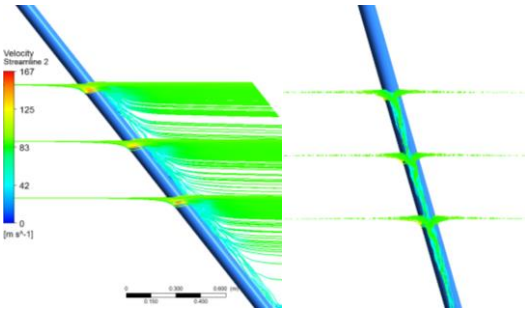
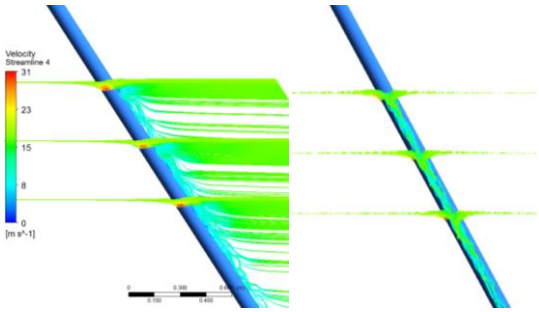
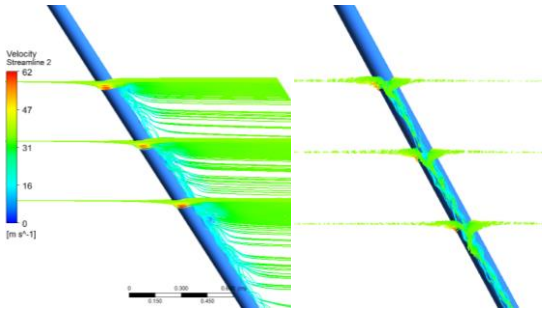


Figure G: Axial flow visualization, velocity streamlines

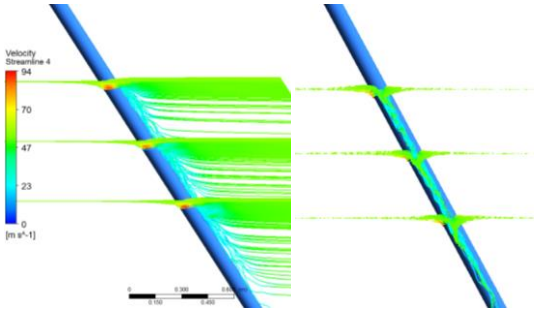
i) $\phi = 60.5°$; $\alpha = 50°$, $\beta = 40°$
i) Re = 1.1×10^5;



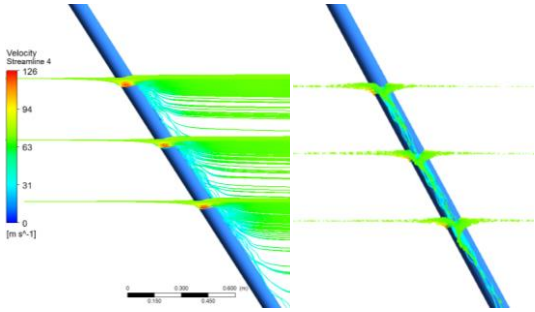
i) $\phi = 60.5°$; $\alpha = 50°$, $\beta = 40°$
ii) Re = 2.2×10^5;



i) $\phi = 60.5°$; $\alpha = 50°$, $\beta = 40°$
iii) Re = 3.3×10^5;



i) $\phi = 60.5°$; $\alpha = 50°$, $\beta = 40°$
iv) Re = 4.4×10^5;



i) $\phi = 60.5°$; $\alpha = 50°$, $\beta = 40°$
v) Re = 5.5×10^5;

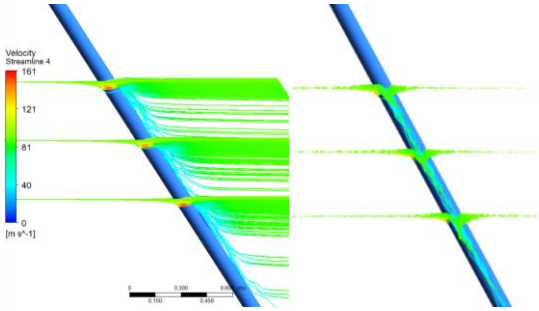
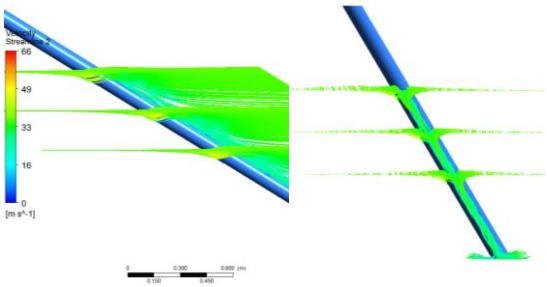
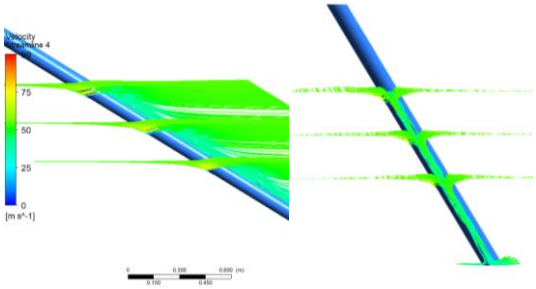


Figure G: Axial flow visualization, velocity streamlines

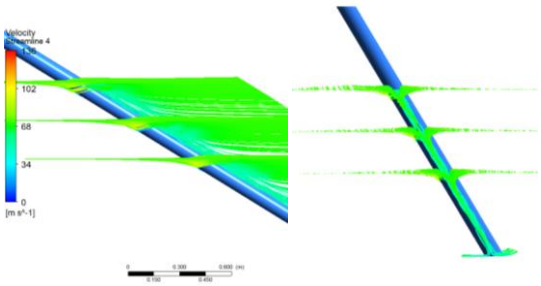
j) $\phi = 35.5°$; $\alpha = 30°$, $\beta = 20°$
Re = 2.2×10^5;



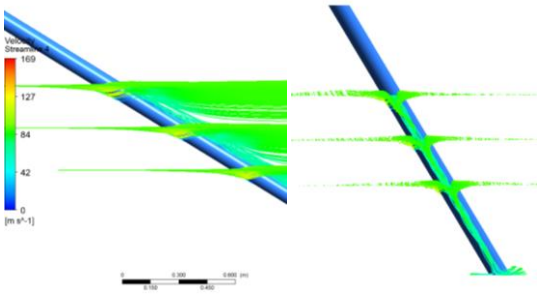
j) $\phi = 35.5°$; $\alpha = 30°$, $\beta = 20°$
Re = 3.3×10^5;



j) $\phi = 35.5°$; $\alpha = 30°$, $\beta = 20°$
Re = 4.4×10^5;



j) $\phi = 35.5°$; $\alpha = 30°$, $\beta = 20°$
Re = 5.5×10^5;

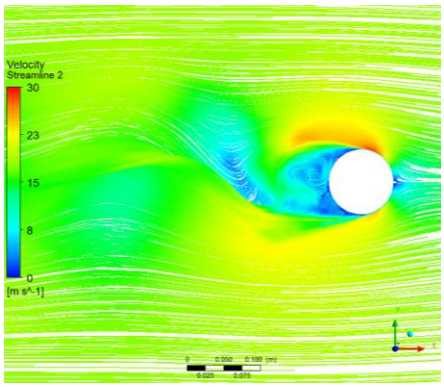


Appendix H: Velocity Streamlines

Figure H: Velocity streamlines

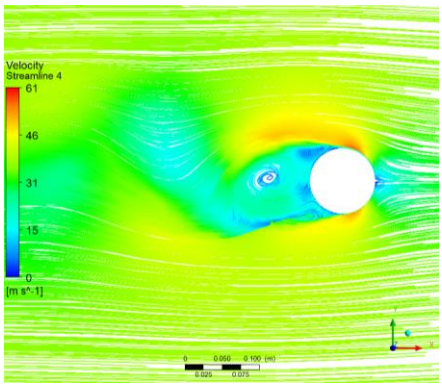
a) $\phi = 0°$; $\alpha = 0°$, $\beta = 0°$

i) Re = 1.1×10^5;



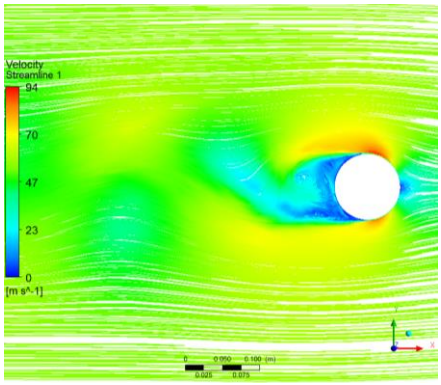
a) $\phi = 0°$; $\alpha = 0°$, $\beta = 0°$

ii) Re = 2.2×10^5;



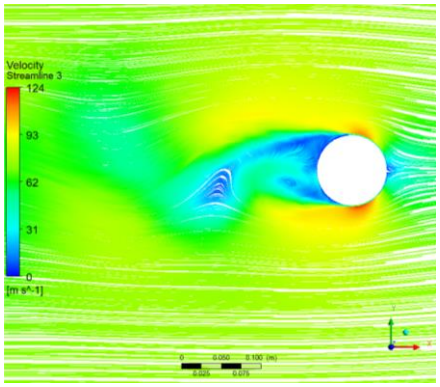
a) $\phi = 0°$; $\alpha = 0°$, $\beta = 0°$

iii) Re = 3.3×10^5;



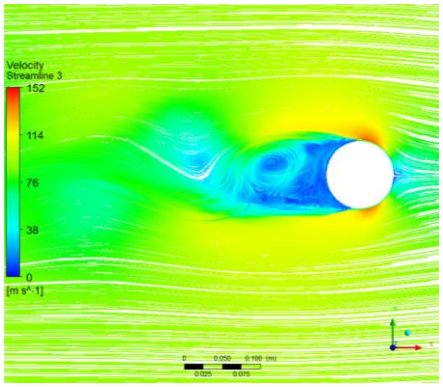
a) $\phi = 0°$; $\alpha = 0°$, $\beta = 0°$

iv) Re = 4.4×10^5;



a) $\phi = 0°$; $\alpha = 0°$, $\beta = 0°$

v) Re = 5.5×10^5;



a) $\phi = 0°$; $\alpha = 0°$, $\beta = 0°$

vi) Re = 6.7×10^5;

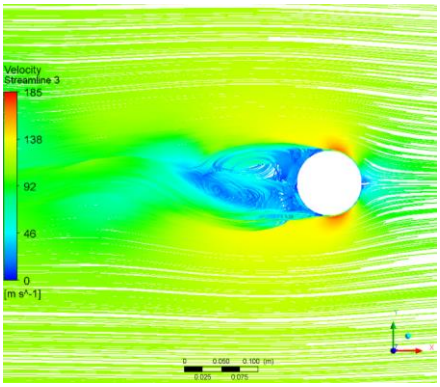
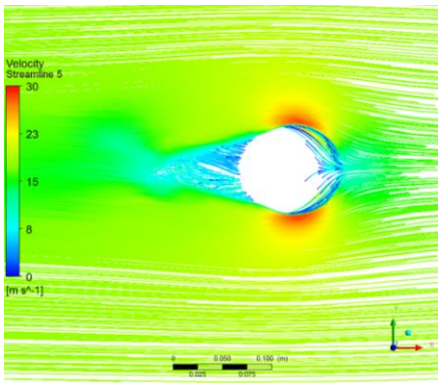


Figure H: Velocity streamlines

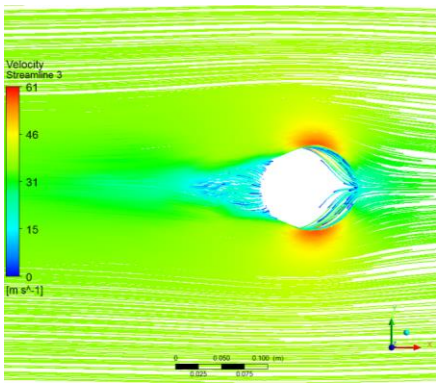
b) $\phi = 60°$; $\alpha = 60°$, $\beta = 0°$

i) Re = 1.1×10^5;



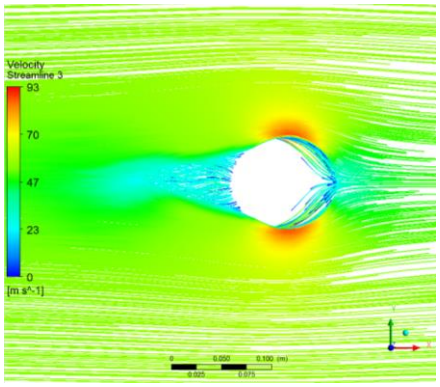
b) $\phi = 60°$; $\alpha = 60°$, $\beta = 0°$

ii) Re = 2.2×10^5;



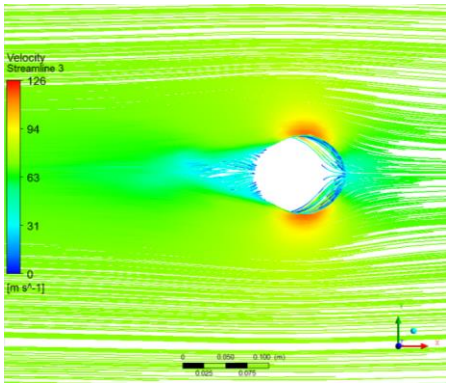
b) $\phi = 60°$; $\alpha = 60°$, $\beta = 0°$

iii) Re = 3.3×10^5;



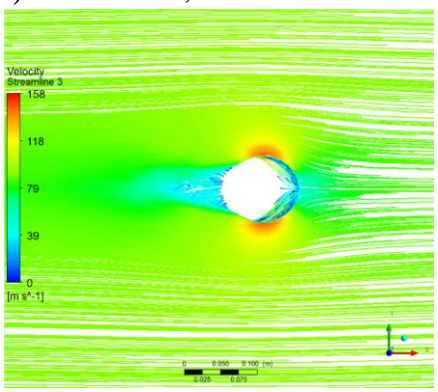
b) $\phi = 60°$; $\alpha = 60°$, $\beta = 0°$

iv) Re = 4.4×10^5;



b) $\phi = 60°$; $\alpha = 60°$, $\beta = 0°$

v) Re = 5.5×10^5;



b) $\phi = 60°$; $\alpha = 60°$, $\beta = 0°$

vi) Re = 6.7×10^5;

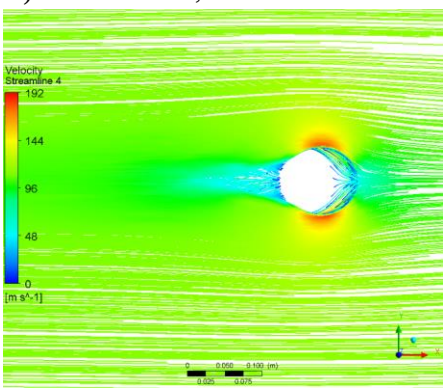
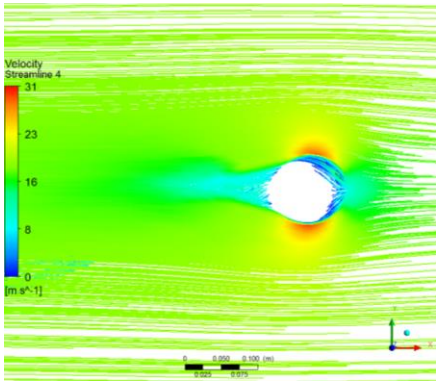


Figure H: Velocity streamlines

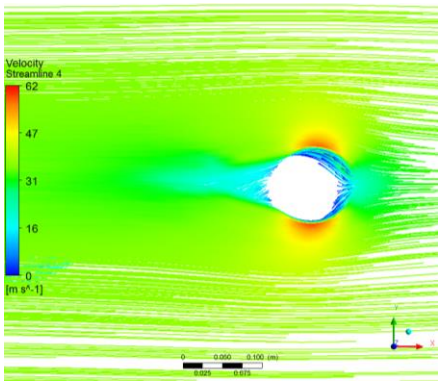
c) $\phi = 62°$; $\alpha = 60°$, $\beta = 20°$

i) Re = 1.1×10^5;



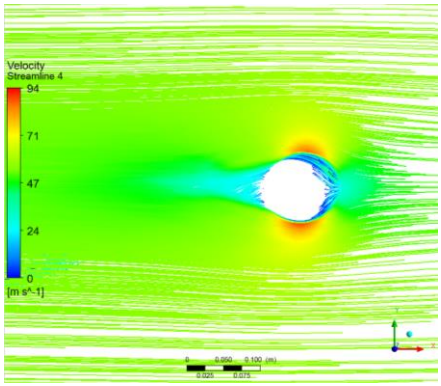
c) $\phi = 62°$; $\alpha = 60°$, $\beta = 20°$

ii) Re = 2.2×10^5;



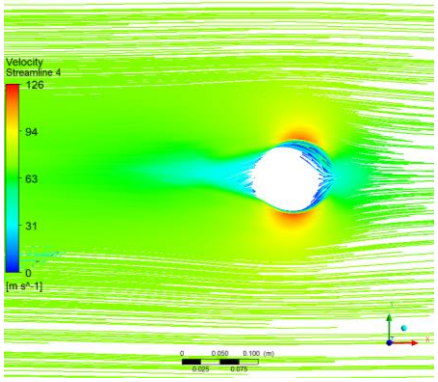
c) $\phi = 62°$; $\alpha = 60°$, $\beta = 20°$

iii) Re = 3.3×10^5;



c) $\phi = 62°$; $\alpha = 60°$, $\beta = 20°$

iv) Re = 4.4×10^5;



c) $\phi = 62°$; $\alpha = 60°$, $\beta = 20°$

v) Re = 5.5×10^5;

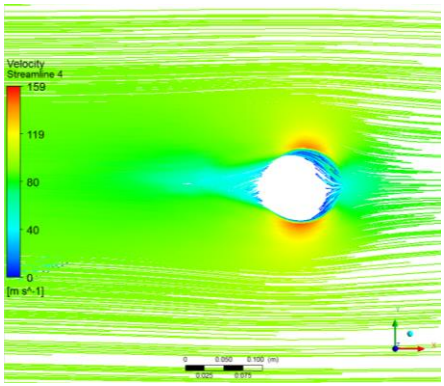
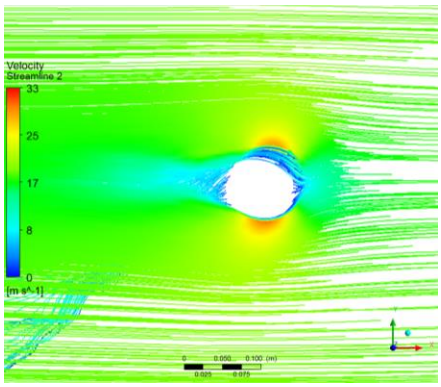


Figure H: Velocity streamlines

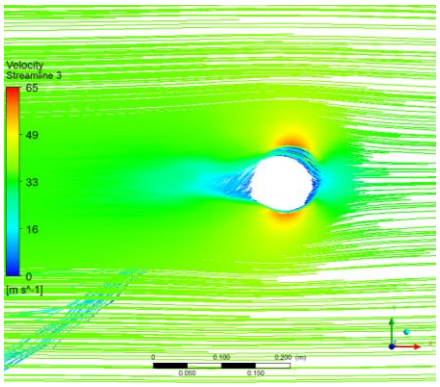
d) $\phi = 67.5°$; $\alpha = 60°$, $\beta = 40°$

i) Re = 1.1×10^5;



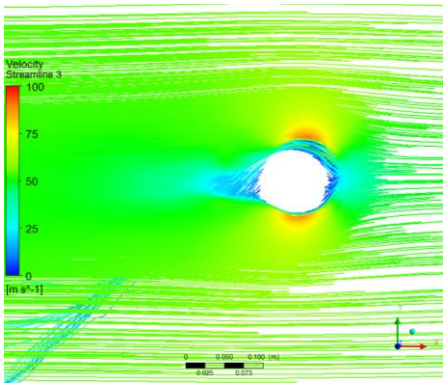
d) $\phi = 67.5°$; $\alpha = 60°$, $\beta = 40°$

ii) Re = 2.2×10^5;



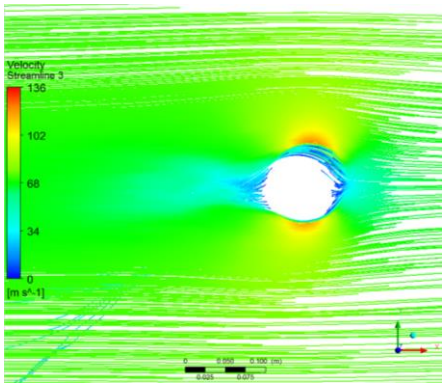
d) $\phi = 67.5°$; $\alpha = 60°$, $\beta = 40°$

iii) Re = 3.3×10^5;



d) $\phi = 67.5°$; $\alpha = 60°$, $\beta = 40°$

iv) Re = 4.4×10^5;



d) $\phi = 67.5°$; $\alpha = 60°$, $\beta = 40°$

v) Re = 5.5×10^5;

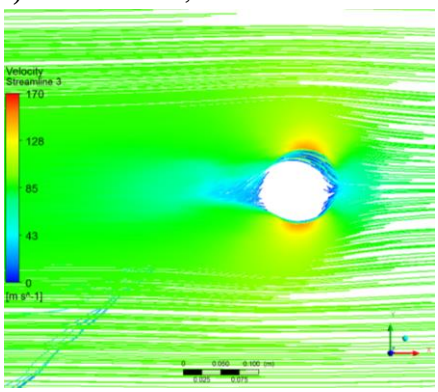
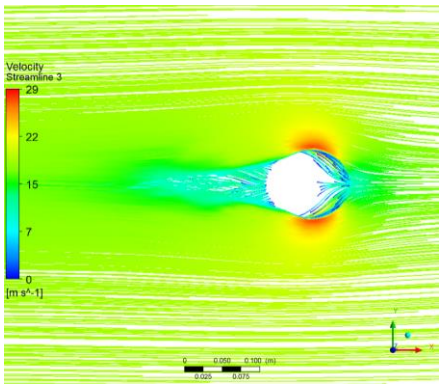


Figure H: Velocity streamlines

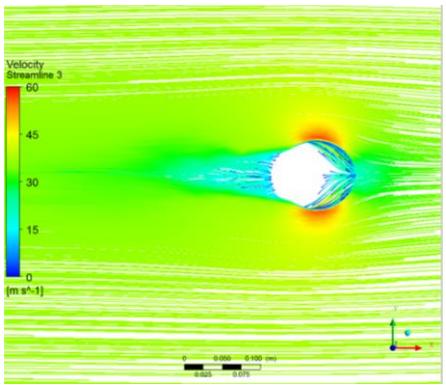
e) $\phi = 54.7°$; $\alpha = 54.7°$, $\beta = 0°$

i) Re = 1.1×10^5;



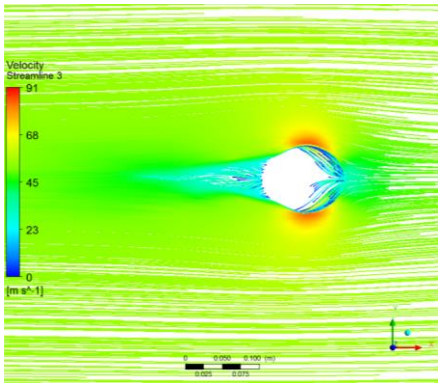
e) $\phi = 54.7°$; $\alpha = 54.7°$, $\beta = 0°$

ii) Re = 2.2×10^5;



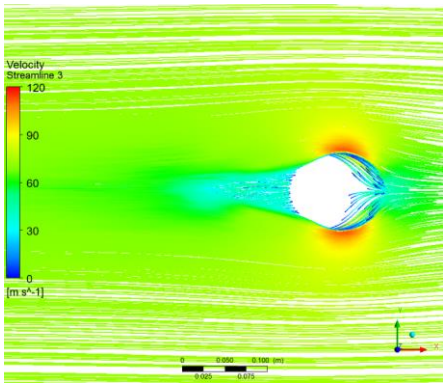
e) $\phi = 54.7°$; $\alpha = 54.7°$, $\beta = 0°$

iii) Re = 3.3×10^5;



e) $\phi = 54.7°$; $\alpha = 54.7°$, $\beta = 0°$

iv) Re = 4.4×10^5;



e) $\phi = 54.7°$; $\alpha = 54.7°$, $\beta = 0°$

v) Re = 5.5×10^5;

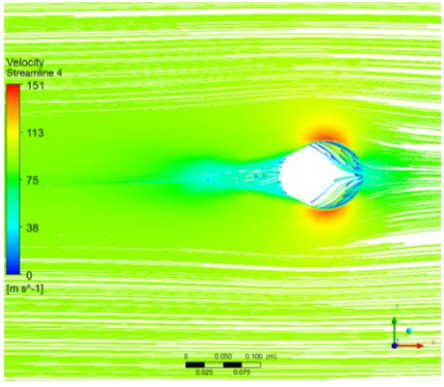
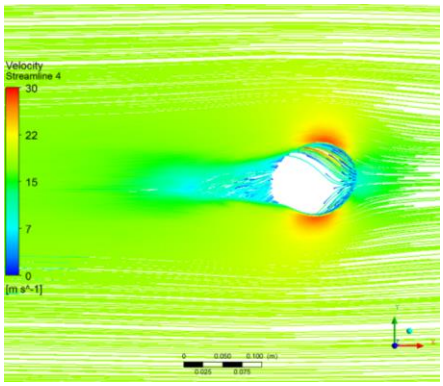
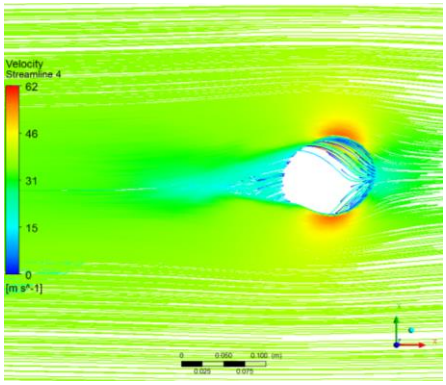


Figure H: Velocity streamlines

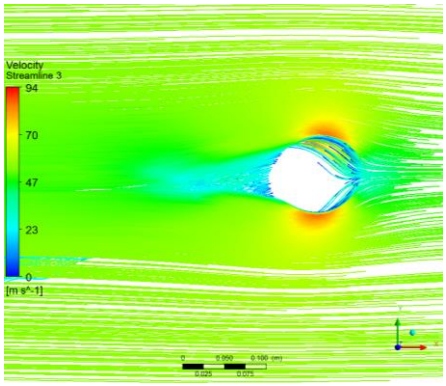
f) $\phi = 57.1°$; $\alpha = 54.7°$, $\beta = 20°$
i) Re = 1.1×10^5;



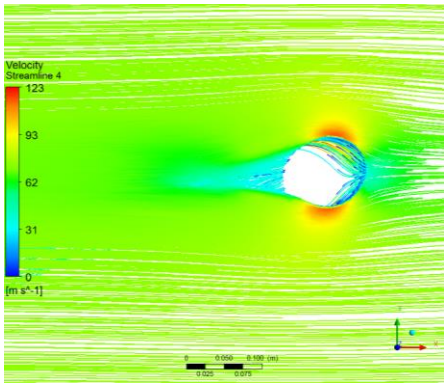
f) $\phi = 57.1°$; $\alpha = 54.7°$, $\beta = 20°$
ii) Re = 2.2×10^5;



f) $\phi = 57.1°$; $\alpha = 54.7°$, $\beta = 20°$
iii) Re = 3.3×10^5;



f) $\phi = 57.1°$; $\alpha = 54.7°$, $\beta = 20°$
iv) Re = 4.4×10^5;



f) $\phi = 57.1°$; $\alpha = 54.7°$, $\beta = 20°$
v) Re = 5.5×10^5;

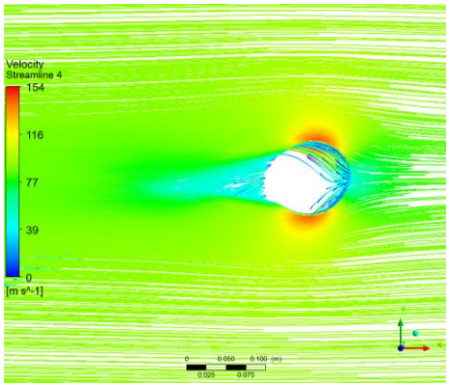
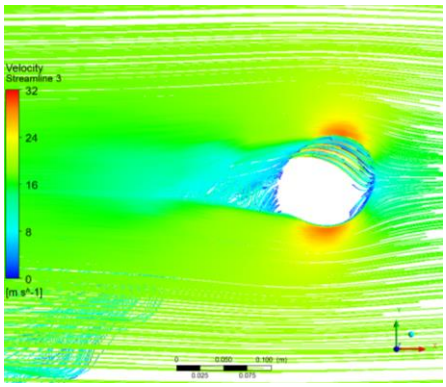


Figure H: Velocity streamlines

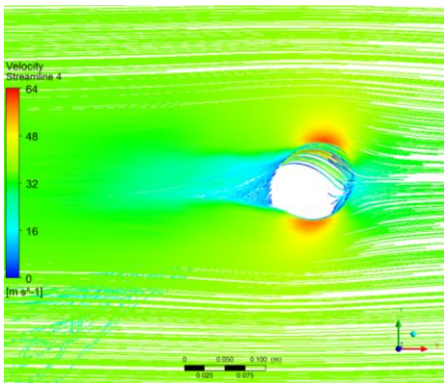
g) $\phi = 64°$; $\alpha = 54.7°$, $\beta = 40°$

i) Re = 1.1×10^5;



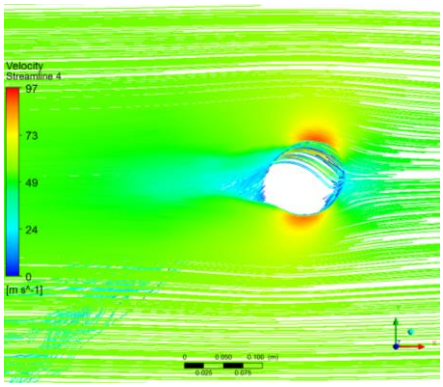
g) $\phi = 64°$; $\alpha = 54.7°$, $\beta = 40°$

ii) Re = 2.2×10^5;



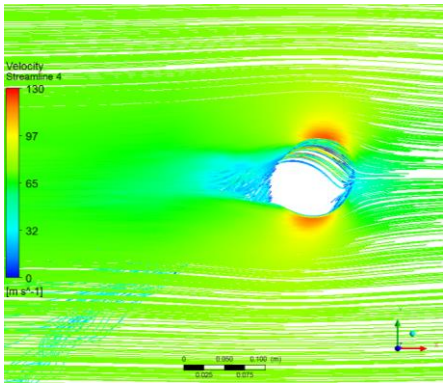
g) $\phi = 64°$; $\alpha = 54.7°$, $\beta = 40°$

iii) Re = 3.3×10^5;



g) $\phi = 64°$; $\alpha = 54.7°$, $\beta = 40°$

iv) Re = 4.4×10^5;



g) $\phi = 64°$; $\alpha = 54.7°$, $\beta = 40°$

v) Re = 5.5×10^5;

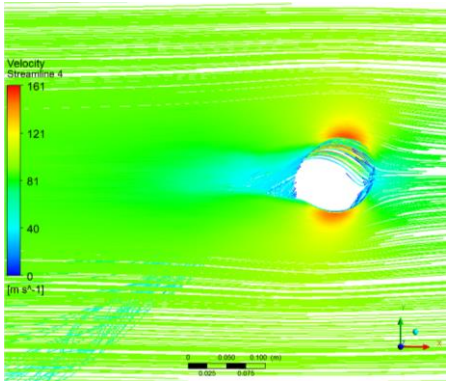
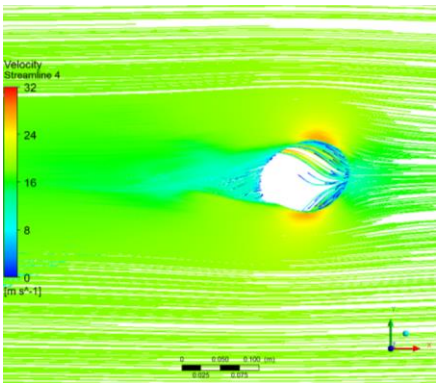


Figure H: Velocity streamlines

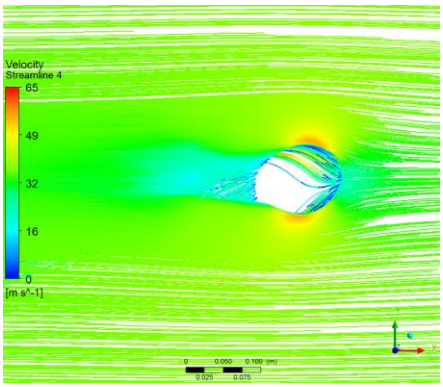
h) $\phi = 53°$; $\alpha = 50°$, $\beta = 20°$

i) Re = 1.1×10^5;



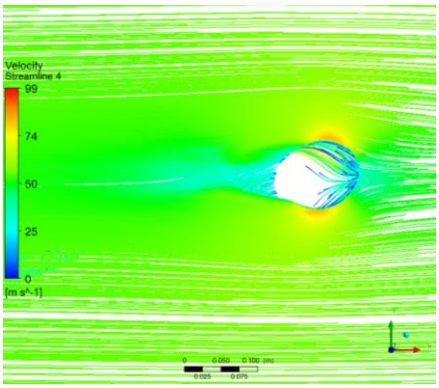
h) $\phi = 53°$; $\alpha = 50°$, $\beta = 20°$

ii) Re = 2.2×10^5;



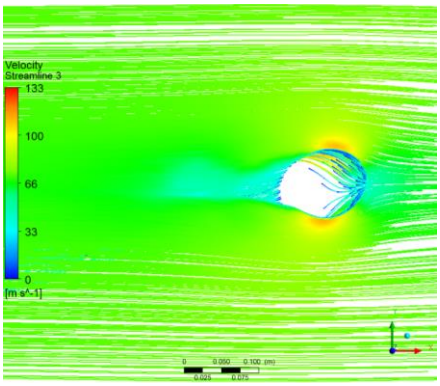
h) $\phi = 53°$; $\alpha = 50°$, $\beta = 20°$

iii) Re = 3.3×10^5;



h) $\phi = 53°$; $\alpha = 50°$, $\beta = 20°$

iv) Re = 4.4×10^5;



h) $\phi = 53°$; $\alpha = 50°$, $\beta = 20°$

v) Re = 5.5×10^5;

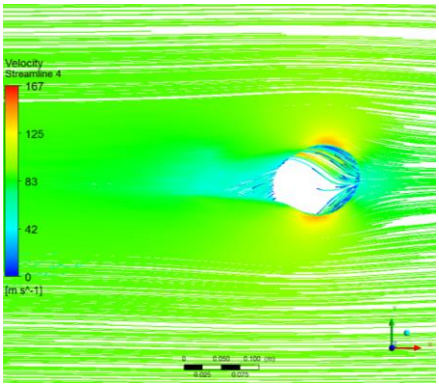
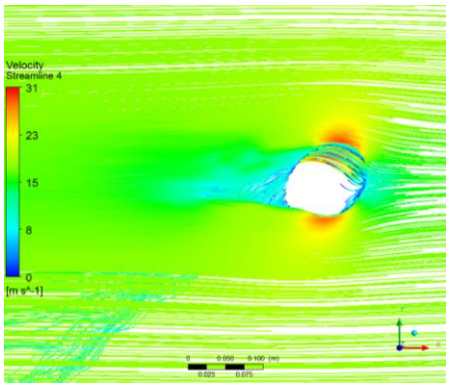


Figure H: Velocity streamlines

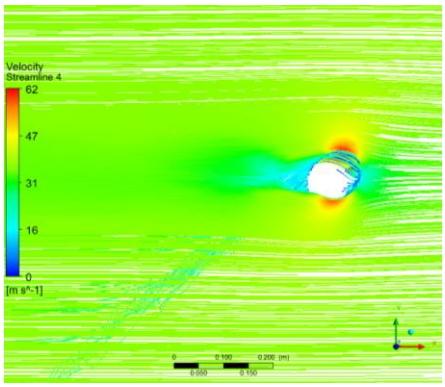
i) $\phi = 60.5°$; $\alpha = 50°$, $\beta = 40°$

i) Re = 1.1×10^5;



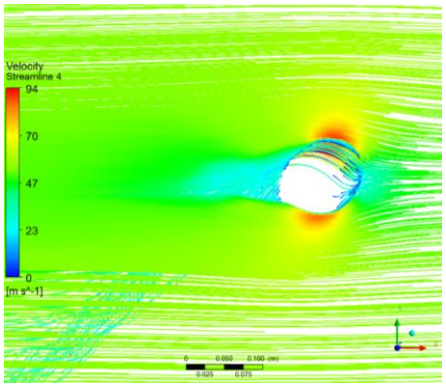
i) $\phi = 60.5°$; $\alpha = 50°$, $\beta = 40°$

ii) Re = 2.2×10^5;



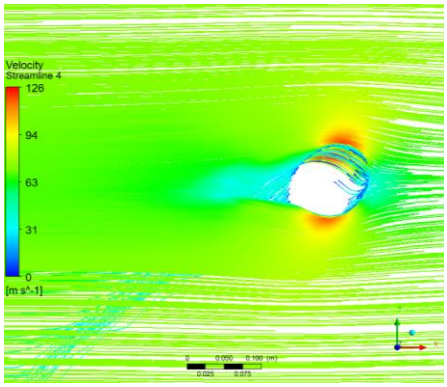
i) $\phi = 60.5°$; $\alpha = 50°$, $\beta = 40°$

iii) Re = 3.3×10^5;



i) $\phi = 60.5°$; $\alpha = 50°$, $\beta = 40°$

iv) Re = 4.4×10^5;



i) $\phi = 60.5°$; $\alpha = 50°$, $\beta = 40°$

v) Re = 5.5×10^5;

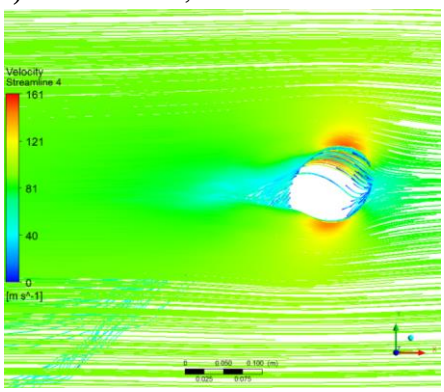
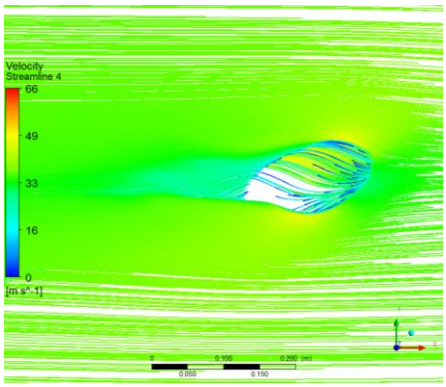
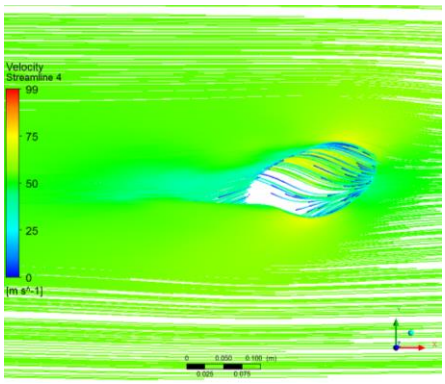


Figure H: Velocity streamlines

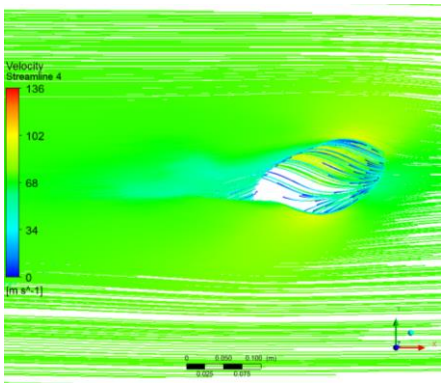
j) $\phi = 35.5°$; $\alpha = 30°$, $\beta = 20°$
Re = 2.2×10^5;



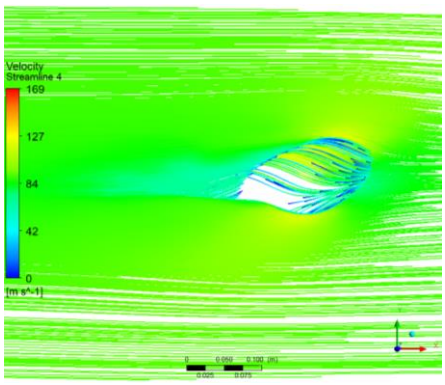
j) $\phi = 35.5°$; $\alpha = 30°$, $\beta = 20°$
Re = 3.3×10^5;



j) $\phi = 35.5°$; $\alpha = 30°$, $\beta = 20°$
Re = 4.4×10^5;



j) $\phi = 35.5°$; $\alpha = 30°$, $\beta = 20°$
Re = 5.5×10^5;

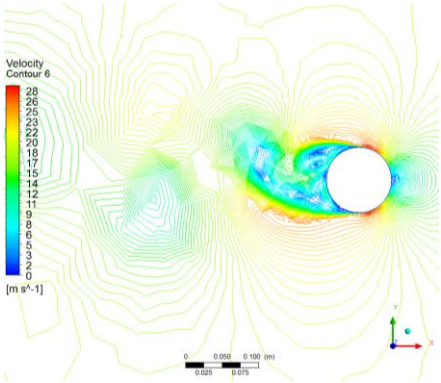


Appendix I: Dominant Velocity Zones and Flow Patterns

Figure I: Dominant velocity zones and flow pattern

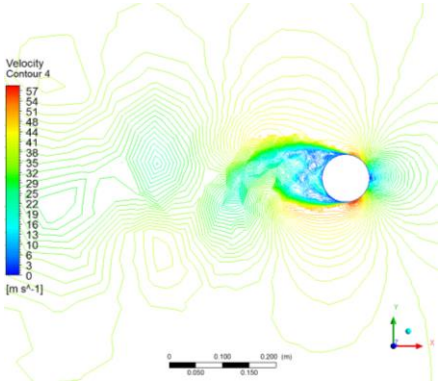
a) $\phi = 0°$; $\alpha = 0°$, $\beta = 0°$

i) Re = 1.1×10^5;



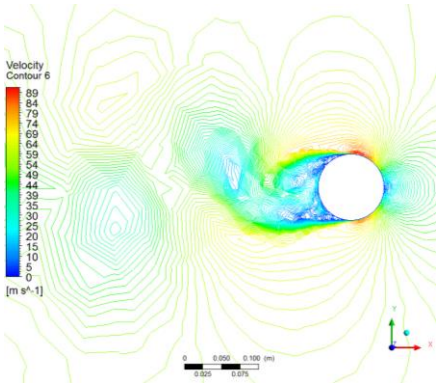
a) $\phi = 0°$; $\alpha = 0°$, $\beta = 0°$

ii) Re = 2.2×10^5;



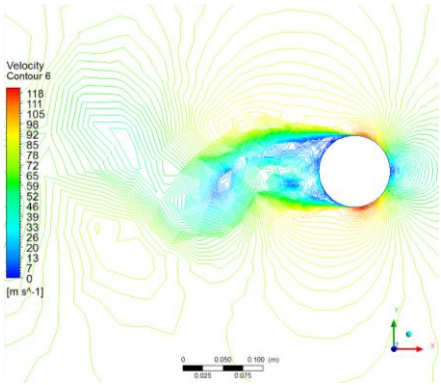
a) $\phi = 0°$; $\alpha = 0°$, $\beta = 0°$

iii) Re = 3.3×10^5;



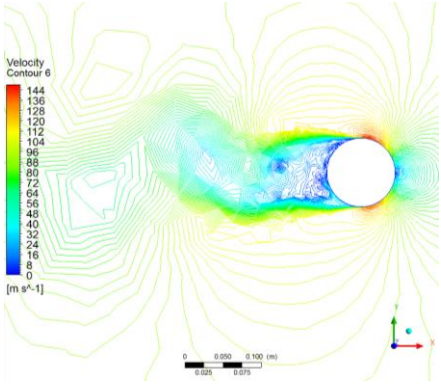
a) $\phi = 0°$; $\alpha = 0°$, $\beta = 0°$

iv) Re = 4.4×10^5;



a) $\phi = 0°$; $\alpha = 0°$, $\beta = 0°$

v) Re = 5.5×10^5;



a) $\phi = 0°$; $\alpha = 0°$, $\beta = 0°$

vi) Re = 6.7×10^5;

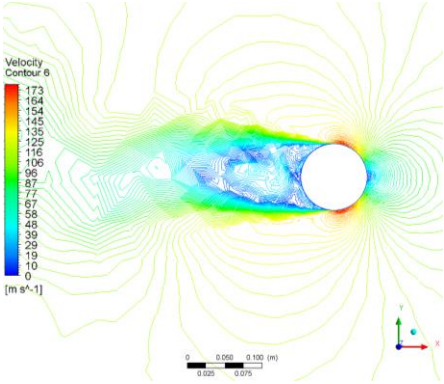
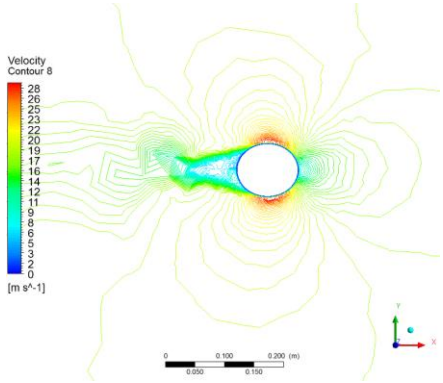
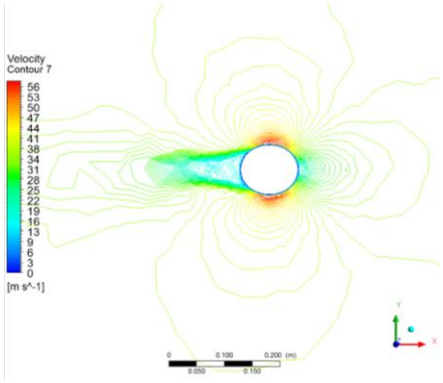


Figure I: Dominant velocity zones and flow pattern

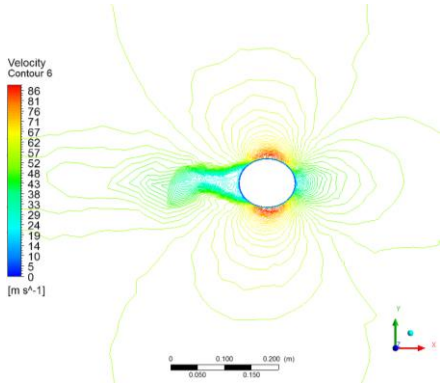
b) $\phi = 60°$; $\alpha = 60°$, $\beta = 0°$
i) Re = 1.1×10^5;



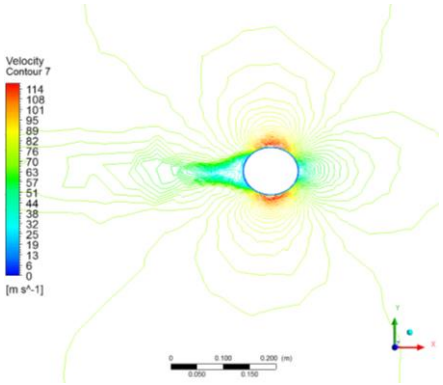
b) $\phi = 60°$; $\alpha = 60°$, $\beta = 0°$
ii) Re = 2.2×10^5;



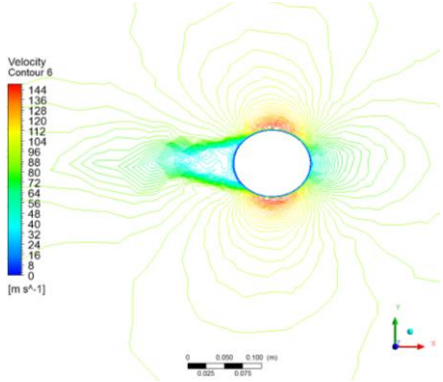
b) $\phi = 60°$; $\alpha = 60°$, $\beta = 0°$
iii) Re = 3.3×10^5;



b) $\phi = 60°$; $\alpha = 60°$, $\beta = 0°$
iv) Re = 4.4×10^5;



b) $\phi = 60°$; $\alpha = 60°$, $\beta = 0°$
v) Re = 5.5×10^5;



b) $\phi = 60°$; $\alpha = 60°$, $\beta = 0°$
vi) Re = 6.7×10^5;

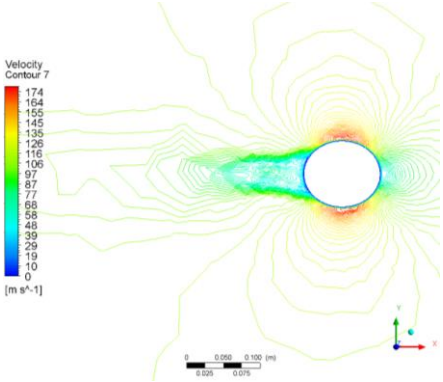
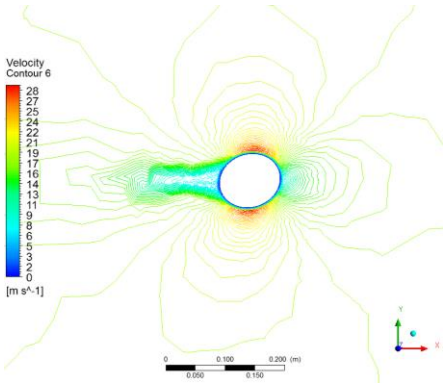


Figure I: Dominant velocity zones and flow pattern

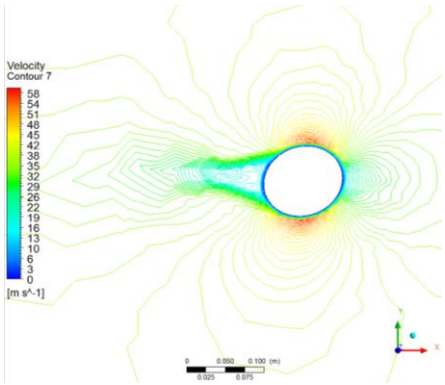
c) $\phi = 62°$; $\alpha = 60°$, $\beta = 20°$

i) Re = 1.1×10^5;



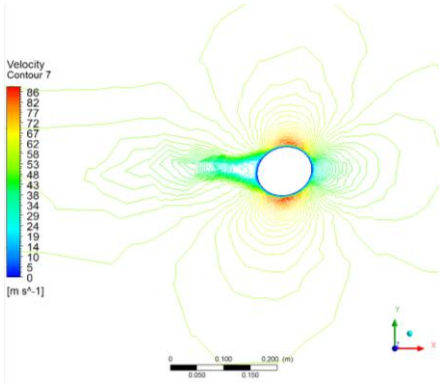
c) $\phi = 62°$; $\alpha = 60°$, $\beta = 20°$

ii) Re = 2.2×10^5;



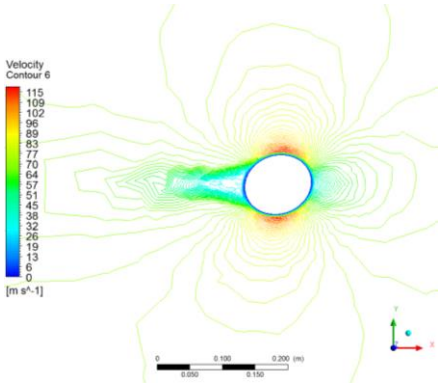
c) $\phi = 62°$; $\alpha = 60°$, $\beta = 20°$

iii) Re = 3.3×10^5;



c) $\phi = 62°$; $\alpha = 60°$, $\beta = 20°$

iv) Re = 4.4×10^5;



c) $\phi = 62°$; $\alpha = 60°$, $\beta = 20°$

v) Re = 5.5×10^5;

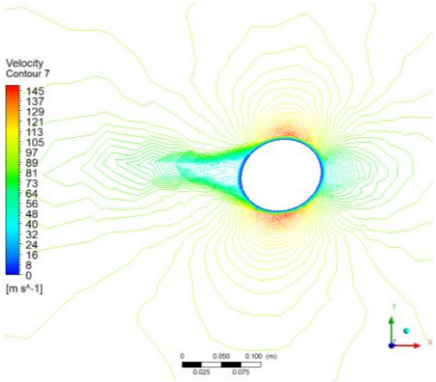
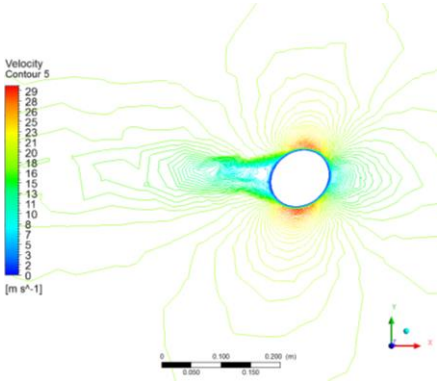
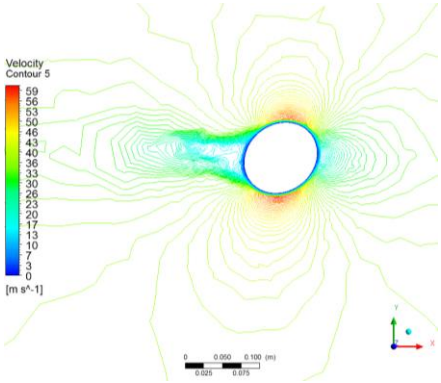


Figure I: Dominant velocity zones and flow pattern

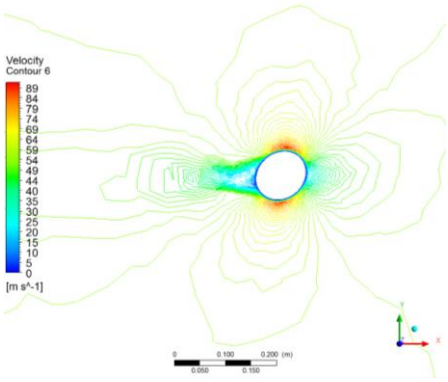
d) $\phi = 67.5°$; $\alpha = 60°$, $\beta = 40°$
i) Re = 1.1×10^5;



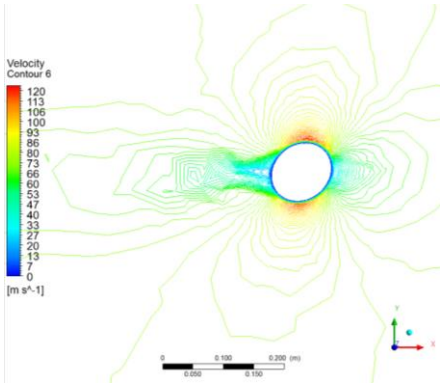
d) $\phi = 67.5°$; $\alpha = 60°$, $\beta = 40°$
ii) Re = 2.2×10^5;



d) $\phi = 67.5°$; $\alpha = 60°$, $\beta = 40°$
iii) Re = 3.3×10^5;



d) $\phi = 67.5°$; $\alpha = 60°$, $\beta = 40°$
iv) Re = 4.4×10^5;



d) $\phi = 67.5°$; $\alpha = 60°$, $\beta = 40°$
v) Re = 5.5×10^5;

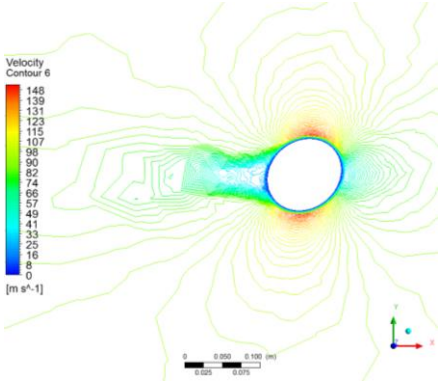
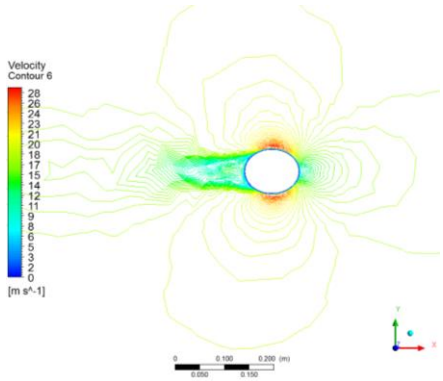
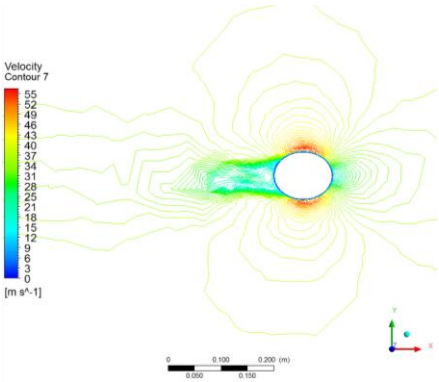


Figure I: Dominant velocity zones and flow pattern

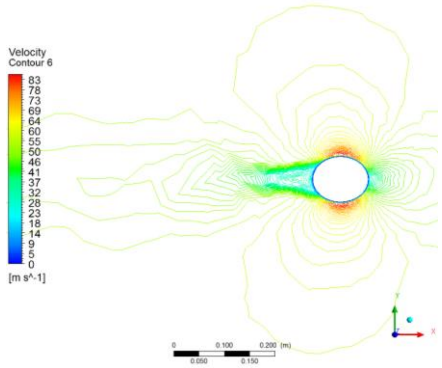
e) $\phi = 54.7°$; $\alpha = 54.7°$, $\beta = 0°$
i) Re = 1.1×10^5;



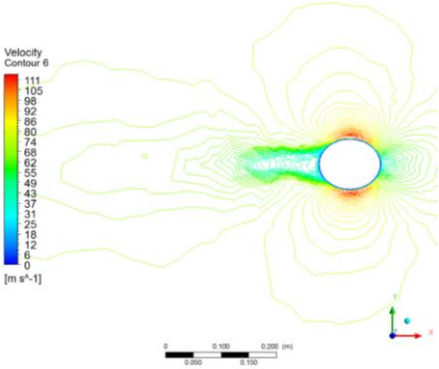
e) $\phi = 54.7°$; $\alpha = 54.7°$, $\beta = 0°$
ii) Re = 2.2×10^5;



e) $\phi = 54.7°$; $\alpha = 54.7°$, $\beta = 0°$
iii) Re = 3.3×10^5;



e) $\phi = 54.7°$; $\alpha = 54.7°$, $\beta = 0°$
iv) Re = 4.4×10^5;



e) $\phi = 54.7°$; $\alpha = 54.7°$, $\beta = 0°$
v) Re = 5.5×10^5;

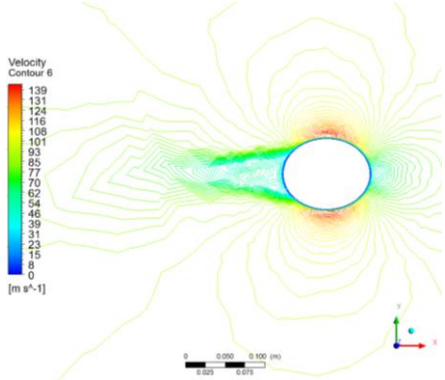
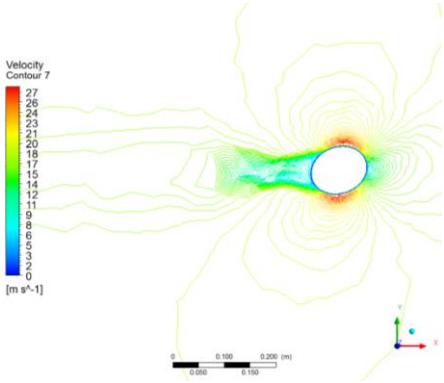
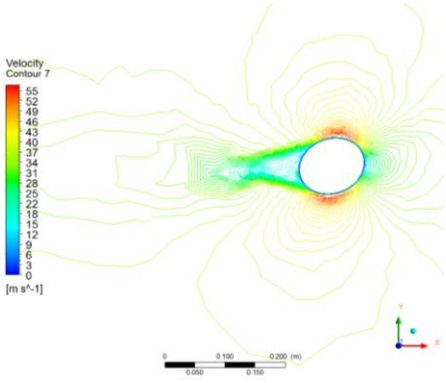


Figure I: Dominant velocity zones and flow pattern

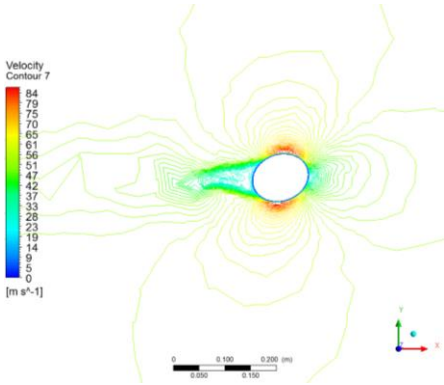
f) $\phi = 57.1°$; $\alpha = 54.7°$, $\beta = 20°$
i) Re = 1.1×10^5;



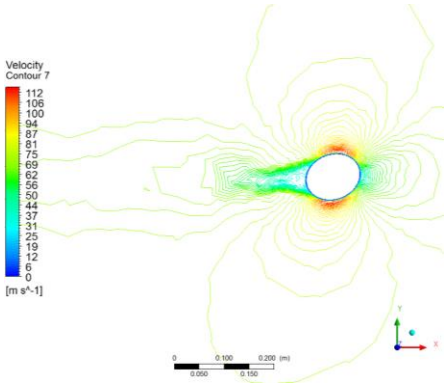
f) $\phi = 57.1°$; $\alpha = 54.7°$, $\beta = 20°$
ii) Re = 2.2×10^5;



f) $\phi = 57.1°$; $\alpha = 54.7°$, $\beta = 20°$
iii) Re = 3.3×10^5;



f) $\phi = 57.1°$; $\alpha = 54.7°$, $\beta = 20°$
iv) Re = 4.4×10^5;



f) $\phi = 57.1°$; $\alpha = 54.7°$, $\beta = 20°$
v) Re = 5.5×10^5;

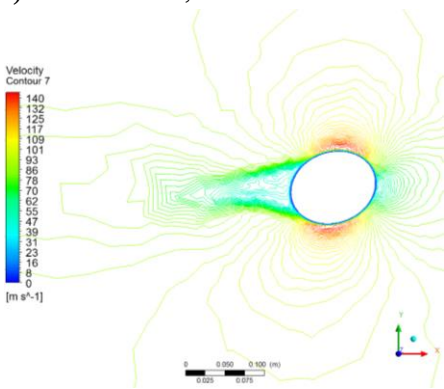
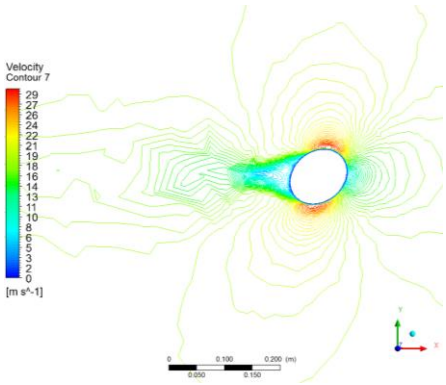
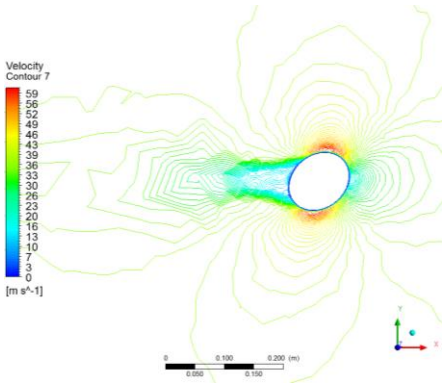


Figure I: Dominant velocity zones and flow pattern

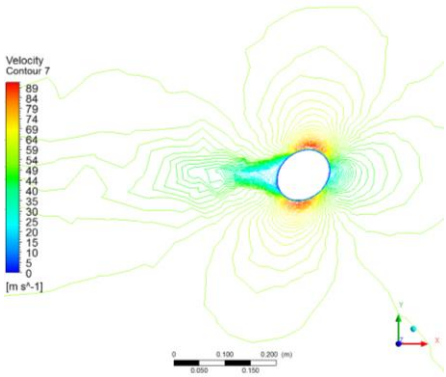
g) $\phi = 64°$; $\alpha = 54.7°$, $\beta = 40°$
i) Re = 1.1×10^5;



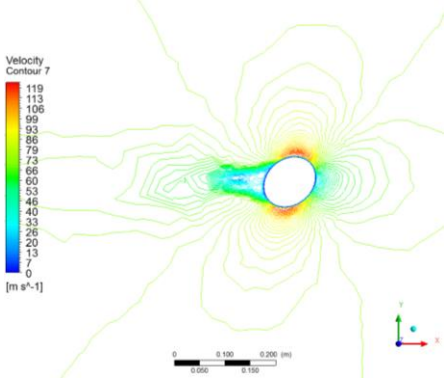
g) $\phi = 64°$; $\alpha = 54.7°$, $\beta = 40°$
ii) Re = 2.2×10^5;



g) $\phi = 64°$; $\alpha = 54.7°$, $\beta = 40°$
iii) Re = 3.3×10^5;



g) $\phi = 64°$; $\alpha = 54.7°$, $\beta = 40°$
iv) Re = 4.4×10^5;



g) $\phi = 64°$; $\alpha = 54.7°$, $\beta = 40°$
v) Re = 5.5×10^5;

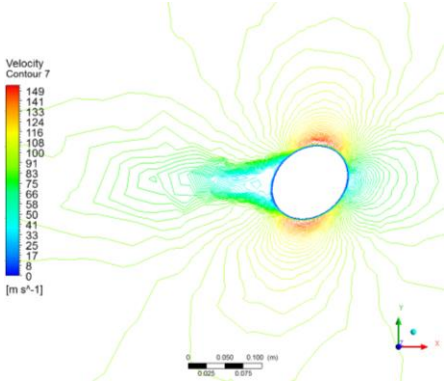
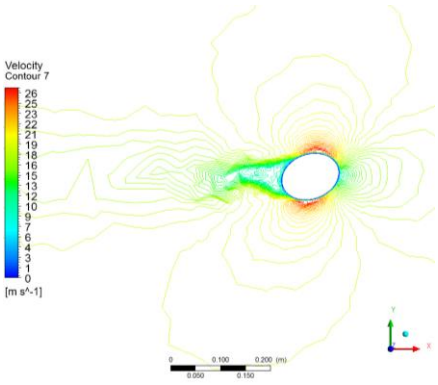
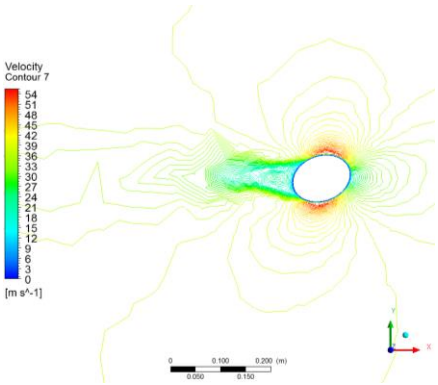


Figure I: Dominant velocity zones and flow pattern

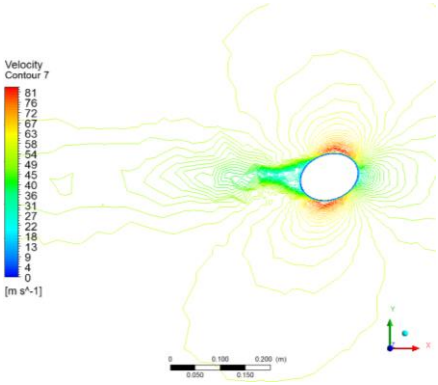
h) $\phi = 53°$; $\alpha = 50°$, $\beta = 20°$
i) Re = 1.1×10^5;



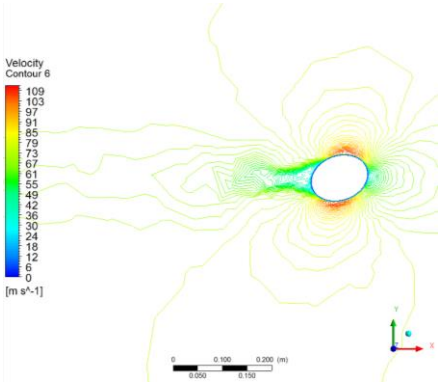
h) $\phi = 53°$; $\alpha = 50°$, $\beta = 20°$
ii) Re = 2.2×10^5;



h) $\phi = 53°$; $\alpha = 50°$, $\beta = 20°$
iii) Re = 3.3×10^5;



h) $\phi = 53°$; $\alpha = 50°$, $\beta = 20°$
iv) Re = 4.4×10^5;



h) $\phi = 53°$; $\alpha = 50°$, $\beta = 20°$
v) Re = 5.5×10^5;

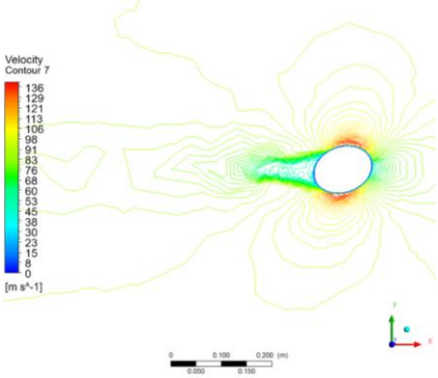
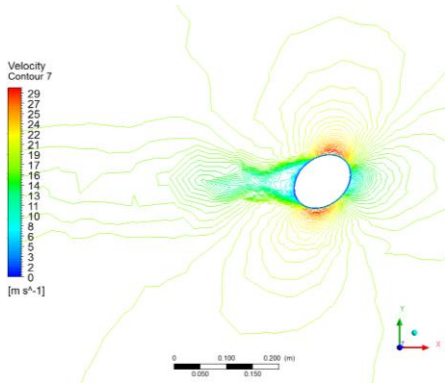


Figure I: Dominant velocity zones and flow pattern

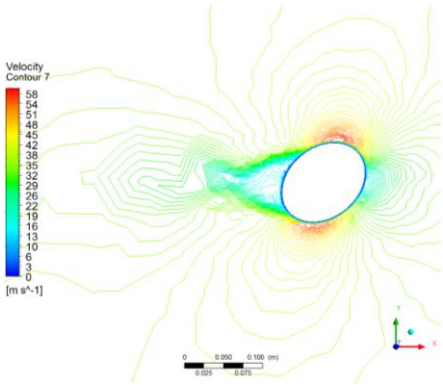
i) $\phi = 60.5°$; $\alpha = 50°$, $\beta = 40°$

i) Re = 1.1×10^5;



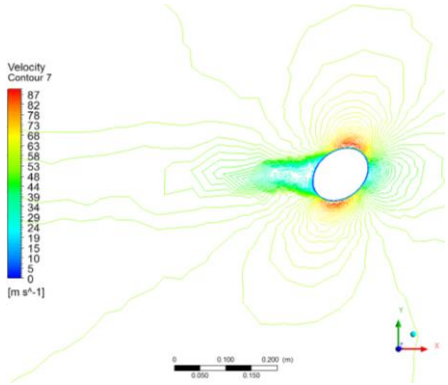
i) $\phi = 60.5°$; $\alpha = 50°$, $\beta = 40°$

ii) Re = 2.2×10^5;



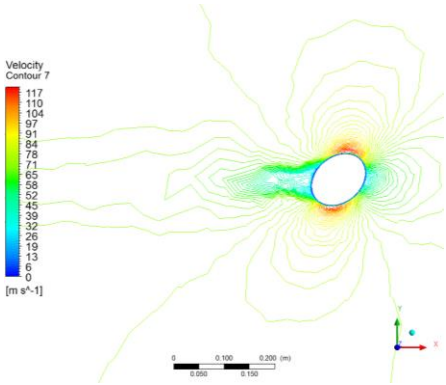
i) $\phi = 60.5°$; $\alpha = 50°$, $\beta = 40°$

iii) Re = 3.3×10^5;



i) $\phi = 60.5°$; $\alpha = 50°$, $\beta = 40°$

iv) Re = 4.4×10^5;



i) $\phi = 60.5°$; $\alpha = 50°$, $\beta = 40°$

v) Re = 5.5×10^5;

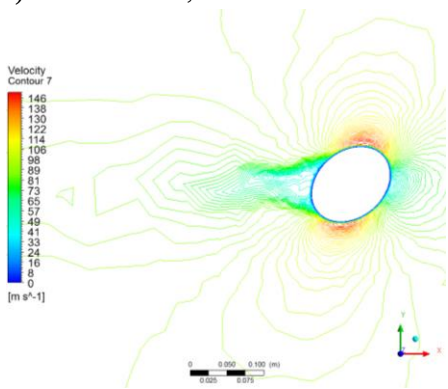
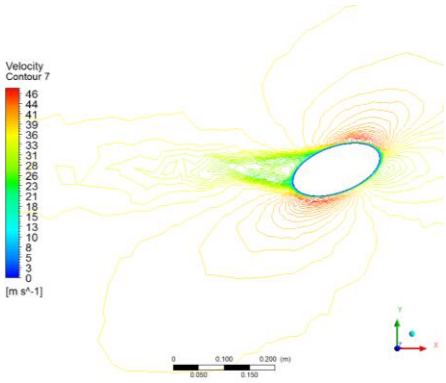
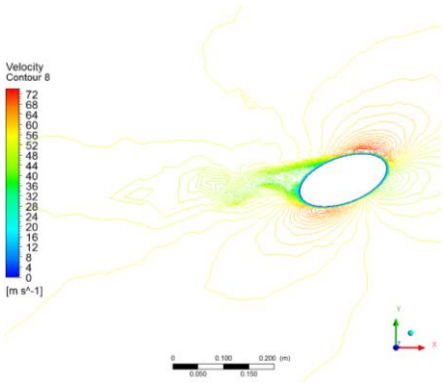


Figure I: Dominant velocity zones and flow pattern

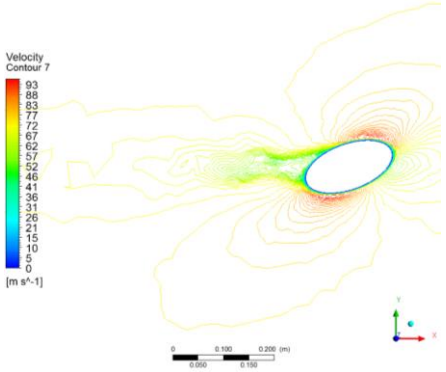
j) $\phi = 35.5°$; $\alpha = 30°$, $\beta = 20°$
ii) Re = 2.2×10^5;



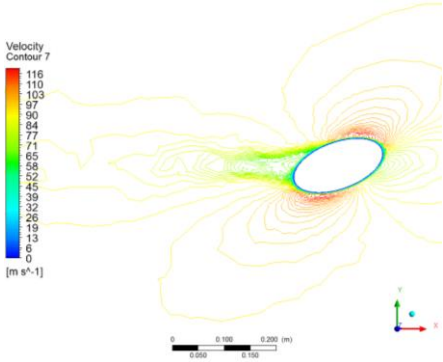
j) $\phi = 35.5°$; $\alpha = 30°$, $\beta = 20°$
iii) Re = 3.3×10^5;



j) $\phi = 35.5°$; $\alpha = 30°$, $\beta = 20°$
iv) Re = 4.4×10^5;



j) $\phi = 35.5°$; $\alpha = 30°$, $\beta = 20°$
v) Re = 5.5×10^5;

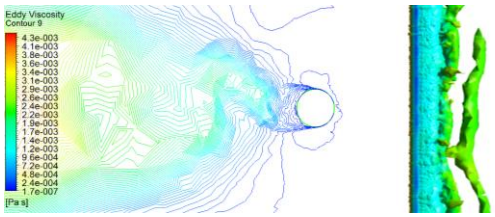


Appendix J: Two-dimensional Eddy Viscosity Profiles and Associated Three-dimensional Visualization of the Q-criterion

Figure J: Two-dimensional eddy viscosity profiles and associated three-dimensional visualization of the Q-criterion

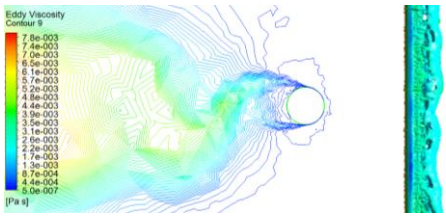
a) $\phi = 0°$; $\alpha = 0°$, $\beta = 0°$

i) Re = 1.1×10^5;



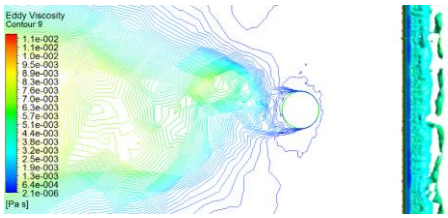
a) $\phi = 0°$; $\alpha = 0°$, $\beta = 0°$

ii) Re = 2.2×10^5;



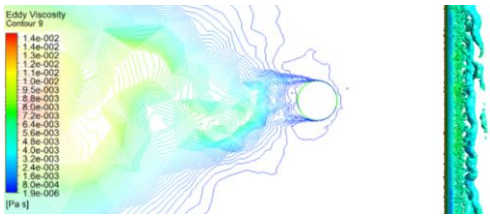
a) $\phi = 0°$; $\alpha = 0°$, $\beta = 0°$

iii) Re = 3.3×10^5;



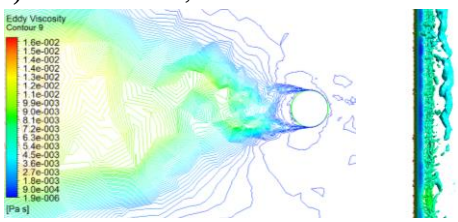
a) $\phi = 0°$; $\alpha = 0°$, $\beta = 0°$

iv) Re = 4.4×10^5;



a) $\phi = 0°$; $\alpha = 0°$, $\beta = 0°$

v) Re = 5.5×10^5;



a) $\phi = 0°$; $\alpha = 0°$, $\beta = 0°$

vi) Re = 6.7×10^5;

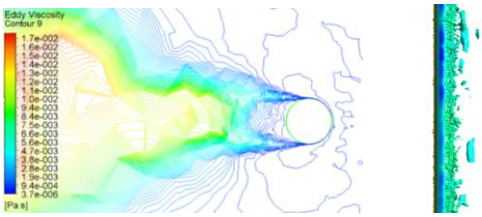
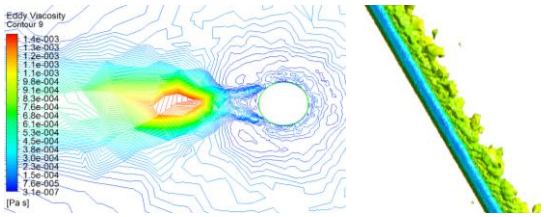


Figure J: Two-dimensional eddy viscosity profiles and associated three-dimensional visualization of the Q-criterion

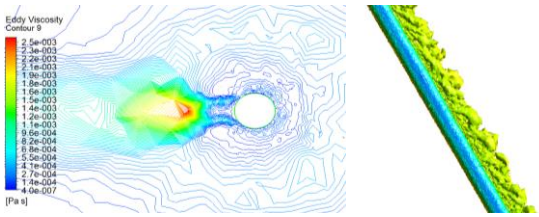
b) $\phi = 60°$; $\alpha = 60°$, $\beta = 0°$

i) Re = 1.1×10^5;



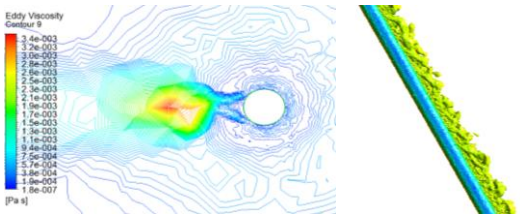
b) $\phi = 60°$; $\alpha = 60°$, $\beta = 0°$

ii) Re = 2.2×10^5;



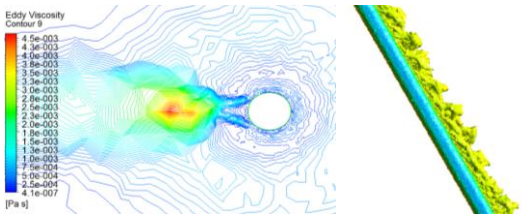
b) $\phi = 60°$; $\alpha = 60°$, $\beta = 0°$

iii) Re = 3.3×10^5;



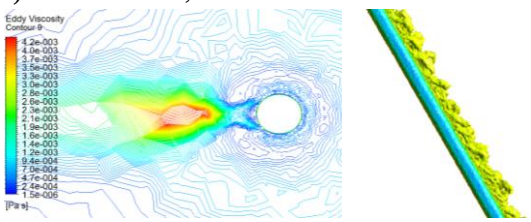
b) $\phi = 60°$; $\alpha = 60°$, $\beta = 0°$

iv) Re = 4.4×10^5;



b) $\phi = 60°$; $\alpha = 60°$, $\beta = 0°$

v) Re = 5.5×10^5;



b) $\phi = 60°$; $\alpha = 60°$, $\beta = 0°$

vi) Re = 6.7×10^5;

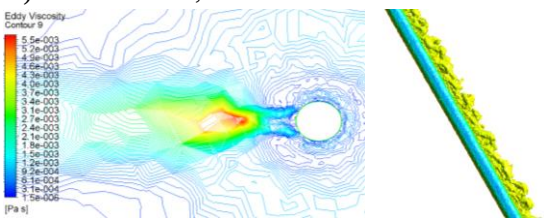
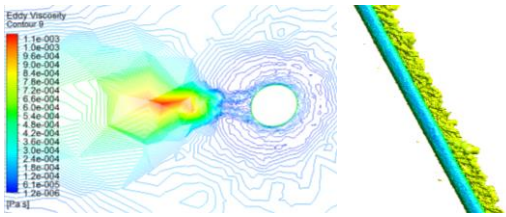


Figure J: Two-dimensional eddy viscosity profiles and associated three-dimensional visualization of the Q-criterion

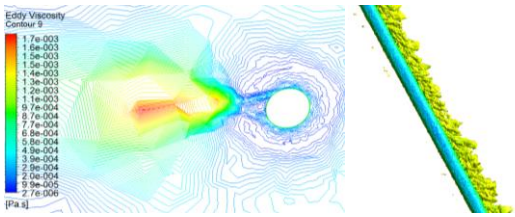
c) $\phi = 62°$; $\alpha = 60°$, $\beta = 20°$

i) Re = 1.1×10^5;



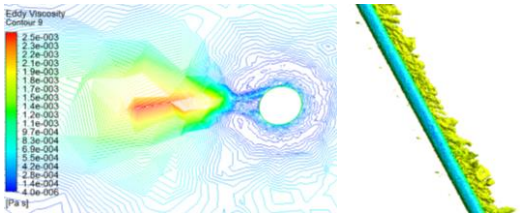
c) $\phi = 62°$; $\alpha = 60°$, $\beta = 20°$

ii) Re = 2.2×10^5;



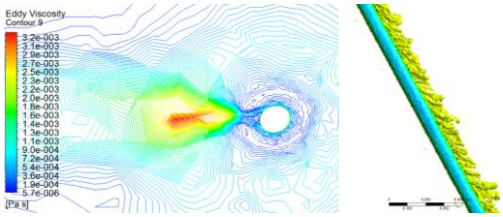
c) $\phi = 62°$; $\alpha = 60°$, $\beta = 20°$

iii) Re = 3.3×10^5;



c) $\phi = 62°$; $\alpha = 60°$, $\beta = 20°$

iv) Re = 4.4×10^5;



c) $\phi = 62°$; $\alpha = 60°$, $\beta = 20°$

v) Re = 5.5×10^5;

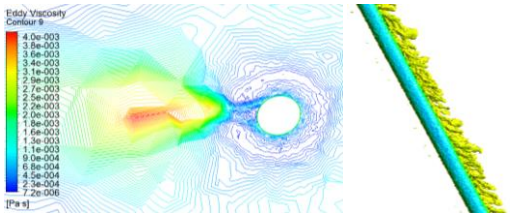
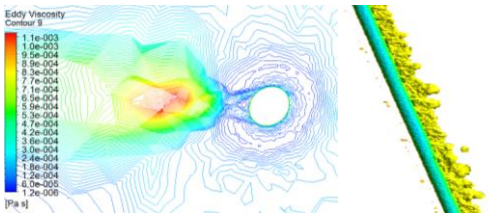


Figure J: Two-dimensional eddy viscosity profiles and associated three-dimensional visualization of the Q-criterion

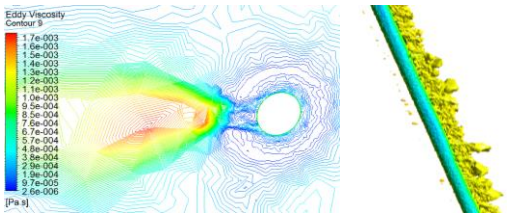
d) $\phi = 67.5°$; $\alpha = 60°$, $\beta = 40°$

i) Re = 1.1×10^5;



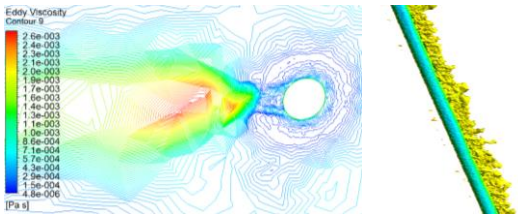
d) $\phi = 67.5°$; $\alpha = 60°$, $\beta = 40°$

ii) Re = 2.2×10^5;



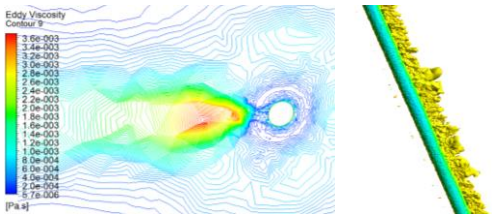
d) $\phi = 67.5°$; $\alpha = 60°$, $\beta = 40°$

iii) Re = 3.3×10^5;



d) $\phi = 67.5°$; $\alpha = 60°$, $\beta = 40°$

iv) Re = 4.4×10^5;



d) $\phi = 67.5°$; $\alpha = 60°$, $\beta = 40°$

v) Re = 5.5×10^5;

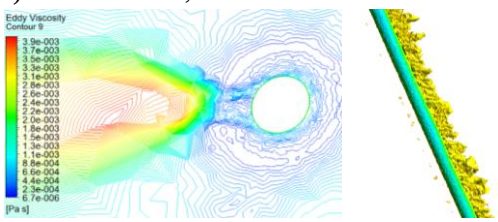
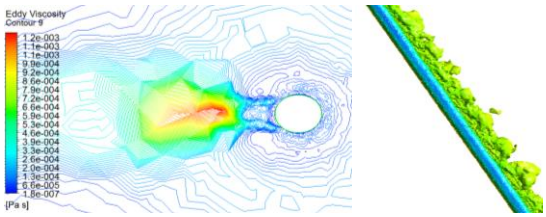


Figure J: Two-dimensional eddy viscosity profiles and associated three-dimensional visualization of the Q-criterion

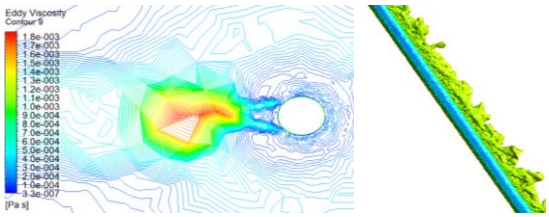
e) $\phi = 54.7°$; $\alpha = 54.7°$, $\beta = 0°$

i) Re = 1.1×10^5;



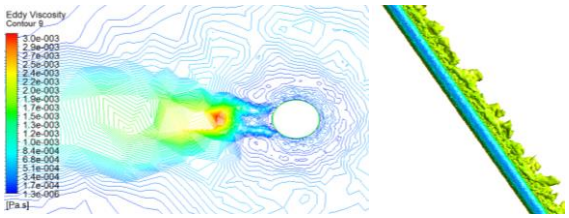
e) $\phi = 54.7°$; $\alpha = 54.7°$, $\beta = 0°$

ii) Re = 2.2×10^5;



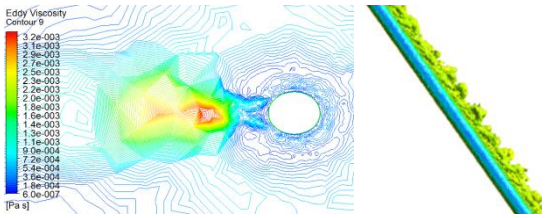
e) $\phi = 54.7°$; $\alpha = 54.7°$, $\beta = 0°$

iii) Re = 3.3×10^5;



e) $\phi = 54.7°$; $\alpha = 54.7°$, $\beta = 0°$

iv) Re = 4.4×10^5;



e) $\phi = 54.7°$; $\alpha = 54.7°$, $\beta = 0°$

v) Re = 5.5×10^5;

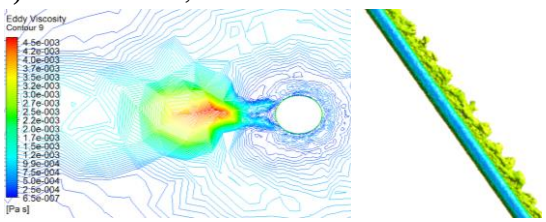
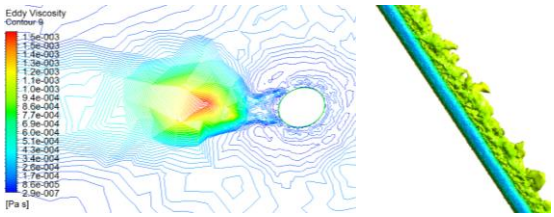


Figure J: Two-dimensional eddy viscosity profiles and associated three-dimensional visualization of the Q-criterion

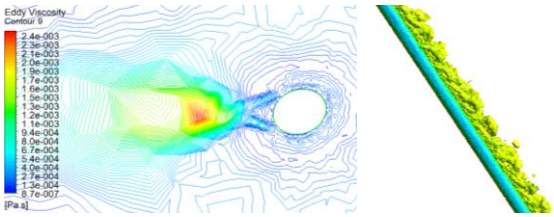
f) $\phi = 57.1°$; $\alpha = 54.7°$, $\beta = 20°$

i) Re = 1.1×10^5;



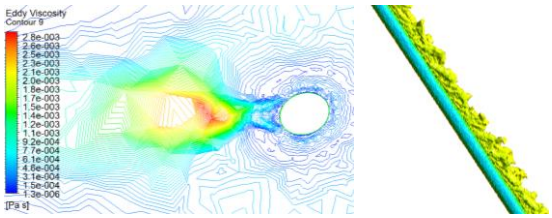
f) $\phi = 57.1°$; $\alpha = 54.7°$, $\beta = 20°$

ii) Re = 2.2×10^5;



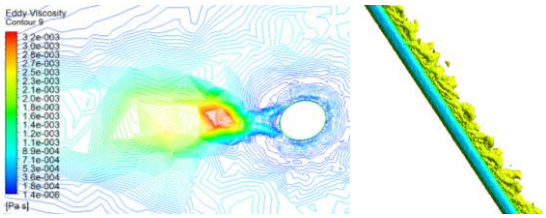
f) $\phi = 57.1°$; $\alpha = 54.7°$, $\beta = 20°$

iii) Re = 3.3×10^5;



f) $\phi = 57.1°$; $\alpha = 54.7°$, $\beta = 20°$

iv) Re = 4.4×10^5;



f) $\phi = 57.1°$; $\alpha = 54.7°$, $\beta = 20°$

v) Re = 5.5×10^5;

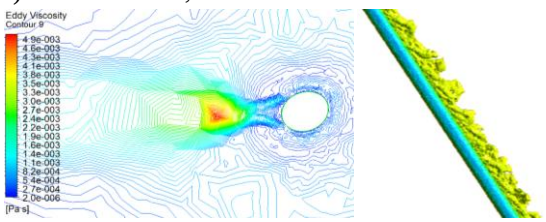
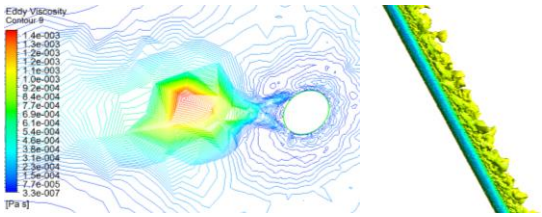


Figure J: Two-dimensional eddy viscosity profiles and associated three-dimensional visualization of the Q-criterion

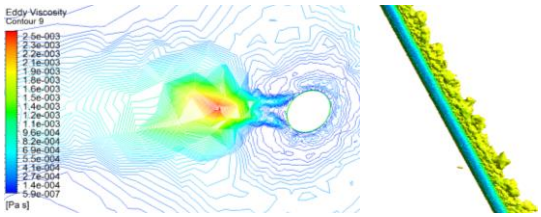
g) $\phi = 64°$; $\alpha = 54.7°$, $\beta = 40°$

i) Re = 1.1×10^5;



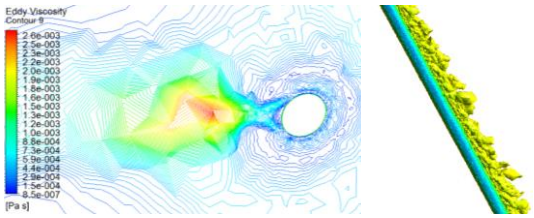
g) $\phi = 64°$; $\alpha = 54.7°$, $\beta = 40°$

ii) Re = 2.2×10^5;



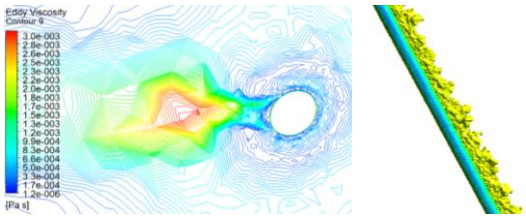
g) $\phi = 64°$; $\alpha = 54.7°$, $\beta = 40°$

iii) Re = 3.3×10^5;



g) $\phi = 64°$; $\alpha = 54.7°$, $\beta = 40°$

iv) Re = 4.4×10^5;



g) $\phi = 64°$; $\alpha = 54.7°$, $\beta = 40°$

v) Re = 5.5×10^5;

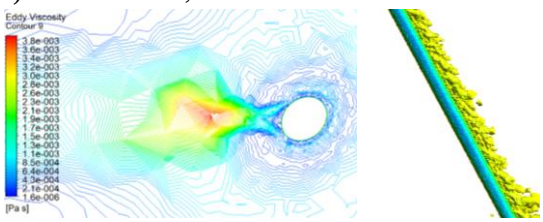
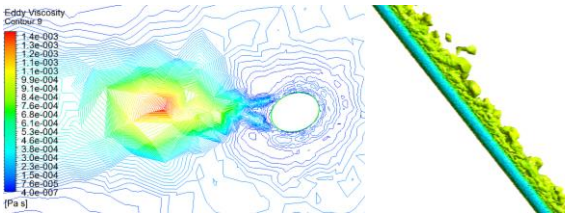


Figure J: Two-dimensional eddy viscosity profiles and associated three-dimensional visualization of the Q-criterion

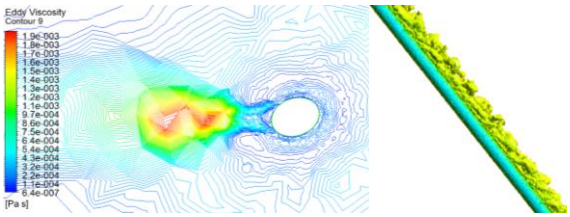
h) $\phi = 53°$; $\alpha = 50°$, $\beta = 20°$

i) Re = 1.1×10^5;



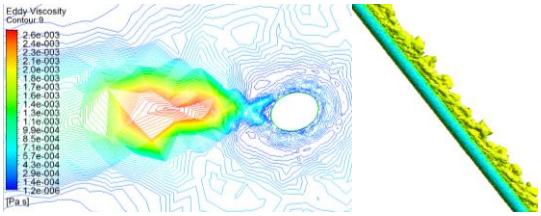
h) $\phi = 53°$; $\alpha = 50°$, $\beta = 20°$

ii) Re = 2.2×10^5;



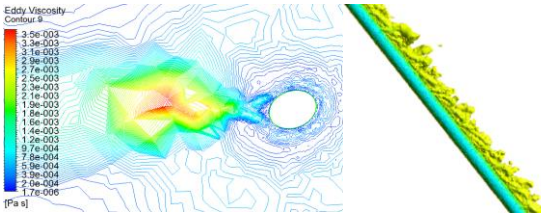
h) $\phi = 53°$; $\alpha = 50°$, $\beta = 20°$

iii) Re = 3.3×10^5;



h) $\phi = 53°$; $\alpha = 50°$, $\beta = 20°$

iv) Re = 4.4×10^5;



h) $\phi = 53°$; $\alpha = 50°$, $\beta = 20°$

v) Re = 5.5×10^5;

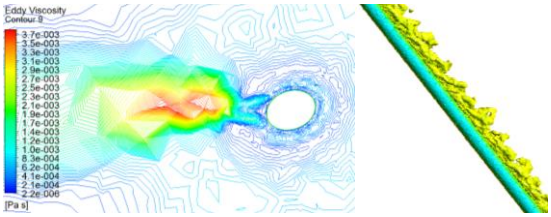
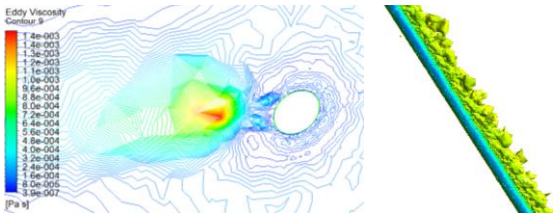


Figure J: Two-dimensional eddy viscosity profiles and associated three-dimensional visualization of the Q-criterion

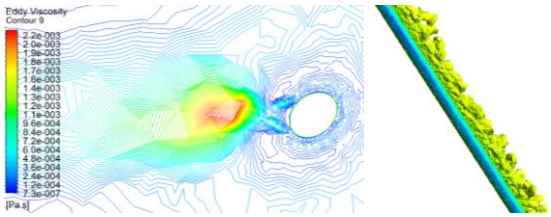
i) $\phi = 60.5°$; $\alpha = 50°$, $\beta = 40°$

i) Re = 1.1×10^5;



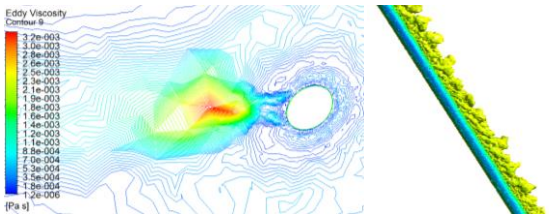
i) $\phi = 60.5°$; $\alpha = 50°$, $\beta = 40°$

ii) Re = 2.2×10^5;



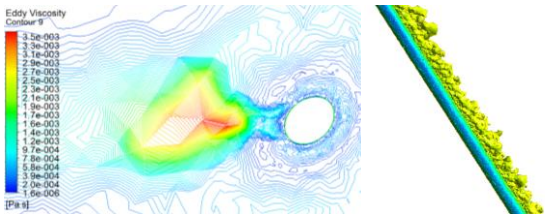
i) $\phi = 60.5°$; $\alpha = 50°$, $\beta = 40°$

iii) Re = 3.3×10^5;



i) $\phi = 60.5°$; $\alpha = 50°$, $\beta = 40°$

iv) Re = 4.4×10^5;



i) $\phi = 60.5°$; $\alpha = 50°$, $\beta = 40°$

v) Re = 5.5×10^5;

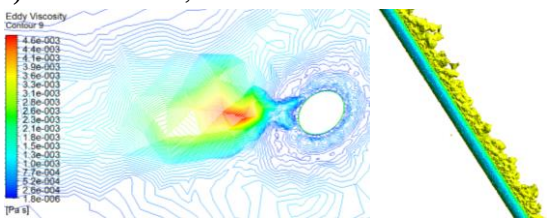
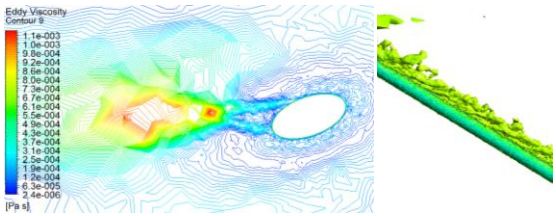
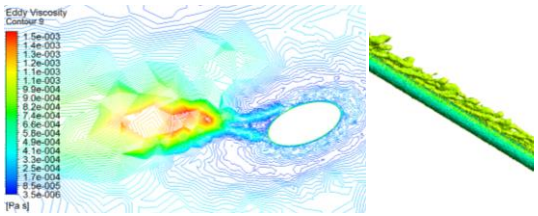


Figure J: Two-dimensional eddy viscosity profiles and associated three-dimensional visualization of the Q-criterion

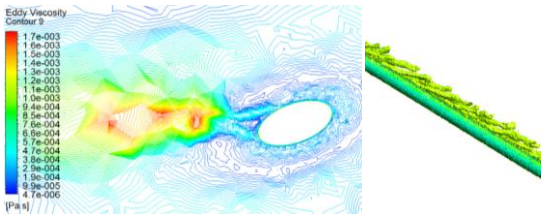
j) $\phi = 35.5°$; $\alpha = 30°$, $\beta = 20°$
Re = 2.2×10^5;



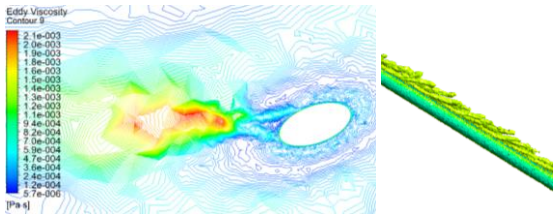
j) $\phi = 35.5°$; $\alpha = 30°$, $\beta = 20°$
Re = 3.3×10^5;



j) $\phi = 35.5°$; $\alpha = 30°$, $\beta = 20°$
Re = 4.4×10^5;



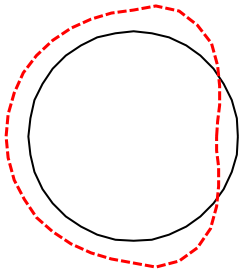
j) $\phi = 35.5°$; $\alpha = 30°$, $\beta = 20°$
Re = 5.5×10^5;



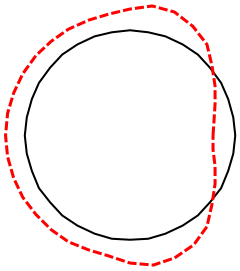
Appendix K: Mean Pressure Distribution about a Circular Cylinder

Figure K: Mean pressure distribution about a circular cylinder:

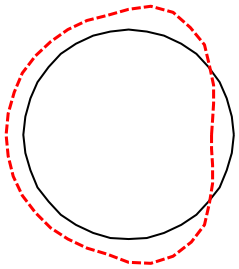
a) $\phi = 0°$; $\alpha = 0°$, $\beta = 0°$
i) Re = 1.1×10^5;



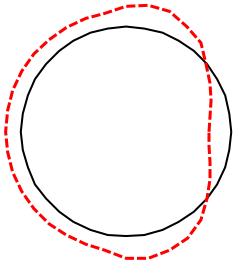
a) $\phi = 0°$; $\alpha = 0°$, $\beta = 0°$
ii) Re = 2.2×10^5;



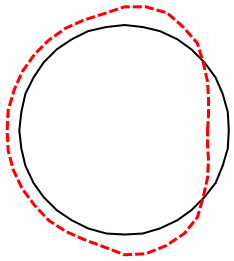
a) $\phi = 0°$; $\alpha = 0°$, $\beta = 0°$
iii) Re = 3.3×10^5;



a) $\phi = 0°$; $\alpha = 0°$, $\beta = 0°$
iv) Re = 4.4×10^5;



a) $\phi = 0°$; $\alpha = 0°$, $\beta = 0°$
v) Re = 5.5×10^5;



a) $\phi = 0°$; $\alpha = 0°$, $\beta = 0°$
vi) Re = 6.7×10^5;

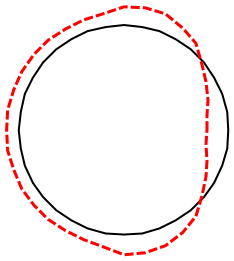
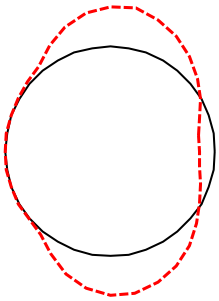
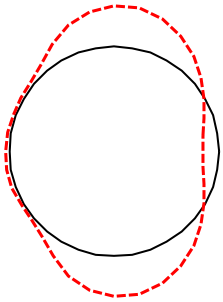


Figure K: Mean pressure distribution about a circular cylinder:

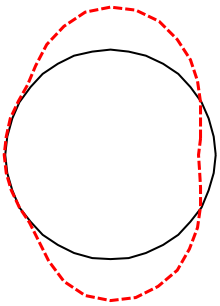
b) $\phi = 60°$; $\alpha = 60°$, $\beta = 0°$
i) Re = 1.1×10^5;



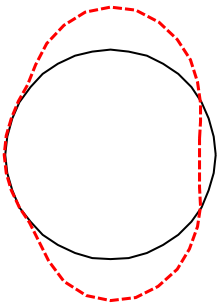
b) $\phi = 60°$; $\alpha = 60°$, $\beta = 0°$
ii) Re = 2.2×10^5;



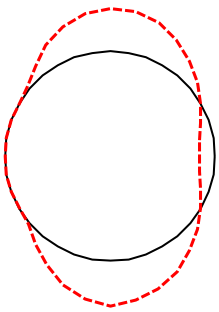
b) $\phi = 60°$; $\alpha = 60°$, $\beta = 0°$
iii) Re = 3.3×10^5;



b) $\phi = 60°$; $\alpha = 60°$, $\beta = 0°$
iv) Re = 4.4×10^5;



b) $\phi = 60°$; $\alpha = 60°$, $\beta = 0°$
v) Re = 5.5×10^5;



b) $\phi = 60°$; $\alpha = 60°$, $\beta = 0°$
vi) Re = 6.7×10^5;

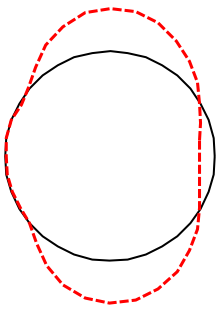
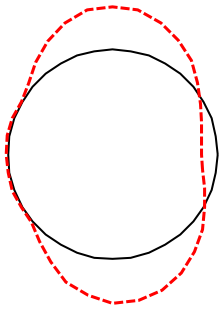
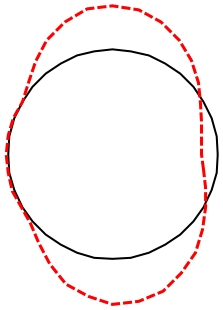


Figure K: Mean pressure distribution about a circular cylinder:

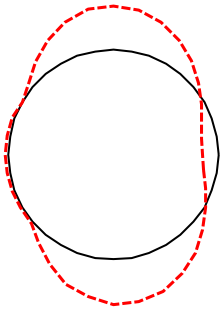
c) $\phi = 62°$; $\alpha = 60°$, $\beta = 20°$
i) Re = 1.1×10^5;



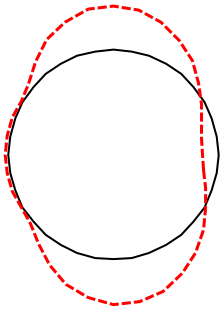
c) $\phi = 62°$; $\alpha = 60°$, $\beta = 20°$
ii) Re = 2.2×10^5;



c) $\phi = 62°$; $\alpha = 60°$, $\beta = 20°$
iii) Re = 3.3×10^5;



c) $\phi = 62°$; $\alpha = 60°$, $\beta = 20°$
iv) Re = 4.4×10^5;



c) $\phi = 62°$; $\alpha = 60°$, $\beta = 20°$
v) Re = 5.5×10^5;

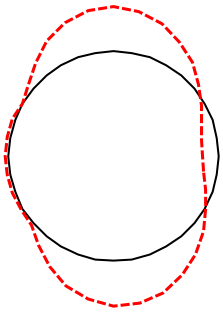
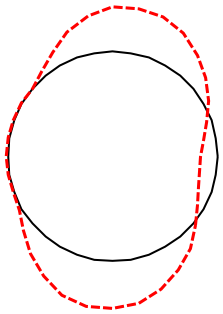
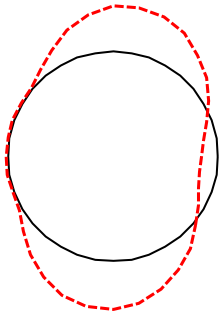


Figure K: Mean pressure distribution about a circular cylinder:

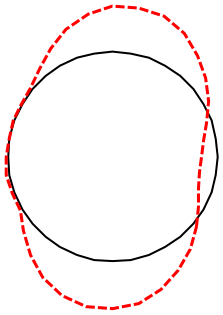
d) $\phi = 64°$; $\alpha = 60°$, $\beta = 40°$
i) Re = 1.1×10^5;



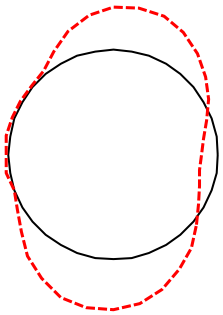
c) $\phi = 62°$; $\alpha = 60°$, $\beta = 20°$
ii) Re = 2.2×10^5;



c) $\phi = 62°$; $\alpha = 60°$, $\beta = 20°$
iii) Re = 3.3×10^5;



c) $\phi = 62°$; $\alpha = 60°$, $\beta = 20°$
iv) Re = 4.4×10^5;



c) $\phi = 62°$; $\alpha = 60°$, $\beta = 20°$
v) Re = 5.5×10^5;

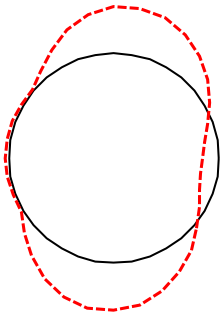
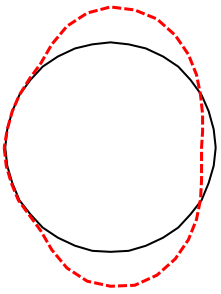
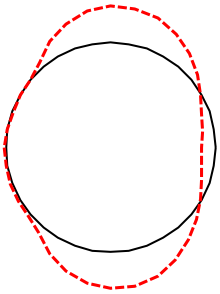


Figure K: Mean pressure distribution about a circular cylinder:

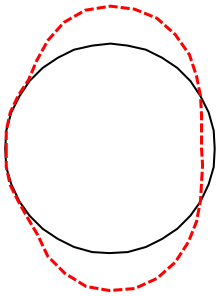
e) $\phi = 54.7°$; $\alpha = 54.7°$, $\beta = 0°$
i) Re = 1.1×10^5;



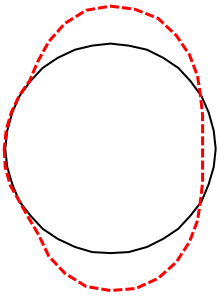
e) $\phi = 54.7°$; $\alpha = 54.7°$, $\beta = 0°$
ii) Re = 2.2×10^5;



e) $\phi = 54.7°$; $\alpha = 54.7°$, $\beta = 0°$
iii) Re = 3.3×10^5;



e) $\phi = 54.7°$; $\alpha = 54.7°$, $\beta = 0°$
iv) Re = 4.4×10^5;



e) $\phi = 54.7°$; $\alpha = 54.7°$, $\beta = 0°$
v) Re = 5.5×10^5;

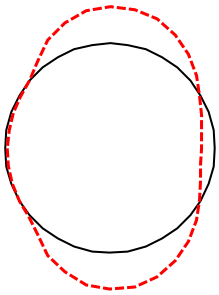
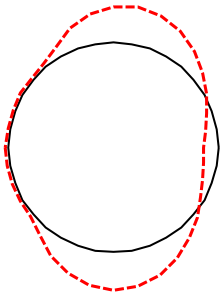
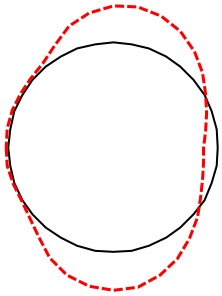


Figure K: Mean pressure distribution about a circular cylinder:

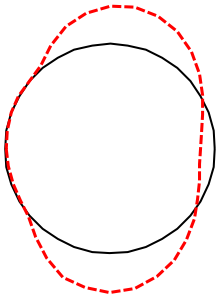
f) $\phi = 57.1°$; $\alpha = 54.7°$, $\beta = 20°$
i) Re = 1.1×10^5;



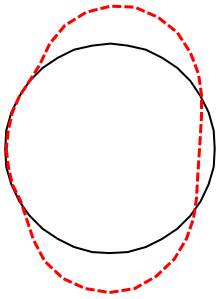
f) $\phi = 57.1°$; $\alpha = 54.7°$, $\beta = 20°$
ii) Re = 2.2×10^5;



f) $\phi = 57.1°$; $\alpha = 54.7°$, $\beta = 20°$
iii) Re = 3.3×10^5;



f) $\phi = 57.1°$; $\alpha = 54.7°$, $\beta = 20°$
iv) Re = 4.4×10^5;



f) $\phi = 57.1°$; $\alpha = 54.7°$, $\beta = 20°$
v) Re = 5.5×10^5;

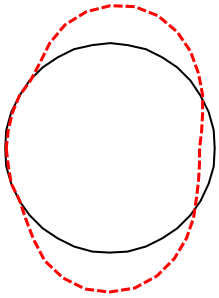
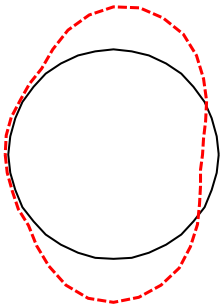
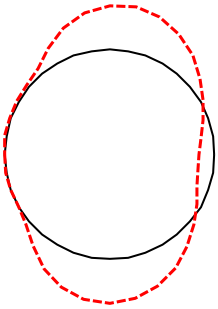


Figure K: Mean pressure distribution about a circular cylinder:

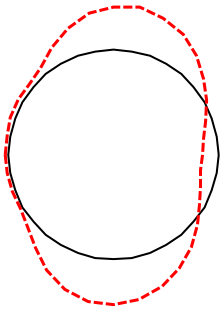
g) $\phi = 64.0°$; $\alpha = 54.7°$, $\beta = 40°$
i) Re = 1.1×10^5;



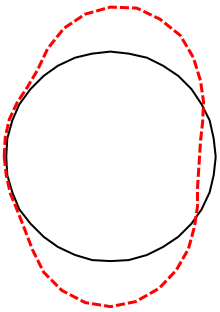
g) $\phi = 64.0°$; $\alpha = 54.7°$, $\beta = 40°$
ii) Re = 2.2×10^5;



g) $\phi = 64.0°$; $\alpha = 54.7°$, $\beta = 40°$
iii) Re = 3.3×10^5;



g) $\phi = 64.0°$; $\alpha = 54.7°$, $\beta = 40°$
iv) Re = 4.4×10^5;



g) $\phi = 64.0°$; $\alpha = 54.7°$, $\beta = 40°$
v) Re = 5.5×10^5;

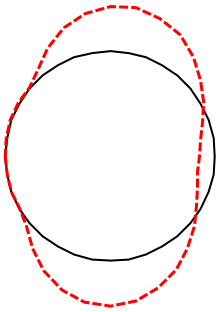
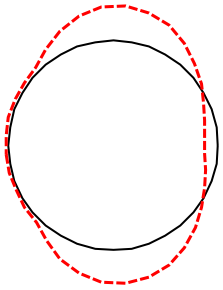
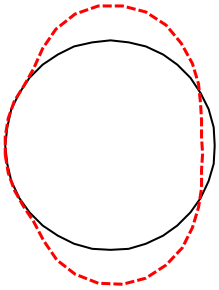


Figure K: Mean pressure distribution about a circular cylinder:

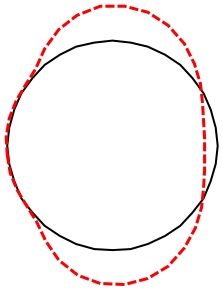
h) $\phi = 53.0°$; $\alpha = 50°$, $\beta = 20°$
i) Re = 1.1×10^5;



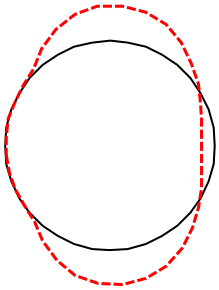
h) $\phi = 53.0°$; $\alpha = 50°$, $\beta = 20°$
ii) Re = 2.2×10^5;



h) $\phi = 53.0°$; $\alpha = 50°$, $\beta = 20°$
iii) Re = 3.3×10^5;



h) $\phi = 53.0°$; $\alpha = 50°$, $\beta = 20°$
iv) Re = 4.4×10^5;



h) $\phi = 53.0°$; $\alpha = 50°$, $\beta = 20°$
v) Re = 5.5×10^5;

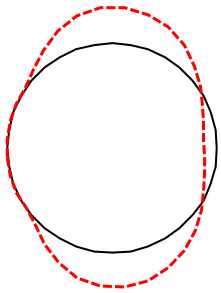
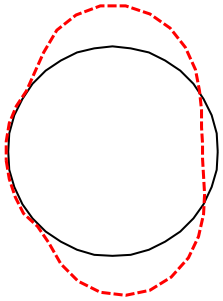
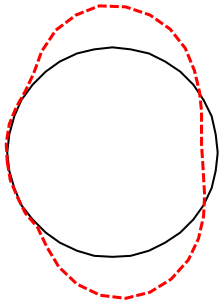


Figure K: Mean pressure distribution about a circular cylinder:

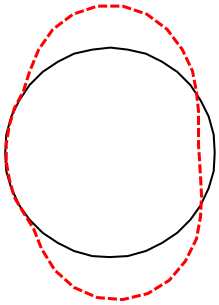
i) $\phi = 60.5°$; $\alpha = 50°$, $\beta = 40°$
i) Re = 1.1×10^5;



i) $\phi = 60.5°$; $\alpha = 50°$, $\beta = 40°$
ii) Re = 2.2×10^5;



i) $\phi = 60.5°$; $\alpha = 50°$, $\beta = 40°$
iii) Re = 3.3×10^5;



i) $\phi = 60.5°$; $\alpha = 50°$, $\beta = 40°$
iv) Re = 4.4×10^5;

i) $\phi = 60.5°$; $\alpha = 50°$, $\beta = 40°$
v) Re = 5.5×10^5;

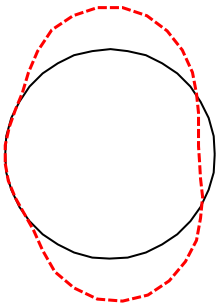
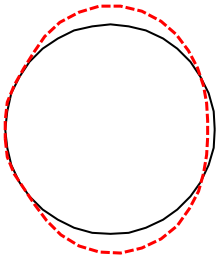
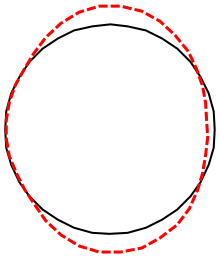


Figure K: Mean pressure distribution about a circular cylinder:

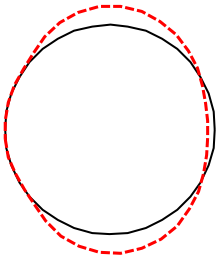
j) $\phi = 35.5°$; $\alpha = 30°$, $\beta = 20°$
ii) Re = 2.2×10^5;



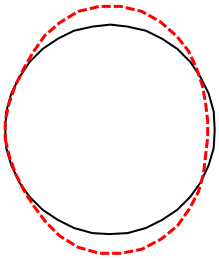
j) $\phi = 35.5°$; $\alpha = 30°$, $\beta = 20°$
iii) Re = 3.3×10^5;



j) $\phi = 35.5°$; $\alpha = 30°$, $\beta = 20°$
iv) Re = 4.4×10^5;



j) $\phi = 35.5°$; $\alpha = 30°$, $\beta = 20°$
v) Re = 5.5×10^5;

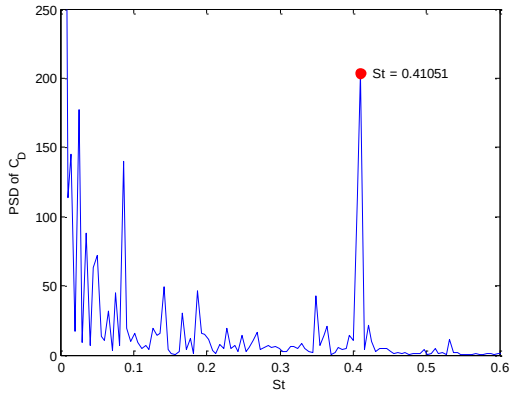


Appendix L: Fast Fourier Transform (FFT) Results for C_D

Figure L: FFT results C_D:

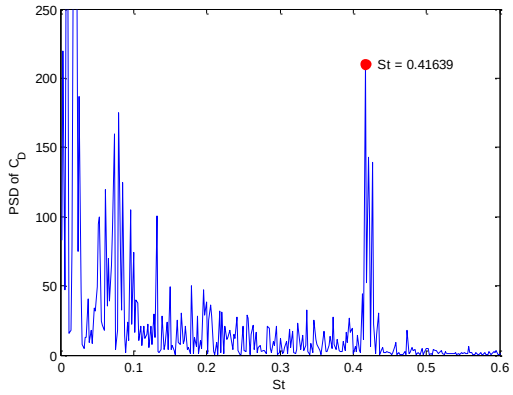
a) $\phi = 0°$; $\alpha = 0°$, $\beta = 0°$

i) Re = 1.1×10^5;



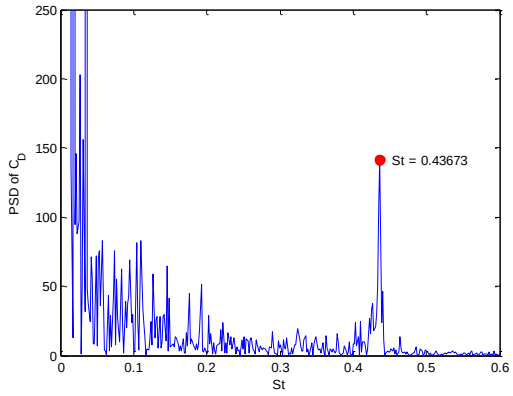
a) $\phi = 0°$; $\alpha = 0°$, $\beta = 0°$

ii) Re = 2.2×10^5;



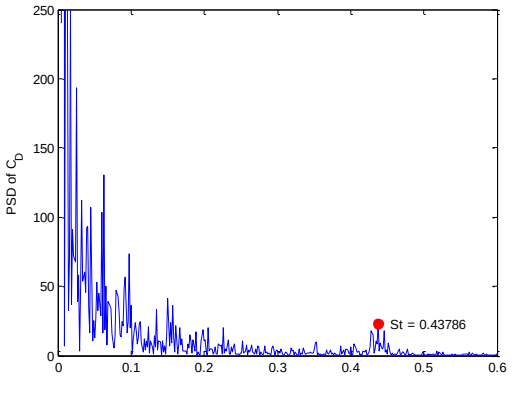
a) $\phi = 0°$; $\alpha = 0°$, $\beta = 0°$

iii) Re = 3.3×10^5;



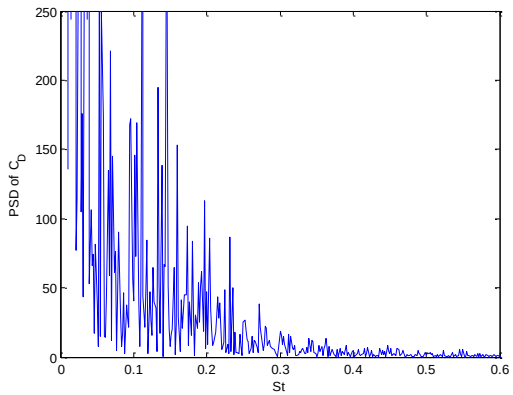
a) $\phi = 0°$; $\alpha = 0°$, $\beta = 0°$

iv) Re = 4.4×10^5;



a) $\phi = 0°$; $\alpha = 0°$, $\beta = 0°$

v) Re = 5.5×10^5;



a) $\phi = 0°$; $\alpha = 0°$, $\beta = 0°$

vi) Re = 6.7×10^5;

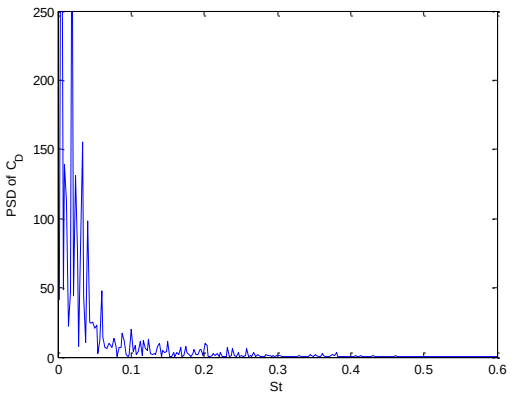
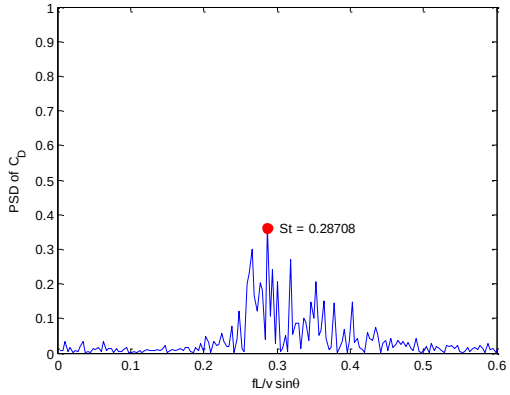
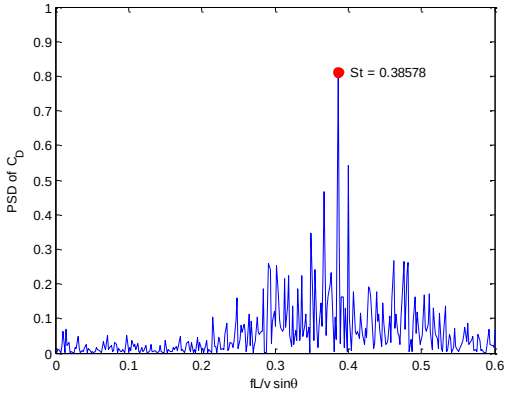


Figure L: FFT results C_D:

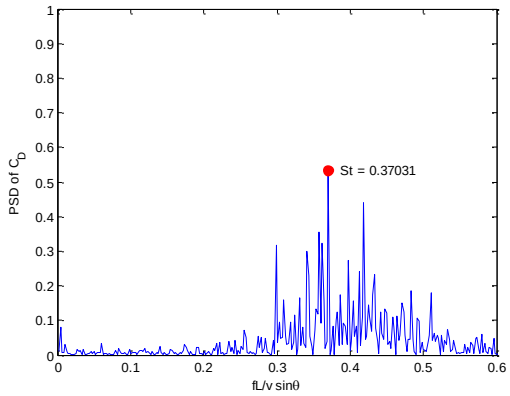
b) $\phi = 60°$; $\alpha = 60°$, $\beta = 0°$
i) Re = 1.1×10^5;



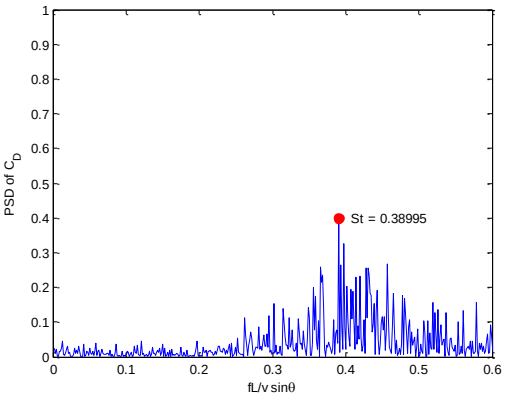
b) $\phi = 60°$; $\alpha = 60°$, $\beta = 0°$
ii) Re = 2.2×10^5;



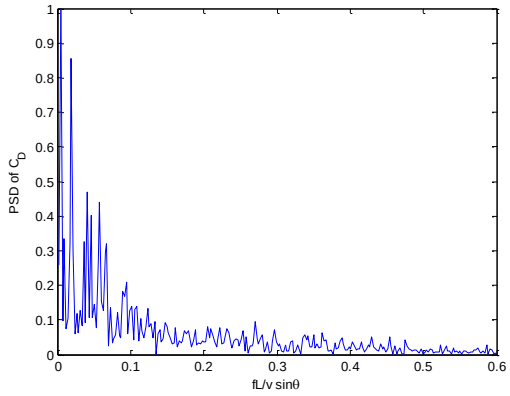
b) $\phi = 60°$; $\alpha = 60°$, $\beta = 0°$
iii) Re = 3.3×10^5;



b) $\phi = 60°$; $\alpha = 60°$, $\beta = 0°$
iv) Re = 4.4×10^5;



b) $\phi = 60°$; $\alpha = 60°$, $\beta = 0°$
v) Re = 5.5×10^5;



b) $\phi = 60°$; $\alpha = 60°$, $\beta = 0°$
vi) Re = 6.7×10^5;

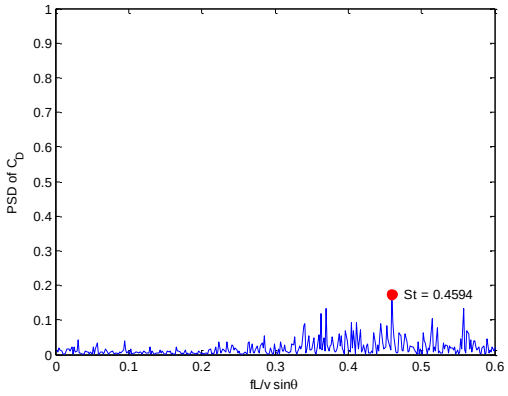
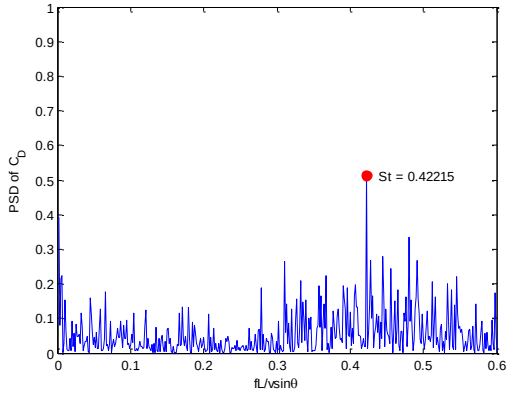
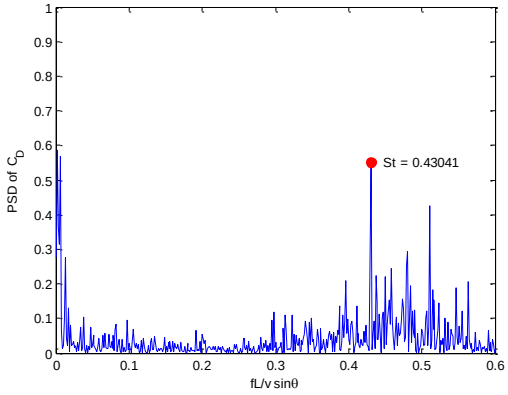


Figure L: FFT results C_D:

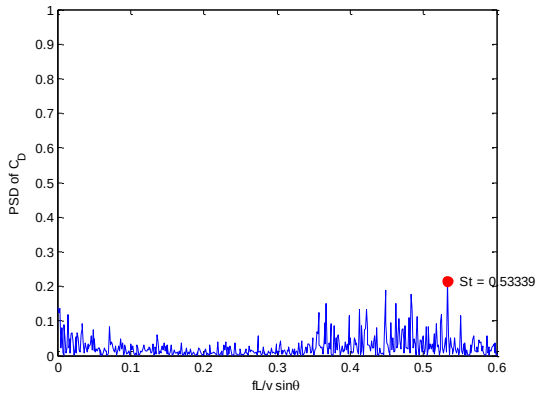
c) $\phi = 62°$; $\alpha = 60°$, $\beta = 20°$
i) Re = 1.1×10^5;



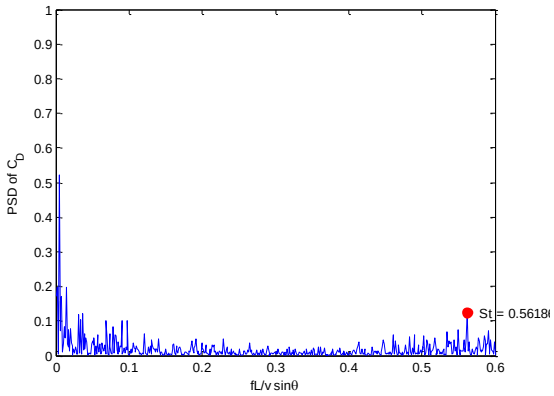
c) $\phi = 62°$; $\alpha = 60°$, $\beta = 20°$
ii) Re = 2.2×10^5;



c) $\phi = 62°$; $\alpha = 60°$, $\beta = 20°$
iii) Re = 3.3×10^5;



c) $\phi = 62°$; $\alpha = 60°$, $\beta = 20°$
iv) Re = 4.4×10^5;



c) $\phi = 62°$; $\alpha = 60°$, $\beta = 20°$
v) Re = 5.5×10^5;

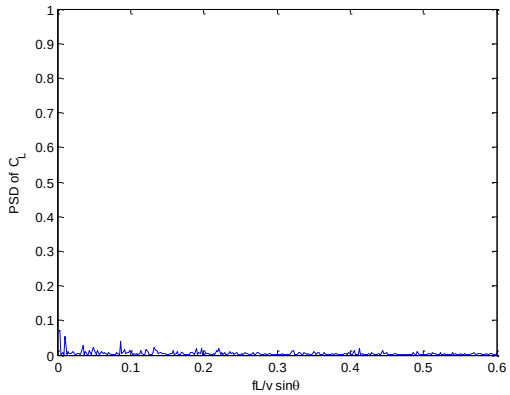
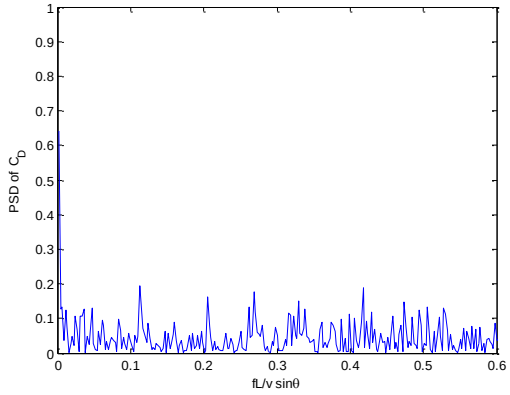
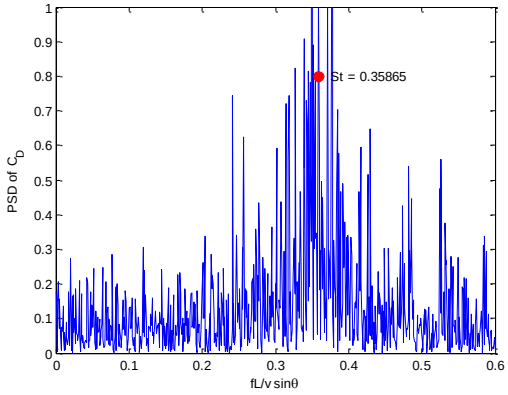


Figure L: FFT results C_D:

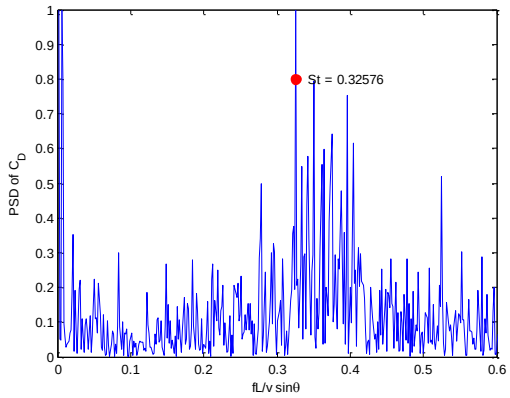
d) $\phi = 67.5°$; $\alpha = 60°$, $\beta = 40°$
i) Re = 1.1×10^5;



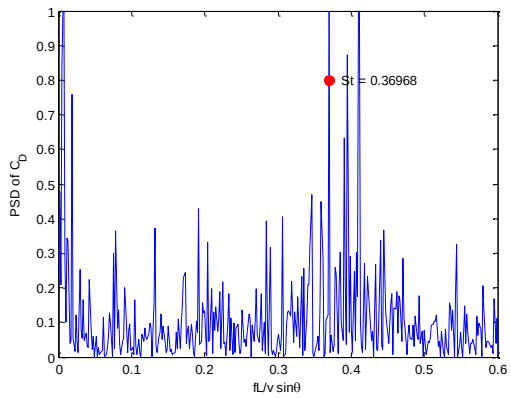
d) $\phi = 67.5°$; $\alpha = 60°$, $\beta = 40°$
ii) Re = 2.2×10^5;



d) $\phi = 67.5°$; $\alpha = 60°$, $\beta = 40°$
iii) Re = 3.3×10^5;



d) $\phi = 67.5°$; $\alpha = 60°$, $\beta = 40°$
iv) Re = 4.4×10^5;



d) $\phi = 67.5°$; $\alpha = 60°$, $\beta = 40°$
v) Re = 5.5×10^5;

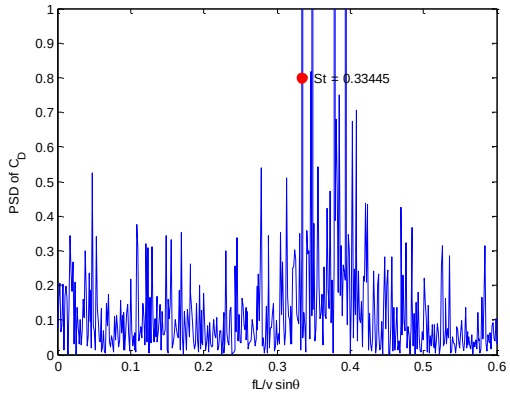
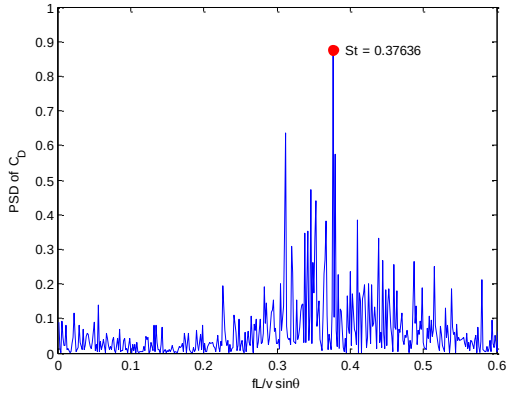
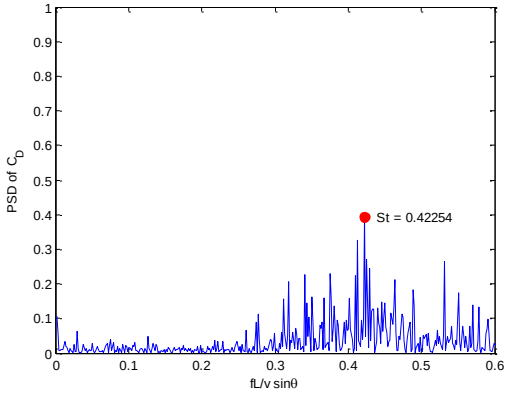


Figure L: FFT results C_D:

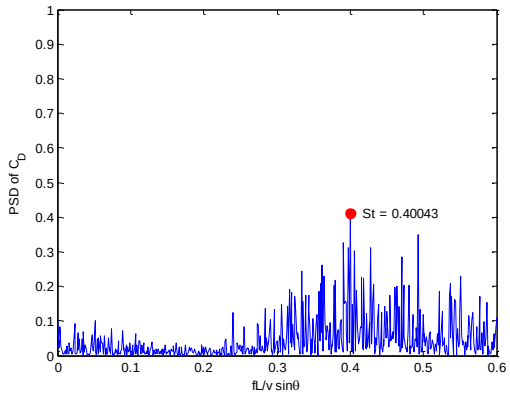
e) $\phi = 54.7°$; $\alpha = 54.7°$, $\beta = 0°$
i) Re = 1.1×10^5;



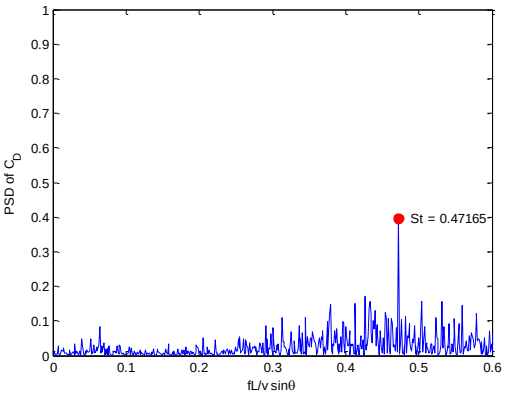
e) $\phi = 54.7°$; $\alpha = 54.7°$, $\beta = 0°$
ii) Re = 2.2×10^5;



e) $\phi = 54.7°$; $\alpha = 54.7°$, $\beta = 0°$
iii) Re = 3.3×10^5;



e) $\phi = 54.7°$; $\alpha = 54.7°$, $\beta = 0°$
iv) Re = 4.4×10^5;



e) $\phi = 54.7°$; $\alpha = 54.7°$, $\beta = 0°$
v) Re = 5.5×10^5;

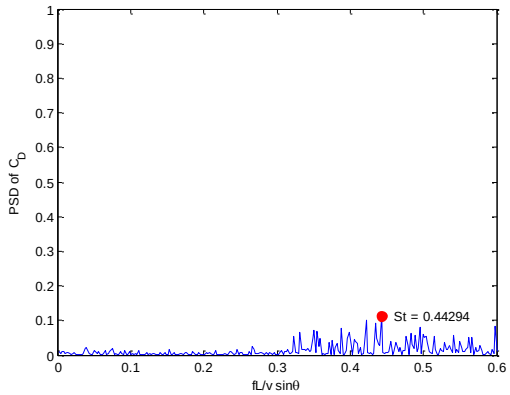
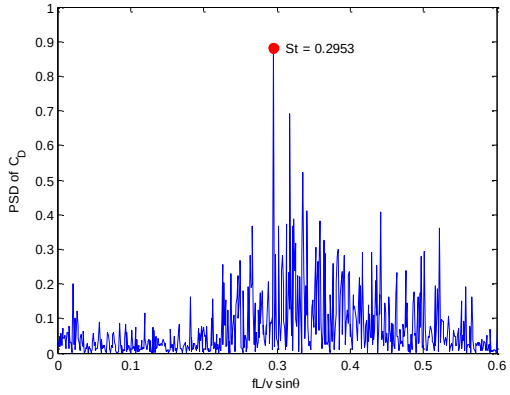
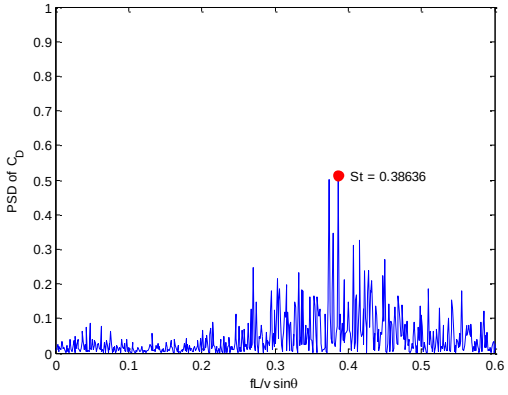


Figure L: FFT results C_D:

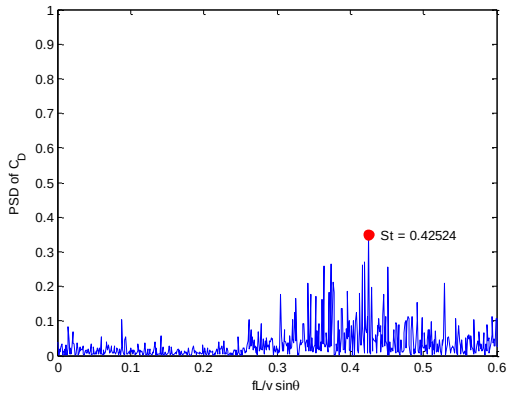
f) $\phi = 57.1°$; $\alpha = 54.7°$, $\beta = 20°$
i) Re = 1.1×10^5;



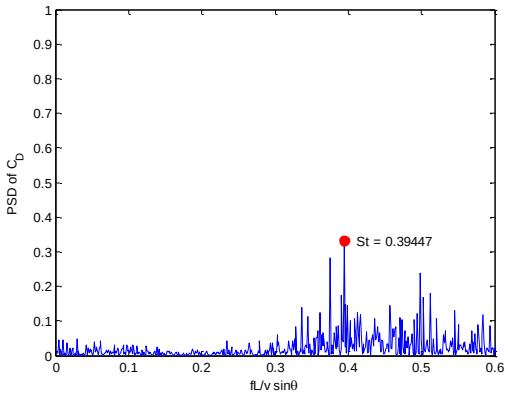
f) $\phi = 57.1°$; $\alpha = 54.7°$, $\beta = 20°$
ii) Re = 2.2×10^5;



f) $\phi = 57.1°$; $\alpha = 54.7°$, $\beta = 20°$
iii) Re = 3.3×10^5;



f) $\phi = 57.1°$; $\alpha = 54.7°$, $\beta = 20°$
iv) Re = 4.4×10^5;



f) $\phi = 57.1°$; $\alpha = 54.7°$, $\beta = 20°$
v) Re = 5.5×10^5;

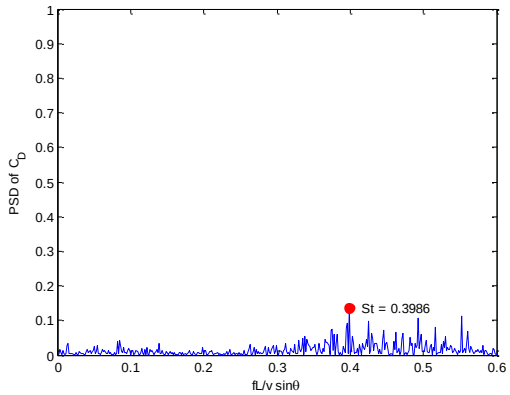
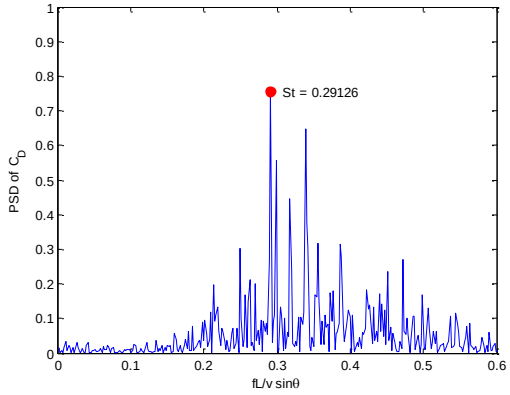
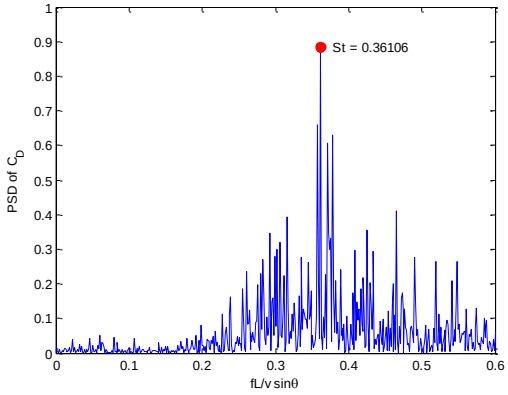


Figure L: FFT results C_D:

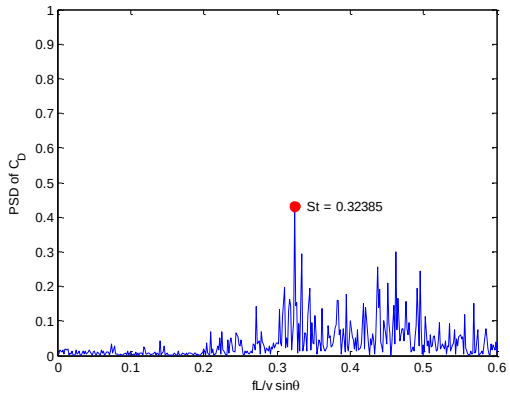
g) $\phi = 64.0°$; $\alpha = 54.7°$, $\beta = 40°$
i) Re = 1.1×10^5;



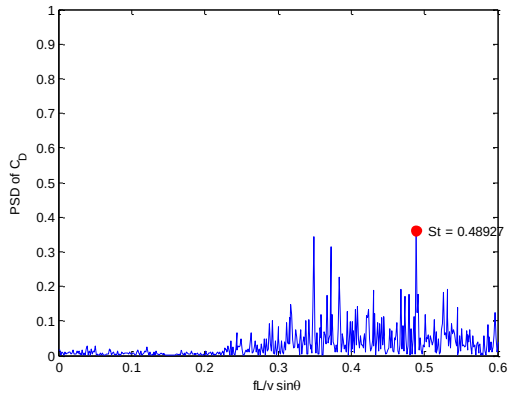
g) $\phi = 64.0°$; $\alpha = 54.7°$, $\beta = 40°$
ii) Re = 2.2×10^5;



g) $\phi = 64.0°$; $\alpha = 54.7°$, $\beta = 40°$
iii) Re = 3.3×10^5;



g) $\phi = 64.0°$; $\alpha = 54.7°$, $\beta = 40°$
iv) Re = 4.4×10^5;



g) $\phi = 64.0°$; $\alpha = 54.7°$, $\beta = 40°$
v) Re = 5.5×10^5;

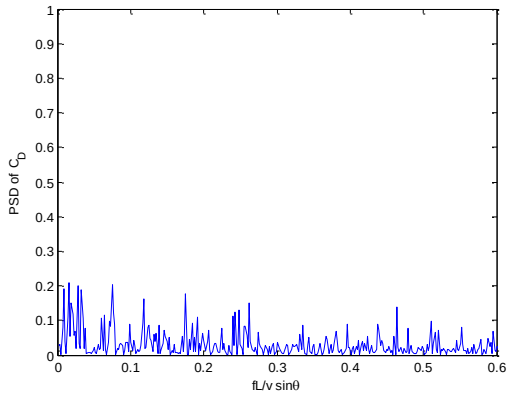
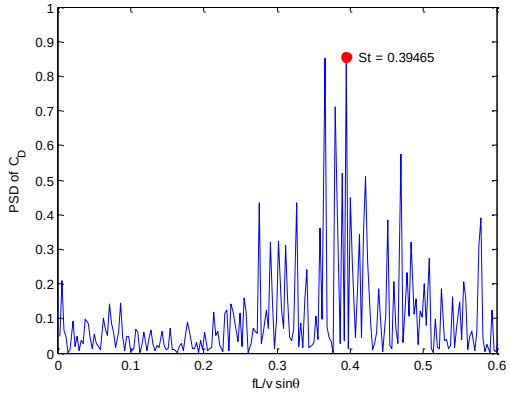
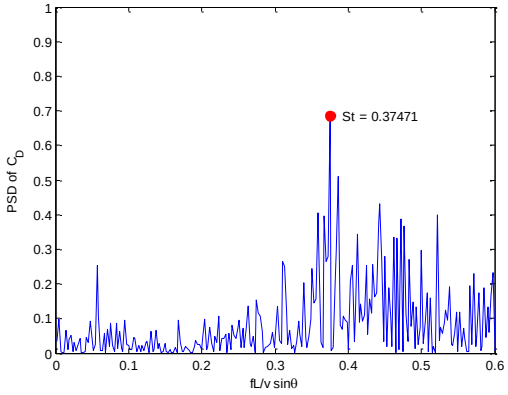


Figure L: FFT results C_D:

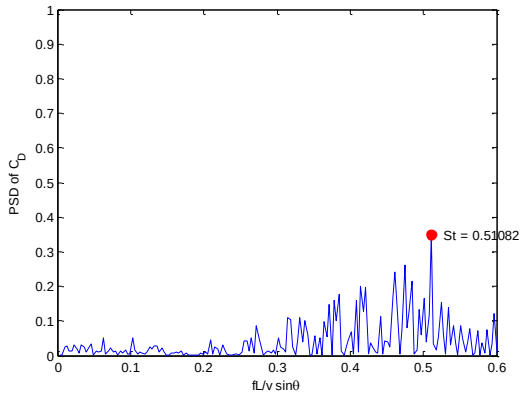
h) $\phi = 53.0°$; $\alpha = 50°$, $\beta = 20°$
i) Re = 1.1×10^5;



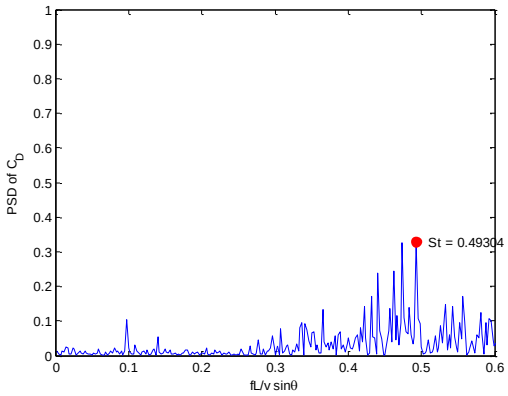
h) $\phi = 53.0°$; $\alpha = 50°$, $\beta = 20°$
ii) Re = 2.2×10^5;



h) $\phi = 53.0°$; $\alpha = 50°$, $\beta = 20°$
iii) Re = 3.3×10^5;



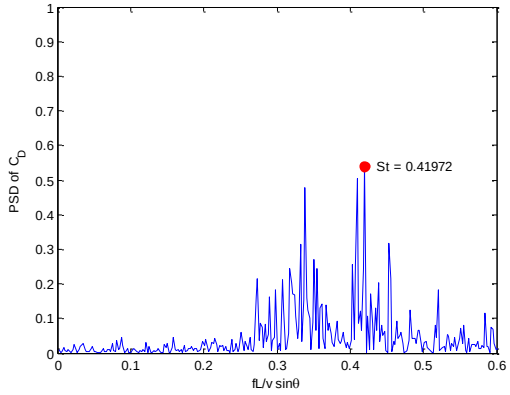
h) $\phi = 53.0°$; $\alpha = 50°$, $\beta = 20°$
iv) Re = 4.4×10^5;



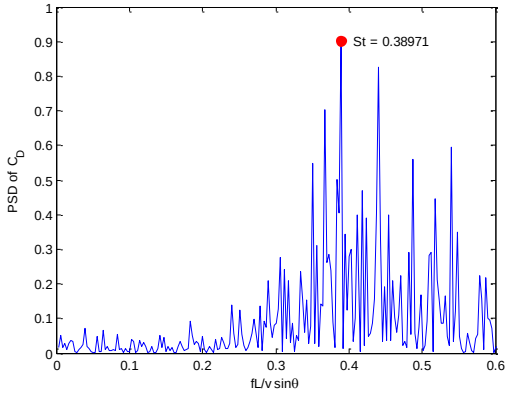
h) $\phi = 53.0°$; $\alpha = 50°$, $\beta = 20°$
v) Re = 5.5×10^5;

Figure L: FFT results C_D:

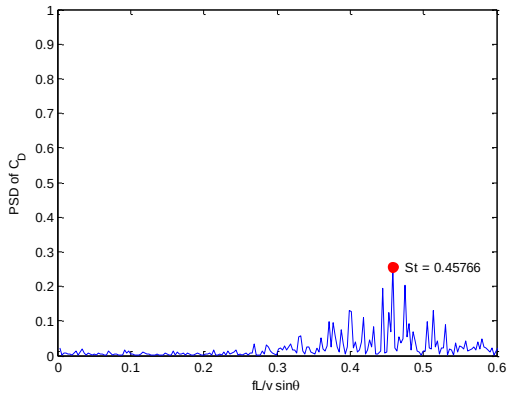
i) $\phi = 60.5°$; $\alpha = 50°$, $\beta = 40°$
i) Re = 1.1×10^5;



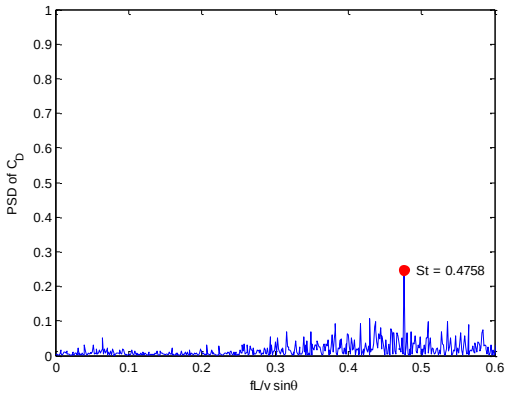
i) $\phi = 60.5°$; $\alpha = 50°$, $\beta = 40°$
ii) Re = 2.2×10^5;



i) $\phi = 60.5°$; $\alpha = 50°$, $\beta = 40°$
iii) Re = 3.3×10^5;



i) $\phi = 60.5°$; $\alpha = 50°$, $\beta = 40°$
iv) Re = 4.4×10^5;



i) $\phi = 60.5°$; $\alpha = 50°$, $\beta = 40°$
v) Re = 5.5×10^5;

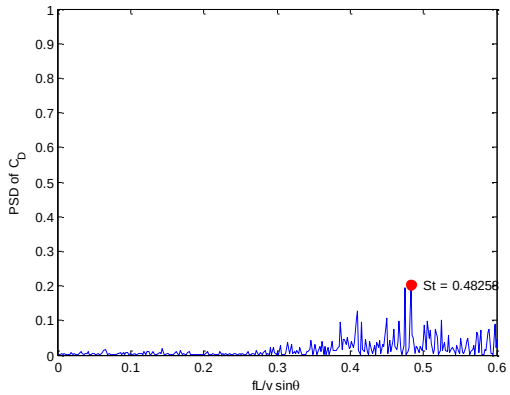
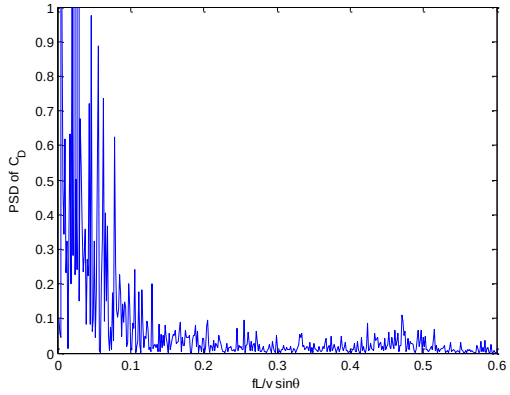


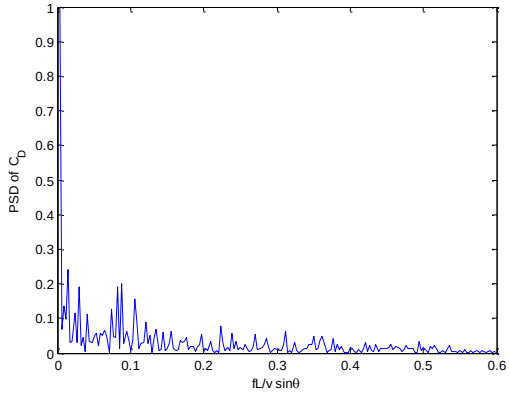
Figure L: FFT results C_D:

j) $\phi = 35.5°$; $\alpha = 30°$, $\beta = 20°$

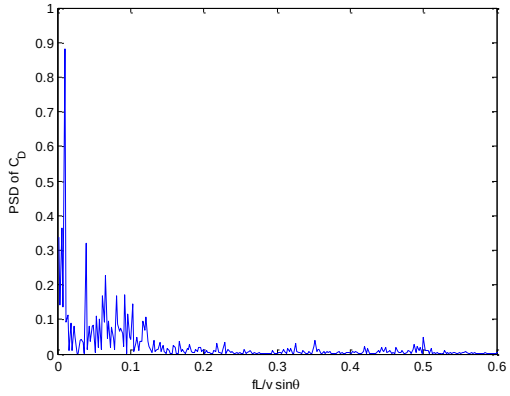
ii) Re = 2.2×10^5;



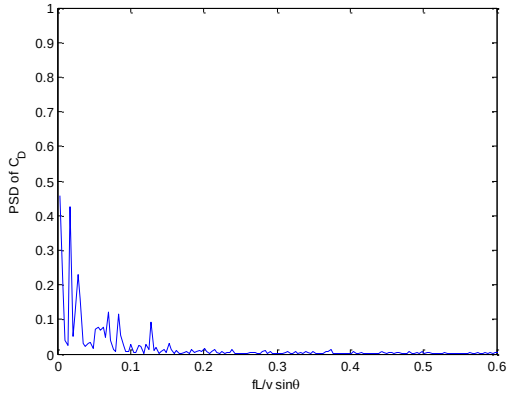
iii) Re = 3.3×10^5;



iv) Re = 4.4×10^5;



v) Re = 5.5×10^5;

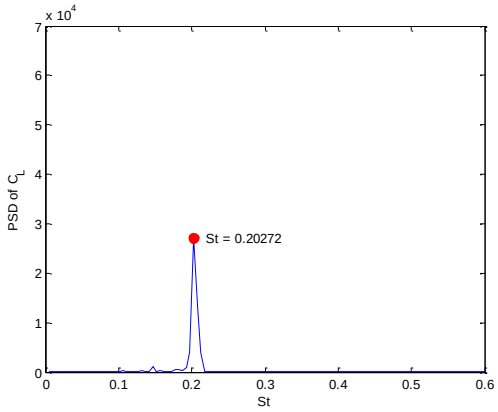


Appendix M: Fast Fourier Transform (FFT) Results for C_L

Figure M: FFT results C_L:

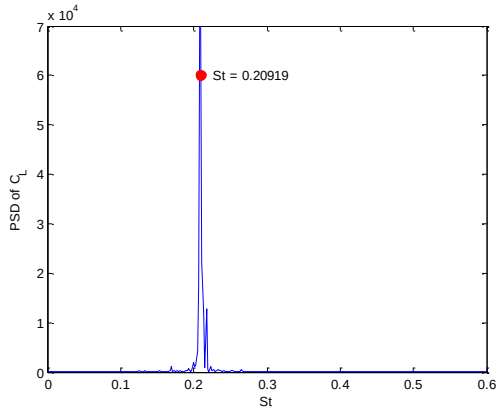
a) $\phi = 0°$; $\alpha = 0°$, $\beta = 0°$

i) Re = 1.1×10^5;



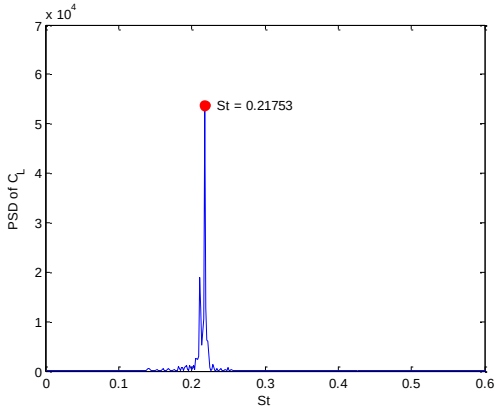
a) $\phi = 0°$; $\alpha = 0°$, $\beta = 0°$

ii) Re = 2.2×10^5;



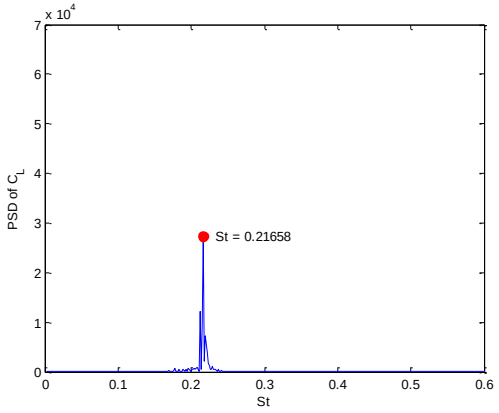
a) $\phi = 0°$; $\alpha = 0°$, $\beta = 0°$

iii) Re = 3.3×10^5;



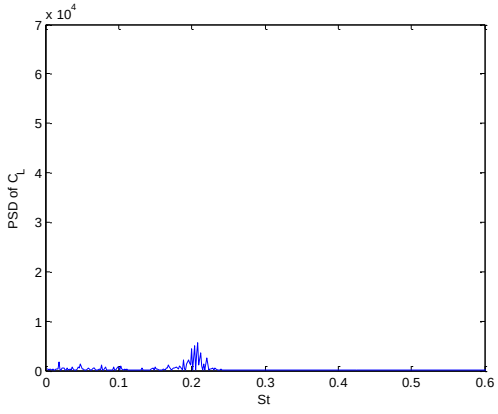
a) $\phi = 0°$; $\alpha = 0°$, $\beta = 0°$

iv) Re = 4.4×10^5;



a) $\phi = 0°$; $\alpha = 0°$, $\beta = 0°$

v) Re = 5.5×10^5;



a) $\phi = 0°$; $\alpha = 0°$, $\beta = 0°$

iv) Re = 6.7×10^5;

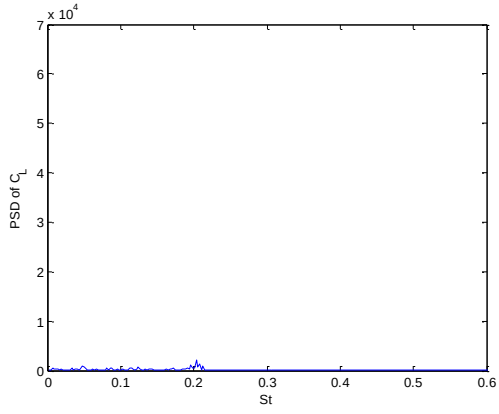
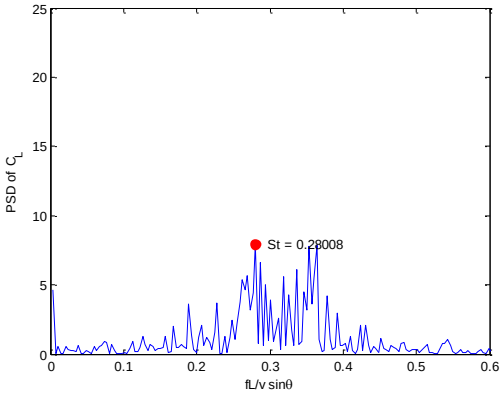
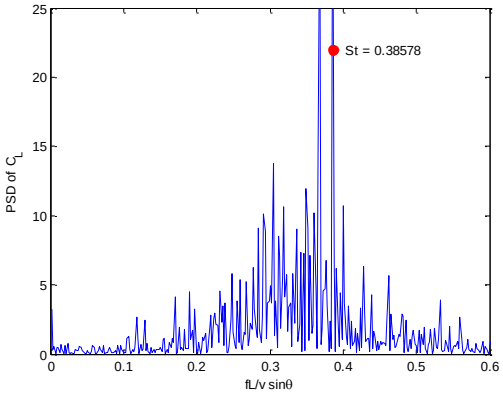


Figure M: FFT results C_L:

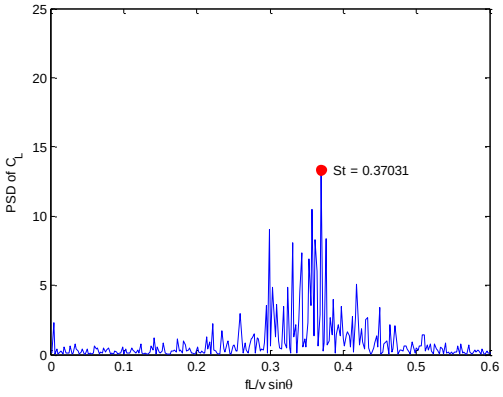
b) $\phi = 60°$; $\alpha = 60°$, $\beta = 0°$
i) Re = 1.1×10^5;



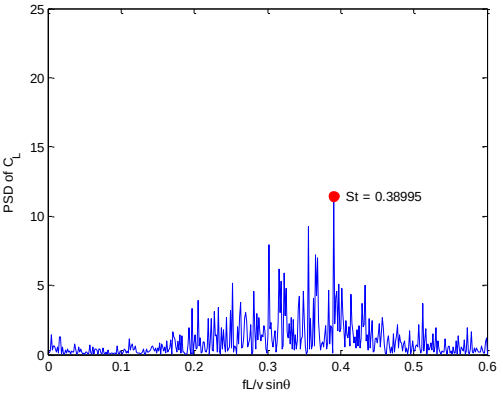
b) $\phi = 60°$; $\alpha = 60°$, $\beta = 0°$
ii) Re = 2.2×10^5;



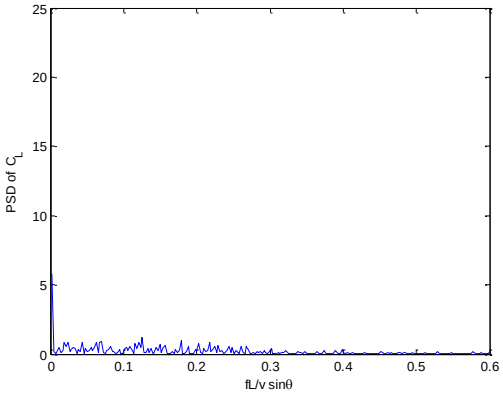
b) $\phi = 60°$; $\alpha = 60°$, $\beta = 0°$
iii) Re = 3.3×10^5;



b) $\phi = 60°$; $\alpha = 60°$, $\beta = 0°$
iv) Re = 4.4×10^5;



b) $\phi = 60°$; $\alpha = 60°$, $\beta = 0°$
v) Re = 5.5×10^5;



b) $\phi = 60°$; $\alpha = 60°$, $\beta = 0°$
vi) Re = 6.7×10^5;

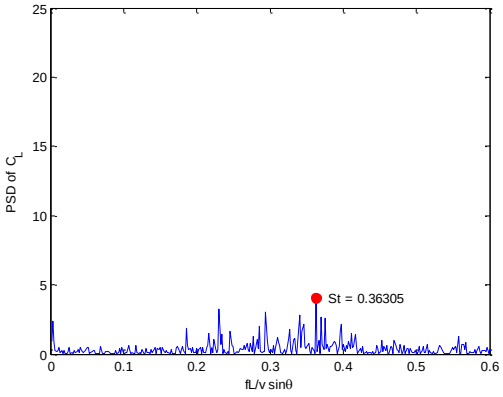
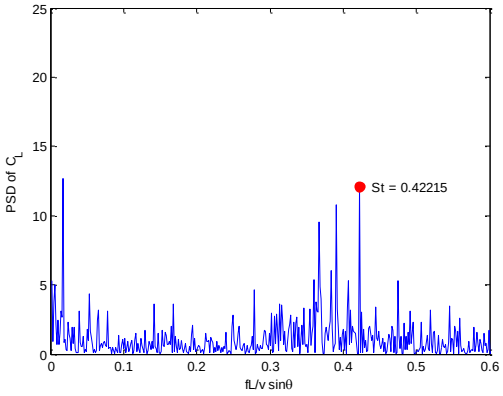
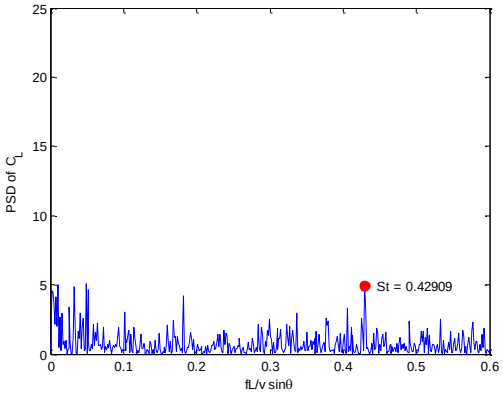


Figure M: FFT results C_L:

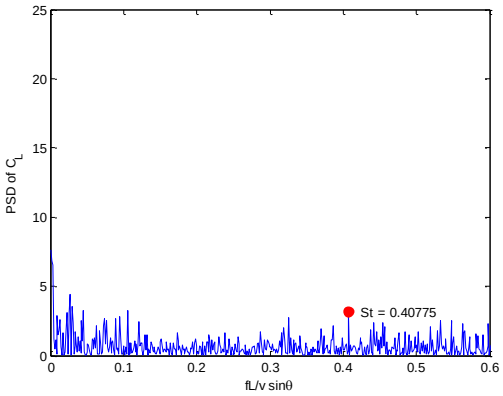
c) $\phi = 62°$; $\alpha = 60°$, $\beta = 20°$
i) Re = 1.1×10^5;



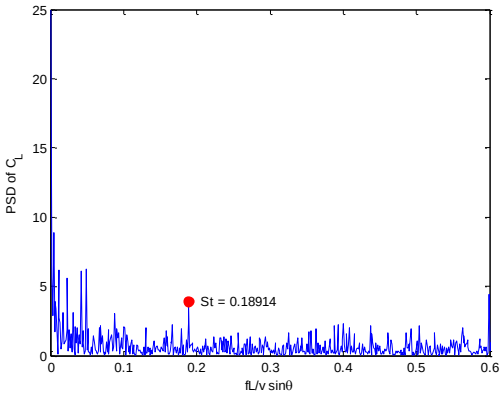
c) $\phi = 62°$; $\alpha = 60°$, $\beta = 20°$
ii) Re = 2.2×10^5;



c) $\phi = 62°$; $\alpha = 60°$, $\beta = 20°$
iii) Re = 3.3×10^5;



c) $\phi = 62°$; $\alpha = 60°$, $\beta = 20°$
iv) Re = 4.4×10^5;



c) $\phi = 62°$; $\alpha = 60°$, $\beta = 20°$
v) Re = 5.5×10^5;

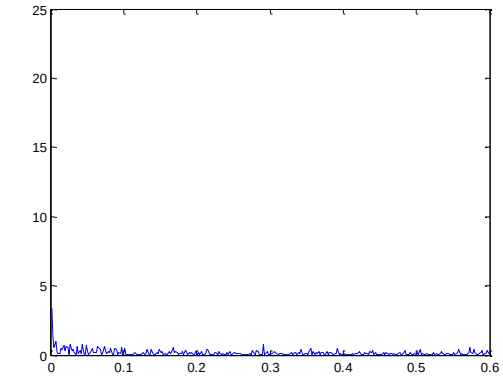
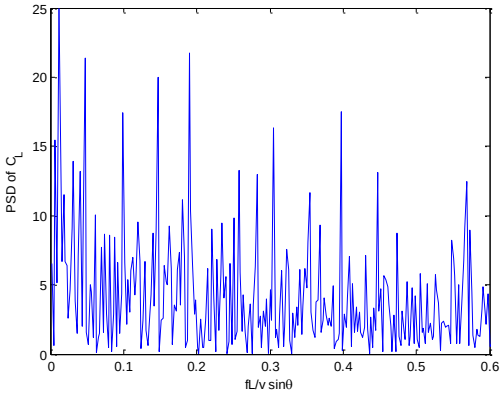
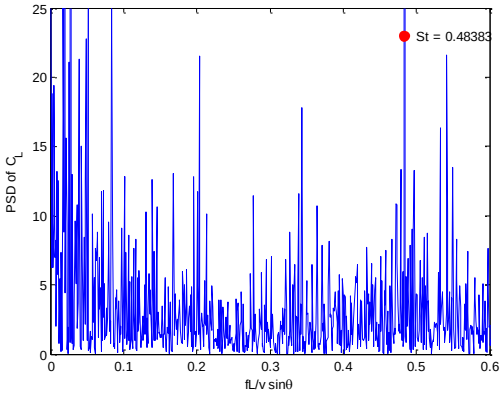


Figure M: FFT results C_L:

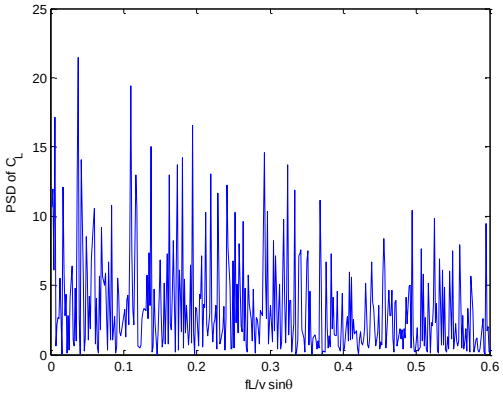
d) $\phi = 67.5°$; $\alpha = 60°$, $\beta = 40°$
i) Re = 1.1×10^5;



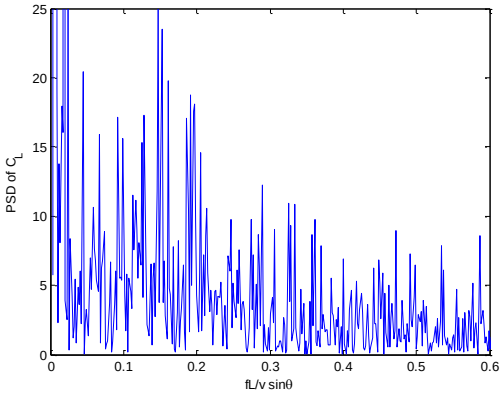
d) $\phi = 67.5°$; $\alpha = 60°$, $\beta = 40°$
ii) Re = 2.2×10^5;



d) $\phi = 67.5°$; $\alpha = 60°$, $\beta = 40°$
iii) Re = 3.3×10^5;



d) $\phi = 67.5°$; $\alpha = 60°$, $\beta = 40°$
iv) Re = 4.4×10^5;



d) $\phi = 67.5°$; $\alpha = 60°$, $\beta = 40°$
v) Re = 5.5×10^5;

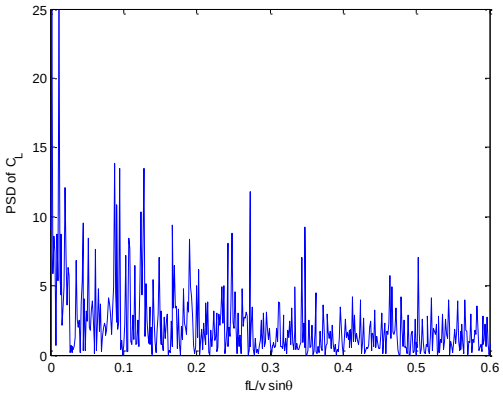
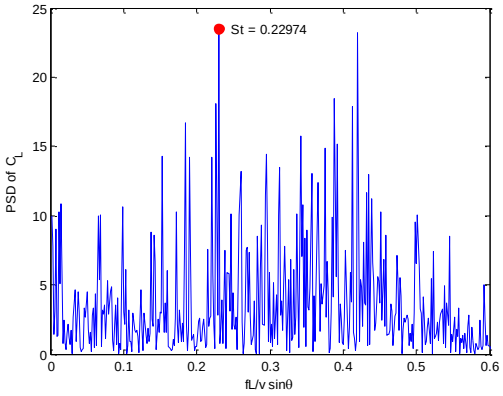
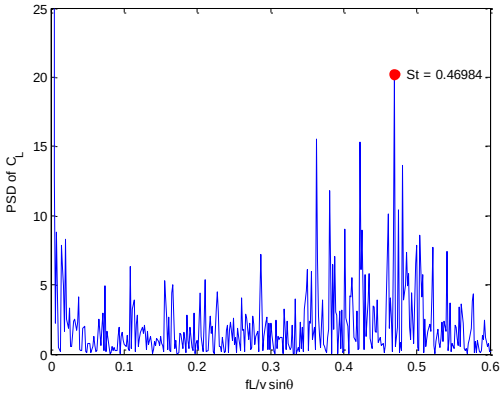


Figure M: FFT results C_L:

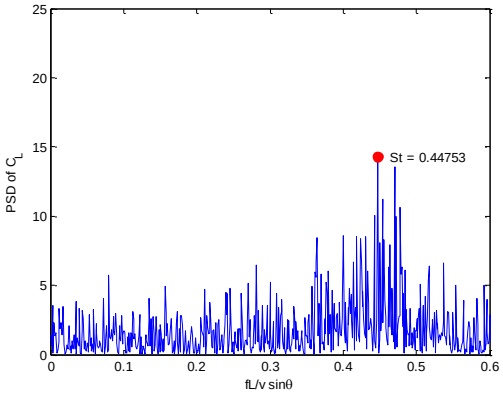
e) $\phi = 54.7°$; $\alpha = 54.7°$, $\beta = 0°$
i) Re = 1.1×10^5;



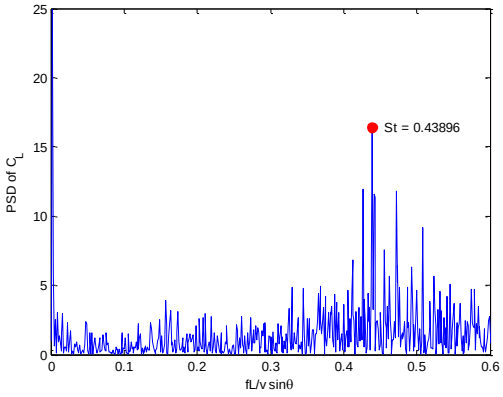
e) $\phi = 54.7°$; $\alpha = 54.7°$, $\beta = 0°$
ii) Re = 2.2×10^5;



e) $\phi = 54.7°$; $\alpha = 54.7°$, $\beta = 0°$
iii) Re = 3.3×10^5;



e) $\phi = 54.7°$; $\alpha = 54.7°$, $\beta = 0°$
iv) Re = 4.4×10^5;



e) $\phi = 54.7°$; $\alpha = 54.7°$, $\beta = 0°$
v) Re = 5.5×10^5;

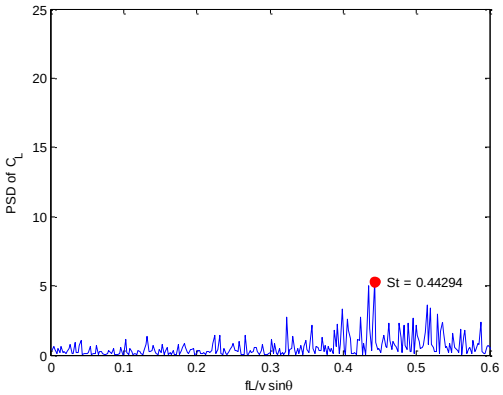
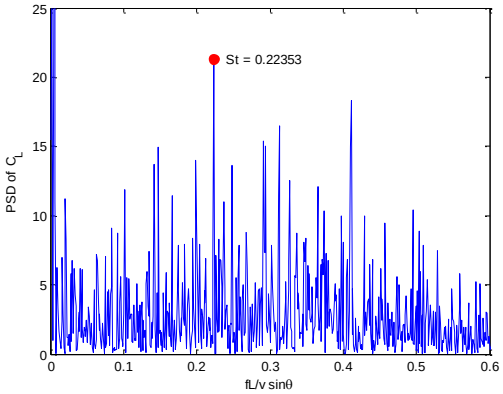
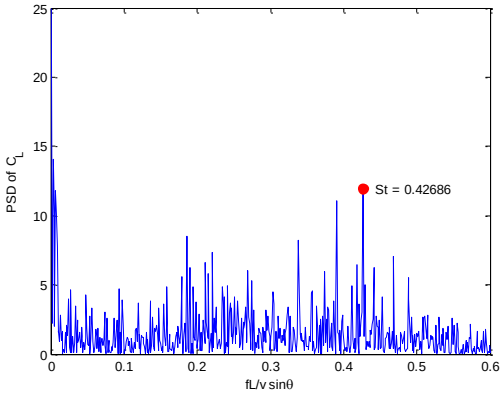


Figure M: FFT results C_L:

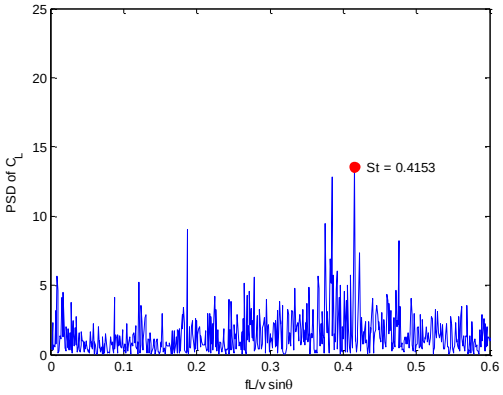
f) $\phi = 57.1°$; $\alpha = 54.7°$, $\beta = 20°$
i) Re = 1.1×10^5;



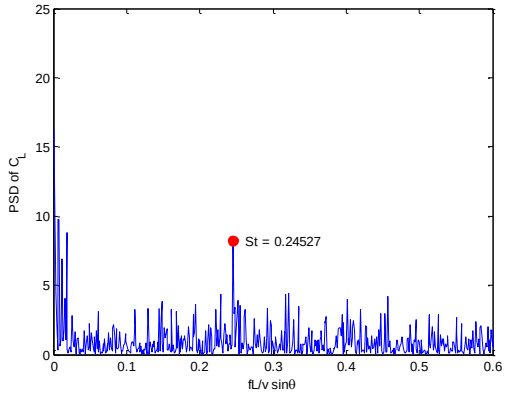
f) $\phi = 57.1°$; $\alpha = 54.7°$, $\beta = 20°$
ii) Re = 2.2×10^5;



f) $\phi = 57.1°$; $\alpha = 54.7°$, $\beta = 20°$
iii) Re = 3.3×10^5;



f) $\phi = 57.1°$; $\alpha = 54.7°$, $\beta = 20°$
iv) Re = 4.4×10^5;



f) $\phi = 57.1°$; $\alpha = 54.7°$, $\beta = 20°$
v) Re = 5.5×10^5;

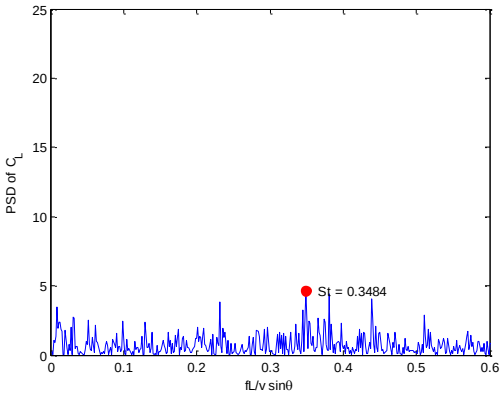
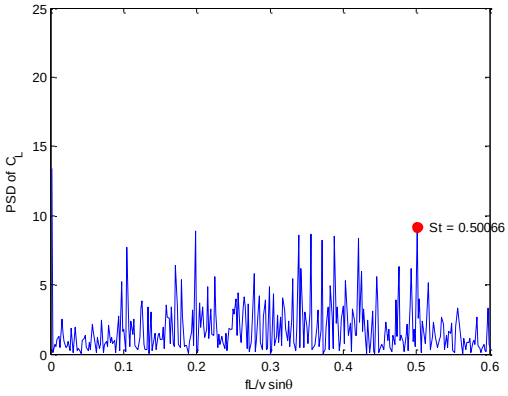
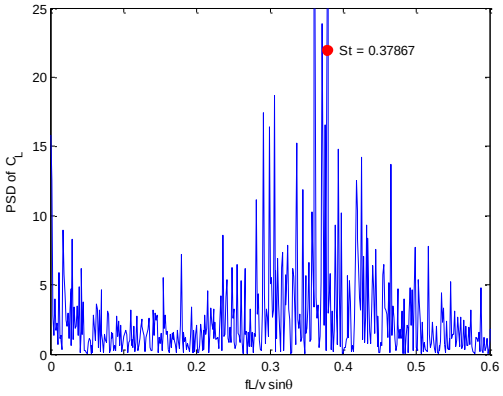


Figure M: FFT results C_L:

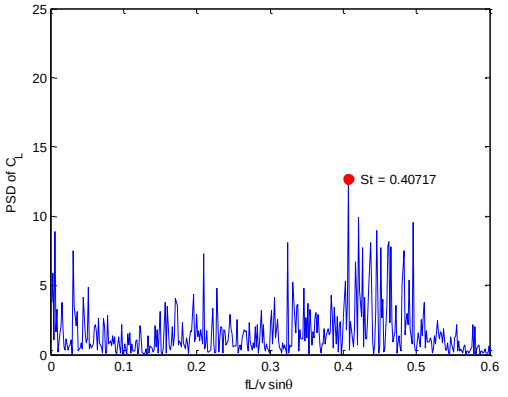
g) $\phi = 64.0°$; $\alpha = 54.7°$, $\beta = 40°$
i) Re = 1.1×10^5;



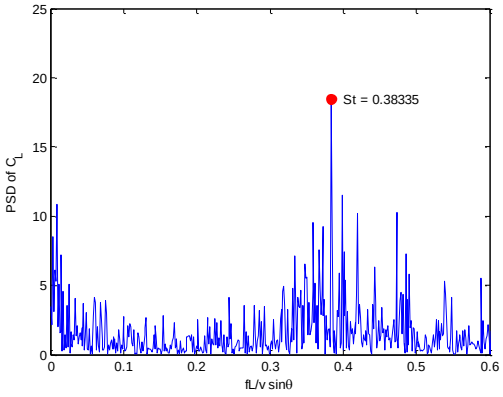
g) $\phi = 64.0°$; $\alpha = 54.7°$, $\beta = 40°$
ii) Re = 2.2×10^5;



g) $\phi = 64.0°$; $\alpha = 54.7°$, $\beta = 40°$
iii) Re = 3.3×10^5;



g) $\phi = 64.0°$; $\alpha = 54.7°$, $\beta = 40°$
iv) Re = 4.4×10^5;



g) $\phi = 64.0°$; $\alpha = 54.7°$, $\beta = 40°$
v) Re = 5.5×10^5;

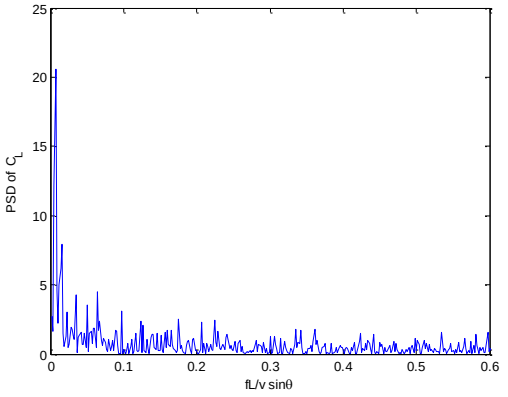
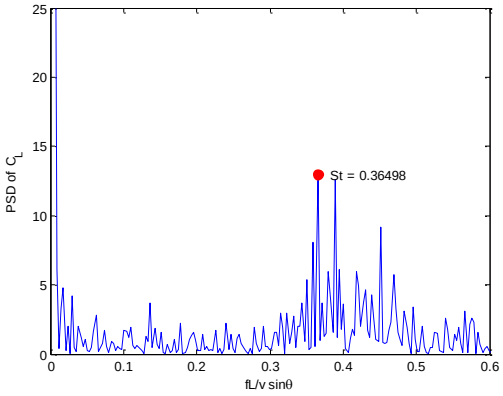
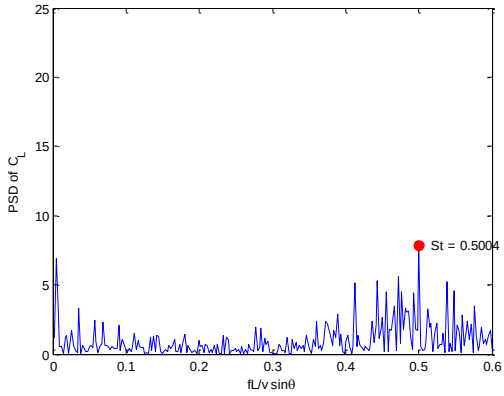


Figure M: FFT results C_L:

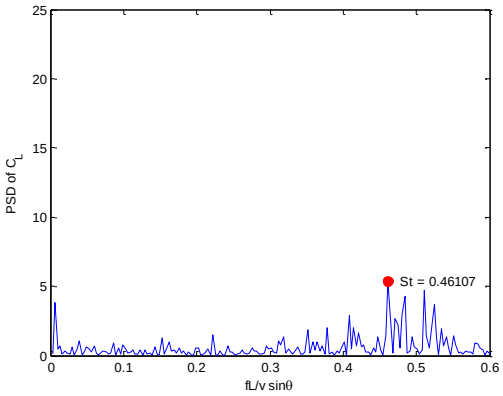
h) $\phi = 53.0°$; $\alpha = 50°$, $\beta = 20°$
i) Re = 1.1×10^5;



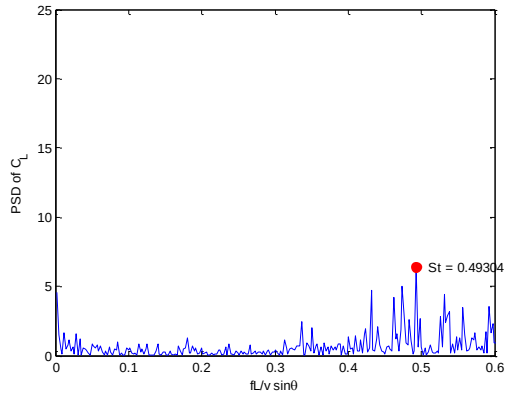
h) $\phi = 53.0°$; $\alpha = 50°$, $\beta = 20°$
ii) Re = 2.2×10^5;



h) $\phi = 53.0°$; $\alpha = 50°$, $\beta = 20°$
iii) Re = 3.3×10^5;



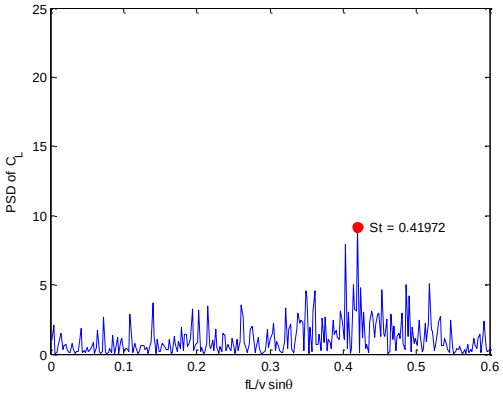
h) $\phi = 53.0°$; $\alpha = 50°$, $\beta = 20°$
iv) Re = 4.4×10^5;



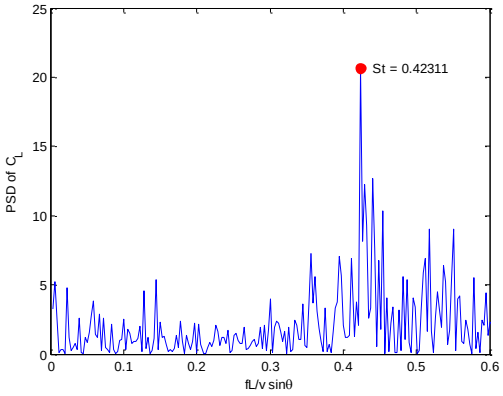
h) $\phi = 53.0°$; $\alpha = 50°$, $\beta = 20°$
v) Re = 5.5×10^5;

Figure M: FFT results C_L:

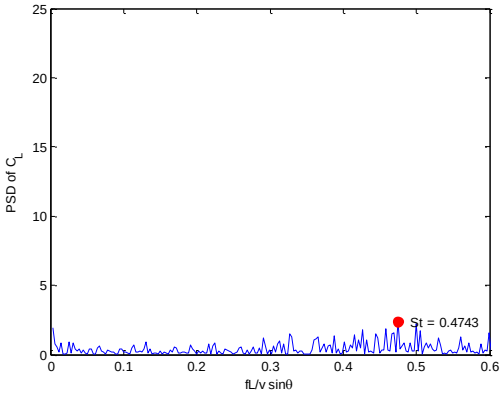
i) $\phi = 60.5°$; $\alpha = 50°$, $\beta = 40°$
i) Re = 1.1×10^5;



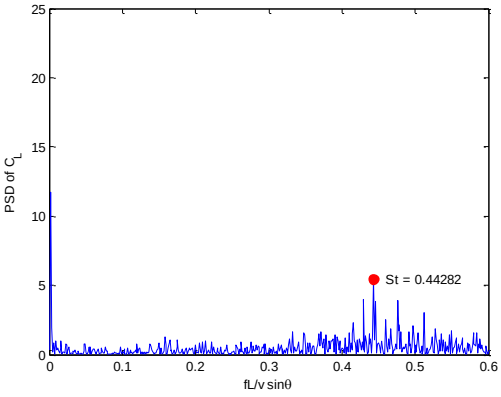
i) $\phi = 60.5°$; $\alpha = 50°$, $\beta = 40°$
ii) Re = 2.2×10^5;



i) $\phi = 60.5°$; $\alpha = 50°$, $\beta = 40°$
iii) Re = 3.3×10^5;



i) $\phi = 60.5°$; $\alpha = 50°$, $\beta = 40°$
iv) Re = 4.4×10^5;



i) $\phi = 60.5°$; $\alpha = 50°$, $\beta = 40°$
v) Re = 5.5×10^5;

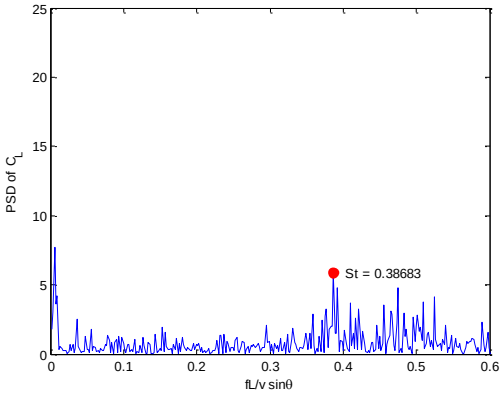
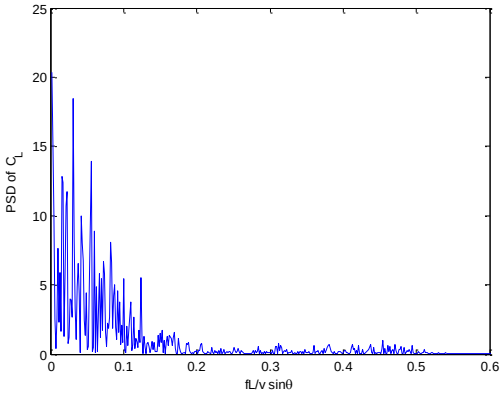


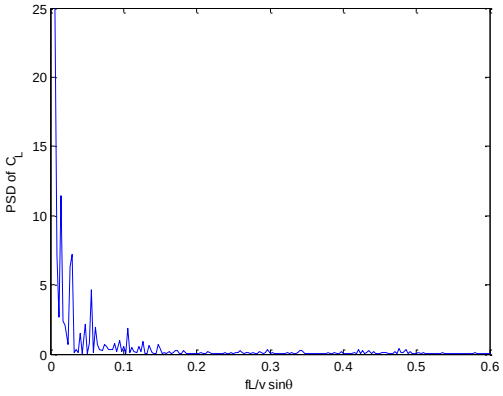
Figure M: FFT results C_L:

j) $\phi = 35.5°$; $\alpha = 30°$, $\beta = 30°$

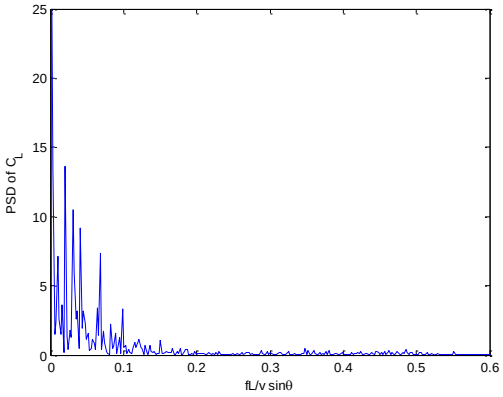
Re = 2.2×10^5;



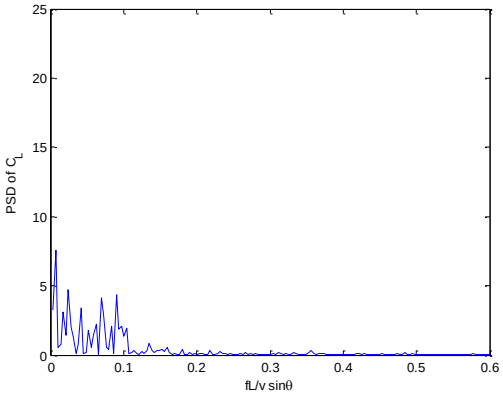
Re = 3.3×10^5;



Re = 4.4×10^5;



Re = 5.5×10^5;



Appendix N: Fast Fourier Transform (FFT) Results for Leeward Points

Figure N: FFT results Leeward Points:

a) $\phi = 0°$; $\alpha = 0°$, $\beta = 0°$

i) Re = 1.1×10^5;

Leeward

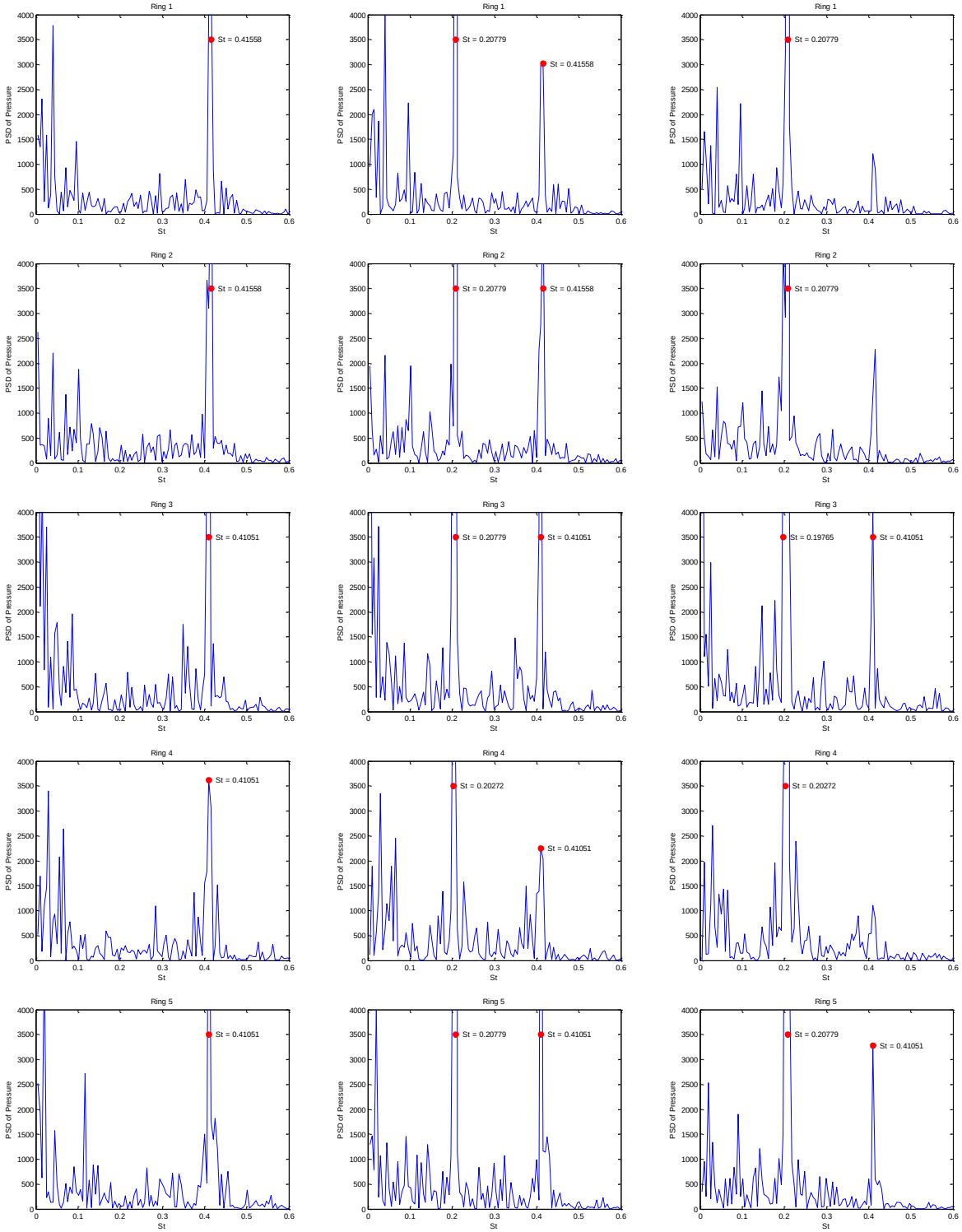


Figure N: FFT results Leeward Points:

a) $\phi = 0°$; $\alpha = 0°$, $\beta = 0°$

ii) Re = 2.2×10^5;

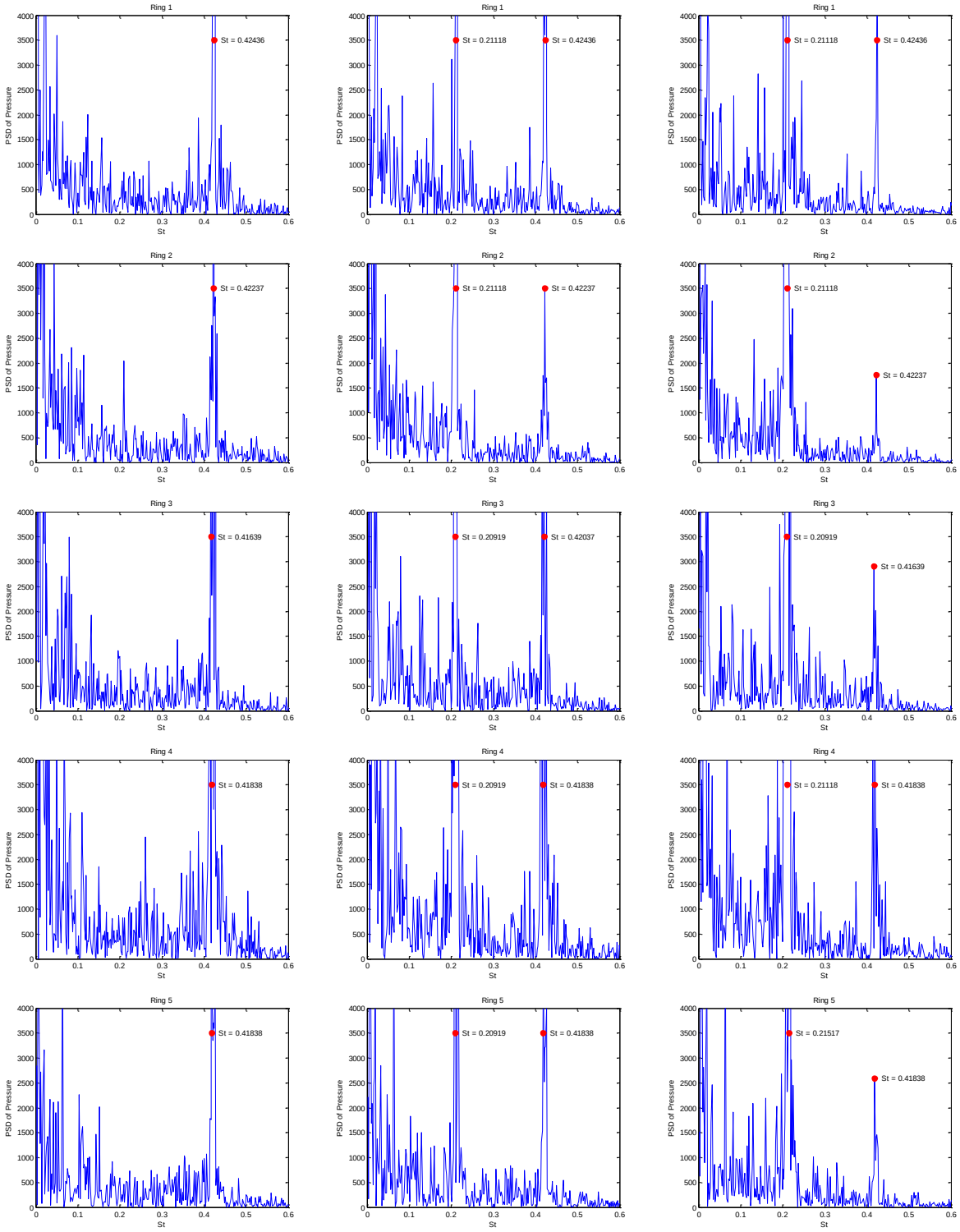


Figure N: FFT results Leeward Points:

a) $\phi = 0°$; $\alpha = 0°$, $\beta = 0°$

iii) Re = 3.3×10^5;

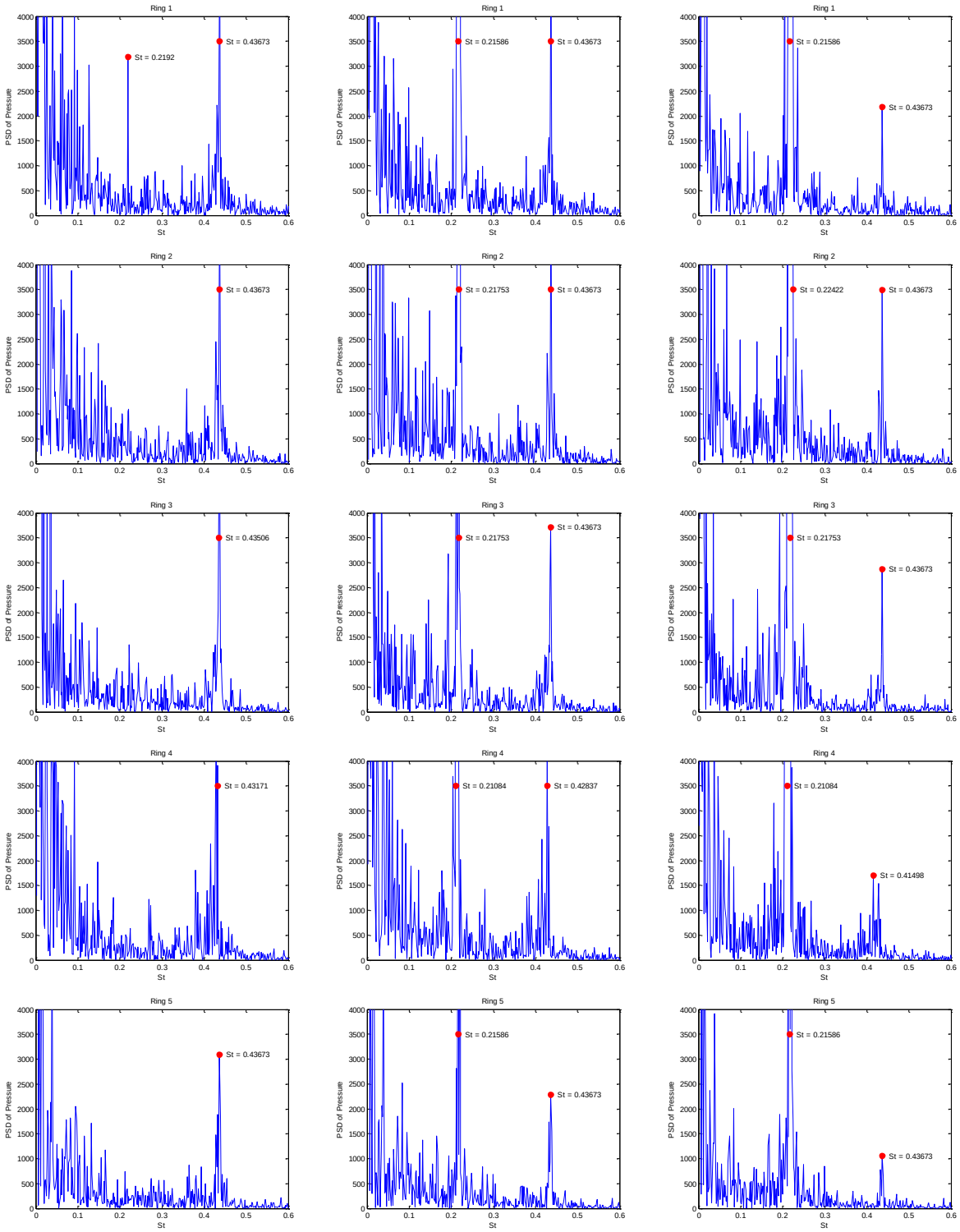


Figure N: FFT results Leeward Points:

a) $\phi = 0°$; $\alpha = 0°$, $\beta = 0°$

iv) Re = 4.4×10^5;

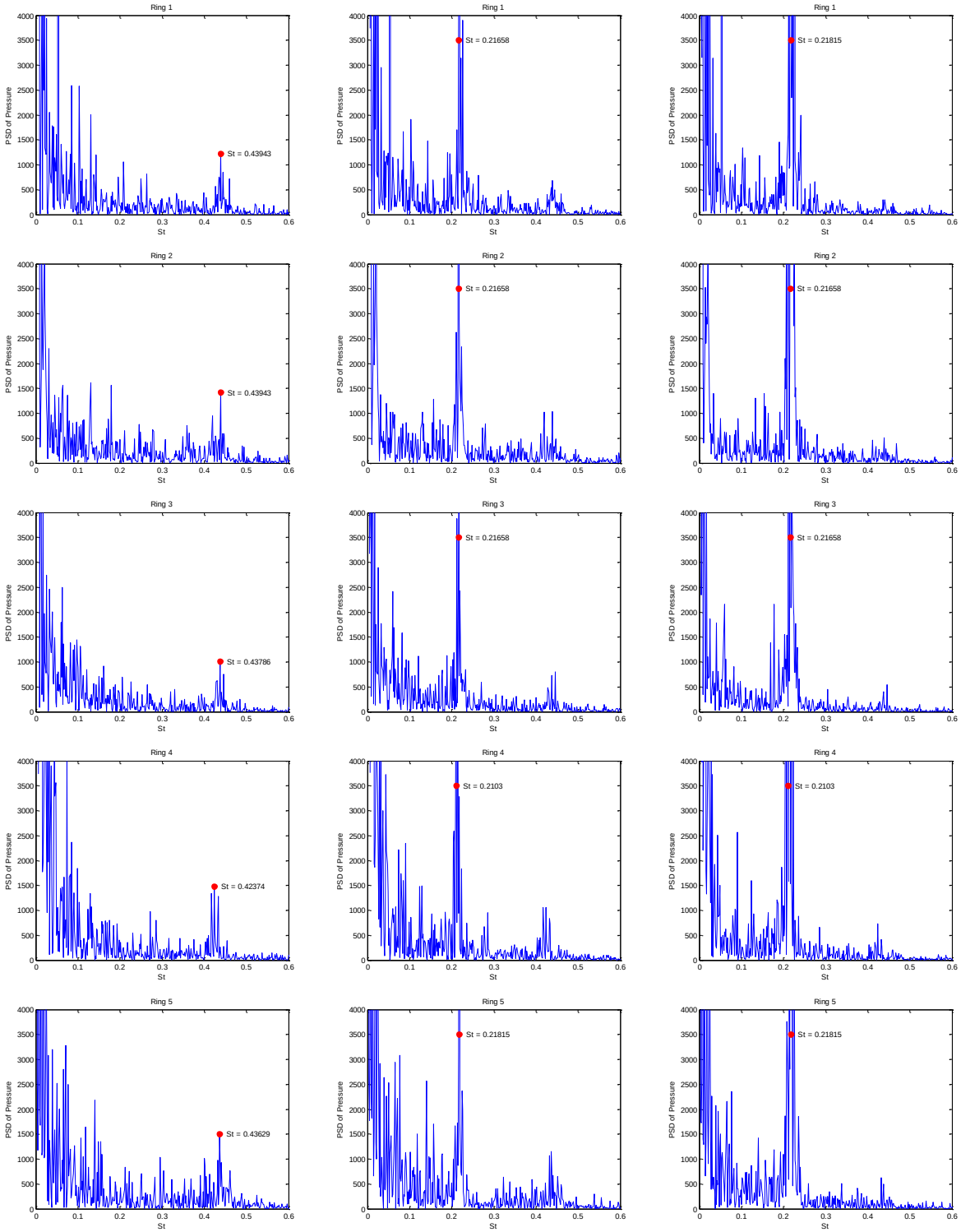


Figure N: FFT results Leeward Points:

a) $\phi = 0°$; $\alpha = 0°$, $\beta = 0°$

v) Re = 5.5×10^5;

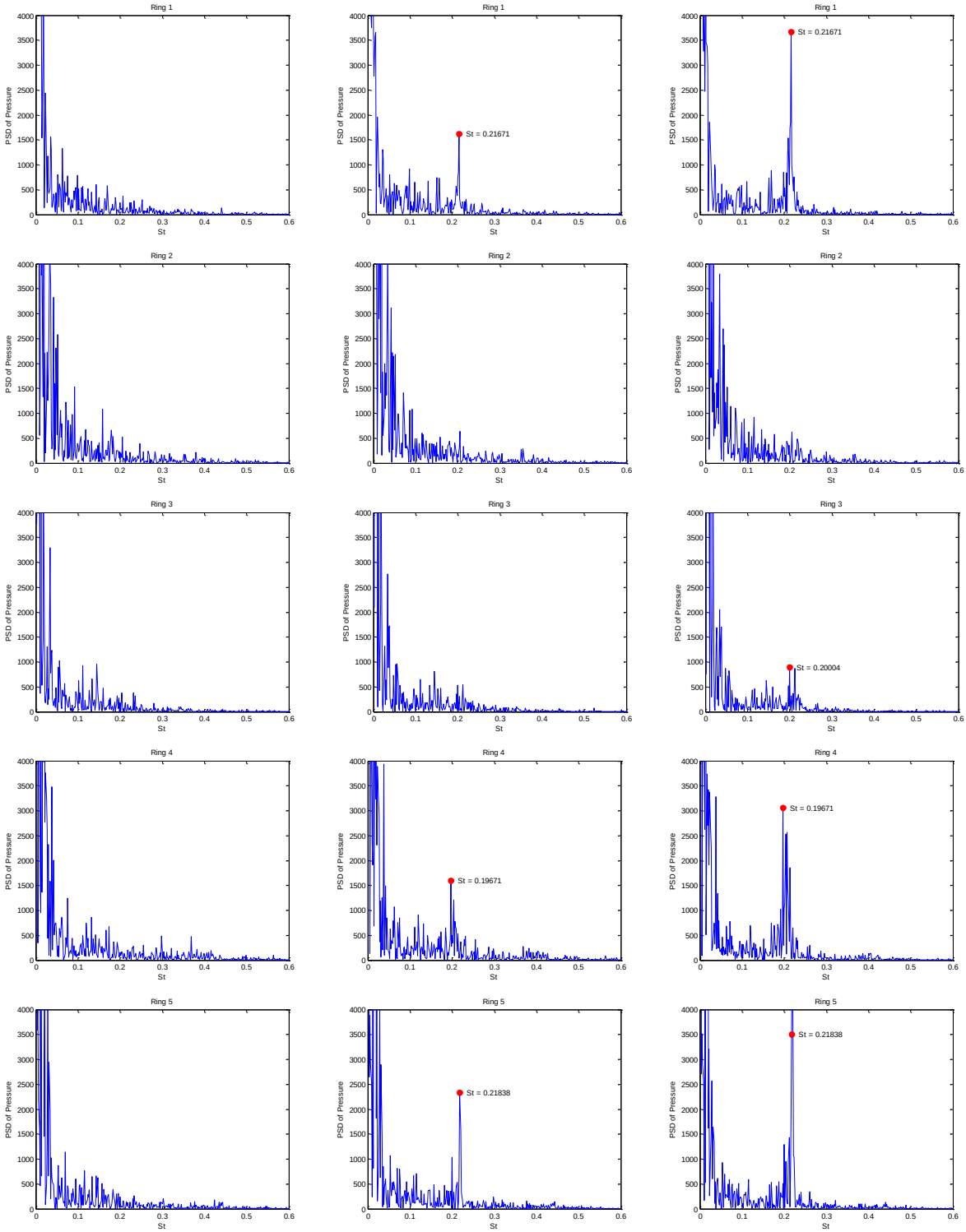


Figure N: FFT results Leeward Points:

a) $\phi = 0°$; $\alpha = 0°$, $\beta = 0°$

vi) Re = 6.7×10^5;

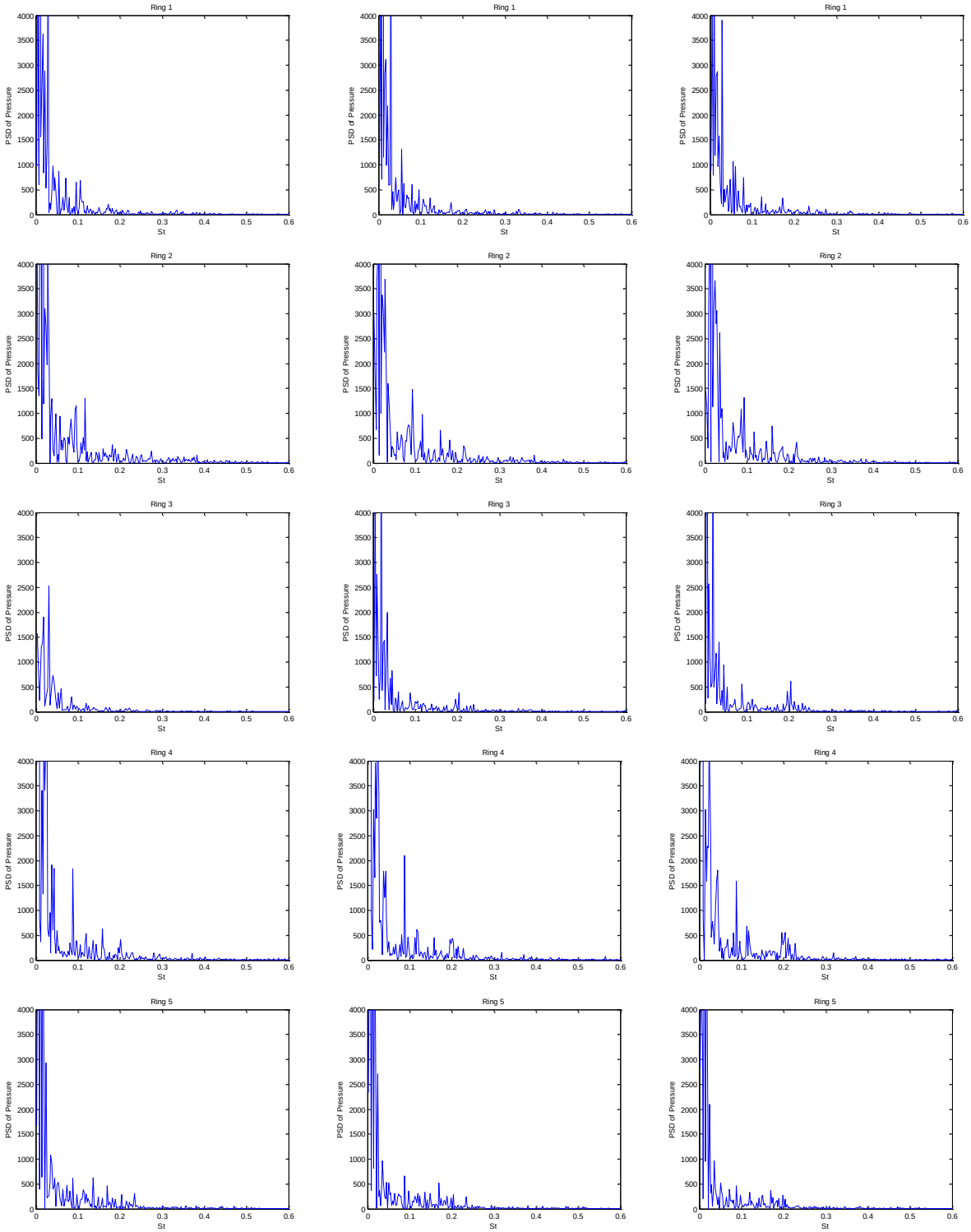


Figure N: FFT results Leeward Points:

b) $\phi = 60°$; $\alpha = 60°$, $\beta = 0°$

i) Re = 1.1×10^5;

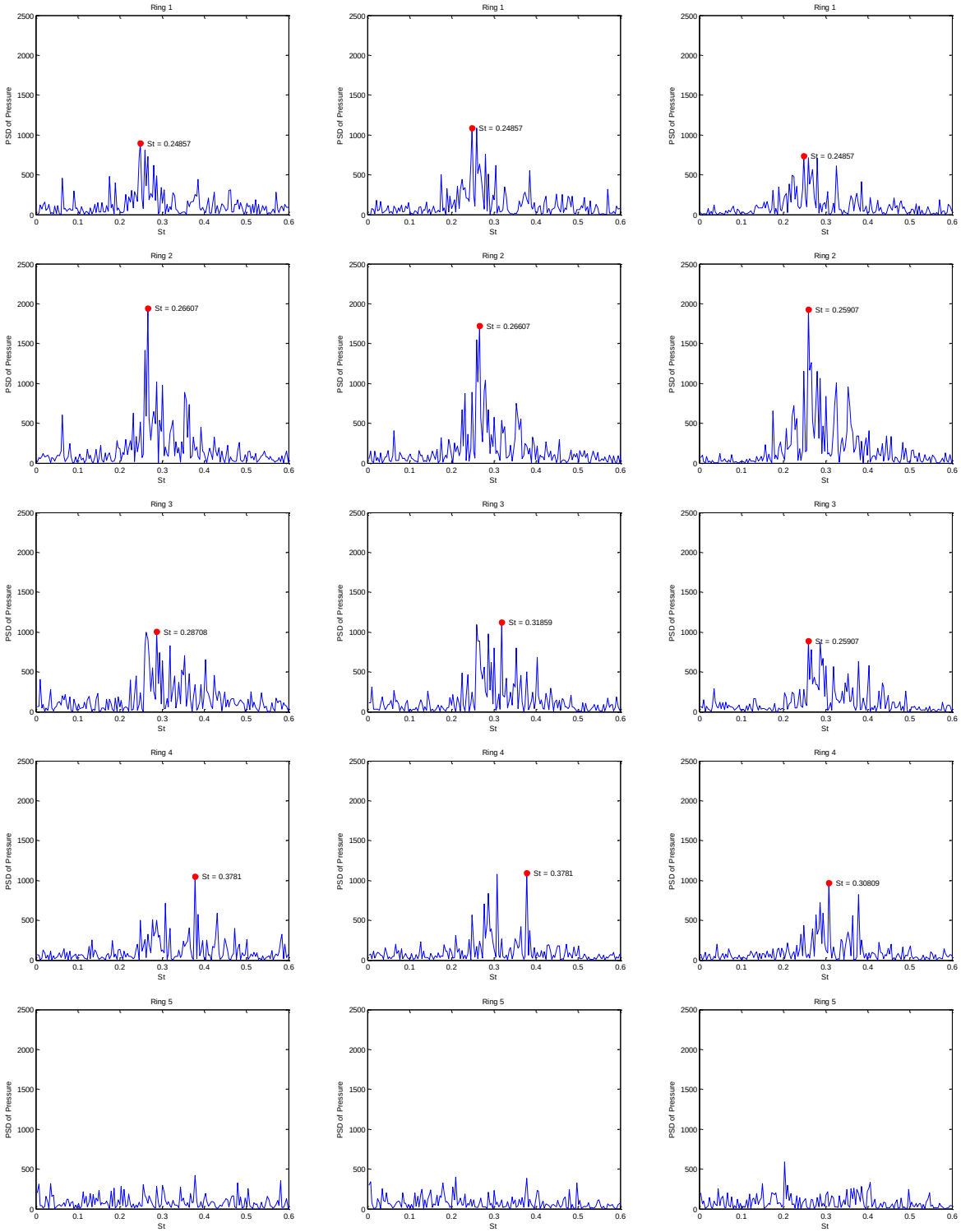


Figure N: FFT results Leeward Points:

b) $\phi = 60°$; $\alpha = 60°$, $\beta = 0°$

ii) Re = 2.2×10^5;

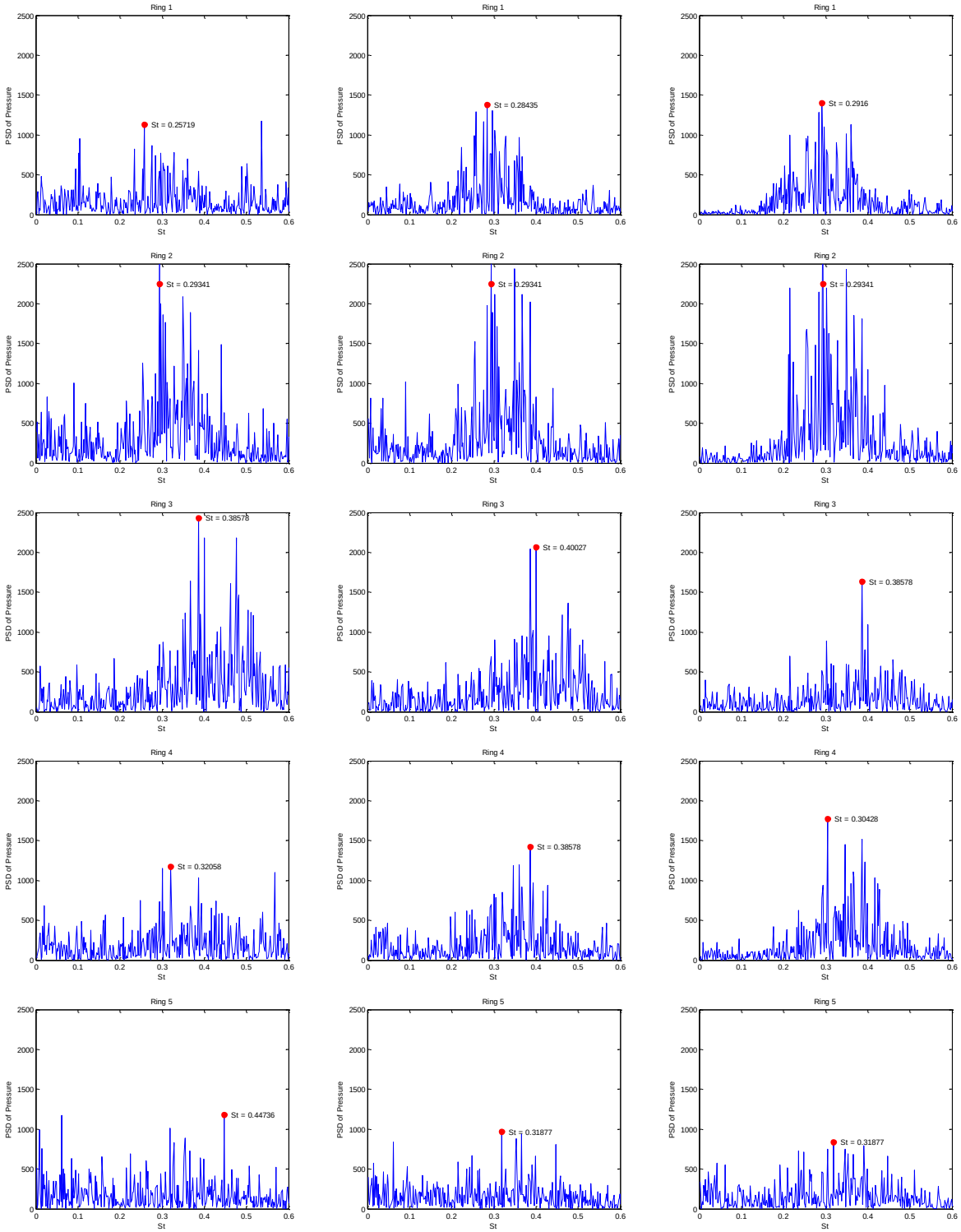


Figure N: FFT results Leeward Points:

b) $\phi = 60°$; $\alpha = 60°$, $\beta = 0°$

iii) Re = 3.3×10^5;

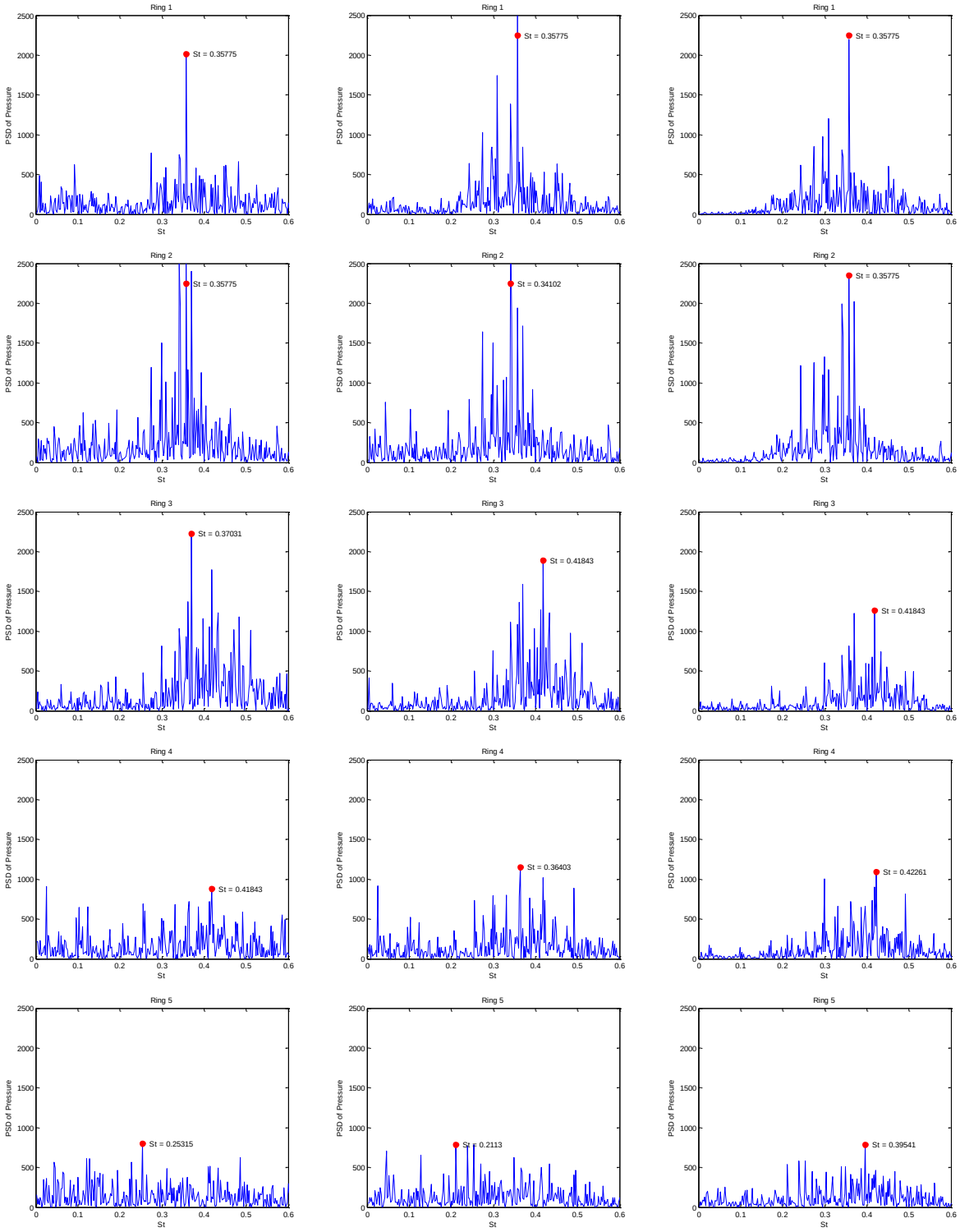


Figure N: FFT results Leeward Points:

b) $\phi = 60°$; $\alpha = 60°$, $\beta = 0°$

iv) Re = 4.4×10^5;

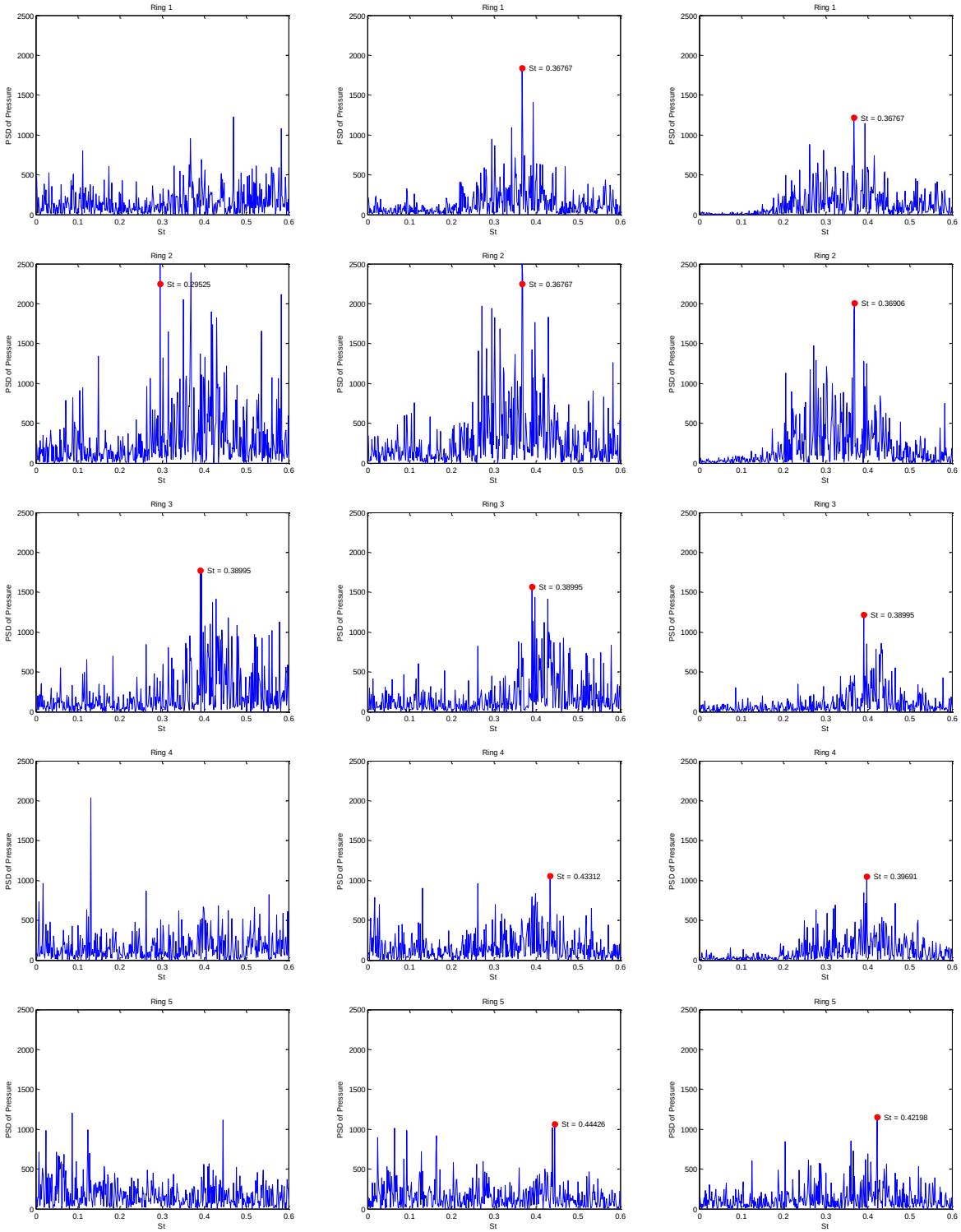


Figure N: FFT results Leeward Points:

b) $\phi = 60°$; $\alpha = 60°$, $\beta = 0°$

v) Re = 5.5×10^5;

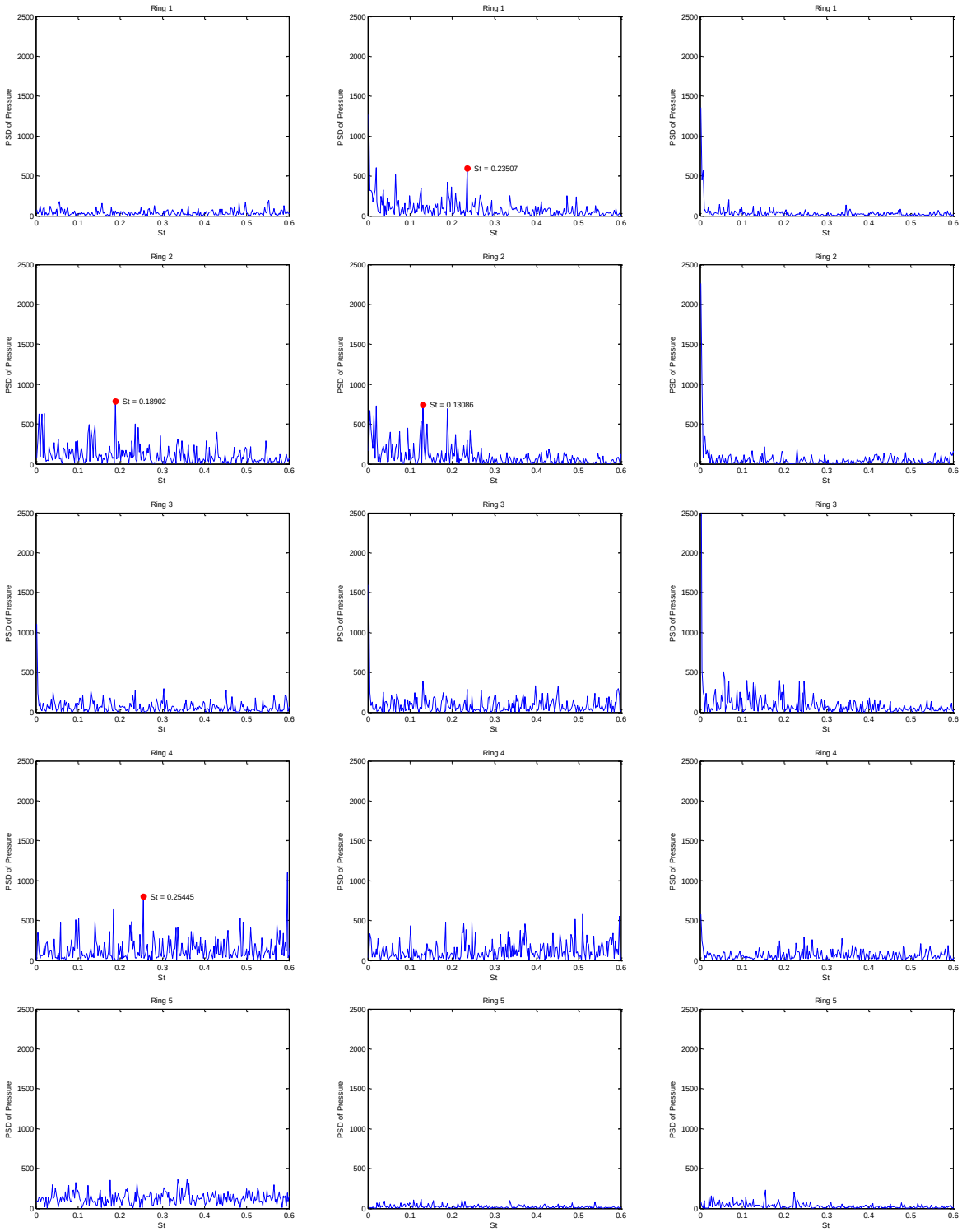


Figure N: FFT results Leeward Points:

b) $\phi = 60°$; $\alpha = 60°$, $\beta = 0°$

vi) Re = 6.7×10^5;

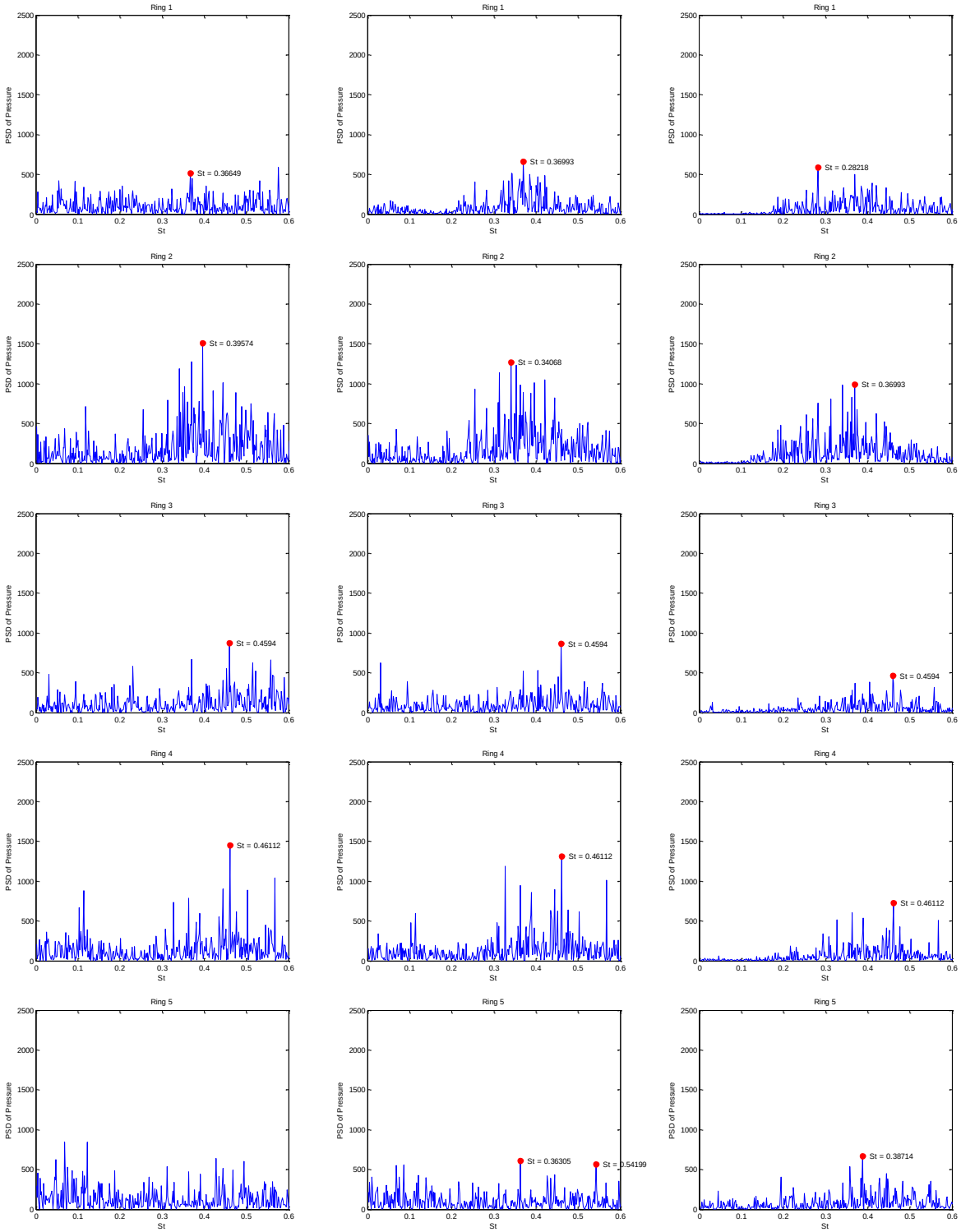


Figure N: FFT results Leeward Points:

c) $\phi = 62°$; $\alpha = 60°$, $\beta = 20°$

i) Re = 1.1×10^5;

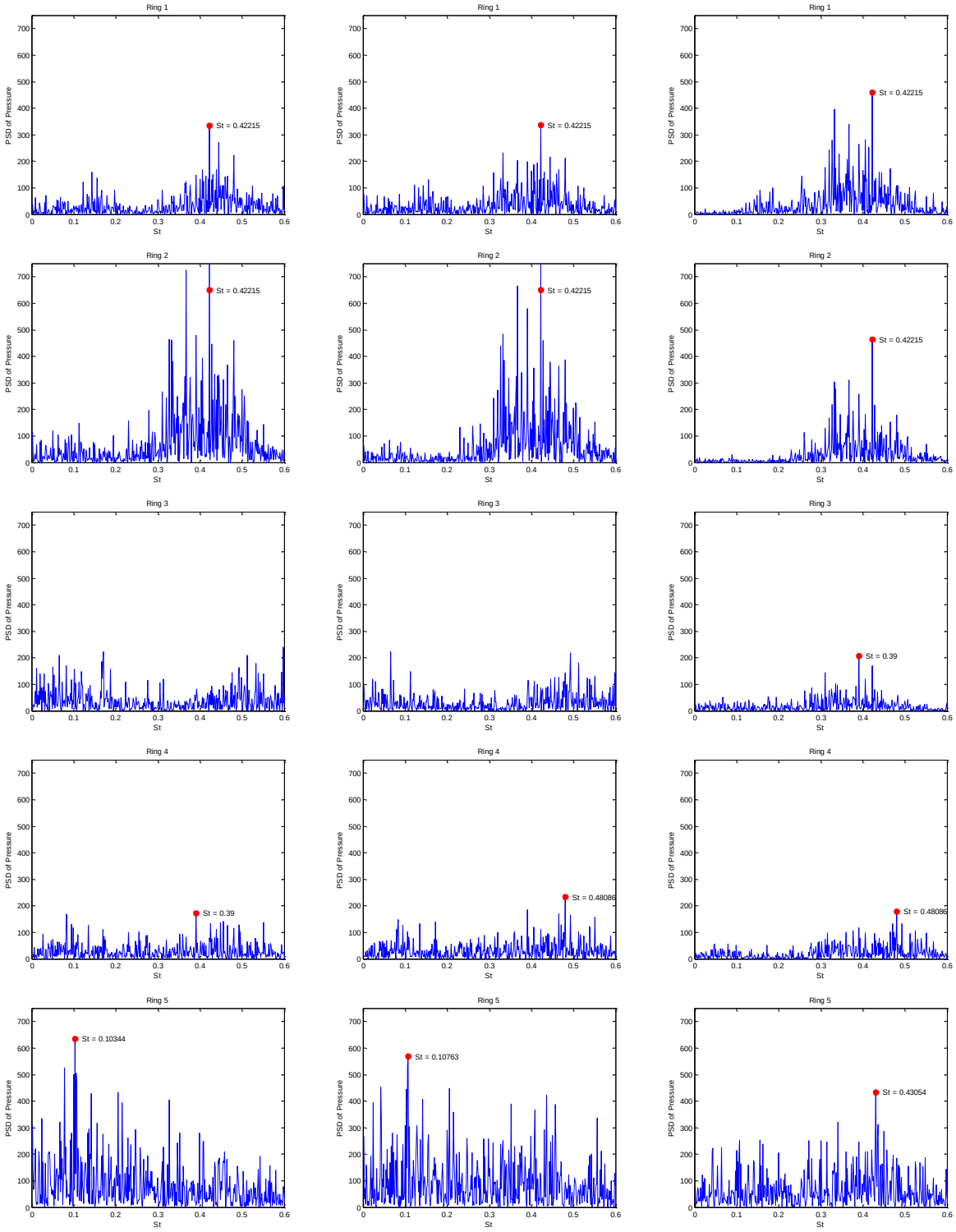


Figure N: FFT results Leeward Points:

c) $\phi = 62°$; $\alpha = 60°$, $\beta = 20°$

ii) Re = 2.2×10^5;

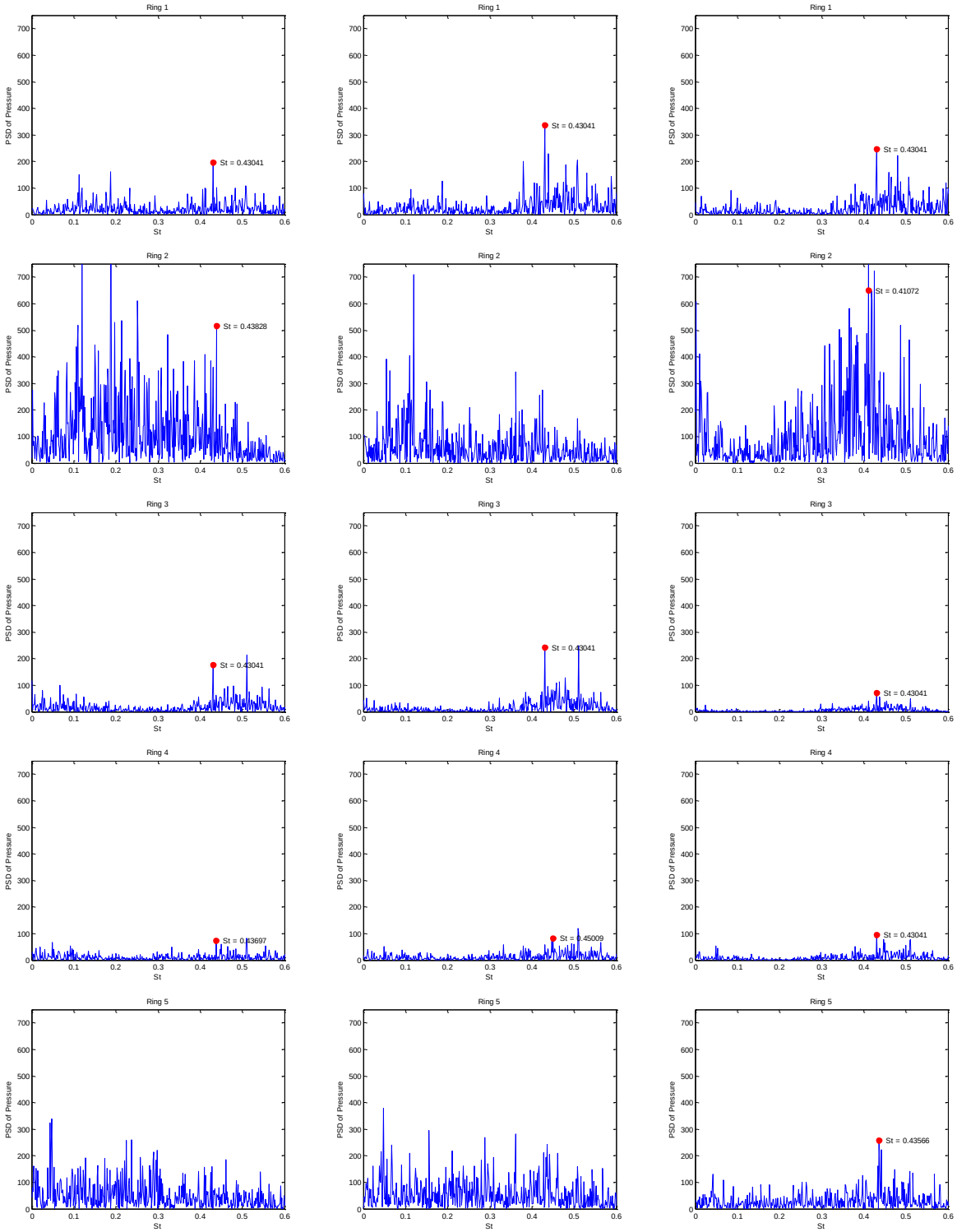


Figure N: FFT results Leeward Points:

c) $\phi = 62°$; $\alpha = 60°$, $\beta = 20°$

iii) Re = 3.3×10^5;

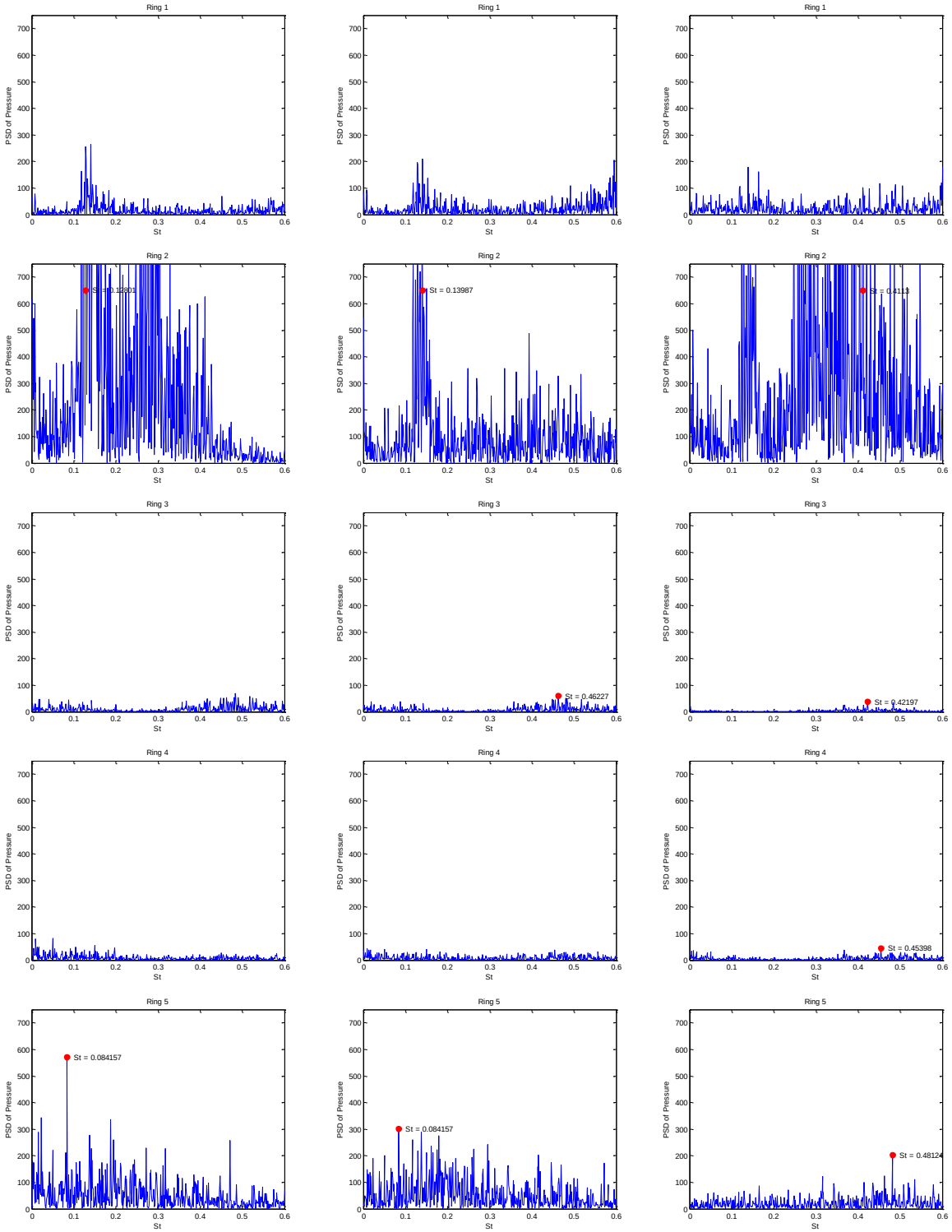


Figure N: FFT results Leeward Points:

c) $\phi = 62°$; $\alpha = 60°$, $\beta = 20°$

iv) Re = 4.4×10^5;

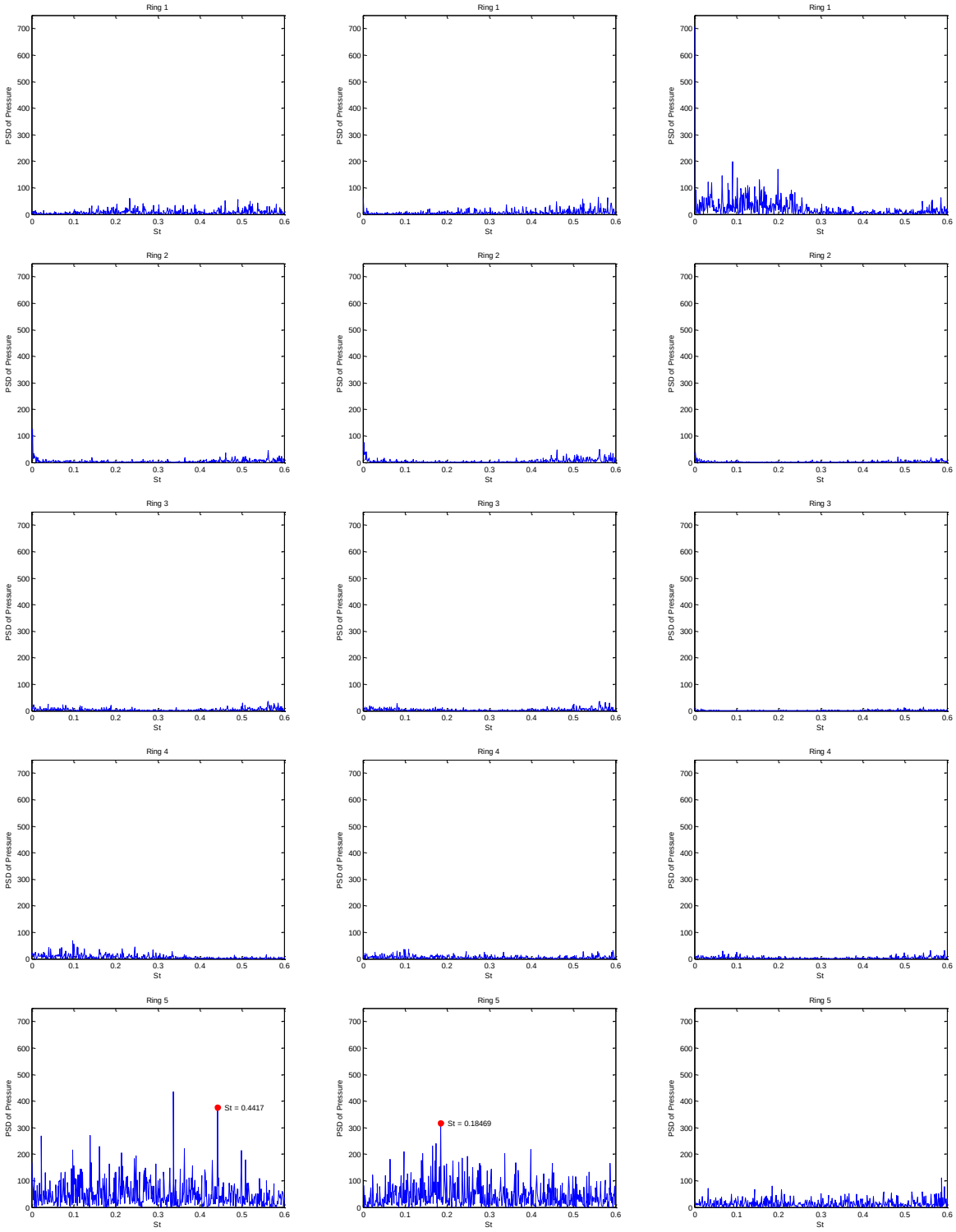


Figure N: FFT results Leeward Points:

c) $\phi = 62°$; $\alpha = 60°$, $\beta = 20°$

v) Re = 5.5×10^5;

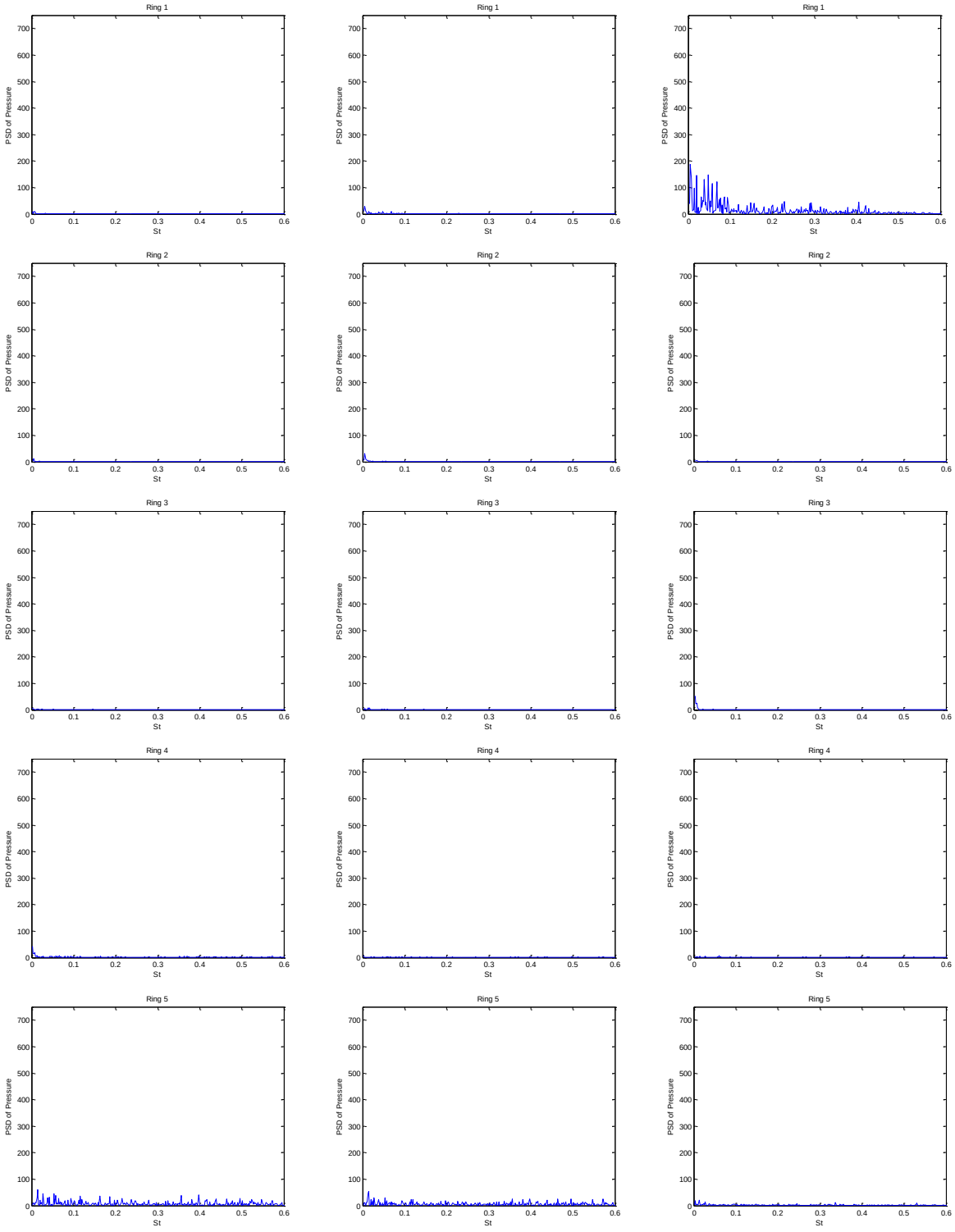


Figure N: FFT results Leeward Points:

d) $\phi = 67.5°$; $\alpha = 60°$, $\beta = 40°$

i) Re = 1.1×10^5;

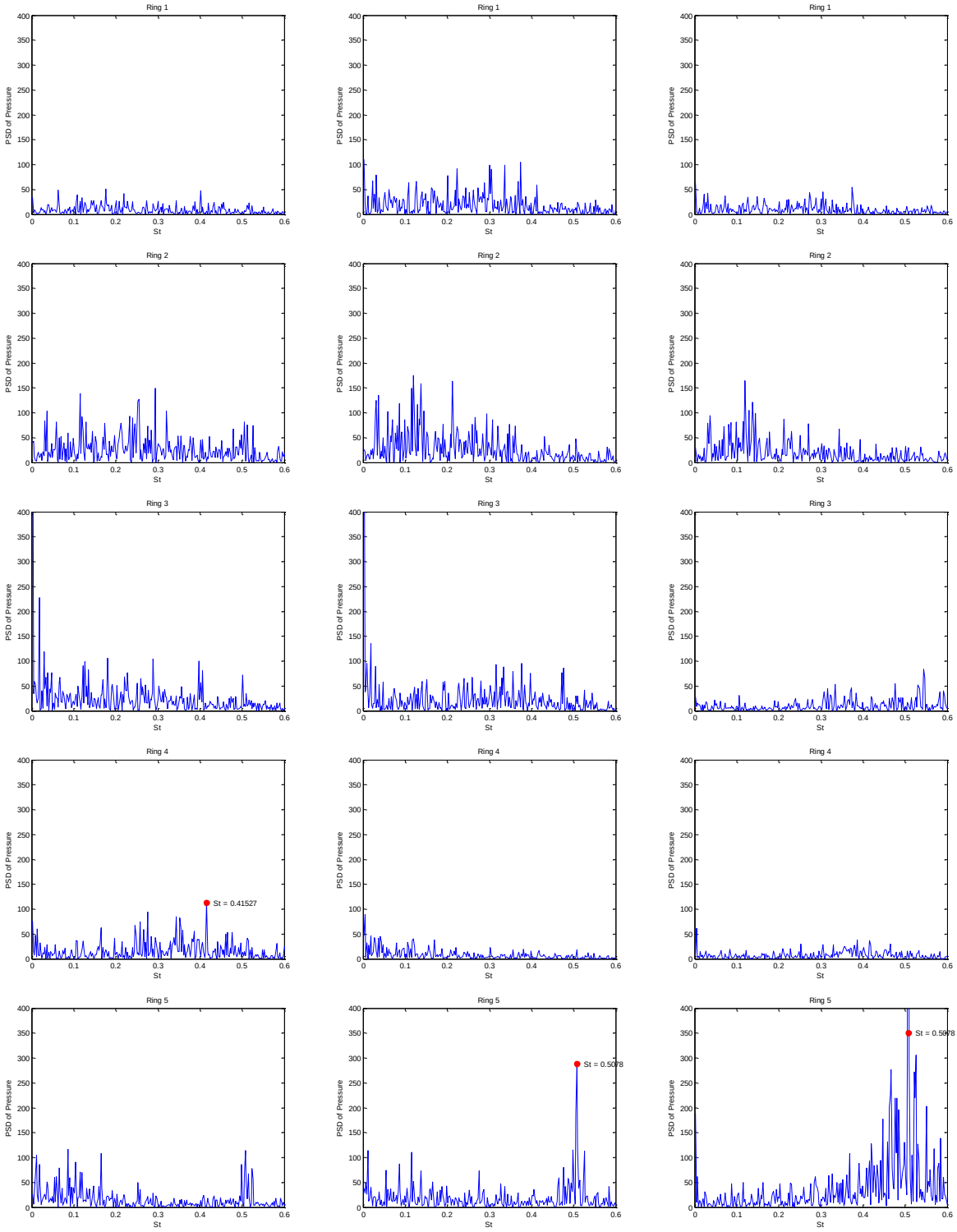


Figure N: FFT results Leeward Points:

d) $\phi = 67.5°$; $\alpha = 60°$, $\beta = 40°$

ii) Re = 2.2×10^5;

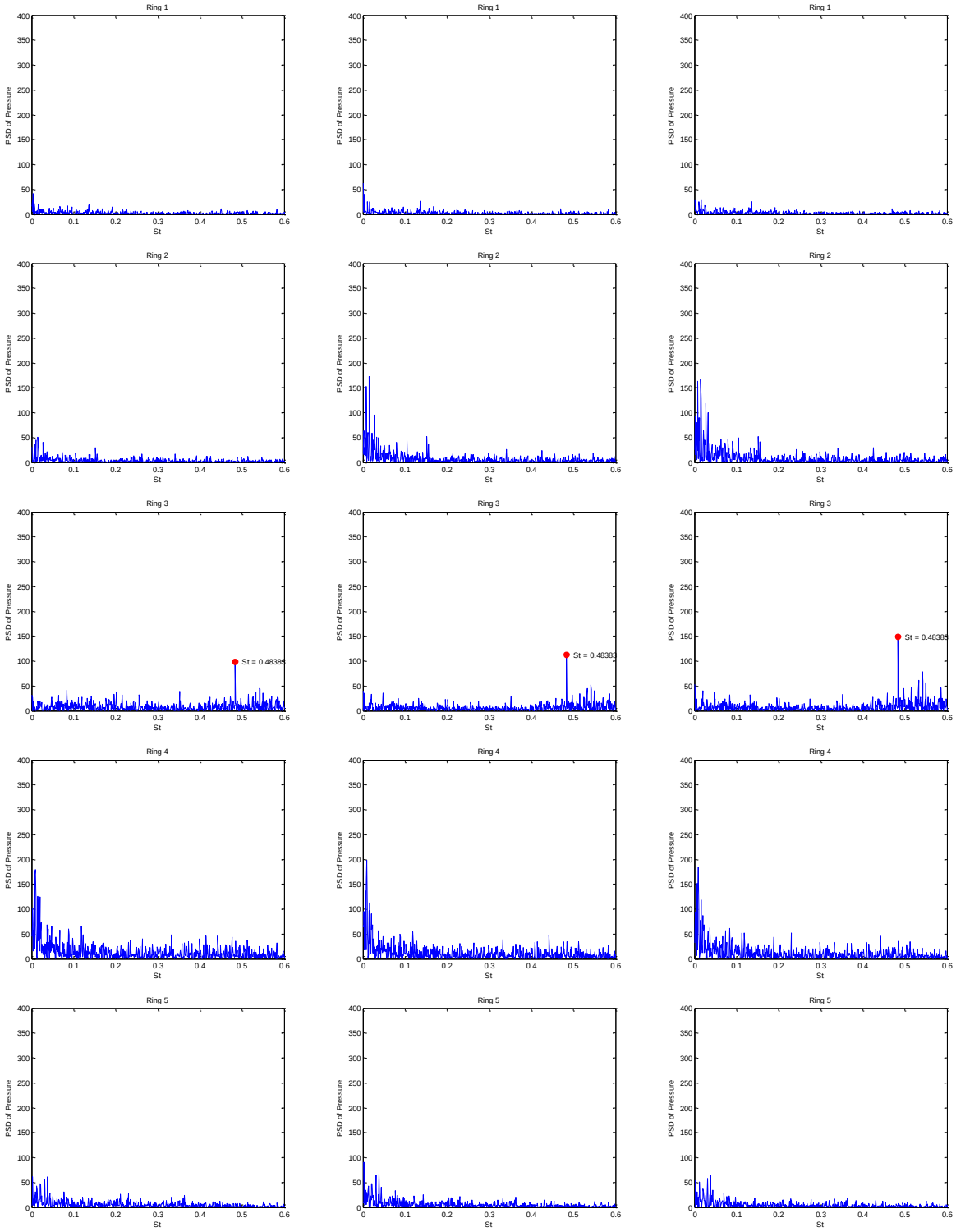


Figure N: FFT results Leeward Points:

d) $\phi = 67.5°$; $\alpha = 60°$, $\beta = 40°$

iii) Re = 3.3×10^5;

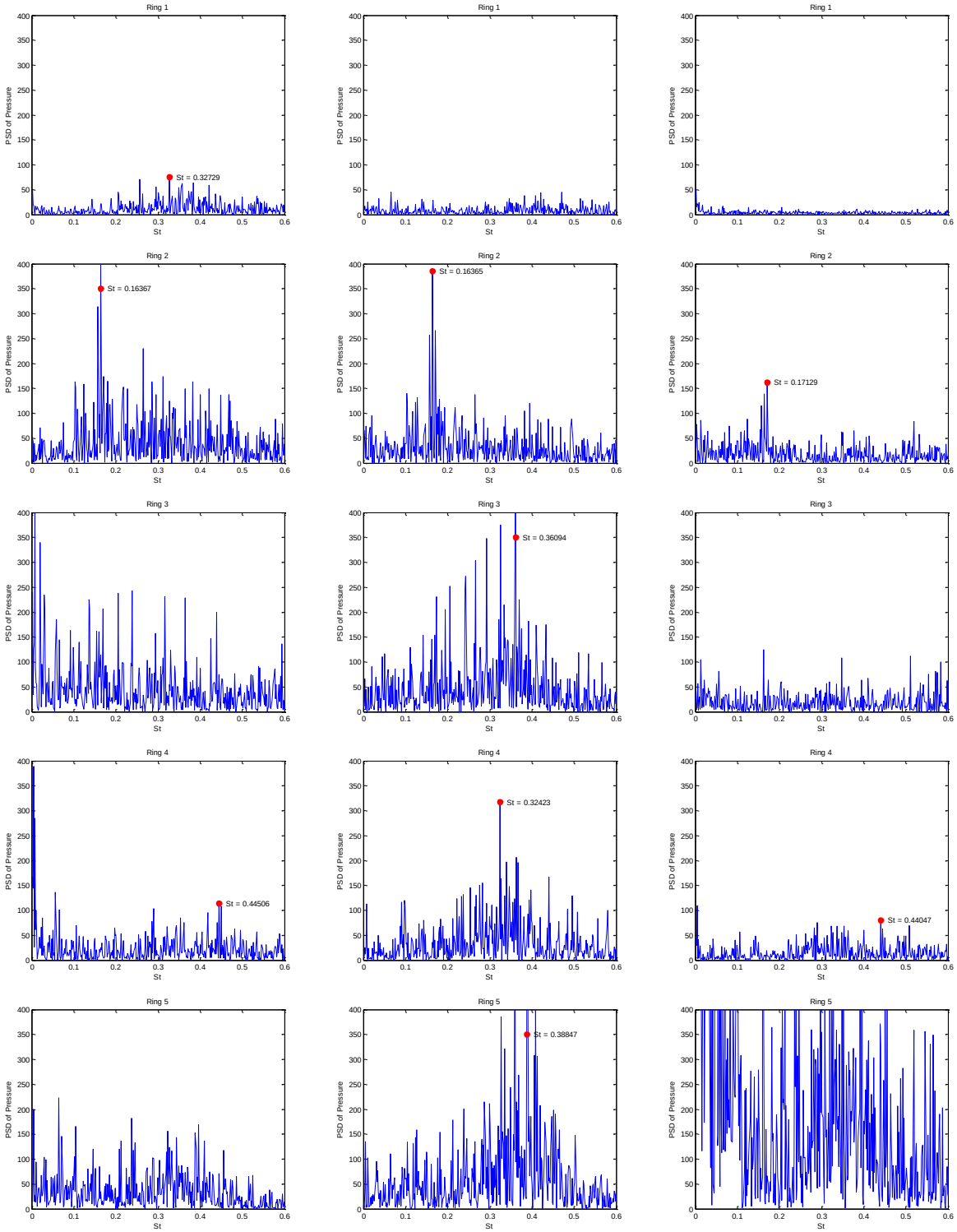


Figure N: FFT results Leeward Points:

d) $\phi = 67.5°$; $\alpha = 60°$, $\beta = 40°$

iv) Re = 4.4×10^5;

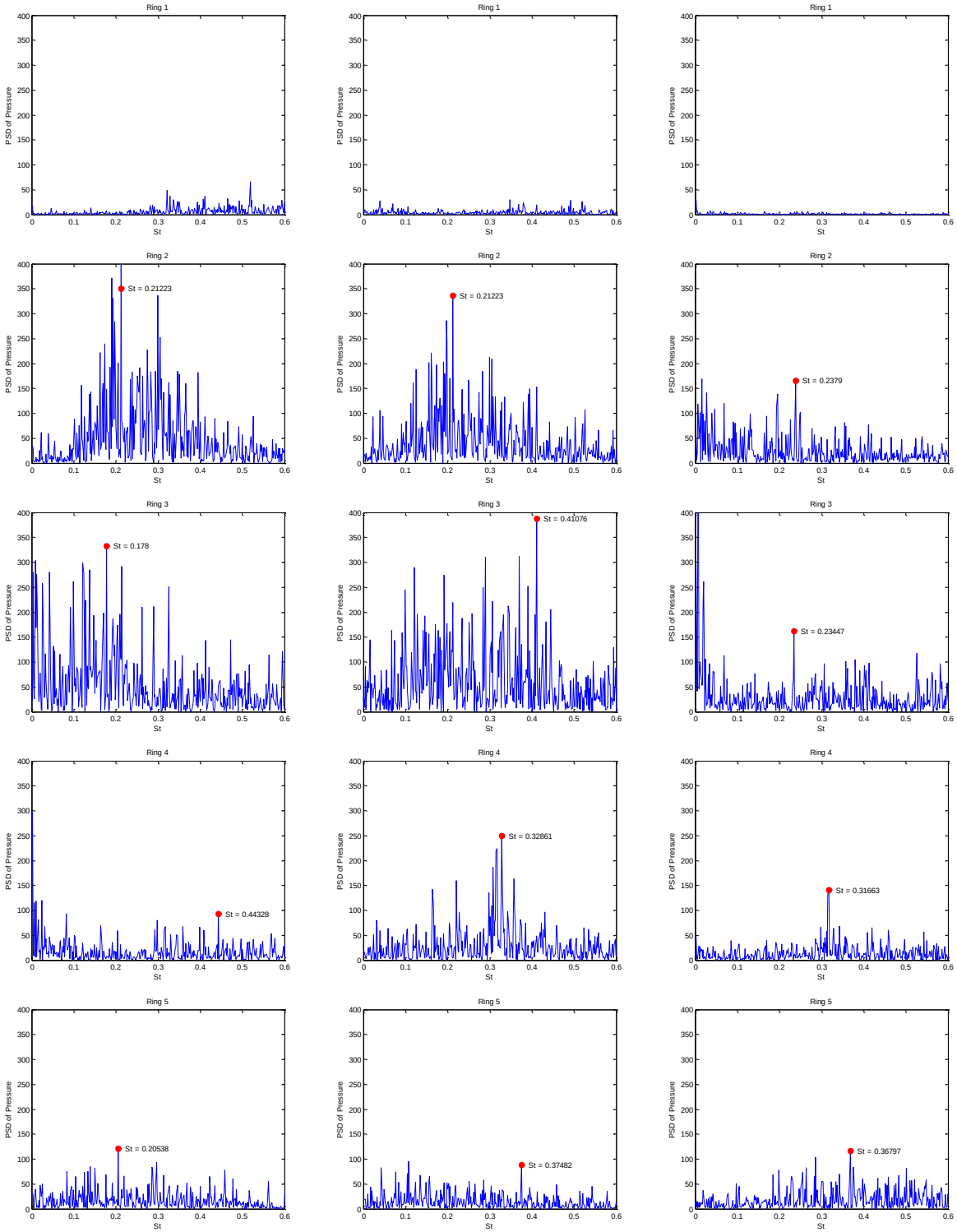


Figure N: FFT results Leeward Points:

d) $\phi = 67.5°$; $\alpha = 60°$, $\beta = 40°$

v) Re = 5.5×10^5;

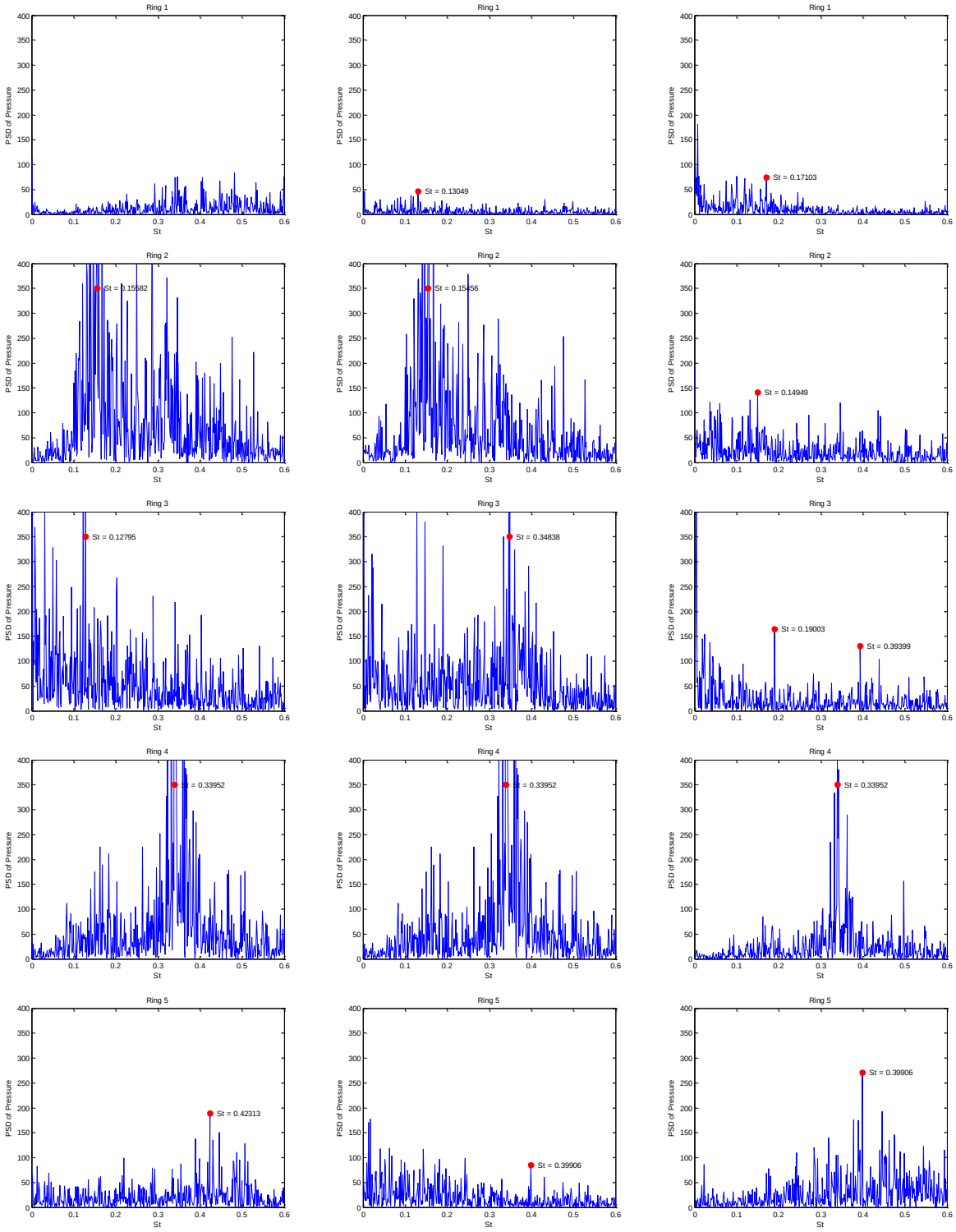


Figure N: FFT results Leeward Points:

e) $\phi = 54.7°$; $\alpha = 54.7°$, $\beta = 0°$

i) Re = 1.1×10^5;

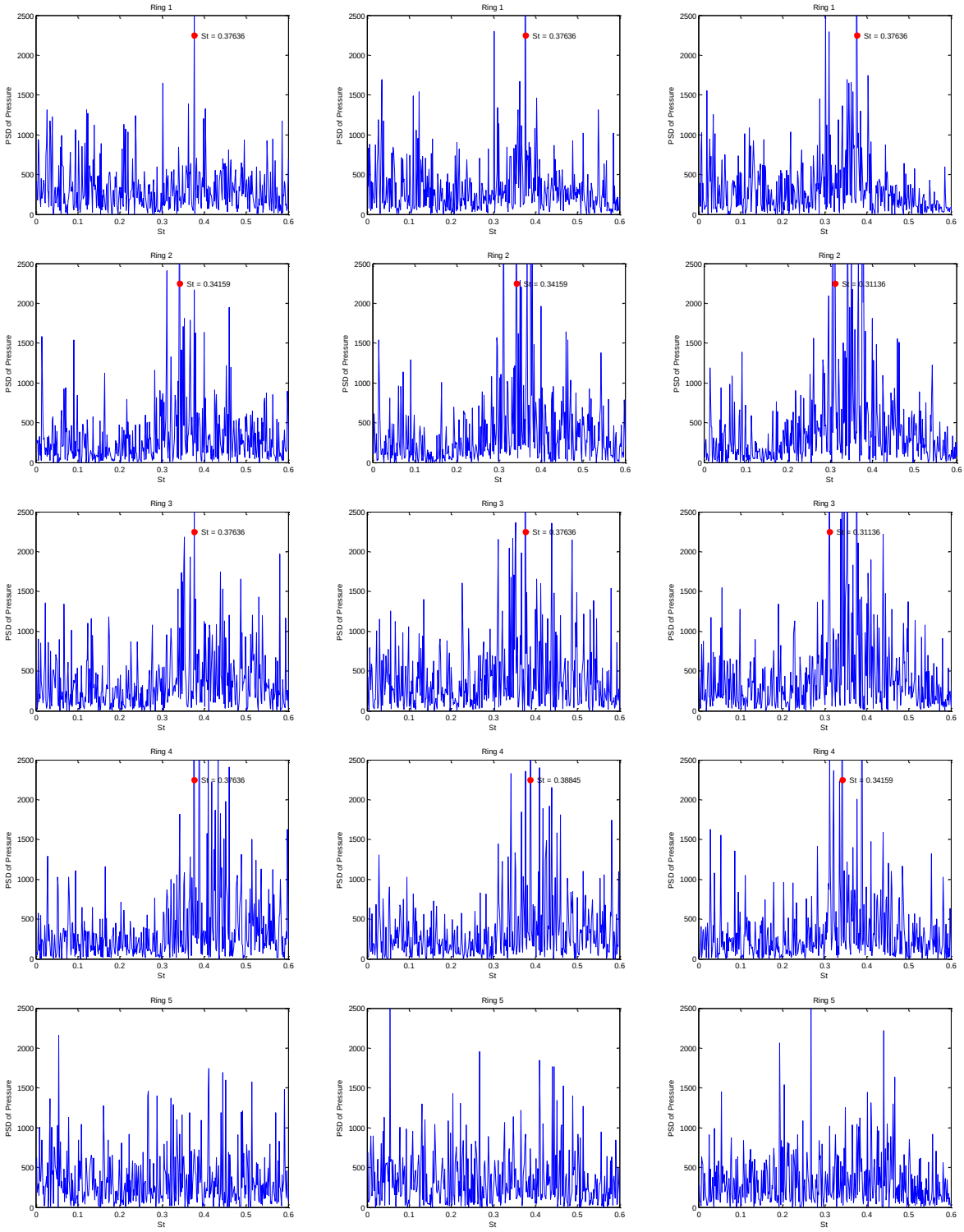


Figure N: FFT results Leeward Points:

e) $\phi = 54.7°$; $\alpha = 54.7°$, $\beta = 0°$

ii) Re = 2.2×10^5;

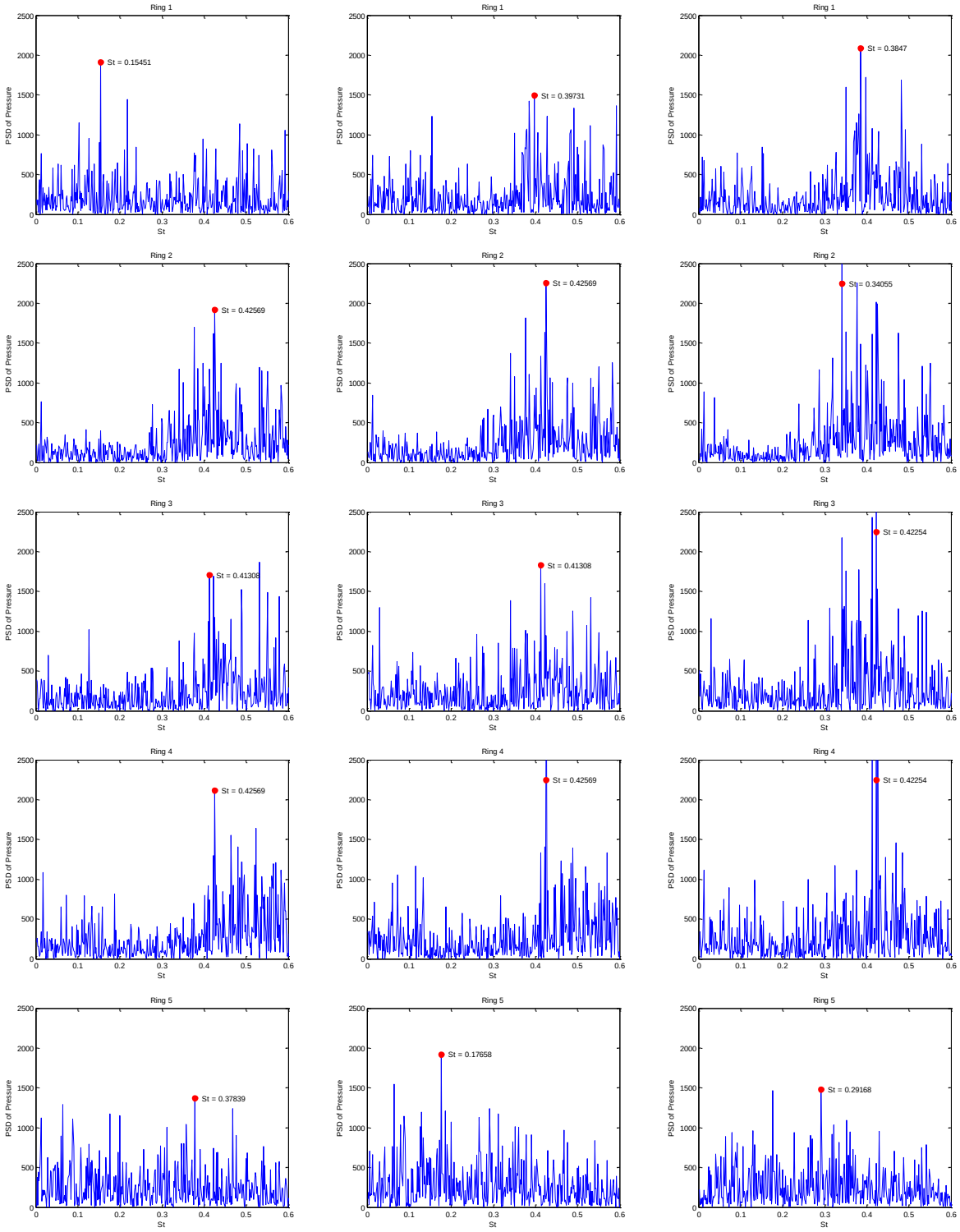


Figure N: FFT results Leeward Points:

e) $\phi = 54.7°$; $\alpha = 54.7°$, $\beta = 0°$

iii) Re = 3.3×10^5;

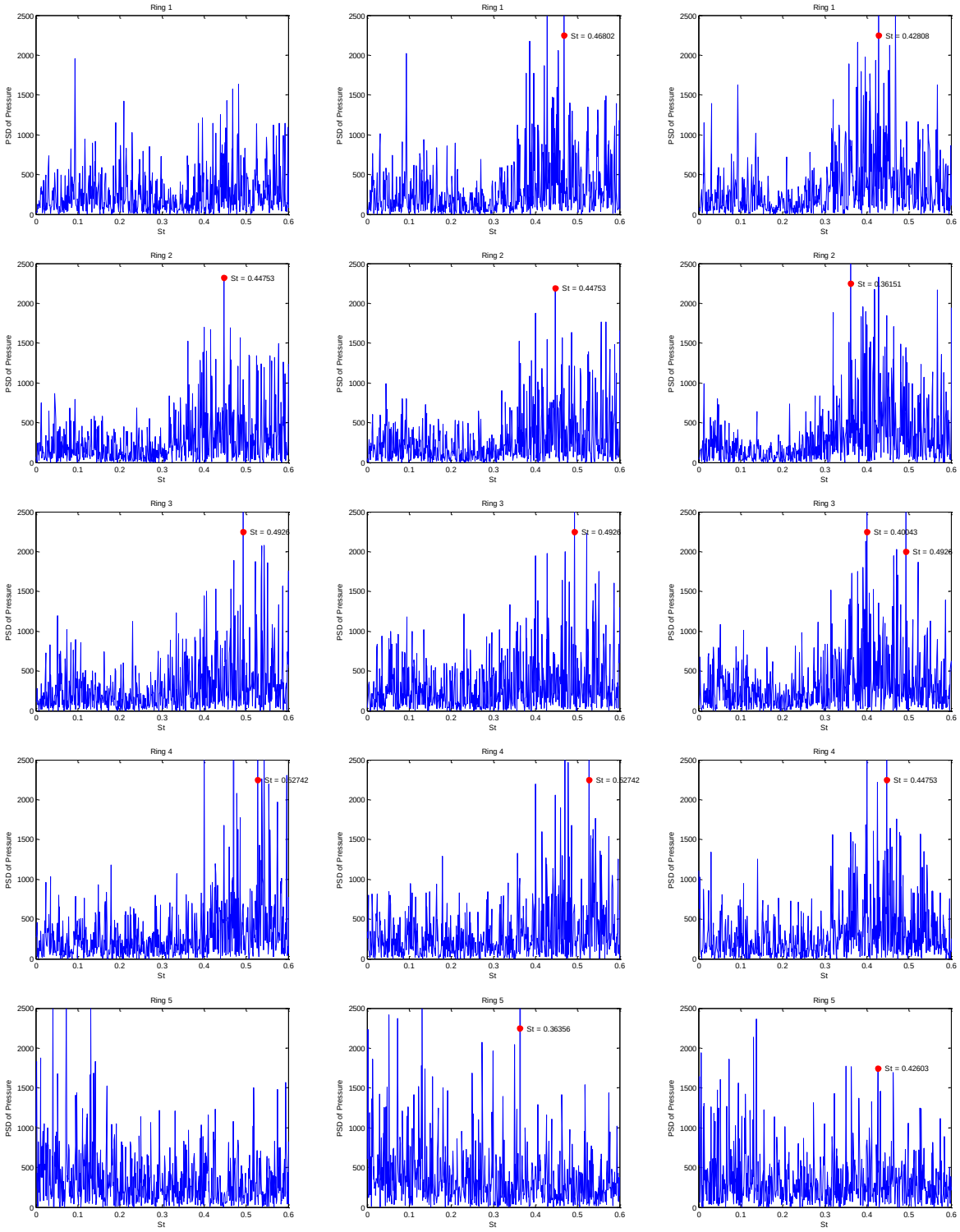


Figure N: FFT results Leeward Points:

e) $\phi = 54.7°$; $\alpha = 54.7°$, $\beta = 0°$

iv) Re = 4.4×10^5;

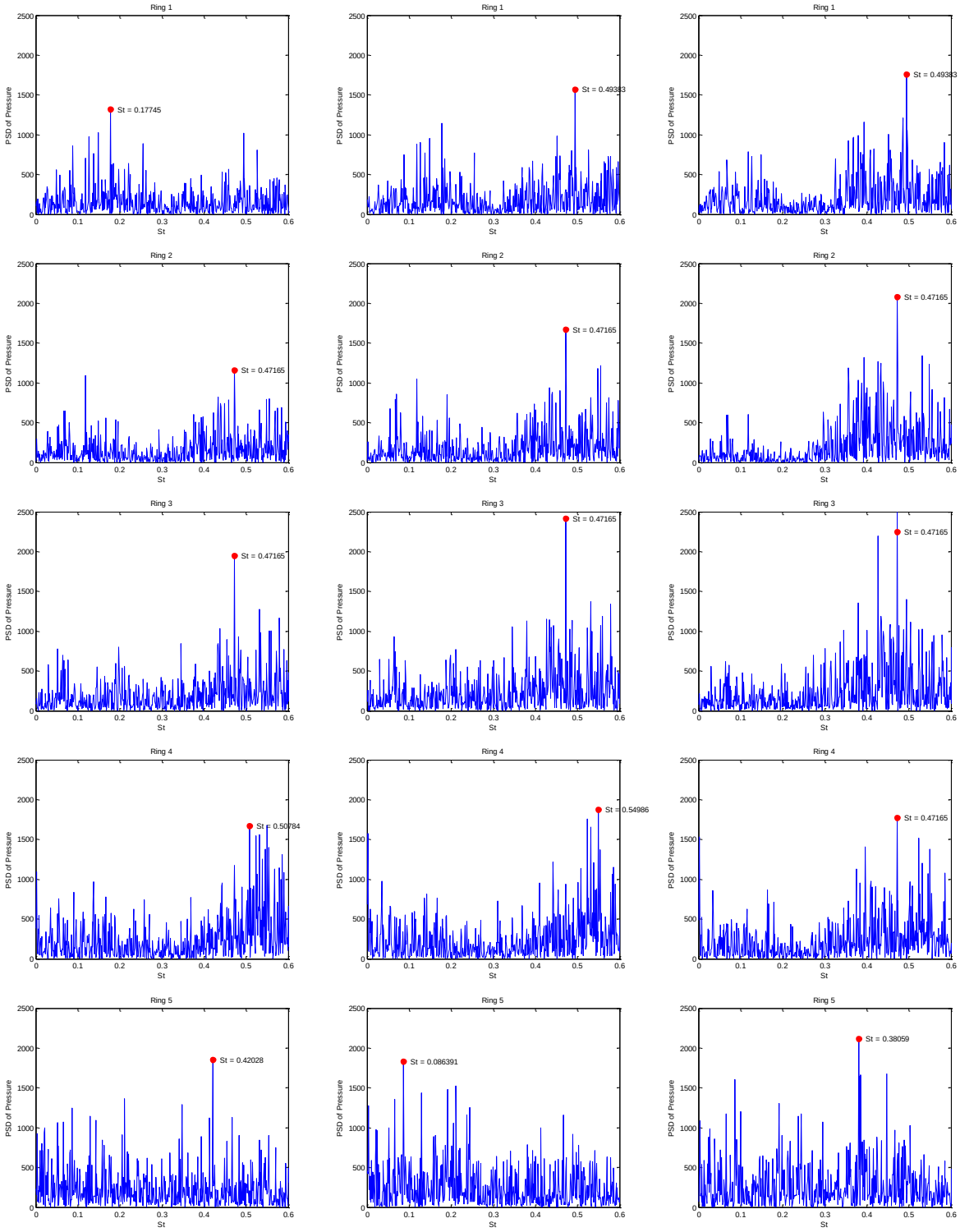


Figure N: FFT results Leeward Points:

e) $\phi = 54.7°$; $\alpha = 54.7°$, $\beta = 0°$

v) Re = 5.5×10^5;

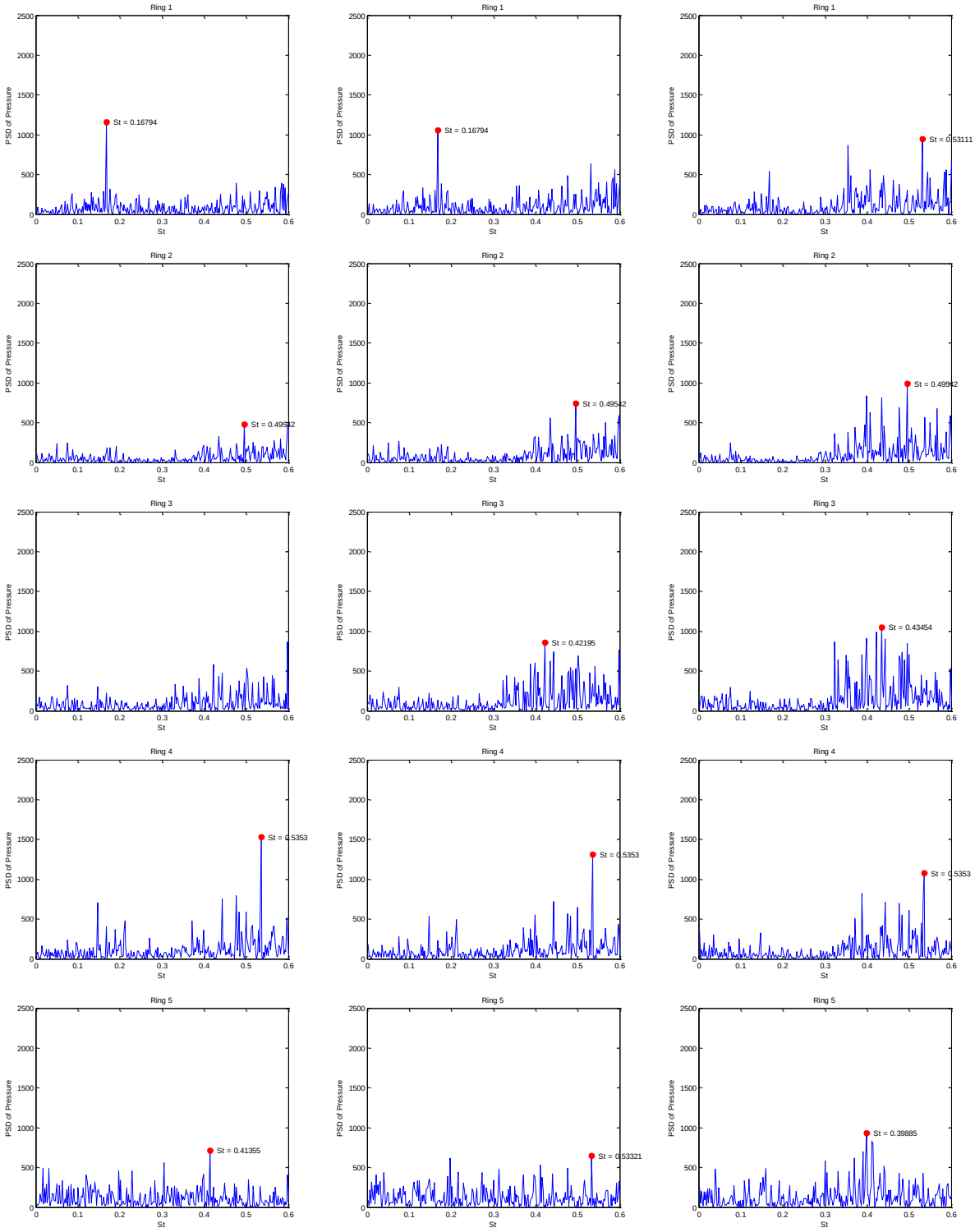


Figure N: FFT results Leeward Points:

f) $\phi = 57.1°$; $\alpha = 54.7°$, $\beta = 20°$

i) Re = 1.1×10^5;

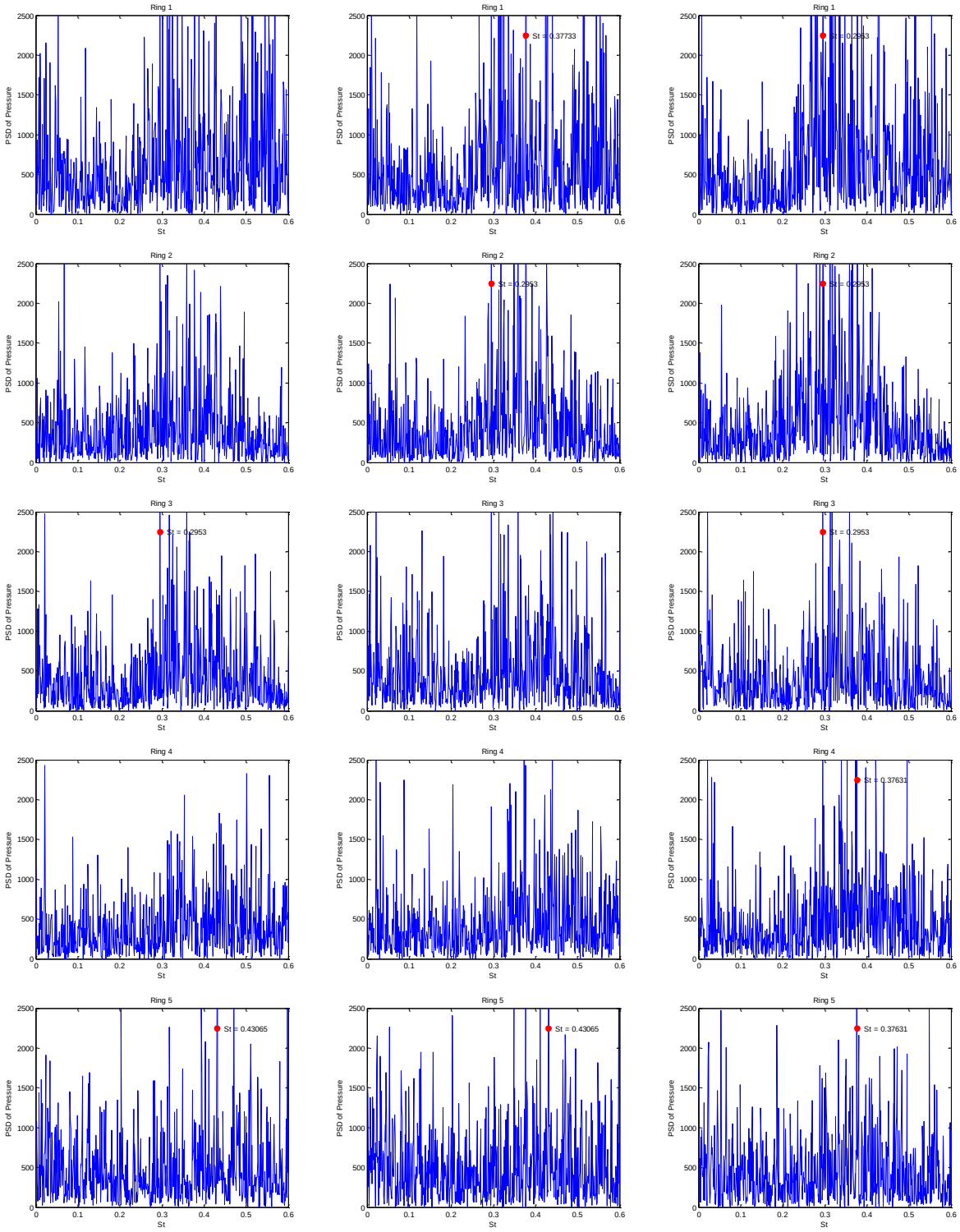


Figure N: FFT results Leeward Points:
f) $\phi = 57.1°$; $\alpha = 54.7°$, $\beta = 20°$
ii) Re = 2.2×10^5;

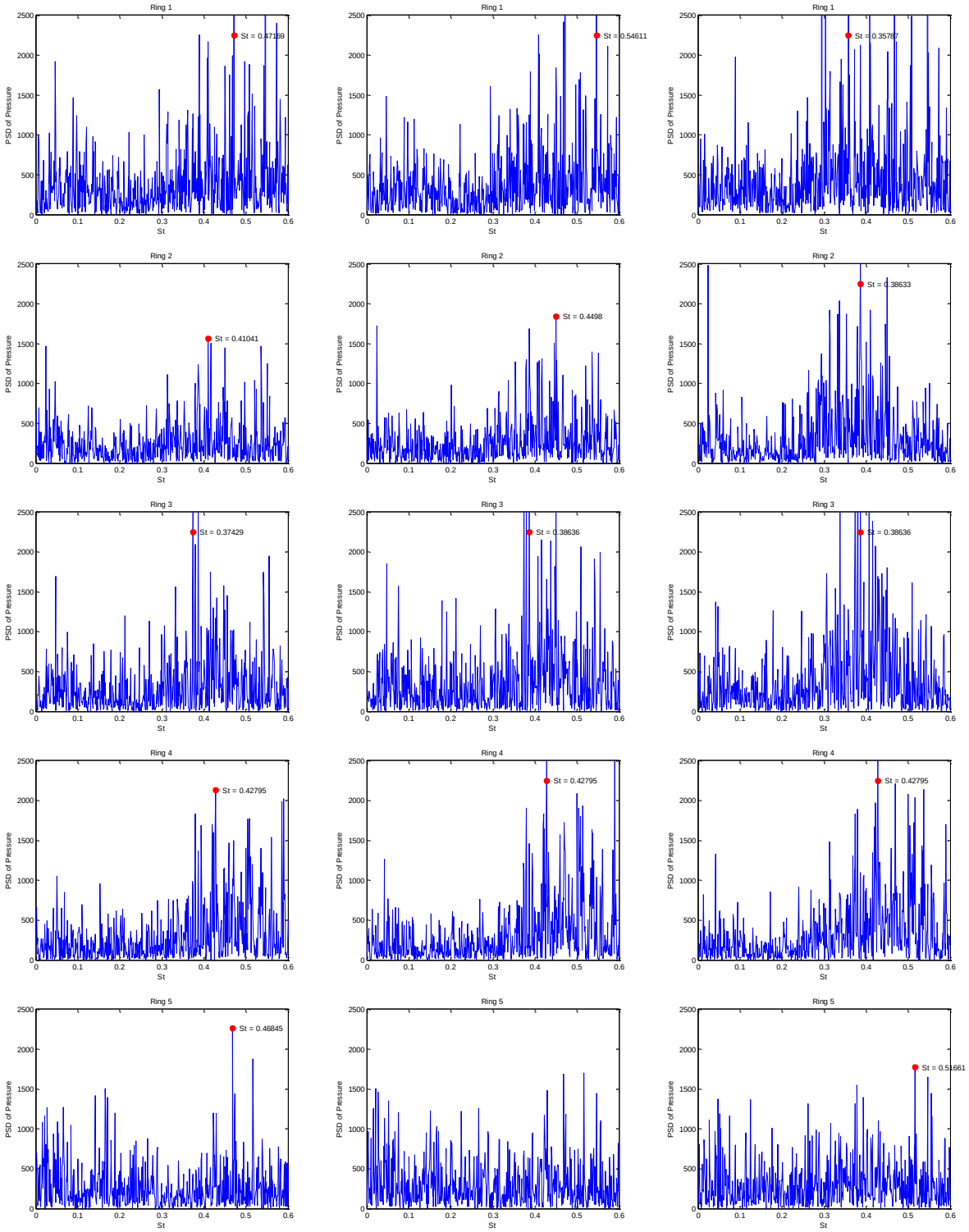


Figure N: FFT results Leeward Points:

f) $\phi = 57.1°$; $\alpha = 54.7°$, $\beta = 20°$

iii) Re = 3.3×10^5;

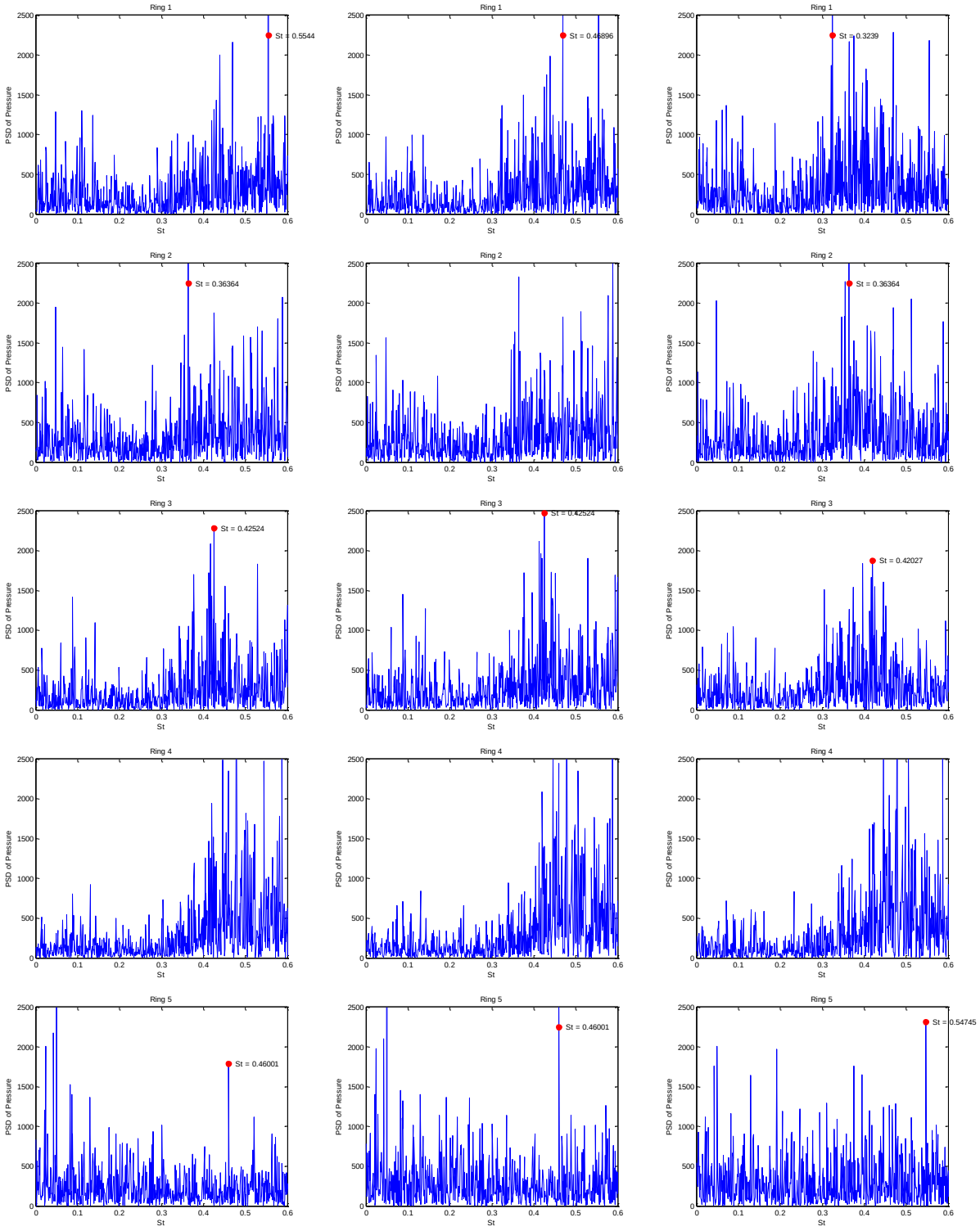


Figure N: FFT results Leeward Points:
f) $\phi = 57.1°$; $\alpha = 54.7°$, $\beta = 20°$
iv) Re = 4.4×10^5;

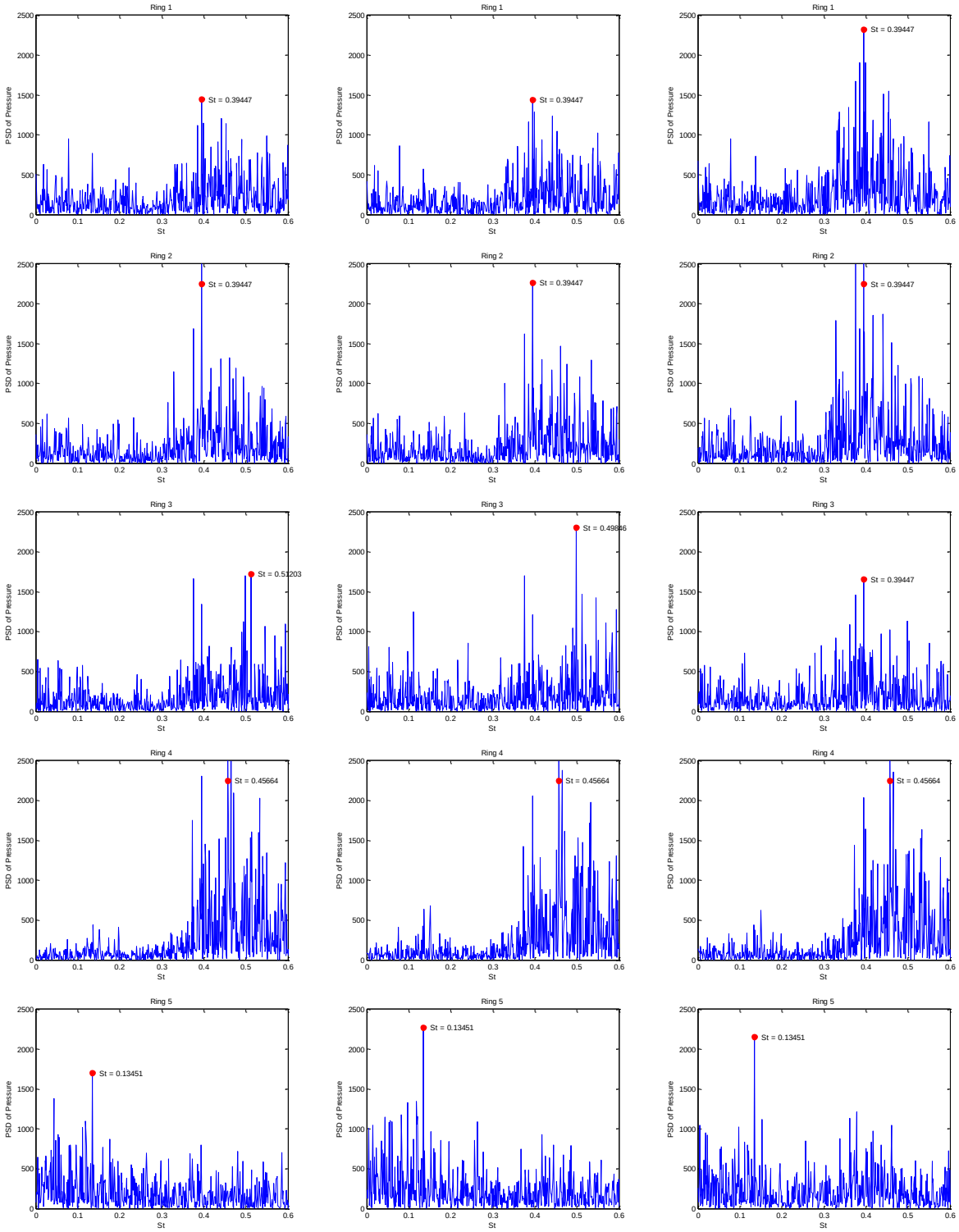


Figure N: FFT results Leeward Points:

f) $\phi = 57.1°$; $\alpha = 54.7°$, $\beta = 20°$

v) Re = 5.5×10^5;

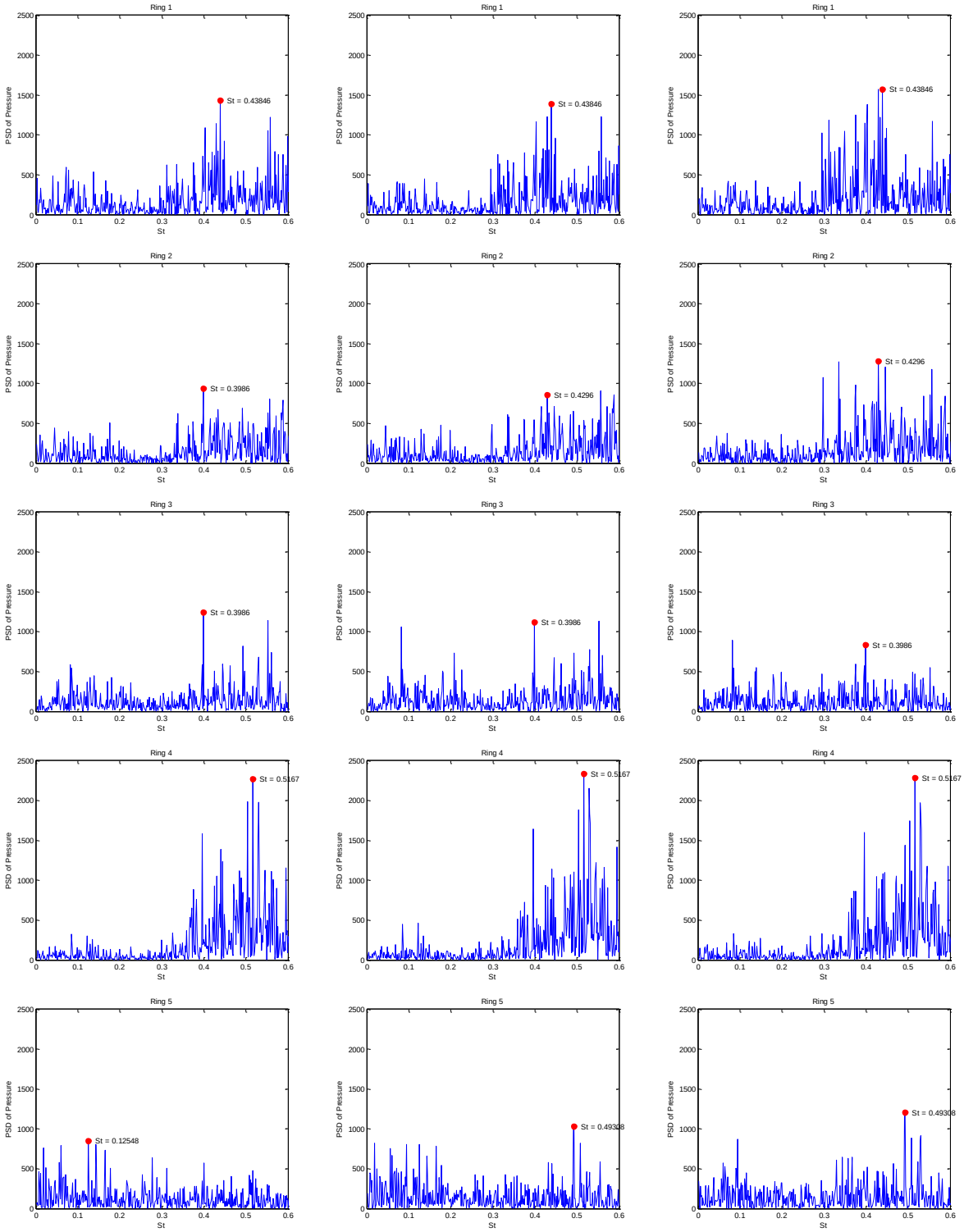


Figure N: FFT results Leeward Points:

g) $\phi = 64.0°$; $\alpha = 54.7°$, $\beta = 40°$

i) Re = 1.1×10^5;

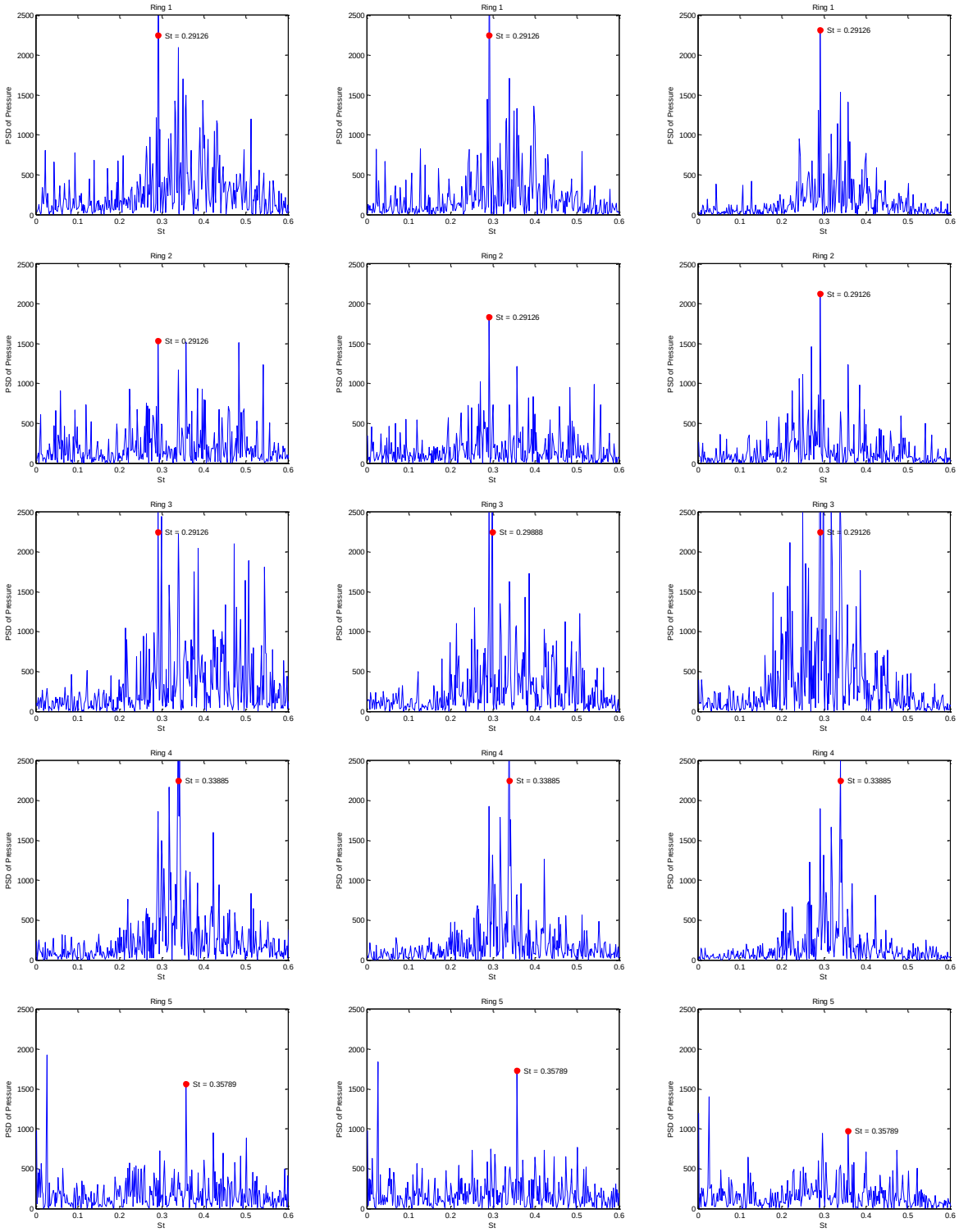


Figure N: FFT results Leeward Points:

g) $\phi = 64.0°$; $\alpha = 54.7°$, $\beta = 40°$

ii) Re = 2.2×10^5;

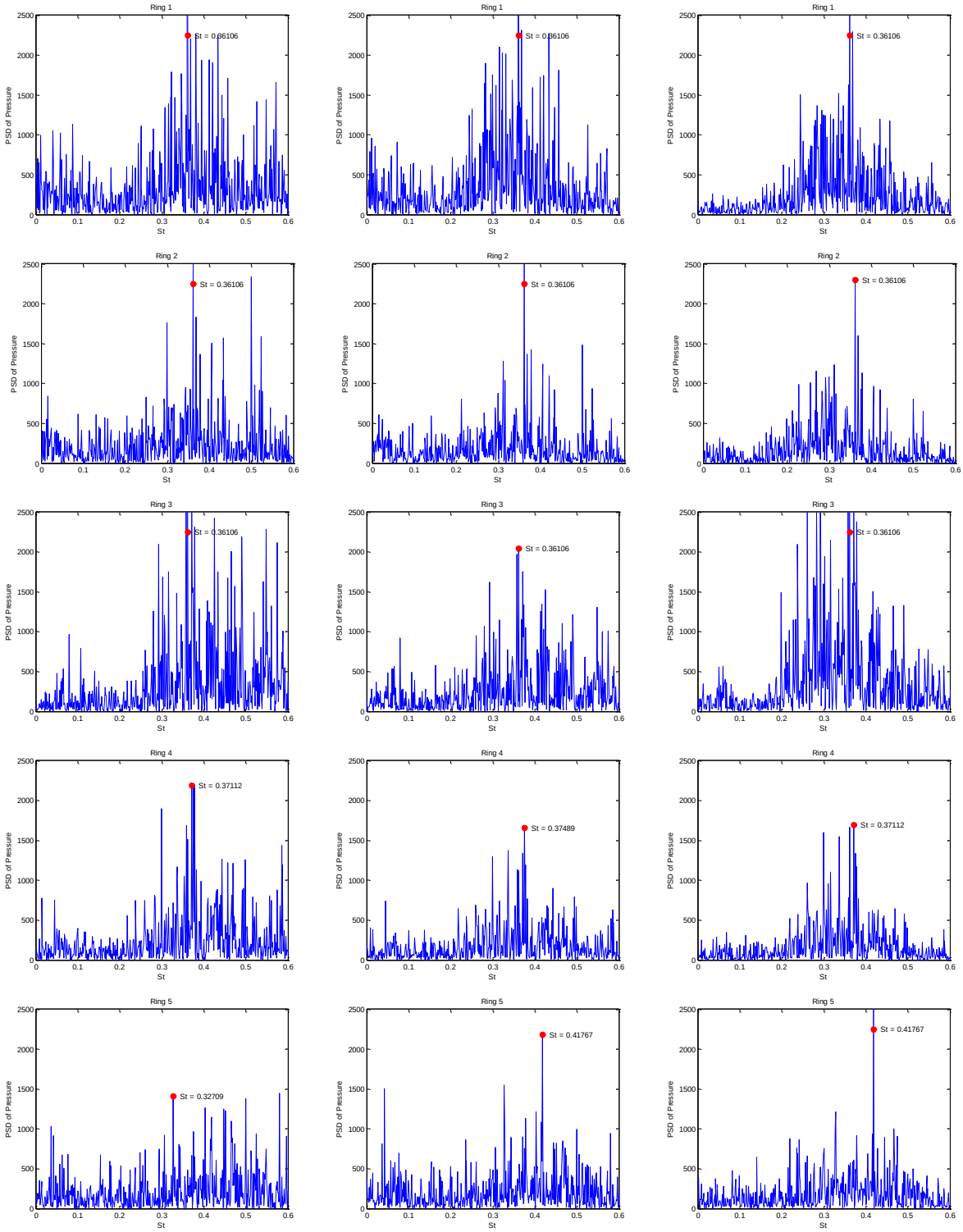


Figure N: FFT results Leeward Points:

g) $\phi = 64.0°$; $\alpha = 54.7°$, $\beta = 40°$

iii) Re = 3.3×10^5;

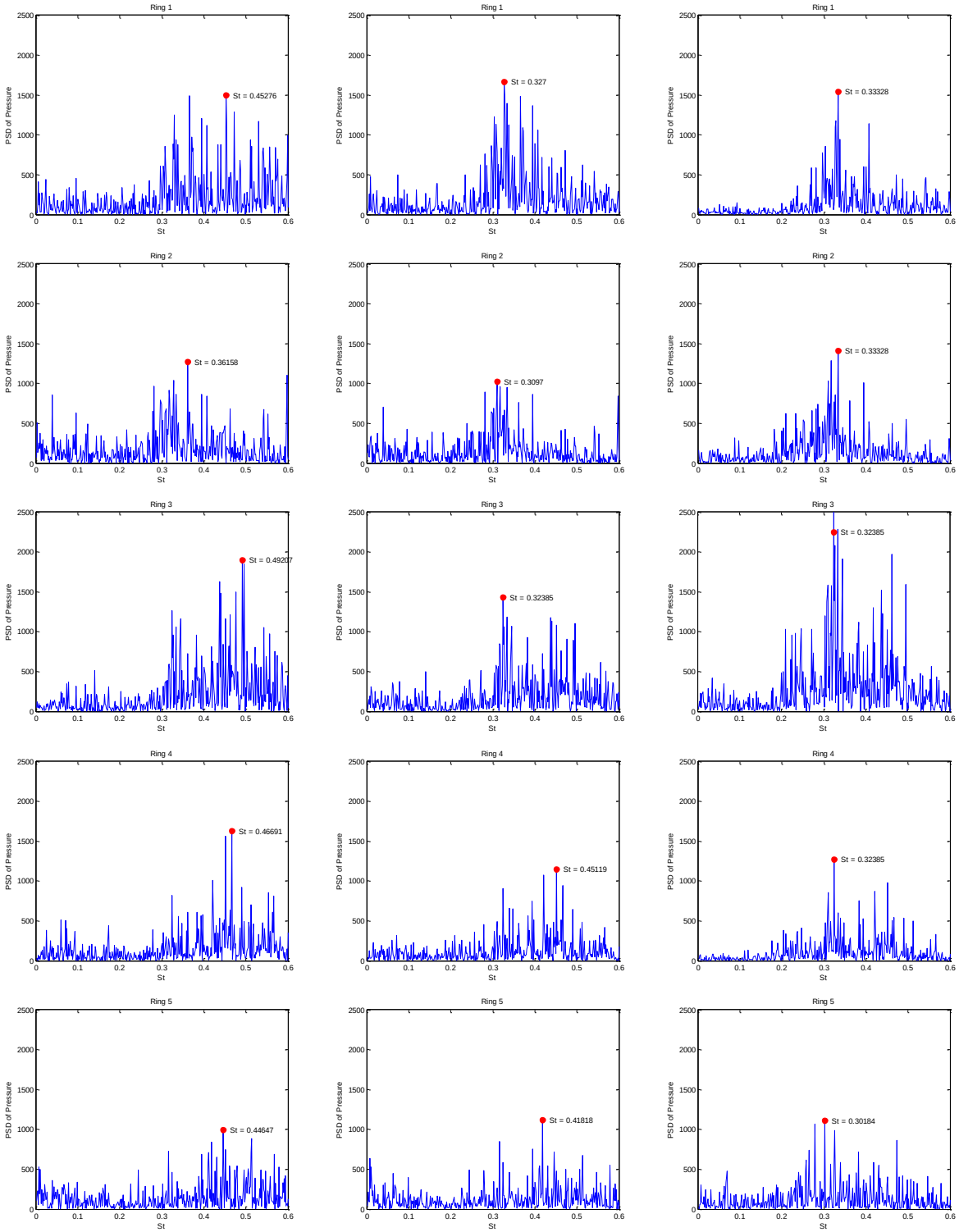


Figure N: FFT results Leeward Points:
g) $\phi = 64.0°$; $\alpha = 54.7°$, $\beta = 40°$
iv) Re = 4.4×10^5;

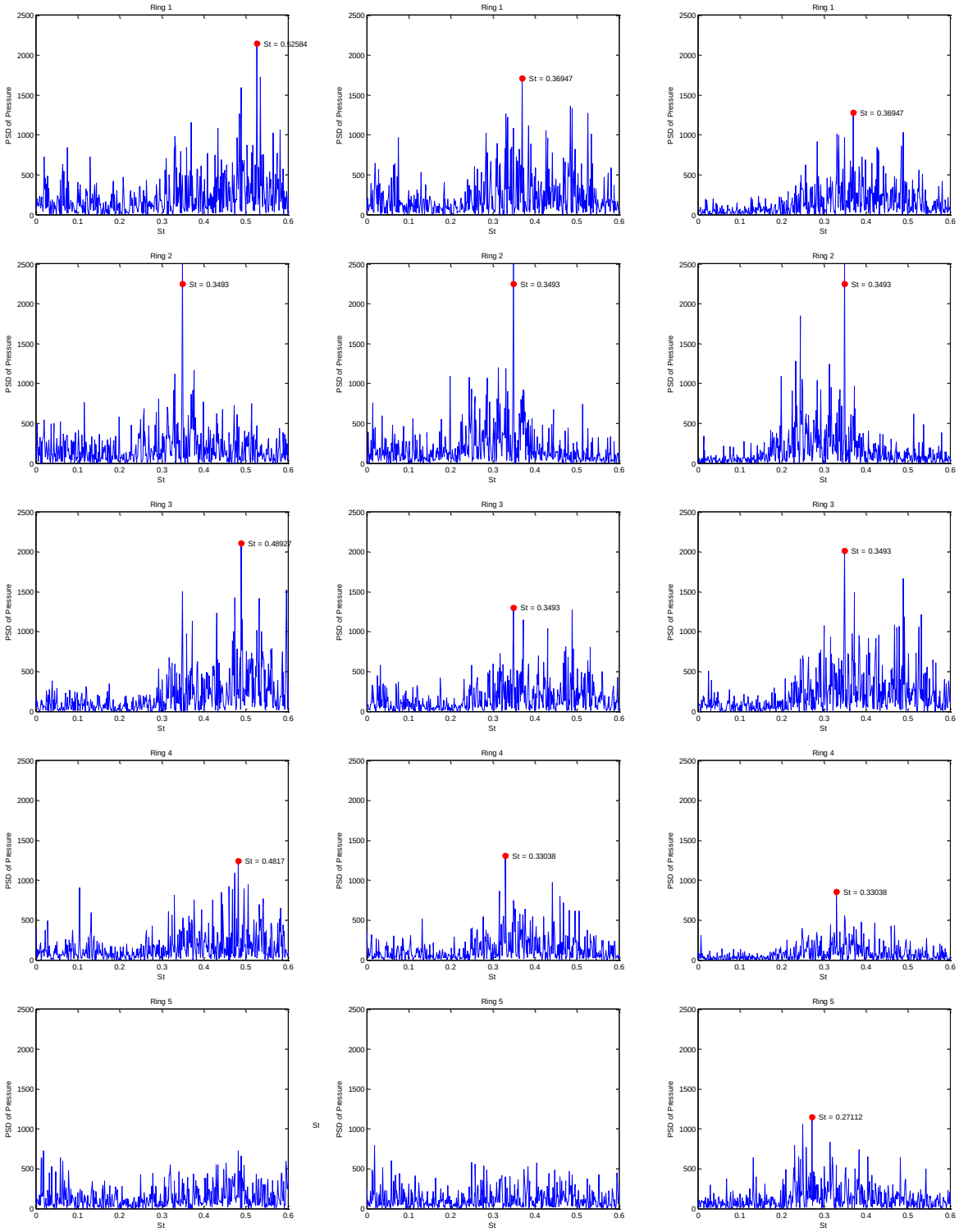


Figure N: FFT results Leeward Points:

g) $\phi = 64.0°$; $\alpha = 54.7°$, $\beta = 40°$

v) Re = 5.5×10^5;

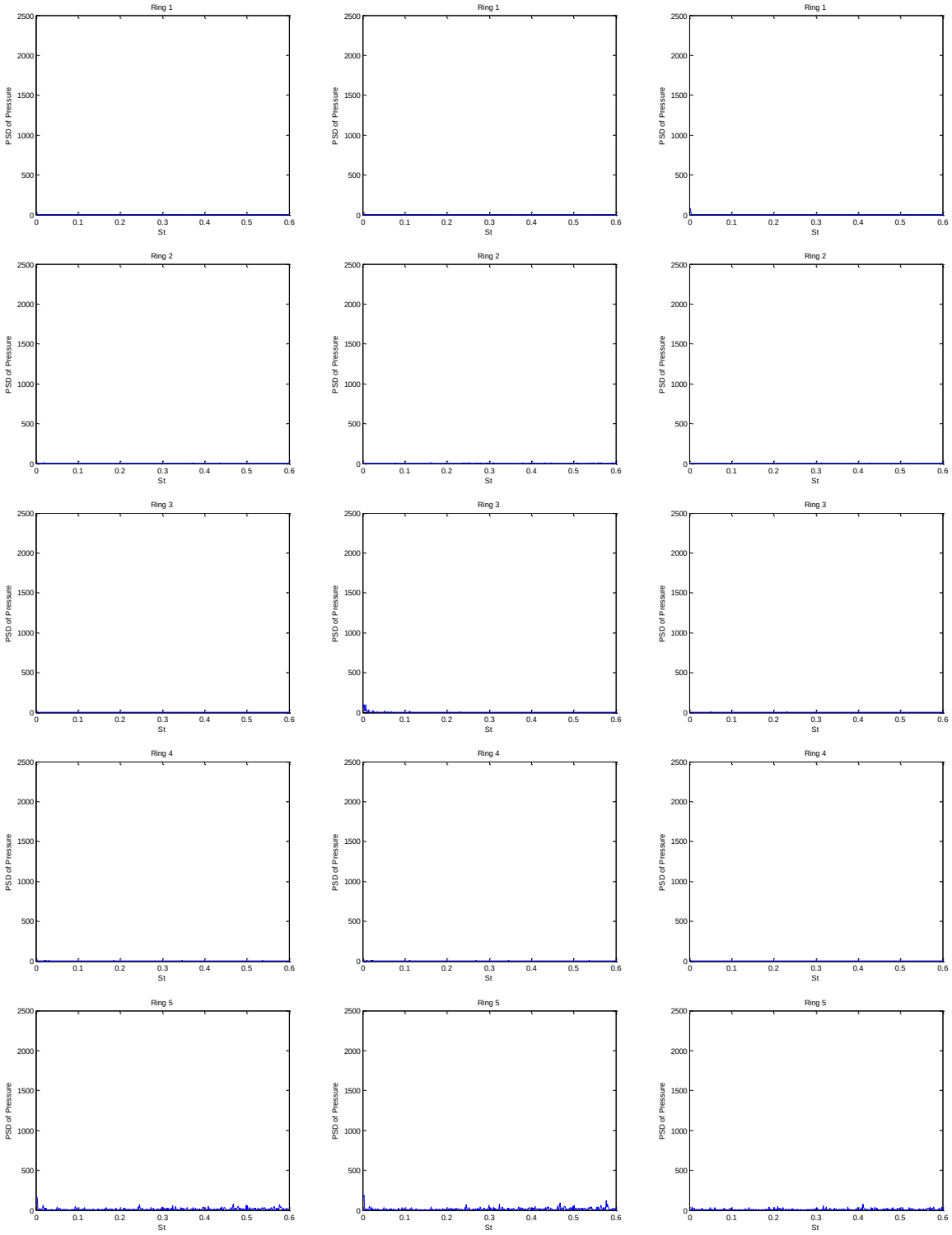


Figure N: FFT results Leeward Points:

h) $\phi = 53.0°$; $\alpha = 50°$, $\beta = 20°$

i) Re = 1.1×10^5;

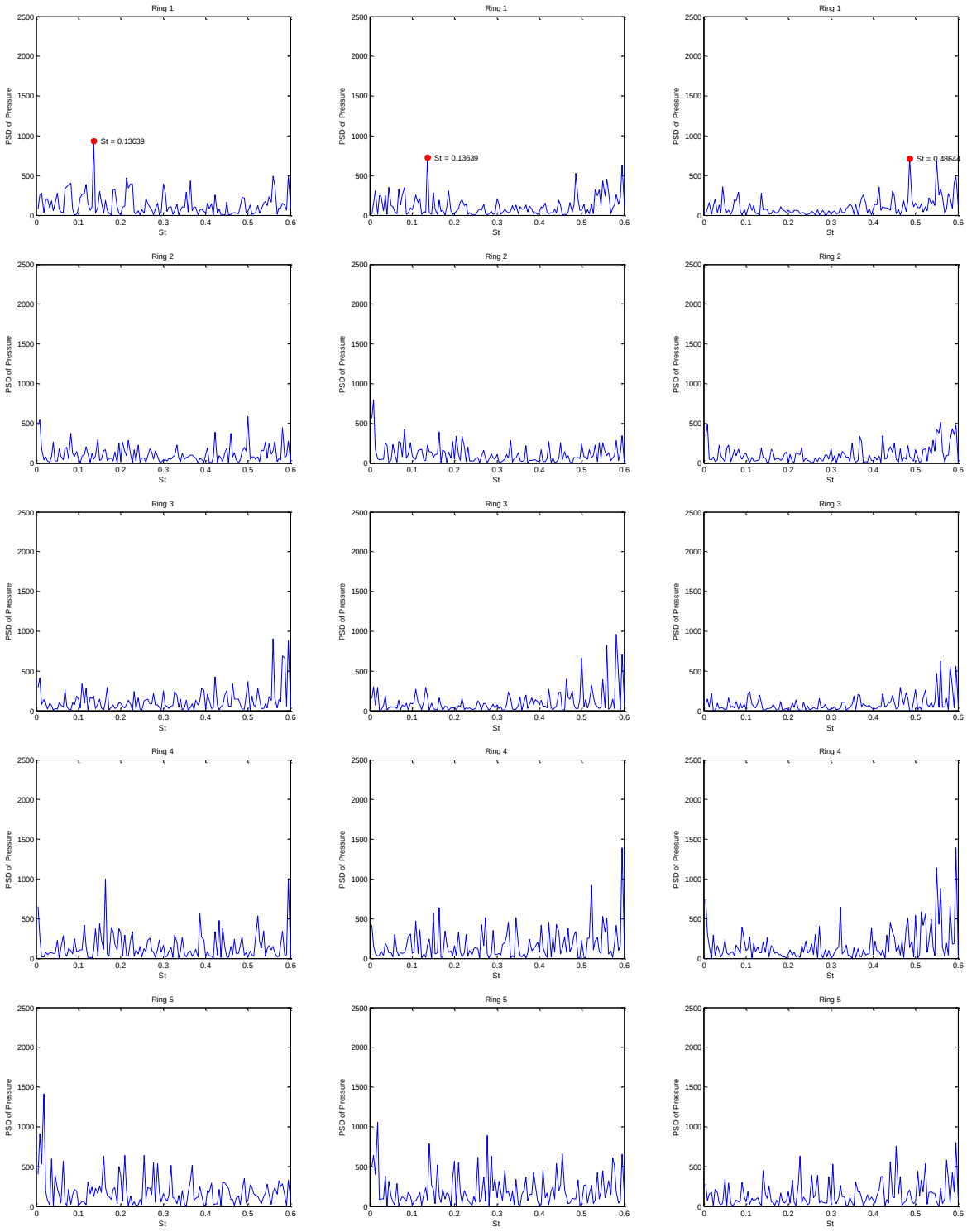


Figure N: FFT results Leeward Points:

h) $\phi = 53.0°$; $\alpha = 50°$, $\beta = 20°$

ii) Re = 2.2×10^5;

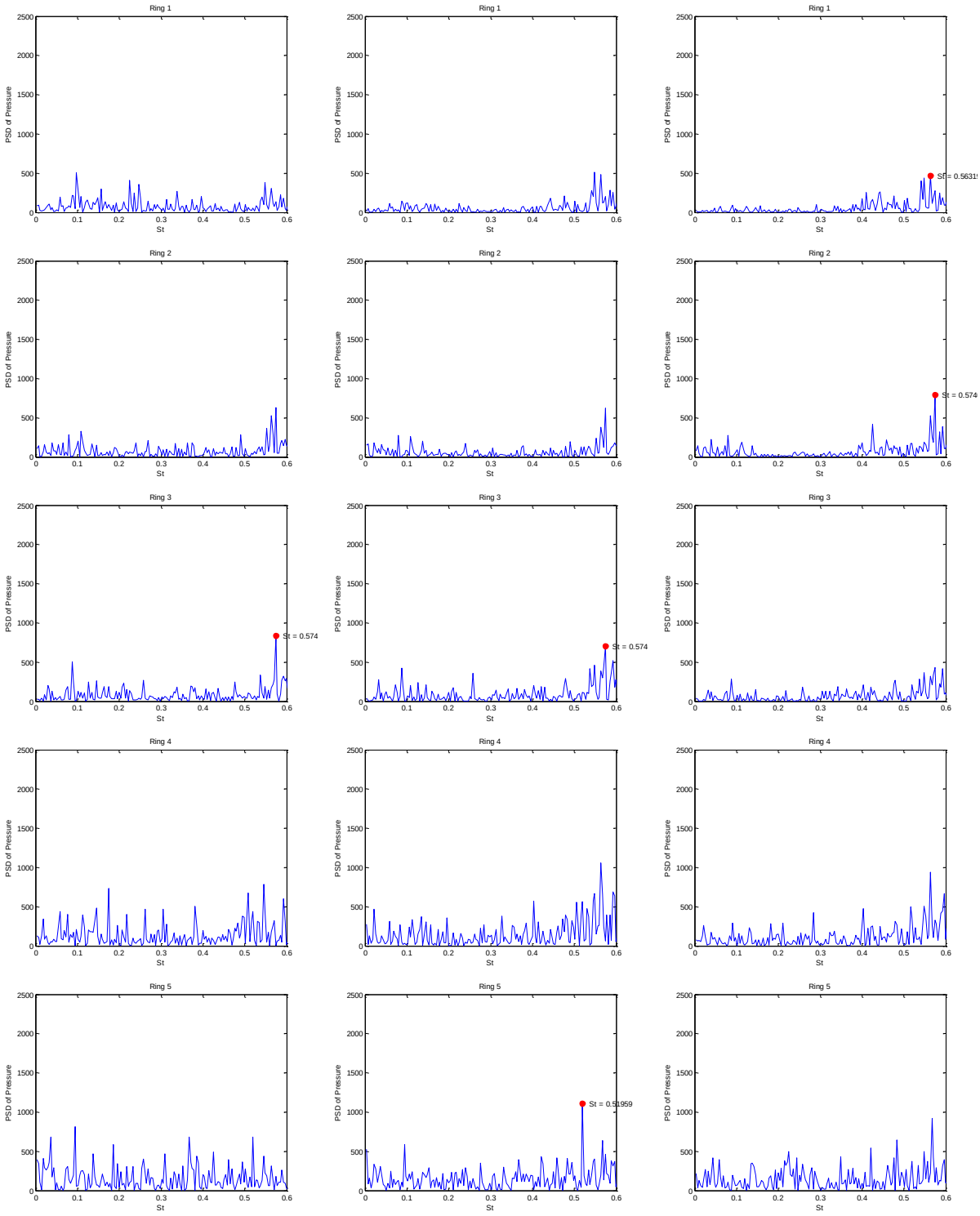


Figure N: FFT results Leeward Points:

h) $\phi = 53.0°$; $\alpha = 50°$, $\beta = 20°$

iii) Re = 3.3×10^5;

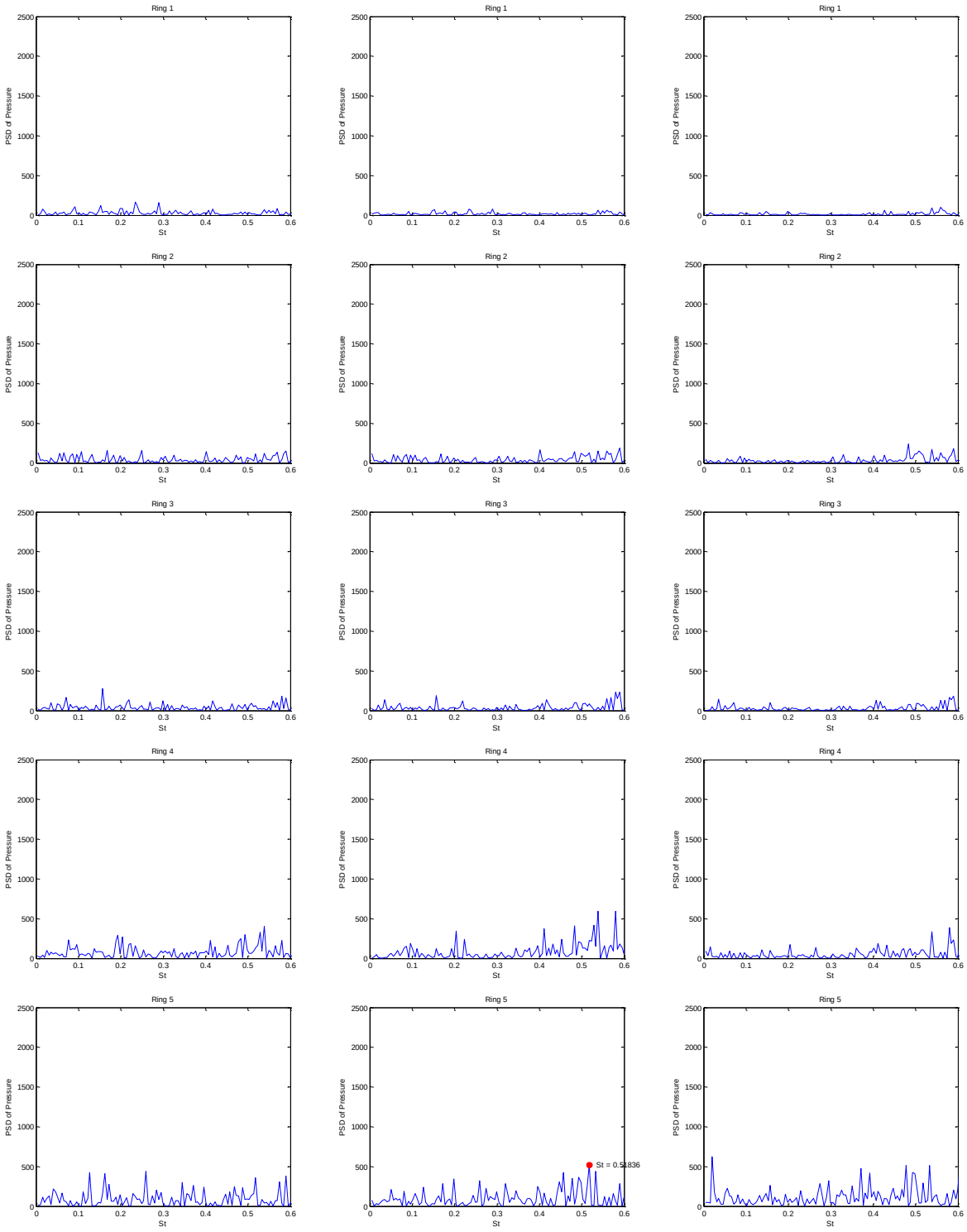


Figure N: FFT results Leeward Points:

h) $\phi = 53.0°$; $\alpha = 50°$, $\beta = 20°$

iv) Re = 4.4×10^5;

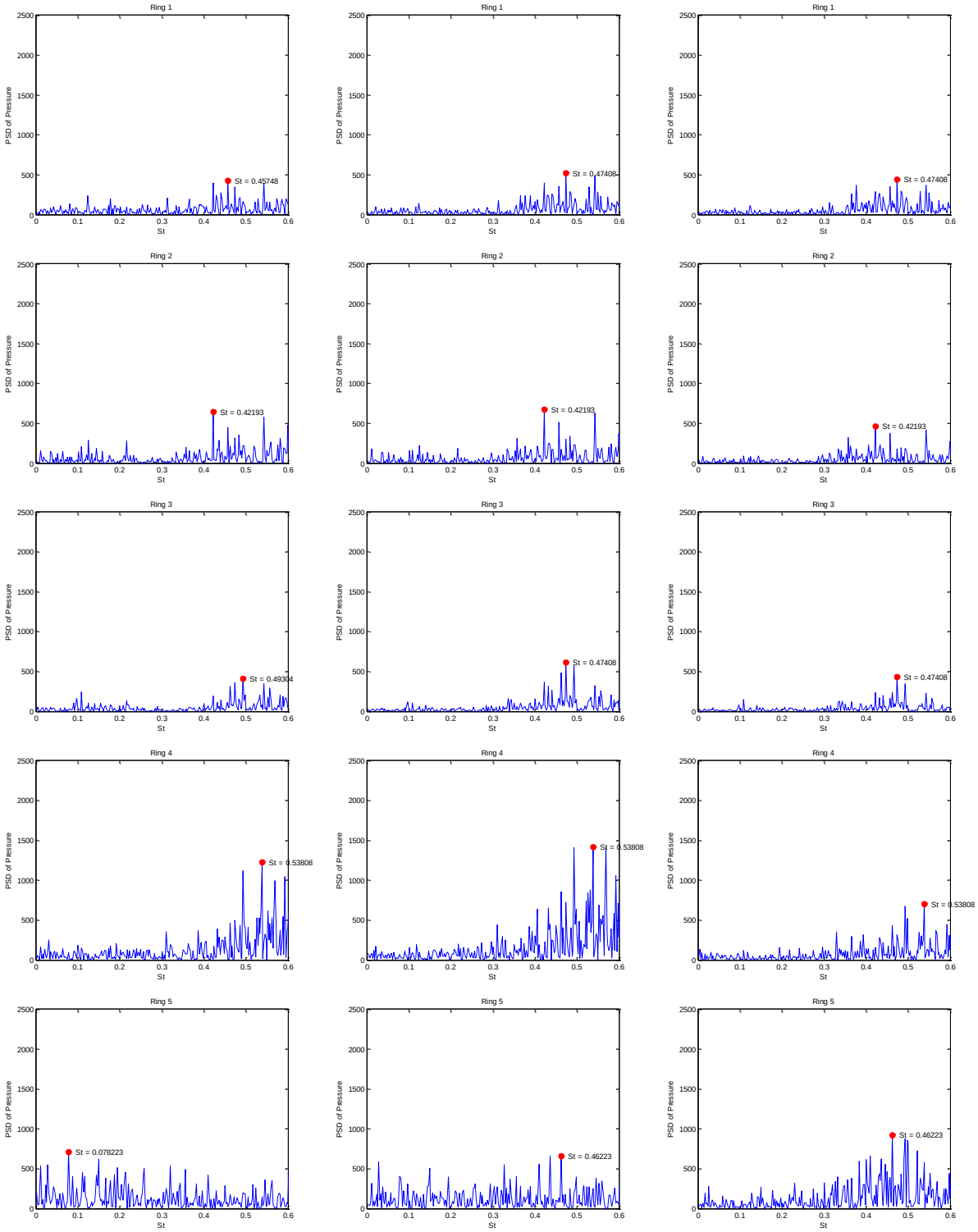


Figure N: FFT results Leeward Points:

h) $\phi = 53.0°$; $\alpha = 50°$, $\beta = 20°$

v) Re = 5.5×10^5;

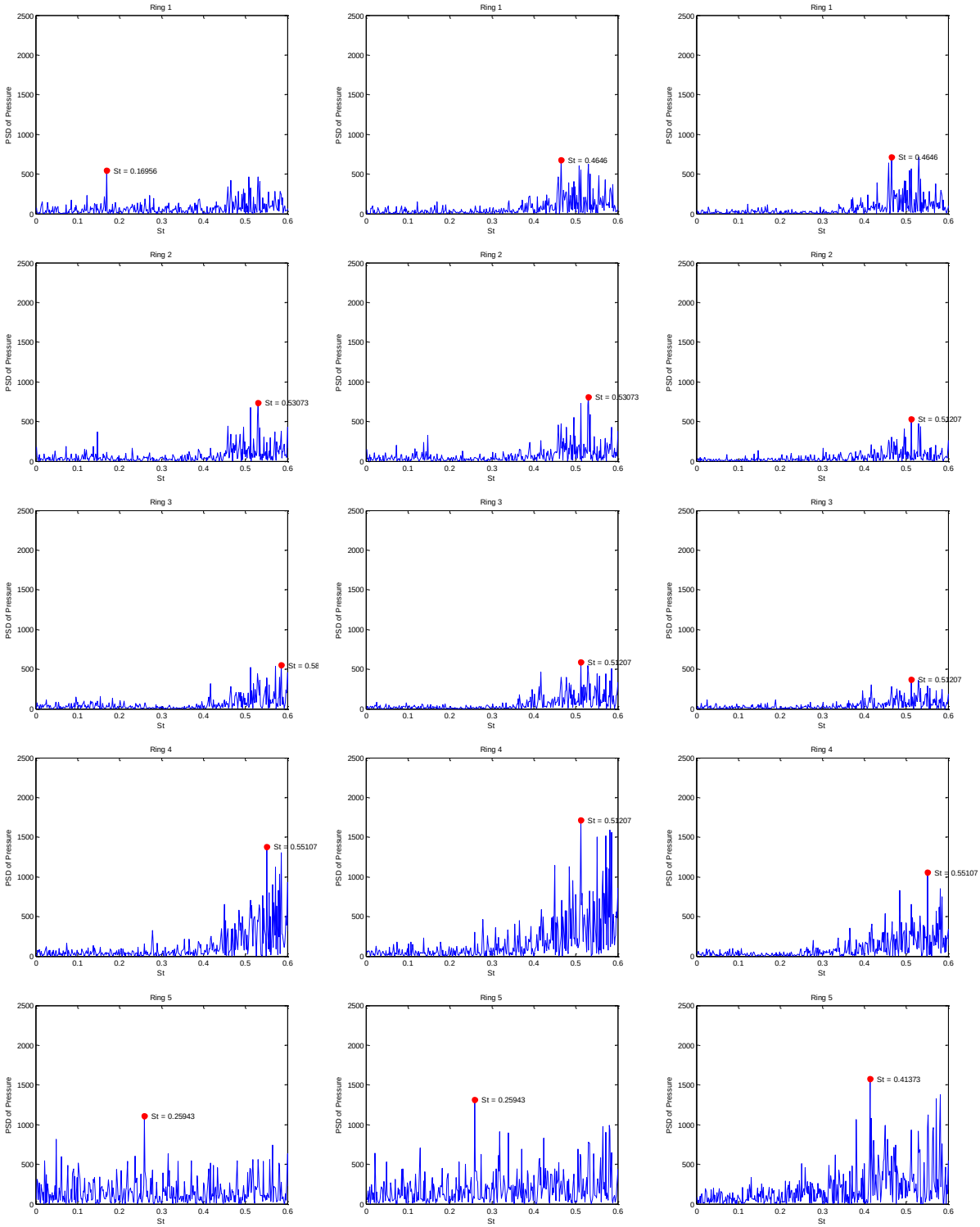


Figure N: FFT results Leeward Points:

i) $\phi = 60.5°$; $\alpha = 50°$, $\beta = 40°$

i) Re = 1.1×10^5;

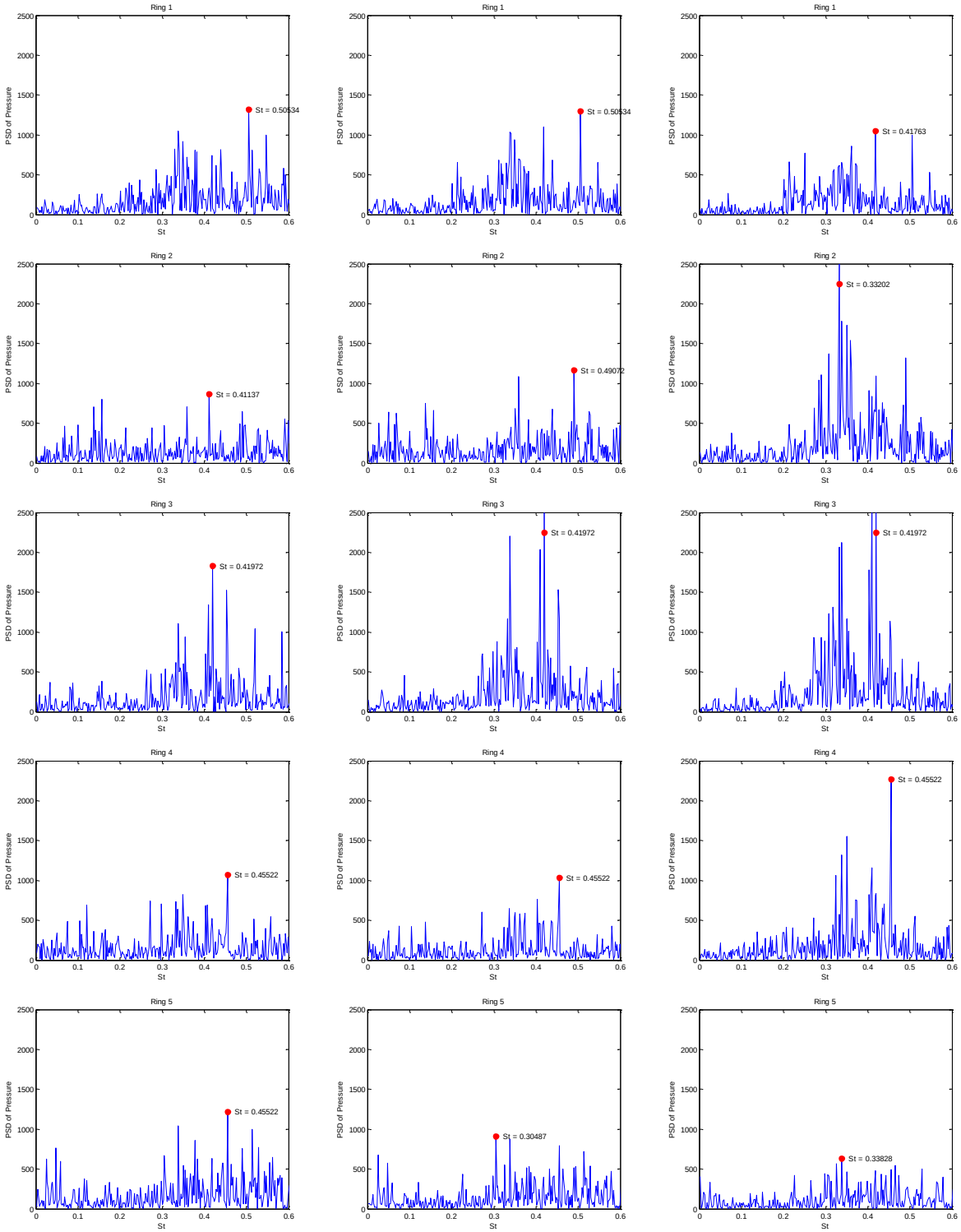


Figure N: FFT results Leeward Points:

i) $\phi = 60.5°$; $\alpha = 50°$, $\beta = 40°$

ii) Re = 2.2×10^5;

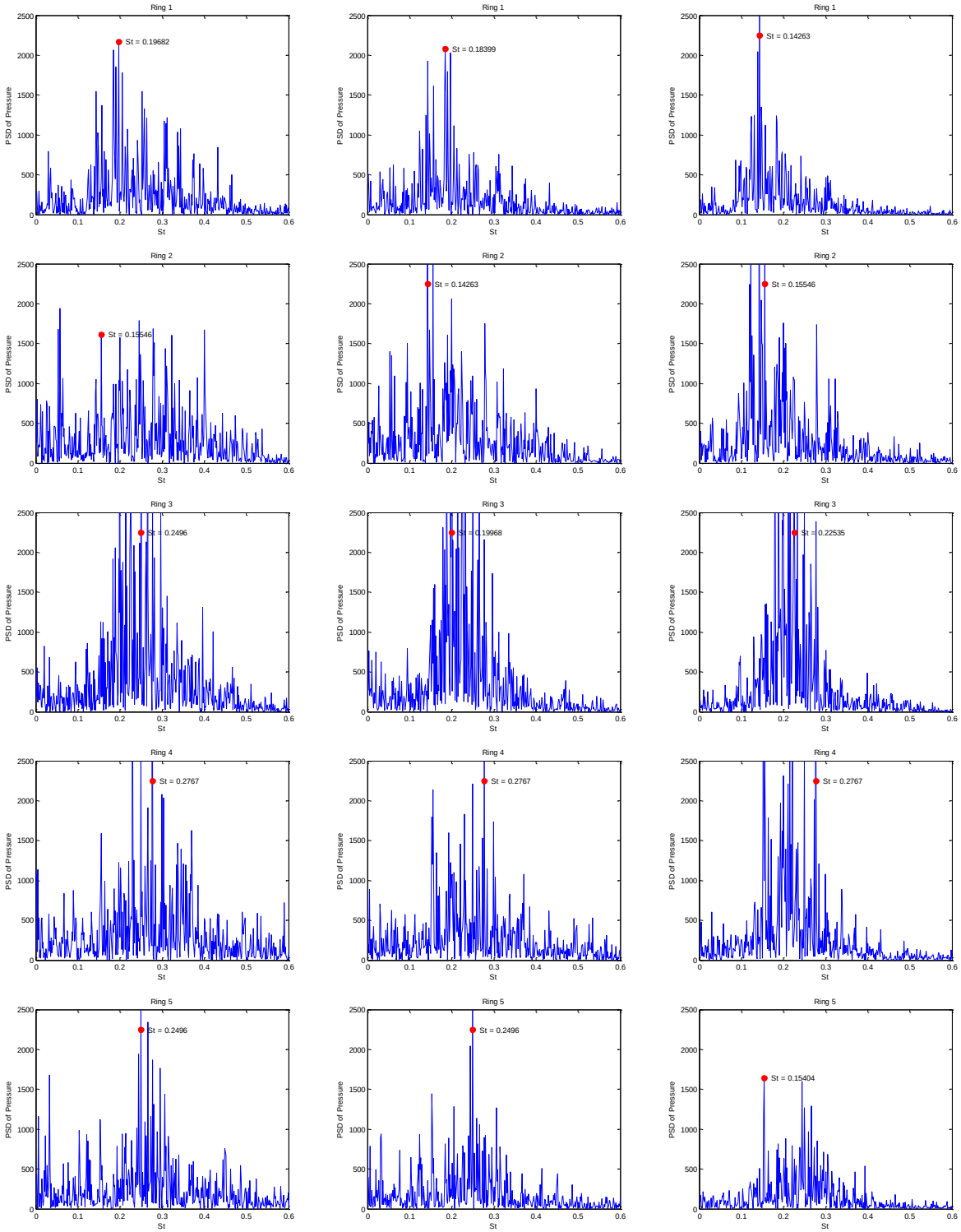


Figure N: FFT results Leeward Points:

i) $\phi = 60.5°$; $\alpha = 50°$, $\beta = 40°$

iii) Re = 3.3×10^5;

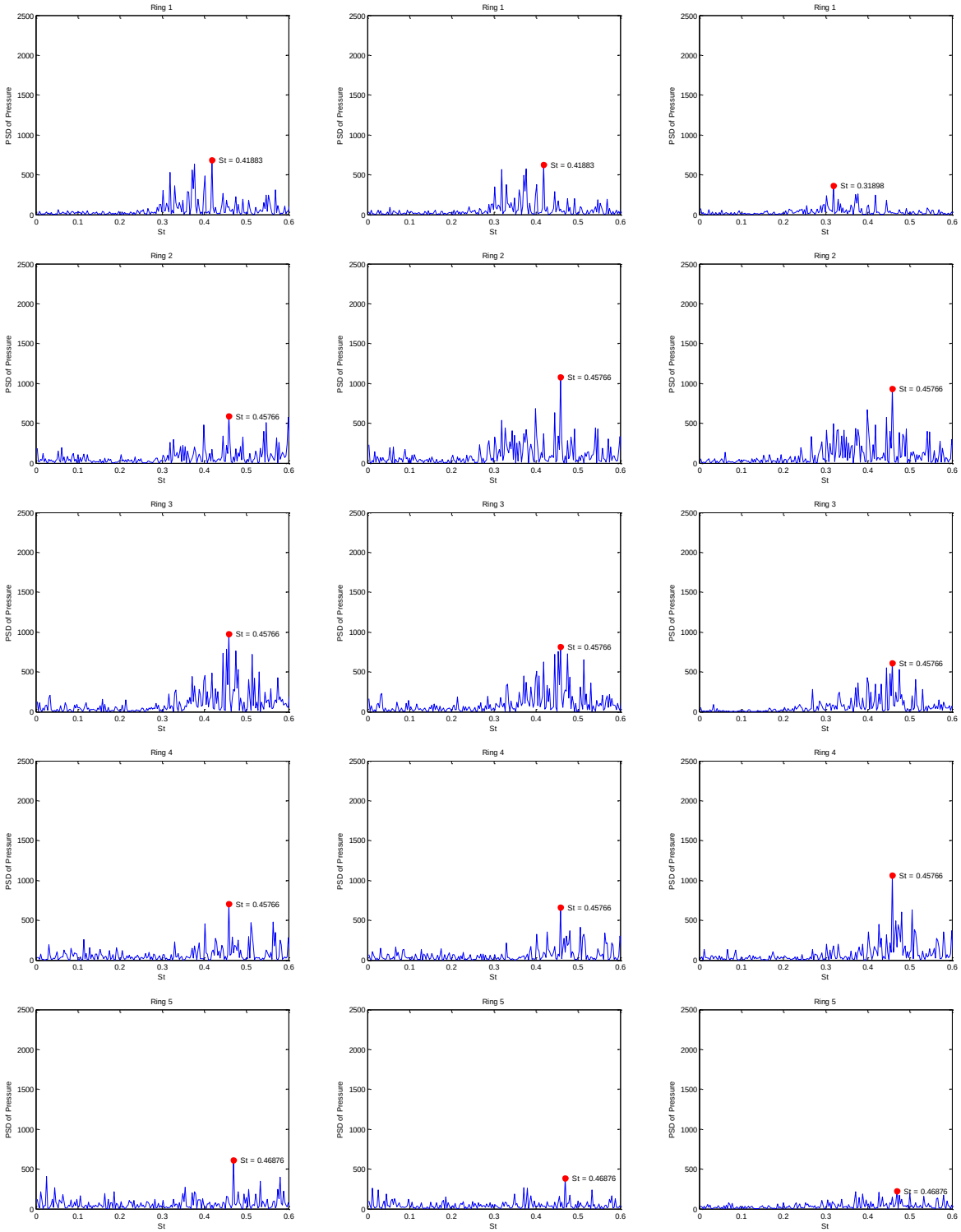


Figure N: FFT results Leeward Points:

i) $\phi = 60.5°$; $\alpha = 50°$, $\beta = 40°$

v) Re = 5.5×10^5;

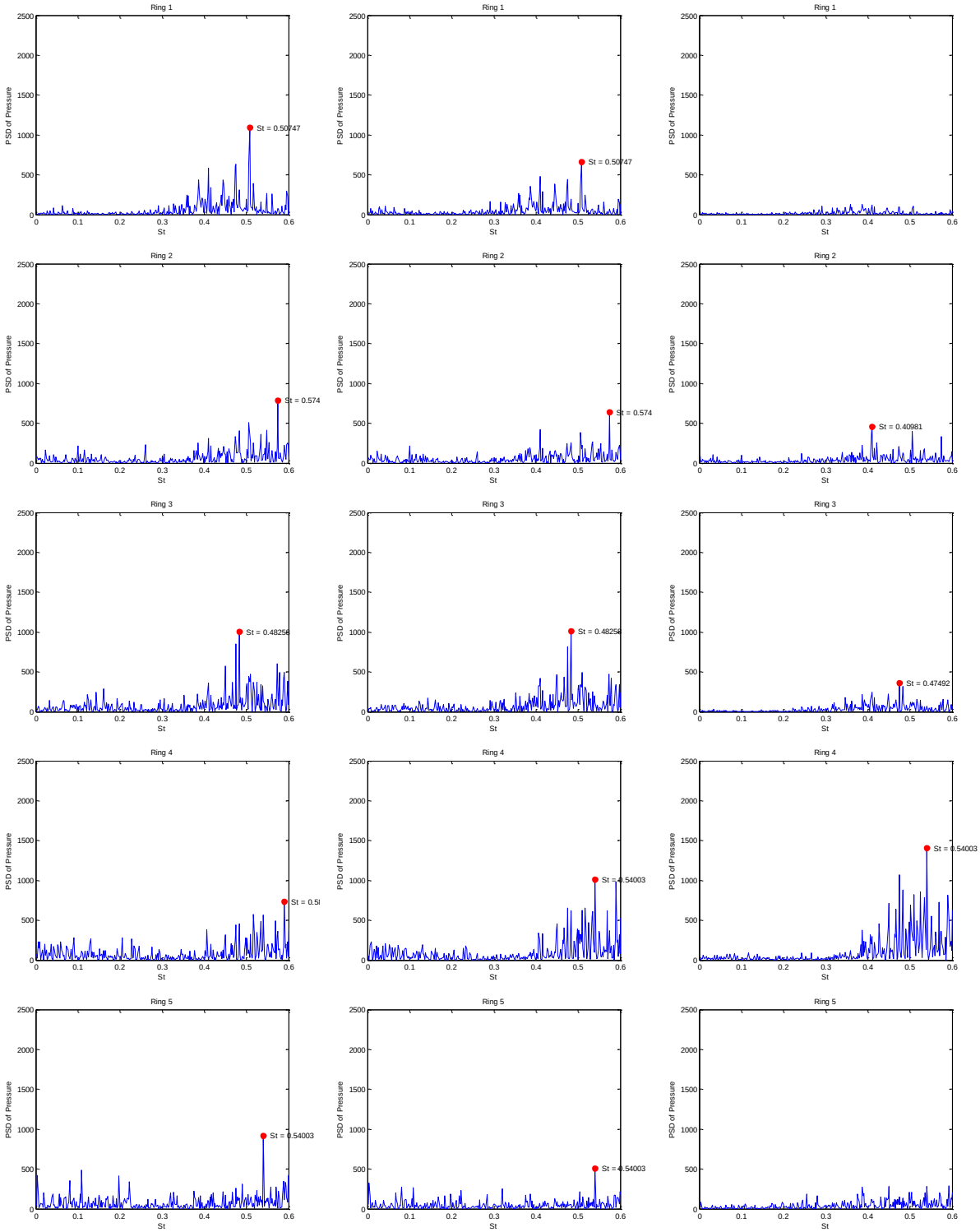


Figure N: FFT results Leeward Points:

j) $\phi = 35.5°$; $\alpha = 30°$, $\beta = 20°$

ii) Re = 2.2×10^5;

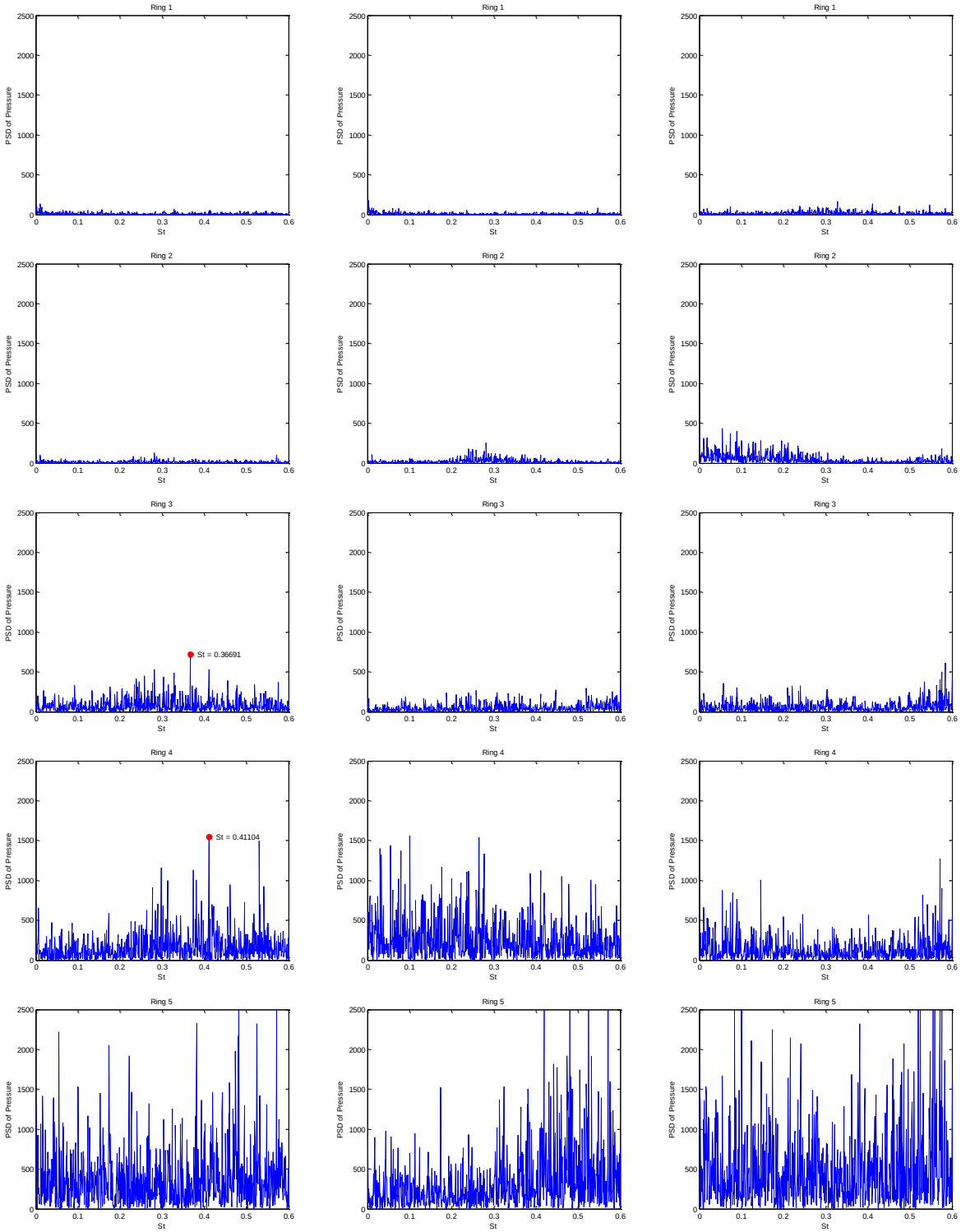


Figure N: FFT results Leeward Points:

j) $\phi = 35.5°$; $\alpha = 30°$, $\beta = 20°$

iii) Re = 3.3×10^5;

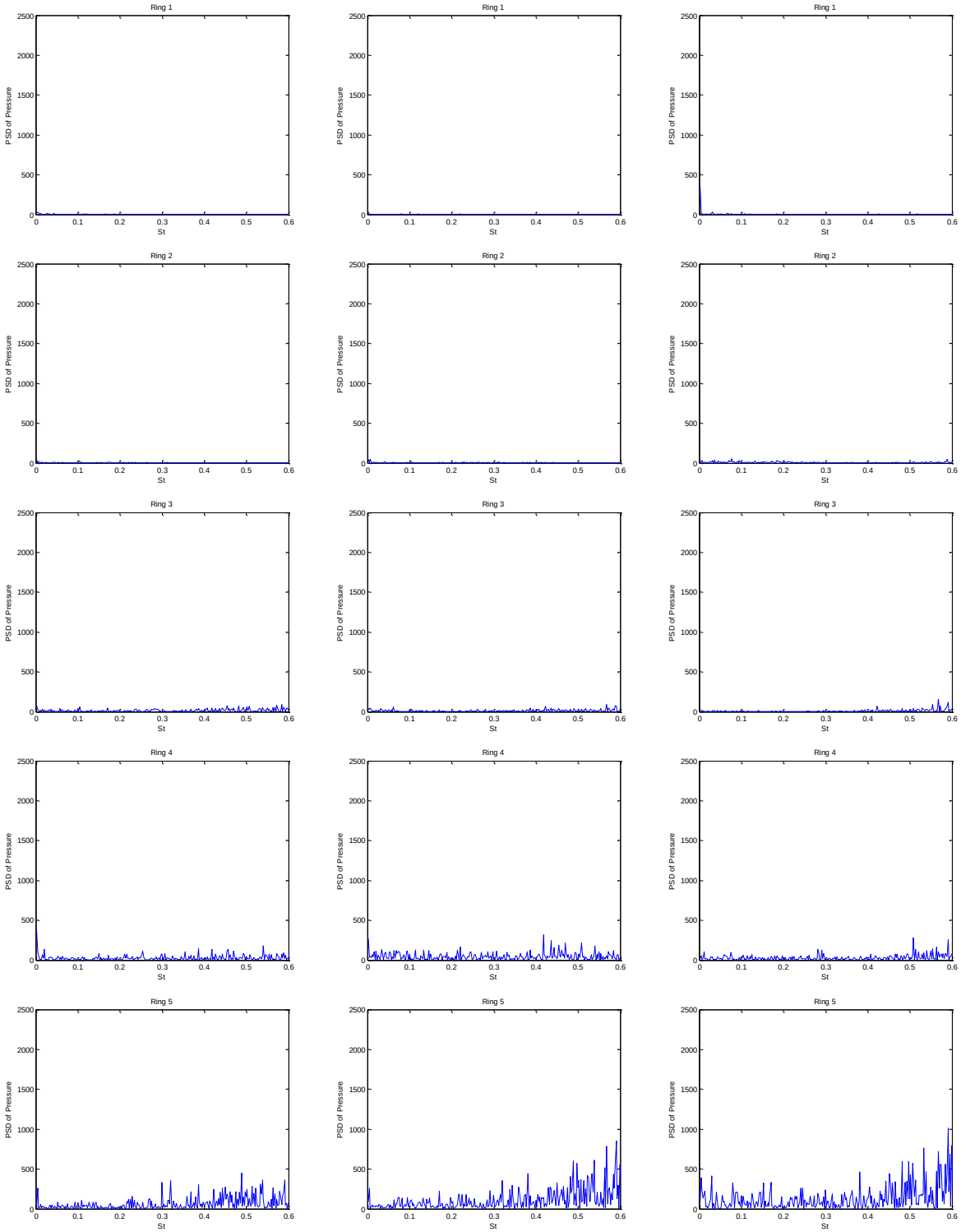


Figure N: FFT results Leeward Points:

j) $\phi = 35.5°$; $\alpha = 30°$, $\beta = 20°$

iv) Re = 4.4×10^5;

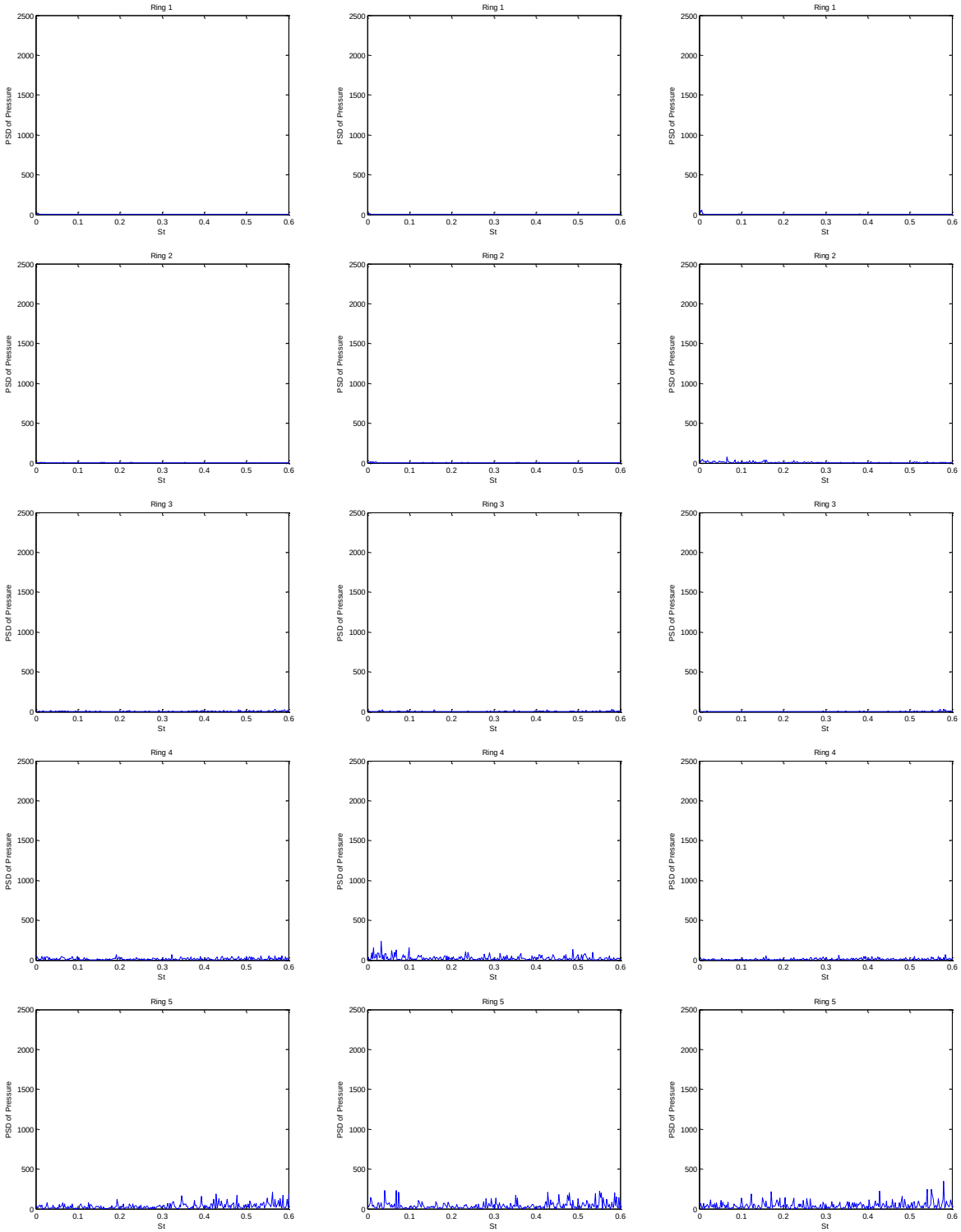
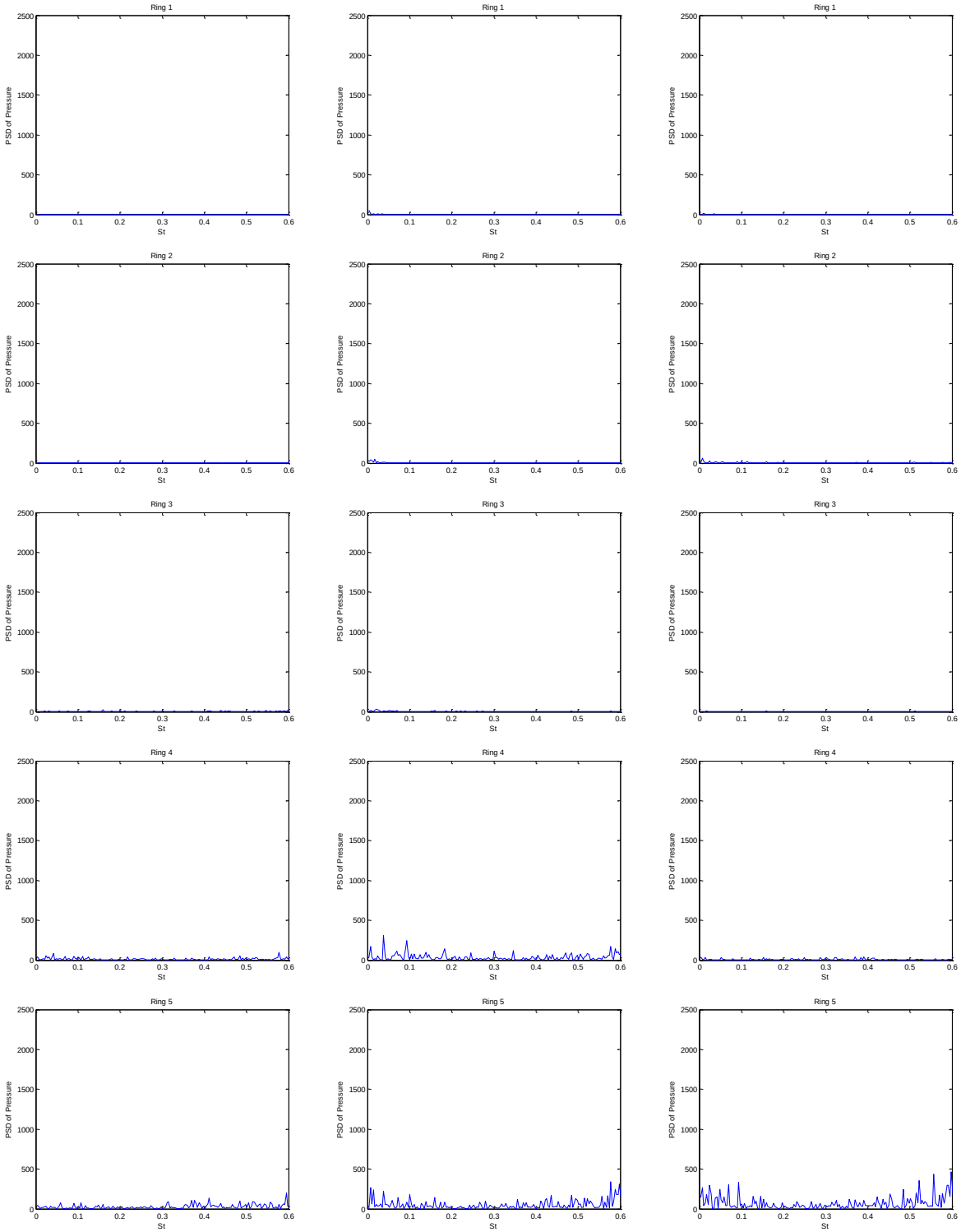


Figure N: FFT results Leeward Points:

j) $\phi = 35.5°$; $\alpha = 30°$, $\beta = 20°$

v) Re = 5.5×10^5;



Appendix O: Fast Fourier Transform (FFT) Results for Leeward Velocity

Figure O: FFT results Leeward Velocity:

a) $\phi = 0°$; $\alpha = 0°$, $\beta = 0°$

i) Re = 1.1×10^5;

Direction of Flow | Axial Flow | Total Velocity

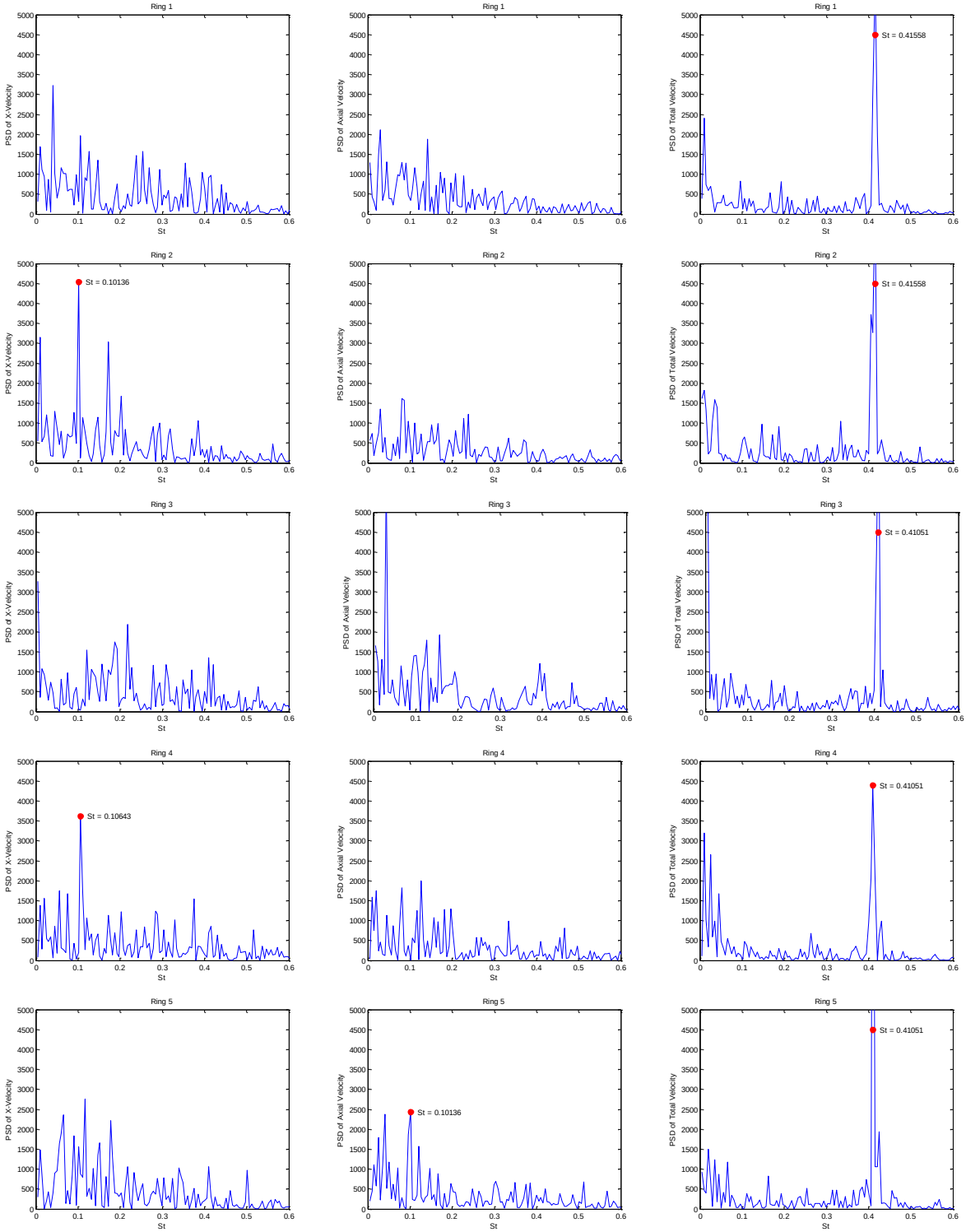


Figure O: FFT results Leeward Velocity:

a) $\phi = 0°$; $\alpha = 0°$, $\beta = 0°$

ii) Re = 2.2×10^5;

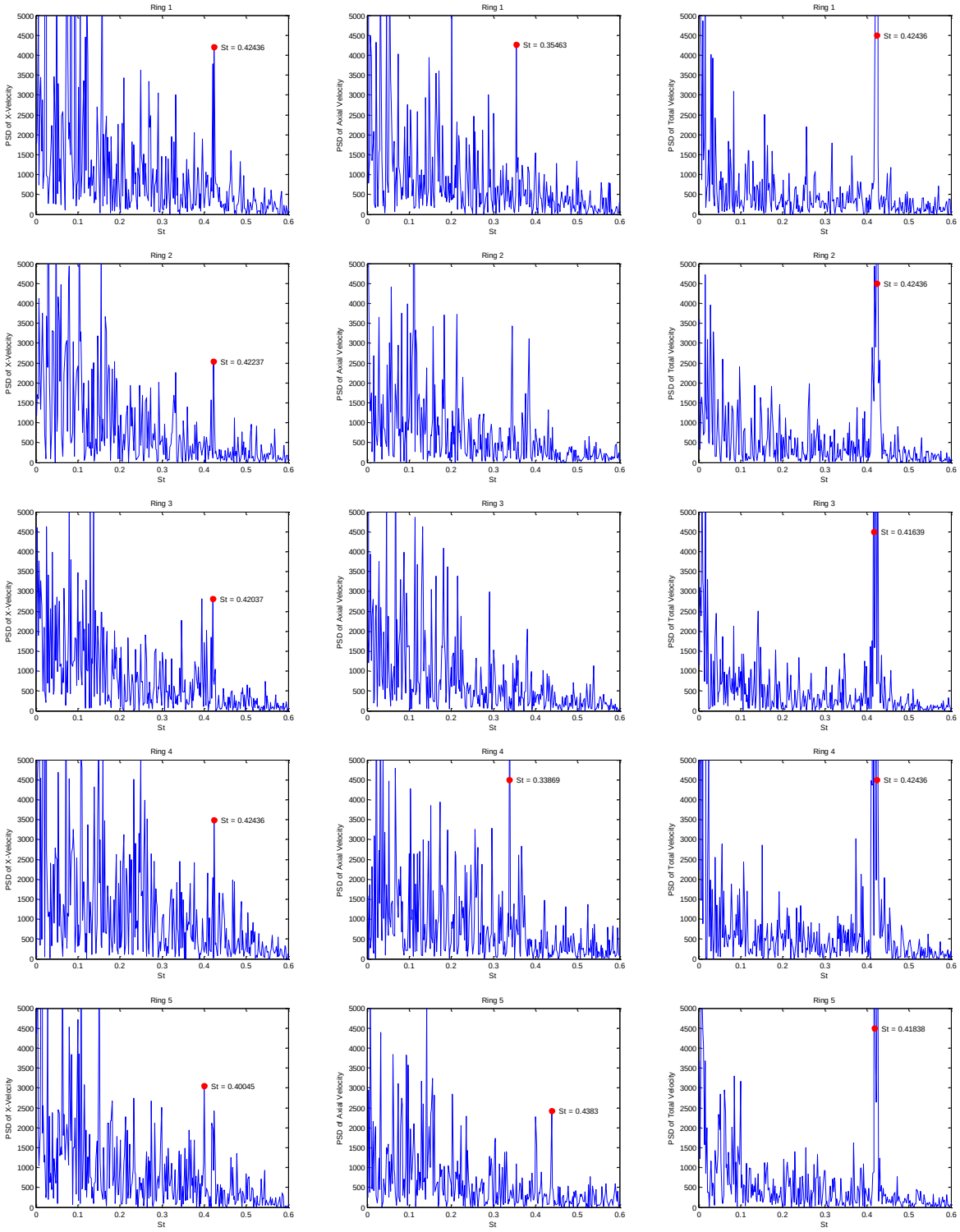


Figure O: FFT results Leeward Velocity:

a) $\phi = 0°$; $\alpha = 0°$, $\beta = 0°$

iii) Re = 3.3×10^5;

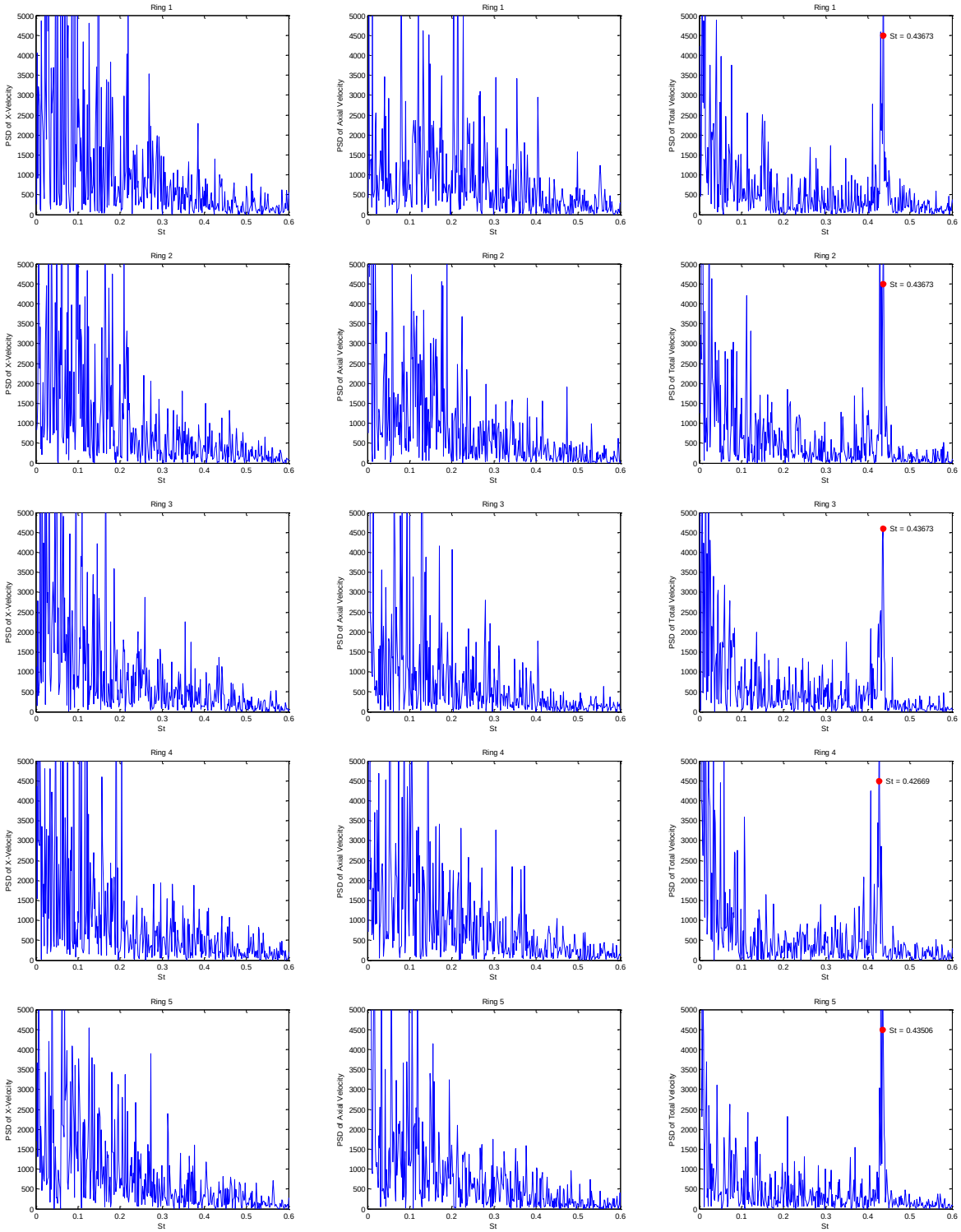


Figure O: FFT results Leeward Velocity:

a) $\phi = 0°$; $\alpha = 0°$, $\beta = 0°$

iv) Re = 4.4×10^5;

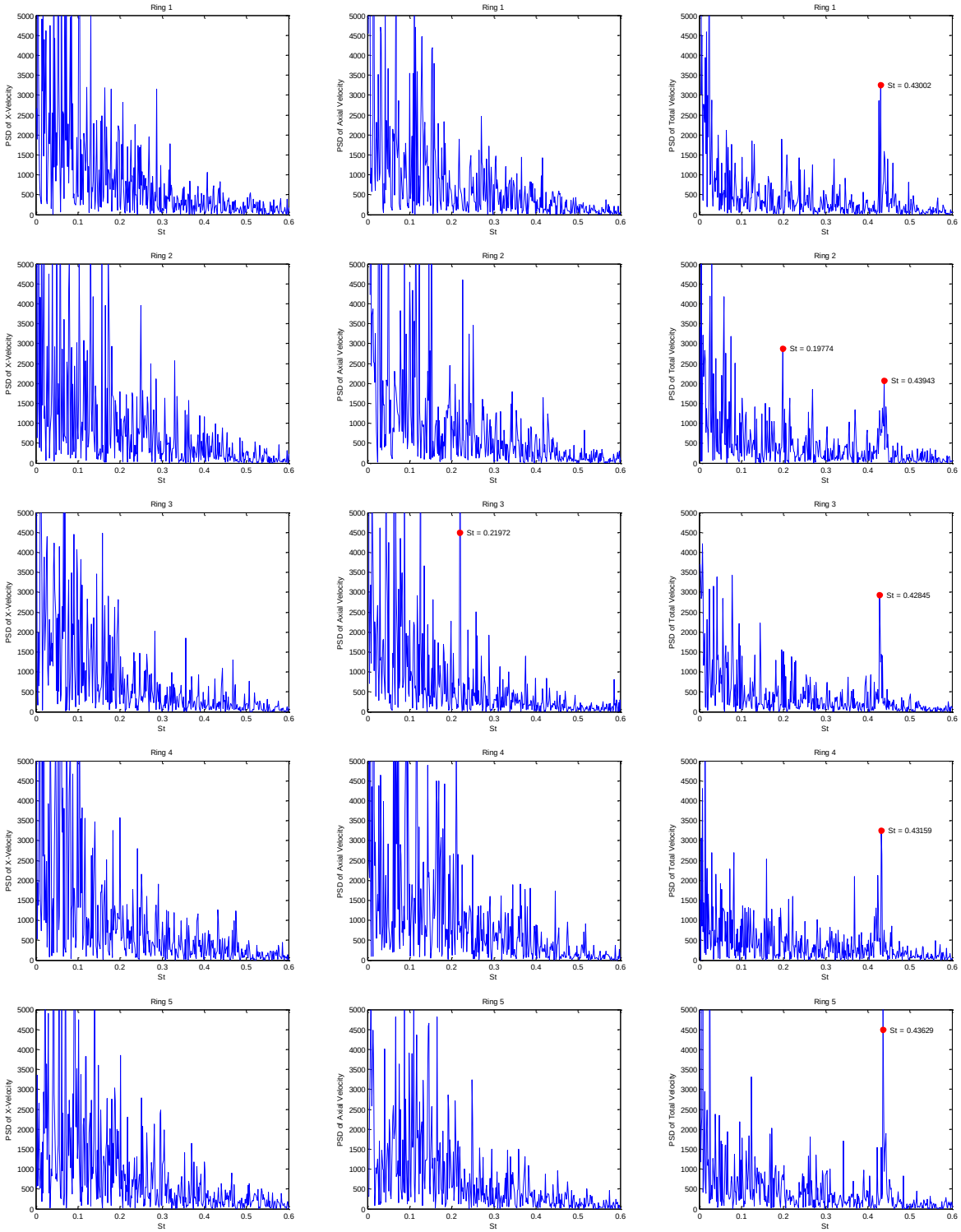


Figure O: FFT results Leeward Velocity:

a) $\phi = 0°$; $\alpha = 0°$, $\beta = 0°$

v) Re = 5.5×10^5;

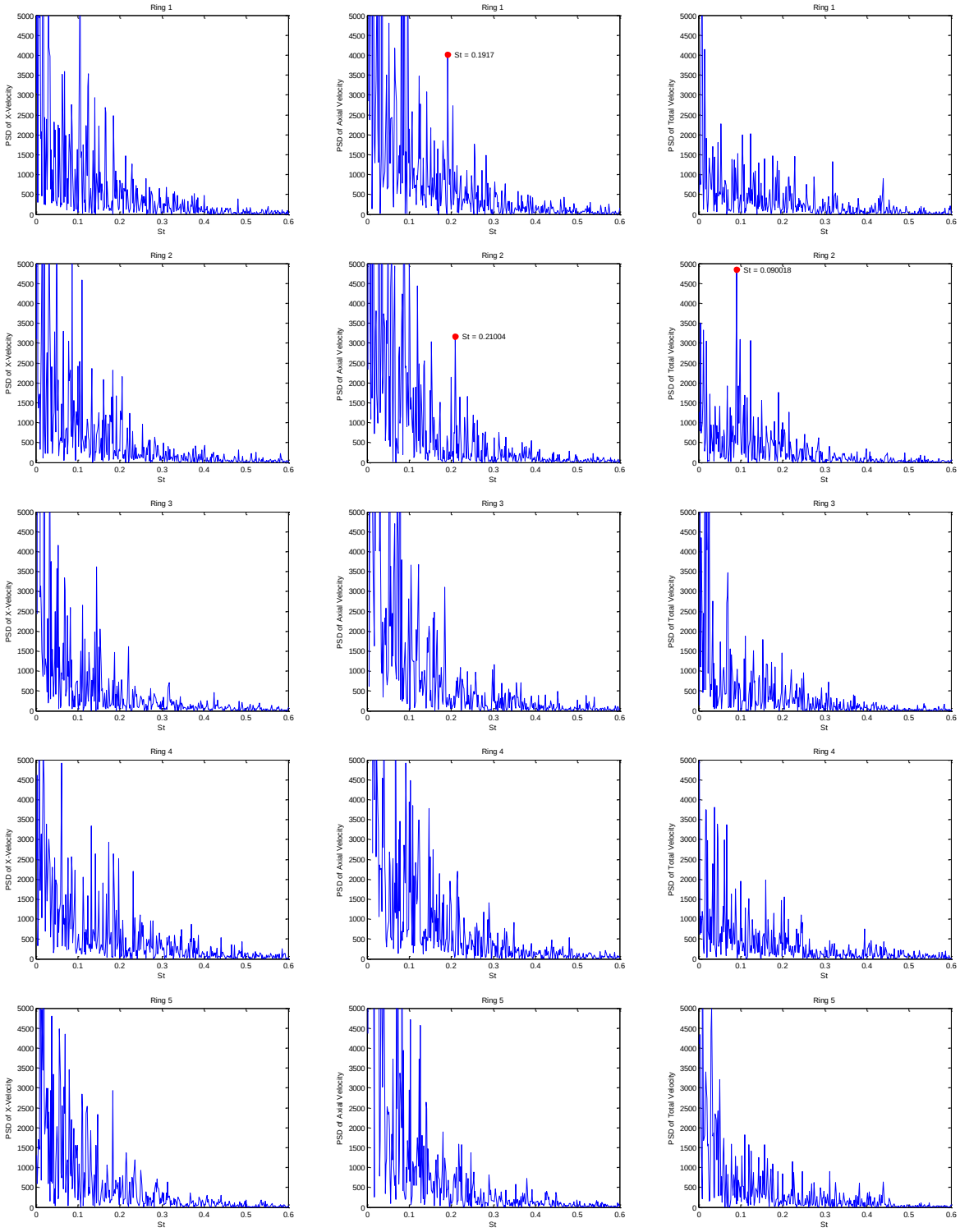


Figure O: FFT results Leeward Velocity:

a) $\phi = 0°$; $\alpha = 0°$, $\beta = 0°$

vi) Re = 6.7×10^5;

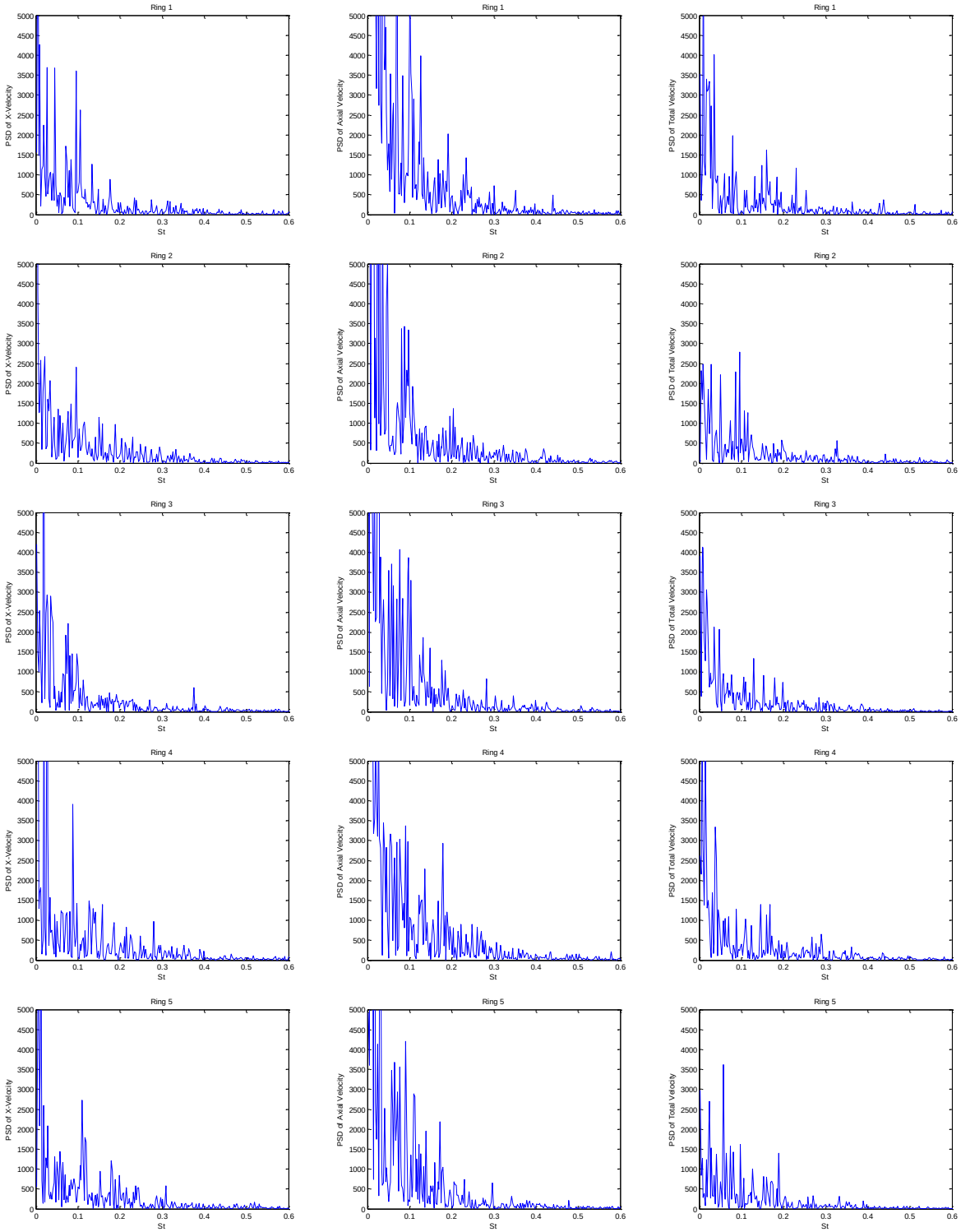


Figure O: FFT results Leeward Velocity:

b) $\phi = 60°$; $\alpha = 60°$, $\beta = 0°$

i) Re = 1.1×10^5;

Direction of Flow | Axial Flow | Total Velocity

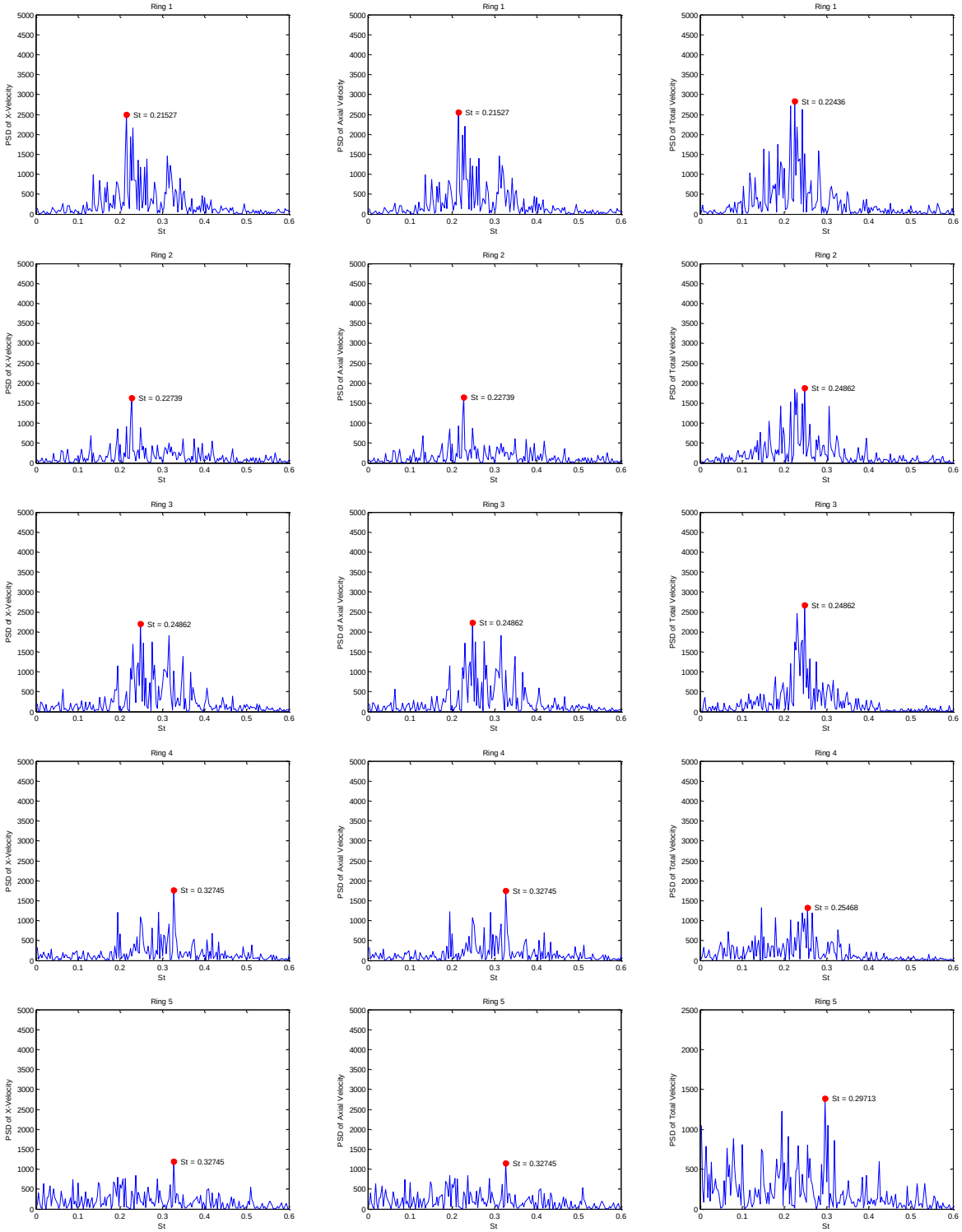


Figure O: FFT results Leeward Velocity:

b) $\phi = 60°$; $\alpha = 60°$, $\beta = 0°$

ii) Re = 2.2×10^5;

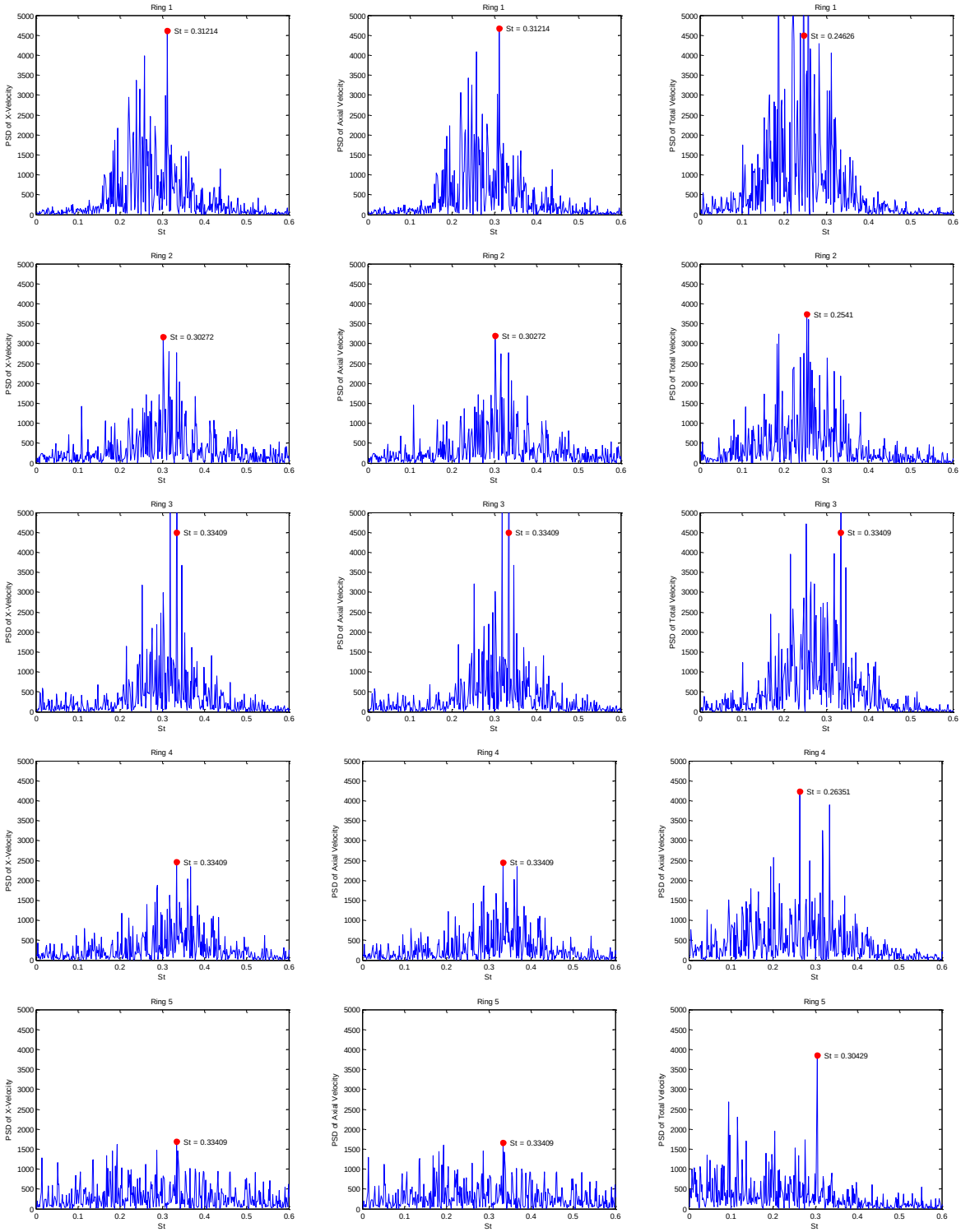


Figure O: FFT results Leeward Velocity:

b) $\phi = 60°$; $\alpha = 60°$, $\beta = 0°$

iii) Re = 3.3×10^5;

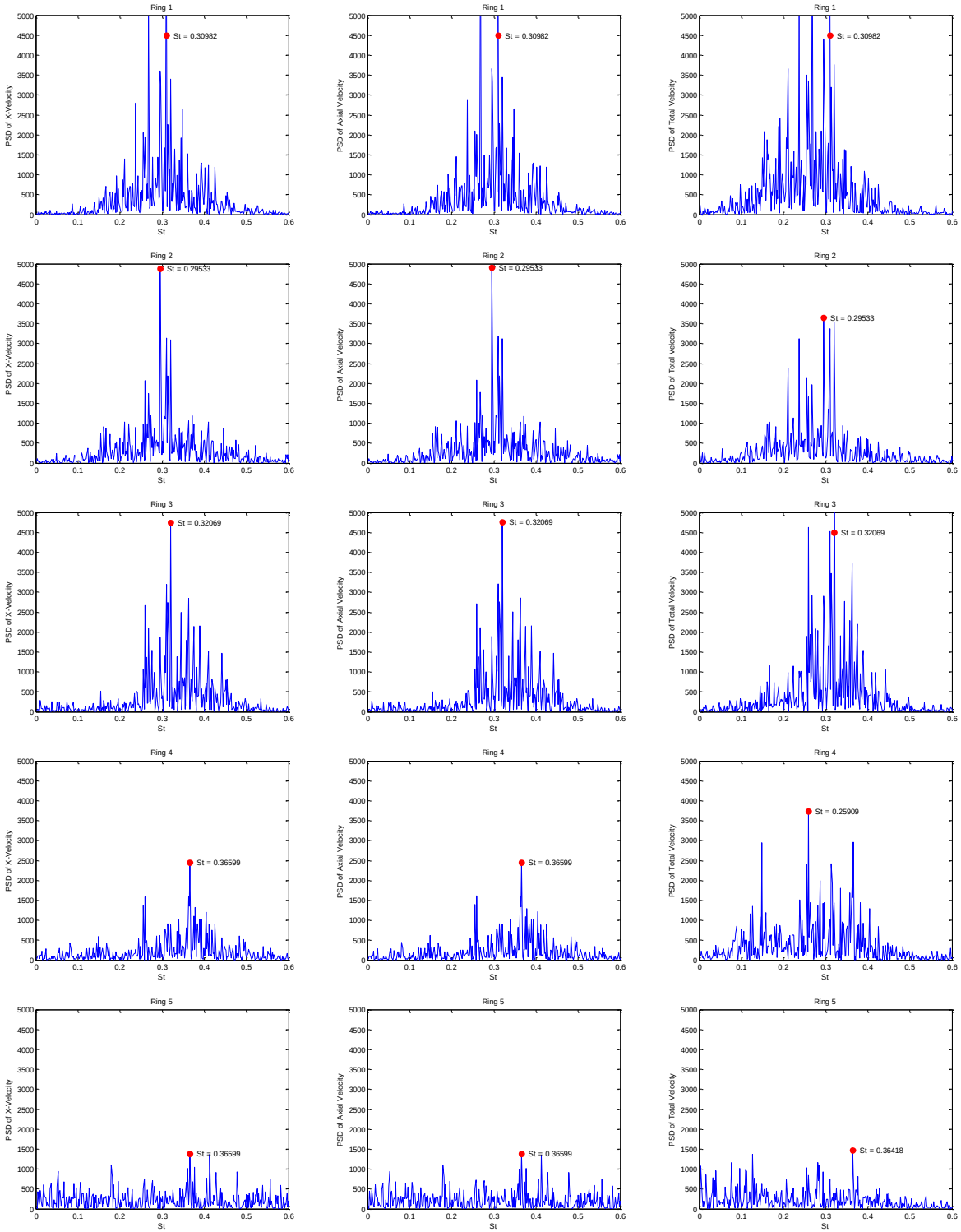


Figure O: FFT results Leeward Velocity:

b) $\phi = 60°$; $\alpha = 60°$, $\beta = 0°$

iv) Re = 4.4×10^5;

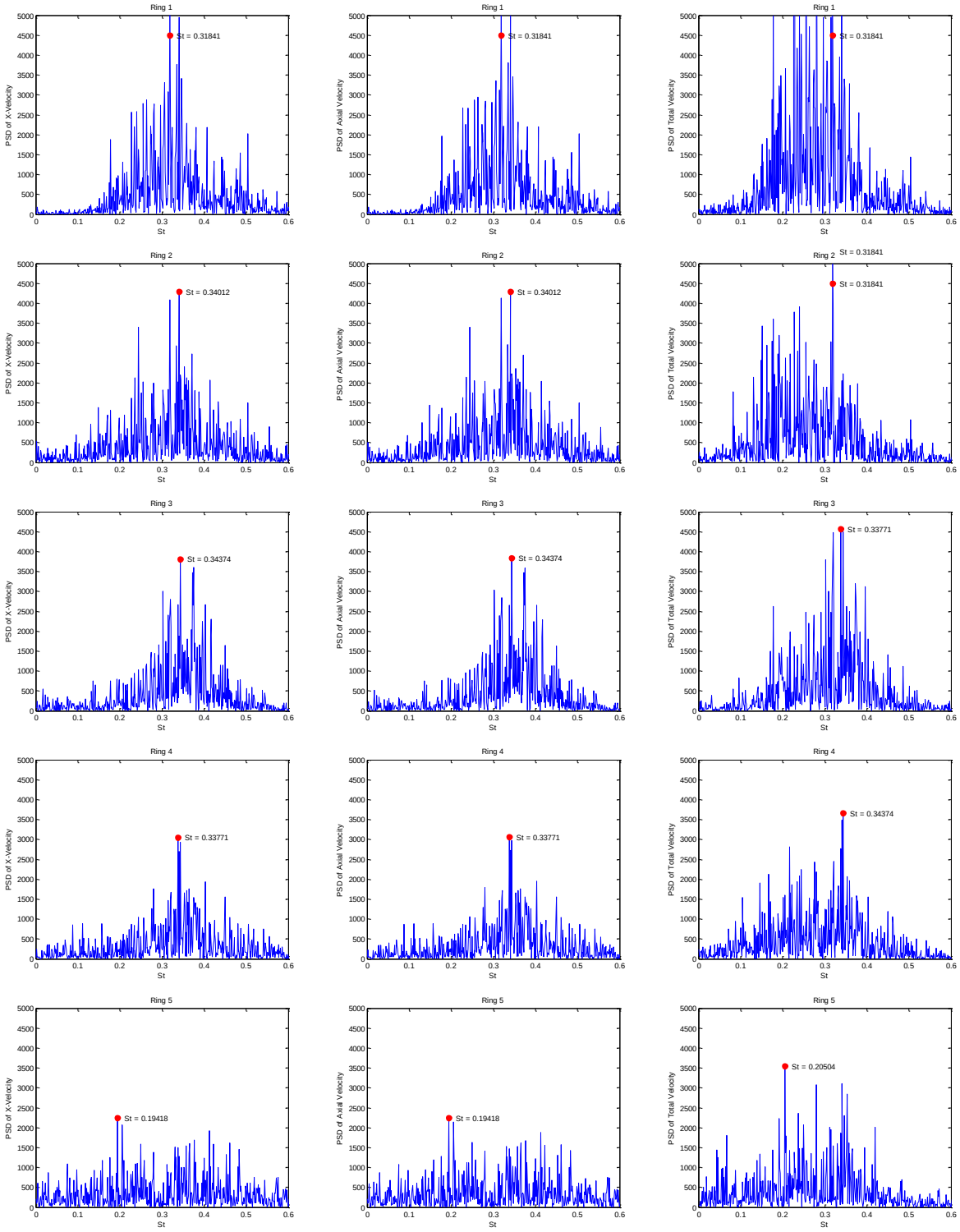


Figure O: FFT results Leeward Velocity:

b) $\phi = 60°$; $\alpha = 60°$, $\beta = 0°$

v) Re = 5.5×10^5;

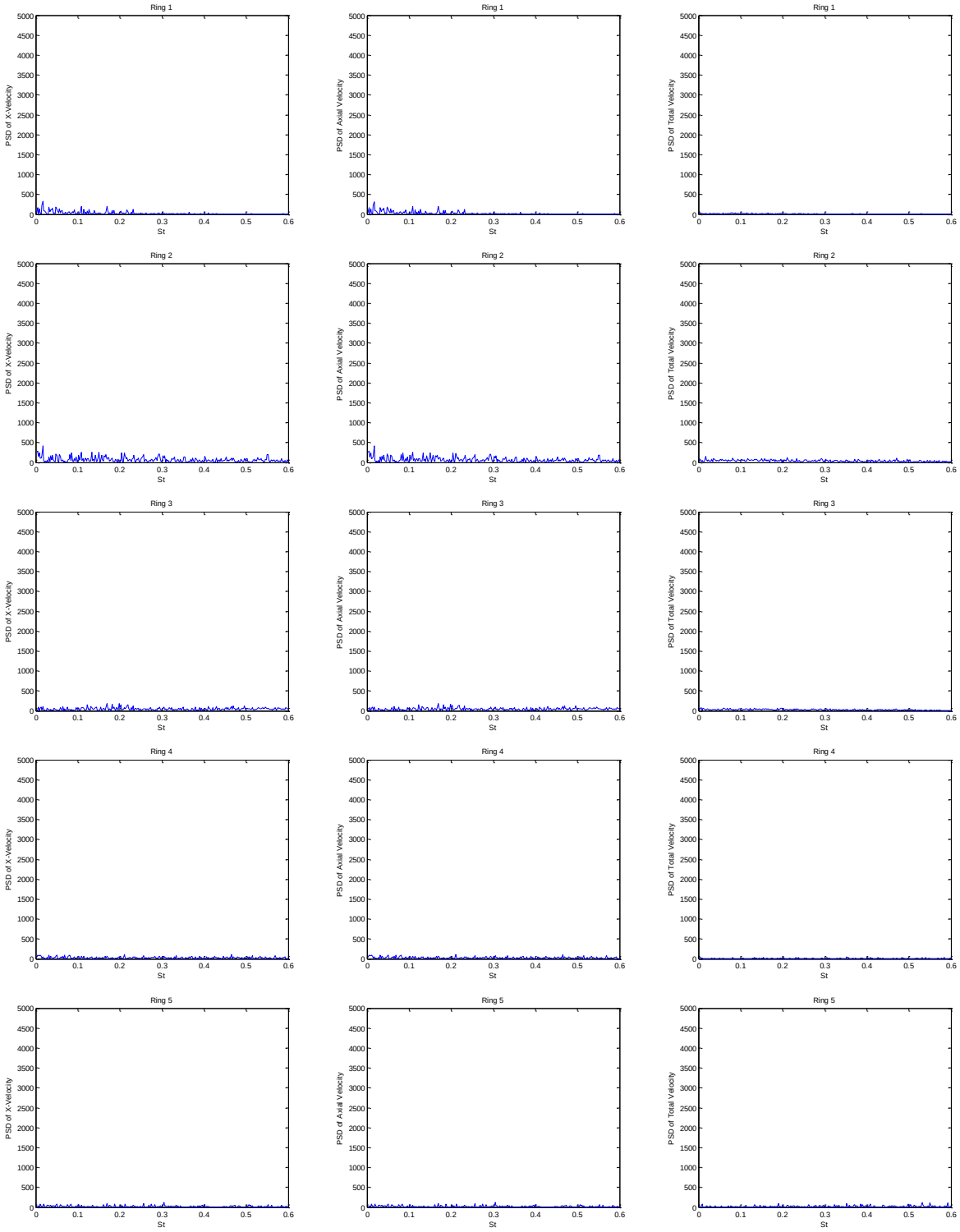


Figure O: FFT results Leeward Velocity:

b) $\phi = 60°$; $\alpha = 60°$, $\beta = 0°$

vi) Re = 6.7×10^5;

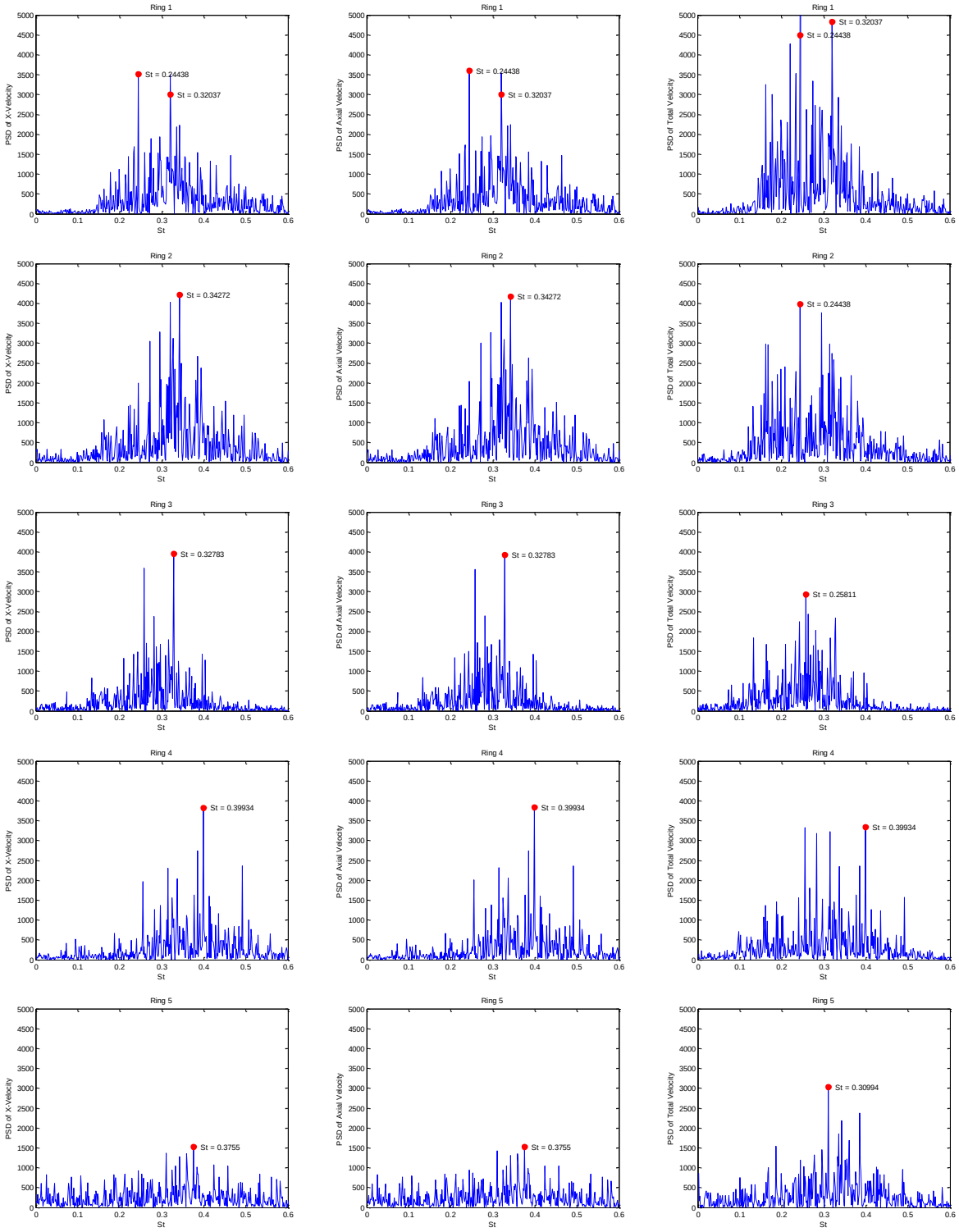


Figure O: FFT results Leeward Velocity:

c) $\phi = 62°$; $\alpha = 60°$, $\beta = 20°$

i) Re = 1.1×10^5;

Direction of Flow | Axial Flow | Total Velocity

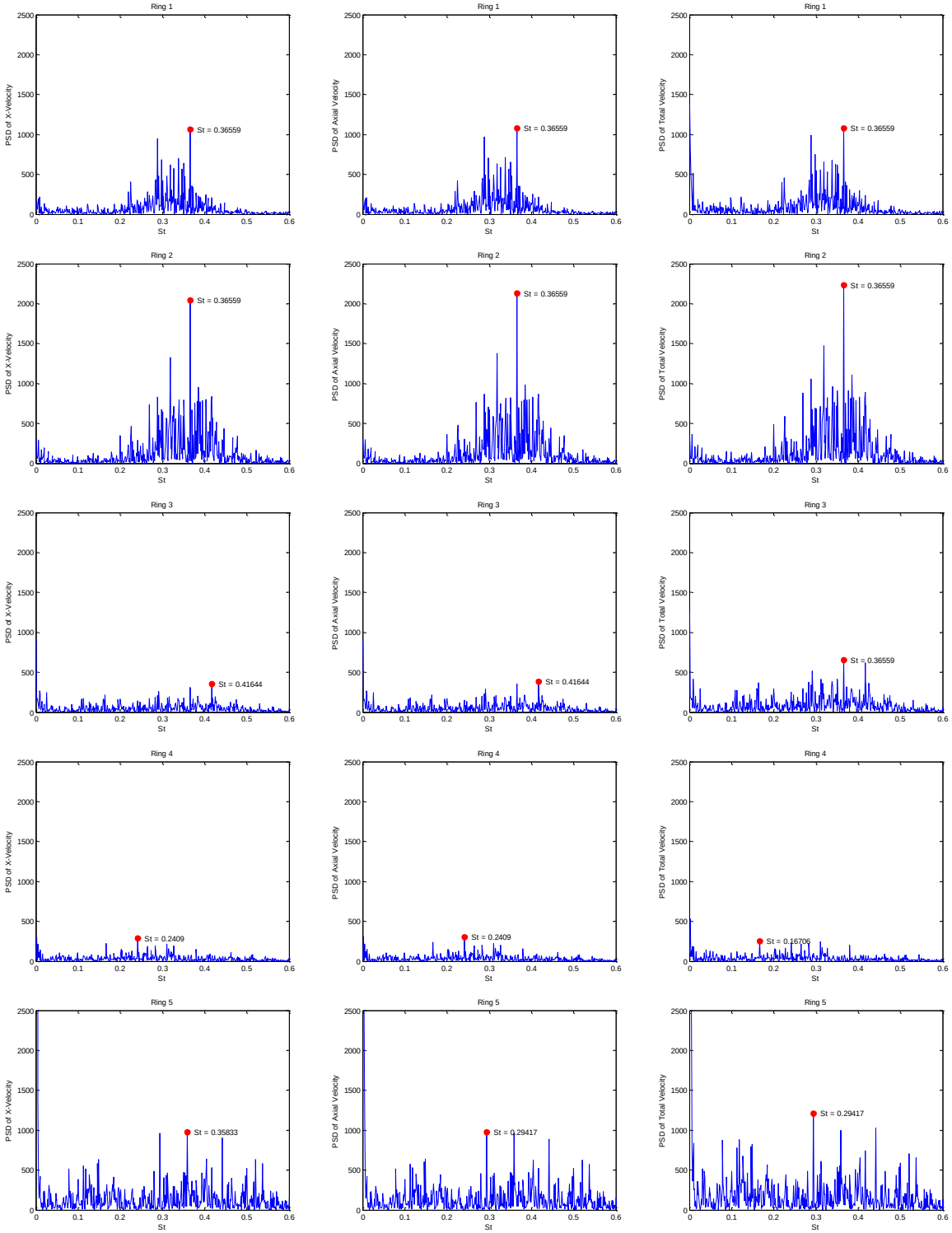


Figure O: FFT results Leeward Velocity:

c) $\phi = 62°$; $\alpha = 60°$, $\beta = 20°$

ii) Re = 2.2×10^5;

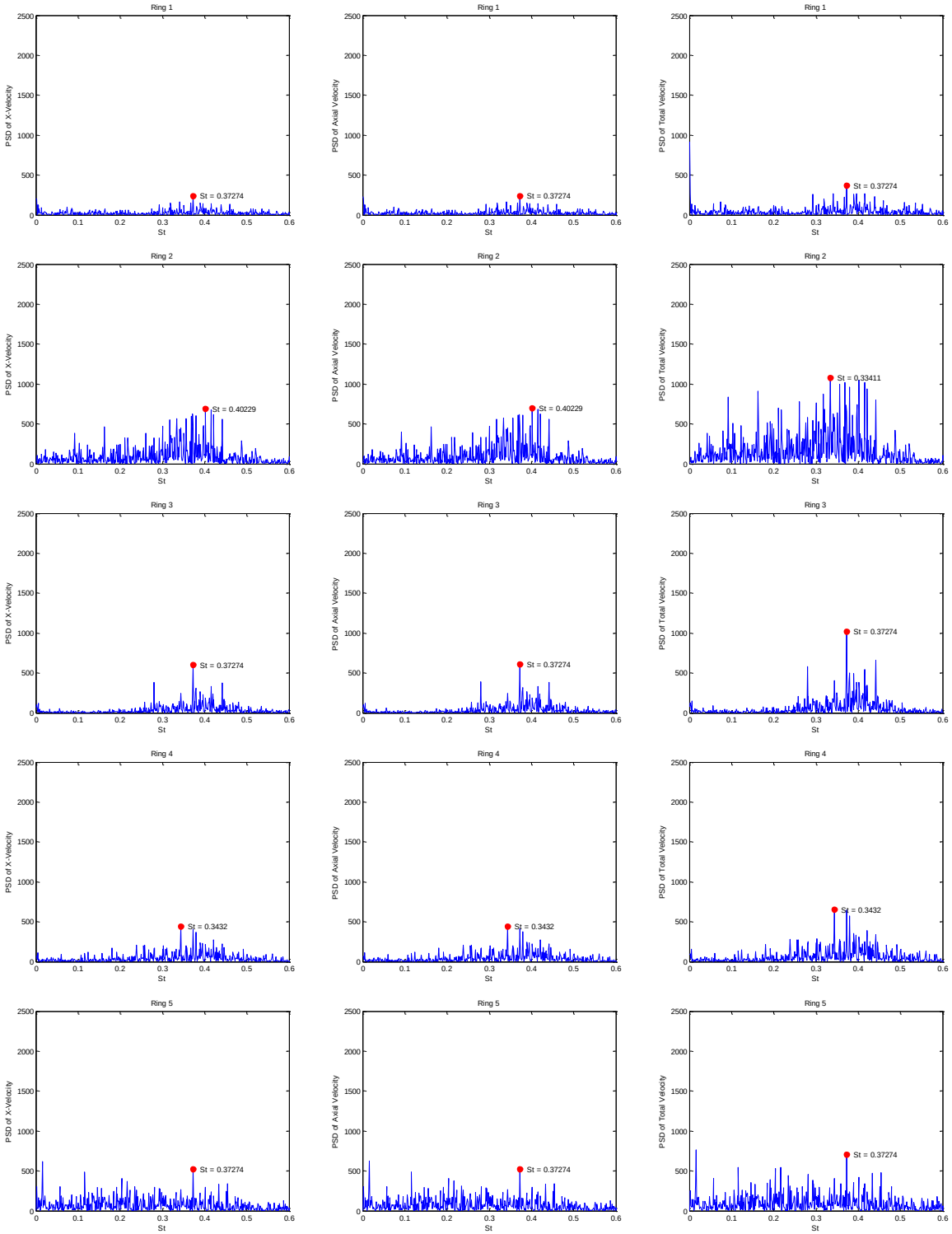


Figure O: FFT results Leeward Velocity:

c) $\phi = 62°$; $\alpha = 60°$, $\beta = 20°$

iii) Re = 3.3×10^5;

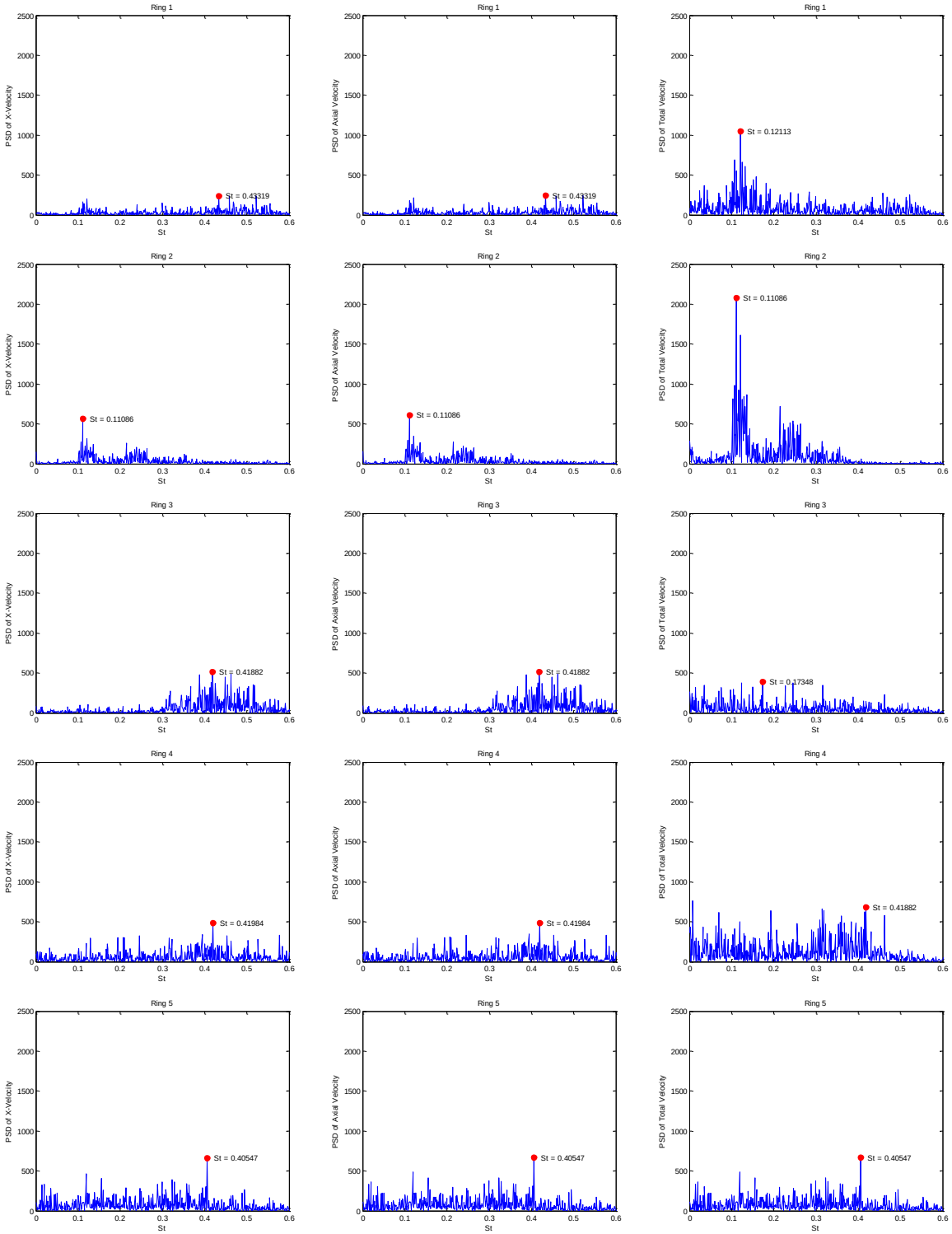


Figure O: FFT results Leeward Velocity:

c) $\phi = 62°$; $\alpha = 60°$, $\beta = 20°$

iv) Re = 4.4×10^5;

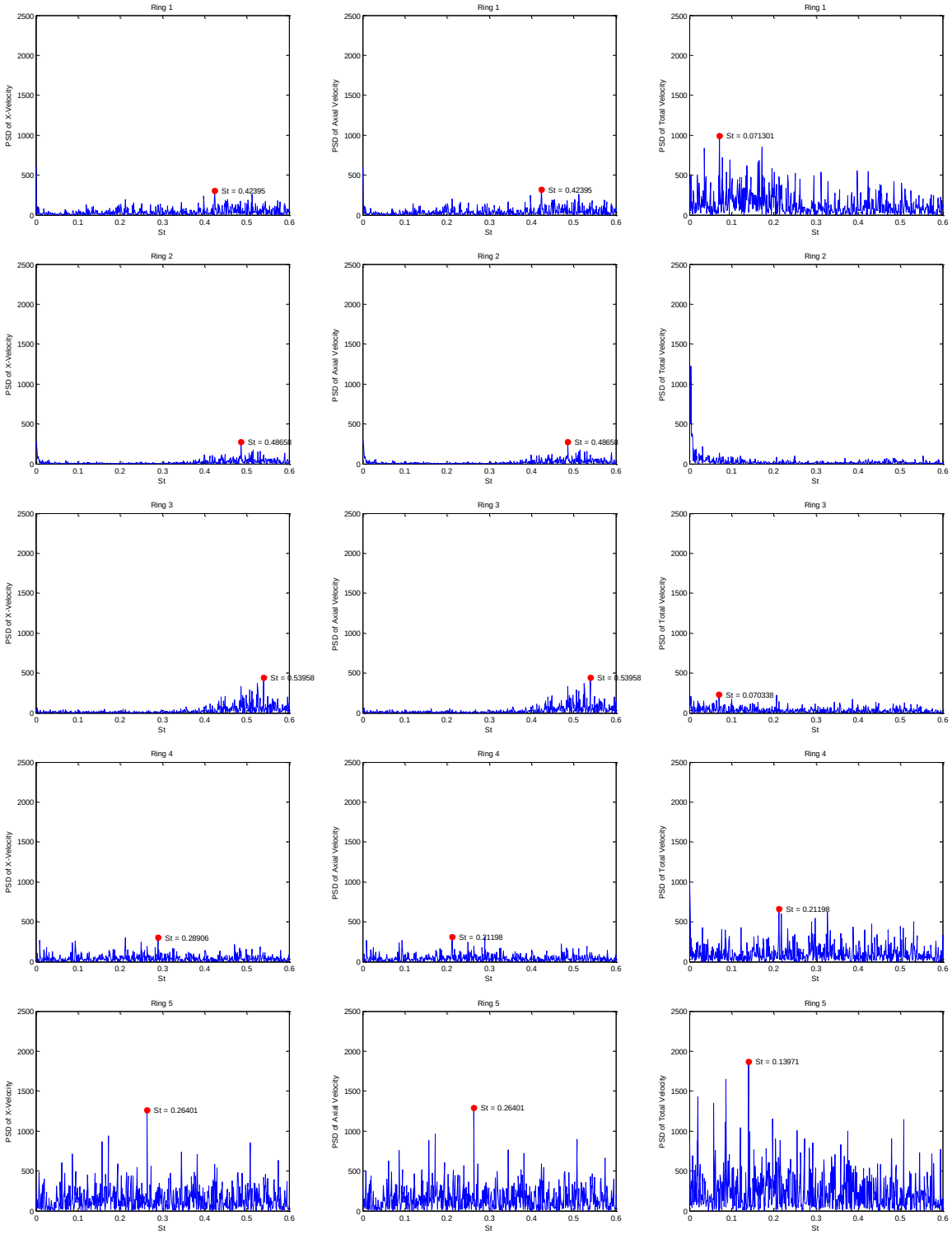


Figure O: FFT results Leeward Velocity:

c) $\phi = 62°$; $\alpha = 60°$, $\beta = 20°$

v) Re = 5.5×10^5;

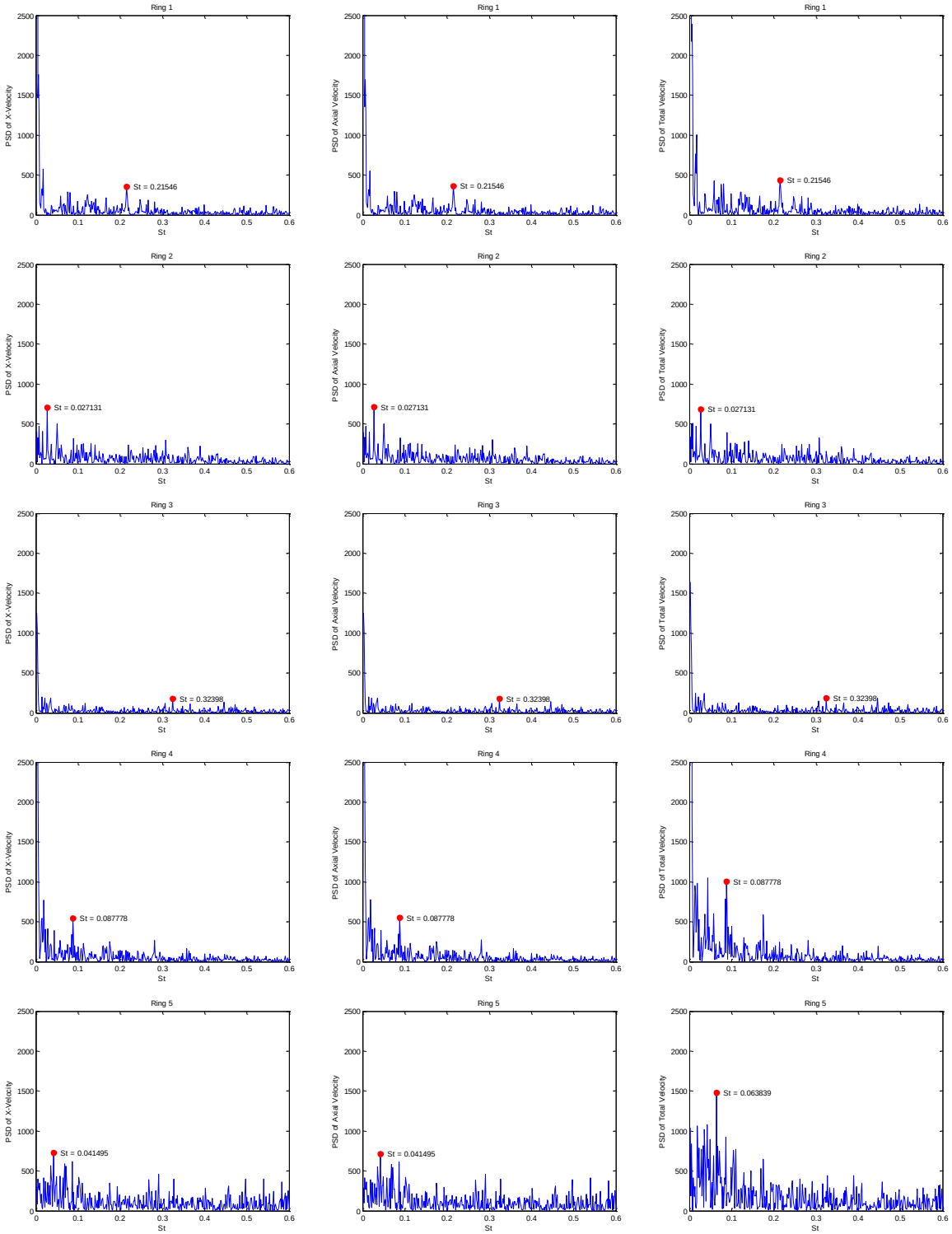


Figure O: FFT results Leeward Velocity:

d) $\phi = 67.5°$; $\alpha = 60°$, $\beta = 40°$

i) Re = 1.1×10^5;

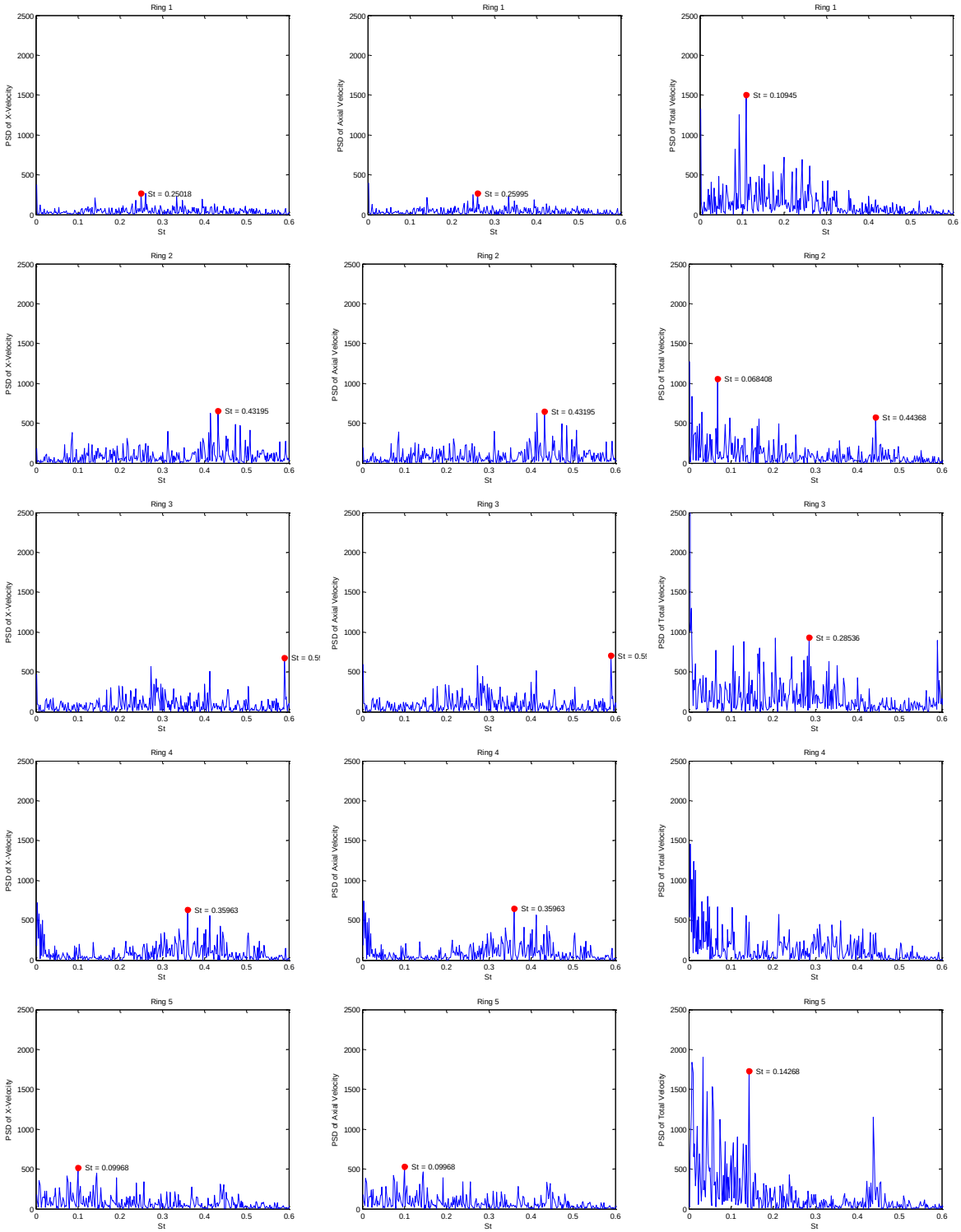


Figure O: FFT results Leeward Velocity:

d) $\phi = 67.5°$; $\alpha = 60°$, $\beta = 40°$

iii) Re = 3.3×10^5;

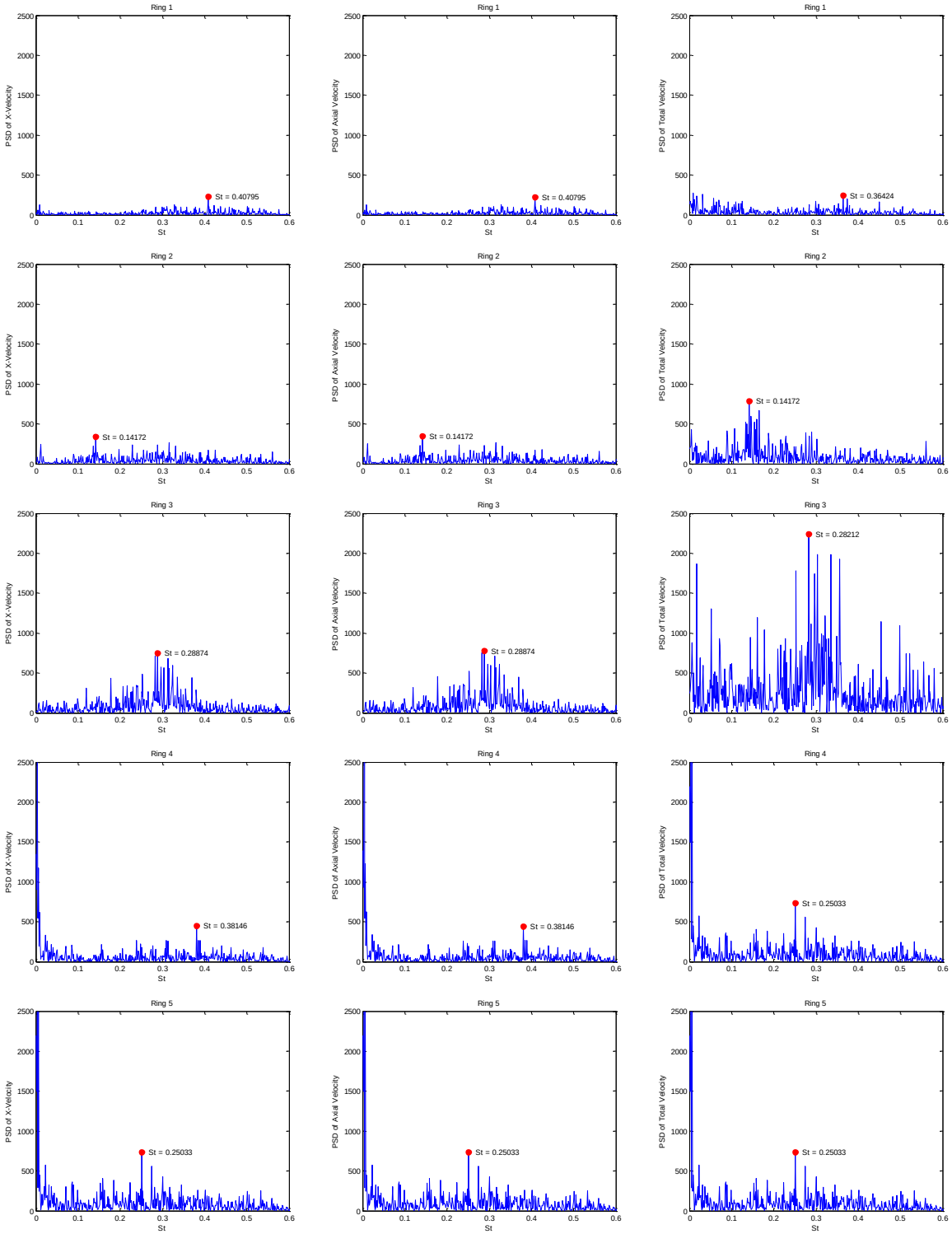


Figure O: FFT results Leeward Velocity:

d) $\phi = 67.5°$; $\alpha = 60°$, $\beta = 40°$

iv) Re = 4.4×10^5;

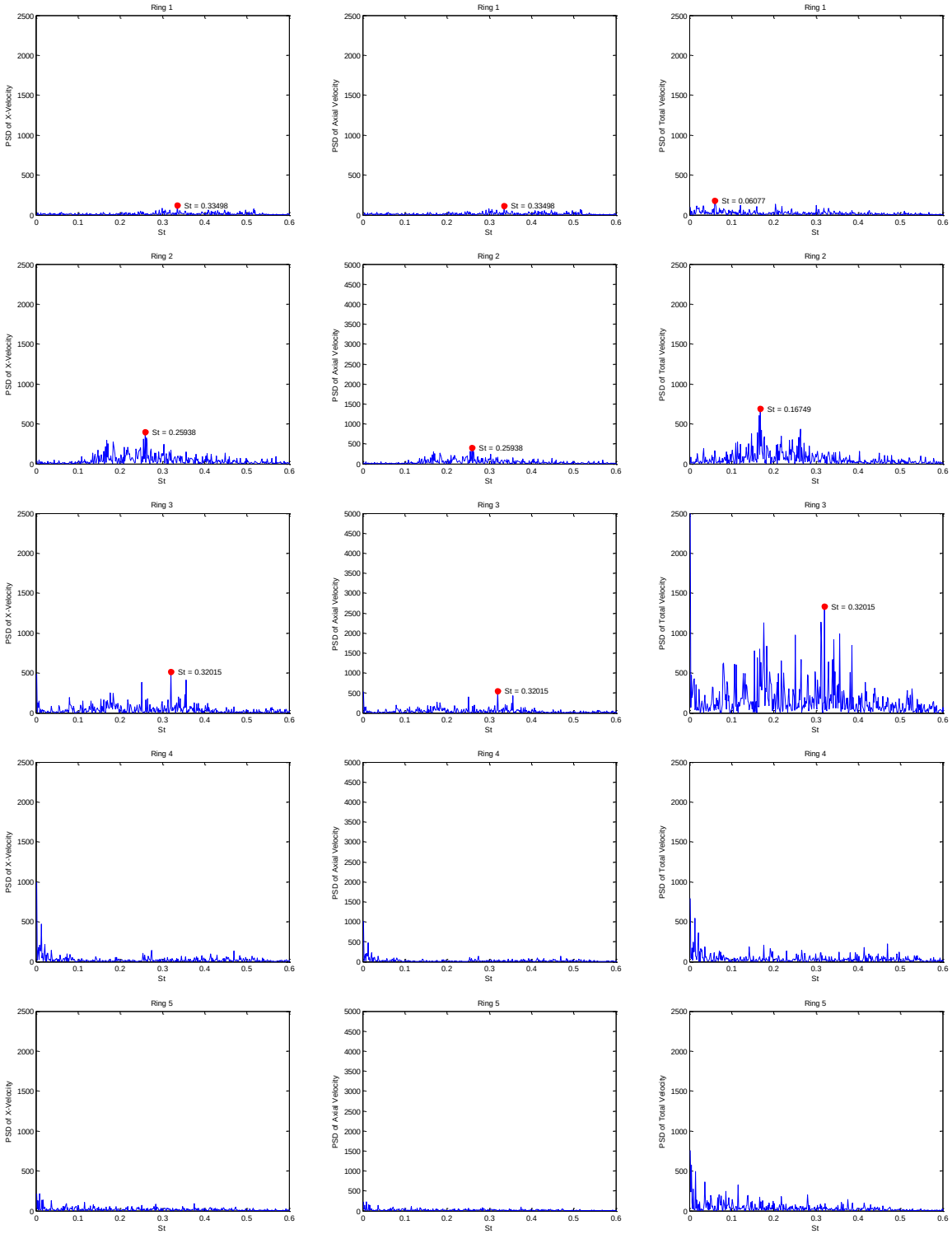


Figure O: FFT results Leeward Velocity:

d) $\phi = 67.5°$; $\alpha = 60°$, $\beta = 40°$

v) Re = 5.5×10^5;

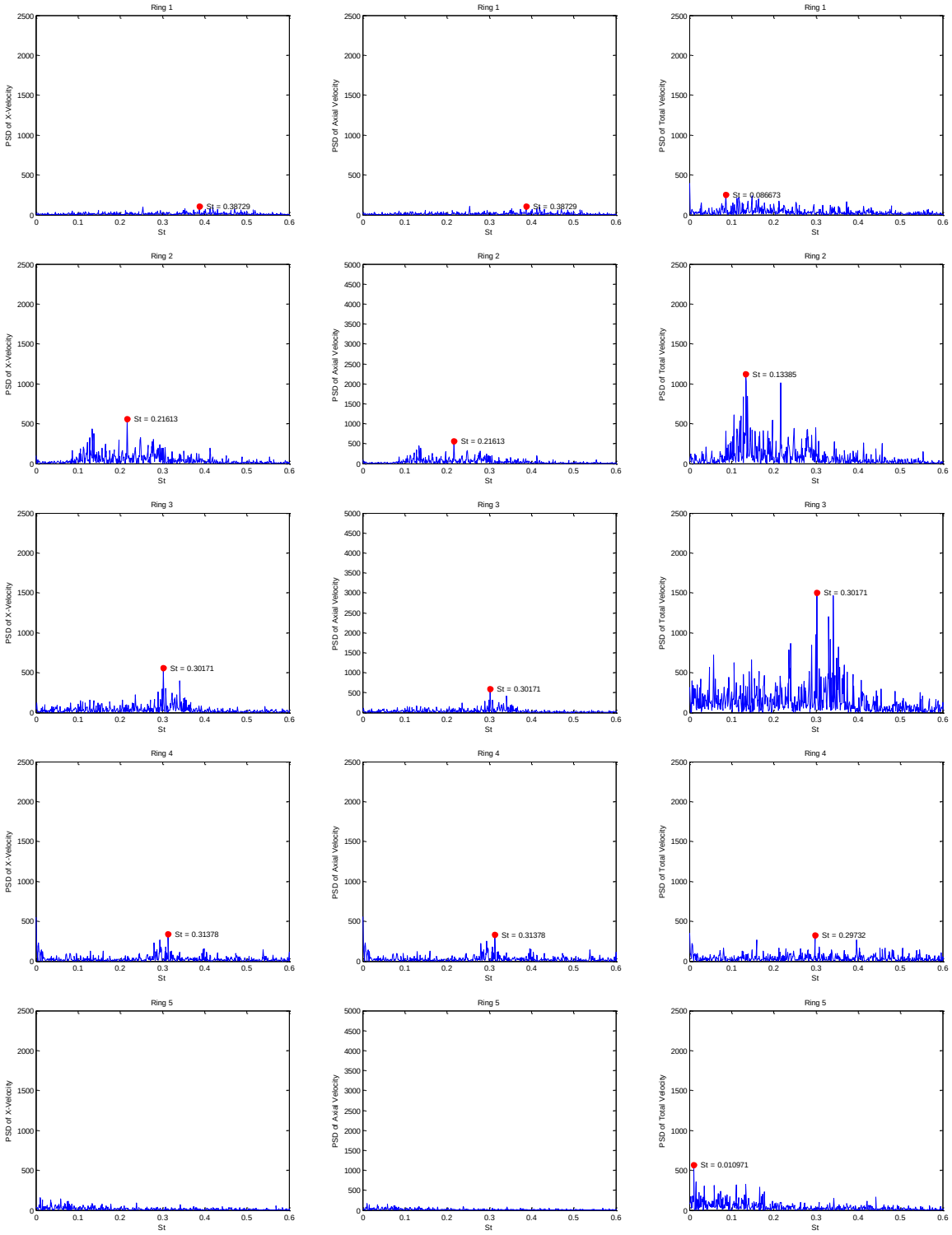


Figure O: FFT results Leeward Velocity:

e) $\phi = 54.7°$; $\alpha = 54.7°$, $\beta = 0°$

i) Re = 1.1×10^5;

Direction of Flow | Axial Flow | Total Velocity

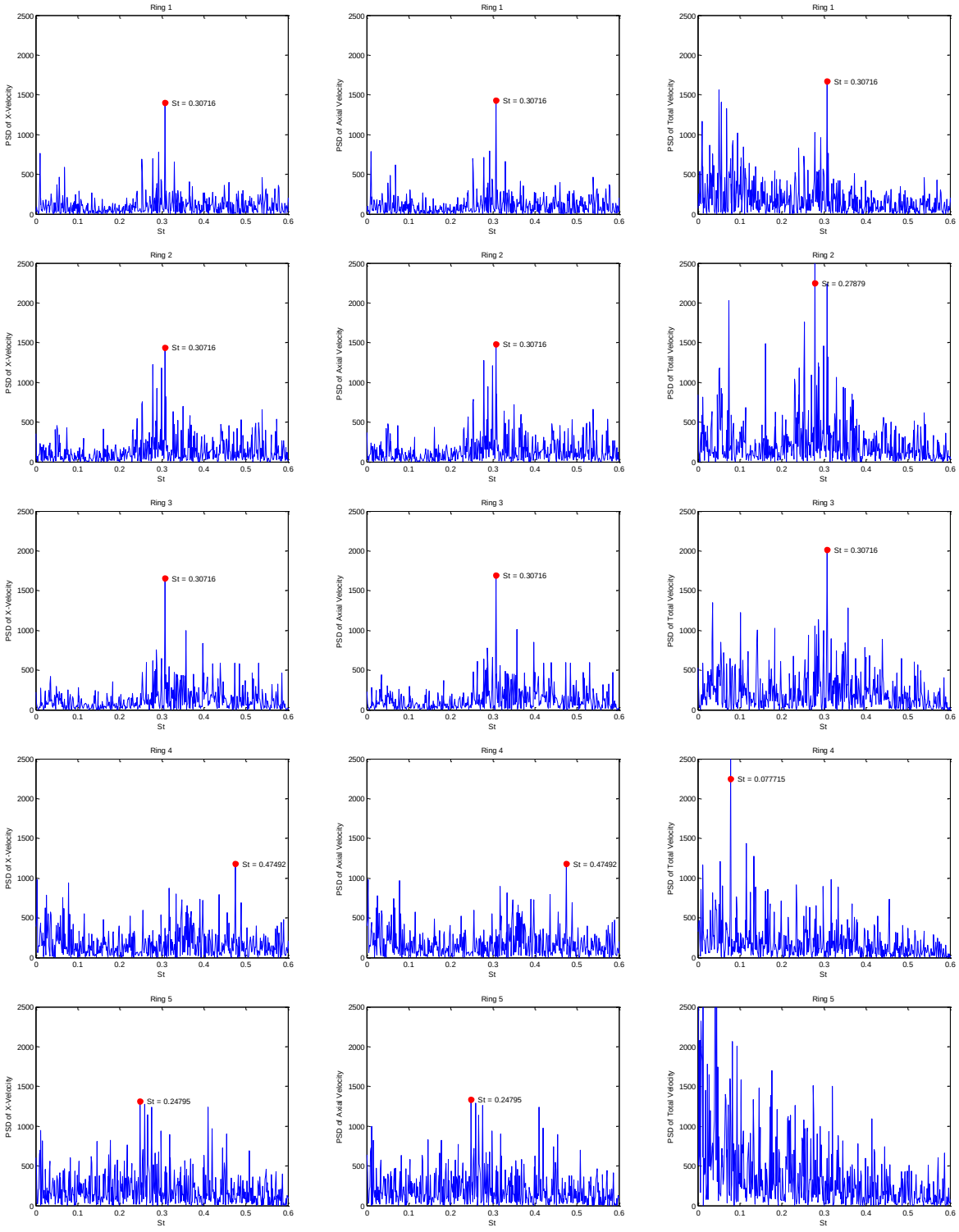


Figure O: FFT results Leeward Velocity:

e) $\phi = 54.7°$; $\alpha = 54.7°$, $\beta = 0°$

ii) Re = 2.2×10^5;

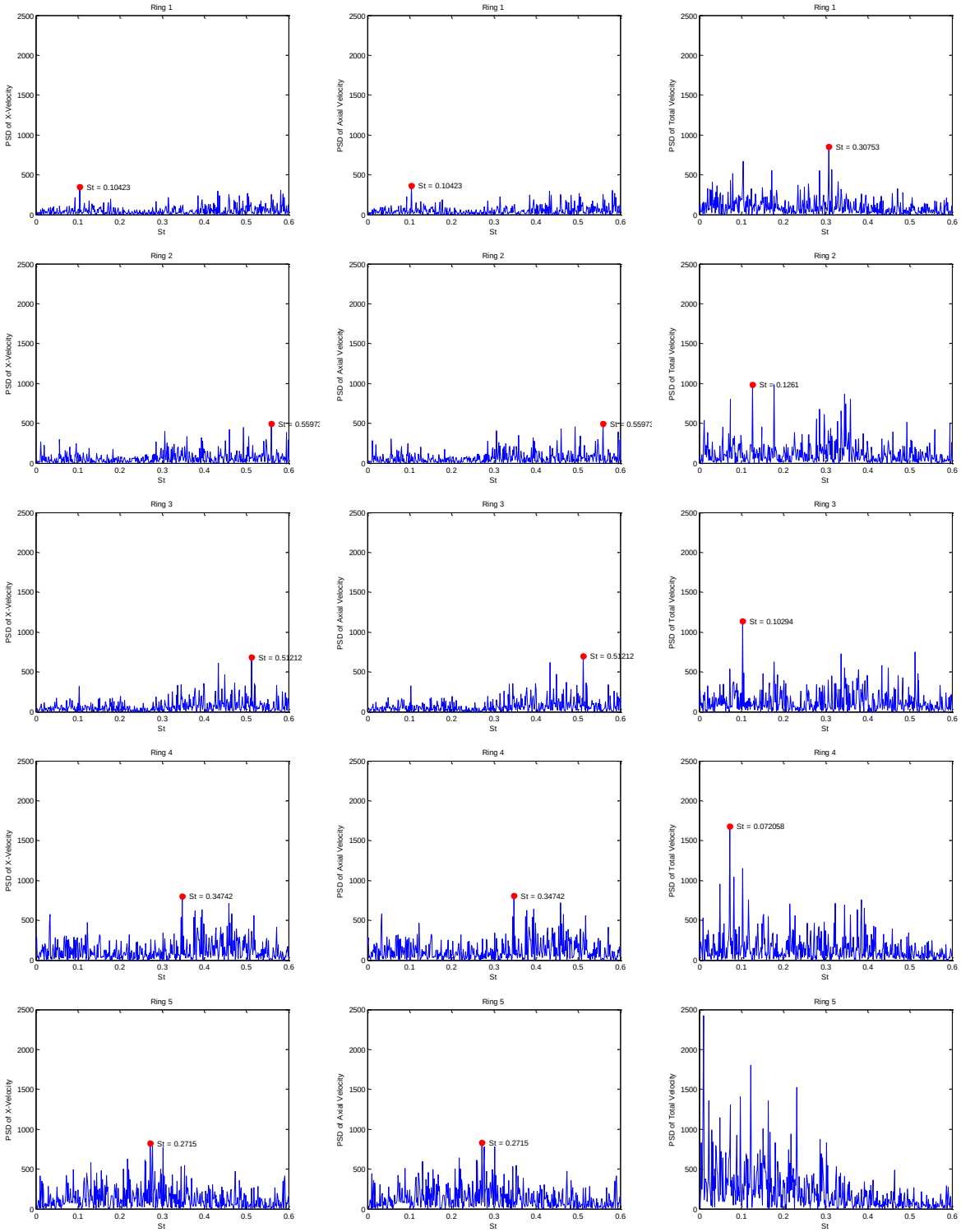


Figure O: FFT results Leeward Velocity:

e) $\phi = 54.7°$; $\alpha = 54.7°$, $\beta = 0°$

iii) Re = 3.3×10^5;

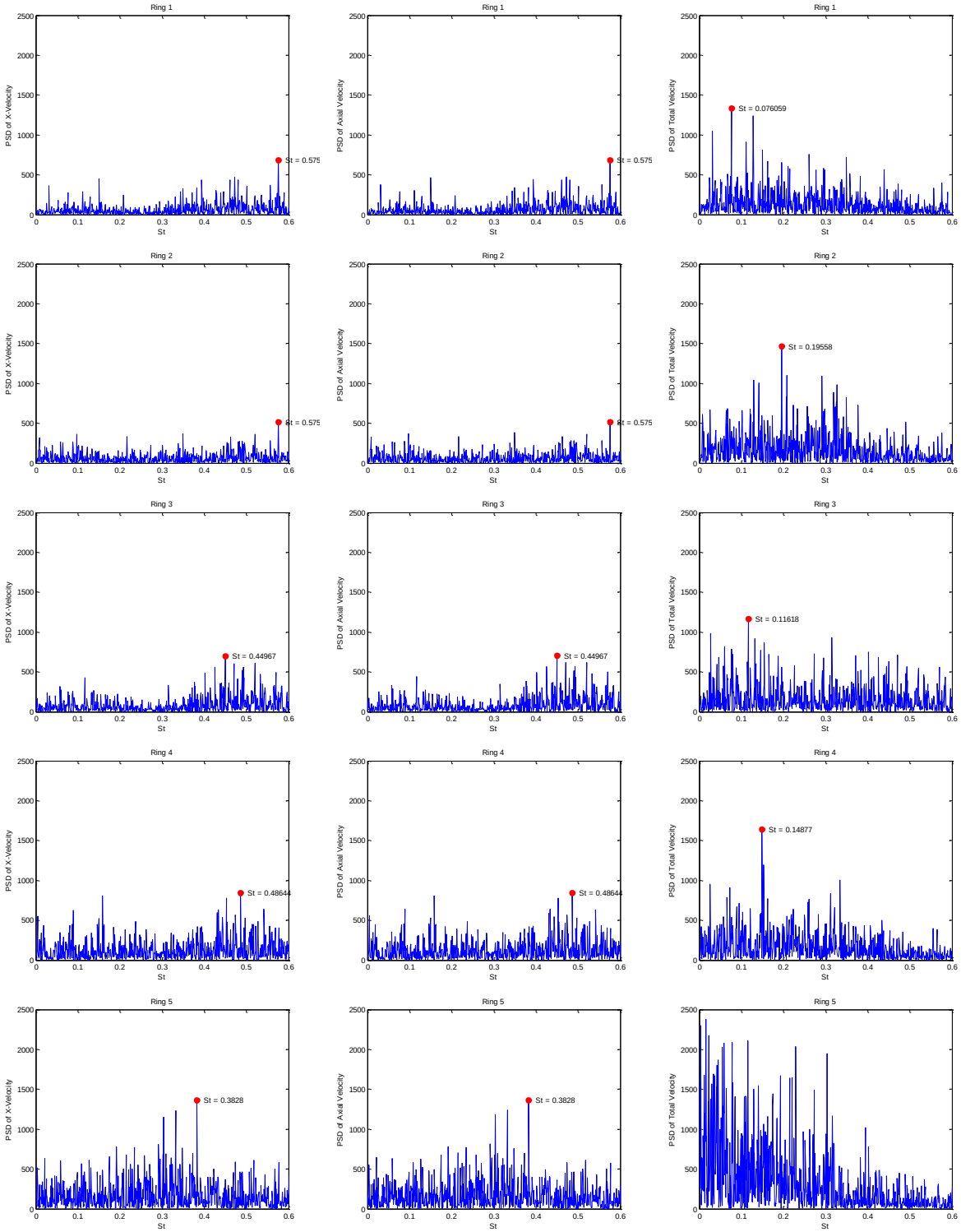


Figure O: FFT results Leeward Velocity:

e) $\phi = 54.7°$; $\alpha = 54.7°$, $\beta = 0°$

iv) Re = 4.4×10^5;

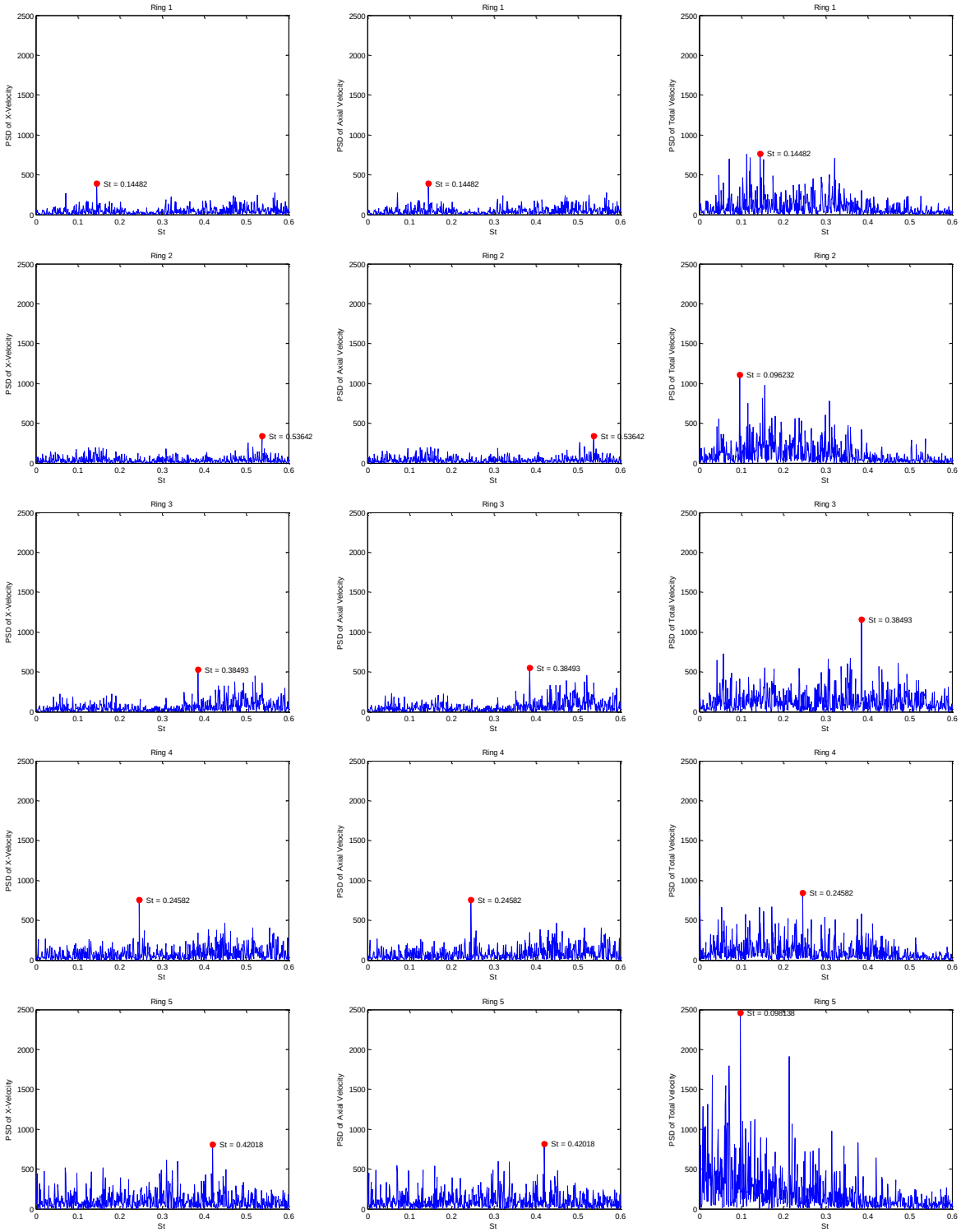


Figure O: FFT results Leeward Velocity:

e) $\phi = 54.7°$; $\alpha = 54.7°$, $\beta = 0°$

v) Re = 5.5×10^5;

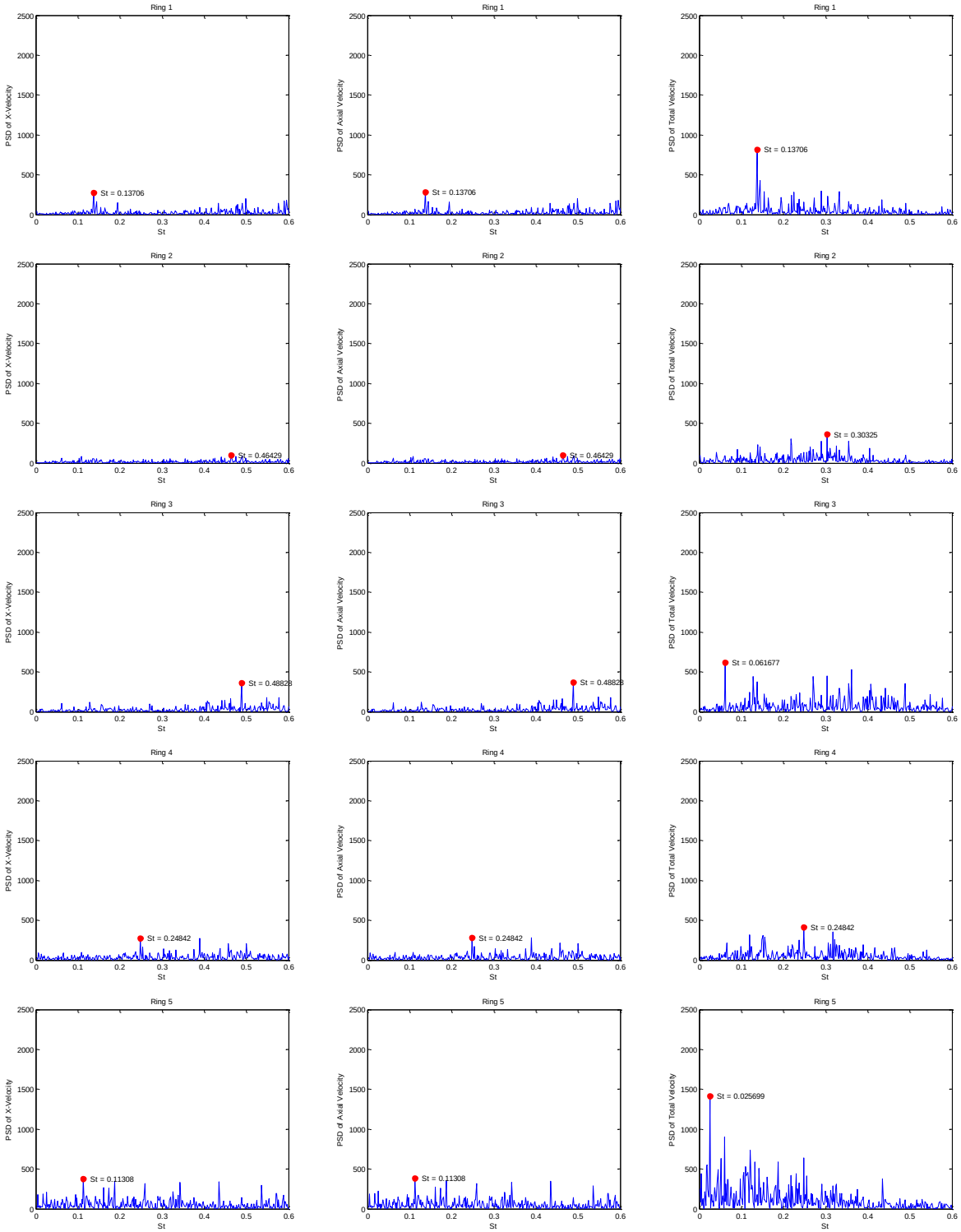


Figure O: FFT results Leeward Velocity:

f) $\phi = 57.1°$; $\alpha = 54.7°$, $\beta = 20°$

i) Re = 1.1×10^5;

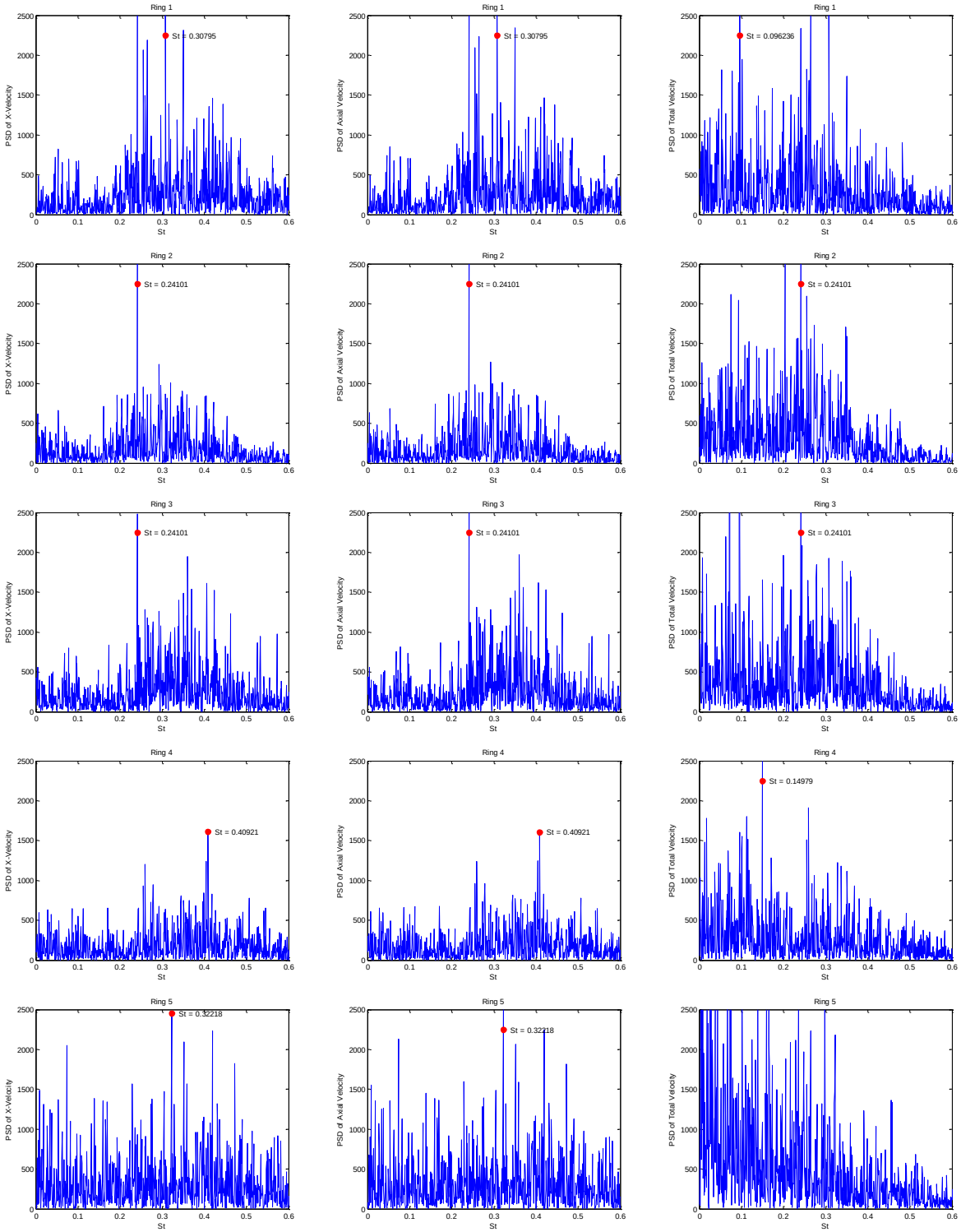


Figure O: FFT results Leeward Velocity:

f) $\phi = 57.1°$; $\alpha = 54.7°$, $\beta = 20°$

ii) Re = 2.2×10^5;

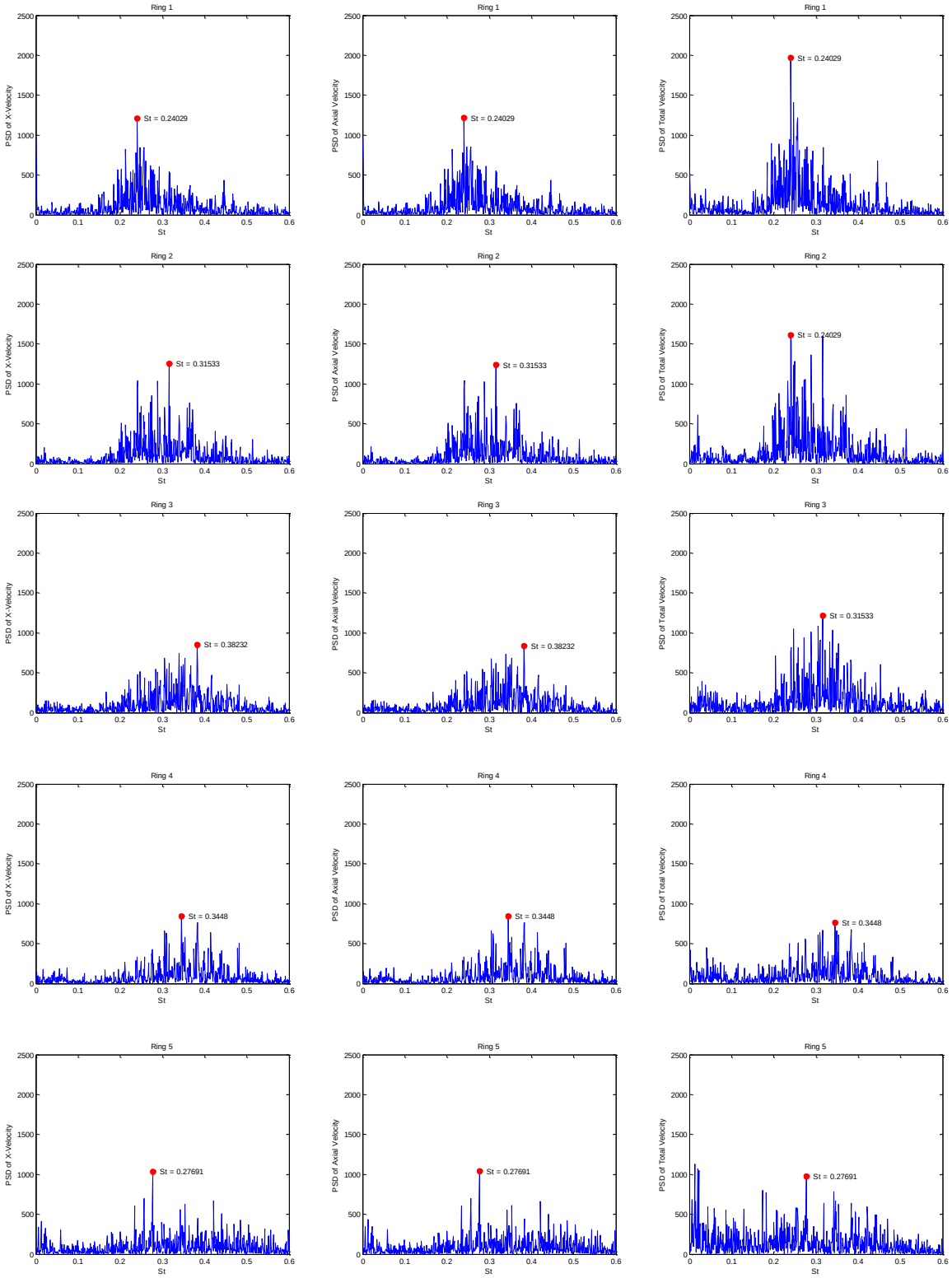


Figure O: FFT results Leeward Velocity:

f) $\phi = 57.1°$; $\alpha = 54.7°$, $\beta = 20°$

iii) Re = 3.3×10^5;

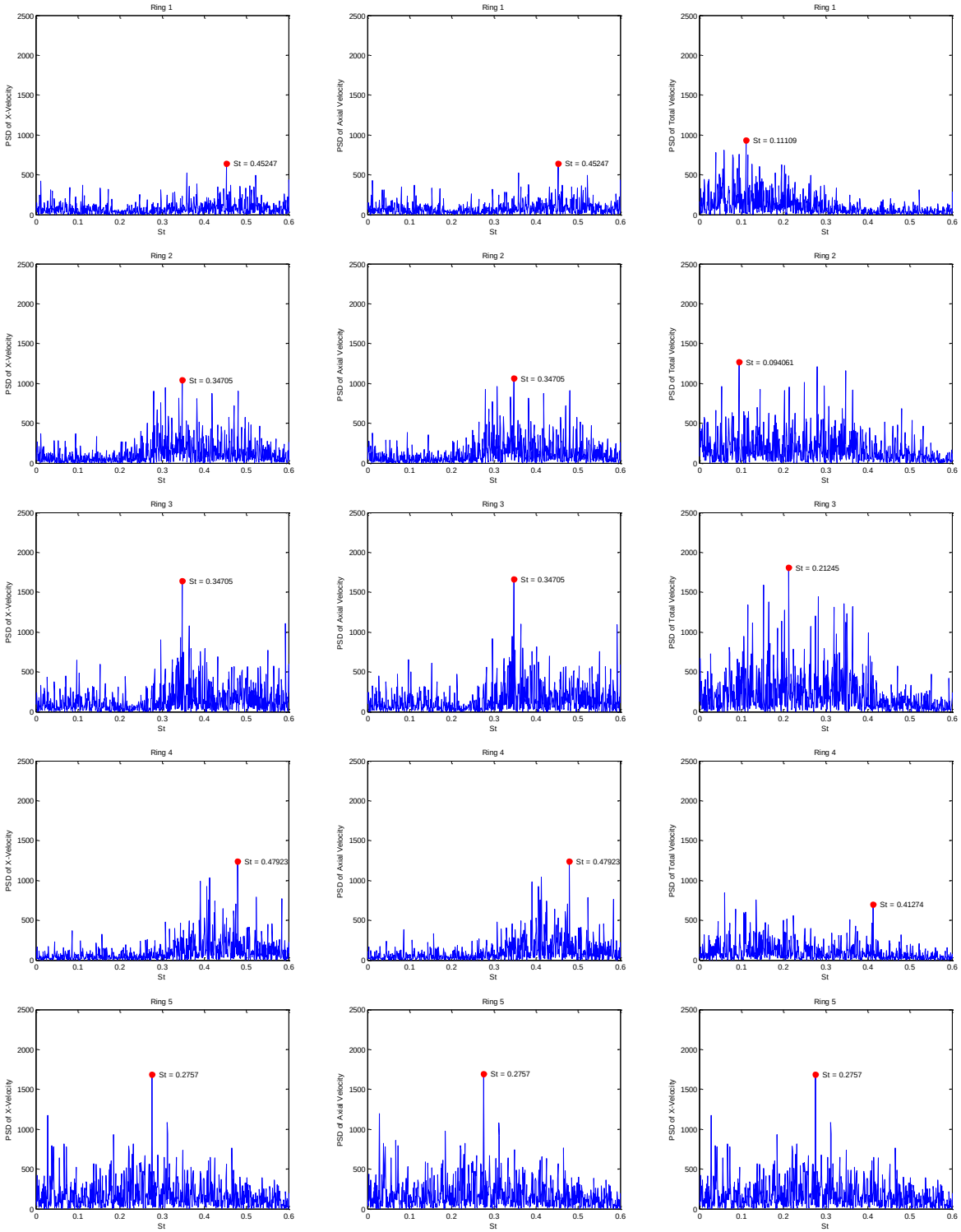


Figure O: FFT results Leeward Velocity:

f) $\phi = 57.1°$; $\alpha = 54.7°$, $\beta = 20°$

iv) Re = 4.4×10^5;

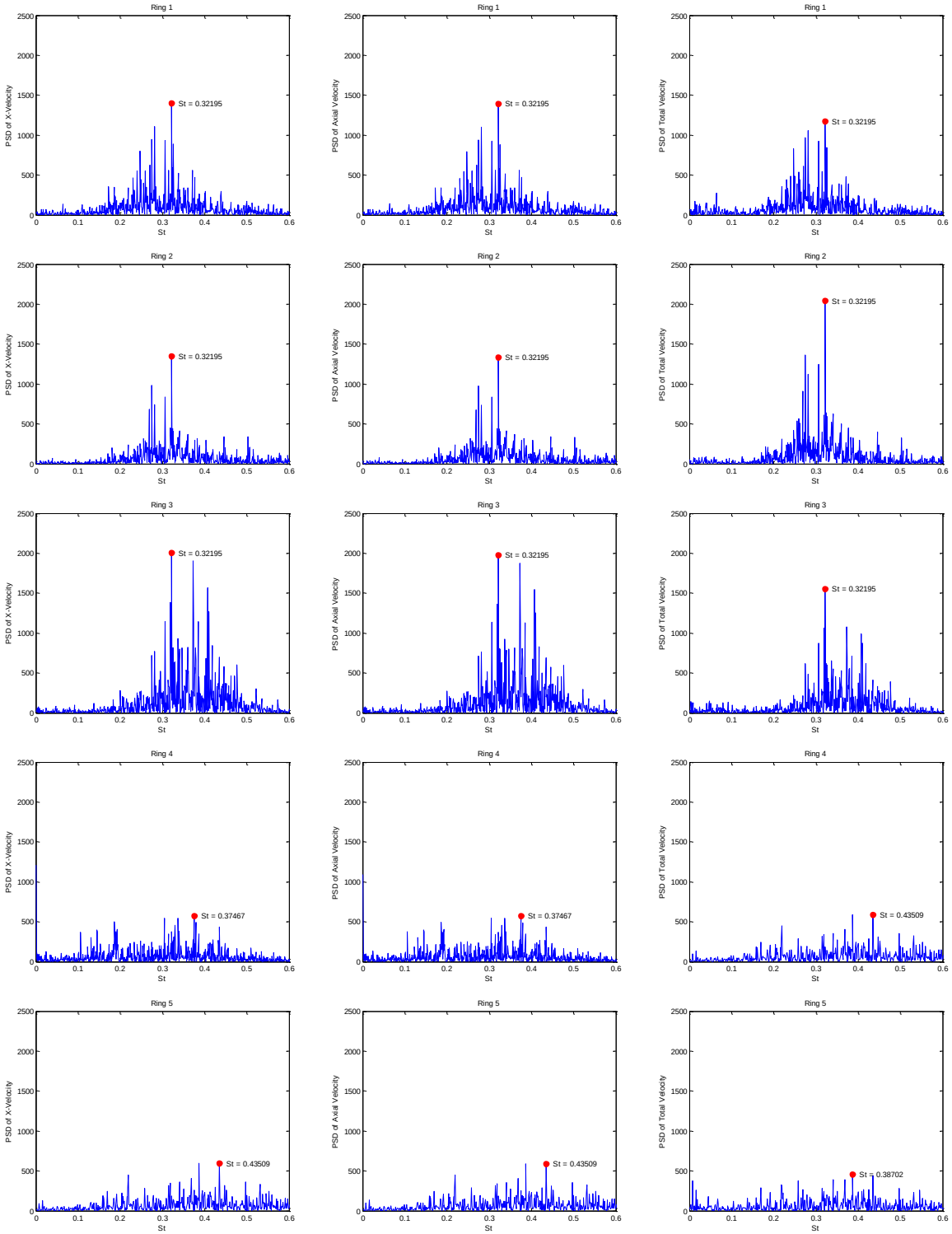


Figure O: FFT results Leeward Velocity:

f) $\phi = 57.1°$; $\alpha = 54.7°$, $\beta = 20°$

v) Re = 5.5×10^5;

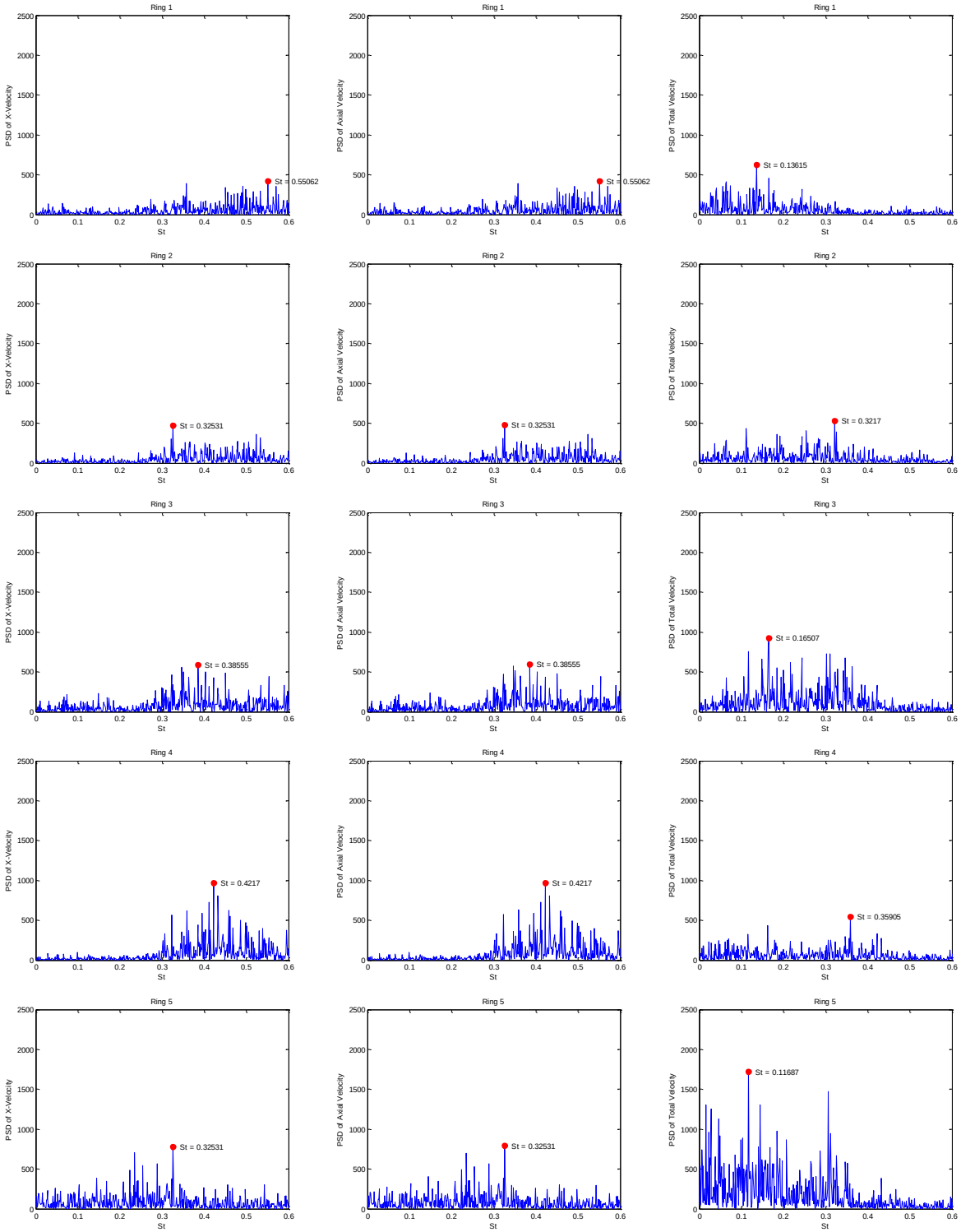


Figure O: FFT results Leeward Velocity:

g) $\phi = 64.0°$; $\alpha = 54.7°$, $\beta = 40°$

i) Re = 1.1×10^5;

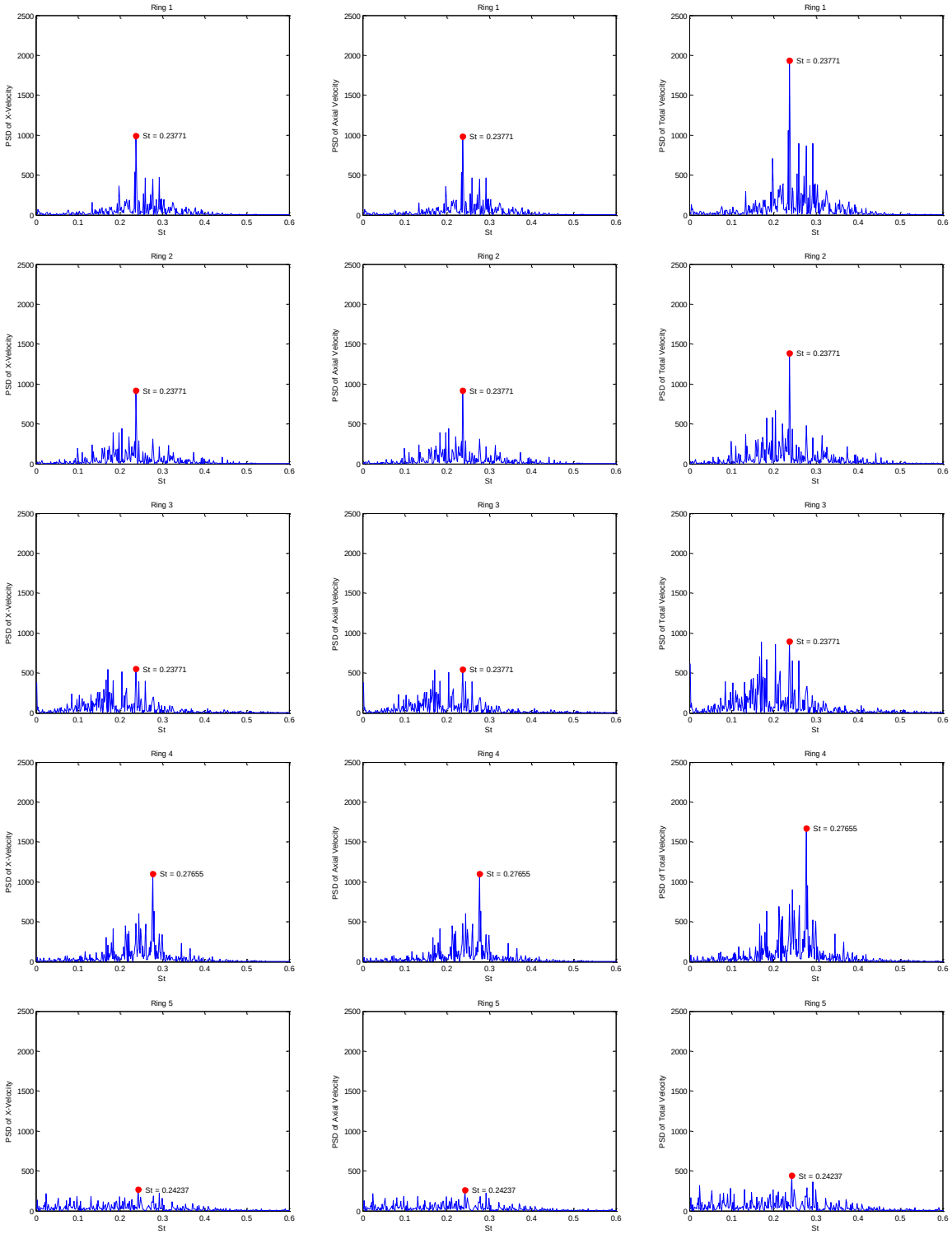


Figure O: FFT results Leeward Velocity:

g) $\phi = 64.0°$; $\alpha = 54.7°$, $\beta = 40°$

ii) Re = 2.2×10^5;

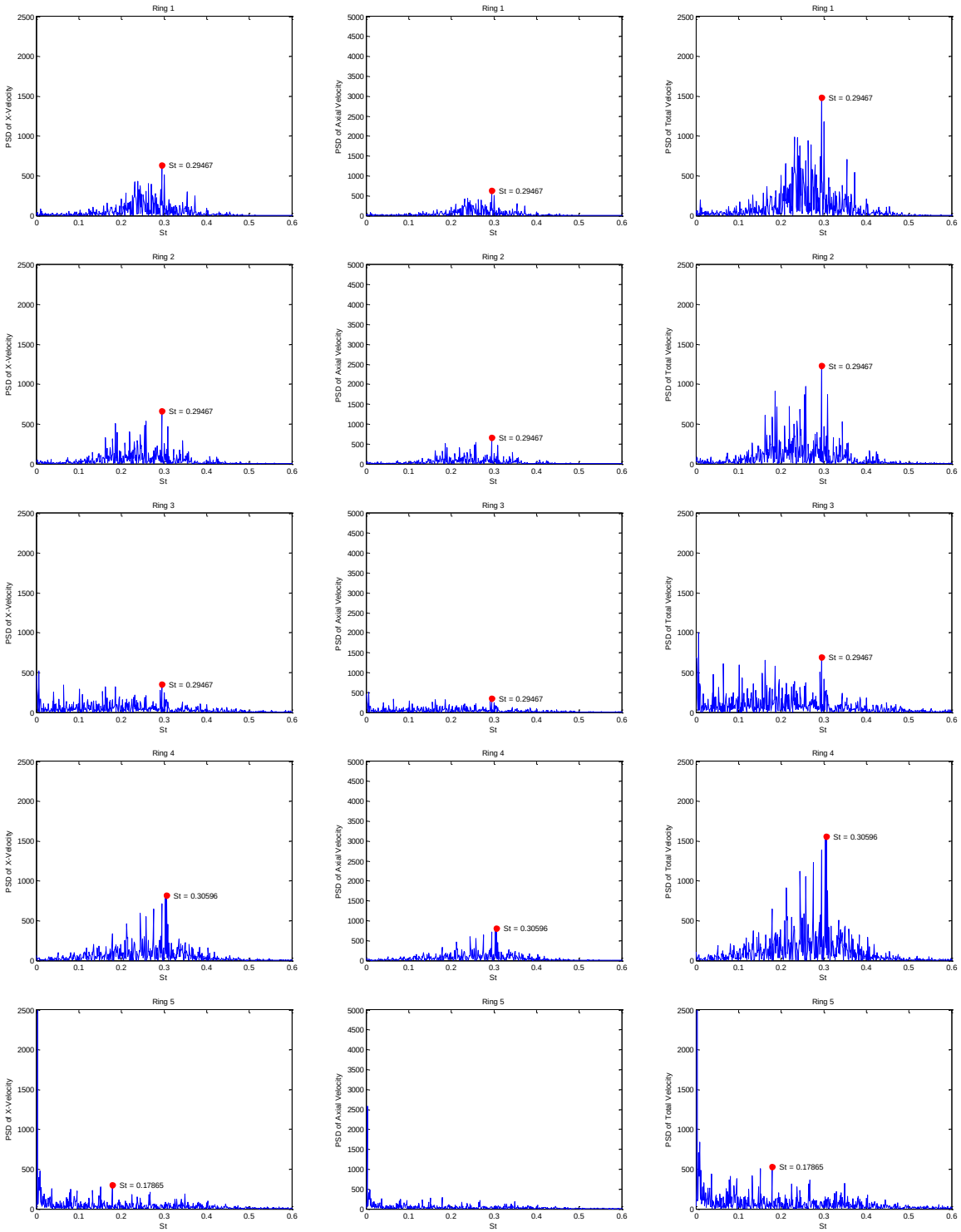


Figure O: FFT results Leeward Velocity:

g) $\phi = 64.0°$; $\alpha = 54.7°$, $\beta = 40°$

iii) Re = 3.3×10^5;

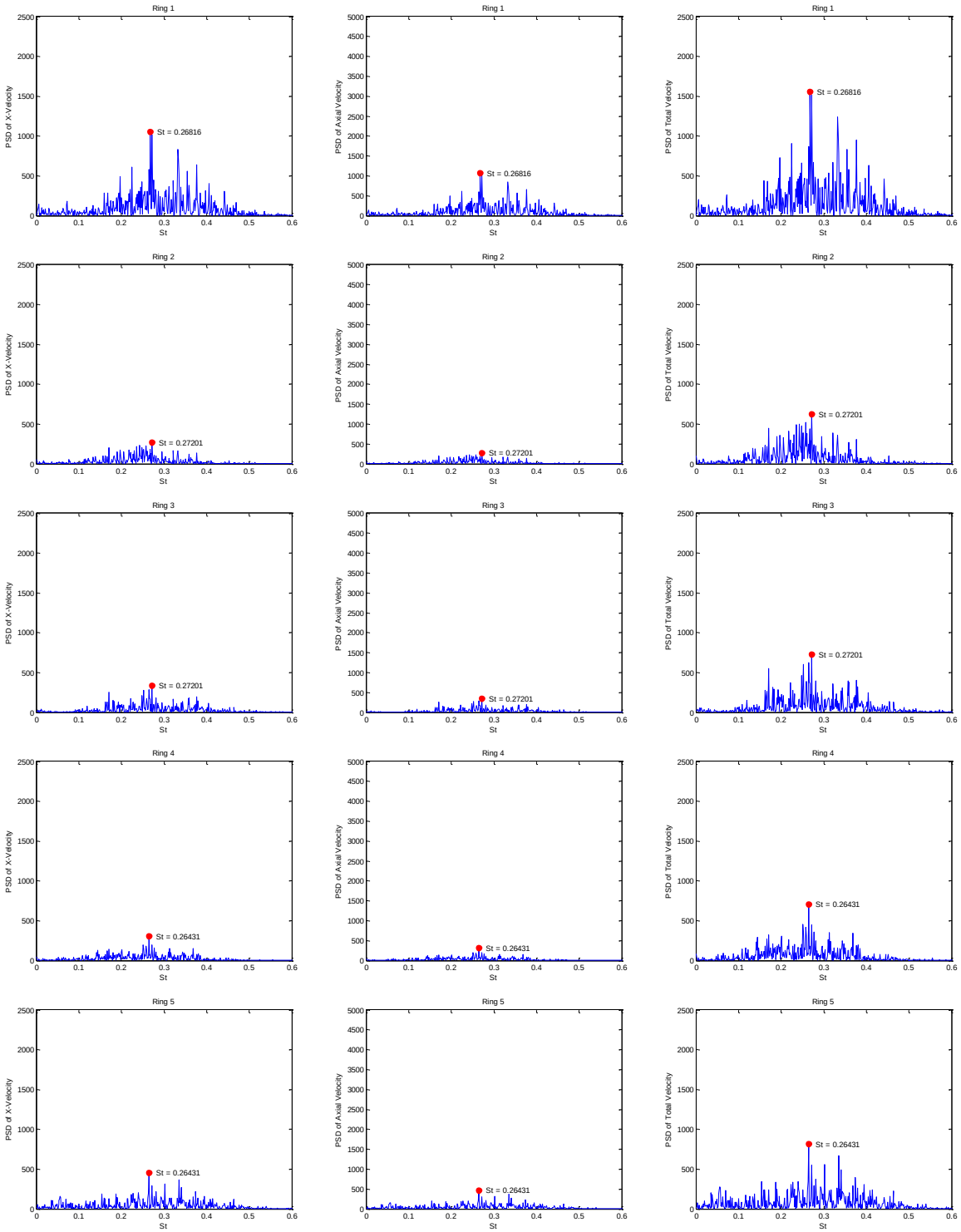


Figure O: FFT results Leeward Velocity:

g) $\phi = 64.0°$; $\alpha = 54.7°$, $\beta = 40°$

iv) Re = 4.4×10^5;

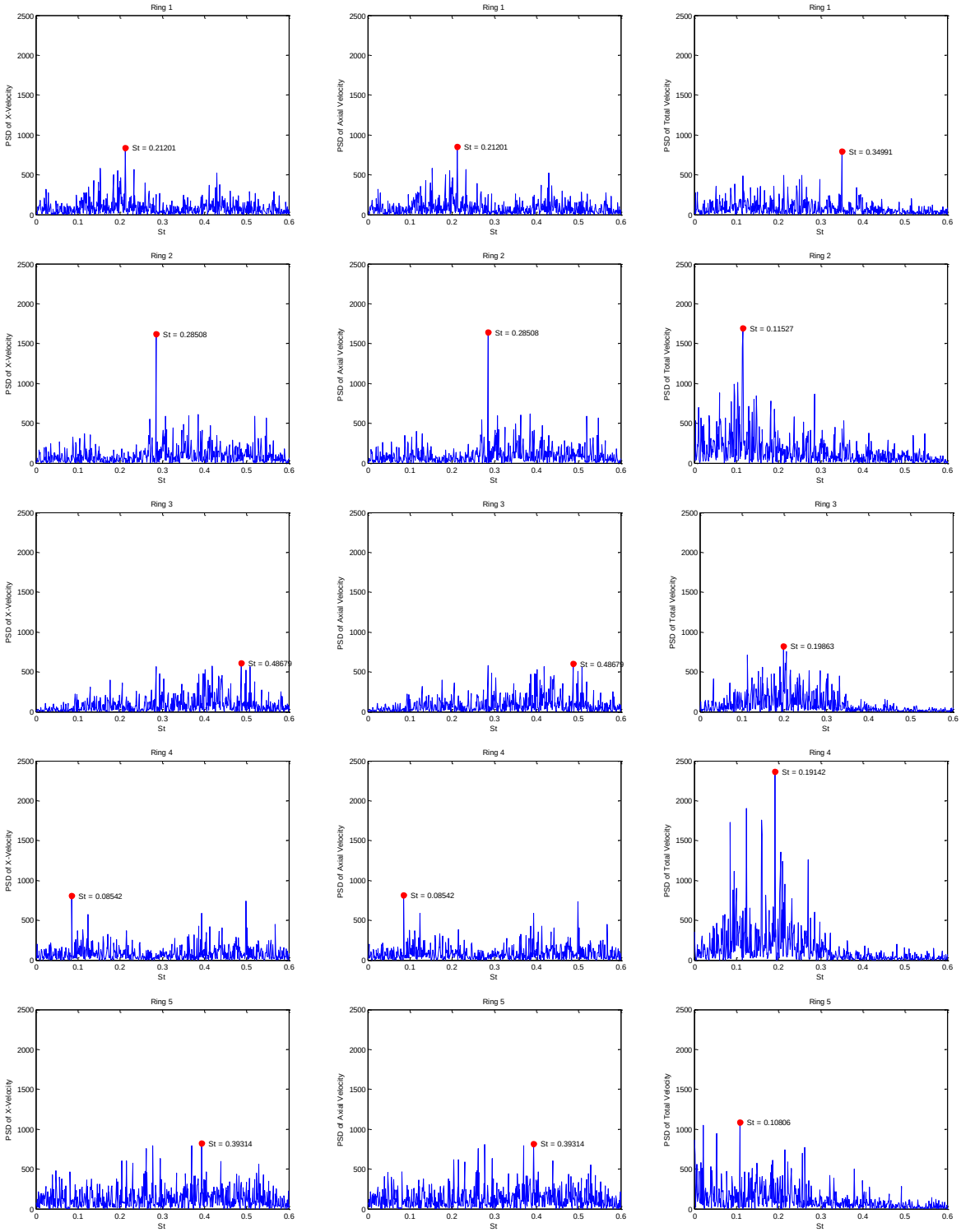


Figure O: FFT results Leeward Velocity:

g) $\phi = 64.0°$; $\alpha = 54.7°$, $\beta = 40°$

v) Re = 5.5×10^5;

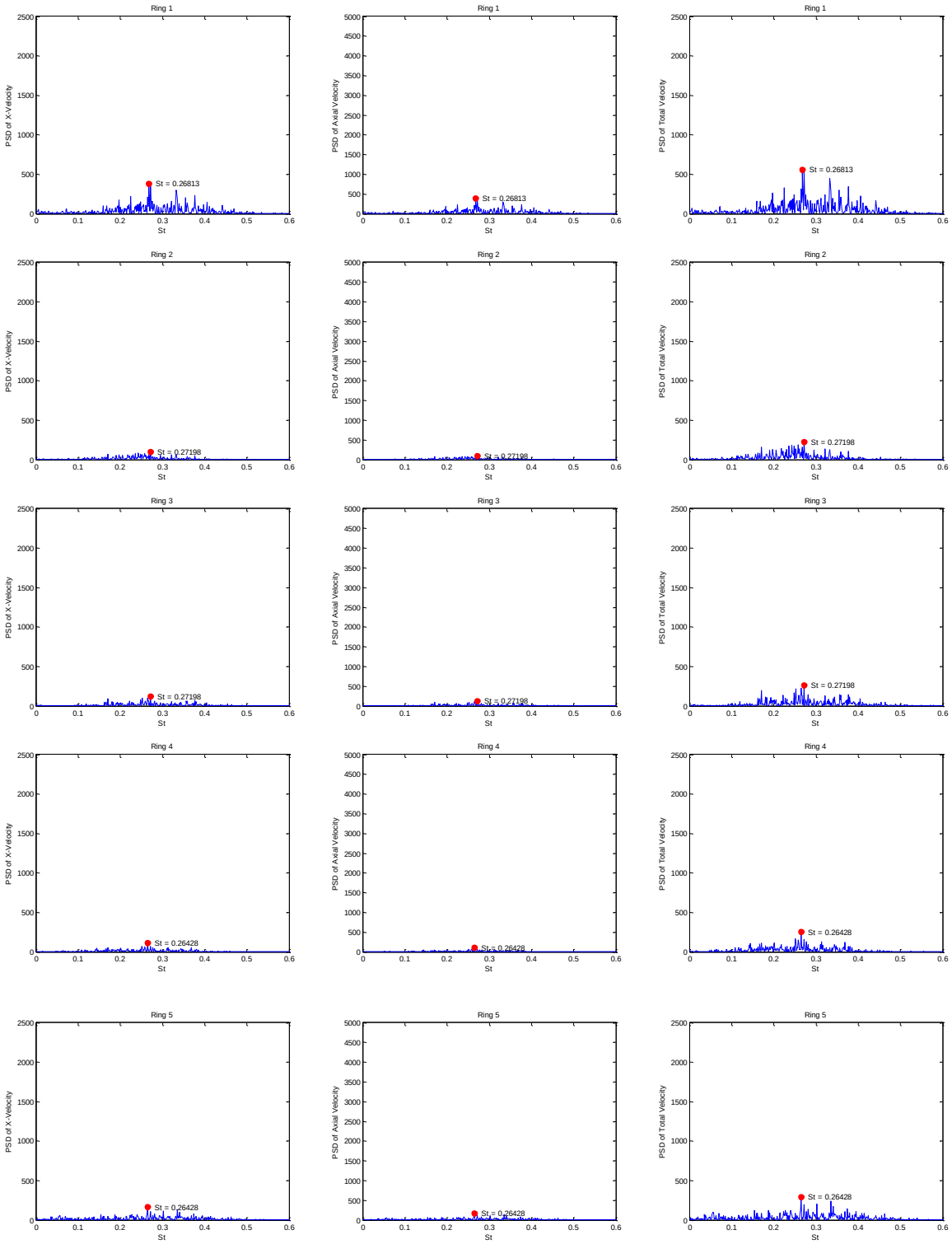


Figure O: FFT results Leeward Velocity:

h) $\phi = 53.0°$; $\alpha = 50°$, $\beta = 20°$

i) Re = 1.1×10^5;

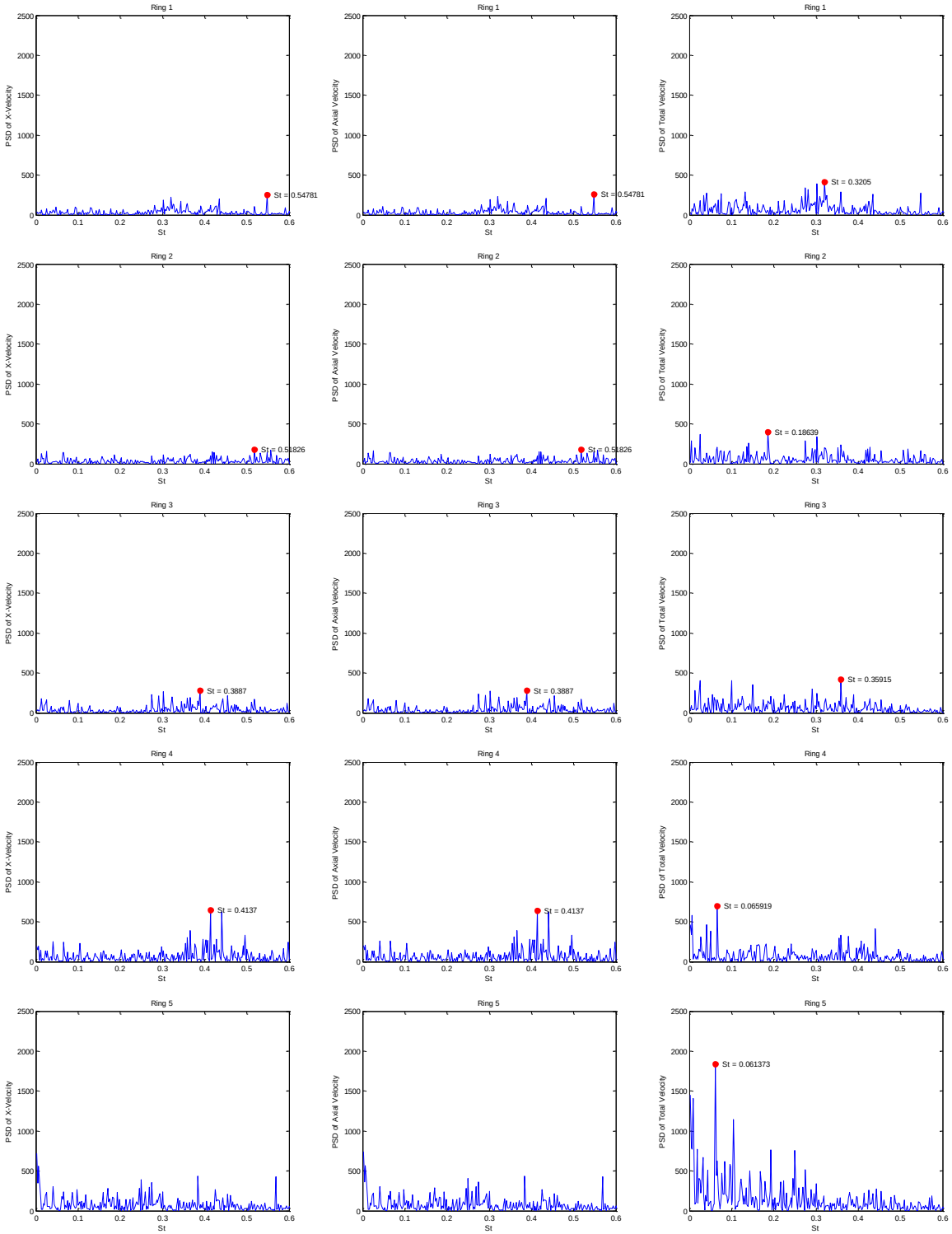


Figure O: FFT results Leeward Velocity:

h) $\phi = 53.0°$; $\alpha = 50°$, $\beta = 20°$

ii) Re = 2.2×10^5;

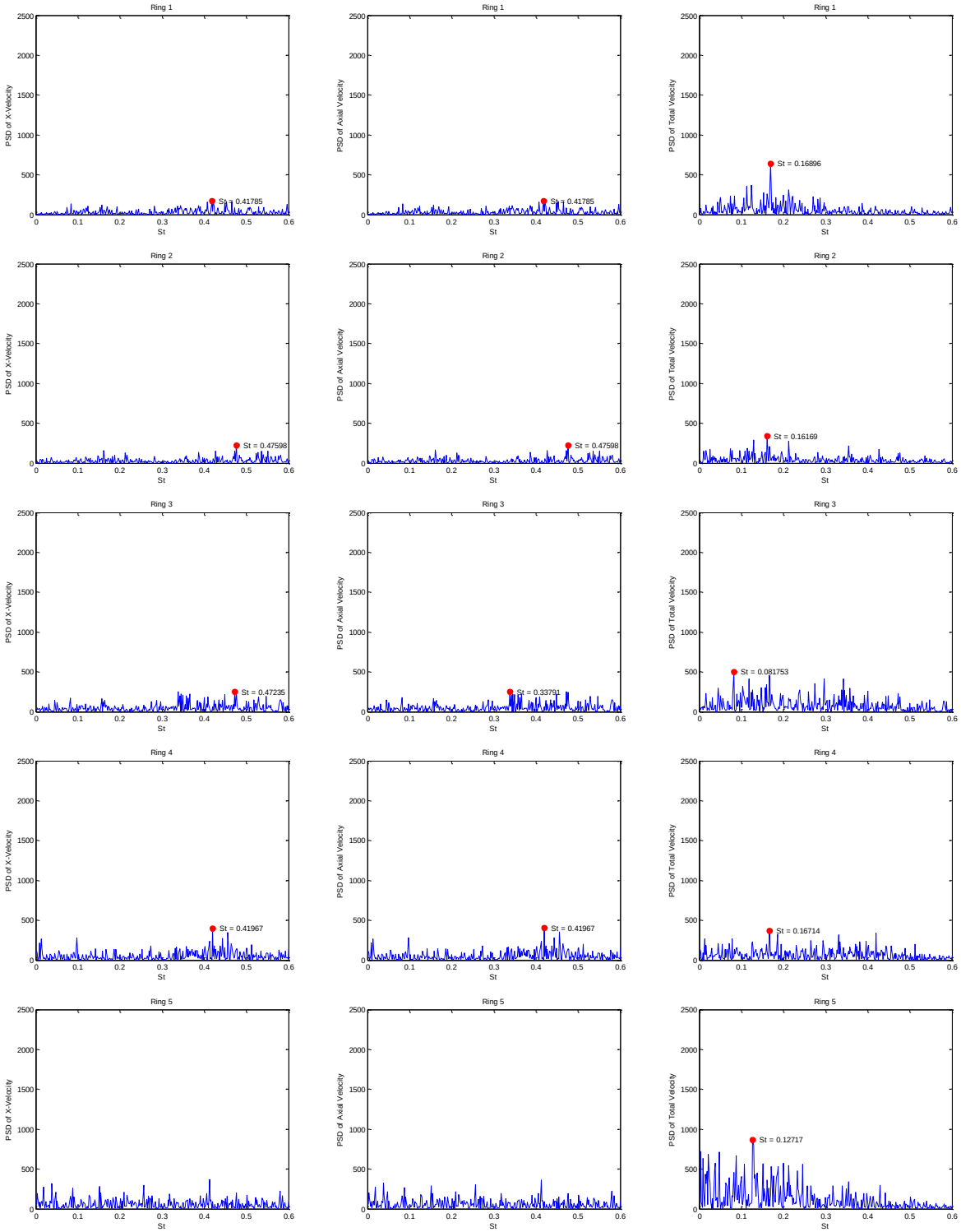


Figure O: FFT results Leeward Velocity:

h) $\phi = 53.0°$; $\alpha = 50°$, $\beta = 20°$

iii) Re = 3.3×10^5;

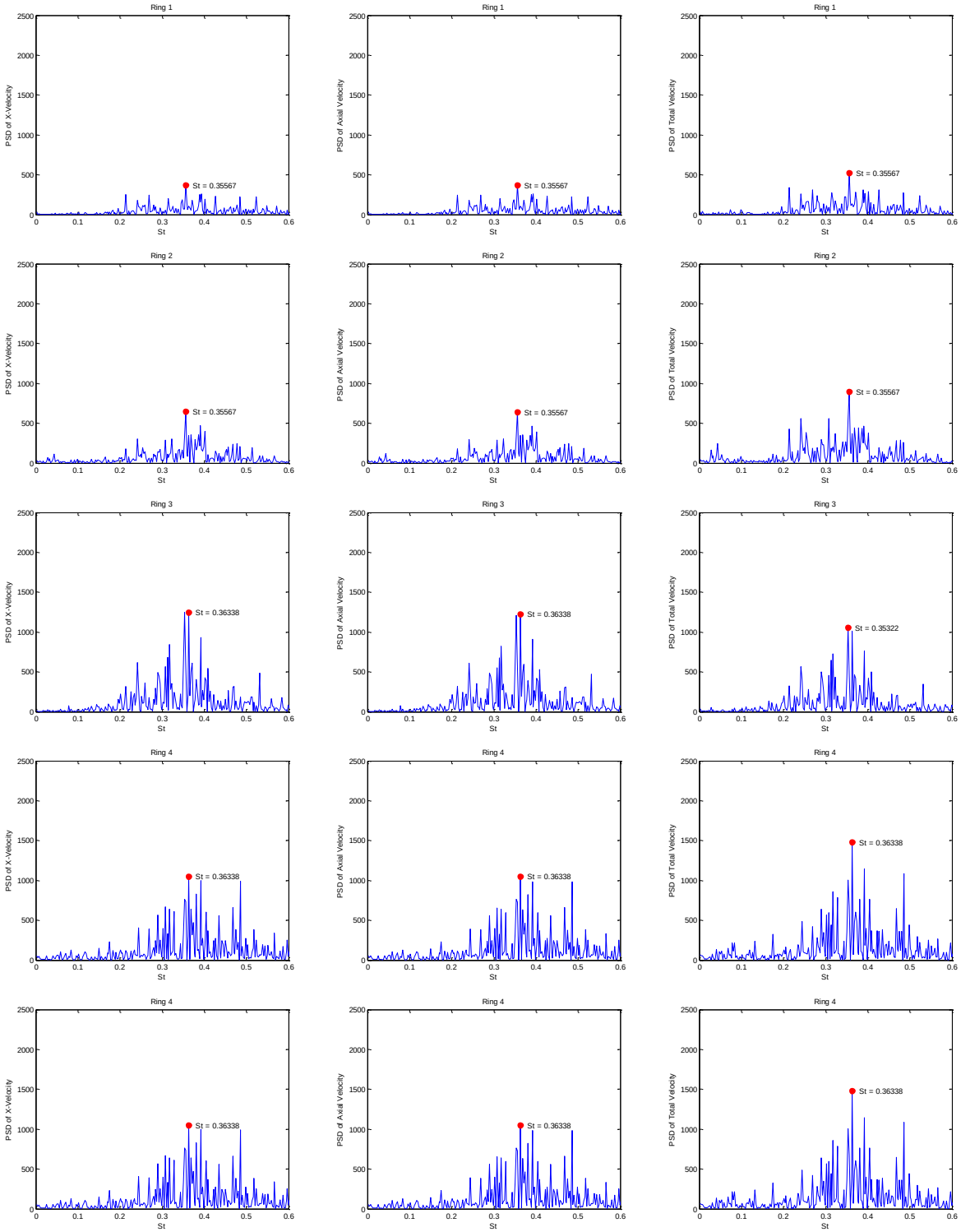


Figure O: FFT results Leeward Velocity:

h) $\phi = 53.0°$; $\alpha = 50°$, $\beta = 20°$

iv) Re = 4.4×10^5;

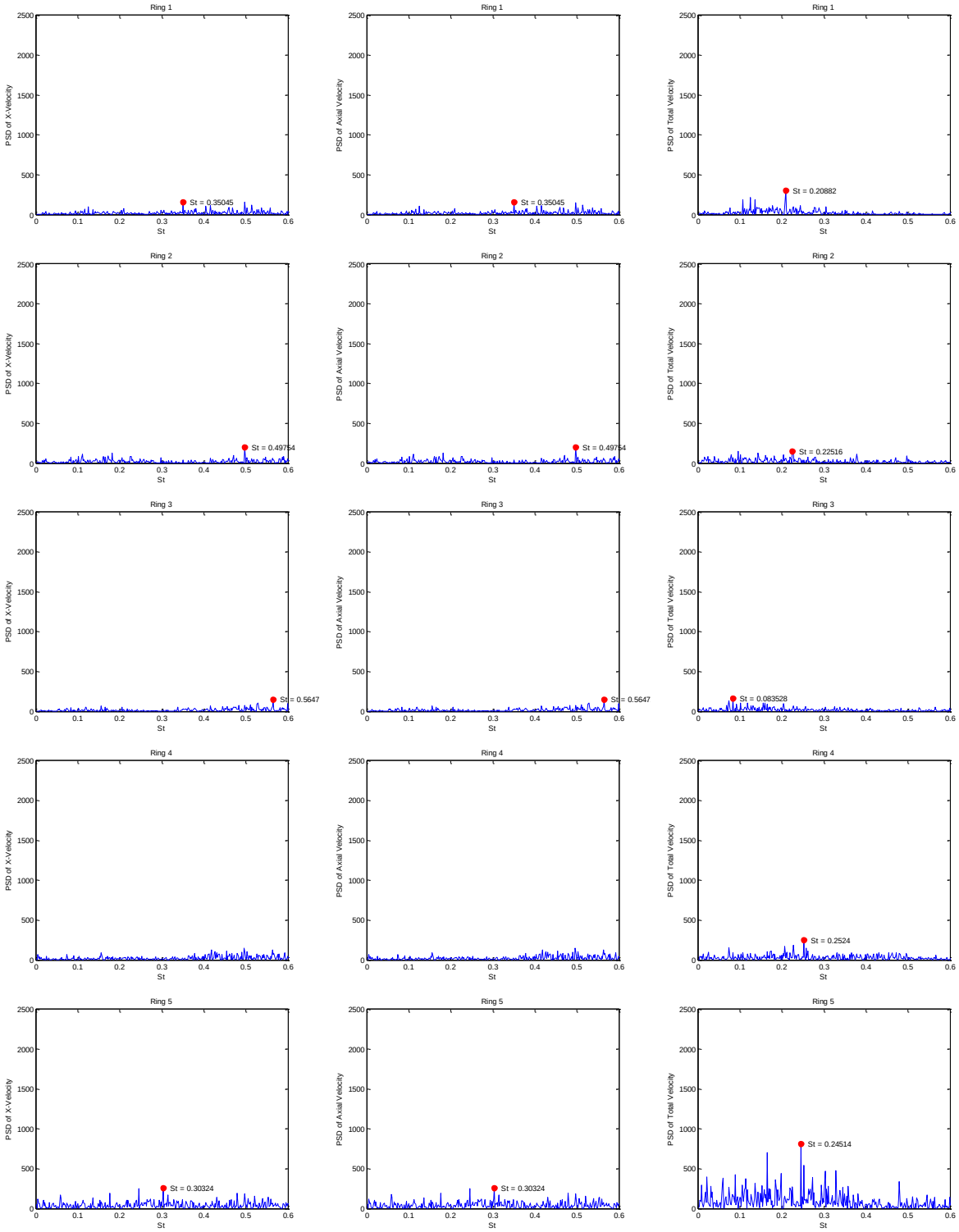


Figure O: FFT results Leeward Velocity:

h) $\phi = 53.0°$; $\alpha = 50°$, $\beta = 20°$

v) Re = 5.5×10^5;

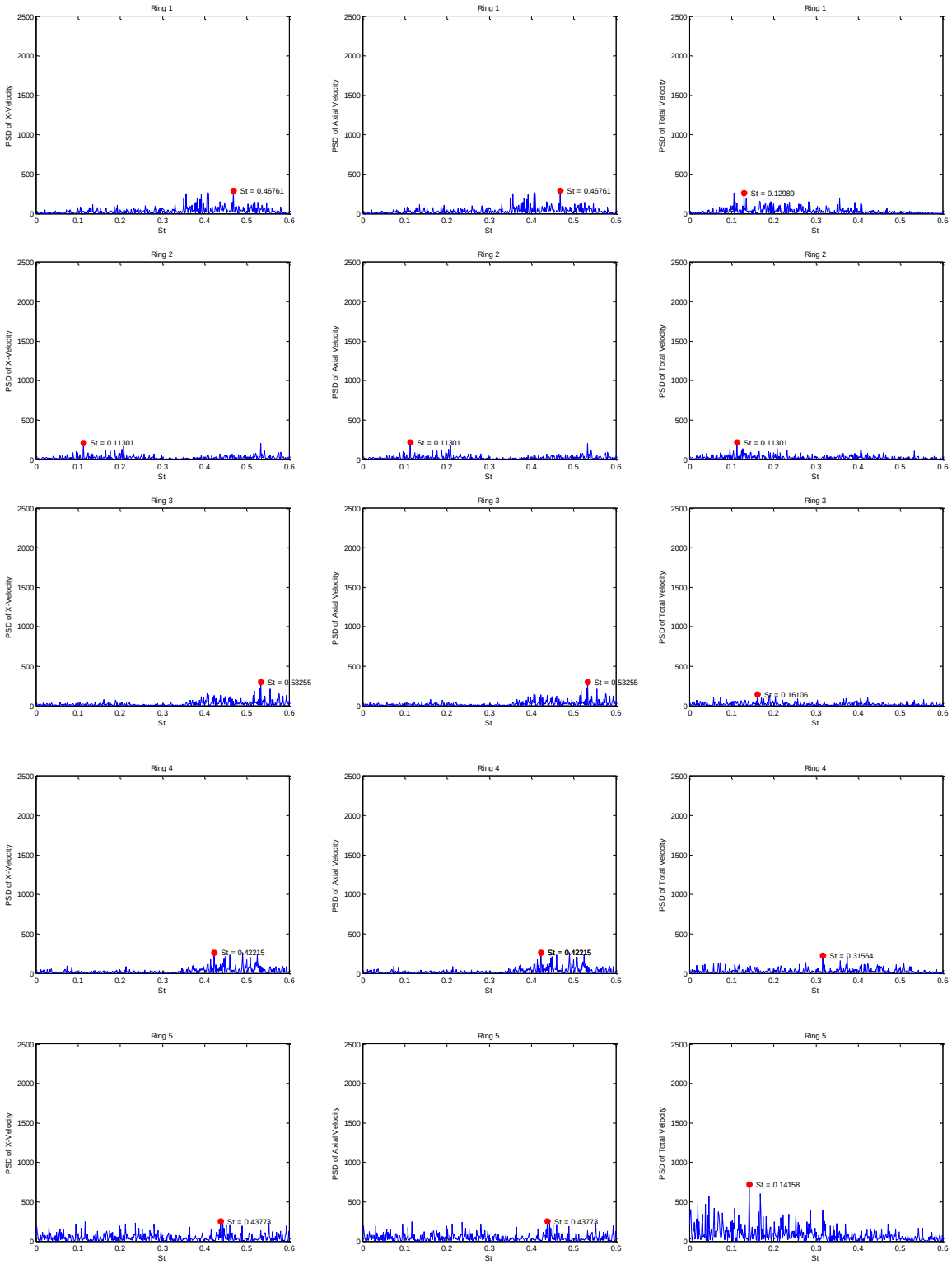


Figure O: FFT results Leeward Velocity:

i) $\phi = 60.5°$; $\alpha = 50°$, $\beta = 40°$

i) Re = 1.1×10^5;

Direction of Flow | Axial Flow | Total Velocity

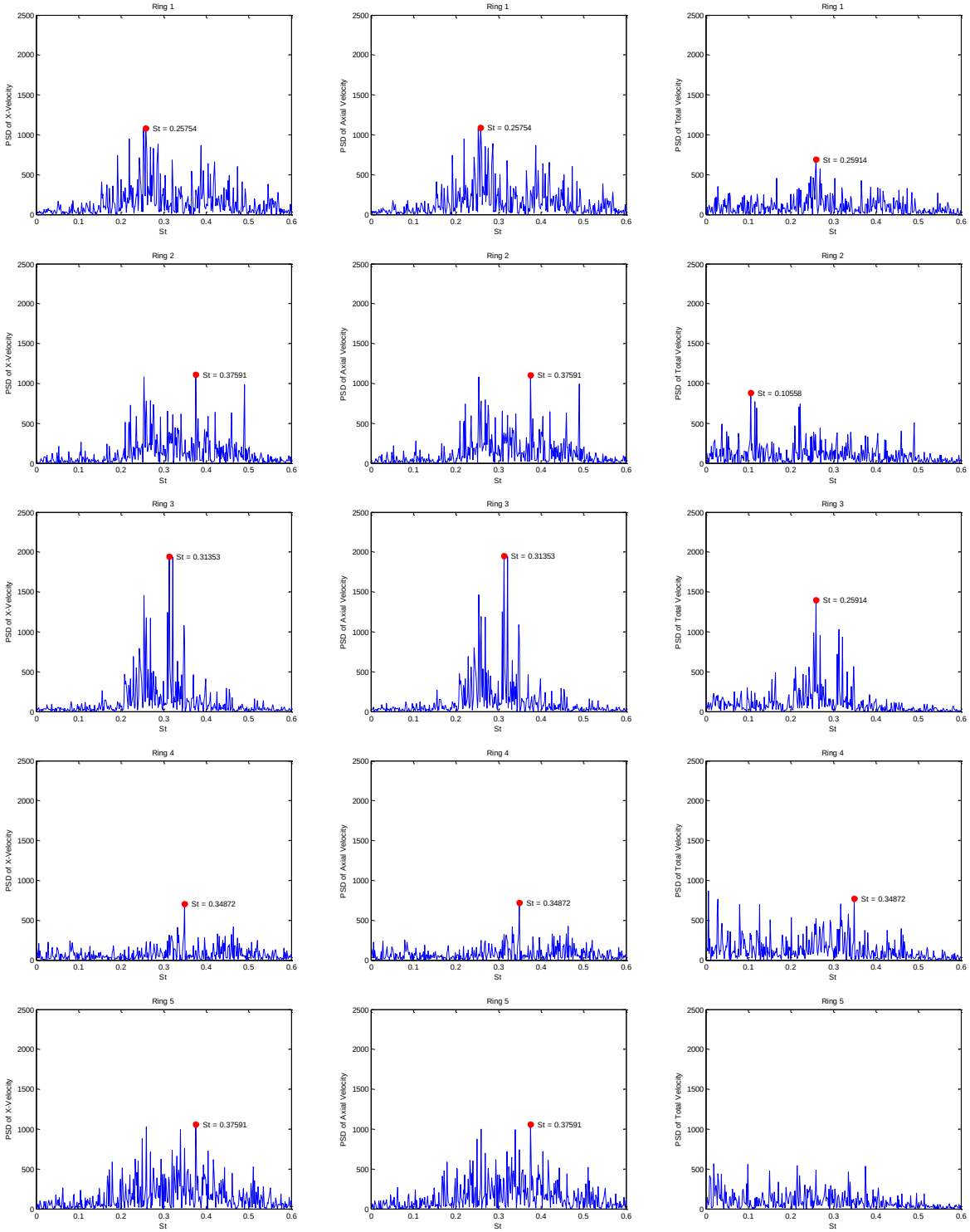


Figure O: FFT results Leeward Velocity:

i) $\phi = 60.5°$; $\alpha = 50°$, $\beta = 40°$

ii) Re = 2.2×10^5;

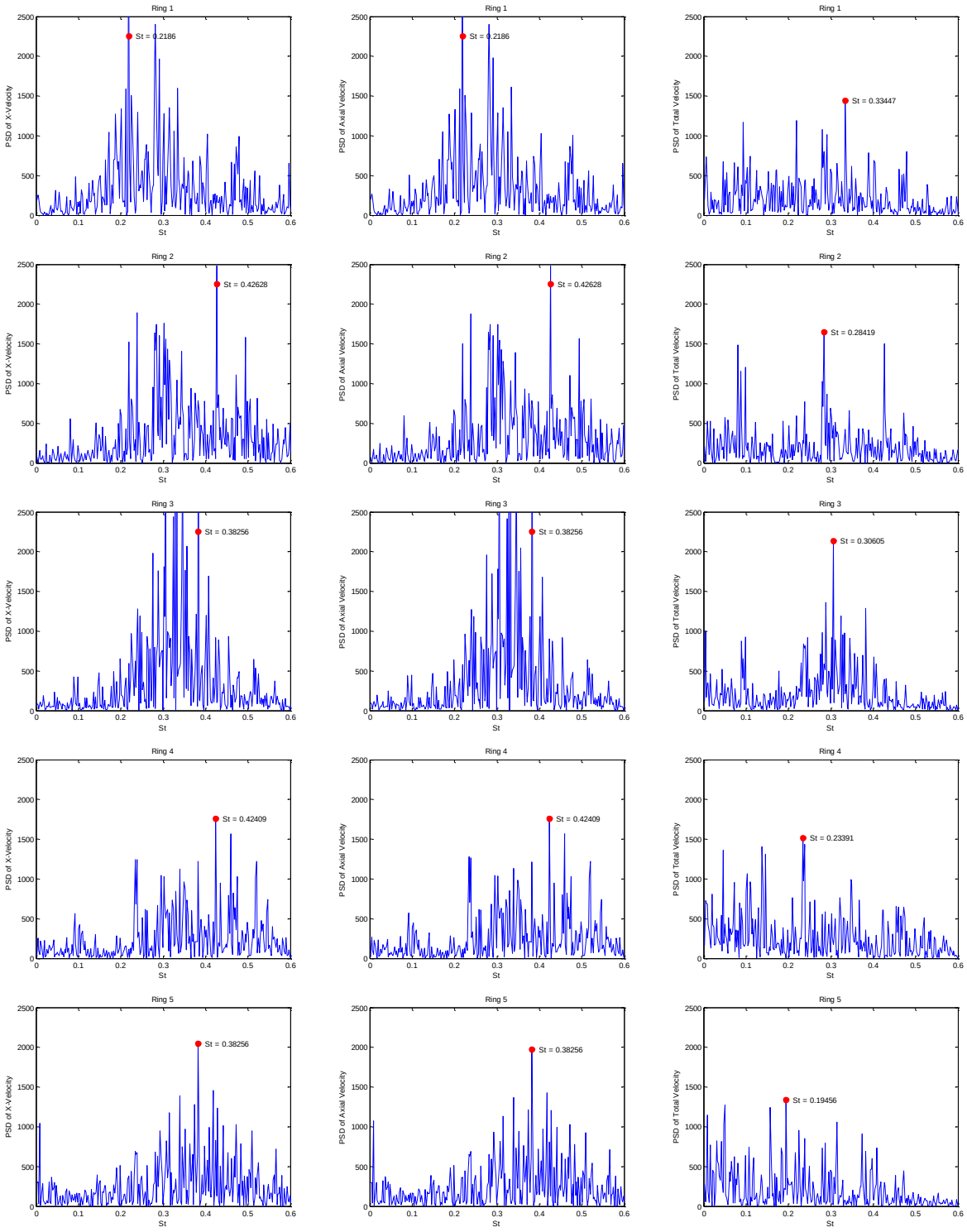


Figure O: FFT results Leeward Velocity:

i) $\phi = 60.5°$; $\alpha = 50°$, $\beta = 40°$

iv) Re = 4.4×10^5;

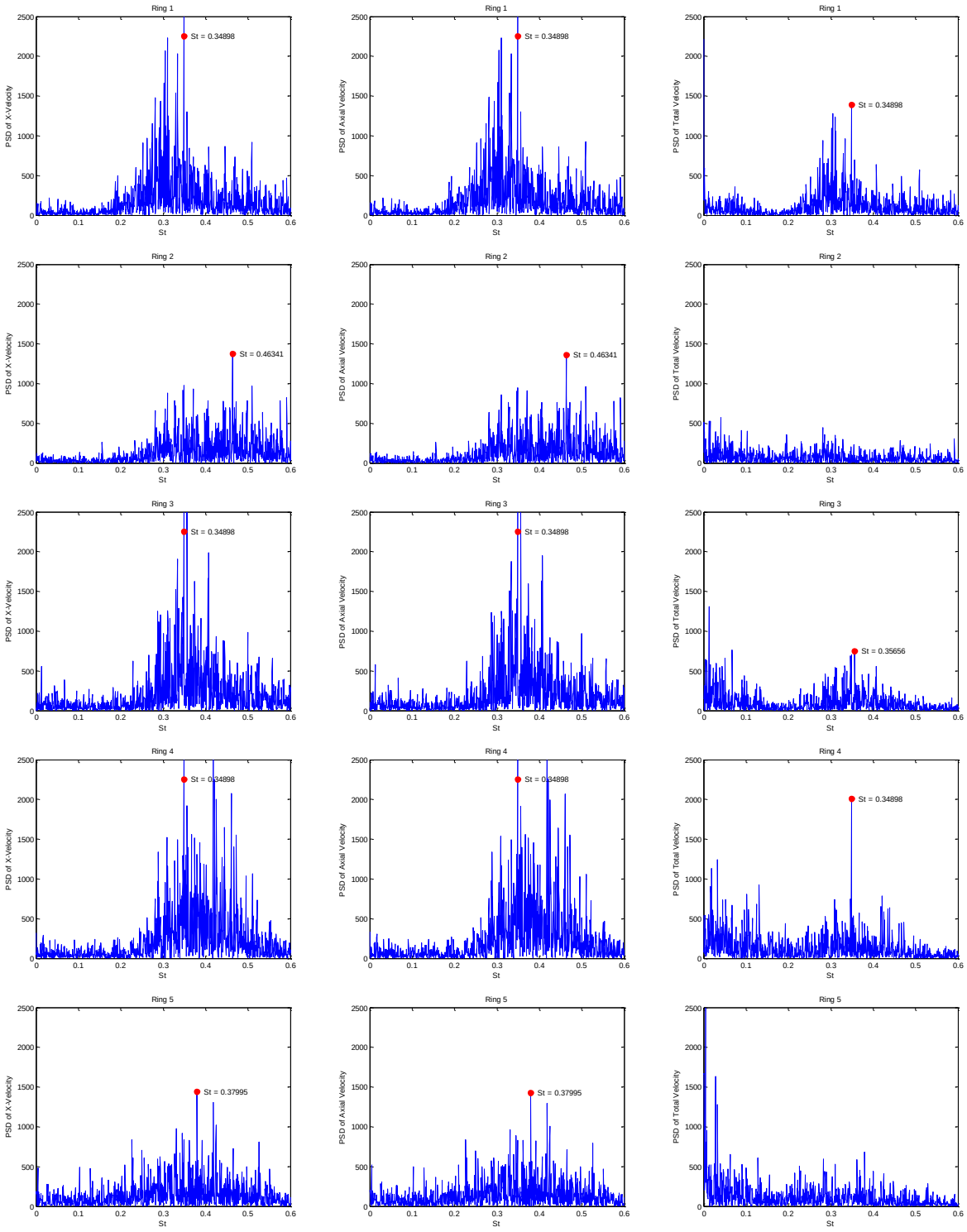


Figure O: FFT results Leeward Velocity:

i) $\phi = 60.5°$; $\alpha = 50°$, $\beta = 40°$

v) Re = 5.5×10^5;

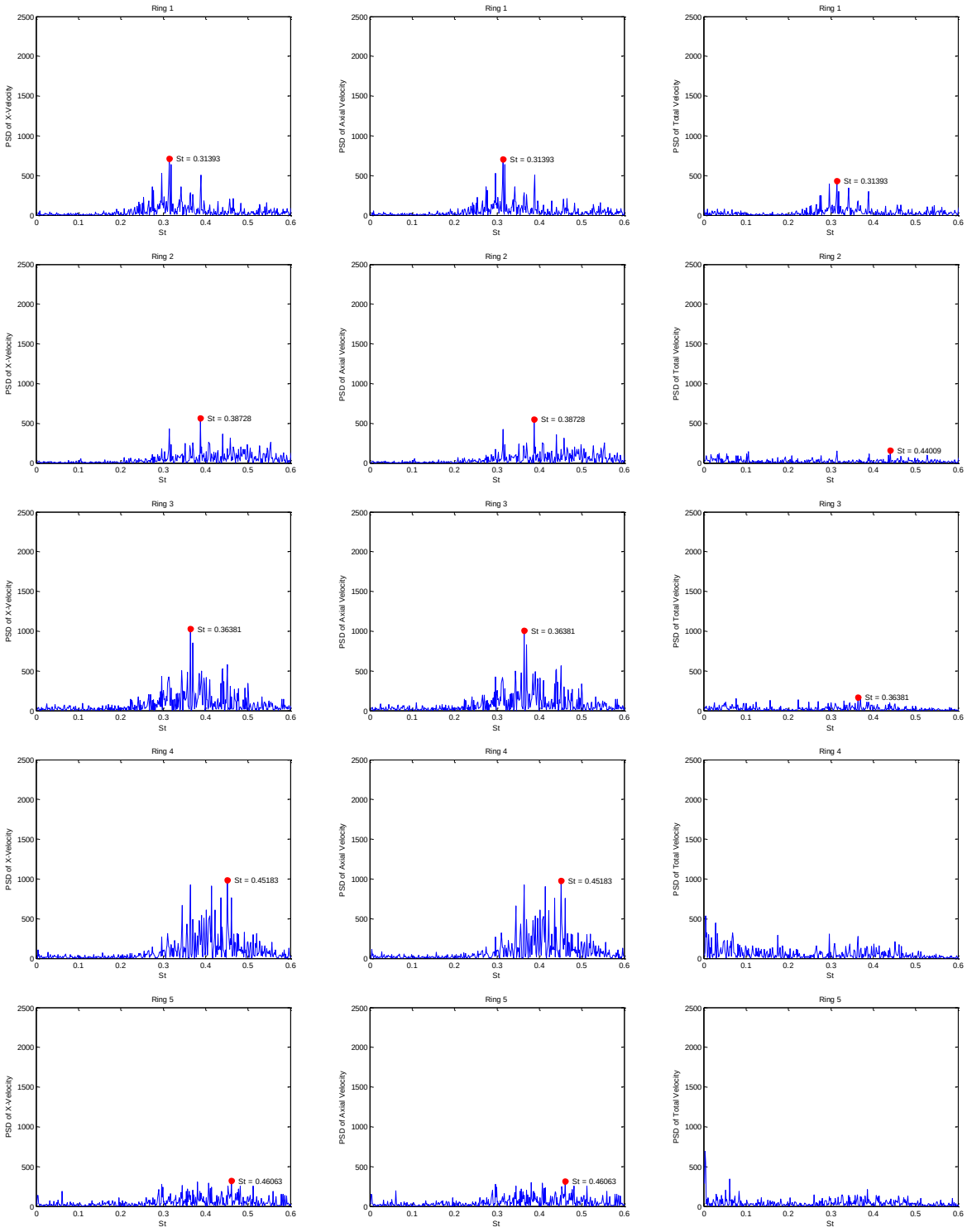


Figure O: FFT results Leeward Velocity:

j) $\phi = 35.5°$; $\alpha = 30°$, $\beta = 20°$

ii) Re = 2.2×10^5;

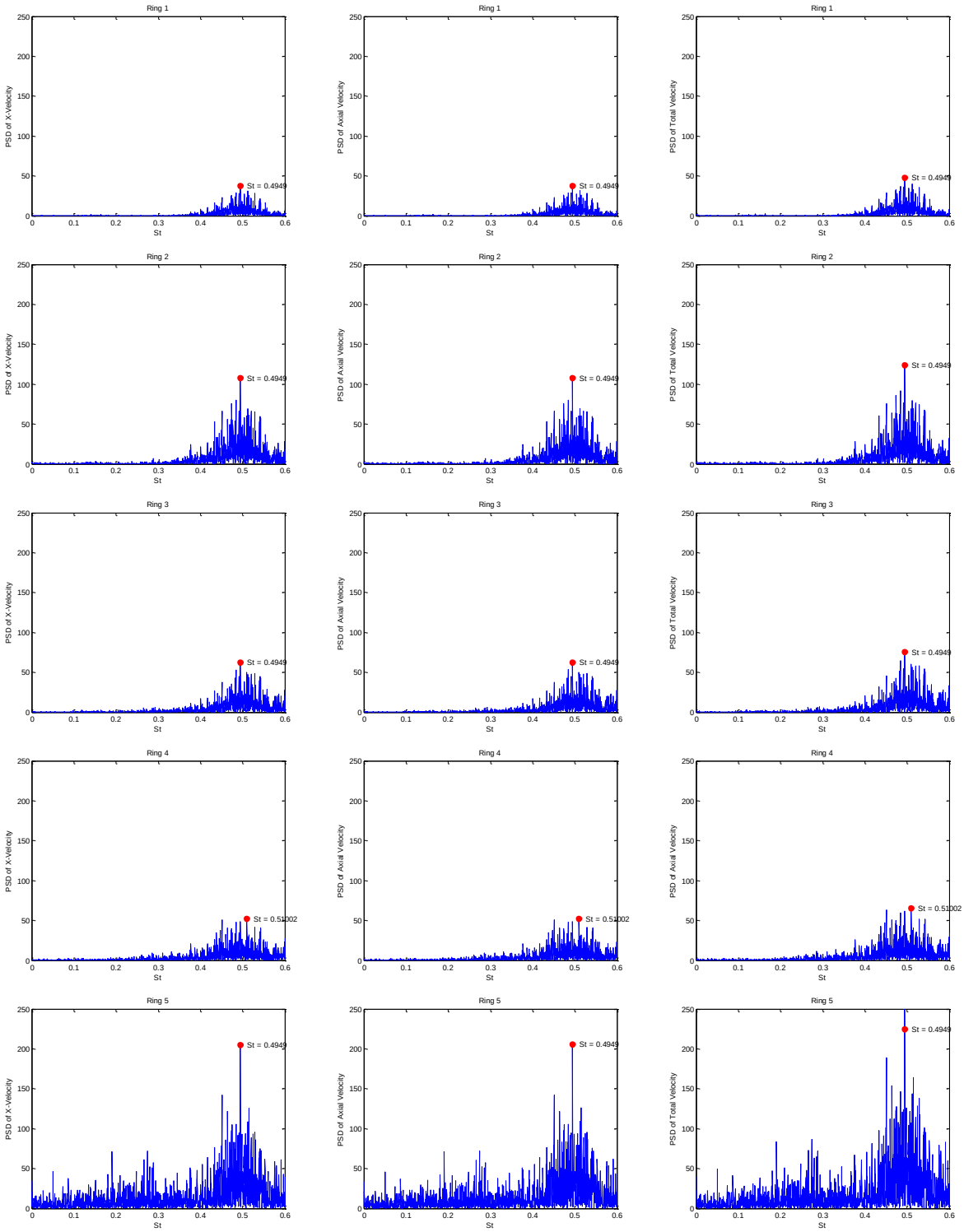


Figure O: FFT results Leeward Velocity:

j) $\phi = 35.5°$; $\alpha = 30°$, $\beta = 20°$

iii) Re = 3.3×10^5;

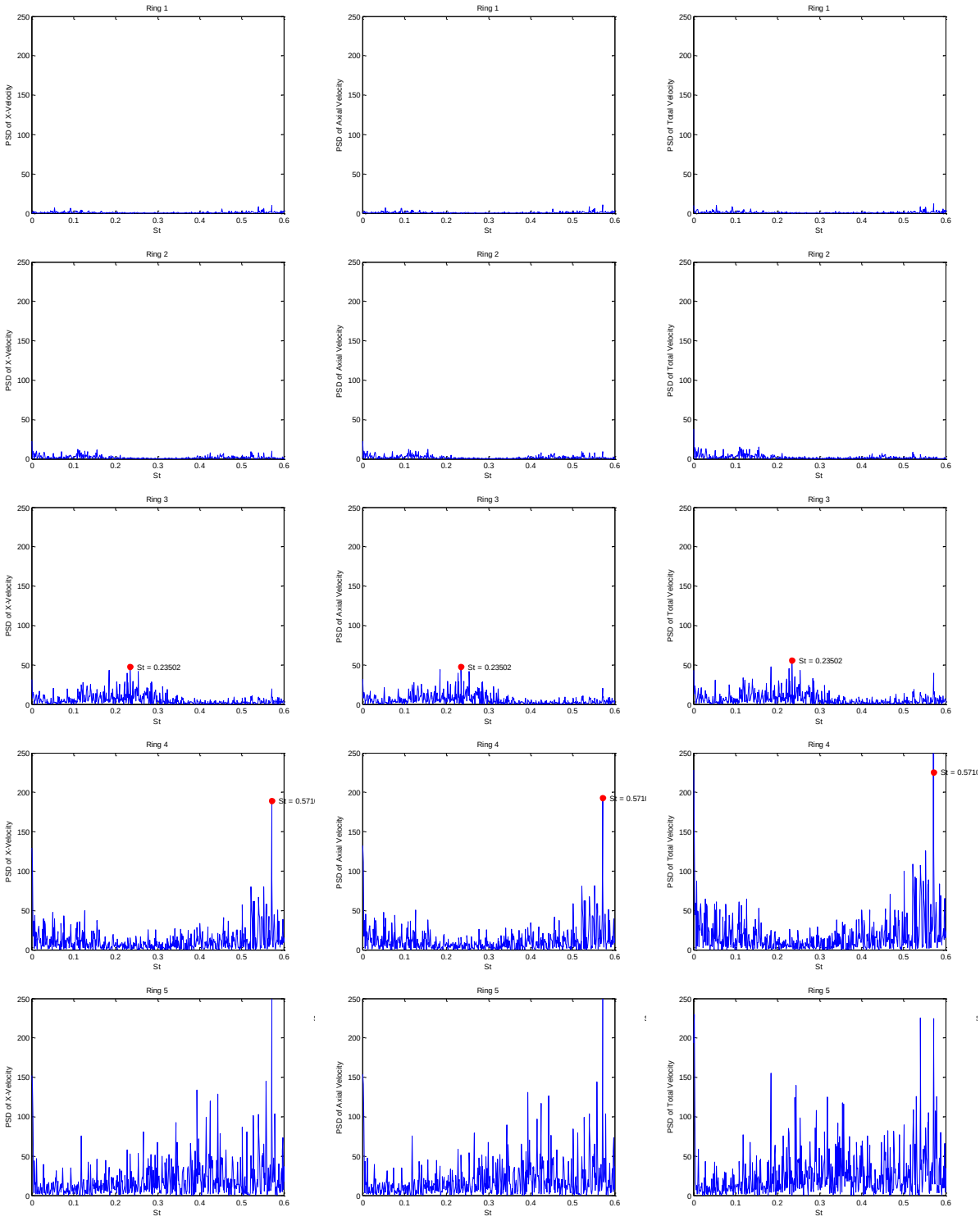


Figure O: FFT results Leeward Velocity:

j) $\phi = 35.5°$; $\alpha = 30°$, $\beta = 20°$

iv) Re = 4.4×10^5;

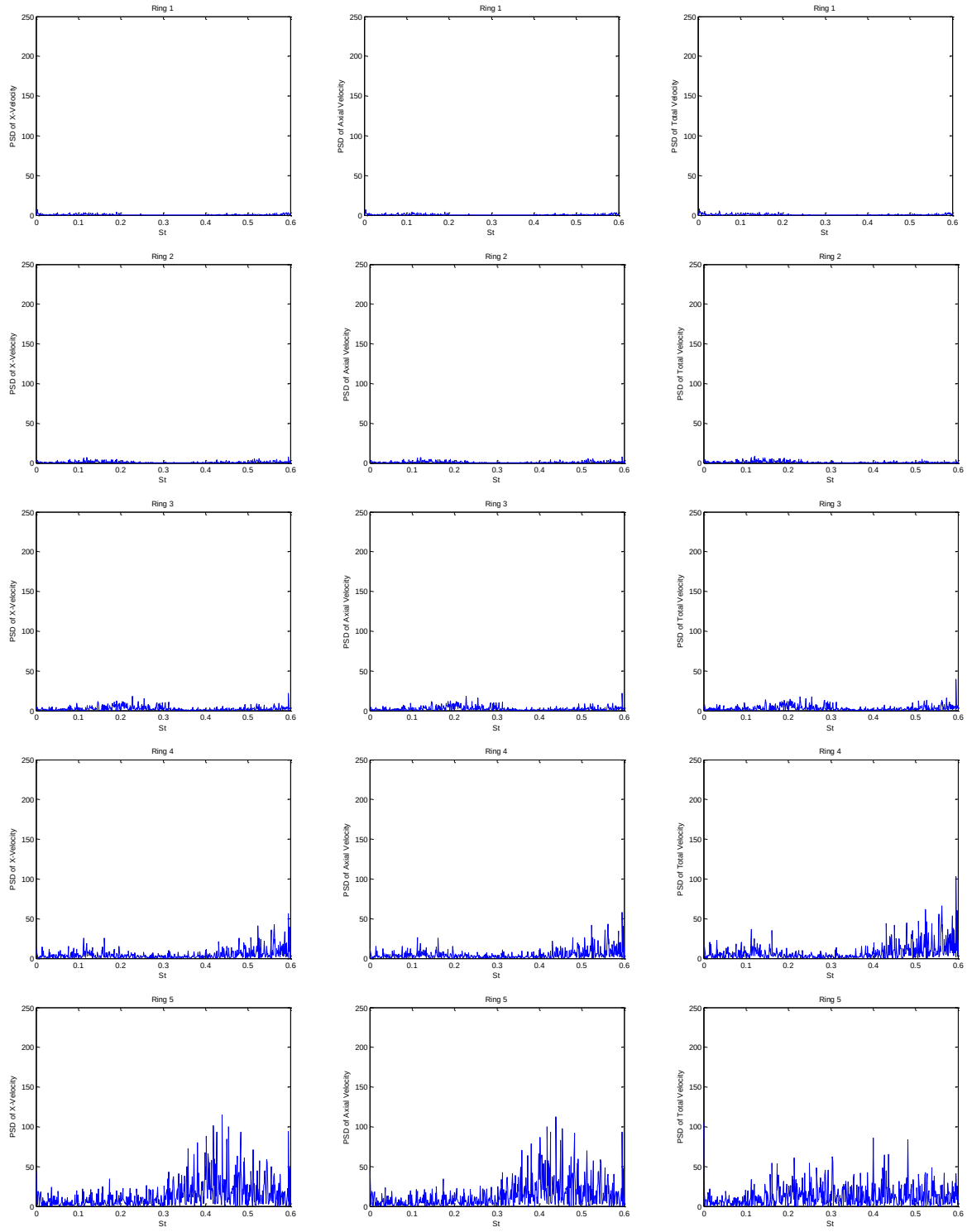
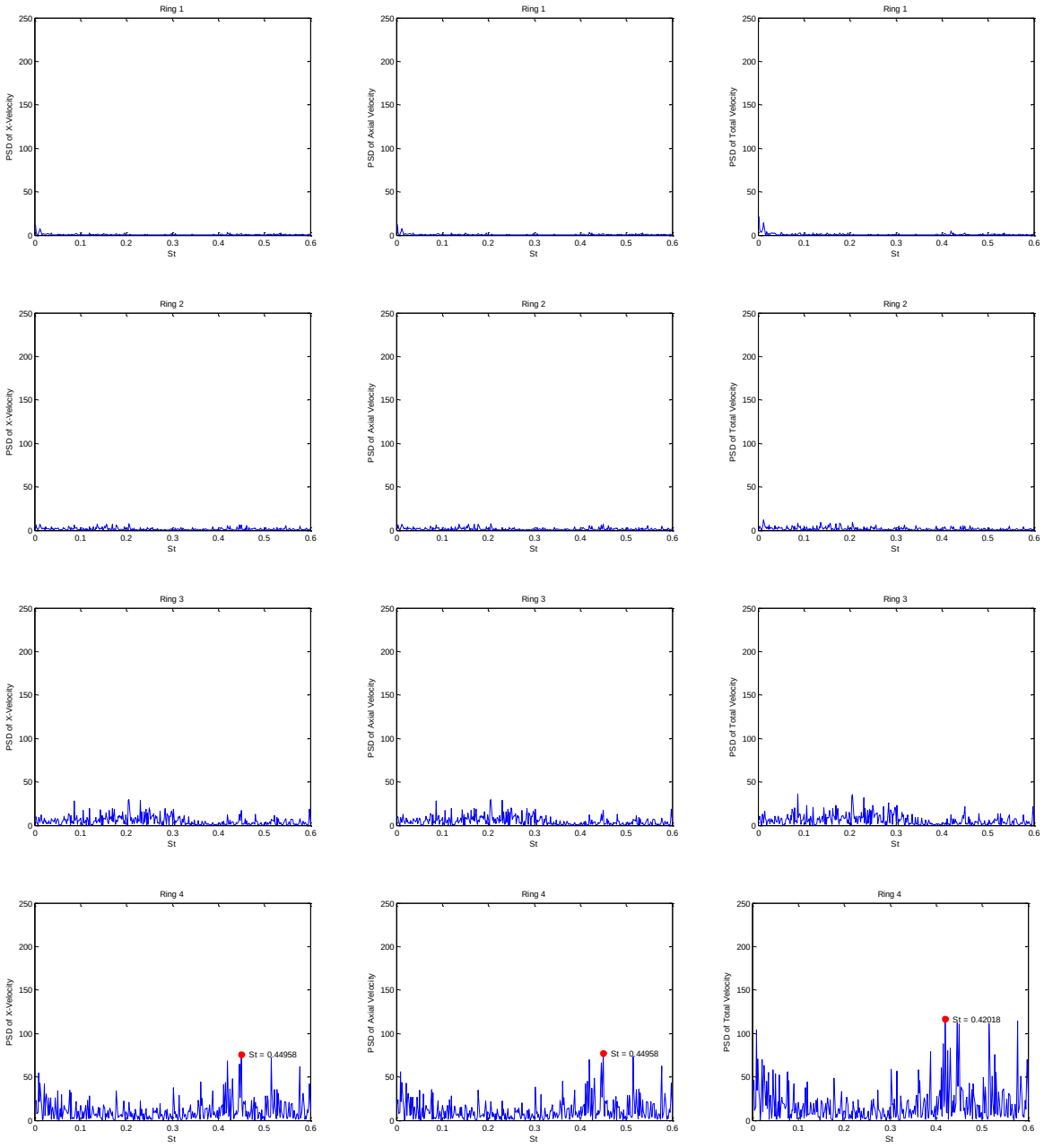


Figure O: FFT results Leeward Velocity:

j) $\phi = 35.5°$; $\alpha = 30°$, $\beta = 20°$

v) Re = 5.5×10^5;



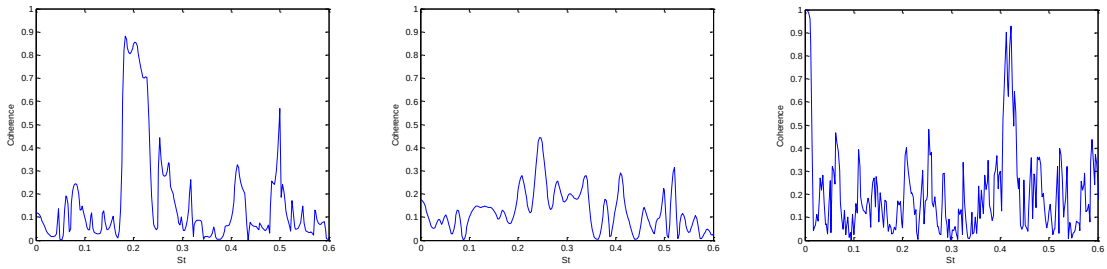
Appendix P: Coherence and Cross-Coherence.

Figure P: Coherence

a) $\phi = 0°$; $\alpha = 0°$, $\beta = 0°$

i) Re = 1.1×10^5;

C_L-Pressure C_L-Total Velocity Pressure-Total Velocity



Cross-coherence: C_L-Pressure-Total Velocity

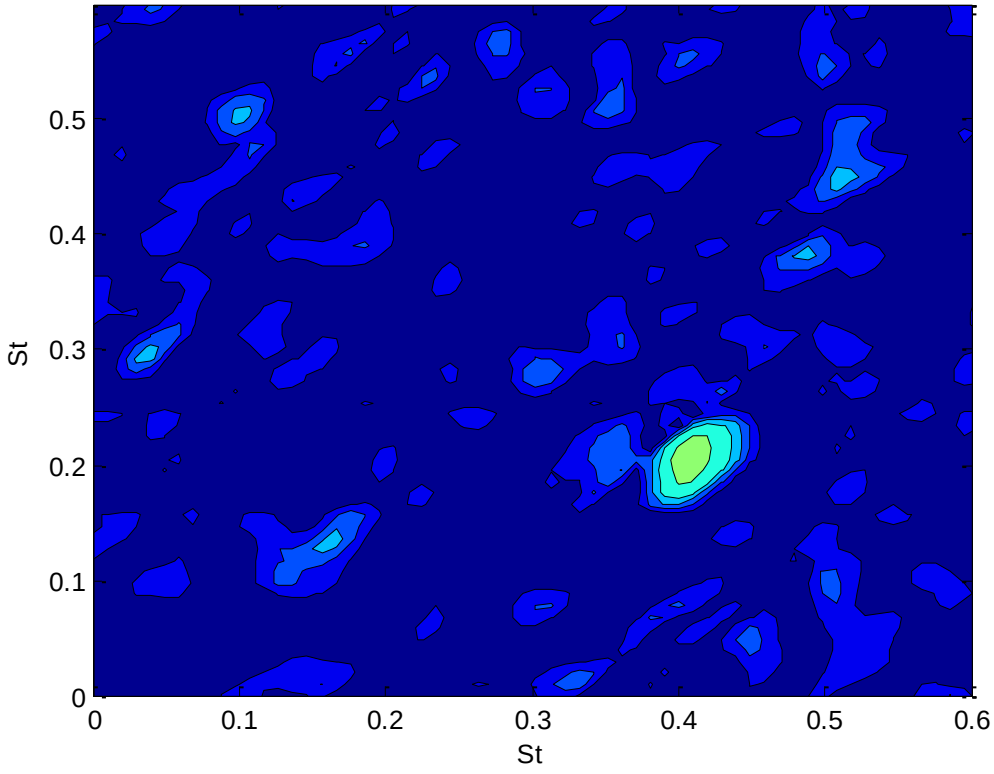
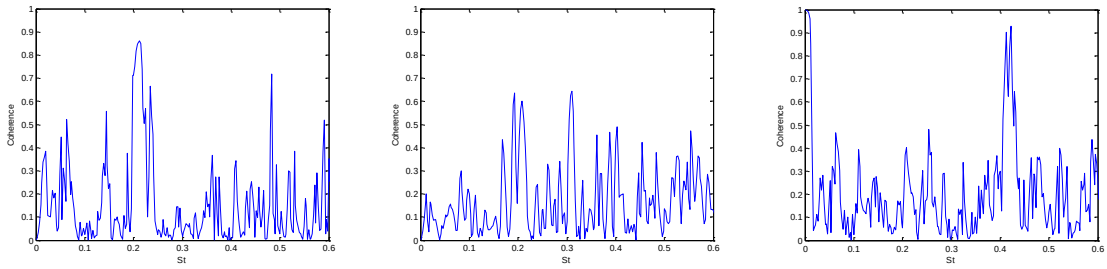


Figure P: Coherence

a) $\phi = 0°$; $\alpha = 0°$, $\beta = 0°$

ii) Re = 2.2×10^5;

C_L-Pressure C_L-Total Velocity Pressure-Total Velocity



Cross-coherence: C_L-Pressure-Total Velocity

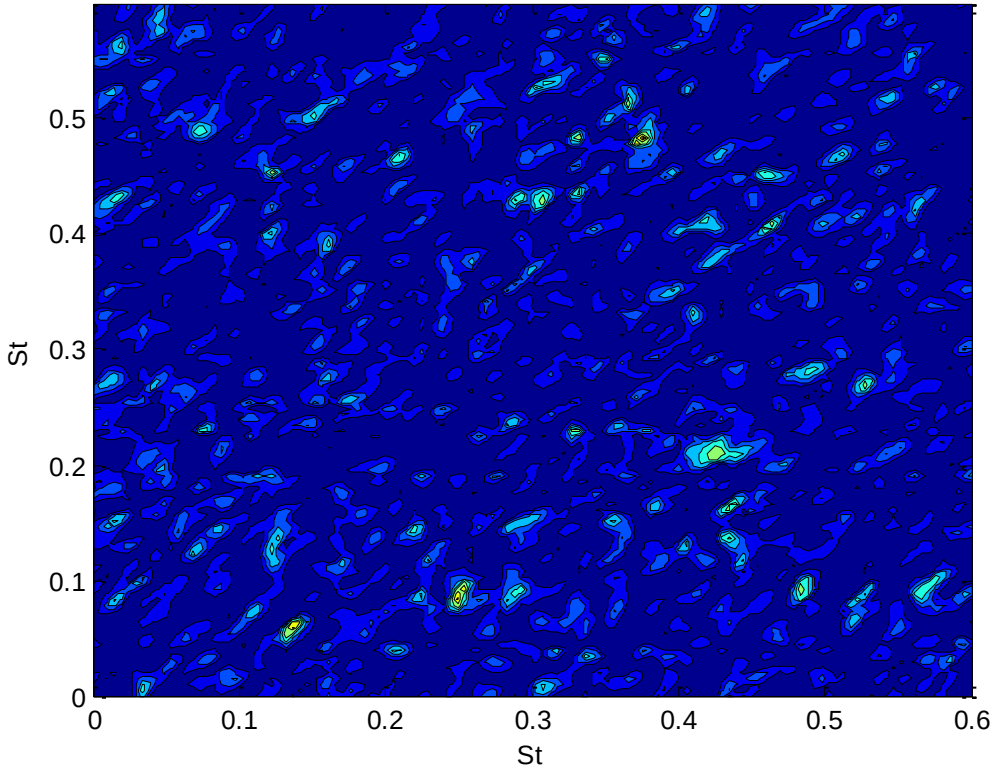
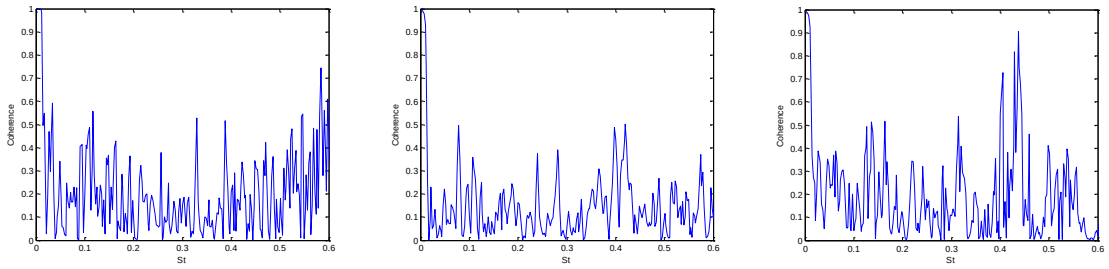


Figure P: Coherence

a) $\phi = 0°$; $\alpha = 0°$, $\beta = 0°$

iii) Re = 3.3×10^5;

C_L-Pressure C_L-Total Velocity Pressure-Total Velocity



Cross-coherence: C_L-Pressure-Total Velocity

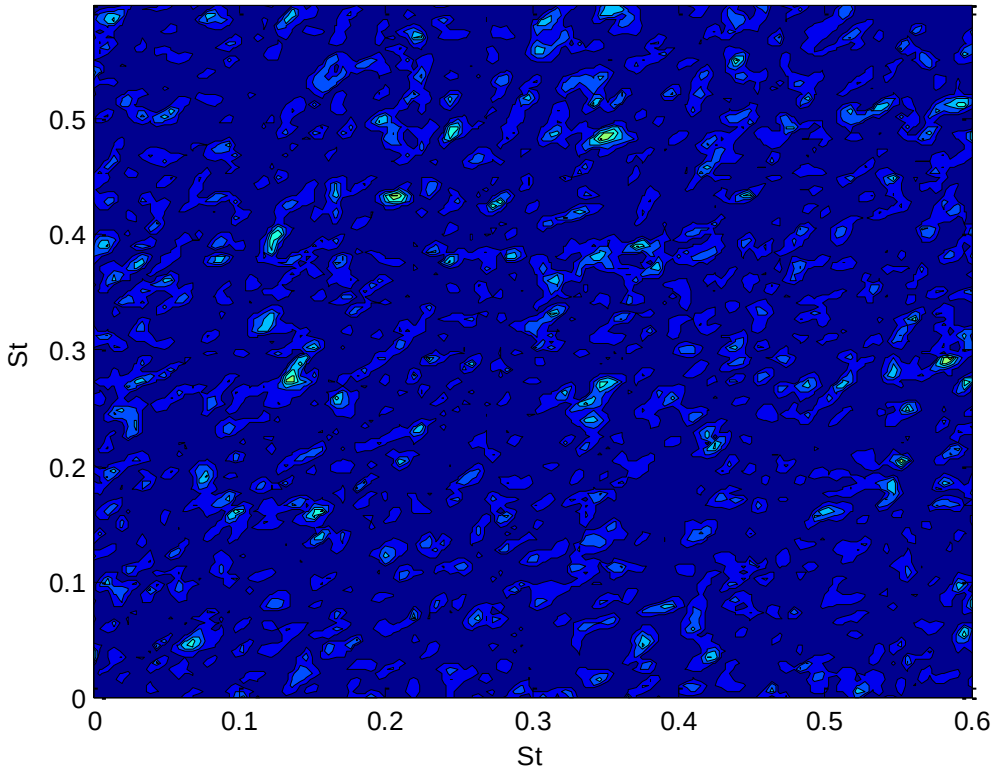
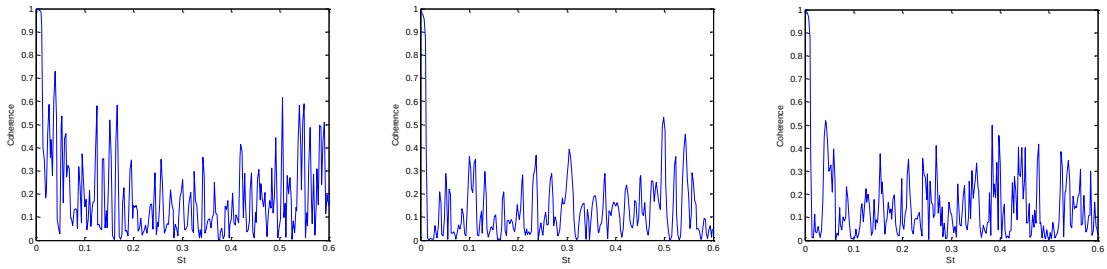


Figure P: Coherence

a) $\phi = 0°$; $\alpha = 0°$, $\beta = 0°$

iv) Re = 4.4×10^5;

C_L-Pressure C_L-Total Velocity Pressure-Total Velocity



Cross-coherence: C_L-Pressure-Total Velocity

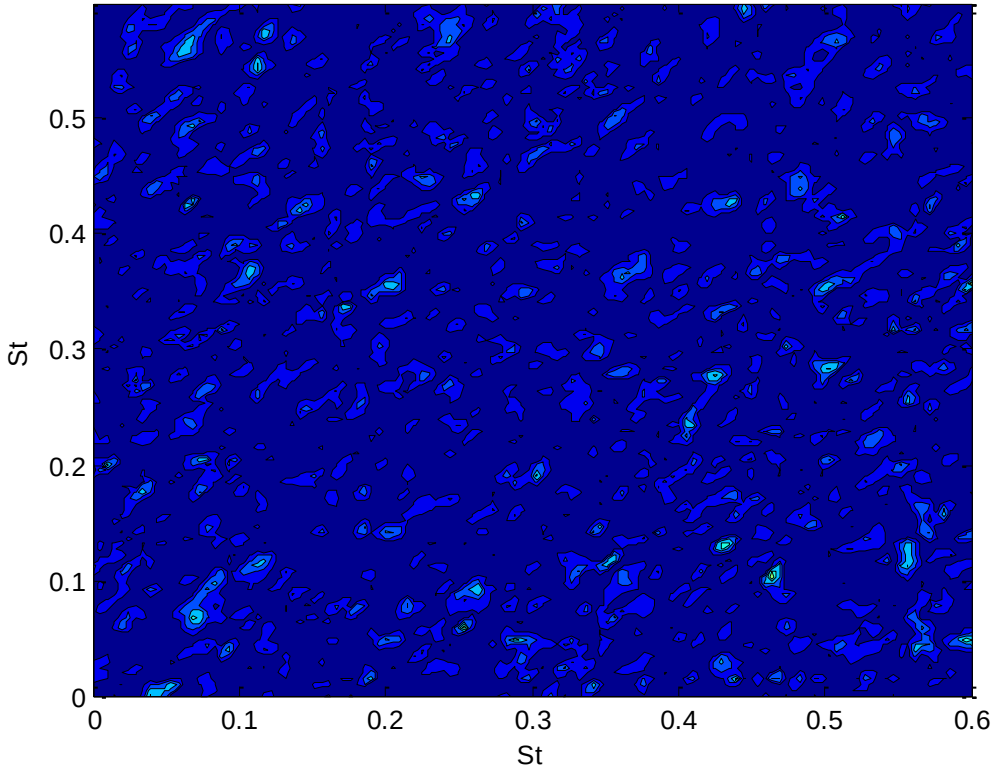
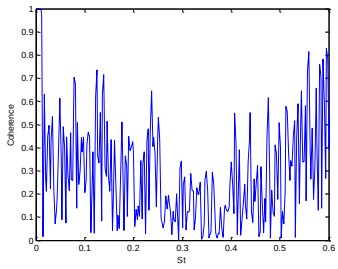


Figure P: Coherence

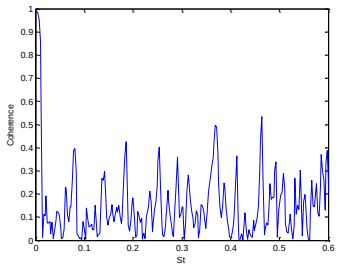
a) $\phi = 0°$; $\alpha = 0°$, $\beta = 0°$

v) Re = 5.5×10^5;

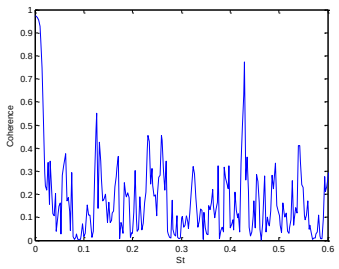
C_L-Pressure



C_L-Total Velocity



Pressure-Total Velocity



Cross-coherence: C_L-Pressure-Total Velocity

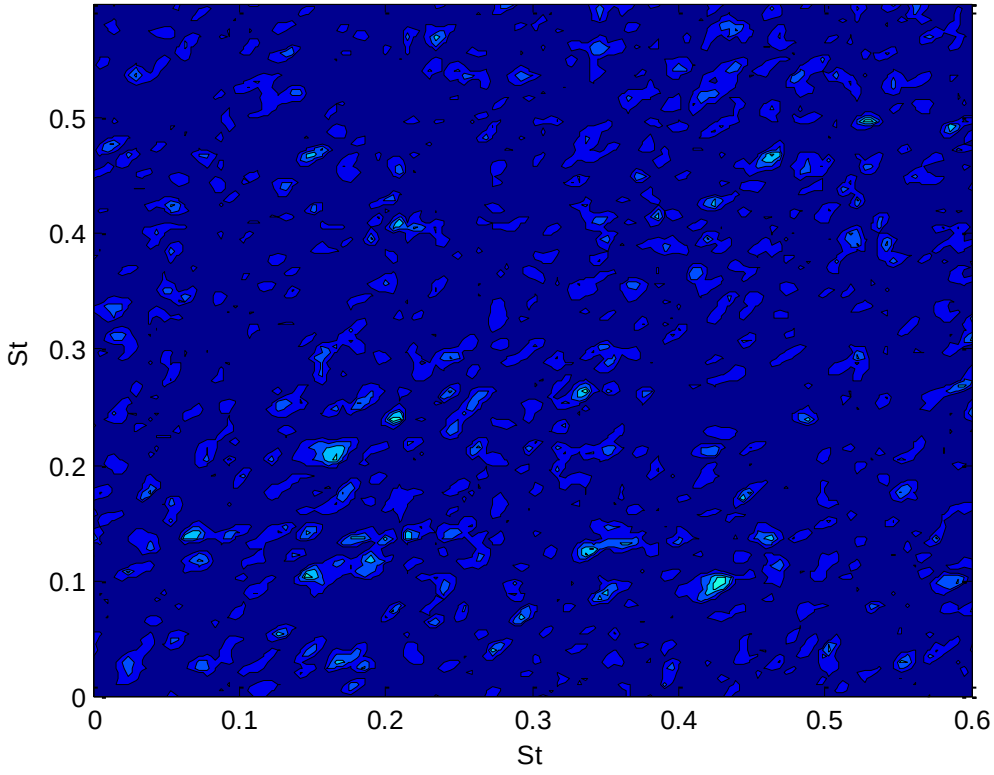
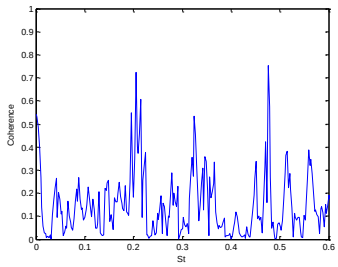


Figure P: Coherence

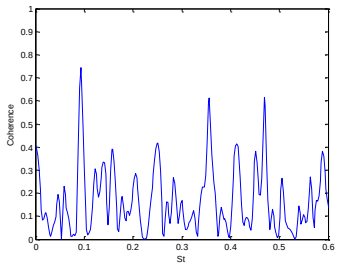
a) $\phi = 0°$; $\alpha = 0°$, $\beta = 0°$

vi) Re = 6.7×10^5;

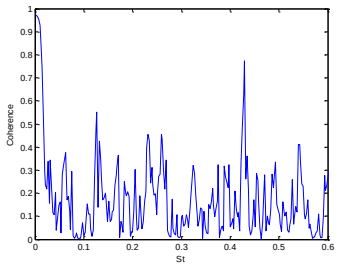
C_L-Pressure



C_L-Total Velocity



Pressure-Total Velocity



Cross-coherence: C_L-Pressure-Total Velocity

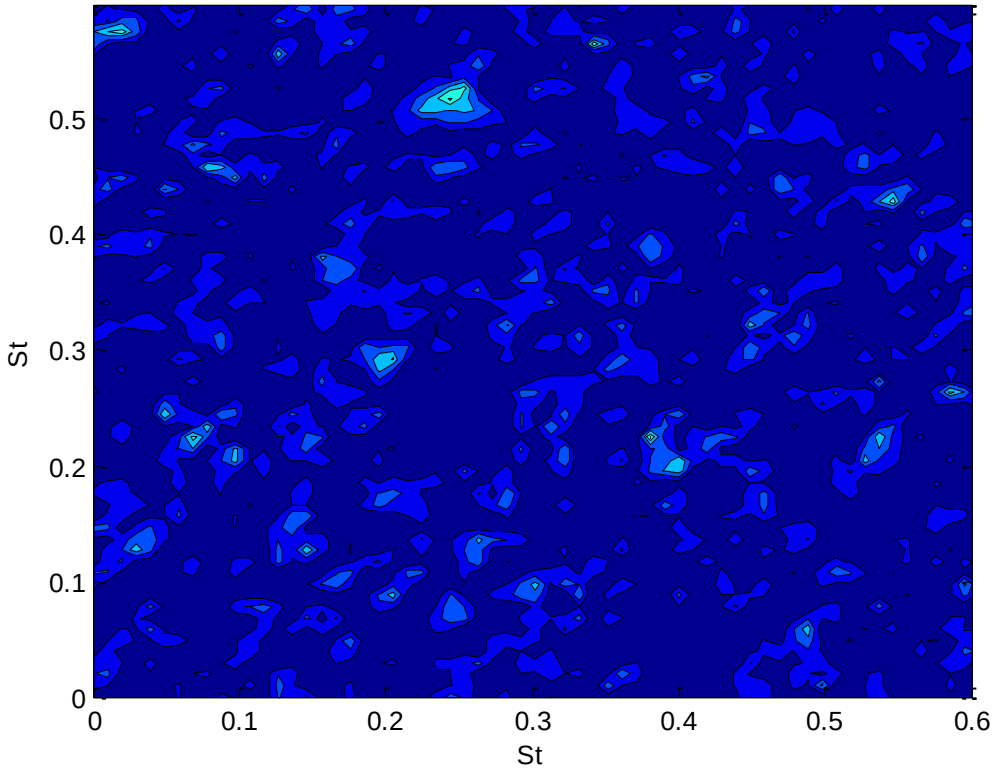
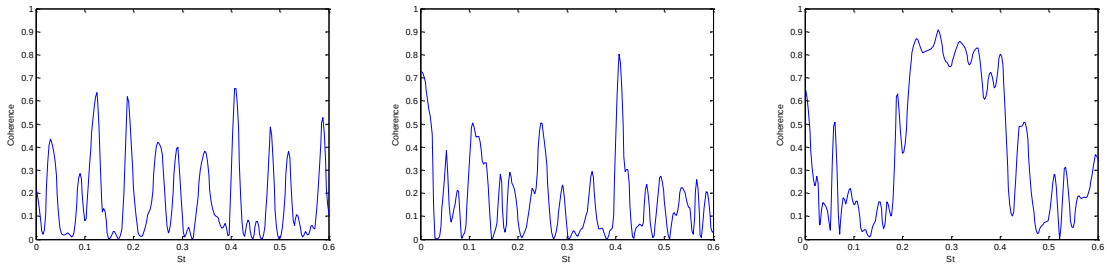


Figure P: Coherence

b) $\phi = 60°$; $\alpha = 0°$, $\beta = 60°$

i) Re = 1.1×10^5;

C_L-Pressure C_L-Total Velocity Pressure-Total Velocity



Cross-coherence: C_L-Pressure-Total Velocity

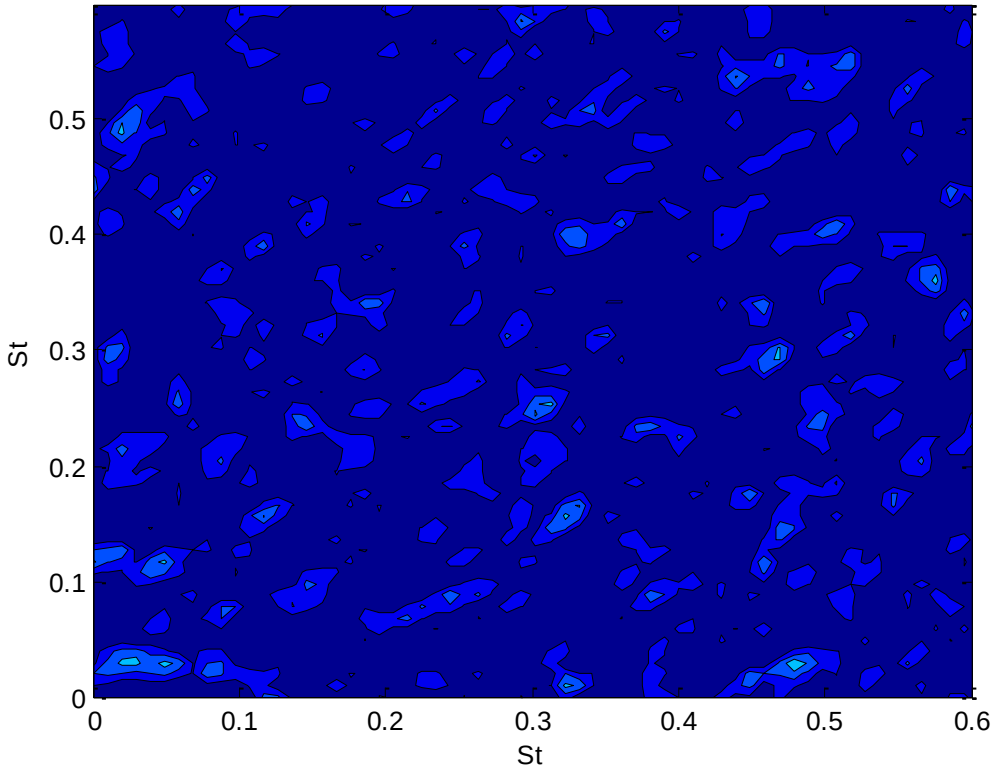
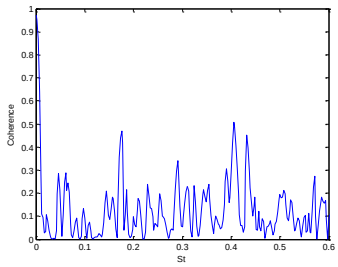


Figure P: Coherence

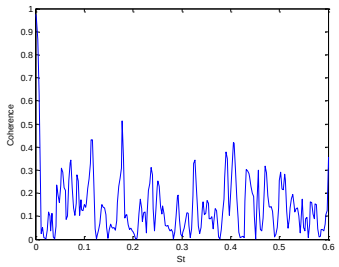
b) $\phi = 60°$; $\alpha = 0°$, $\beta = 60°$

ii) Re = 2.2×10^5;

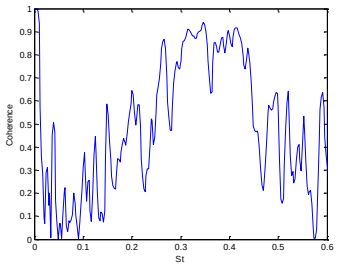
C_L-Pressure



C_L-Total Velocity



Pressure-Total Velocity



Cross-coherence: C_L-Pressure-Total Velocity

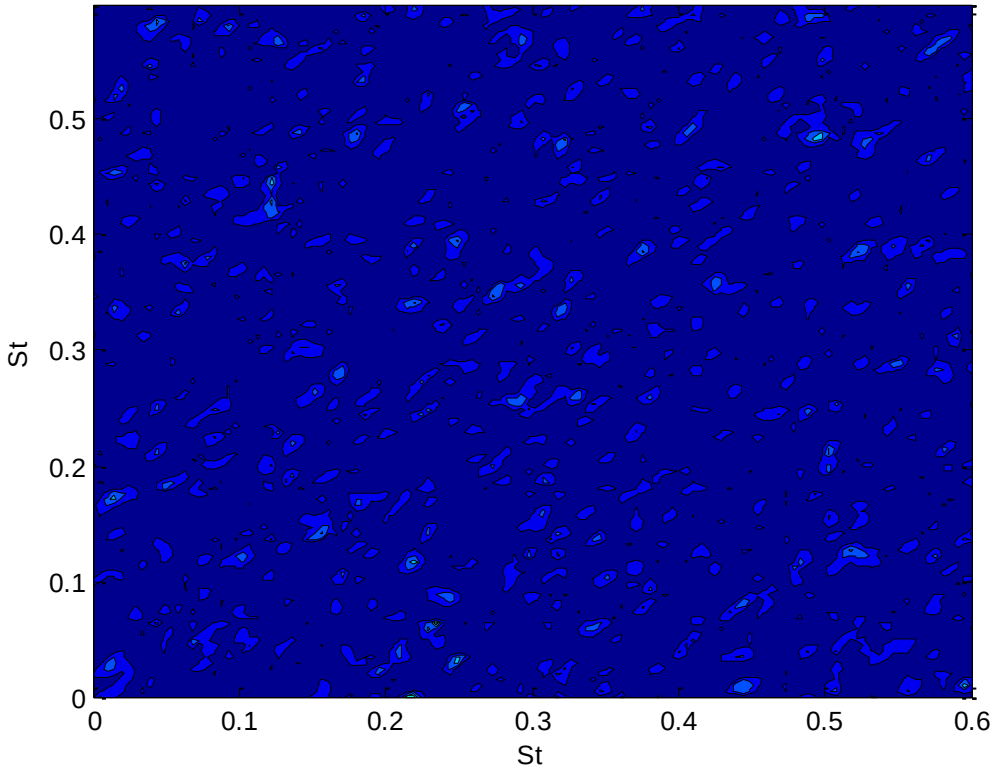
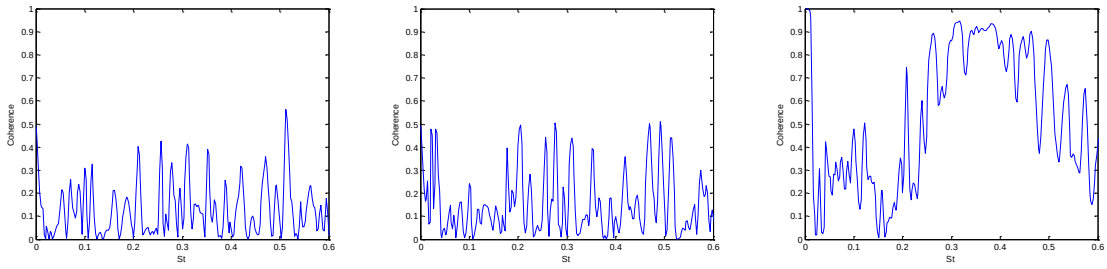


Figure P: Coherence

b) $\phi = 60°$; $\alpha = 0°$, $\beta = 60°$

iii) Re = 3.3×10^5;

C_L-Pressure C_L-Total Velocity Pressure-Total Velocity



Cross-coherence: C_L-Pressure-Total Velocity

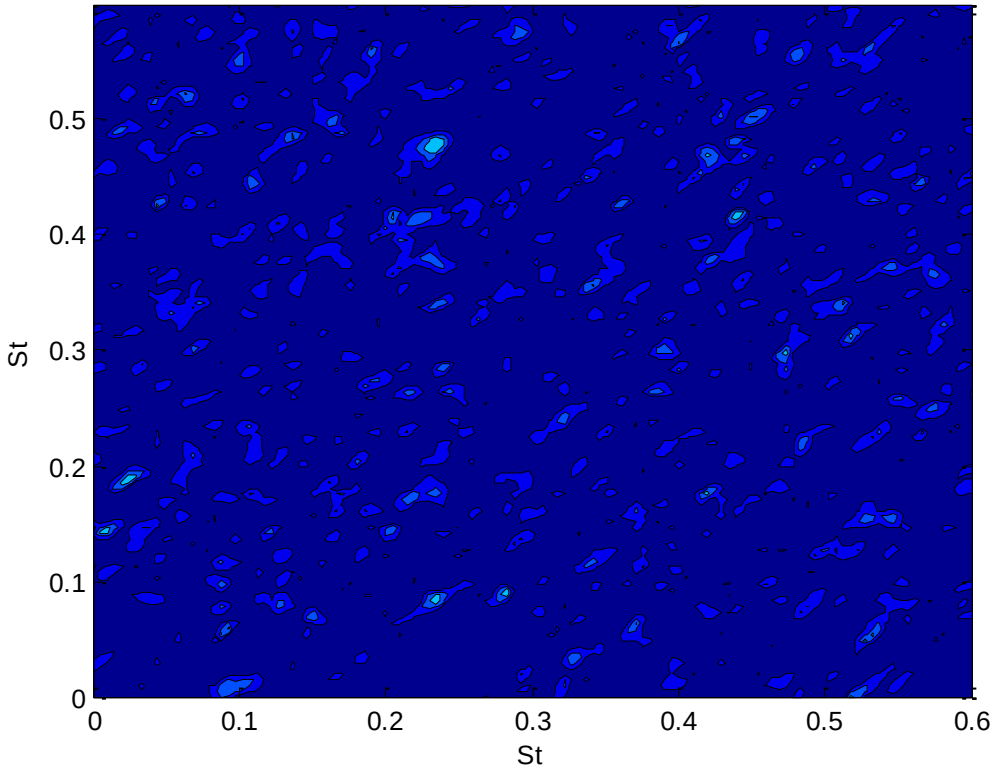
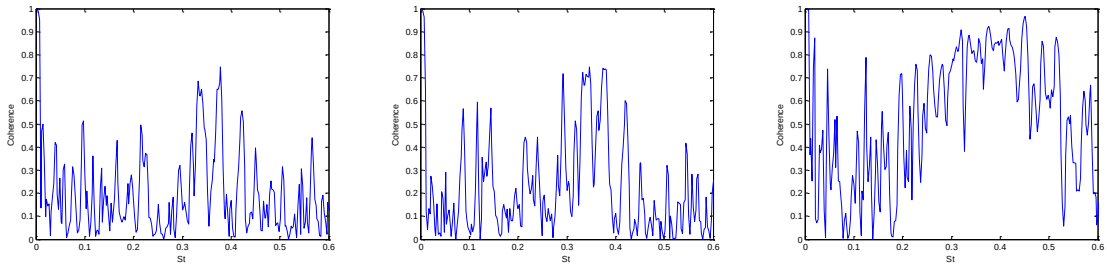


Figure P: Coherence

b) $\phi = 60°$; $\alpha = 0°$, $\beta = 60°$

iv) Re = 4.4×10^5;

C_L-Pressure C_L-Total Velocity Pressure-Total Velocity



Cross-coherence: C_L-Pressure-Total Velocity

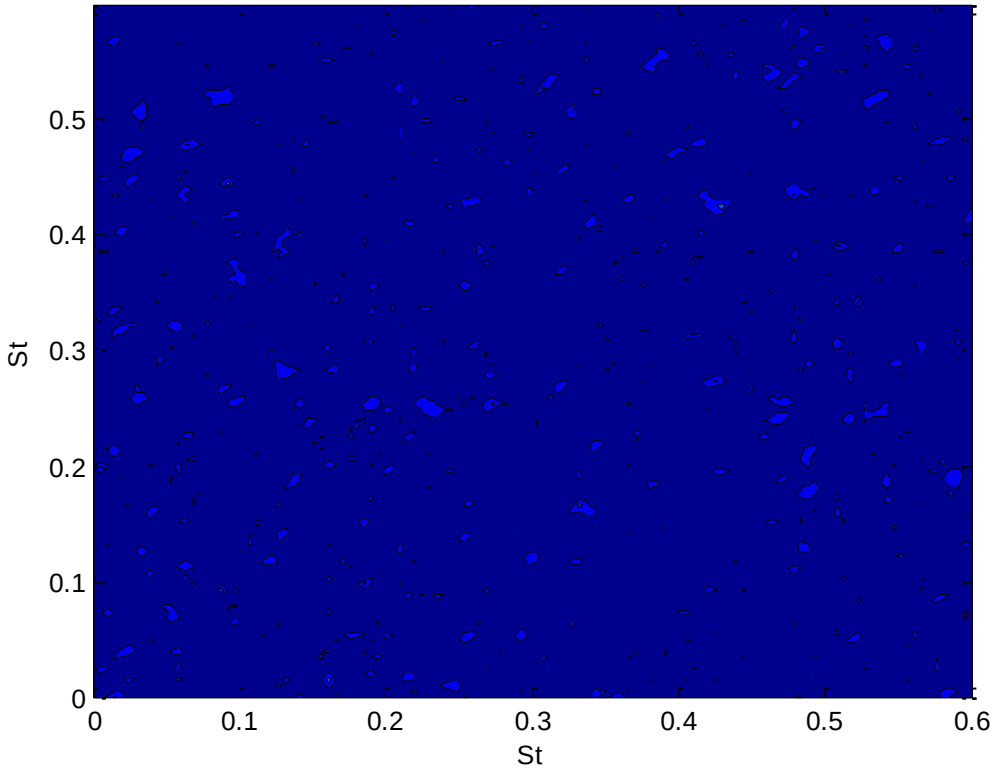
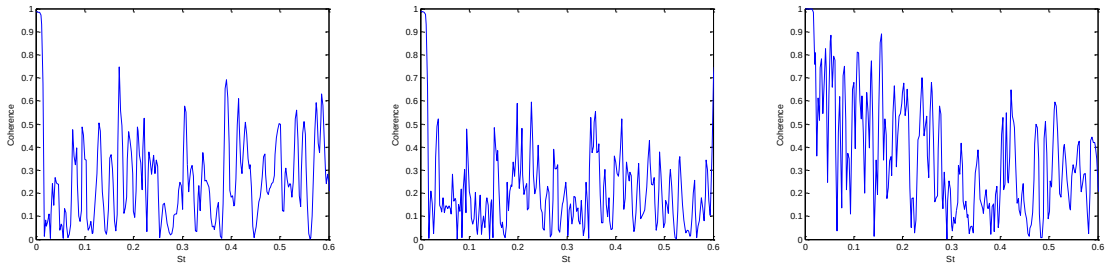


Figure P: Coherence

b) $\phi = 60°$; $\alpha = 0°$, $\beta = 60°$

v) Re = 5.5×10^5;

C_L-Pressure C_L-Total Velocity Pressure-Total Velocity



Cross-coherence: C_L-Pressure-Total Velocity

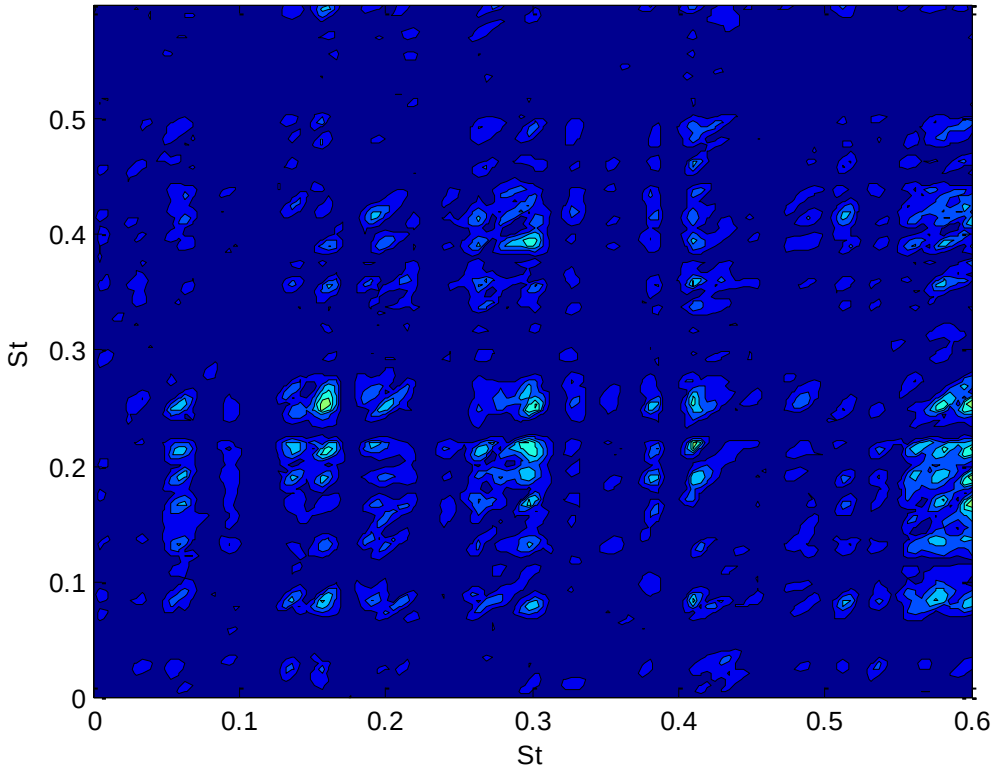
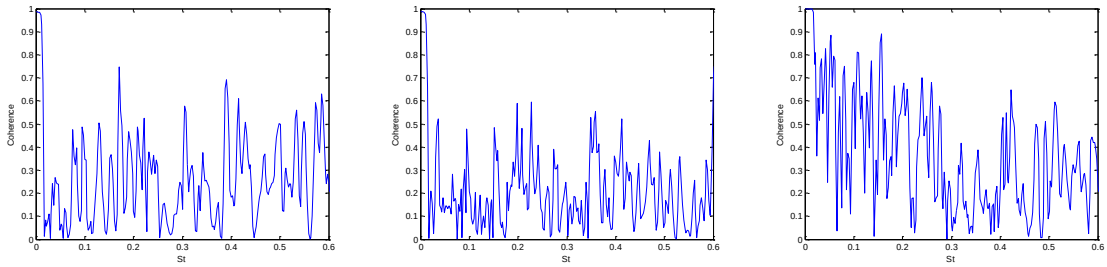


Figure P: Coherence

b) $\phi = 60°$; $\alpha = 0°$, $\beta = 60°$

vi) Re = 6.7×10^5;

C_L-Pressure C_L-Total Velocity Pressure-Total Velocity



Cross-coherence: C_L-Pressure-Total Velocity

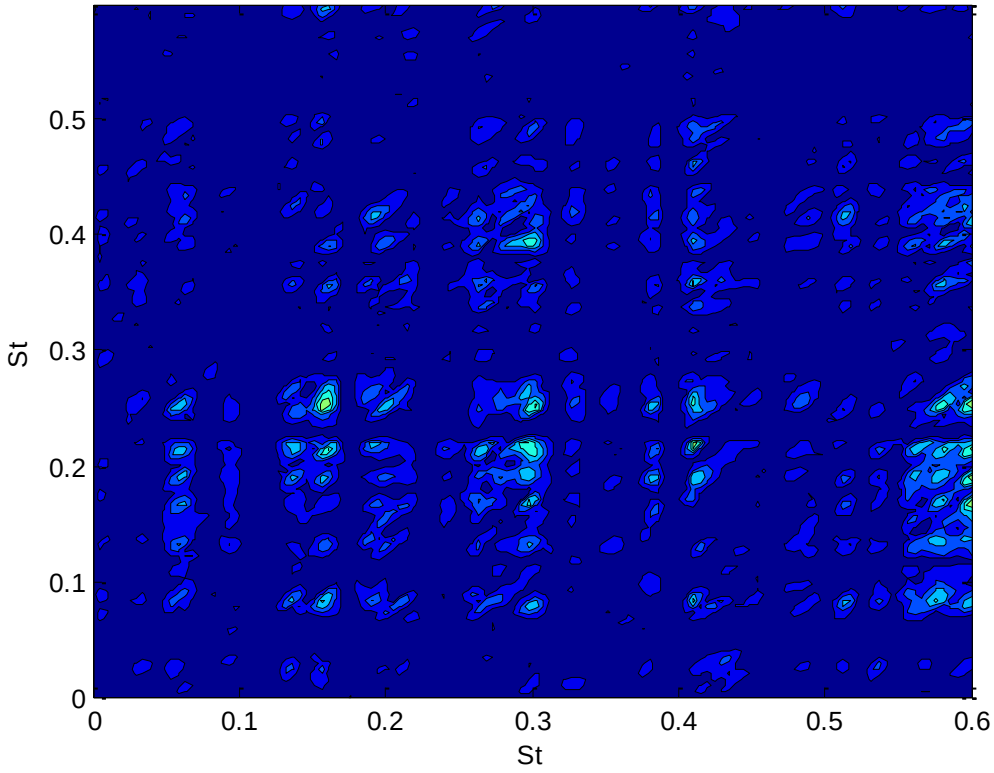
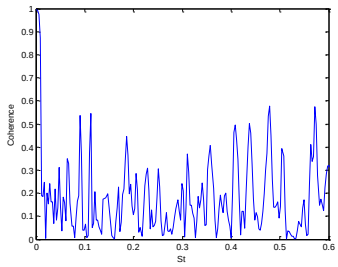


Figure P: Coherence

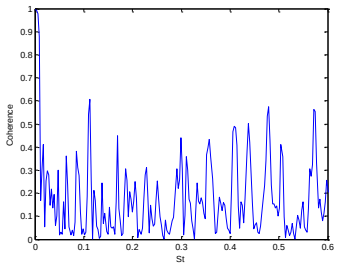
c) $\phi = 62°$; $\alpha = 60°$, $\beta = 20°$

i) Re = 1.1×10^5;

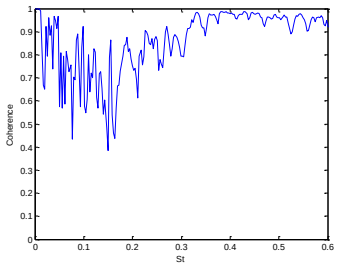
C_L-Pressure



C_L-Total Velocity



Pressure-Total Velocity



Cross-coherence: C_L-Pressure-Total Velocity

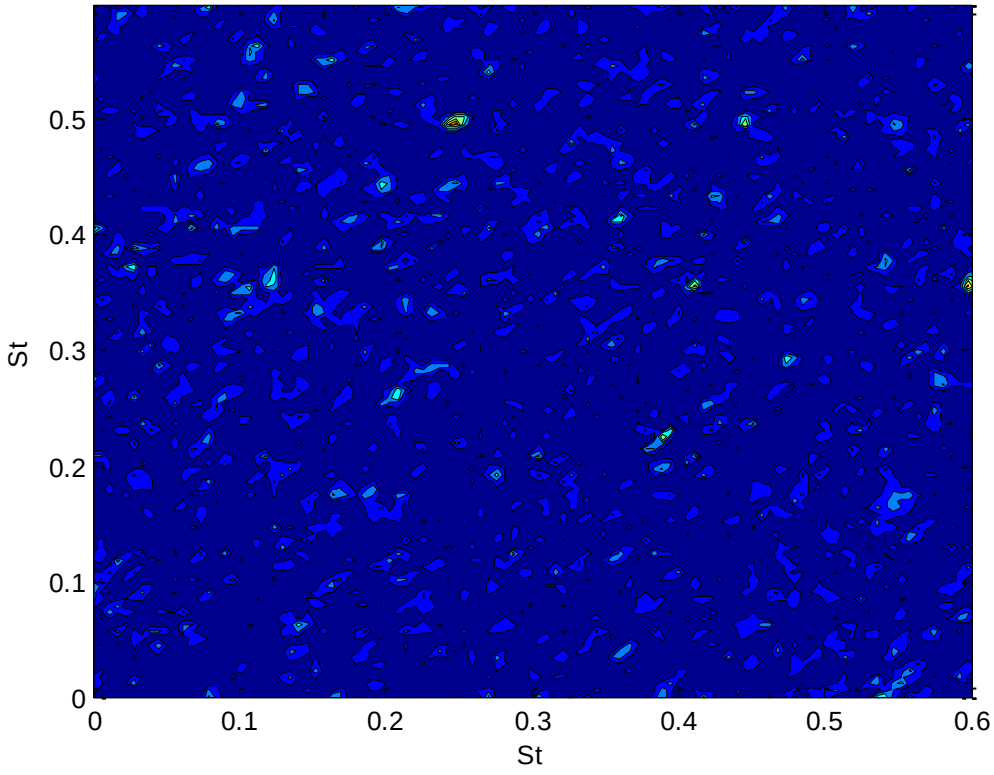
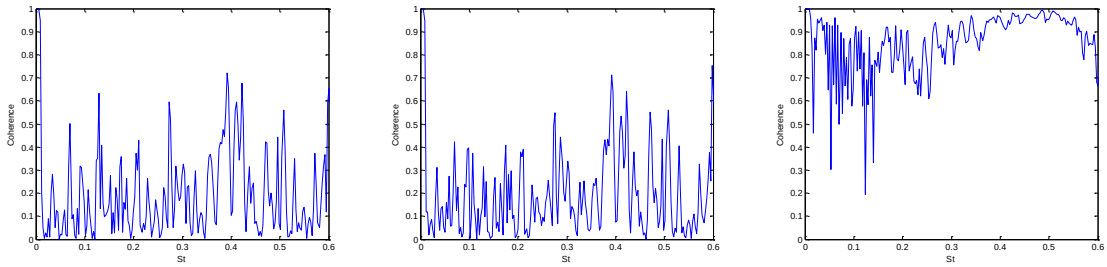


Figure P: Coherence

c) $\phi = 62°$; $\alpha = 60°$, $\beta = 20°$

ii) Re = 2.2×10^5;

C_L-Pressure C_L-Total Velocity Pressure-Total Velocity



Cross-coherence: C_L-Pressure-Total Velocity

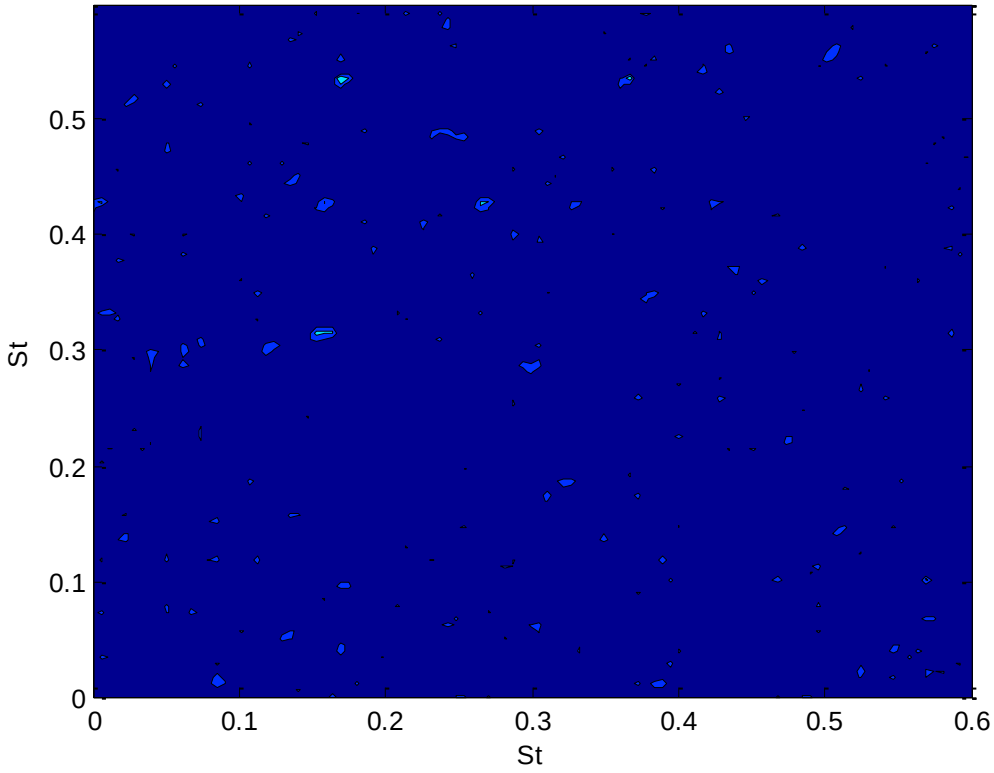
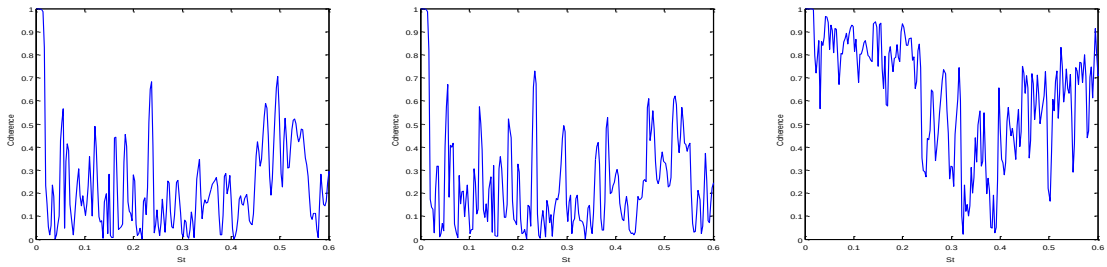


Figure P: Coherence

c) $\phi = 62°$; $\alpha = 60°$, $\beta = 20°$

iii) Re = 3.3×10^5;

C_L-Pressure C_L-Total Velocity Pressure-Total Velocity



Cross-coherence: C_L-Pressure-Total Velocity

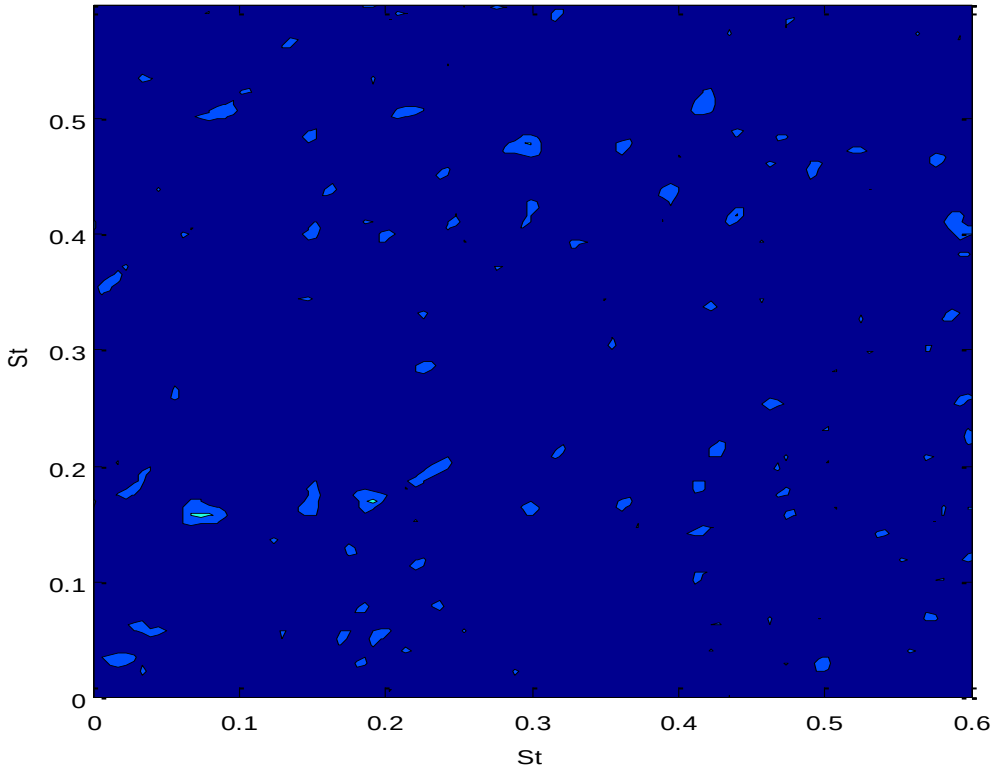
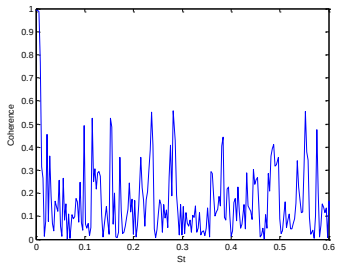


Figure P: Coherence

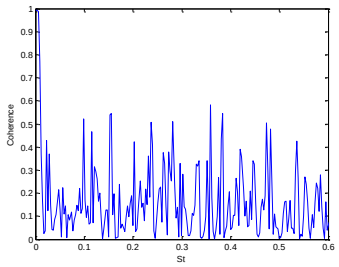
c) $\phi = 62°$; $\alpha = 60°$, $\beta = 20°$

iv) Re = 4.4×10^5;

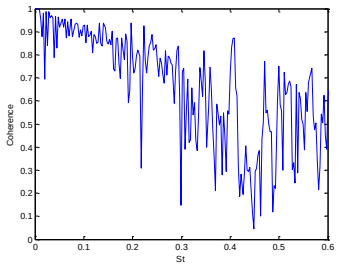
C_L-Pressure



C_L-Total Velocity



Pressure-Total Velocity



Cross-coherence: C_L-Pressure-Total Velocity

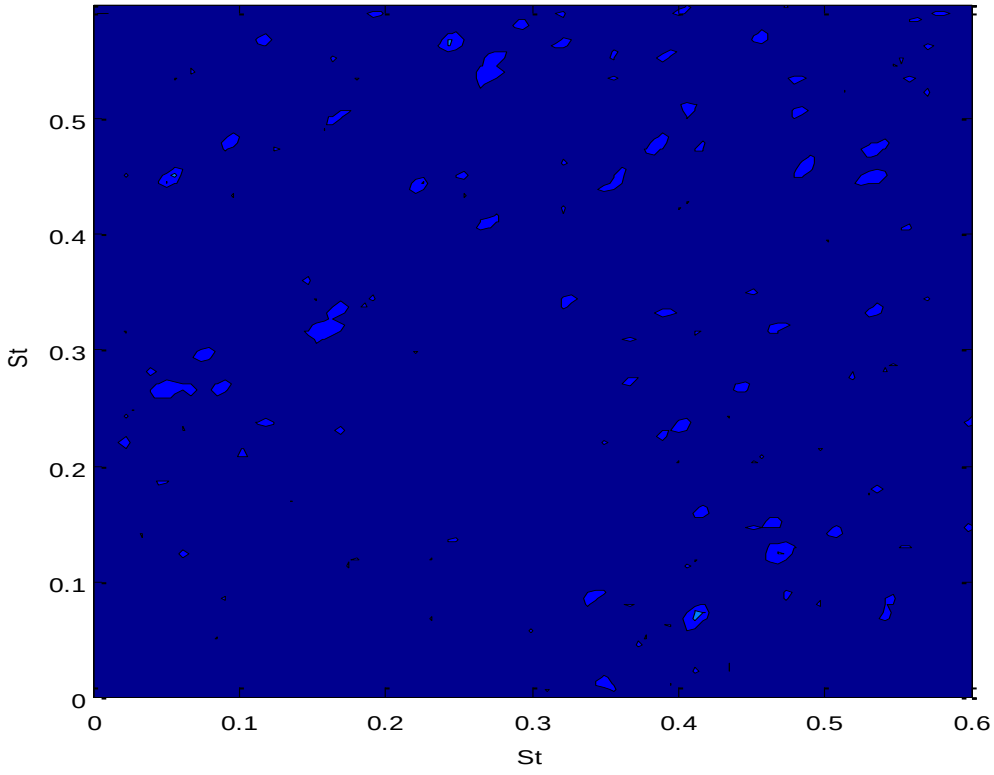
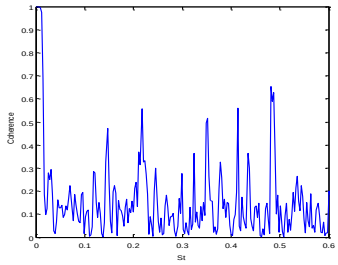


Figure P: Coherence

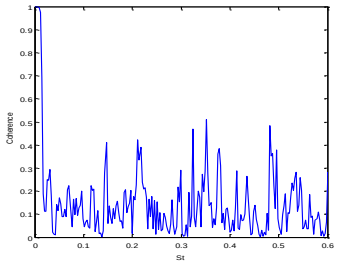
c) $\phi = 62°$; $\alpha = 60°$, $\beta = 20°$

v) Re = 5.5×10^5;

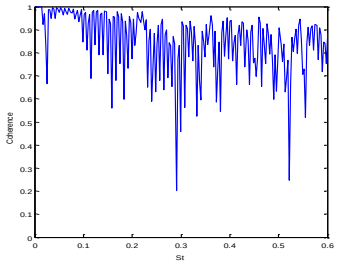
C_L-Pressure



C_L-Total Velocity



Pressure-Total Velocity



Cross-coherence: C_L-Pressure-Total Velocity

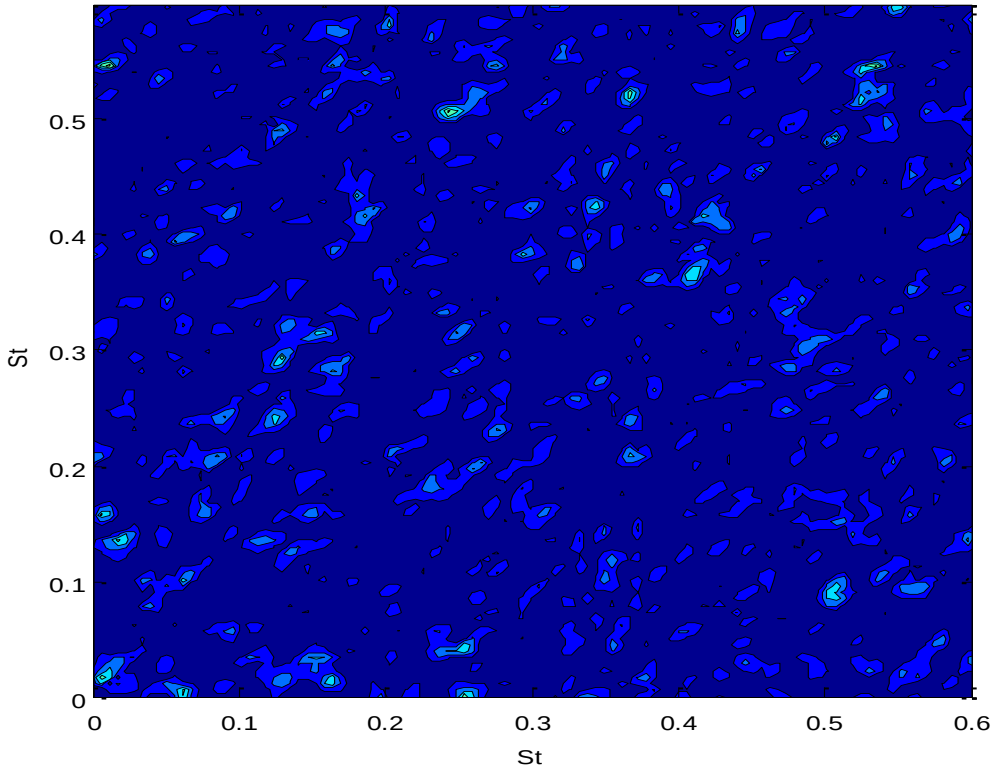
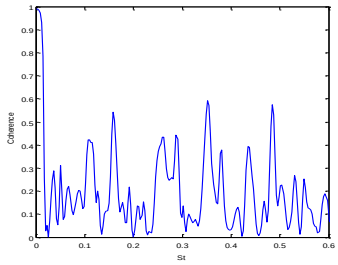


Figure P: Coherence

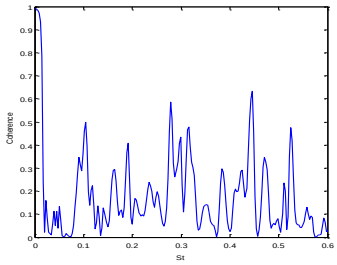
d) $\phi = 67.5°$; $\alpha = 60°$, $\beta = 40°$

i) Re = 1.1×10^5;

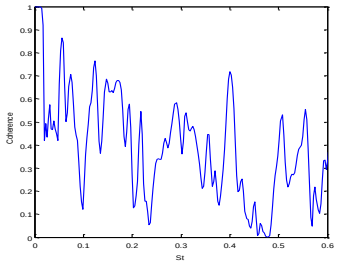
C_L-Pressure



C_L-Total Velocity



Pressure-Total Velocity



Cross-coherence: C_L-Pressure-Total Velocity

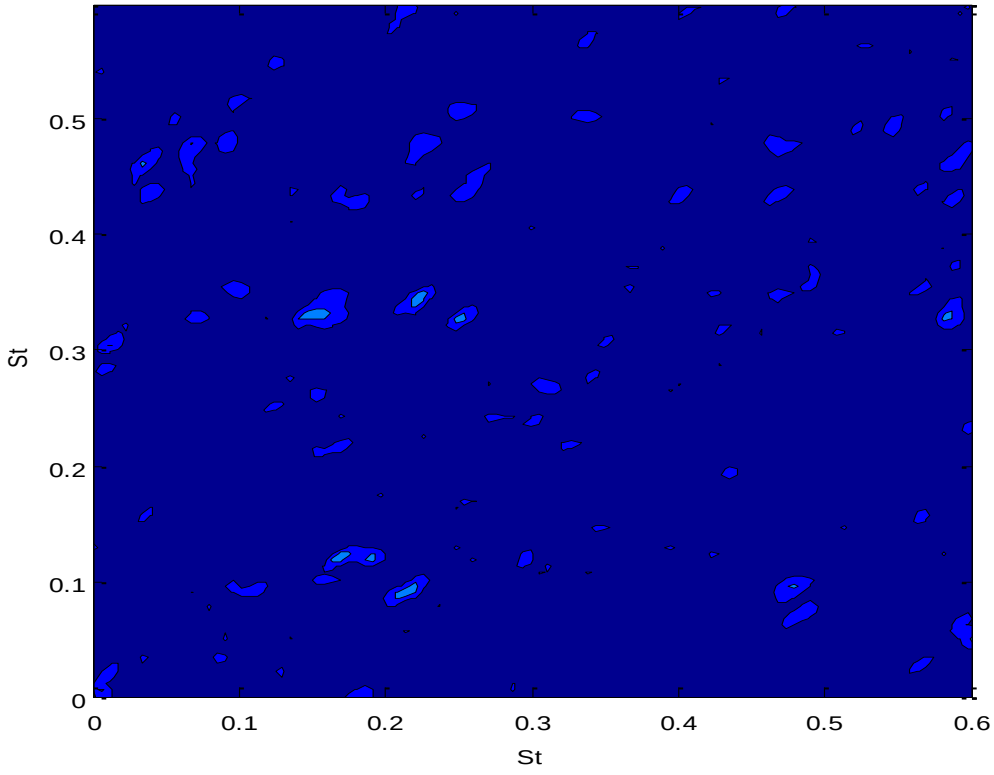
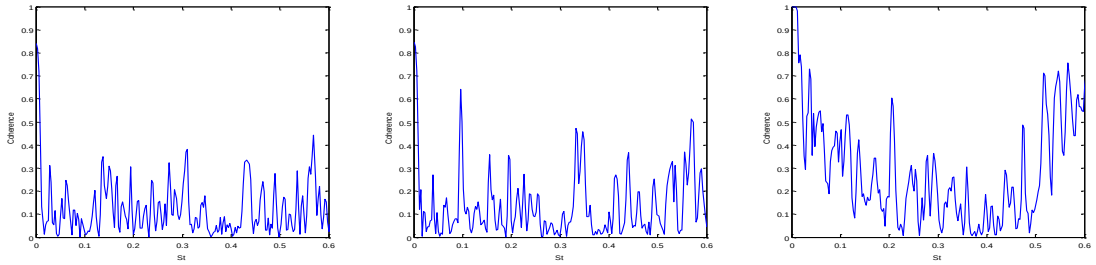


Figure P: Coherence

d) $\phi = 67.5°$; $\alpha = 60°$, $\beta = 40°$

iii) Re = 3.3×10^5;

C_L-Pressure C_L-Total Velocity Pressure-Total Velocity



Cross-coherence: C_L-Pressure-Total Velocity

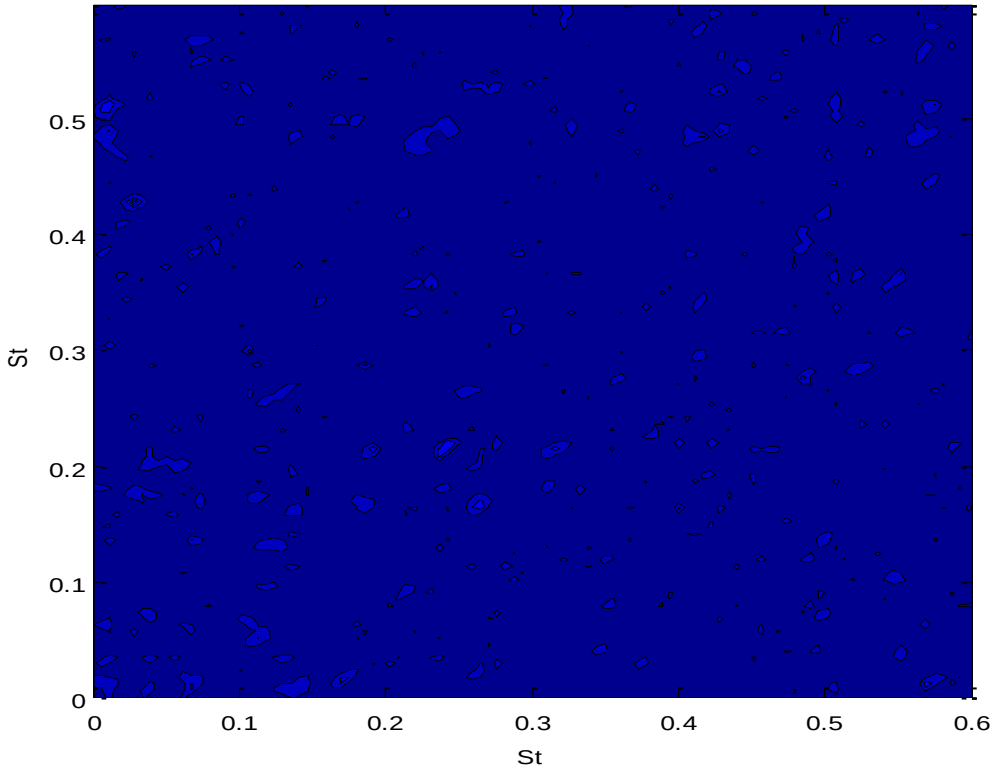
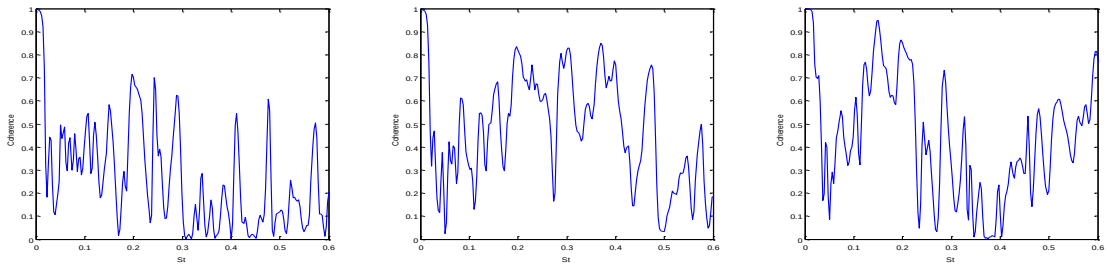


Figure P: Coherence

d) $\phi = 67.5°$; $\alpha = 60°$, $\beta = 40°$

iv) Re = 4.4×10^5;

C_L-Pressure C_L-Total Velocity Pressure-Total Velocity



Cross-coherence: C_L-Pressure-Total Velocity

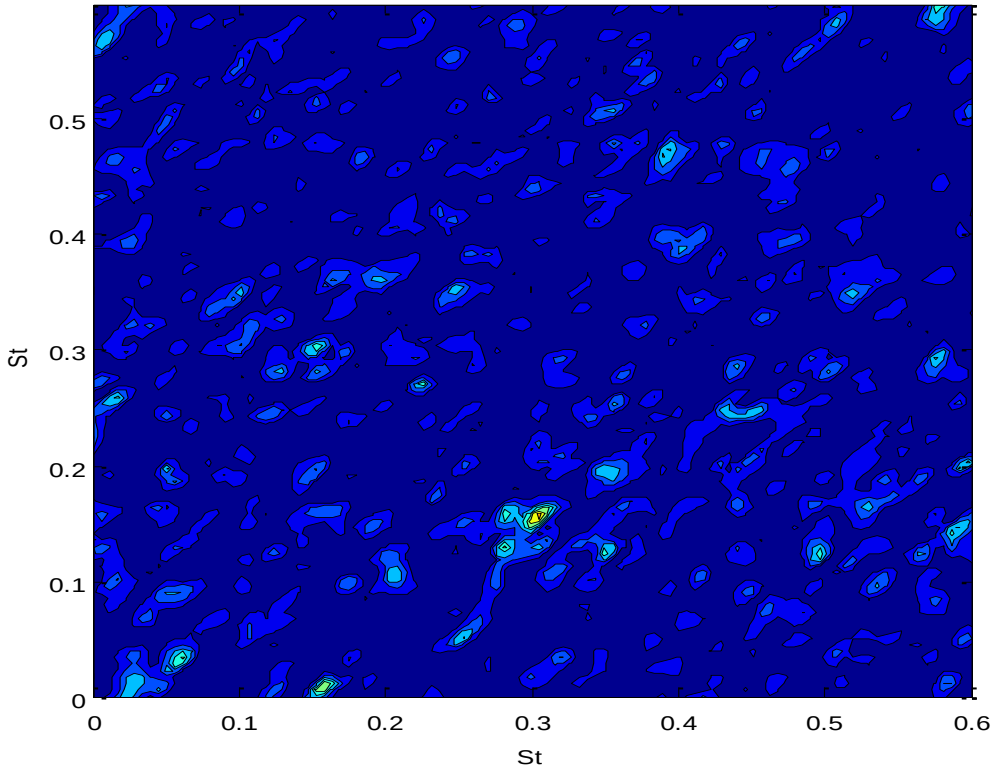
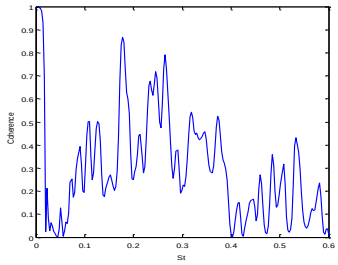


Figure P: Coherence

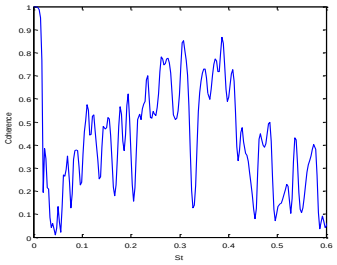
d) $\phi = 67.5°$; $\alpha = 60°$, $\beta = 40°$

v) Re = 5.5×10^5;

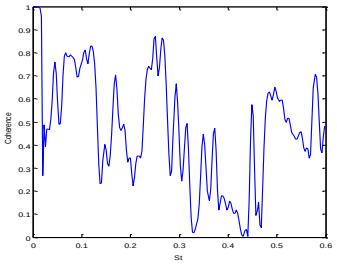
C_L-Pressure



C_L-Total Velocity



Pressure-Total Velocity



Cross-coherence: C_L-Pressure-Total Velocity

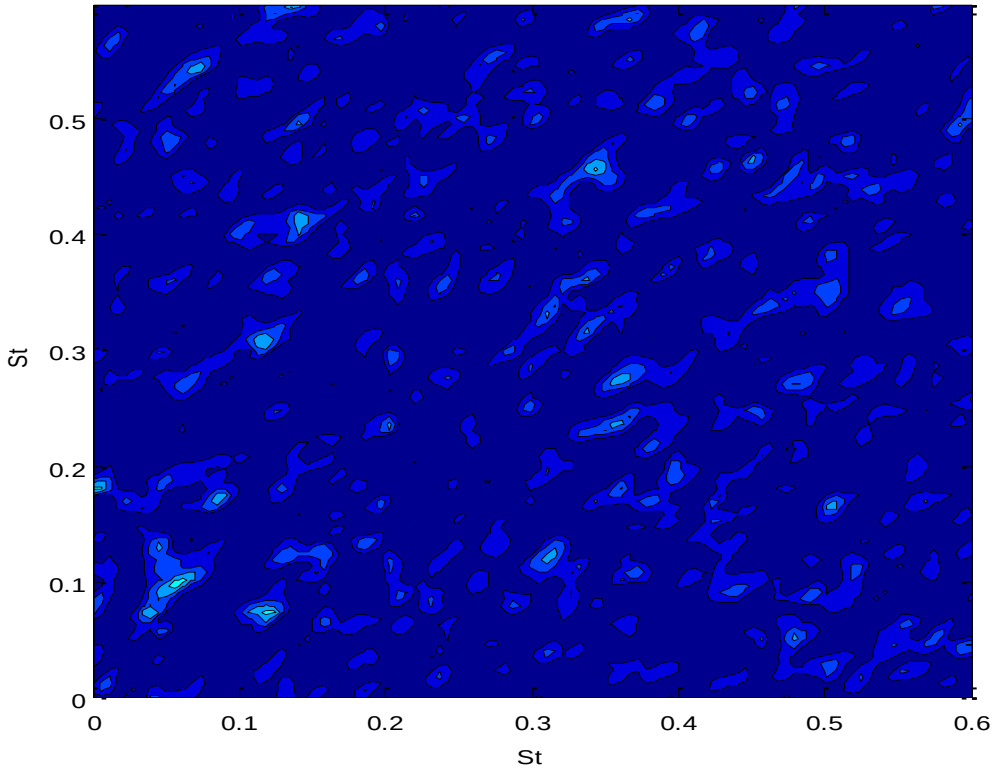
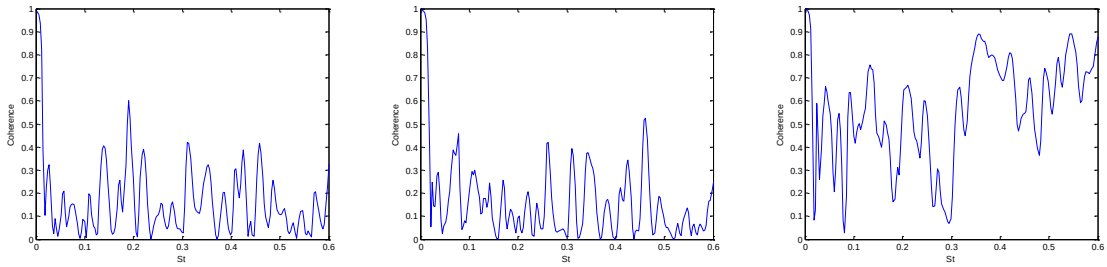


Figure P: Coherence

e) $\phi = 54.7°$; $\alpha = 54.7°$, $\beta = 0°$

i) Re = 1.1×10^5;

C_L-Pressure C_L-Total Velocity Pressure-Total Velocity



Cross-coherence: C_L-Pressure-Total Velocity

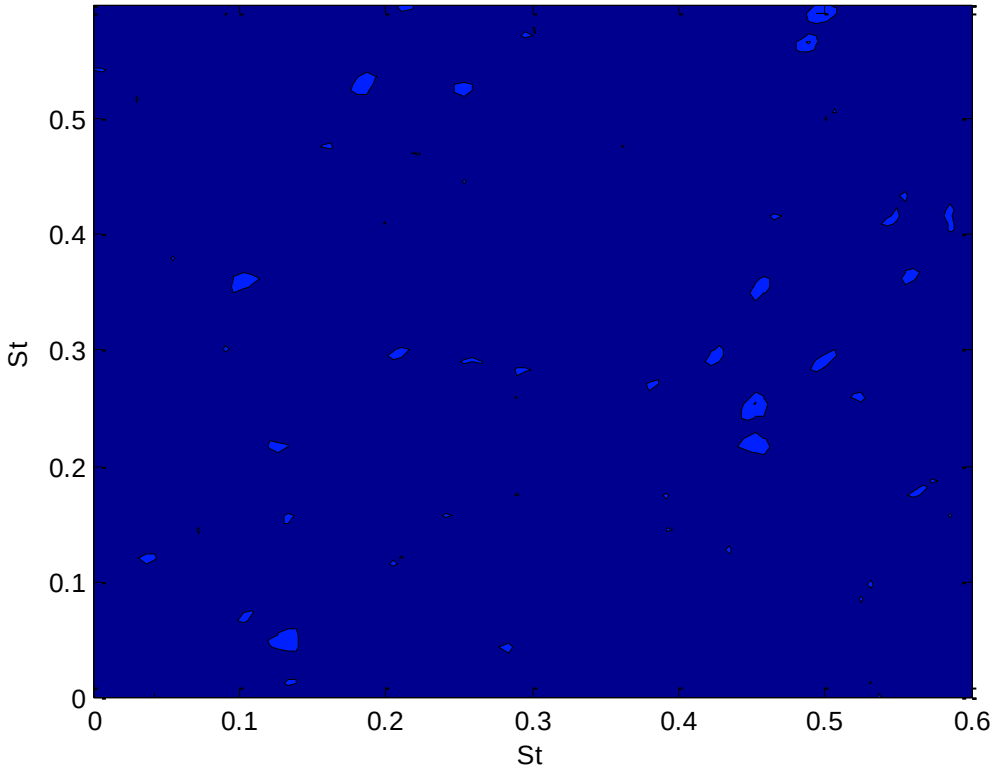
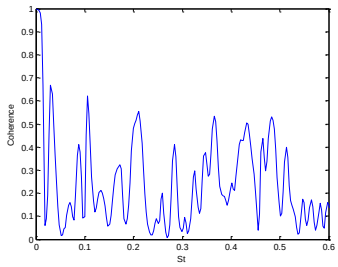


Figure P: Coherence

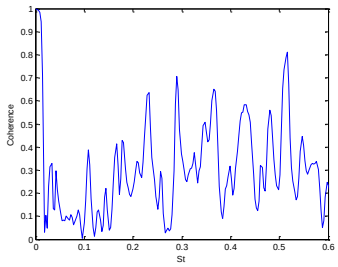
e) $\phi = 54.7°$; $\alpha = 54.7°$, $\beta = 0°$

ii) Re = 2.2×10^5;

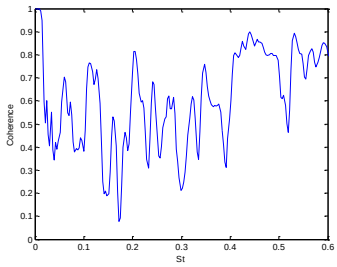
C_L-Pressure



C_L-Total Velocity



Pressure-Total Velocity



Cross-coherence: C_L-Pressure-Total Velocity

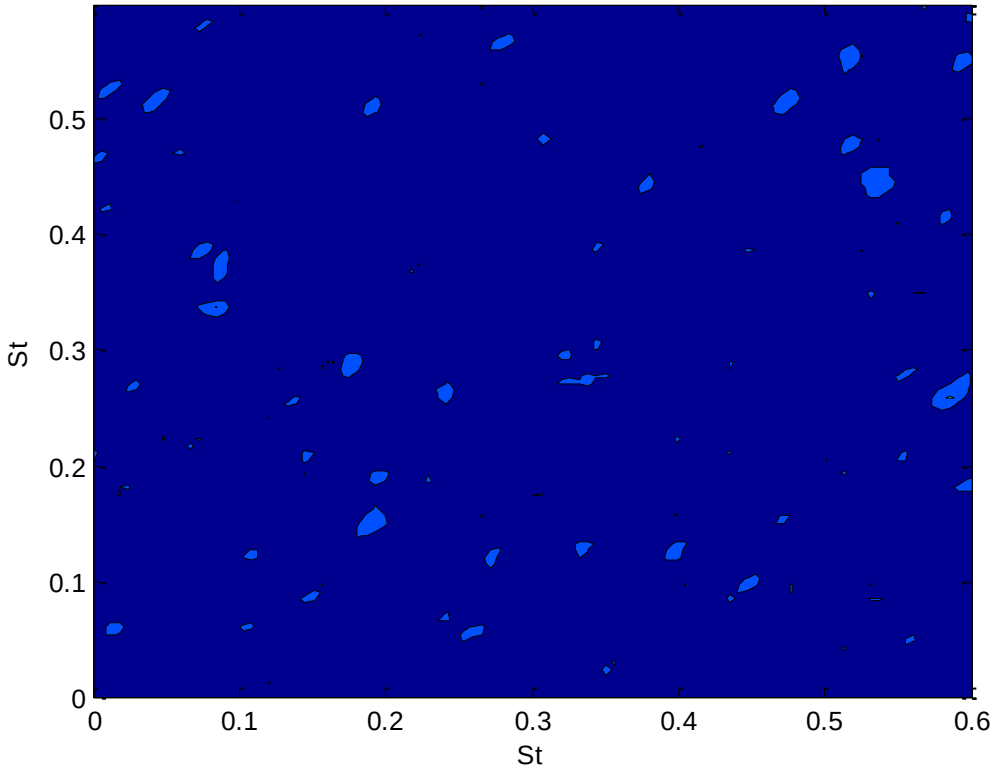
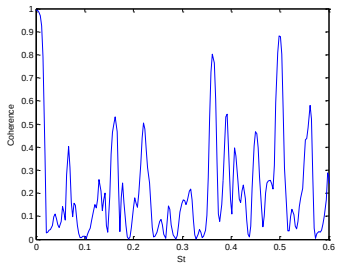


Figure P: Coherence

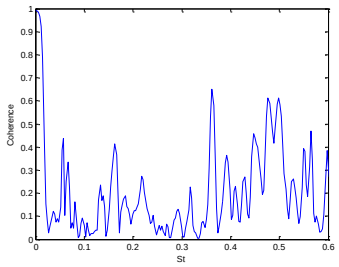
e) $\phi = 54.7°$; $\alpha = 54.7°$, $\beta = 0°$

iii) Re = 3.3×10^5;

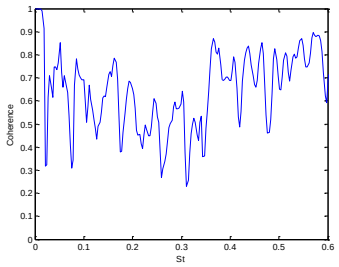
C_L-Pressure



C_L-Total Velocity



Pressure-Total Velocity



Cross-coherence: C_L-Pressure-Total Velocity

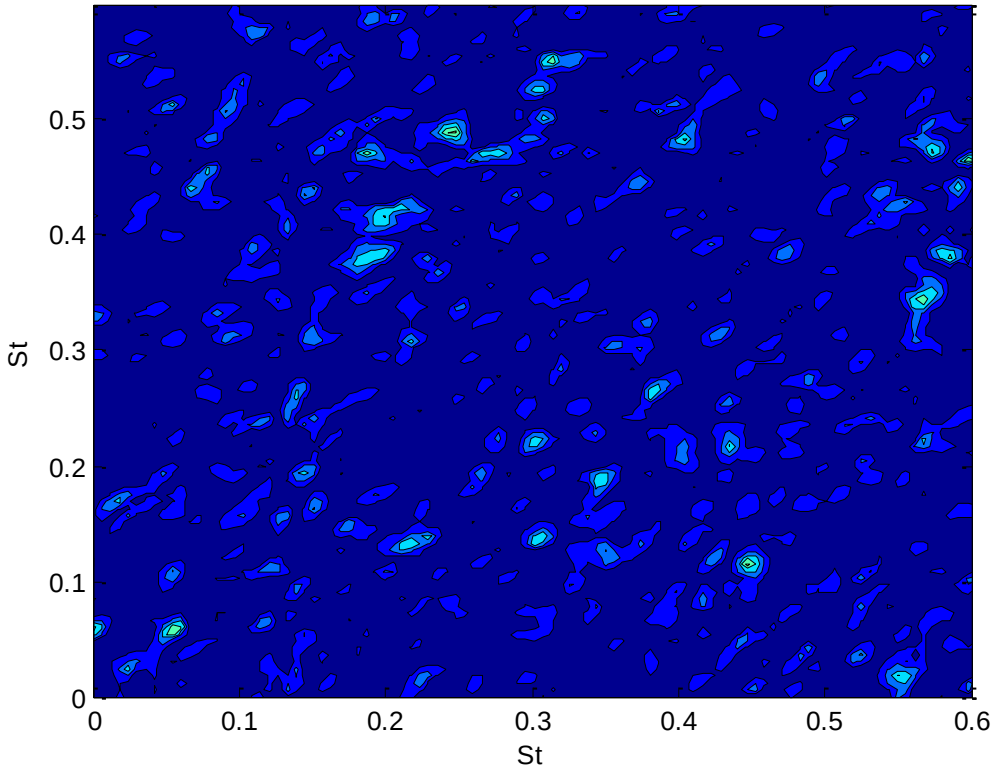
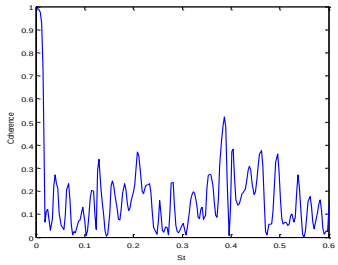


Figure P: Coherence

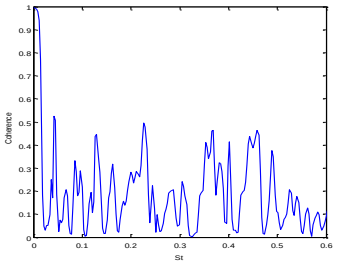
e) $\phi = 54.7°$; $\alpha = 54.7°$, $\beta = 0°$

iv) Re = 4.4×10^5;

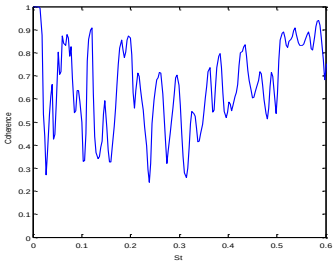
C_L-Pressure



C_L-Total Velocity



Pressure-Total Velocity



Cross-coherence: C_L-Pressure-Total Velocity

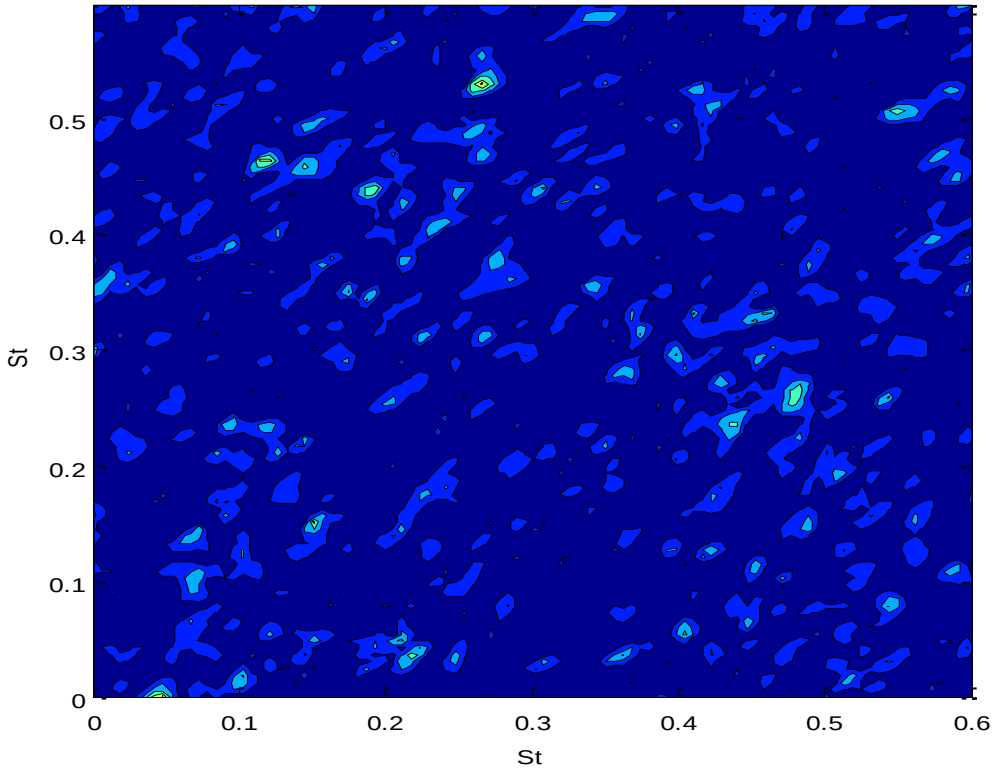
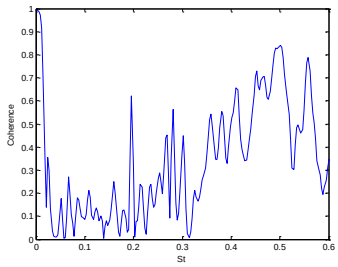


Figure P: Coherence

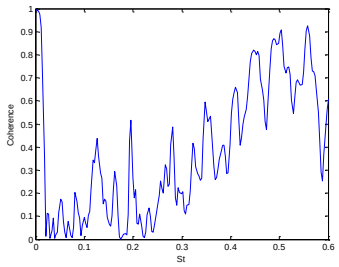
e) $\phi = 54.7°$; $\alpha = 54.7°$, $\beta = 0°$

v) Re = 5.5×10^5;

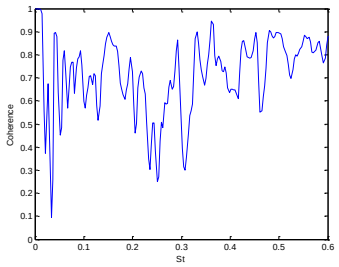
C_L-Pressure



C_L-Total Velocity



Pressure-Total Velocity



Cross-coherence: C_L-Pressure-Total Velocity

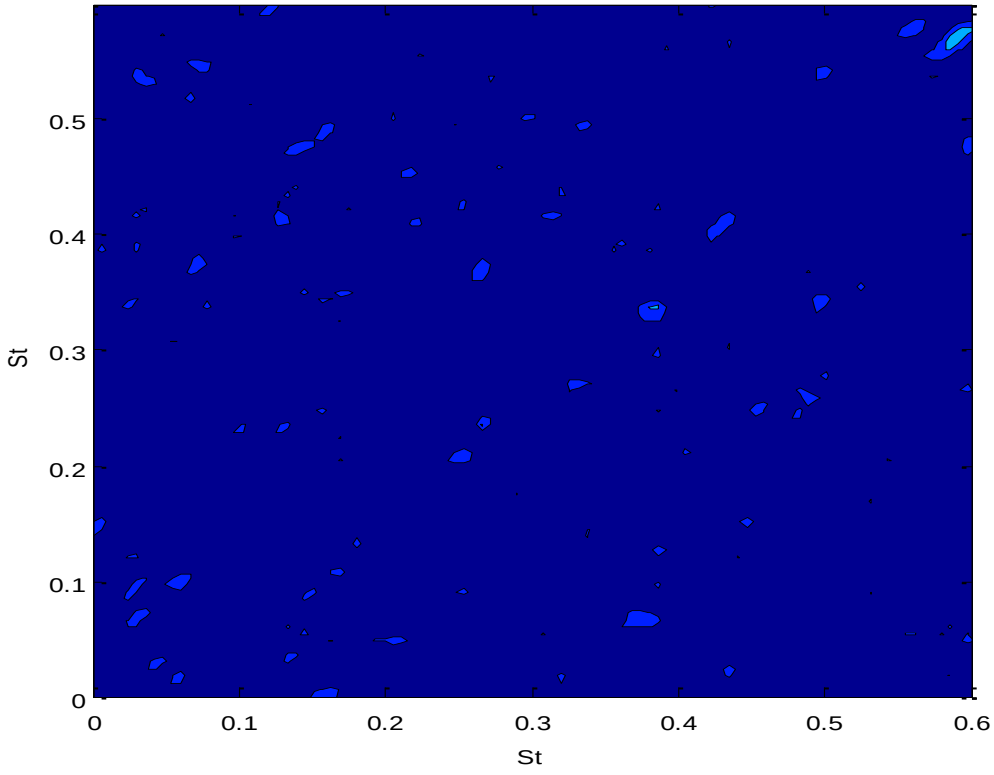
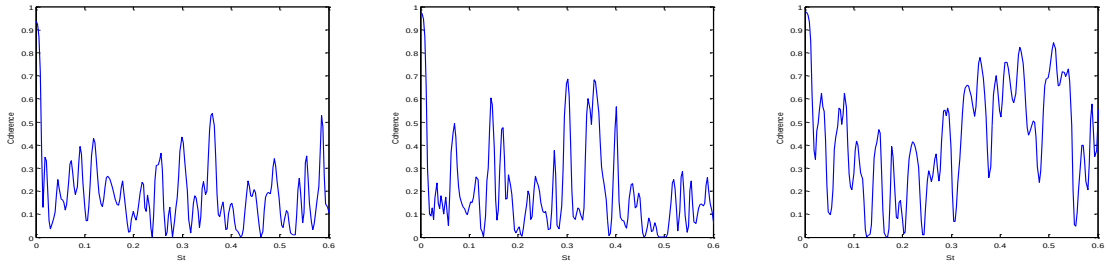


Figure P: Coherence

f) $\phi = 57.1°$; $\alpha = 54.7°$, $\beta = 20°$

i) Re = 1.1×10^5;

C_L-Pressure C_L-Total Velocity Pressure-Total Velocity



Cross-coherence: C_L-Pressure-Total Velocity

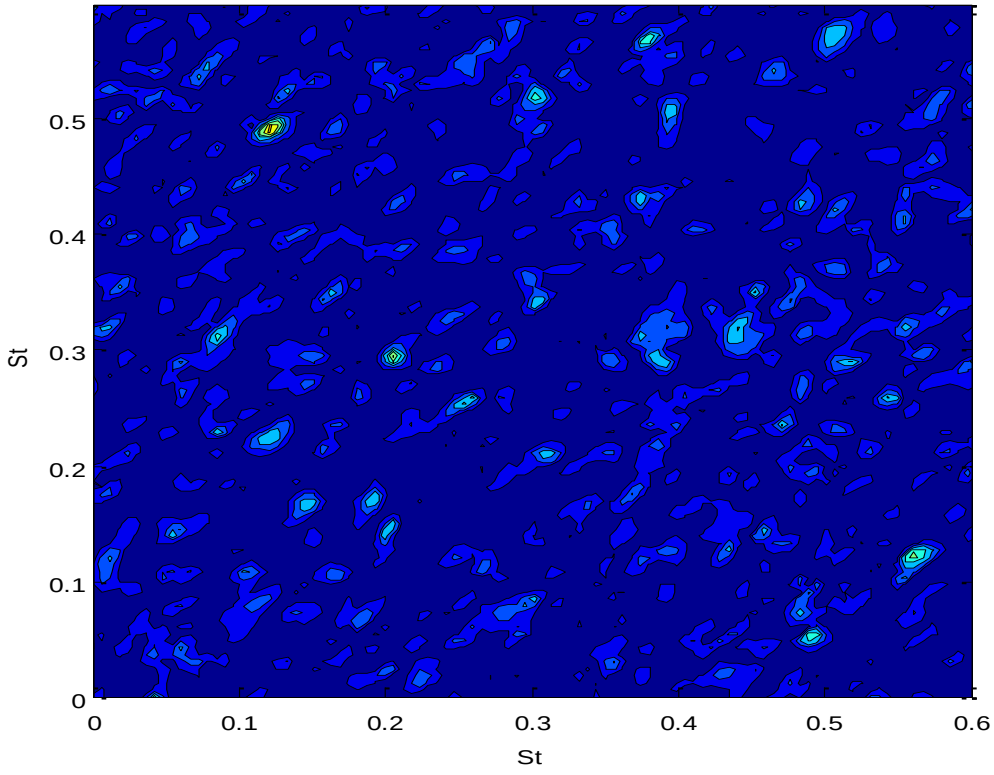
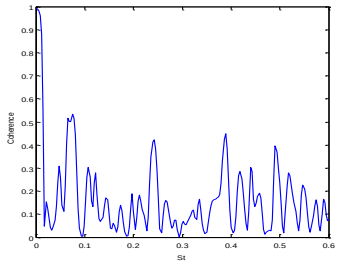


Figure P: Coherence

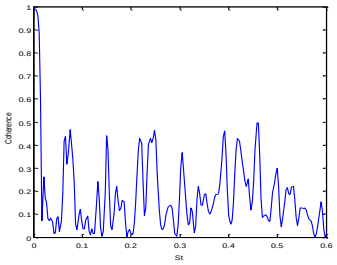
f) $\phi = 57.1°$; $\alpha = 54.7°$, $\beta = 20°$

ii) Re = 2.2×10^5;

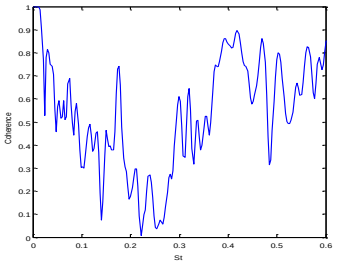
C_L-Pressure



C_L-Total Velocity



Pressure-Total Velocity



Cross-coherence: C_L-Pressure-Total Velocity

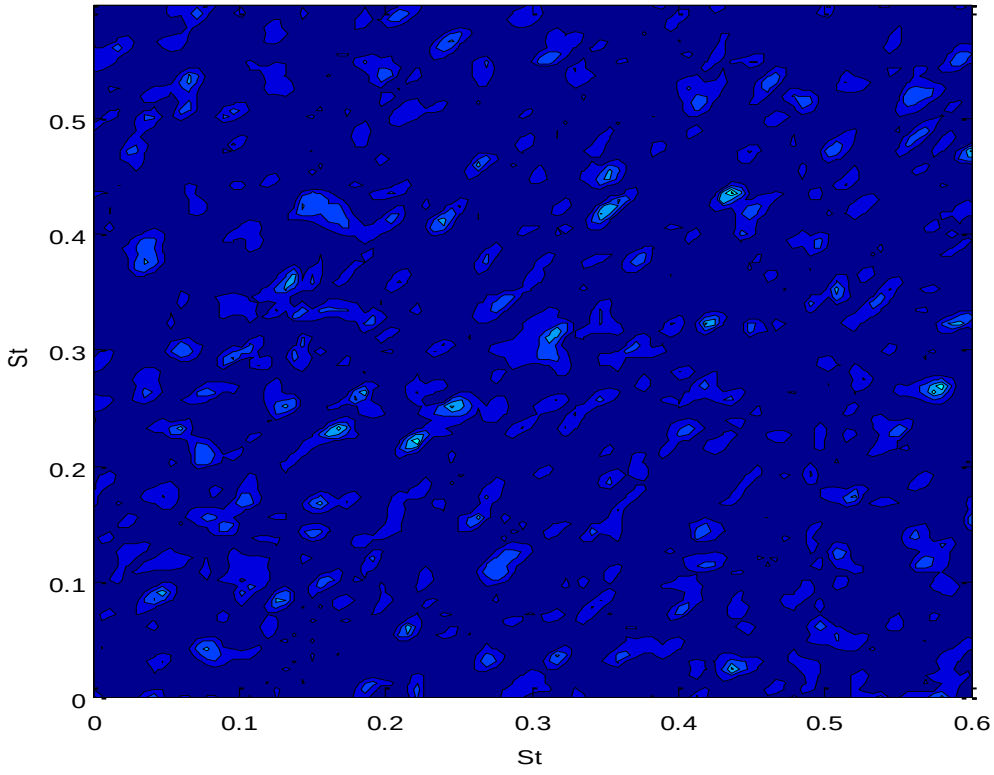
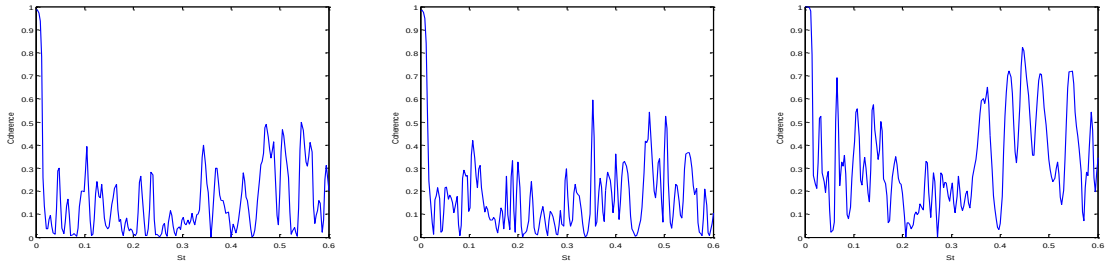


Figure P: Coherence

f) $\phi = 57.1°$; $\alpha = 54.7°$, $\beta = 20°$

iii) Re = 3.3×10^5;

C_L-Pressure C_L-Total Velocity Pressure-Total Velocity



Cross-coherence: C_L-Pressure-Total Velocity

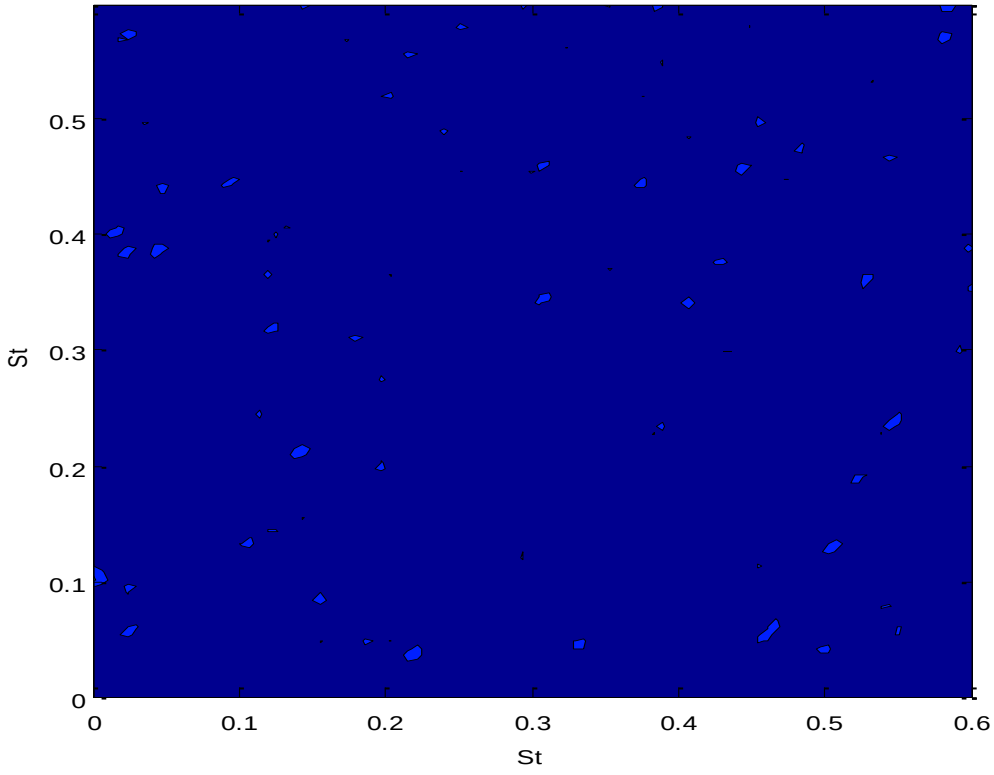
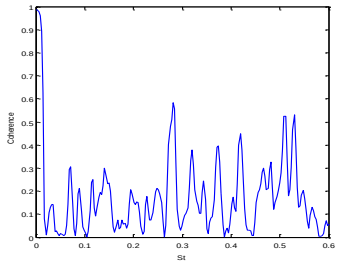


Figure P: Coherence

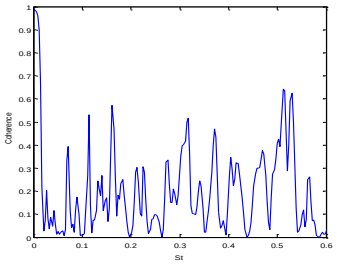
f) $\phi = 57.1°$; $\alpha = 54.7°$, $\beta = 20°$

iv) Re = 4.4×10^5;

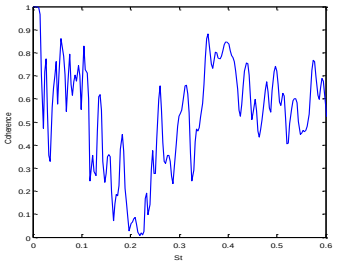
C_L-Pressure



C_L-Total Velocity



Pressure-Total Velocity



Cross-coherence: C_L-Pressure-Total Velocity

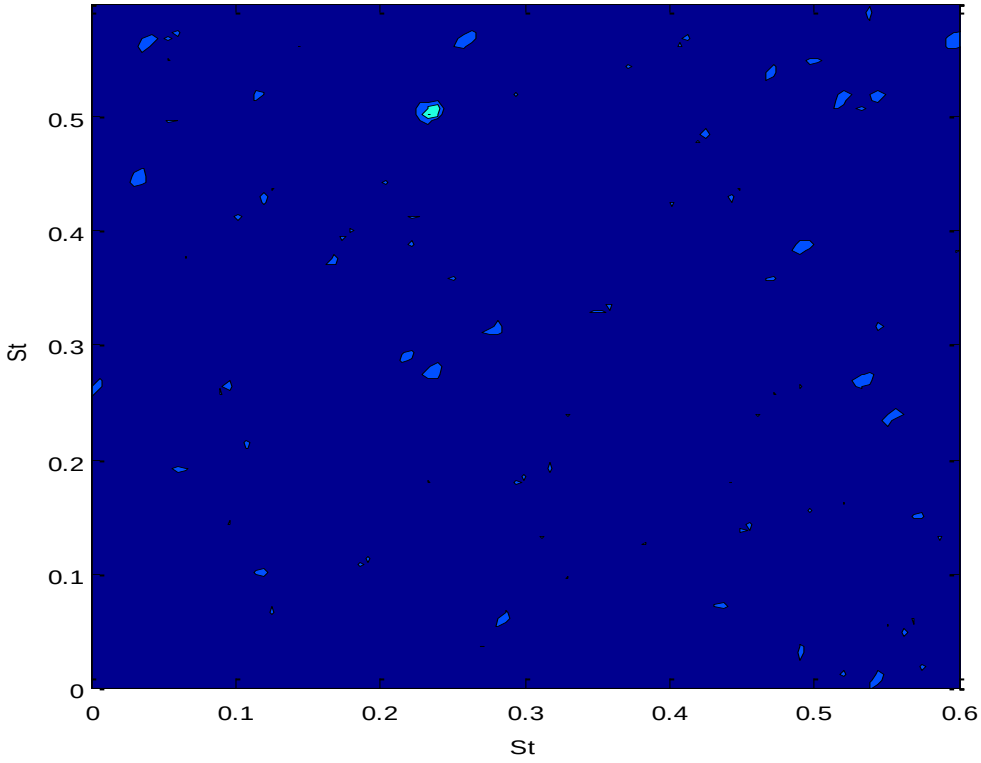
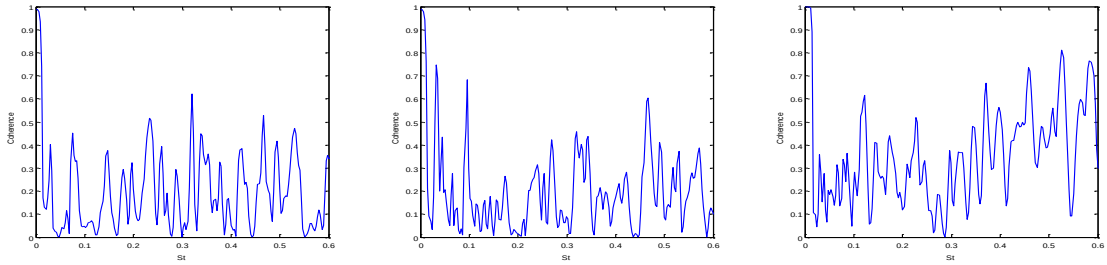


Figure P: Coherence

f) $\phi = 57.1°$; $\alpha = 54.7°$, $\beta = 20°$

v) Re = 5.5×10^5;

C_L-Pressure C_L-Total Velocity Pressure-Total Velocity



Cross-coherence: C_L-Pressure-Total Velocity

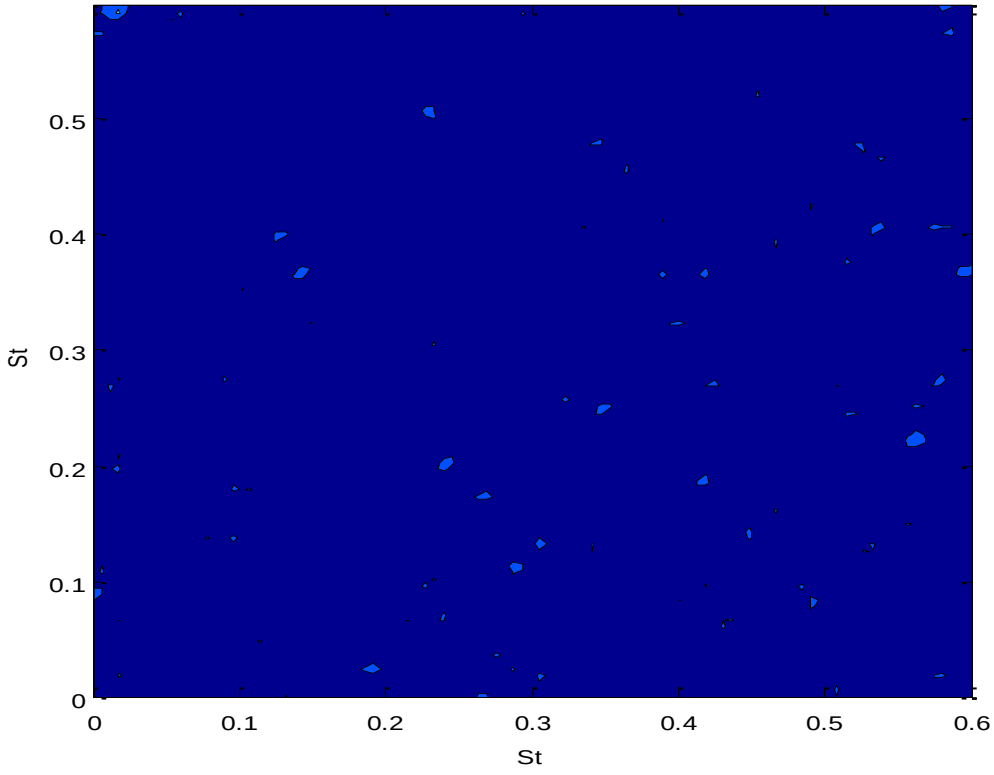
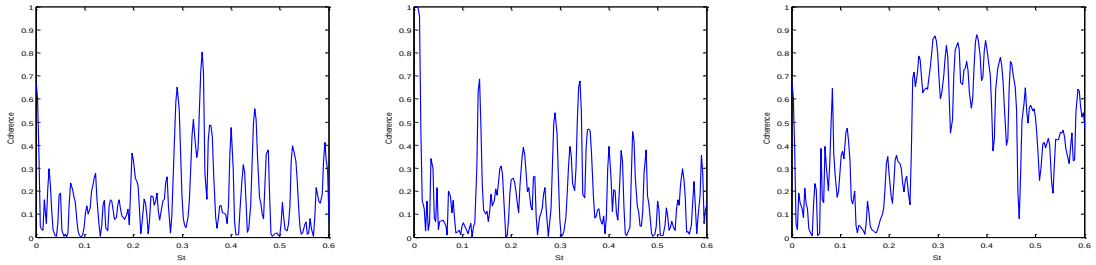


Figure P: Coherence

g) $\phi = 64°$; $\alpha = 54.7°$, $\beta = 40°$

i) Re = 1.1×10^5;

C_L-Pressure C_L-Total Velocity Pressure-Total Velocity



Cross-coherence: C_L-Pressure-Total Velocity

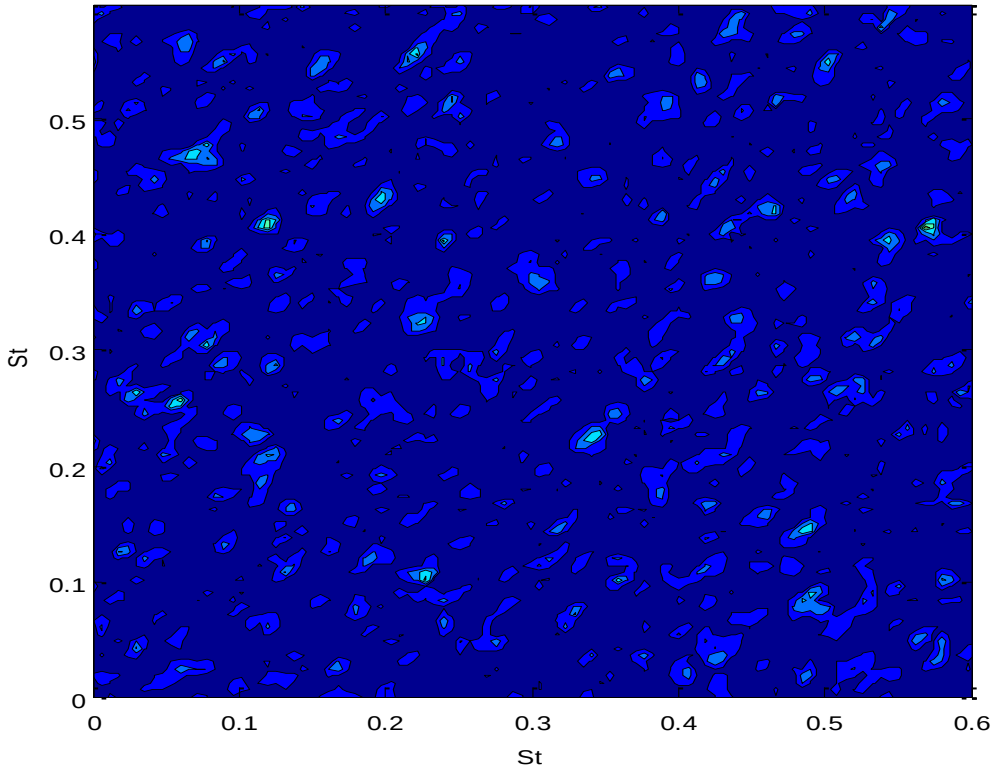
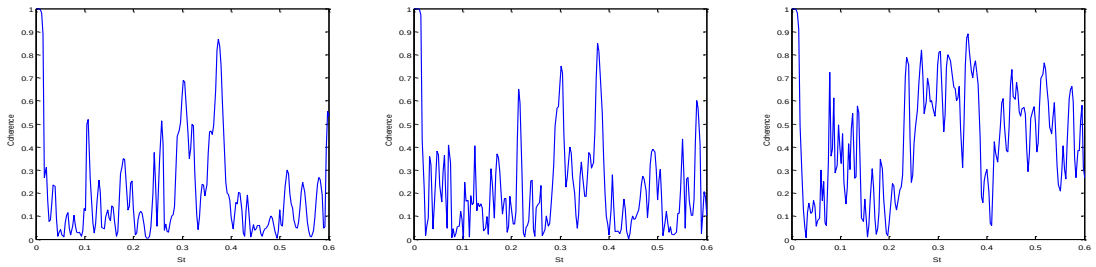


Figure P: Coherence

g) $\phi = 64°$; $\alpha = 54.7°$, $\beta = 40°$

ii) Re = 2.2×10^5;

C_L-Pressure C_L-Total Velocity Pressure-Total Velocity



Cross-coherence: C_L-Pressure-Total Velocity

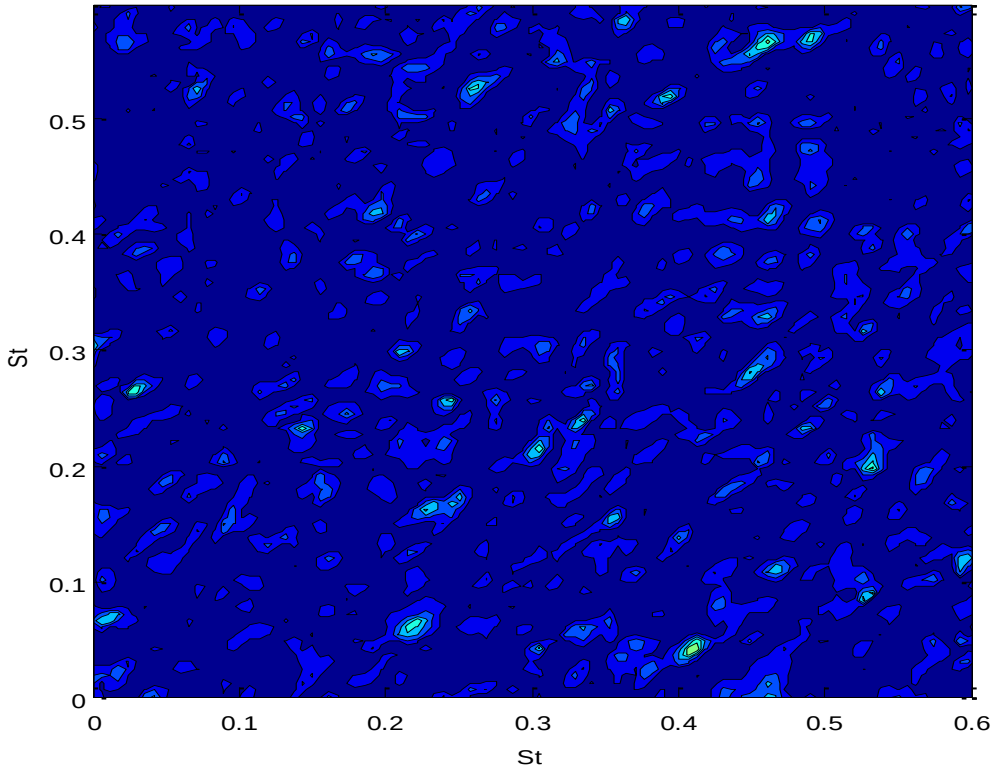
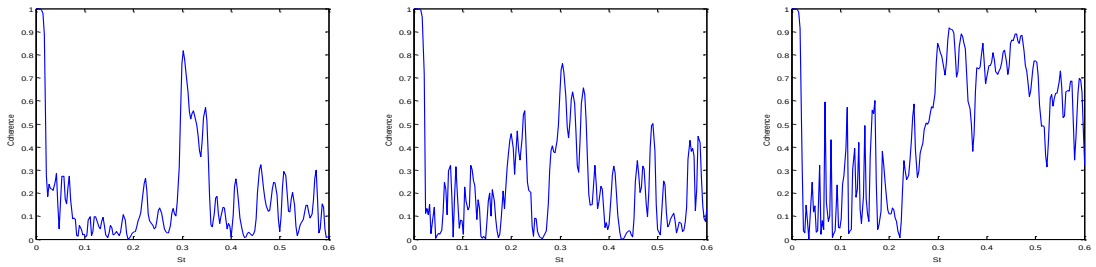


Figure P: Coherence

g) $\phi = 64°$; $\alpha = 54.7°$, $\beta = 40°$

iii) Re = 3.3×10^5;

C_L-Pressure C_L-Total Velocity Pressure-Total Velocity



Cross-coherence: C_L-Pressure-Total Velocity

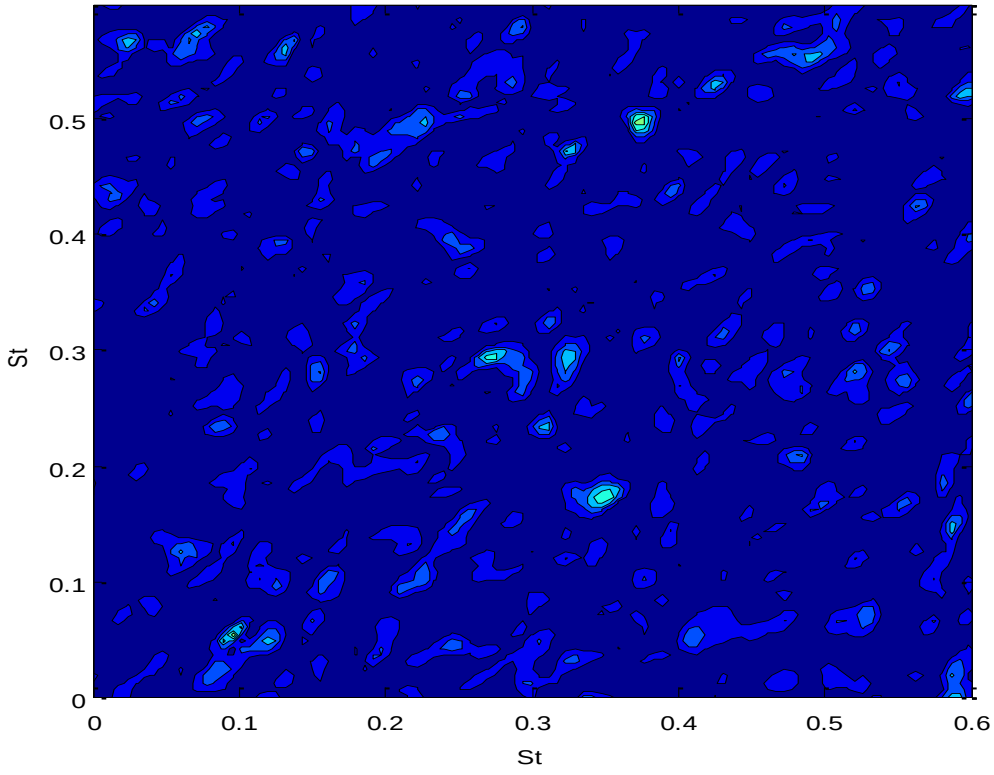
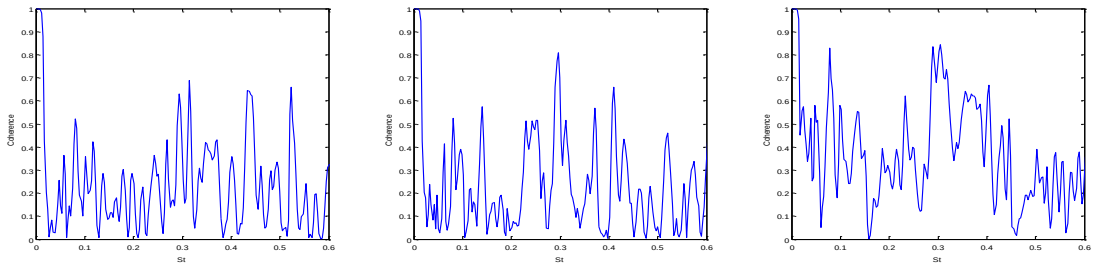


Figure P: Coherence

g) $\phi = 64°$; $\alpha = 54.7°$, $\beta = 40°$

iv) Re = 4.4×10^5;

C_L-Pressure C_L-Total Velocity Pressure-Total Velocity



Cross-coherence: C_L-Pressure-Total Velocity

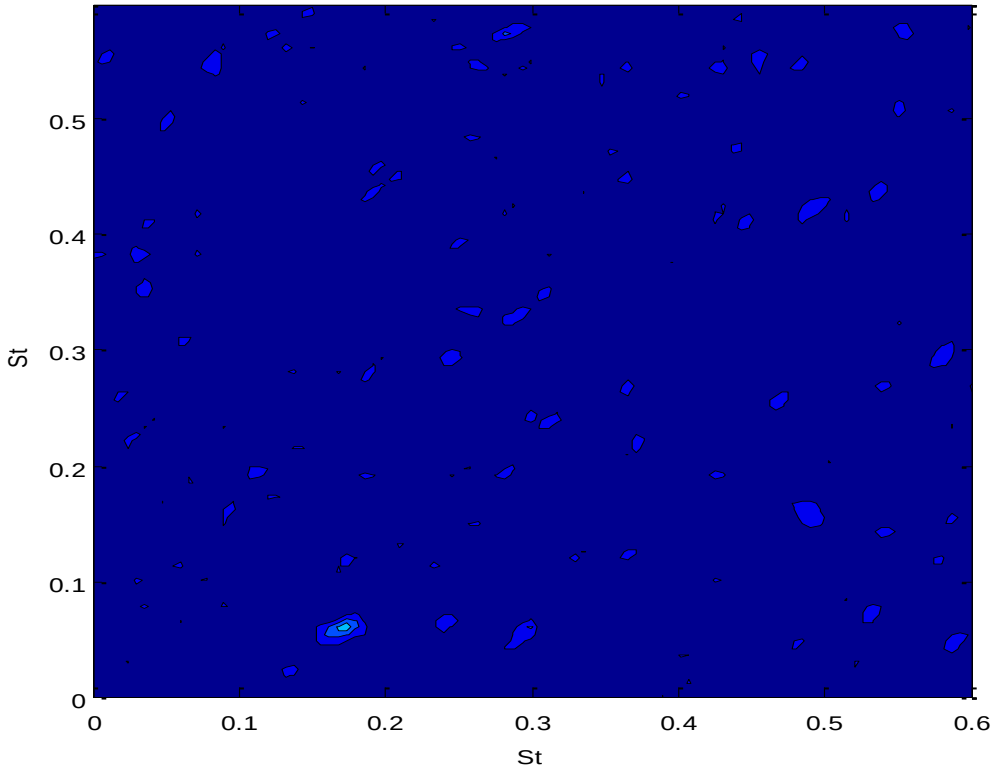
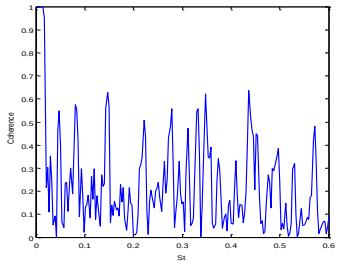


Figure P: Coherence

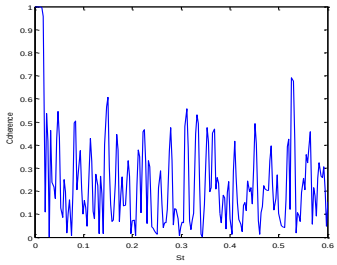
g) $\phi = 64°$; $\alpha = 54.7°$, $\beta = 40°$

v) Re = 5.5×10^5;

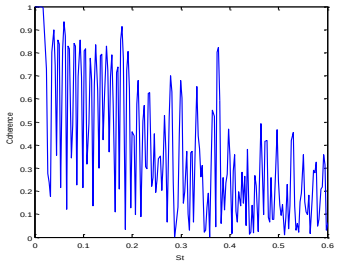
C_L-Pressure



C_L-Total Velocity



Pressure-Total Velocity



Cross-coherence: C_L-Pressure-Total Velocity

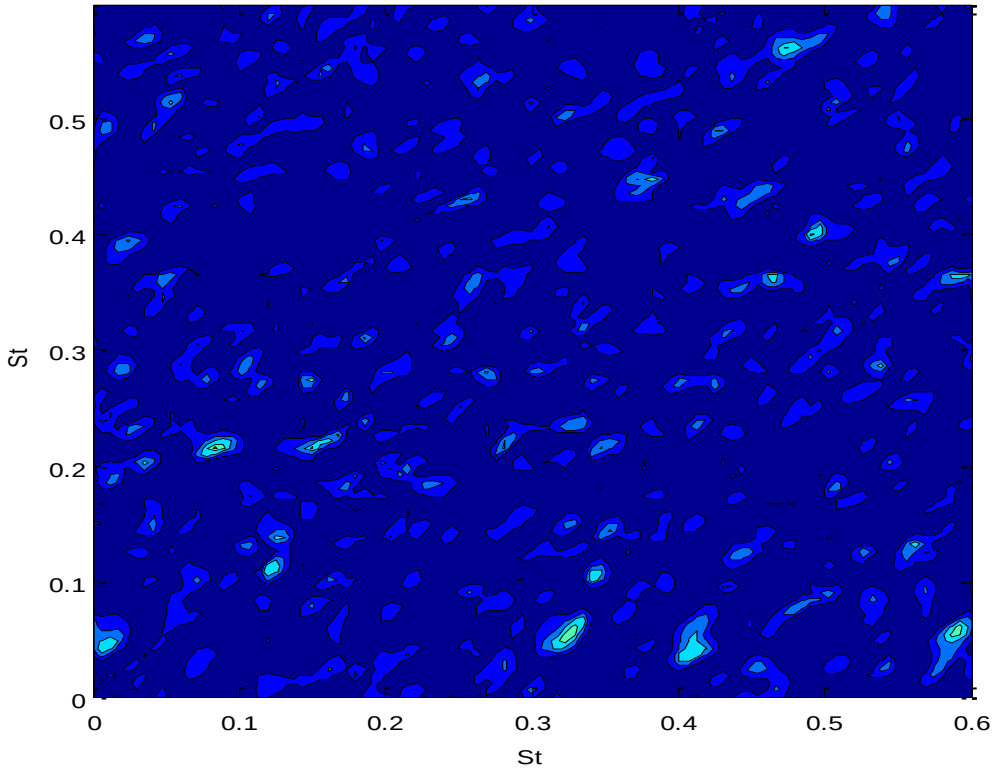
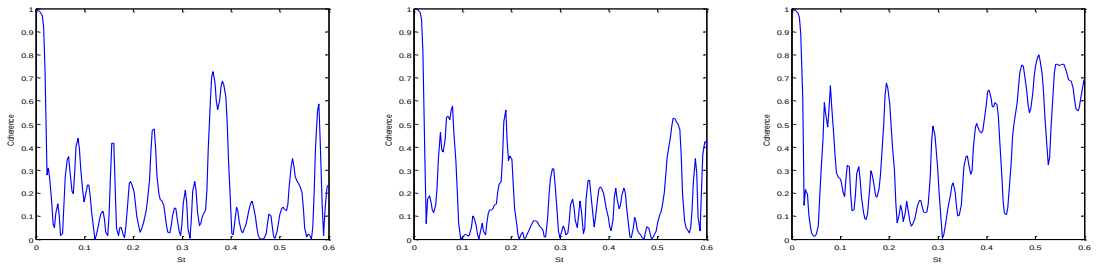


Figure P: Coherence

h) $\phi = 53°$; $\alpha = 50°$, $\beta = 20°$

i) Re = 1.1×10^5;

C_L-Pressure C_L-Total Velocity Pressure-Total Velocity



Cross-coherence: C_L-Pressure-Total Velocity

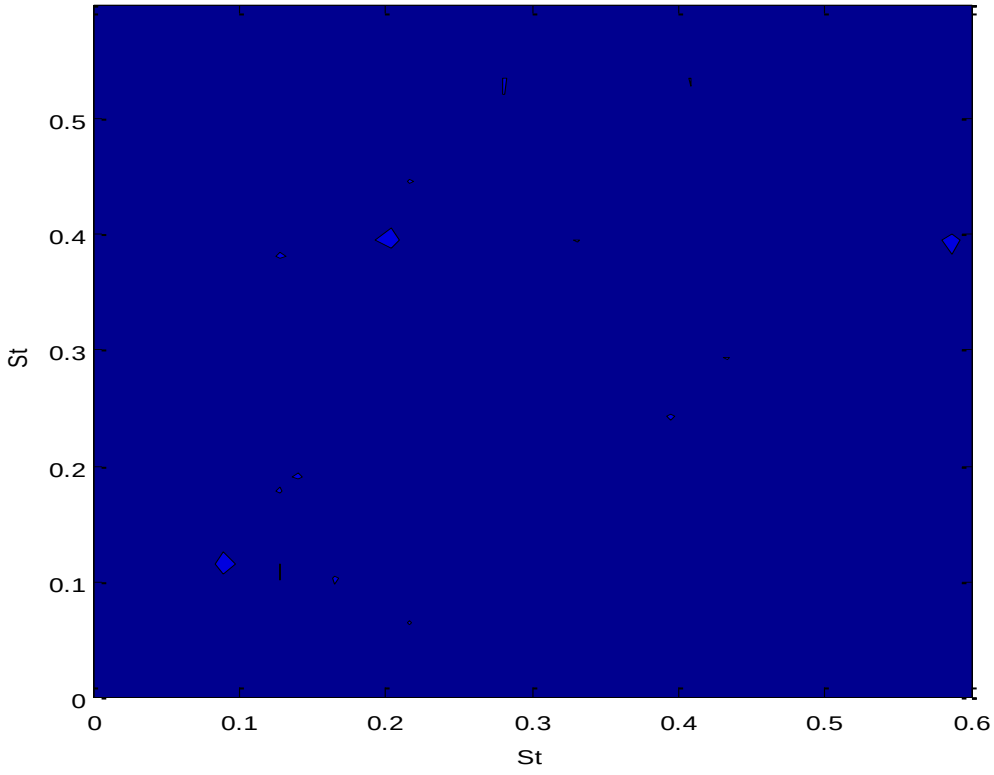
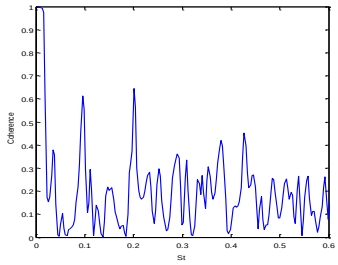


Figure P: Coherence

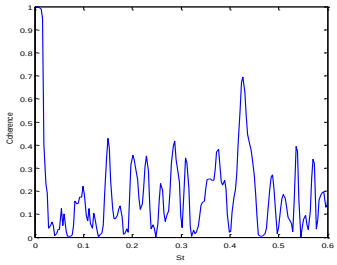
h) $\phi = 53°$; $\alpha = 50°$, $\beta = 20°$

ii) Re = 2.2×10^5;

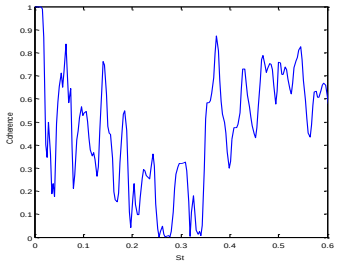
C_L-Pressure



C_L-Total Velocity



Pressure-Total Velocity



Cross-coherence: C_L-Pressure-Total Velocity

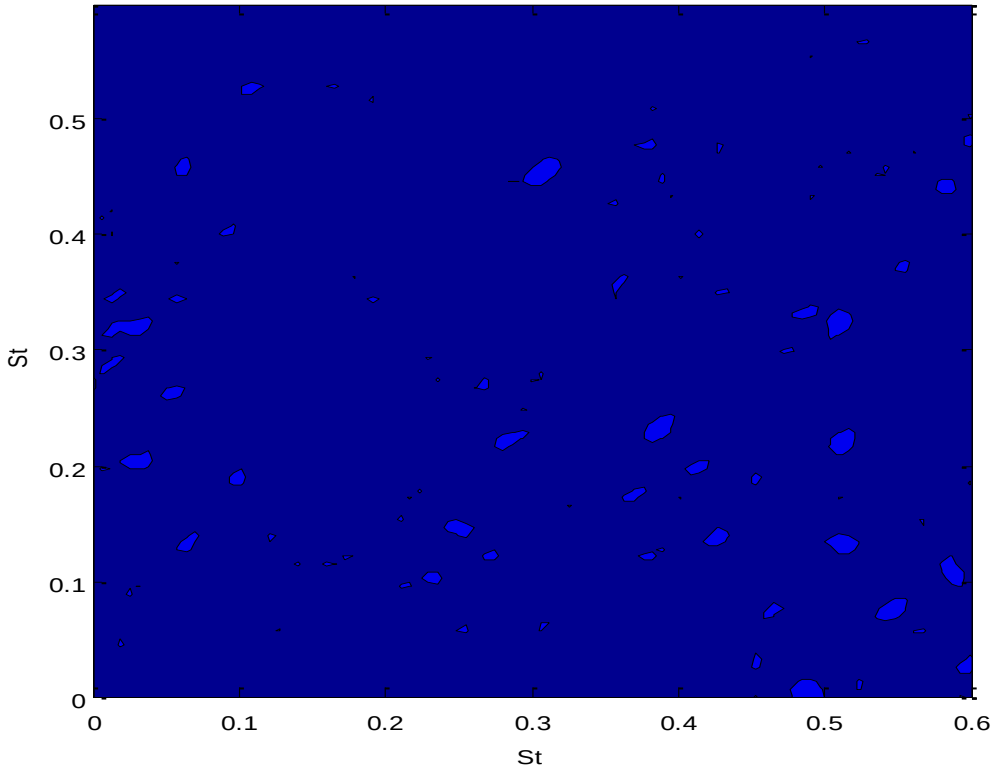
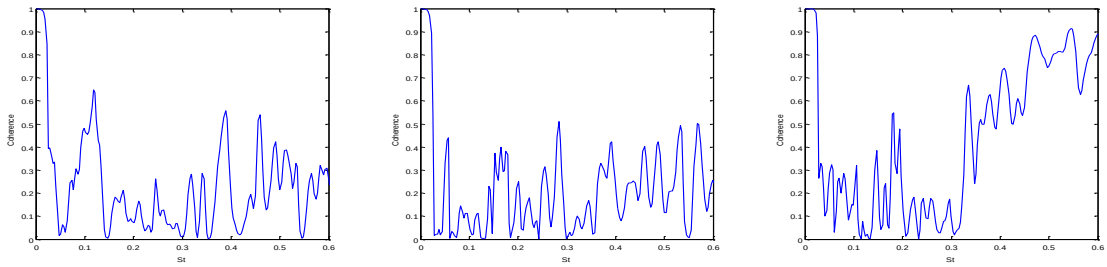


Figure P: Coherence

h) $\phi = 53°$; $\alpha = 50°$, $\beta = 20°$

iii) Re = 3.3×10^5;

C_L-Pressure C_L-Total Velocity Pressure-Total Velocity



Cross-coherence: C_L-Pressure-Total Velocity

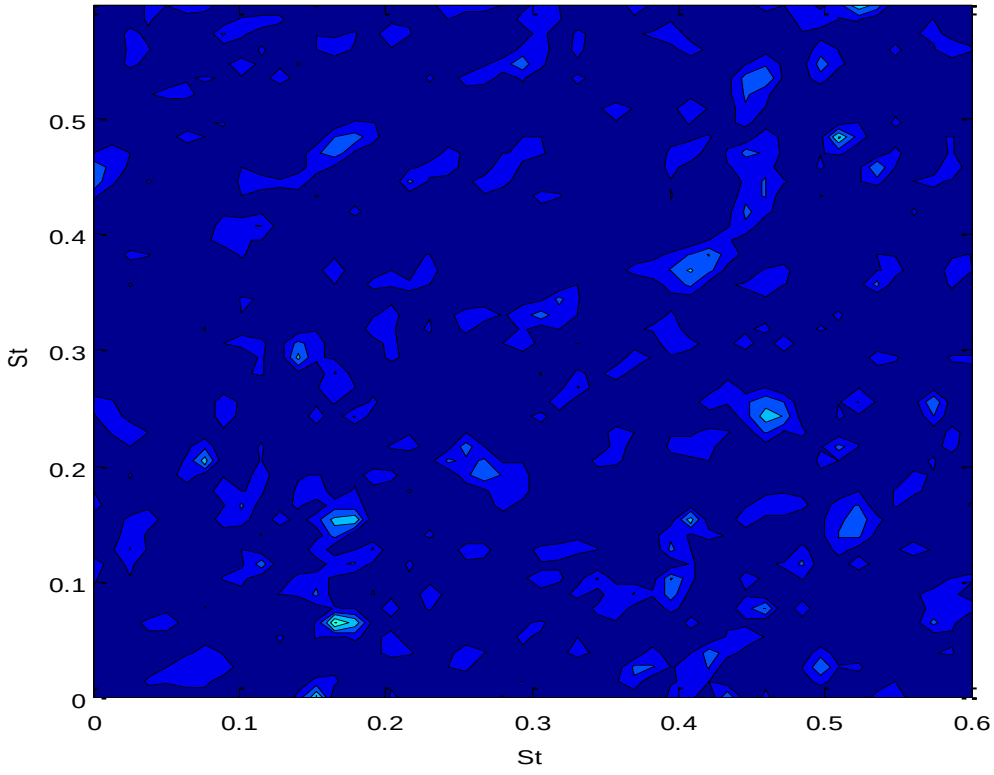
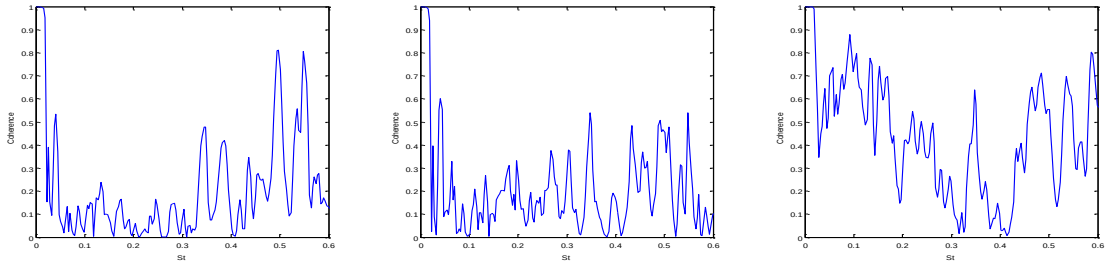


Figure P: Coherence

h) $\phi = 53°$; $\alpha = 50°$, $\beta = 20°$

iv) Re = 4.4×10^5;

C_L-Pressure C_L-Total Velocity Pressure-Total Velocity



Cross-coherence: C_L-Pressure-Total Velocity

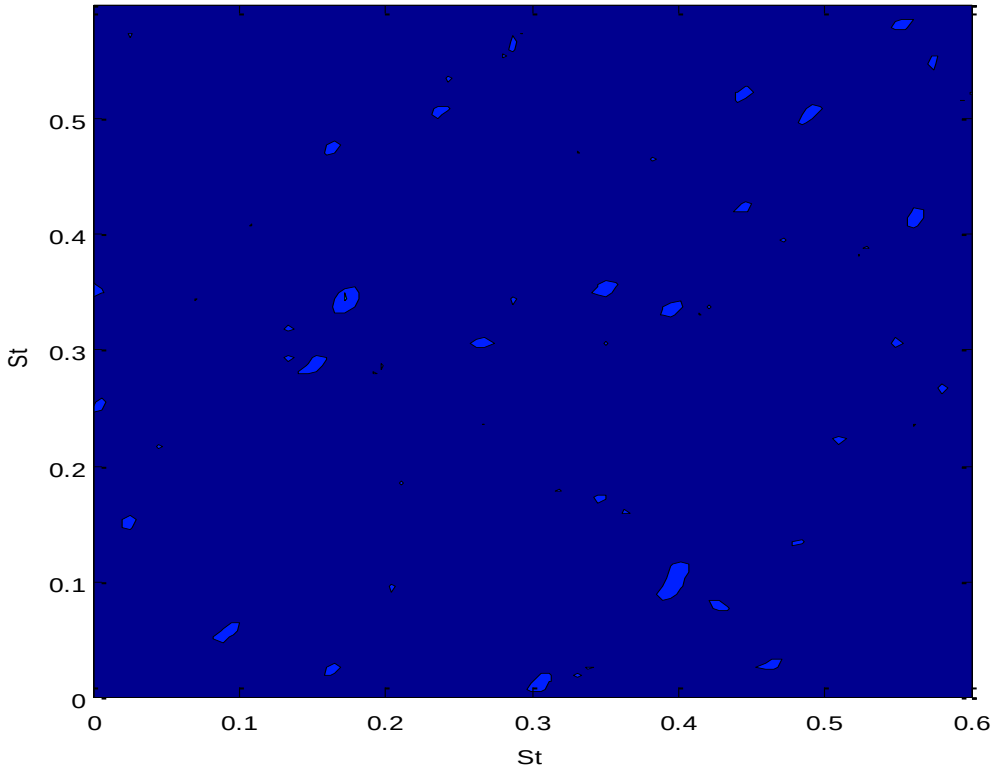
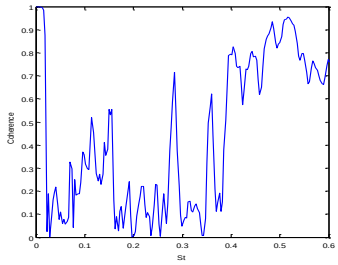


Figure P: Coherence

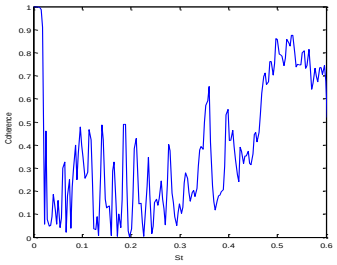
h) $\phi = 53°$; $\alpha = 50°$, $\beta = 20°$

v) Re = 5.5×10^5;

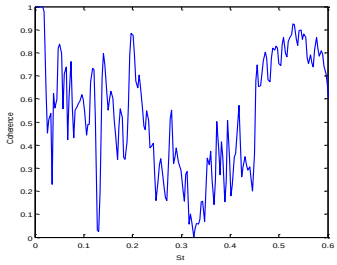
C_L-Pressure



C_L-Total Velocity



Pressure-Total Velocity



Cross-coherence: C_L-Pressure-Total Velocity

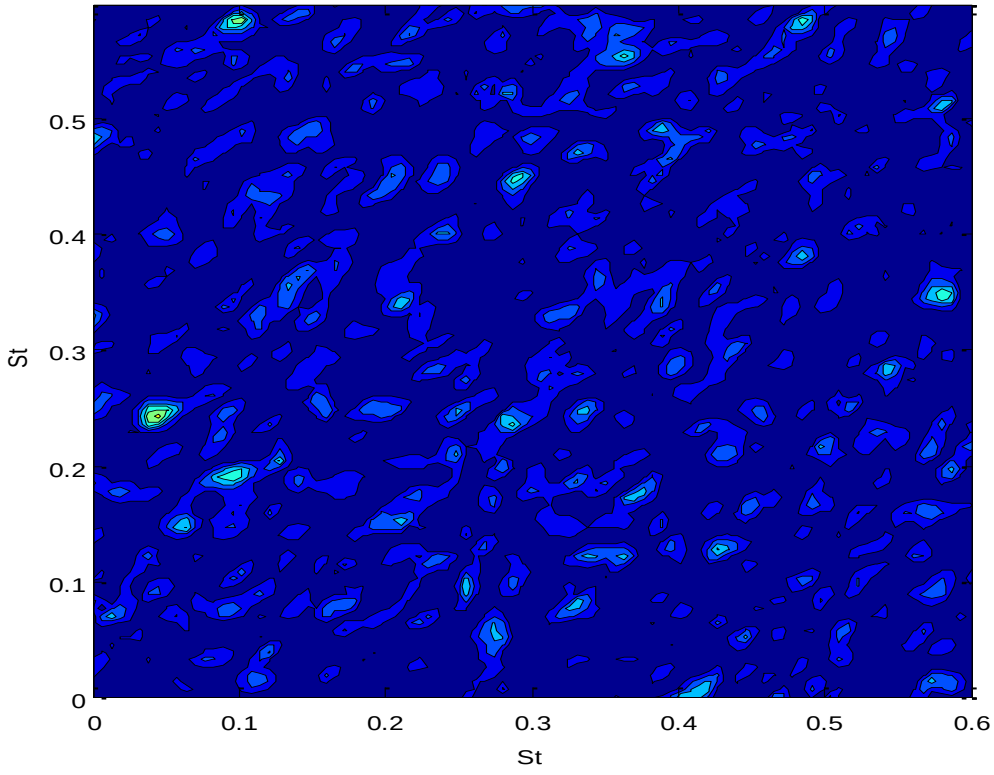
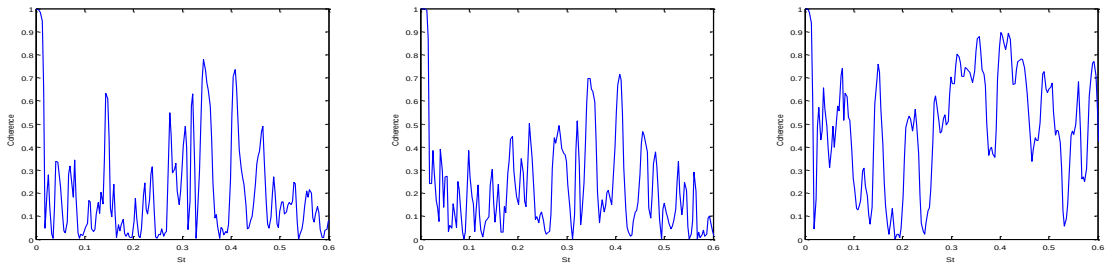


Figure P: Coherence

i) $\phi = 60.5°$; $\alpha = 50°$, $\beta = 40°$

i) Re = 1.1×10^5;

C_L-Pressure C_L-Total Velocity Pressure-Total Velocity



Cross-coherence: C_L-Pressure-Total Velocity

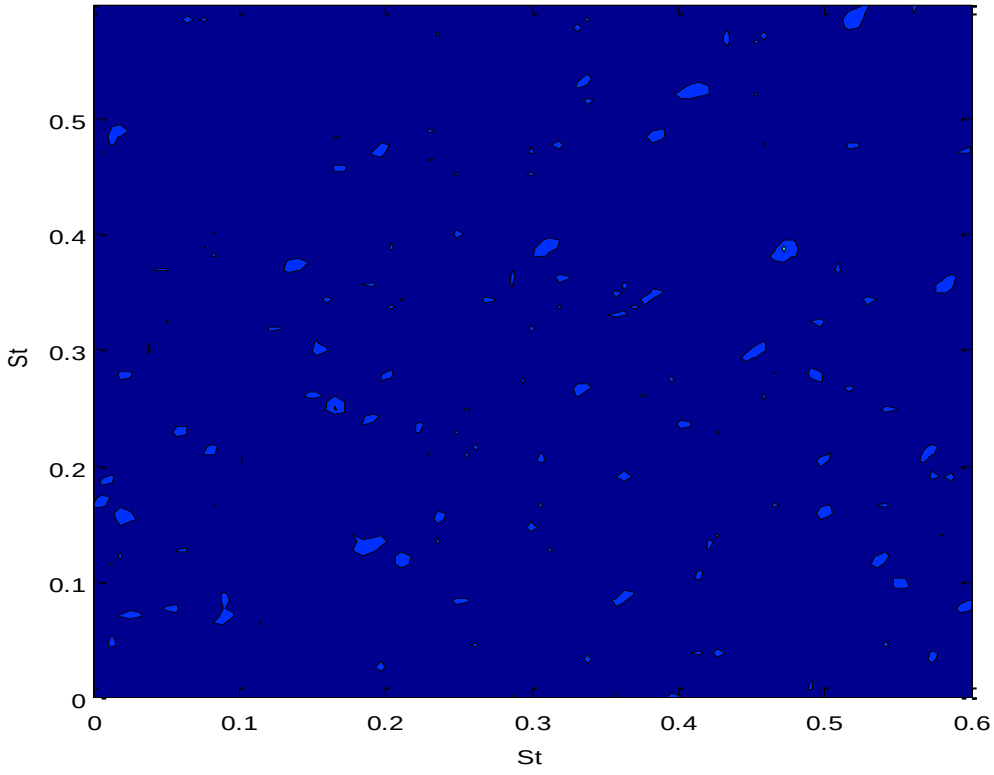
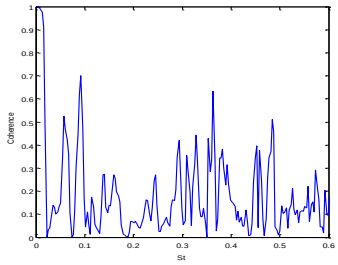


Figure P: Coherence

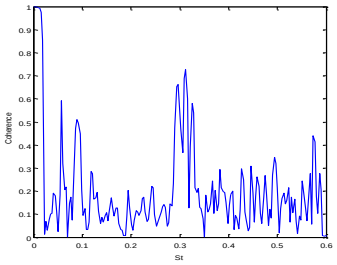
i) $\phi = 60.5°$; $\alpha = 50°$, $\beta = 40°$

ii) Re = 2.2×10^5;

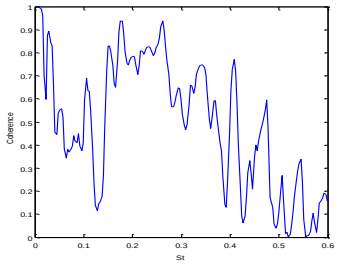
C_L-Pressure



C_L-Total Velocity



Pressure-Total Velocity



Cross-coherence: C_L-Pressure-Total Velocity

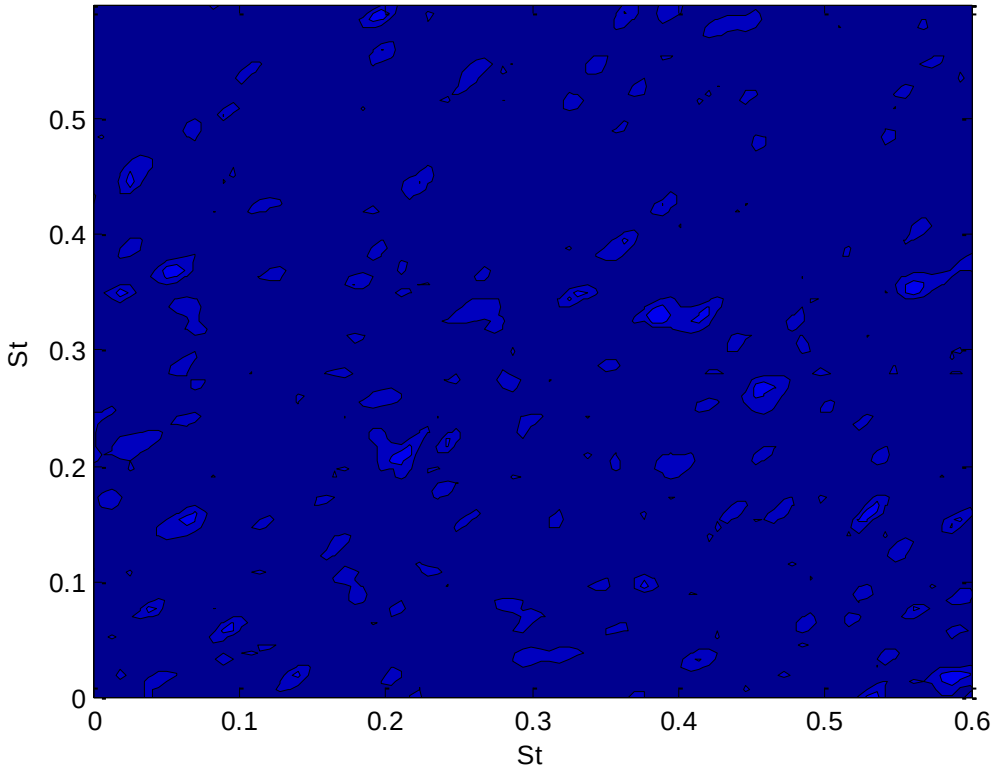
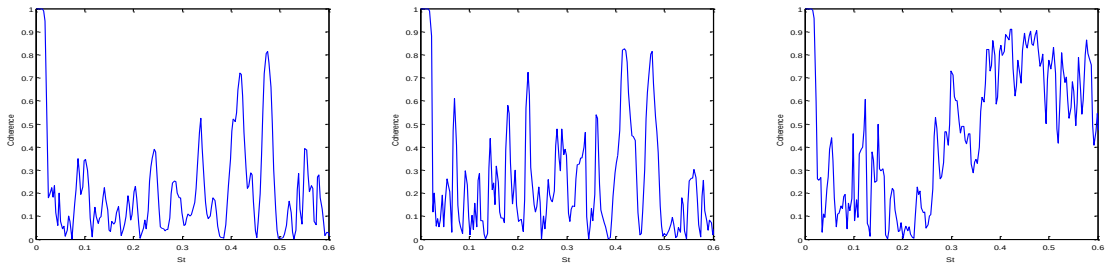


Figure P: Coherence

i) $\phi = 60.5°$; $\alpha = 50°$, $\beta = 40°$

iii) Re = 3.3×10^5;

C_L-Pressure C_L-Total Velocity Pressure-Total Velocity



Cross-coherence: C_L-Pressure-Total Velocity

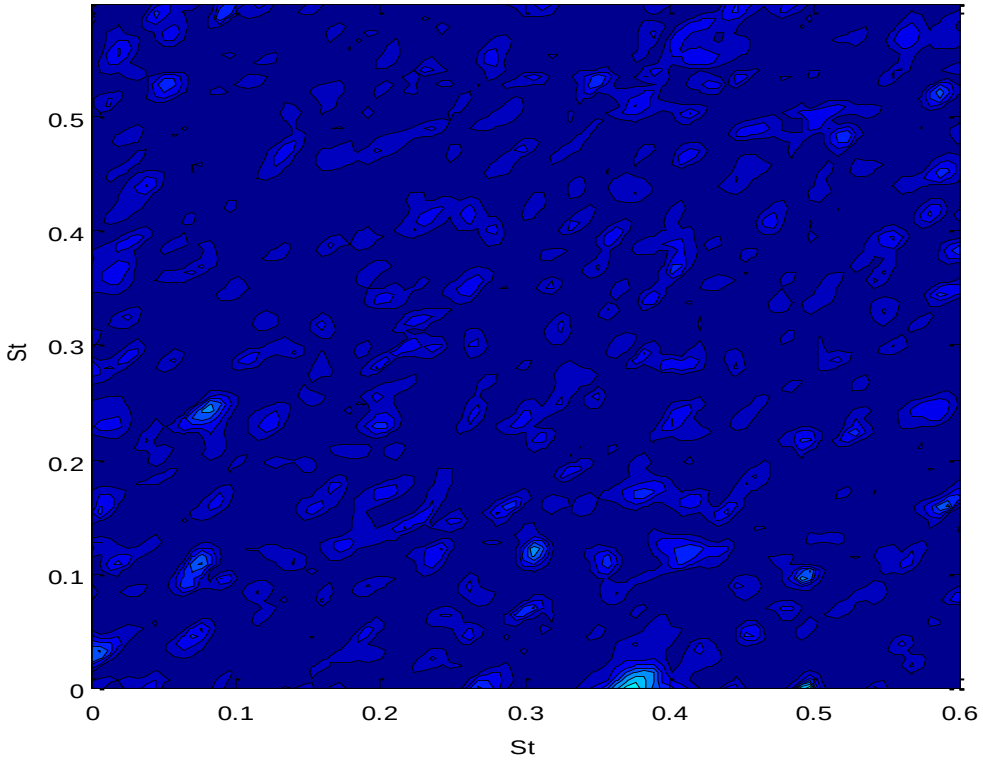
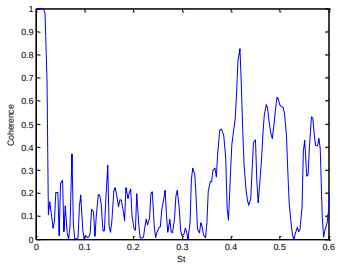


Figure P: Coherence

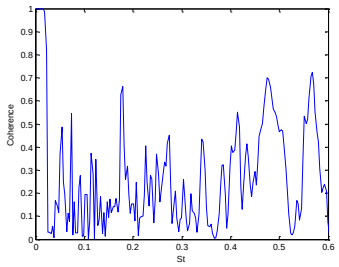
i) $\phi = 60.5°$; $\alpha = 50°$, $\beta = 40°$

v) Re = 5.5×10^5;

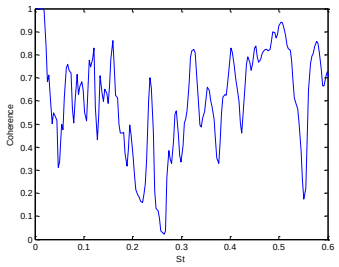
C_L-Pressure



C_L-Total Velocity



Pressure-Total Velocity



Cross-coherence: C_L-Pressure-Total Velocity

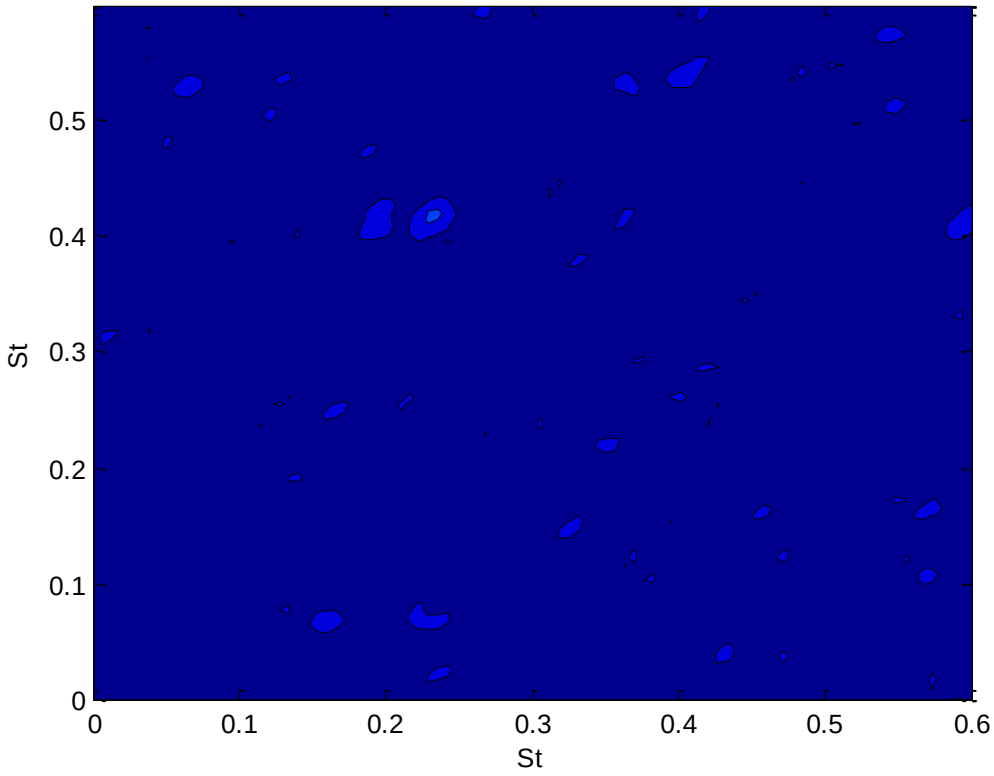
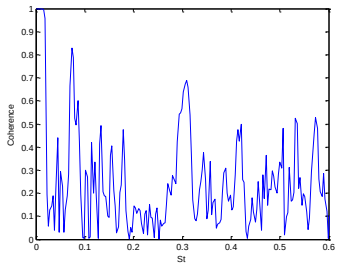


Figure P: Coherence

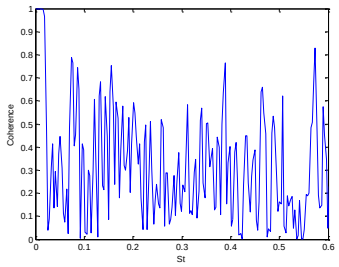
j) $\phi = 35.5°$; $\alpha = 30°$, $\beta = 20°$

ii) Re = 2.2×10^5;

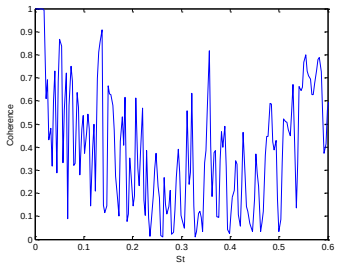
C_L-Pressure



C_L-Total Velocity



Pressure-Total Velocity



Cross-coherence: C_L-Pressure-Total Velocity

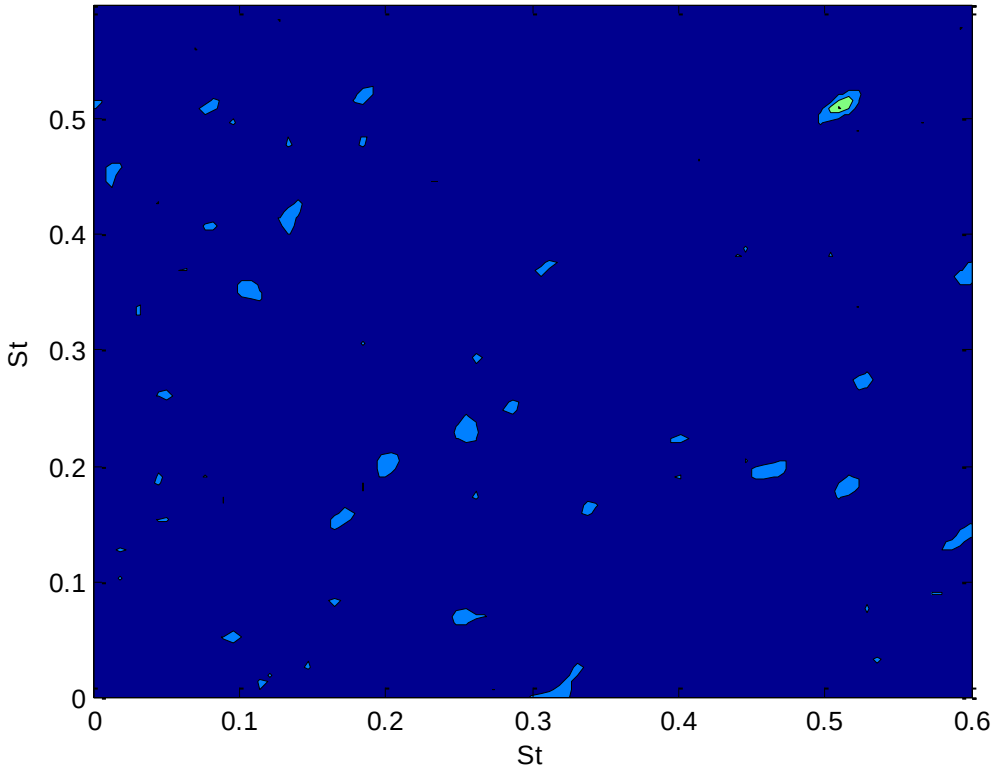
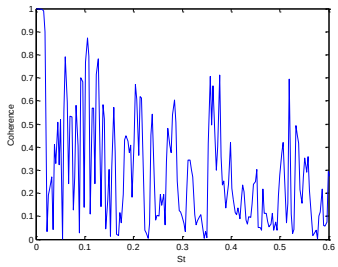


Figure P: Coherence

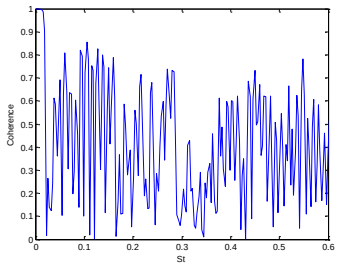
j) $\phi = 35.5°$; $\alpha = 30°$, $\beta = 20°$

iii) Re = 3.3×10^5;

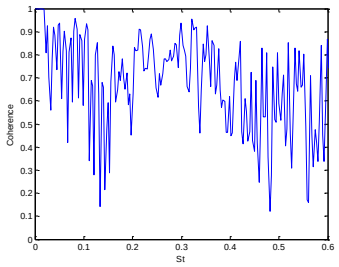
C_L-Pressure



C_L-Total Velocity



Pressure-Total Velocity



Cross-coherence: C_L-Pressure-Total Velocity

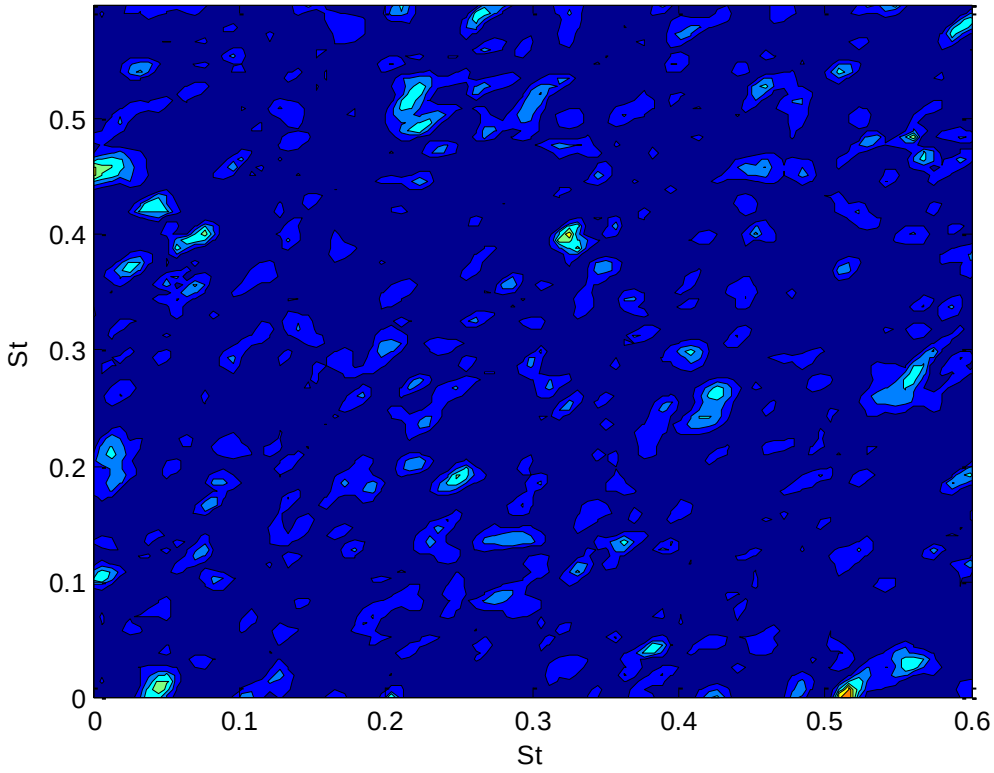
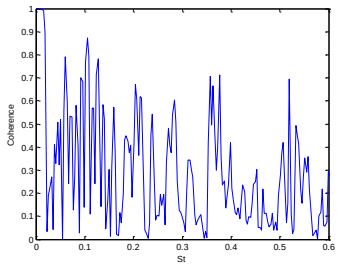


Figure P: Coherence

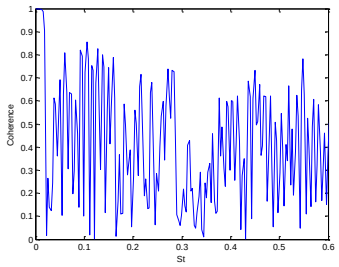
j) $\phi = 35.5°$; $\alpha = 30°$, $\beta = 20°$

iv) Re = 4.4×10^5;

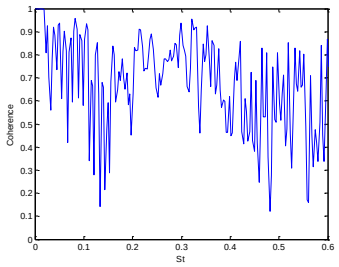
C_L-Pressure



C_L-Total Velocity



Pressure-Total Velocity



Cross-coherence: C_L-Pressure-Total Velocity

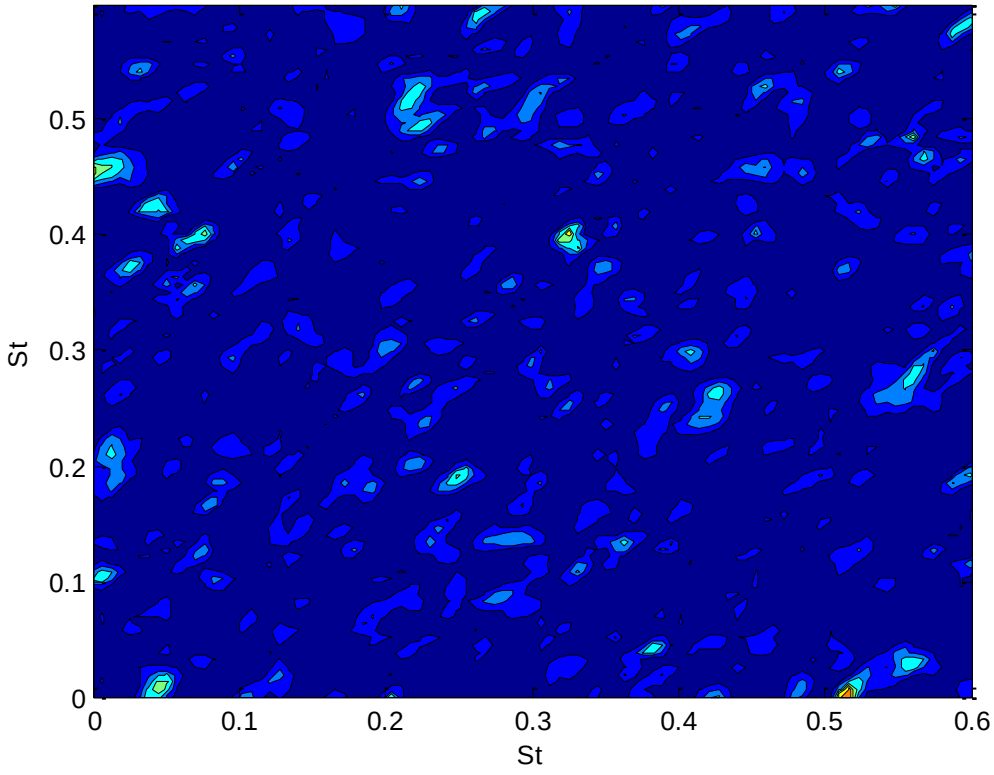
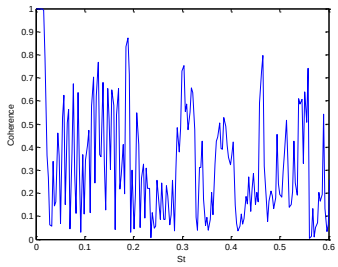


Figure P: Coherence

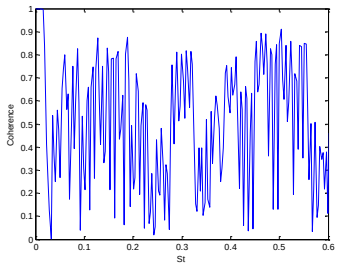
j) $\phi = 35.5°$; $\alpha = 30°$, $\beta = 20°$

v) Re = 5.5×10^5;

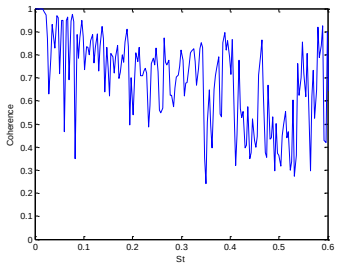
C_L-Pressure



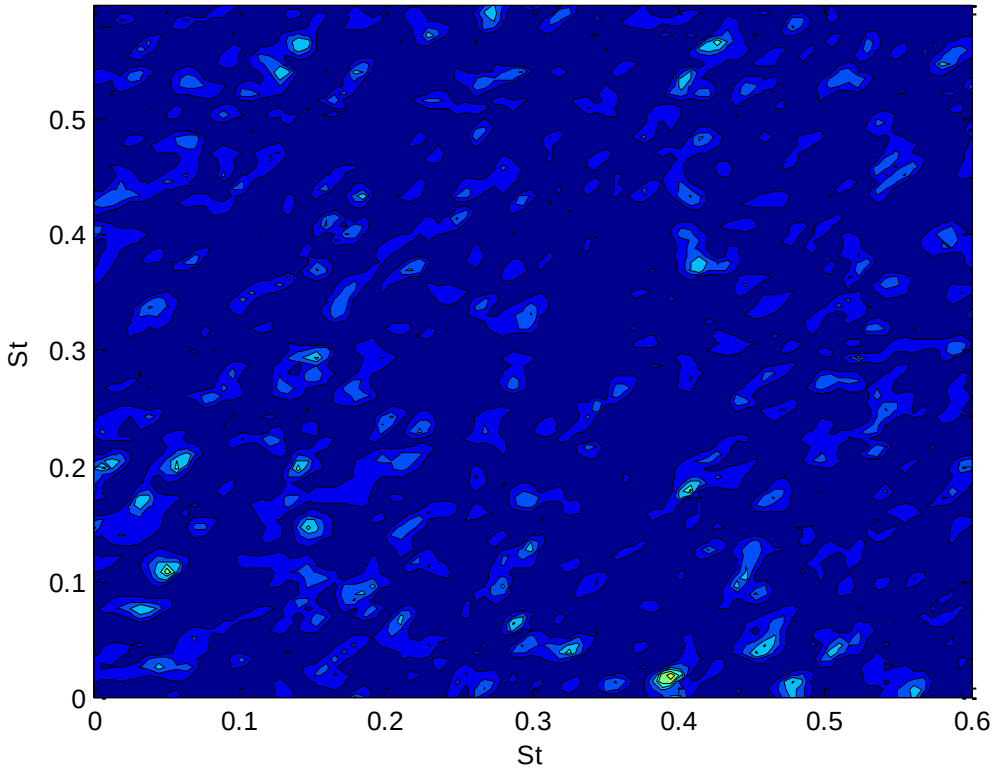
C_L-Total Velocity



Pressure-Total Velocity



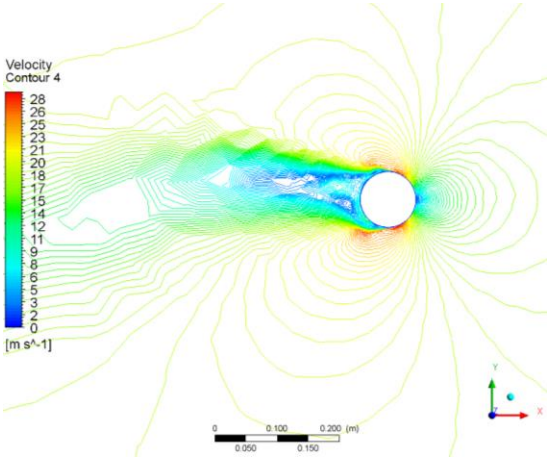
Cross-coherence: C_L-Pressure-Total Velocity

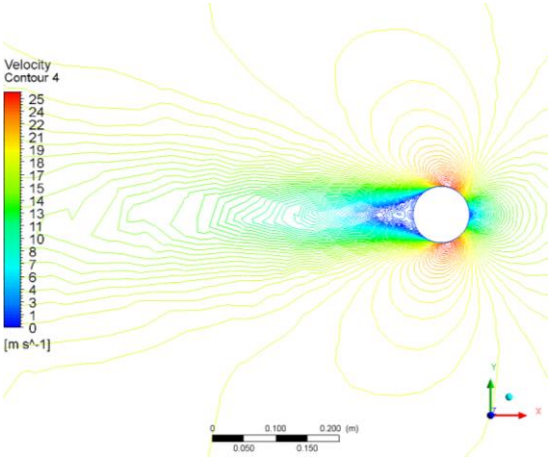


Appendix Q: Comparison of Results for Laminar Flow, k-ε Model, and LES Model

Appendix Q: Comparison of Results for Laminar Flow, k-ε Model, and LES Model

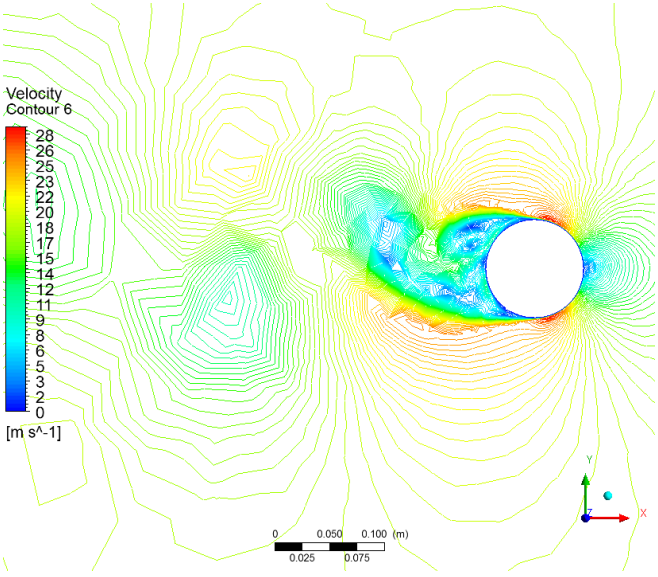
Figure Q: Results for $\alpha = 0°$, $\beta = 0°$, Re = 1.1×10^5.



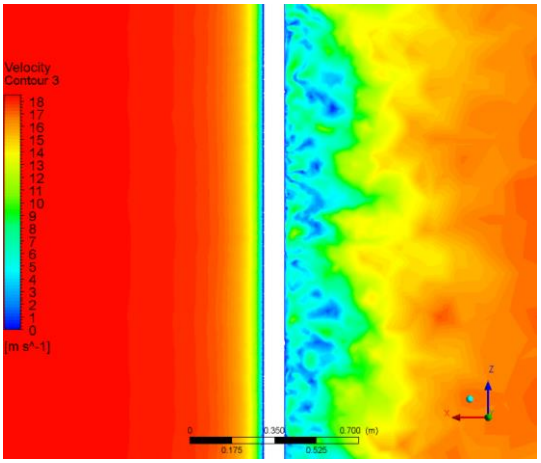


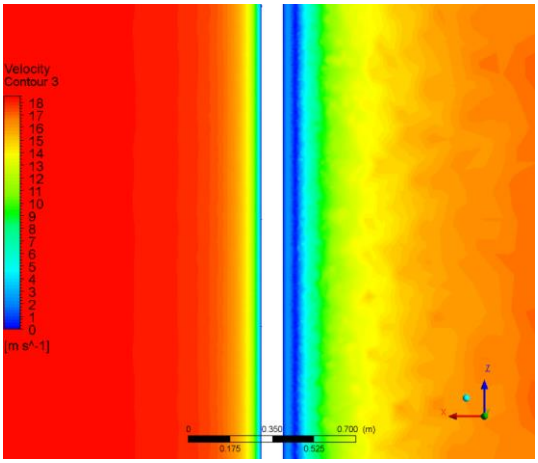
i) Velocity Profiles, $\alpha = 0°$, $\beta = 0°$, Re = 1.1×10^5.
Laminar Option

i) Velocity Profiles, $\alpha = 0°$, $\beta = 0°$, Re = 1.1×10^5.
k-ε Model



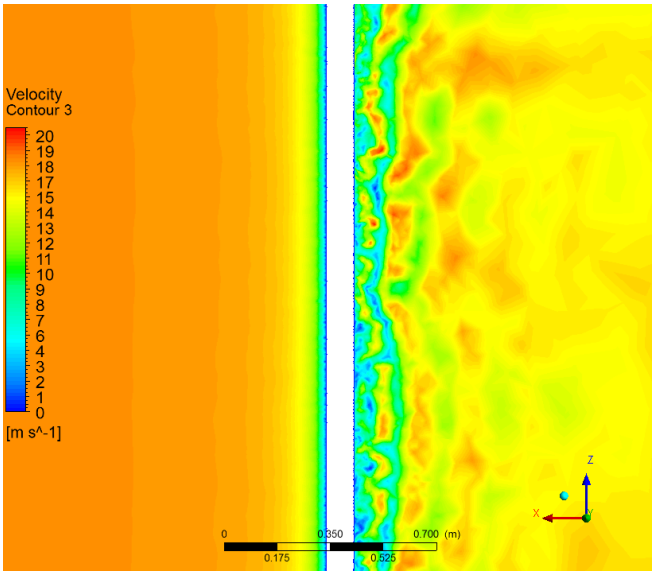
i) Velocity Profiles, $\alpha = 0°$, $\beta = 0°$, Re = 1.1×10^5.
LES Model



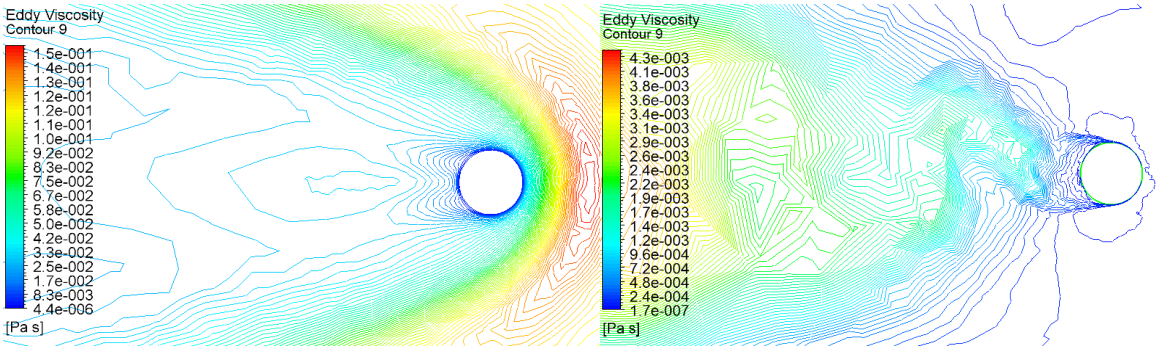


i) Velocity Profiles, $\alpha = 0°$, $\beta = 0°$, Re = 1.1×10^5.
Laminar Option

k-ε Model

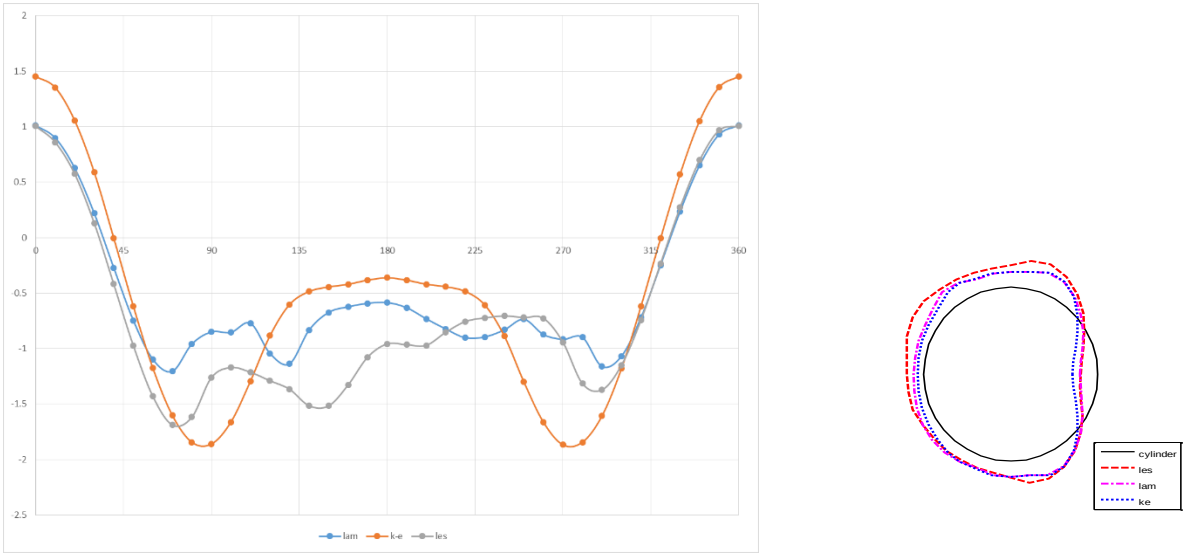


i) Velocity Profiles, $\alpha = 0°$, $\beta = 0°$, Re = 1.1×10^5.
LES Model



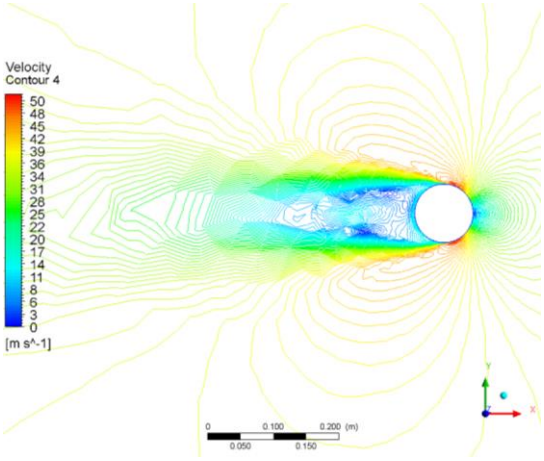
i) Eddy Viscosity, $\alpha = 0°$, $\beta = 0°$, Re = 1.1×10^5.

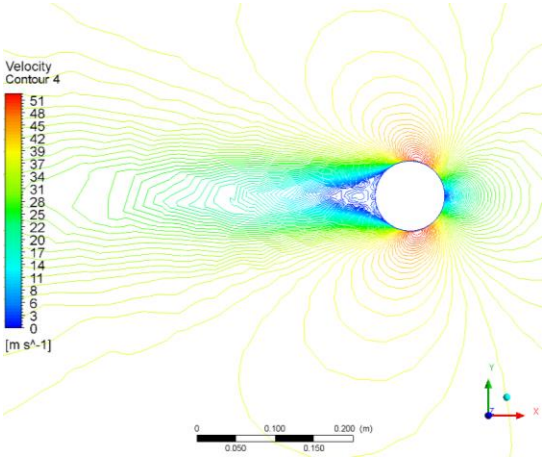
k-ε Model LES Model



i) Pressure Profiles, $\alpha = 0°$, $\beta = 0°$, Re = 1.1×10^5.

Figure Q: Results for $\alpha = 0°$, $\beta = 0°$, Re = 2.2×10^5.

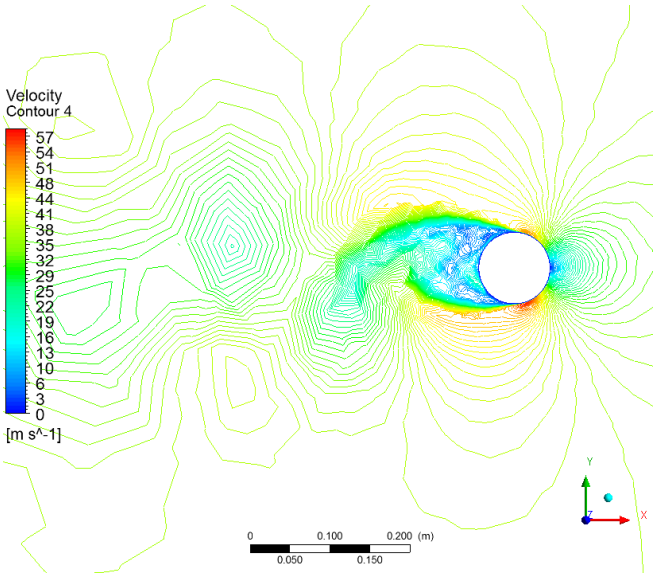




ii) Velocity Profiles, $\alpha = 0°$, $\beta = 0°$, Re = 2.2×10^5.

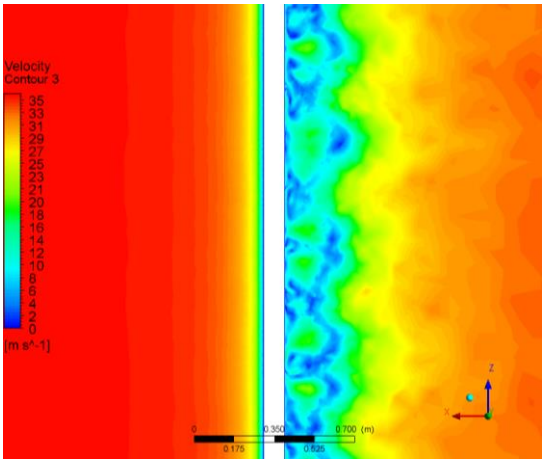
Laminar Option

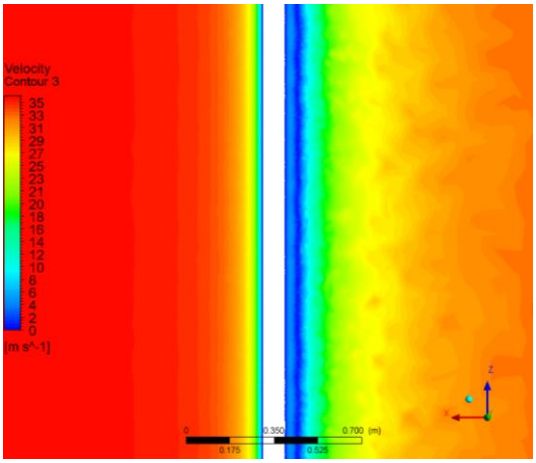
k-ε Model



ii) Velocity Profiles, $\alpha = 0°$, $\beta = 0°$, Re = 2.2×10^5.

LES Model

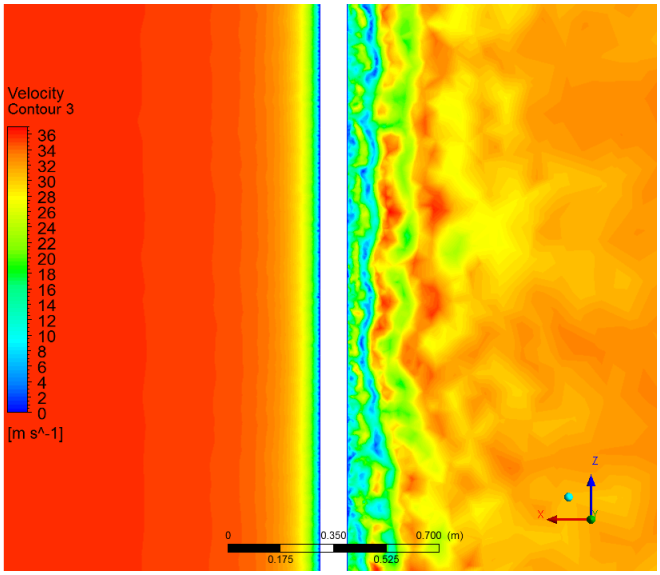




ii) Velocity Profiles, $\alpha = 0°$, $\beta = 0°$, Re = 2.2×10^5.

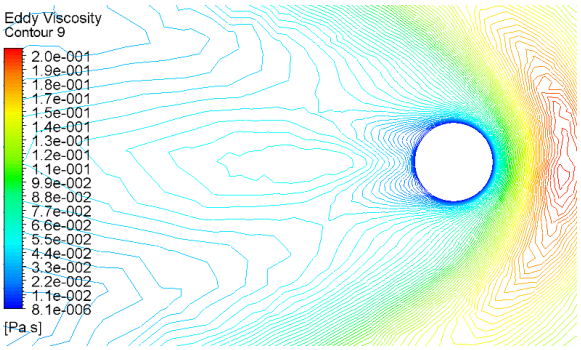
Laminar Option

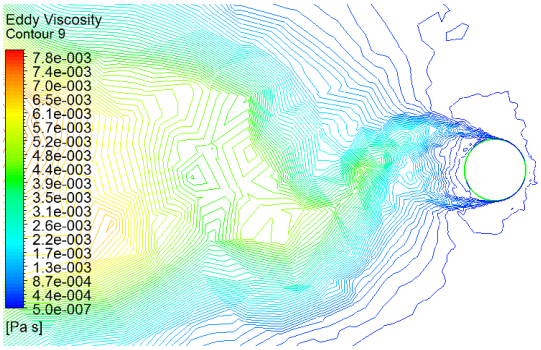
k-ε Model



ii) Velocity Profiles, $\alpha = 0°$, $\beta = 0°$, Re = 2.2×10^5.

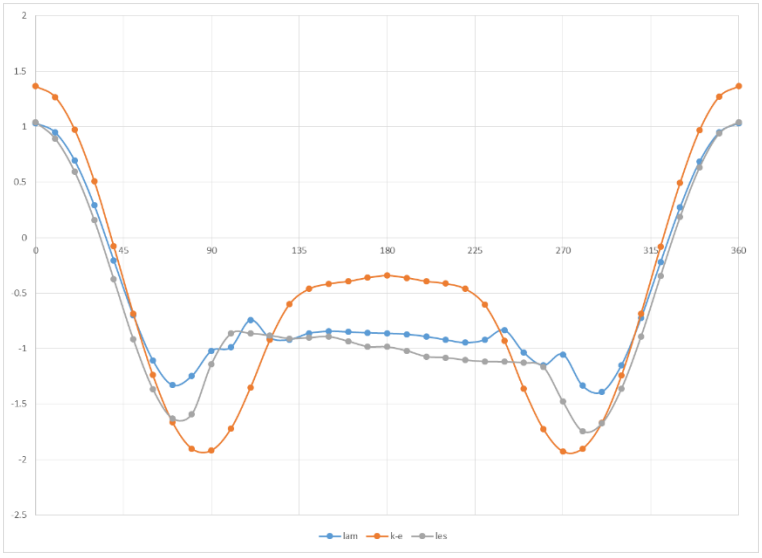
LES Model

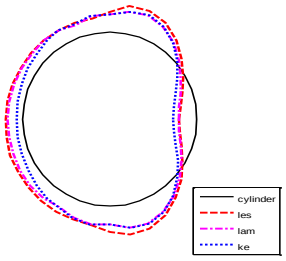




ii) Eddy Viscosity, $\alpha = 0°$, $\beta = 0°$, Re = 2.2×10^5.

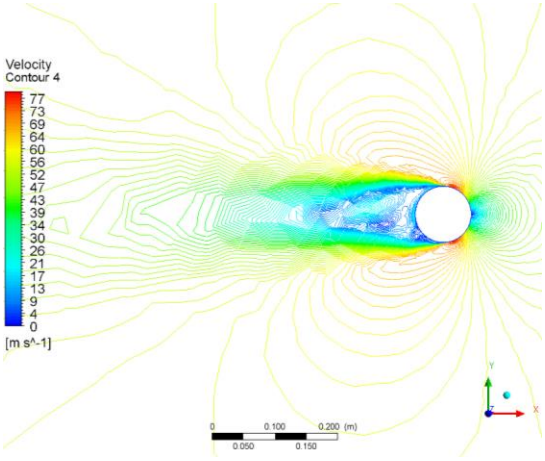
k-ε Model LES Model

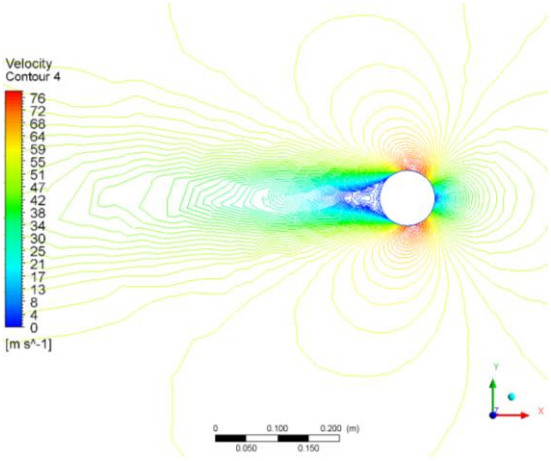




ii) Pressure Profiles, $\alpha = 0°$, $\beta = 0°$, Re = 2.2×10^5.

Figure Q: Results for $\alpha = 0°$, $\beta = 0°$, Re = 3.3×10^5.

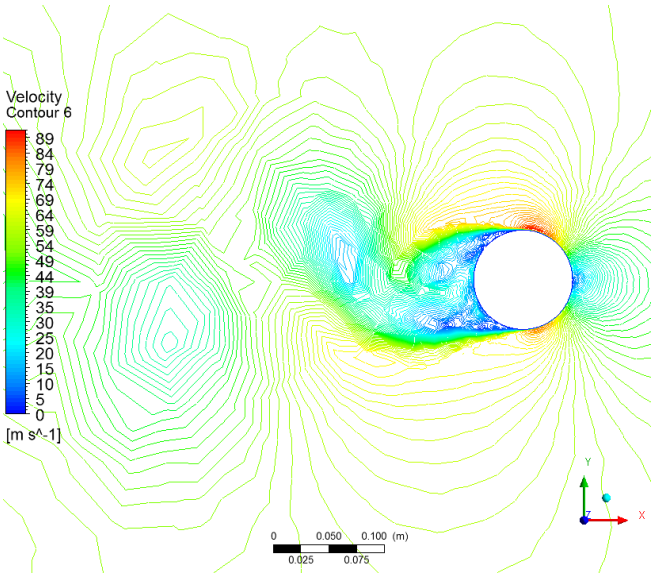




iii) Velocity Profiles, $\alpha = 0°$, $\beta = 0°$, Re = 3.3×10^5.

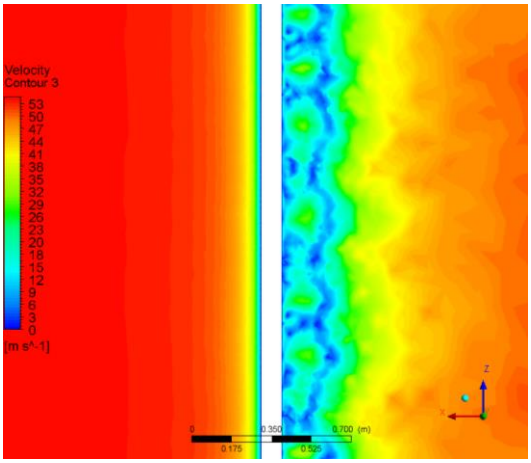
Laminar Option

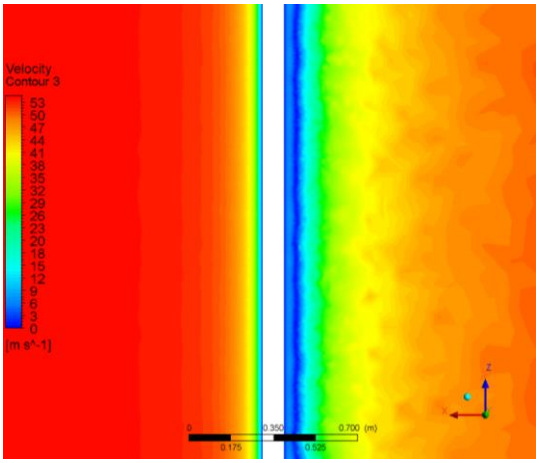
k-ε Model



iii) Velocity Profiles, $\alpha = 0°$, $\beta = 0°$, Re = 3.3×10^5.

LES Model

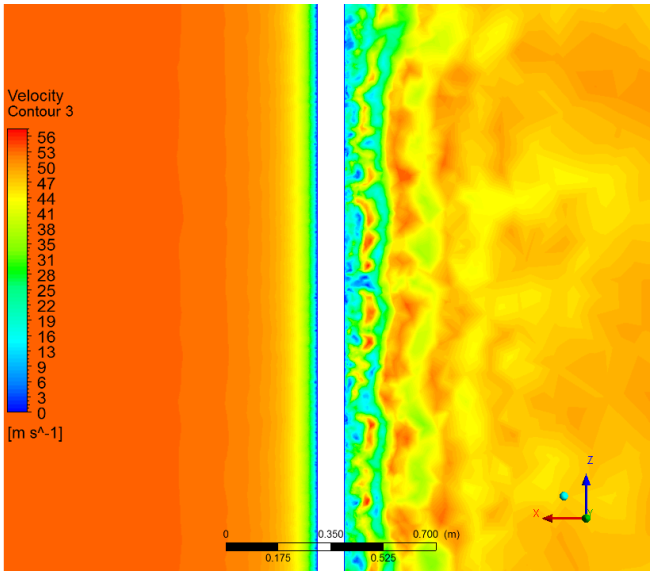




iii) Velocity Profiles, $\alpha = 0°$, $\beta = 0°$, Re = 3.3×10^5.

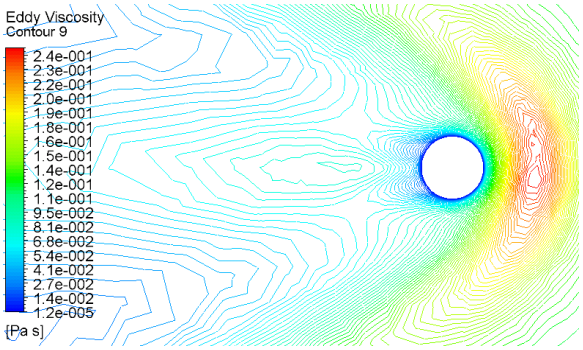
Laminar Option

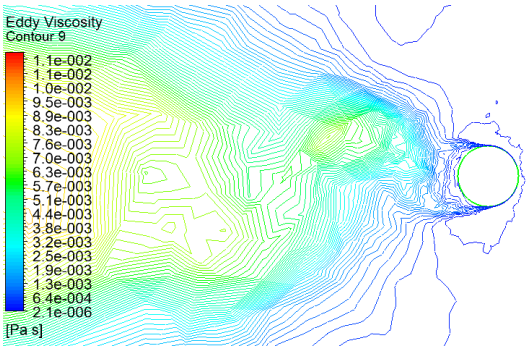
k-ε Model



iii) Velocity Profiles, $\alpha = 0°$, $\beta = 0°$, Re = 3.3×10^5.

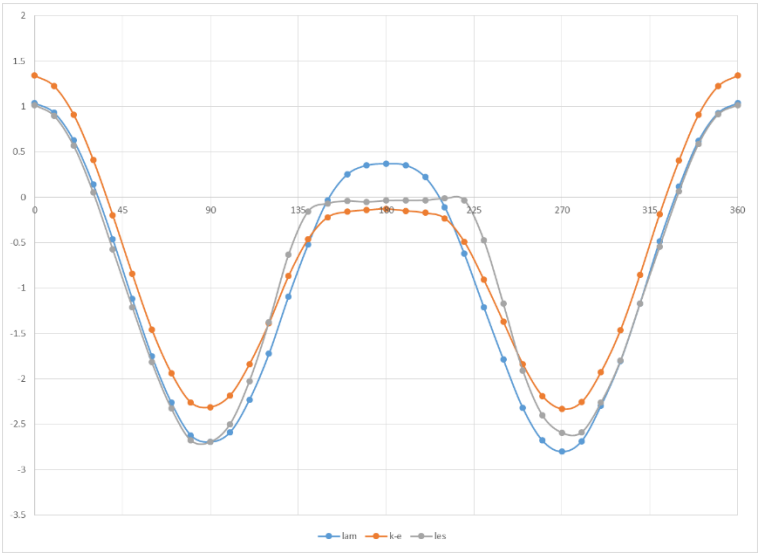
LES Model

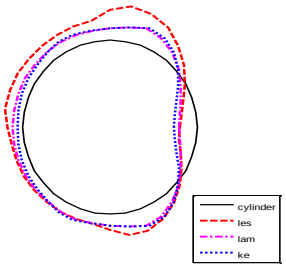




iii) Eddy Viscosity, $\alpha = 0°$, $\beta = 0°$, Re = 3.3×10^5.

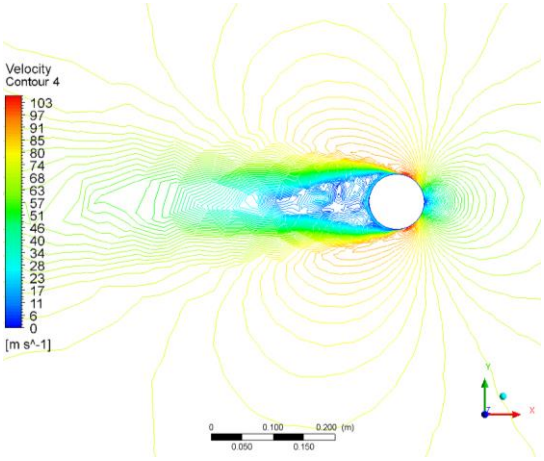
k-ε Model LES Model

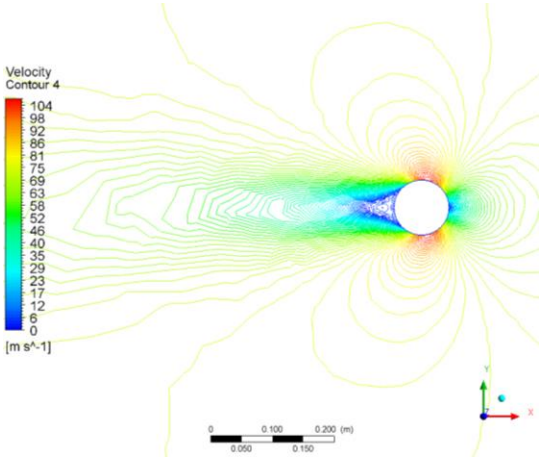




iii) Pressure Profiles, $\alpha = 0°$, $\beta = 0°$, Re = 3.3×10^5.

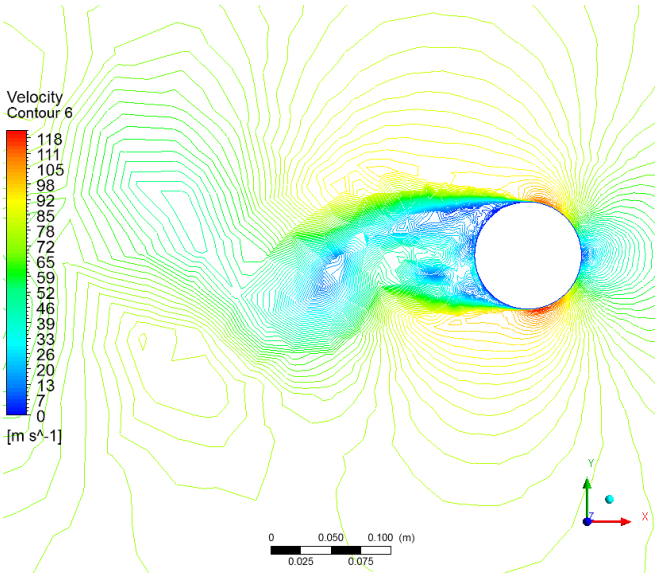
Figure Q: Results for $\alpha = 0°$, $\beta = 0°$, Re = 4.4×10^5.





iv) Velocity Profiles, $\alpha = 0°$, $\beta = 0°$, Re = 4.4×10^5.

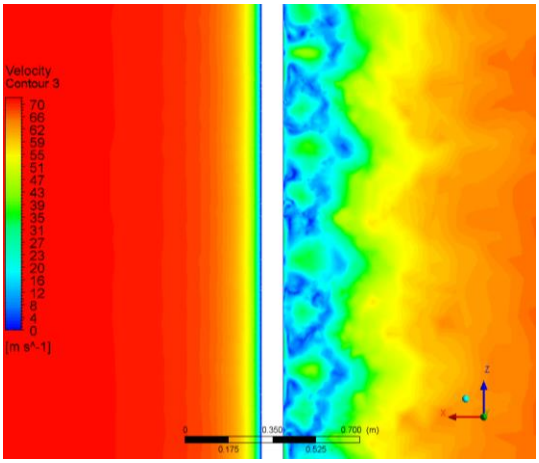
Laminar Option

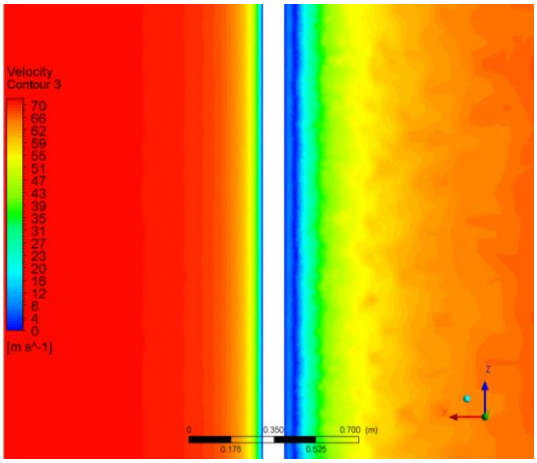


iv) Velocity Profiles, $\alpha = 0°$, $\beta = 0°$, Re = 4.4×10^5.

k-ε Model

LES Model

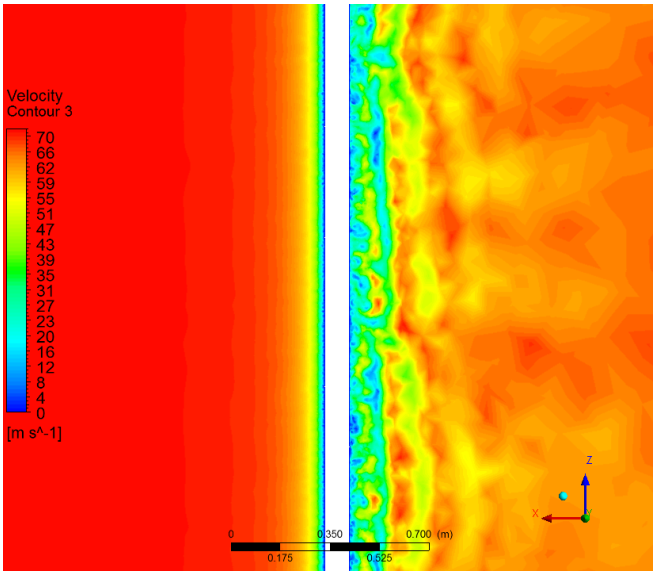




iv) Velocity Profiles, $\alpha = 0°$, $\beta = 0°$, Re = 4.4×10^5.

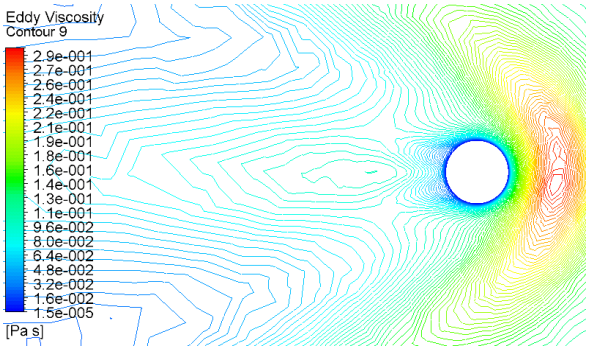
Laminar Option

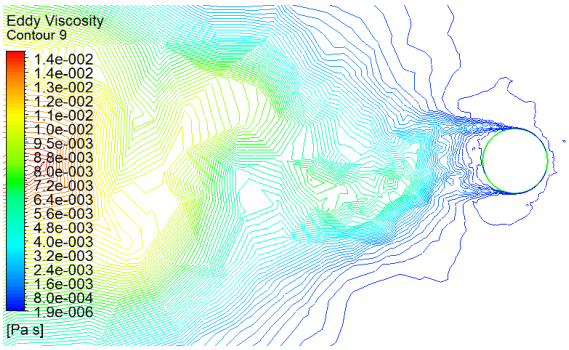
k-ε Model



iv) Velocity Profiles, $\alpha = 0°$, $\beta = 0°$, Re = 4.4×10^5.

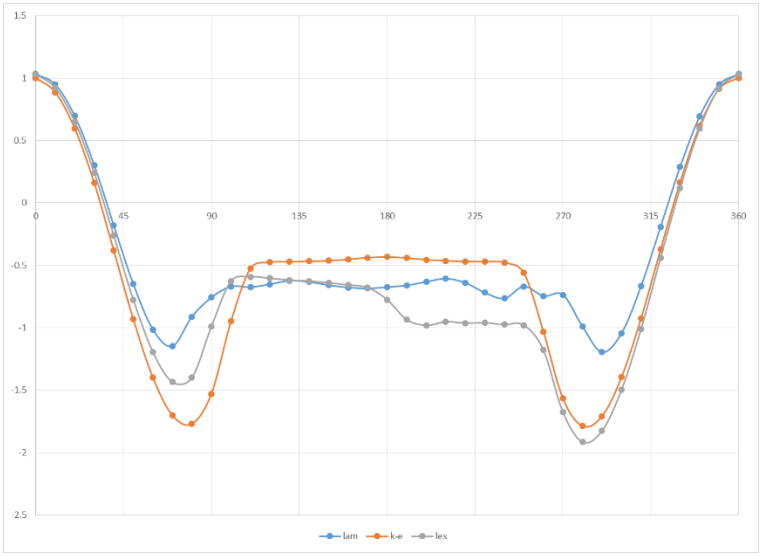
LES Model

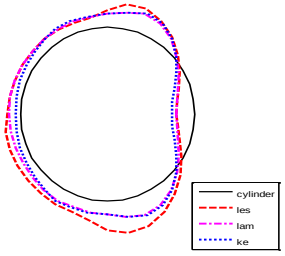




iv) Eddy Viscosity, $\alpha = 0°$, $\beta = 0°$, Re = 4.4×10^5.

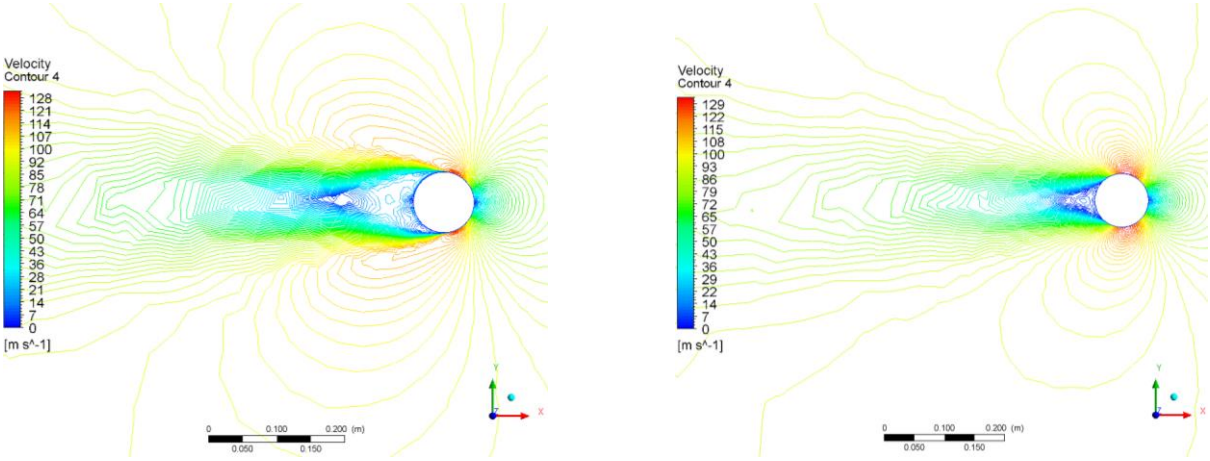
k-ε Model LES Model





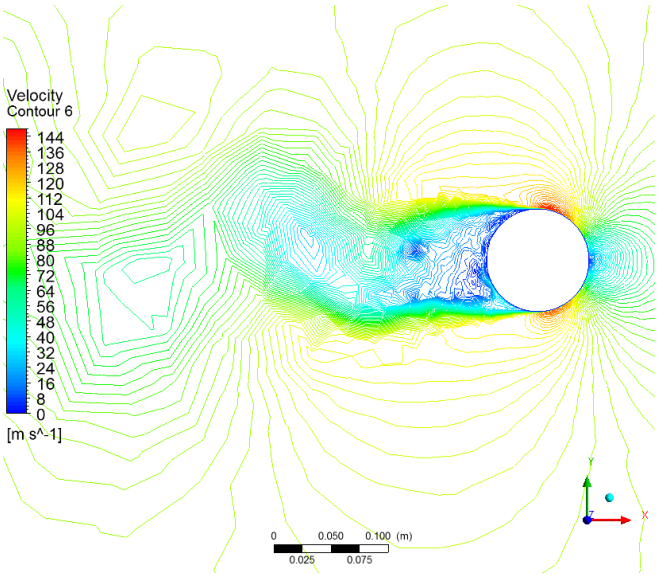
iv) Pressure Profiles, $\alpha = 0°$, $\beta = 0°$, Re = 4.4×10^5.

Figure Q: Results for $\alpha = 0°$, $\beta = 0°$, Re = 5.5×10^5.



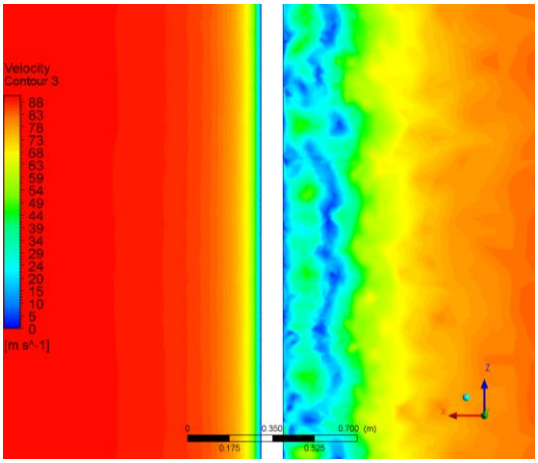
v) Velocity Profiles, $\alpha = 0°$, $\beta = 0°$, Re = 5.5×10^5.

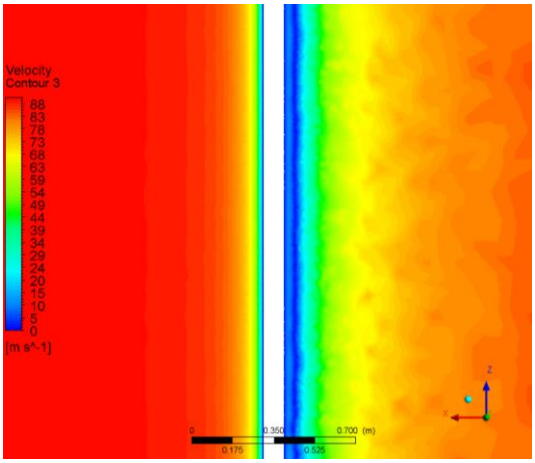
Laminar Option k-ε Model



v) Velocity Profiles, $\alpha = 0°$, $\beta = 0°$, Re = 5.5×10^5.

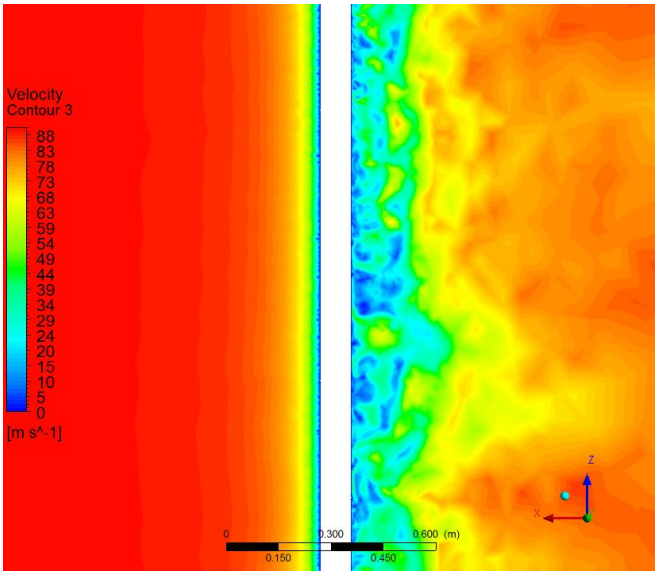
LES Model



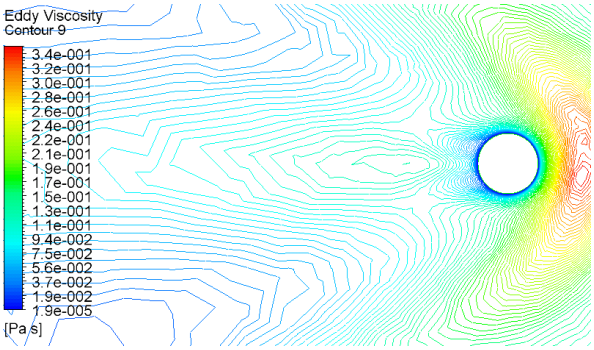


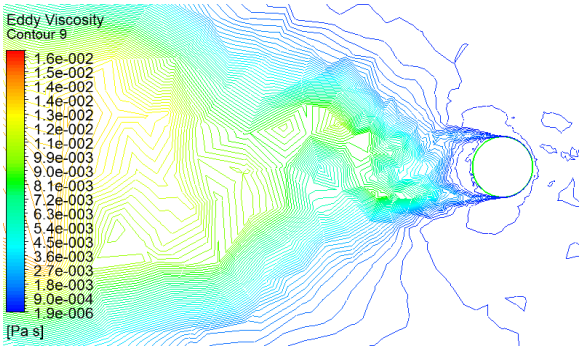
v) Velocity Profiles, $\alpha = 0°$, $\beta = 0°$, Re = 5.5×10^5.
Laminar Option

v) Velocity Profiles, $\alpha = 0°$, $\beta = 0°$, Re = 5.5×10^5.
k-ε Model



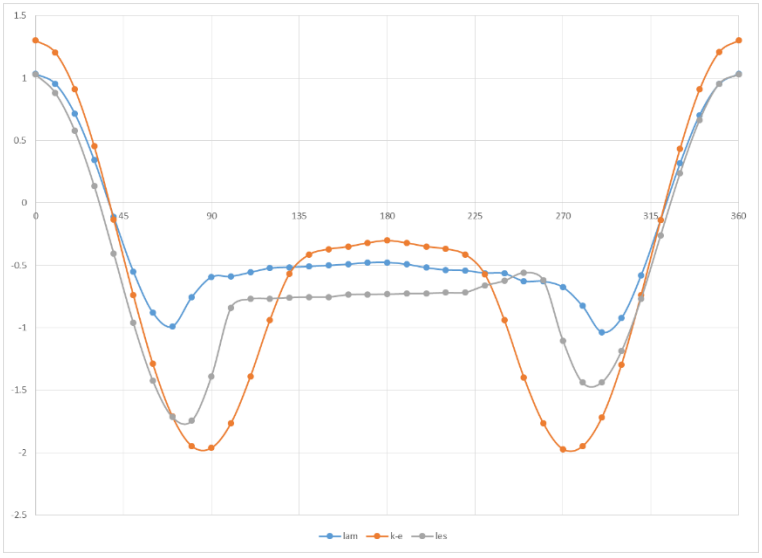
v) Velocity Profiles, $\alpha = 0°$, $\beta = 0°$, Re = 5.5×10^5.
LES Model

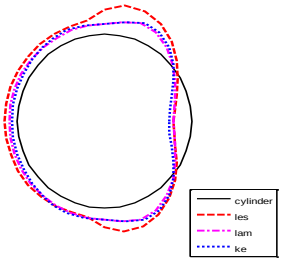




v) Eddy Viscosity, $\alpha = 0°$, $\beta = 0°$, Re = 5.5×10^5.

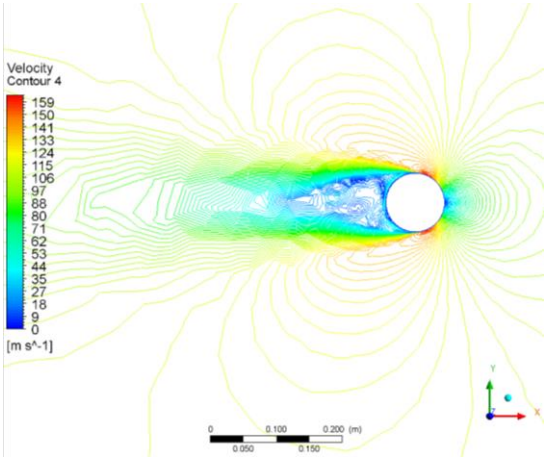
k-ε Model LES Model

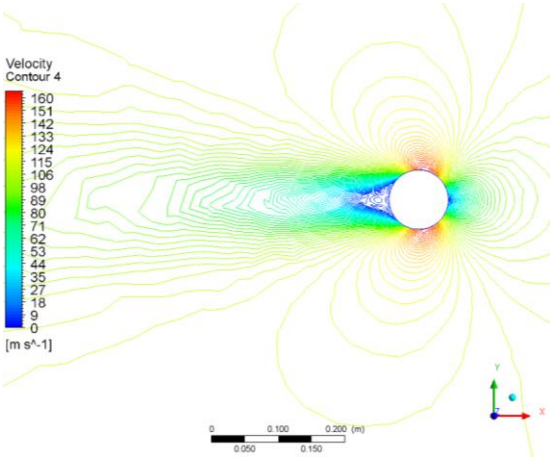




v) Pressure Profiles, $\alpha = 0°$, $\beta = 0°$, Re = 5.5×10^5.

Figure Q: Results for $\alpha = 0°$, $\beta = 0°$, Re = 6.7×10^5.

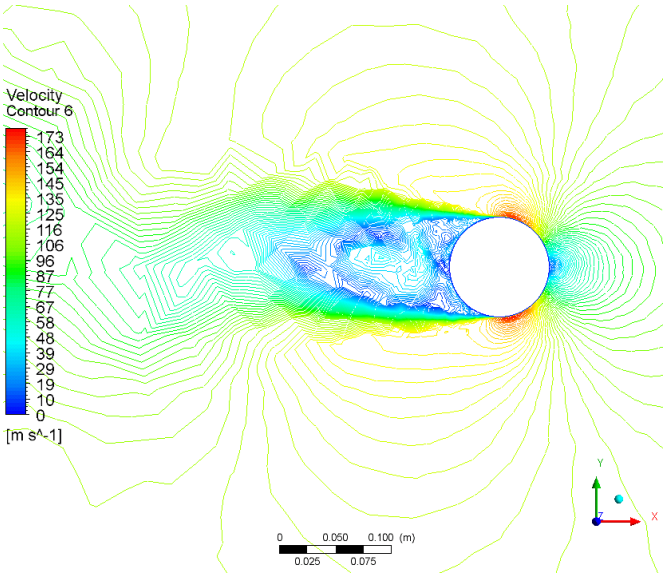




vi) Velocity Profiles, $\alpha = 0°$, $\beta = 0°$, Re = 6.7×10^5.

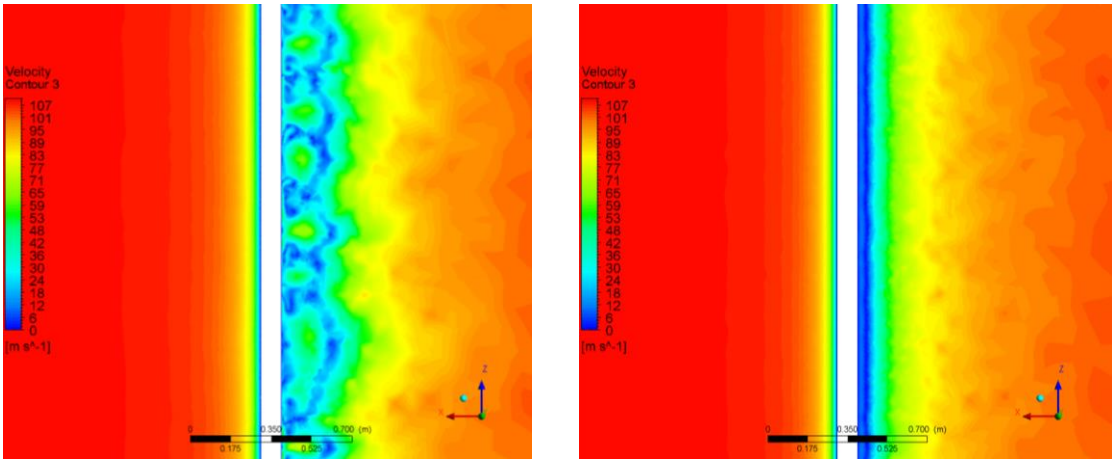
Laminar Option

k-ε Model



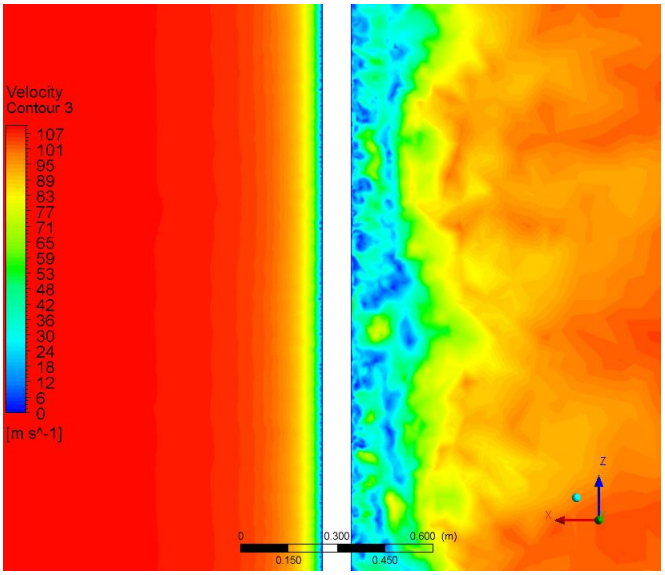
vi) Velocity Profiles, $\alpha = 0°$, $\beta = 0°$, Re = 6.7×10^5.

LES Model



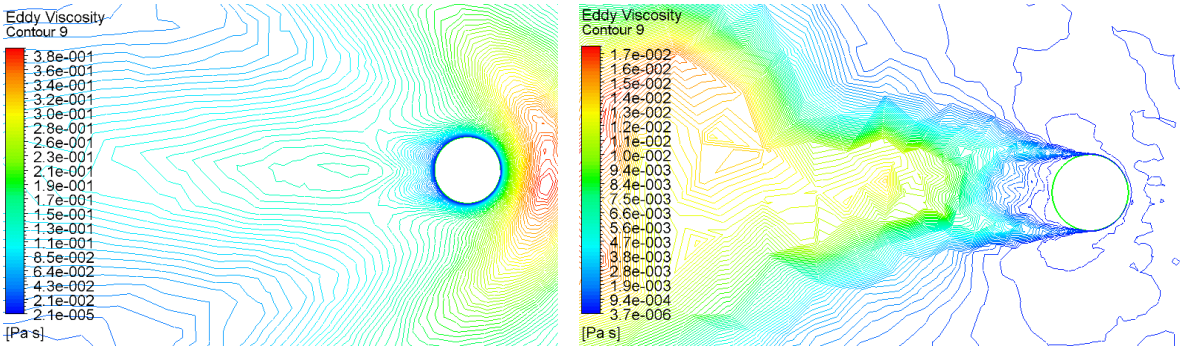
vi) Velocity Profiles, $\alpha = 0°$, $\beta = 0°$, Re = 6.7×10^5.

Laminar Option k-ε Model



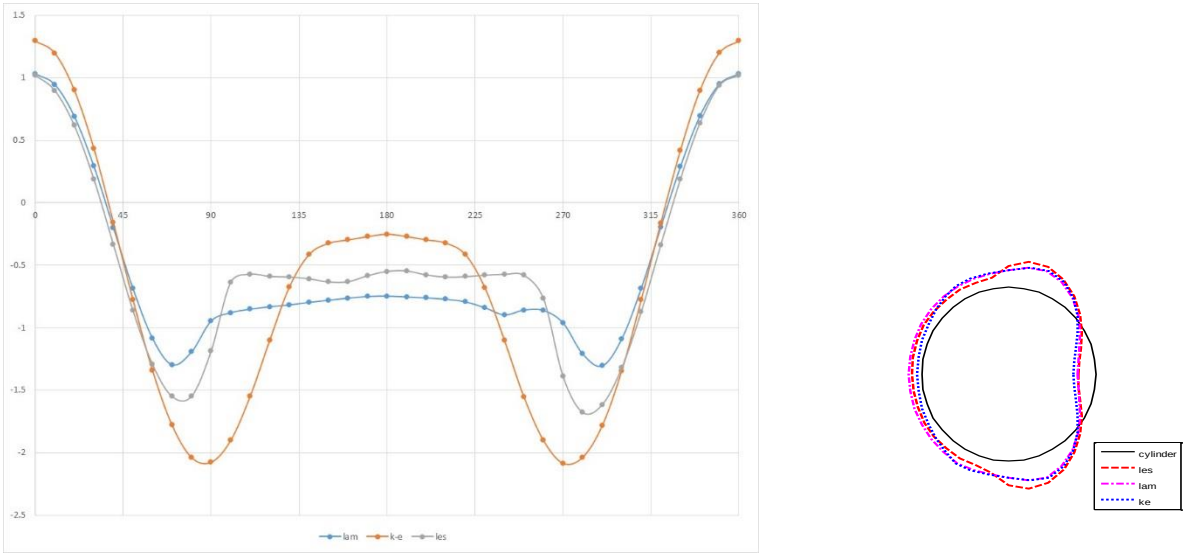
vi) Velocity Profiles, $\alpha = 0°$, $\beta = 0°$, Re = 6.7×10^5.

LES Model



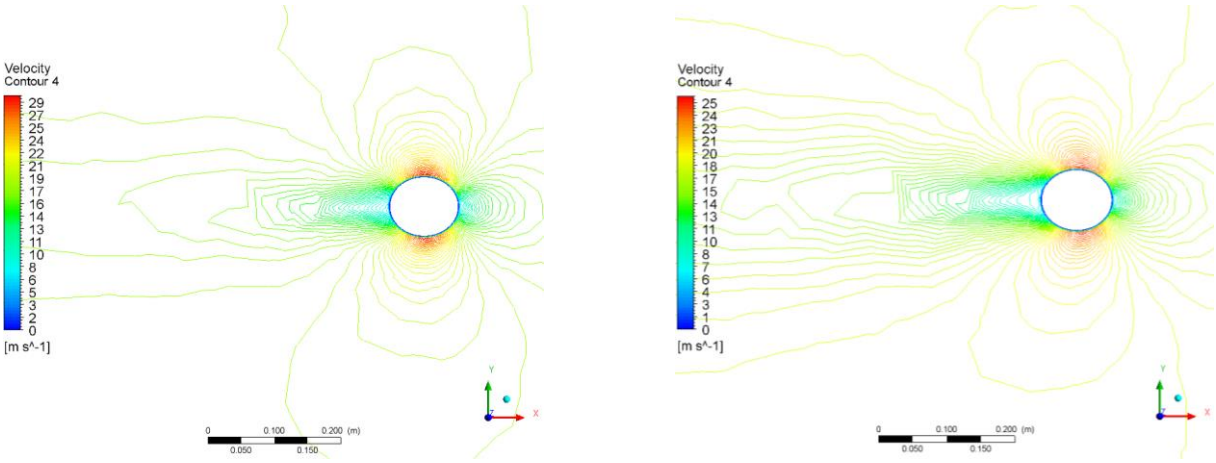
vi) Eddy Viscosity, $\alpha = 0°$, $\beta = 0°$, Re = 6.7×10^5.

k-ε Model LES Model



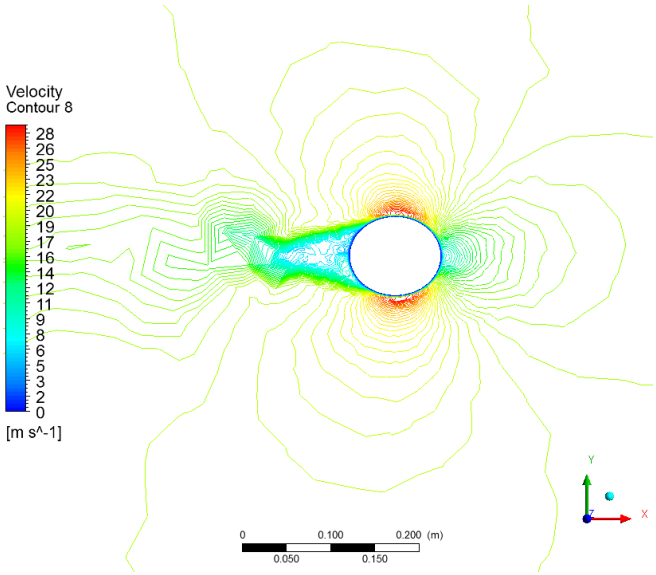
vi) Pressure Profiles, $\alpha = 0°$, $\beta = 0°$, Re = 6.7×10^5.

Figure Q: Results for $\alpha = 60°$, $\beta = 0°$, Re = 1.1×10^5.



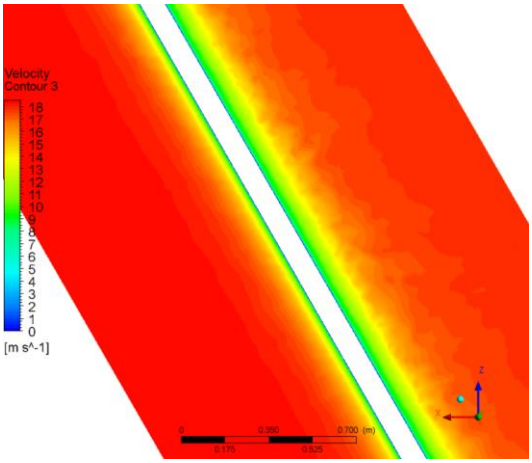
vii) Velocity Profiles, $\alpha = 60°$, $\beta = 0°$, Re = 1.1×10^5.

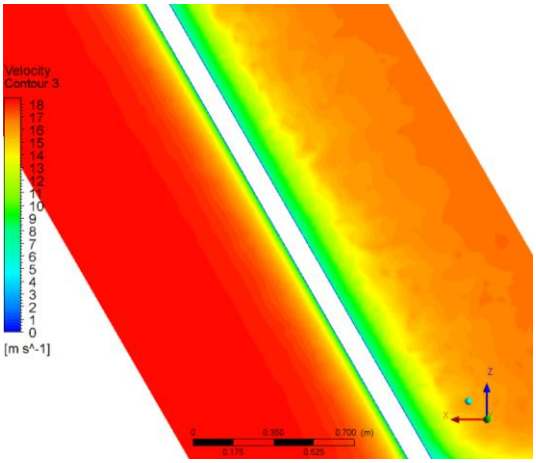
Laminar Option k-ε Model



vii) Velocity Profiles, $\alpha = 60°$, $\beta = 0°$, Re = 1.1×10^5.

LES Model

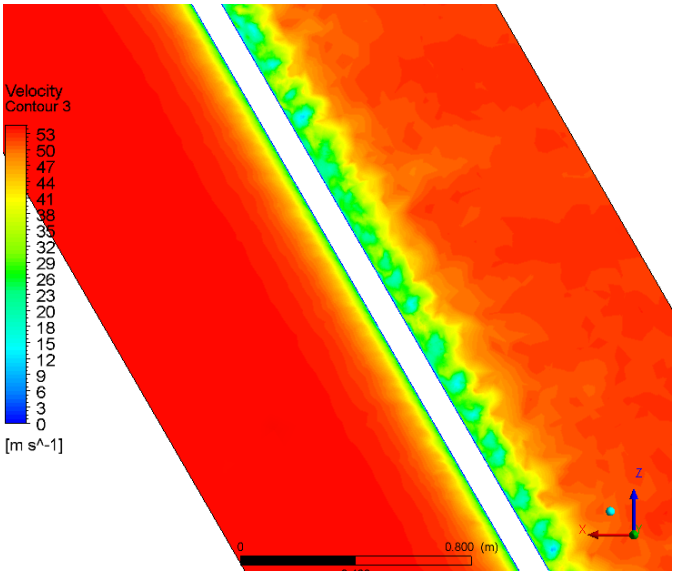




vii) Velocity Profiles, $\alpha = 60°$, $\beta = 0°$, Re = 1.1×10^5.

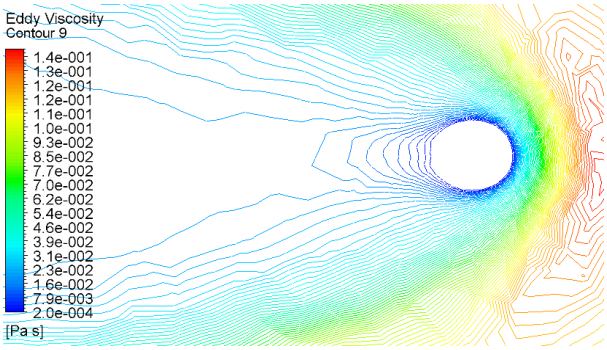
Laminar Option

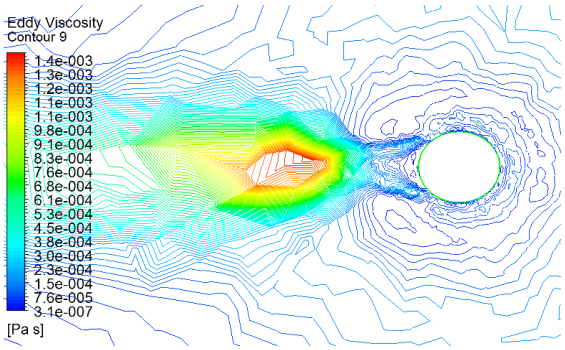
k-ε Model



vii) Velocity Profiles, $\alpha = 60°$, $\beta = 0°$, Re = 1.1×10^5.

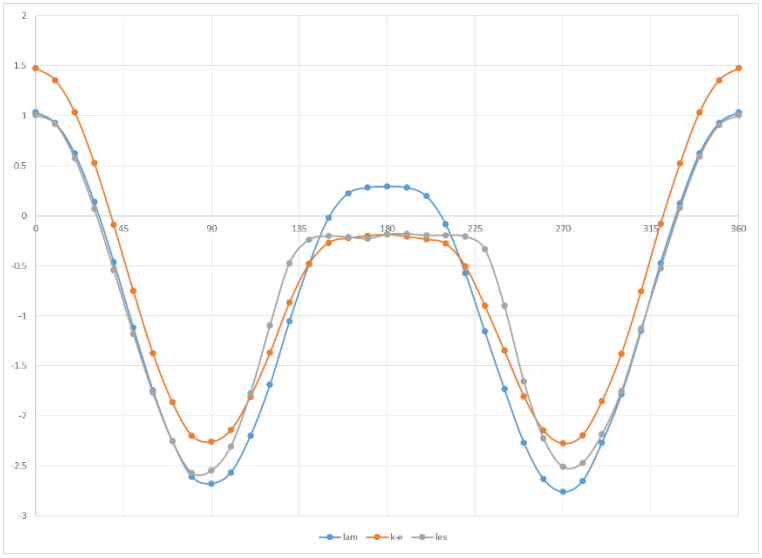
LES Model

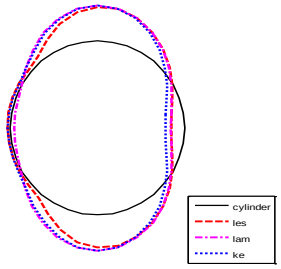




vii) Eddy Viscosity, $\alpha = 60°$, $\beta = 0°$, Re = 1.1×10^5.

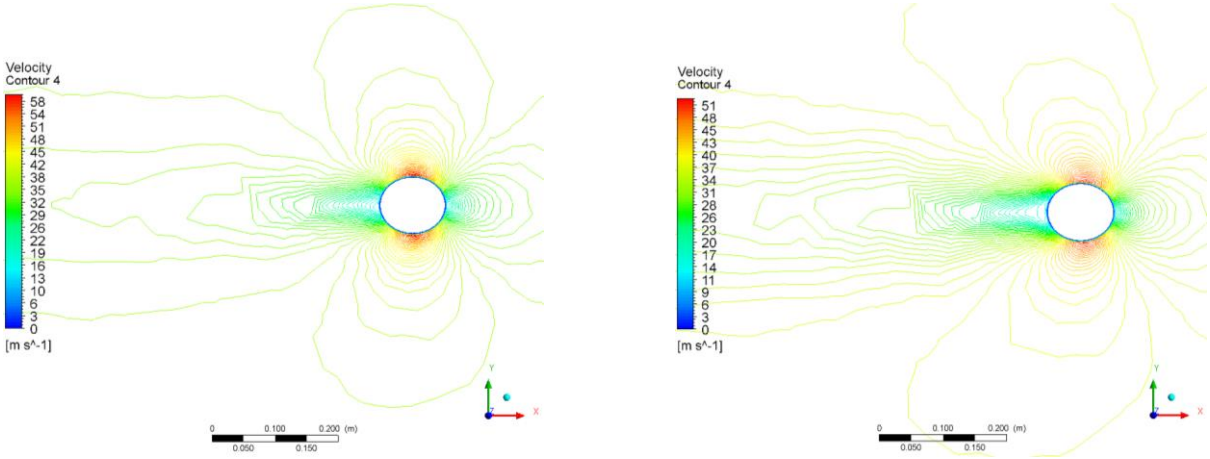
k-ε Model LES Model





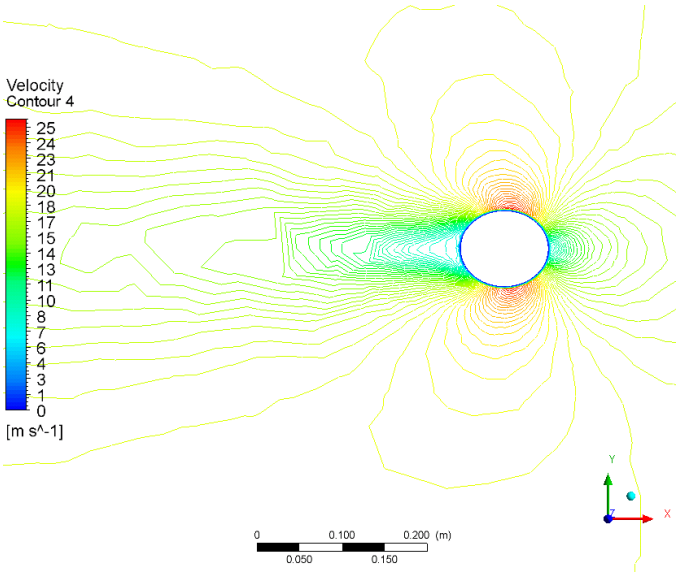
vii) Pressure Profiles, $\alpha = 60°$, $\beta = 0°$, Re = 1.1×10^5.

Figure Q: Results for $\alpha = 60°$, $\beta = 0°$, Re = 2.2×10^5.



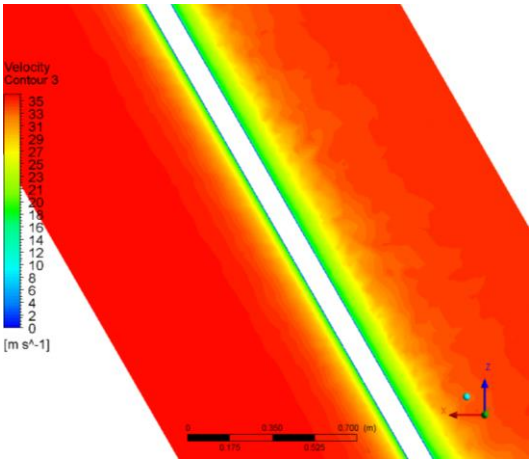
viii) Velocity Profiles, $\alpha = 60°$, $\beta = 0°$, Re = 2.2×10^5.

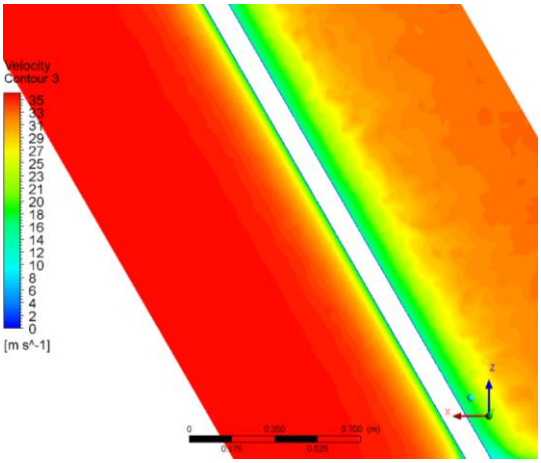
Laminar Option k-ε Model



viii) Velocity Profiles, $\alpha = 60°$, $\beta = 0°$, Re = 2.2×10^5.

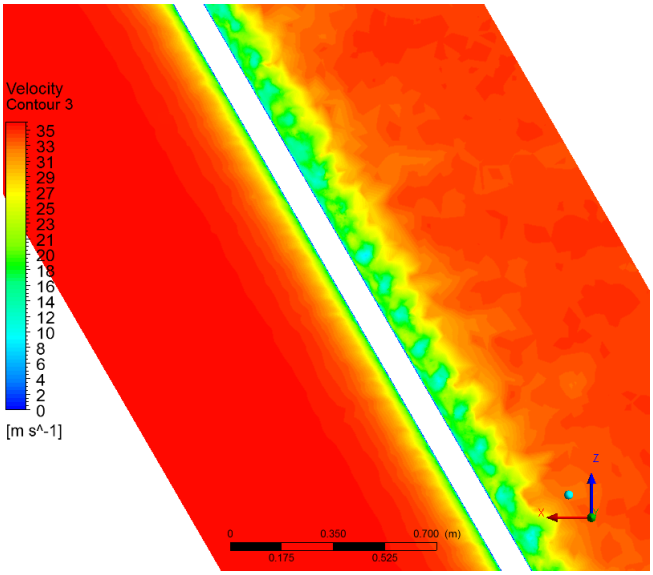
LES Model





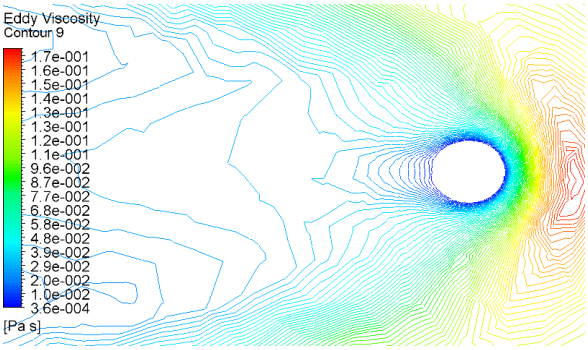
viii) Velocity Profiles, $\alpha = 60°$, $\beta = 0°$, Re = 2.2×10^5.

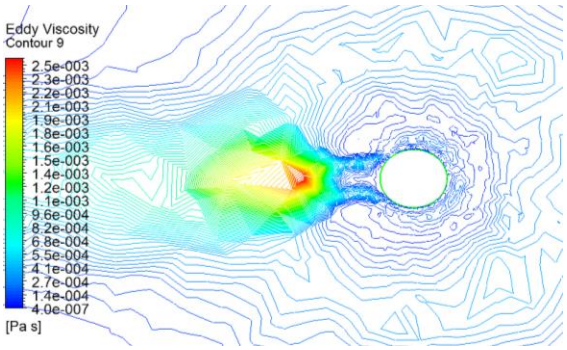
Laminar Option k-ε Model



viii) Velocity Profiles, $\alpha = 60°$, $\beta = 0°$, Re = 2.2×10^5.

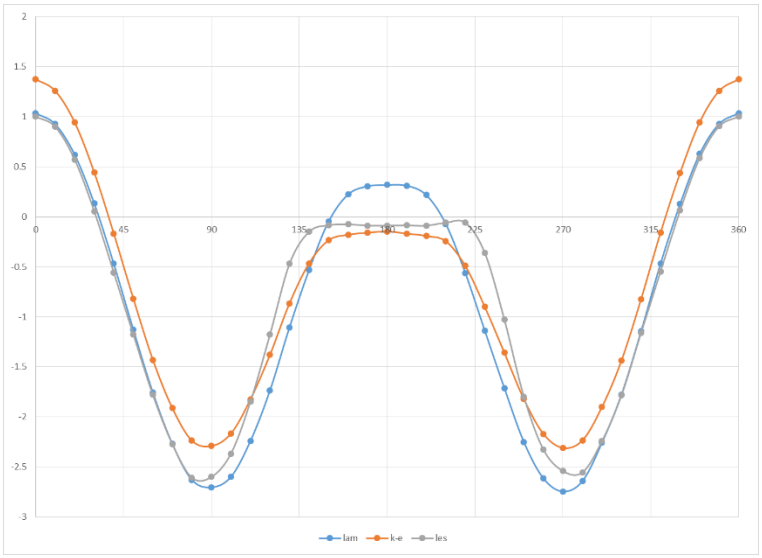
LES Model

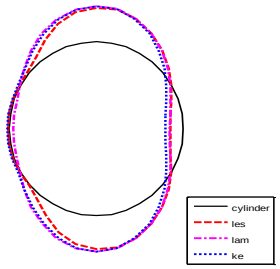




viii) Eddy Viscosity, $\alpha = 60°$, $\beta = 0°$, Re = 2.2×10^5.

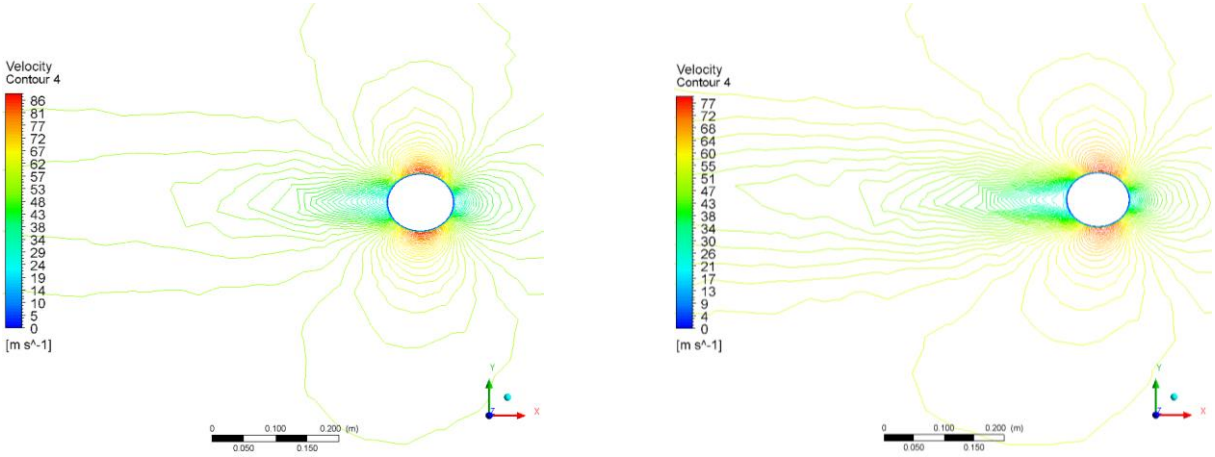
k-ε Model LES Model





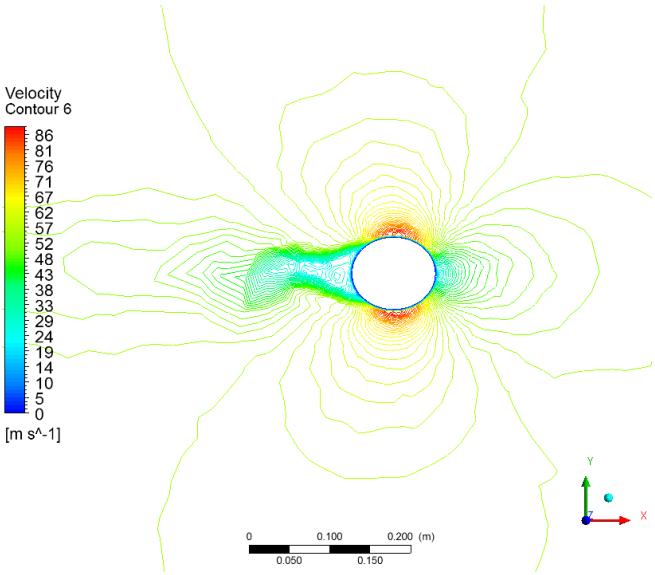
viii) Pressure Profiles, $\alpha = 60°$, $\beta = 0°$, Re = 2.2×10^5.

Figure Q: Results for $\alpha = 60°$, $\beta = 0°$, Re = 3.3×10^5.



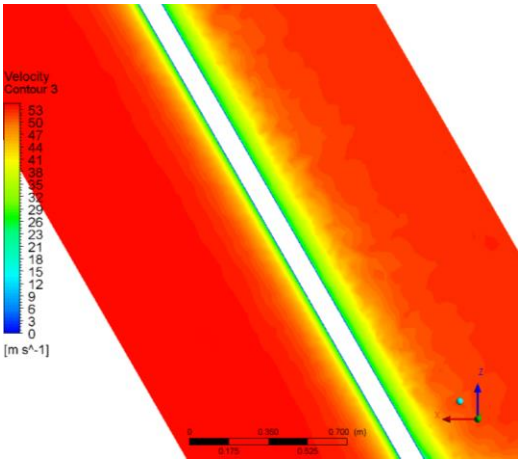
ix) Velocity Profiles, $\alpha = 60°$, $\beta = 0°$, Re = 3.3×10^5.

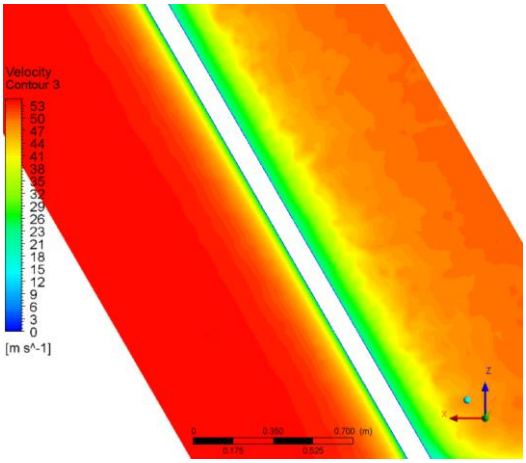
Laminar Option k-ε Model



ix) Velocity Profiles, $\alpha = 60°$, $\beta = 0°$, Re = 3.3×10^5.

LES Model

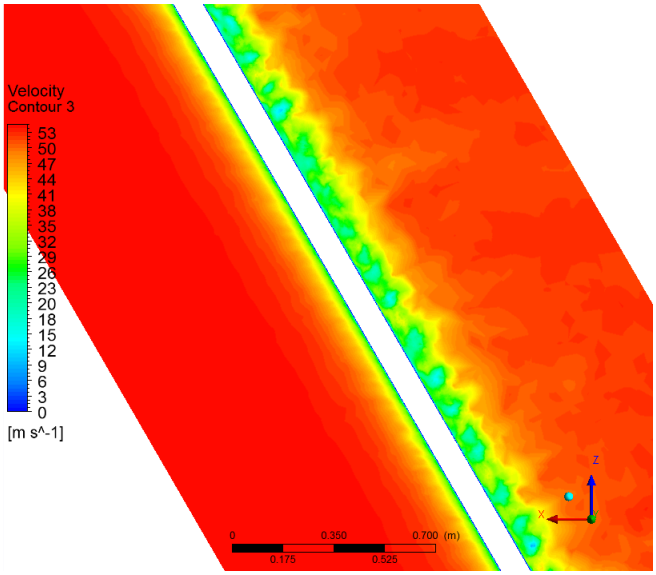




ix) Velocity Profiles, $\alpha = 60°$, $\beta = 0°$, Re = 3.3×10^5.

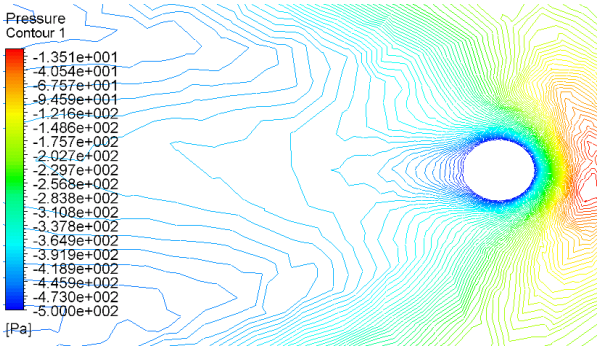
Laminar Option

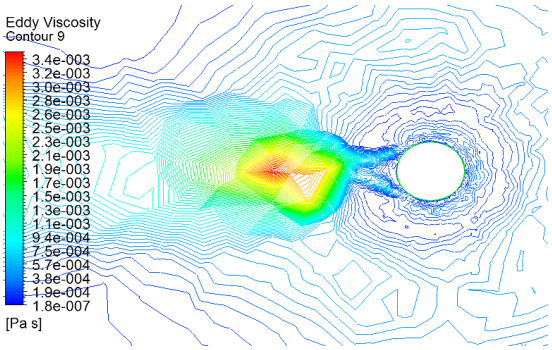
k-ε Model



ix) Velocity Profiles, $\alpha = 60°$, $\beta = 0°$, Re = 3.3×10^5.

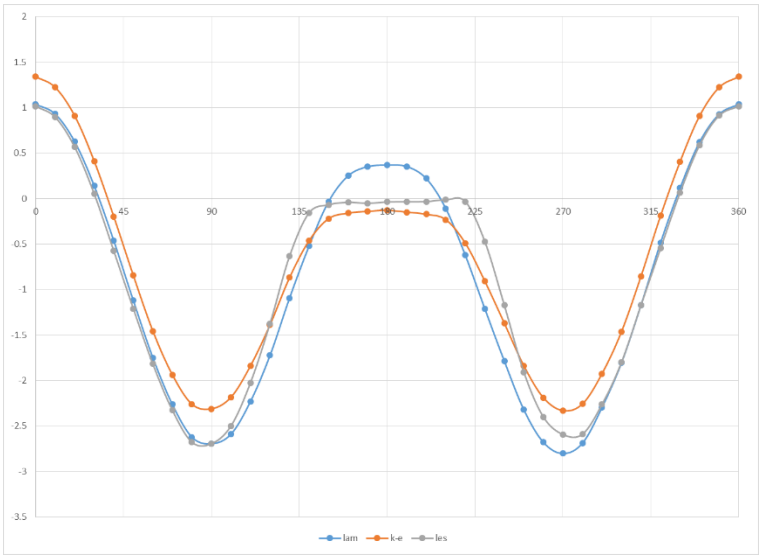
LES Model

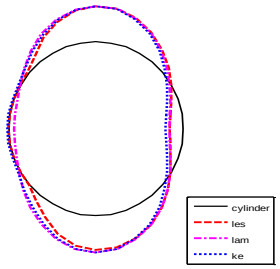




ix) Eddy Viscosity, $\alpha = 60°$, $\beta = 0°$, Re = 3.3×10^5.

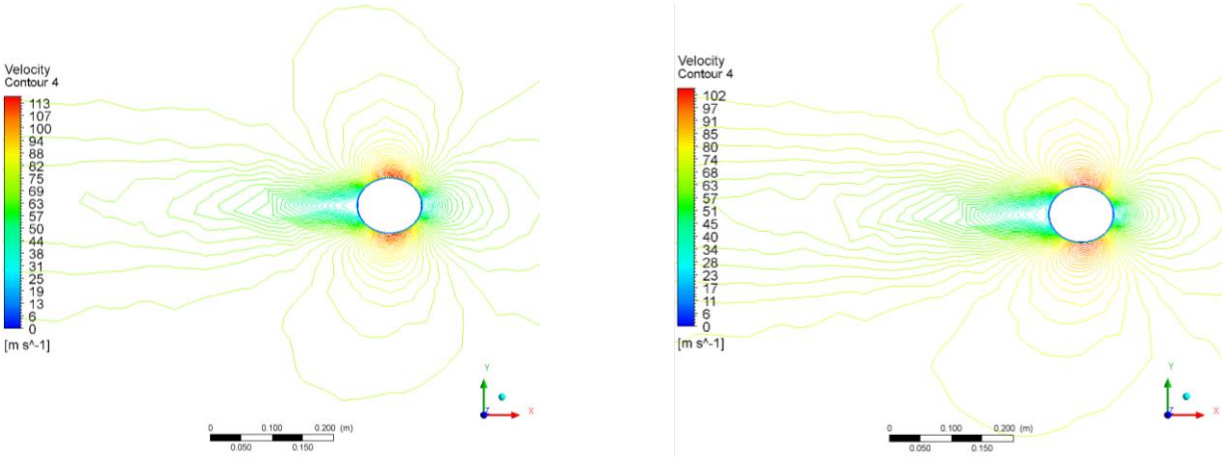
k-ε Model LES Model





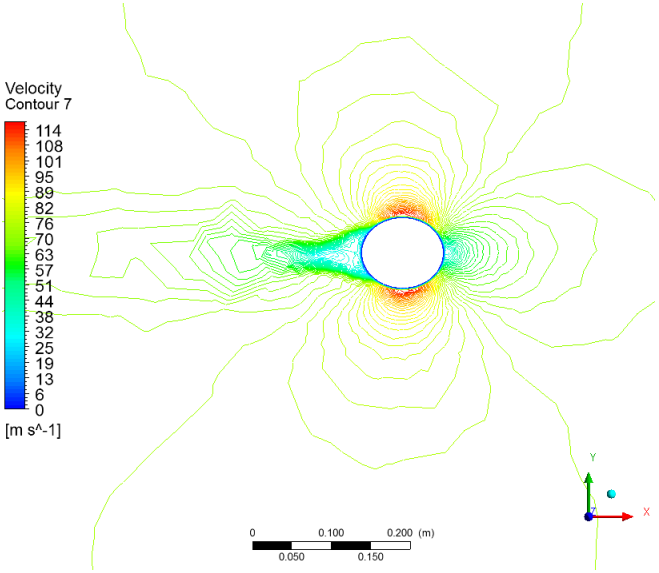
ix) Pressure Profiles, $\alpha = 60°$, $\beta = 0°$, Re = 3.3×10^5.

Figure Q: Results for $\alpha = 60°$, $\beta = 0°$, Re = 4.4×10^5.



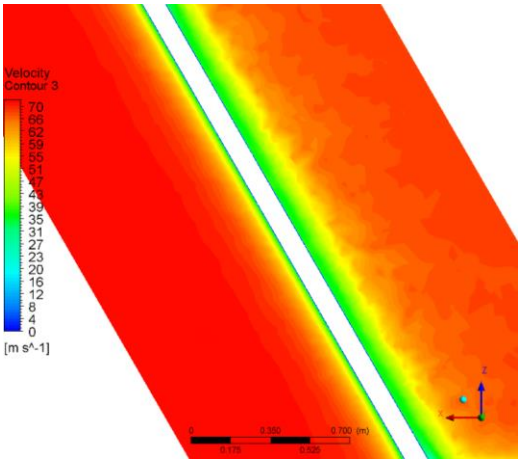
x) Velocity Profiles, $\alpha = 60°$, $\beta = 0°$, Re = 4.4×10^5.

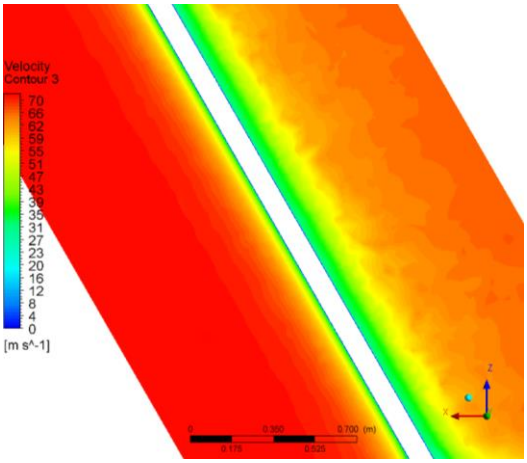
Laminar Option k-ε Model



x) Velocity Profiles, $\alpha = 60°$, $\beta = 0°$, Re = 4.4×10^5.

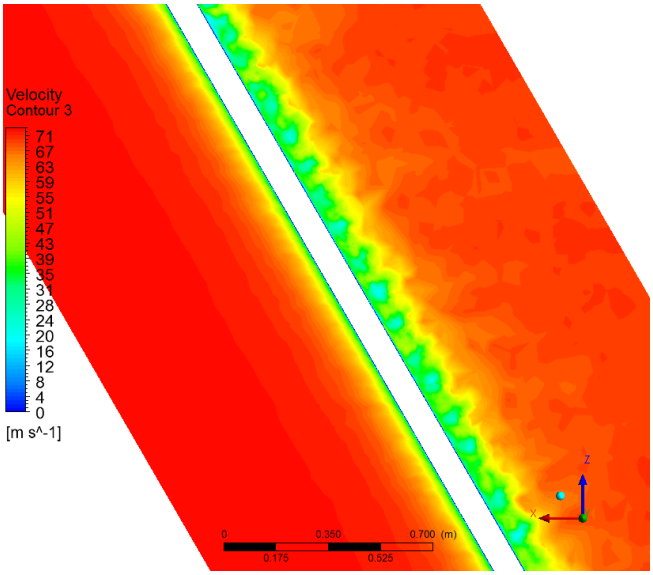
LES Model





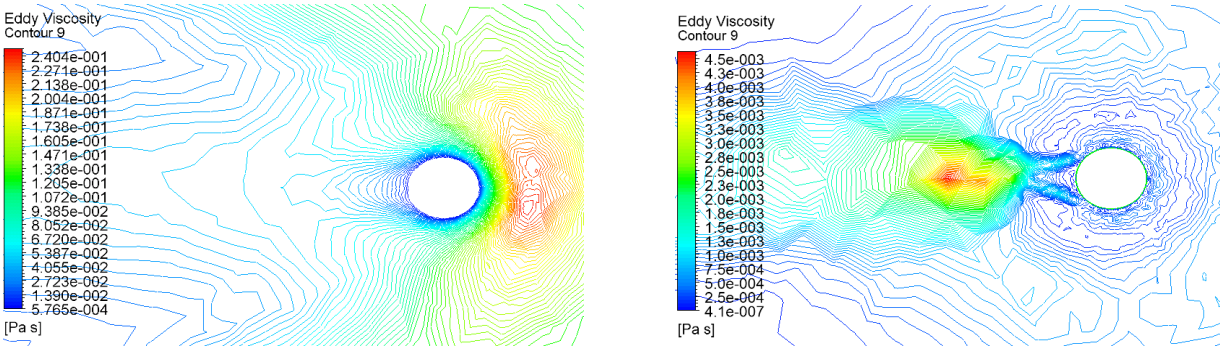
x) Velocity Profiles, $\alpha = 60°$, $\beta = 0°$, Re = 4.4×10^5.

Laminar Option k-ε Model



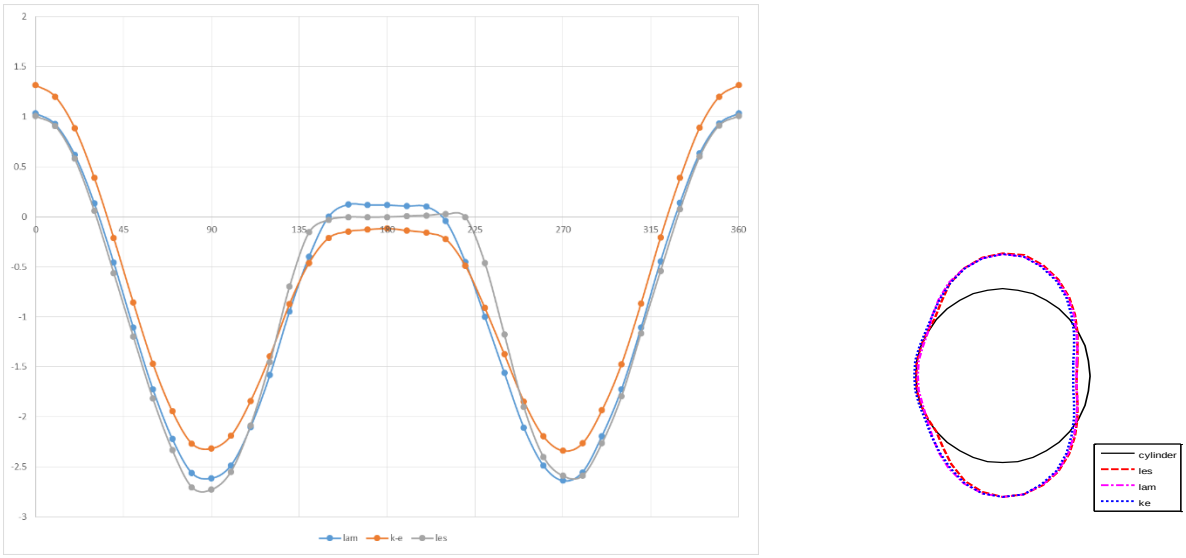
x) Velocity Profiles, $\alpha = 60°$, $\beta = 0°$, Re = 4.4×10^5.

LES Model



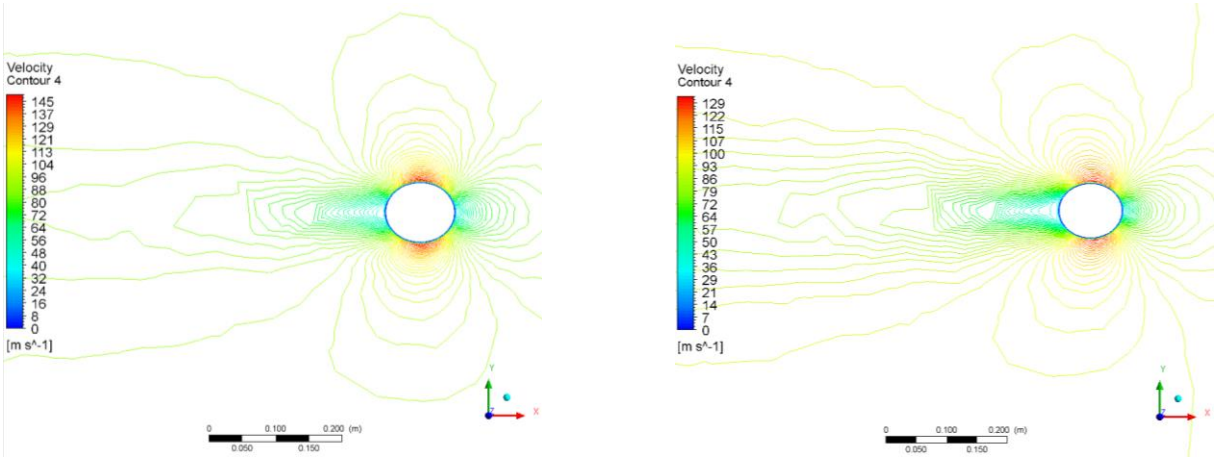
x) Eddy Viscosity, $\alpha = 60°$, $\beta = 0°$, Re = 4.4×10^5.

k-ε Model LES Model



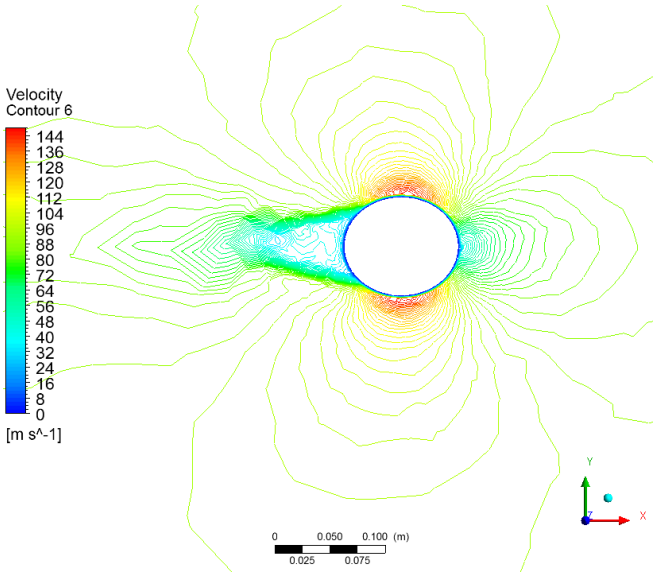
x) Pressure Profiles, $\alpha = 60°$, $\beta = 0°$, Re = 4.4×10^5.

Figure Q: Results for $\alpha = 60°$, $\beta = 0°$, Re = 5.5×10^5.



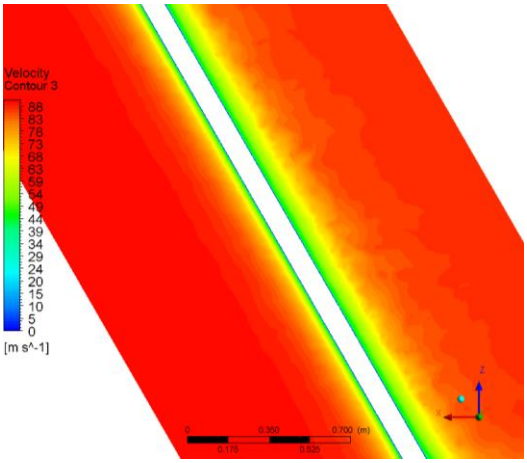
xi) Velocity Profiles, $\alpha = 60°$, $\beta = 0°$, Re = 5.5×10^5.

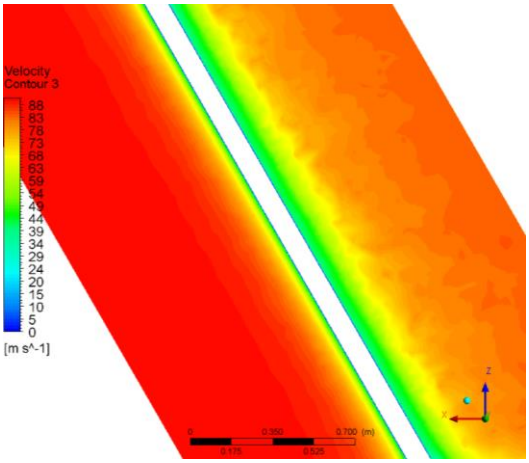
Laminar Option k-ε Model



xi) Velocity Profiles, $\alpha = 60°$, $\beta = 0°$, Re = 5.5×10^5.

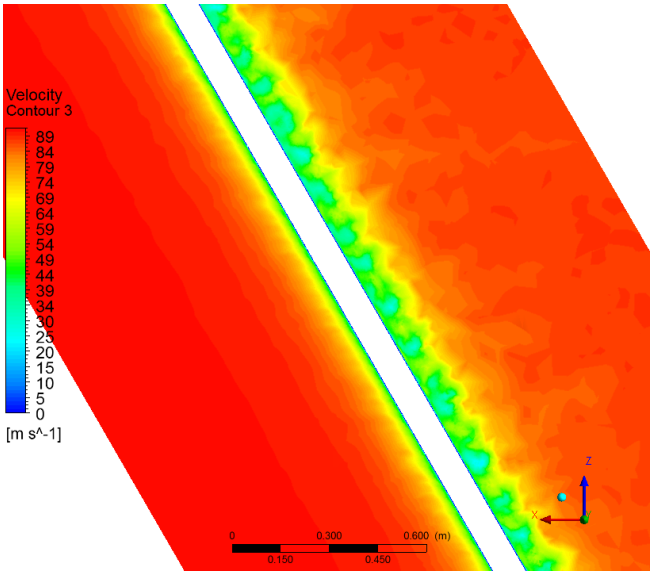
LES Model





xi) Velocity Profiles, $\alpha = 60°$, $\beta = 0°$, Re = 5.5×10^5.

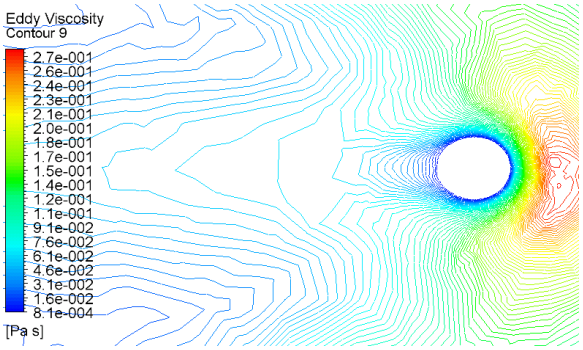
Laminar Option k-ε Model

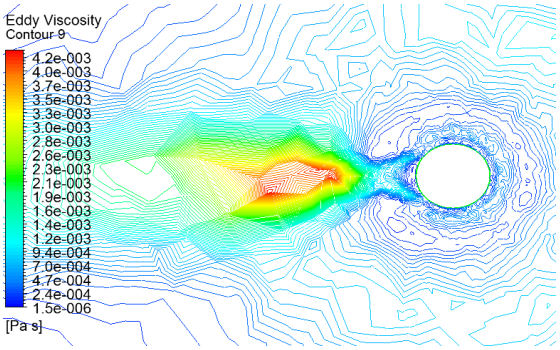


xi) Velocity Profiles, $\alpha = 60°$, $\beta = 0°$, Re = 5.5×10^5.

LES Model

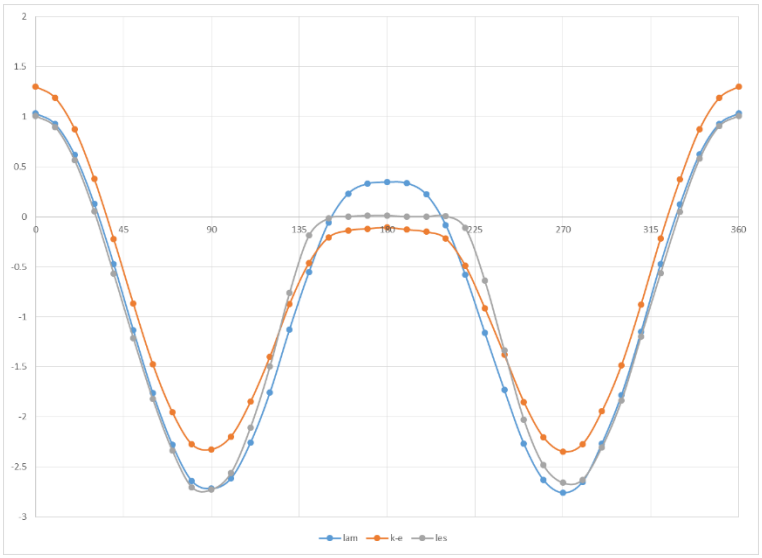
les height = 7.5 cm

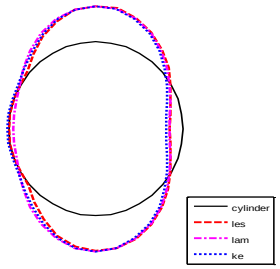




xi) Eddy Viscosity, $\alpha = 60°$, $\beta = 0°$, Re = 5.5×10^5.

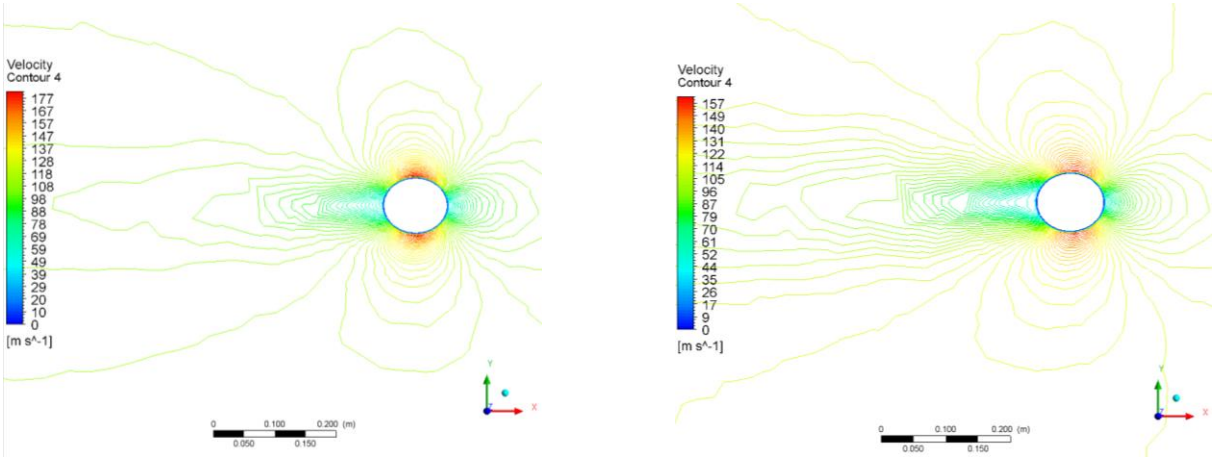
k-ε Model LES Model





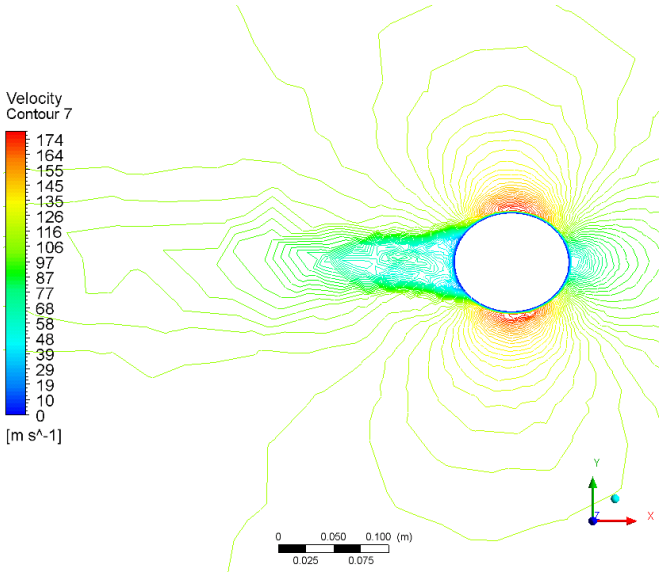
xi) Pressure Profiles, $\alpha = 60°$, $\beta = 0°$, Re = 5.5×10^5.

Figure Q: Results for $\alpha = 60°$, $\beta = 0°$, Re = 6.7×10^5.



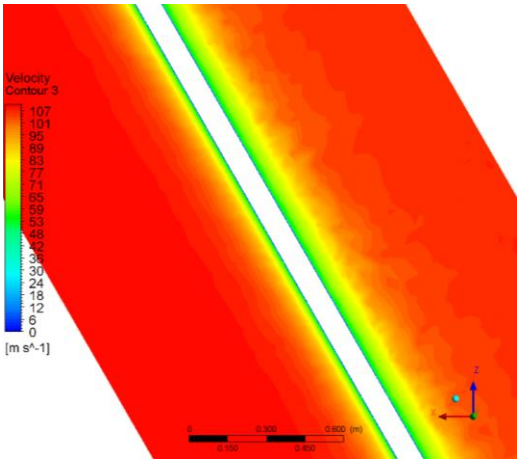
xii) Velocity Profiles, $\alpha = 60°$, $\beta = 0°$, Re = 6.7×10^5.

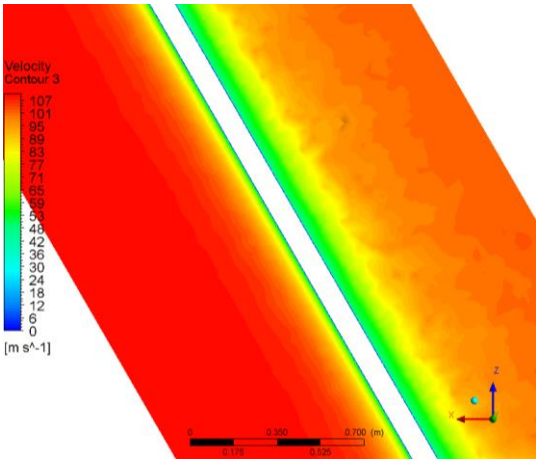
Laminar Option k-ε Model



xii) Velocity Profiles, $\alpha = 60°$, $\beta = 0°$, Re = 6.7×10^5.

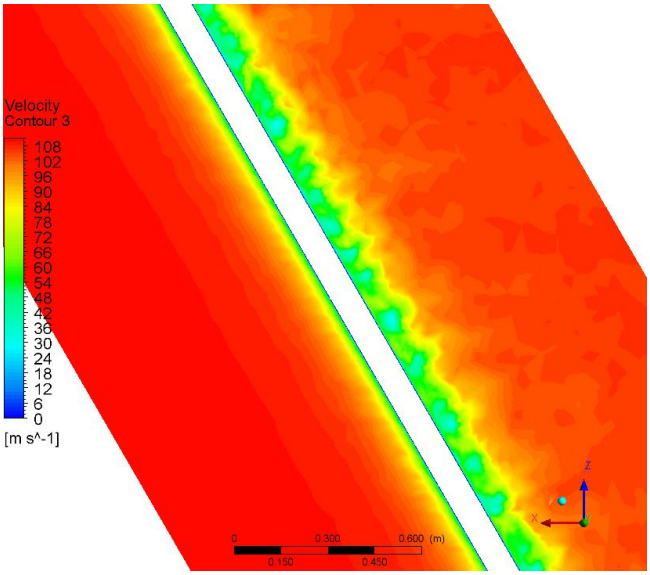
LES Model





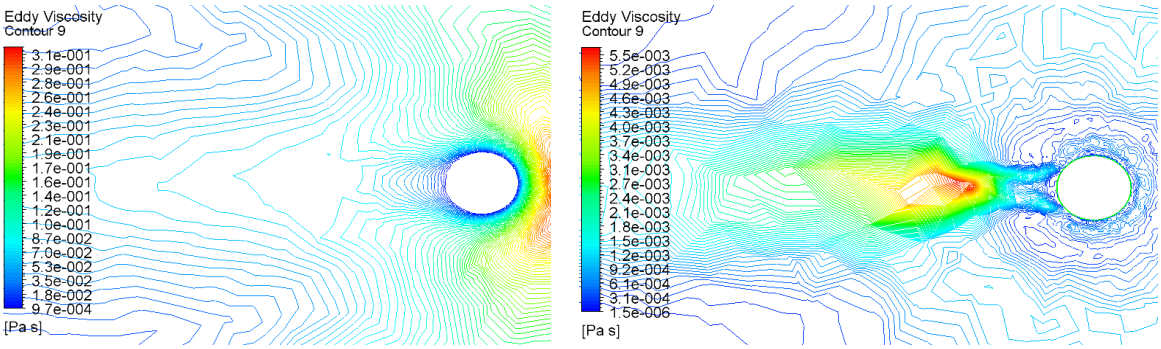
xii) Velocity Profiles, $\alpha = 60°$, $\beta = 0°$, Re = 6.7×10^5.

Laminar Option k-ε Model



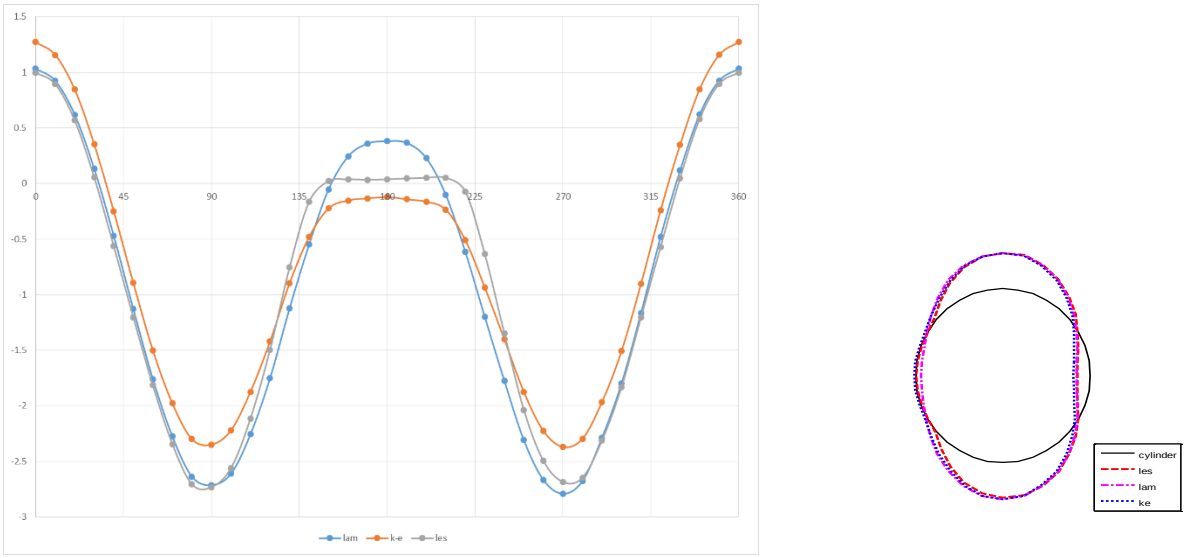
xii) Velocity Profiles, $\alpha = 60°$, $\beta = 0°$, Re = 6.7×10^5.

LES Model



xii) Eddy Viscosity, $\alpha = 60°$, $\beta = 0°$, Re = 6.7×10^5.

k-ε Model LES Model



xii) Pressure Profiles, $\alpha = 60°$, $\beta = 0°$, Re = 6.7×10^5.